AD-A074 425 OHIO UNIV ATHENS DEPT OF ELECTRICAL ENGINEERING F/G 17/7
IN-SERVICE IMPROVEMENTS AND MODERNIZATION OF ALL COMPONENTS OF --ETC(U)
JUL 78 DOT-FA75WA-3549
UNCLASSIFIED EER-35-1 FAA-RD-78-112-1 NL

1 OF 8
AD A074425

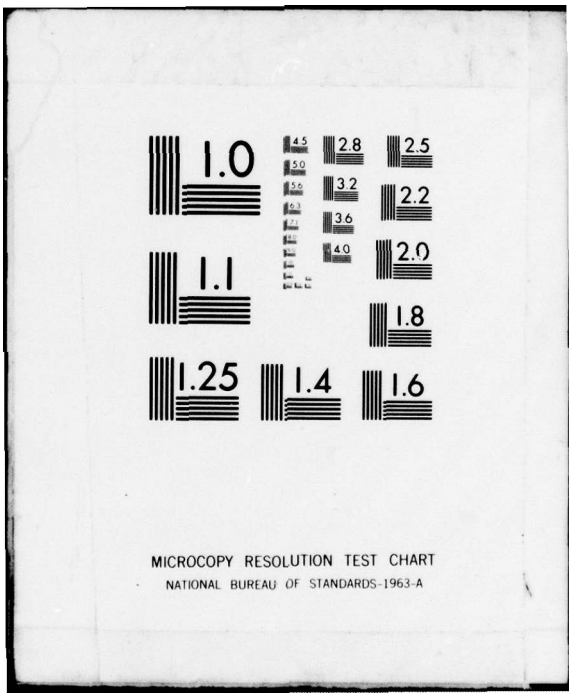
1.0
1.1
1.25
1.4
1.6
1.8
2.0
2.2
2.5
2.8
3.2
3.6
4.0
4.5
5.0
5.6
MICROCOPY RESOLUTION TEST CHART
NATIONAL BUREAU OF STANDARDS-1963-A

Report No. FAA-RD-78-112,I

LEVEL II

IN-SERVICE IMPROVEMENTS AND MODERNIZATION OF ALL COMPONENTS OF THE INSTRUMENT LANDING SYSTEMS

VOLUME I - Sections I Through X

Avionics Engineering Center
Department of Electrical Engineering
Ohio University
Athens, Ohio 45701

JULY 1978

FINAL REPORT

Prepared for

U.S. DEPARTMENT OF TRANSPORTATION
FEDERAL AVIATION ADMINISTRATION
Systems Research & Development Service
Washington, D.C. 20590

NOTICE

This document is disseminated under the sponsorship of the Department of Transportation in the interest of information exchange. The United States Government assumes no liability for the contents or use thereof.

TECHNICAL REPORT STANDARD TITLE PAGE

1. Report No.	2. Government Accession No.	3. Recipient's Catalog No.
FAA-RD-78-112-I		

4. Title and Subtitle
IN-SERVICE IMPROVEMENTS AND MODERNIZATION OF ALL COMPONENTS OF THE INSTRUMENT LANDING SYSTEMS, VOLUME I, SECTIONS I THROUGH X

5. Report Date
July 1978

6. Performing Organization Code

7. Author(s)
Avionics Engineering Center Staff

8. Performing Organization Report No.
EER-35-1

9. Performing Organization Name and Address
Avionics Engineering Center
Department of Electrical Engineering
Ohio University
Athens, Ohio 45701

10. Work Unit No.

11. Contract or Grant No.
DOT-FA75WA-3549

13. Type of Report and Period Covered
Final Report
October 1974—July, 1978

12. Sponsoring Agency Name and Address
Department of Transportation
Federal Aviation Administration
800 Independence Avenue, S.W.
Washington, D.C. 20591

14. Sponsoring Agency Code

15. Supplementary Notes

679p.

16. Abstract

Volume I of a Two Volume Report
Volume II Contains Sections XI and XII

This final report covering over three-years' work on ILS improvement and alternative uses gives results of Ohio University's evaluation of localizer and glide-slope systems emphasizing antenna and monitor performance, terrain effects and the effects of obstructions. Also, details of analyses and flight evaluations of Alford and Hollins localizer systems are provided together with findings during evaluations of the Watts Mark 1, 2, and 3 endfire, glide-slope systems.

Technical results of development and evaluation work on the FAA-suggested techniques for determining range-rate and position during approach using the localizer signal are given.

Non-destructive ILS system fault testing techniques are described, as is a plan for development of an airport systems control/display facility. Further, special devices and techniques for use in ILS field work such as a mini-laboratory for collection of airborne data, digital data collection system, time domain reflectometry, and mathematical modeling to predict localizer and glide slope performance and facilitate setups are discussed.

17. Key Words	18. Distribution Statement
ILS, localizer, glide slope, monitor, ground-speed, marker, endfire array, slotted cable, mathematical modeling, terrain effects, flight evaluation	This document is available to the U.S. public through the National Technical Information Service, Springfield, Virginia 22161.

19. Security Classif. (of this report)	20. Security Classif. (of this page)	21. No. of Pages	22. Price
Unclassified	Unclassified	Vol. I - 598 Vol. II - 782	

Form DOT F 1700.7 (8-69)

267 460

JOB

METRIC CONVERSION FACTORS

Approximate Conversions to Metric Measures

Symbol	When You Know	Multiply by	To Find	Symbol
	LENGTH			
in	inches	*2.5	centimeters	cm
ft	feet	30	*centimeters*	cm
yd	yards	0.9	meters	m
mi	miles	1.6	*kilometers*	*km*
	AREA			
in^2	square inches	6.5	square centimeters	cm^2
ft^2	square feet	0.09	*square meters*	m^2
yd^2	square yards	0.8	square meters	m^2
mi^2	square miles	2.6	square kilometers	km^2
	acres	0.4	hectares	ha
	MASS (weight)			
oz	ounces	28	grams	g
lb	pounds	0.45	kilograms	kg
	short tons (2000 lb)	0.9	tonnes	t
	VOLUME			
tsp	teaspoons	5	*milliliters*	ml
Tbsp	tablespoons	15	milliliters	ml
fl oz	fluid ounces	30	*milliliters*	*ml*
c	cups	0.24	liters	l
pt	pints	0.47	liters	l
qt	quarts	0.95	liters	l
gal	gallons	3.8	liters	l
ft^3	cubic feet	0.03	cubic meters	m^3
yd^3	cubic yards	0.76	cubic meters	m^3
	TEMPERATURE (exact)			
°F	*Fahrenheit temperature*	5/9 (after subtracting 32)	Celsius *temperature*	°C

*1 in = 2.54 (exactly). For other exact conversions and more detailed tables, see NBS Misc. Publ. 286, *Units of Weights and Measures*, Price $2.25, SD Catalog No. C13.10:286.

Approximate Conversions from Metric Measures

Symbol	When You Know	Multiply by	To Find	Symbol
	LENGTH			
mm	millimeters	0.04	inches	in
cm	centimeters	0.4	inches	in
m	meters	3.3	feet	ft
m	meters	1.1	yards	yd
km	kilometers	0.6	miles	mi
	AREA			
cm^2	square centimeters	0.16	square inches	in^2
m^2	square meters	1.2	square yards	yd^2
km^2	square kilometers	0.4	*square miles*	mi^2
ha	hectares (10,000 m^2)	2.5	acres	
	MASS (weight)			
g	grams	0.035	ounces	oz
kg	kilograms	2.2	pounds	lb
t	tonnes (1000 kg)	1.1	short tons	
	VOLUME			
ml	milliliters	0.03	fluid ounces	fl oz
l	liters	2.1	pints	pt
l	liters	1.06	quarts	qt
l	liters	0.26	gallons	gal
m^3	cubic meters	35	cubic feet	ft^3
m^3	cubic meters	1.3	cubic yards	yd^3
	TEMPERATURE (exact)			
°C	Celsius temperature	9/5 (then add 32)	Fahrenheit temperature	°F

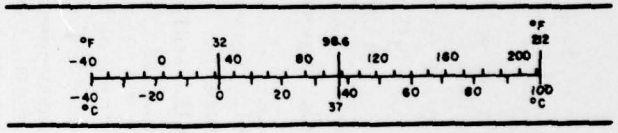

TABLE OF CONTENTS

VOLUME I - Sections I Through X

		PAGE
	List of Figures	xiv
	List of Tables	lxix
	Foreword	lxxvi
I	INTRODUCTION	1-1
II	REVIEW	2-1
III	SUMMARY	3-1
IV	GENERAL TOPICS	4-1
	A. New Tamiami Airport, Florida, Test Site	4-1
	1. Ground Facilities	4-1
	2. Flight Check Aircraft	4-5
	B. The Minilab Airborne Data-Collection Systems	4-10
	1. Mark I Minilab	4-10
	2. Mark II Minilab	4-10
	3. Mark III Minilab	4-10
	a. Introduction	4-10
	b. Functional Description	4-10
	c. Mechanical Description	4-15
	d. Specifications	4-15
	e. Antenna Requirements	4-17
	f. Digital Data Collection Subsystem (DDCS)	4-17
	C. Phase-Locked Loop 90 Hz Generator	4-23
	1. Introduction	4-23
	2. Basic Design	4-23
	3. Results	4-25
	D. The 90-150 Hz Phase Measurement Device	4-26
	1. Introduction	4-26
	2. Discussion	4-26
	a. Filtering	4-26
	b. Interfacing	4-26
	c. Phase Detection	4-27
	d. Amplification and Readout	4-27
	e. Testing	4-27
	f. Field Use	4-27

TABLE OF CONTENTS (CONTINUED)

		PAGE
E.	Time Domain Reflectometry in ILS Fault Testing	4-36
	1. TDR Analysis of ILS System Components	4-37
	a. Cabling System Analysis	4-37
	b. TDR Analysis of RF Combining Bridges	4-55
	c. TDR Fault Analysis of Three Glide Slope Antennas	4-78
	d. V-Ring Localizer TDR Study	4-106
	2. Sample TDR Signatures of Commissioned ILS Facilities	4-122
	a. Localizer TDR Signature Samples	4-122
	b. Glide Slope TDR Signature Samples	4-132
	3. General Conclusions	4-139
F.	Airport Systems Control and Display	4-140
	1. Introduction: Existing ILS Monitoring Scheme at O'Hare International Airport	4-140
	a. Relaying ILS Status Information to Air Traffic Controllers	4-140
	b. ILS Data Logging	4-143
	c. ILS Control	4-148
	2. Proposed ILS Control and Display System	4-150
	a. Remote Data Processor (RDP)	4-153
	b. Protocol	4-155
	c. I/O Multiplexer, Central Processor, Operating System Software, and Peripherals	4-156
	d. Video Display	4-158
	3. Equipment Specifications	4-161
	a. Remote Data Processor (RDP)	4-161
	b. MODEM	4-162
	c. I/O Multiplexer and Central Processor	4-163
	d. Operating System Software	4-163
	e. Peripherals	4-164
	f. Video Display System	4-164
	4. Future Capabilities	4-165
	a. Maintenance Feature	4-165
	b. Administrative Features	4-166
	5. Summary and Conclusions	4-169
G.	Marker Beacon Precision Location	4-170
	1. Marker Beacon and Flight Path Geometry	4-170
	2. Signal Processing Analysis	4-170
	a. Doppler System	4-170
	b. Amplitude System	4-173
	c. Differential Phase Measurement System	4-173

TABLE OF CONTENTS (CONTINUED)

		PAGE
3.	Prototype System Design	4-175
	a. Modification of Standard Marker Beacon Receiver	4-175
	b. Trigger Circuitry	4-175
	c. Flight Evaluation	4-175
4.	Conclusions	4-179
	a. Differential Phase-Measurement System Continuation	4-186
	b. Two-Dimensional Beacon Locator	4-186
	c. Marker Beacon Test Transmitter	4-186
H.	Comparison of Common ILS Data Acquired Using a DC-3 and a Beechcraft 35	4-188
1.	Introduction and Summary	4-188
2.	Background	4-188
3.	Procedure of Analysis	4-189
4.	Experimental Results	4-190
5.	Conclusions	4-191
I.	*References and Bibliography for Section IV*	4-201
V	LOCALIZERS	5-1
A.	General	5-1
B.	Alford 14-Element Two-Frequency Localizer Systems Tests	5-1
1.	Background	5-1
2.	Ground-Based Measurements	5-4
3.	Flight Data	5-4
4.	Conclusions	5-4
C.	Initial Comparison of Wilcox 14-Element Distribution Unit with Alford 12-Element Box	5-14
1.	Tests	5-14
2.	Conclusions and Results	5-14
D.	Final Comparison of Performance of 12-Element V-Ring Array Fed First with an Alford Distribution Box and Then with a Wilcox Stripline Unit	5-26
1.	Introduction	5-26
2.	Discussion of Data	5-27
	a. Comments on Data Reduction	5-49
3.	Conclusions	5-54
E.	Figure of Merit Analysis for Alford 14/6 Array	5-55
1.	Introduction	5-55
2.	Presentation of Data	5-55
3.	Conclusions	5-57

TABLE OF CONTENTS (CONTINUED)

		PAGE
F.	Investigation of Alford MC 14/6 Two-Frequency Localizer Monitor Performance Under Attenuation and Phase Fault Conditions	5-57
	1. Introduction	5-57
	2. Data and Analysis	5-63
	3. Tests to Determine Operating Parameters of Equipment	5-63
G.	Discussion of Total Monitor System Response	5-81
	1. Pre-Combiner Clearance Monitor	5-81
	2. Monitor Response to Far-Field Out-of-Tolerance Conditions	5-89
	a. Low Clearance Conditions	5-89
	b. Course Alignment or Course Width Out-of-Tolerance	5-90
	3. Conclusions	5-90
H.	1976 Tests of Monitor Performance of the Alford MC 14/6 Two Frequency Localizer System Under Attenuation and Phase Fault Conditions	5-92
	1. Introduction	5-92
	2. Data Collection	5-94
	3. Results	5-94
	4. Conclusions	5-134
I.	Watts-Hollins Small Aperture Slotted-Cable Localizer	5-138
	1. Introduction	5-138
	2. Discussion of Data	5-138
J.	Flight Test Results of the Small and Medium Aperture Hollins Slotted-Cable Localizer Antenna Array	5-143
	1. Introduction	5-143
	2. Data Collection	5-143
	3. Results	5-149
	4. Conclusions	5-149
	a. Small Aperture Array	5-149
	b. Medium Aperture Array	5-155
VI	TERRAIN-SENSITIVE MODELING OF ILS SYSTEMS	6-1
A.	The Ohio University ILS Modeling Center	6-1
	1. Introduction	6-1
	2. Background	6-1
	3. Available Glide Slope Models	6-2
	4. The Ohio University GTD Glide Slope Model	6-11
	a. Theoretical Background for GTD Model	6-12

TABLE OF CONTENTS (CONTINUED)

		PAGE
	b. Ray Geometry for GTD Model	6-16
	c. Physical Optics and GTD Comparison	6-19
5.	OUGS--The Hybrid Glide Slope Program	6-41
6.	Localizer Models	6-44
7.	Supplemental Data	6-45
	a. Input Data Format for the OUGS Hybrid Glide Slope Terrain Model	6-45
	b. POSTOUGS Program	6-52
	c. Mathematical Modeling of Receiver Capture Effect	6-54
8.	ILS Modeling Center Facilities	6-69
9.	Summary	6-71
B.	Theoretical Models Applied to the Kodiak, Alaska Glide Slope	6-71
1.	Airfield Geometry	6-71
2.	Calculated Results for Null Reference and Sideband Reference Systems Compared with Flight Measurements	6-72
3.	Predicted Results for Possible Future Glide Slope Installation at Kodiak	6-79
4.	Summary and Conclusions	6-81
C.	Validation of Mathematical Models Using the Kodiak, Alaska Glide Slope	6-81
1.	Introduction	6-81
2.	Results	6-83
3.	Data Requirements for Accurate Modeling	6-100
4.	Documentation of Data Used in Model Validation	6-103
	a. Excitation Currents in Antennas	6-103
	b. Positions of the Radiators	6-104
	c. Terrain Data	6-104
	d. Aircraft Position	6-104
5.	Summary	6-104
6.	Conclusions	6-110
D.	Mathematical Prediction of Effects of Hangar Construction on the Denver Stapleton Airport Localizer	6-110
1.	Introduction	6-110
2.	Results	6-112
3.	Summary	6-112
4.	Conclusions	6-112
E.	Mathematical Modeling Applied to Ship Interference with the Hoquiam, Washington Localizer	6-116
1.	Introduction	6-116
2.	Approach and Results	6-116

TABLE OF CONTENTS (CONTINUED)

		PAGE
	3. Summary	6-124
	4. Conclusions	6-124
	F. References for Section VI	6-126
VII	SINGLE FREQUENCY DISCRIMINATION AGAINST REFLECTIONS (MULTIPATH)	7-1
	A. General	7-1
VIII	SYSTEM PERFORMANCE STANDARDS	8-1
	A. Proposed Criteria for Classification of Glide Slope Records with Respect to Quality	8-1
	1. General	8-1
	2. Definition of Classes of Records	8-1
	3. Rationale	8-1
	B. STI Report	8-4
IX	RANGE MEASUREMENT FROM LOCALIZER SIGNALS	9-1
	A. System Descritpion	9-1
	B. System Assembly for Concept Demonstration	9-1
	1. Predicted System Parameters	9-1
	2. Ground Installation	9-4
	3. Airborne Installation - RF	9-8
	4. Airborne Installation - Audio Processor	9-8
	C. Detailed Description of the Airborne Processing Circuitry	9-12
	1. Analog Circuits	9-12
	2. Digital Circuitry	9-12
	D. Calibration	9-15
	E. Flight Evaluation	9-19
	F. Approach Range-Rate and Windspeed: Evaluation and Development	9-25
	1. General	9-25
	2. Approach Range-Rate System	9-26
	a. Range-Rate System Description	9-26
	b. Initial System Evaluation	9-26
	c. RF-Link Tests	9-26

TABLE OF CONTENTS (CONTINUED)

		PAGE
	d. Individual Module Checkout	9-29
	e. Preliminary Conclusions from Module Checkout and System Re-Evaluation	9-31
	f. System Modification and Development	9-31
	g. Schematics	9-32
	3. Analog Wind Telemetry System	9-39
	a. Introduction	9-39
	b. Ground Installation	9-45
	c. Airborne Installation	9-45
	d. Results	9-58
	4. Digital Wind Telemetry System	9-58
	a. Anemometer Transmitter	9-58
	b. Transmitter Modulator	9-59
	c. Receiver	9-59
	d. Transmitted Data Format	9-60
	e. System Schematic Diagrams	9-60
	5. Data and Discussion	9-60
G.	Conclusions and Recommendations	9-85
X	PROCESSING OF ILS FLIGHT DATA	10-1
A.	General	10-1
	1. Analog Strip-Chart to Digital Data Translator	10-1
	a. Introduction	10-1
	b. Setup and Operating Procedure	10-2
	c. *Circuit Description*	10-5
	d. Sample Data Sets	10-10
	e. Recommendations	10-10

VOLUME II - Sections XI and XII

XI	GLIDE SLOPE	11-1
A.	Computer Model for Image Glide Slope Systems	11-1
	1. General	11-1
	2. The Model	11-1
B.	Fault Studies on a Capture-Effect Glide Slope and Its Computer Model	11-11
	1. Introduction and Summary	11-11
	2. Analytical Methods	11-11
	3. Ground Data	11-12
	4. Preliminary Setup Procedures	11-12
	5. Error Analysis	11-13
	6. Results	11-15

TABLE OF CONTENTS (CONTINUED)

		PAGE
C.	Evaluation of Endfire Glide Slope System	11-123
	1. Introduction	11-123
	2. Watts Mark I System	11-124
	a. Goals	11-124
	b. Measurements	11-127
	c. Conclusions Concerning Operation of Mark I Curvilinear System	11-138
	3. The Watts Mark 2 System	11-138
	a. General	11-138
	b. Data Collection	11-139
	c. Measurements on the Mark 2	11-139
	d. Monitoring of the Watts Mark 2	11-148
	4. The Mark 3 System Evaluation	11-191
	a. General	11-191
	b. Discussion of Experiments	11-194
	c. Discussion of the Data	11-197
	d. Monitor Investigation for the Mark 3	11-207
	e. Monitor Investigation	11-207
	f. Off-Centerline Path Characteristics for the Mark 3	11-224
	g. Special Tests to Examine Special Characteristics of the Array	11-232
	h. Conclusions Concerning the Mark 3 System	11-239
	5. Prediction of Performance of the Watts Mark 1 Endfire Glide Slope System	11-246
	a. Theory and Analysis of the Effects of Irregular Terrain on Watts Endfire Glide Slope	11-248
	b. Experimental and Theoretical Results (Tamiami, Staunton)	11-249
	c. Characteristics of Off-Centerline Theoretical Prediction	11-271
	d. Conclusions	11-280
	6. Evaluation of the Watts Mark 3 Endfire Glide Slope at Rock Springs, Wyoming	11-285
	a. Introduction	11-285
	b. Background	11-285
	c. Flight Evaluation, November 1977	11-285
	d. Flight Evaluation, May 1978	11-297
D.	ILS Glide Slope Set-Up Measurements Using Thruline Meters	11-321
	1. General	11-321
	2. Theory - The A-Ratio	11-321
	3. Power Measurement - The Thruline Meter	11-322
	4. Using the Thruline Meter to Set-Up Antenna Current Ratios	11-323
	5. Experimental Verification of K Equal to 0.80	11-325

TABLE OF CONTENTS (CONTINUED)

		PAGE
E.	Monitoring Tilt of a Null-Reference Glide Slope Mast with Near Field Detectors	11-329
	1. General	11-329
	2. Analysis	11-329
F.	Integral Path Monitor Test Circuit for Null-Reference Glide Slope	11-339
	1. Introduction	11-339
	2. Circuit Description	11-339
	3. Experiment and Results	11-342
	4. Conclusions	11-342
G.	Effects of Carrier Sideband Leakage into Sideband Only Signal on ILS Glide Slope Performance	11-345
	1. Frequency Components in Detected SBO + CSB Signals	11-345
	2. Effect of CSB Leakage into SBO Signal on Null Reference and Capture-Effect Path Width and Symmetry	11-345
	3. Conclusions	11-345
H.	Mobile Glide Slope Facility	11-351
I.	On-Site Glide Slope Evaluation Activities	11-353
	1. Westinghouse Broadside Glide Slope Array Tests (Lynchburg)	11-353
	a. Mission 1: August 4-6, 1976	11-353
	b. Mission 2: August 12-13, 1976	11-353
	c. Mission 3: August 19-20, 1976	11-354
	d. Mission 4: September 29, 1976	11-355
	e. Mission 5: October 12, 1976	11-355
	2. Documentary Flight Data for a Capture Effect Glide Slope System Operating at a Typical Upslope Site (Lawton)	11-356
	a. Introduction	11-356
	b. Glide Slope System Parameters	11-357
	c. Antenna Current Measurements	11-357
	d. Faults	11-357
	e. Terrain Features	11-360
	f. Ground Measurements at the 360° Monitor Point	11-360
	g. Graphical Data Presentation	11-369
	h. Results	11-369
	i. Recommendations	11-369
	3. Documentary Flight Data for a Capture Effect Glide Slope System Operating at an Unimproved Site	11-486
	a. Introduction	11-486
	b. The Addison System	11-486
	c. Procedures for Probe Measurement Taking on CEGS Systems	11-487

TABLE OF CONTENTS (CONTINUED)

		PAGE
	d. Probe Measurement Results	11-488
	e. Terrain and Site Peculiarities	11-489
	f. Data Processing	11-489
	g. Documentary Data	11-492
	h. Comparison of Near-Field Monitor Response with Far-Field Observations	11-492
4.	Documentary Flight Data for a Capture Effect Glide Slope System Operating with a Truncated Ground Plane (Redbird)	11-531
	a. Optimization	11-531
	b. Perturbational Study	11-540
5.	Documentary Flight Data for a Capture Effect Glide Slope System Operating with a Two-Level Ground Plane (Columbus)	11-634
	a. Introduction	11-634
	b. Equipment	11-634
	c. Procedures for Probe Measurement-Taking on CEGS Systems	11-636
	d. Terrain and Site Peculiarities	11-640
	e. Data Processing	11-640
	f. Documentary Data	11-640
	g. Comparison of Near-Field Alarm Values and Observed Far-Field Response	11-641
J.	Measurement and Monitoring of Glide Slope Antennas	11-695
1.	Introduction	11-695
2.	Relationship Between Radiated Signal and Monitor Port Output	11-695
	a. Single-Element Antennas	11-696
	b. Multi-Element Antennas	11-696
3.	Recommended Measurement Techniques	11-697
4.	Hand-Held Probe Performance	11-698
5.	Development of the Jig-Held Probe	11-703
	a. Probe Placement and Stability	11-703
	b. Experimental Results	11-712
6.	Far-Field Response to Antenna Currents	11-712
7.	Multi-Element Antenna Array Radiation Patterns	11-719
8.	Antenna Diagnostics	11-725
9.	Conclusions	11-725
10.	Recommendations	11-730
K.	Experimental Investigation of Contemporary Glide Slope Antennas	11-732
1.	Introduction	11-732
	a. History of Glide Slope Antennas	11-732
	b. History of Signal Sampling for Monitoring	11-732
2.	Specific Antennas Involved in Tests	11-733

TABLE OF CONTENTS (CONTINUED)

		PAGE
3.	Measurement and Techniques	11-734
a.	Test Range	11-734
b.	Specific Tests	11-735
4.	Matrix of Results	11-738
a.	Baseline Data	11-738
b.	Fault Data on the AIL FA8651	11-752
5.	Correlation of Signal Samples with Monitor Response	11-762
6.	Summary	11-762
7.	Conclusions	11-766
8.	Recommendations	11-767
L.	Minimum Site Preparation for an Image Glide Slope	11-768
1.	Introduction	11-768
2.	General Case	11-768
3.	Engineering for Minimum Costs	11-769
a.	Reduced Length of Ground Plane	11-772
b.	Reduced Depth of Fill	11-772
c.	Allow Longitudinal Slope of 1 Degree	11-772
d.	Allow Transverse Slope of 2.5%	11-776
e.	Methods for Additional Cost Savings	11-776
4.	Conclusions	11-776
5.	Recommendations	11-777
M.	References for Section XI	11-778
XII	INVESTIGATORS AND ACKNOWLEDGEMENTS	12-1

LIST OF FIGURES

		PAGE
Figure 4-1.	Aerial Photograph of Tamiami Site Prior to Installation of Facilities.	4-2
Figure 4-2.	Ohio University Test Sites - New Tamiami Airport.	4-3
Figure 4-3.	Control Points for ILS Site at New Tamiami Airport, Florida.	4-4
Figure 4-4.	Contour Map, Tamiami, Glide Slope Area.	4-6
Figure 4-5.	Capture-Effect Glide Slope Evaluation Underway at Tamiami.	4-7
Figure 4-6.	A Ohio University Research Technician Shown Performing Repairs on Monitor Detector at Tamiami, Florida.	4-8
Figure 4-7.	Mark I Minilab Showing Typical Aircraft Installation.	4-11
Figure 4-8.	Mark II Minilab Flight Data-Collection Package.	4-11
Figure 4-9.	Mark III Minilab Installed in Beechcraft 35 Bonanza.	4-12
Figure 4-10.	Alarm Panel.	4-13
Figure 4-11.	Mark III Minilab Block Diagram.	4-14
Figure 4-12.	DDCS Block Diagram.	4-18
Figure 4-13.	DDCS Sample CDI Output.	4-19
Figure 4-14.	Analog CDI Test Trace for DDC System.	4-21
Figure 4-15.	PLL 90 Hz Generator.	4-24
Figure 4-16.	Interface Circuit.	4-26
Figure 4-17.	MC 4044P Input/Output Waveforms.	4-28
Figure 4-18.	Plot of Analysis Data.	4-30

LIST OF FIGURES (CONTINUED)

		PAGE
Figure 4-19.	Amplification and Readout Circuit.	4-31
Figure 4-20.	Test Circuit Block Diagram.	4-31
Figure 4-21.	Plot of Test Data.	4-33
Figure 4-22.	Schematic of 90-150 Hz Phase Detector.	4-34
Figure 4-23.	Block Diagram, 90-150 Hz Phase Detector.	4-35
Figure 4-24.	Circuit Model for a Short Length of Transmission Line.	4-38
Figure 4-25.	Theoretical TRD Plot of a 50Ω Line Terminated in 70 Ohms.	4-38
Figure 4-26.	Reflection Diagram for the Quarter-Wave Transformer Matched System.	4-41
Figure 4-27.	TDR Signature and Terminal Voltage Plot for the Quarter-Wave Transformer in Figure 4-26.	4-43
Figure 4-28.	TDR Analysis of Quarter-Wavelength Transformer.	4-44
Figure 4-29.	Graphs Displaying Short, Open, and Properly Terminated 50Ω Cables.	4-45
Figure 4-30.	TDR Graphs Showing Wetted Cable Terminations.	4-46
Figure 4-31.	TDR Graphs Showing Sliced Cables; Dry and Wet.	4-48
Figure 4-32.	Coaxial Cable with Pinhole Fault.	4-49
Figure 4-33.	Corroded Connector Experiment One.	4-50
Figure 4-34.	Corroded Connector Experiment Two.	4-52
Figure 4-35.	Example of Resistive Loss in Cables.	4-54
Figure 4-36.	*Capture Effect Glide Slope Antenna and Monitor* Cable Traces Obtained at the Tamiami Airport.	4-56

LIST OF FIGURES (CONTINUED)

		PAGE
Figure 4-37.	Two Typical Cable Traces Obtained from a Null Reference Glide Slope at Wood County Airport.	4-57
Figure 4-38.	An Example of TDR Analysis of Cable Other than Coaxial.	4-58
Figure 4-39.	Trace of a Glide Path Monitor Cable Used at Tri-State Airport in Huntington, W. Va.	4-59
Figure 4-40.	A Piece of RG-58 (50 Ω) and RG-59 (72 Ω) Cable Spliced Together to Show a Trace of Cables with Different Characteristic Impedances.	4-59
Figure 4-41.	Examples of Cable Faults.	4-60
Figure 4-42.	Tektronic 1502 TDR Measurement of a Sliced Cable Fault.	4-61
Figure 4-43.	Photograph of RF Signal Devices Used in an APCU.	4-63
Figure 4-44.	TDR Signature and Diagram of Test Set-Up for Coaxial Bridge.	4-64
Figure 4-45.	No Fault Bounce Diagram for Bridges of Figures 4-44 and 4-50b.	4-66
Figure 4-46.	TDR Signatures of Faulted Experimental Coaxial Bridge Connections.	4-67
Figure 4-47.	Effect of Shorted Port Connector on TDR Pulse Transmission.	4-68
Figure 4-48.	J2 Open Fault Bounce Diagram for Bridges of Figures 4-46a and 4-50b.	4-70
Figure 4-49.	Shorted Bounce Diagram for Bridges of Figures 4-46b and 4-51c.	4-71
Figure 4-50.	TDR Signature of a Coaxial Bridge on Sideband Input to a Localizer Distribution System.	4-72

LIST OF FIGURES (CONTINUED)

		PAGE
Figure 4-51.	TDR Signatures of Scanwell Model 110 Bridge.	4-73
Figure 4-52.	TDR Signature and Diagram of Test Set-Up for Scanwell SX-28 Bridge.	4-74
Figure 4-53.	No Fault Bounce Diagram for Scanwell SX-28 Bridge.	4-76
Figure 4-54.	Signatures of Faulted SX-28 Bridge Connections.	4-77
Figure 4-55.	Detailed Diagram of the FA-8976 and Bent Dipole Type Antennas.	4-79
Figure 4-56.	Detailed Diagram of FA-8730 Antenna.	4-80
Figure 4-57.	TDR and TDR Recording of a Scanwell Model 110 Bridge.	4-81
Figure 4-58.	TDR and TDR Chart Recording of the Communications Antenna Shown.	4-82
Figure 4-59.	Probe Measurements of a Scanwell FA-8730 Glide Slope Antenna.	4-83
Figure 4-60.	TDR Antenna Signature Test.	4-86
Figure 4-61.	TDR Pulse Degradation Due to Line Loss.	4-86
Figure 4-62.	Antenna FA-8976 TDR Antenna Signatures of Different Cable Lengths Between TDR and Antenna.	4-88
Figure 4-63.	Antenna FA-8976 with Dipoles Individually Opened - Antenna Port Pulsed.	4-89
Figure 4-64.	Antenna FA-8976 with Dipoles Individually Shorted - Antenna Port Pulsed.	4-91
Figure 4-65.	Antenna FA-8976 TDR Signatures - Antenna Port Pulsed.	4-92
Figure 4-66.	FA-8976 Antenna TDR Signatures of Integral Monitor Input Pulsed.	4-93

LIST OF FIGURES (CONTINUED)

		PAGE
Figure 4-67.	Antenna FA-8730 TDR Signatures of Antenna Port with Two Cable Lengths Between TDR and Antenna.	4-95
Figure 4-68.	Bounce Diagram for First Two Feet of TDR Pulse Transmission through the Antenna Port.	4-96
Figure 4-69.	Antenna FA-8730 Antenna Port Pulsed.	4-97
Figure 4-70.	Antenna FA-8730 Antenna Port Pulsed.	4-98
Figure 4-71.	Antenna FA-8730 Antenna Port Pulsed.	4-100
Figure 4-72.	Antenna FA-8730 TDR Signatures of the Inputs of Dipole A1 and J1.	4-101
Figure 4-73.	Antenna FA-8730 TDR Signatures of Integral Monitor Input.	4-104
Figure 4-74.	TDR Signatures of Bent Dipole Type Antenna.	4-105
Figure 4-75.	V-Ring Localizer Antenna Block Diagram.	4-107
Figure 4-76.	V-Ring Localizer Cables.	4-109
Figure 4-77.	V-Ring Antenna Element Construction.	4-110
Figure 4-78.	V-Ring Antenna TDR Signature.	4-111
Figure 4-79.	Expanded Signature Views of a V-Ring Antenna.	4-112
Figure 4-80.	TDR V-Ring Fault Analysis and Associated VSWR Values.	4-114
Figure 4-81.	V-Ring Antenna 2A(E6), Ohio University Localizer.	4-117
Figure 4-82.	Type FA-8720 V-Ring Monitor Signature and Circuit Diagram.	4-118
Figure 4-83.	V-Ring Localizer APCU Signatures of SB Input (Z3, J1).	4-120

LIST OF FIGURES (CONTINUED)

		PAGE
Figure 4-84.	V-Ring Localizer APCU Signatures of Power Divider, Z2, Input.	4-123
Figure 4-85.	TDR Signature Example of Traveling Wave Antennas and TWA Monitor.	4-124
Figure 4-86.	Carrier Input for 8-Element TWA Localizer APCU, Raleigh County Airport.	4-127
Figure 4-87.	GRN/27 TWA Localizer Course Antenna Signatures, Detroit Metropolitan Airport.	4-128
Figure 4-88.	Alford Loop Antenna Diagrams.	4-130
Figure 4-89.	Alford Loop Antenna Pair Signatures, Port Columbus Airport.	4-131
Figure 4-90.	Alford Loop Antenna Signatures.	4-133
Figure 4-91.	Glide Slope Antenna Signatures.	4-134
Figure 4-92.	Antenna and Path Monitor Signatures from GRN/27 Glide Slopes.	4-137
Figure 4-93.	O'Hare Runway Map with Monitor Points.	4-141
Figure 4-94.	Future TRACON Configuration at O'Hare.	4-142
Figure 4-95.	Overall System Concept - ASCD.	4-151
Figure 4-96.	Remote Data Processor Block Diagram.	4-154
Figure 4-97.	Configuration for RDP/CP Interface.	4-157
Figure 4-98.	Controller Display When ILS Operating Properly.	4-159
Figure 4-99.	Controller Display After ILS Failure has Occurred.	4-160
Figure 4-100.	Example of Maintenance Feature.	4-167
Figure 4-101.	A.C. Measurements Using High-Speed Sample Capability.	4-168

LIST OF FIGURES (CONTINUED)

		PAGE
Figure 4-102.	ILS Middle Marker Beacon Flight Geometry.	4-171
Figure 4-103.	Horizontal Radiation Patterns Obtained from an ILS Marker.	4-172
Figure 4-104.	Simultaneous-Phase-Comparison Radar.	4-174
Figure 4-105.	Differential Phase System.	4-176
Figure 4-106.	Developmental Model - Differential Phase Marker Beacon Locator.	4-177
Figure 4-107.	Differential Phase System - Trigger Circuitry.	4-178
Figure 4-108.	Flight Test #7.	4-180
Figure 4-109.	Flight Test #8.	4-181
Figure 4-110.	Flight Test #9.	4-182
Figure 4-111.	Calibration Pass: Detailed Phase Plot.	4-183
Figure 4-112.	Phase Shift vs. RF Amplitude KR-21.	4-184
Figure 4-113.	Aircraft Angle of Attack Required for Zero Phase Difference.	4-185
Figure 4-114.	Single-Receiver Marker Locator Concept.	4-187
Figure 5-1.	Schematic of Localizer Distribution System for Alford Two-Frequency Array.	5-2
Figure 5-2.	Recording of CDI Observed During Orbit, 6 Miles Range, Elevation 1500 Feet.	5-8
Figure 5-3.	CDI Crossover of Course Array to 45 Degrees.	5-9
Figure 5-4.	CDI Crossover of Clearance Array to 45 Degrees.	5-10
Figure 5-5.	Data Taken During 6-Mile Orbit, 1500 Feet Elevation.	5-11

LIST OF FIGURES (CONTINUED)

		PAGE
Figure 5-6.	Recording of CDI and Differential Amplifier Output Showing Difference Between CDI and Theodolite Track.	5-12
Figure 5-7.	Recording of CDI and Differential Amplifier Approach to Landing Shown in Previous Figure.	5-13
Figure 5-8.	Broad Alarm - CDI - North to South Runs.	5-15
Figure 5-9.	Broad Alarm - CDI - South to North Runs.	5-16
Figure 5-10.	Broad Alarm - Signal Strength - South to North Runs.	5-17
Figure 5-11.	Broad Alarm - Signal Strength - North to South Runs.	5-18
Figure 5-12.	Antenna Feed Line Electrical Length Test Setup.	5-19
Figure 5-13.	Antenna Element Test Setup.	5-20
Figure 5-14.	Alford 12-Element Test Setup.	5-21
Figure 5-15.	Wilcox 14-Element Test Setup.	5-22
Figure 5-16.	Sideband Test Setup.	5-23
Figure 5-17.	Carrier Test Setup.	5-24
Figure 5-18.	System Normal Test Setup.	5-25
Figure 5-19.	Plot of CDI versus Azimuth, Alford Box, 108.5 MHz.	5-28
Figure 5-20.	Plot of CDI versus Azimuth, Alford Box, 109.7 MHz.	5-29
Figure 5-21.	Plot of CDI versus Azimuth, Alford Box, 111.9 MHz.	5-30
Figure 5-22.	Plot of CDI versus Azimuth, Wilcox Box, 108.5 MHz.	5-31
Figure 5-23.	Plot of CDI versus Azimuth, Wilcox Box, 109.7 MHz.	5-32
Figure 5-24.	Plot of CDI versus Azimuth, Wilcox Box, 111.9 MHz.	5-33
Figure 5-25.	Plot of CDI versus Azimuth, Alford and Wilcox Boxes, 108.5 MHz.	5-34

LIST OF FIGURES (CONTINUED)

		PAGE
Figure 5-26.	Plot of CDI versus Azimuth, Alford and Wilcox Boxes, 109.7 MHz.	5-35
Figure 5-27.	Plot of CDI versus Azimuth, Alford and Wilcox Boxes, 111.9 MHz.	5-36
Figure 5-28.	Plot of CDI versus Azimuth, Alford Distribution Box, 108.5 MHz, 109.7 MHz, 111.9 MHz.	5-37
Figure 5-29.	Plot of CDI versus Azimuth, Wilcox Distribution Box, 108.5 MHz, 109.7 MHz, 111.9 MHz.	5-38
Figure 5-30.	Plot of Sideband Signal versus Azimuth, Alford and Wilcox Boxes, 108.5 MHz.	5-39
Figure 5-31.	Plot of Sideband Signal versus Azimuth, Alford and Wilcox Boxes, 109.7 MHz.	5-40
Figure 5-32.	Plot of Sideband Signal versus Azimuth, Alford and Wilcox Boxes, 111.9 MHz.	5-41
Figure 5-33.	Plot of Sideband Signal versus Azimuth, Alford Distribution Box, 108.5 MHz, 109.7 MHz, 111.9 MHz.	5-42
Figure 5-34.	Plot of Sideband Signal versus Azimuth, Wilcox Distribution Box, 108.5 MHz, 109.7 MHz, 111.9 MHz.	5-43
Figure 5-35.	Plot of Carrier Strength versus Azimuth, Alford and Wilcox Boxes, 108.5 MHz.	5-44
Figure 5-36.	Plot of Carrier Strength versus Azimuth, Alford and Wilcox Boxes, 109.7 MHz.	5-45
Figure 5-37.	Plot of Carrier Strength versus Azimuth, Alford and Wilcox Boxes, 111.9 MHz.	5-46
Figure 5-38.	Plot of Carrier Strength versus Azimuth, Alford Distribution Box, 108.5 MHz, 109.7 MHz, 111.9 MHz.	5-47

LIST OF FIGURES (CONTINUED)

		PAGE
Figure 5-39.	Plot of Carrier Strength versus Azimuth, Wilcox Distribution Box, 108.5 MHz, 109.7 MHz, 111.9 MHz.	5-48
Figure 5-40.	Plot of AGC Derived Signal Strength versus Azimuth, Alford and Wilcox Boxes, 108.5 MHz.	5-51
Figure 5-41.	Plot of AGC Derived Signal Strength versus Azimuth, Alford and Wilcox Boxes, 109.7 MHz.	5-52
Figure 5-42.	Plot of AGC Derived Signal Strength versus Azimuth, Alford and Wilcox Boxes, 111.9 MHz.	5-53
Figure 5-43.	Normalized Main Carrier Pattern.	5-56
Figure 5-44.	Normalized Clearance Carrier Pattern.	5-58
Figure 5-45.	Normalized Sideband Difference (NSD) - Main Sideband.	5-59
Figure 5-46.	Normalized Sideband Difference (NSD) - Clearance Sideband.	5-60
Figure 5-47.	Main and Clearance NSD Patterns.	5-61
Figure 5-48.	Criteria for Assessing Acceptability of System Status.	5-63
Figure 5-49.	30° Dephasing, Centerline Readings, Mini-Lab.	5-79
Figure 5-50.	Width Reading of Monitor, Mini-Lab and PFCD for 30° Dephasing at 111.9 MHz.	5-80
Figure 5-51.	Block Diagram - MC-14/6 Alford Array System.	5-82
Figure 5-52.	Block Diagram - MC-14/6 Alford Array System Revised 1976 Tests.	5-93
Figure 5-53.	Run 18-21 (FAA-DC-6), Normal Configuration, ±35° Clearance Orbit--March 18, 1976.	5-115
Figure 5-54.	Ground Run, 47° Phase Retard in Line A-7, ±35° Clearance Orbit--March 13, 1976,	5-117

LIST OF FIGURES (CONTINUED)

		PAGE
Figure 5-55.	Orbit, 46° Phase Retard in Line A-7, ±35° Clearance Orbit--March 17, 1976.	5-118
Figure 5-56.	Run 18-18 (FAA-DC-6), 47° Phase Retard in Line A-7, ±35° Clearance Orbit--March 18, 1976.	5-119
Figure 5-57.	Run 18-30 (FAA-DC-6), 31° Phase Retard in M-14 SO Line, ±35° Clearance Orbit--March 18, 1976.	5-121
Figure 5-58.	Run 19-2 (FAA-DC-6), 45° Phase Retard in Line A-7, Broad Course and Clearance Path Widths--March 19, 1976.	5-123
Figure 5-59.	Run 19-8 (FAA-DC-6), 41° Phase Retard in Line A-7, Normal Course and Clearance Path Widths--March 19, 1976.	5-125
Figure 5-60.	Run 19-2 (FAA-DC-6), 51° Phase Retard in Line A-8, Broad Course and Clearance Path Widths--March 19, 1976.	5-127
Figure 5-61.	Run 19-9 (FAA-DC-6), 40° Phase Retard in Line A-8, Normal Course and Clearance Path Widths--March 19, 1976.	5-129
Figure 5-62.	Run 19-4 (FAA-DC-6), 36° Phase Retard in M-14 SO Line, Broad Course and Clearance Path Widths--March 19, 1976.	5-131
Figure 5-63.	Run 19-11 (FAA-DC-6), 44° Phase Retard in M-14 SO Line, Normal Course and Clearance Path Widths--March 19, 1976.	5-132
Figure 5-64.	Comparison of 6 and 2-Mile Orbits of Small Aperture Slotted-Cable Localizer.	5-139
Figure 5-65.	Low Approach - Small Aperture Slotted Cable Localizer - January 25, 1976.	5-140
Figure 5-66.	Plot of Localizer CDI vs. Azimuth for a 2 mile run at f= 111.9 on January 27, 1976 of Localizer Array.	5-142

LIST OF FIGURES (CONTINUED)

		PAGE
Figure 5-67.	Course Width at Borad Alarm, 1500' Altitude at 6 Nautical Miles for the Medium Aperture Antenna Array at 108.5 MHz.	5-150
Figure 5-68.	Course Width at Broad Alarm, 1500' Altitude at 6 Nautical Miles for the Small Aperture Antenna Array at 111.9 MHz.	5-151
Figure 5-69.	Back Course Orbit, 1000' Altitude at 6 Nautical Miles for the Medium Aperture Antenna Array at 108.5 MHz.	5-152
Figure 5-70.	Back Course Orbit, 1000' Altitude at 6 Nautical Miles for the Small Aperture Antenna Array at 108.5 MHz.	5-153
Figure 5-71.	Structure Runs for the Medium (Top) and Small Aperture Antenna Arrays on 109.7 MHz.	5-154
Figure 6-1.	Examples of Terrain Reflection Mechanisms Normally Neglected in Physical Optics Terrain Models.	6-3
Figure 6-2.	Terrain Approximated as Perfectly-Conducting Plates.	6-5
Figure 6-3.	Geometry of Glide Slope Terrain Problem as Treated by Westinghouse Using Half-Plane Diffraction.	6-7
Figure 6-4.	Geometry of Glide Slope Terrain Problem as Treated by OU Far Zone GTD Model.	6-9
Figure 6-5.	The 8 Types of Ray Contributions Included in the Ohio University GTD Glide Slope Model.	6-10
Figure 6-6.	Wedge Diffraction Geometry and Coordinates.	6-13
Figure 6-7.	Illustration of Diffraction Unit Vectors.	6-13
Figure 6-8.	Diffraction Angle β_0 and Cone of Diffracted Rays.	6-15

LIST OF FIGURES (CONTINUED)

		PAGE
Figure 6-9.	Numbering of Terrain Profile Plates and Curves.	6-17
Figure 6-10.	Profile of Terrain in the Reflecting Zone of the Kodiak, Alaska Glide Slope.	6-20
Figure 6-11.	Calculated CDI for 1000 Foot Level Run for Terrain Profile of Figure 6-10.	6-21
Figure 6-12.	Calculated Radiation Pattern for Upper Antenna for Terrain Profile of Figure 6-10.	6-22
Figure 6-13.	Calculated Radiation Pattern for the Lower Antenna for the Terrain Profile of Figure 6-10.	6-23
Figure 6-14.	Profile of Terrain in the Reflecting Zone for Carswell AFB, Texas.	6-24
Figure 6-15.	Calculated CDI for the Terrain Profile of Figure 6-14.	6-25
Figure 6-16.	Calculated Radiation Pattern for the Upper Antenna for the Terrain Profile of Figure 6-14.	6-26
Figure 6-17.	Calculated Radiation Pattern for the Lower Antenna for the Terrain Profile of Figure 6-14.	6-27
Figure 6-18.	Test Profile No. 1.	6-28
Figure 6-19.	Calculated CDI for Test Profile No. 1, Figure 6-18.	6-29
Figure 6-20.	Calculated Radiation Pattern for the Upper Antenna for Test Profile No. 1, Figure 6-18.	6-30
Figure 6-21.	Calculated Radiation Pattern for the Lower Antenna for Test Profile No. 1, Figure 6-18.	6-31
Figure 6-22.	Test Profile No. 2.	6-32
Figure 6-23.	Calculated CDI for Test Profile No. 2, Figure 6-22.	6-33
Figure 6-24.	Calculated Radiation Pattern for the Upper Antenna for Test Profile No. 2, Figure 6-22.	6-34

LIST OF FIGURES (CONTINUED)

		PAGE
Figure 6-25.	Calculated Radiation Pattern for the Lower Antenna for Test Profile No. 2, Figure 6-22.	6-35
Figure 6-26.	Test Profile No. 3.	6-36
Figure 6-27.	Calculated CDI for Test Profile No. 3, Figure 6-26.	6-37
Figure 6-28.	Calculated Radiation Patterns for the Upper Antenna for Test Profile No. 3, Figure 6-26.	6-38
Figure 6-29.	Calculated Radiation Patterns for the Lower Antenna for Test Profile No. 3, Figure 6-26.	6-39
Figure 6-30.	Organization of OUGS and POSTOUGS Programs.	6-43
Figure 6-31a.	Sample Input Data for OUGS Program.	6-46
Figure 6-31b.	Sample Output Data from OUGS Program.	6-47
Figure 6-32.	Coordinate System for Input to OUGS.	6-49
Figure 6-33.	Sample Input Data for POSTOUGS Program.	6-53
Figure 6-34.	Calculated Values of DDM Versus the Ratio of the Clearance Carrier Signal (E_{cc}) to the Course Carrier Signal (E_c) for Various Values of Course Signal Only DDM.	6-55
Figure 6-35.	Calculated Values of DDM Versus the Ratio of the Clearance Carrier Signal (E_{cc}) to the Course Carrier Signal (E_c) for Various Values of Course Signal Only DDM.	6-56
Figure 6-36.	Measured Values of DDM Versus the Ratio of the Clearance Signal (E_{cc}) to the Course Carrier Signal (E_c) for Various Values of Course Signal Only DDM.	6-58
Figure 6-37.	Measured Values of DDM Versus the Ratio of the Clearance Carrier Signal (E_{cc}) to the Course Carrier Signal (E_c) for Various Values of Course Signal Only DDM.	6-59

		PAGE
Figure 6-38.	Block Diagram of the Experiment Setup Used to Obtain the Measured Curves of Figures 6-36 and 6-37.	6-60
Figure 6-39.	Block Diagram of the Audio Processor Used to Obtain the Values of DDM Shown in Figures 6-36 and 6-37 and Indicated in the Block Diagram of Figure 6-38.	6-61
Figure 6-40.	Circuit Schematic of the Audio Source Used to Obtain the Values of DDM Shown in Figures 6-36 and 6-37 and Indicated in the Block Diagram of Figure 6-38.	6-62
Figure 6-41.	Calculated Values of DDM Versus the Ratio of the Clearance Carrier Signal (E_{cc}) to the Course Carrier Signal (E_c) for Various Values of Course Signal DDM Calculated Using the Alford Equation.	6-63
Figure 6-42.	Digital Decwriter II30 Character/Second Terminal and Hewlett-Packard 7203A Graphic Plotter.	6-70
Figure 6-43.	Model of Kodiak Airfield.	6-73
Figure 6-44.	DDM vs. Path Angle for the Kodiak Sideband Reference Glide Slope Calculated Using the GTD Code.	6-77
Figure 6-45.	Calculated Antenna Patterns for the Kodiak Geometry and an Ideal Flat Ground Plane Subtracted to Show Perturbing Effect of Ocean Reflections.	6-78
Figure 6-46.	Calculated Flyability Runs for a Capture Effect System with Antenna Heights of 51', 34', and 17' and an A ratio of 0.289.	6-80
Figure 6-47.	Calculated and Measured Curves of CDI vs. Elevation Angle Alpha for a 1000' High Level Run (Pattern B) Flight Measurement Along the Runway Centerline for the Null Reference System at High Tide.	6-87
Figure 6-48.	Calculated and Measured Curves of CDI vs. Elevation Angle Alpha for a 1000' High Level Run (Pattern B) Flight Measurement Along the Runway Centerline for the Null Reference System at Mean Tide.	6-88

LIST OF FIGURES (CONTINUED)

		PAGE
Figure 6-49.	Calculated and Measured Curves of CDI vs. Elevation Angle Alpha for a 1000' High Level Run (Pattern B) Flight Measurement Along the Runway Centerline for the Null Reference System at Low Tide.	6-89
Figure 6-50.	Calculated and Measured Curves of CDI vs. Elevation Angle Alpha for a 1000' High Level Run (Pattern B) Flight Measurement Along the Runway Centerline for the Sideband Reference System at High Tide.	6-90
Figure 6-51.	Calculated and Measured Curves of CDI vs. Elevation Angle Alpha for a 1000' High Level Run (Pattern B) Flight Measurement Along the Runway Centerline for the Sideband Reference System at Mean Tide.	6-91
Figure 6-52.	Calculated and Measured Curves of CDI vs. Elevation Angle Alpha for a 1000' High Level Run (Pattern B) Flight Measurement Along the Runway Centerline for the Sideband Reference System at Low Tide.	6-92
Figure 6-53.	Calculated and Measured Curves of CDI vs. Distance for a Pattern A Flight Along the Runway Centerline for the Null Reference System at High Tide.	6-93
Figure 6-54.	Calculated and Measured Curves of CDI vs. Distance for a Pattern A Flight Along the Runway Centerline for the Null Reference System at Mean Tide.	6-94
Figure 6-55.	Calculated and Measured Curves of CDI vs. Distance for a Pattern A Flight Along the Runway Centerline for Null Reference System at Low Tide.	6-95
Figure 6-56.	Calculated and Measured Curves of CDI vs. Distance for a Pattern A Flight Along the Runway Centerline for the Sideband Reference System at High Tide.	6-96

LIST OF FIGURES (CONTINUED)

		PAGE
Figure 6-57.	Calculated and Measured Curves of CDI vs. Distance for a Pattern A Flight Along the Runway Centerline for the Sideband Reference System at Mean Tide.	6-97
Figure 6-58.	Calculated and Measured Curves of CDI vs. Distance for a Pattern A Flight Along the Runway Centerline for the Sideband Reference System at Low Tide.	6-98
Figure 6-59.	Ground Profile for Kodiak Modeling Calculations.	6-102
Figure 6-60.	Graph for Experimental Determination of Upper Antenna Height for NR.	6-105
Figure 6-61.	Portion of the Terrain Contour Map for Kodiak Runway 25 Glide Slope.	6-106
Figure 6-62.	Flight Log for Null Reference Tests.	6-107
Figure 6-63.	Tide Plots for NR Tests.	6-108
Figure 6-64.	Tide Plots for SBR Tests.	6-109
Figure 6-65.	Building A Geometry and Relation to Localizer Antenna - Denver Stapleton Runway 26L-8R.	6-111
Figure 6-66.	Calculated Front Course (26L) for Circular Orbit 15,000 Ft. from Localizer Antenna.	6-113
Figure 6-67.	Calculated Back Course (8R) for Circular Orbit 15,000 Ft. from Localizer Antenna.	6-114
Figure 6-68.	Stapleton Field Localizer CDI Envelope for a 2.75° Flight Angle (from Horizontal) Above Runway Centerline Due to Derogation Caused by Proposed Hangar A.	6-115
Figure 6-69.	Hoquiam, Washington Localizer CDI Envelope for a 3.0° Flight Angle (from Horizontal) Above Runway Centerline.	6-117

LIST OF FIGURES (CONTINUED)

		PAGE
Figure 6-70.	Hoquiam, Washington Localizer CDI Envelope for a 3.0° Flight Angle (from Horizontal Above Runway Centerline.	6-118
Figure 6-71.	Hoquiam, Washington Localizer CDI Envelope for a 3.0° Flight Angle (from Horizontal) Above Runway Centerline.	6-119
Figure 6-72.	Predicted CDI for Orbital Flight at 1000 Ft. Altitude and 6 Mile Radius with No Ship Present.	6-120
Figure 6-73.	Predicted CDI for Orbital Flight at 1000 Ft. Altitude and 6 Mile Radius with Ship Positioned 2000 ft.	6-121
Figure 6-74.	Predicted CDI for Orbital Flight at 1000 Ft. Altitude and 6 Mile Radius with Ship Positioned 4000 Ft.	6-122
Figure 6-75.	Antenna Radiation Patterns for 14-Element Mark ID LPD Array.	6-123
Figure 6-76.	Ship Modeled Using Five Vertical Plat Plates.	6-125
Figure 9-1.	ILS Distance Measuring System.	9-2
Figure 9-2.	Groundspeed System Block Diagram.	9-5
Figure 9-3.	Pulser No. 1 - Ground.	9-6
Figure 9-4.	Pulser No. 2 - Airborne.	9-6
Figure 9-5.	Transmitter Modulation Generating Circuitry.	9-7
Figure 9-6.	21 KHz Input Conditioning and 5 KHz Phase Detector.	9-9
Figure 9-7.	Input Conditioning Circuitry for the 5.250 KHz Reference Tone Modulated on the Localizer.	9-10
Figure 9-8.	Directional Phase Detector.	9-11
Figure 9-9.	Processor Control Circuit.	9-13
Figure 9-10.	Groundspeed Computational Circuitry.	9-14

LIST OF FIGURES (CONTINUED)

		PAGE
Figure 9-11.	Mixer and Filter for Full Doppler Processing.	9-16
Figure 9-12.	Physical Layout of the Groundspeed Processor.	9-17
Figure 9-13.	Calibration Data for the Flight Tests on July 2, 1978.	9-18
Figure 9-14.	Four Low Approaches from the Flight Test on July 26, 1976.	9-20
Figure 9-15.	360° Turns Made at Ohio University Test Site at Albany, Ohio.	9-21
Figure 9-16.	Two 360° Turns from the Flight Test on July 26, 1976.	9-22
Figure 9-17.	Sample Run from Flight Test on July 26, 1976.	9-23
Figure 9-18.	Initial Test Configuration - Audio Range-Rate System.	9-27
Figure 9-19.	Range-Rate System Tests with RF Generator.	9-28
Figure 9-20.	Revised Synchronous Processing of 1 MHz Data.	9-33
Figure 9-21.	ILS Groundspeed System, Seiko Filter Module, Model SL-62R.	9-34
Figure 9-22.	ILS Groundspeed System 1 MHz Multiplier Detector Module.	9-35
Figure 9-23.	ILS Groundspeed System 5 MHz Multiplier Detector Module.	9-37
Figure 9-24.	ILS Groundspeed System - Doppler Processor Module.	9-40
Figure 9-25.	ILS Groundspeed System, Fast-Slow Module.	9-41
Figure 9-26.	ILS Groundspeed System Clock Module, Modified.	9-43
Figure 9-27.	Circuit Schematic Anemometer Transmitter Analog Wind Telemetry System.	9-46
Figure 9-28.	Localizer Modulator Circuit.	9-47

LIST OF FIGURES (CONTINUED)

		PAGE
Figure 9-29.	Component Layout, Anemometer Transmitter, Analog Wind Telemetry System.	9-48
Figure 9-30.	Circuit Schematic Analog Data Processor, Analog Wind Telemetry System.	9-50
Figure 9-31.	Components Layout, Analog Data Processor, Analog Wind Telemetry System.	9-51
Figure 9-32a.	Circuit Schematic Digital Data Processor, Analog Wind Telemetry System.	9-53
Figure 9-32b.	Circuit Schematic Digital Data Processor, Analog Wind Telemetry System.	9-55
Figure 9-33.	Components Layout, Digital Data Processor, Analog Wind Telemetry System.	9-57
Figure 9-34.	Photograph of Wind Telemetry Anemometer and Transmitter at Ohio University Airport.	9-61
Figure 9-35.	Wind Telemetry System Pictorial.	9-62
Figure 9-36.	Wind Telemetry System Ground Anemometer Transmitter Unit.	9-63
Figure 9-37a.	Wind Telemetry System: Ground Installation at Localizer.	9-64
Figure 9-37b.	Digital Wind Telemetry Receiver Component Layout.	9-65
Figure 9-37c.	Block Diagram: Wind Telemetry Receiver/ Display Module.	9-66
Figure 9-38a.	Anemometer Transmitter: Data Multiplexer and Serializer.	9-67
Figure 9-38b.	Anemometer Transmitter: Data Multiplexer and Serializer.	9-68
Figure 9-39.	Components Layout, Anemometer Transmitter Digital Wind Telemetry System.	9-69

LIST OF FIGURES (CONTINUED)

		PAGE
Figure 9-40.	Anemometer Transmitter: Tone Generation and Switching.	9-70
Figure 9-41.	Anemometer Transmitter: Clock Generation and Controller.	9-71
Figure 9-42.	Localizer Transmitter: Timing and Synchronizing Tone Generation.	9-72
Figure 9-43.	Localizer Modulator Synchronization Pulse Generation.	9-73
Figure 9-44.	Localizer Modulator: Tone Detection, Tone Generation and Modulation.	9-75
Figure 9-45.	Localizer Modulator and Sync Tone Generator (Viewed from Component Side of Board).	9-77
Figure 9-46.	Groundspeed and Airspeed Traces Using Synchronous Processor with the 5 MHz Detector.	9-79
Figure 9-47.	Groundspeed Outputs Using the 5 MHz Detector and the Non-Synchronous Processor.	9-81
Figure 9-48.	Simultaneous Ground and Aircraft Traces, Digital Wind Telemetry System.	9-83
Figure 9-49.	Simultaneous Wind Telemetry and Groundspeed Outputs.	9-86
Figure 9-50.	Simultaneous Wind Telemetry and Groundspeed Tests with a Change in Airspeed.	9-87
Figure 9-51.	Simultaneous Ground and Aircraft Traces, Analog Wind Telemetry System.	9-88
Figure 10-1.	Analog Strip-Chart to Digital Data Translator.	10-3
Figure 10-2.	Data Translator Operational Setup.	10-4
Figure 10-3.	Remote Manual Sample Control Switch for Analog/Digital Data Translator.	10-6

LIST OF FIGURES (CONTINUED)

		PAGE
Figure 10-4.	Analog/Digital Data Translator Sample Rate Control Circuit.	10-7
Figure 10-5.	Analog/Digital Data Translator Schematic.	10-8
Figure 10-6.	Timing Diagram.	10-9
Figure 10-7.	Data Translator Power Supply.	10-9
Figure 10-8.	Calcomp Plot of Sample Sinusoid and Triangular Waveforms.	10-11
Figure 10-9.	Calcomp Plot of Glide Slope Summer Output.	10-12
Figure 10-10.	Actual Glide Slope Data Used for Data Conversion Comparison.	10-13
Figure 11-1.	Sample Output of Glide Slope Model.	11-9
Figure 11-2.	Example Output: Far Field CDI vs Angle - Capture Effect Glide Slope.	11-10
Figure 11-3.	Near Field (360° Point) CDI vs Angle - Normal Glide Slope.	11-23
Figure 11-4.	Far Field CDI vs Angle - Normal Glide Slope.	11-24
Figure 11-5.	Near Field (360° Point) CDI vs Angle - Sidebands Retarded 20°.	11-25
Figure 11-6.	Far Field CDI vs Angle - Sidebands Retarded 20°.	11-26
Figure 11-7.	Near Field (360° Point) CDI vs Angle - Sidebands Retarded 20°.	11-27
Figure 11-8.	Far Field CDI vs Angle - Sidebands Retarded 20°.	11-28
Figure 11-9.	Near Field (360° Point) CDI vs Angle - Sidebands Retarded 20°.	11-29
Figure 11-10.	Far Field CDI vs Angle - Sidebands Retarded 20°.	11-30
Figure 11-11.	Near Field (360° Point) CDI vs Angle - Sidebands Retarded 30°.	11-31

LIST OF FIGURES (CONTINUED)

		PAGE
Figure 11-12.	Far Field CDI vs Angle - Sidebands Retarded 30°.	11-32
Figure 11-13.	Near Field (360° Point) CDI vs Angle - Sidebands Retarded 30°.	11-33
Figure 11-14.	Far Field CDI vs Angle - Sidebands Retarded 30°.	11-34
Figure 11-15.	Near Field (360° Point) CDI vs Angle - Sidebands Retarded 40°.	11-35
Figure 11-16.	Far Field CDI vs Angle - Sidebands Retarded 40°.	11-36
Figure 11-17.	Near Field (360° Point) CDI vs Angle - Sidebands Retarded 50°.	11-37
Figure 11-18.	Far Field CDI vs Angle - Sidebands Retarded 50°.	11-38
Figure 11-19.	Near Field (360° Point) CDI vs Angle - Lower Antenna Advanced 10°.	11-39
Figure 11-20.	Far Field CDI vs Angle - Lower Antenna Advanced 10°.	11-40
Figure 11-21.	Near Field (360° Point) CDI vs Angle - Lower Antenna Advanced 20°.	11-41
Figure 11-22.	Far Field CDI vs Angle - Lower Antenna Advanced 20°.	11-42
Figure 11-23.	Near Field (360° Point) CDI vs Angle - Lower Antenna Advanced 30°.	11-43
Figure 11-24.	Far Field CDI vs Angle - Lower Antenna Advanced 30°.	11-44
Figure 11-25.	Near Field (360° Point) CDI vs Angle - Middle Antenna Retarded 12°.	11-45
Figure 11-26.	Far Field CDI vs Angle - Middle Antenna Retarded 12°.	11-46
Figure 11-27.	Near Field (360° Point) CDI vs Angle - Middle Antenna Retarded 14°.	11-47

LIST OF FIGURES (CONTINUED)

		PAGE
Figure 11-28.	Far Field CDI vs Angle - Middle Antenna Retarded 14°.	11-48
Figure 11-29.	Near Field (360° Point) CDI vs Angle - Middle Antenna Advanced 14°.	11-49
Figure 11-30.	Far Field CDI vs Angle - Middle Antenna Advanced 14°.	11-50
Figure 11-31.	Near Field (360° Point) CDI vs Angle - Middle Antenna Retarded 20°.	11-51
Figure 11-32.	Far Field CDI vs Angle - Middle Antenna Retarded 20°.	11-52
Figure 11-33.	Near Field (360° Point) CDI vs Angle - Middle Antenna Retarded 30°.	11-53
Figure 11-34.	Far Field CDI vs Angle - Middle Antenna Retarded 30°.	11-54
Figure 11-35.	Near Field (360° Point) CDI vs Angle - Middle Antenna Retarded 40°.	11-55
Figure 11-36.	Far Field CDI vs Angle - Middle Antenna Retarded 40°.	11-56
Figure 11-37.	Near Field (360° Point) CDI vs Angle - Middle Antenna Retarded 50°.	11-57
Figure 11-38.	Far Field CDI vs Angle - Middle Antenna Retarded 50°.	11-58
Figure 11-39.	Near Field (360° Point) CDI vs Angle - Middle Antenna Retarded 60°.	11-59
Figure 11-40.	Far Field CDI vs Angle - Middle Antenna Retarded 60°.	11-60
Figure 11-41.	Near Field (360° Point) CDI vs Angle - Upper Antenna Retarded 30°.	11-61
Figure 11-42.	Far Field CDI vs Angle - Upper Antenna Retarded 30°.	11-62
Figure 11-43.	Near Field (360° Point) CDI vs Angle - Upper Antenna Retarded 40°.	11-63
Figure 11-44.	Far Field CDI vs Angle - Upper Antenna Retarded 40°.	11-64

LIST OF FIGURES (CONTINUED)

		PAGE
Figure 11-45.	Near Field (360° Point) CDI vs Angle - Upper Antenna Retarded 50°.	11-65
Figure 11-46.	Far Field CDI vs Angle - Upper Antenna Retarded 50°.	11-66
Figure 11-47.	Near Field (360° Point) CDI vs Angle - Upper Antenna Retarded 60°.	11-67
Figure 11-48.	Far Field CDI vs Angle - Upper Antenna Retarded 60°.	11-68
Figure 11-49.	Near Field (360° Point) CDI vs Angle - Upper Antenna Advanced 60°.	11-69
Figure 11-50.	Far Field CDI vs Angle - Upper Antenna Advanced 60°.	11-70
Figure 11-51.	Near Field (360° Point) CDI vs Angle - Upper Antenna Retarded 70°.	11-71
Figure 11-52.	Far Field CDI vs Angle - Upper Antenna Retarded 70°.	11-72
Figure 11-53.	Near Field (360° Point) CDI vs Angle - Upper Antenna Retarded 80°.	11-73
Figure 11-54.	Far Field CDI vs Angle - Upper Antenna Retarded 80°.	11-74
Figure 11-55.	Near Field (360° Point) CDI vs Angle - Upper Antenna Retarded 90°.	11-75
Figure 11-56.	Far Field CDI vs Angle - Upper Antenna Retarded 90°.	11-76
Figure 11-57.	Near Field (360° Point) CDI vs Angle - Lower Antenna Attenuated 1 dB.	11-77
Figure 11-58.	Far Field CDI vs Angle - Lower Antenna Attenuated 1 dB.	11-78
Figure 11-59.	Near Field (360° Point) CDI vs Angle - Lower Antenna Attenuated 3 dB.	11-79
Figure 11-60.	Far Field CDI vs Angle - Lower Antenna Attenuated 3 dB.	11-80
Figure 11-61.	Near Field (360° Point) CDI vs Angle - Lower Antenna Attenuated 7 dB.	11-81

LIST OF FIGURES (CONTINUED)

		PAGE
Figure 11-62.	Far Field CDI vs Angle - Lower Antenna Attenuated 7 dB.	11-82
Figure 11-63.	Near Field (360° Point) CDI vs Angle - Middle Antenna Attenuated 1 dB.	11-83
Figure 11-64.	Far Field CDI vs Angle - Middle Antenna Attenuated 1 dB.	11-84
Figure 11-65.	Near Field (360° Point) CDI vs Angle - Middle Antenna Attenuated 2 dB.	11-85
Figure 11-66.	Far Field CDI vs Angle - Middle Antenna Attenuated 2 dB.	11-86
Figure 11-67.	Near Field (360° Point) CDI vs Angle - Middle Antenna Attenuated 4 dB.	11-87
Figure 11-68.	Far Field CDI vs Angle - Middle Antenna Attenuated 4 dB.	11-88
Figure 11-69.	Near Field (360° Point) CDI vs Angle - Upper Antenna Attenuated 3 dB.	11-89
Figure 11-70.	Far Field CDI vs Angle - Upper Antenna Attenuated 3 dB.	11-90
Figure 11-71.	Near Field (360° Point) CDI vs Angle - Upper Antenna Attenuated 6 dB.	11-91
Figure 11-72.	Far Field CDI vs Angle - Upper Antenna Attenuated 6 dB.	11-92
Figure 11-73.	Near Field (360° Point) CDI vs Angle - Upper Antenna Attenuated 10 dB.	11-93
Figure 11-74.	Far Field CDI vs Angle - Upper Antenna Attenuated 10 dB.	11-94
Figure 11-75.	Near Field (360° Point) CDI vs Angle - Lower Antenna Out.	11-95
Figure 11-76.	Far Field CDI vs Angle - Lower Antenna Open.	11-96

LIST OF FIGURES (CONTINUED)

		PAGE
Figure 11-77.	Near Field (360° Point) CDI vs Angle - Lower Antenna Out.	11-97
Figure 11-78.	Far Field CDI vs Angle - Lower Antenna Shorted.	11-98
Figure 11-79.	Near Field (360° Point) CDI vs Angle - Middle Antenna Out.	11-99
Figure 11-80.	Far Field CDI vs Angle - Middle Antenna Open.	11-100
Figure 11-81.	Near Field (360° Point) CDI vs Angle - Middle Antenna Out.	11-101
Figure 11-82.	Far Field CDI vs Angle - Middle Antenna Shorted.	11-102
Figure 11-83.	Near Field (360° Point) CDI vs Angle - Upper Antenna Out.	11-103
Figure 11-84.	Far Field CDI vs Angle - Upper Antenna Open.	11-104
Figure 11-85.	Near Field (360° Point) CDI vs Angle - Upper Antenna Out.	11-105
Figure 11-86.	Far Field CDI vs Angle - Upper Antenna Shorted.	11-106
Figure 11-87.	Near Field (360° Point) CDI vs Angle - Modulation Index = .28.	11-107
Figure 11-88.	Far Field CDI vs Angle - Modulation Index = .28.	11-108
Figure 11-89.	Near Field (360° Point) CDI vs Angle - Modulation Index = 0.5.	11-109
Figure 11-90.	Far Field CDI vs Angle - Modulation Index = 0.5.	11-110
Figure 11-91.	Near Field (360° Point) CDI vs Angle - No Clearance.	11-111
Figure 11-92.	Far Field CDI vs Angle - No Clearance.	11-112
Figure 11-93.	Near Field (360° Point) CDI vs Angle - Maximum Clearance Modulation.	11-113
Figure 11-94.	Far Field CDI vs Angle - Maximum Clearance Modulation.	11-114

		PAGE
Figure 11-95.	Far Field CDI vs Angle - Power Divider A+ Clockwise.	11-115
Figure 11-96.	Far Field CDI vs Angle - Power Divider A- Counterclockwise.	11-116
Figure 11-97.	Far Field CDI vs Angle - Power Divider B+ Clockwise.	11-117
Figure 11-98.	Far Field CDI vs Angle - Power Divider B- Counterclockwise.	11-118
Figure 11-99.	Far Field CDI vs Angle - Power Divider Carrier +.	11-119
Figure 11-100.	Far Field CDI vs Angle - Power Divider Carrier -.	11-120
Figure 11-101.	Far Field CDI vs Angle - Z8 Clockwise.	11-121
Figure 11-102.	Far Field CDI vs Angle - Z8 Counterclockwise.	11-122
Figure 11-103.	Watts Mark I Glide Slope Array at New Tamiami, Florida.	11-125
Figure 11-104.	Watts Mark I Antenna Being Lowered for Tests to Determine Path Independence of Antenna Height.	11-126
Figure 11-105.	Antenna Positioning for Seventh Series of Watts Slotted Cable Glide Slope Tests.	11-128
Figure 11-106.	Ground-Based Measurement of Elevation of Zero DDM Line Above Ground at Threshold.	11-129
Figure 11-107.	Flight Recording of Glide Slope CDI Made on a Level Flight Through the Path Structure on Runway Centerline Extended at 1500-feet above the Array.	11-131
Figure 11-108.	Airborne Measurement of Zero DDM Line Made at a Distance of 4.8 Miles from Transmitter Antennas.	11-132
Figure 11-109.	Airborne Measurement of Zero DDM Line Made at a Distance Equal to the Distance of the 100-foot Decision Point on the Glide Slope (ILS Point C).	11-133
Figure 11-110.	Flight Recording of the Mark I, Curvilinear System Made During Low Approach for Landing.	11-134

LIST OF FIGURES (CONTINUED)

		PAGE
Figure 11-111.	Airborne Measurement of Zero DDM Line Made at a Distance of 4.8 Miles.	11-135
Figure 11-112.	Perpendicular Measurement Subsequent to Figure 11-111 Data But With Sideband Dephased 30 Degrees (advance).	11-136
Figure 11-113.	Measurement of Perpendicular Path Structure with the Sideband Energy Retarded 30 Degrees.	11-137
Figure 11-114.	Tamiami Site Layout for Initial Series of Tests on Watts Mark 2 System.	11-140
Figure 11-115.	Copy of Flight Recording - Level Pass, 1000 Feet.	11-141
Figure 11-116.	Copy of Flight Recording Made During Low Approach for Watts Mark 2 System.	11-142
Figure 11-117.	Three Differential Amplifier Traces Superimposed.	11-144
Figure 11-118.	Copy of Flight Recording, Perpendicular-Cut to Runway Centerline at 5.4 Miles.	11-145
Figure 11-119.	Comparison of Calculated and Measured Cross Sections of the Watts Glide Path.	11-146
Figure 11-120.	Comparison of Calculated and Measured Flyability Runs for Watts Mark 2 System.	11-147
Figure 11-121.	Truck Positions for Fault Tests Mark 2 System.	11-152
Figure 11-122.	Watts Mark II Glide Slope Array with Deliberate Alignment Fault.	11-158
Figure 11-123a.	Perpendicular Path Structure from the Watts Array When Fed by the TU-4 and Wilcox Transmitters.	11-161
Figure 11-123b.	Perpendicular Path Structure from the Watts Array When Fed by the TU-4 Transmitter.	11-162
Figure 11-124.	Perpendicular Path Structure from the Watts Array Showing the Effects of Antenna Misalignment.	11-164

LIST OF FIGURES (CONTINUED)

		PAGE
Figure 11-125.	Far-Field Monitor #1 RF Level and DDM and Far-Field Monitor #2 DDM responses.	11-169
Figure 11-126.	Watts Mark 2 Glide-Slope Set Up at the Ohio University Test Site, Tamiami, Florida.	11-171
Figure 11-127.	Response of the Integral Monitor, Far-Field Monitor, and the Modulator Carrier to Changes in Transmitter Parameters.	11-173
Figure 11-128.	Monitor Response for the Period of September 18 to September 21, 1975.	11-175
Figure 11-129a.	Monitor Response, September 18, 1975, from 0630 hours to 0800 hours.	11-176
Figure 11-129b.	Monitor Response, September 18, 1975, from 0930 hours to 1100 hours.	11-177
Figure 11-129c.	Monitor Response, September 19, 1975, from 1400 hours to 1530 hours.	11-178
Figure 11-130.	Far-Field Monitor RF Level, September 18, 1975.	11-180
Figure 11-131.	Effects Due to a Fault in the Monitor Circuit.	11-181
Figure 11-132.	RF Cable Diagram for 2-Antenna End-Fire Glide Slope Junction Box.	11-183
Figure 11-133.	Monitor Response for the Period of September 26 to September 29, 1975.	11-184
Figure 11-134a.	Monitor Response, September 27, 1975, from 0800 hours to 0930 hours.	11-185
Figure 11-134b.	Monitor Response, September 27, 1975, from 1300 hours to 1430 hours.	11-186
Figure 11-134c.	Monitor Response, September 27, 1975, from 1445 hours to 1615 hours.	11-187
Figure 11-134d.	Monitor Response, September 27, 1975, from 2000 hours to 2130 hours.	11-188

LIST OF FIGURES (CONTINUED)

		PAGE
Figure 11-135.	Monitor Response, September 30, 1975, During Varying Rain Conditions.	11-189
Figure 11-136.	Layout of the Watts System at the Tamiami Airport.	11-192
Figure 11-137.	Watts Mark III End-Fire Glide Slope Array Installed at Tamiami.	11-193
Figure 11-138.	Shown in the Foreground are Three Slotted-Cable Monitor Antennas Serving the Rear Antenna Which is Partially Evident.	11-195
Figure 11-139.	Watts Mark III Glide Slope Arrray.	11-196
Figure 11-140.	Level Pass 1000 Feet Above Runway Centerline Extended Normal Daytime Turbulence.	11-198
Figure 11-141.	CDI, Theodolite, and Differential Amplifier Recordings from Run 25-20.	11-199
Figure 11-142.	Completion of a Pattern A Run with the Bonanza 35 Aircraft During Watts Mark III Testing at Tamiami.	11-200
Figure 11-143.	Differential Amplifier Traces from Five Different Runs Made on February 25, 1977.	11-201
Figure 11-144.	Recording of CDI on Transverse Cut to Localizer at 5.2 Miles Range from the Glide Slope Array.	11-203
Figure 11-145.	Comparison of Perpendicular Structures with Different Configurations of the Watts Endfire Glide-Slope Array.	11-204
Figure 11-146.	Comparison of Transverse Patterns from Spinner's Yagi Array in 1956 and the Watts Mark 3 in 1977.	11-205
Figure 11-147.	Transverse Crosspointer Curves Calculated by Watts to Which has been Added the Measured CDI Values During a Perpendicular Cut, Run 25-9.	11-206
Figure 11-148.	Locations of Specific Faults.	11-211
Figure 11-149.	Transverse Path Structure in the Absence of the Clearance Transmitter.	11-213

		PAGE
Figure 11-150.	Recording of Glide-Slope CDI During Level Flight Along Localizer Course, 1000 Feet Altitude.	11-217
Figure 11-151.	Recording of Glide-Slope CDI During Level Flight Perpendicular to Localizer, 5.4 Miles from Runway, 1600 Feet Altitude.	11-219
Figure 11-152.	Recordings of CDI and Differential Amplifier Output During Low Approach.	11-221
Figure 11-153.	Recording of Theodolite Trace for FAA Saberliner Flight with a Hand-Calculated Differential Trace Added.	11-225
Figure 11-154.	Effects of Clearance Transmitter Power Level on Perpendicular Structure as Seen at 5.4 Miles, 1600 Feet	11-227
Figure 11-155.	Composite of Seven Differential Amplifier Traces Taken at Different Azimuth Approach Angles to the Runway.	11-229
Figure 11-156.	Tracings of the Flight Records of Transverse Structure for the Standard and Expanded Aperture for the Watts Mark 3 Endfire Glide Slope Array.	11-234
Figure 11-157.	Plot of CDI Contours in the Vertical Plane Containing the Runway Threshold and Perpendicular to the Runway Centerline.	11-235
Figure 11-158.	Comparison of Transverse Structure Before and After the Interchange of Single Sections of the Front and Rear Antennas.	11-237
Figure 11-159.	Photograph of Modification of Front Antenna to Lower Its Height Gradually from 42 Inches to 21 Inches at the Runway End.	11-240
Figure 11-160.	Tracing of Two Records Showing the Transverse Path Structures Before and After Lowering of the End Portion of the Front Antenna Element.	11-241
Figure 11-161.	Diagram of Carrier and Sideband Being Fed into the Antenna.	11-247
Figure 11-162.	Relative Slot Excitations of Rear Antenna, Tamiami.	11-250

LIST OF FIGURES (CONTINUED)

		PAGE
Figure 11-163.	Relative Slot Excitations of Front Antenna, Tamiami.	11-251
Figure 11-164.	Watts Slotted-Cable Glide-Slope Layout, Tamiami.	11-252
Figure 11-165.	Relative Slot Excitations of Rear Antenna, Staunton.	11-253
Figure 11-166.	Relative Slot Excitations of Front Antenna, Staunton.	11-254
Figure 11-167.	Watts Slotted Cable Glide Slope Layout, Staunton.	11-255
Figure 11-168.	Terrain Profile of Shenandoah Valley Airport, Staunton.	11-257
Figure 11-169.	Extended Terrain Profile of Shenandoah Valley Airport, Staunton.	11-258
Figure 11-170.	Schematic of Flight Tracks on Watts Slotted-Cable Glide Slope.	11-259
Figure 11-171.	Low Approach, Run 29-5, Tamiami.	11-260
Figure 11-172.	Low Approach, Run 29-6, Tamiami.	11-261
Figure 11-173.	Low Approach, Run 29-8, Tamiami.	11-262
Figure 11-174.	Perpendicular Cut, Altitude 1600', Run 18-17, Tamiami.	11-264
Figure 11-175.	Perpendicular Cut, Altitude 1700', N-S, Tamiami.	11-265
Figure 11-176.	Level Pass, Altitude 1000', Run 18-6, Tamiami.	11-266
Figure 11-177.	Low Approach, Staunton.	11-267
Figure 11-178.	Perpendicular Cut, Altitude 1300', Run 1-7, Staunton.	11-268
Figure 11-179.	Perpendicular Cut, Altitude 1500', Run 1-4, Staunton.	11-269
Figure 11-180.	Perpendicular Cut, Altitude 1500', Staunton.	11-270
Figure 11-181.	Level Run, Altitude 1000', Staunton.	11-271

LIST OF FIGURES (CONTINUED)

		PAGE
Figure 11-182.	Level Run, Altitude 1500', Run Number 1-8, Staunton.	11-272
Figure 11-183.	Low Approaches 4° South and North of Runway Centerline.	11-273
Figure 11-184.	Low Approach 6° South and North of Centerline.	11-274
Figure 11-185.	Low Approach 8° South and North of Centerline, Tamiami.	11-275
Figure 11-186.	Above and Below .35° Approaches, Tamiami.	11-276
Figure 11-187.	Level Pass, Altitude 1000', 3° North and South of Centerline.	11-277
Figure 11-188.	Level Pass, Altitude 1000', 4° North and South of Centerline.	11-277
Figure 11-189.	Level Pass, Altitude 1000', 5° North and South of Centerline.	11-278
Figure 11-190.	Level Pass, Altitude 1000', 6° North and South of Centerline.	11-278
Figure 11-191.	Level Pass, Altitude 1000', 7° North and South of Centerline, Tamiami.	11-279
Figure 11-192.	Level Pass, Altitude 1000', 8° North and South of Centerline, Tamiami.	11-279
Figure 11-193.	Theoretical Low Approach, 4° North and South of Centerline, Staunton.	11-281
Figure 11-194.	Theoretical Low Approach, 6° North and South of Centerline, Staunton.	11-282
Figure 11-195.	Theoretical Low Approach, 8° North and South of Centerline.	11-283
Figure 11-196.	Diagram to Show the Conical Structure of the Watts Array.	11-284

LIST OF FIGURES (CONTINUED)

		PAGE
Figure 11-197.	Layout of the Watts System at Rock Springs Airport.	11-287
Figure 11-198.	Level Pass 1000 Feet Above Runway Centerline Extended.	11-289
Figure 11-199.	Differential Amplifier Recording Made During Low Approach at RKS.	11-291
Figure 11-200.	Recordings of CDI on Transverse Cut to Localizer.	11-295
Figure 11-201.	Conceptual Drawing Depicting the Effect of Theodolite Placement on the Measured Path Structure Near Threshold.	11-299
Figure 11-202.	Pertinent Dimensions for Determining and Measuring the Localizer Edge.	11-301
Figure 11-203.	Layout of the Watts System at Rock Springs Airport.	11-302
Figure 11-204.	Level Pass 1000 Feet Above Runway Centerline Extended.	11-305
Figure 11-205.	Three Differential Amplifier Recordings Made During Low Approaches at Rock Springs.	11-307
Figure 11-206.	Recordings of CDI On Transverse Cut to Localizer.	11-311
Figure 11-207.	Low Angle Transverse Cut to the Localizer.	11-315
Figure 11-208.	Averaged Signal Strength Measured by a 360° Orbit.	11-317
Figure 11-209.	Test Set-Up for Verifying K.	11-328
Figure 11-210.	Phasor Diagram.	11-329
Figure 11-211.	Coordinate System.	11-331
Figure 11-212.	Plots of Path-Width Changes Seen in the Far-Field (30,000 ft.).	11-334
Figure 11-213.	Plots of Path-Width Changes Seen at 5,000 ft. Due to Mast Tilt in the Plane Parallel to Runway Centerline.	11-335
Figure 11-214.	Plots of Changes Seen at 0.7° Below Path at the 180° Proximity Point Due to Mast Tilt in the Plane Parallel to the Runway.	11-336

LIST OF FIGURES (CONTINUED)

		PAGE
Figure 11-215.	Plot of Changes Seen at 0.7° Above Path at the 180° Proximity Point Due to Mast Tilt in the Plane Parallel to the Runway.	11-337
Figure 11-216.	Plot of Near Field Responses at ± 0.7° to Mast Tilt in the Plane Perpendicular to Runway.	11-338
Figure 11-217.	Conventional Null-Reference Monitor System.	11-340
Figure 11-218.	Integral Path and Width Monitor for a Null-Reference System.	11-340
Figure 11-219.	Null-Reference Monitor Test Unit.	11-341
Figure 11-220.	Vertical Lobe Structures for Null-Reference and Perturbed Null-Reference Glide Slope.	11-343
Figure 11-221.	Mobile Glide Slope Facility During Tests at Ohio University Airport.	11-352
Figure 11-222.	Lawton, Oklahoma, Municipal Airport, Runway 35.	11-363
Figure 11-223.	Lawton, Oklahoma, Municipal Airport, Runway 35.	11-364
Figure 11-224.	Profile of the Terrain Along a Straight Line Down from the Tower Base to the Middle Marker (Lawton, Oklahoma, Municipal Airport).	11-365
Figure 11-225.	Detailed Terrain Profile Runway 35 Approach Lawton, Oklahoma.	11-367
Figure 11-226.	Ground Data (Commissioned) - Clearance On.	11-370
Figure 11-227.	Ground Data (Commissioned) - Clearance Off.	11-371
Figure 11-228.	Ground Data (Commissioned) -10° Delay in Middle Antenna, Clearance On.	11-372
Figure 11-229.	Ground Data (Commissioned) -10° Delay in Middle Antenna, Clearance Off.	11-373
Figure 11-230.	Ground Data (Commissioned) -10° Advance in Middle Antenna, Clearance Off.	11-374

LIST OF FIGURES (CONTINUED)

		PAGE
Figure 11-231.	Ground Data (Commissioned) -10° Advance in Middle Antenna, Clearance On.	11-375
Figure 11-232.	Ground Data (Commissioned) -2 dB Attenuation in Middle Antenna, Clearance On.	11-376
Figure 11-233.	Ground Data (Commissioned) -6 dB Attenuation in Upper Antenna, Clearance On.	11-377
Figure 11-234.	Ground Data (Commissioned) -3 dB Attenuation in Lower Antenna -10° Retard in Middle Antenna, Clearance On.	11-378
Figure 11-235.	Ground Data (Theoretical Phasing) - Clearance Off.	11-380
Figure 11-236.	Ground Data (Theoretical Phasing) - Clearance On.	11-381
Figure 11-237.	Ground Data (Theoretical Phasing) 10° Delay Middle Antenna, Clearance Off.	11-382
Figure 11-238.	Ground Data (Theoretical Phasing) -20° Delay Middle Antenna, Clearance Off.	11-383
Figure 11-239.	Ground Data (Theoretical Phasing) -30° Delay in Middle Antenna, Clearance Off.	11-384
Figure 11-240.	Ground Data (Theoretical Phasing) -10° Advance in Middle Antenna.	11-385
Figure 11-241.	Approach 17-02 BR Commissioned - Normal with Clearance.	11-389
Figure 11-242.	Approach 17-03 BR Commissioned - Normal with Clearance - (Repeat 17-02 BR).	11-390
Figure 11-243.	Approach 17-04 Commissioned - Normal without Clearance.	11-391
Figure 11-244.	Approach 17-05 BR Commissioned - A2 +15 Degrees, Clearance Off.	11-392
Figure 11-245.	Approach 17-06 Commissioned - A2 +15 Degrees, with Clearance.	11-393

LIST OF FIGURES (CONTINUED)

		PAGE
Figure 11-246.	Approach 17-07 BR Commissioned - A2 -15 Degrees, with Clearance.	11-394
Figure 11-247.	Approach 17-08 BR Commissioned - A3 +45 Degrees, with Clearance.	11-395
Figure 11-248.	Approach 17-09 BR Commissioned - A3 -45 Degrees, with Clearance.	11-396
Figure 11-249.	Approach 17-11 BR Theoretical - Normal with Clearance.	11-397
Figure 11-250.	Approach 17-23 BR Theoretical - Without Clearance.	11-398
Figure 11-251.	Approach 17-15 BR Theoretical - A2 +15 Degrees.	11-399
Figure 11-252.	Approach 17-16 BR Theoretical - A2 -15 Degrees.	11-400
Figure 11-253.	Approach 17-17 BR Theoretical - Normal - (Repeat 17-12 BR).	11-401
Figure 11-254.	Approach 17-18 Theoretical - A1 -10 Degrees.	11-402
Figure 11-255.	Approach 17-19 BR Theoretical - A1 -20 Degrees.	11-403
Figure 11-256.	Approach 17-20 BR Theoretical - A1 -30 Degrees.	11-404
Figure 11-257.	Approach 17-21 BR Theoretical - A1 +20 Degrees.	11-405
Figure 11-258.	Approach 17-22 BR Theoretical - A2 -10 Degrees.	11-406
Figure 11-259.	Approach 17-23 BR Commissioned - A2 -20 Degrees.	11-407
Figure 11-260.	Approach 17-24 Commissioned - A2 -30 Degrees.	11-408
Figure 11-261.	Approach 17-25 BR Commissioned - A2 +20 Degrees.	11-409
Figure 11-262.	Approach 17-26 BR Commissioned - A2 -40 Degrees.	11-410
Figure 11-263.	Approach 17-27 BR Commissioned - A2 -50 Degrees.	11-411
Figure 11-264.	Approach 17-28 BR Commissioned - A2 -60 Degrees.	11-412

LIST OF FIGURES (CONTINUED)

		PAGE
Figure 11-265.	Approach 17-30 BR Commissioned - A3 -30 Degrees.	11-413
Figure 11-266.	Approach 17-31 BR Commissioned -A3 -40 Degrees.	11-414
Figure 11-267.	Approach 17-32 BR Commissioned - A3 -50 Degrees.	11-415
Figure 11-268.	Approach 17-33 BR Commissioned - A3 -60 Degrees.	11-416
Figure 11-269.	Approach 17-34 BR Commissioned - A3 -70 Degrees.	11-417
Figure 11-270.	Approach 17-35 BR Commissioned - A3 -80 Degrees.	11-418
Figure 11-271.	Approach 17-36 BR Commissioned - A3 -90 Degrees.	11-419
Figure 11-272.	Approach 17-37 BR Commissioned - A3 +60 Degrees.	11-420
Figure 11-273.	Approach 18-01 BR Theoretical - Normal.	11-421
Figure 11-274.	Approach 18-02 BR Theoretical - A2 +10 Degrees.	11-422
Figure 11-275.	Approach 18-03 BR Theoretical - A2 +20 Degrees.	11-423
Figure 11-276.	Approach 18-04 BR Theoretical - A2 +20 Degrees (Repeat 18-03 BR).	11-424
Figure 11-277.	Approach 18-05 BR Theoretical - A2 -10 Degrees.	11-425
Figure 11-278.	Approach 18-06 BR Theoretical - A2 -20 Degrees.	11-426
Figure 11-279.	Approach 18-07 BR Theoretical - Normal (Repeat 18-01 BR).	11-427
Figure 11-280.	Approach 18-08 BR Theoretical - A2 -30 Degrees.	11-428
Figure 11-281.	Approach 18-09 BR Theoretical - A2 -20 Degrees.	11-429
Figure 11-282.	Approach 18-10 BR Theoretical - A2 -40 Degrees.	11-430
Figure 11-283.	Approach 18-11 BR Experimental - Normal.	11-431
Figure 11-284.	Approach 18-12 BR Experimental - Normal (Mod Equality Reset).	11-432

		PAGE
Figure 11-285.	Approach 18-13 BR Experimental - Normal (Repeat 18-12 BR).	11-433
Figure 11-286.	Approach 18-14 BR Experimental - A2 -10 Degrees.	11-434
Figure 11-287.	Approach 18-15 BR Experimental - A2 -20 Degrees.	11-435
Figure 11-288.	Approach 18-16 BR Experimental - A2 -30 Degrees.	11-436
Figure 11-289.	Approach 18-17 BR Experimental - A2 +10 Degrees.	11-437
Figure 11-290.	Approach 18-18 BR Experimental - A3 +40 Degrees.	11-438
Figure 11-291.	Approach 18-19 BR Experimental - A3 -40 Degrees.	11-439
Figure 11-292.	Approach 18-20 BR Experimental - A2 -10 Degrees A1 -1 dB.	11-440
Figure 11-293.	Approach 18-21 BR Experimental - A2 -10 Degrees, A1 -3 dB.	11-441
Figure 11-294.	Approach 18-22 BR Experimental - A2 -10 Degrees, A1 -7 dB.	11-442
Figure 11-295.	Approach 18-23 BR Experimental - A2 -10 Degrees, A1 Shorted.	11-443
Figure 11-296.	Approach 18-24 BR Experimental - A2 -10 Degrees, A1 Open.	11-444
Figure 11-297.	Approach 18-25 BR Experimental - A2 -10 Degrees, A1 -1 dB.	11-445
Figure 11-298.	Approach 18-26 BR Experimental - A1 -10 Degrees, A2 -2 dB.	11-446
Figure 11-299.	Approach 18-27 BR Experimental - A2 -10 Degrees, A2 -4 dB.	11-447
Figure 11-300.	Approach 18-28 BR Experimental - A2 Shorted.	11-448
Figure 11-301.	Approach 18-29 BR Experimental - A2 Open.	11-449

LIST OF FIGURES (CONTINUED)

		PAGE
Figure 11-302.	Approach 18-30 BR Experimental - A2 -10 Degrees, A3 -3 dB.	11-450
Figure 11-303.	Approach 18-31 BR Experimental - A2 -10 Degrees, A3 -6 dB.	11-451
Figure 11-304.	Approach 18-32 BR Experimental - A2 -10 Degrees, A3 -10 dB.	11-452
Figure 11-305.	Approach 18-33 BR Experimental - A2 -10 Degrees, A3 Shorted.	11-453
Figure 11-306.	Approach 18-34 BR Experimental - A2 -10 Degrees, A3 Open.	11-454
Figure 11-307.	Approach 18-36 BR Experimental - A2 -10 Degrees (Repeat 18-14 BR).	11-455
Figure 11-308.	Approach 18-37 BR Experimental - A2 -10 Degrees, 20 Degrees SBO Dephase.	11-456
Figure 11-309.	Approach 18-38 BR Experimental - A2 -10 Degrees, 30 Degrees SBO Dephase.	11-457
Figure 11-310.	Approach 18-39 BR Experimental - A2 -10 Degrees, 50 Degrees SBO Dephase.	11-458
Figure 11-311.	Approach 18-40 BR Experimental - A2 -10 Degrees, Clearance -3 dB.	11-459
Figure 11-312.	Approach 18-41 BR Experimental - A2 -10 Degrees, Clearance -6 dB.	11-460
Figure 11-313.	Approach 18-42 BR Experimental - A2 -10 Degrees, Clearance +3 dB.	11-461
Figure 11-314.	Approach 18-43 BR Experimental - A2 -10 Degrees, Clearance = +5.2 dB.	11-462
Figure 11-315.	Approach 18-44 BR Experimental - A2 -10 Degrees, Clearance Mod at Alarm CI - 0 dB.	11-463

LIST OF FIGURES (CONTINUED)

		PAGE
Figure 11-316.	Approach 18-45 BR Experimental - A2 -10 Degrees, PWR Divider A Clockwise.	11-464
Figure 11-317.	Approach 18-46 BR Experimental - A2 -10 Degrees, PWR Divider A CCW.	11-465
Figure 11-318.	Approach 18-47 BR Experimental - A2 -10 Degrees, PWR Divider B Clockwise.	11-466
Figure 11-319.	Approach 18-48 BR Experimental - A2 -10 Degrees, PWR Divider B CCW.	11-467
Figure 11-320.	Approach 18-49 BR Experimental - A2 -10 Degrees, Carrier PWR Divider Clockwise.	11-468
Figure 11-321.	Approach 18-50 BR Experimental - A2 -10 Degrees, Carrier PWR Divider CCW.	11-469
Figure 11-322.	Approach 18-51 BR Experimental - A2 -10 Degrees, Control Z8 Clockwise.	11-470
Figure 11-323.	Approach 18-52 BR Experimental - A2 -10 Degrees, Control Z8 CCW.	11-471
Figure 11-324.	Approach 18-53 BR Experimental - A2 -10 Degrees, Normal (Repeat 18-36 BR).	11-472
Figure 11-325.	Approach 18-54 BR Experimental - A2 -10 Degrees, Normal -8 Degree W.	11-473
Figure 11-326.	Approach 19-01 BR Theoretical - Normal.	11-474
Figure 11-327.	Approach 19-03 BR Theoretical - Normal (Repeat 19-01 BR).	11-475
Figure 11-328.	Approach 19-04 BR Theoretical - Normal, Clearance Off.	11-476
Figure 11-329.	Approach 19-05 BR Theoretical - Normal, Clearance Off (Repeat 19-04 BR).	11-477
Figure 11-330.	Approach 19-06 BR Theoretical - Normal, Clearance Off (Repeat 19-04 BR).	11-478

LIST OF FIGURES (CONTINUED)

		PAGE
Figure 11-331.	Approach 19-07 BR Theoretical - Normal, Clearance Off (Repeat 19-04 BR).	11-479
Figure 11-332.	Approach 19-08 BR Theoretical - A2 -10 Degrees.	11-480
Figure 11-333.	Approach 19-09 BR Theoretical - A2 -20 Degrees.	11-481
Figure 11-334.	Approach 19-10 BR Theoretical - A2 -30 Degrees.	11-482
Figure 11-335.	Approach 19-11 BR Theoretical - A2 -40 Degrees.	11-483
Figure 11-336.	Approach 19-23 BR Theoretical Commissioned - Normal, Clearance Off.	11-484
Figure 11-337.	Approach 19-24 BR Commissioned - Normal, Clearance On.	11-485
Figure 11-338.	Centerline Profile.	11-490
Figure 11-339.	Topographical Map Indicating Terrain Around Glide Slope Reflecting Area.	11-491
Figure 11-340.	Approach 18-2 BR, Normal.	11-495
Figure 11-341.	Approach 18-3 BR, Normal.	11-496
Figure 11-342.	Approach 18-4 BR, Normal.	11-497
Figure 11-343.	Approach 18-5 BR, Normal.	11-498
Figure 11-344.	Approach 18-6 BR, Normal, No Clearance.	11-499
Figure 11-345.	Approach 18-8 BR, SBO Reduced to Alarm.	11-500
Figure 11-346.	Approach 18-9 BR, SBO Reduced to Alarm.	11-501
Figure 11-347.	Approach 18-11 BR, Normal, 8° West of Centerline.	11-502
Figure 11-348.	Approach 18-12 BR, Normal, 8° East of Centerline.	11-503
Figure 11-349.	Approach 18-13 BR, Middle Antenna Phase Advanced 15° to Alarm.	11-504

		PAGE
Figure 11-350.	Approach 18-15 BR, Middle Antenna Phase Retarded 14° to Alarm.	11-505
Figure 11-351.	Approach 18-17 BR, Middle Antenna Phase Advanced 28° to Twice Alarm.	11-506
Figure 11-352.	Approach 18-19 BR, Middle Antenna Phase Retarded 28° to Twice Alarm.	11-507
Figure 11-353.	Approach 18-21 BR, Middle Antenna Phase Advanced 28° to Twice Alarm, No Clearance.	11-508
Figure 11-354.	Approach 18-22 BR, Upper Antenna Phase Advanced 22° to Alarm.	11-509
Figure 11-355.	Approach 18-24 BR, Upper Antenna Phase Retarded 22° to Alarm.	11-510
Figure 11-356.	Approach 18-26 BR, Upper Antenna Phase Advanced 44° to Twice Alarm.	11-511
Figure 11-357.	Approach 18-28 BR, Upper Antenna Phase Retarded 44° to Twice Alarm.	11-512
Figure 11-358.	Approach 18-30 BR, Lower Antenna Phase Advanced 15° to Alarm.	11-513
Figure 11-359.	Approach 18-32 BR, Lower Antenna Phase Retarded 10° to Alarm.	11-514
Figure 11-360.	Approach 18-34 BR, Lower Antenna Phase Advanced 30° to Twice Alarm.	11-515
Figure 11-361.	Approach 18-36 BR, Lower Antenna Phase Retarded 20° to Twice Alarm.	11-516
Figure 11-362.	Approach 18-44 BR, Middle Antenna Attenuated 1 dB to Alarm.	11-517
Figure 11-363.	Approach 18-46 BR, Middle Antenna Attenuated 2 dB to Twice Alarm.	11-518
Figure 11-364.	Approach 18-48 BR, Upper Antenna Attenuated 2 dB to Alarm.	11-519

LIST OF FIGURES (CONTINUED)

		PAGE
Figure 11-365.	Approach 18-50 BR, Upper Antenna Attenuated 4 dB to Twice Alarm.	11-520
Figure 11-366.	Approach 18-52 BR, Lower Antenna Attenuated 1 dB to Alarm.	11-521
Figure 11-367.	Approach 18-54 BR, Lower Antenna Attenuated 2 dB to Twice Alarm.	11-522
Figure 11-368.	Approach 18-56 BR, CSB to SBO Phase Shifted 30° to Alarm.	11-523
Figure 11-369.	Approach 18-57 BR, CSB to SBO Phase Shifted 30° to Alarm (Advance).	11-524
Figure 11-370.	Approach 18-58 BR, SBO Power Increased to Sharp Alarm.	11-525
Figure 11-371.	Approach 19-59 BR, Normal.	11-526
Figure 11-372.	Approach 18-60 BR, Normal.	11-527
Figure 11-373.	Approach 18-39 AR, Normal.	11-528
Figure 11-374.	Approach 18-40 AR, Normal.	11-529
Figure 11-375.	Approach 18-41 AR, Normal.	11-530
Figure 11-376.	Dual Recording of CDI Made with Different Scales on a Flight on the Localizer Centerline 1600 Feet Above the Site Elevation.	11-533
Figure 11-377.	Redbird Airport CDI and Differential Amplifier Traces.	11-535
Figure 11-378.	Geometry for Angle Correction.	11-539
Figure 11-379.	Redbird Profile Starting at Center of Tower Base.	11-543
Figure 11-380.	Topographic Map of Area Around Glide Slope Antennas at Redbird Airport.	11-544
Figure 11-381.	Continuation of Topographic Map Showing Region in Front of Antennas Parallel to Centerline.	11-545

LIST OF FIGURES (CONTINUED)

		PAGE
Figure 11-382.	Approach 12-6, Normal.	11-548
Figure 11-383.	Approach 12-7, Normal.	11-549
Figure 11-384.	Approach 12-8, East Localizer Edge.	11-550
Figure 11-385.	Approach 12-9, West Localizer Edge.	11-551
Figure 11-386.	Approach 12-12, 8° East.	11-552
Figure 11-387.	Approach 12-13, 8° West.	11-553
Figure 11-388.	Approach 12-14, Normal.	11-554
Figure 11-389.	Approach 12-15, Normal.	11-555
Figure 11-390.	Approach 12-16, Normal.	11-556
Figure 11-391.	Approach 12-17, Normal.	11-557
Figure 11-392.	Approach 12-18, Normal.	11-558
Figure 11-393.	Approach 12-19, East Localizer Edge.	11-559
Figure 11-394.	Approach 12-20, West Localizer Edge.	11-560
Figure 11-395.	Approach 12-21, 8° West.	11-561
Figure 11-396.	Approach 12-26, Normal, Without Clearance.	11-562
Figure 11-397.	Approach 13-1, Normal.	11-563
Figure 11-398.	Approach 13-8, Normal.	11-564
Figure 11-399.	Approach 13-9, Increasing SBO.	11-565
Figure 11-400.	Approach 13-10, Increasing SBO.	11-566
Figure 11-401.	Approach 13-11, Increasing SBO.	11-567
Figure 11-402.	Approach 13-12, 8° West.	11-568

LIST OF FIGURES (CONTINUED)

		PAGE
Figure 11-403.	Approach 13-13, 8° West.	11-569
Figure 11-404.	Approach 13-14, 8° West.	11-570
Figure 11-405.	Approach 13-15, 8° West.	11-571
Figure 11-406.	Approach 13-16, Normal, Without Clearance.	11-572
Figure 11-407.	Approach 13-17, Normal.	11-573
Figure 11-408.	Approach 13-18, Middle Antenna Phase Retarded 15°.	11-574
Figure 11-409.	Approach 13-19, Middle Antenna Phase Retarded 12°.	11-575
Figure 11-410.	Approach 13-20, Normal.	11-576
Figure 11-411.	Approach 13-21, Middle Antenna Phase Advanced 12°.	11-577
Figure 11-412.	Approach 13-22, SBO Decreased to Broad Alarm.	11-578
Figure 11-413.	Approach 13-24, SBO Decreased to Broad Alarm.	11-579
Figure 11-414.	Approach 13-27, Middle Antenna Phase Retarded 11°.	11-580
Figure 11-415.	Approach 13-28, Middle Antenna Phase Advanced 9°.	11-581
Figure 11-416.	Approach 13-29, Middle Antenna Phase Advanced 7°.	11-582
Figure 11-417.	Approach 14-2, Normal.	11-583
Figure 11-418.	Approach 14-3, 8° West.	11-584
Figure 11-419.	Approach 14-4, 8° East.	11-585
Figure 11-420.	Approach 14-5, 8° East.	11-586
Figure 11-421.	Approach 14-7, SBO Decreased to Broad Alarm.	11-587
Figure 11-422.	Approach 14-8, SBO Decreased to Broad Alarm.	11-588
Figure 11-423.	Approach 14-9, Normal.	11-589
Figure 11-424.	Approach 14-10, SBO Decreased to Broad Alarm.	11-590

		PAGE
Figure 11-425.	Approach 14-11, SBO Decreased to Broad Alarm.	11-591
Figure 11-426.	Approach 14-12, SBO Decreased to Broad Alarm.	11-592
Figure 11-427.	Approach 14-15, SBO Increased to Sharp Alarm.	11-593
Figure 11-428.	Approach 14-18, SBO Phase Retarded 30°.	11-594
Figure 11-429.	Approach 14-19, SBO Phase Advanced 30°.	11-595
Figure 11-430.	Approach 14-20, Middle Antenna Phase Advanced 8°.	11-596
Figure 11-431.	Approach 14-21, Middle Antenna Phase Retarded 8°.	11-597
Figure 11-432.	Approach 14-22, Upper Antenna Phase Advanced 10°.	11-598
Figure 11-433.	Approach 14-24, Upper Antenna Phase Retarded 17°.	11-599
Figure 11-434.	Approach 14-32, Normal.	11-600
Figure 11-435.	Approach 15-3, Normal.	11-601
Figure 11-436.	Approach 15-4, Normal.	11-602
Figure 11-437.	Approach 15-5, SBO Decreased to Broad Alarm.	11-603
Figure 11-438.	Approach 15-6, Lower Antenna Phase Advanced 20°.	11-604
Figure 11-439.	Approach 15-8, Lower Antenna Phase Retarded 8°.	11-605
Figure 11-440.	Approach 15-10, Lower Antenna Phase Advanced 40°.	11-606
Figure 11-441.	Approach 15-12, Lower Antenna Phase Retarded 16°.	11-607
Figure 11-442.	Approach 15-14, Middle Antenna Attenuated 1 dB.	11-608
Figure 11-443.	Approach 15-16, Middle Antenna Attenuated 2 dB.	11-609
Figure 11-444.	Approach 15-18, Upper Antenna Attenuated 1 dB.	11-610
Figure 11-445.	Approach 15-20, Upper Antenna Attenuated 2 dB.	11-611
Figure 11-446.	Approach 15-22, Lower Antenna Attenuated 1 dB.	11-612

LIST OF FIGURES (CONTINUED)

		PAGE
Figure 11-447.	Approach 15-26, Normal.	11-613
Figure 11-448.	Approach 15-27, 8° West.	11-614
Figure 11-449.	Approach 15-28, 8° East.	11-615
Figure 11-450.	Approach 15-30, SBO Doubled.	11-616
Figure 11-451.	Approach 15-31, SBO Increased to Sharp Alarm.	11-617
Figure 11-452.	Approach 15-32, Normal.	11-618
Figure 11-453.	Approach 15-34, Normal.	11-619
Figure 11-454.	Approach 15-35, Normal.	11-620
Figure 11-455.	Approach 2-5, Normal.	11-621
Figure 11-456.	Approach 2-6, Normal.	11-622
Figure 11-457.	Approach 2-8, SBO Reduced to Broad Alarm.	11-623
Figure 11-458.	Approach 2-9, SBO Reduced to Broad Alarm.	11-624
Figure 11-459.	Approach 2-10, Normal.	11-625
Figure 11-460.	Approach 2-11, Middle Antenna Phase Advanced 13°.	11-626
Figure 11-461.	Approach 2-12, Middle Antenna Phase Advanced 13°.	11-627
Figure 11-462.	Approach 2-13, Middle Antenna Phase Advanced 18°.	11-628
Figure 11-463.	Approach 2-14, Lower Antenna Phase Retarded 18°.	11-629
Figure 11-464.	Approach 2-16, Lower Antenna Phase Advanced 15°.	11-630
Figure 11-465.	Approach 2-17, Lower Antenna Attenuated .5 dB.	11-631
Figure 11-466.	Approach 2-18, Middle Antenna Attenuated .5 dB.	11-632
Figure 11-467.	Approach 2-19, Lower Antenna Attenuated 1.5 dB.	11-633
Figure 11-468.	Topographic Map of Columbus 10 R Glide Slope Area.	11-635

		PAGE
Figure 11-469.	Centerline Profile for Port Columbus 10R.	11-637
Figure 11-470.	Approach 19-4BC, Normal.	11-644
Figure 11-471.	Approach 19-6BC, SBO Decreased to Broad Alarm.	11-645
Figure 11-472.	Approach 19-8BC, Middle Antenna Phase Retarded 15°.	11-646
Figure 11-473.	Approach 19-9BC, Middle Antenna Phase Retarded 15°.	11-647
Figure 11-474.	Approach 19-10BC, Middle Antenna Phase Advanced 15°.	11-648
Figure 11-475.	Approach 19-11BC, Middle Antenna Phase Advanced 15°.	11-649
Figure 11-476.	Approach 19-13BC, Normal, Without Clearance.	11-650
Figure 11-477.	Approach 19-21BC, SBO Phase Advanced 30°.	11-651
Figure 11-478.	Approach 19-22BC, SBO Phase Advanced 30°.	11-652
Figure 11-479.	Approach 19-23BC, Middle Antenna Phase Retarded 13°.	11-653
Figure 11-480.	Approach 19-24BC, Middle Antenna Phase Advanced 8°.	11-654
Figure 11-481.	Approach 19-25BC, Middle Antenna Phase Retarded 18°.	11-655
Figure 11-482.	Approach 19-26BC, Middle Antenna Phase Advanced 24°.	11-656
Figure 11-483.	Approach 19-27BC, Lower Antenna Phase Retarded 14°.	11-657
Figure 11-484.	Approach 19-28BC, Lower Antenna Phase Advanced 10°.	11-658
Figure 11-485.	Approach 19-33BC, Upper Antenna Phase Retarded 85°.	11-659
Figure 11-486.	Approach 19-34BC, Upper Antenna Phase Advanced 84°.	11-660
Figure 11-487.	Approach 19-35BC, Upper Antenna Phase Advanced 60° and 3 dB Attenuation in Clearance.	11-661
Figure 11-488.	Approach 19-37BC, Upper Antenna Phase Retarded 58° and 3 dB Attenuation in Clearance.	11-662
Figure 11-489.	Approach 19-38BC, Upper Antenna Attenuated 5 dB.	11-663

LIST OF FIGURES (CONTINUED)

		PAGE
Figure 11-490.	Approach 19-39BC, Upper Antenna Attenuated 10 dB.	11-664
Figure 11-491.	Approach 19-41BC, Middle Antenna Attenuated 2 dB.	11-665
Figure 11-492.	Approach 19-43BC, Middle Antenna Attenuated 3 dB.	11-666
Figure 11-493.	Approach 19-44BC, Lower Antenna Attenuated 2 dB.	11-667
Figure 11-494.	Approach 19-45BC, Lower Antenna Attenuated 3 dB.	11-668
Figure 11-495.	Approach 19-17BC, Normal-Low Approach.	11-669
Figure 11-496.	Approach 20-4BC, Normal, Null-Reference.	11-670
Figure 11-497.	Approach 20-5BC, Normal, SBO Adjusted for Normal Width.	11-671
Figure 11-498.	Approach 20-8BC, Normal, Null-Reference.	11-672
Figure 11-499.	Approach 20-9BC, Normal, Aircraft at 500' AGL.	11-673
Figure 11-500.	Approach 20-13BC, System Restored to Normal CEGS.	11-674
Figure 11-501.	Lower Antenna Attenuated 3 dB to Greater than 200% Alarm.	11-675
Figure 11-502.	Phase of Lower Antenna Advanced 15° to Twice Alarm.	11-676
Figure 11-503.	Phase of Lower Antenna Advanced 10° to Alarm.	11-677
Figure 11-504.	Sideband/Carrier Dephasing; -30°.	11-678
Figure 11-505.	Sideband/Carrier Dephasing; +30°.	11-679
Figure 11-506.	Phase of Middle Antenna Advanced 8° to Alarm.	11-680
Figure 11-507.	Phase of Middle Antenna Advanced 24° to Twice Alarm.	11-681
Figure 11-508.	Phase of Lower Antenna Retarded 14° to Alarm.	11-682
Figure 11-509.	Phase of Lower Antenna Retarded 19° to Twice Alarm.	11-683
Figure 11-510.	Phase of Middle Antenna Retarded 13° to Alarm.	11-684

LIST OF FIGURES (CONTINUED)

		PAGE
Figure 11-511.	Upper Antenna Retarded 50° to Alarm (Clearance Reduced 3 dB).	11-685
Figure 11-512.	Upper Antenna Advanced 60° to Alarm (Clearance Reduced 3 dB).	11-686
Figure 11-513.	Upper Antenna Attenuated 5 dB to Alarm.	11-687
Figure 11-514.	Upper Antenna Attenuated 10 dB to 133% Alarm.	11-688
Figure 11-515.	Lower Antenna Attenuated 2 dB to 114% Alarm.	11-689
Figure 11-516.	Middle Antenna Attenuated 3 dB to 170% Alarm.	11-690
Figure 11-517.	Middle Antenna Attenuated 2 dB to 128% Alarm.	11-691
Figure 11-518.	Phase of Upper Antenna Advanced 84° to Alarm.	11-692
Figure 11-519.	Normal Run.	11-693
Figure 11-520.	Comparison of Monitor Response to Measured Far-Field Response.	11-694
Figure 11-521.	Configuration for Making Probe Measurements.	11-699
Figure 11-522.	Jog-Held Probe Placement on an FA-8976 Antenna Element.	11-700
Figure 11-523.	Photograph of Magnetic Induction Probe.	11-701
Figure 11-524.	Schematic Representation of Magnetic Induction Probe.	11-702
Figure 11-525.	Element Dimensions for the FA-8976 Glide Slope Antenna.	11-705
Figure 11-526.	Coordinate System for Magnetic Field Analysis.	11-706
Figure 11-527.	Probe Measured Amplitude of Elements of the FA-8976 Antenna Versus Distance.	11-709
Figure 11-528.	Probe Measured Phase of Elements of the FA-8976 Antenna Versus Distance.	11-710

LIST OF FIGURES (CONTINUED)

		PAGE
Figure 11-529a.	Isometric Projection of Probe Jig.	11-713
Figure 11-529b.	Drawing of Probe Jig with Dimensions.	11-714
Figure 11-530.	Change in Capture Effect Glide Slope Path Angle (3.0° Normal) Caused by Antenna Dephasing.	11-715
Figure 11-531.	Change in Capture Effect Glide Slope Path Width (.7° Normal) Caused by Antenna Dephasing.	11-716
Figure 11-532.	Change in Capture Effect Glide Slope Path Angle (3.0° Normal) Caused by Signal Attenuation.	11-717
Figure 11-533.	Change in Capture Effect Glide Slope Path Width (.7° Normal) Caused by Signal Attenuation.	11-718
Figure 11-534.	Horizontal Free Space Radiation Pattern for Antenna Array.	11-720
Figure 11-535.	Measured Radiation Pattern for a Typical FA-8976 Antenna Along with FAA Specifications.	11-722
Figure 11-536.	Theoretical Three-Element Array Compared with APC FA-8976 Antenna - Amplitude Horizontal Pattern.	11-723
Figure 11-537.	Theoretical Horizontal Phase Pattern for Three-Element Array Compared with Measured Pattern for APC FA-8976.	11-724
Figure 11-538.	Simulated Radiation Pattern for a FA-8976 Antenna with a 3 dB Attenuation in the Third Element.	11-728
Figure 11-539.	Plot of Phase of a Simulated Radiation Pattern for a FA-8976 Antenna with a 3 dB Attenuation in the Third Element.	11-729
Figure 11-540.	Antenna Test Range Layout.	11-734
Figure 11-541.	The Tamiami Antenna Test Range.	11-735
Figure 11-542.	Impedance and VSWR Test Configuration.	11-735

		PAGE
Figure 11-543a.	The Antenna under Test as seen from the Far-Field Measurement Position.	11-736
Figure 11-543b.	The Far-Field Receiving Dipole as seen from the Far-Field Measurement Point.	11-736
Figure 11-544.	Probe Measurements on the APC FA-8976.	11-738
Figure 11-545a.	Horizontal Radiation Pattern for AIL FA-8651 S/N 126.	11-740
Figure 11-545b.	Horizontal Phase Pattern for the AIL FA-8651 S/N 126.	11-741
Figure 11-546a.	Horizontal Radiation Pattern for AIL FA-8651 S/N 132.	11-742
Figure 11-546b.	Horizontal Phase Pattern for the AIL FA-8651 S/N 132.	11-743
Figure 11-547a.	Horizontal Radiation Pattern for AIL FA-8651 S/N 132.	11-744
Figure 11-547b.	Horizontal Phase Pattern for the AIL FA-8651 S/N 153.	11-745
Figure 11-548a.	Horizontal Radiation Pattern for AIL FA-8651 S/N 160.	11-746
Figure 11-548b.	Horizontal Phase Pattern for the AIL FA-8651 S/N 160.	11-747
Figure 11-549a.	Horizontal Radiation Pattern for SCA FA-8730.	11-748
Figure 11-549b.	Horizontal Phase Pattern for the SCA FA-8730.	11-749
Figure 11-550a.	Horizontal Radiation Pattern for APC FA-8976.	11-750
Figure 11-550b.	Horizontal Phase Pattern for the APC FA-8976.	11-751
Figure 11-551.	Input Port TDR Trace - AIL, FA-8651 S/N 126.	11-753
Figure 11-552.	Input Port TDR Trace - AIL, FA-8651 S/N 132.	11-753
Figure 11-553.	Input Port TDR Trace - AIL, FA-8651 S/N 153.	11-753
Figure 11-554.	Input Port TDR Trace - AIL, FA-8651 S/N 160.	11-754
Figure 11-555.	Input Port TDR Trace, Scanwell FA-8730, S/N 9.	11-754
Figure 11-556.	Input Port TDR Trace, APC FA-8976, S/N C013.	11-754

IV. GENERAL TOPICS

A. New Tamiami Airport, Florida, Test Site.

LIST OF FIGURES (CONTINUED)

		PAGE
Figure 11-557a.	"Bubble Pad" Wrapped Around the Center Dipole of the AIL FA-8651 Glide Slope Antenna.	11-757
Figure 11-557b.	Shorted Center Dipole Test of the AIL FA-8651.	11-757
Figure 11-557c.	Spraying the Right Dipole Elements of the AIL FA-8651.	11-758
Figure 11-557d.	Injection of Water in the Feed Area of the Stripline of the AIL FA-8651.	11-758
Figure 11-558.	Polyurethane Foam Being Cut Away.	11-759
Figure 11-559.	Water Corrosion on the Left Dipole of the FA-8651.	11-760
Figure 11-560.	Corrosion on the Stripline Device.	11-761
Figure 11-561.	A Perturbational Influence Impacting the Glide Slope Antenna May be Expected to be Evident in the Far-Field Radiation, the Antenna's Monitor Port, and Possibly at the Input Port.	11-763
Figure 11-562.	Generalized Site in Rolling Terrain with Proposed Runway Extension.	11-770
Figure 11-563.	Generalized Case for Ground Plane Fill.	11-771
Figure 11-564.	Illustration of Truncated and Lowering Ground Plane.	11-774
Figure 11-565.	Illustration of Truncating and Lowering Ground Plane.	11-775

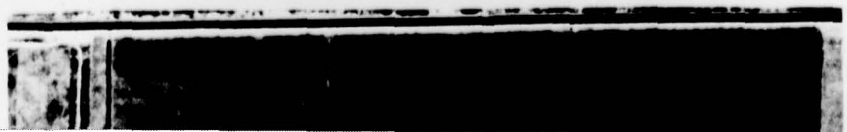

LIST OF TABLES

		PAGE
Table 4-1.	Harmonics Levels Present in 90 Hz Output.	4-25
Table 4-2.	Analysis Data.	4-29
Table 4-3.	Test Data.	4-32
Table 4-4.	List of Faults Induced in the Three Glide Slope Antennas Tested.	4-84
Table 4-5.	Difference Values Observed Between DC-3 and Beechcraft 35.	4-190
Table 4-6.	Reference Data.	4-192
Table 4-7.	Experimental Data.	4-193
Table 5-1.	Data Illustrating Localizer Processor Relative Performance of Collins 51R-3 and Ohio University Processor Working with a Narco NAV 11.	5-3
Table 5-2.	Clearance System.	5-5
Table 5-3.	Course System.	5-6
Table 5-4.	Course System Carrier Input Fed.	5-7
Table 5-5.	Antenna Feed Line Measurements.	5-19
Table 5-6.	Antenna Element Measurements.	5-20
Table 5-7.	Alford 12-Element Distributions.	5-21
Table 5-8.	Wilcox 14-Element Distributions.	5-22
Table 5-9.	Sideband Distributions as Measured on Antennas.	5-23
Table 5-10.	Carrier Distributions as Measured on Antennas.	5-24
Table 5-11.	System Normal - Antenna Amplitudes and Phases.	5-25
Table 5-12.	dB Taper for Three Frequencies with Alford and Wilcox Distribution Systems.	5-49

LIST OF TABLES (CONTINUED)

		PAGE
Table 5-13.	Microvolts at Receiver Input as Function of Distance from Array Along Extended Centerline at 1500 Feet Altitude.	5-50
Table 5-14.	Listing of Low Clearance Points.	5-62
Table 5-15.	Monitor Response Data, 108.5 MHz.	5-64
Table 5-16.	Monitor Response Data, 109.7 MHz.	5-65
Table 5-17.	Monitor Response Data, 111.9 MHz.	5-66
Table 5-18.	Monitor Response Data, 108.5 MHz.	5-67
Table 5-19.	Monitor Response Data, 109.7 MHz, May 14, 1975.	5-68
Table 5-20.	Monitor Response Data, 111.9 MHz.	5-69
Table 5-21.	Monitor Response to Phase Lags Just Sufficient to Initiate Alarm, 108.5 MHz.	5-70
Table 5-22.	Monitor Response to Phase Lags Just Sufficient to Initiate Alarm, 109.7 MHz.	5-71
Table 5-23.	Monitor Response to Phase Lags Just Sufficient to Initiate Alarm, 111.9 MHz.	5-72
Table 5-24.	Summary of Monitor Alarms Classified According to Figure 5-43.	5-73
Table 5-25.	Null Checks of Antenna Pairs.	5-74
Table 5-26.	Null Checks of Center Antenna Pairs.	5-75
Table 5-27.	Antenna Feedline Power.	5-75
Table 5-28.	Power at Monitor Box Inputs.	5-76
Table 5-29.	Course Transmitter Phasing.	5-76
Table 5-30.	Clearance Transmitter Phasing.	5-77
Table 5-31.	Carrier Equality Drift Measurements.	5-77

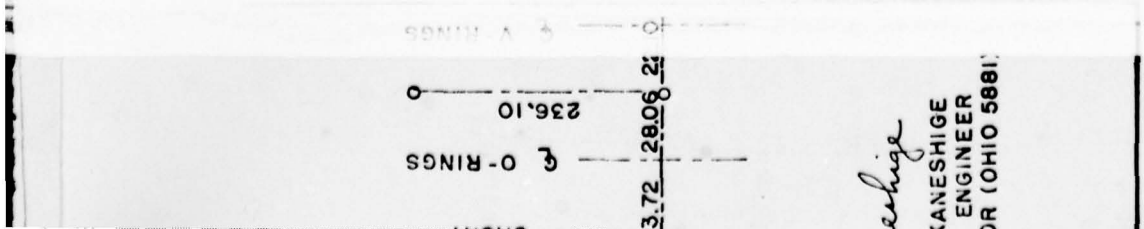

LIST OF TABLES (CONTINUED)

		PAGE
Table 5-32.	Antenna Phase Changes.	5-78
Table 5-33.	Transmitter Power Drift.	5-78
Table 5-34.	Simulated Clearance and Pre-Combiner Clearance Monitor Responses to 3 dB Fault Test at 109.7 MHz.	5-83
Table 5-35.	Simulated Clearance and Pre-Combiner Clearance Monitor Responses to 3 dB Fault at 108.5 MHz.	5-84
Table 5-36.	Simulated Clearance and Pre-Combiner Clearance Monitor Responses to 3 dB Fault Test at 111.9 MHz.	5-85
Table 5-37.	Simulated Clearance and Pre-Combiner Clearance Monitor Response to 30° Phase Fault at 109.7 MHz.	5-86
Table 5-38.	Simulated Clearance and Pre-Combiner Clearance Monitor Response to 30° Phase Fault at 108.5 MHz.	5-87
Table 5-39.	Simulated Clearance and Pre-Combiner Clearance Monitor Response to 30° Phase Fault at 111.9 MHz.	5-88
Table 5-40.	Monitor Alarms for Out-of-Tolerance Conditions of Course Centerline Alginment or Course Width.	5-91
Table 5-41.	Summary of Localizer Standard Flight Check.	5-95
Table 5-42.	Flight Check Results for Selected Faults.	5-96
Table 5-43.	Ground Orbit Results for Those Faults Which Showed Less than 2000 Microamperes Clearance or Excessive Course Width Changes.	5-98
Table 5-44.	Variable Phase Fault Data.	5-101
Table 5-45.	3 dB Attenuation Fault Data.	5-108
Table 5-46.	A Comparison of the Field Responses on Centerline and the Phase Faults Necessary to Produce a Monitor Alarm for the Three Test Frequencies.	5-135
Table 5-47.	Summary of Ohio University Flight Test Results.	5-144

noise is not a problem. Small aircraft traffic can under normal circumstances be diverted to a parallel, Runway 9 Right, and this has in past times permitted as many as 50 flight records to be collected without interruption due to other traffic.

LIST OF TABLES (CONTINUED)

		PAGE
Table 5-48.	Data Summary for Small Aperture Array for FAA Flight Test Data.	5-145
Table 5-49.	Data Summary for Medium Aperture Array for FAA Flight Test Data.	5-146
Table 5-50.	Summary of Usable Distance.	5-147
Table 5-51.	Carrier/SBO Dephasing.	5-148
Table 6-1.	Comparisons of CPU Running Time Between the Physical Optics (P.O.) Approximation and the High Frequency Theory of Diffraction Approximation (GTD).	6-40
Table 6-2.	Kodiak Path Angle Calculations by Two Different Methods.	6-74
Table 6-3.	Kodiak Path Width and Symmetry Calculations.	6-75
Table 6-4.	Calculated Path Angles for Untried Capture Effect System.	6-79
Table 6-5.	Comparison of Measured and Calculated Results for Kodiak NR and SBR Tests.	6-83
Table 6-6.	Path Data for Several Untried Systems Calculated Using Physical Optics.	6-84
Table 6-7.	Path Data for Several Untried Systems Calculated Using the Geometrical Theory of Diffraction.	6-85
Table 8-1.	Proposed Criteria for Glide Slope Recordings.	8-2
Table 9-1.	Predicted System Parameters at 110.497 MHz.	9-3
Table 11-1.	Summary of Reaction Time Delays.	11-14
Table 11-2.	Time in Seconds for Selected Angular Intervals of 1000 Foot Level Flight at 140 Kts.	11-14
Table 11-3.	Comparison of Calculated Values for Path Angle and Width to Measured Values.	11-16

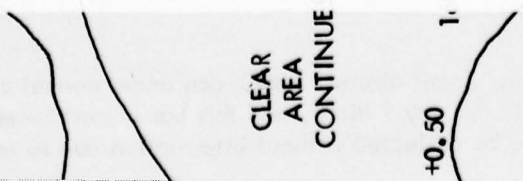

LIST OF TABLES (CONTINUED)

		PAGE
Table 11-4.	Fault Events.	11-153
Table 11-5.	Monitor Responses and Flight Check Results for 30 Faults Introduced into the Watts Glide-Slope System.	11-154
Table 11-6.	Effects of Changing Transmitters on the Watts System.	11-163
Table 11-7.	Effects of Antenna Misalignment.	11-163
Table 11-8.	Fault Events.	11-166
Table 11-9.	Monitor Response and Flight Check Results for Seven Faults Introduced into the Watts Glide-Slope System.	11-168
Table 11-10.	Responses to System Faults.	11-209
Table 11-11.	Nominal Values for Transverse Path Structure Seen at 5.4 Nautical Mile Range, 1600 Feet Altitude.	11-223
Table 11-12.	Path Angle and Width Values as a Function of Azimuth.	11-231
Table 11-13.	Listing of Quality Figures for Several Fault Conditions.	11-231
Table 11-14.	Comparison of Quality Figures for the Standard and Expanded Aperture Versions of the Watts Mark 3 Endfire Glide-Slope Antenna.	11-233
Table 11-15.	Quality Figures Derived from Records Taken of Transverse Path Structures Before and After Changes of Antenna Sections and Antenna Heights.	11-236
Table 11-16.	Figures of Merit for Perpendicular Structure.	11-293
Table 11-17.	Figures of Merit for Perpendicular Cut Data.	11-309
Table 11-18.	Calculated Performance Along Localizer Edge.	11-313
Table 11-19.	Summary of Fault Test Results.	11-319
Table 11-20.	Experimental Results.	11-327
Table 11-21.	Path Angle for Zero DDM in Degrees for Indicated Tilt and Displacement of Upper Antenna.	11-333

LIST OF TABLES (CONTINUED)

		PAGE
Table 11-22.	Comparison of Flight Test Data and Monitor Results.	11-342
Table 11-23.	Relative Amplitudes of Frequency Components in Detected SBO + CSB Signal as Function of C_a/A Ratio.	11-347
Table 11-24.	Relative Amplitudes of Frequency Components in Detected SBO + CSB Signal as Function of C_a/S Ratio where $C_a/ < 0$.	11-348
Table 11-25.	Null Reference.	11-349
Table 11-26.	Capture Effect.	11-350
Table 11-27.	Antenna Currents.	11-358
Table 11-28.	APCU Calibration.	11-360
Table 11-29.	Ground Monitor Data Site as Commissioned.	11-361
Table 11-30.	Ground Monitor Data Site as Commissioned.	11-362
Table 11-31.	Ground Monitor Data Theoretical Phasing.	11-379
Table 11-32.	Airborne Data.	11-386
Table 11-33.	Comparison of Near-Field/Far-Field Results for Various Fault Conditions.	11-494
Table 11-34.	Fault Data.	11-537
Table 11-35.	Azimuthal Data.	11-538
Table 11-36.	Far-Field and Monitor Response to Certain Fault Conditions.	11-547
Table 11-37.	System Outputs, Columbus 10R.	11-639
Table 11-38.	Far-Field Response.	11-642
Table 11-39.	Hand-Held Probe Measurements Taken from the Lower Antenna of a Commissioned Glide Slope Facility.	11-704

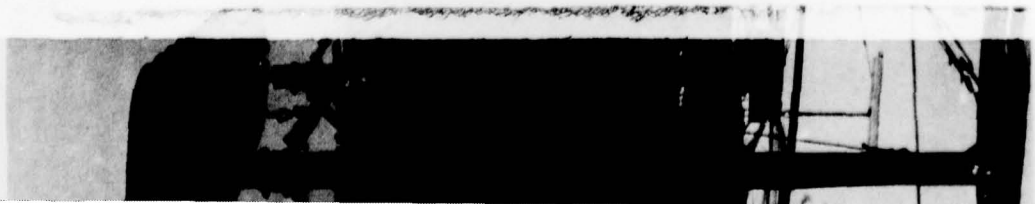

LIST OF TABLES (CONTINUED)

		PAGE
Table 11-40.	Matrix of Characteristics.	11-739
Table 11-41.	Normalized Fault Data for AIL FA-8651 S/N 126.	11-755
Table 11-42.	AIL Mark 1B Monitor Response to Lower Antenna Monitor Line Faults.	11-764
Table 11-43.	AIL Mark 1B Monitor Response to Middle Antenna Monitor Line Faults.	11-765
Table 11-44.	Budget for Reducing Fill.	11-773

aircraft contains instrumentation necessary for collecting data on localizer and glide slope facilities. The Ohio University DC-3 N4002 carries an independent complement of Avionics equipment for routine flight. This permits the aircraft to operate in an IFR

FOREWORD

Since 1963, the Avionics Engineering Center, Ohio University, has carried out research and engineering tasks involving Instrument Landing System improvements. The Federal Aviation Agency has supported this effort under a series of contracts with the Systems Research and Development Service and the Airway Facilities Service.

This Final Report describes results obtained during contract FA75WA-3549 through its 1974-78 period of performance. As will be seen in this document, a wide range of ILS analytical and experimental studies have been performed, with results pointing to improvements and alternative uses for existing ILS signals in space.

The Avionics Engineering Center is an integral part of the Department of Electrical Engineering at Ohio University. Accordingly, the Center is able to offer opportunities to graduate and undergraduate students and faculty members, for participation in the ongoing FAA-sponsored work. Benefits accrue to the FAA, the Center, and to the individual, through participation in real-world engineering tasks with their requirement for quality work on schedule. The FAA and the aviation industry benefit from the availability of trained and educated engineers with experience in existing and developmental navigation and communication systems.

B. The Minilab Airborne Data-Collection Systems. The Avionics Engineering Center utilizes light aircraft in ILS flight evaluation studies to minimize fuel usage and cost. To obtain flight recordings in such aircraft, fabrication of new instrumentation

I. INTRODUCTION

This report presents results of FAA-supported work on improvement, documentation and alternative utilization of ILS glide slope and localizer systems. Detailed report sections on each of the major work efforts are presented. Due to the diverse nature of project activity, results and conclusions are distributed throughout the report, in those sections where they apply.

The general conclusion is that the ILS remains a highly flexible and important navigational aid, with many possibilities for improvement and alternative use still waiting to be fully realized.

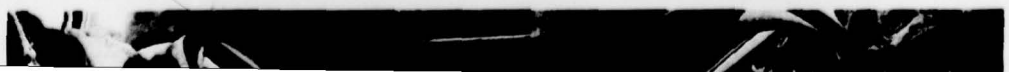

II. REVIEW

The research performed in fulfillment of the requirements of Contract DOT-FA75WA-3549 is described in three main categories of work statement set forth in the contract and its applicable modifications (Amend 1, Mod 3, Mod 9 and Mod 10). Each of these categories has several subdivisions covering details of the task. The purpose of this chapter is to provide a prospectus for the remainder of the report correlating tasks and accomplishments.

Work statement A, headed "General" calls for the establishment of an ILS (instrument landing system) test facility at an airport with low activity and near-perfect electromagnetic environment. Fulfillment of this requirement is discussed in Section A of Chapter IV of this report. Section B of Chapter IV describes the satisfaction of the next contract requirement (i.e., A.2) for ground and airborne test equipment necessary to check the radiated performance of the facilities.

Work statement A.3, as amended by Mod 3, calls for four (4) specialized test equipment studies: a) a prototype far-field localizer and glide slope recording instrument, b) a relative phase meter for the 90-150 Hz navigation tones, c) a coaxial cable fault detector and locator, and d) real-time remote test and performance evaluation equipment. Accomplishment of these tasks is detailed in Chapter IV, Sections C, D, E, and F, respectively.

Work statement A.4 envisioned the establishment of a marker test facility using Government-furnished equipment. Unavailability of the equipment precluded the accomplishment of this project with Government-furnished equipment; however, a marker was assembled at the Ohio University Airport and used as described in Section G of Chapter IV in carrying out work under work statement B.7.

Chapter V of this report describes the work specified by work statements B.1 and B.2 (as amended by Mod 9). Items from Mod 9 are specifically covered in Sections I and J of Chapter V.

The tasks described under work statement B.4 was initiated but then de-emphasized. The priority was lowered to the point where funding was insufficient to accomplish the task. Accordingly, the 8-loop and T-bar arrays were not furnished by the FAA. Similarly with work statement B.5, there was insufficient priority to allow this work to be fully accomplished. Chapter VII mentions the single frequency system for discrimination against multipath interference.

Chapter VIII discusses the study and analysis of overall air-ground ILS system performance standards required by work statement B.6.

Work statement B.7 (as amended by Amendment 1 and Mod 9) specifies work which was accomplished. It is described in Chapter IX, "Range Measurement from Localizer Signals".

The work delineated under work statement C.1 was accomplished at Tamiami with the exception of the broadside array tests which were conducted instead at Lynchburg, Virginia. Chapter XI discusses the work and the results. Work statement C.2 requirements were met with the work described in Sections F and I or Chapter XI. Sideband reference system work was not requested specifically; hence, no shorter mast was provided. Configuration suitable for sideband reference was made available on the 50-foot tower.

Extensive work was done consistent with work statement C.3. Three versions of the Watts endfire system were evaluated and the reporting is done principally in Section C of Chapter XI. The mobile facility identified in work statement C.4 was provided and the discussion of this facility is given in Section H of Chapter XI. Finally the investigation of effects ofseverely limited terrain and tilt of the terrain in the area of the first Fresnel zone for the image glide slopes is described in Chapter VI.

One of the glide slope receivers is modified to receive the telemetry signal from the theodolite on 329.0 MHz for RTT operation. Front panel RF padding is available on the Miniloh for the localizer RF and the glide slope RF independently.

III. SUMMARY

The work performed under Contract DOT-F A75WA-3549 represents continuous effort from October, 1974 through July, 1978. During this time a variety of tasks was completed using facilities at Ohio University, Athens, Ohio, and the operational test facility maintained at the Tamiami Airport, Florida. Additionally, work was performed as necessary at other locations or facilities throughout the United States.

At the outset of the contract, work was logically directed at those tasks which were to pave the way for the efficient and timely completion of other assigned tasks. This initial thrust included physical preparation of the Tamiami test facility for subsequent glide slope and localizer array evaluations. The test facility was flyable and fully operational by December, 1974. This preparation and set-up included operational null reference and capture effect glide slopes as well as V-ring and traveling-wave-antenna localizers. Work efforts involving these systems was completed by January, 1975.

Also started very early in the contract period was the work done on both airborne test and measurement equipment and a digital data collection system (DDCS). Work on the DDCS continued through December, 1976 while a continuing effort to provide improved airborne instrumentation was sustained during the entire contract period. Similarly, work on the limited and tilted terrain studies was maintained for the duration of the contract.

Work on several tasks began in January, 1975. Included in these tasks were capture effect monitors and range determination utilizing localizer signals. Work was completed on these efforts in June, 1976 and July, 1978, respectively. Additionally, engineering evaluations of newly-developed glide slope arrays such as the Watts Mark I, II and III arrays and the Westinghouse broadside system began in June, 1975 and continued for the duration of the contract period. During this same time frame a mobile glide slope facility was developed and used for on-site engineering analysis.

Tasks addressing non-destructive ILS fault testing, ILS control and display, and general ILS performance standards began in June, 1976. The study to recommend further development of ILS control and display techniques and equipment came to a close in November, 1976. Work on general system performance standards was completed in April, 1977 while non-destructive ILS testing efforts drew to a close by August of 1977.

This final report for DOT-FA75WA-3549 began with the submission of the proposed outline in January, 1977 and continued until the completion of contract commitments, amended by Modifications 1 through 15, in July, 1978.

IV. GENERAL TOPICS

A. New Tamiami Airport, Florida, Test Site.

1. Ground Facilities. Ohio University's Avionics Engineering Center for a number of years has maintained and operated several test sites for use in experimentally examining and evaluating instrument landing system localizer and glide-slope performance. Sites which are available include the Ohio University ILS Test Site, Runway 9L, at the New Tamiami Airport, Miami, Florida. This is the principal all-weather test site which has been used in support of the ILS work. Ohio University also has available test sites at the Ohio University Airport, Albany, Ohio and at the Houghton County Airport, Houghton, Michigan. These additional test sites are for use in evaluating particular environmental problems, snow and adverse weather conditions.

Figure 4-1 shows an aerial view of the site associated with Runway 9L at Tamiami. A number of possible test sites were evaluated and this particular one was selected as an outstanding example of an interference-free site for use in ILS field measurements. Ohio University has performed ILS work at this site for approximately four years. Following are comments relating to characteristics of the Tamiami Test Site. See Figure 4-2 for a site map and Figure 4-3 for survey control points.

1) The Runway 9L at the Tamiami Airport is 5000 feet long and 150 feet wide. An overrun area for this runway extends approximately 2000 feet in each direction beyond the threshold. If a simulated threshold is provided, then it is possible to work alongside the simulated runway and move onto the simulated runway without obstructing traffic flow on Runway 9L.

2) The location of the Ohio University Test Site at Tamiami Airport has been shown during four years of operation to be quite suitable for year-round use. Ohio University operations have taken place at this site during every calendar month of the year and there has not been one day without some flyable weather for data taking.

3) The Miami area is virtually pollution and fog free and permits excellent opportunities for optical tracking. Fog is infrequent and occurs in shallow layers during very early morning hours, but has been no problem. Pollution in the area is at a minimum. The worst problems are the Everglades burning and smoke drifting into the test area. In general the visibility is not reduced below five miles and the Everglades fires have not been found to be an operational problem.

4) The high density traffic area of Miami International Airport is well removed from the Tamiami Airport. The New Tamiami is a general aviation airport and the approach region and traffic pattern are free from large aircraft traffic problems. Experience has shown that cooperation with the ATC personnel has given minimum traffic problems when performing glide slope and localizer system measurements. The approach region extends out over the everglades in an unpopulated area and

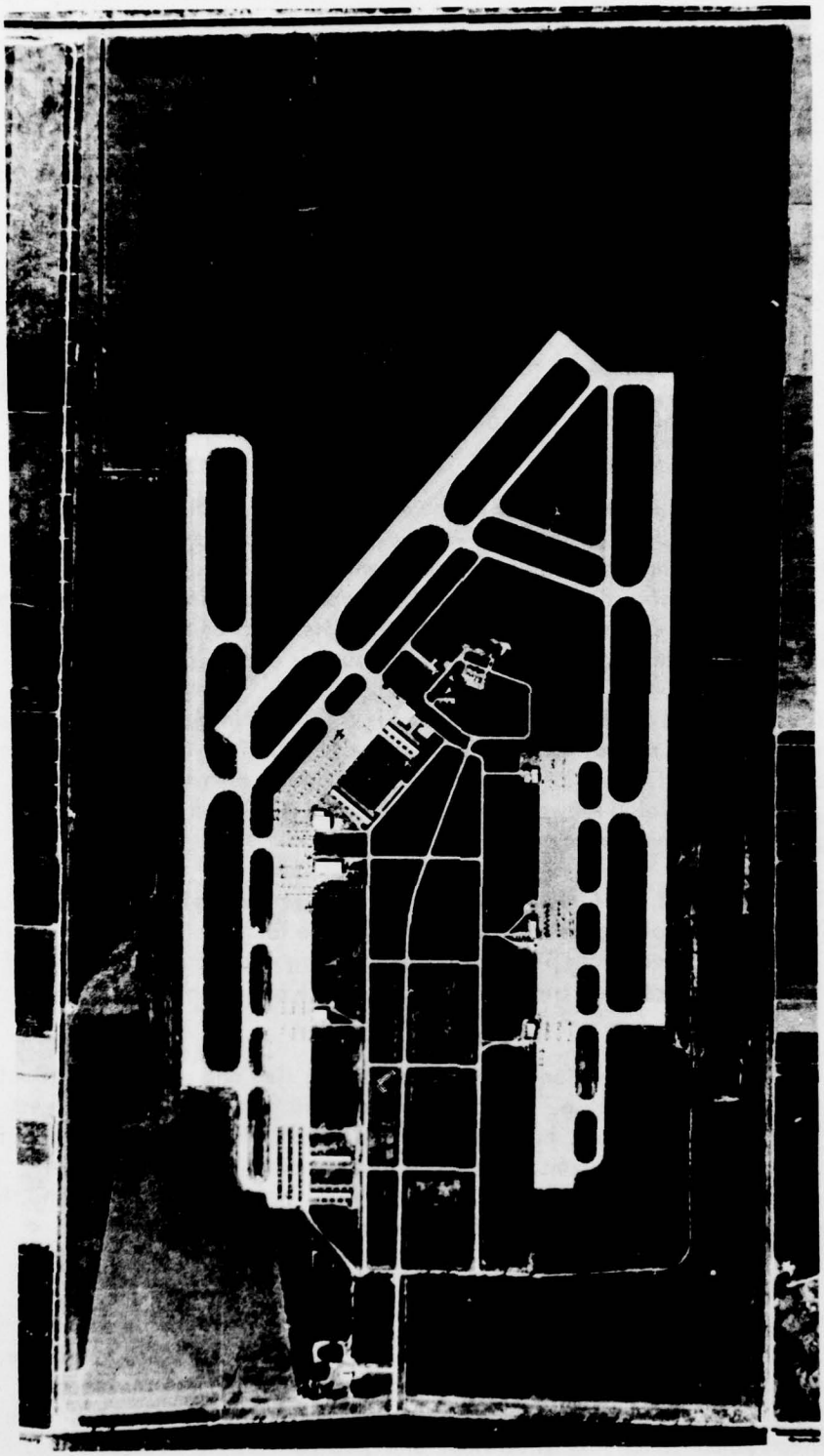

Figure 4-1. Aerial Photograph of Tamiami Site Prior to Installation of Facilities. (Courtesy of Coast Geodetic Survey.)

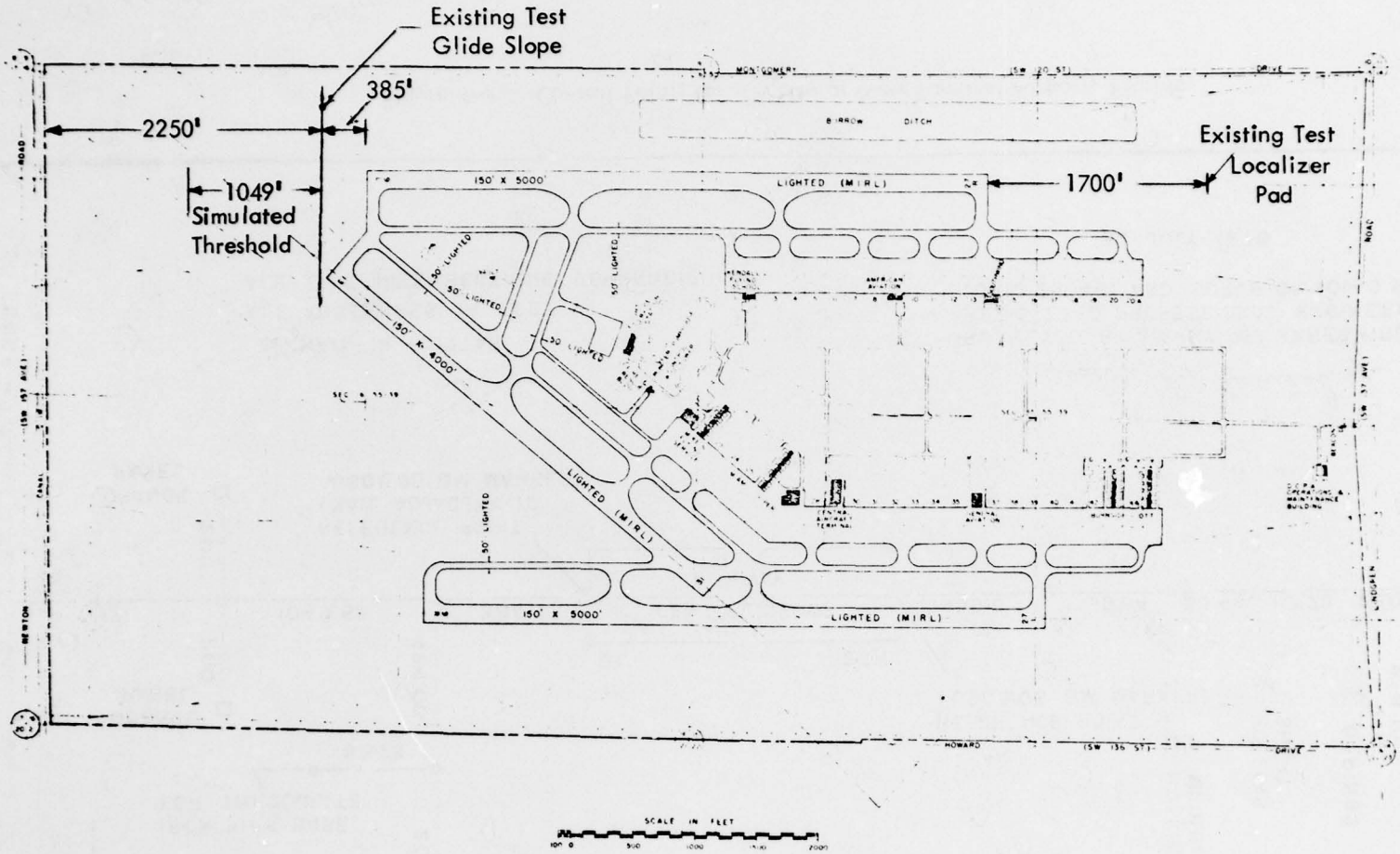

Figure 4-2. Ohio University Test Sites - New Tamiami Airport.

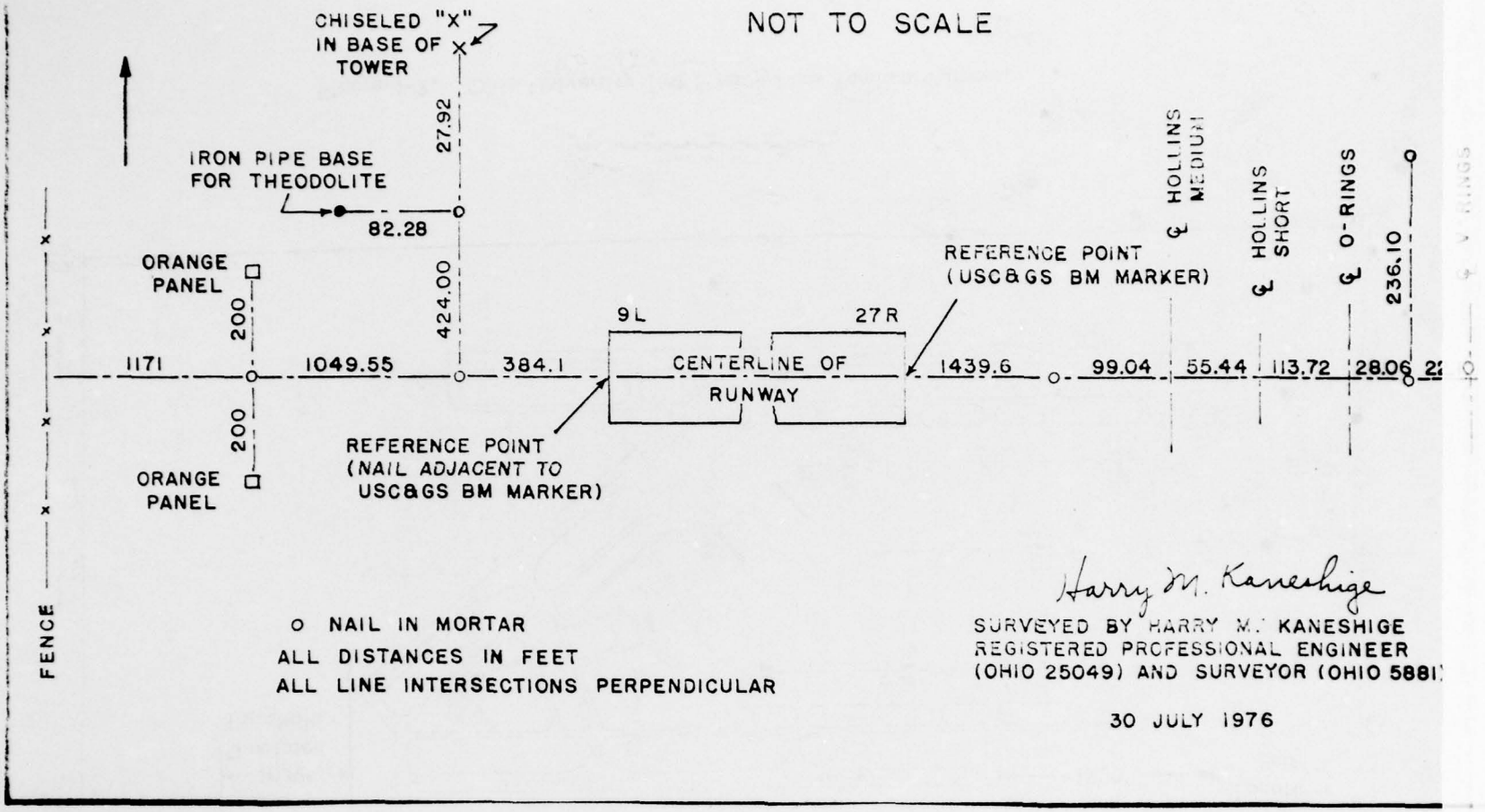

Figure 4-3. Control Points for ILS Site at New Tamiami Airport, Florida.

noise is not a problem. Small aircraft traffic can under normal circumstances be diverted to a parallel, Runway 9 Right, and this has in past times permitted as many as 50 flight records to be collected without interruption due to other traffic.

5) Full cooperation from local airport authorities is evident from the history of four years of operation. The Dade County Aviation Department, which operates the airport, and the local FAA Traffic Control and Flight Service Personnel have been extremely cooperative in providing assistance during local data collection missions.

6) No large hangars or reflecting surfaces exist on the New Tamiami Airport. The airport is relatively new. There are approximately six hangars on the airport, but these are modest in size, small by today's standards, and are well removed from the localizer and glide slope areas.

7) The terrain surrounding the localizer and glide slope sites is extremely flat. Florida typically is level country and the area on the Tamiami Airport is an excellent example of very large flat, grass sod areas. A contour map especially prepared to show the terrain and glide slope reflecting area is included (see Figure 4-4). Figures 4-5 and 4-6 illustrate the flat terrain and show typical site installations.

8) A clear localizer critical area exists. This includes a rectangular area extending approximately 800 feet either side of the centerline and 1500 feet each side of the localizer array. A 12 element V-ring localizer has been installed 1700 feet from the stop end of Runway 9L and is approximately 1500 feet from the boundary fence of the airport.

9) The glide slope critical area is 800 feet wide allowing 400 feet between the transmitting antennas and the boundary fence and 450 feet from the transmitting antennas of the runway centerline extended. The critical area extends approximately 2600 feet from the actual runway threshold. When a simulated threshold is established, a ratio of 100 feet to 1500 feet can be met. Evidence from four years of operation clearly shows that these critical areas are free from reflection problems.

10) Ohio University has in effect FCC licenses for ILS test operation at the Tamiami Site. They are:

Localizer	111.9 MHz, 108.5 MHz, 109.7 MHz
Glide Slope	331.1 MHz, 333.2 MHz, 329.9 MHz
Telemetry	329.0 MHz
Ground to Air Communication	123.2 MHz

Both aircraft used by Ohio University are licensed for the ground-to-air communications channel 123.2 MHz.

2. Flight Check Aircraft. Two specially instrumented aircraft are used in collecting airborne data. The first is a DC-3 formerly owned by the FAA. This

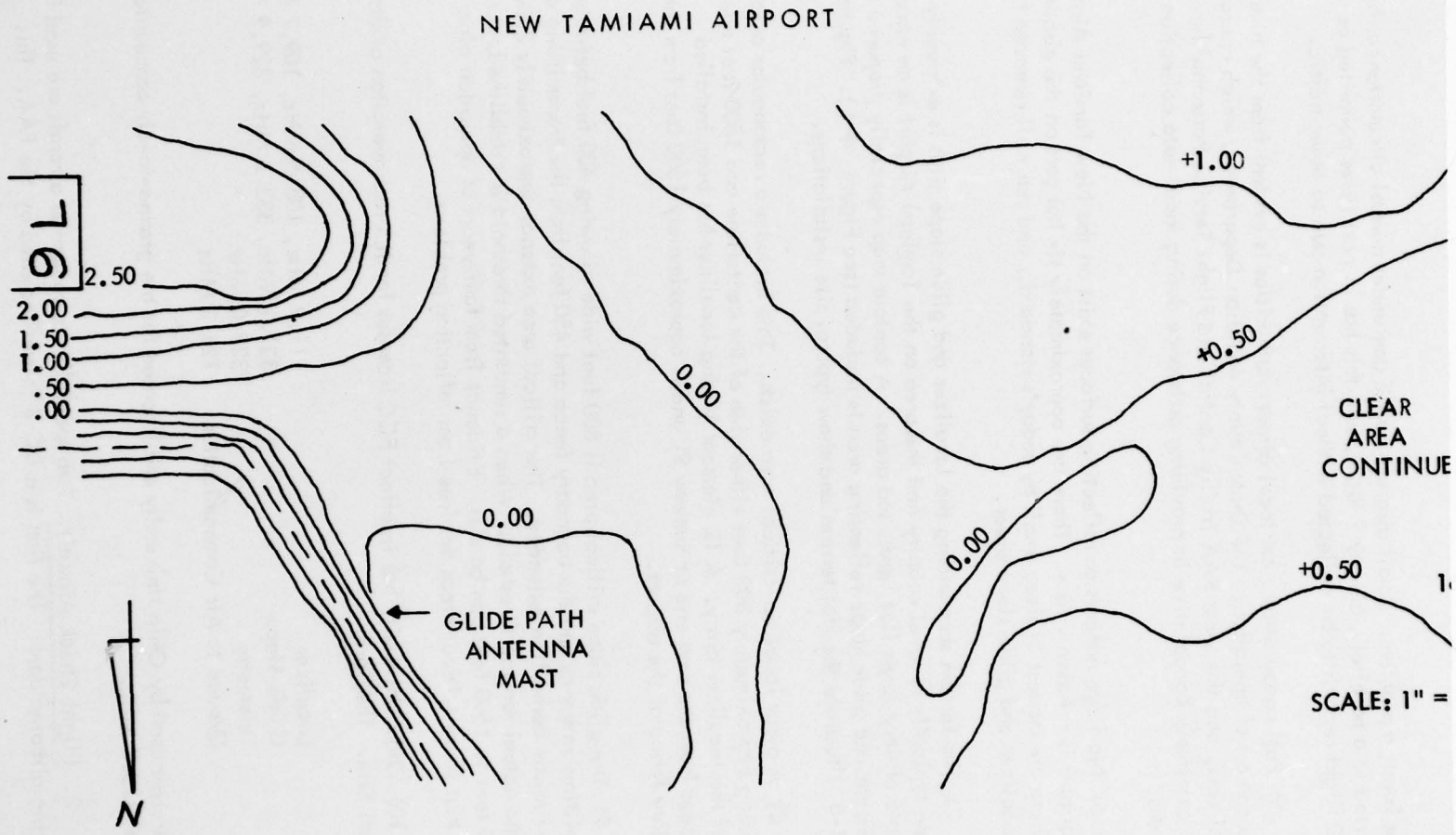

Figure 4-4. Contour Map, Tamiami, Glide Slope Area.

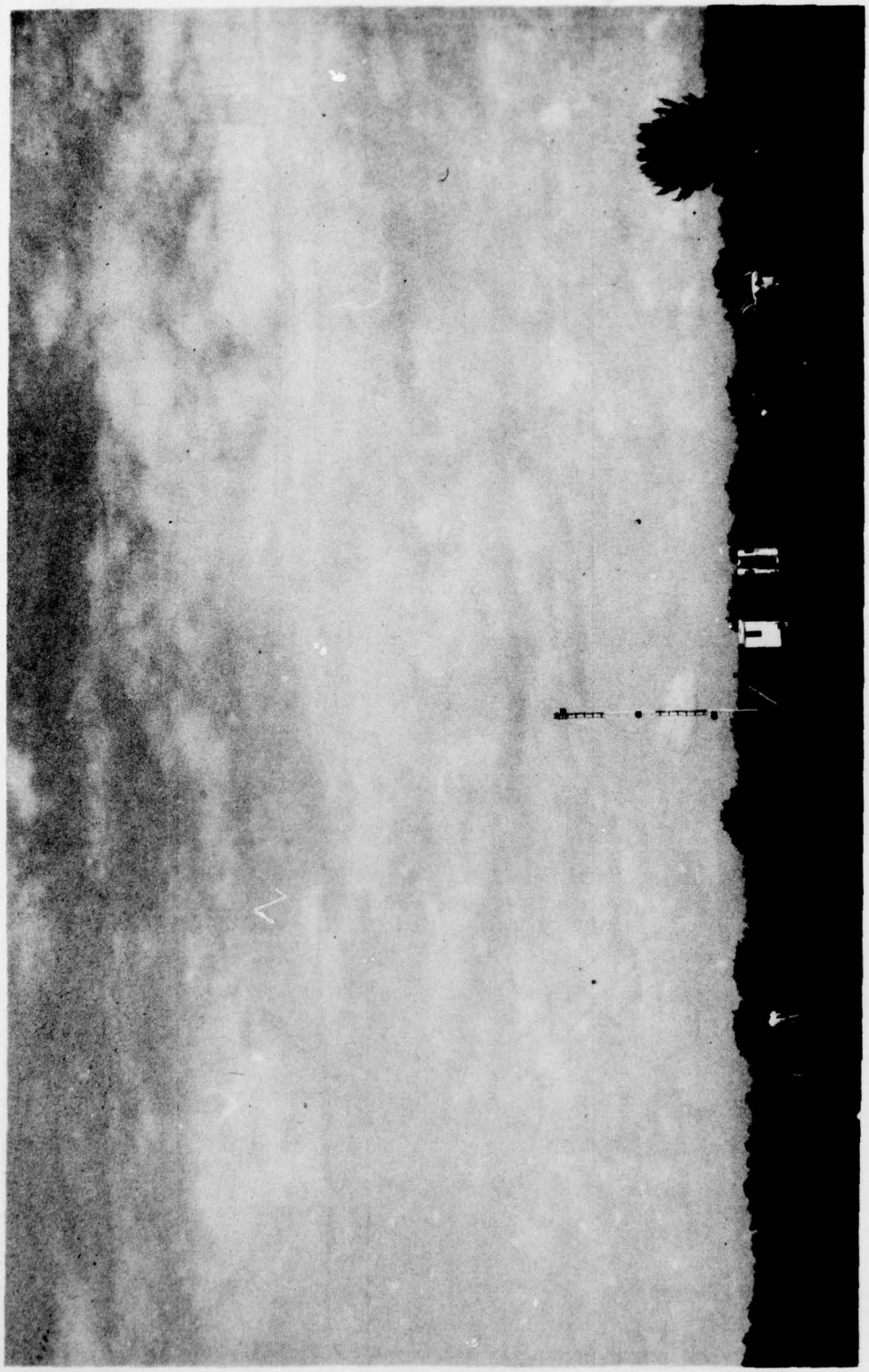

Figure 4-5. Capture-Effect Glide Slope Evaluation Underway at Tamiami.

Antenna of a Commissioned Glide Slope Facility.

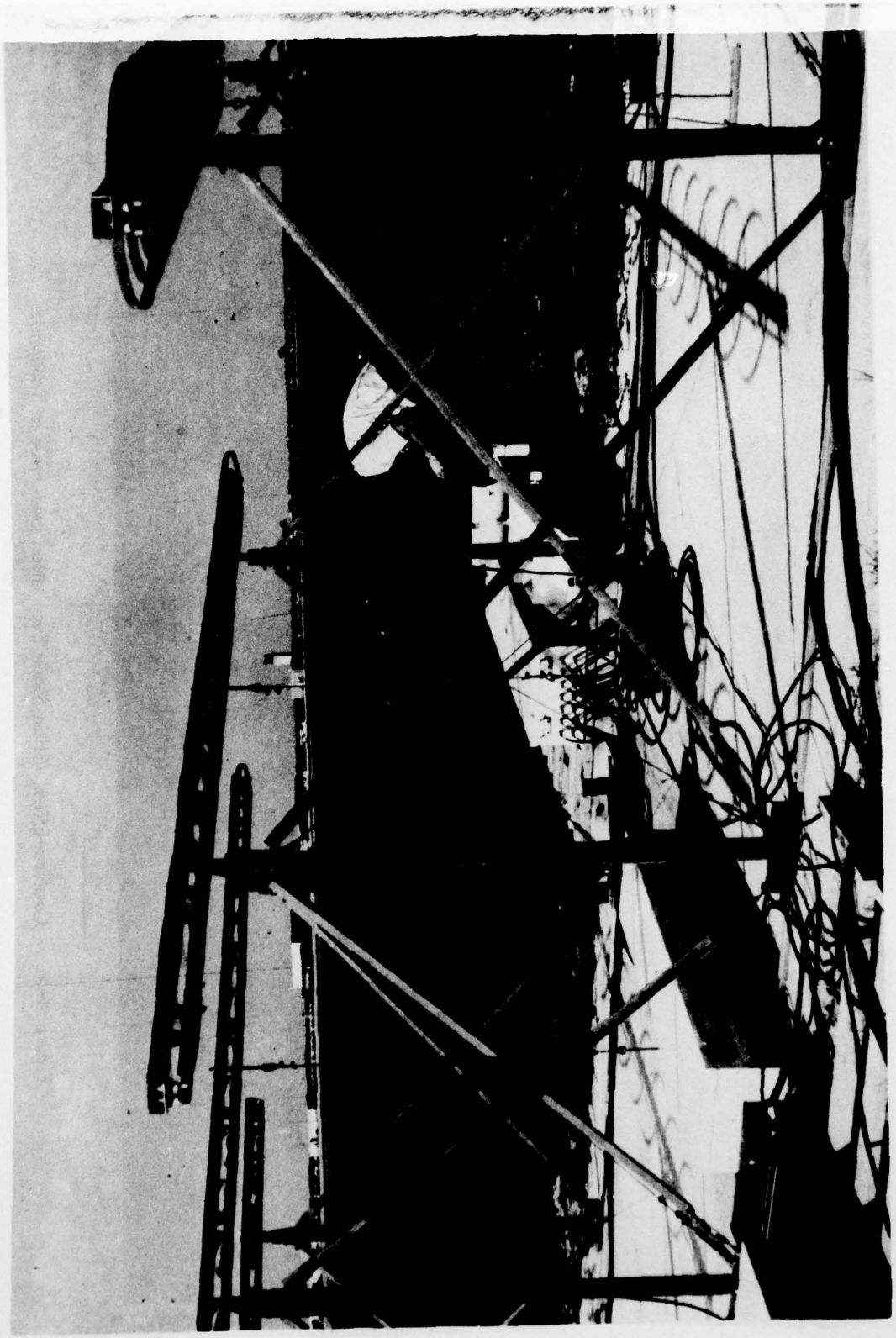

Figure 4-6. A Ohio University Research Technician is Shown Performing Repairs on Monitor Detector Used with 2-Frequency Localizer at Ohio University Test Site, Tamiami, Florida.

aircraft contains instrumentation necessary for collecting data on localizer and glide slope facilities. The Ohio University DC-3 N4002 carries an independent complement of Avionics equipment for routine flight. This permits the aircraft to operate in an IFR environment and to move from site to site in a normal manner. The aircraft is unrestricted for flight operation. A second DC-3 has recently been obtained from the FAA and NASA and is used as a backup.

The second operational aircraft, a Beechcraft Model 35 Bonanza, is equipped with special recording equipment in the form of a package known as the Ohio University Minilab (see Section IV-B of this report). This aircraft has the advantage of high speed, maneuverability, and low operating costs which provide definite advantages for certain types of data collection. It has the capability of receiving glide slope signals, telemetry signals, and localizer and marker beacon information. The information is processed using a differential amplifier to give indication of the true path position taken from glide slope and theodolite telemetry signals. This aircraft, while limited to carrying the minilab package, 1 observer, 1 operator, and the pilot, has six hours of endurance and has been found to be an extremely versatile aircraft not only for collecting data but moving the equipment and personnel to and from the test sites. It has an area navigation system which can, for example, provide a digital readout of miles to the Tamiami Site. Cost of operation of the Beechcraft is approximately 1/5 that of the DC-3.

Supporting these two aircraft is the Ohio University FAA approved repair station at Ohio University with a satellite at Tamiami which provides standards and calibration equipment for adjusting the airborne equipment to known references. These references may be traced to the National Bureau of Standards.

It is essential that the same references and standards be applied to measurements made with the Ohio University Aircraft and FAA flight inspection aircraft. Cross calibration with FAA facilities is maintained to insure compatability of Ohio University data with that collected by the FAA. This has been accomplished as a part of the Watts glide slope antenna measurement program at Tamiami, with flights by Ohio University and the FAA on the same day.

B. The Minilab Airborne Data-Collection Systems. The Avionics Engineering Center utilizes light aircraft in ILS flight evaluation studies to minimize fuel usage and cost. To obtain flight recordings in such aircraft, fabrication of new instrumentation has been necessary to operate within size and weight constraints of small aircraft without sacrificing data quality. The Minilab series of airborne data-collection systems has been developed to support ILS data collection missions.

1. Mark I Minilab. In 1972, the Mark I Minilab was developed, with basic glide slope and theodolite receiving and processing functions. The Mark I used a single Honeywell analog chart recorder for primary data output. The unit was designed to mount in place of the right front seat of the Beech Bonanza aircraft (Figure 4-7).

2. Mark II Minilab. In 1974, the Minilab Mark II was designed, recognizing the need for additional flight recording capability. This unit, pictured in Figure 4-8 featured a custom, precision glide-slope audio processor plus a backup glide-slope receiver, ground-telemetered event mark circuitry plus marker-beacon event channel, and localizer recording capability. Two Honeywell chart recorders provided a total of four output channels of data. Extensive flight experience was gained with the Mark II, which could be mounted either in the right front seat or, if a copilot is required for a mission, the Mark II could be put in place of a rear seat. The Minilab makes use of existing antennas, requiring no significant modification of the aircraft.

3. Mark III Minilab.

a. Introduction. The Mark III Minilab shown in Figure 4-9 is the airborne instrumentation package currently in use for ILS evaluations. The Minilab contains the necessary receivers and additional circuitry to receive, detect, compare, and record the parameters of interest for both glide slope and localizer signals. These parameters are the CDI, flag, and AGC. The Minilab also has RTT capability.

The size and weight of this package permit installation in light aircraft such as the Beechcraft Model 35.

b. Functional Description. The Mark III Minilab is an airborne instrumentation package equipped with six receivers. Two localizer, three glide slope, and a marker beacon receiver are used. One of the glide slope receivers is used primarily as a theodolite telemetry receiver.

The localizer receivers are a King KX-175 and a Narco NAV 11. Both the KX-175 and the NAV 11 cover 200 channels at 50 KHz spacing over a frequency range of 108.00 to 117.95 MHz. The VOR capability of the NAV 11 is not utilized in the Minilab. Additionally, the KX-175 COMM transceiver section covers 360 channels with 50 KHz spacing over a frequency range of 118.00 to 139.95 MHz. The transmitter power output is 5 watts into 50 ohms.

The glide slope receivers are Narco UGR-2/2A/3. The UGR-2 operates over 20 channels at a 300 KHz spacing from 329.3 to 335.0 MHz. The UGR-2A and the UGR-3 are 40 channel units with 150 KHz spacing over the same frequency range.

Figure 4-7. Mark I Minilab Showing Typical Aircraft Installation.

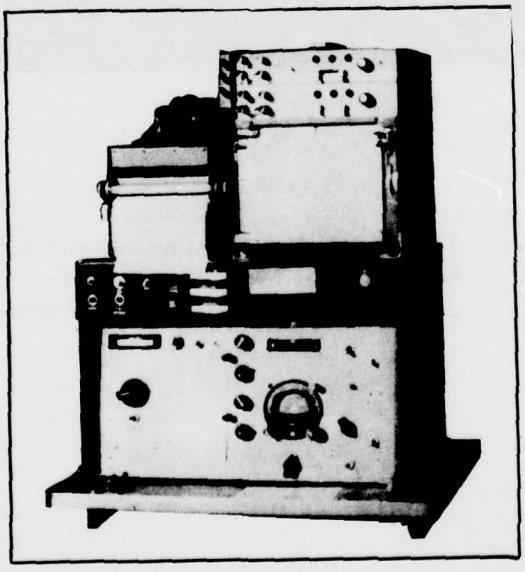

Figure 4-8. Mark II Minilab Flight Data-Collection Package.

Localizer Signals".

Figure 4-9. Mark III Minilab Installed in Beechcraft 35 Bonanza. The Mark III is the current flight data-collection package for ILS evaluations.

One of the glide slope receivers is modified to receive the telemetry signal from the theodolite on 329.0 MHz for RTT operation. Front panel RF padding is available on the Minilab for the localizer RF and the glide slope RF independently.

The AGC and the audio outputs from all five receivers are used. As shown in Figure 4-11, all AGC signals are buffered and presented to the AGC switching for selection. The selected AGC is then routed to the front panel AGC meter. The selection of the proper AGC signal for the meter is accomplished by using a three-bit digital control word from the AGC thumbwheel switch on the front panel. This three-bit word electronically switches the proper AGC signal to the AGC meter. The number appearing in the window of the thumbwheel switch is an indication of which of the available inputs has been selected. All signal switching in the Minilab is done in this manner. For example, a five appearing in the AGC thumbwheel window indicates that the theodolite AGC is currently displayed on the AGC meter.

Each of the five receivers has a precision audio processing card dedicated to it. The audio processors in the receivers are not used. Each processor card has a CDI and a flag output. As with the AGC selection, all CDI and flag signals are made available to their respective selection circuits. The CDI's for each of the receivers is also made available to the summer selection circuits. Two independent summers are available on the Minilab. Any two CDI signals may be summed in a summer. The summers would most often be used in RTT operation. The outputs of the two summers are available to the CDI selection circuits and may be displayed on the CDI meter.

Figure 4-10 shows the layout of the alarm panel on the Minilab. The audible alarm may be disabled but the appropriate alarm lamp remains lighted as long as the associated fault is present.

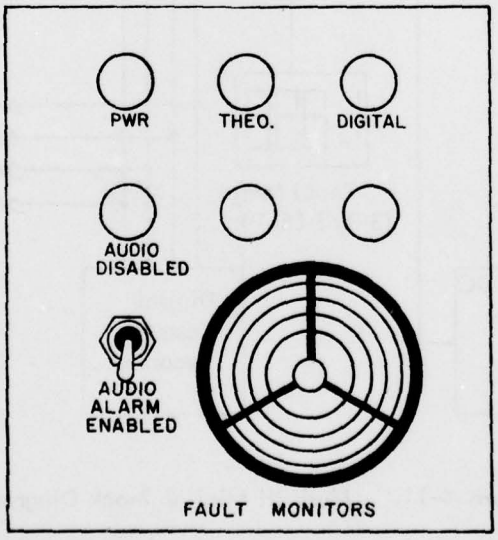

Figure 4-10. Alarm Panel.

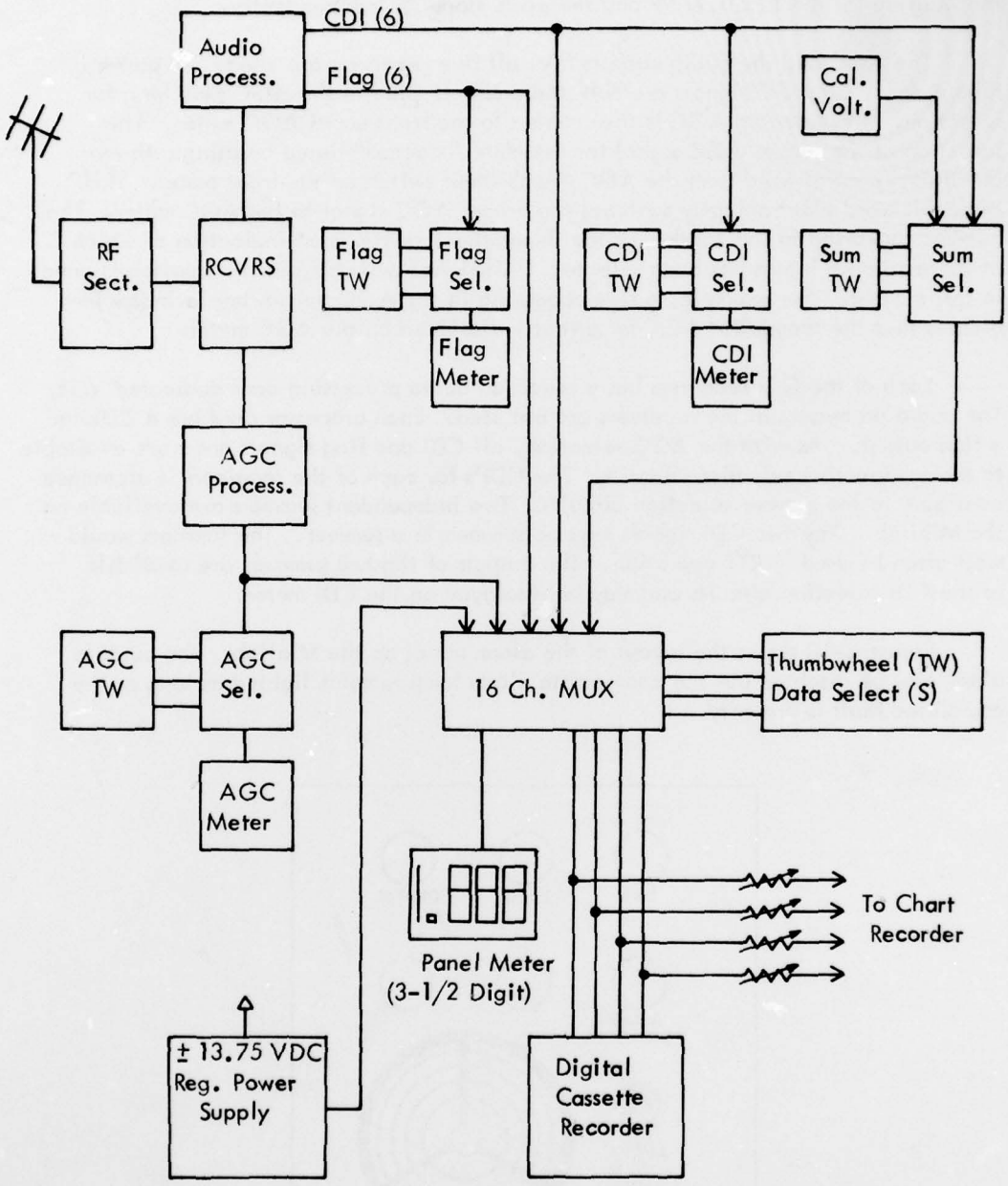

Figure 4-11. Mark III Minilab Block Diagram.

AD-A074 425 OHIO UNIV ATHENS DEPT OF ELECTRICAL ENGINEERING F/G 17/7
IN-SERVICE IMPROVEMENTS AND MODERNIZATION OF ALL COMPONENTS OF --ETC(U)
JUL 78 DOT-FA75WA-3549
UNCLASSIFIED EER-35-1 FAA-RD-78-112-1 NL

2 OF 8
AD
A074425

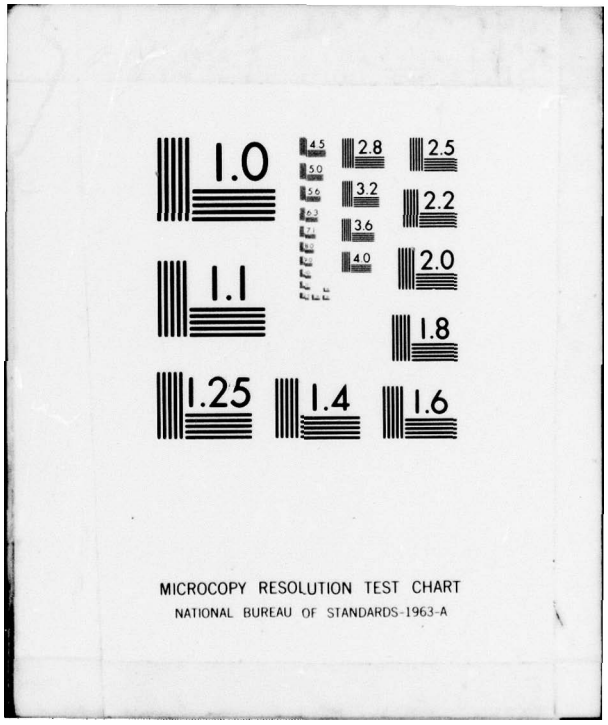
1.0
1.1
1.25
1.4
1.6
1.8
2.0
2.2
2.5
2.8
3.2
3.6
4.0
4.5
5.0
5.6
6.3
7.1
MICROCOPY RESOLUTION TEST CHART
NATIONAL BUREAU OF STANDARDS-1963-A

The power supply in the lower package of the Minilab converts the 12-14 VDC aircraft battery to 13.75 VDC REG for the receiver operation. Additional modular power supplies in the upper package provide supply voltages for all the instrumentation.

c. Mechanical Description. The Mark III Minilab is comprised of two packages that are electrically connected with a 32 pin umbilical cable. The upper (instrumentation) package is secured to the lower (receiver/power-supply) package by guide pins at the rear of the units and Dzus snaps at the front. The same mounting mechanism secures the lower package to a pallet that is mounted in the aircraft. The two analog chart recorders mount atop the upper package and lock in place with their appropriate snaps. This mounting system precludes the need for any specialized tools during installation.

The lower package houses all of the receivers and the 13.75 VDC regulated power supply. All receiver frequency selections and RF padding is done from the front panel of the lower package.

The upper package contains all the signal conditioning and instrumentation circuitry on three rows of plug-in printed circuit boards. All of the meters, switches, and indicators are located on the front panel for easy access by the operator. When secured together, the upper/lower package combination measures 21"L x 20"W x 16"H. The recorders add an additional 14" to the height of the system when mounted atop the Minilab.

A power inverter to operate the 110 VAC recorders is mounted beside the Minilab on the pallet. The total weight of the system including, all units, cables, and connectors is 185 lbs.

d. Specifications.

Size: 21"L x 20"W x 16"H (exclusive of recorders)

Weight: 185 lbs. (includes pallet, all units, all necessary cables and connectors)

Power Requirements: 18 amps total from 12-14V aircraft Batt.

Minilab: 10 amps
± 15V supply and inverter: 8 amps

Antenna Input Impedance: All antennas 50 ohm

*Sensitivity:

Glide Slope:

UGR-2/2A/3: An input signal of 2 μV at antenna is required for CDI to be ± 6% of a calibrated 78 μA at 100 μA.

*Sensitivity and flag sensitivity specifications are for that receiver at the appropriate antenna input. Any change in the preamplifier/splitter configuration of the Mark III Minilab may change these specifications.

Localizer:

Nav 11: 3 μV maximum for 6dB S+N/N ratio
King 175: 2 μV maximum for 6 dB S+N/N Ratio

Comm:

King 175: 2.5 μV for 6dB S+N/N ratio at 1 KHz and 30% modulation

*Flag Sensitivity:

Glide Slope:

UGR-2/2A/3: 1 μV maximum for 250 μA flag

Localizer:

Nav 11: 4 μV maximum for full flag
King 175: 3 μV maximum for full flag

**Frequency Range:

Glide Slope: 329.3 to 335.0 MHz, 20 channels at 300 KHz spacing
Localizer: 108.00 to 117.95 MHz, 200 channels at 50 KHz spacing
Comm: 108.00 to 135.95 MHz, 360 channels at 50 KHz spacing

Transmitter:

VHF power output: 5W into 50 ohms
Microphone: Carbon or dynamic (with preamp) to provide 120 mV rms 2 into 500 ohms
Duty Cycle: 1 min. on, 4 min. off

Audio Output: 5W

Analog Recorder Outputs: ± 7.5V DC max into high Z load (2K ohms min.)

Connectors:

Antennas: All BNC type
Umbilical Cable: Cannon type DAPL-32-34S and mate

*Sensitivity and flag sensitivity specifications are for that receiver at the appropriate antenna input. Any change in the preamplifier/splitter configuration of the Mark III Minilab may change these specifications.

**Glide slope receiver No. 5 has been modified for telemetry operation on 329.00 MHz (a non-standard glide slope frequency).

e. Antenna Requirements. Depending upon the type of data collection being done, the Mark III Minilab can have a requirement for as many as four separate RF inputs. All RF inputs to the minilab are made on the rear panel of the lower package and are of the BNC type. All antenna impedances are 50 ohms. The following four RF inputs may be required:

1) Glide Slope
2) Localizer
3) Communications
4) Marker Beacon

f. Digital Data Collection Subsystem (DDCS). The Digital Data Collection Subsystem is an integral part of the Mark III Minilab. Figure 4-12 shows a block diagram of the DDCS, including input signal selection, digitizer and multiplexer, and digital cassette tape recorder.

The DDCS consists of an eight-channel analog multiplexer, feeding an analog-to-digital converter and cassette recorder. Input can be selected from any of the parameters measurable by the Minilab. The event mark is permanently wired to one digital channel. Tape output consists of eight words of digital data per frame, with a sampling rate of 4 per second for each measured parameter. Any parameter which can be displayed in analog format using the chart recorders can also be digitized and recorded on cassette digital tape.

Figure 4-13 shows a test DDC run, using a glide slope CDI recording as a sample. Figure 4-14 is the analog trace of the CDI, recorded simultaneously. The DDCS graph was prepared by retrieving cassette data and decommutating the CDI word from each data frame using Ohio University's System/370 Model 158 computer. Then, the resulting data were plotted against an X-axis scale showing sample number. The excellent agreement between these two graphs illustrates the desirability of the digital system.

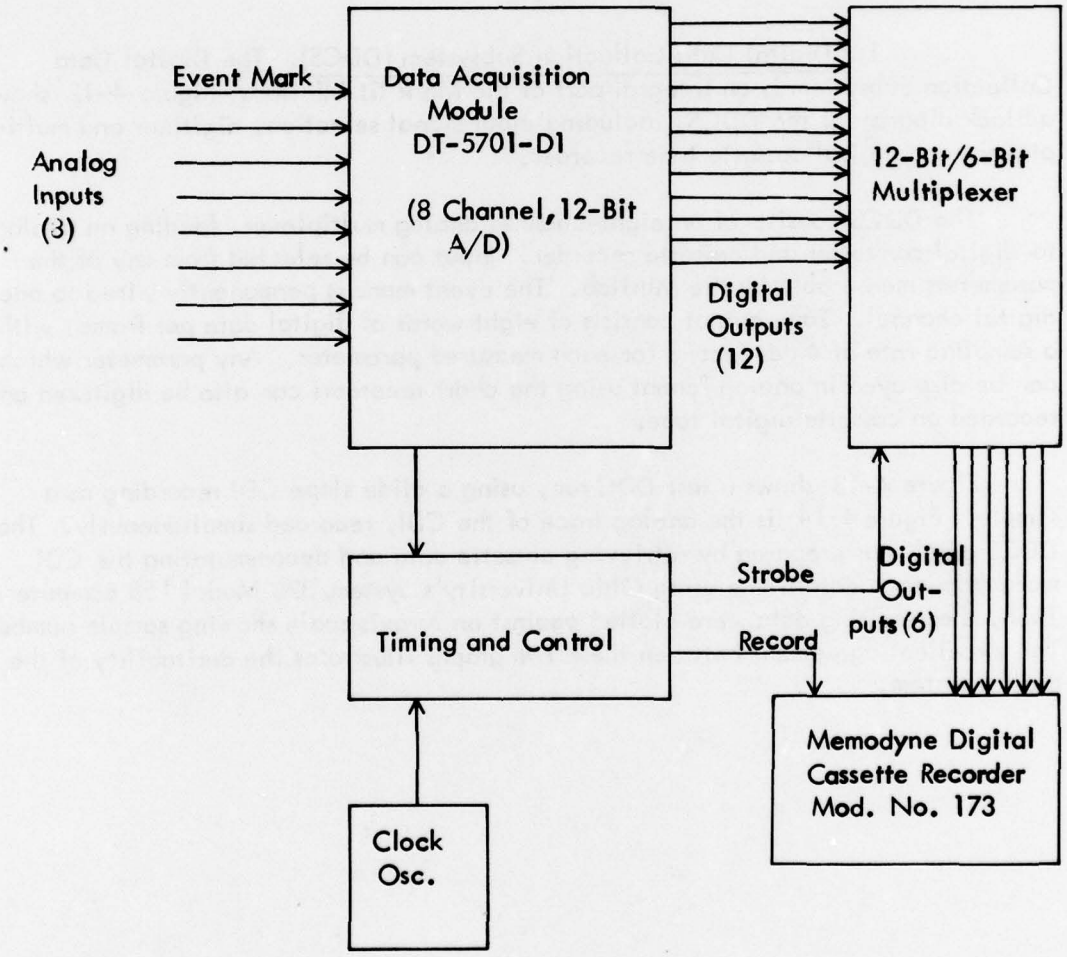

Figure 4-12. DDCS Block Diagram.

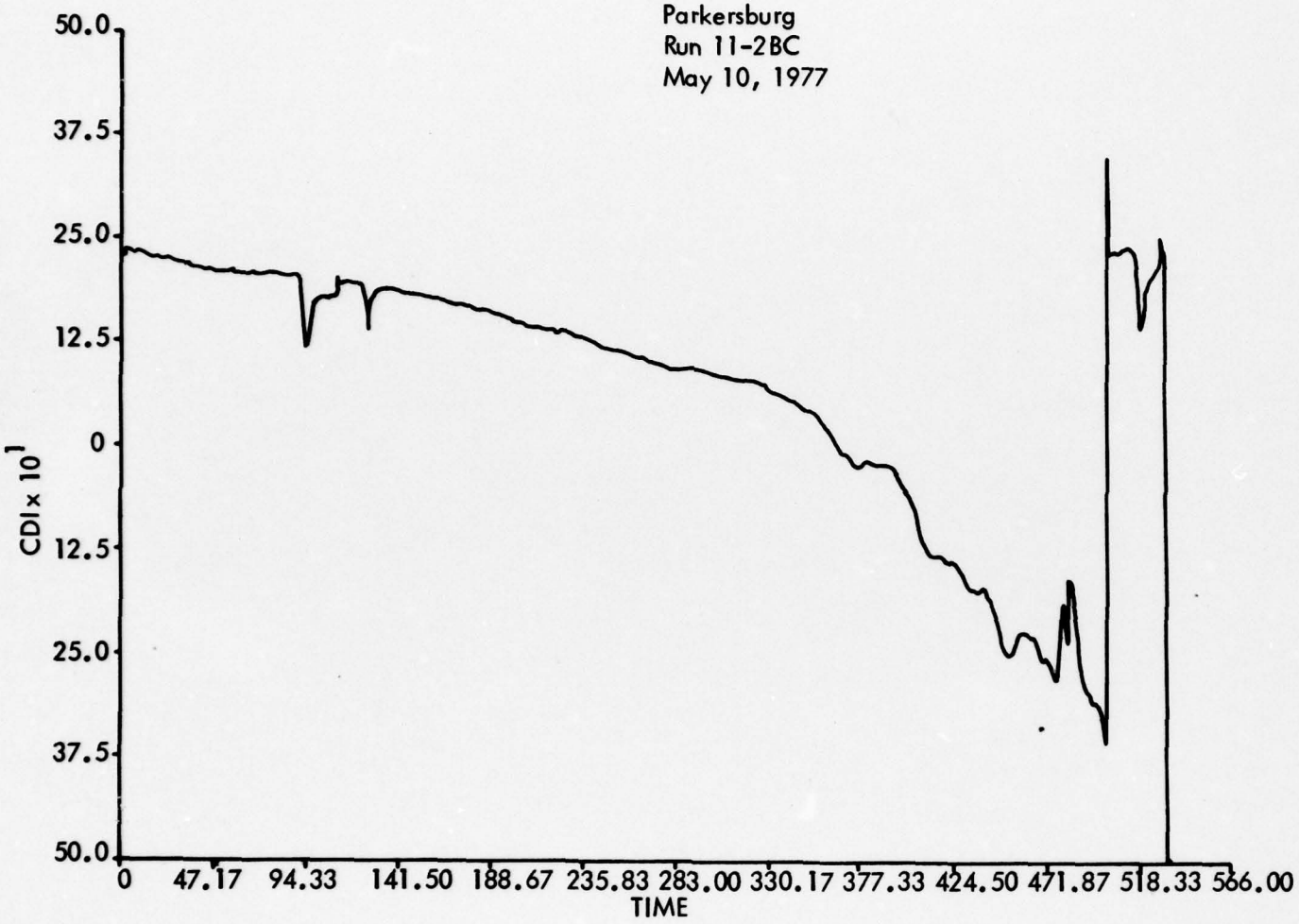

4-19/4-20

Figure 4-13. DDCS Sample CDI Output.

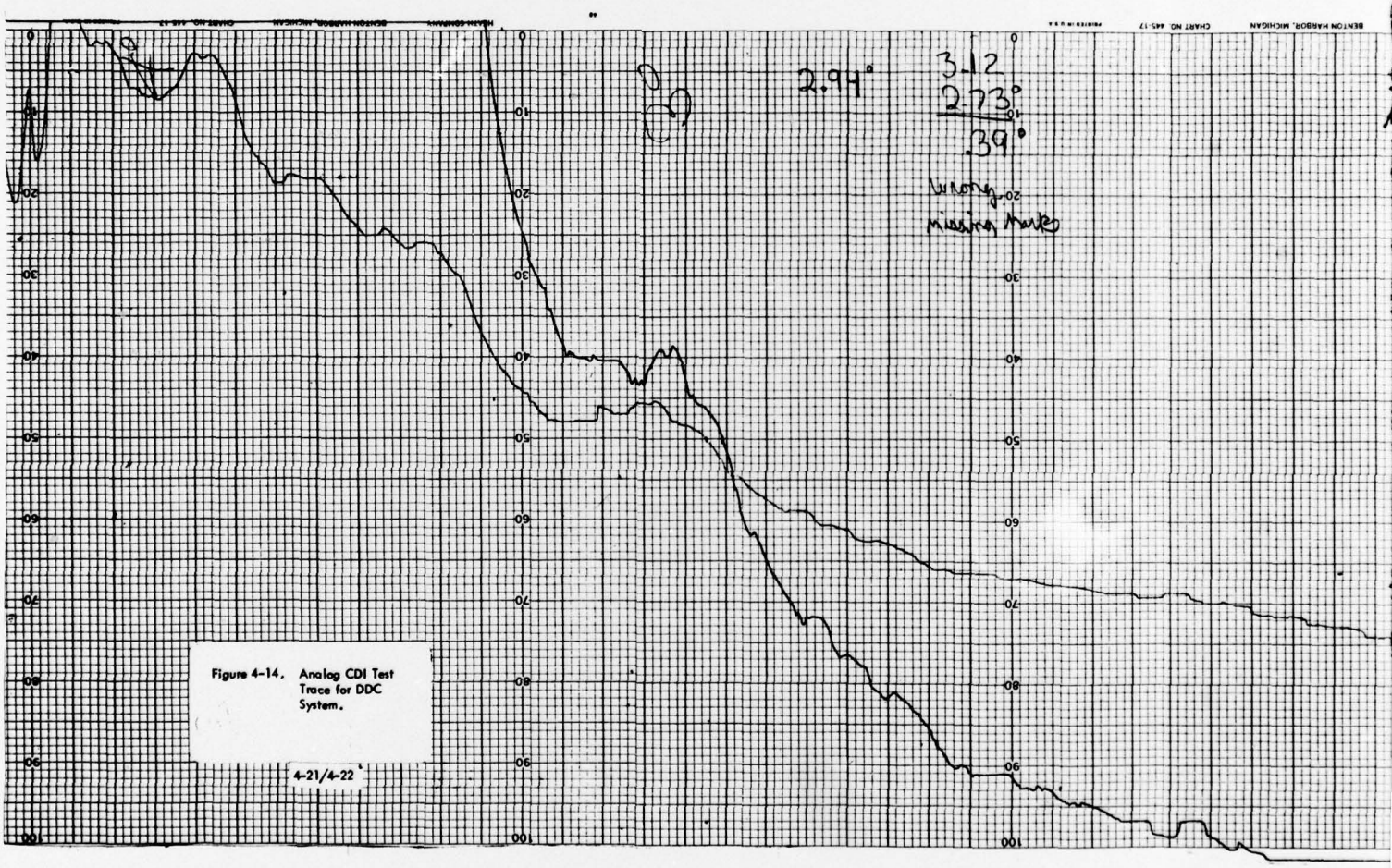

Figure 4-14. Analog CDI Test Trace for DDC System.

4-21/4-22

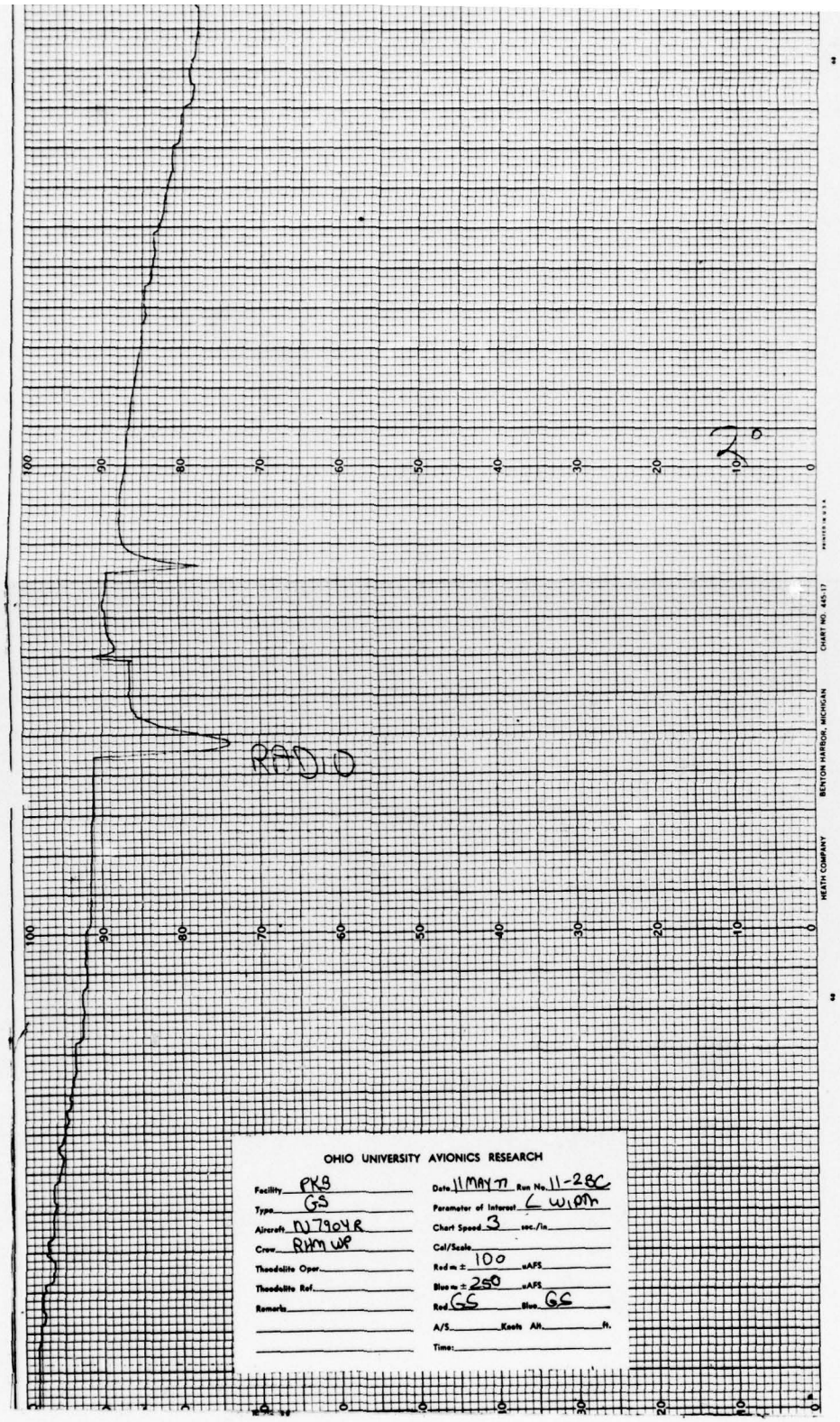
100
90
80
70
60
50
40
30
20
10
0
RADIO
HEATH COMPANY BENTON HARBOR, MICHIGAN CHART NO. 445-17
OHIO UNIVERSITY AVIONICS RESEARCH
Facility PKB
Type GS
Aircraft N7904R
Crew RHM WP
Theodolite Oper.
Theodolite Ref.
Remarks
Date 11 MAY 77 Run No. 11-28C
Parameter of Interest L WIDTH
Chart Speed 3 sec./in.
Cal/Scale
Red m ± 100 uAFS
Blue m ± 250 uAFS
Red GS Blue GS
A/S. Knots Alt. ft.
Time:

C. Phase-Locked Loop 90 Hz Generator.

1. Introduction. A below-path glide slope far-field monitor operating on the capture effect principle was designed and 12 prototype models built and delivered to FAA under a previous contract (FA69WA-2066). This device operates by producing a slightly offset carrier modulated by a 90 Hz signal and fed into a monitor receiver along with the glide slope signal from the monitor antenna. Capture by the 90 Hz modulated signal caused by a decrease in the glide slope signal being monitored produces a dramatic change in the DDM shown by the monitor CDI. In order to use these monitors where the navigation tones are not directly derived from the power line frequency, it becomes necessary to generate a 90 Hz signal and to lock it in phase with the 90 Hz of the transmitted signal.

2. Basic Design. 90 Hz in the audio recovered from the glide slope signal is used as a reference in a special phase locked loop to control an Intersil 8038 voltage controlled oscillator (VCO). This VCO has square, triangular, and sine wave outputs, the sine being approximated by first integrating the square wave and then switching the slope of the resulting triangular wave to approximate the sine with less than 1% harmonic distortion. The integration process results in a 90° phase relation between square and sinewave outputs. This is useful since in this design phase lock occurs when the square wave is 90° out of phase with the reference sinewave thus making the VCO sinewave in phase with the reference.

Two operational amplifiers connected as precision half-wave rectifiers of opposite polarity have their outputs added by a third operational amplifier connected as a summer. These three amplifiers thus constitute a class B push-pull stage with no crossover distortion. The recovered audio from the glide slope signal is applied to the two inverting inputs in phase.

The square wave from the VCO is added to these inputs through a phase splitter and, since its amplitude is always greater than that of the audio it suppresses both outputs when it causes the input polarity to be that not passed by the rectifiers. On the alternate half cycles of the square wave diodes block it from the inputs allowing only the audio signal to reach the outputs. This action multiplies the audio by the square wave.

The audio is also fed directly to the summer without inversion through the 100K resistor (cf. Figure 4-15). Since this input resistor to the summer is twice the value of the other two (each 49.9K + the output resistance of the rectifiers) the overall effect is to multiply the audio by a zero average unity peak-to-peak square wave.

It can be shown by multiplying the audio reference, $A\sin 2\pi 90t + B\sin 2\pi 150t$, by the series expansion of the square wave, $0.25\pi(\cos\omega t - (\cos 3\omega t)/3 + (\cos 5\omega t)/5 - \ldots\ldots)$, term by term, that the lowest frequency present is (90 - f) where f is the square wave fundamental frequency. The next lowest frequency is (150 - f) which is about 60Hz.

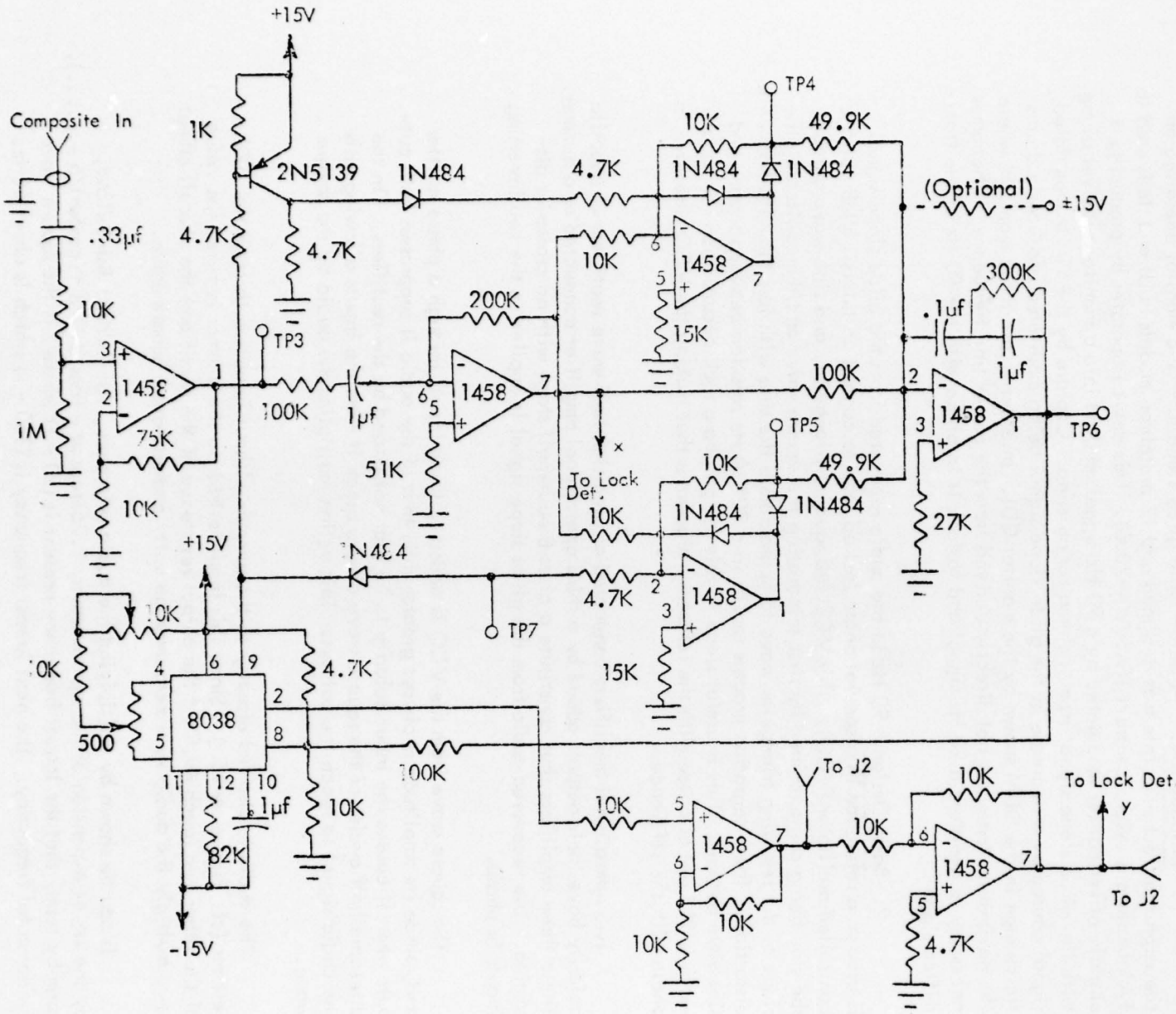

Figure 4-15. PLL 90 Hz Generator.

A low-pass filter is used to remove the higher frequency terms and the lowest frequency is used to adjust the frequency of the VCO.

Similarly it can be shown by inserting a phase angle term in the above term by-term multiplication that this feedback loop will lock the phase of the square wave to the 90 Hz component of the audio in quadrature thus locking the VCO sine wave in phase with the reference.

3. Results. Using this design approach, a phase locked loop realization (Figure 4-15) was built and tested. The finished circuit performed up to the desired standards:

1. No more than 1% total harmonic distortion due to frequency modulation of the VCO by the phase detector.

2. The fastest possible loop transient response commensurate with the harmonic distortion requirement of 1.

3. Type II system so that phase error is independent of reference frequency (within limits).

Laboratory tests showed that a small step change in reference phase is followed by the output in less than a second.

Table 4-1 gives measured values of harmonic distortion due both to frequency modulation and to distortion inherent in the VCO sine approximation.

Frequency	DB Amplitude Relative to 90 Hz Output	Amplitude as a % of 90 Hz Output
30	-43.5	0.67
60	-52.0	0.25
90	0.0	100.
120	-50.0	0.32
150	-42.2	0.78
180	-36.8	1.45
270	-46.4	0.48
630	-48.0	0.40

Square root of the sum of the squares (RSS) total harmonic distortion (THD) based on the predominant harmonics listed above: 1.93%

Table 4-1. Harmonics Levels Present in 90 Hz Output.

D. The 90-150 Hz Phase Measurement Device.

1. Introduction. The purpose of the device described in this section is to measure the phase relationship between the 90 Hz and 150 Hz ILS navigation tones. The device is entirely self-contained and requires no external equipment for readout after initial calibration. The task is accomplished using minimum circuitry by filtering to separate the 90 Hz and 150 Hz tones, interfacing the tones to digital circuitry, phase detection, and amplification and readout.

A 90-150 Hz phase measurement technique has been demonstrated. The small amount of hardware required and consequent low-power requirement lend the device to portable use. This device should be very useful in the initial set-up of navigational systems requiring a phase measurement of 90 Hz and 150 Hz tones.

2. Discussion.

a. Filtering. For test purposes two Burr-Brown active bandpass filters were used to separate the two frequencies. This could also be accomplished using any good bandpass filter system.

b. Interfacing. The circuit shown in Figure 4-16 was used for interfacing both frequencies. To interface the sine wave output from the 90-150 Hz generator or from the audio detectors in a navigation system, a CMOS 4050 non-inverting buffer was used. The buffer was used as an amplifier with high gain and the output is clipped at a convenient logic level. The logic levels chosen were five volts and zero volts. The input level on the 4050 may be at a higher level than the supply voltage but the output level varies only between supply voltage levels.

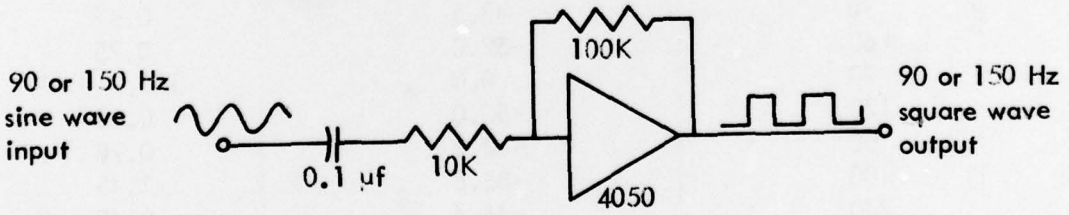

Figure 4-16. Interface Circuit.

c. Phase Detection. The Motorola MC 4044P Phase/Frequency detector was used for phase detection. The MC 4044P consists of two phase-frequency detectors, a charge pump, and amplifier. Only phase detector number one was used for this device. Figure 4-17 illustrates the action of this phase detector.

A computer program was developed for analysis of the phase detector using unequal input frequencies. For the program and the actual circuit, 90 Hz was chosen as the reference input and 150 Hz as the variable phase input.

The "in phase" point of the two signals is defined as the point at which both waveforms pass through zero with either positive or negative slope simultaneously. Plotting the two waveforms, it is seen that they will be in phase every third period of the 90 Hz waveform and every fifth period of the 150 Hz waveform. The maximum amount of phase shift that may occur before the waveforms are back in phase is one-third the period of the 150 Hz signal or 120°. This is true whether the 150 Hz signal is leading or lagging the 90 Hz signal. This maximum phase shift was used in the computer analysis to determine that the output waveform of the MC 4044P phase detector has an average value monotonic in relation to the phase shift between zero and 120°.

The analysis determined that a near-linear relationship exists between the average output and the amount of phase shift for the case of a 90 Hz reference and a 150 Hz variable phase input. See Table 4-2 and Figure 4-18.

d. Amplification and Readout. An operational amplifier circuit was used to interface the phase detector signal to analog form for measurement. Since the output waveform area in one period is proportional to the phase shift the average or DC voltage is also proportional. For test purposes the output was amplifier using an LM 741 operational amplifier and then measured directly using a DC voltmeter. The circuit of Figure 4-19 was used for this purpose.

e. Testing. The circuit of Figure 4-20 was used for testing and data collection.

The phase of the 150 Hz signal was shifted in 10° increments in relationship to the 90 Hz signal. The test data obtained is in Table 4-3 and a plot of the difference in voltage and the phase appears in Figure 4-21. The data obtained shows that the circuitry gives a usable output which with a properly calibrated meter gives a direct readout of the phase relationship. Figure 4-22 is the schematic diagram of the test circuitry.

f. Field Use. An actual field model of the 90-150 Hz phase detector was not constructed. However, as seen from the schematic diagram of Figure 4-22 and the block diagram of Figure 4-23, a field model of the circuit could be constructed in a very small package. The use of the detector in the field would require only that the technician connect the 90-150 Hz detected ILS audio to the device and then read the phase directly. When the phase shift is zero the reading would be a minimum.

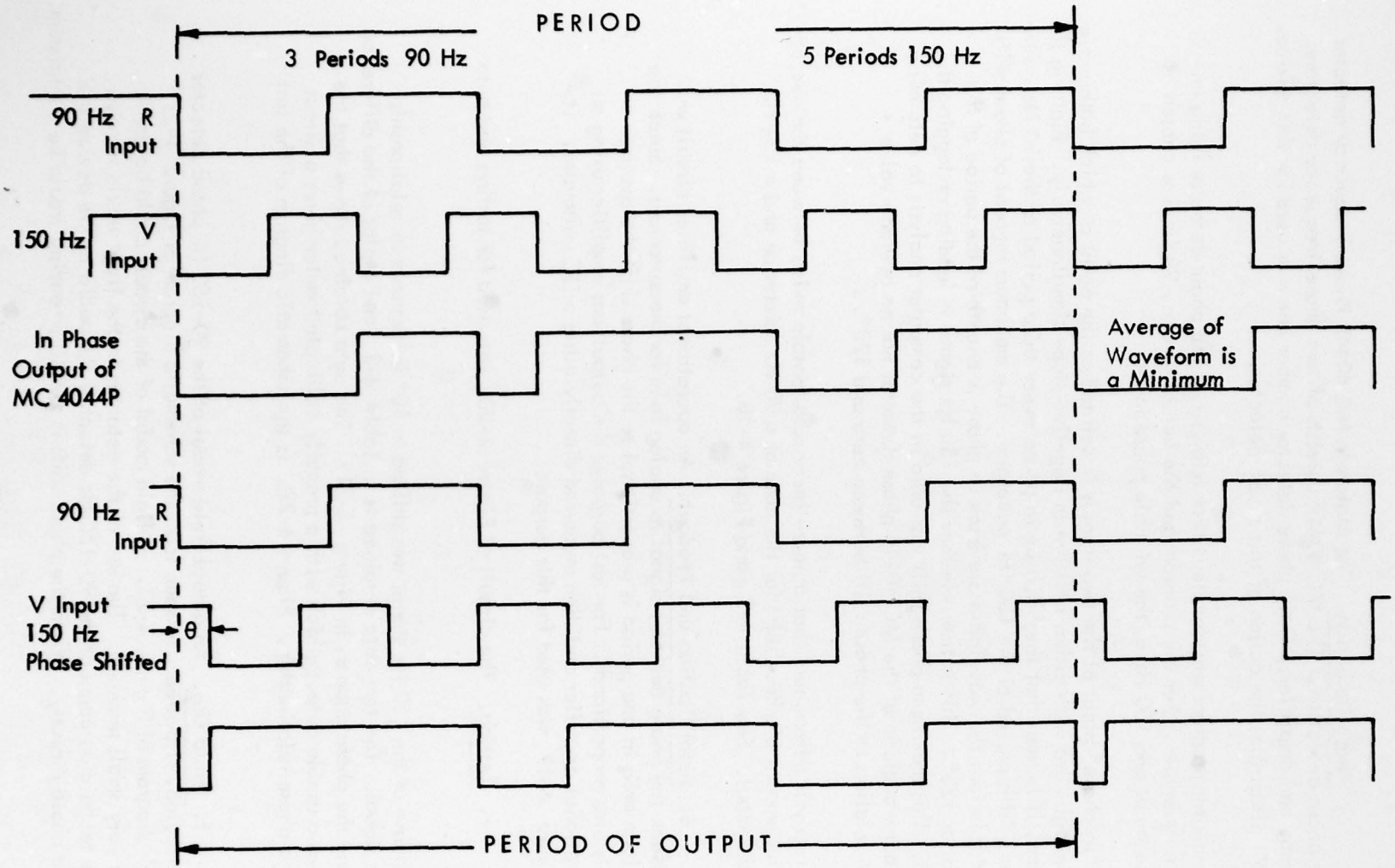

Figure 4-17. MC 4044P Input/Output Waveforms.

Average	Phase Shift
95.	0.0
97.	0.1257
99.	0.2513
101.	0.3770
103.	0.5027
105.	0.6283
107.	0.7540
109.	0.8796
111.	1.0053
113.	1.1310
115.	1.2566
117.	1.3823
118.	1.5080
120.	1.6336
122.	1.7593
124.	1.8850
126.	2.0106
96.	2.1363

Table 4-2. Analysis Data.

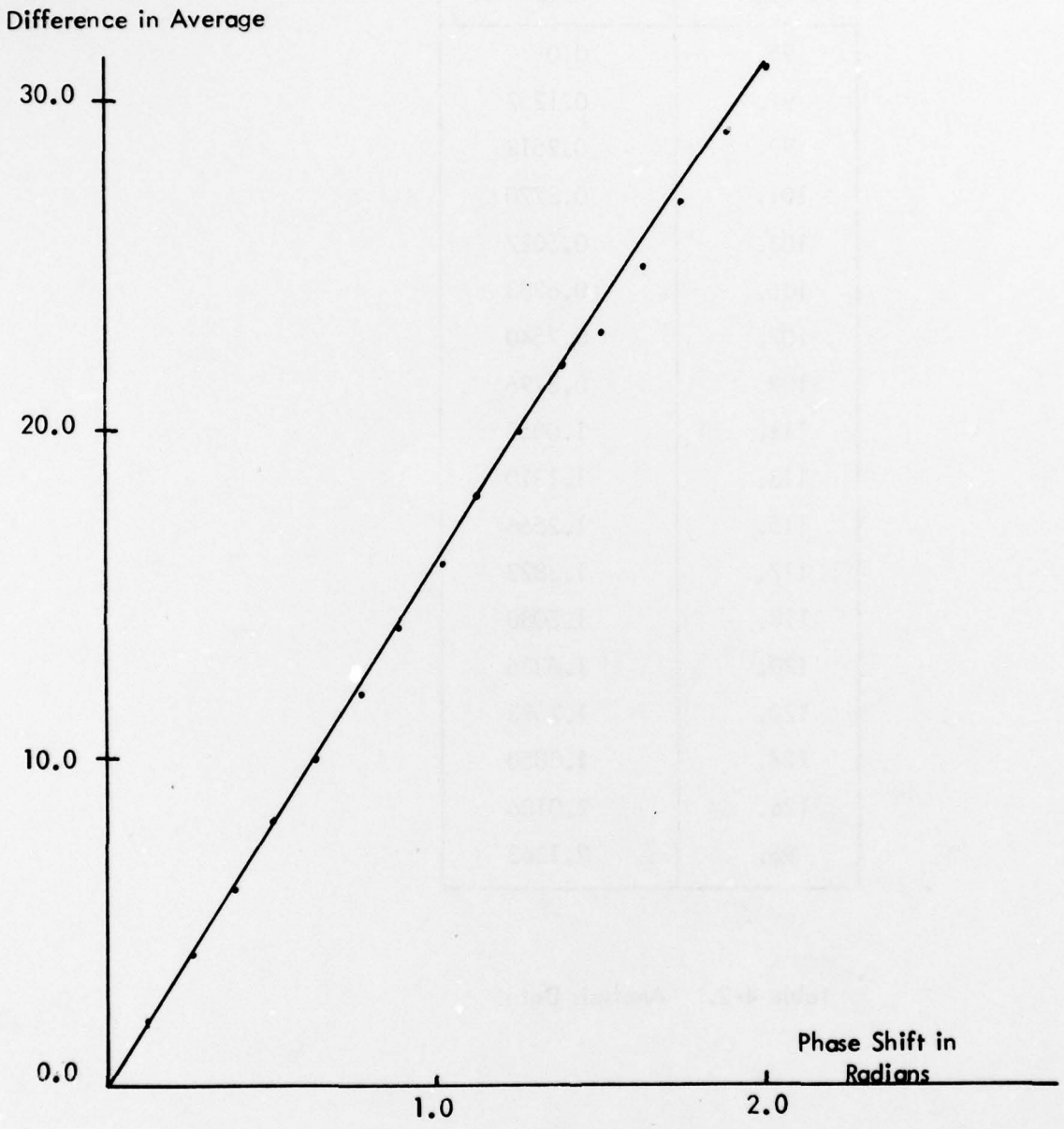

Figure 4-18. Plot of Analysis Data.

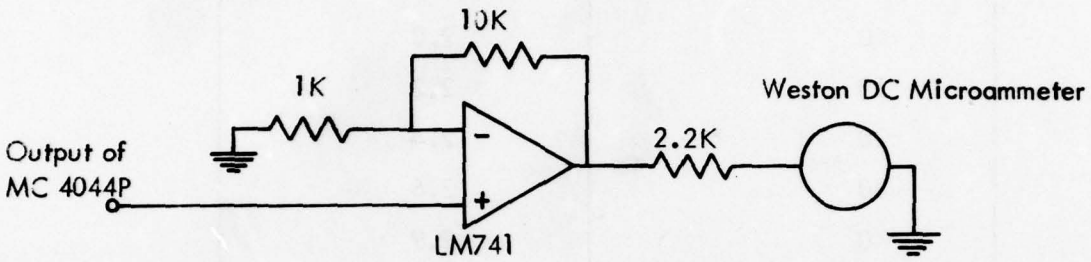

Figure 4-19. Amplification and Readout Circuit.

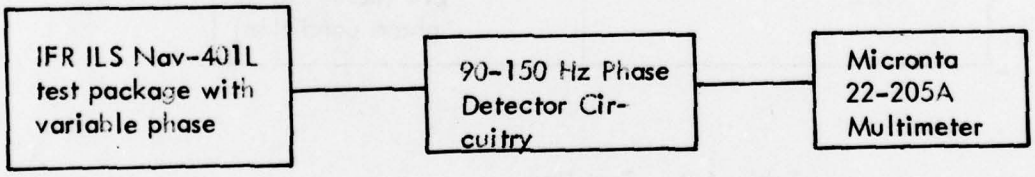

Figure 4-20. Test Circuit Block Diagram.

Test Signal Phase Shift (Degrees) 90 Hz and 150 Hz	Voltage Reading (Volts)
0	2.0
10	2.2
20	2.4
30	2.6
40	2.9
50	3.1
60	3.4
70	3.6
80	3.8
90	4.1
100	4.3
110	4.6
120	2.0 (Return to in-phase condition)

Table 4-3. Test Data.

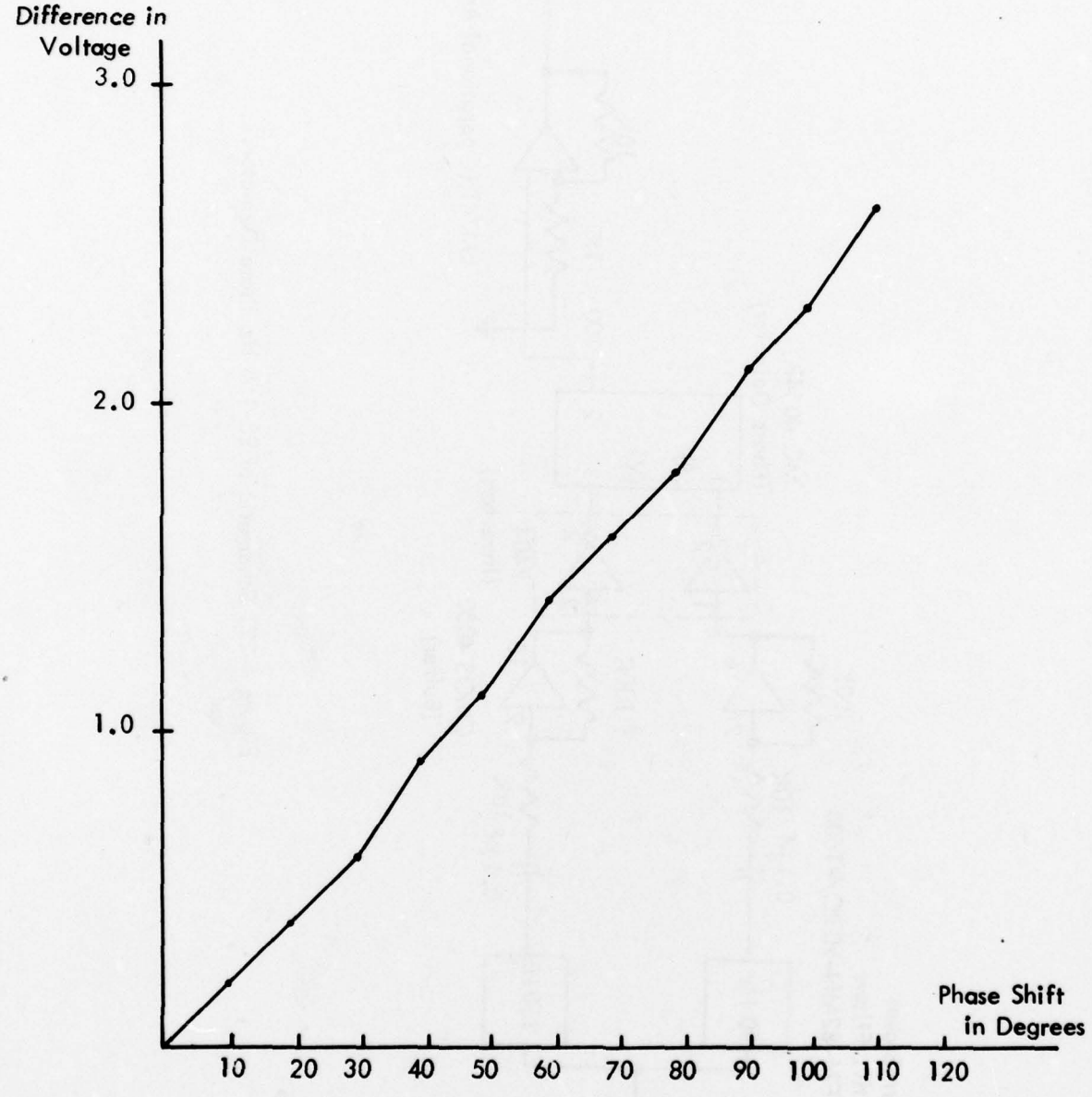

Figure 4-21. Plot of Test Data.

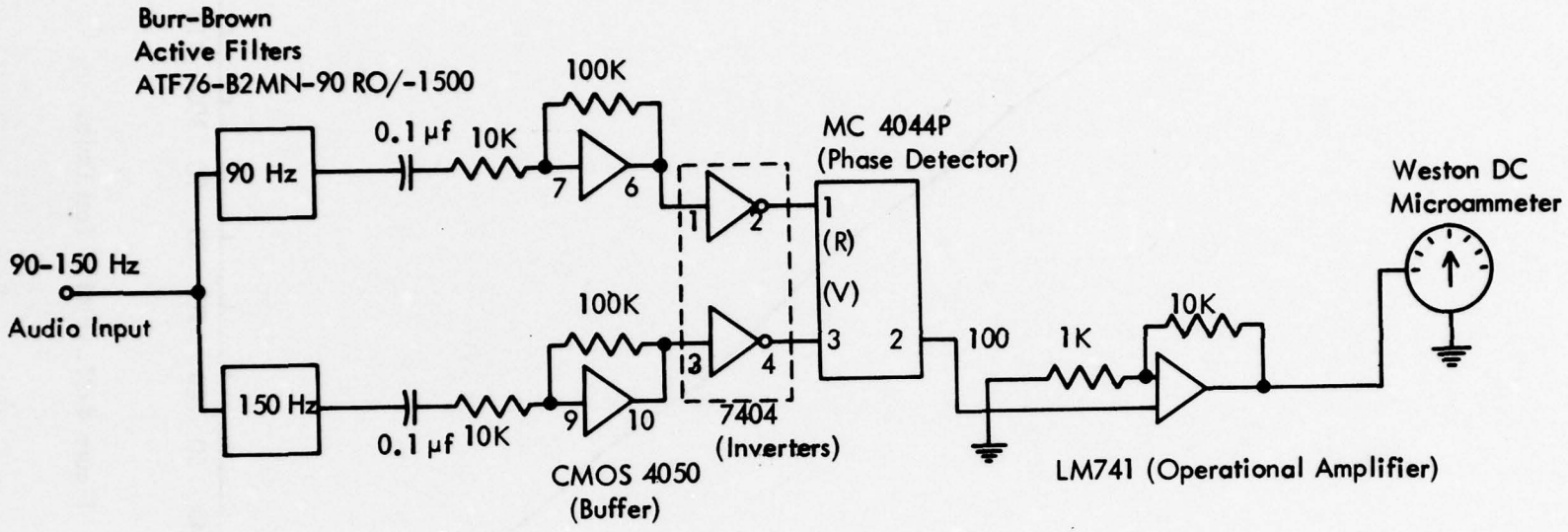

Figure 4-22. Schematic of 90-150 Hz Phase Detector.

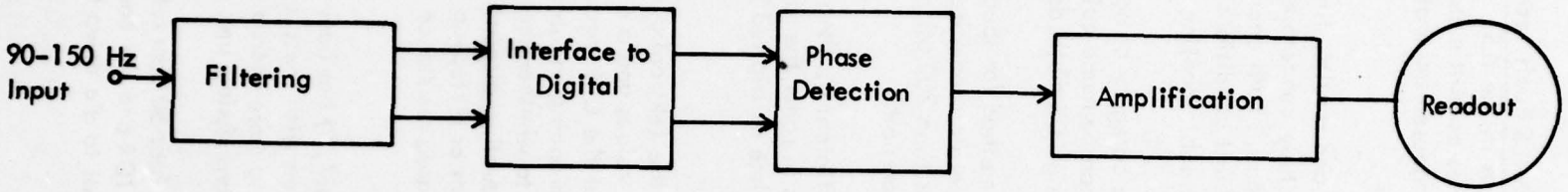

Figure 4-23. Block Diagram, 90–150 Hz Phase Detector.

E. Time Domain Reflectometry in ILS Fault Testing. Periodic health checks have been used to locate or prevent faults in the ILS. Health check instrumentation has generally been limited to such devices as multimeters and portable detectors. Often, troubles with a system have not been diagnosed accurately and guesswork fault diagnosis has been used.

To improve health check methods and results, time domain reflectometry (TDR) is suggested. This section reports on a study concerning the applicability of TDR to locate faults in Instrument Landing Systems. Both operating installations and laboratory set-ups were tested under fault and no fault conditions to determine guidelines and procedures for using the TDR as an ILS troubleshooting instrument.

These TDR checks come under the category of nondestructive testing as opposed to destructive testing. Health checks can be made quickly, easily, and without detrimental effects on the system by using TDR methods.

Time Domain Reflectometry is a method for locating and identifying system problems (faults). The TDR operates like a closed-circuit radar system in that it sends a step (pulse) with a short rise time (less than 200 ps) down a cable and displays reflections from any discontinuity in the transmission path.

The TDR plots the reflection coefficient ρ, the ratio of the reflected voltage to the incident voltage, vs. distance. As in radar the distance to the target, or discontinuity, is one-half the round trip time multiplied by the velocity of the pulse in the cable.

In the tests done for this report, the Tektronix 1502 TDR was used. The 1502 has a CRT to display reflection coefficient values and a chart recorder which provides an expanded permanent graphical record of the CRT trace. The returned voltage from a discontinuity is superimposed on the advancing incident step and will appear as a step-up or step-down on the TDR according to whether the reflection is of the same or opposite sense with respect to the incident. Inductive discontinuities or discontinuities of increased resistance will cause positive reflections or a step-up in the TDR trace. Capacitive discontinuities or discontinuities of decreased resistance will cause negative reflections or a step-down in the TDR trace.

Though the TDR is a "cable tester", it has been used to test ILS components such as bridges, antennas and monitors. Even with these components, though, cables are still being tested. The bridge is nothing more than a transmission line ring, and the antenna and monitors tested contain transmission line networks terminated in dipoles.

For most tests, a precision three foot 50 ohm reference cable provided with the TDR was used to connect between the TDR and the component being tested. This cable also allows any incident pulse overshoot to die down before the device to be tested is reached.

1. TDR Analysis of ILS System Components.

a. Cabling System Analysis.

(1) Transmission Line Transient Analysis for TDR Measurements.[1,2]*

The words "time domain" indicate concern with quantities which are functions of time. The frequency domain is concerned with the steady state performance which is independent of time. Fourier and Laplace transforms can be used to go from one domain to another in order to relate them.

Consider a uniform transmission line (say, a coaxial cable) of infinite length. If a pulse of voltage is sent down this line, there will be no reflection from the far end since the line is infinite and the pulse travels at a finite speed and thus never reaches the far end. The ratio of current to voltage on such a line is called the characteristic impedance of the line. If Z is the series impedance per unit length of the conductors and Y is the shunt admittance between the conductors per unit length, the characteristic impedance can be shown to be $Z_o = \sqrt{Z/Y}$ (see Figure 4-24). Here, for steady state sine waves, $Z = R + jX$ ohms per meter and $Y = G + jB$ mhos per meter. So that, in general, Z_o is complex. However, high quality lines may usually be satisfactorily analyzed by assuming that R and G are negligibly small so that $Z_o = \sqrt{L/C}$. Losses are then taken into account by using an appropriate attenuation factor.

If one now looks at a finite line terminated in an impedance Z_t, the possibility of reflection at the termination must be considered. There will be a forward traveling wave and a reverse traveling wave on the line. At the termination these must add to satisfy the equation $V_t = Z_t I_t$. For the forward wave call the voltage V_f and the current I_f and for the reverse or backward traveling wave the voltage and current are V_r and I_r. Then $V_f = Z_o I_f$ and $V_r = Z_o I_r$. The forward and reverse voltages add at the terminating impedance giving $V_t = V_f + V_r$ but the current in the reverse wave subtracts from that in the forward wave giving $I_t = I_f - I_r$. Combining these equations we get:

$$Z_t = \frac{V_t}{I_t} = \frac{V_f + V_r}{V_f - V_r} Z_o = \frac{1 + \rho}{1 - \rho} Z_o \qquad (4.1)$$

where ρ is the reflection factor, V_r/V_f .

From (1) $\rho = (Z_t - Z_o) / (Z_t + Z_o)$, which gives:

$\rho = 0$ when $Z_t = Z_o$

$\rho = 1$ when $Z_t = \infty$, open line

$\rho = -1$ when $Z_t = 0$, shorted line

and $-1 < \rho < +1$ for other real values of Z_t. It is clear that in order to avoid reflections the line must be matched at every point; that is, it must have no discontinuities in impedance.

*References are listed at the end of each section. See page 4-201 for references for Section IV.

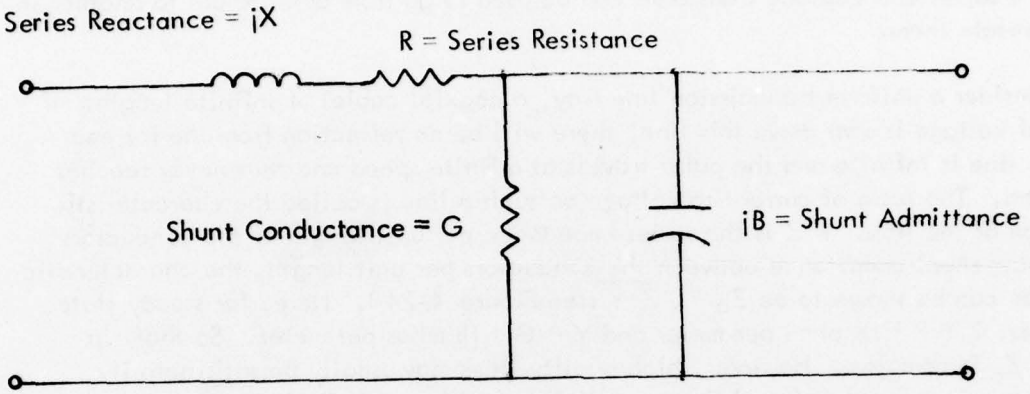

Figure 4-24. Circuit Model for a Short Length of Transmission Line.

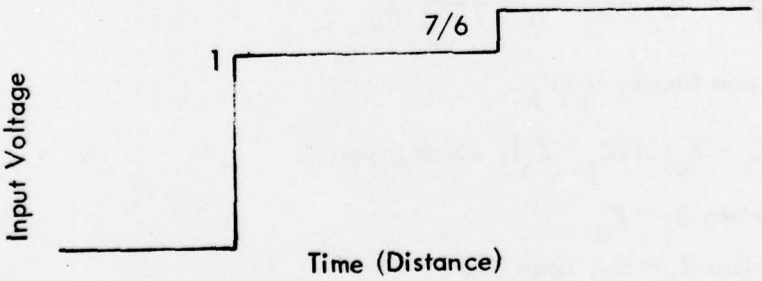

Figure 4-25. Theoretical TDR Plot of a 50Ω Line Terminated in 70 Ohms.

Suppose that a step of voltage is applied by a generator having a 50 ohm internal impedance to a 50 ohm line (Z_o = 50 ohms) which is terminated in 70 ohms. ρ will be (70-50)/(70+50) = 1/6. The voltage at the input to the line will rise to one half the open circuit generator voltage. The input voltage will remain at this value for twice the time it takes for the step to travel to the load (the 50 to 70 ohm discontinuity). It will then rise by 1/6 of its initial value vecause 1/6 of the forward wave has been reflected back to the input. Since the generator is matched in this case, the backward wave will not be reflected by the generator (as would be the case if the generator were not matched to the line). Note that this is just the voltage that would appear across the 70 ohm load if it were connected directly to the 50 ohm generator. The TDR which presents the input voltage as a function of time after the step function is launched down the line would plot this as in Figure 4-25. If, as is usual, the wave travels at a known constant speed in the line, time is proportional to distance and the horizontal axis is calibrated in feet or meters per division. The vertical scale gives the reflection coefficient.

Consider now sending a steady state sine wave down the line terminated in the above mismatch. The wave going down the line (forward wave) will be $E\cos(\omega t-\beta x)$* while the reflected wave will be $\rho E\cos(\omega t+\beta x)$*. The total wave will be:

$$E(x,t) = E\cos(\omega t-\beta x) + \rho E\cos(\omega t+\beta x) \tag{4.2}$$

Using familiar trigonometric identities for cosines of sum and difference angles (4.2) may be written:

$$E(x,t) = (1-\rho)\, E\cos(\omega t-\beta x) + 2\rho E\cos\omega t\cos\beta x \tag{4.3}$$

The first term on the right is a forward traveling wave, while the second term is a stationary or standing wave. The voltage standing wave ratio (VSWR) on the line is defined as the ratio of the maximum voltage to the minimum voltage. The maximum voltage occurs when the two terms of (4.3) are in phase opposition. Thus S, the VSWR, can be shown to be $(1+|\rho|)/(1-|\rho|)$. For the 50 ohm line terminated in 70 ohms this gives S = 1.4. Since the reflection factor, ρ, can be determined from the TDR plot, the VSWR can also be determined in this simple case.

The impedance (for single frequency steady state sine waves) seen looking into a transmission line depends on the length of the line, its characteristic impedance, and the terminating impedance. This may be shown to be:

$$Z_{in} = Z_o \frac{Z_t\cos\beta L + jZ_o\sin\beta L}{Z_o\cos\beta L + jZ_t\sin\beta L} \tag{4.4}$$

---

* That these terms represent traveling waves may be seen by imagining an observer riding on a point of fixed value on the wave. For this value to remain fixed the argument of the cosine must remain constant which requires that $\omega t-\beta x = c$ and thus that $\omega(dt) = \beta(dx) = 0$ or $dx/dt = \omega/\beta$. From the $\cos(\omega t+\beta x)$ term $dx/dt = -\omega/\beta$, a velocity in the reverse direction.

$\beta = 2\pi/\lambda$

l = length of the cable

λ = the wavelength in the cable

It is convenient to normalize this equation (4.4) by expressing impedance in terms of the characteristic impedance of the line. Equation (4.4) then becomes:

$$z_{in} = (z_t \cos\beta L + j\sin\beta L) / (\cos\beta L + j z_t \sin\beta L) \qquad (4.5)$$

where $z = Z/Z_o$

From (4.5) it is seen that if the line is an odd number of quarter wavelengths long $z_{in} = 1/z_t$ or the line is said to invert the impedance.

A use of this phenomenon is in the quarter wave transformer used to match two lines (or a line and a load) of different characteristic impedance.

Take, for example, a 98 ohm line terminated in 98 ohms. If this combination must be driven from a 50 ohm cable, ρ will be (98-50)/(98+50) or about 1/3 and the standing wave ratio (VSWR) will be 1.96. If now a quarter wavelength of 70 ohm line is inserted between the 50 ohm line and the 98 ohm line, z_t becomes 98/70 and z_{in} is, therefore, 70/98 (due to the inverting property of the quarter wave transformer) so that $Z_{in} = 70x70/98 = 50$ ohms. Thus the 50 ohm line is terminated in its characteristic impedance and the reflection factor for this particular frequency is zero. One says the line is flat and the load is matched to the line, hence the term quarter wave transformer. The source sees no discontinuities between it and the load.

What does the TDR see? It sends a step of voltage down the 50 ohm line which is partly reflected by the discontinuity at the input to the quarter wave transformer. The reflection factor is given by (70-50)/(70+50) = 1/6. A voltage of 7/6 appears across the input to the 70 ohm line and travels down toward the 98 ohm line. When this step reaches the discontinuity, it is reflected back toward the input with a reflection factor of (98-70)/(98+70) = 1/6. Arriving at the input of the quarter wave transformer it is again reflected toward the load with a reflection factor of (50-70)/(50+70) = -1/6 and transmitted through to the 50 ohm line with a transmission factor of 5/6. This process quickly becomes difficult to follow, so a technique known as the bounce diagram [3] is employed to analyze reflections from discontinuities in a system. The bounce diagram plots the progress of the voltage waves as a function of time and distance. In Figure 4-26, the bounce diagram is shown for the quarter-wave transformer where time advances down the page and distance from the source increases toward the right. The magnitude of each portion of the wavefront is shown in the center of each column in the diagram and the TDR terminal voltage at the discontinuity where $\rho = \rho_1$ is shown at the left side.

The reflected voltage, E_r, from the discontinuities is found by multiplying the incident voltage, E_i, at the discontinuity by the reflection coefficient since $\rho = \frac{E_r(\text{voltage reflected})}{E_i(\text{voltage incident})}$ or $E_r = E_i \cdot \rho$. The voltage transmitted through a discontinuity is equal to $E_r + E_i$.

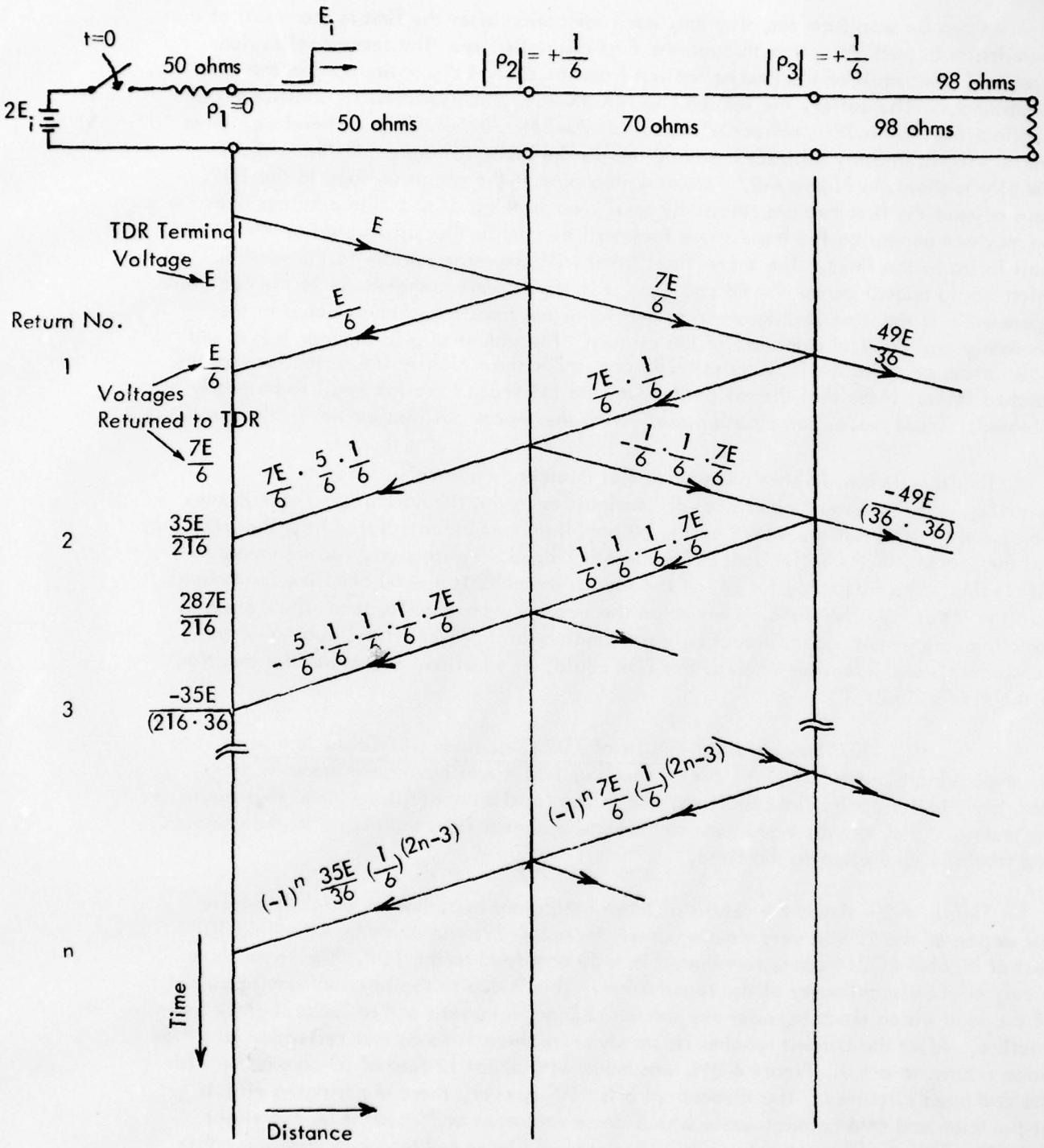

Figure 4-26. Reflection Diagram for the Quarter-Wave Transformer Matched System.

As can be seen from the diagram, each reflection after the first is the result of a transmission in each direction through the first discontinuity. The second reflection to return is the result of the first reflection from the second discontinuity and the two transmissions. Thereafter, the succeeding returns have each suffered an additional pair of reflections, one with a reflection factor of (70-50)/(70+50) = 1/6. Therefore, these returns will alternately subtract from and add to the input voltage. The theoretical TDR plot is shown in Figure 4-27 along with a plot of the return voltage to the TDR. Steps beyond the first two are relatively small, each being a/36 of the previous one and may not appear on the trace since they will be still further attenuated by the small losses in the lines. The theoretical trace will converge rapidly to the voltage which would appear across the 98 ohm load if it were connected directly to the generator. Figure 4-28 is the circuit diagram for a quarter-wave transformer constructed in the laboratory and the TDR signature of the circuit. The values of ρ in Figures 4-27a and 4-28 compare quite well. Figures 4-28b and 4-28c show clearly the reflections on the matched lines. Note that the reflections beyond the second are too small to be easily detected. These traces correspond closely with the theory outlines earlier in this section.

Thus a system which has been made flat (matched, non-reflecting) in the frequency domain shows a number of discontinuities in the time domain. The TDR sees the discontinuities but the VSWR on the 50 ohm line must be calculated from the frequency and the spacing of the reflections. On the other hand, the frequency domain measurements will indicate the frequency for which the load is matched to the 50 ohm line but cannot, from the input, see the standing waves on the quarter wave transformer. The frequency domain measurements could detect only a mismatch (high VSWR) if the quarter-wave transformer were defective whereas the TDR could, in addition, determine the location of the defect (fault).

(2) Experimental Results of TDR Connector and Cable Analysis. The accompanying Figures (4-29 to 4-41) showing TDR traces have been made in the laboratory under controlled conditions and in the field on operating systems shut down for testing. They are arranged here so that one proceeds from the simple to the complex and from the laboratory to the field.

Figure 4-29 shows the results of three laboratory experiments which illustrate the action of the TDR in very simple cases. Figure 4-29a was made by attaching 10 feet of 50 ohm RG214 cable terminated in a 50 ohm load to the TDR. The trace shows a very slight discontinuity at the termination. This is due to the physical configuration of the load which tends to resist any sudden change in current and so looks slightly inductive. After the current reaches its steady state there is no further reflection and the trace returns to ρ = 0. Figure 4-29b was made with about 12 feet of 50 ohm cable with the end open circuited. The theoretical ρ is +1; however, there are fringing effects at the open end of a coaxial cable which cause radiation and account for the slight deviation from the theoretical value. The trace of Figure 4-29c made with the cable shorted shows ρ very nearly equal to the theoretical -1. The scale of this trace indicates 2.5 times the vertical sensitivity of that of Figure 4-29b.

Figure 4-30 shows the effect of water in the cable termination. Figure 4-30a was made by wetting the 50 ohm load. Water, having a high dielectric constant, causes a capacitive effect which looks like a low impedance to the sharply rising step function.

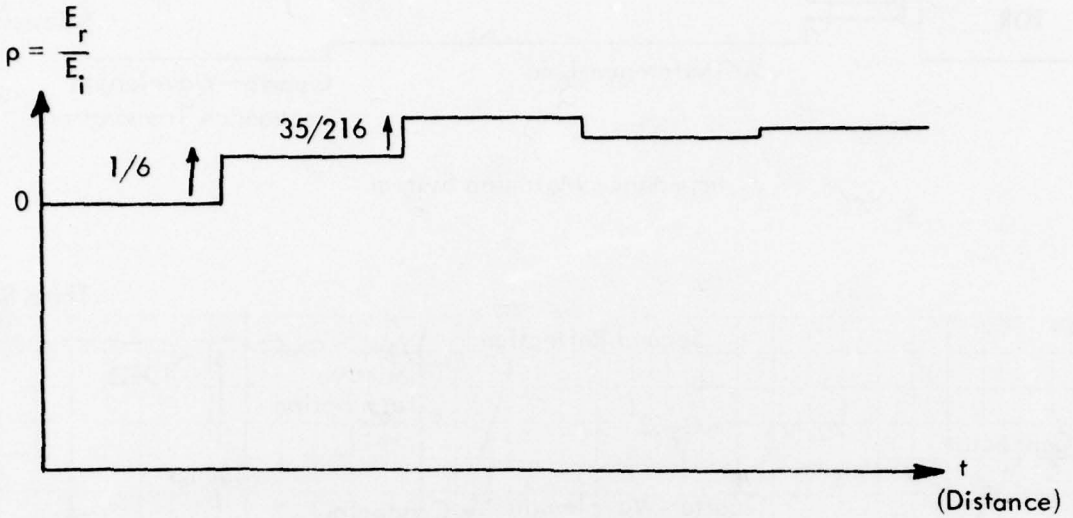

a. Theoretical TDR Signature for Circuit of a Quarter-Wave Transformer Matching 50Ω to 98Ω.

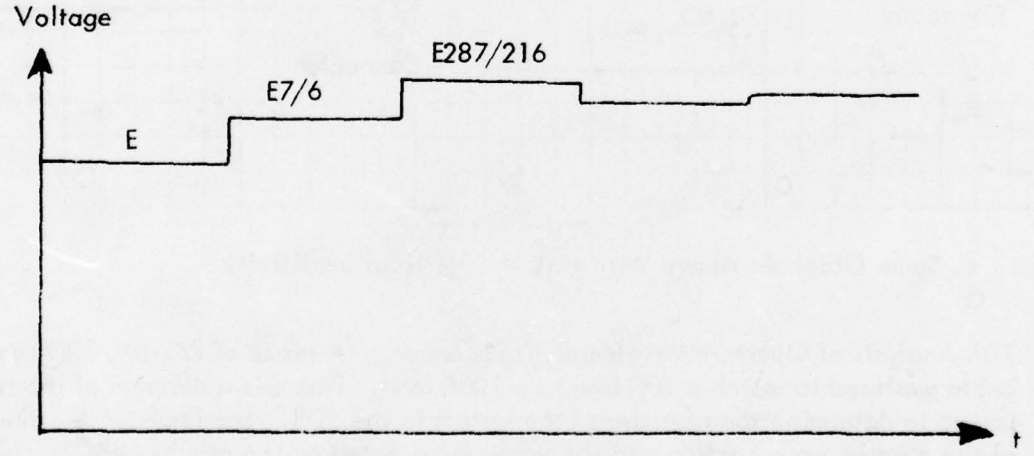

b. TDR Terminal Voltage for Circuit of a Quarter-Wave Transformer Matching 50Ω to 98Ω.

Figure 4-27. TDR Signature and Terminal Voltage Plot for the Quarter-Wave Transformer in Figure 4-26.

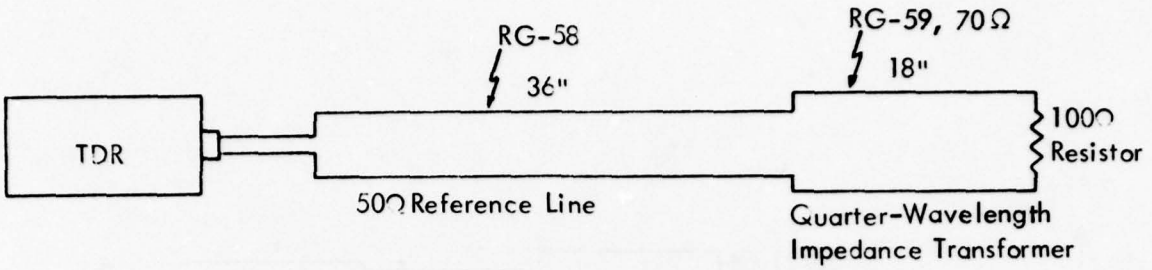

a. Impedance Matching System

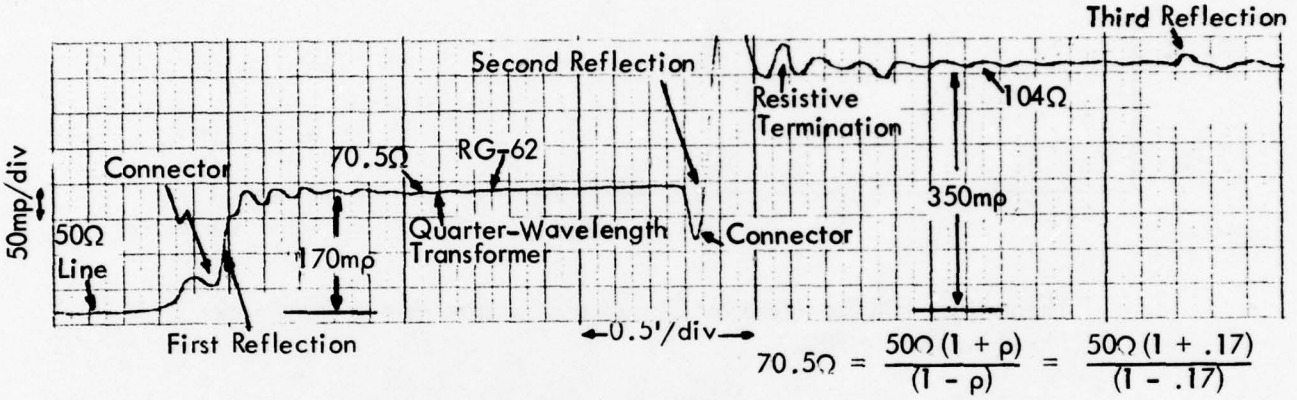

b. Impedance Transformer

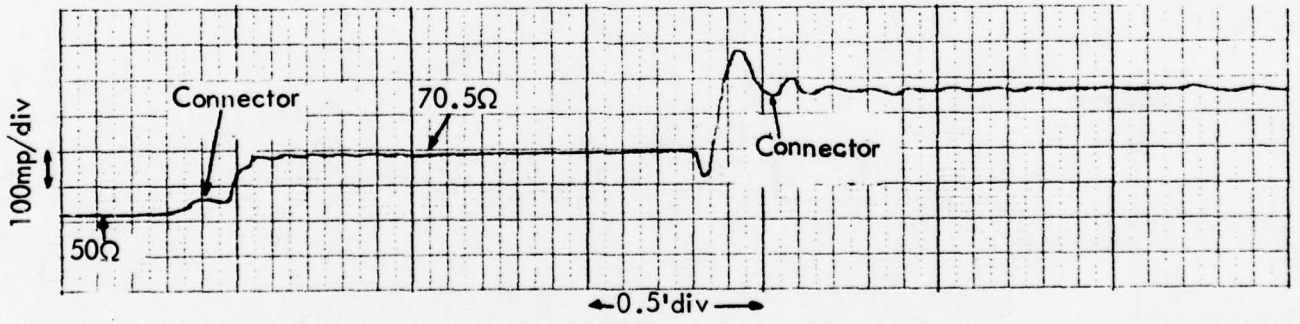

c. Same Graph As Above With Half the Vertical Sensitivity

Figure 4-28. TDR Analysis of Quarter-Wavelength Transformer. A piece of RG-59, 72Ω coaxial cable was used to match a 50Ω line to a 100Ω load. Part a is a diagram of the test set-up to determine the response of the system to the TDR. The impedance values of the quarter wave section and the termination noted on the graphs were calculated from the measured values of rho (ρ) using the 50Ω line as a reference. The discontinuity in the area of the connector is caused by the connector itself as well as small multiple reflections due to the change in impedances in the system.

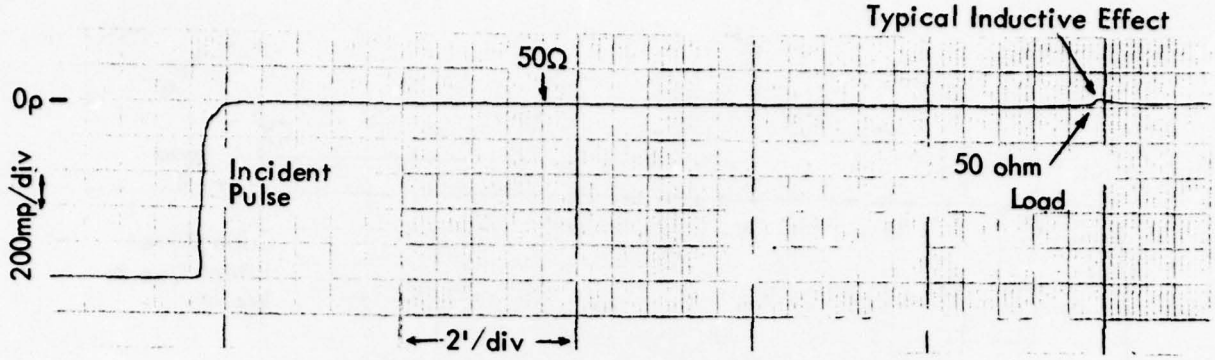

a. RG 214 Cable Terminated in 50Ω Load

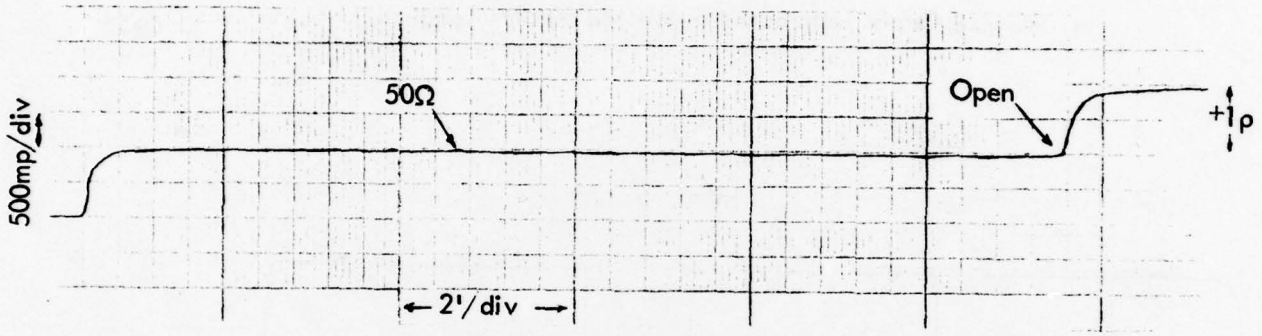

b. Open Cable

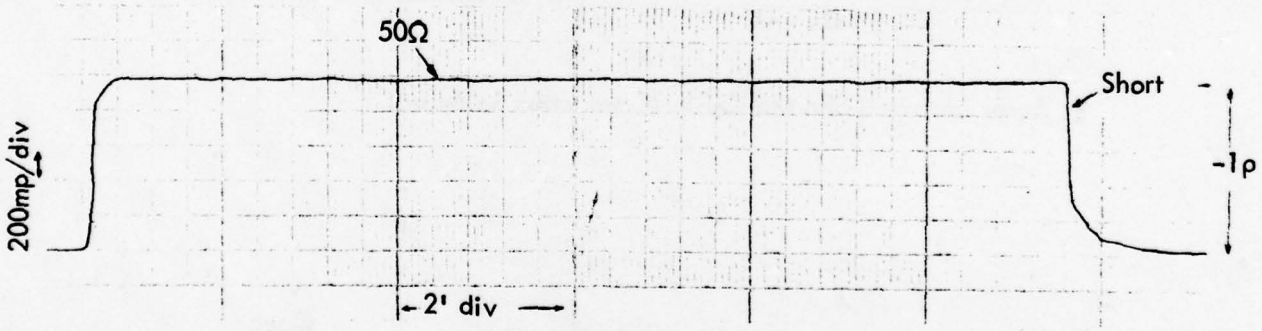

c. Shorted Cable

Figure 4-29. Graphs Displaying Short, Open, and Properly Terminated 50Ω Cables. The top of the incident pulse is the 0 reflection reference. The first graph is a cable terminated in 50Ω. Because the load is not precisely 50 ohms, it causes a small reflection. The open cable reflects all of the wave in phase with the incident, thus +1ρ step up, while the shorted cable reflects all of the wave with reverse polarity, or -1ρ.

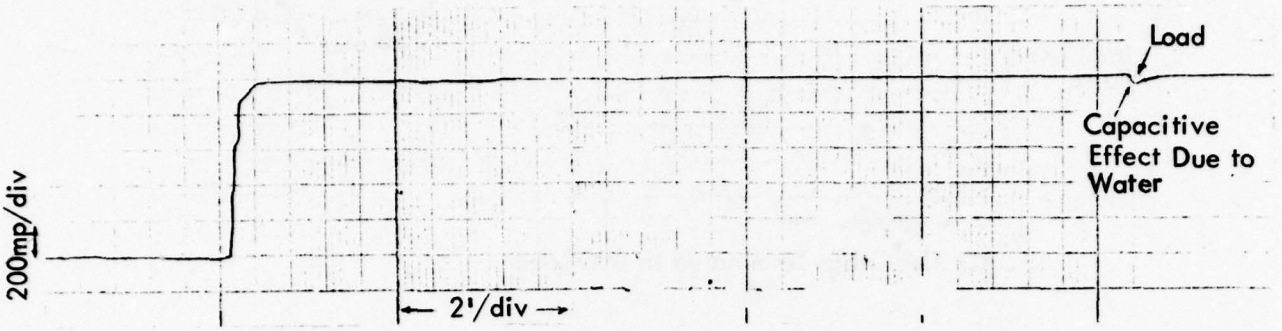

a. RG 214 Cable Terminated in Wetted 50 ohm Load

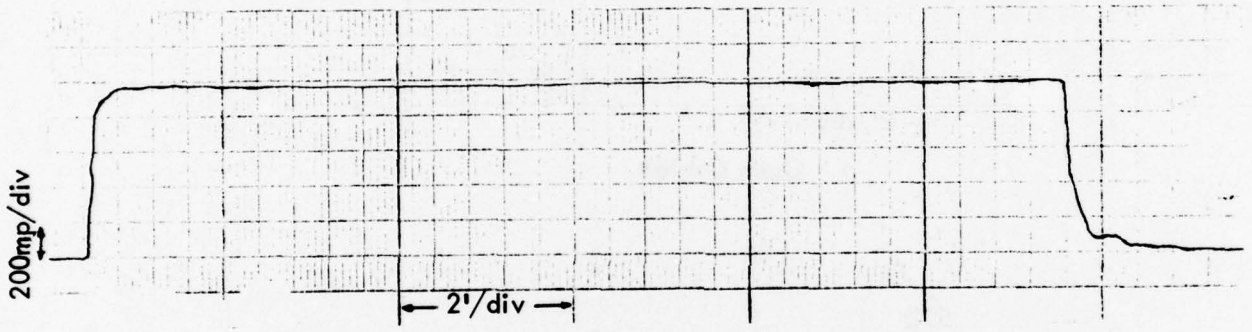

b. Water Immersed Shorted Cable (Conductors Soldered)

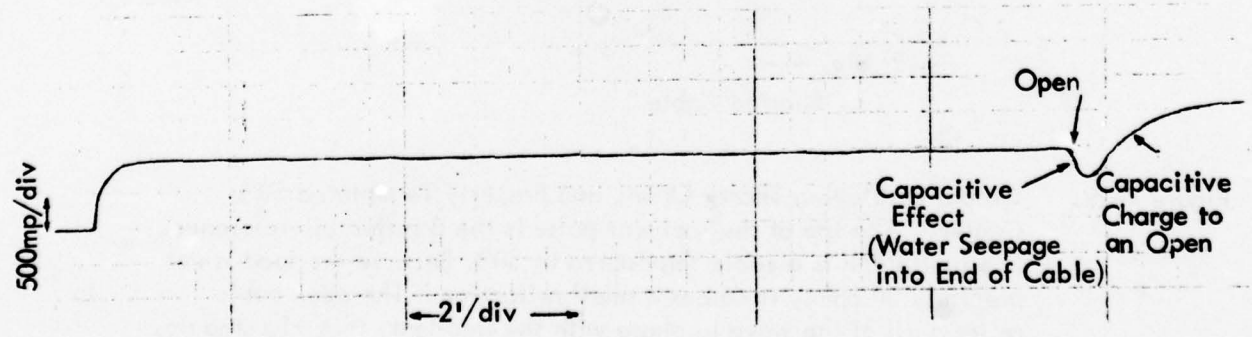

c. Water Immersed Open Cable

Figure 4-30. TDR Graphs Showing Wetted Cable Terminations.

Unless there is conductivity the water has no effect on the final value of the reflection. In other words, the capacitor charges and the voltage returns to normal. Figure 4-30b was made with a water immersed short at the end of the cable (conductors soldered). This is much the same as Figure 4-29c except that the addition of some high dielectric (water) tends to cause the reflection to occur more abruptly. For Figure 4-30c the open cable was immersed in water. The low impedance effect of the high dielectric constant is clearly shown. (Comments about Figure 4-29b apply here also).

An 11.5 foot length of 50 ohm cable was sliced for one inch about 2 feet from the load end. Figure 4-31a indicates that this cable exhibits a moderately high impedance discontinuity ($\rho > 0$). Figure 4-31b shows the effect of a light wetting of the slice. Not much change is noticed. However, taking into account the doubling of the vertical sensitivity between Figures 4-31a and 4-31b one might detect a slight reduction of the inductive effect. Figure 4-31c , however, leaves no doubt as to the effect of water in the cable since the lowering of the impedance (capacitive effect) is quite obvious.

Figure 4-32 depicts the result of an experiment in which a small pinhole in RG214 cable was immersed in water to test the ability of the TDR to detect this type of fault. Figure 4-32a indicates that the pinhole itself caused no observable discontinuity. After only 5 minutes in water a noticeable effect appeared (Figure 4-32b). This figure again illustrates the capacitive effect of the water in the cable. Figure 4-32c, taken after 18 hours immersion in water, shows the extent of the seepage.

To investigate the results of corrosion due to seepage of acidic ground water into buried connectors or to the condensation of atmospheric pollutants on exposed contact surfaces, some accelerated corrosion tests were performed. 97% sulfuric acid was used to induce the corrosion, first diluted with an equal amount of water and then undiluted.

Figure 4-33 shows the series of traces obtained using the 50% solution. Figures 4-33a and 4-33b show no effect during the first two days of daily rewetting the mating surfaces. The acid solution is a good conductor. Figures 4-33c and 4-33d show the effect of daily rewetting for 3 days. (Note the different horizontal and vertical sensitivities.) After the three days of rewetting daily, the connector was allowed to dry and Figures 4-33e and 4-33f were made.

Figure 4-34 shows the effect of the 97% acid. Figure 4-34a shows the untreated connector located by the usual small inductive reflection. Figures 4-34b and 4-34c show the onset of corrosion effect indicated by a lowering of the impedance to 46 ohms. After one day the impedance seen has dropped to 39 ohms as shown in Figure 4-34d. Figure 4-34e shows still further lowering of the impedance to 27 ohms. In Figure 4-34f, after four days, the impedance has fallen to 10 ohms. After two weeks of drying Figure 4-34g indicates a high impedance type of failure probably due to high contact resistance.

Figure 4-35 shows field measurements of lossy cable made at Wood County Airport, Parkersburg, West Virginia.

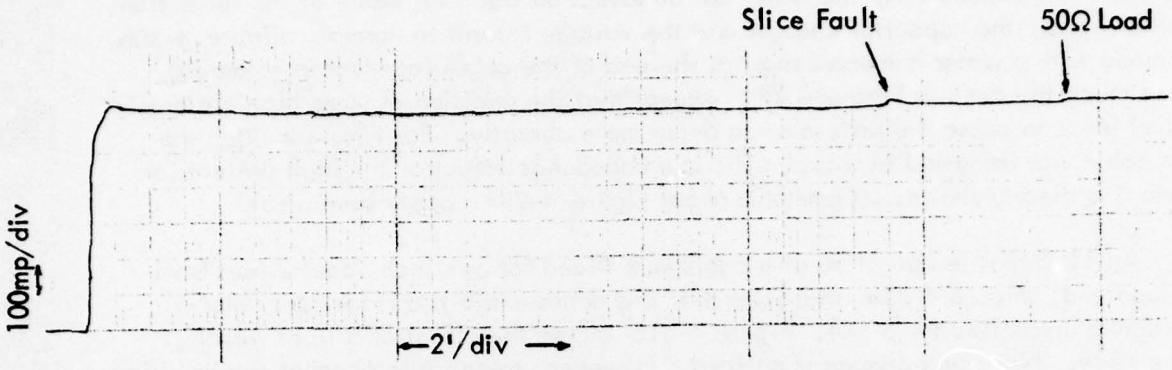

a. Dry Sliced Cable, 1" Long Slice to Center Conductor

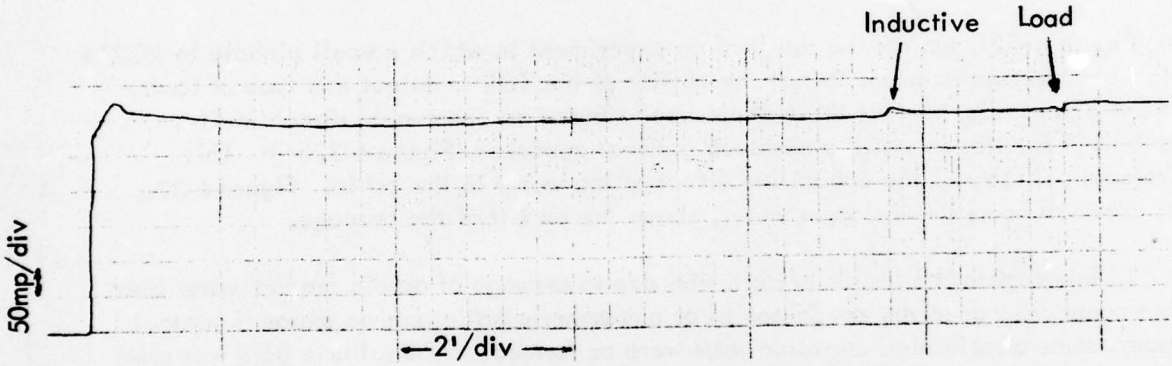

b. Same Cable and Fault As Above, But Wetted.

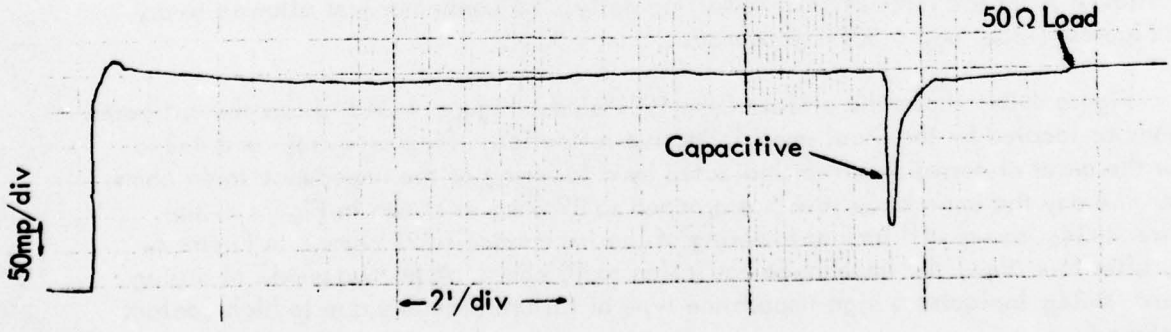

c. Water Submerged Sliced Cable. Large Capacitive Fault Due to Water.

Figure 4-31. TDR Graphs Showing Sliced Cable; Dry and Wet.

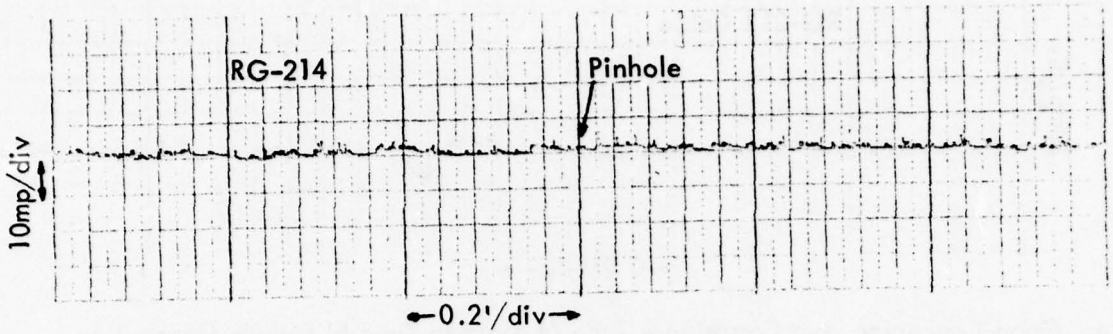

a. Pinhole Through Outer Conductor and Insulator (No Fault Noticeable)

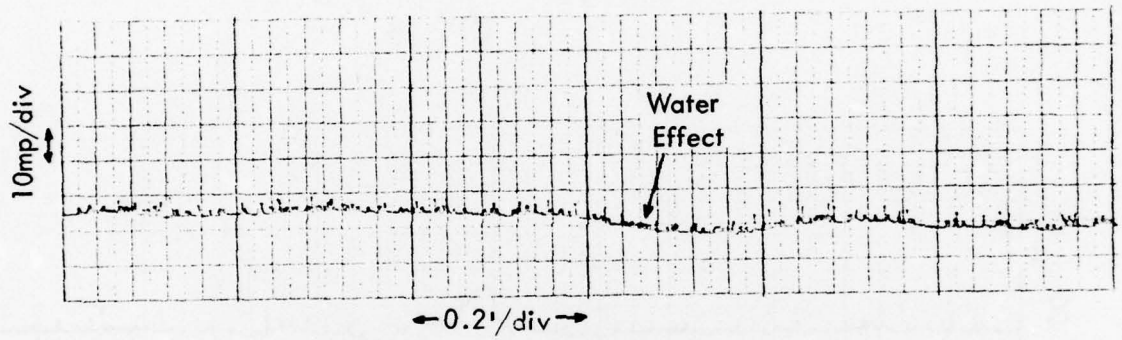

b. 5 Minutes After Cable Submerged in Water

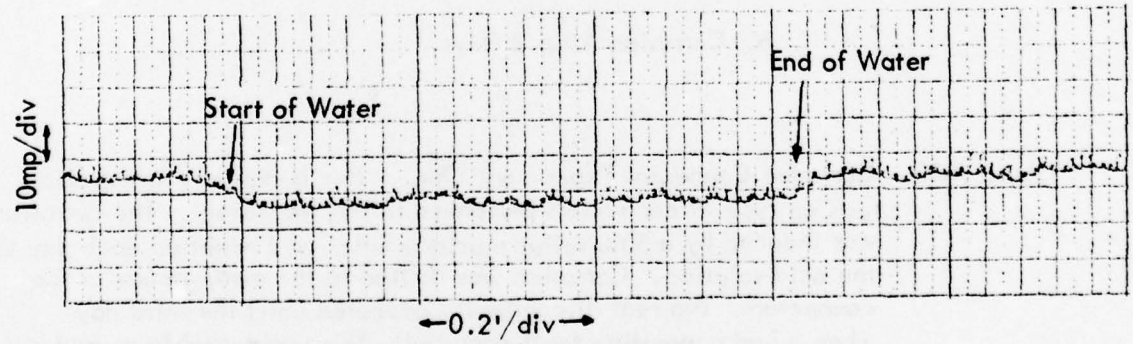

c. 18 Hours After Cable Submerged

Figure 4-32. Coaxial Cable with Pinhole Fault. A pinhole about 1/10" in diameter was made through the outer insulator and conductor of a piece of RG-214 cable. The cable was then submerged in water. The typical effect of a decrease in impedance caused by water seepage under the outer insulator was seen immediately by the TDR.

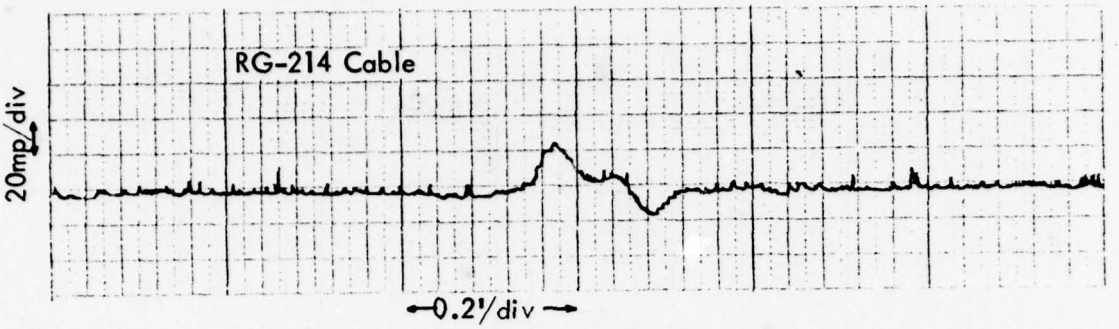

a. Good Connector, No Corrosion - Type N Male to Type N Female Connection

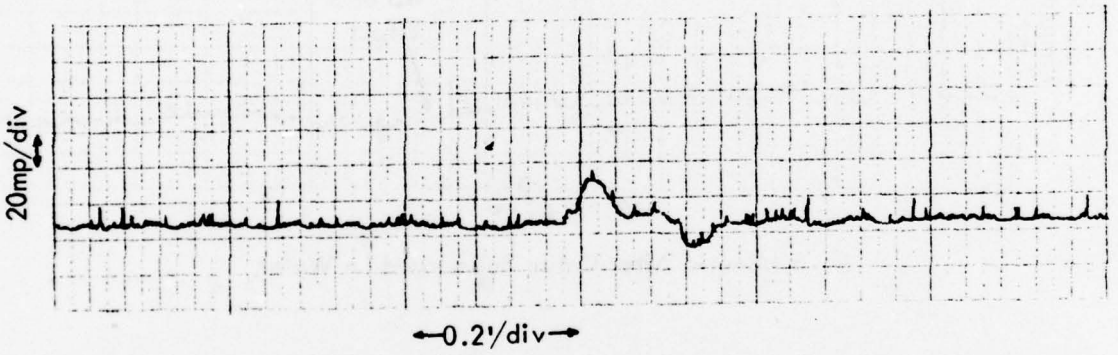

b. Corrosion After 2 Days

Figure 4-33. Corroded Connector Experiment One. This is one of two corrosion tests on Type N connectors performed in the laboratory. The corrosion was induced by a 50% sulfuric acid solution and rewetted each day with the acid solution. Corrosion was limited to the mating parts of the connectors. No real discontinuity appeared until the third day when a bad capacitive fault occurred. This was probably caused by the liquid solution itself more than the corrosion factor as indicated by the fact that when the connectors were allowed to dry, the discontinuity was similar to that measured before the acid solution was applied.

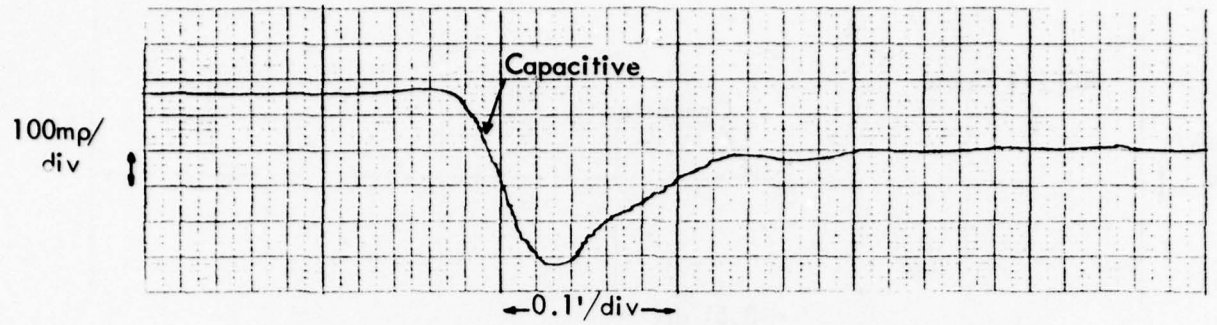

c. Wet Corroded Connector (Rewetted) - 3 Days

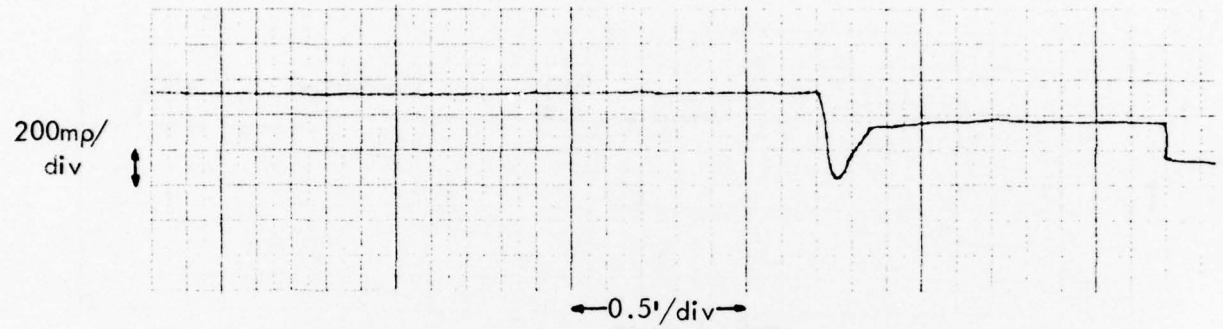

d. Wet Corroded Connector (Rewetted) - 3 Days

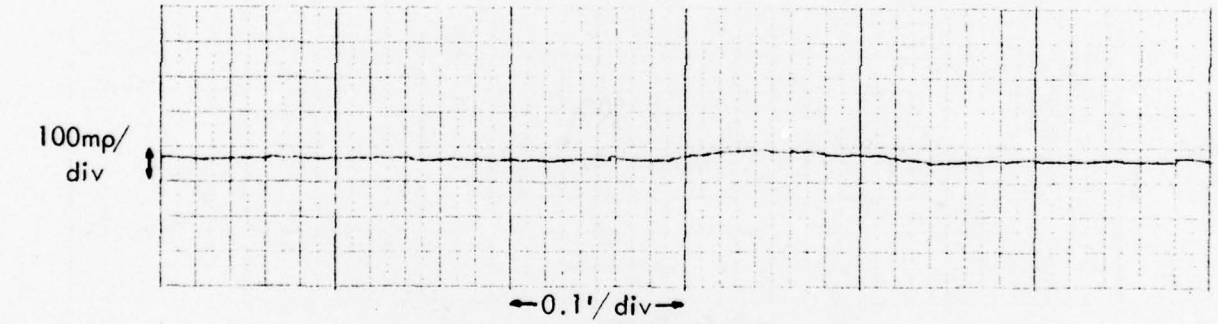

e. Dry Corrosion After 10 Days

f. Dry Corrosion After 10 Days - Graph Essentially the Same as Graph a.

Figure 4-33 (continued).

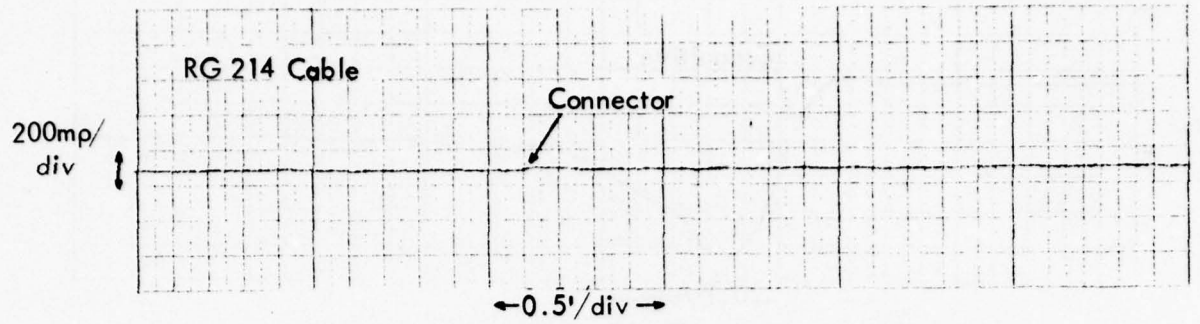

a. Type N Male to Type N Female Connection - No Corrosion

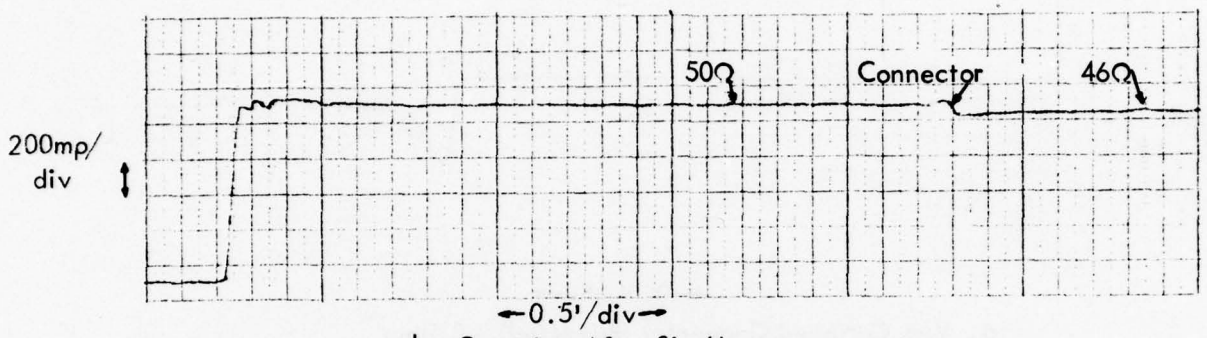

b. Corrosion After Six Hours

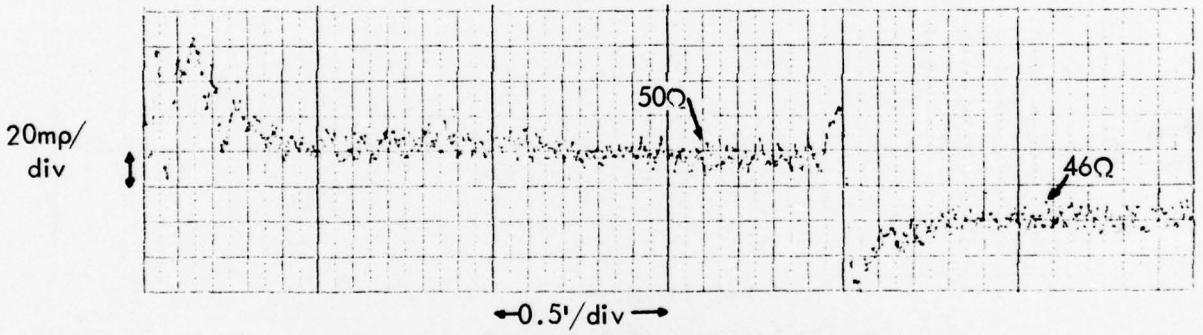

c. Expanded Vertical Scale of Above Graph

Figure 4-34. Corroded Connector Experiment Two. A strong acid solution was applied daily to a type N male to type N female connection on the total surface of the connectors. A discontinuity appeared in just a few hours and continued to become worse. After this test, analysis of the connectors revealed the fault to be caused mainly by corroded material between the outer and inner conductor of the connector. This corrosion fault caused the reduction in impedance. In the last graph the same fault caused an open. The conclusion of this test is that the initial few days of corrosion was wet and caused the reduced impedance effect. After 2 weeks of thorough drying and corrosion, the connector was making a high resistance contact especially in the area where the combed outer conductor and connector clamp meet.

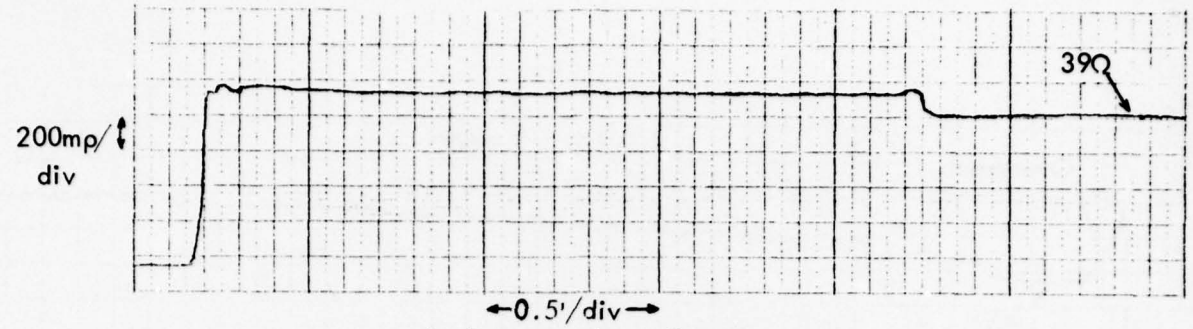

d. Corrosion After One Day

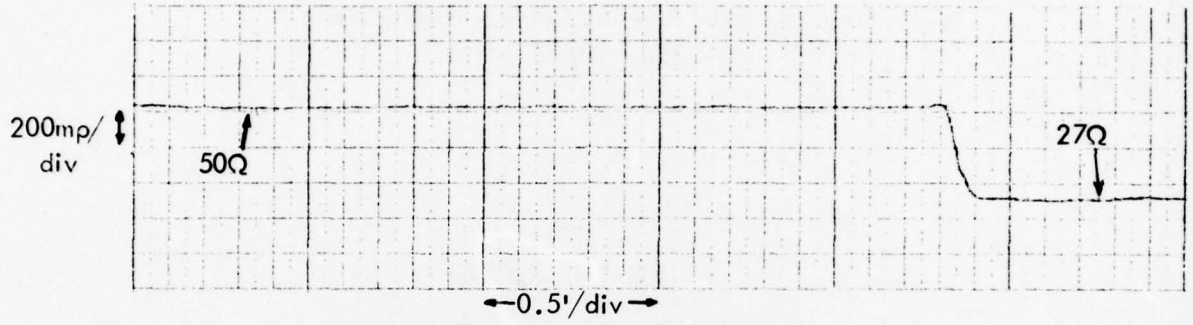

e. Corrosion After Two Days

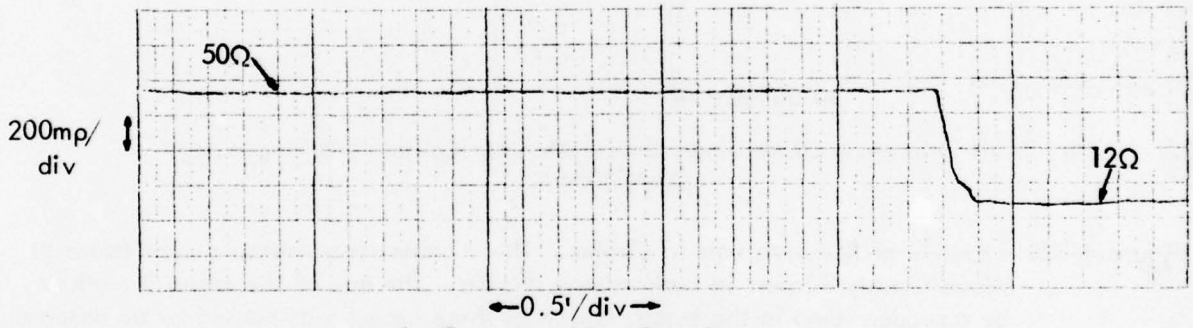

f. Corrosion After Four Days

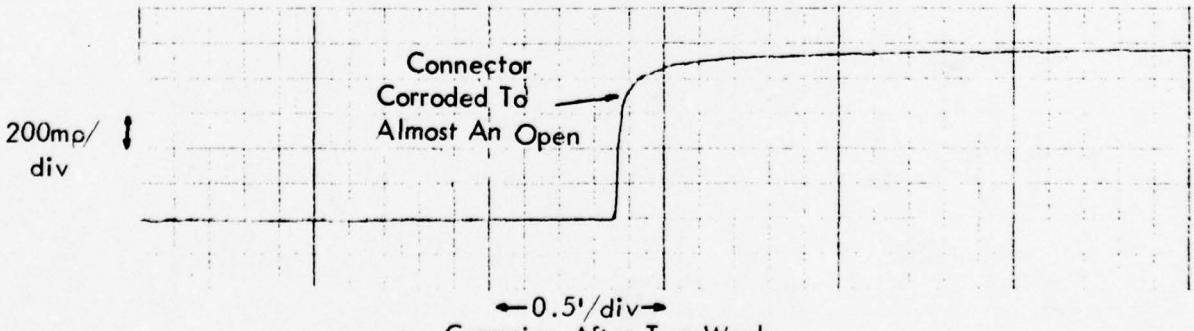

g. Corrosion After Two Weeks

Figure 4-34 (continued.)

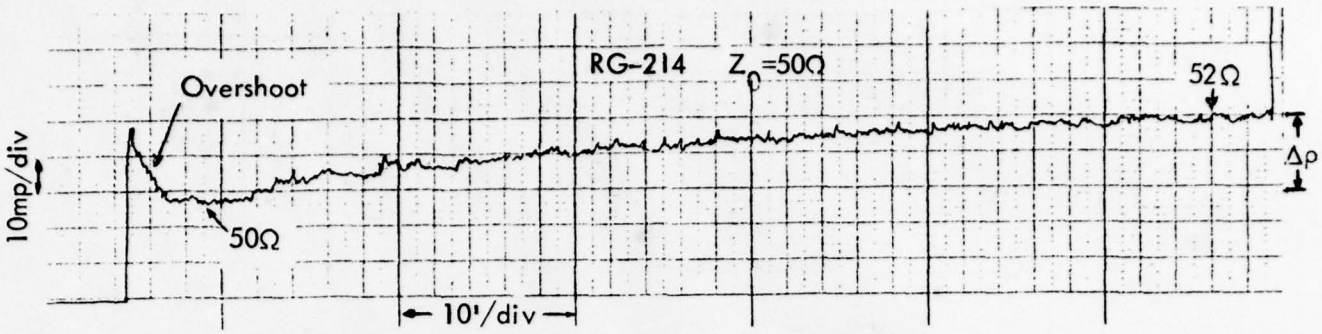

a. V-Ring Localizer Antenna Cable - 62 Feet Long
(Δρ = 22mρ)

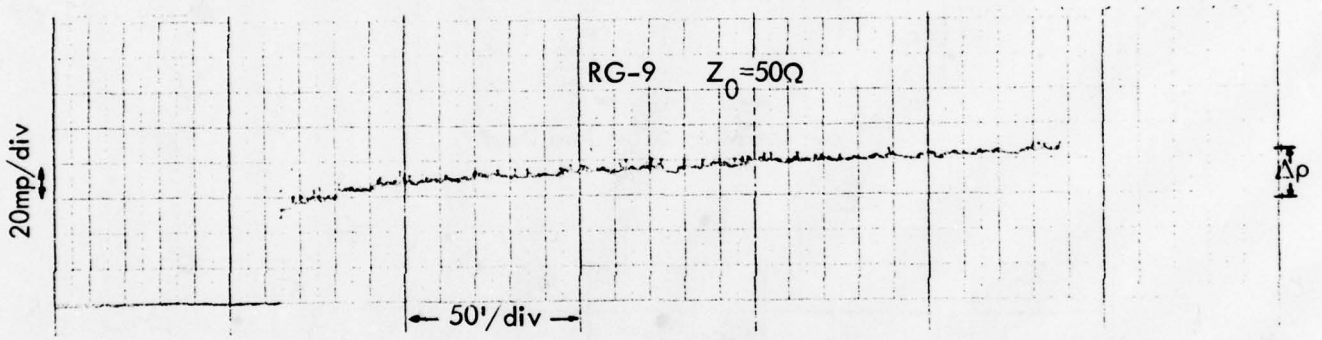

b. Null Reference Glide Slope Course Monitor Cable - 190 Feet Long
(Δρ = 30mρ)

Figure 4-35. Example of Resistive Loss in Cables. These cable measurements were taken at Wood County Airport in Parkersburg, W.Va. The end of the cable is marked by a sudden jump in the trace, which in these cases, was caused by an antenna or monitor on the end of the cable. Each cable has a constant rise called the "dribble-up" effect caused by resistive loss.

Figure 4-36 was obtained during field measurements made on antenna and monitor cables of the capture effect glide slope test facility at the Tamiami test site.

Figure 4-37 records measured traces of null reference glide slope antenna cables at Wood County Airport, Parkersburg, West Virginia.

Figure 4-38 gives examples of non-coaxial transmission line such as may be used for transmission of d.c. or low-frequency audio information.

Figure 4-39 was made at Tri-State Airport, Huntington, West Virginia. This figure shows the very low loss in a length of high quality cable.

Figure 4-40 shows the effect of a discontinuity between RG-58, 50 ohm cable and RG-59, 72 ohm cable.

Figure 4-41 depicts two cable faults detected and accurately located during a check at the Ohio University experimental localizer site at Albany, Ohio. The loose connector fault was cleared by tightening the connector giving a normal trace (not shown).

Figure 4-42 is a photograph of the TDR used to detect a slice fault in a coaxial cable.

(3) Conclusions. As shown by the figures, the TDR readily detects and locates discontinuities in simple cable runs. Since various connectors and adaptors are detectable and accurately locatable the TDR may be used for mapping simple cable runs. Such maps of properly installed and terminated simple cable runs will be valuable signatures for comparison with later traces to determine whether and where changes have taken place.

The experiment with the quarter wave transformer shows that some valuable information can be obtained even in the case of frequency dependent structures (a resonant line in this case) but that care must be exercised in interpreting the information obtained. In frequency dependent (tuned) networks many discontinuities occur in the time domain which are not seen in the frequency domain. This fact will be seen again in the next section on TDR analysis of RF combining bridges.

In summary, the TDR works best on simple cable runs properly terminated. On simple frequency dependent structures, care must be taken in interpretation of the traces.

b. TDR Analysis of RF Combining Bridges.

(1) Introduction. The ILS bridge or hybrid is necessary for the proper combination of RF signals in the antenna and monitor systems. Bridge faults caused by improper manufacturing, connection corrosion, and faulty cable connectors on the bridge ports result in improper operation of the ILS. It is, therefore, important that bridge faults be immediately detected and corrected.

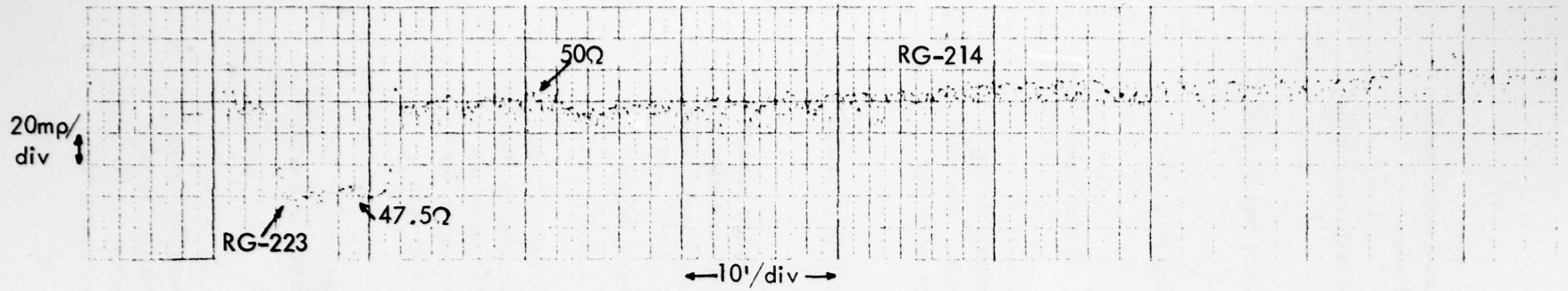

a. Portion of Middle Antenna Cable

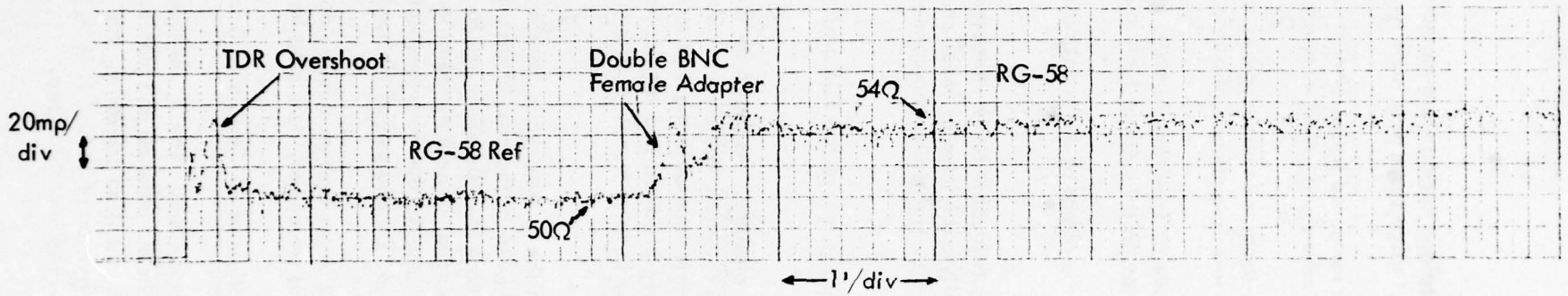

b. Portion of Lower Antenna Integral Monitor Cable

Figure 4-36. Capture Effect Glide Slope Antenna and Monitor Cable Traces Obtained at the Tamiami Airport in Miami, Florida. The three antenna cables (91.50', 91.75', 91.45') and three monitor cables (60.20', 58.00', 60.20') were measured to within ± 0.6 inches using the CRT readout and the distance dial. The RG-214 cable has an effective resistance of 2Ω/80 ft. as measured on the graph, while the RG-58 has an effective resistance of 2Ω/10 ft. Note the high characteristic impedance of 54 ohms for the RG-58 cable.

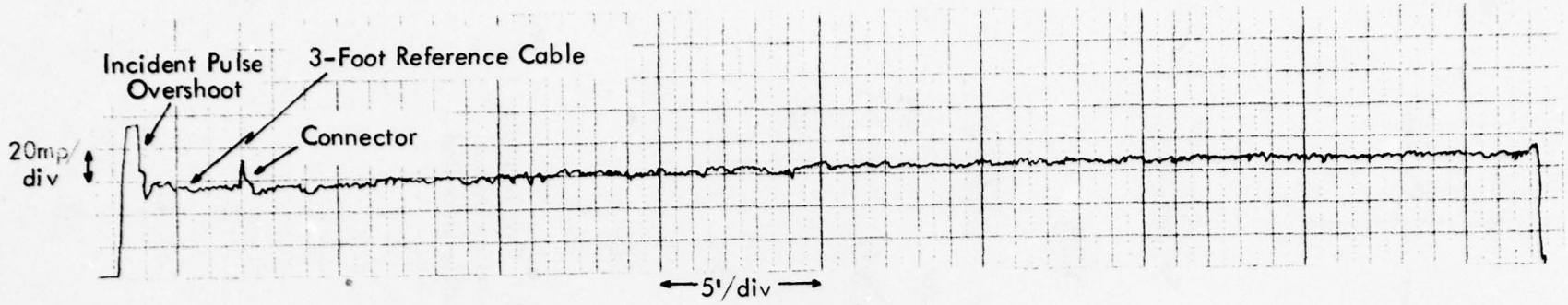

a. Glide Slope Lower Antenna Cable

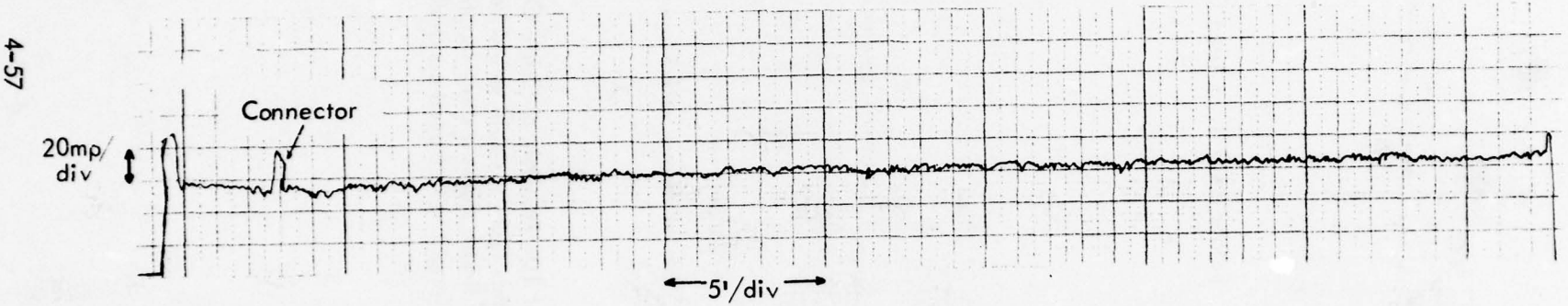

b. Glide Slope Upper Antenna Cable

Figure 4-37. Two Typical Cable Traces Obtained from a Null Reference Glide Slope at Wood County Airport, Parkersburg, W.Va. The cable before the connector is a three foot piece of precision 50Ω cable. This provides a 50Ω reference for comparison with the cable being measured as well as enabling the incident pulse overshoot to die down before the cable to be measured begins on the graph.

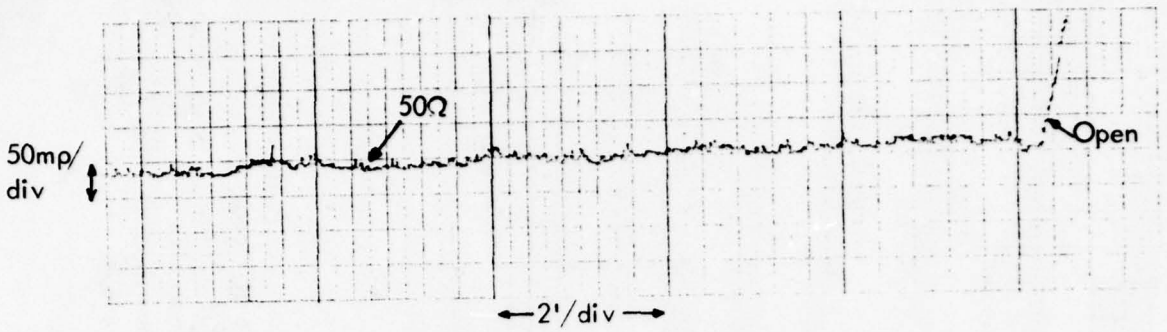

a. Belden 8451 Twin Lead Cable

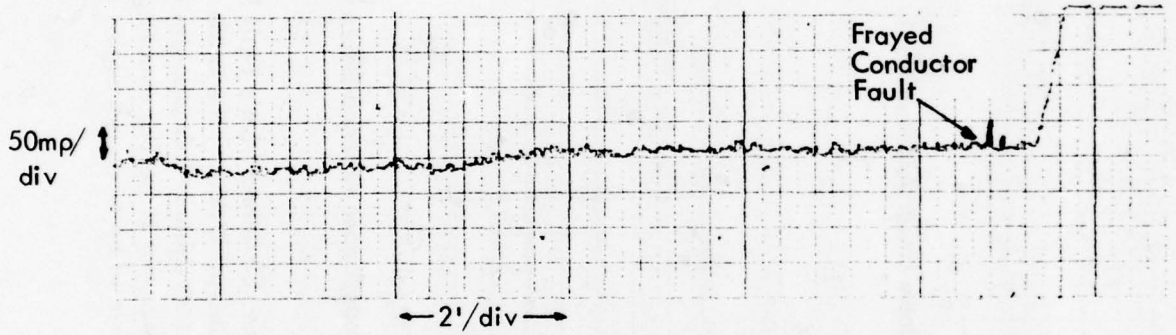

b. Same Cable as Above with Frayed Conductors

Figure 4-38. An Example of TDR Analysis of Cable Other Than Coaxial. One example of the use of this type of cable would be for a DC voltage return from a monitor. The figure shows a short length of Belden 8451 cable unfaulted and the same length with frayed conductors.

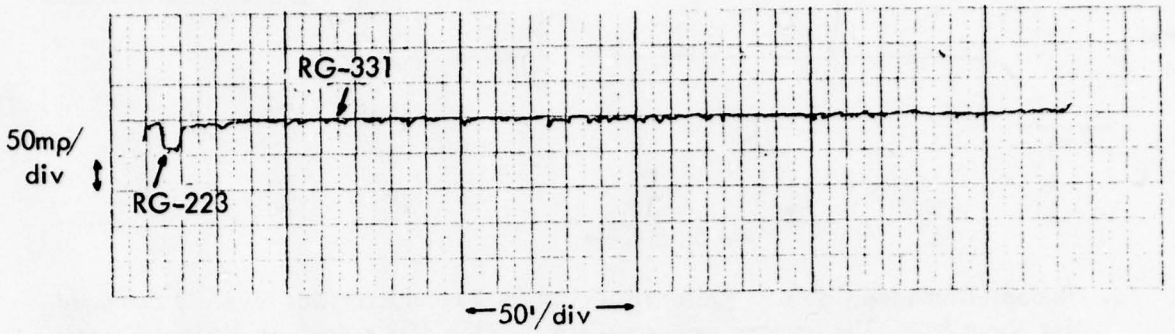

Figure 4-39. Trace of a Glide Path Monitor Cable Used at Tri-State Airport in Huntington, W. Va. The cable is composed of a small piece of RG-223 which runs from the monitor at the transmitter to connect to a length of RG-331 foamflex. The foamflex is a high quality cable used to run long distances underground. Note the very low resistive loss and small cable discontinuity.

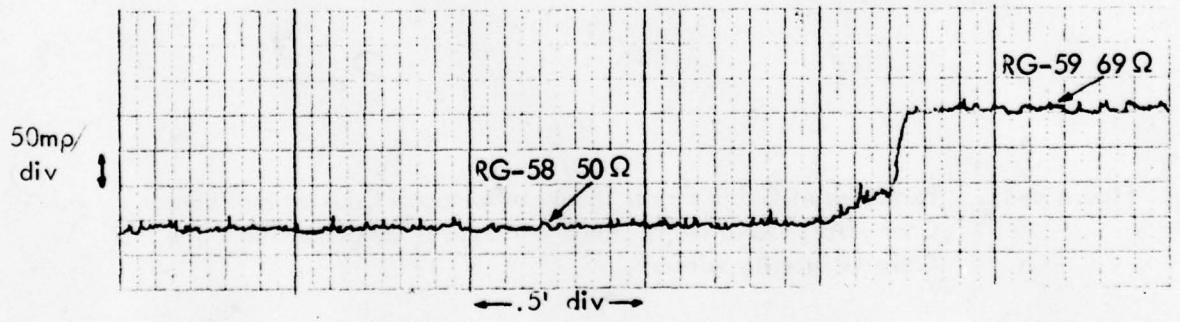

Figure 4-40. A Piece of RG-58 (50Ω) and RG-59 (72Ω) Cable Spliced Together to Show a Trace of Cables with Different Characteristic Impedances.

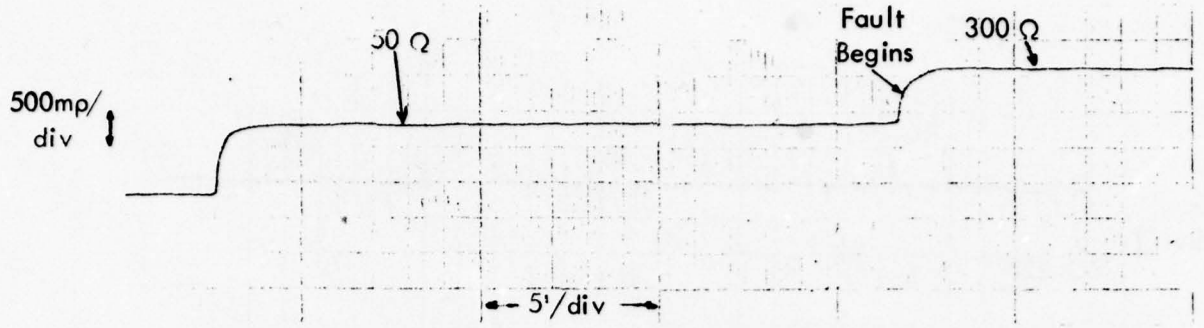

a. Rodent-Damaged Cable. Outer insulation and conductor was severely damaged for about 8". The damage was so severe that the TDR pulse was dissipated, thus the reason for the graph not returning to 50 ohms.

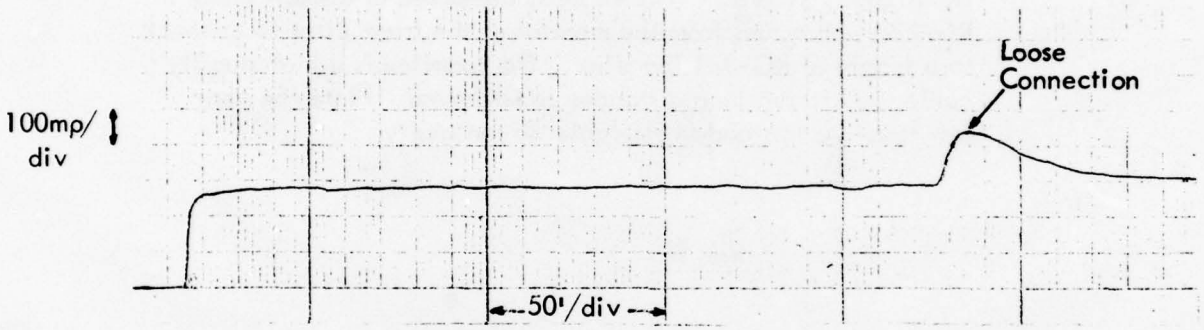

b. Loose Type N Female to Type N Male Connectors at a Buried Cable Junction Box

Figure 4-41. Examples of Cable Faults (Rodent-Damaged Coaxial and Loose Connector) Obtained at the Experimental Localizer Near the Ohio University Airport.

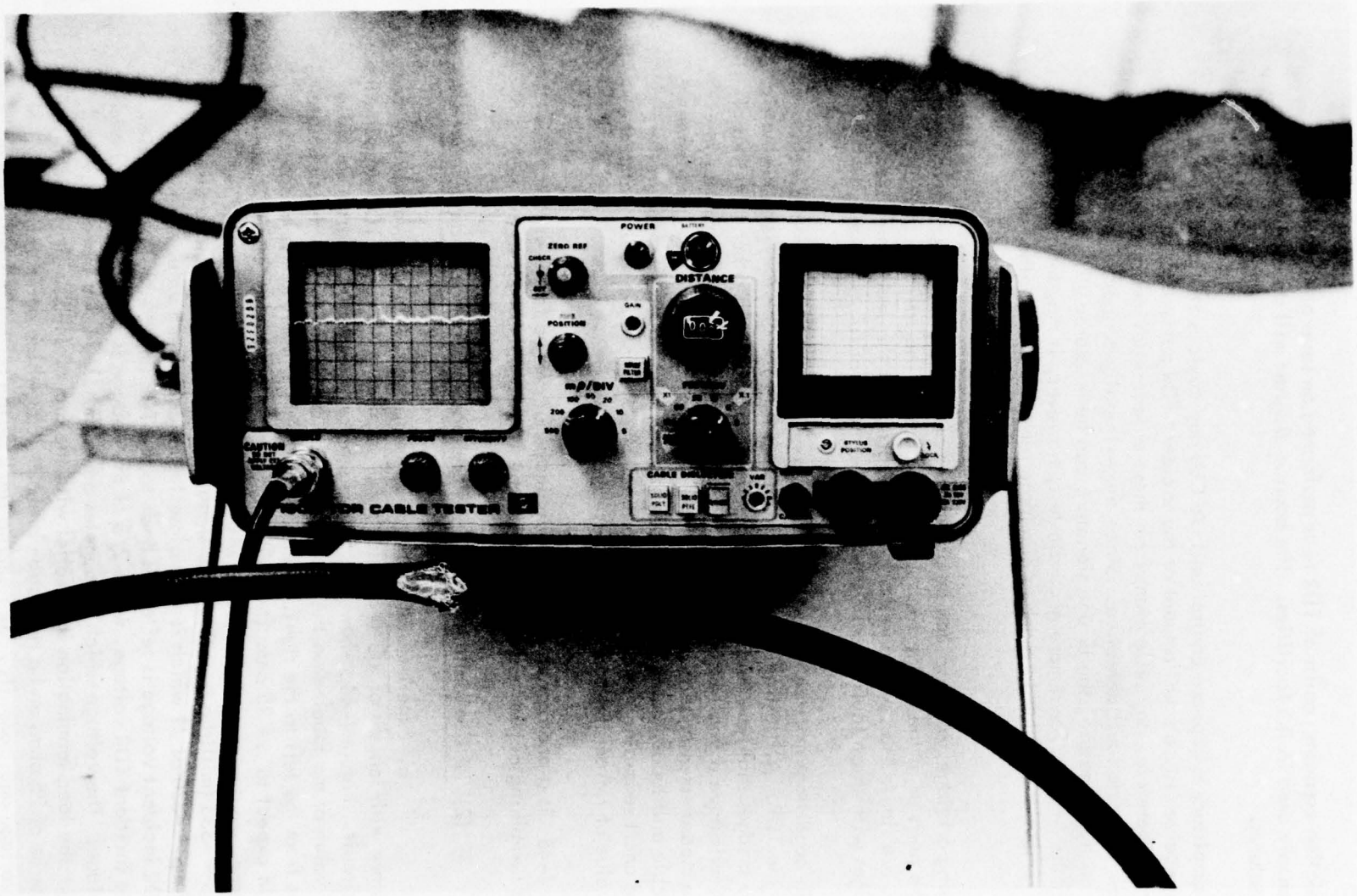

Figure 4-42. Tektronix 1502 TDR Measurement of a Sliced Cable Fault.

This section contains results of TDR tests performed on several RF combining bridges commonly used in ILS facilities. The bounce diagram will be used to analyze the TDR signatures.

In an amplitude and phase control unit (APCU) any devices connected to the bridge ports receive only a small amount of the incident TDR pulse when the TDR pulses a bridge port. Therefore, any reflections from these external devices are usually too small to allow accurate fault detection. Since the externally connected devices have little effect on the signature, the bridge signature can be measured with the bridge connected in the APCU. For a more accurate test, however, it may be necessary to electrically remove the bridge in order to eliminate reflections from other devices in the APCU.

In testing a bridge, any port can be pulsed and any fault of sufficient severity located at the ports or in the bridge lines can be detected. The faults in the following examples are limited to opens and shorts at the ports, but the techniques used to analyze bridges with these faults can be used for other types of faults as well.

Certain conditions must be recognized and taken into account when analyzing bridges with the TDR. All testing was done with the TDR in the polyethylene dielectric setting. Any bridges that have transmission line dielectric constants other than that of polyethylene will have a small error in their distance plot. Because of variables involved in the measurements, such as deviation from nominal characteristic impedance of coaxial cable and loads, cable loss, non-ideal connectors, and tolerances in the TDR gain and chart recording, some signature values of ρ may not precisely match the theoretical value of ρ from the bounce diagram.

Figure 4-43 is a photograph of several devices that can be found in ILS RF distribution and combining networks and tested with the TDR.

(2) RF Combining Bridge TDR Signature and Bounce Diagram Analysis.

a) Experimental Coaxial Cable Bridge. A bridge was constructed in the laboratory with lengths of RG-8 coaxial cable to allow a thorough TDR examination of a bridge circuit. Figure 4-44 shows the TDR signature and circuit diagram for this bridge. The value of mp labeled on the signature is the change in mp, as the signature moves in time from the left to the right. When examining the input to the bridge at J1, one would expect to see 25 ohms (two 50 ohm cables in parallel). The TDR, being a 50 ohm source, would see a discontinuity with a reflection coefficient of (25-50)/(25+50) or mp = -333 (millirho = -333). The signature for the bridge shows a discontinuity of mp = -320 at J1 which is very close to the calculated value. At J1, 1/3 of the TDR incident voltage is reflected back to the TDR (mp = -333) of opposite sense with the incident TDR voltage, while 2/3 of the voltage is transmitted down each arm of the bridge. The voltage which propagates down the J1-J4 arm travels 2.7 ft. and encounters the load termination in parallel with the arm of J4-J3. This discontinuity has an impedance of 25 ohms and a reflection of mp = -333 which again reflects 1/3 of the incident voltage and transmits 2/3. Keeping track of the reflections and voltage levels

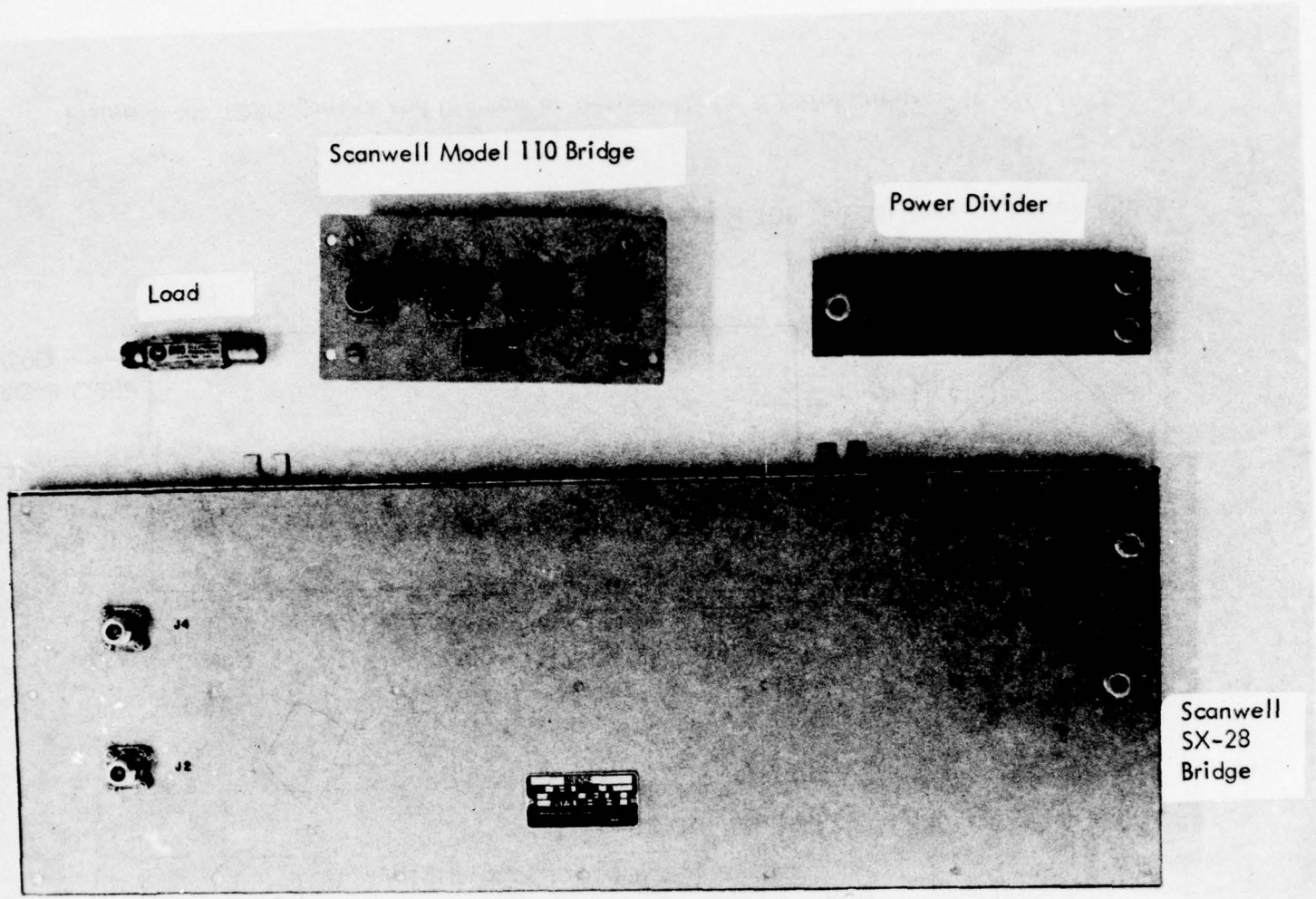
Scanwell Model 110 Bridge
Power Divider
Load
J4
J2
Scanwell
SX-28
Bridge

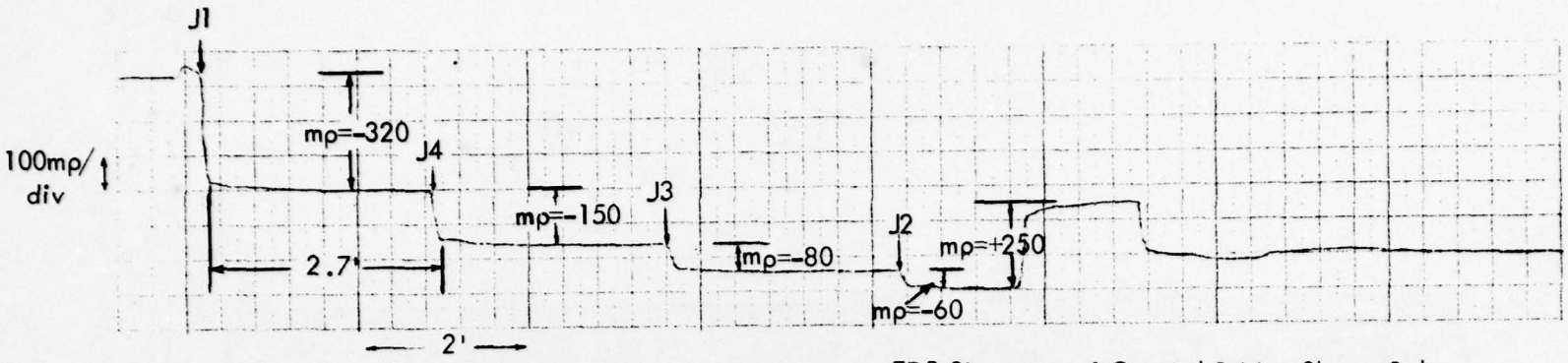

a. TDR Signature of Coaxial Bridge Shown Below-No Fault.

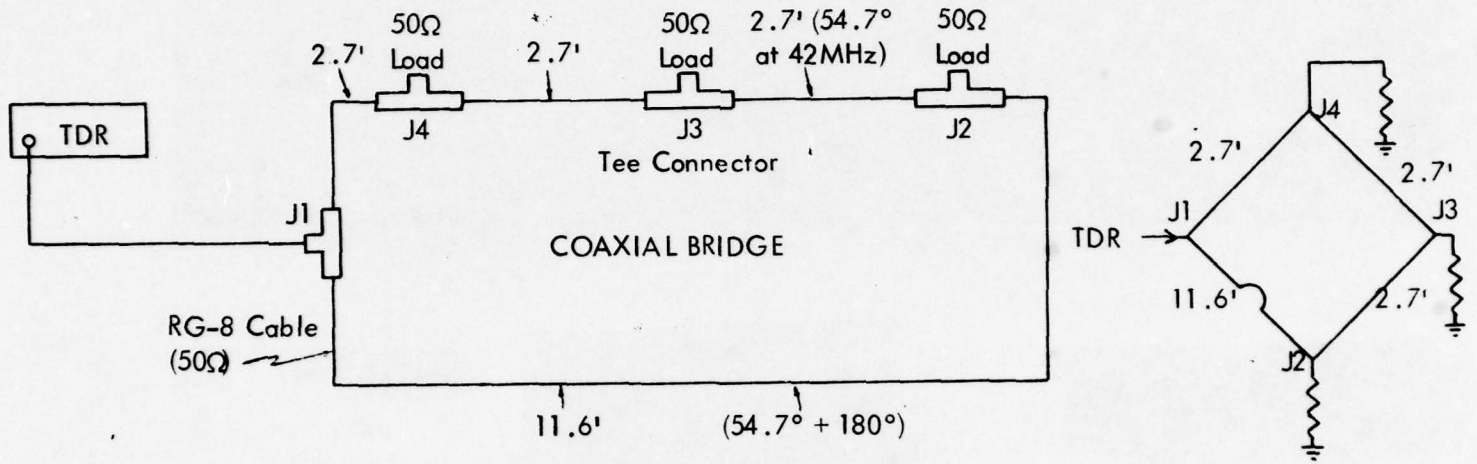

b. Diagram of TDR Test Set-Up for Coaxial Bridge.

Figure 4-44. TDR Signature and Diagram of Test Set-Up for Coaxial Bridge.

quickly becomes very cumbersome, but can be accomplished with the bounce diagram shown in Figure 4-45. The table lists values of ρ obtained from the signature and the bounce diagram for common distances.

At the point where the TDR pulse enters the bridge there are two directions (down each arm of the bridge) for the pulse to propagate. On the bounce diagram, the bridge ports J1, J2, J3 and J4 are labeled across the top. J1 appears at the top two corners since the TDR pulse travels down each adjacent arm at J1. Any voltage reflections transmitted bacj to J1 are also transmitted to the TDR. These transmitted voltages are shown on each side of the diagram. Since $\rho = \frac{E_r(\text{the reflected voltage})}{E_i(\text{the incident voltage})}$, the corresponding values of ρ were calculated and are labeled next to the voltages transmitted to the TDR. It should be noted that voltages transmitted to the TDR as shown on each side of the bounce diagram add when they arrive at a common time. This means that the reflection coefficient values also add.

Figure 4-46 contains TDR signatures for the bridge just discussed under fault conditions. The top signature was measured with J2 open. For this fault, the pulse must travel around three arms of the bridge of 8.1 feet before the discontinuity is seen. Until them, the signature is identical to the no fault signature for the bridge. From an open, or increase in impedance, one would expect a rise in the value of ρ. This increase in ρ is evident in the signature in Figure 4-46.

The bottom signature is of the same bridge with J3 shorted now. Again, no fault is apparent on the signature until the pulse reaches the faulted area which in this case is J3. From a short, or decrease in impedance, one would expect a decrease in ρ. The decrease in ρ is seen on the signature.

One effect of opened and shorted ports requires closer examination. The port connector, generally a female N type, has a finite length (about 1"). When an open or a short is placed on the end of the bridge port connector, the finite connector length still can act as a short piece of 50 ohm transmission in which a wave can travel. The effect of this short piece of transmission line is to cause the "blips" in Figure 4-46. It also contributed to the sloping effect of the trace at J3 and J2 in Figure 4-46B. due to the multiply-reflected waves arriving back at the TDR at different times. The difference in time is the amount of time needed for the wave to travel up the port connector to the short at J3 and back.

To help clarify the port connector transmission line effect as seen in Figure 4-46, Figure 4-47 provides an expanded view of the shorted port being pulsed by the TDR. The TDR pulse is introduced at one end of the Tee connector. The bounce diagram for the TDR pulse is given in Figure 4-47a. There is actually only one point where $\rho = -1/3$, but two points are drawn to show that there are two different paths for the wave to travel at the discontinuity B. In Figure 4-47a, the pulse from the TDR travels down the cable, A, and encounters a discontinuity of $\rho = -1/3$ at B and reflects $-E/3$ back to the TDR and transmits $2E/3$ down the cable, D, and $2E/3$ toward the short. At the short ($\rho = -1$) the wave is reflected and $-2E/3$ travels back to the discontinuity at B where $2E/9$ is reflected

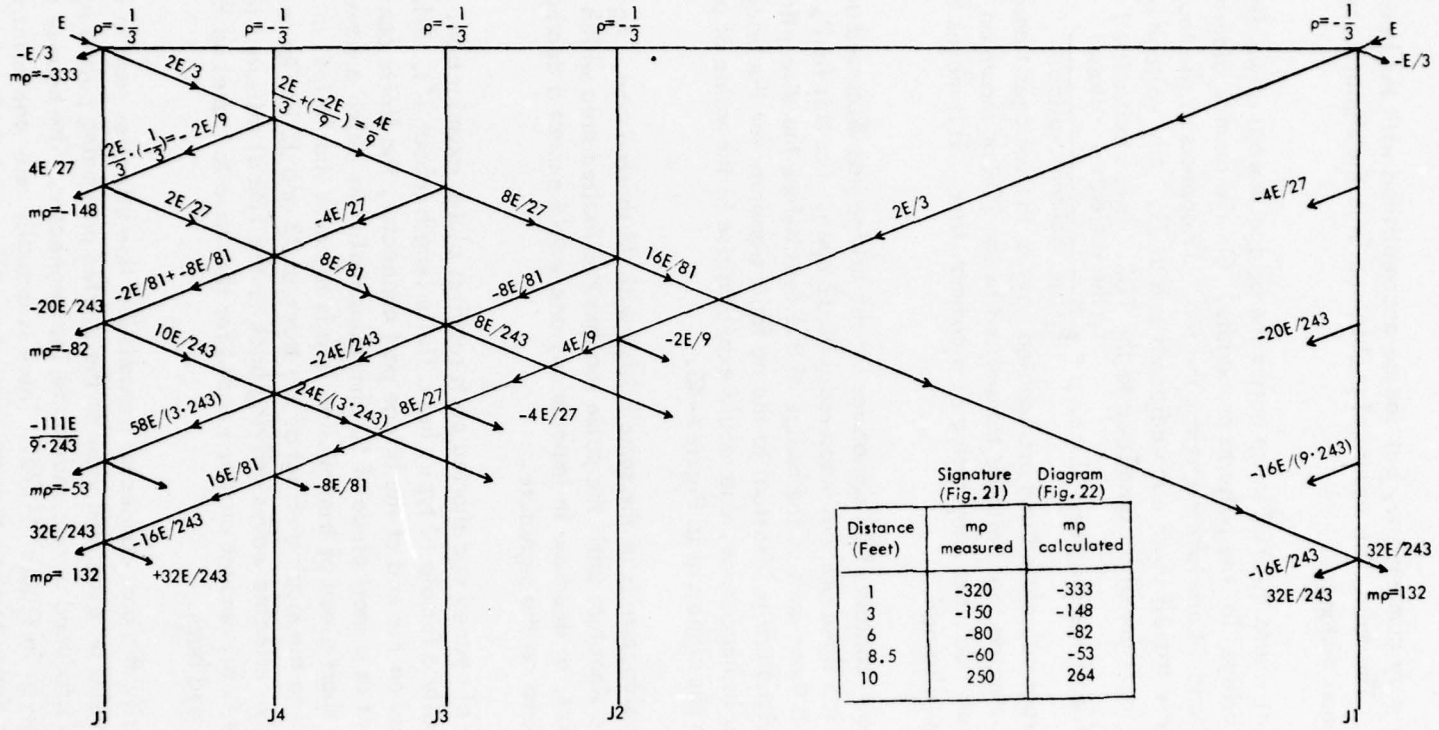

Distance (Feet)	Signature (Fig. 21) mρ measured	Diagram (Fig. 22) mρ calculated
1	-320	-333
3	-150	-148
6	-80	-82
8.5	-60	-53
10	250	264

Figure 4-45. No Fault Bounce Diagram for Bridges of Figures 4-44 and 4-50b.

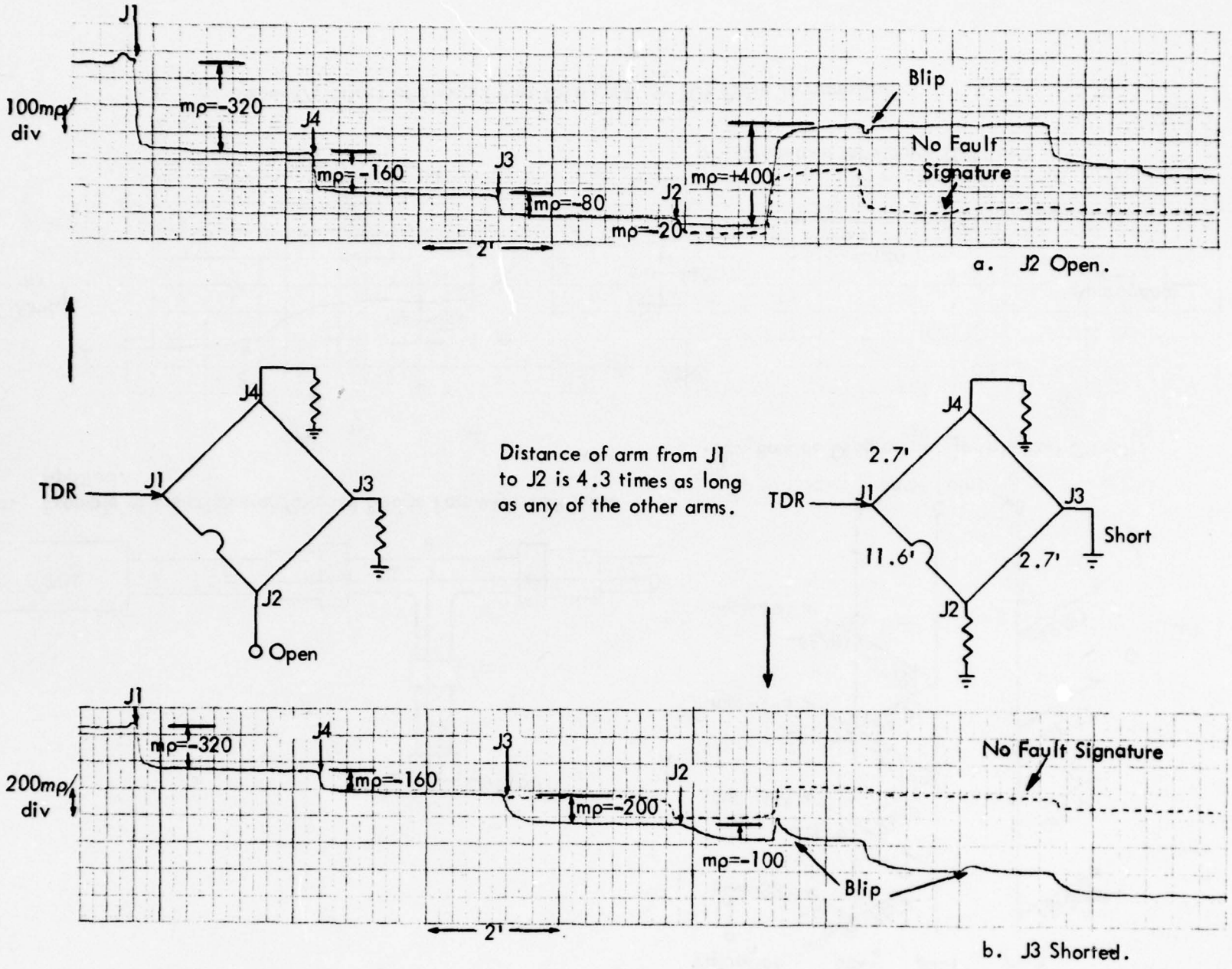

Figure 4-46. TDR Signatures of Faulted Experimental Coaxial Bridge Connections.

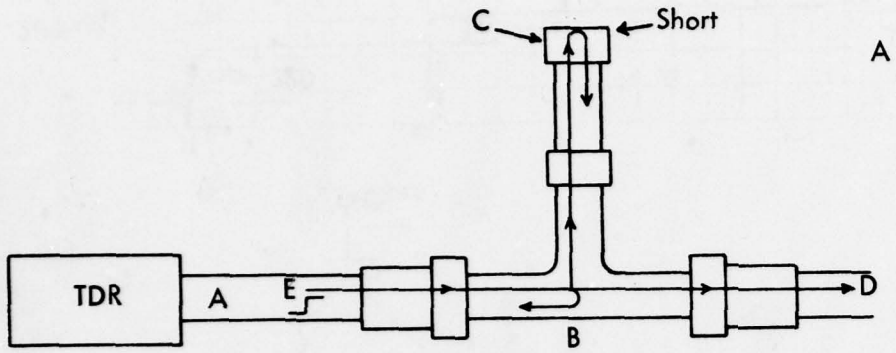

a. Example of Experimental Coaxial Bridge Port with TDR Pulse Applied.

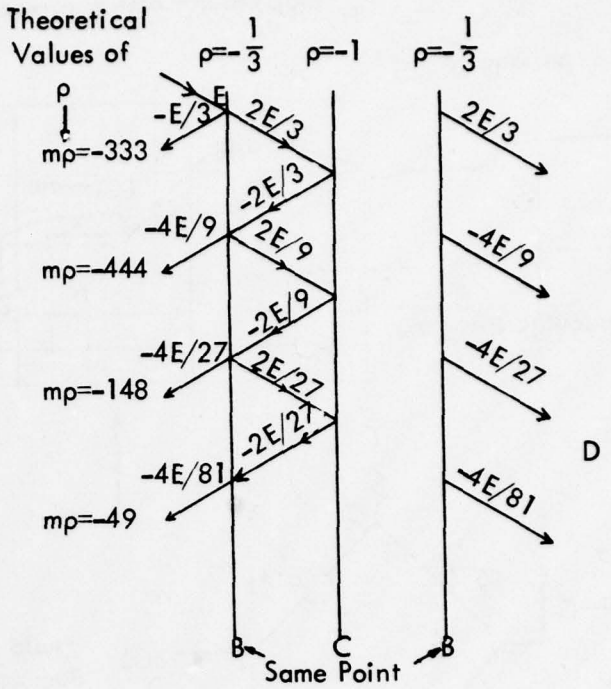

b. Bounce Diagram for Sample Port Circuit.

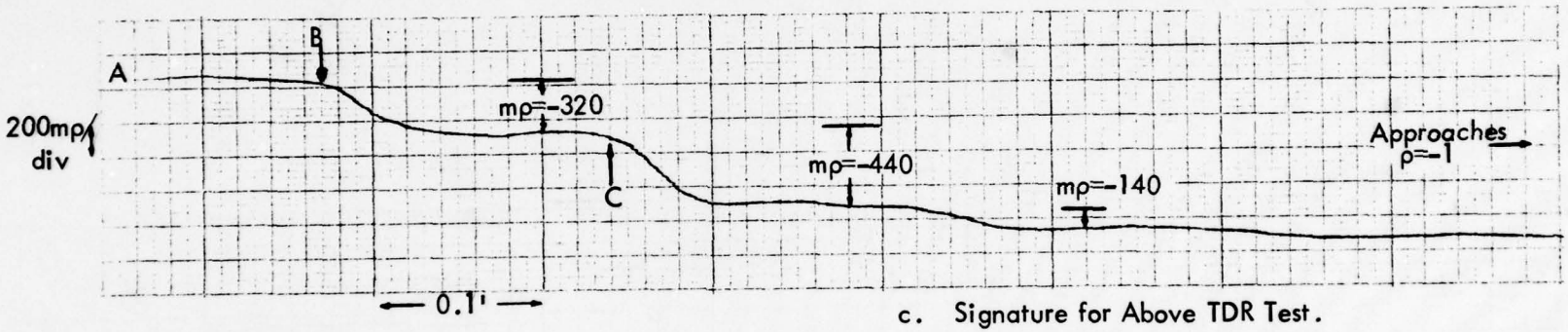

c. Signature for Above TDR Test.

Figure 4-47. Effect of Shorted Port Connector on TDR Pulse Transmission.

toward the short again and -4E/9 is transmitted down cables A and D. The reflecting and transmitting of waves goes on forever, but a steady-state value of $\rho = -1$ is being approached as is seen in the TDR signature in Figure 4-47c. In Figure 4-47c, the ρ values are measured from the signature and compare very well to the theoretical values of ρ obtained from the bounce diagram.

Bounce diagrams for the fault conditions of Figure 4-46 are given in Figures 4-48 and 4-49. These bounce diagrams do not consider the effect of wave transmission on the small length of the bridge port as studied earlier. The significant difference in the bounce diagram if the effect were considered would be the presence of the transient blips noted in Figure 4-46. Since all ports and bridge arms are indicated on the signature by the time J2 is reached, the contribution of these "blips" is small because they appear significantly only after J2. The values of ρ obtained from the bounce diagrams for the examples given closely agree with the values of ρ as measured on the TDR signatures.

b) Localizer Coaxial Cable Bridge. Figure 4-50 is the TDR signature for both the no fault and a fault condition of a coaxial cable type bridge that was tested in an APCU at a commissioned localizer site. The results of those tests provide a comparison with the experimental coaxial bridge studied.

Since the bridge was tested while connected to other devices in the APCU, the signature is a record of the bridge alone only until reflections from the external devices reach the TDR. This could conceivably mask faults at J2 unless one had a previous knowledge of the no fault signature (Figure 4-50a).

The impedance and length ratios for the localizer bridge and the experimental coaxial bridge analyzed earlier are identical; therefore, the bounce diagrams in Figures 4-45 and 4-47 also apply to the localizer bridge to the point where reflections from other devices complicate the signature. Bounce diagrams could conceivably be constructed with external devices taken into consideration, but this would be a difficult task.

c) Scanwell Model 110 Bridge. Another bridge similar to the previous two bridges of this section if the Scanwell Model 110. It is shown in the photograph in Figure 4-43. Various signatures of the 110 shown in Figure 4-51 are similar to the signatures of the two bridges previously discussed. Even though line lengths of the 110 are the same as those in the localizer coaxial bridge, because of smaller diameter cable and tight coiling the 110 takes up much less space. Since the impedance and line length ratios are identical to both preceding bridges, the bounce diagrams for them also apply for the 110.

d) Scanwell SX-28 Bridge. The SX-28 bridge by Scanwell is made using stripline construction where a dielectric substrate is the base on which strips of copper transmission line run to form the arms of the bridges. One arm of the bridge is three times the length of any other arm. In Figure 4-52 the TDR signature and diagram of the bridge are given. According to the TDR signature, the first discontinuity (at J1)

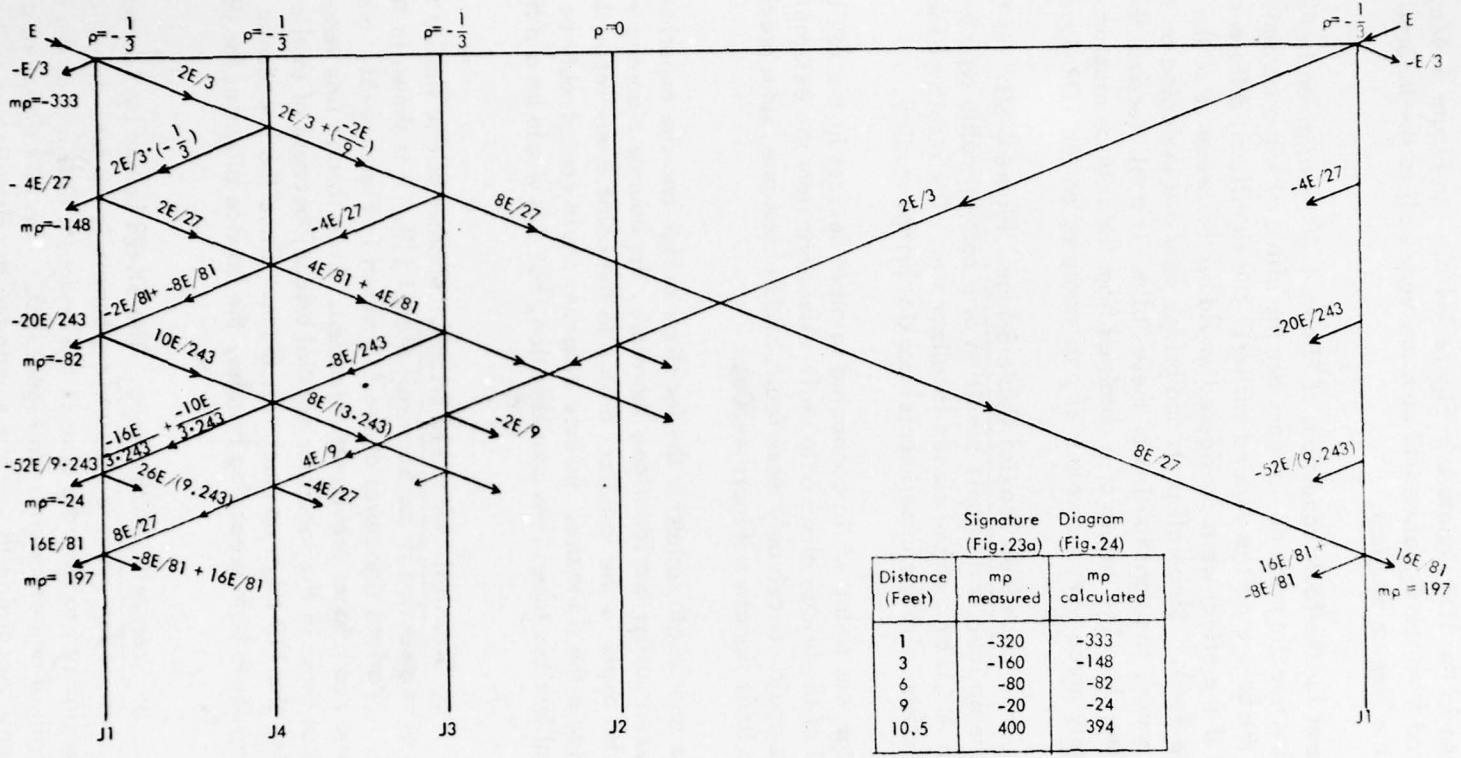

Distance (Feet)	Signature (Fig. 23a) mρ measured	Diagram (Fig. 24) mρ calculated
1	-320	-333
3	-160	-148
6	-80	-82
9	-20	-24
10.5	400	394

Figure 4-48. J2 Open Fault Bounce Diagram for Bridges of Figures 4-46a and 4-50b.

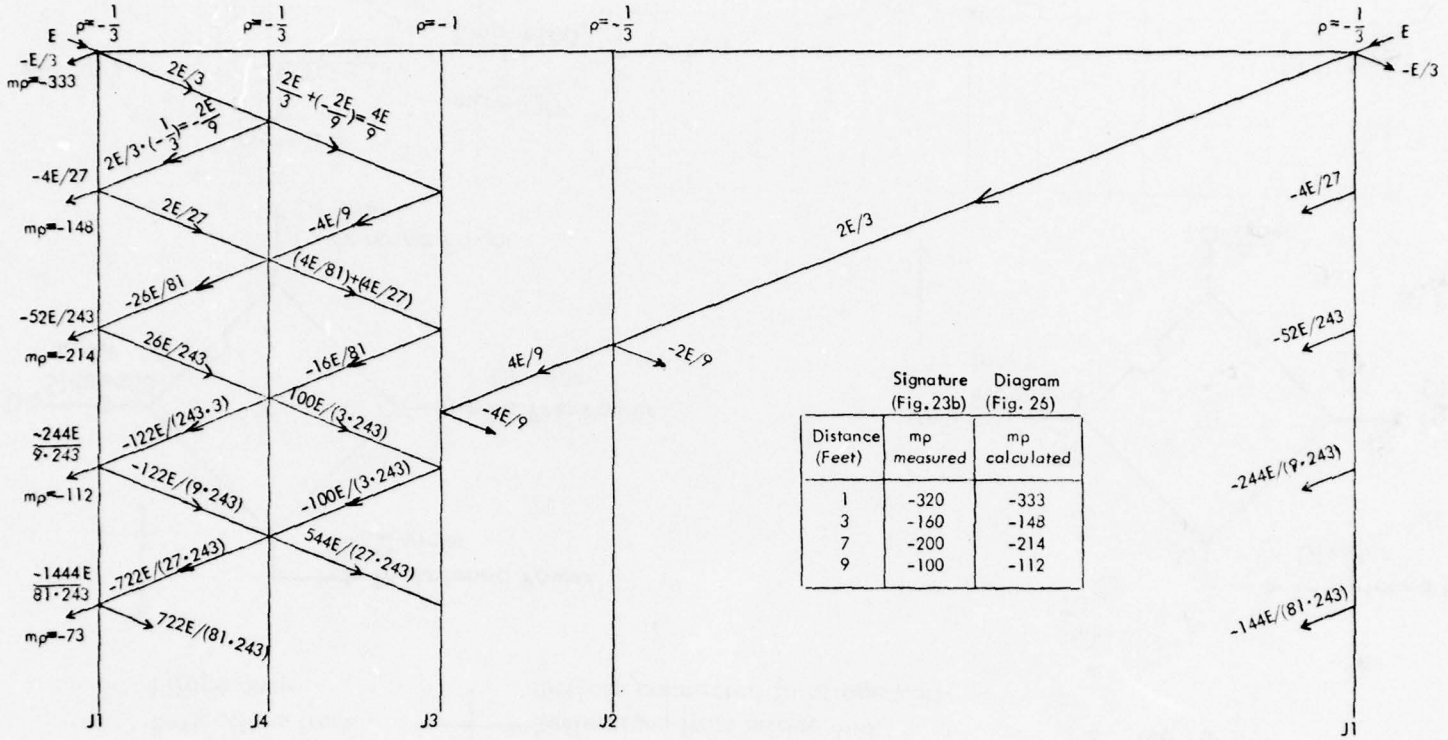

Distance (Feet)	Signature (Fig. 23b) mp measured	Diagram (Fig. 26) mp calculated
1	-320	-333
3	-160	-148
7	-200	-214
9	-100	-112

Figure 4-49. Shorted Bounce Diagram for Bridges of Figures 4-46b and 4-51c.

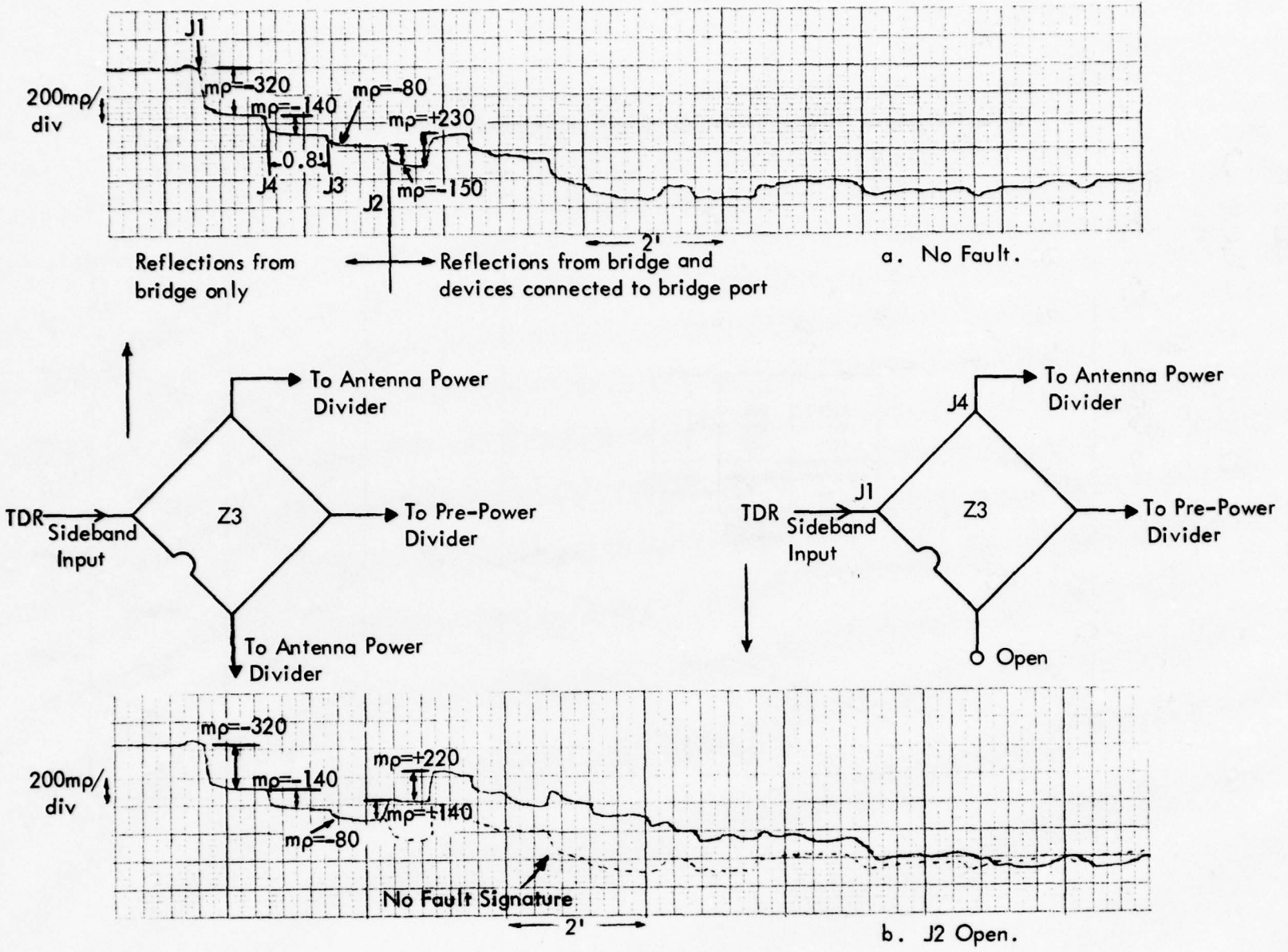

Figure 4-50. TDR Signature of a Coaxial Bridge on Sideband Input to a Localizer Distribution System - Detroit City Airport.

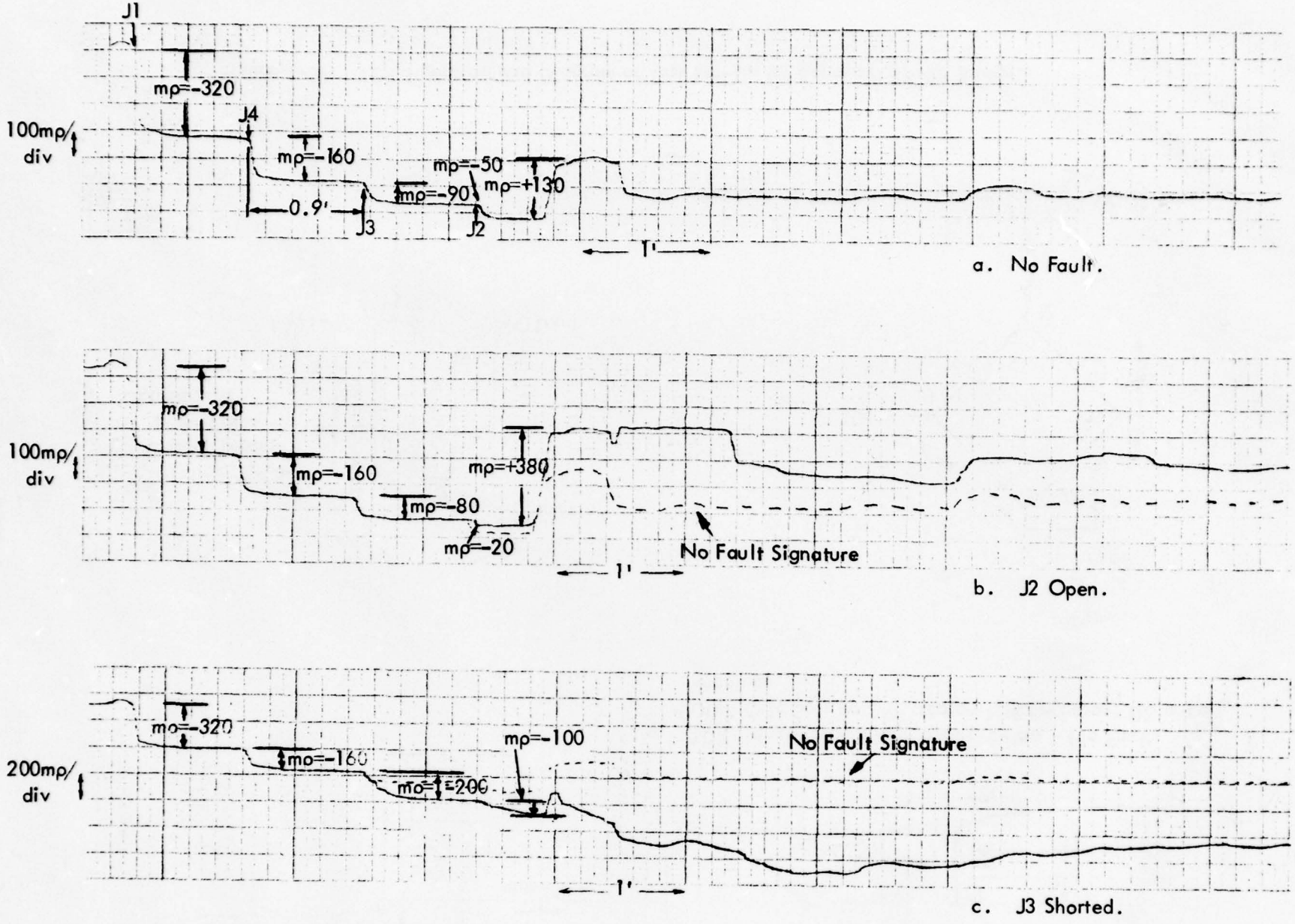

Figure 4-51. TDR Signatures of Scanwell Model 110 Bridge.

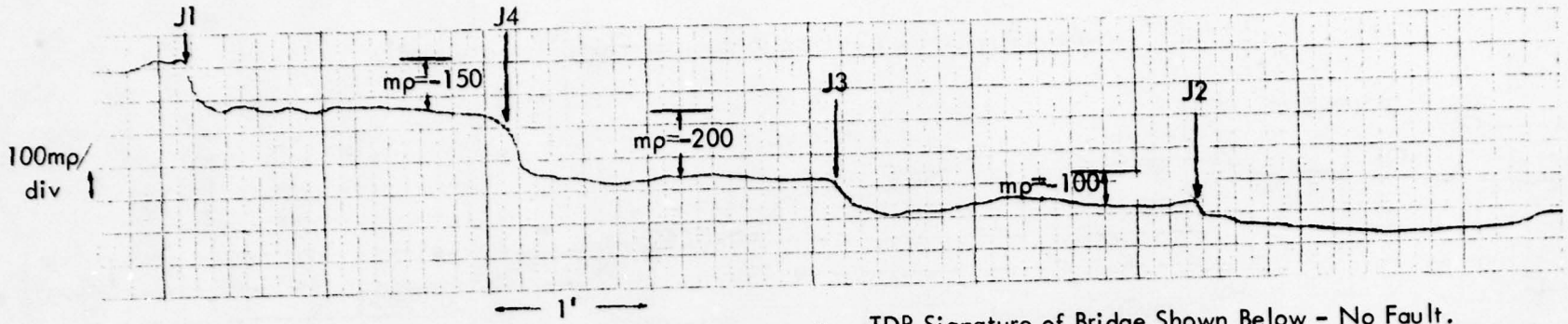

a. TDR Signature of Bridge Shown Below - No Fault. Dielectric Setting Adjusted on TDR for Proper Distance Reading.

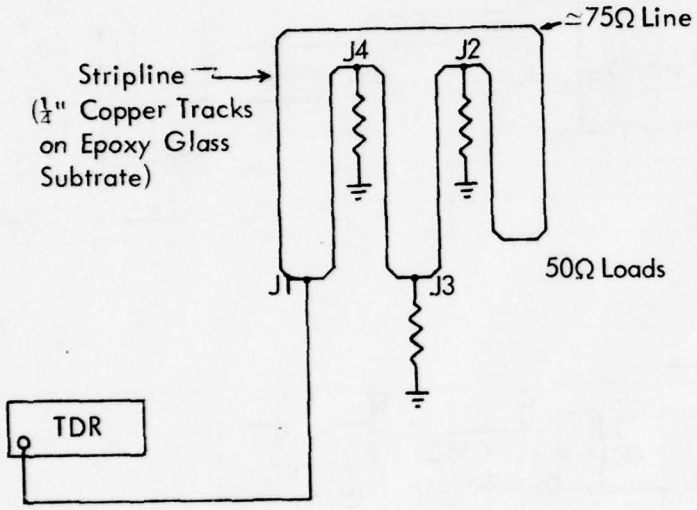

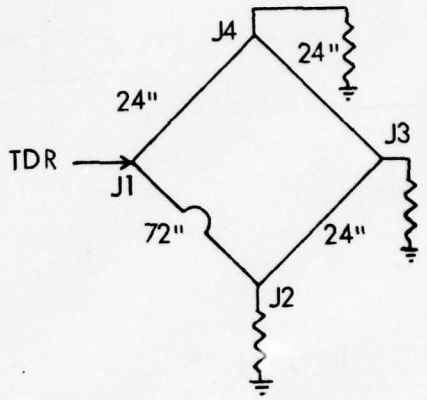

b. Diagram of TDR Test Set-Up for Scanwell SX-28 Bridge.

Figure 4-52. TDR Signature and Diagram of Test Set-Up for Scanwell SX-28 Bridge.

has a reflection coefficient of approximately mp = -140. From $Zr = Zo \frac{1-\rho}{1+\rho}$, where Zr is the discontinuity impedance and Zo is the impedance of the TDR transmission line (50 ohms), Zr is calculated to be 36 ohms. Since the discontinuity is caused by two parallel lines of equal impedance, then $36 = \frac{(Zo')^2}{2Zo}$ where Zo' is the characteristic impedance of the stripline which is found to be 72 ohms. This calculated value of characteristic impedance is a standard transmission line impedance for bridges of this type. At each of the other corners of the bridge, a similar analysis can be performed since the 72 ohm transmission line meets a discontinuity of 72 ohms and 50 ohms (port termination) in parallel at each corner. Voltage levels and reflections soon become hard to keep track of, so a bounce diagram is useful (Figure 4-53). The mp value looking into J1 from the TDR as mentioned earlier is -160 or about -1/6. When the waves transmitted from J4 and J2 reach J1 they see a discontinuity of reflection coefficient (72//50 - 72)/(72//50 + 72) or about $\rho = -3/7$. Thus, the two reflection coefficient values are labeled on each corner of the top of the bounce diagram. The diagram is carried out to three reflections back to the TDR.

Two fault condition signatures are depicted in Figure 4-54 for the SX-28. The bottom trace is actually two stacked signature recordings formed by adjusting the TDR vertical trace positioning for each recording in order that the 100 mp/div. resolution can be maintained. Both faults are quite easily detected by comparing the faulted and unfaulted TDR signatures.

(3) Conclusions. Based on the theoretical and experimental work presented in this section, the TDR is a credible tool for ILS work. The conclusions are:

1. It is useful in both locating and identifying faults in RF combining bridges. In comparison, frequency tests including vector voltmeter measurements, determine the presence, but not the location and characteristics of the fault.

2. The TDR is instrumental in providing an immediate, permanent record of the bridge fault test results in the form of a strip chart recording. The fault location is the point on the signature where the trace first deviates from the expected value. Experience has shown that signature deviations greater than 5% of the expected value at any point strongly indicate a fault condition.

3. It is easy to use the TDR in performing measurements. To fault check a bridge it is often only necessary to connect the TDR output to a port of the bridge and examine the returns on the TDR.

4. The TDR is a singular device for fault tests. The TDR needs no peripheral equipment for its measurements such as an oscilloscope, couplers, or signal generator. The integrated battery pack enables use independent of external power.

5. Faults can often be diagnosed by simple transmission line analysis and a basic knowledge of bridge characteristics such as arm lengths and line impedances. For this technique to be most effective, the bridge should be electrically removed from the APCU; however, in some cases adequate results may be obtained without this removal.

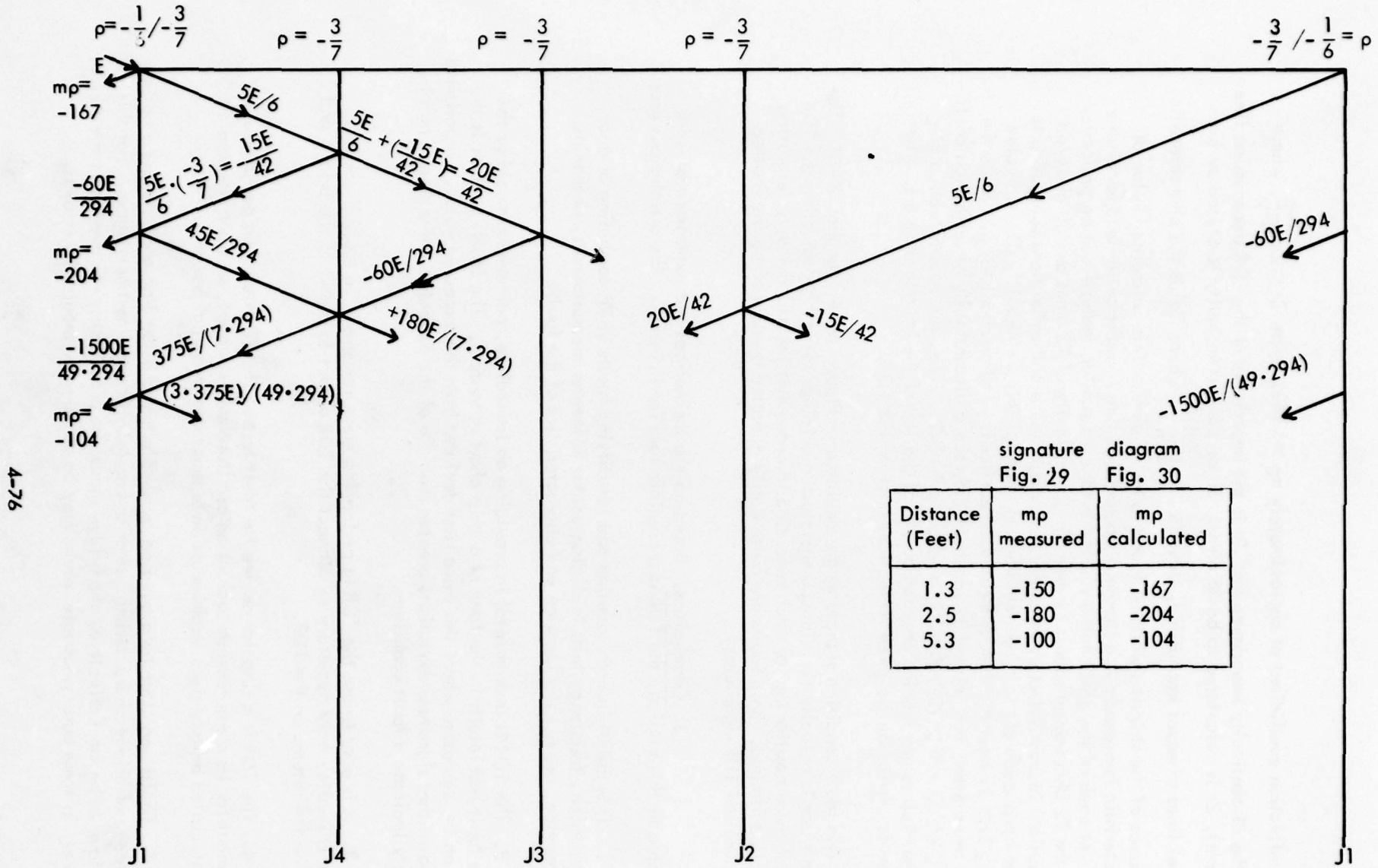

Distance (Feet)	signature Fig. 29 mρ measured	diagram Fig. 30 mρ calculated
1.3	-150	-167
2.5	-180	-204
5.3	-100	-104

Figure 4-53. No Fault Bounce Diagram for Scanwell SX-28 Bridge.

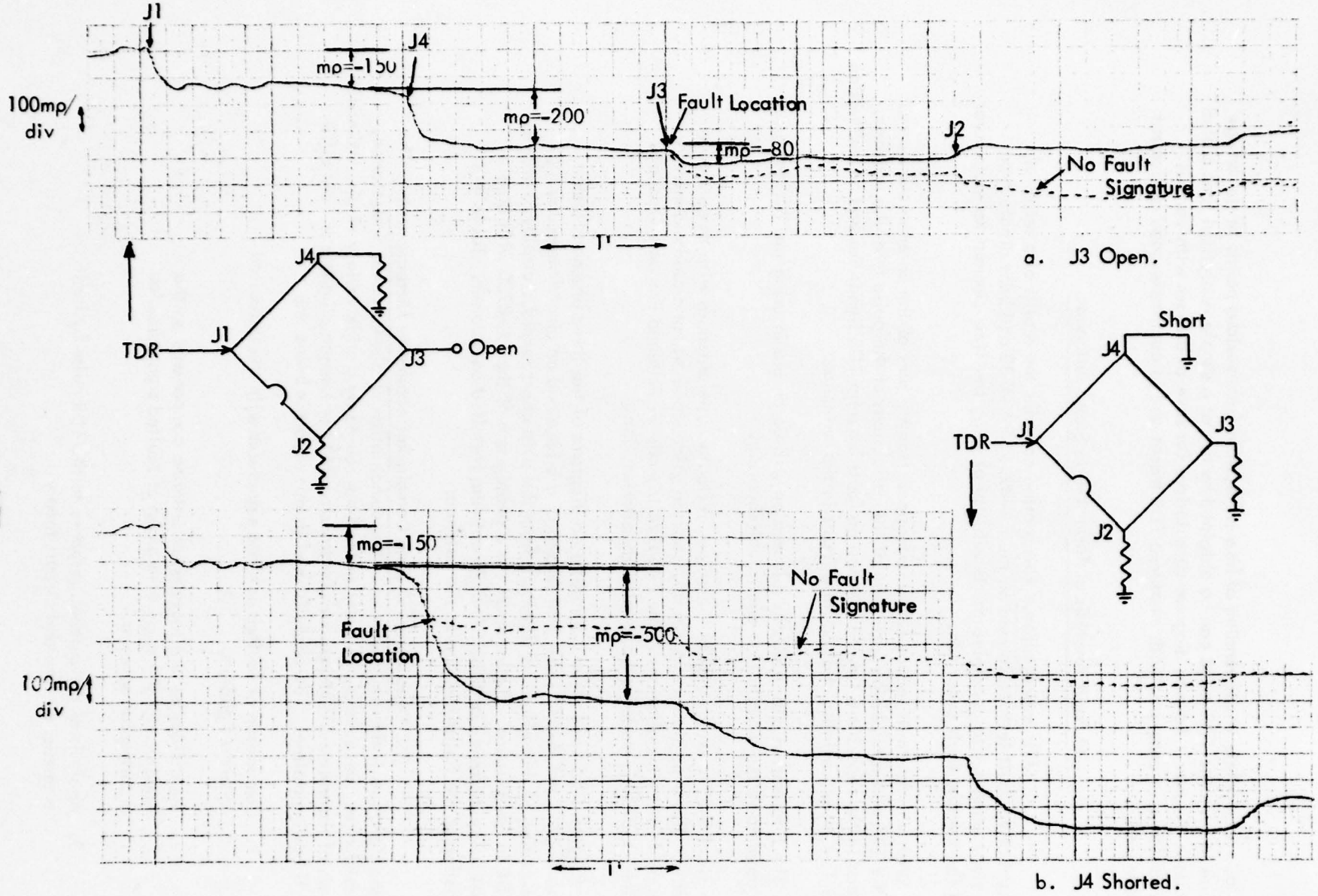

Figure 4-54. Signatures of Faulted SX-28 Bridge Connections.

6. A complete understanding of how reflections from various points in the bridge combine to form the TDR trace can be obtained by use of a simple analytical tool called the bounce diagram. Bounce diagram calculations for several bridges with various terminations were compared with measured TDR traces and in each case good agreement was obtained.

c. *TDR Fault Analysis of Three Glide Slope Antennas.*

(1) Introduction. This section contains the results of a series of nondestructive fault tests performed on the FA-8976, FA-8730 and bent dipole type glide slope antennas to determine the feasibility of using the Time Domain Reflectometer (TDR) for antenna fault detection.

With a given fault induced, the antenna or monitor port of the antenna was pulsed with the TDR and a recording was made of the reflections of the pulse from the antenna. Included in the report is a set of fault and no fault antenna TDR signatures and an evaluation of the TDR in determining and locating faults in the antennas.

The information and results in this section will be an aid in using the TDR for glide slope antenna system installation and troubleshooting.

The FA-8976 and FA-8730 are corner-reflector type antennas with three dipole elements. The bent dipole is a simple, common glide slope antenna used extensively in the past in ILS installations. The FA-8976 is made by Antenna Products Company and the FA-8730 is made by Scanwell Laboratories, Inc.

Figures 4-55 and 4-56 are detailed diagrams of the three antennas tested. Figures 4-57 and 4-58 show TDR testing of a bridge and an aircraft antenna with the recording of the reflection signature from the strip chart recorder displayed above the TDR in each figure. Figure 4-59 is a photograph of the FA-8730 with dipole current being measured and the FA-8976 antenna installed on a tower. Table 4-4 is a listing of the faults induced in the antennas.

(2) Description of Time Domain Reflectometer Measurements. The antenna signature is the result of a complex combination of capacitance, inductance, and resistance. Because of the many reflections caused by a wide variety of discontinuities, analysis of the antenna TDR response by transforms [4] or bounce diagrams is very difficult, if not impossible. The analysis used in this report is based on:

1. Comparison of faulted antenna signatures with the unfaulted antenna signature.

2. Identification and location of antenna components on the signature by the study of a group of faulted signatures for a particular antenna.

3. Analysis of the antenna response to the TDR pulse by basic transmission line and circuit theory.

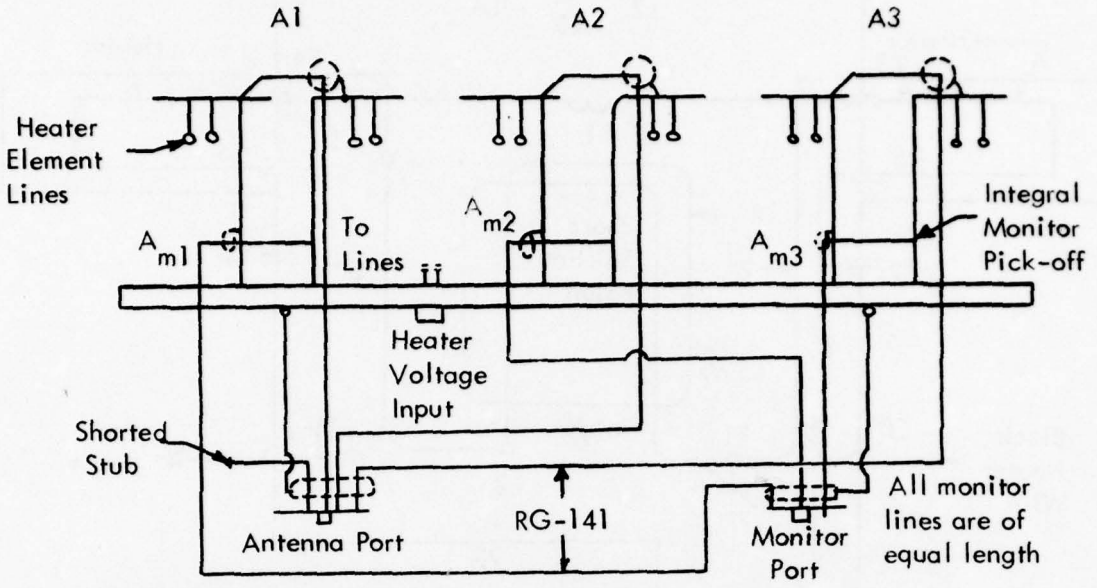

FA-8976 Antenna

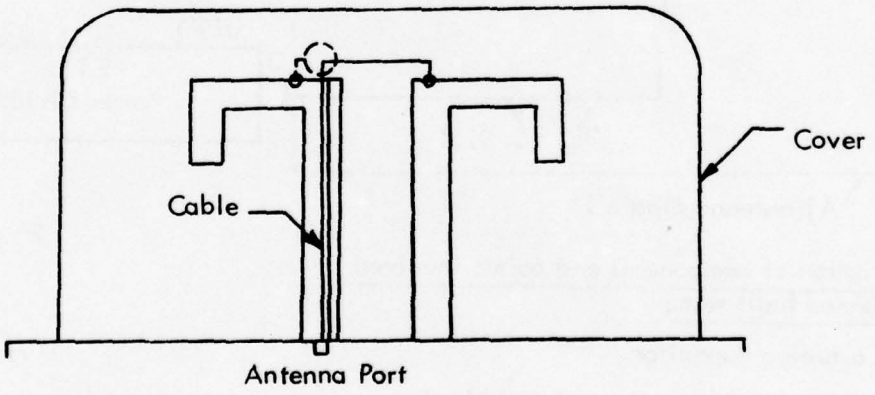

Bent Dipole Antenna

Figure 4-55. Detailed Diagram of the FA-8976 and Bent Dipole Type Antennas.

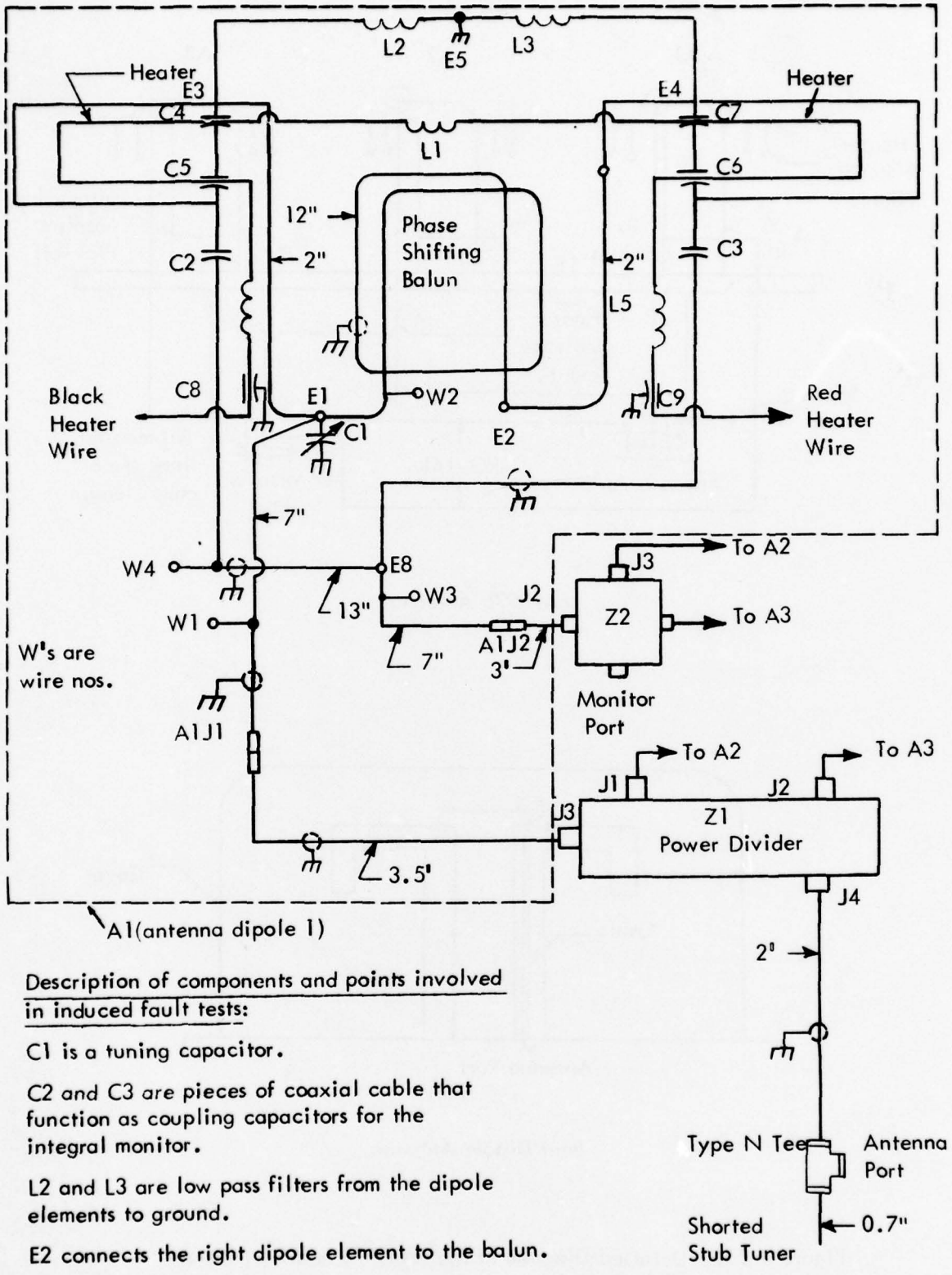

Description of components and points involved in induced fault tests:

C1 is a tuning capacitor.

C2 and C3 are pieces of coaxial cable that function as coupling capacitors for the integral monitor.

L2 and L3 are low pass filters from the dipole elements to ground.

E2 connects the right dipole element to the balun.

Figure 4-56. Detailed Diagram of FA-8730 Antenna.

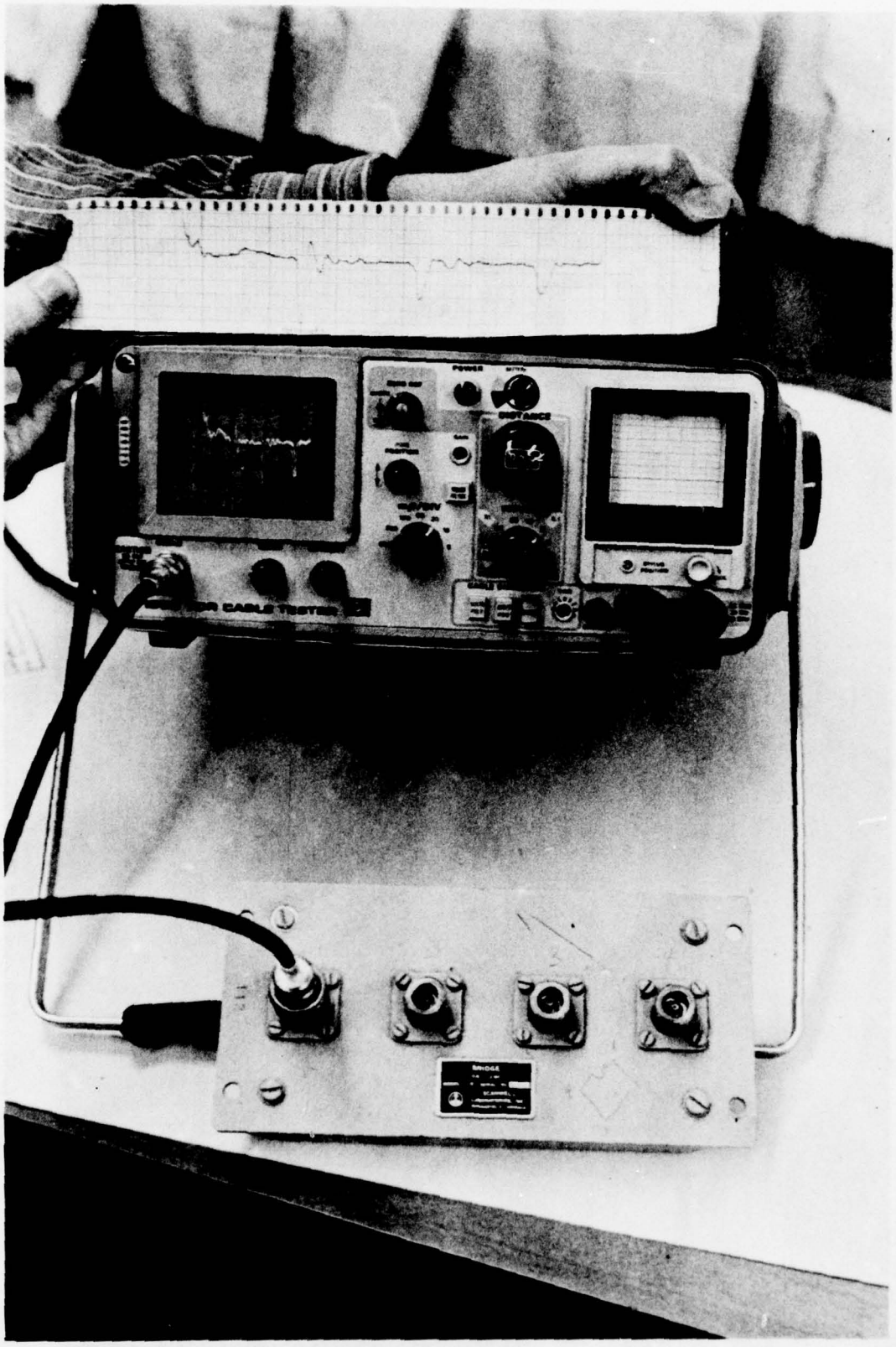

Figure 4-57. TDR and TDR Recording of a Scanwell Model 110 Bridge.

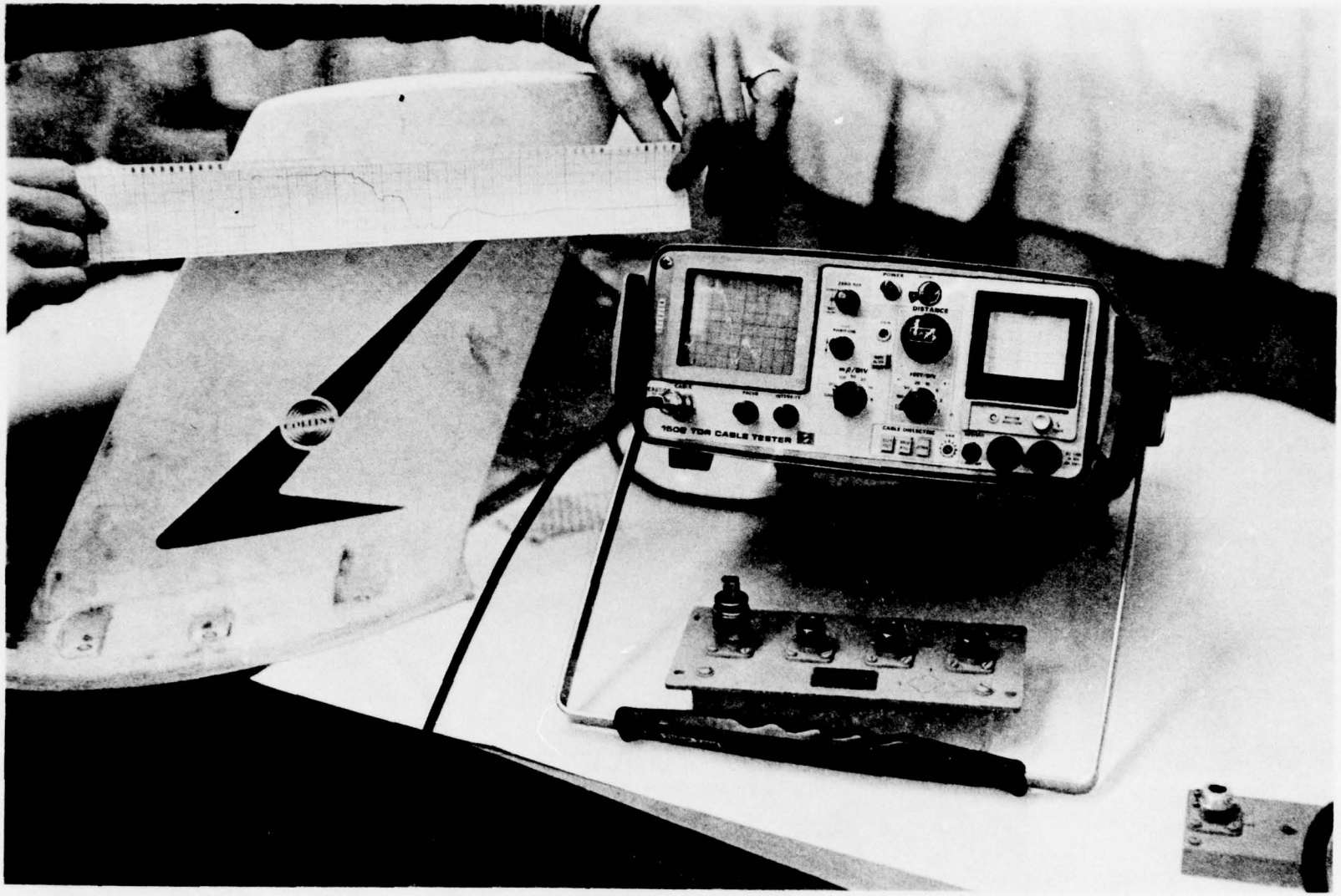

Figure 4-58. TDR and TDR Chart Recording of the Communications Antenna Shown.

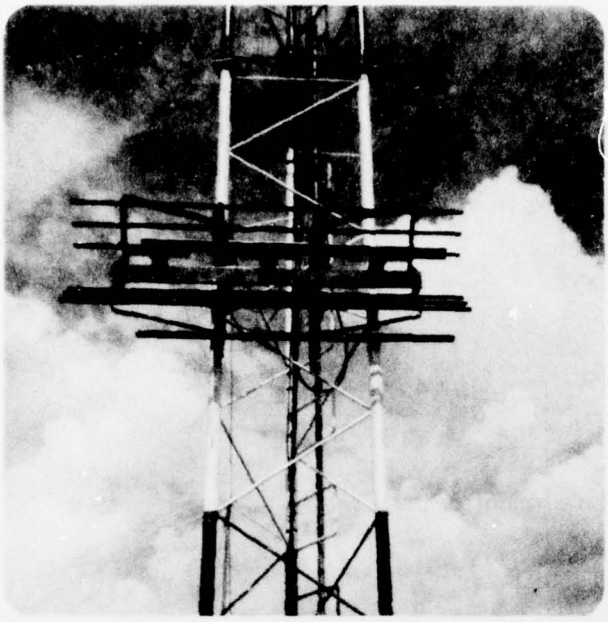

FA-8976 Antenna Installed on a Tower as Part of a Glide Slope Antenna Array

Figure 4-59. Probe Measurements of a Scanwell FA-8730 Glide Slope Antenna.

Antenna: FA-8976

Fault No.	Fault Description
1	A1 (dipole 1) open
2	A2 (dipole 2) open
3	A3 (dipole 3) open
4	A1 shorted
5	A2 shorted
6	A3 shorted
7	A_{m1} (A1 integral monitor) open at monitor port
8	Wet antenna port

Antenna: FA-8730

9	A3, C2 open
10	A1, C2 shorted
11	A1, L2 shorted
12	A2, Point E2 (balun) shorted to ground
13	A1 open
14	A1 shorted at Z1, J3
15	Stub tuner open
16	Stub tuner connector shorted
17	Z2, J3 open
18	A2, J2 open
19	Wet antenna port

Antenna: Bent Dipole

20	Wet antenna port
21	Open dipole elements

Table 4-4. List of Faults Induced in the Three Glide Slope Antennas Tested.

The reflections from a discontinuity is quantitatively described by the reflection coefficient ρ (rho), which is equal to (Zr-Zo)/(Zr+Zo), where Zo is the characteristic impedance of the first medium and Zr is the characteristic impedance of the second medium.

The settings on the TDR for the FA-8976 and the FA-8730 antenna signatures used for all fault and no fault conditions were 2.0 ft/div horizontal and 0.2ρ/div vertical. The settings for the bent dipole were 0.5 ft/div horizontal and 0.2ρ/div vertical.

For each fault measurement, tests were made with 7 ft. and 70 ft. lengths of RG-8 coaxial cable placed between the TDR and glide slope antenna under test (see Figure 4-60). The 70 ft. cable was used to simulate testing through the antenna cable at an ILS facility. Series resistance losses on the TDR transmission line tend to reduce the amplitude of the TDR pulse. Shunt capacitance losses filter out the high frequency content of the pulse and cause a smoothing of the TDR signature.

Due to low cable loss, a sharp pulse reached the antenna through the 7 ft. cable, but due to the cable losses through the 70 ft. cable the pulse was degraded, resulting in a smoother signature trace with less amplitude than for the signature made using the 7 ft. cable (see Figure 4-61).

While the signature for the FA-8976 antenna using the 7 ft. TDR cable provides the better trace, testing using the 70 ft. cable was in most cases adequate to identify a specific fault. This means that the antenna can often be checked from the transmitter through the antenna cable. For more accuracy, or when doubts arise concerning a fault, it is advisable to use a short TDR cable length even if it means climbing a tower to do so. The 16 pound TDR used is a field unit with a battery pack, so this type of testing is possible.

The FA-8730 is a more complicated type of construction than the FA-8976 antenna (see Figures 4-55 and 4-56). The power divider on the FA-8730 antenna input reflects a large portion of the incident TDR pulse back to the TDR. Thus, only a small amount of voltage is transmitted to the dipoles and adequate fault detection for the dipoles is difficult. This problem is worsened when the 70 ft. cable is used because of the pulse degradation due to line losses as described above. The traces made employing the 70 ft. line were found to be unsatisfactory in accurate fault identification of the FA-8730, but the traces using the 7 ft. cable are sometimes usable.

After a set of fault and no fault data was obtained for each antenna, an experiment was conducted to help determine fault identification ability using the set of TDR charts. One person introduced a fault, while another, not knowing the fault, attempted to determine the fault using the TDR. In every case a successful identification of the fault was made by comparison of the TDR trace taken of the unknown fault with the set of TDR fault graphs taken previously. The faults diagnosed in the experiment were fault numbers 1,3,4, and 5.

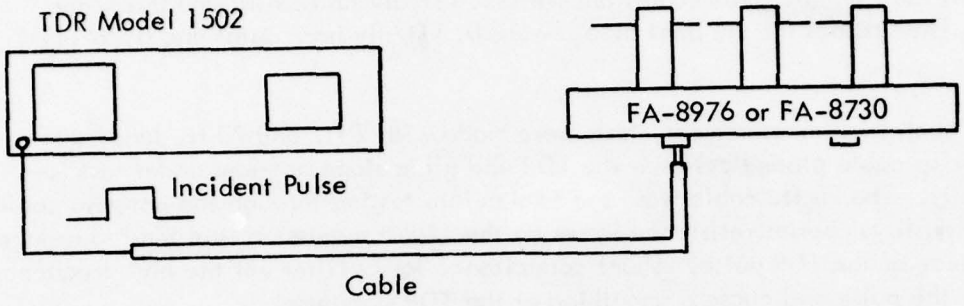

Figure 4-60. TDR Antenna Signature Test.

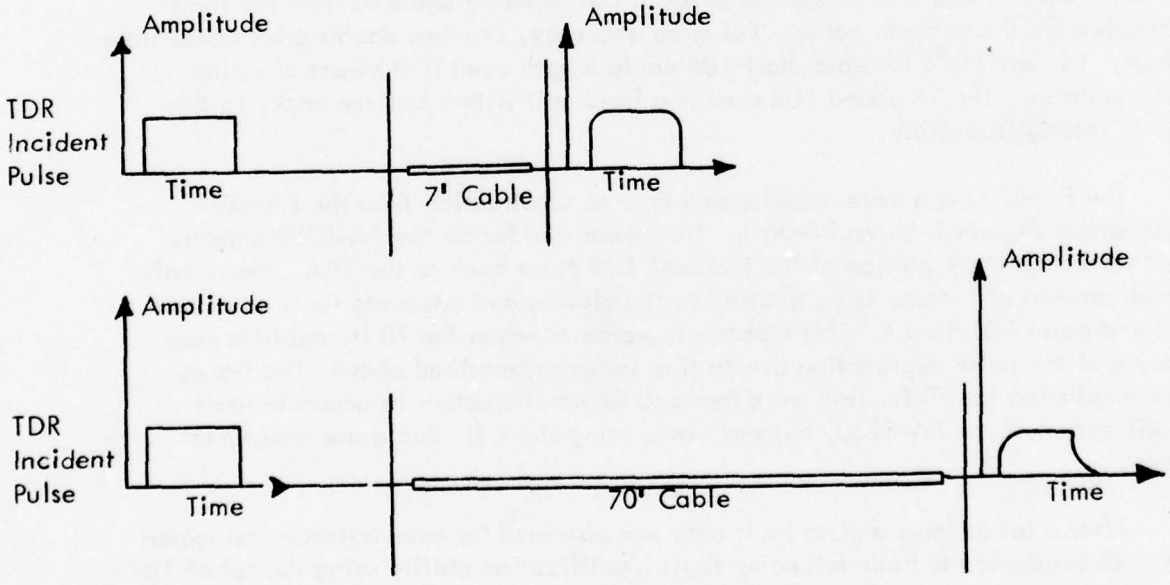

Figure 4-61. TDR Pulse Degradation Due to Line Loss.

(3) TDR Antenna Signature Analysis.

a) Introduction. In this section a list of antenna TDR signatures made with the antenna faulted in various ways is compiled. The no fault antenna signature is displayed first for each set of antenna graphs, and is shown for different line lengths between the TDR and antenna to illustrate the effects of different lengths on the signature. The fault signatures are for a 7 ft. cable only between the TDR and antenna, since the signatures using that cable have more resolution and amplitude than the signatures using the 70 ft. TDR cable. This enables a more accurate analysis to be performed in fault location and identification since discontinuities can be more easily determined.

In many cases, the no fault signature has been dotted in on the faulted signature to provide better comparison of the two.

The antenna fault for a particular signature is identified under the signature trace by the number of the faulted component. The fault description corresponding to that number can be found in Table 4-4. Location of the fault in the antenna can be found in the diagrams in Figures 4-55 and 4-56.

b) FA-8976 Antenna Signature Analysis.

(i) FA-8976 antenna--no fault signatures. Figure 4-62 is a series of three graphs of the FA-8976 under no fault conditions with varied lengths of cable between the TDR and the antenna. The dipole locations are marked for A1, A2, and A3. The part of the trace before A2 is caused by the dipole feed cables and the shorted stub tuner. In this part, the reflections from the stub contributes to the oscillations. The frequency and amplitude loss due to the TDR cable is evident in the signatures with the 70 and 130 ft. line lengths.

(ii) FA-8976 antenna--open dipole fault signatures. Figure 4-63 is a set of signatures with dipoles open-circuited. Since the value of impedance on a transmission line repeats every half wavelength, the manufacturer took advantage of this principle to save cable when constructing the antenna. The cables from the antenna port to dipoles A1 and A3 are one-half wavelength (1.5') longer than the cable from the port to A2. A2 is located close to the antenna port so the interconnecting cable can be shorter (1.5') than the other dipole cables but still have the same RF impedance. The graphs in Figure 4-63a and 4-63c are identical since the same fault occurs at the same location for each. In Figure 4-63b, the same fault discontinuity occurs as in 4-63a and 4-63c but one-half wavelength earlier. The discontinuity causes the trace to go upward at each opened dipole, indicating an increase in impedance as would be expected from the open-circuited dipole. Note that the graphs of the fault conditions are the same as the no fault graph until the reflections from the open dipole are received at the TDR. This is an aid in identifying and locating the fault.

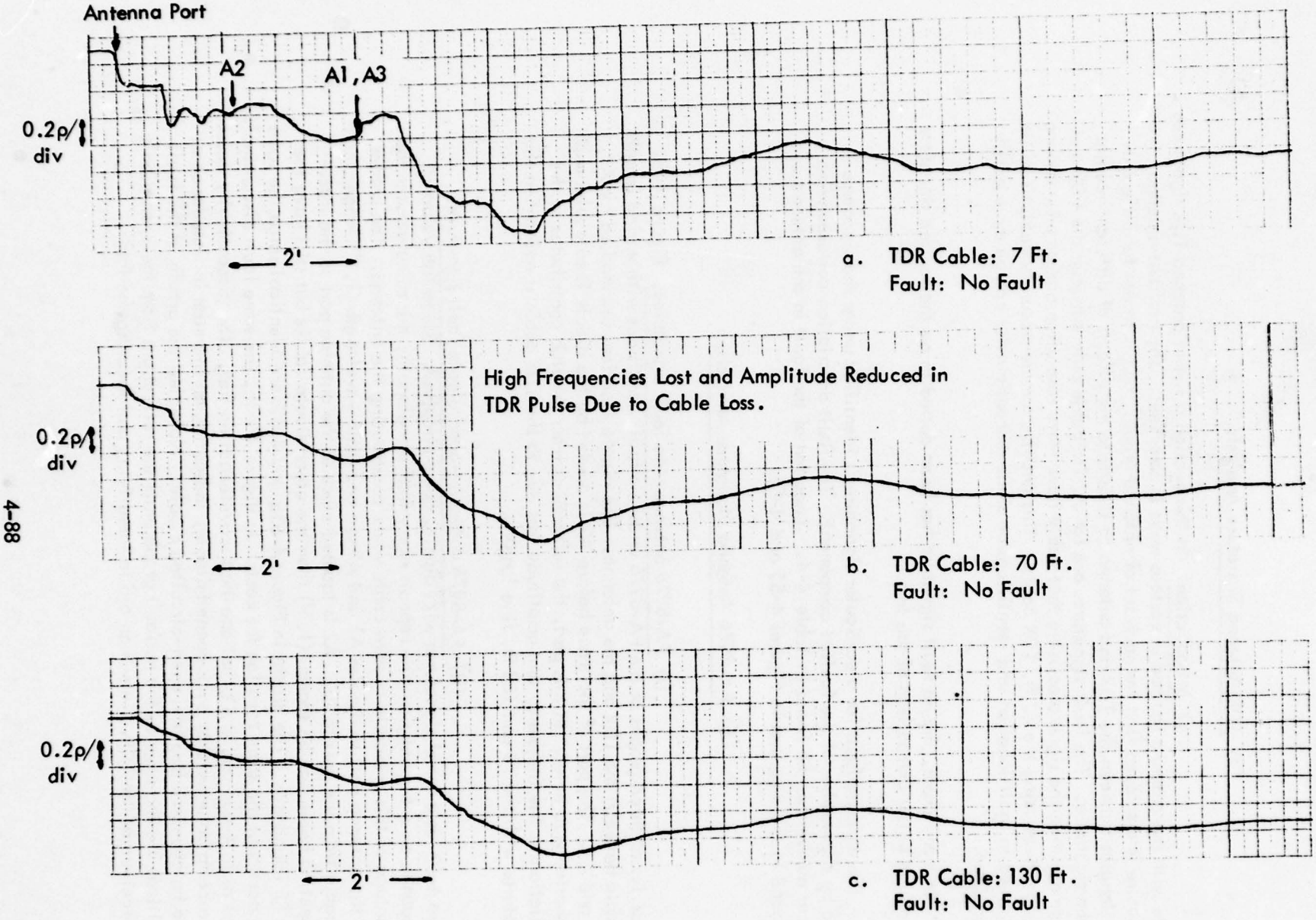

Figure 4-62. Antenna FA-8976 TDR Antenna Signatures of Different Cable Lengths Between TDR and Antenna.

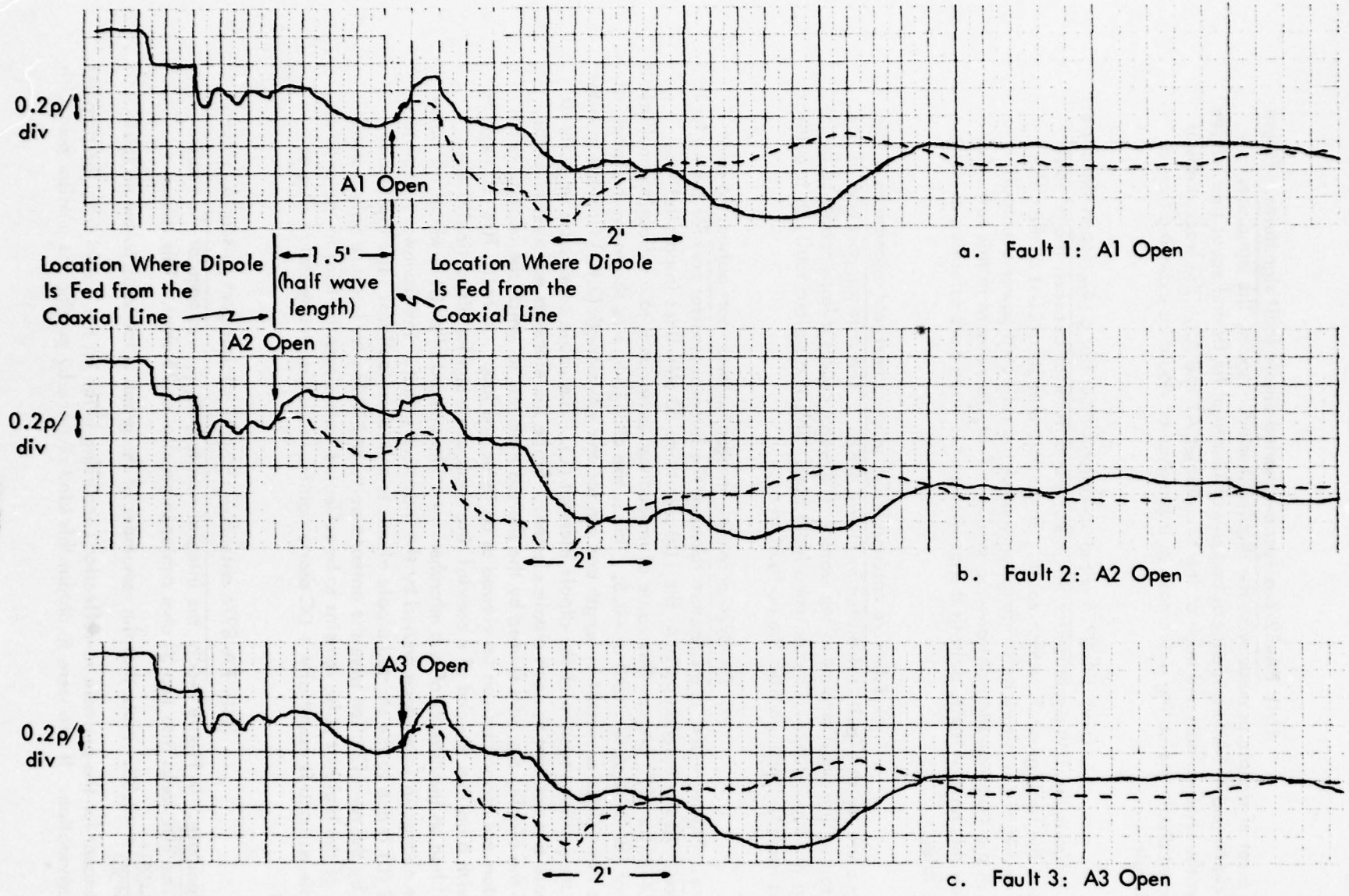

Figure 4-63. Antenna FA-8976 with Dipoles Individually Opened - Antenna Port Pulsed.

(iii) FA-8976 antenna--shorted dipole fault signatures. Figure 4-64 is a set of signatures made with the dipoles shorted. Again, the signatures in Figure 4-64a and 4-64c are identical because of identical faults and equal line lengths between the antenna port and each of the two dipoles A1 and A3. The trace drops at the shorted dipole indicating a decrease in impedance as would be expected from a short circuit.

(iv) FA-8976 antenna--integral monitor a (A_{m1}) open signatures. Figure 4-65a is the TDR signature for this test. No difference between the no fault graph and the fault graph is recognizable. Since only a small amount of the pulse power reaches the monitor, only a small amount of the reflected power eventually returns to the TDR from the monitor--too small, in fact, to measure in this test. For detecting this type of fault, pulsing the monitor port is much more effective as will be seen later.

(v) FA-8976 antenna--wet antenna port fault signatures. The TDR signature for this fault is depicted in Figure 4-65b. The antenna port was wetted in this test with a small amount of tap water. The water causes a low impedance by increasing the capacitance at the antenna input port. This is a serious fault, as is evident from the radical departure from the no fault trace.

(vi) FA-8976 antenna--integral monitor port pulsed; no fault signature. Figure 4-66a is a signature taken at the integral monitor port for the no fault condition. At the antenna port (A) the TDR sees three 50 ohm lines in parallel (see Figure 4-55) or 50/3 ohms. This value of impedance corresponds to a reflection coefficient ρ (rho) of (50/3-50)/(50/3+50) or -0.5. This is the change in ρ as shown on the graph at B. The three lines are equal in length and run for one wavelength (3 ft.) from the monitor port to the vertical section of the dipole element (C). The cable conductors separate at the dipole and connect to each dipole element. Since the elements are shorted at the base of the dipole, the path formed by the shorted elements to which the coaxial cable conductors are connected can be viewed as an inductive loop. In fact, TDR lab experiments with a coil on the end of a coaxial line produced a similar discontinuity when the coil had an inductance of two microhenries. The upward blip (C) is where the pulse sees the change in impedance caused by the inductive effect. The downward slope to $\rho = 1/2$ (D) is due to the shorted dipole elements and re-reflections. The dip at E is caused by the re-reflection from the antenna port, and is smaller because only a small portion of the incident pulse remains to be reflected from discontinuities in the antenna. Since the antenna is essentially a DC short, point F shows the steady state value of $\rho = -1$.

(vii) FA-8976 antenna--integral monitor port pulsed; A_{m1} open fault signature. In Figure 4-66b the integral monitor, A_{m1}, was open at the monitor port. The TDR looks into two 50 ohm cables in parallel or 25 ohms. This causes a $\rho = \frac{(25-50)}{(25+50)} = -0.33$. Note that the remainder of the graph is the same as the no fault graph except for the periodic re-reflection (occurring twice on the graph) from the parallel cable connection. If one were to obtain this kind of trace by pulsing the monitor port with

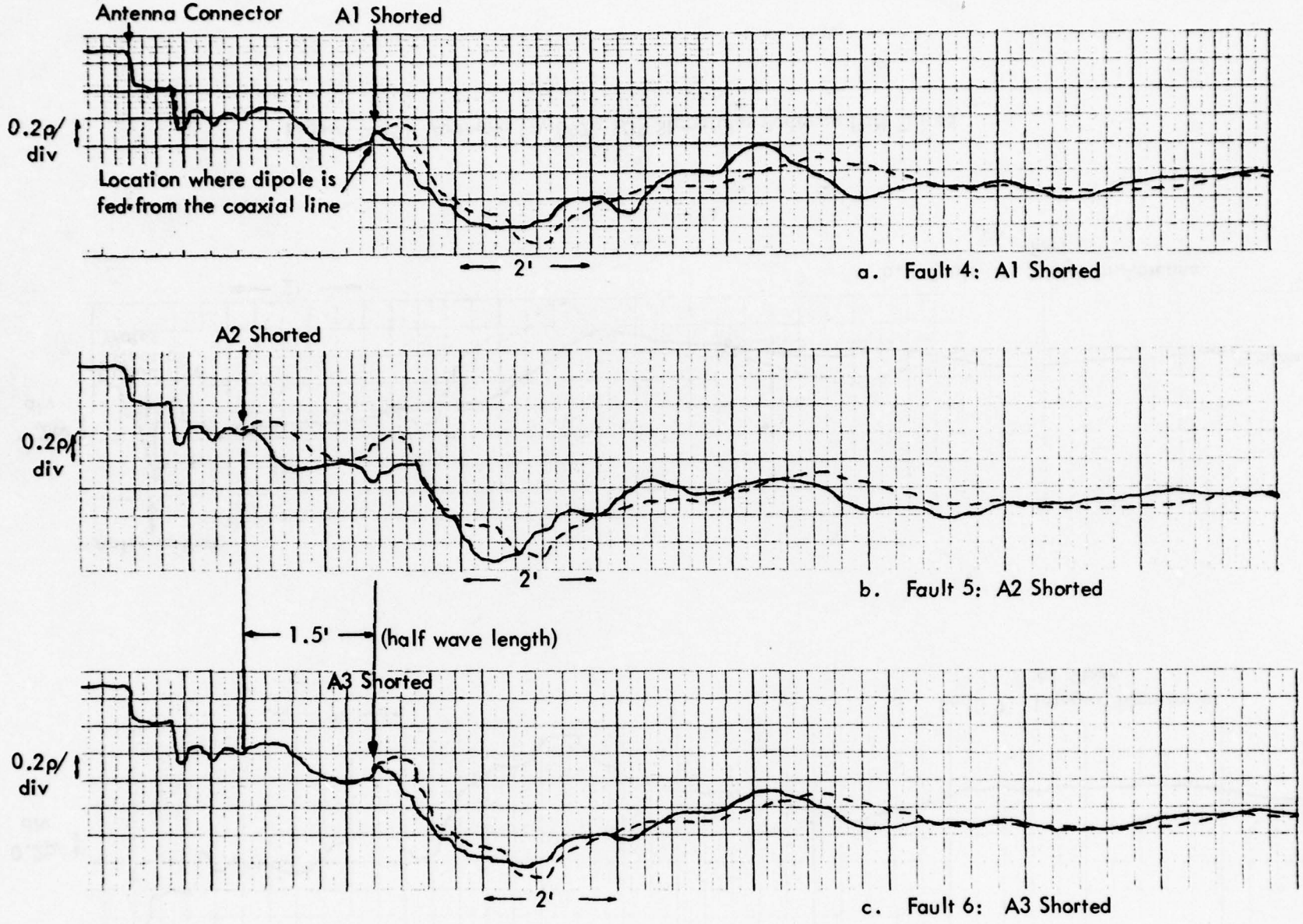

Figure 4-64. Antenna FA-8976 with Dipoles Individually Shorted - Antenna Port Pulsed.

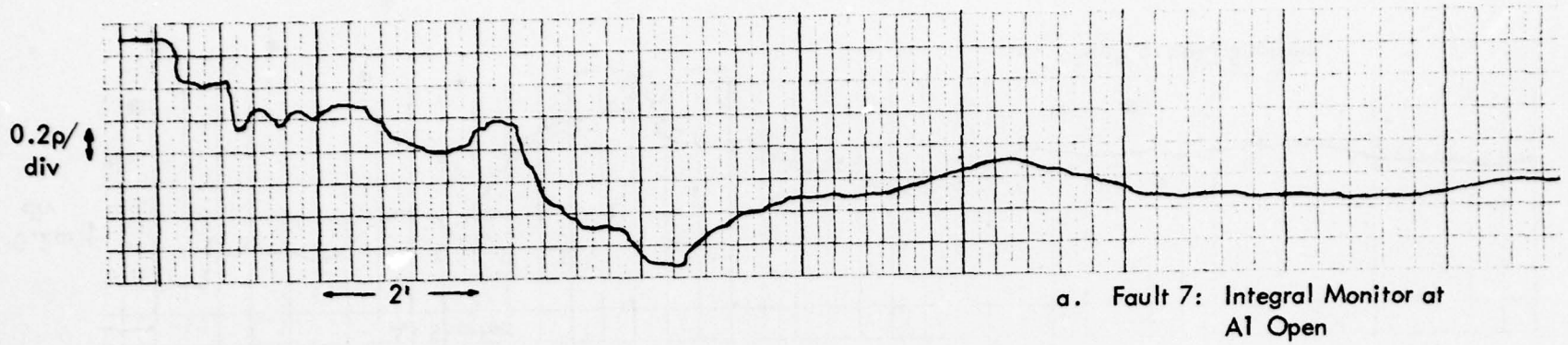

a. Fault 7: Integral Monitor at A1 Open

b. Fault 8: Water in Antenna Port

Figure 4-65. Antenna FA-8976 TDR Signatures-Antenna Port Pulsed.

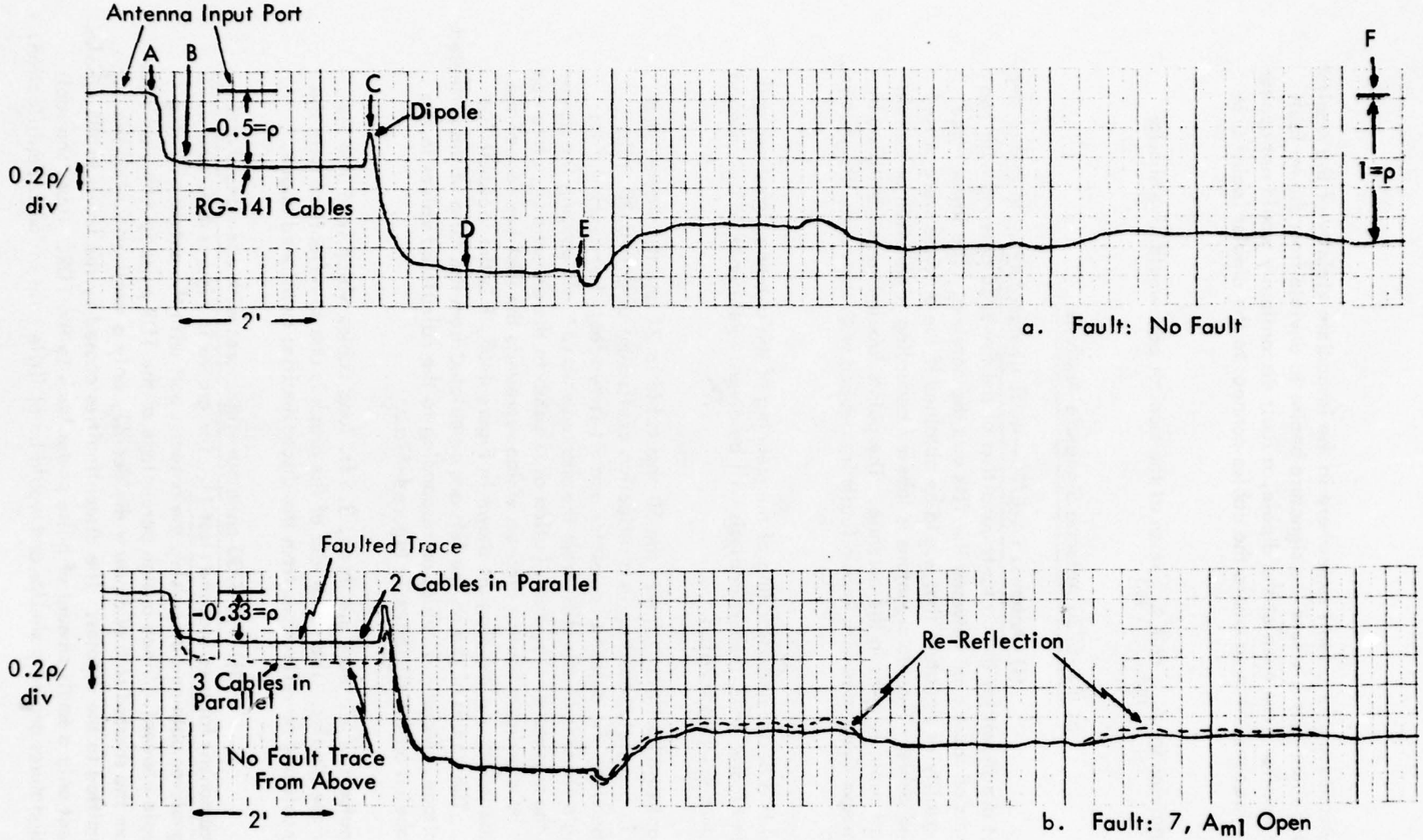

Figure 4-66. FA-8976 Antenna TDR Signatures of Integral Monitor Input Pulsed.

the TDR, he would look for a fault somewhere in the immediate vicinity of the monitor input connector since that is where the signature begins to deviate from the no fault graph. If the monitor were open at the dipole, a fault discontinuity would not appear until the pulse reached the area where the cables connect to the dipoles (point C in Figure 4-66a).

The signatures for A_{m2} and A_{m3} open at the monitor port would give similar traces.

c) FA-8730 Antenna Signature Analysis.

(i) Antenna FA-8730--no fault signatures. In Figure 4-67 TDR signatures are shown for the no fault condition of the FA-8730 antenna with two different lengths of cable used between the TDR and the antenna. The lower trace simulates the quality of signature that would be obtained if the antenna were pulsed through its feed cable. The top signature is labeled according to location of certain components and cable lengths in the antenna. The points labeled were identified by comparing antenna signatures with known faults introduced with the no fault signatures in Figure 4-67.

To provide a better understanding of the meaning of the antenna signatures and the labeling in Figure 4-67, a short analysis will be given. Reference to the antenna diagram in Figure 4-56 is advised.

At the antenna port the TDR sees the 50 ohm cable to Z1 and the shorted stub (50 ohm line) in parallel, resulting in a reflection coefficient of $\rho = -0.33$. The cable length between the antenna connector and Z1 is two feet, but every 0.7 ft. along this length there is a reflection from the shorted stub ($\rho = -1$) causing the downward steps on the signature. The contribution of the stub to the antenna signature can be easily seen by drawing a bounce diagram which represents the first two feet of the TDR pulse transmission. In the diagram shown in Figure 4-68, E is the incident TDR voltage pulse. The values of rho on the left are calculated from the ratio of the reflected to incident voltage. Measured values corresponding to the calculated values in the diagram are labeled on the signature in Figure 4-67a .

At the outputs of Z1 there are three, 3.5 ft. long cables which lead into the connectors for the dipoles. The remainder of the graph is due to reflections from the dipole components and re-reflections from the discontinuities mentioned above.

(ii) FA-8730 antenna--signatures with open and shorted dipoles and component failures induced (test 1). The graphs in Figures 4-69 and 4-70 are sample signatures obtained by pulsing the antenna port with the antenna faulted in a given dipole element. Since a high percentage of the TDR pulse is reflected back to the TDR from the shorted stub and power divider Z1, only a small amount of the pulse power is transmitted to the dipoles. The discontinuities caused by the faults in the dipoles therefore reflect only a small amount of pulse power back to the TDR. Thus, the fault and no fault signatures are very similar and would be of little help in fault identification.

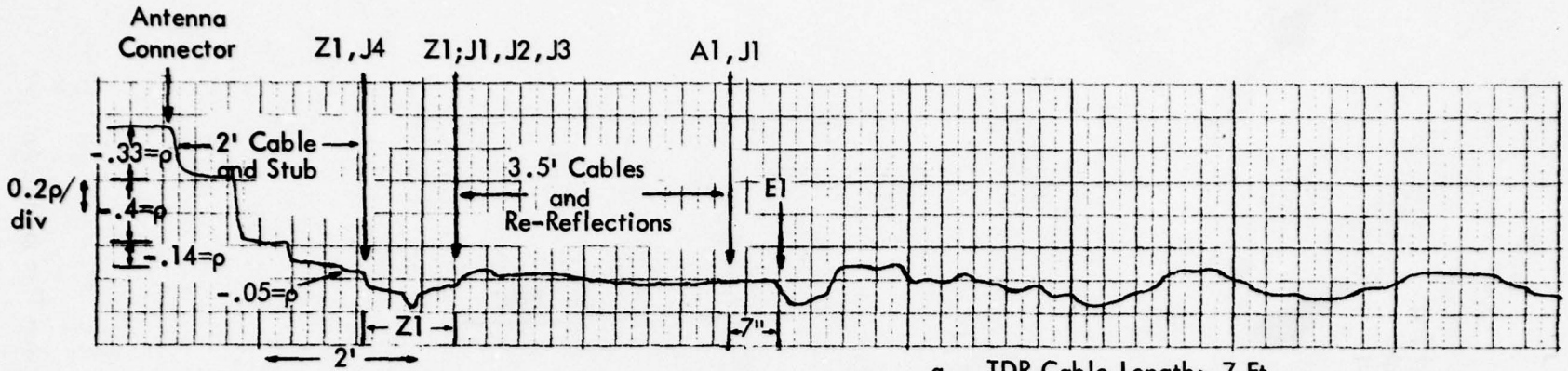

a. TDR Cable Length: 7 Ft.
Fault: No Fault

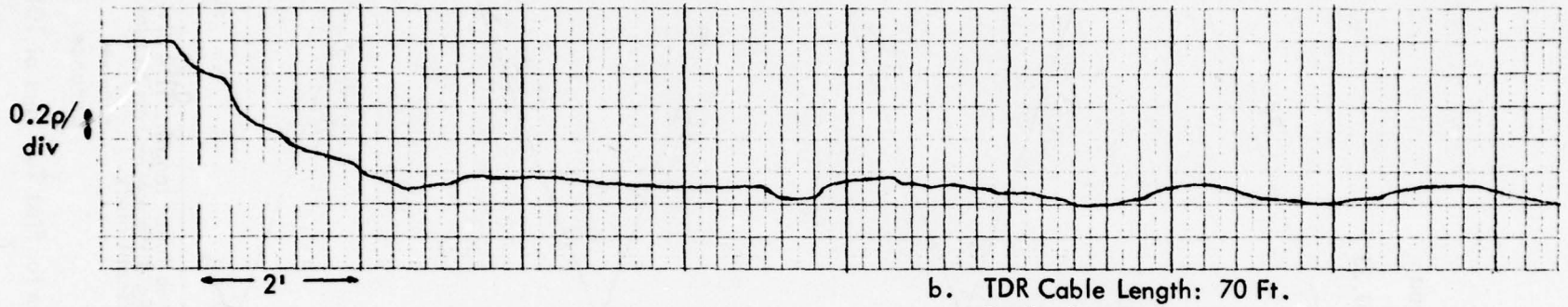

b. TDR Cable Length: 70 Ft.
Fault: No Fault

Figure 4-67. Antenna FA-8730 TDR Signatures of Antenna Port with Two Cable Lengths Between TDR and Antenna.

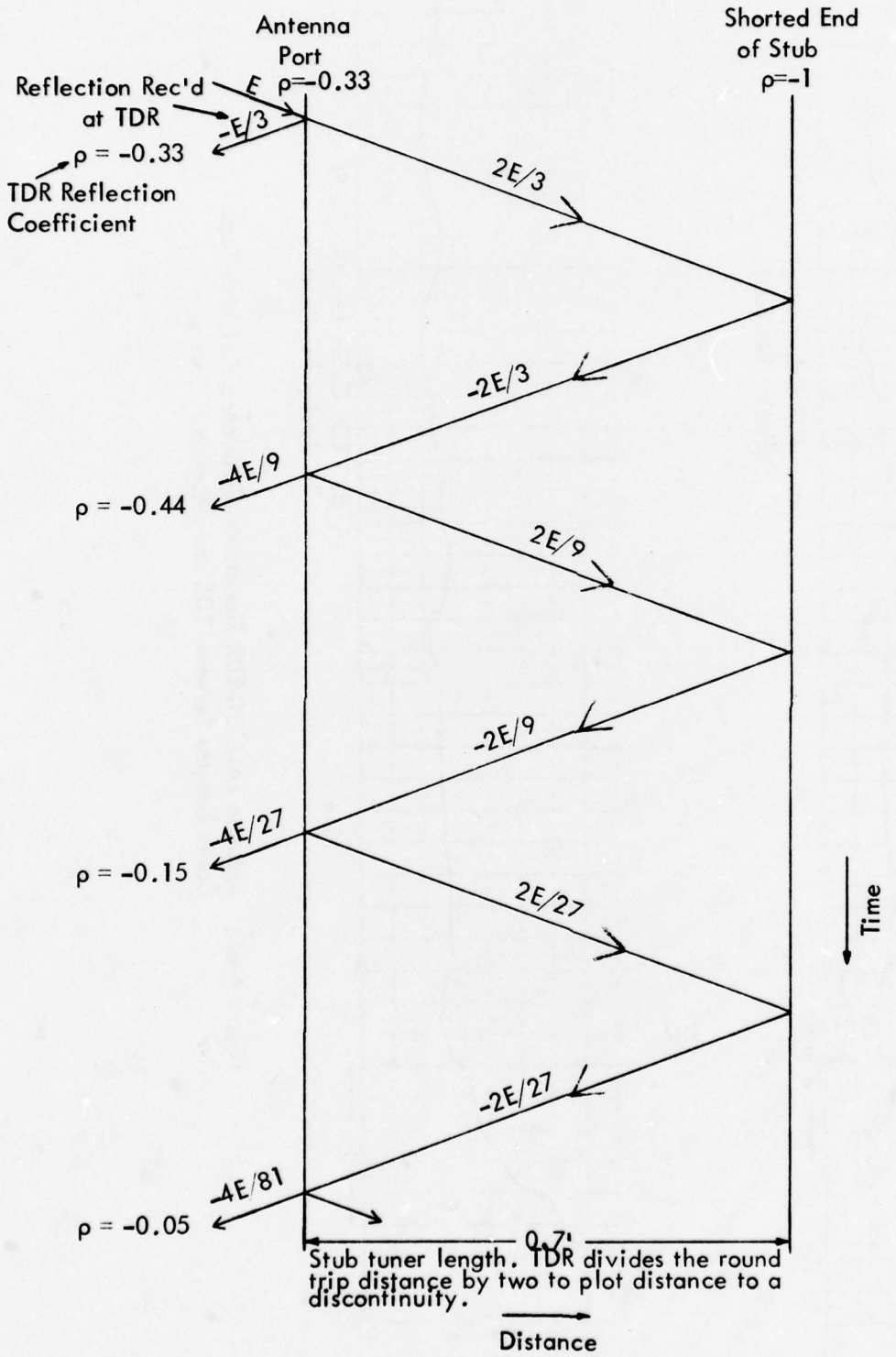

Figure 4-68. Bounce Diagram for First Two Feet of TDR Pulse Transmission Through the Antenna Port.

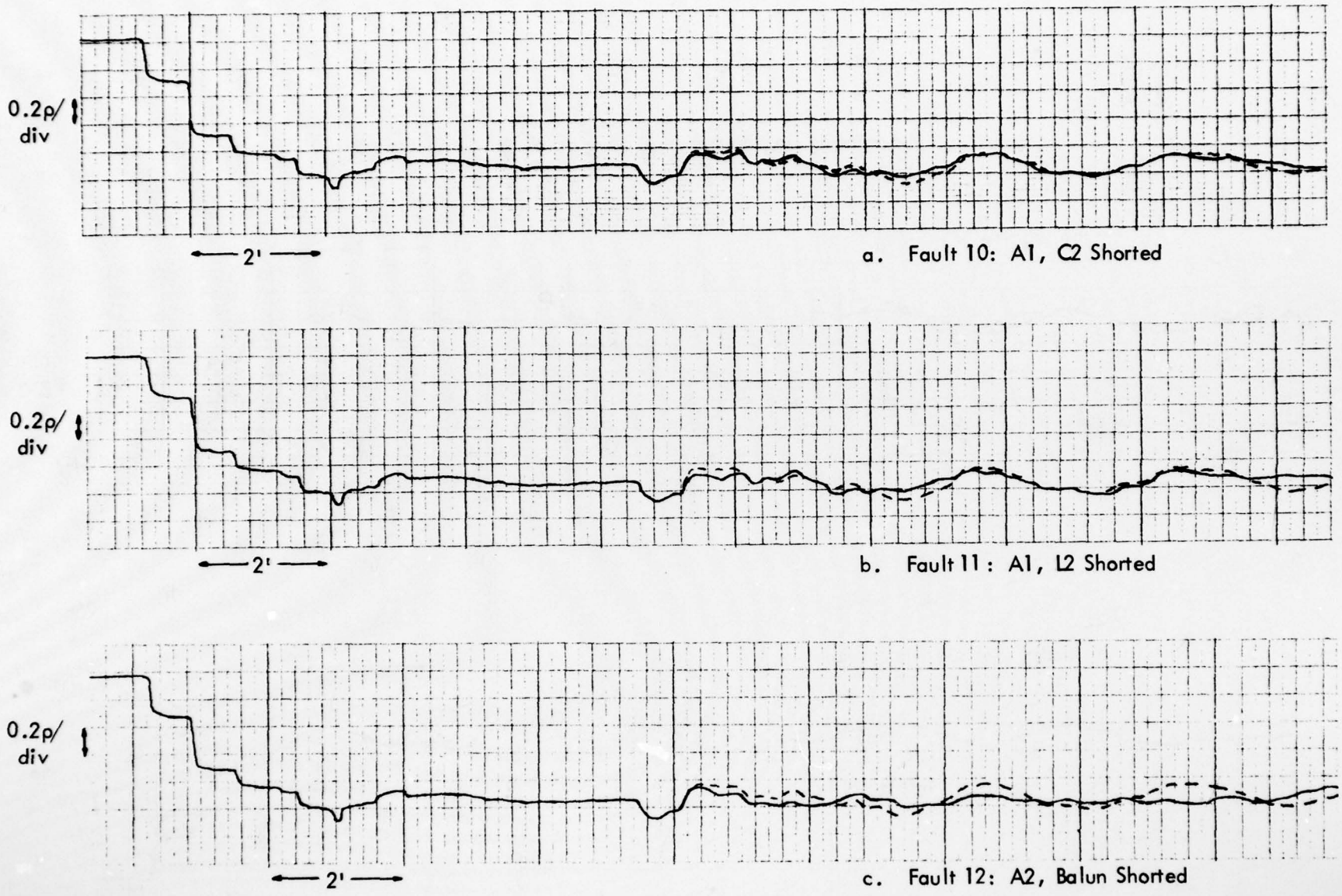

Figure 4-69. Antenna FA-8730 Antenna Port Pulsed.

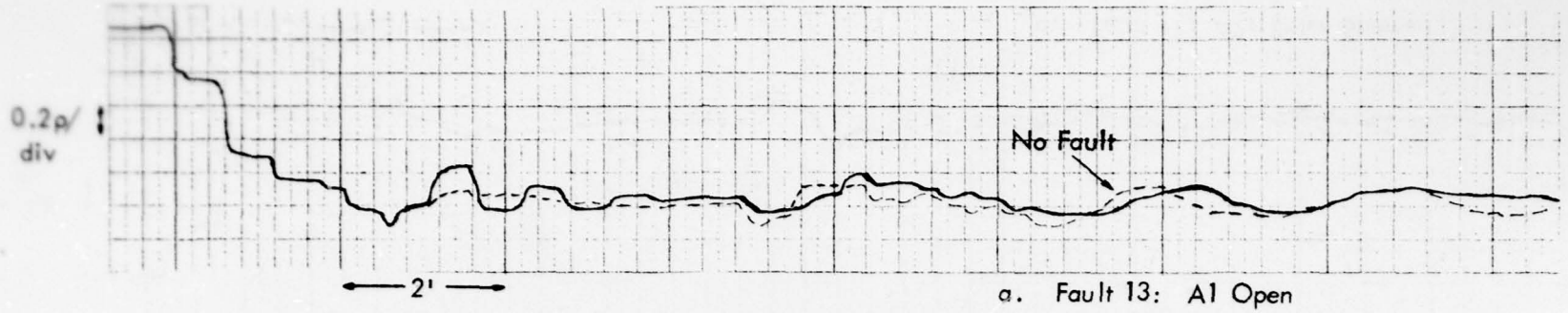

a. Fault 13: A1 Open

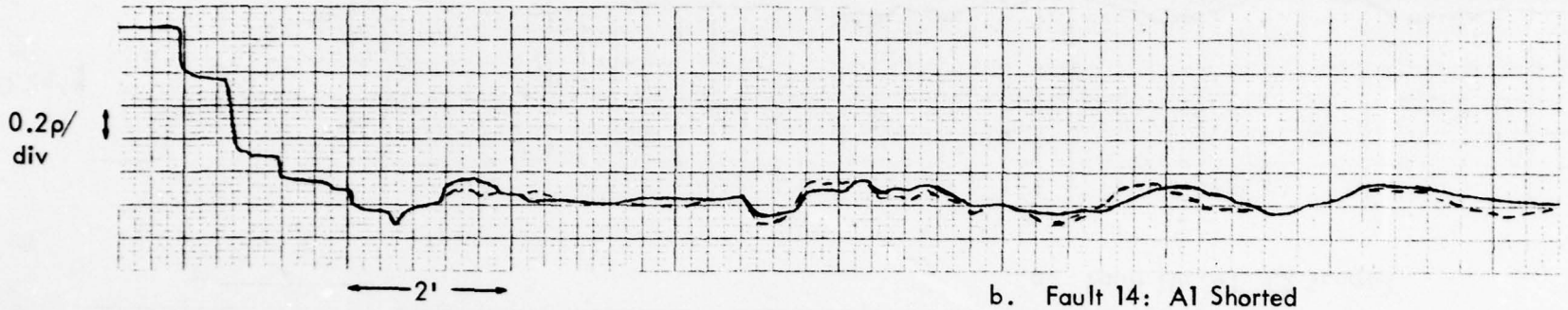

b. Fault 14: A1 Shorted

Figure 4-70. Antenna FA-8730 Antenna Port Pulsed.

(iii) Antenna FA-8730--antenna signatures with opened and shorted stub tuner connector and wet antenna port faults. The stub tuner on the antenna input is mounted on a type N male connector. This connector was removed to produce a fault condition. The fault could be readily identified in the antenna signature in Figure 4-71a because of the severity (an open is created where before a shorted cable, the stub tuner, existed) and the location of the fault (at the antenna port where the pulse from the TDR enters).

Figure 4-71b is a signature of the antenna port with a short across the stub connection. The downward blip two feet from the antenna connector is due to the connection Z1, J4. The graph shows the fault as essentially a short since the TDR looks into a Tee terminated in a short and the input to Z1. Reflections from the short at the Tee cause the $\rho = -1$ on the graph. The trace remains at -1 until the reflection from Z1 is received. The reflections farther down the trace are mainly from the dipoles.

Figure 4-71c is the antenna signature with the antenna port wetted with a small amount of water. The capacitive effect of the water is evident at the antenna connector input since the trace falls sharply. This fault also causes a deviation in the remainder of the signature from the no fault signature since the pulse transmitted by the TDR has been abnormally reflected by the wet connector.

(iv) Antenna FA-8730--antenna signatures with open and shorted dipoles and component failure faults induced (test 2). The signatures in Figures 4-69 and 4-70 were seen to be inadequate for reliable fault determination. In Figure 4-70, signatures for some of those same faults are depicted, but in these instances, the TDR is connected to the output of the dipole (A1, J1 in this example) in which the fault occurs, thus bypassing power divider Z1. These signatures would locate the particular faulted dipole and general area in the dipole where the fault occurs, but identification of the precise component causing the fault would still be difficult due to the complexity of the reflections from the dipole circuits.

Obtaining the signatures of Figure 4-72 requires removal of the antenna backplate in order to get to the dipole inputs. This type of procedure is on the border of destructive testing. It is hoped, though, that an initial test at the antenna port would tell whether or not the area up to and including Z1 is unfaulted. If the area is unfaulted, then subsequent tests directly into the dipole may be necessary.

In Figure 4-72b, C2, which connected left dipole element to the right one and to Z3, is shorted. The signature reflection coefficients are more negative than for the no fault signature except for the dipole inductances which raise the final third of the signature.

In Figure 4-72c, shorting L2 reduces the inductive effect in the circuit causing a general lowering of the graph.

In Figure 4-72d, shorting E2 to ground also shorts L3 and the right dipole element to ground which again lowers the graph.

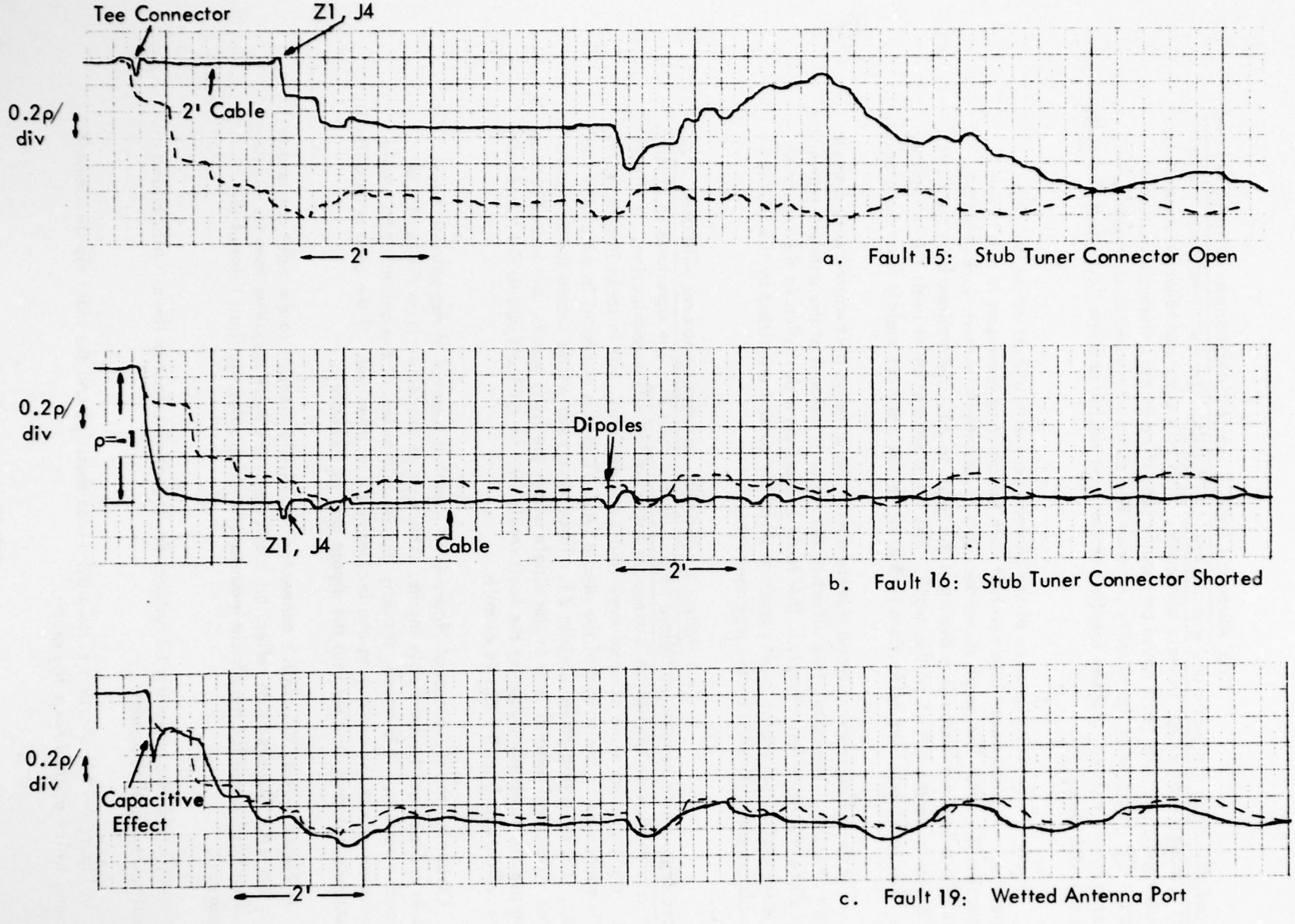

Figure 4-71. Antenna FA-8730 Antenna Port Pulsed.

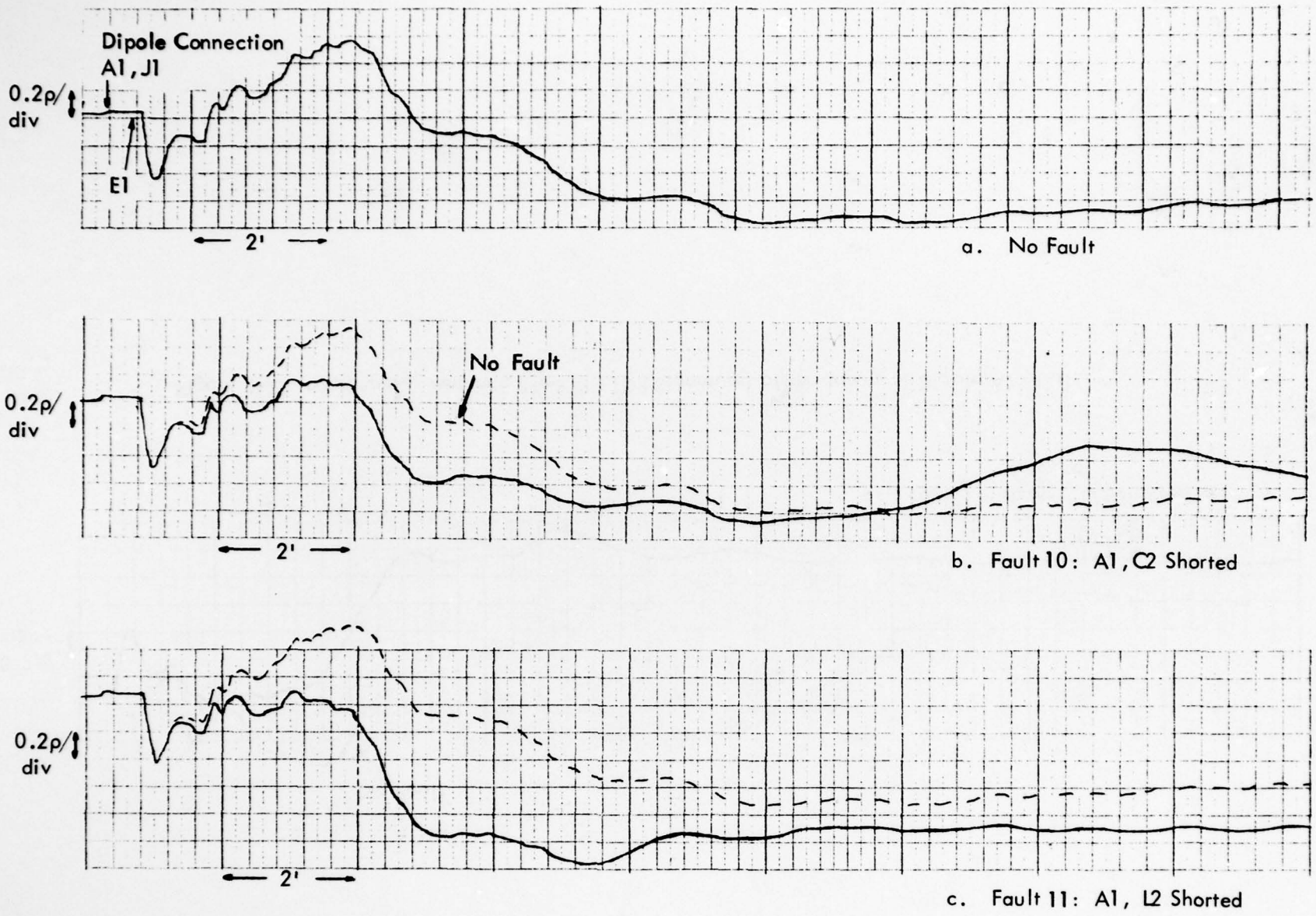

Figure 4-72. Antenna FA-8730 TDR Signatures of the Inputs of Dipole A1 at J1.
(Continued on Next Page)

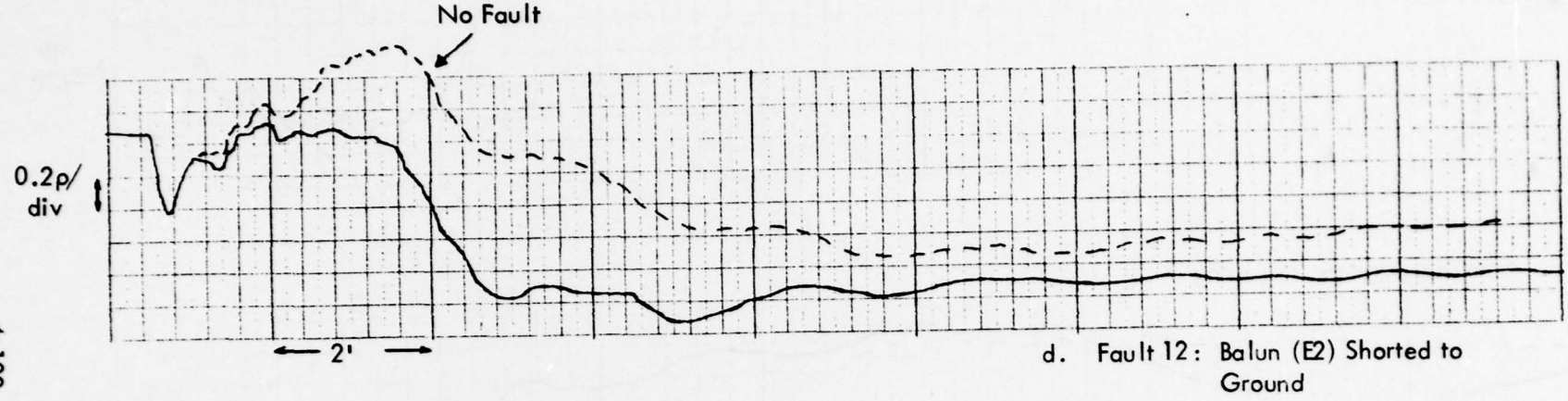

Figure 4-72 (continued). Antenna FA-8730 TDR Signatures of the Inputs of Dipole A1 at J1.

(v) Antenna FA-8730--monitor output fault and no fault signature. Figure 4-73 demonstrates a few examples of the results from measurements where the monitor port of the antenna was pulsed with the TDR. The no fault signature and the A3, C2 open fault signature are given in Figure 4-73a. The signatures are the same, i.e., the fault has no effect on the signature. The TDR is shown to be inadequate in finding faults produced in the dipoles when connected to the monitor due to the small amount of reflection from the dipole component.

The no fault signature shown in Figure 4-73a is qualitatively analyzed as follows. At the monitor input, the TDR sees three cables from the dipole monitors in parallel at the four-way connector Z2. The parallel cable impedance of 50/3 ohms causes a reflection coefficient of $\rho = -0.5$. Then, for 3.5 feet, the monitor cables run to the dipole inputs at J2 where another cable runs in the dipole cavity for 7 inches to C3 and the remainder of the dipole network.

Figure 4-73b is the monitor signature of the Z2, J3 open fault condition. The TDR looks into two parallel 50 ohm lines causing a ρ of -0.33. The fault condition causes the entire signature to be offset from the no fault signature.

In Figure 4-73c, the monitor cable of A2 was opened to produce the signature shown. The change of ρ at J2 is 0.17 since the impedance goes from three parallel lines ($\rho = -0.5$) to two parallel lines ($\rho = -0.33$).

d) Bent Dipole Antenna TDR Signatures. Bent dipoles have been used extensively in the past in glide slope antenna arrays. The construction is simply a cable feeding two elements shorted at one end (see Figure 4-55). Figure 4-74 contains the no fault and two faulted signatures for the bent dipole.

(4) Recommendations and Conclusions. The results of the time domain reflectometer tests on the glide slope antennas show that the TDR can often differentiate between normal and abnormal antenna conditions. This indicates the usefulness of the TDR as a test instrument for antennas as well as other parts of the ILS such as monitors, hybrids and, of course, cables.

The TDR is known as a "cable tester". As the name implies, its use has mainly been limited to cable testing. In the antenna tests reported here, though, TDR signatures were recorded for antennas in order to investigate the fault locating and identifying potentialities of the TDR. With the particular TDR used, the pulse generator, sampler, CRT, chart recorder, and battery pack are housed in one unit. Because of this, the TDR is quite capable of performing field tests.

The results of these tests proved the ability of the TDR to identify certain common faults in the antennas. Not only is the presence of a fault detectable, but often identification of the nature of the fault is possible. In some cases, simply pulsing the antenna port was adequate, but some faults were best detected by pulsing the integral monitor port or entering the antenna itself to bypass certain areas. In some cases where extensive fault analysis is necessary, lab tests may be done where the TDR pulse is first applied to

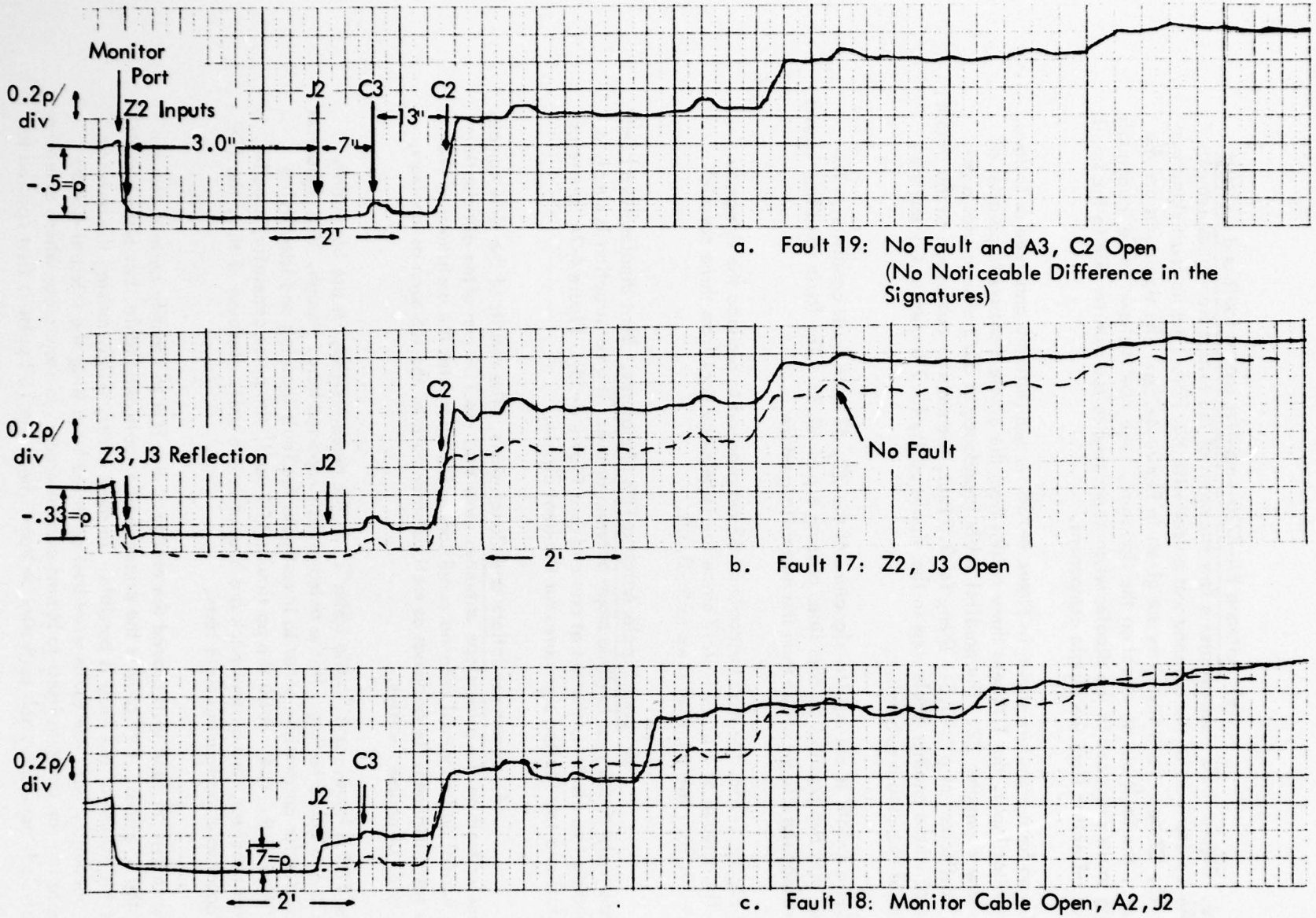

Figure 4-73. Antenna FA-8730 TDR Signatures of Integral Monitor Input.

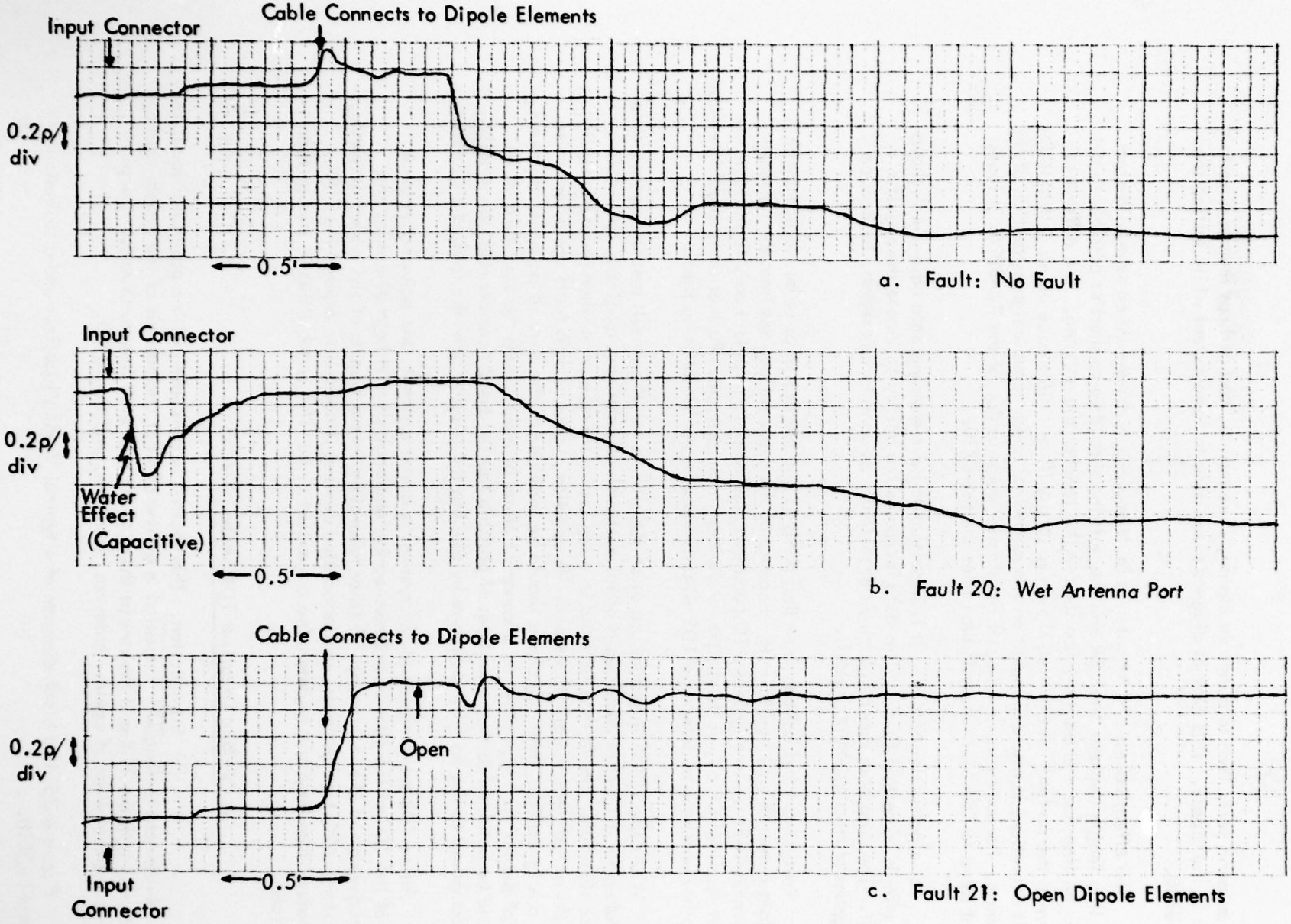

Figure 4-74. TDR Signatures of Bent Dipole Type Antenna.

the antenna port, then to a certain dipole, if necessary, and perhaps then to a certain area in the dipole. This type of diagnosis was done to some extent while testing the FA-8730.

The effectiveness of TDR antenna fault analysis is dependent on several factors. The line length between the TDR and the antenna should be as short as possible to cut down on line loss and assure that a sharp pulse reaches the antenna. The difference between the no fault and faulted signature (a significant difference being desirable for fault detection) is also dependent on the electrical and mechanical construction of the antenna. For example, because of the simpler construction of the FA-8976, it lends itself more to TDR fault analysis than does the FA-8730.

For a particular antenna, it is important to have a strong data base which shows the effects of certain faults. This data increases the ability to locate the specific fault. The data base can be obtained empirically as done in this report, by bounce diagrams or from computer models.

Preliminary indications show that analysis and prediction of pulse reflections in certain antennas will be difficult. Because of the many reflections from the numerous discontinuities in some systems, TDR analysis may be able to detect only faults near the input terminals; i.e., up to the power divider in an antenna. Further study should be done on other antennas to determine TDR effectiveness in troubleshooting them.

When the TDR is in actual use at an ILS site, a set of no fault measurements should be taken for all system components of interest such as antennas, monitors, and cables. These signatures should then be filed in a log for future reference when periodic health checks or maintenance are performed. In addition, when certain fault conditions arise and are identified, their signatures should be included in the log. If possible, an overlay of the no fault signatures (a transparent piece of plastic with the signature on it) should be obtained so that signatures of possible faulted system components can readily be compared to the no fault signature by placing the overlay over the faulted signature.

Since TDR measurement of ILS systems is a new concept, the actual day-to-day use of the TDR at ILS sites in troubleshooting and analysis will help determine the effectiveness of the instrument. Further laboratory measurements of ILS system antennas, monitors, APCU components, and associated devices is needed to expand the TDR signature data base and to determine the extent of the TDR capabilities in testing these devices.

d. V-Ring Localizer TDR Study.

(1) Introduction. This section is concerned with a particular localizer the 14-element V-Ring.[5] Presented is a view of what components of the system could be tested with the TDR and the results that can be expected from such tests. Sample signatures are given of cables, antennas, monitors, and the APCU.

Figure 4-75 is a block diagram of a typical V-Ring localizer and distribution system (APCU).

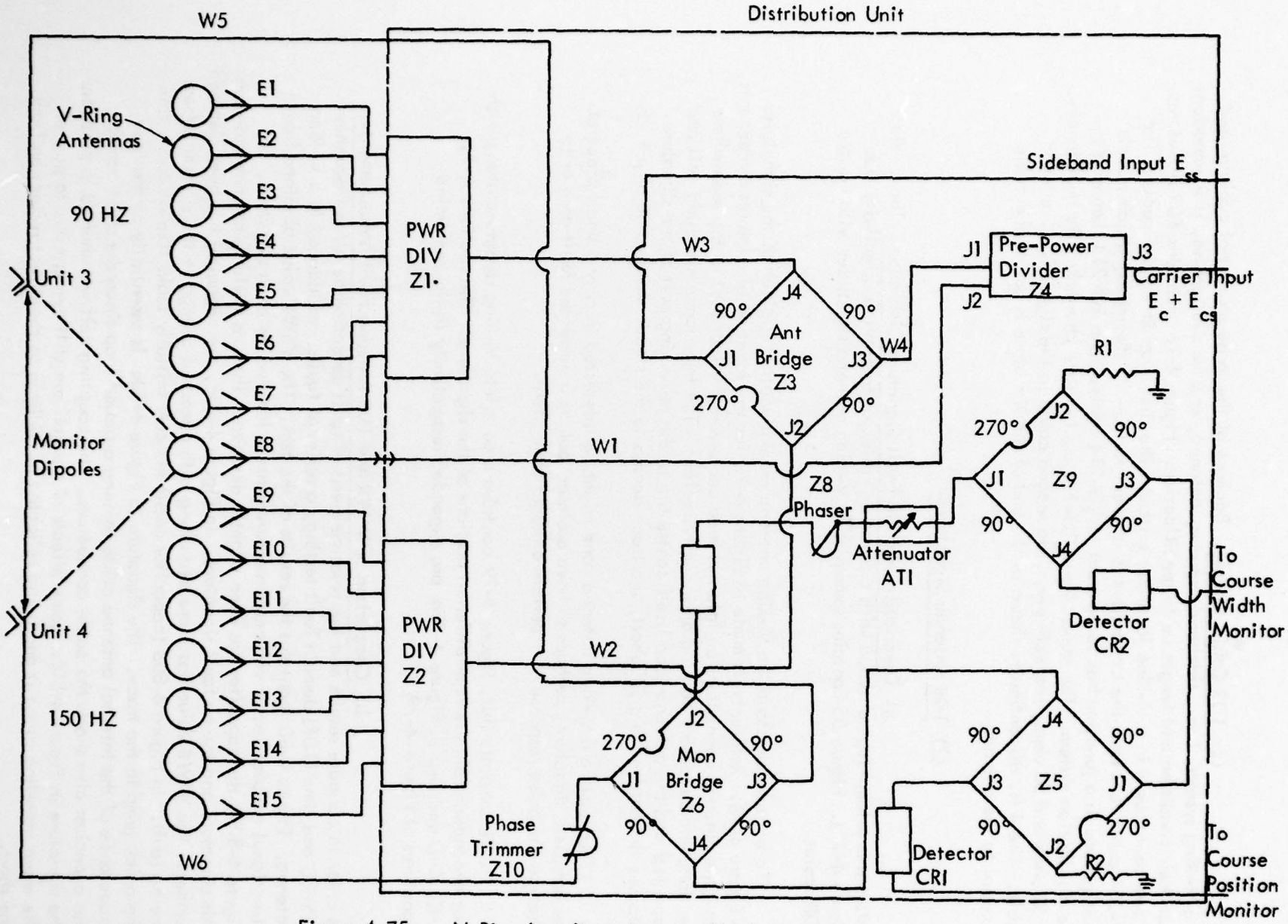

Figure 4-75. V-Ring Localizer Antenna Block Diagram.

(2) TDR Cable Checks. Because of the large amount of cabling used in a V-Ring system, i.e., sideband, carrier, antenna, and monitor cables, it is important that their condition and length be to specification. Figure 4-76 contains TDR signatures of two cables used in a V-Ring localizer system. The first is an RF carrier cable. The RF-214 cable runs from the transmitter to connect to RG-331 (foamflex) which travels underground to a junction box to connect to RG-214 again. The RG-214 then runs to the distribution system. The RG-214 and RG-331 cables have characteristic impedances of 52 ohms and 50 ohms, respectively. The second cable in the figure is an antenna cable. The 4 ft. discontinuity shown at the end of the signature is due to the cable internal to the antenna.

(3) TDR Antenna Signatures.

a) Description and No Fault Signature Discussion. The V-Ring antenna is a loop-type antenna with a parasitic reflector to provide directivity (see Figure 4-77). Figure 55 contains examples of V-Ring antenna signatures with various TDR scales.

To better understand the V-Ring antenna an explanation is given of the signatures in Figure 4-78. Reference is made to Figure 4-77 for the location of antenna components. From the antenna connector, an internal feed cable runs for four feet in the loop where the conductors separate causing an inductive effect. The impedance matching coil and capacitor and the antenna loop itself contribute to the remaining part of the signature. Because the antenna is a DC short, the trace decays to the steady state value of $\rho = -1$.

When testing a V-Ring antenna, one might be interested in only a small piece of the complete signature, perhaps to have a closer look at a suspected fault area or to analyze the pulse response of a certain antenna component.

To demonstrate this, Figure 4-79 contains a complete V-Ring signature along with four expanded scale views of different portions of the signature. The sections A-B, B-C, C-D and D-E in Figure 4-79a are expanded respectively in the remaining signatures of Figure 4-79.

b) Comparison of VSWR and TDR Antenna Fault Measurements. In order to compare results and the relative merit of fault detection between frequency (VSWR) and time (TDR) domain fault testing, a series of faults was induced in a V-Ring antenna. Figure 4-80 contains the results of the test. The VSWR value obtained from directional coupler vector voltmeter measurements is labeled for each signature. In Figure 4-80b, the capacitor has been slightly detuned. There is little difference between this signature and the no fault signature. In Figure 4-80c, the capacitor has been detuned further. The VSWR value has increased along with a marked change in the signature from the no fault. In Figure 4-80d (capacitor open) the coil initially looks like an open, thus the quick jump in the trace. The signature in Figure 4-80e is essentially of the lead inductance of the internal antenna cable forming a closed loop since the short across the capacitor also shorts the cable conductors. The coupling coil was shorted to produce the signature in Figure 4-80f. Some effects of the coil are still evident due to part of the wave traveling along it and being reflected in addition to the direct reflection from the short.

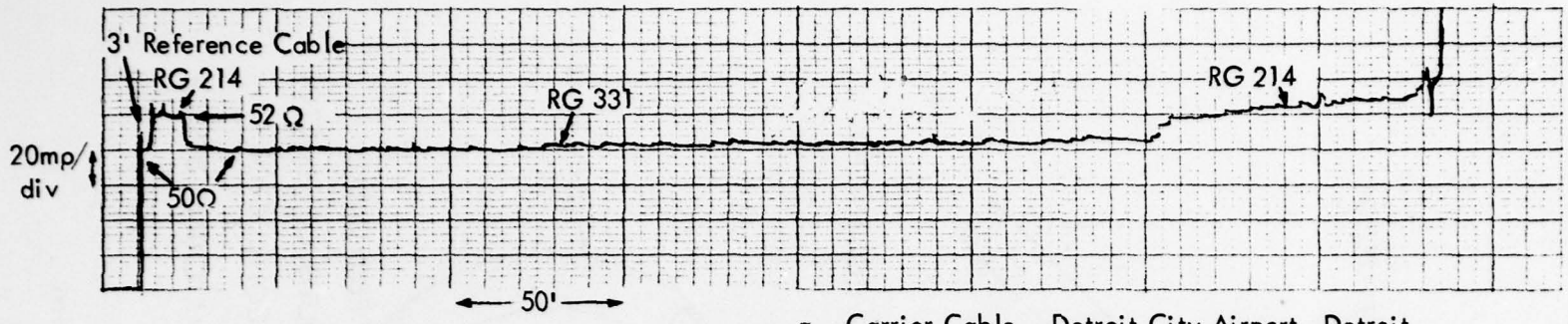

a. Carrier Cable. Detroit City Airport, Detroit, Michigan.

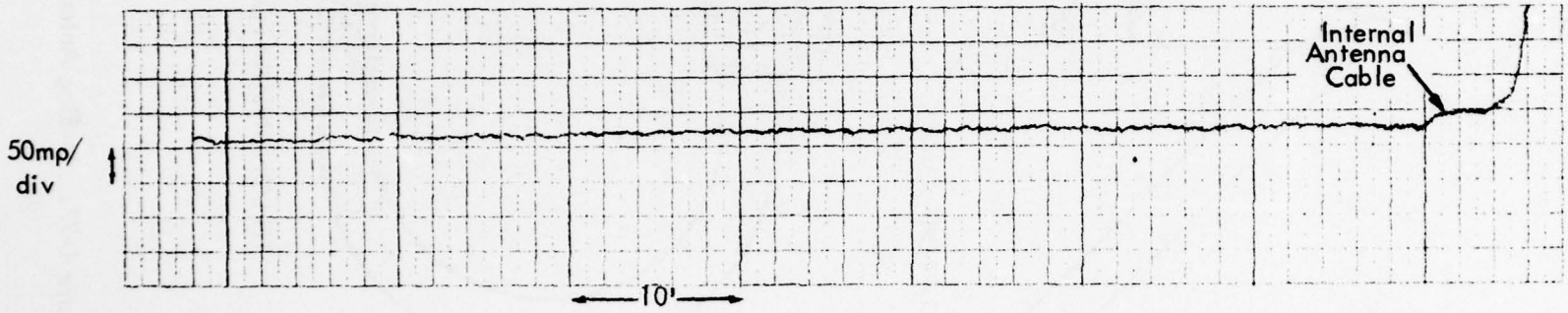

b. Antenna Cable. Tri-State Airport, Parkersburg, W. Va.

Figure 4-76. V-Ring Localizer Cables.

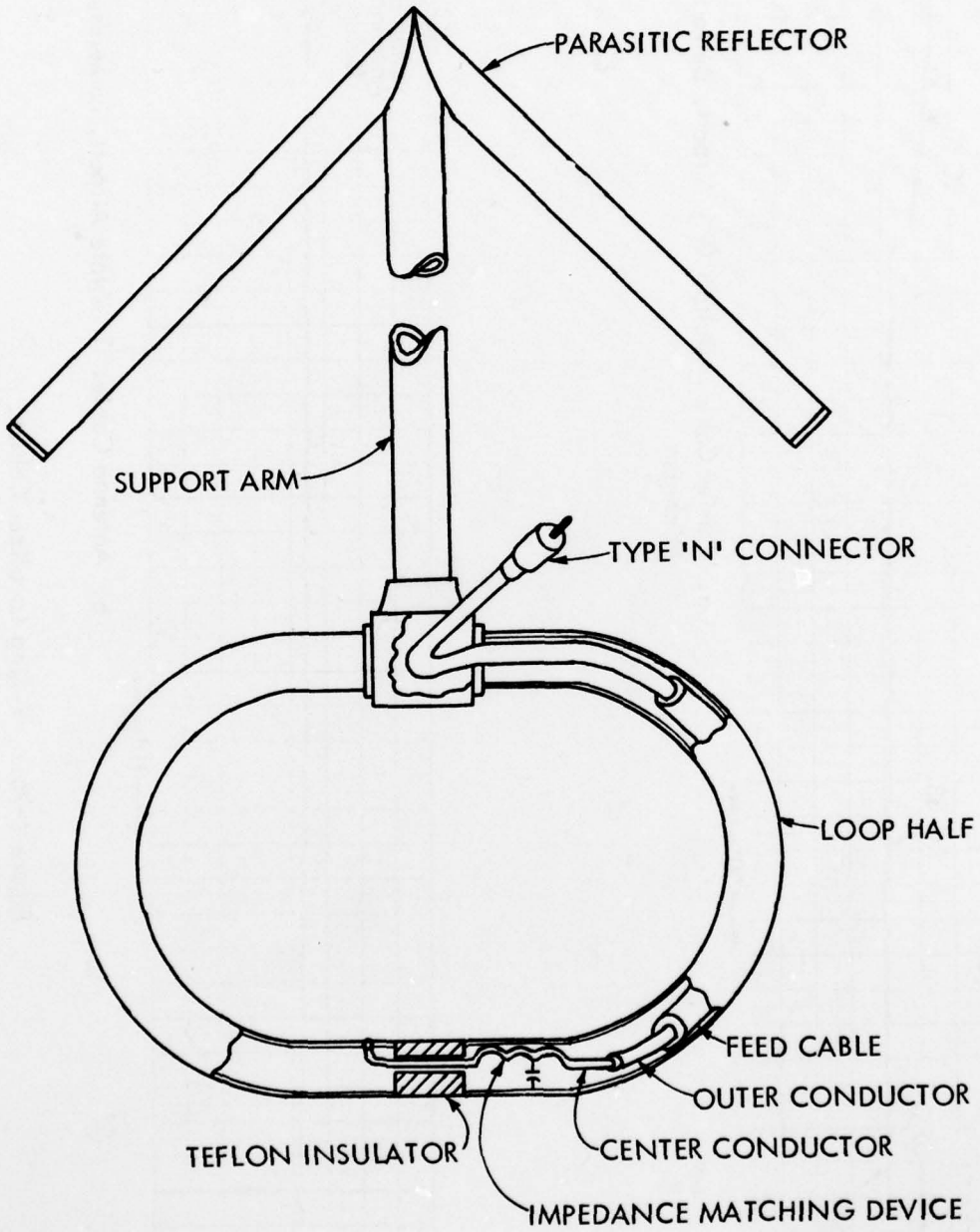

Figure 4-77. V-Ring Antenna Element Construction.

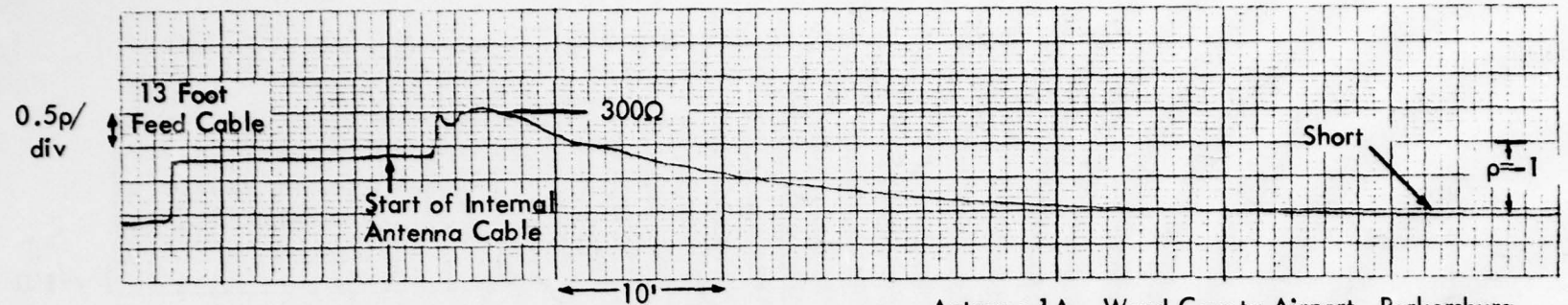

a. Antenna 1A - Wood County Airport, Parkersburg, W. Va.

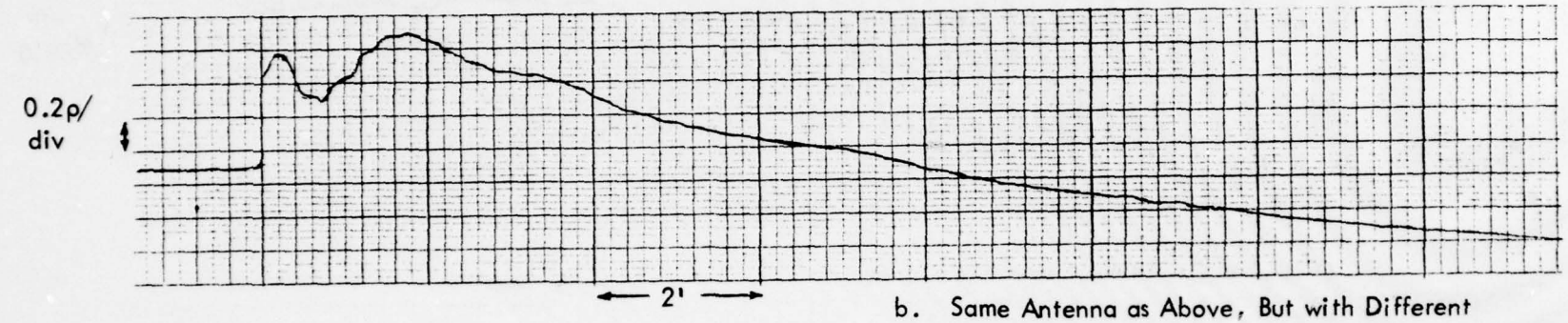

b. Same Antenna as Above, But with Different Scales.

Figure 4-78. V-Ring Antenna TDR Signatures.

AD-A074 425 OHIO UNIV ATHENS DEPT OF ELECTRICAL ENGINEERING F/G 17/7
IN-SERVICE IMPROVEMENTS AND MODERNIZATION OF ALL COMPONENTS OF --ETC(U)
JUL 78 DOT-FA75WA-3549
UNCLASSIFIED EER-35-1 FAA-RD-78-112-1 NL

3 OF 8
AD A074425

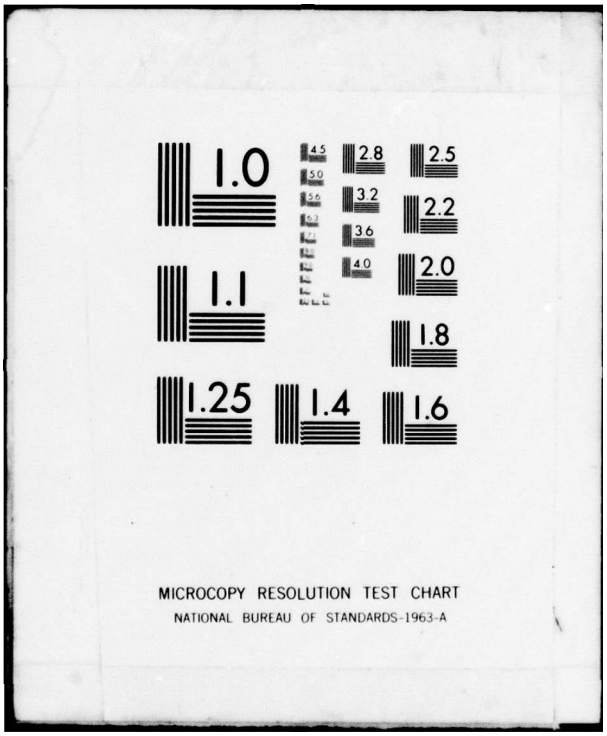
1.0
1.1
1.25
1.4
1.6
1.8
2.0
2.2
2.5
2.8
3.2
3.6
4.0
4.5
5.0
5.6
6.3
7.1
8.0
9.0
MICROCOPY RESOLUTION TEST CHART
NATIONAL BUREAU OF STANDARDS-1963-A

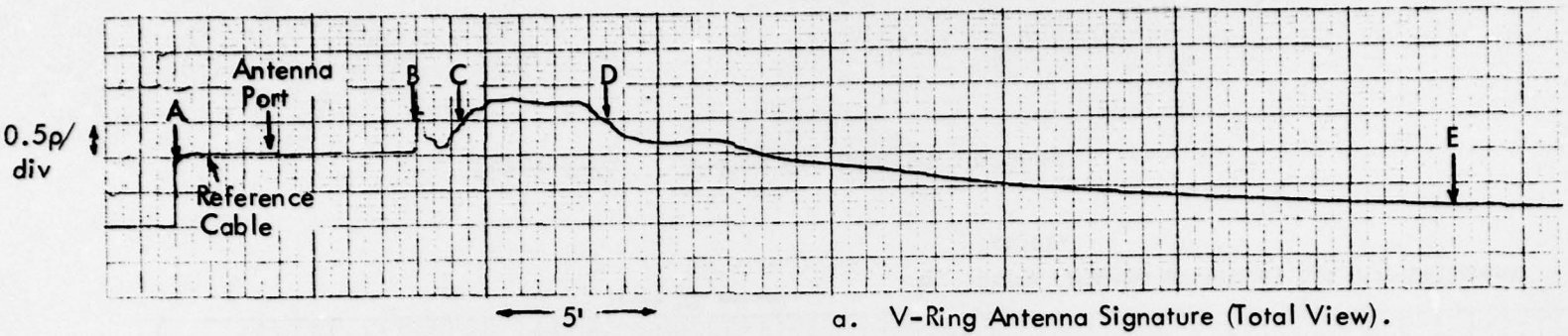

a. V-Ring Antenna Signature (Total View).

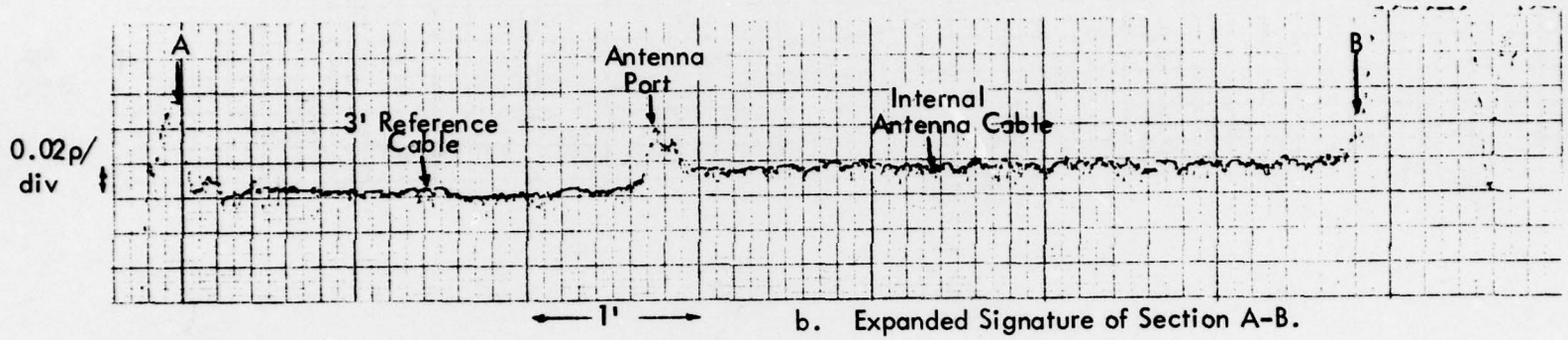

b. Expanded Signature of Section A-B.

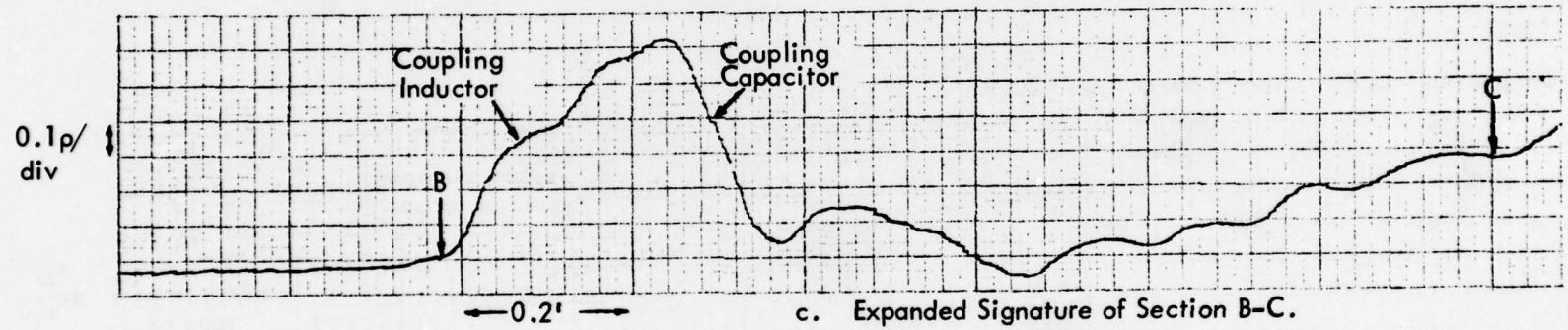

c. Expanded Signature of Section B-C.

Figure 4-79. Expanded Signature Views of a V-Ring Antenna.

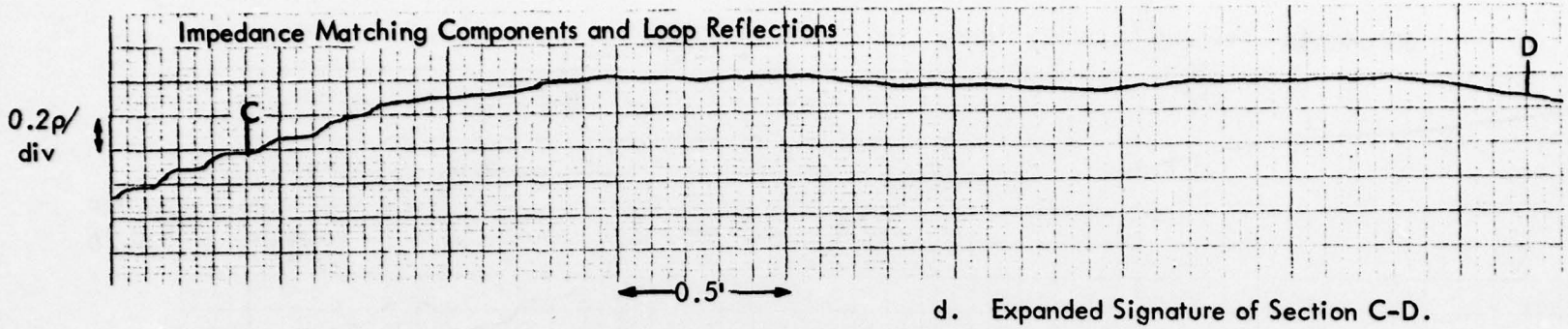

d. Expanded Signature of Section C-D.

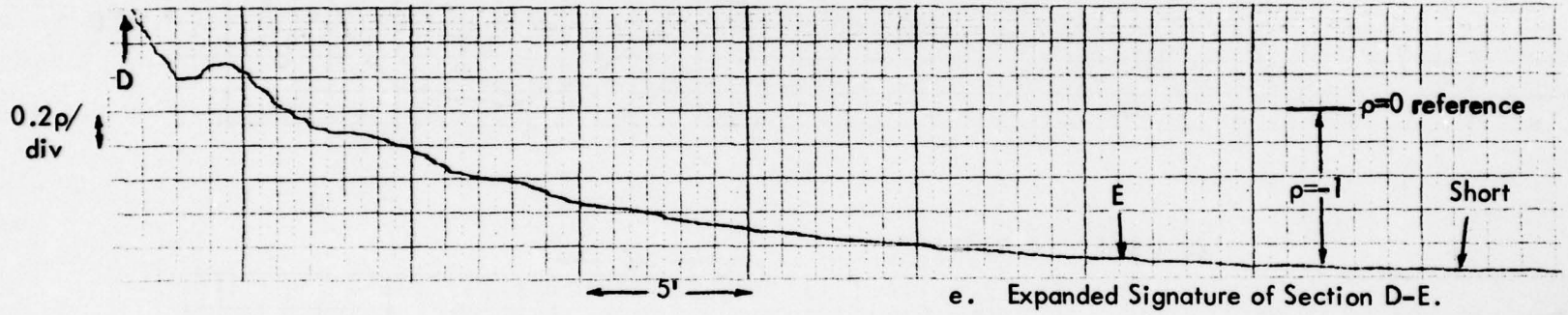

e. Expanded Signature of Section D-E.

Figure 4-79 (continued).

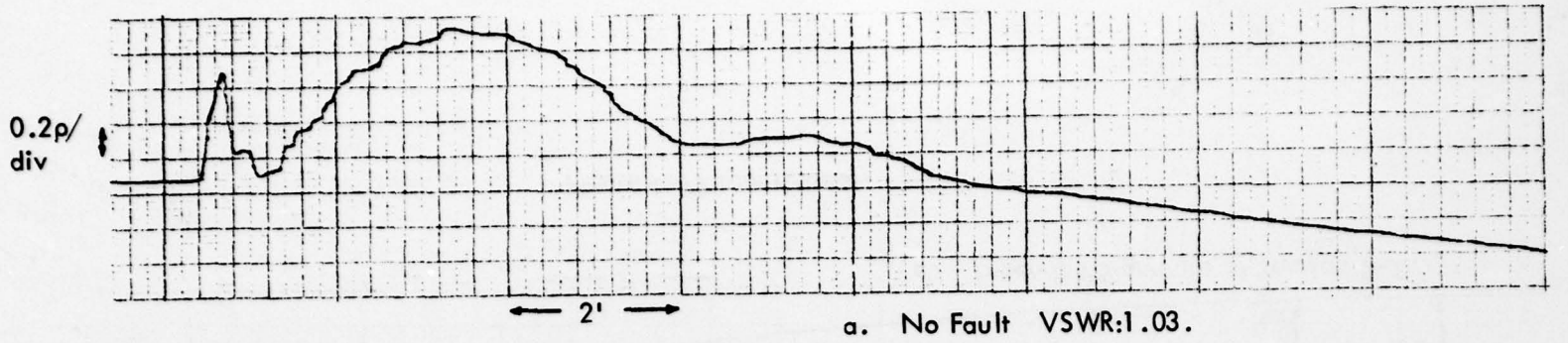

a. No Fault VSWR:1.03.

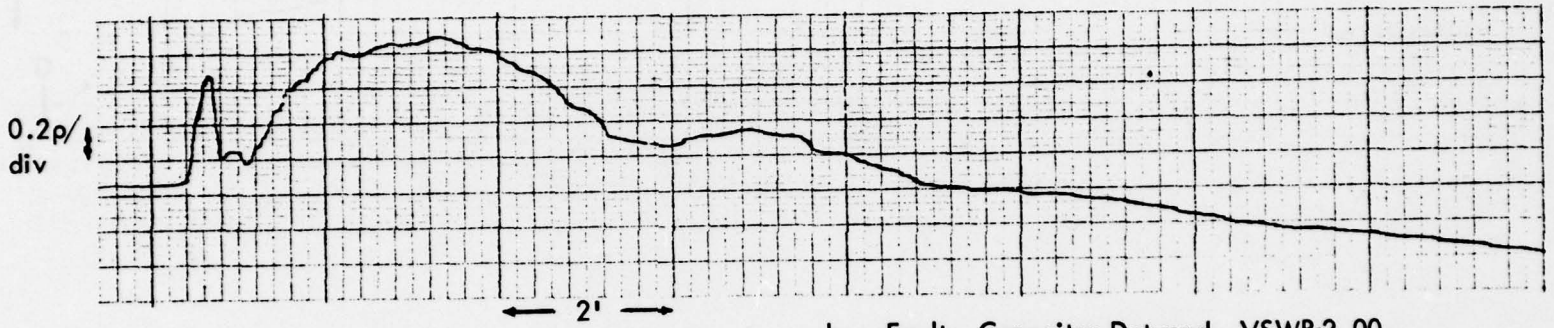

b. Fault: Capacitor Detuned VSWR:2.00

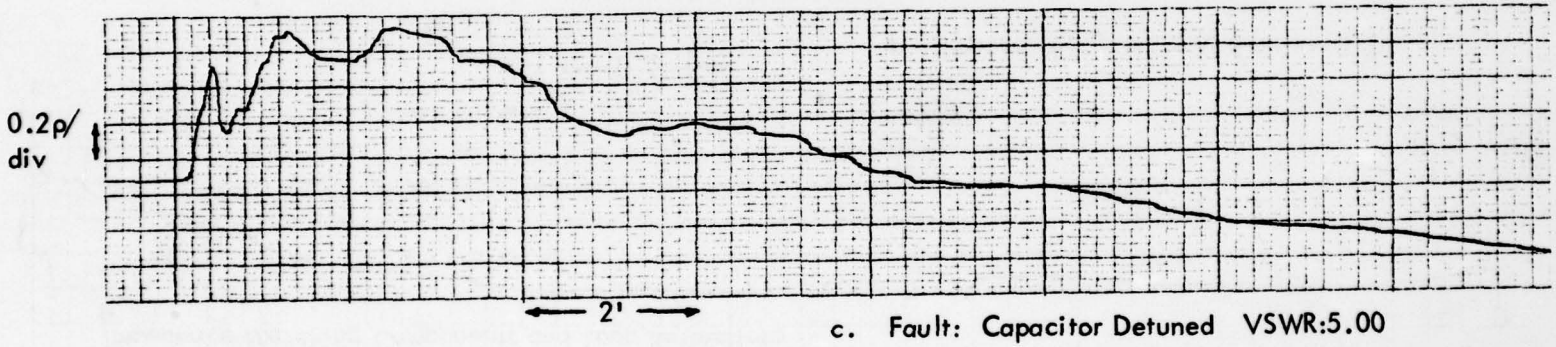

c. Fault: Capacitor Detuned VSWR:5.00

Figure 4-80. TDR V-Ring Fault Analysis and Associated VSWR Values.

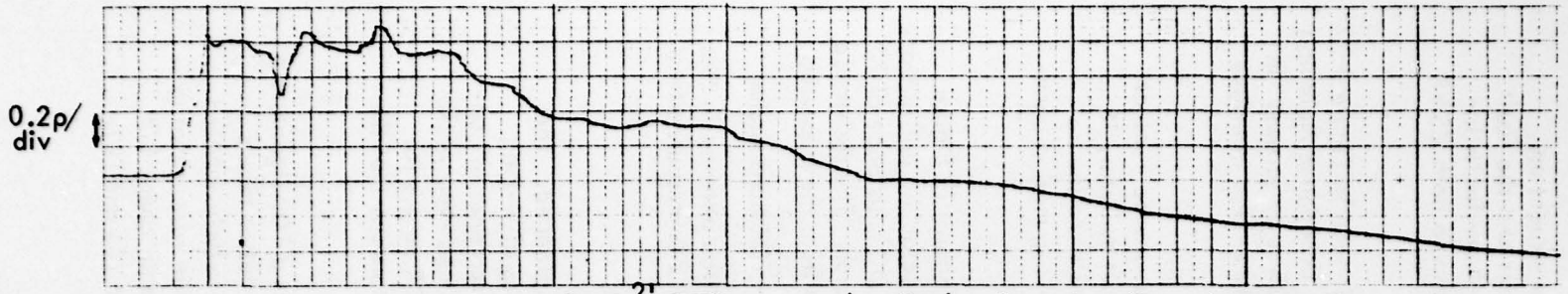

d. Fault: Capacitor Open VSWR:8.52

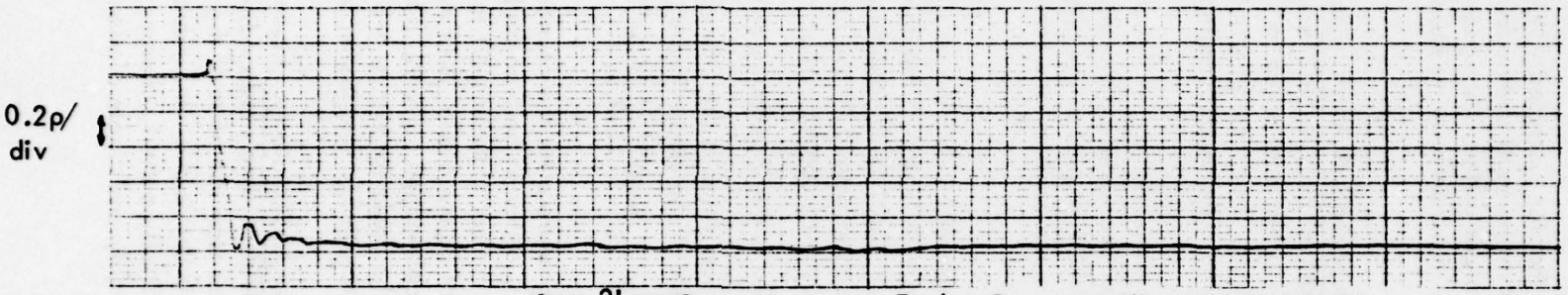

e. Fault: Capacitor Shorted VSWR:9.00.

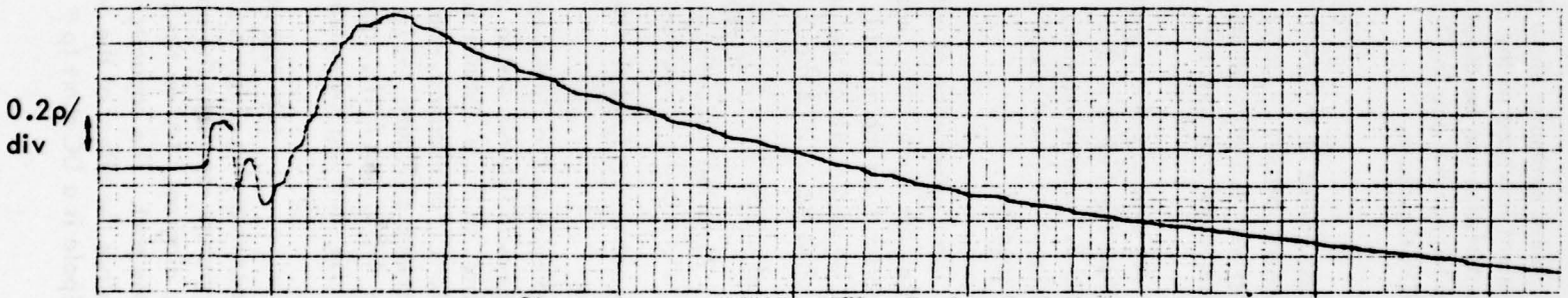

f. Fault: Coil Shorted VSWR:9.00.

Figure 4-80 (continued).

These examples show generally that for increased VSWR, one can expect an equivalent increase in the differences in the fault and no fault signatures and the fault characteristics can be obtained by analysis of the TDR signature. All of the faults induced except the one in Figure 4-80b have definite measurable qualities in both VSWR and TDR signature.

c) Field Measurements of Antenna Faults. As is seen in Figure 4-77 the loop halves of the V-Ring are separated by a teflon insulator. The impedance matching components attach to plates which are in turn connected to the loop halves by screws. In talking with ILS maintenance technicians, they stated that often the plate-loop interface becomes dirty and corroded necessitating a thorough cleaning.

An example of a signature for an antenna with just such a high resistance contact is depicted in Figure 4-81. Instead of the signature showing a DC short as usual, it shows a 5.5 ohm resistance. Because the first part of the graph was similar to the no fault signature (therefore unfaulted), a bad contact between the plate-loop mating parts was suspected.

The consequence of a loose connector on an antenna signature is shown in Figure Because part of the pulse was abnormally reflected at the antenna connector the entire trace is distorted from the no fault signature. The TDR signature indicates a DC resistance of 75 ohms also as a result of the poor connection caused by the loose connector. The resistance of 75 ohms (as well as the 5.5 ohm resistance above) can be calculated from the measured value of ρ from $Z_L = Zo\frac{(1+\rho)}{(1-\rho)}$ where Zo is the impedance of the TDR or TDR transmission cable, Z_L is the discontinuity impedance which is the DC resistance of the antenna in this case, and ρ is the reflection coefficient of the discontinuity. A ρ of 0.2 is measured from the signature in Figure 4-81b, therefore $Z_L = 50\frac{(1+0.2)}{(1-0.2)} = 75$ ohms.

Figure 4-81c is the resultant signature after the connector was tightened. The signatures in Figures 4-81a and 4-81c, although both no fault signatures of V-Ring antennas, do have distinct differences. This is due in part to slight differences in construction. For instance, the antenna of Figure 4-81a is of the fixed-tuned type while the antenna of Figure 4-81c is a variable-tuned variety. Also, the TDR cables for Figure 4-81c was 50 ft. longer than the cable for Figure 4-81a, which means that the TDR pulse reaching the antenna of Figure 4-81c had higher losses.

(4) TDR Monitor Dipole Signatures. Figure 4-82a is a TDR signature and accompanying diagram of an FA-8720 V-Ring monitor dipole. The letter labels on the signature represent the contributions from the parts of the monitor similarly labeled on the diagram. (A) on the signature is due to the lead inductance of the wires running from the port. The capacitor at (B) initially a short, charges quickly to an open, but not before the effect of the balun assembly and dipole elements begin at (C) and (D). The dipole is a DC short ($\rho = -1$).

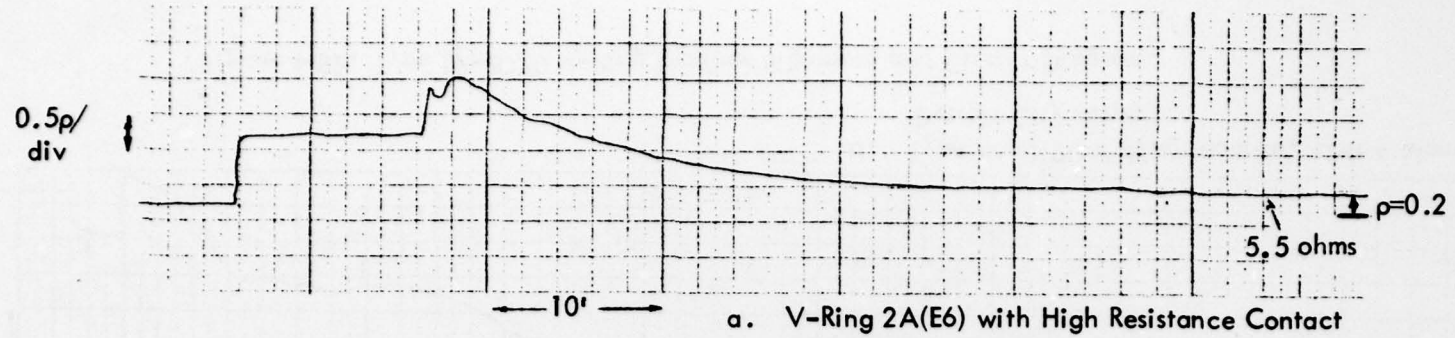

a. V-Ring 2A(E6) with High Resistance Contact
Wood County Airport.

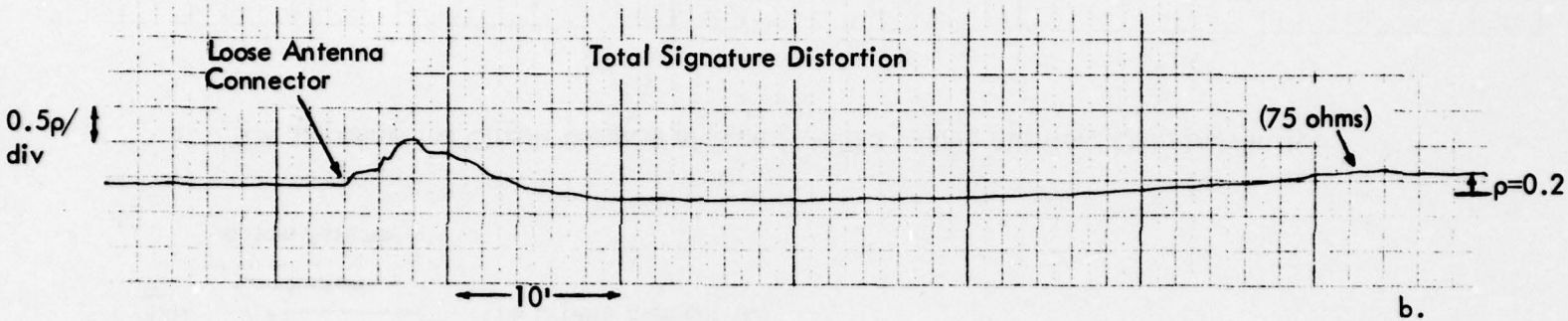

b.

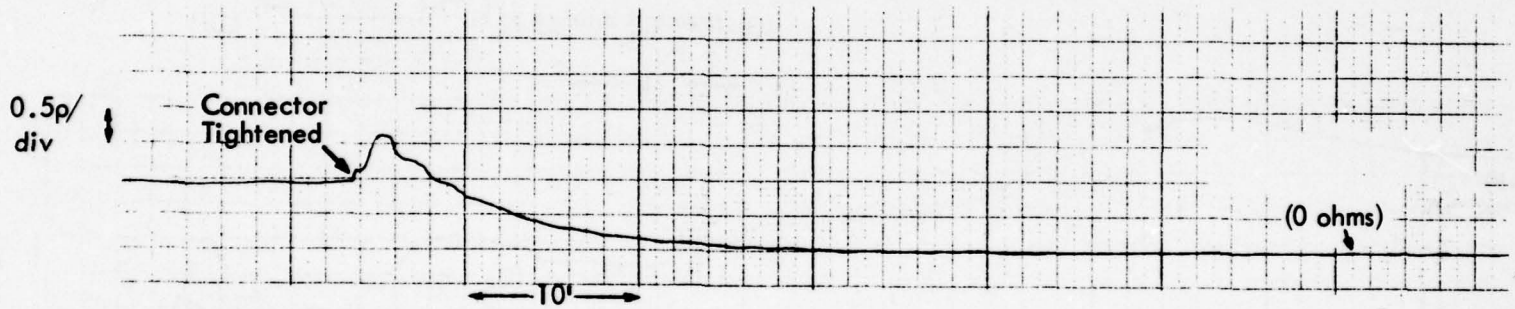

c.

Figure 4-81. V-Ring Antenna 2A(E6), Ohio University Localizer.

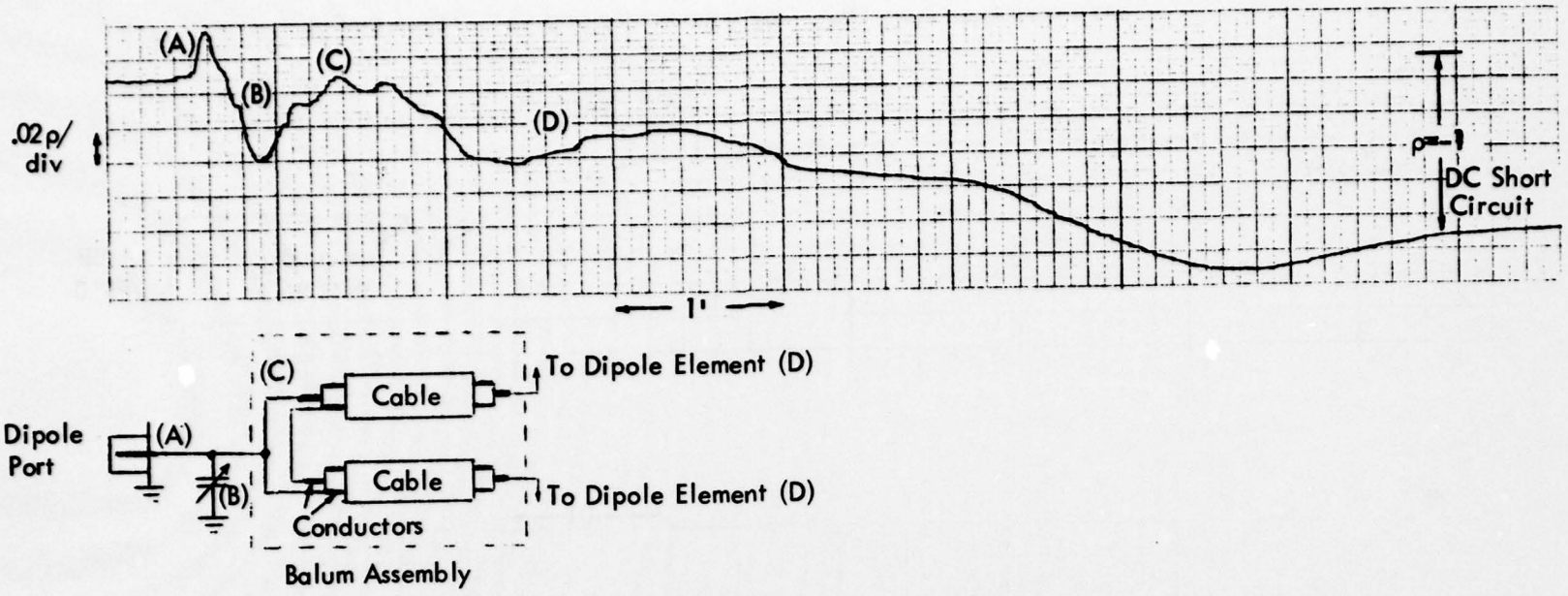

a. TDR Signature and Circuit Diagram of Type FA-8720 V-Ring Monitor, Ohio University.

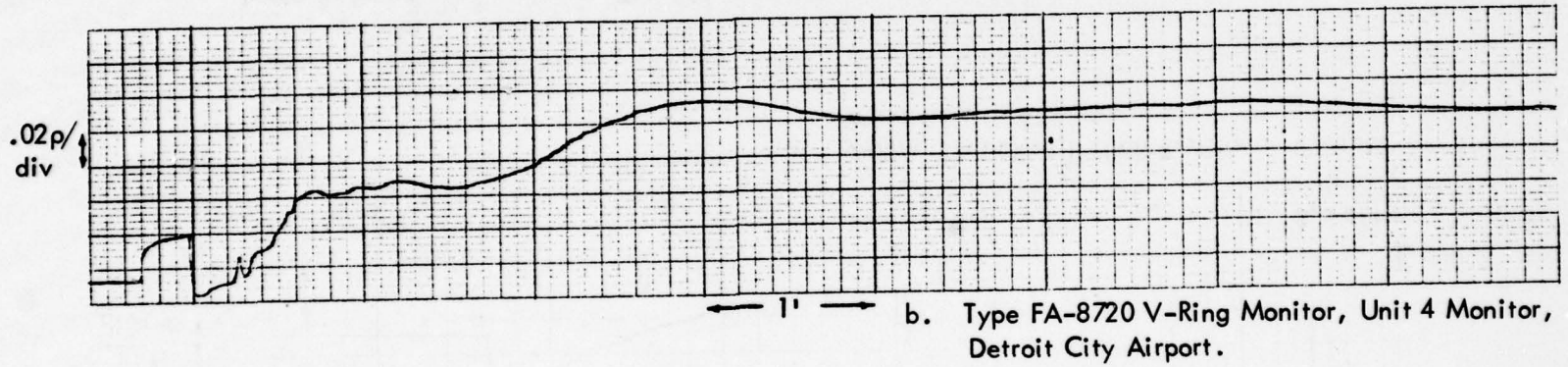

b. Type FA-8720 V-Ring Monitor, Unit 4 Monitor, Detroit City Airport.

Figure 4-82. Type FA-8720 V-Ring Monitor Signature and Circuit Diagram.

The signature at the bottom of Figure 4-82b is from a FA-5696 type V-Ring monitor dipole. The steady state value of the previous TDR signature was $\rho = -1$ where the steady state value for this signature is $\rho = +1$. The FA-8720 monitor is, therefore, a DC short and the FA-5696 is a DC open.

(5) Localizer Distribution System. As was seen in Figure 4-75, the localizer APCU is composed of power dividers, bridges, attenuators and detectors. In the signature of the sideband input to the APCU in Figure 4-83a, the return is mainly from the bridge (Scanwell SX-28) since only a small amount of the pulse power is transmitted beyond Z3. If the horizontal scale was reduced to 2 ft/div more of the reflections beyond Z3 would be shown, but they would be inappropriately small for fault detection. For this reason, it has been found that the most effective way to test an APCU component is to electrically isolate it. This was also suggested earlier in the section on bridge analysis. In some cases, though, fault checks can be accomplished with the APCU components connected. The following examples help enforce these thoughts and provide procedures and samples for fault checks.

The signatures in Figures 4-83b-83f are examples of faults introduced near where the TDR pulse enters at Z3, J1. The 90° arm lengths of the bridge are two feet long and the 270° arm is 6 ft. Because the dielectric setting of the TDR was for polyethylene while dielectric of the bridge is epoxy glass (stripline construction), the proper arm distances are not plotted on the TDR signatures. The lengths are consistent from signature to signature, so fault analysis is not hampered significantly. One could always use the variable dielectric setting to match the stripline dielectric if for some reason it was necessary for testing.

A short discussion of each signature follows. See Figure 4-75 for component location and identification.

Figure 4-83b: Sideband input (Z3), J2 open: With Z3, J2 open, W2 is opened and eliminated from the signature. Thus the pulse path around J2 is essentially a constant impedance path. There is an upward jump of the signature due to reflections from Z3, J1 at the same time as the returns from J2 are received at the TDR.

Figure 4-83c: Z2 input open: The fault here produces an open cable which causes a rise in the signature.

Figure 4-83d: Z3, J4 open: With Z3, J4 open, W3 is opened and eliminated from the signature. The pulse path around J4 is essentially a constant impedance as is shown in the signature. Note that the remainder of the signature is vertically offset from but similar to the no fault signature. The drop at Z3, J3 for the faulted signature condition is larger than for the no fault since little of the wave was reflected at Z3, J4 and a larger portion than usual is transmitted to J3 producing a larger reflection.

Figure 4-83e: Carrier input open (Z4, J3): The fault produces little change from no fault voltage waves transmitted back to the TDR. Therefore, little change in the TDR signature.

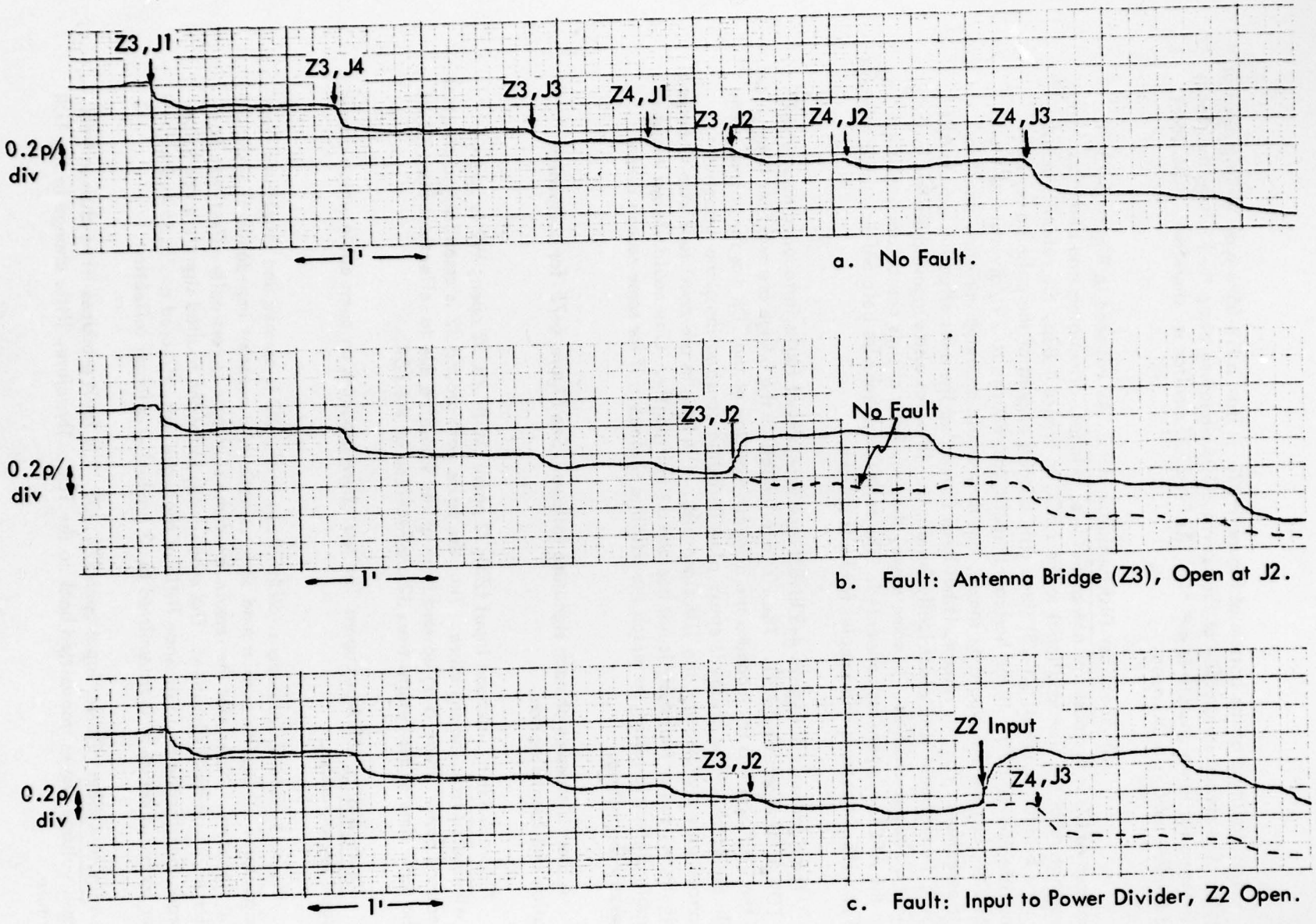

Figure 4-83. V-Ring Localizer APCU Signatures of SB Input (Z3, J1).

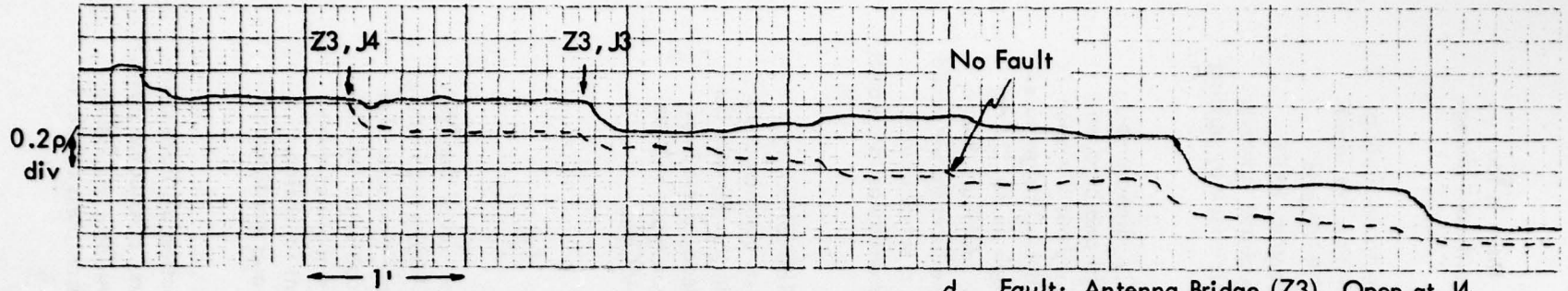

d. Fault: Antenna Bridge (Z3), Open at J4.

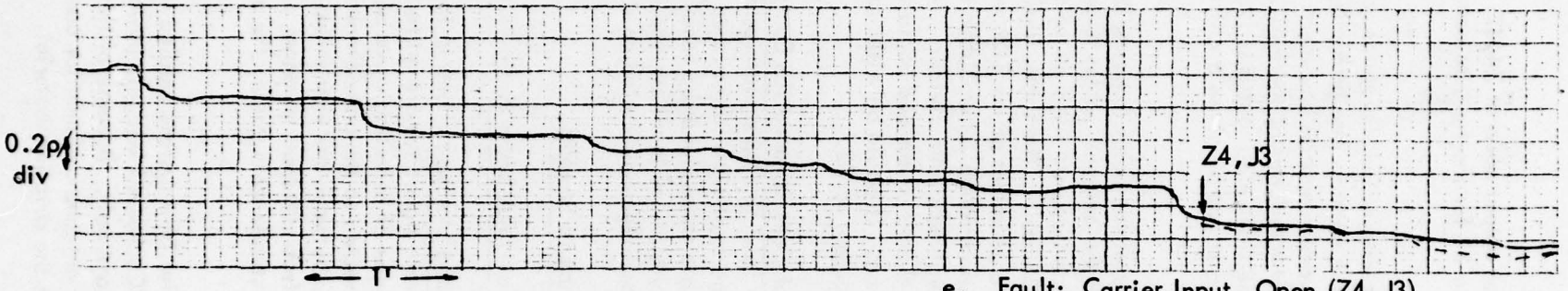

e. Fault: Carrier Input, Open (Z4, J3).

f. Fault: Pre-Power Divider Output, Open at Z4, J2.

Figure 4-83 (continued).

Figure 4-83f: Pre-power divider output open at Z4, J2: Again, there is too little of the wave power transmitted to Z4 for the fault to cause any significant change in the signature.

Conclusions regarding the preceding APCU signatures are that the fault-finding ability of the TDR is evident for devices within close proximity of the TDR pulse input point. Appropriate fault detection is dependent on how much of the TDR wave is transmitted to a device and on the characteristics of the fault. For example, fault testing the pre-power divider when the sideband input is pulsed is inadequate; however, bridge Z3 and any cables connected to it can be given a sufficient fault check by pulsing the sideband input.

Figure 4-84 is a signature study of the input to power divider Z2. Signatures in Figure 4-84b and 4-84c represent the antenna cables to antenna E14 and E9 open, respectively. Both produce the expected upward jump at the fault point, but the open at J6(6B) produces the more severe TDR fault. The faults as shown by the TDR signatures are functions of the reflections and transmissions of the TDR wave through power divider Z2. Determining the pulse propagation through Z2 would be extremely difficult due to the multiple paths and components involved in the divider. Tests of the kind shown would be of little value for antenna health checks unless one could establish a set of unique TDR signatures for each faulted antenna. It would be wiser to test the antennas individually by disconnecting their cables at the output of Z2.

2. Sample TDR Signatures of Commissioned ILS Facilities. The following material is a sample set of instrument landing TDR signatures obtained at commissioned sites. Since cable and APCU tests and analysis were covered earlier in this report, the signatures that follow will not duplicate those signature samples. Instead, a group of antenna and monitor signatures for a variety of localizer and glide slope types will be presented. The only deviation will be a short discussion on stripline APCU's.

a. Localizer TDR Signature Samples.

(1) APC and Wilcox TWA Systems.

a) Antennas and Monitors. Due to the construction of the TWA antennas and monitors studied here there signatures are quite simple. Figure 4-85 shows some example signatures of various types of traveling wave antennas and monitors. For these measurements the TDR was connected to the antenna or monitor cables at the distribution system. Note the similarity between the first three antenna signatures even though the signatures were obtained from different antennas at different facilities. Since the traces tend to $\rho = -1$ for a steady state value, the antennas and monitors represented are essentially DC shorts.

b) APCU. The TWA systems studied in this section all have stripline type APCU's. The stripline APCU has all bridges, power dividers, attenuators, and associated components fabricated as one unit. Because of this construction, any faults usually occur at load terminations or antenna and monitor connections on ports connecting to the stripline rather than inside the stripline material.

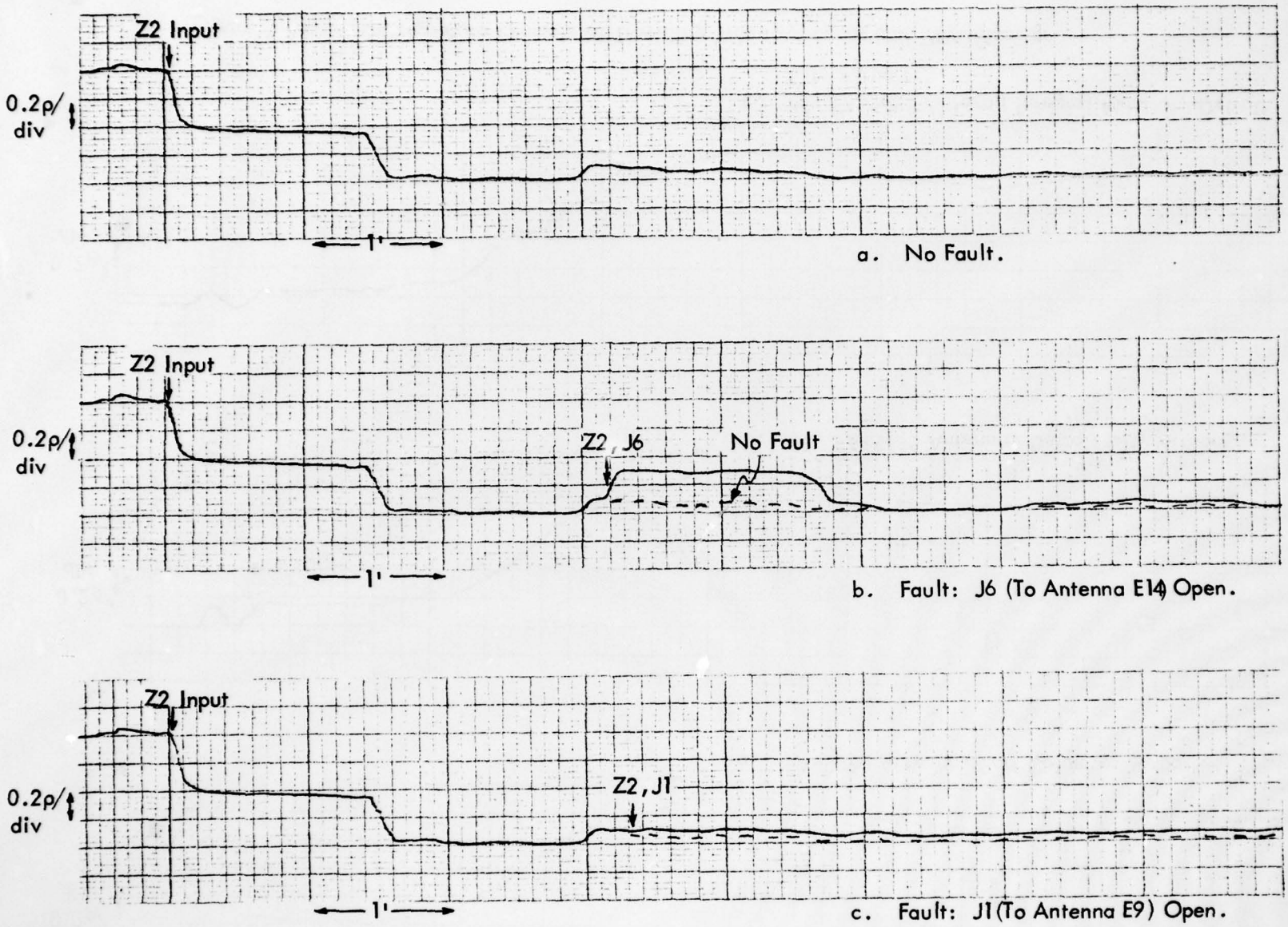

Figure 4-84. V-Ring Localizer APCU Signatures of Power Divider, Z2, Input.

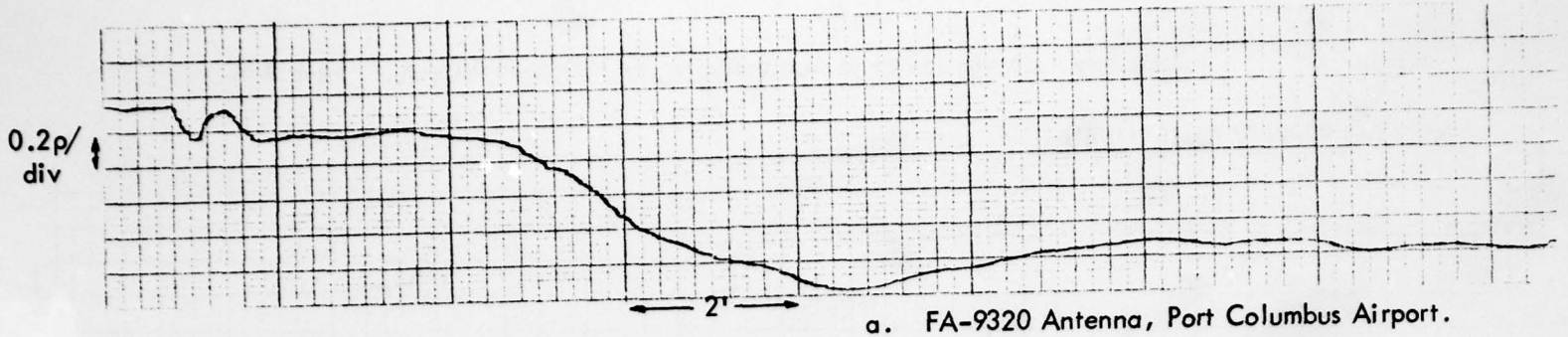

a. FA-9320 Antenna, Port Columbus Airport.

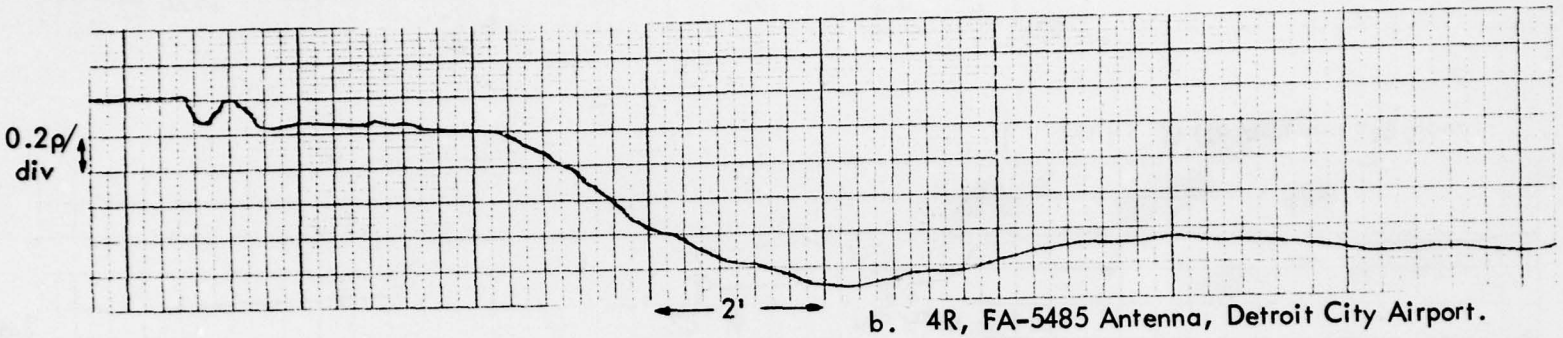

b. 4R, FA-5485 Antenna, Detroit City Airport.

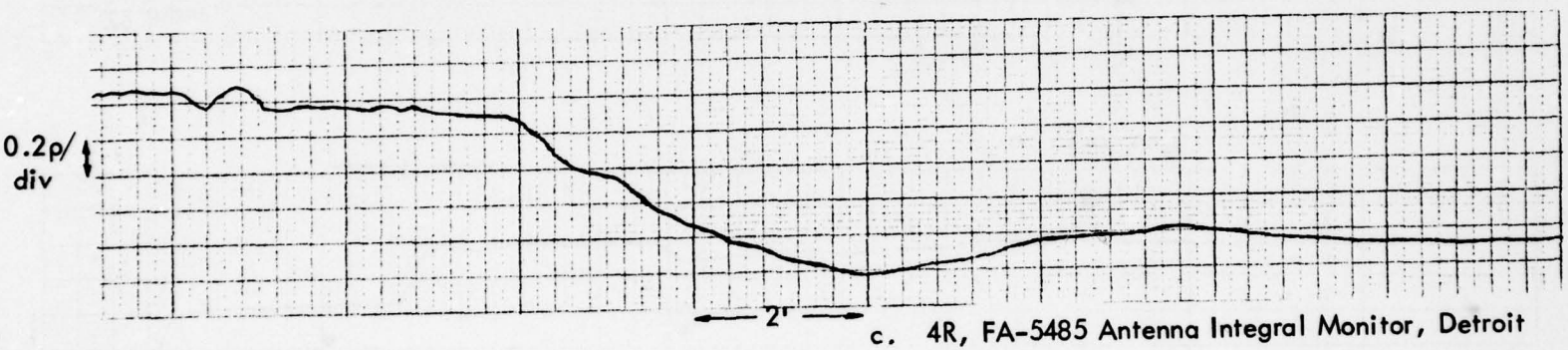

c. 4R, FA-5485 Antenna Integral Monitor, Detroit City Airport.

Figure 4-85. TDR Signature Example of Traveling Wave Antennas and TWA Monitor.

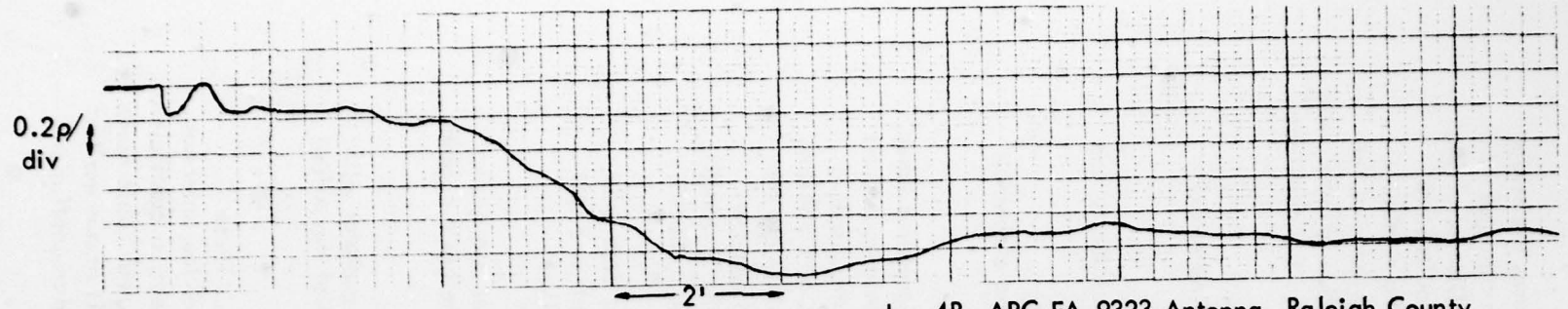

d. 4R, APC FA-9323 Antenna, Raleigh County Airport.

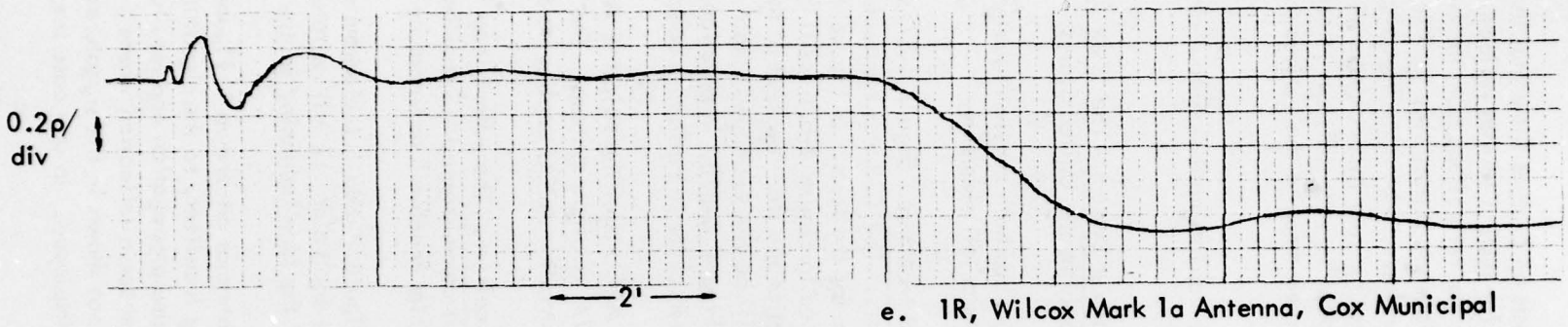

e. 1R, Wilcox Mark 1a Antenna, Cox Municipal Airport.

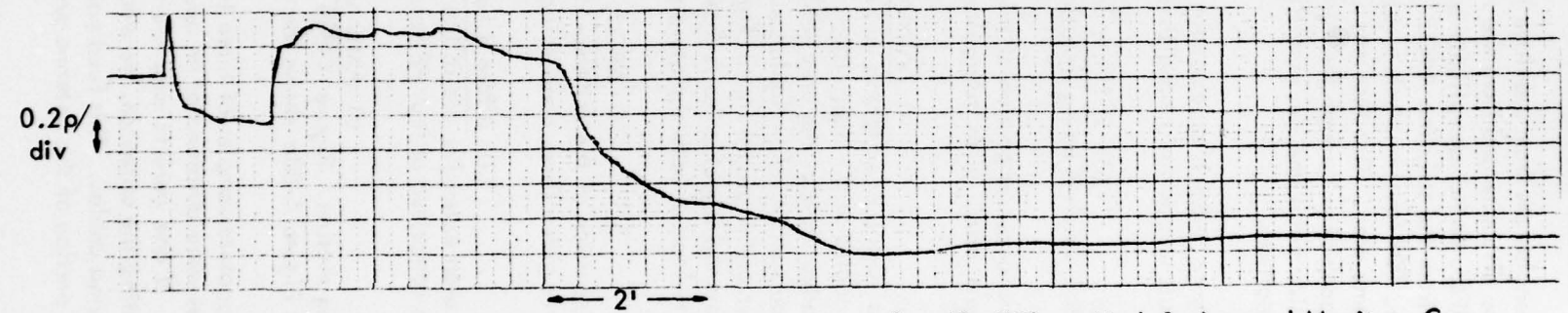

f. 4R, Wilcox Mark 1a Integral Monitor, Cox Municipal Airport.

Figure 4-85 (continued).

Conclusions from previous TDR tests on bridges show that in most cases the bridge should be disconnected from the APCU for testing so that reflections from other devices in the APCU do not complicate or mask the reflections from the bridge. Disconnecting devices from the stripline APCU is obviously not possible, so if internal faults were suspected TDR fault analysis would often have to be done by comparing the signature of the same area. This test may even yet be very inconclusive since knowledge of the pulse propagation through the APCU would be very difficult to ascertain due to multiple transmission paths and the inability to keep trace of the various pulse wave transmissions and reflections.

Figure 4-86 is an example of the carrier input signature of a stripline APCU under fault and no fault conditions.

(2) TI GRN/27 Localizer System. The GRN/27 is a relatively new type of ILS which is being installed widely in the United States.

The localizer portion of this system has both course (14-element) and clearance (6-element) arrays with integral monitors on all elements.

a) Antennas and Monitors. Figure 4-87 shows signatures taken of typical GRN/27 antennas and monitors. The TDR was connected to the antenna and monitor cables at the distribution system for the tests. In Figure 4-87b, the graph is an expanded view of the area (ab) marked in Figure 4-87a. All antennas and monitors tested had similar reflection characteristics the first few feet of the signature, so the remainder of the graphs in this figure will be the expanded, more interesting, part of the antenna signature as is shown in Figure 4-87b. In practice, though, it would be wise to look at both signature scales in order to perform a complete fault check.

b) APCU. The APCU is of the stripline variety as described in the discussion of the Wilcox-APC TWA localizer systems. The comments and test procedures given there concerning the stripline APCU applies here as well.

(3) Alford 8 Loop Localizer. The Alford loop localizer is a system that has seen extensive use in the past at commissioned ILS facilities. The basic antenna system is comprised of four RF power cables feeding 8 antennas by pairs.

a) Antennas. Figure 4-88a is a diagram of loop radiator with balancing section. Figure 4-88b is the equivalent circuit representation of the Alford loop and Figure 4-88c shows the use of the loop balancing section.

Signature samples of three loop antennas are shown in Figure 4-89. These signatures were obtained at an operating localizer, so the signatures are of the antennas in pairs. If one were to examine the pulse propagation and resultant reflection coefficient when testing the antennas, he would first see a reflection where the RF power cable feeds two antenna cables. This feed point is not shown in the signatures since it occurs earlier than the portion of the antenna system displayed. In any case the reflection coefficient

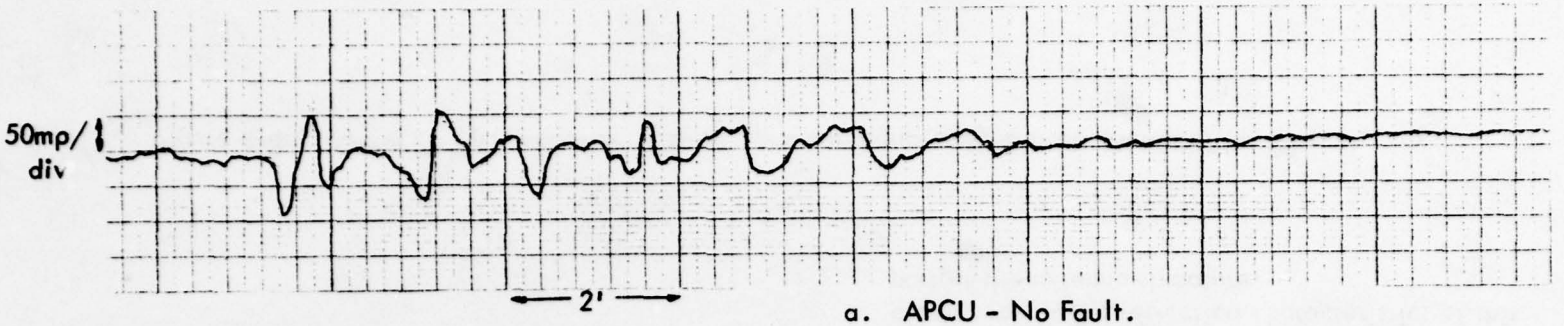

a. APCU - No Fault.

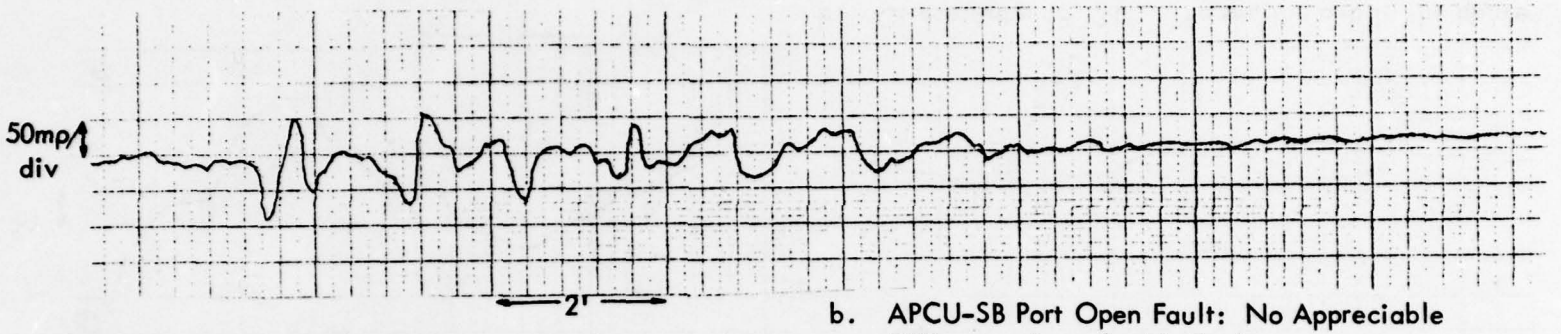

b. APCU-SB Port Open Fault: No Appreciable Difference from the No Fault

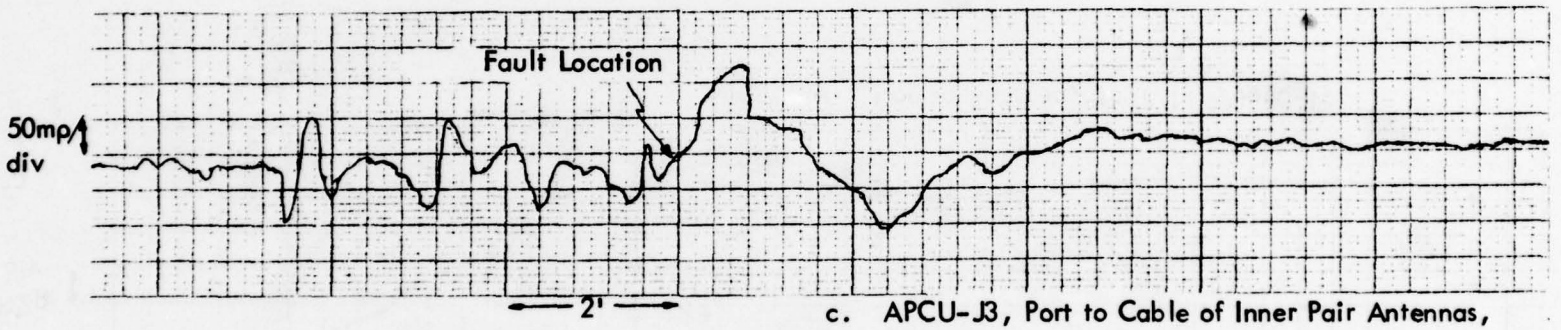

c. APCU-J3, Port to Cable of Inner Pair Antennas, Shorted.

Figure 4-86. Carrier Input for 8-Element TWA Localizer APCU, Raleigh County Airport.

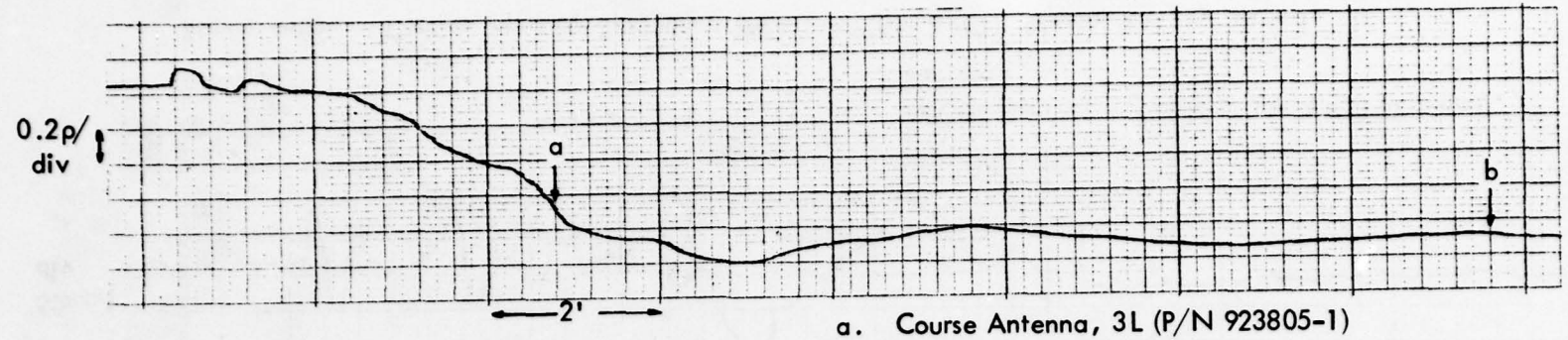

a. Course Antenna, 3L (P/N 923805-1)

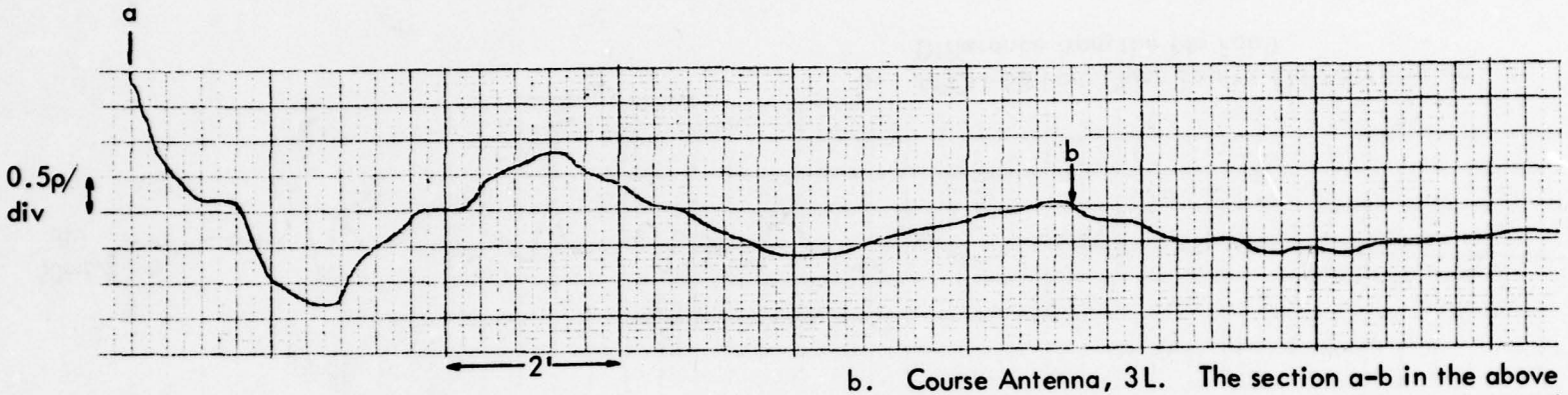

b. Course Antenna, 3L. The section a-b in the above signature is the same as section a-b here except with a more sensitive vertical scale. This provides a closer look at the reflection characteristics of this part of the antenna signature.

Figure 4-87. GRN/27 TWA Localizer Course Antenna Signatures, Detroit Metropolitan Airport.

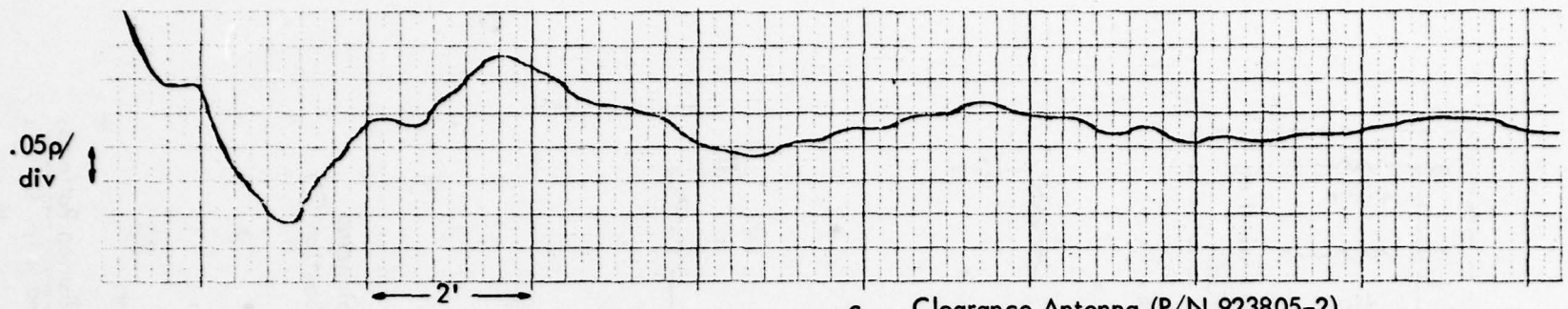

c . Clearance Antenna (P/N 923805-2).

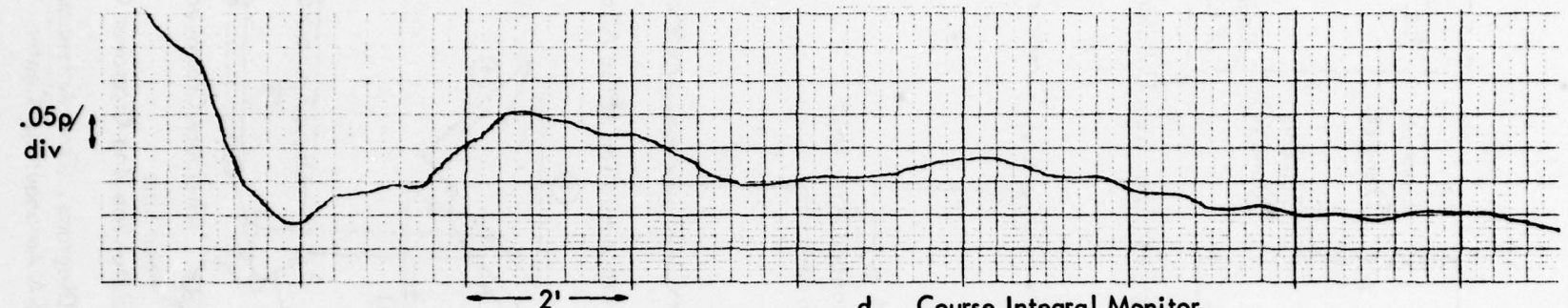

d . Course Integral Monitor.

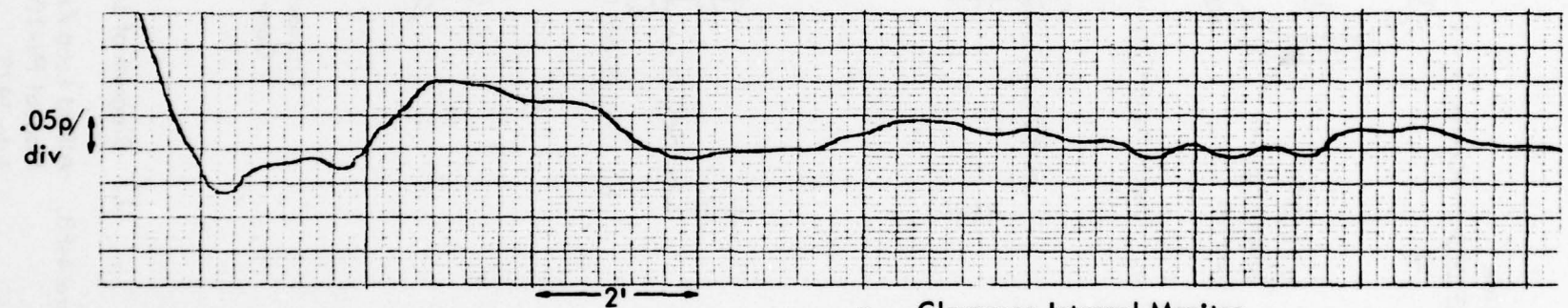

e . Clearance Integral Monitor.

Figure 4-87 (continued).

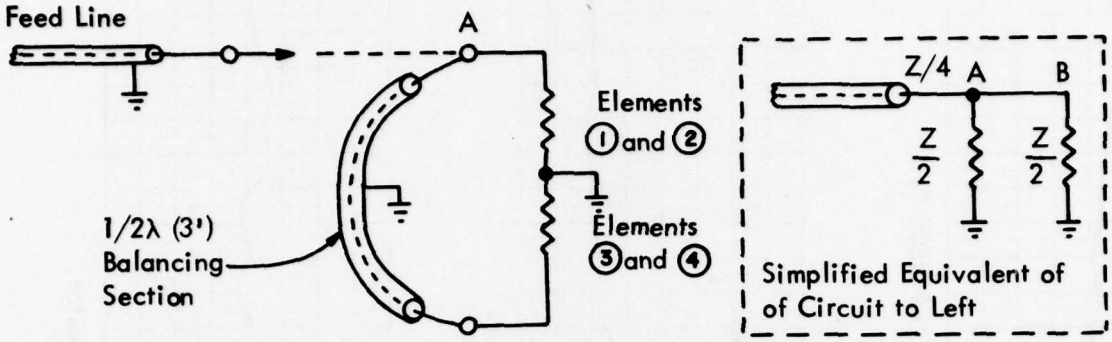

a. Use of Balancing Section to Feed Loop from Unbalanced Line.

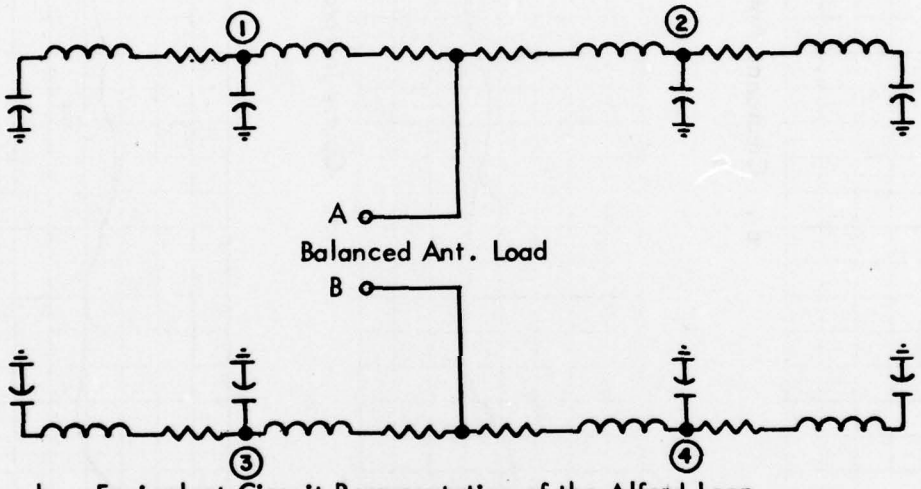

b. Equivalent Circuit Representation of the Alford Loop.

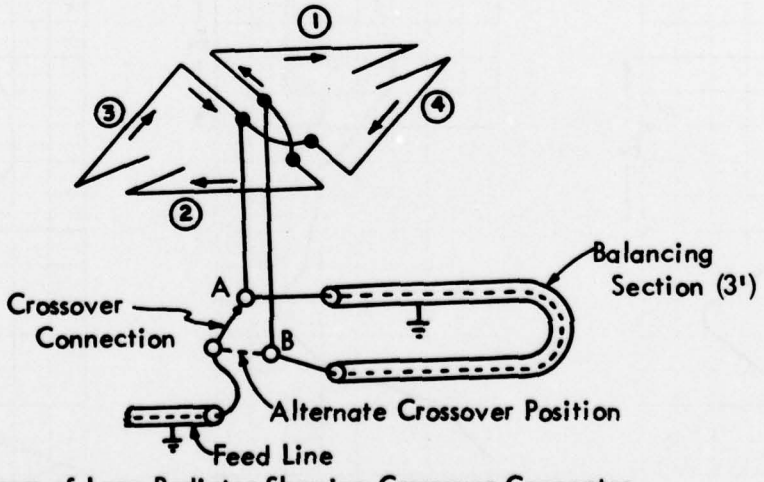

c. Diagram of Loop Radiator Showing Crossover Connector.

Figure 4-88. Alford Loop Antenna Diagrams. (From Antennas and Radiation Patterns, Manual FV-108-1, FAA Aeronautical Center, Oklahoma City, Okla., July 1975.

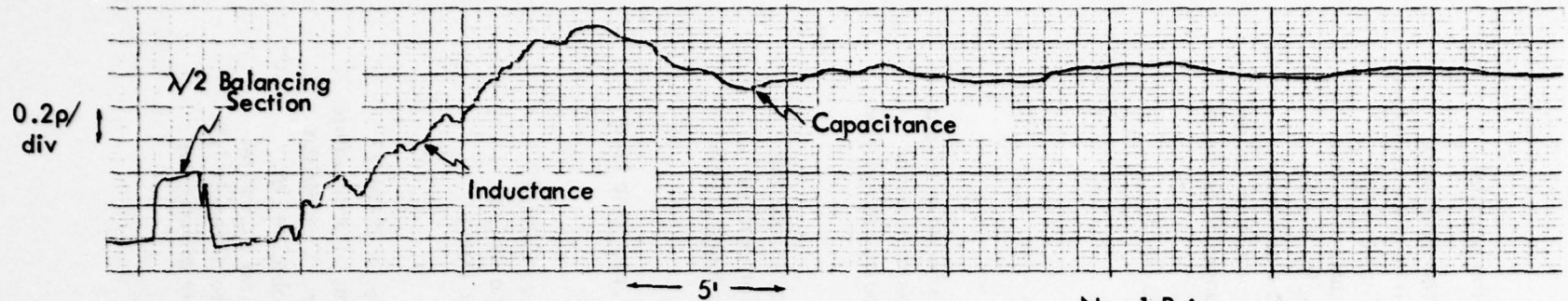

a. No. 1 Pair.

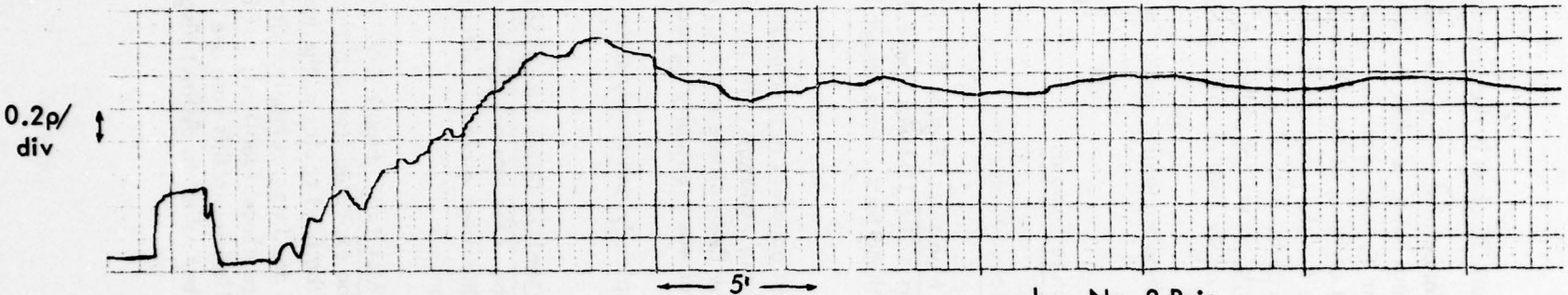

b. No. 2 Pair.

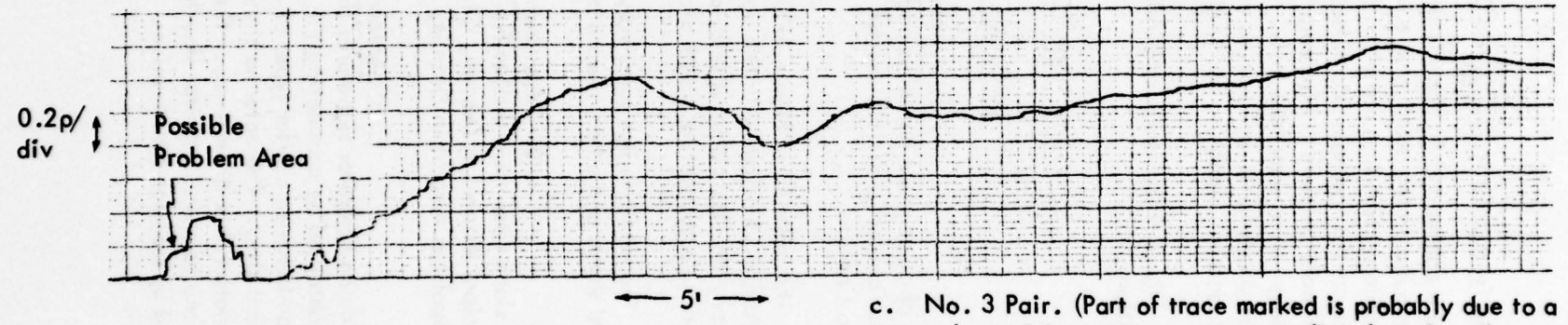

c. No. 3 Pair. (Part of trace marked is probably due to a pulse arriving at one antenna earlier than the other because of different antenna line lengths.

Figure 4-89. Alford Loop Antenna Pair Signatures, Port Columbus Airport.

for the feed point is $\frac{25-50}{25+50} = -0.5$, where 25 ohms is the impedance of the parallel antenna cables and 50 ohms is the impedance of the RF power cable. When each part of the pulse transmitted down each antenna cable reaches the antennas, it sees the balancing cable section in parallel with the line to loop sections 1 and 2. In Figure 4-89c, it appears that perhaps the pulses are not arriving at the antennas at the same time due to different antenna cable lengths. Thus the stair step effect where normally the reflections return simultaneously. The resistive, inductive, and capacitive equivalent circuit components are labeled accordingly on the top signature. The steady state value of the antenna signature is +1ρ since the equivalent circuit capacitor changes to an open.

Figure 4-90 is a set of individual loop signatures under fault and no fault conditions.

b. Glide Slope TDR Signature Samples.

(1) APC, AIL and Wilcox System.

a) Antennas and Monitors. Figure 4-91 is signatures from several types of glide slope antennas and monitors. The TDR was connected to the antenna or monitor cables in the transmitter hut for these tests. Thus, there is TDR pulse degradation due to line loss.

The antenna in Figure 4-91c has an apparent high impedance fault. Since the signature is identical with the upper antenna signature until the dipole elements are reached, the fault is in at least one of the three dipole elements in the antenna. This antenna was suspect in a path problem and was eventually replaced.

The monitor signatures vary in complexity and steady state value; i.e., some tend toward shorts and others toward opens.

(2) Texas Instrument GRN/27 Glide Slope System. Two GRN/27 glide slope sites were visited for TDR tests. One was a null reference type at Cox Municipal Airport in Dayton, Ohio and the other a capture effect type at Detroit Metropolitan Airport in Detroit, Michigan.

a) Antennas and Monitors. Figure 4-92 is a series of GRN/27 antenna and monitor signatures that can be expected from a typical system. The signatures were obtained by connecting the TDR to the feed cables at the transmitter. Comparison is made between similar types of antenna and integral monitor signatures obtained at different sites. The antenna signatures are almost identical, but the monitor signatures have noticeable differences. The dissimilarities in this case are not due to different TDR line lengths (i.e., monitor line lengths) but rather to distinct discontinuity differences caused by monitor construction.

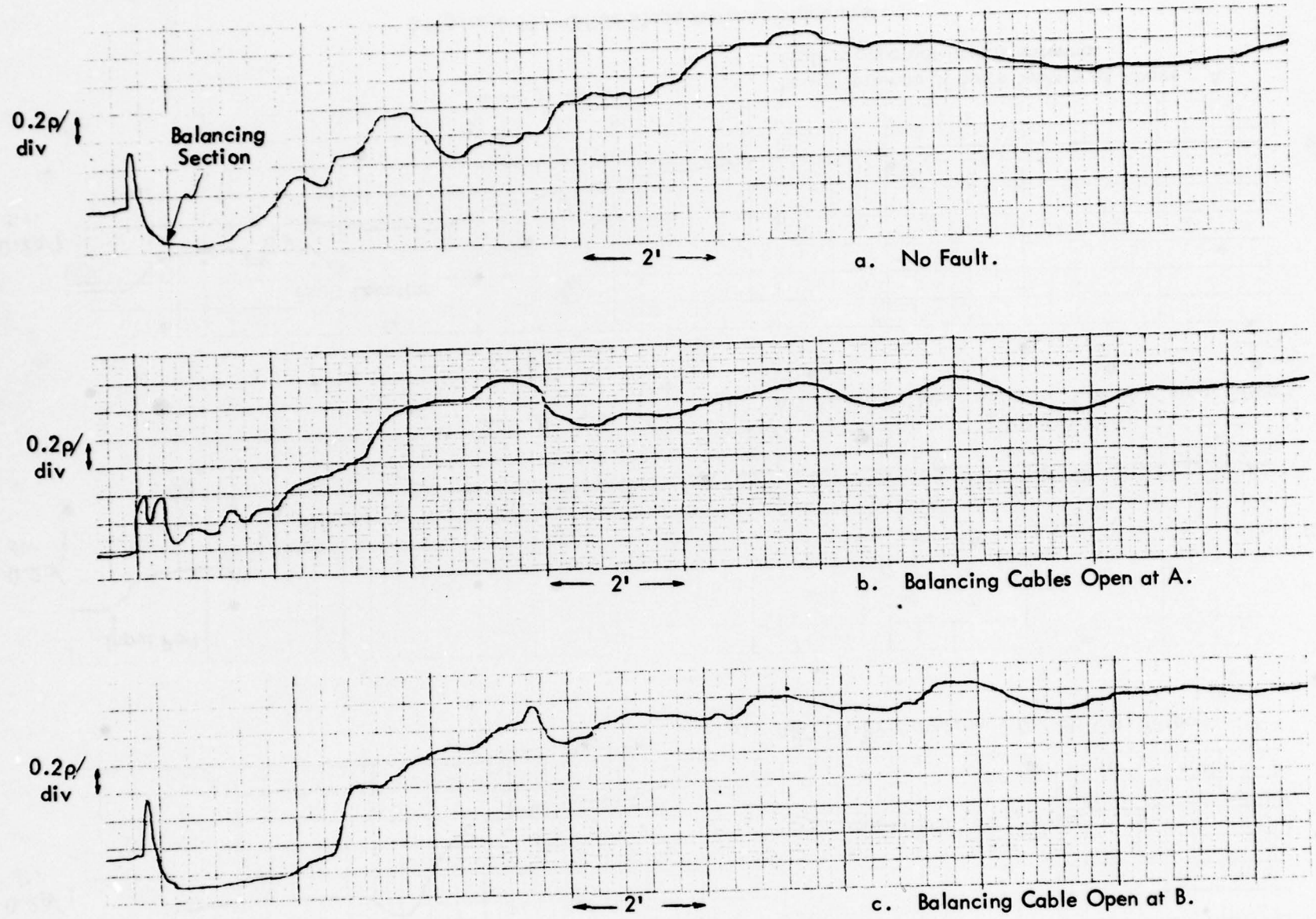

Figure 4-90. Alford Loop Antenna Signatures.

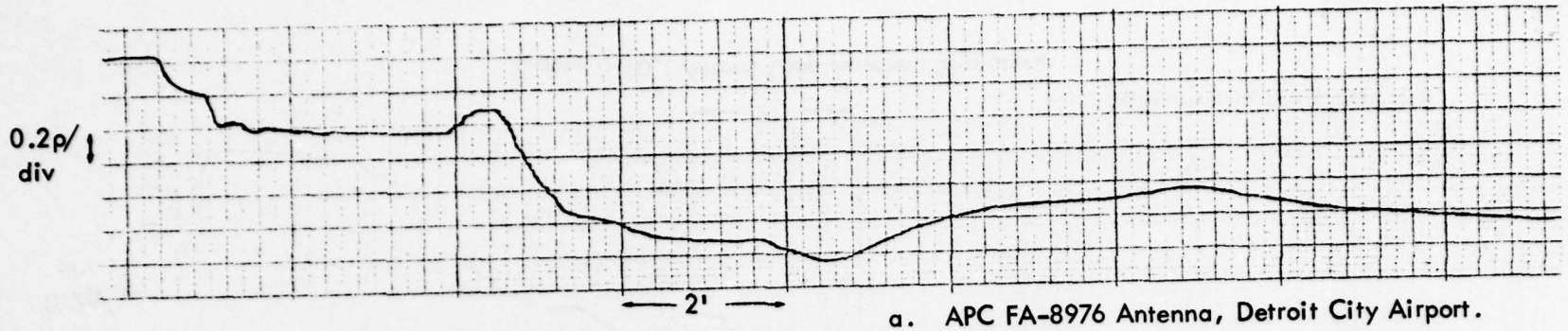

a. APC FA-8976 Antenna, Detroit City Airport.

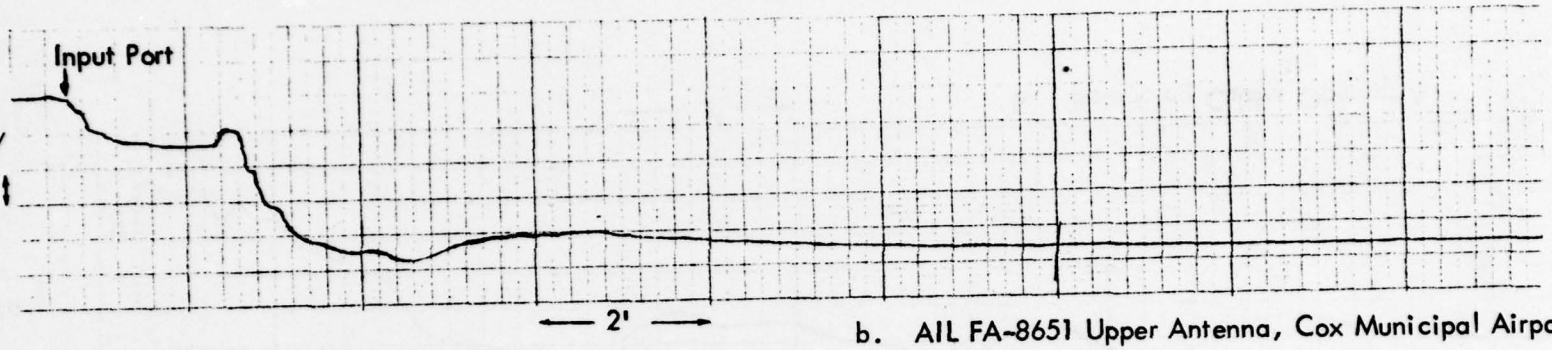

b. AIL FA-8651 Upper Antenna, Cox Municipal Airport.

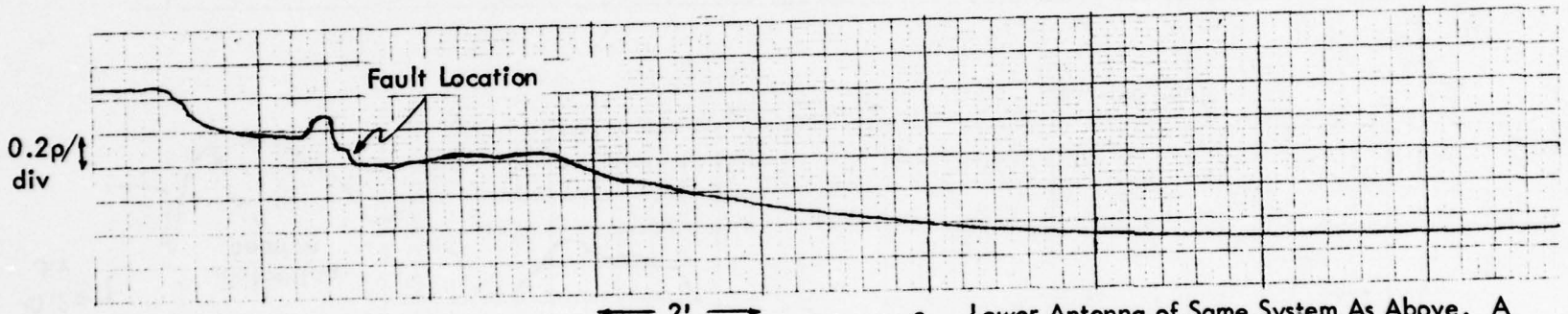

c. Lower Antenna of Same System As Above. A fault is apparent in this antenna.

Figure 4-91. Glide Slope Antenna Signatures.

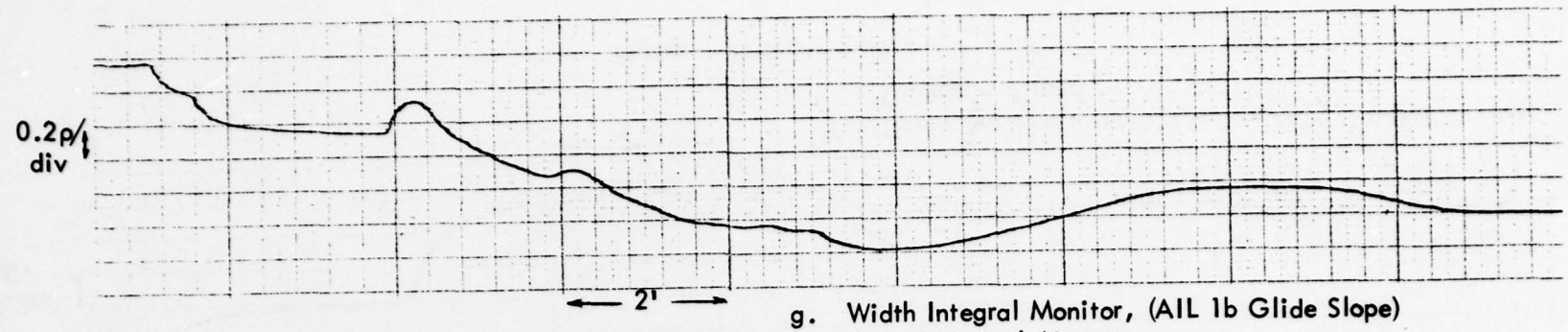

g. Width Integral Monitor, (AIL 1b Glide Slope) Cox Municipal Airport.

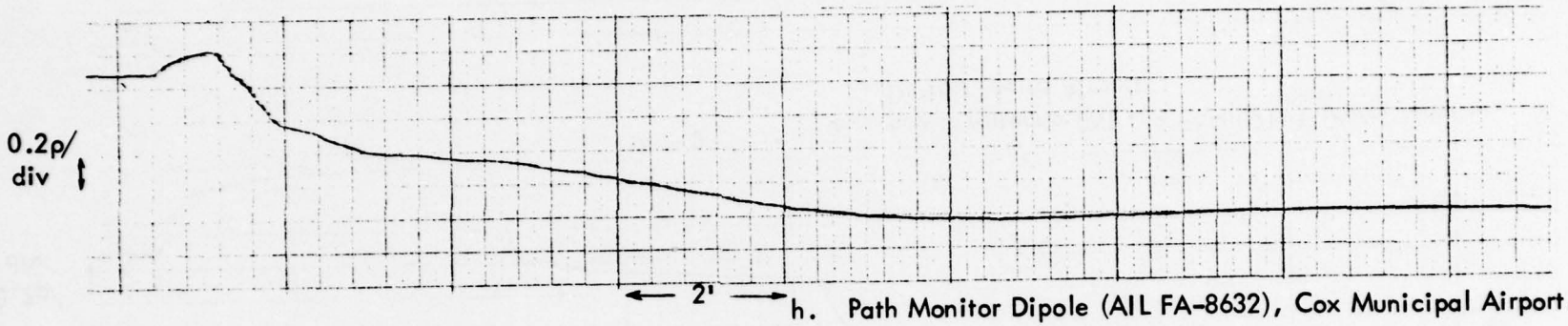

h. Path Monitor Dipole (AIL FA-8632), Cox Municipal Airport.

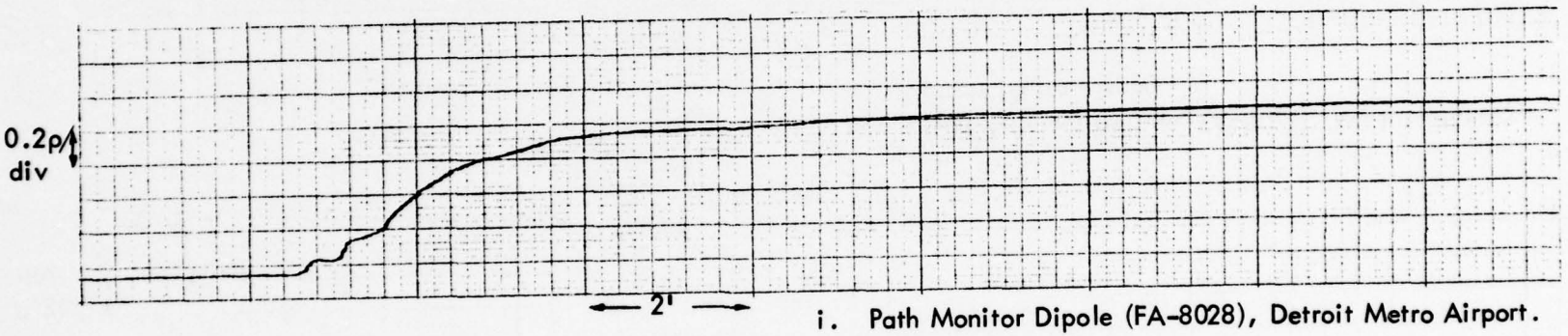

i. Path Monitor Dipole (FA-8028), Detroit Metro Airport.

Figure 4-91 (continued).

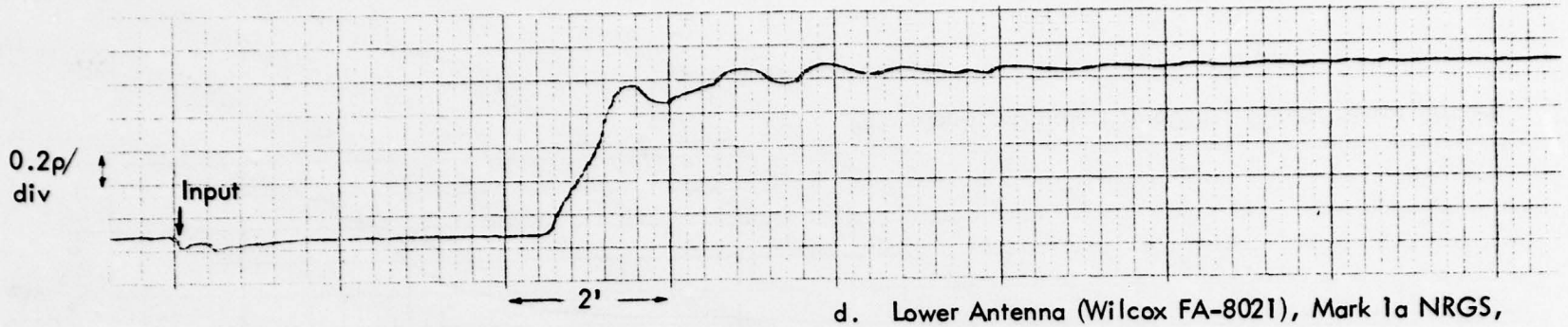

d. Lower Antenna (Wilcox FA-8021), Mark 1a NRGS, Detroit Metro Airport.

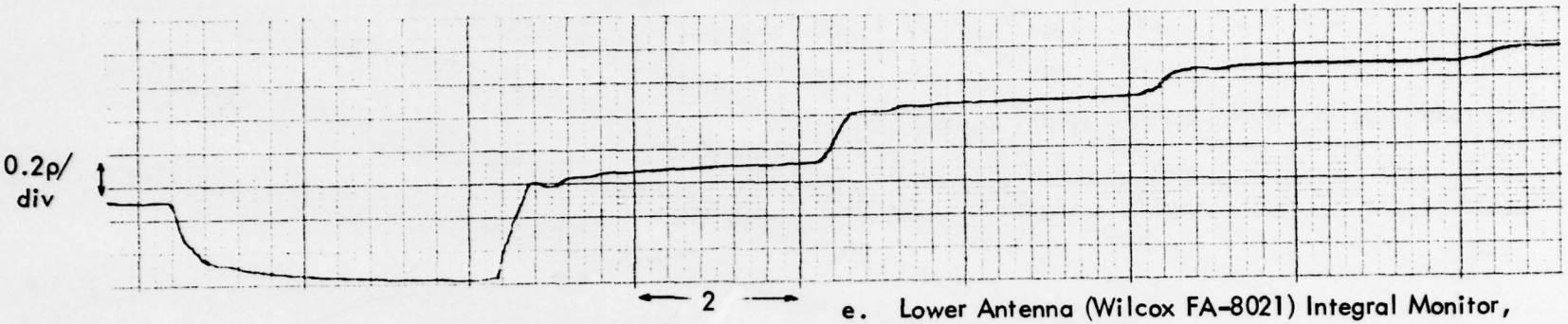

e. Lower Antenna (Wilcox FA-8021) Integral Monitor, Detroit Metro Airport.

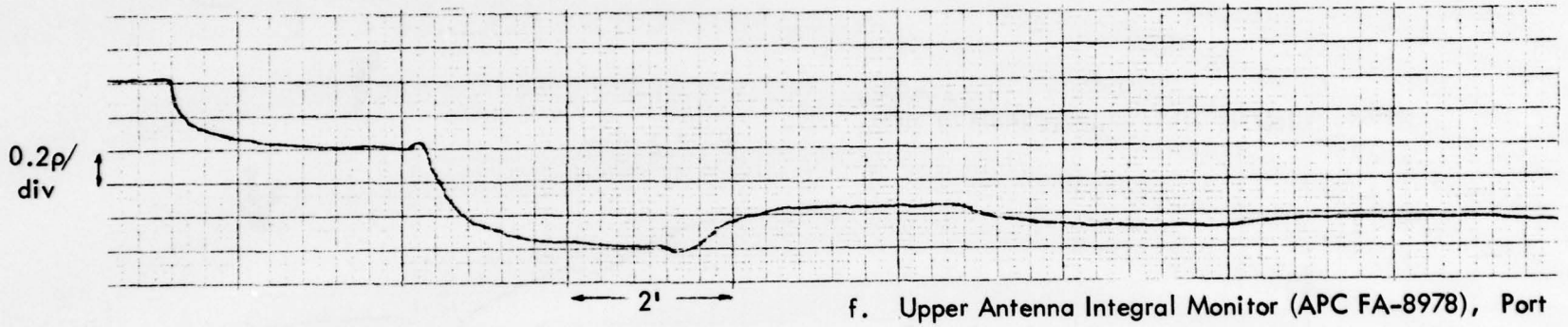

f. Upper Antenna Integral Monitor (APC FA-8978), Port Columbus Airport.

Figure 4-91 (continued).

a. Middle Antenna (2 Lambda Type), Detroit Metro Airport.

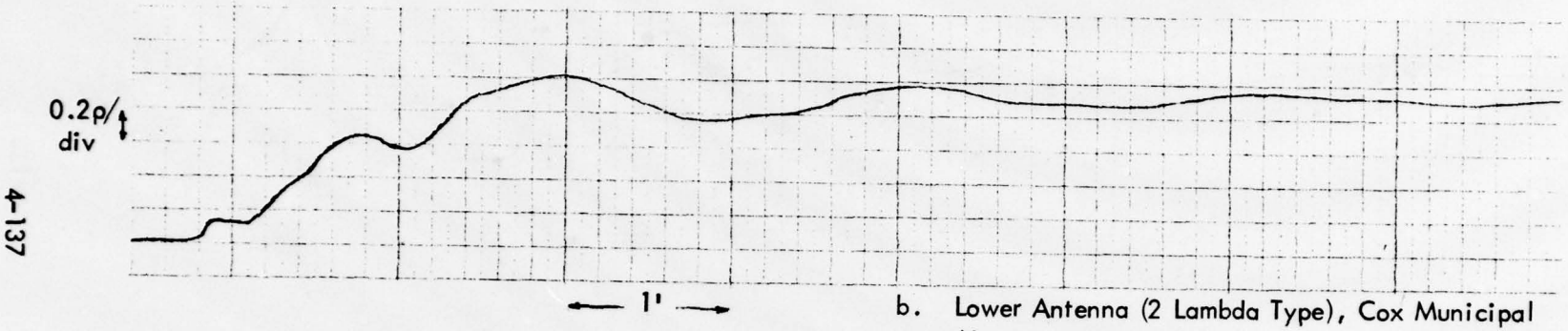

b. Lower Antenna (2 Lambda Type), Cox Municipal Airport.

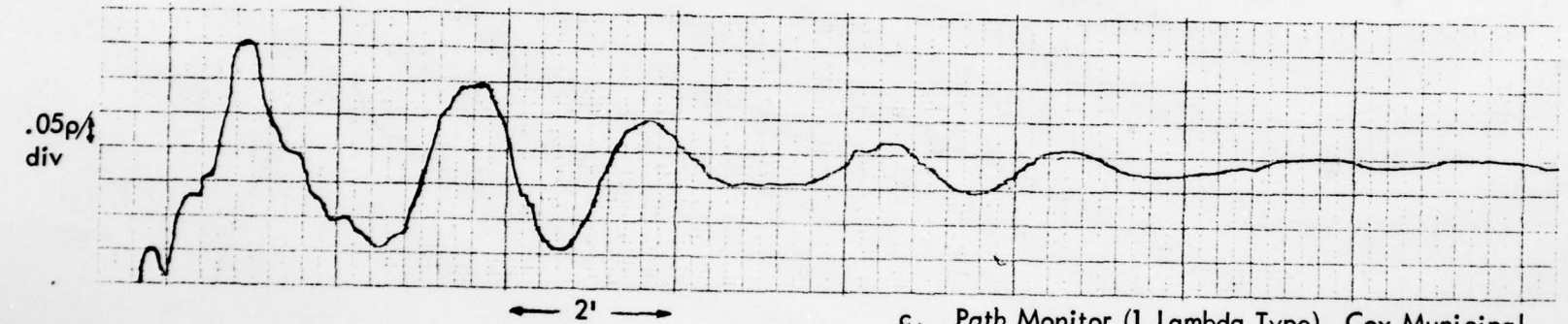

c. Path Monitor (1 Lambda Type), Cox Municipal Airport

Figure 4-92. Antenna and Path Monitor Signatures from GRN/27 Glide Slopes.

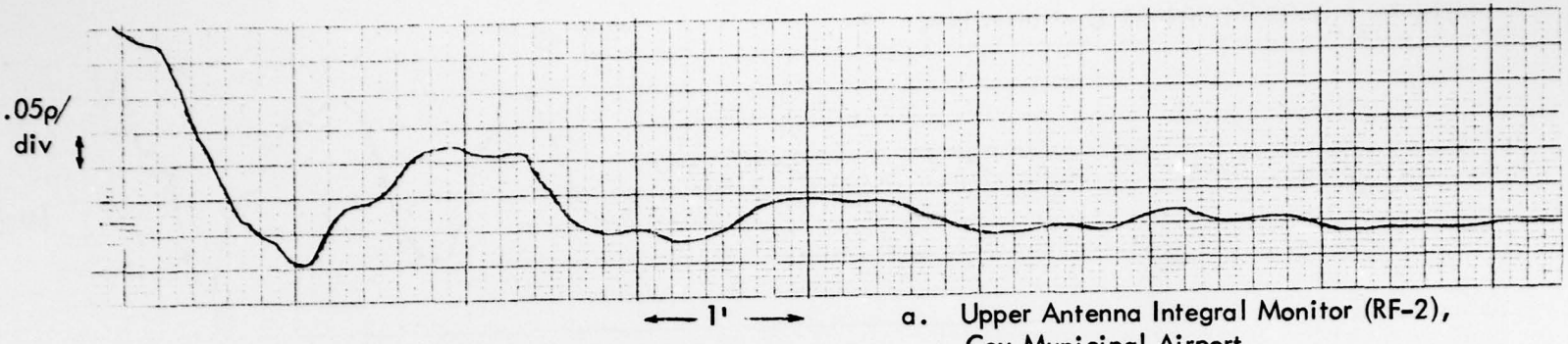

a. Upper Antenna Integral Monitor (RF-2), Cox Municipal Airport.

b. Lower Antenna Integral Monitor (RF-2), Detroit Metropolitan Airport.

Figure 4-92 (continued).

3. General Conclusions. The TDR has definite applications to ILS health checks and troubleshooting. For cable runs such as antenna, monitor, and RF power lines, the TDR readily locates and identifies faults such as opens, shorts, slices, corroded connections, loose connections, and the presence of water in cabling.

In the ILS fault test study presented here, the use of the TDR has been advanced beyond cable testing to include fault checks of antenna systems, monitors and RF amplitude and phase components such as the combining bridge and the phasor. In addition to fault checking and troubleshooting systems components, much can be determined concerning the construction of the component from the examination of the TDR signature. This examination entails comparison of faulted and unfaulted signatures and analysis of the antenna response to the TDR pulse by basic circuit theory and transmission line transient analysis.

Care must be taken in both selecting devices which lend themselves to TDR testing and interpreting the signatures of these devices. In some cases fault conditions that exist in a system may not be able to be detected. This, of course, depends on the severity of the fault and the reflections from the fault that are returned to the TDR. When used in a conscientious manner, the TDR provides a quick, simple, and accurate method for fault testing certain ILS components and detecting many, but not all, of the faults that may exist in those components.

F. Airport Systems Control and Display.

1. Introduction: Existing ILS Monitoring Scheme at O'Hare International Airport. O'Hare Airport, one of the busiest in the world, employs instrument landing systems (ILS) on 12 of its 14 runways. Each ILS incorporates 2 separate systems, a glide slope and localizer, to give the pilot guidance in both approach angle and azimuth, respectively. O'Hare, then, has 23 separate ILS sites (runway 04L has localizer only) that must be continuously monitored when the runway it is serving is in use. In addition, there are marker beacons associated with each ILS that also need to be monitored; two markers for Category I (outer and middle), and three for Categories II and III (outer, middle, and inner).

Figure 4-93 shows the runway configuration at O'Hare with the ILS sites represented by dots. Information about ILS status from these sites is transmitted to the terminal radar control room (TRACON) via buried cables. These cables also contain control signals from the TRACON to the ILS sites that switch the ILS on or off. It is the utilization and display of the information carried by these cables and of information not currently available in real-time that is the primary concern of this paper.

a. Relaying ILS Status Information to Air Traffic Controllers. ILS status is of particular interest to TRACON personnel, since the approach controllers located there are responsible for aligning the incoming aircraft with the runway. Presently, ILS status is displayed on the wall furthest from the approach controllers (see Figure 4-94 for the layout of the TRACON; ILS status display is denoted "monitor panel"). When a failure occurs at any of the operating ILS sites, an audio alarm sounds and lights indicating the nature and location of the failure are actuated on this panel. Unfortunately, these lights are not readily decipherable by the controller since he is physically located away from the panel and also because there are inconsistent error indicators from the various displays on the panel, comprised as it is of equipment from several manufacturers.

Typically, when a failure does occur, the watch supervisor interprets the monitor panel and verbally conveys the nature of the problem to the appropriate controller. This system may be effective during good weather and slow traffic times, but can be quite demanding on ATC personnel during IFR and peak traffic periods. For example, if an approach controller is landing aircraft at the maximum rate under IFR conditions and hears the alarm, it is at least a distraction from his primary duties. Cost and safety considerations associated with any traffic delay caused by false alarm or unnecessary traffic pattern changes are formidable. It should be noted that the alarm is sounded whenever a stand-by transmitter is switched in to replace a primary transmitter; i.e., the alarm may sound even though the ILS signals remain navigable.

The proposed system described in subsequent paragraphs addresses itself to rectifying the above problems. Specifically, a color TV monitor is proposed for each controller to give him an immediate indication in the event of an ILS failure (this, in itself, is not a new idea[6]). In addition, more detailed displays are proposed for the watch supervisor and maintenance personnel in order that they might have more information about the status of the ILS systems.

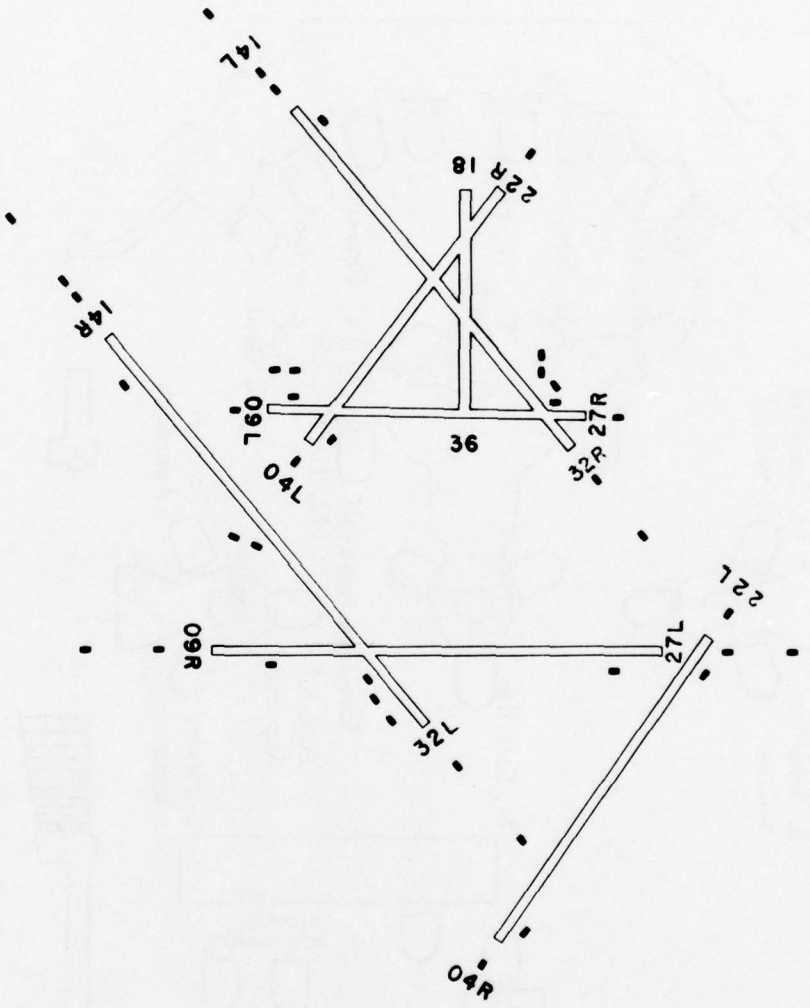

Figure 4-93. O'Hare Runway Map with Monitor Points.

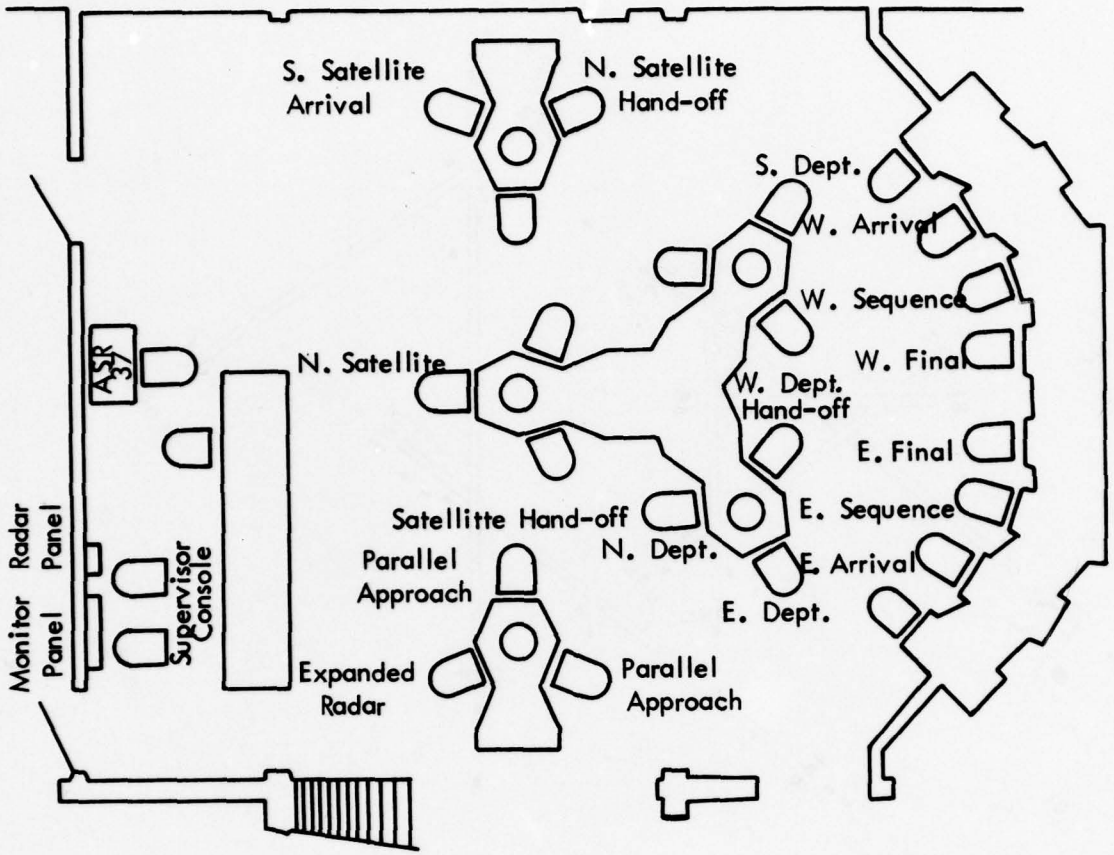

Figure 4-94. Future TRACON Configuration at O'Hare.

b. ILS Data Logging. FAA policy dictates that ILS sites must periodically have certain parameters logged to certify the integrity of the system. This procedure must also be performed in the event of an accident involving an approach aircraft on an ILS runway in order to determine what effect, if any, the ILS had on the accident. This information can be crucial in litigation. Depending on the type of ILS, this logging operation might have to be performed daily taking from one to two and a half hours per site not including transportation to and from the site. If there is an accident involving an approach aircraft, there will be a time delay before the ILS involved can be logged due to travel time to the site, and logging time. This factor can be critical in the courtroom when proof is needed that at the time of the accident (not some time later) the ILS was within tolerance.

It has been suggested that if certain ILS parameters could be continuously monitored, incipient failures could be detected by maintenance personnel well before the ILS exceeded specific tolerances. Such prediction would allow for effective preventative maintenance, thus minimizing outages. However, this scheme is not practicable with present logging methods.

In the proposed system, a microprocessor at the ILS site would gather data that a technician would normally record during a logging operation along with other selected parameters and send this information to a central site. Comprehensive and continuous status information about each ILS would then be available for the required logging and for prediction without delays or human error.

The listing given below identifies more specifically the monitor points which could be made available to maintenance and traffic personnel in the Control and Display System.

Note that parameters forming the system input and control data are grouped into classes:

A. Analog Parameters provide sampled data for use by maintenance personnel in certification or analysis of navaid performance.

B. Digital Parameters provide additional information for maintenance personnel from navaid circuit points which are inherently digital (on-off) functions.

C. High-Rate Parameters are those navaid signals which can be observed by maintenance personnel using rapid sampled-data techniques to recover waveforms for display and analysis. The high-rate feature is intended as a service aid, and not as a continuous monitor mode.

D. Control Functions relate to navaid remote control from the maintenance central site. Such control functions generally are restricted to on/off functions which can be exercised by maintenance or the Watch Supervisor from their system consoles. With suitable navaid equipment modifications, more complex control functions can be implemented.

E. Alarm Functions relate to those conditions at the navaid which cause instantaneous signals to alert ATC and maintenance personnel of a navaid failure or out-of-tolerance condition. Basic system philosophy is to provide the alarm to ATC as at present, with minimal supporting data to avoid confusion. The Watch Supervisor can call up supporting data to determine the nature of the failure at the navaid, if he desires. Maintenance personnel can call up detailed fault data "snapshots" taken at the instant of alarm.

F. Supplemental Parameters are those test points selected by maintenance personnel at the navaid site through use of the Remote Probe Unit.

It is emphasized that the Remote Data Processor (RDP) units are software-controlled and highly flexible. Each unit is capable of measuring up to 64 analog signals. Addition or alteration of the parameter lists given here causes very little change at the RDP.

Similar Parameter Lists could be formulated for NDB, VOR or other navigation and communications facilities; we have concentrated on the locations on-site at Chicago O'Hare for this prototype study.

The reference for this tabulation has been the FAA publication Number 403232 "AN/GRN-27 (Category II ILS)", January, 1974. We recognize the parameter lists will differ somewhat among equipment types. In essence, we have attempted to remote virtually all navaid display functions offered by BITE equipment and monitor panels to the central site. Inherent system flexibility allows convenient restructuring of the parameter complement even as system design proceeds.

(1) Marker Beacon Transmitter Site

A. Analog Parameters
   1. Transmitter Input Voltage
   2. Transmitter Input Current
   3. Output Power (Forward)
   4. Output Power (Reverse)
   5. Percentage Modulation
   6. Battery Voltage

B. Digital Parameters
   1. Power Source External
   2. Power Source Battery
   3. Monitor Status (Local/Remote)
   4. Monitor Bypassed

C. High-Rate Parameters
   1. Keyer Waveform
   2. Audio Waveform

D. Control Functions
   1. Transmitter On/Off
   2. [Keyer Mode CW/MCW/KMCW]

E. Alarm Functions (Real-Time)
   1. Transmitter Alarm (Maintenance and ATC)
   2. Monitor Bypassed (Maintenance Only)
   3. Power Source Transfer from External to Battery (Maintenance Only)
   4. Abnormal

F. Supplemental Parameters
   1. As Selected On-Site

(2) Localizer Transmitter Site

A. Analog Parameters
   1. Power Supply Voltages for Two Transmitter Units
      a. -50
      b. -50
      c. -18
      d. -18
      e. +5
      f. +5
      g. +28
   2. Battery Voltage

Note: Monitors existing as part of the transmitting equipment provide signals for RD level, SDM and DDM for clearance and course channels of each transmitter unit. In addition, far-field monitors provide DDM values. Power output at the transmitter ports is also provided by probe units.

   3. Clearance On-Course 1 and 2
      a. RF
      b. SDM
      c. DDM

   4. Off-Course Sensitivity 1 and 2
      a. RF
      b. SDM
      c. DDM

   5. Monitors 1 and 2
      a. Far-Field DDM

6. Output Power Monitors
    a. Carrier Plus Sideband
    b. Clearance Sideband
    c. Course Sideband

B. Digital Parameters
    1. Power Source External
    2. Power Source Battery
    3. Transmitter 1 On
    4. Transmitter 2 On
    5. Monitor Bypass
    6. Monitor Local/Remote Status
    7. Interlock Status
    8. Monitor Mismatch
    9. Transfer
    10. AC Power Failure
    11. Batt Charger Failure
    12. Temperature

C. High-Rate Parameters
    1. Carrier Port Audio
    2. 90 Hz Audio
    3. 150 Hz Audio

D. Control Functions
    1. Transmitter 1 On/Off
    2. Transmitter 2 On/Off
    3. Transmitter 1 Ident On/Off
    4. Transmitter 2 Ident On/Off

E. Alarm Functions
    1. Abnormal

F. Supplemental Parameters
    1. As Selected by Maintenance Personnel On-Site

(3) Glide Slope Transmitter Site

A. Analog Parameters
    1. Power Supply Voltages for Two Units
        a. -50
        b. -50
        c. -18
        d. -18
        e. +5
        f. +5
        g. +28

2. Battery Voltage

Note: Monitors existing in the transmitter unit provide outputs for RF level, SDM and DDM for clearance and course signals. Additionally, near-field monitor and sens monitors outputs are available.

3. Clearance 1 and 2
   a. RF
   b. SDM
   c. DDM

4. Course 1 and 2
   a. RF
   b. SDM
   c. DDM

5. Sensitivity 1 and 2
   a. RF
   b. SDM
   c. DDM

6. Near-Field 1 and 2
   a. RF
   b. SDM
   c. DDM

7. Antenna Power Monitors
   a. Upper Antenna
   b. Middle Antenna
   c. Lower Antenna

8. Power Monitors
   a. Course, Carrier + Sideband
   b. Course, Sideband Only
   c. Clearance, Carrier + Sideband

B. Digital Parameters
   1. Power Source External
   2. Power Source Battery
   3. Transmitter 1 On
   4. Transmitter 2 On
   5. Monitor Bypass
   6. Monitor Remote/Local
   7. Interlock Status
   8. Monitor Mismatch
   9. Transfer

10. AC Power Failure
11. Batt Charger Failure
12. Temperature

C. High-Rate Parameters
1. Carrier Port Audio
2. 90 Hz Audio
3. 150 Hz Audio

D. Control Functions
1. Transmitter 1 On/Off
2. Transmitter 2 On/Off
3. [Transmitter 1 Ident On/Off]
4. [Transmitter 2 Ident On/Off]

E. Alarm Functions
1. Abnormal

F. Supplemental Parameters
1. As Selected by Maintenance Personnel On-Site

c. ILS Control. Because of noise abatement policy and changes in the wind, the active runway configuration at O'Hare is often rearranged. When this reconfiguration involves an ILS runway, the ILS's must be appropriately switched.

Presently, runway reconfiguration is handled by the watch supervisor in the TRACON who, by performing the proper switching operation at the monitor panel, can turn ILS's on or off. Again, since the monitor panel is comprised of equipment from different manufacturers, the switching operation may take some experience before it can be performed efficiently. Even by an experienced watch supervisor this process takes a good deal of time as after an ILS is switched on, he must wait to see that it has come up within specified tolerances.

The watch supervisor may want to determine if an ILS on a runway that is presently not in use will come up properly when required. This is presently accomplished by a process called "quick look" where the ILS is turned on and then turned off after it has met specified tolerances.

Both of the above procedures require a good deal of time from the watch supervisor. In the proposed system, he would insert the desired runway configuration into a control keyboard and would be given a graphic indication when the ILS's came up to specified tolerances. For example, the watch supervisor would first indicate which runway ILS's he wanted turned off. After the computer controlling the system sent a request to the remote site and then verified that the site had been shut down, it would indicate this fact to the watch supervisor (this process would be almost instantaneous). Next, the watch supervisor would insert the runways he wanted on. The computer would send this command to the remote site and verify proper operation on the console when the ILS

came up to specified tolerances (this would take the length of time required for an ILS to come up to specified tolerances). If the watch supervisor attempted to configure the runways in an improper fashion, such as turning the ILS's on at both ends of the runway, the computer would display an error flag and require override procedures to perform the requested command. The advantages of the proposed system is that the watch supervisor would have an easily readable display indicating which ILS's were on and which were off. If desired, the computer could then print out a hard copy indicating the entire airport ILS status whenever a change was made and the time that the change was made. "Quick look" would be accomplished by the watch supervisor by inserting into the console the ILS runway number he wanted to check. With the present system, the watch supervisor must stand by to shut the selected system down as soon as it met the specified tolerance. This quick shutdown is most important as it is undesirable to have ILS signals radiating from a runway that is not in use. In the proposed system, the ILS could be shut down after either a specified time or after the ILS came up to within specified tolerances; the results of this test would be clearly displayed on the console. With such a system, the watch supervisor would be free to do other duties during the quick look operation.

From a total system standpoint, use of general-purpose computing processors, programmed with desired system operating logic, offers a tremendous increase in system flexibility over hard-wired designs. For example, it is recognized at the outset that the runway changeover represents a heavy workload period for all TRACON personnel, perhaps especially the watch supervisor. The system should relieve this workload if possible, at least as far as ILS system configuration changes are concerned.

In this particular case, the software control allows just such a workload decrease. Where in a manual system the ILS systems must be changed over element by element and checked for proper operation, with the proposed system, a super-command, or MACRO command, can be coded in advance to perform the entire changeover instantly. A long series of operator commands may be combined into a MACRO and stored under a particular name:

MACRO Name (entered by watch supervisor):	CONFIG 1	
Information returned by computer:	GS14L-ON	SDISPL=14L
	GS14R-ON	SDISPL=14R
	LOC14L-ON	WFINAL=14R
	LOC14R-ON	EFINAL=14L
	GS32L-OFF	.
	GS32R-OFF	.
	LOC32L-OFF	.
	LOC32R-OFF	etc.

It can be seen that a complicated changeover has been cataloged under the name CONFIG1. All the watch supervisor must do is call CONFIG1 and the glide slope and localizer systems are changed, a summary display of both systems is provided for the watch supervisor, and 14L is assigned to the Number 1 video channel for the East Final Approach controller. This incomplete example also indicates a few of the proposed commands being considered in the preliminary study work.

2. Proposed ILS Control and Display System. The previous section was devoted to a description of the present ILS monitoring system at O'Hare; this section is concerned with the description of a system that will improve operational considerations of that system. A block diagram for this proposed system is shown in Figure 4-95. The function of this system is to display ILS status to controllers, to log and to present detailed information about the ILS to appropriate supervisory and maintenance personnel, and to control various aspects of the ILS operation. A brief component description is given below to give a basic understanding of the system; more detailed component descriptions comprise subsequent paragraphs of this section.

A remote data processor (RDP) is to be located at each ILS equipment site. The RDP design, as developed during this study, has 64 inputs capable of accepting and measuring analog signals between $\pm$ 10 volts, 8 digital sense inputs (this can be expanded in multiples of 8 if necessary), and 8 relay outputs for control purposes at the ILS site. It is intended that the RDP measure certain parameters of the equipment at the ILS site and relay this information to the central processor (CP) located in the TRACON upon command. The RDP will in no way alter the operation of the present monitoring system. Its function is to relay the official status and operational parameters of the monitor and the transmitting equipment to the central processor where this information can be disseminated to appropriate persons.

Although the RDP is capable of measuring almost any parameter at the site, some tentative measurements have been suggested: (1) official monitor status, (2) RF power from the monitor, (3) SDM from the monitor, (4) DDM from the monitor, (5) room temperature at the site, (6) security sensors, (7) power source (line or battery), and (8) monitor bypass. It should be noted that these inputs to the RDP can be changed at a later time to parameters felt to be more important with very little difficulty. Such a change would involve only a software change at the Central Processor (CP) and changing the parameter inputs to the RDP.

Data are transferred from the RDP's to the CP using tone signaling techniques to minimize the effects of lightning and transients on the transmission lines.[7] The device that encodes and decodes the transmission is known as a modulator/demodulator (MODEM) and is located at both the RDP and CP.

This status indication may be determined by a checksum. In this processor, the RDP adds up all of its instructions (which are coded numerically in machine language) and sends the result to the CP. If the sum produced by the RDP matches the sum that the CP has stored in its memory for that RDP, the RDP is operating correctly; otherwise, a failure has occurred in the RDP.

The CP will evaluate the information from the RDP's and based on that information and information from RVR outputs, present an easily-interpreted, color-coded video display to the air traffic controllers. Although specific designs for these displays are presented later, it should be noted that these displays can be tailored to almost any conceivable format as they are defined by software. Controller displays consist of color video monitors, under control of the watch supervisor, and provide for each controller position the runway in use, the RVR data and any necessary fault information relating to the ILS elements serving that runway. Letter or background color indicates runway systems status:

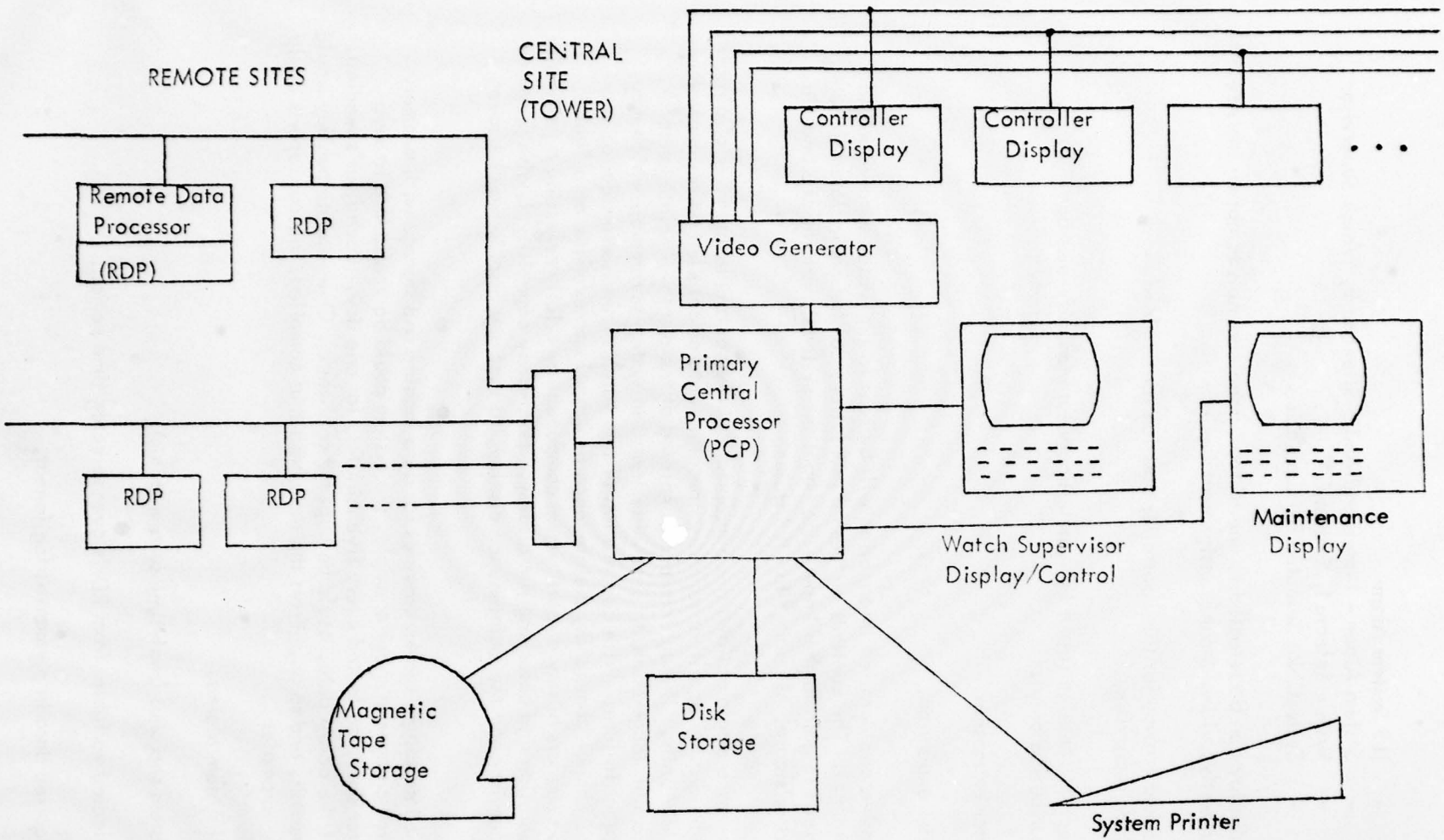

Figure 4-95. Overall System Concept - ASCD.

Red	-	ILS System Alarm
Amber	-	System Alarm - Noted and Audio Silenced by Watch Supervisor
Green	-	System Selected, System OK
Blue	-	System Not Selected for Operation

Each controller display can be selected to one of four video channels to obtain the needed information. Currently, video channel assignment is:

1. Current runway for this controller position (determined by watch supervisor).

2. Weather Message (input by watch supervisor manually-message distribution only).

3. Later expansion.

4. Later expansion.

Comprehensive and detailed information will be sent to the watch supervisor and maintenance personnel. The contents of these presentations can be manipulated through a keyboard interface to gain further knowledge about the systems' performance and, in the watch supervisor's case, to change the ILS status.

The maintenance display allows the appropriate personnel a detailed view of airport system operation by displaying either summary operating data or detailed parameter values provided by the RDP units. Through commands entered at the display, maintenance personnel can examine logged data to determine trends in system parameters which may indicate an incipient failure. With cooperation of the watch supervisor insofar as airport systems status change commands, maintenance personnel can examine on a "quick look" basis the parameters of any airport system component by briefly selecting a particular ILS system for operation and observing the display. Hard-copy capability is also proposed for the watch supervisor and the maintenance display, so that any display may be saved for later use.

The proposed prototype system provides for data logging and storage with summary printouts in several categories. For example, the system could be configured to save detailed parameter data, collected every five minutes, for one day. Each hour's reading, or one-twelfth of the detail data, could be kept for one week. One reading per day would be kept for one month, and so on. From the data base thus compiled, various reports could be prepared. For example:

1. All system alarms.

2. System shapshot (real-time system status).

3. Selected variables from RDP's over selected time period.

4. Required data in permanent log format.

a. Remote Data Processor (RDP). The RDP which is located at the ILS transmitter sites is one of the most crucial components in terms of total system cost and performance. There will be a large number of RDP's, and the RDP's will provide the major source of inputs for the system.

Most representative computer manufacturers contacted have off-the-shelf units available that are capable of performing the intended functions of the RDP. All of these units basically have the same design architecture: a microprocessor-controller measuring device that could relay the measured information to the host computer. One drawback to these commercial devices, however, is that their cost would make the total system cost unacceptable. One reason for the high cost is that the ready-made units offer functions which would not be needed for RDP operation and require certain options to be added.

In order to lower the cost of the RDP's, several small microcomputer companies were contacted with hopes of custom-building a low-cost RDP. Microcomputer Associates, Incorporated, [8] responded by submitting a tentative design meeting of all the RDP specifications (to be given later) at a cost substantially lower than off-the-shelf equipment with the same capabilities. A block diagram for this RDP is shown in Figure 4-96. The heart of the system is the MOS technology 6502 microprocessor integrated circuit which controls the operation of the RDP. The program that defined the microprocessor operation is stored on a 2K byte programmable read-only memory (PROM). This memory is non-volatile, meaning that its memory will not be lost in the event of a power outage. A random access memory (RAM) is used as a "scratch pad" by the microprocessor to store data temporarily so that the microprocessor can fill up this memory with information from analog and digital inputs when the RDP is not being interrogated by the CP, and send information to the CP directly from memory when it is interrogated. Such a scheme shortens transmission time and eases the burden on the CP over a system that performs measurements on-line with the CP.

Analog inputs to the RDP are multiplexed into an 8-bit A/D converter which is fed under program control into RAM. The analog inputs are of high enough impedance as not to load significantly the circuit being measured. The $\pm$ 10 Volt input limits were established by assuming that any parameter of interest could be scaled to within those limits. [9]

Analog measurement under RDP software control provides wide flexibility. For example, RDP programming can alter measurement interval or provide variable-interval integration under control of the Central Processor. Alternatively, relatively high-speed sampling of selected parameters can be accomplished, with data stored at the RDP, to be transmitted at the 300 baud line rate on command. Such high-speed sampled data can then be processed by the CP to yield statistics or graphs.

Digital sense inputs to the RDP are intended to measure the official status of the monitor. Digital inputs were chosen for this function as monitors typically present their status in a binary form, i.e., either a parameter is in-tolerance (1) or out-of-tolerance (0). The results of this measurement will also be stored in RAM.

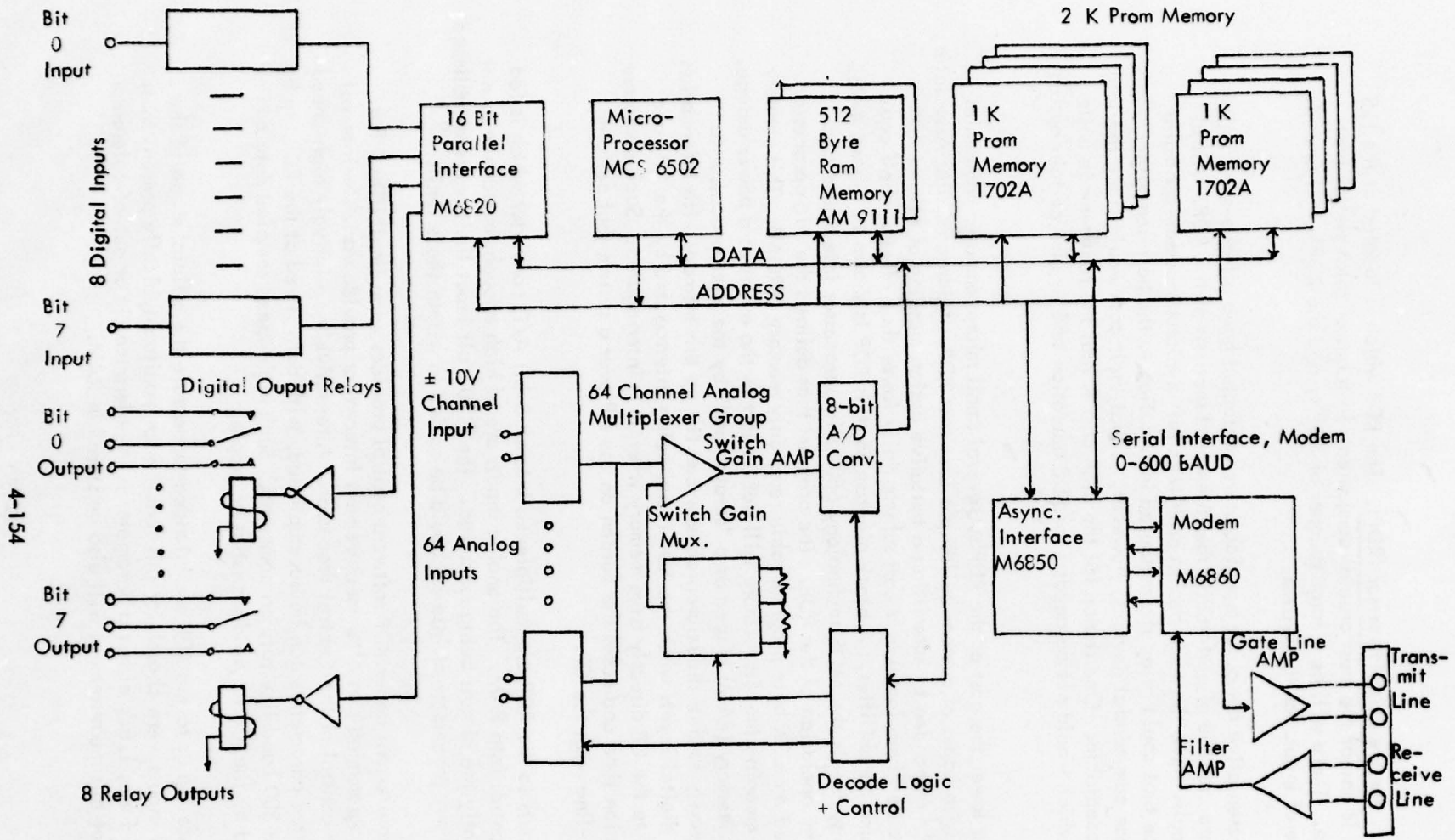

Figure 4-96. Remote Data Processor Block Diagram.

The RDP will have 8 relay outputs that can be switched with appropriate commands from the CP. As only one of these relays is required for the ILS switch on/off operation, there are several unused switch outputs that would be available for future use. As a possible suggestion, these relays might be used to control heating and air-conditioning units at the site. Since room (or equipment) temperature can be monitored by the RDP, the heating and cooling devices might be more stably controlled by a temperature sensor located closer to the ILS equipment and not at the heating/cooling device as is presently the case.

Some attractive aspects of the Microcomputer Associates RDP is that it has a built in modem and power supply. The entire RDP is contained in a fuse-box style enclosure. Power requirements are 110 volts at 60 Hz.

It should be mentioned that RDP's offered by other manufacturers could be substituted into the proposed system which would operate in the same manner as the custom-designed RDP; the primary consideration for suggesting the custom-designed RDP is cost and secondly size (the custom RDP is more size-efficient as it has a self-contained power supply and modem).

A by-product of the RDP configuration described above is its ability to operate at a truly remote site, which may be serviced only by a standard dial telephone line. The RDP modem can communicate over such lines utilizing a data interface unit provided by the telephone company. The CP must be provided with a telephone dial unit under software control. The CP can then call the RDP on the dial network and command the return of specified data from the remote navaid installation.

b. Protocol. One important aspect of any data communication system is the data communication protocol, which defines how various components in the system interact with each other. If protocol is chosen improperly, such as having normally-idle processors periodically interrupt a normally-active processor, the system will not perform efficiently or may not even operate at all; as a result of thumb, the busiest machine should interrupt the least-busy machine so that the former can run at maximum efficiency.

Protocol also defines data transmission rate; if this rate is too fast, more errors will occur during transmission which would require additional procedures to detect and rectify. If the data rate is too slow, there will be delays between system updates causing lags between the time an event occurs and the time that event is reported.

Protocol is an important factor in troubleshooting the system since it defines the codes involved in data transmission. If non-standard codes are used, or codes which require special timing pulses, the trouble-shooting process will require that all systems are functioning in order to provide each other with the required codes and timing pulses. However, if standard asynchronous codes, such as ASCII, are used, the equipment can be evaluated independently with a teleprinter placed directly on line.

All of the above were considered in the development of a protocol for the proposed system.

All communication between the CP and the RDP are specified in ASCII at a rate of 300 baud (about 30 characters per second). The CP, which is the most active component in the system, will initiate all communication, and the RDP will respond according to a pre-programmed format. By arranging the protocol in this manner, the RDP's can be interrogated and debugged without a CP. The appropriate commands could be entered on a standard data terminal and the RDP's would respond in a code that the terminal could interpret without further computation. The major advantage of this scheme is that the RDP's and the CP, which will most likely come from different manufacturers in this prototype system, could be debugged independently.

Each RDP will be assigned its own coded address, which will be stored in its PROM storage. The RDP will not respond to any command unless its address, along with appropriate codes, are sent from the CP.

There are at least four different commands to which the RDP is to respond: (1) a request about the sense inputs which indicate the status of the ILS monitor, (2) a request for a dump of the analog data corresponding to different data points in the monitors, (3) a request to change one of the RDP outputs such as turning on or off one of the ILS transmitters, and (4) a request for the status of the RDP. The status indication may be determined by a checksum. In this process, the RDP adds up all of its instructions (which are coded numerically in machine language) and sends the result to the CP. If the sum produced by the RDP matches the sum that the CP has stored in its memory for that RDP, the RDP is operating correctly; otherwise a failure has occurred in the RDP.

ASCII codes have one bit reserved for parity (odd or even) to determine if an error has occurred during transmission. This is accomplished by setting the parity bit high if there is an odd number of bits on in the transmitted ASCII code with odd parity or setting the parity bit high if there is an even number of bits on with even parity. If the received code differs from what the parity bit indicates, it can be assumed that an error occurred during transmission. In the event that such an error does occur with the proposed system, the transmission sequence will be repeated, thus making sure that no bad data is accepted into the system. If the number of errors received from a RDP exceeds a predetermined threshold, maintenance personnel will be notified via their display console. The RDP can then be given a self-test to determine what type of corrective action should be taken.

c. I/O Multiplexer, Central Processor, Operating System Software, and Peripherals. Figure 4-97 is a block diagram indicating the connections between the RDP's and the CP. As shown in Figure 4-97, up to 20 RDP's can be connected, via MODEM's, to one CP I/O port in parallel; such a connection is also referred to as a party-line drop. Grouping RDP's in this manner is desirable from both a hardware and software standpoint since I/O ports are expensive and space-consuming and would require additional software to address.

Although up to 20 RDP's can be effectively party-line dropped, it is felt that the number in a group should be limited to 5 or 6, so that in the event of a major RDP or line failure, only a small group would be disabled and the problem of pinpointing the failure would be eased. This limitation on the number of RDP's per group results in the need for multiple I/O ports or an I/O multiplexer. The I/O multiplexer was seen

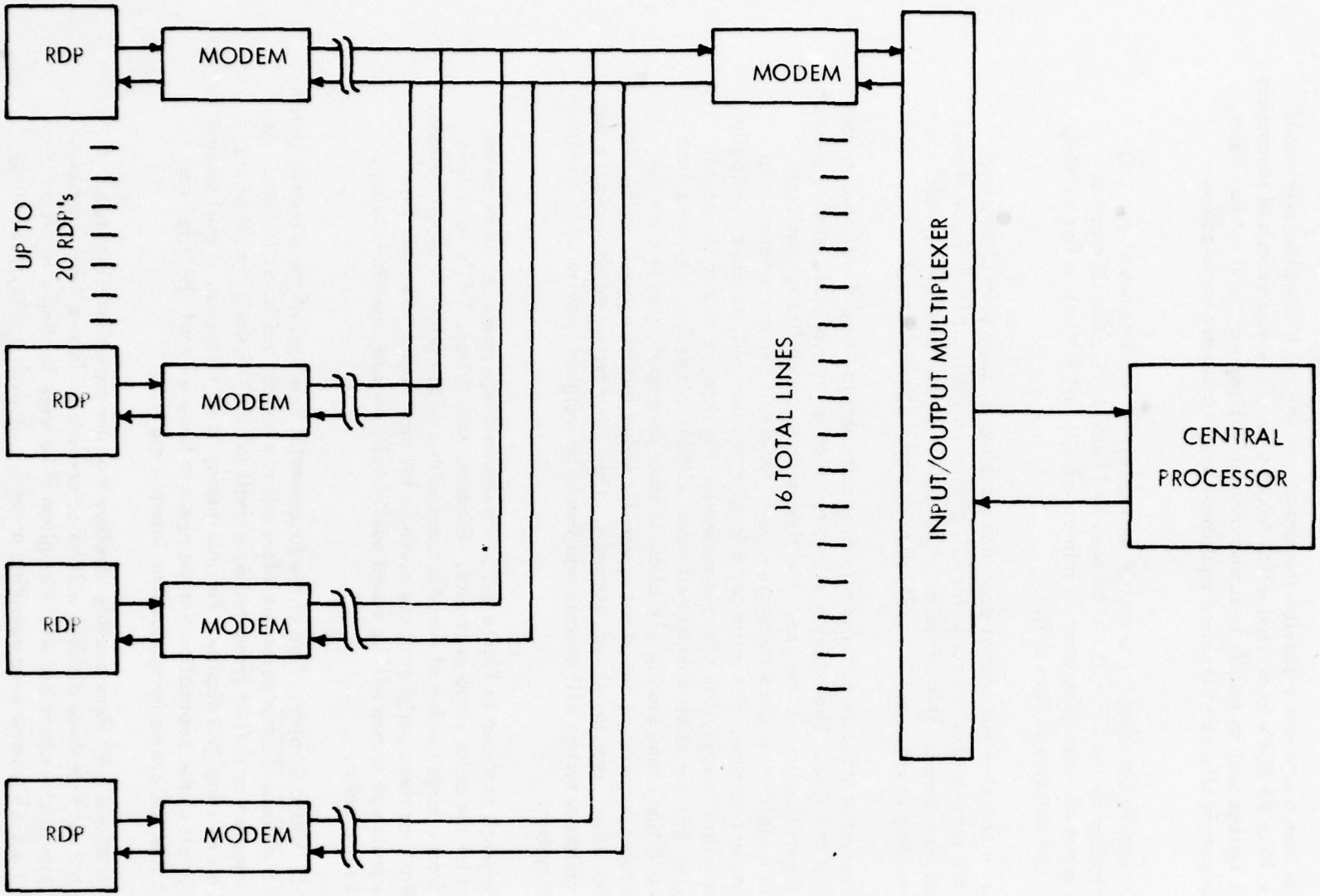

Figure 4-97. Configuration for RDP/CP Interface.

as advantageous from a cost and expansion standpoint. A 16-port I/O multiplexer would allow up to 6 x 16 or 96 RDP's to be used which would allow for measurements of parameters of other airport systems such as marker beacons, communications gear, and runway lights. The I/O multiplexer is offered as standard equipment by all computer manufacturers contacted.

The I/O multiplexer connects to the CP through either the data bus or one I/O port and is controlled by the CP. As can be seen by Figure 4-95, the CP also has control over a group of video generators, 2 interactive displays (TVT's), a line printer, a disk storage, and a magnetic tape unit.

Whenever a computer has control over such peripherals, some form of software which defines the priority that the computer will give to an interrupt from any of these peripherals must be created. This software, which is part of the "operating system", is quite time-consuming to write and is usually provided by the manufacturer.

Operating system software can also allow the computer to "time share" several computer programs at one time. Time sharing allows one program to run while another program is waiting for inputs from an I/O device. The time-sharing capability is considered important for this application since there are several types of computer programs that might be running at one time. For instance, a logging program will be run periodically to take data from disk storage, analyze and summarize the data, and store the results on magnetic tape; this operation must be performed without interfering with the system operation. In addition, time sharing will allow O'Hare personnel to write their own FORTRAN computer programs to run on the system for either further analysis of the RDP input data or for other, even unrelated, purposes. Operating system software plays a big part in how a computer system will operate and should be weighed heavily when considering a computer system.

The peripherals as shown in Figure 4-95 are standard equipment in the computer industry except for the color video generator. Printers, tape drives, TVT's, and disks are available from a large number of manufacturers with a wide variety of specifications. The specifications for these peripherals are given in the next pages; however, final selection for a prototype system will be based additionally on cost, maintainability, reliability, size and noise.

d. Video Display. One of the fundamental functions of the proposed system is to present ILS status and other pertinent information to the air traffic controllers. As planned, this information will be presented on a small (6" x 8") color TV monitor that could replace his existing RVR display. For this display to be effective, it must present to the controller all of the information that he needs to know without cluttering the presentation so that the controller spends time interpreting it.

Figures 4-98 and 4-99 show possible displays that the controller might see. It should be pointed out that these displays will be color-coded. Figure 4-98 represents the type of display that a controller would be given if he were landing aircraft on runway 14L and all ILS systems were operating properly. In such a case, the runway

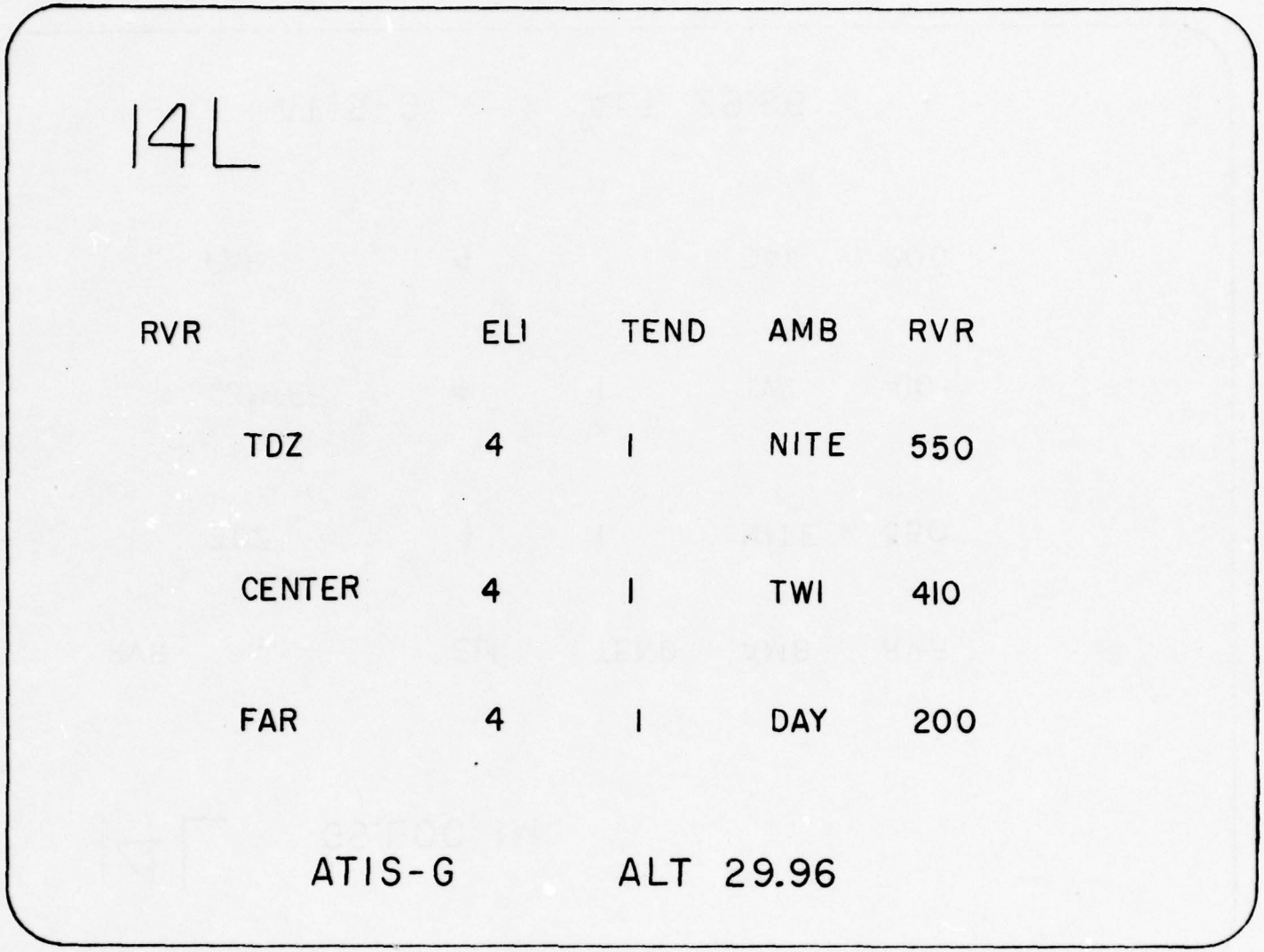

Figure 4-98. Controller Display When ILS Operating Properly.

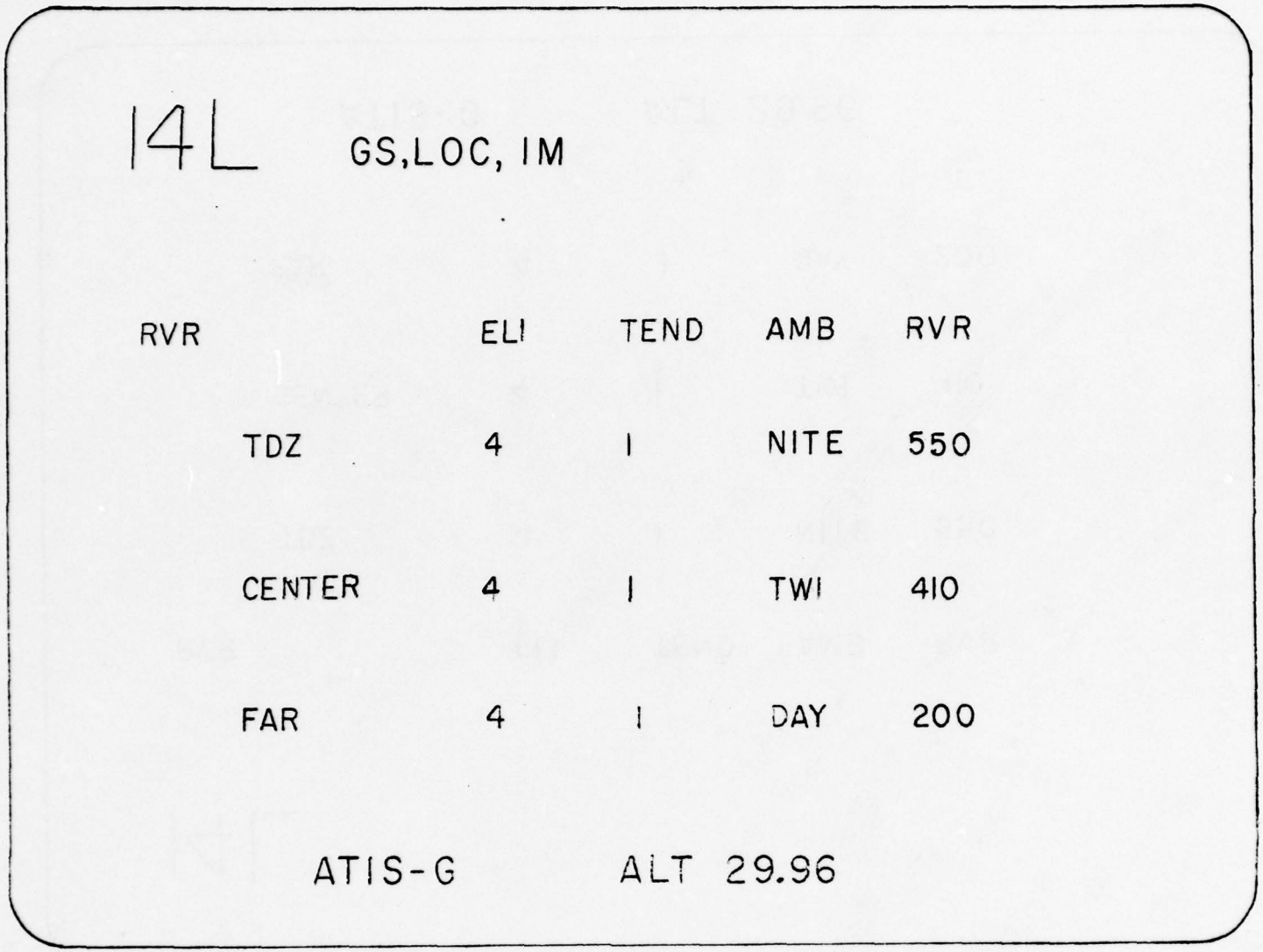

Figure 4-99. Controller Display After ILS Failure Has Occurred.

numbers would appear in green letters on a black background. If there were an ILS malfunction, these letters would turn red and the malfunctioning component would be indicated next to the runway numbers (see Figure 4-99).

Below the ILS status line is a section allocated for RVR information from measurements taken at the touchdown zone (TDZ), runway center and far end of the runway; this data is retrieved from existing RVR equipment. Edge light intensity (ELI), RVR tendency (TEND:increase) (I), decrease (D), or no change (-)), ambient light (AMB) and runway visual range (RVR, in feet) are also displayed. If any of these values go below minimums, that reading will appear in red.

The automatic terminal information service (ATIS) code being used will be displayed along with the altimeter reading on the bottom line of the display.

If all systems are operating properly and RVR readings are all above minimums, the entire display will consist of green characters on a black background. Any out-of-tolerance or below minimums parameter would appear in red.

Several buttons will be located adjacent to the controllers' display that will enable him to select different video channels. These additional channels might contain weather information, ATIS comments, or any other information that might be of interest to the controller. Messages would be input by the watch supervisor. As the video equipment selected for the proposed system is capable of displaying computer-created pictures as well as characters, the additional channels might contain approach maps or even graphs indicating various parameter histories, in future systems.

It should be mentioned that the above display concepts are to demonstrate the types of presentation that could be created. Since these presentations are products of software, almost any imaginable format could be created; blinking characters, changing background color, moving characters, bar graphing, and other functions are available. We have presented ideas, to be improved upon by direct consultation with FAA personnel during display design for the prototype hardware at O'Hare.

3. Equipment Specifications. Electronic Industries Association RS-232-C [10] standard has greatly eased the task of specifying these components as the computer industry uses these standards to define their equipment input/output characteristics. For instance, a 300 baud RS-232-C standard teleprinter from DEC will directly substitute for a 300 baud, RS-232-C standard teleprinter from Hewlett-Packard. These standards will be used for the equipment specifications.

The specifications to be presented were chosen as they were felt to be the most universally accepted and most easily applied in the industry.

a. Remote Data Processor (RDP). The RDP is to be located physically at the ILS site and its function is to collect both analog and digital data as well as to control certain ILS parameters (such as switching the ILS transmitter on or off). The

RDP is to communicate with the central processor (CP) through a modulator/demodulator (modem) via existing twisted-pairs of wire. The data rate is 300 baud and communication code to be used is ASCII.

The equipment specifications are as follows:

(1) The RDP must contain its own power supply capable of using 115 VAC 60 Hz.

(2) Be enclosed in a single enclosure. The durability and temperature range of the unit is not critical as the RDP will be located inside the ILS site's controlled environment.

(3) Have 64 analog inputs (and be capable of expanding the number of analog inputs) that are to be converted to a 8 bit digital word. The incoming analog signal will be within ± 10 VDC and single-ended (i.e., a common ground for all 64 inputs). The RDP will also have 8 TTL-compatible digital inputs and 8 outputs capable of driving low-power relays.

(4) If the RDP incorporates a microprocessor, the program directing the data flow must be in read only memory (ROM) or some other form of non-volatile memory.

(5) The RDP must have a serial input/output port in compliance with RS-232 standards; or, if a modem is an integral part of the RDP, the modem must comply with the standards given in a later section.

(6) If the RDP incorporates a microprocessor, there must be a system whereby the microprocessor will restart itself after a power failure has occurred.

(7) The RDP must be able to communicate with the CP according to the protocol given earlier.

(8) The RDP must allow for temporary connection to a local (at the ILS site) printer for technician use.

(9) The RDP must have some form of self-test; the central processor may be used in this process for verification of checksums or other tests.

b. Modem. A modulator/demodulator, or modem, is a device that allows digital information to be transmitted over long distances with minimal interference from transients and electrical spikes on the transmission lines which, in this case, will be twisted pairs. This interference minimization is accomplished by frequency-shift keying (FSK) the output of the modem according to the transmitted serial bit pattern. This FSK signal, which is usually near the center of the pass-band of the transmission line, can then be decoded into the original serial binary at the receiving modem by a frequency discriminator.

The configuration indicating modem application in the proposed ASCD system is shown in Figure 4-97 . As shown, a group of remote data processors (RDP's) are connected party-line fashion to one central processor I/O port. In practice, the number of modems that can be connected in that manner is about 20 due to impedance considerations. As configured, all of the RDP's will receive when the central processor is transmitting, and the central processor will receive when anyone of the RDP's are transmitting. This is known as a 4 wire, half-duplex system according to RS-232 standards.

The specification for a modem to be used in the proposed ASCD system is that it be of the low-speed, asynchronous variety capable of operating in a 4 wire, half-duplex system at 300 baud in compliance with RS-232 standards (Bell model 103 or equivalent).

c. I/O Multiplexer and Central Processor. The I/O multiplexer is the component which allows the CP to communicate with several small groups of RDP's. Since this multiplexer must operate in close cooperation with the CP, it is recommended that the CP and multiplexer come from the same manufacturer; this selection will most likely be mandatory as multiplexer and CP units are generally not interchangable.

The specifications for the I/O multiplexer are that it: (1) have at least 16 I/O ports, (2) be capable of communicating asynchronously with the RDP's, (3) provide appropriate modem control, (4) be capable of sending and receiving ASCII, (5) have a program definable data rate for each I/O port, (6) provide parity generation and checking, (7) have capabilities for direct memory access (DMA), and (8) have a self-contained power supply or be able to use the CP's supply.

The DEC DH-11AD and the IBM-TPMM I/O multiplexers meet the above requirements.

The function of the CP is to interrogate the RDP's, evaluate the information received from them, and output this information on a printer, several types of video displays, a disk, and a magnetic tape unit. The CP will also accept as inputs data from RVR outputs, the watch supervisor terminal, and the maintenance terminal.

The above duties require a minicomputer that is capable of: (1) asynchronous operation, (2) 4 level priority interrupts, (3) hardware-implemented multiply and divide, (4) at least 16 K byte storage, (5) modulator component design, (6) direct memory access (DMA), (7) stack processing, (8) vectored interrupts, (9) power fail protection and restart capability, (10) self-test, (11) automatic bootstrap loader, (12) servicing the peripherals indicated in Figure 4-95 and (13) battery backup.

d. Operating System Software. Most computer manufacturers offer, as an option, operating system software to be used with their equipment. This program dictates the priority that certain peripherals are given, how several programs might be time shared, what types of higher-level languages may be used, and other aspects of system operation.

As local generation of operating system software would be time-consuming, duplicative and expensive, it is suggested that existing vendor basic software be purchased for the proposed system. Such software should be capable of: (1) real-time, event-driven operation, (2) compiling FORTRAN and/or BASIC programs, (3) handling interrupts and "handshake" commands from the peripherals shown in Figure 4-95, (4) multiprogrammed operation (as opposed to sequential operation), (5) scheduling tasks to be performed at a certain time or as the result of an event, (6) spooling output devices, (7) on-line diagnostics, and (8) time-sharing at least 5 programs.

e. Peripherals. The magnetic tape unit, which continuously logs RDP data, should have the following characteristics: (1) 1600 bytes per inch (BPI), (2) 9-track storage, (3) industry compatible data format, (4) read/write capability, (5) data transfer rate of at least 5 K bytes/sec, (6) rewind from program control, and (8) be able to use 2400 ft. tape reel.

The disk drive stores the operating system software and aids in the creation and editing of magnetic tapes. The specifications for the disk unit are as follows: (1) cartridge type disk, (2) 1.2 M byte or greater storage capacity, (3) data transfer rate of 12 μsec or less, (4) maximum track positioning time of 90 msec or less, and (5) be capable of interfacing with the host computer's I/O structure.

The line printer logs all system operations. The specifications for this printer are: (1) 132 characters per line, (2) 120 characters or more per second, (3) variable paper width, (4) vertical forms control, and (5) ability to interface with the host CP.

System terminals allow the watch supervisor and maintenance personnel to interrogate the computer and view the output of the computer on a TV screen. In order to perform the above duties, the terminals should have the following specifications: (1) industry standard color video (CCIR and/or PAL), (2) software definable characters, (3) psuedo-graphics (also software definable) in the form of horizontal and vertical lines, (4) able to communicate through a RS-232-C standard I/O to the host CP, and (5) a hard-copy option.

f. Video Display System. The components described in the previous section are often used in computer systems and are easy to specify with a brief description. Color video display systems, however, are not commonly used and will, therefore, require a more detailed description.

The major problem encountered with finding a video generation system is that up to 8 independent video channels must be serviced by the CP at one time. With most available systems this means either a long time between display updates (5 seconds or more) or a heavy burden on the CP, or both. As both the delay between updates and the burden on the CP are unacceptable, the specification for the proposed system's video display includes the requirement that the video generator be able to refresh each video display at least once per second and require less than 10% of the CP time for the entire video generation operation.

Since video data transmission involves large quantities of data, the method of data transmission can be critical; especially when there are 8 channels that must be continuously updated. There are basically two ways that video data can be transferred from the CP to the video generators: a high speed serial I/O port or directly from the CP's data bus. The former allows for greater flexibility in that any standard high-speed RS-232-C I/O port could supply the data while the latter is capable of much higher data rates.

The specification for data transfer are: either a high-speed (9600 baud), RS-232-C standard serial I/O or direct bus access may be used to provide video data as long as the update and CP dedication requirements are not exceeded.

To keep programming time to a minimum, it is necessary that display contents be readily defined by software. Such software might be written as a subroutine to be called from the main program to write on a particular display. Such software must be able to define: character size, foreground/background color, and a limited graphics capability such as the creation of bar graphs. The characters themselves are to be created by a dot matrix to eliminate stair-step appearance.

The video generator is to have input from the CP and produce 8 video outputs. The specifications for these outputs are that they be industry standard color video (CCIR or PAL).

It should be mentioned that equipment from Industrial Data Terminals[11] meets all of the above requirements. A demonstration video tape has been made on this equipment to be presented to FAA personnel in Washington and at O'Hare for comment. (A similar video tape was created in Grand Rapids, Michigan using equipment produced by Telematron, Inc. The Telematron equipment, however, does not appear suitable for the proposed system due to I/O limitations.)

4. Future Capabilities. The proposed system has been designed in such a manner that expansion could be easily accomplished with minimal investment and down-time. This section will describe some ideas for possible future work. Some of these ideas could be realized with the proposed systems' hardware plus additional software development. The application of these ideas has conservatively been reserved for future work so that the design might be frozen at what has already been presented. However, if any of the following is felt to be of great importance, revisions could be made in the proposed work effort to incorporate these ideas into the system.

a. Maintenance Feature. At the ILS site, there might be an unmonitored parameter that is suspected of being the source of an intermittent problem. The usual procedure for verifying such a problem is to monitor continuously the parameter until the problem manifests itself. As a problem of this type could take much technician time to diagnose, it would be desirable to employ an automatic system to monitor the suspected parameter. A simple chart recorder could be used in such a situation, although considerations such as additional equipment requirements, replacing paper, maintaining ink flow, and travel to and from the site would tend to make the chart recorder undesirable.

A block diagram for an addition to the proposed system that would allow a suspected parameter to be remotely monitored is shown in Figure 4-100. This addition would connect to the RDP and would allow any 4 parameters to be relayed to the TRACON for continuous monitoring (the number of selectable parameters is arbitrarily chosen to be 4).

The CP could aid the troubleshooting effort by providing data vs. time graphs, logging, and alarms when the suspected parameter exceeded pre-determined thresholds. An alarm on a suspected parameter might allow action to be taken before the entire system went out-of-tolerance. A time plot of the suspected parameter along with other monitored parameters might reveal when interrelation existed between the suspected parameter and the system operation. Such information could be most useful in system diagnostics.

There is an additional maintenance feature that could be realized through software development that would allow for high-speed sampling of any of the RDP parameters (this would apply to the probe unit also). It should be noted that with the proposed system, samples from any one parameter will be taken at relatively long intervals (on the order of seconds) due to the slow data transfer rate between the CP and RDP. Since the parameters being measured by the RDP are direct-current voltages, the slow sample rate does not degrade the proposed system's measurement capability.

If, however, it were considered desirable to monitor remotely a waveform, such as the modulation waveform, the RDP would have to be modified. This modification would involve the RDP software and would allow the RDP to sample the selected parameter at a fast rate until the random-access memory became full. The RDP would then relay this information to the CP at the normal data transfer rate. The CP could perform a Fast Fourier Transform on the incoming data to determine the frequency content of the waveform. Since the microprocessor clock in the RDP is crystal controlled, this analysis could be performed rather accurately as the sample intervals would be known within close tolerance. The frequency spectrum of the waveform could be plotted on the maintenance display or, with appropriate modifications, be sent back to a technician at the ILS site who would be able to receive information from the CP on a portable teleprinter. The implementation of this feature is depicted in Figure 4-101.

b. Administrative Features. If the proposed system is implemented, it will provide a larger data base on ILS systems than has ever before been possible. This data base could provide such information as the relationships between failures and other variables such as weather over extended periods.

The proposed system is in no way limited to the measurement of ILS systems. It is comprised of a general purpose computer and flexible analog and digital measurement devices. The system could just as well measure navigational aids (VOR, radar, etc.) or any parameter that could be represented by an analog voltage in the vicinity of the airport. Such a system, suitably expanded, would be capable of displaying the entire airport systems status.

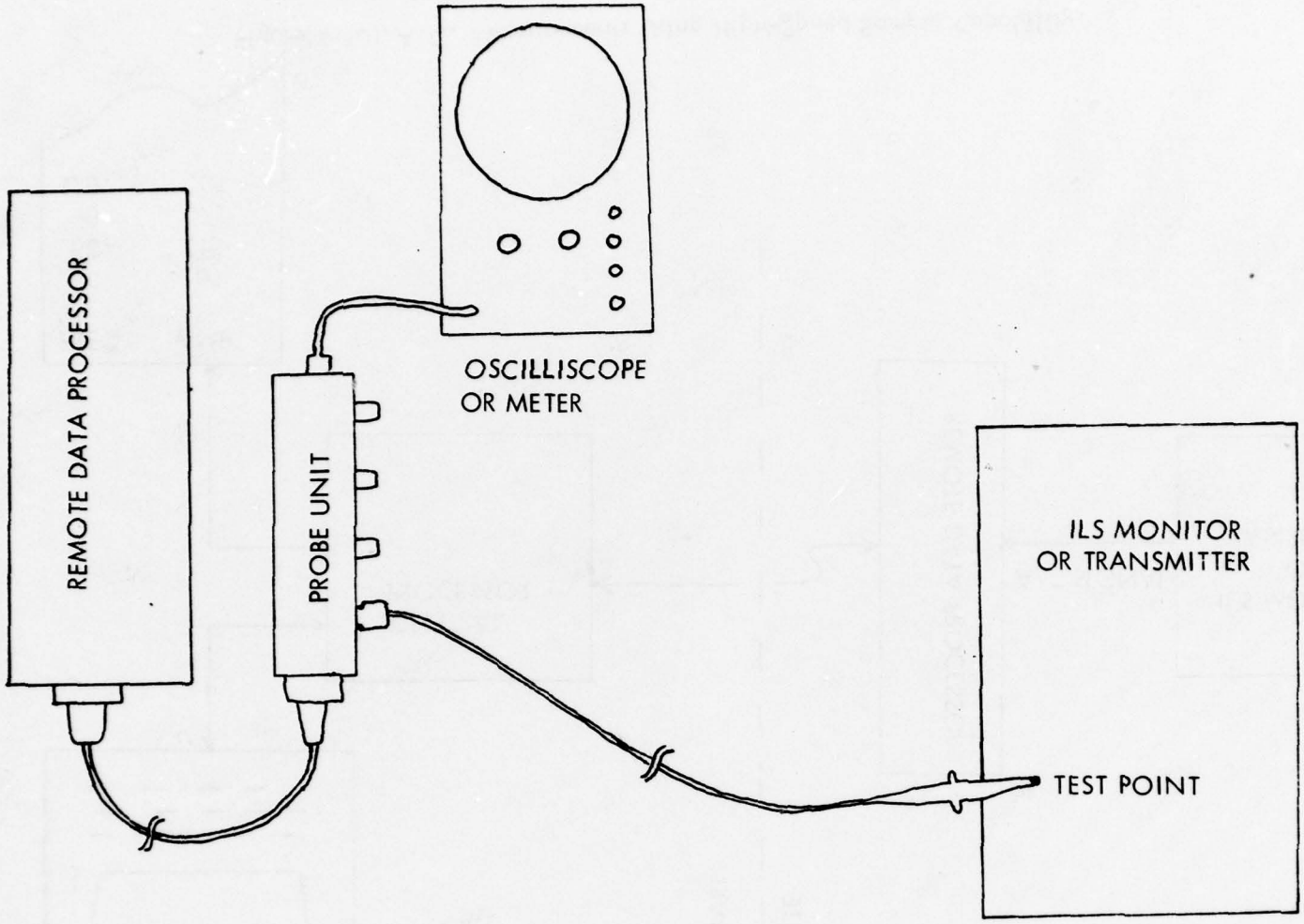

Figure 4-100. Example of Maintenance Feature.

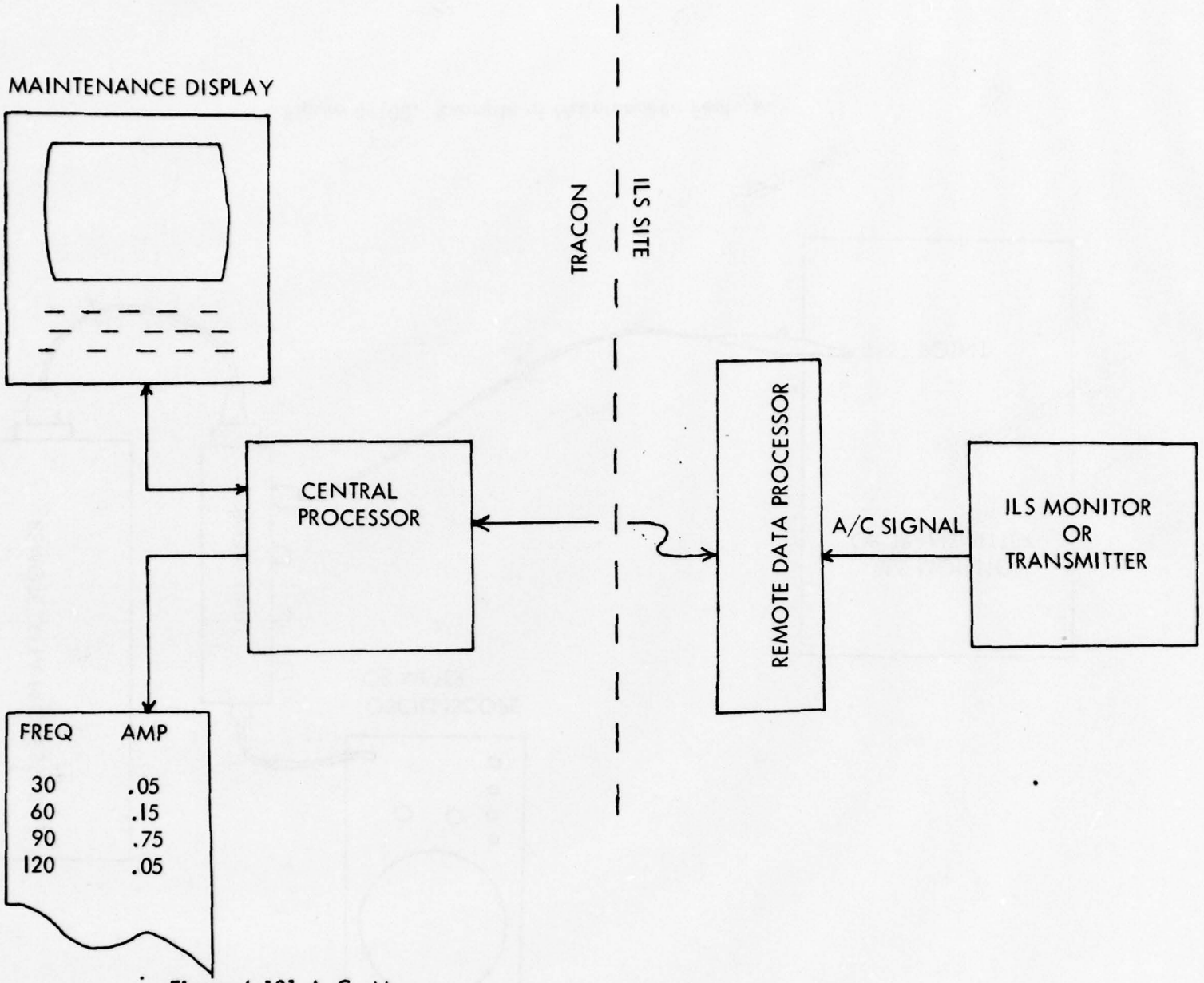

Figure 4-101. A.C. Measurements Using High-Speed Sample Capability.

In the event that the proposed system were implemented at several major airports, summary information could be collected at a central site, Washington, D.C., perhaps, to be used for comprehensive analysis or systems maintenance planning.

There are many possibilities for expansion with the proposed system. It was designed to accommodate these possibilities with minimal effort and cost.

5. Summary and Conclusions. In cooperation with FAA Airway Facilities Service, Ohio University's Avionics Engineering Center has prepared a design for a prototype display and control system, using O'Hare International Airport in Chicago as a focus. Equipment operating parameters of ILS elements and other airport electrical and electronic systems can be measured, with data display for air traffic controllers, display and system control for the watch supervisor and complete system operating measurements plus data storage and retrieval functions available to maintenance personnel. Computer software control of system operation is emphasized, due to its flexibility, growth potential and self-test capabilities. Color-coded video displays are featured for maximum readability and impact.

One objective of this preliminary design study has been to determine the extent to which system components are available "off-the-shelf", with a minimum of custom technology development specifically for this program. The conclusion is that each system element is presently available from more than one manufacturer. In two system areas, however, it is concluded that some custom design is desirable to significantly reduce cost. In the remote data processor and the video generator areas, available equipment is costly since it possesses capabilities far in excess of the requirements for this system.

A general conclusion is that the prototype system can be assembled using present technology and that prototype installation at Chicago O'Hare in parallel with existing ILS status displays will demonstrate operational improvements and maintenance manpower advantages provided by the system.

Indications from manufacturers are that hardware necessary to begin software development could be delivered to Ohio University within 8 weeks of receiving the order. The system would initially be configured at Ohio University in order to give personnel an unrestricted hands-on evaluation of the system without interfering with TRACON operation. After the software development and evaluation phase, which is anticipated to last six months, the system will be configured at O'Hare. The system is expected to be fully operational one year after installation at O'Hare begins.

The total work effort is scheduled to extend over a 3 year period with 3 major goals: (1) software development and system evaluation at Ohio University, (2) system installation at O'Hare, and (3) system support plus software development as needed.

The total cost of the system presented above and described herein is less than $1 million. This includes software development, system installation and support.

G. Marker Beacon Precision Location. A marker beacon transmitter was established at the Ohio University Airport, Albany, Ohio, for use in experiments involving precise location. Three separate marker locator systems were evaluated in bench and flight tests. The two-antenna, differential phase-measurement system gave satisfactory results during flight tests of the development hardware. The two other systems, one a single-antenna phase-measurement system and the other an amplitude-measurement unit, provided results which illustrated the need for additional development to obtain reliable and precise positioning.

With the dual antenna system, marker position was detected to within ±6 feet on normal approach paths during flight tests.

1. Marker Beacon and Flight Path Geometry. Figure 4-102 illustrates the marker beacon and flight path geometry. The middle marker is approximately 3500 feet from the runway threshold. An ideal approach brings the aircraft over the marker at an altitude of 200 feet. The ICAO specifications require the aircraft to be in the beam of the marker for 1000 ± 300 feet (see Figure 4-103). At an approach speed of 220 feet/second the aircraft will be in the beam for 4.5 ± 1.4 seconds.

In an ordinary approach and landing situation, the marker provides the necessary position information to the pilot in order to establish the final approach. However, in flight testing an ILS system or in an auto-landing approach, it is necessary to know the airplane's exact location. Navigation for flight checks is normally handled by an inertial navigation system, but this system must have a point from which to start. The accuracy of the inertial navigation system is dependent on the accuracy of the position fix.

The object of this effort has been to develop a system which can locate the marker within ±10 feet.

2. Signal Processing Analysis. Detection of the marker beacon on-top position can be approached by at least three methods. In the course of this research effort, equipment was constructed to detect the on-top location using each of three methods.

a. Doppler System. The Doppler method makes use of the frequency shift observed in the aircraft as it approaches and passes the marker beacon antenna. The frequency of the marker is not specified exactly, so relative frequency measurement must be made. The change in frequency due to Doppler is small compared to the center frequency so that the received frequency must be mixed down to a lower frequency while preserving the entire Doppler frequency shift. Once the frequency is translated to a suitable IF, the signal may be processed using either a frequency or time-period measurement. A processing method which can be employed with either frequency or period measurements is to take the difference between successive measurements to obtain the first and second derivatives of the Doppler curve. An on-top trigger can, in theory, be obtained directly from either of these signals.

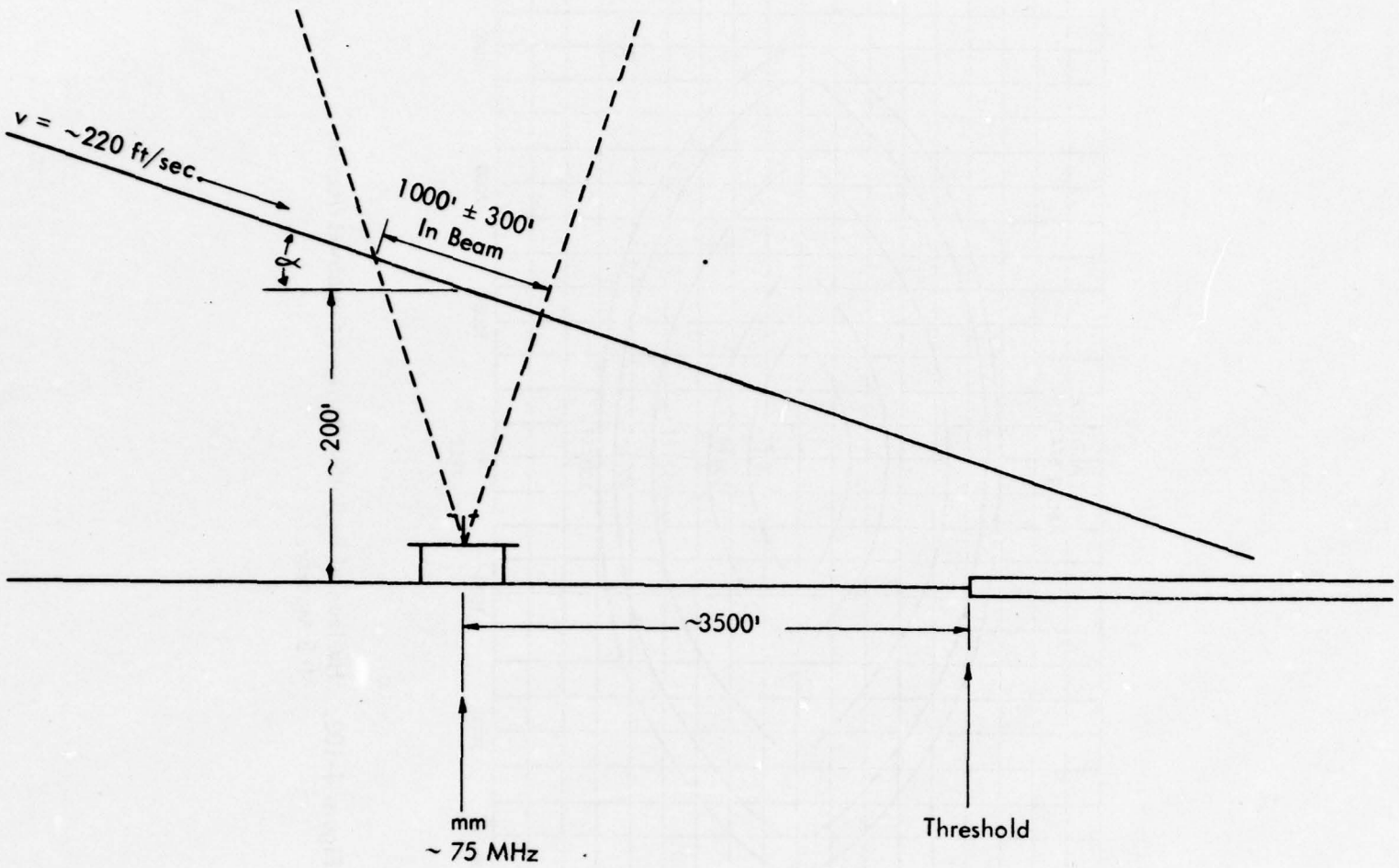

Figure 4-102. ILS Middle Marker Beacon Flight Geometry.

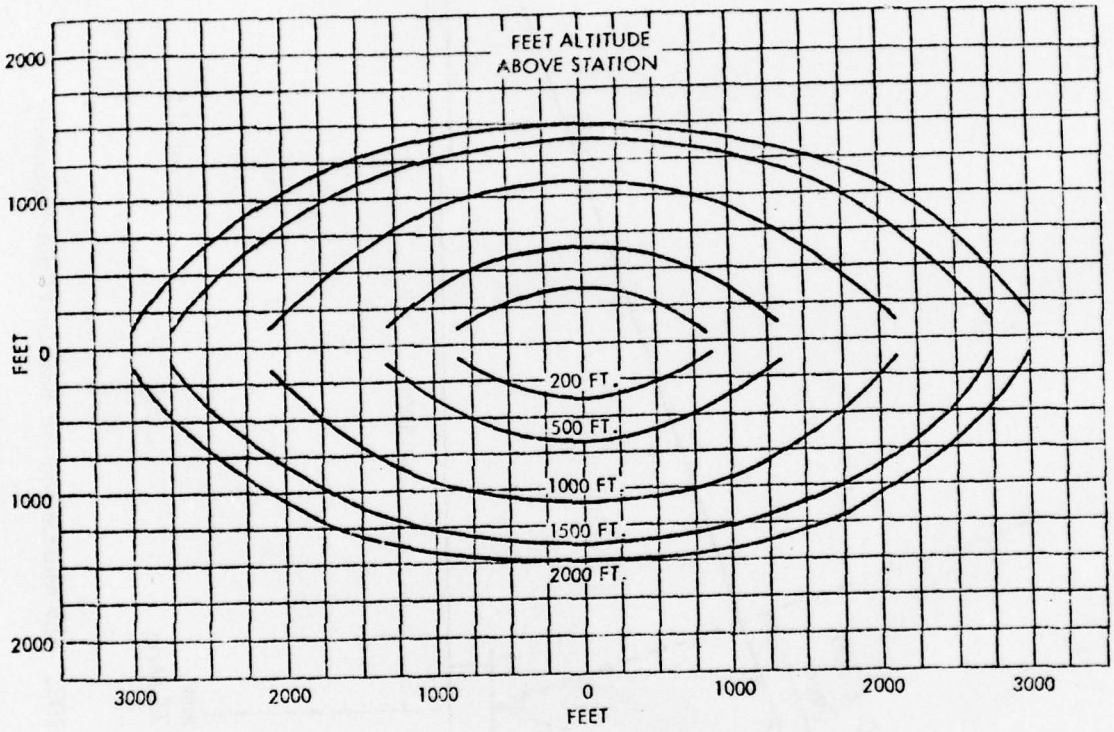

Figure 4-103. Horizontal Padiation Patterns Obtained from an ILS Marker.

b. Amplitude System. The amplitude system can be constructed by disconnecting the AGC loop in a marker beacon receiver and connecting a comparator to the output of the AGC detector. The comparator will turn on at a preset RF level and turn off at the same RF level on the other side of the marker antenna. The on-top position of the marker beacon antenna is assumed to be at the center of the comparator "on" period.

A real-time on-top locator employing this method would provide an event mark and a time-delayed output which would indicate the time since the on-top position was passed.

c. Differential Phase Measurement System. The differential marker beacon locator is essentially a single-plane, phase-comparison monopulse receiving system. Through the use of two antennas and receivers, a developmental design system can measure the phase difference between two antennas with known separation and trigger an on-top indication when incoming signal phases are equal at the two antennas.

System elements for the concept-demonstration locator are described in this section, together with flight evaluation results. The two antennas are separated by a distance d (see Figure 4-104). The distance from a point halfway between the two antennas and the target is R. If R is large compared to d, R_1 and R_2 may be assumed to be parallel, in which case the distance from antenna 1 to the target is:

$$R_1 = R + \frac{d}{2} \sin \theta$$

and the distance from antenna 2 to the target is:

$$R_2 = R - \frac{d}{2} \sin \theta$$

The difference in the distance from the target to the two antennas is:

$$\Delta R = d \sin \theta$$

Thus, the phase difference between the signals received at the two antennas is:

$$\Delta \Phi = \frac{2 \pi}{\lambda} d \sin \theta$$

For a nonambiguous system, the distance between the antennas d must be smaller than one-half wavelength ($\lambda /2$). The phase difference $\Delta \Phi$ will now range from:

$$180° \geq \frac{2 \pi d \sin \theta}{\lambda} \geq -180°$$

and the phase difference $\Delta \Phi$, is zero when angle θ is zero.

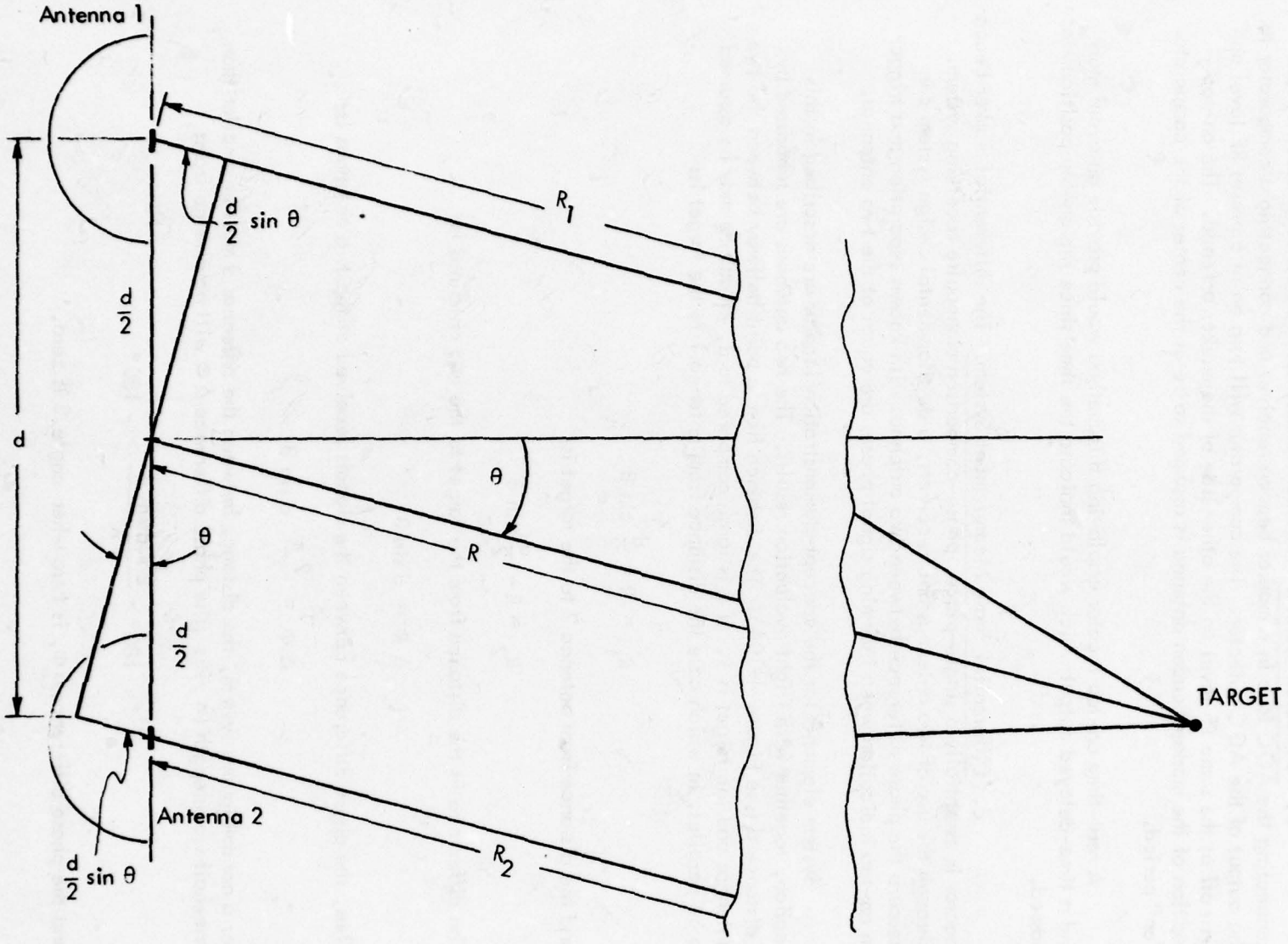

Figure 4-104. Simultaneous-Phase-Comparison Radar.

3. Prototype System Design. A marker beacon locator was designed and constructed which utilizes differential phase comparison or interferometer techniques to trigger an indicator when the marker is equidistant from the two antennas.

A block diagram of the differential phase system is shown in Figure 4-105. The 75 MHz signals from the two antennas are separately mixed to an IF frequency of 10.7 MHz in the front-ends of two modified King KR-21 marker beacon receivers. The modification was necessitated by the requirement of a common local oscillator between the two receivers to eliminate oscillator drift. The phasor in one antenna line compensates for differences in the antenna cable lengths and for differences in the phase-shift of the two receivers. Phase measurement of the resulting two signals was made in a vector voltmeter HP Model 8405A. The phase output of the vector voltmeter was used to trigger the zero-phase point for an on-top indication.

Figure 4-106 shows the differential phase developmental system as installed for flight evaluation.

a. Modification of Standard Marker Beacon Receiver. Two standard King KR-21 Marker Beacon Receivers were obtained for use in the project. Two modifications were made to increase the capabilities of the receiver outputs.

(1) The receiver detector output was brought out on the rear-panel connector for marker signal-strength measurements.

(2) The receiver IF (10.7 MHz) was picked off and connected by shielded cable to the rear-panel connector. The connection is intended for use with a FET-follower circuit in the external system.

(3) An option for external L.O. at 85.7 MHz was added.

b. Trigger Circuitry. Figure 4-107 shows the schematic diagram for the on-top trigger generation. Inputs at CH1 and CH2 are obtained from the 20 KHz outputs of the vector voltmeter. These inputs represent signal phase at each of the two antennas. Each channel is hard-limited and passed to the NAND gate phase detector and latch. When the phase at the two inputs becomes equal, the on-top trigger is generated. The AGC is used to reset the circuitry when the signal drops below a predetermined value.

c. Flight Evaluation. A 75 MHz marker transmitter was installed at the Ohio University Airport approximately 1500 feet from the Runway 24 threshold with 1-watt output at 75 MHz. The middle marker identification keying was activated. After calibration runs at pattern altitude and during low approaches (200 ft. agl. over the marker), data passes were taken at both altitudes.

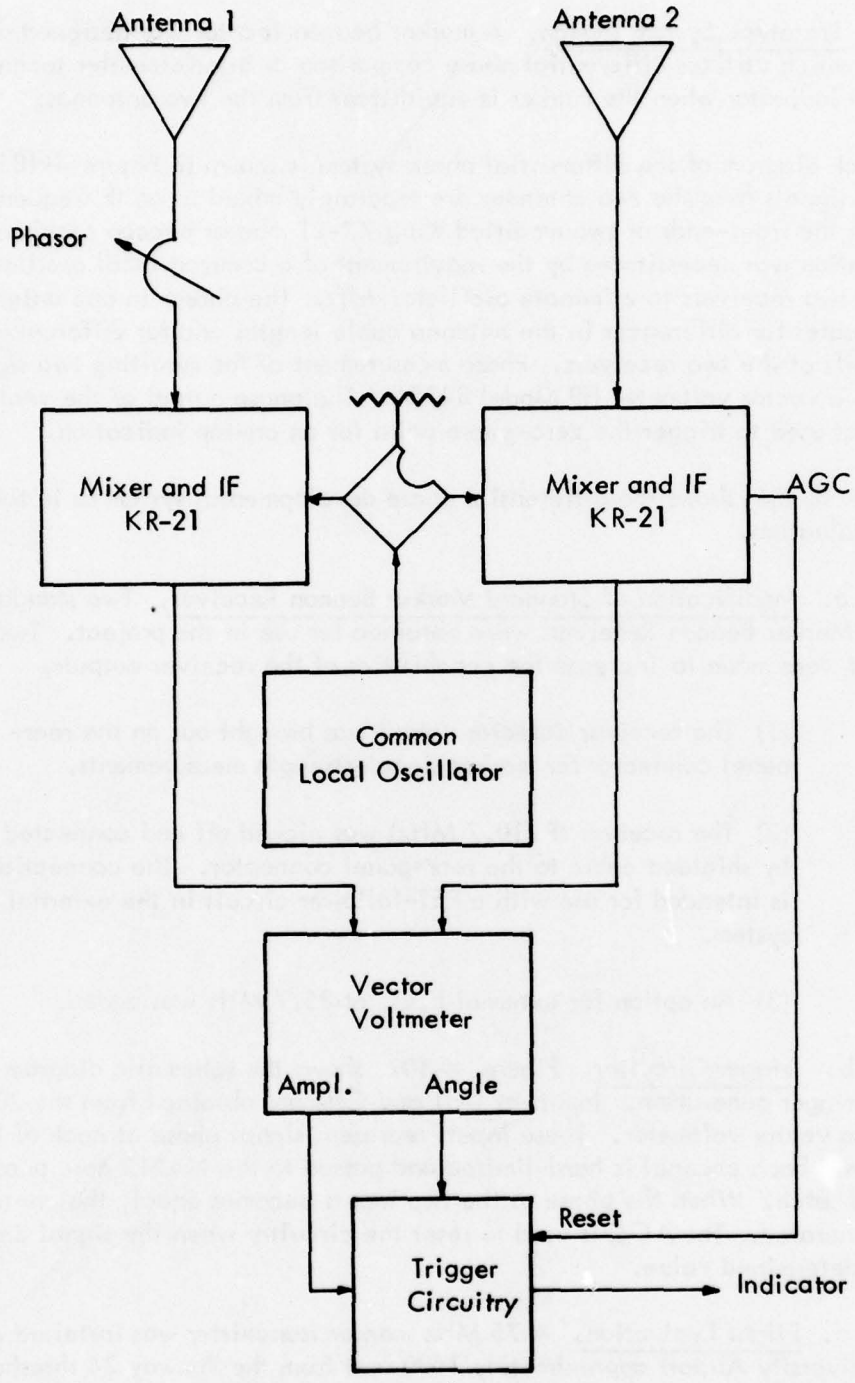

Figure 4-105. Differential Phase System.

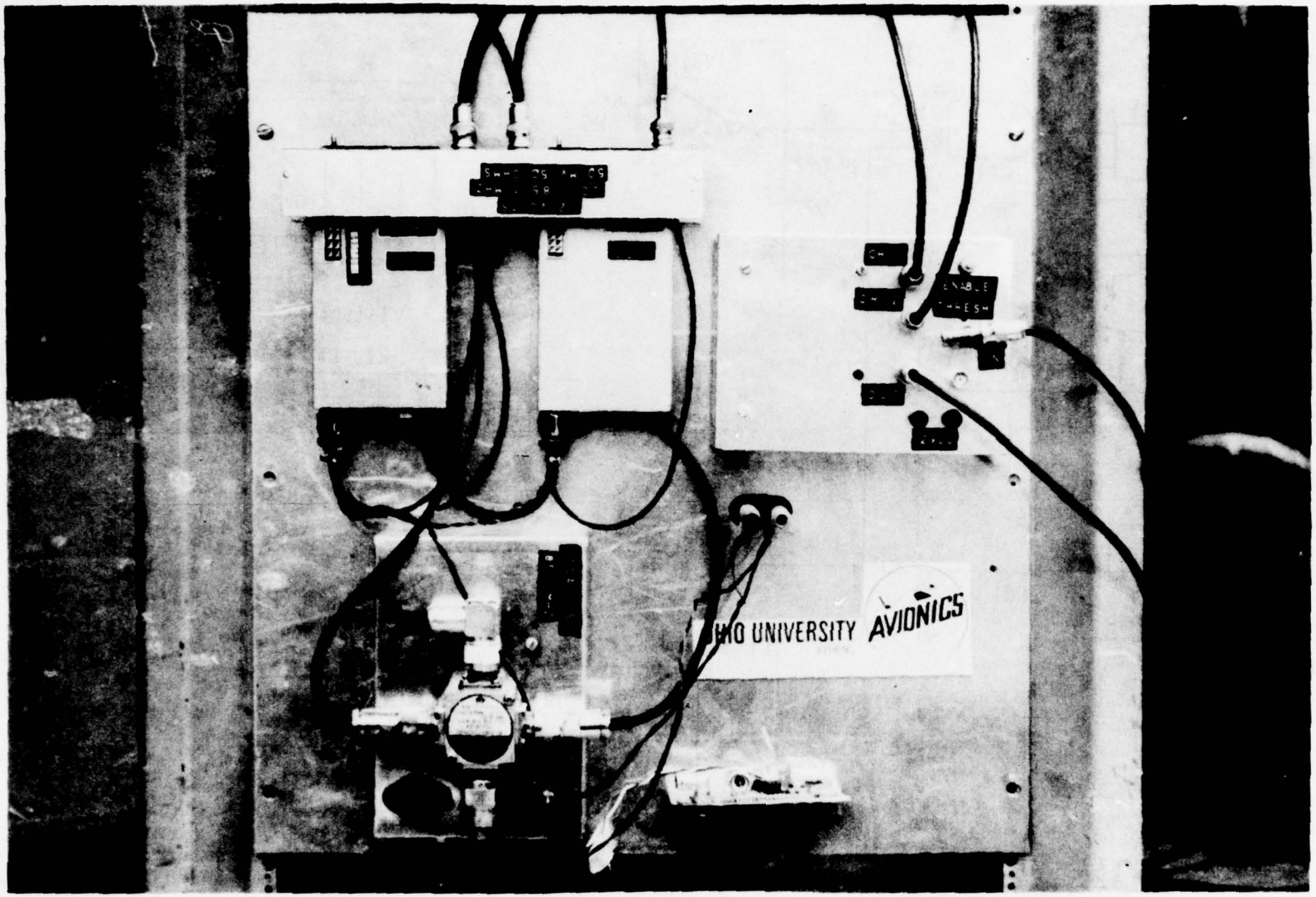

Figure 4-106. Developmental Model - Differential Phase Marker Beacon Locator.

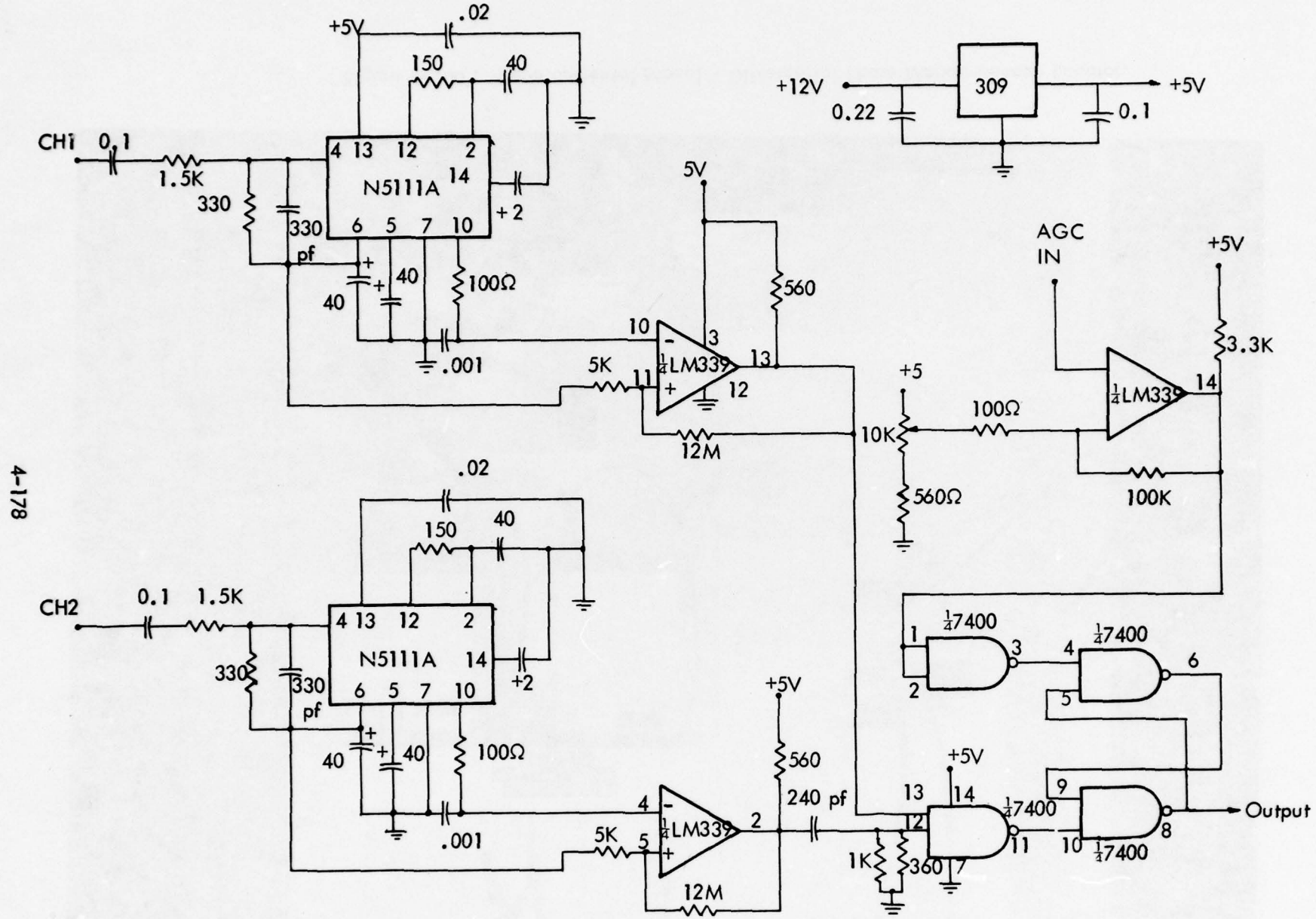

Figure 4-107. Differential Phase System -- Trigger Circuitry.

Results indicate a system repeatability of within ±6 feet for the low approaches performed, using a ground observer sending a radio event-mark recorded in the airplane.

Chart recordings of three low approaches are included as Figures 4-108, 4-109 and 4-110. The three traces are: from top to bottom, Vector Voltmeter (VVM) Amplitude, VVM Phase and on-top trigger. The visual on-top position derived from a ground-based observer was recorded on another channel and has been drawn above the on-top trigger. Chart speed was 50 mm/sec and the approach speed was approximately 130 kts. for all three passes.

The nulls in the amplitude chart recording on either side of the zero phase point are caused by reflections from two ground planes, one being the earth ground and the other a parasitic element $\lambda/4$ below the dipole transmitting antenna. These nulls were not found to be a problem, but they could be reduced significantly in future tests by marker antenna modification.

Data from a calibration flight which consisted of a level pass 1600 feet over the marker was plotted in detail, and is shown in Figure 4-111. As this data represented aircraft position which was inside the antenna sidelobe pattern, additional work was performed to determine the source of the variations in phase indicated in the plot. Figure 4-112 shows the result of a receiver calibration test and aids in explaining the phase variation. The receiver obviously evidences significant phase shift with amplitude changes.

In the differential phase system, aircraft angle of attack will cause phase differentials between antennas. We found that a ±5° change in angle of attack would cause positioning error of ±25 feet. The angle of attack function is illustrated in Figure 4-113.

Results of the flight tests show that the differential phase system has excellent repeatability; however, additional flight tests should be made at other marker installations to determine whether parameter changes in the transmitter power, antenna or site would affect the repeatability of the system.

In addition, multiplexing of a single receiver for phase measurements would be highly desirable in future tests, to avoid differential phase shift between receivers and to minimize the effects of receiver phase shift with amplitude changes.

4. Conclusions. Three methods for precise location of ILS marker beacon transmitters were investigated. Of the three, the amplitude measurement system was least complex and provided ±30 feet repeatability in flight evaluation. The differential-phase method was more complex, utilizing two antennas and two receivers, and its repeatability was ±6 feet. The single-antenna phase (Doppler) system was considerably more complex than either of the other systems, and the design suffered from the extremely small amplitudes of the Doppler velocity and acceleration signals and from frequency and phase stability problems both in the marker transmitter and in the airborne equipment. The Doppler system was not evaluated in flight.

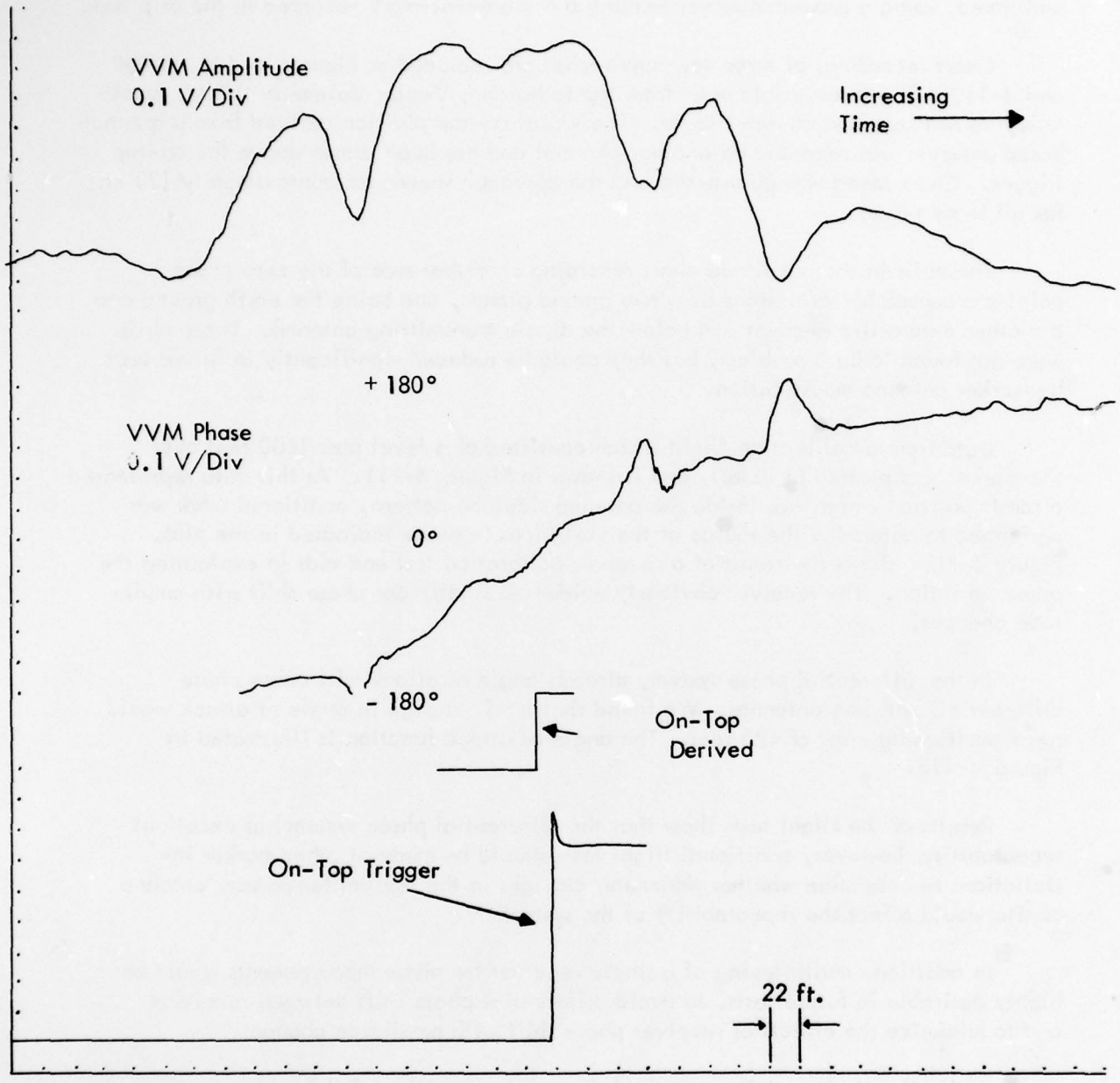

Run #7/October 4, 1975/Albany, Ohio

(1) Chart Speed = 50 mm/sec.
(2) Low Approach at 130 Kts.
(3) 2-Antenna/2-Receiver System.

Figure 4-108. Flight Test #7.

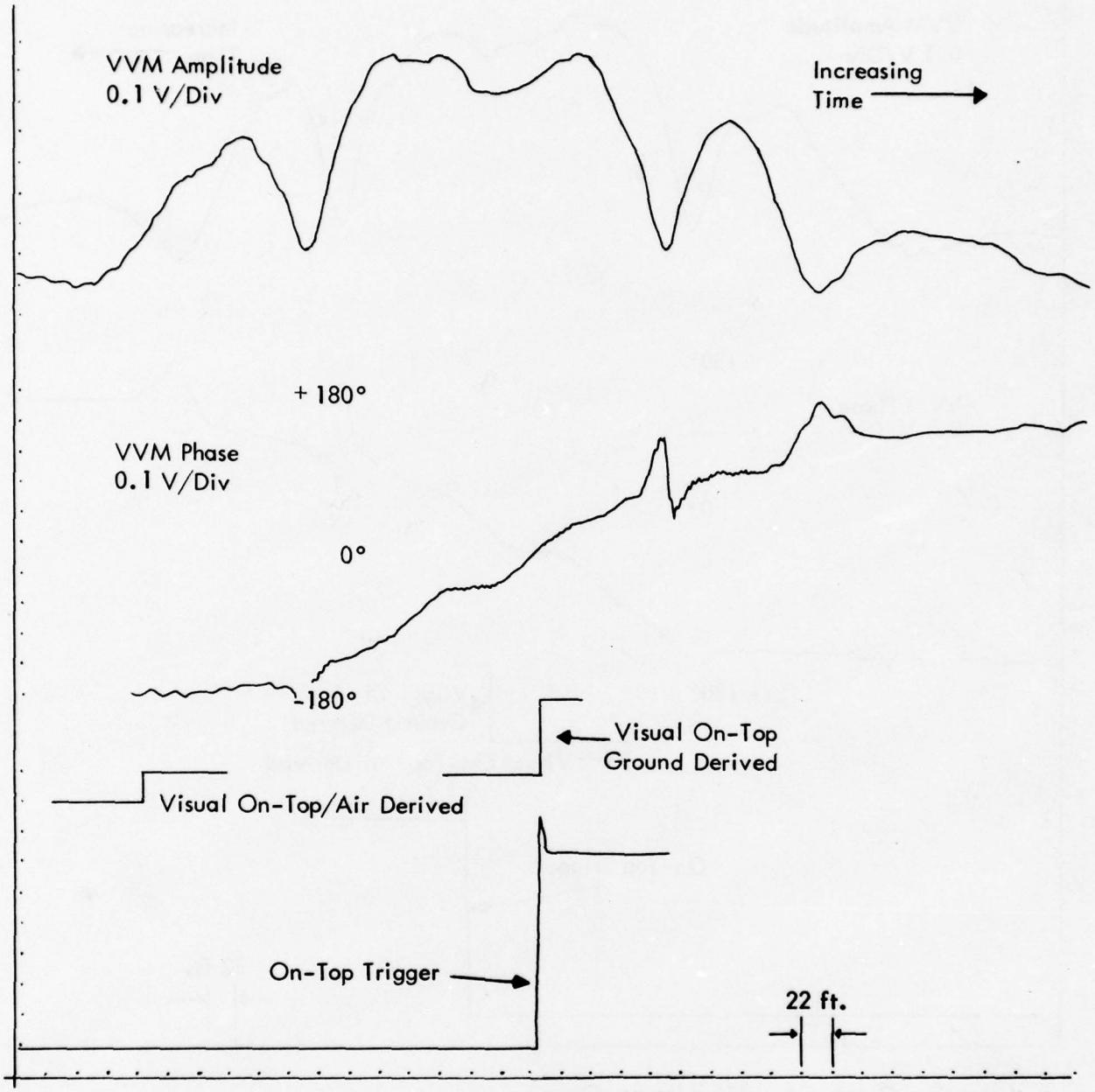

Run #8/October 4, 1975/Albany, Ohio

(1) Chart Speed = 50 mm/sec.
(2) Low-Approach at 130 Kts.
(3) 2-Antenna/2-Receiver System.

Figure 4-109. Flight Test #8.

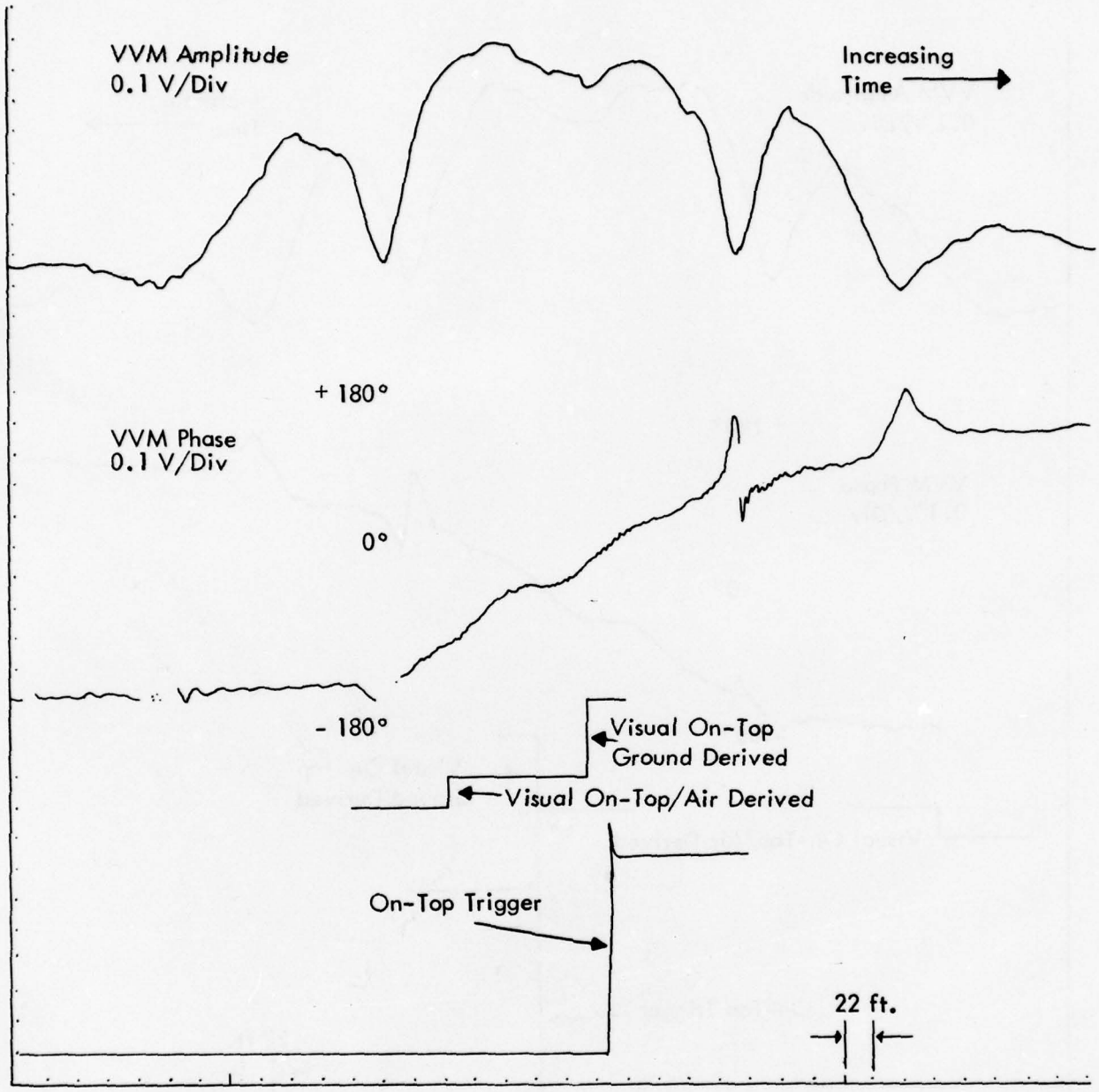

Run #9, October 4, 1975/Albany, Ohio

(1) Chart Speed = 50 mm/sec.
(2) Low-Approach 130 Kts.
(3) 2-Antenna/2-Receiver System.

Figure 4-110. Flight Test #9.

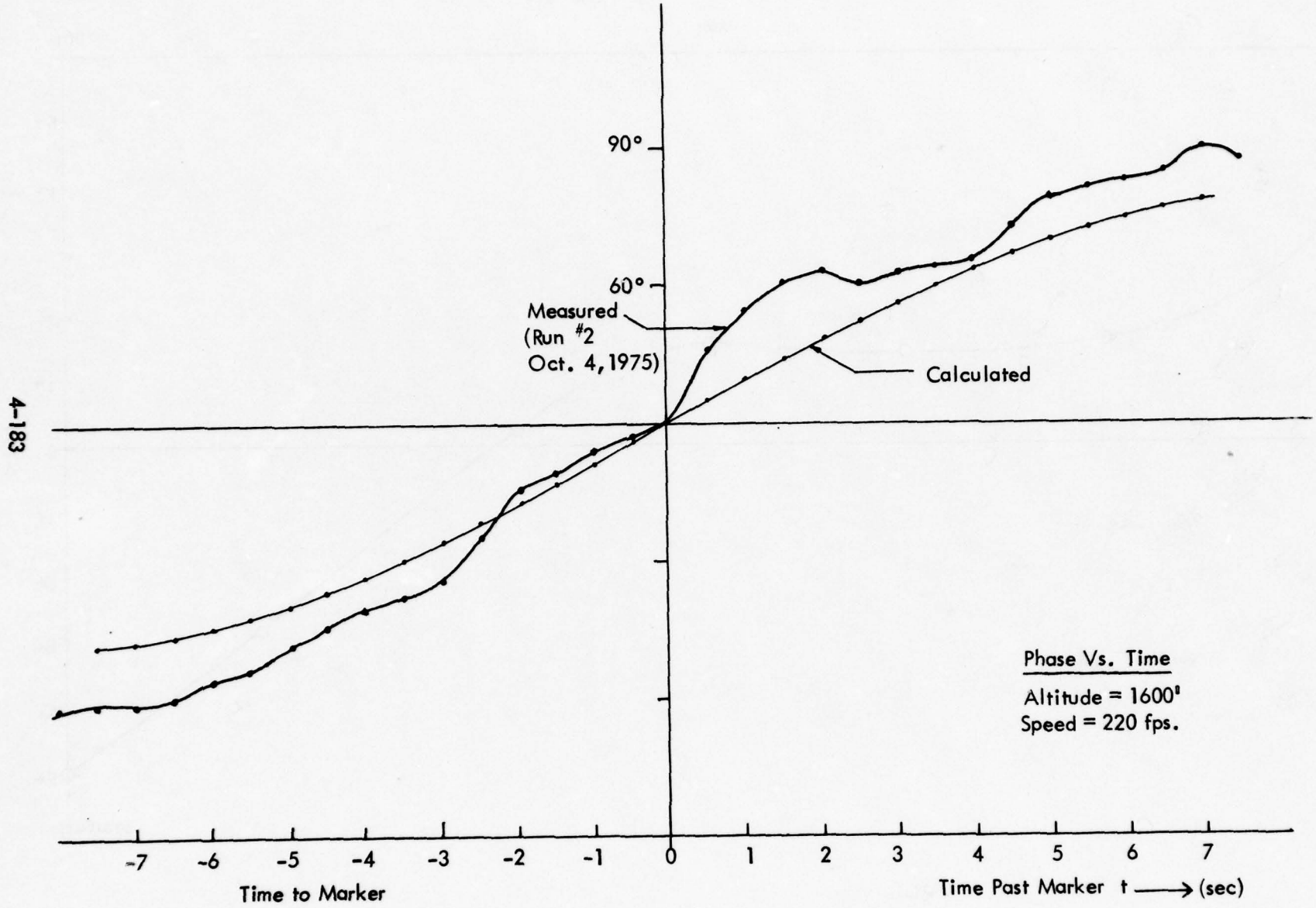

Figure 4-111. Calibration Pass: Detailed Phase Plot.

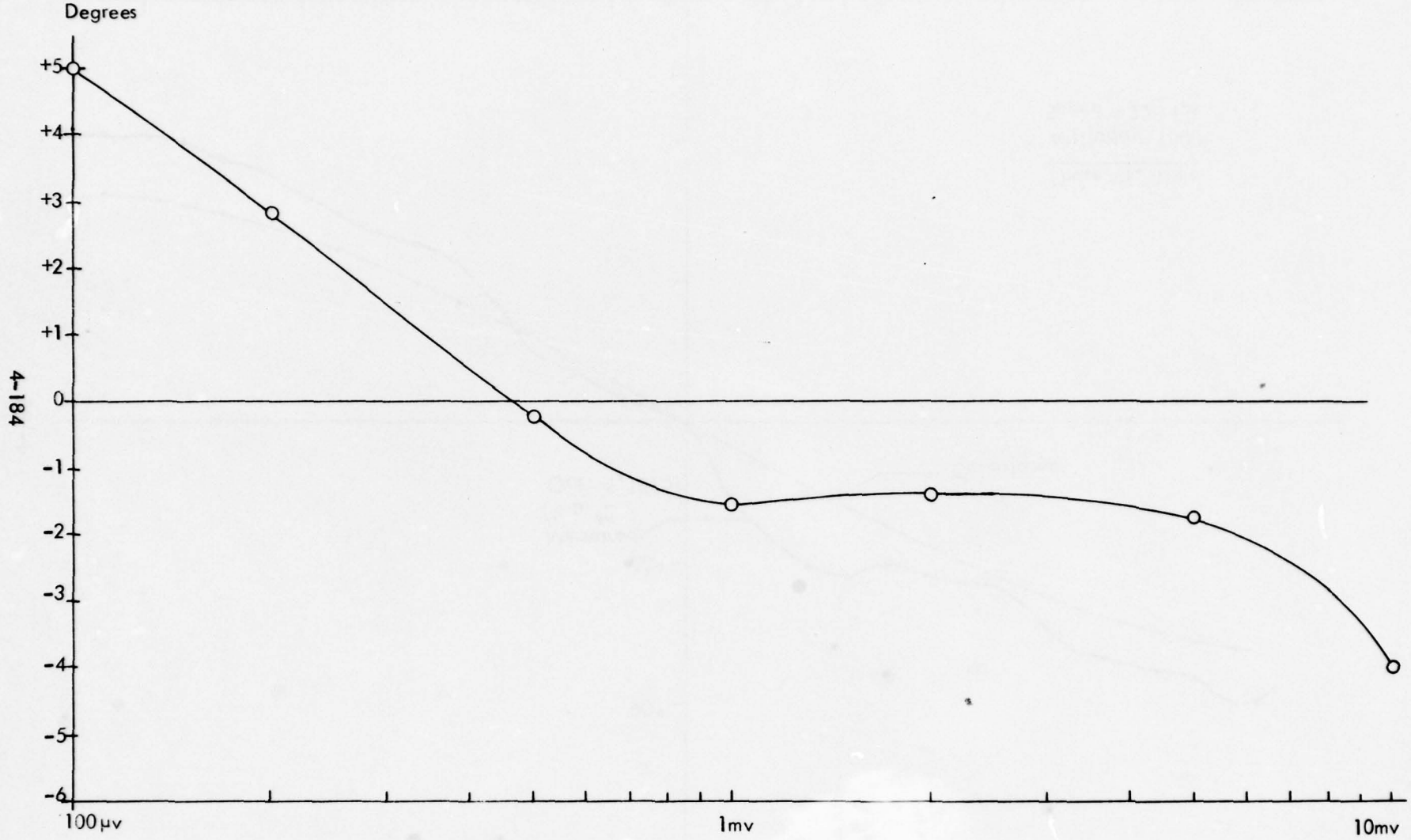

Figure 4-112. Phase Shift vs. RF Amplitude KR-21.

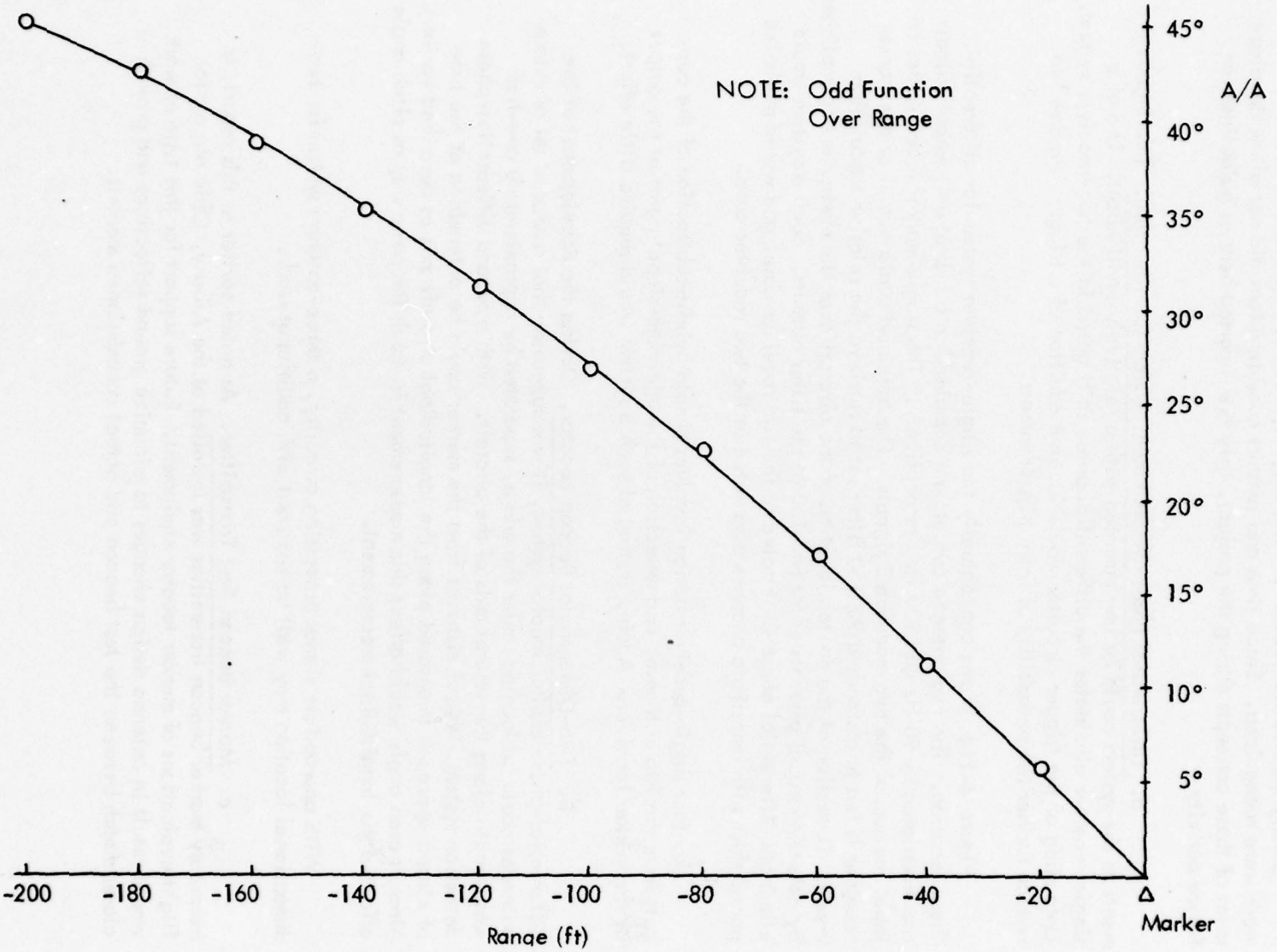

Figure 4-113. Aircraft Angle of Attack Required for Zero Phase Difference.

During the Marker Beacon Locator Project, several possible extensions of the work were recognized. Since time and support considerations did not allow development of these concepts during the project, they are reported here as guidelines for future activity.

a. Differential Phase-Measurement System Continuation. Two improvements to the system could be implemented with a relatively small effort. Use of a single receiver eliminates the differential phase shift noted in the two-receiver system. Upgrading of the trigger circuitry would involve addition of a trigger "window" to reduce further the probability of false trigger events.

Figure 4-114 shows conceptually the single-receiver system for differential phase location. The two antenna outputs are combined in a hybrid unit whose outputs are modulated by 90 Hz and 150 Hz, respectively. The single marker receiver has an input the sum of the two modulated signals. The detected audio output of the marker receiver is fed to a standard 90/150 filter set to retrieve the relative modulation levels. Detection of the on-top location of the aircraft over the marker is accomplished by detecting equal amounts of 90 and 150 at the filter outputs. Such a system would eliminate differential phase shift noted in the two receiver case, and would minimize phase-shift with amplitude changes also noted in the two receiver case.

Another single-receiver option involves simple hybrid-subtraction of the outputs from the two antennas, and detection of the minimum-signal point at the output of the marker receiver. Again, testing of such a system would require little effort.

b. Two-Dimensional Beacon Locator. During the development of the differential-phase marker locator system, it was suggested that a second set of marker antennas could be located under the wings, separated by approximately one-half wavelength along the lateral axis of the aircraft. With a second differential-phase detection system, lateral distance from the marker could be determined at the time of closest approach (measured along the longitudinal aircraft axis as described earlier). Aircraft crab angle would affect this measurement in much the same way as pitch angle affected the longitudinal measurement.

With appropriate signal processing circuitry, a three-antenna system for two-dimensional location may well be realized with additional work.

c. Marker Beacon Test Transmitter. As noted earlier in this report, a temporary marker beacon transmitter was installed at the Albany, Ohio airport for flight evaluations of marker locator equipment. Future support for this type of work would result in antenna design changes to minimize ground reflections and provide a closer match between the test beacon and actual commissioned markers.

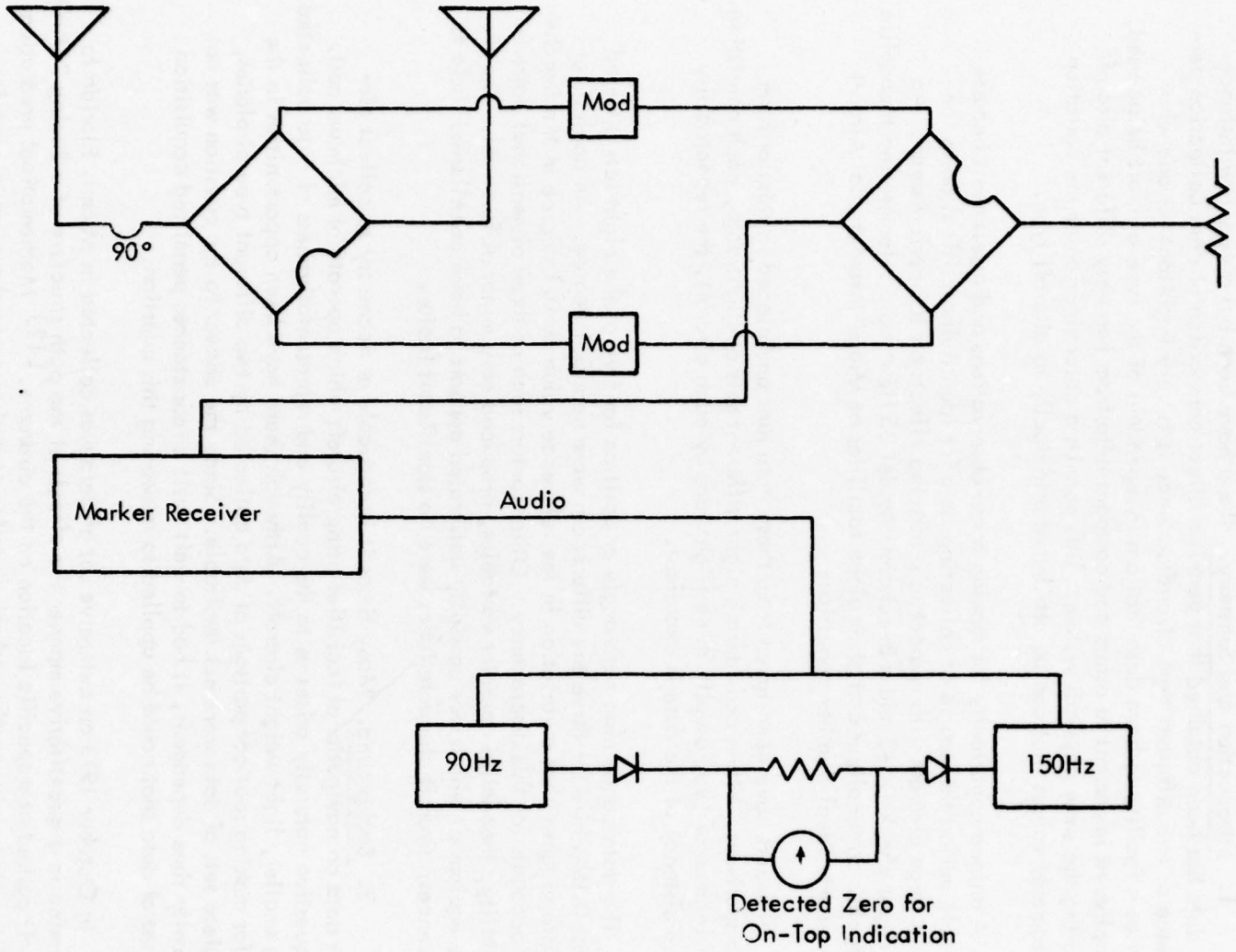

Figure 4-114. Single-Receiver Marker Locator Concept.

H. Comparison of Common ILS Data Acquired Using a DC-3 and a Beechcraft 35.

1. Introduction and Summary. There have been but a very few instances when data has been obtained that permit a direct comparison of data collection performance of two different type aircraft. Since it is very important for one who qualifies a facility to have data that are independent of the type aircraft being used, it is believed important to assess and compare data from two very different aircraft measuring the same physical system. This permits a determination of the variation of parameter values that can be attributed principally to aircraft type.

A unique opportunity for making these observations and assessments became available during the course of collecting data for identifying critical areas for parking large aircraft with respect to producing effects on ILS performance. An FAA flight check DC-3 and a Beechcraft Model 35 flew radio telemetering theodolite approaches on localizer and glide slope facilities at Miami International Airport under nearly ideal weather conditions.

Numbers have been taken from these data runs and placed in tabular form for comparisons. When considering eight different sets of slight data, each consisting of a minimum of two, usually three flight runs by each aircraft, the repeatability and consistency of the data is excellent.

The data concerning path angle or position for five of the eight sets differed at most 0.02 while for three the differences were near 0.1 degree. An analysis of the data suggests that a variation in the reference value by 0.1 degree in the Beechcraft accounts for this discrepancy. Other factors such as three dimensional pattern variability, theodolite operator variables, produced only minor differences. The airborne equipment which was carefully calibrated appears to have contributed little to differences; aircraft characteristics were no significant factor.

2. Background. Many times it is desirable or necessary to collect airborne data on navigational facilities using aircraft which operate at minimum cost. The question naturally arises as to the quality and representativeness of data collected using smaller, light weight aircraft. Although there have been opportunities in the past for making spot comparisons of data collected by two different type airplanes, complete sets of data were not available. Since the answer to the question was not critically time dependent, it had to wait until circumstances permitted acquisition of a set of data that could be applied to answering this question.

In October 1973 an extensive set of data was collected in Miami, Florida to determine in a quantitative manner the effects of the path structure of a Boeing 747 aircraft parked at a specific location on the airdrome. [12] Mathematical predictions had been made using mathematical modeling techniques and there was a need for validating this modeling and assessing the accuracy of the predictions. Through the cooperation of National Airlines a Boeing 747 was parked at 6 different locations for localizer considerations and seven locations for glide-slope measurements.

Once the Boeing 747 was in position six approaches were made, three by the FAA flight check DC-3 and three by a Beechcraft Model 35 (BE-35). There were interlaced or alternated. The same theodolite tracker and instrument were used for pairs of DC-3/BE-35 runs but not the entire set. The time of dat was very early morning including times of darkness, daybreak, and daylight. The atmospheric conditions were very stable.

The Beechcraft 35 carried the Ohio University Mark II Minilab. In this minilab NARCO UGR-2 glide-slope receivers were used for the glide slope and theodolite telemetry. A NARCO NAV II was used for the localizer with special audio processing external to that receiver for increased range and linearity. A differential amplifier was used to provide a direct reading of the difference between course deviation indicator (CDI) and the theodolite reference. The chart recorder was dual channel Honeywell Electronik 19 model.

3. Procedure of Analysis. The parameters of interest in this analysis are the actual path angle in zone 2, and the maximum upper and lower deviations in zone 2 and zone 3.

For each position the data is tabulated separately for the 3 runs. Then the 3 runs are averaged and tabulated for comparison of the DC-3 averages to the BE-35 averages. If 3 data points do not display sufficient correlation the average is not computed and a (~) replaced the average in the corresponding table entry.

In this comparison the zones are defined as follows:

Zone 1 - beyond O.M (not considered)

Zone 2 - O.M to B

Zone 3 - B to C

Chart and airspeed are assumed constant; therefore, distance on the charts are linearly interpolated using the O.M and TH as reference points.

$$\text{Point B on chart} = \left(\frac{TH - B}{TH - O.M}\right) \times \text{Chart Length (TH-O.M)}$$

$$\text{Point C on chart} = \left(\frac{TH - C}{TH - O.M}\right) \times \text{Chart Length (TH-O.M)}$$

The average path angles Φ are figured as follows:

$$G/S\ \Phi = \theta - \frac{\text{Average zone 2 in } \mu A}{150\ \mu A} \times .7^\circ$$

$$\text{LOC } \Delta\,\Phi = \frac{\text{Average zone 2 in } \mu A}{150\ \mu A} \times \tan^{-1}\frac{350}{11{,}500}$$

The maximum deviations, upper and lower, are tabulated and the range at which each occurs is recorded.

4. Experimental Results. Flight records of the Miami facilities are reported in SRDS Report RD-74-57 and will not be repeated here. Instead numerical values typical of those that are filed on official flight inspection FAA form 8240-7 (formerly FAA form 3488) have been extracted from the data and comparisons made based on these.

The rationale for this approach is that, given a flight inspection, these numbers are the ones recorded to characterize the facility performance. Should the use of different aircraft for collecting the data make a difference in numerical values obtained, then this would be an important observation. Intuitively one might imagine the aircraft might have some influence. Impressions given at times by people involved with flight check operations indicate that data values are dependent.

The extensive data collection required to validate the mathematical model for predicting multipath effects due to reflections from a jumbo jet permitted as a by-product an assessment of aircraft dependency. The numerical data is tabulated in this section to permit the reader to make a personal assessment. (See Tables 4-6 and 4-7.

Two rather obvious discrepancies in data appear amounting to approximately 0.1 degree. The difference appears to be consistent within a specific set and does not transfer. Each aircraft produced consistent data per set which indicated that telemetry calibration could have been a problem. The one set of data establishing the reference values for the facilities were the exception to the practice of interlacing flights, in that the Beechcraft flights were made on a Friday with the DC-3 reference values being taken on a Monday.

For purposes of generalization Table 4-5 shows the averages.

Difference: DC-3 - BE-35		
Localizer	Nominal	-.01
	Position 1	.00
	Position 2	-.12
	Position 5	-.11
Glide Slope	Nominal	-.10
	Position 2	.00
	Position 3	.00
	Position 8	-.02

Table 4-5. Difference Values Observed Between DC-3 and Beechcraft 35.

5. Conclusions. From the flight checks performed on the Miami localizer and glide slopes using two different aircraft as vehicles for airborne data collections, the following conclusions are drawn:

a. There is no significance as to the aircraft being used for flight check provided a radio telemetering theodolite is used for reference and the weather is not extremely turbulent.

b. Careful calibration of airborne equipment is, of course, essential to successful data collection. Accomplishing these calibrations insures to a great degree that high quality data is obtained.

c. Theodolite and telemetry operation is potentially a source of significant error. Misindexing, a drift in telemetry transmitter values, personnel proficiency, recency of experience, and theodolite location are all critical items to be considered when attempting to minimize flight check error. Cross checking and use of redundant readings helps identify and eliminate these errors.

d. Differential amplifier and recorder problems are sometimes overlooked and may produce errors that are interpreted as facility problems. Again, the practice of cross checking and, if possible, carrying an onboard calibration source for obtaining checks of equipment through to the recorder output is desirable. Portable calibration standards are invaluable for this purpose.

e. Air-ground equipment compatibility determination is very important. That is to say, for best results the theodolite, telemetry and airborne equipment should be exercised and calibration reference obtained. For example, with a glide slope receiver zero CDI value fed to the differential amplifier, the two traces, i.e., theodolite and differential amplifier output, should present a type of mirrored trace effect as the equation Differential Amplifier value = CDI minus the theodolite is mechanized.

f. Proper warmup and voltage stabilization for equipment is essential for good data.

g. Good agreement between data from different aircraft is obtainable as demonstrated by the Miami flight checks. Some discrepancies are evident in the data and because of the repeatabilities, it is concluded that theodolite indexing or calibration was the problem.

27 L MIA

TH - OM = 27,140'
TH - B = 3,500'
TH - C = 823'
θ = 2.90°
Commissioned Path Angle

27 R VIN

TH - OM = 24,475'
TH - B = 3,500'
TH - C = 846'
θ = 3.00°

Chart range DC-3 was ± 75 μA

Chart range BE-35 was ± 50 μA

Average chart Length TH - OM for DC-3 was 25"

Average chart Length TH - OM for BE-35 was 20"

Chart speeds was 12"/min. for both recorders

Nominal A/S DC-3 120
Nominal A/S BE-35 130

Flight tests run between 9/21/73 and 9/27/73.

Table 4-6. Reference Data.

FACILITY: Miami Glide Slope (Null Reference) 27R

Normal Facility Data Runs: 2,3,4

Summary Averages

Average Path Displacement -	Zone 2	DC-3	3.01°	BE-35	3.11°	
Maximum Deviations -	Zone 2	DC-3	+ ~	(~)	-29	(4,800')
		BE-35	+ 38	(6,600')	+ ~	
	Zone 3	DC-3	~	(2,900')	-29	(~)
		BE-35	+ 46	(1,600')	+11	(2,000')
Average Path Displacement -	Zone 2	DC-3	2.97°, 3.04°, 3.02°			
		BE-35	3.14°, 3.08°, 3.12°			

Maximum course deviations (differential amplifier trace)

Zone 2	DC-3	+26	(16,100')	- 26	(5,900')
	BE-35	+42	(5,700')	+ 12	(4,400')
	DC-3	+12	(4,600')	- 32	(3,500')
	BE-35	+32	(5,600')	+ 2	(11,700')
	DC-3	+14	(21,300')	- 30	(5,000')
	BE-35	+40	(8,500')	+ 3	(7,400')
Zone 3	DC-3	+ 7	(2,600')	- 22	(3,300')
	BE-35	+50	(2,200')	+ 10	(2,600')
	DC-3	+ 6	(3,200')	- 32	(3,500')
	BE-35	+41	(1,600')	+ 8	(1,100')
	DC-3	- 7	(2,800')	- 34	(1,500')
	BE-35	+48	(1,600')	+14	(2,200')

Table 4-7. Experimental Data.

FACILITY: Miami Glide Slope (Null Reference) 27R

Normal Facility Data Runs: 2,3,4

Summary Averages

Average Path Displacement -	Zone 2	DC-3	3.01°	BE-35	3.11°	
Maximum Deviations -	Zone 2	DC-3	+ ~	(~)	-29	(4,800')
		BE-35	+ 38	(6,600')	+ ~	
	Zone 3	DC-3	~	(2,900')	-29	(~)
		BE-35	+ 46	(1,600')	+11	(2,000')
Average Path Displacement -	Zone 2	DC-3	2.97°, 3.04°, 3.02°			
		BE-35	3.14°, 3.08°, 3.12°			

Maximum course deviations (differential amplifier trace)

Zone 2	DC-3	+26	(16,100')	- 26	(5,900')
	BE-35	+42	(5,700')	+ 12	(4,400')
	DC-3	+12	(4,600')	- 32	(3,500')
	BE-35	+32	(5,600')	+ 2	(11,700')
	DC-3	+14	(21,300')	- 30	(5,000')
	BE-35	+40	(8,500')	+ 3	(7,400')
Zone 3	DC-3	+ 7	(2,600')	- 22	(3,300')
	BE-35	+50	(2,200')	+ 10	(2,600')
	DC-3	+ 6	(3,200')	- 32	(3,500')
	BE-35	+41	(1,600')	+ 8	(1,100')
	DC-3	- 7	(2,800')	- 34	(1,500')
	BE-35	+48	(1,600')	+14	(2,200')

Table 4-7. Experimental Data.

FACILITY: Miami Glide Slope (Null Reference) 27R

B-747 Position #2 Data Runs 21,22,23

Summary Averages

Average Path Displacement -	Zone 2	DC-3	2.98°	BE-35	2.98°	
Maximum Deviations -	Zone 2	DC-3	+ 30	(22,000')	- 20	(~)
		BE-35	+ 28*	(23,000')	-25	(11,700')
		DC-3	~	(2,500')	-19	(1,600')
		BE-35	~		-15	(1,900')
Average Path Displacement -	Zone 2	DC-3	2.98°, 2.99°, 2.96°			
		BE-35	2.98°, 2.98°, 2.99°			

Maximum course deviations (differential amplifier trace)

Zone 2	DC-3	+ 26	(24,000')	-24	(4,400')
	BE-35	+ 31	(24,000')	-28	(11,000')
	DC-3	+ 30	(22,000')	-22	(9,000')
	BE-35	+ 19	(15,700')	-23	(7,800')
	DC-3	+ 34	(21,000')	-15	(9,100')
	BE-35	+ 24	(22,000')	-22	(12,400')
Zone 3	DC-3	+ 10	(2,500')	-23	(1,800')
	BE-35	+ 14	(2,600')	-16	(1,800')
	DC-3	+ 4	(2,500')	-20	(1,400')
	BE-35	+ 5	(2,800')	-15	(1,800')
	DC-3	+ 22	(2,500')	-15	(1,500')
	BE-35	+ 22	(1,300')	-13	(2,000')

* Run 9 not included.

Table 4-7. Continued

FACILITY: Miami Glide Slope (Null Reference) 27R

B-747 Position #3 Data Runs: 18, 19, 20; 5, 6, 7

Summary Averages

Actual Path Angle - Zone 2 DC-3: 2.97° BE-35: 2.97°

Maximum Deviations

Zone 2	DC-3	+ 24 μA	(14,500')	- 28 μA	(4,200')
	BE-35	+ ~	(~)	- 23 μA	(6,200')
Zone 3	DC-3	+ 19 μA	(2,400')	- 30 μA	(3,500')
	BE-35	+ 23 μA	(2,500')	- 17 μA	(3,300')

Measured Actual Path Angle - Zone 2 DC-3 2.98°, 2.96°, 2.97°

BE-35 2.97°, 2.99°, 2.95°

Maximum Course Deviations (*differential amplifier trace*)

Zone 2	DC-3	+ 23 μA	(14,500')	- 34 μA	(3,500')
	BE-35	+ 23 μA	(17,100')	- 29 μA	(6,100')
	DC-3	+ 23 μA	(16,400')	- 23 μA	(3,500')
	BE-35	+ 16 μA	(8,200')	- 14 μA	(6,700')
	DC-3	+ 26 μA	(12,700')	- 27 μA	(5,600')
	BE-35	+ 36 μA	(3,800')	- 25 μA	(5,700')
	DC-3	+ 20 μA	(2,500')	- 34 μA	(3,500')
	BE-35	+ 20 μA	(2,100')	- 20 μA	(3,300')
	DC-3	+ 19 μA	(2,500')	-23 μA	(3,500')
	BE-35	+ 25	(2,500')	-14	(3,200')
	DC-3	+ 5 μA	(2,100')	- 34 μA	(2,200')
	BE-35	+ 25 μA	(3,000')	- 16 μA	(3,400')

Table 4-7. Continued

FACILITY: Miami Glide Slope (Null Reference) 27L

B-747 Position #8 Data Runs: 48,49,50

Summary Averages

Average Path Displacement - Zone 2 DC-3: 2.96° BE-35: 2.98°

Maximum Deviations -	Zone 2	DC-3	+ 13	(6,300')	- 33	(16,800')
		BE-35	+ ~	(~)	- 41	(15,400')
	Zone 3	DC-3	+ 26	(920')	- ~	
		BE-35	+ ~	(920')	- 16	(2,800')

Average Path Displacement - Zone 2 DC-3 2.96°, 2.95°, 2.96°

BE-35 2.98°, 2.98°, 2.98°

Maximum Course Deviations (differential amplifier trace)

Zone 2	DC-3	+ 12	(6,200')	-33	(17,300')
	BE-35	+ 13	(5,400')	-40	(15,700')
	DC-3	+ 12	(6,000')	-33	(16,800')
	BE-35	+ 5	(4,200')	-42	(15,400')
	DC-3	+ 15	(6,700')	-34	(16,400')
	BE-35	+ 17	(5,600')	-41	(15,100')
Zone 3	DC-3	+ 30	(850')	- 5	(2,600')
	BE-35	+ 31	(1,000')	- 13	(3,000')
	DC-3	+ 28	(950')	- 10	(1,400')
	BE-35	+ 18	(900')	- 17	(2,700')
	DC-3	+ 21	(950')	- 12	(1,400')
	BE-35	+ 18	(850')	- 18	(2,800')

Table 4-7. Continued

FACILITY: Miami Localizer 27 R

Normal Facility Data Runs: 7, 8, 9

Summary Averages

Average Path Displacement -	Zone 2	DC-3: -.07	Be-35: -.06		
Maximum Deviations -	Zone 2	DC-3	- 12	(~) - 4	(6,700')
		BE-35	+ 12	(4,200') - 4	(5,500')
	Zone 3	DC-3	+ 14	(1,300') - 3	(~)
		BE-35	+ 21	(1,900') -	(~)
Average Path Displacement -	Zone 2	DC-3	-.05, -.05, -.10		
		BE-35	~, -.07, -.05		

Maximum Course Deviations (differential amplifier trace)

Zone 2	DC-3 BE-35	+ 11	(4,200')	- 7	(6,800')
	DC-3	+ 11	(9,000')	- 3	(6,000')
	BE-35	+ 14	(3,600')	- 4	(6,400')
	DC-3	+ 15	(6,400')	- 1	(7,400')
	BE-35	+ 11	(4,700')	- 5	(4,500')
Zone 3	DC-3	+ 12	(1,500')	- 3	(2,100')
	DC-3	+ 11	(990')	-5	(1,900')
	BE-35	+ 19	(2,150')	-2	(2,000')
	DC-3	+ 19	(1,500')	-0	(1,100')
	BE-35	+ 24	(1,700')	-11	(1,100')

Table 4-7. Continued

FACILITY: Miami Localizer 27R

B-747 Position #1 Data Runs: 28,29,30; 3,4,5

Summary Averages

Average Path Displacement - Zone 2 DC-3 +.14° BE-35 + 14°
(+ = Shift to right as seen from approaching aircraft.)

Maximum Deviations

Zone 2 DC-3 + 7.5μA (~) + 18μA (7,300')

BE-35 + 4 (16,400) + 23μA (7,200')

Zone 3 DC-3 + ~ (~) - ~ (~)

BE-35 + ~ (~) - ~ (~)

Average Path Displacement - Zone 2 DC-3 +.15, ~, + .14

BE-35 + .09, + .15, + .19

Maximum Course Deviations (differential amplifier trace)

Zone 2	DC-3	-7.5 μA	(3,600')	-18μA	(6,500')
	BE-35	- 4 μA	(17,000')	+20μA	(7,700')
	DC-3	+ ~	(~)	- ~	(~)
	BE-35	+ 5 μA	(16,500')	+21	(7,000')
	DC-3	+7.5μA	(19,900')	+18μA	(8,000')
	BE-35	+10 μA	(15,700')	+27μA	(7,000')
Zone 3	DC-3	+ 4	(3,100')	+11μA	(2,200')
	BE-35	+ ~		- ~	(~)
	DC-3	+ ~	(~)	- ~	(~)
	BE-35	+ ~		- ~	(~)
	DC-3	+ ~	(~)	- ~	(~)
	BE-35	+ ~		- ~	(~)

Table 4-7. Continued

FACILITY: Miami Localizer 27 R

B-747 Position #2 Data Runs: 31, 32, 33

Summary Averages

Average Path Displacement	- Zone 2	DC-3	-0.43°	BE-35	-.31°	
Maximum Deviations	- Zone 2	DC-3	+ 47 (5,600')	+ 31	(22,000')	
		BE-35	+ 35 (4,900')	+ 19	(~)	
	Zone 3	DC-3	+ 51 (1,700')	+ 38	(3,000')	
		BE-35	+ 47 (1,200')	+ 18	(1,100')	
Average Path Displacement	Zone 2	DC-3	-.45°, -.42, -.42°			
		BE-35	-.25°, -.35°, -.32°			

Maximum Course Deviations (differential amplifier trace)

Zone 2	DC-3	+ 48	(7,600')	+ 30	(24,000')
	BE-35	+ 29	(5,200')	+ 15	(7,500')
	DC-3	+ 46	(5,200')	+ 31	(20,500')
	BE-35	+ 38	(5,000')	+ 21	(4,000')
	DC-3	+ 47	(4,100')	+ 32	(21,300')
	BE-35	+ 38	(4,500')	+22	(14,700')
Zone 3	DC-3	+ 50	(1,360')	+ 40	(2,300')
	BE-35	+ 41	(1,000')	+ 11	(1,450')
	DC-3	+ 51	(2,700')	+ 37	(3,400')
	BE-35	+ 48	(860')	+ 22	(970')
	DC-3	+ 52	(1,000')	+ 37	(3,300')
	BE-35	+ 51	(1,800')	+ 22	(960')

Table 4-7. Continued

FACILITY: Miami Localizer 27 R

B-747 Position #5 Data Runs: 51,52,53, 11,12

Summary Averages

Average Path Displacement	-	Zone 2	DC-3	-.17°	BE-35	-.06°	
Maximum Deviations	-	Zone 2	DC-3	+ 23	(4,100')	(~)	
			BE-35	+ 10	(~)	(~)	
		Zone 3	DC-3	+ 30	(1,100')	+ 14	(16,000')
			BE-35	+ 14	(990')	- 3	(~)
Average Path Displacement	-	Zone 2	DC-3	-.17°, -.19°, -.16°			
			BE-35	-.07°, -.05°			

Maximum Course Deviations (differential amplifier trace)

Zone 2	DC-3	+ 23	(4,000')	+ 9	(6,200')
	BE-35	+ 11	(9,100')	- 1	(6,500')
	DC-3	+ 22	(4,200')	+ 11	(6,600')
	BE-35	+ 9	(3,600')	- 6	(4,800')
	DC-3	+ 23	(4,200')	+ 4	(22,600')
Zone 3	DC-3	+ 34	(1,100')	+ 15	(1,300')
	BE-35	+ 13	(930')	- 2	(2,700')
	DC-3	+ 28	(1,100')	+ 14	(1,700')
		+ 15	(1,050')	- 4	(1,200')
	DC-3	+ 28	(1,100')	+ 12	(1,700')

Table 4-7. Continued

I. References and Bibliography for Section IV.

References

[1] Ramo, Simon, and John R. Whinnery, Fields and Waves in Modern Radio, Second Edition, John Wiley and Sons, Inc., New York, New York, 1953.

[2] Johnson, Walter C., Transmission Lines and Networks, McGraw-Hill, New York, New York, 1950.

[3] Moore, Richard K., Traveling-Wave Engineering, McGraw-Hill, New York, New York, 1960.

[4] Harding, Russ, "Use Pulse Instead of CW Signals to Analyze Discontinuities in High-Frequency Circuits. Time-Domain Reflectometry Can Pinpoint the Problem", Electronic Design, Vol. 22, No. 11, pp.60-67, May 24, 1974.

[5] Fine, Frederick, Low Cost Localizer System, Scanwell Laboratories, Inc., Springfield, Virginia, August, 1968.

[6] "Improved Equipment Arrangements for ARTC Centers," FAA Report No. RD-65-27, March 1965: from the list of conclusions, "A TV monitor, used to display meteorological, navigational, and other pertinent information, was recognized as a necessary controller aid."

[7] "Application of Balanced Lines, Tone Signaling, and Microprocessor Control Techniques to a Category III Instrument Landing System," FAA Report No. FAA-RD-76-24, February, 1976.

[8] Microcomputer Associates, Inc., 2489 Scott Boulevard, Santa Clara, Calif. 95050, Phone 408-247-8940.

[9] Information gained from conversation with Mr. John Miyasaki of Airways Facilities, Chicago O'Hare sector during his visit to Ohio University on May 4 and 5, 1976.

[10] EIA Standard, Electronic Industries Association, 2001 Eye Street, N.W., Washington, D.C. 20006

[11] Industrial Data Terminals, 100 E. Broad St., Columbus, Ohio, Phone 614-461-5832.

[12] "Experimental Validation of Boeing 747 ILS Signal Scattering Calculations for Critical Area Determination," Robert A. Rondini, Richard H. McFarland, SRDS Report FAA-RD-74-57, Federal Aviation Administration, January, 1974.

Bibliography

"Cable Testing with Time Domain Reflectometry," Application Note 67, Hewlett-Packard, Colorado Springs, Colorado.

"1502 Time Domain Reflectometer Instruction Manual," Tektronix, Inc., Beaverton, Oregon 97077.

Ivanov, Ivan P. and John D. Trudel, "TDR for Cable Testing," TDR Cable Tester Application Note 25M1.0, Tektronix, Inc., Beaverton, Oregon 97077.

Moffitt, Lee R., "Selected Articles on Time Domain Reflectometry Applications," Application Note 75, March, 1966, Reprint from EDN 1964 Test Instrument Issue, Hewlett-Packard, Colorado Springs, Colorado.

"Time Domain Reflectometry," Application Note 62, Hewlett-Packard Company, Colorado Springs, Colorado.

"Time Domain Reflectometry-Made Simple," Nelson Hibbs, 18 Minute Videotape, Tektronix, Inc., Beaverton, Oregon 97077.

VHF Transmission Lines, Manual FV-110-1, FAA Aeronautical Center, Oklahoma City, Oklahoma, July, 1975.

V. LOCALIZERS

A. General. The following localizer systems were flight and ground-tested:

1. Alford 14-element two-frequency O-ring traveling-wave system.
2. 12-element V-ring with Wilcox 14-element distribution box and with Alford 12-element distribution box.
3. Alford 14/6 array.
4. Watts-Hollins small aperature slotted cable array.
5. Watts-Hollins medium aperature slotted cable array.

These tests are described and the results are presented in the following sections.

B. Alford 14-Element Two-Frequency Localizer Systems Tests.

1. Background. During the period between December 2 and December 20, 1974, the Alford 14-element, two-frequency localizer system was established on runway 9L at the Ohio University Test Site, New Tamiami Airport, and test flown. This system combines the functions of the typical discrete course and clearance arrays into one physical array of 14 traveling wave "O" ring-type antennas recently developed by the Alford Engineering Company. Distribution of the carrier and sideband signals for the two-frequency system is through the use of a special distribution box also designed, built, and furnished by the Alford Company.

The principal objective of the tests was to determine if full benefits of a two-frequency system could be obtained using one set of localizer antennas. Of the 14-element array used in these tests, the center six-elements served as a clearance array giving coverage out to ± 35°, whereas the complete 14-element array was energized to 8 KHz above the clearance carrier to produce the course signal. See Figure 5-1.

Phase and amplitude readings of signals into and out of the distribution boxes and into and out of the antennas were made considering both the course and clearance array portions of the system. This particular array is monitored in part by an integral technique whereby residual energy at the end of the traveling wave elements is used for sample purposes. These monitor samples were also recorded.

Flight recordings were made using a Beechcraft 35 aircraft. A Narco Nav 11 receiver for RF/IF amplification was used with a specially designed audio processor to permit improved symmetry and DDM response especially in regions where DDM greater than .155 would be expected. Response characteristics of this receiver unit are given in Table 5-1 . One may note by reviewing the material in the table that the DDM is observed to be more symmetrical and to greater limits with the Ohio University design than with the Collins 51R-3, an old flight inspection standard.

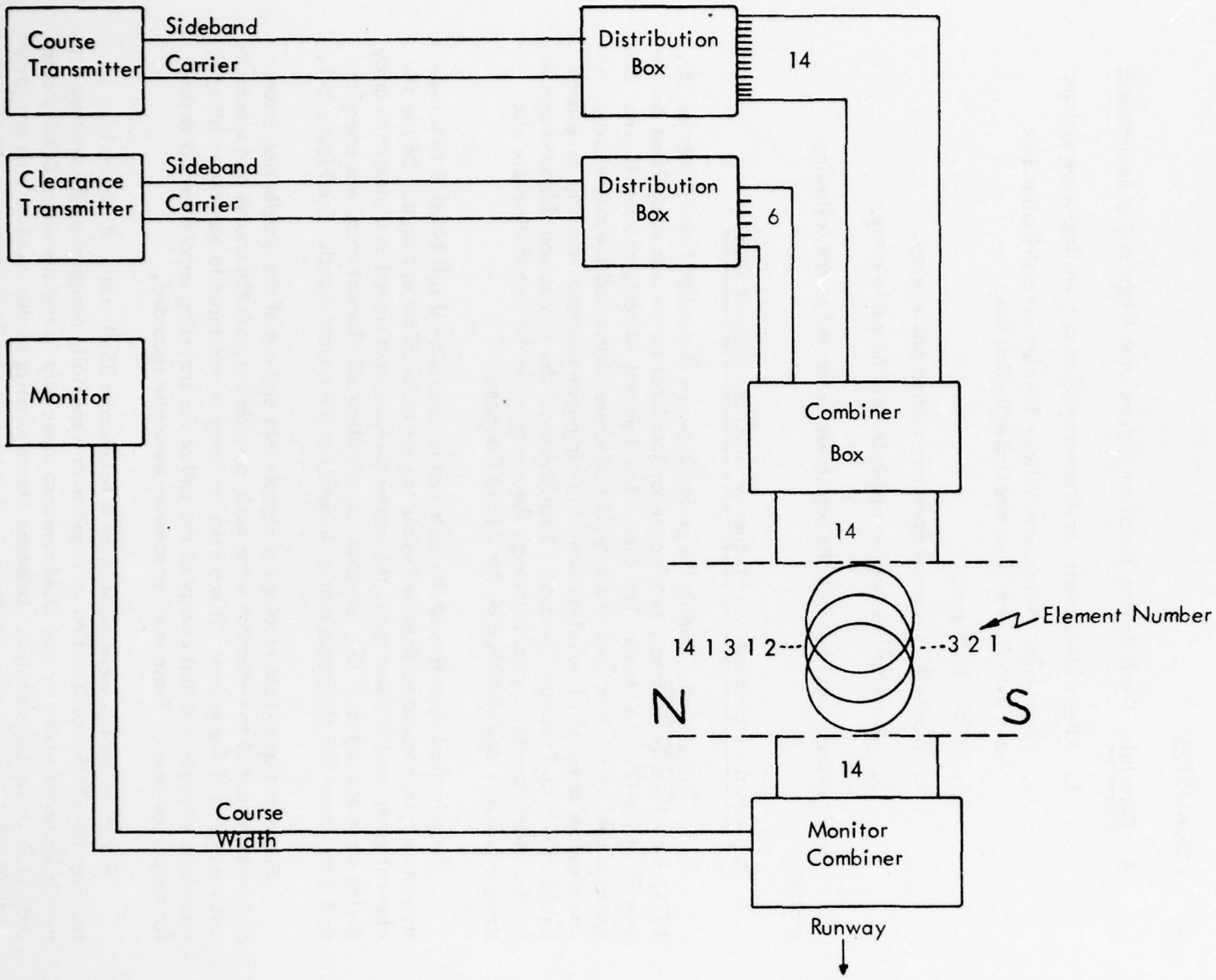

Figure 5-1. Schematic of Localizer Distribution System for Alford Two-Frequency Array.

	479S-3 Tone Ratio (dB)	211A Theoretical	Test Setup OU Processor	1K Microvolt 51R-3 (microampere)
90 Hz	7.5	172.36	170	168
	4.0	89.92	90	90
	2.0	44.66	46	47
	.5	11.14	12	11
	0.0	0.0	2 (90)	1 (150)
150 Hz	.5	11.14	10	14
	2.0	44.66	43	48
	4.0	89.92	90	90
	7.5	112.36	168	160
40% Mod 150 Hz Only	.4 ddm	387	335	270
40% Mod 90 Hz Only	.4 ddm	387	340	280

Table 5-1. Data Illustrating Localizer Processor Relative Performance of Collins 51R-3 and Ohio University Processor Working With a Narco NAV 11.

2. Ground-Based Measurements. The Wilcox Solid State transmitters at Tamiami were set and tuned at 109.7 MHz - 4 KHz for the clearance and 109.7 MHz + 4 KHz for the course. Signal levels were measured and recorded for specific points in the distribution system. Tables 5-2, 5-3, and 5-4 summarize these relative distributions.

3. Flight Data. Flight data was taken on the radio frequency energy distributions of the carrier and sideband feeds for both the course and clearance portions of the array. Course widths of 4 degrees and 8 degrees were set for the course and clearance portions respectively and the combined system performance then observed. Orbital data was collected at 6 miles, 1500 feet elevation, through a ± 45 degree sector about the centerline. Usable distance was checked in accordance with the U.S. Flight Inspection Manual, Paragraph 217.3308 for Sectors 1 and 2 as defined by the manual to be ± 10 degrees and 10-35 degrees either side, respectively. Several low approaches were made to check flyability. All flight data taken at 6 miles or closer was collected using a theodolite with telemetry to the aircraft when appropriate.

Representative samples of the flight data are shown in Figures 5-2, 5-3, and 5-4 . From these, several observations can be made. Records taken during orbits indicate a slight asymmetry but within tolerances. The course alignment was shifted 0.17 degrees. Averaging flight data taken in both directions reduces this into the 150 Hz side. This offset, of course, can be corrected easily by tone balance adjustment. Figure 5-5 shows a 6-mile, 1500 ft. AGL orbit.

Flyability was excellent with the records indicating ± 2 microampere noise. This continued through rollout on the runway. See Figures 5-6 and 5-7 .

4. Conclusions. The following conclusions have been reached concerning the performance of the Alford, 14-element, two-frequency localizer array using traveling wave, "O" ring-type elements. These conclusions are based on both ground-based and flight measurements made at the Tamiami Site.

a. The flyability of the path produced by the Alford localizer is excellent (± 2 microamperes noise).

b. The two-frequency Alford localizer performs well using only one array of 14-elements, all 14-elements radiating the course signal with the center six antennas also transmitting the clearance signal.

c. Independent performance of the course portion and clearance portion of the array can be observed easily and setting made in a normal fashion. The simultaneous operation of the two portions of the array then becomes straightforward. The weighting of the path width in the ± 2.5 degree section seems to be 6.5:1 in favor of the course array.

d. The symmetry of the path observed was in tolerance but not perfect. Ground readings indicate that a slight defect exists in the Number 8 line of the 14-element distribution box.

AD-A074 425 OHIO UNIV ATHENS DEPT OF ELECTRICAL ENGINEERING F/G 17/7
IN-SERVICE IMPROVEMENTS AND MODERNIZATION OF ALL COMPONENTS OF --ETC(U)
JUL 78 DOT-FA75WA-3549
UNCLASSIFIED EER-35-1 FAA-RD-78-112-1 NL

4 OF 8
AD
A074425

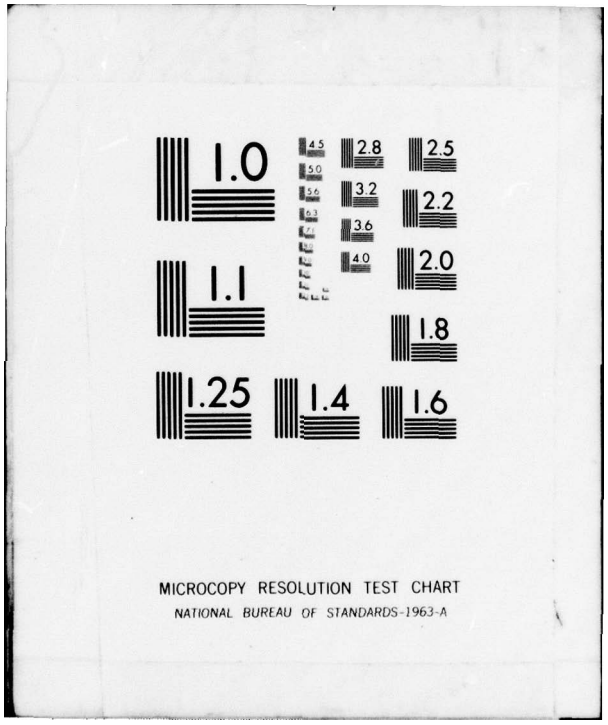
1.0
1.1
1.25
1.4
1.6
1.8
2.0
2.2
2.5
2.8
3.2
3.6
4.0
4.5
5.0
5.6
6.3
MICROCOPY RESOLUTION TEST CHART
NATIONAL BUREAU OF STANDARDS-1963-A

OUT OF SIX ELEMENT DISTRIBUTION BOX			OUT OF COMBINER BOX		
	CARRIER	SIDEBAND		CARRIER	SIDEBAND
Port	Decibels	Decibels	Port	Decibels	Decibels
1	-15.0	-16.5	5	-15.2	-17.0
2	-----	-9.5	6	-----	-10.0
3	0.0	0.0	7	0.0	0.0
4	0.0	0.0	8	-0.4	-0.5
5	-----	-9.5	9	-----	-10.4
6	-15.0	-17.5	10	-15.0	-17.0
OUT OF ANTENNAS AS SEEN BY HANG-ON METER			OUT OF ANTENNAS AS SEEN AT INPUT OF MONITOR BOX		
	CARRIER	SIDEBAND		CARRIER	SIDEBAND
Port	Decibels	Decibels		Decibels	Decibels
5	-14.0	-18.0		-14.5	-18.8
6	-15.0	-15.0		-19.5	-14.4
7	0.0	-1.0		0.0	0.0
8	-0.5	0.0		-1.4	-0.2
9	-16.0	-16.0		-18.2	-15.0
10	-14.0	-21.0		-14.4	-18.6

Table 5-2. Clearance System.

Antennas	CARRIER INPUT PORT FED								SIDEBAND INPUT PORT FED			
	Output Disbribution Box		Output Combiner Box		Monitor End of Antenna (Hang-on Meter)		Input Monitor Box		Output Disbribution Box	Output Combiner Box	Antenna (Hang-on Meter)	Input Monitor Box
	Amp. dB	Phase Degrees	Amp. dB	Phase Degrees	Amp. dB	Phase Degrees	Amp. dB	Phase Degrees	Amp. dB	Amp. dB	Amp. dB	Amp. dB
1	-15.7	-0.6	-15.3	-5.1	-14.4	0.0	-17.1	-6.9	-7.0	-8.8	-7.0	-8.2
2	-15.2	+2.4	-15.6	-1.2	-16.5	+6.0	-18.3	-5.7	-5.0	-5.8	-5.0	-5.7
3	-11.0	-1.8	-11.1	-5.1	-11.5	0.0	-13.1	-2.7	-0.6	-1.3	-0.5	-1.4
4	-5.5	-1.2	-5.6	-0.3	-6.5	-6.0	-6.3	-1.7	0.0	0.0	0.0	0.0
5	-3.5	+0.3	-3.1	+0.6	-4.5	-8.1	-4.0	0.0	0.0	-0.3	0.0	-0.3
6	-0.1	+0.45	0.0	-0.1	0.0	-2.1	0.0	-1.5	-3.0	-4.0	-3.0	-4.0
7	-2.0	+3.0	-1.4	+4.8	-2.5	0.0	-2.0	+7.2	-13.0	-13.5	-13.0	-13.0
8	-3.0	+3.0	-1.9	+6.0	-3.4	+6.0	-3.0	+13.5	-12.0	-13.0	-12.0	-13.6
9*	0.0	-0.9	0.0	+0.7	0.0	+1.2	-0.2	0.0	-3.0	-4.0	-3.0	-4.0
10	-2.8	-1.2	-3.1	+1.8	-3.5	+7.8	-3.8	+4.5	-0.5	-0.6	-0.4	-0.6
11	-5.8	+1.2	-5.8	-1.2	-7.0	-9.0	-5.9	-1.5	-0.2	-0.2	-0.2	-0.2
12	-11.0	-4.05	-11.0	-2.7	-12.6	-1.8	-11.9	+3.0	-1.0	-1.2	-1.0	-1.4
13	-15.8	+1.2	-15.7	-0.9	-16.4	+4.8	-16.2	-0.3	-5.0	-5.5	-5.0	-5.8
14	-16.0	-3.9	-15.3	-0.7	-16.4	+7.8	-16.4	+2.1	-9.0	-8.8	-9.0	-8.8

*Reference Antenna

Table 5-3. Course System.

OUT OF ANTENNAS AS SEEN AT INPUT OF MONITOR BOX				
Antenna	Probe Inserted Between Antenna Line and Monitor Box Input Port		Probe Inserted At End of Antenna Line Into Dummy Load - Monitor Box Input Port Also Dummied	
	Amp. (dB)	Phase	Amp. (dB)	Phase
1	-17.4	-13.0	-15.6	-10.2
2	-18.6	-11.5	-16.5	-7.6
3	-13.3	-8.5	-12.1	-8.8
4	-6.5	-7.8	-5.9	-8.0
5	-4.3	-6.1	-4.0	-7.1
6	-0.2	-7.6	0	-8.8
7*	-2.3	+1.3	-2.1	0
8	-3.3	+7.5	-3.1	+7.0
9	-0.4	-6.2	-0.2	-7.0
10	-4.1	-1.4	-4.1	-2.6
11	-6.1	-7.4	-6.0	-8.0
12	-12.1	-3.0	-12.1	-4.0
13	-16.4	-6.3	-16.2	-5.9
14	-16.6	-4.0	-16.0	-2.2

*Reference Antenna with Line and Associated Port Dummy Loaded

Table 5-4. Course System Carrier Input Fed.

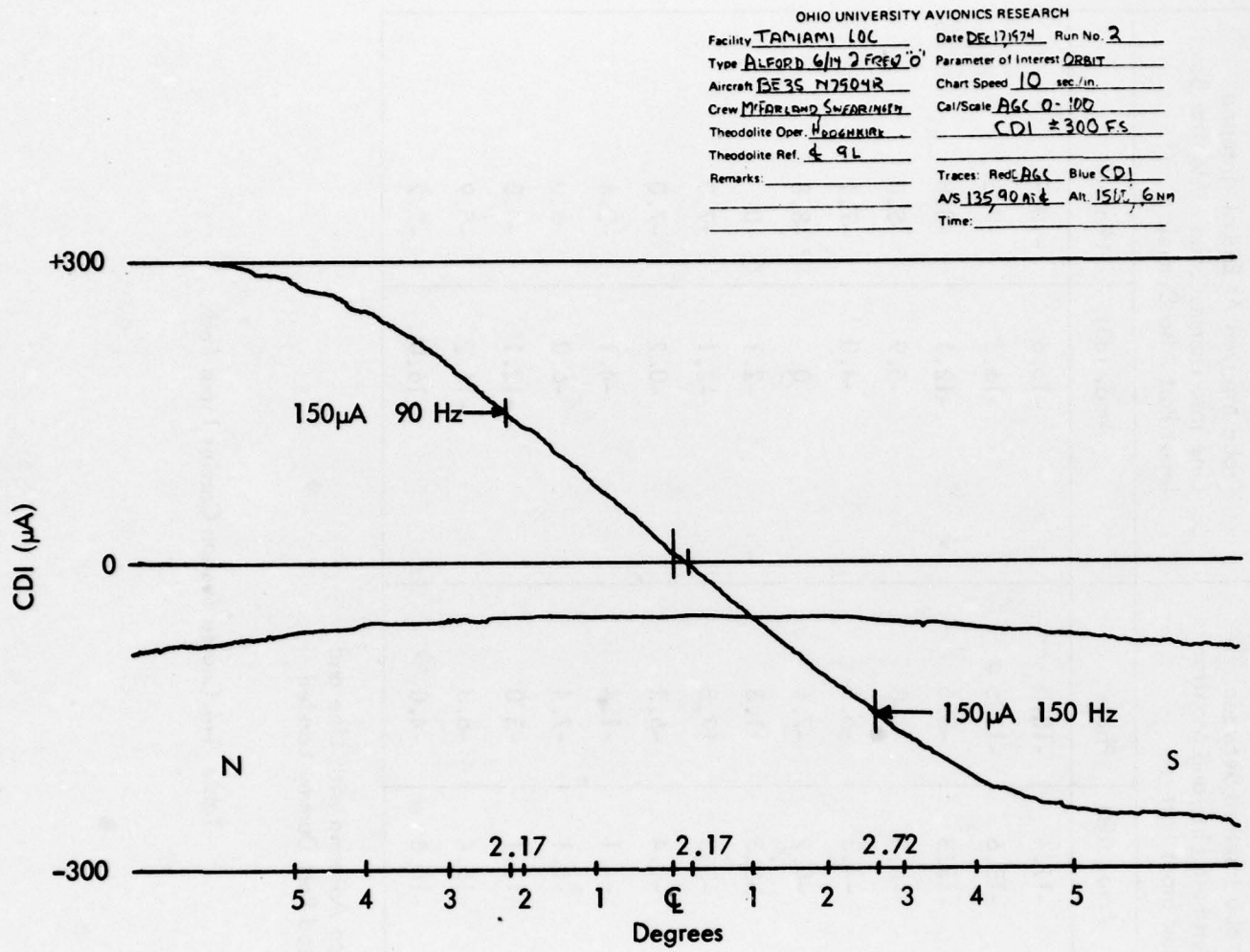

Figure 5-2. Recording of CDI Observed During Orbit, 6 Miles Range, Elevation 1500 Feet. This is for the complete two-frequency array.

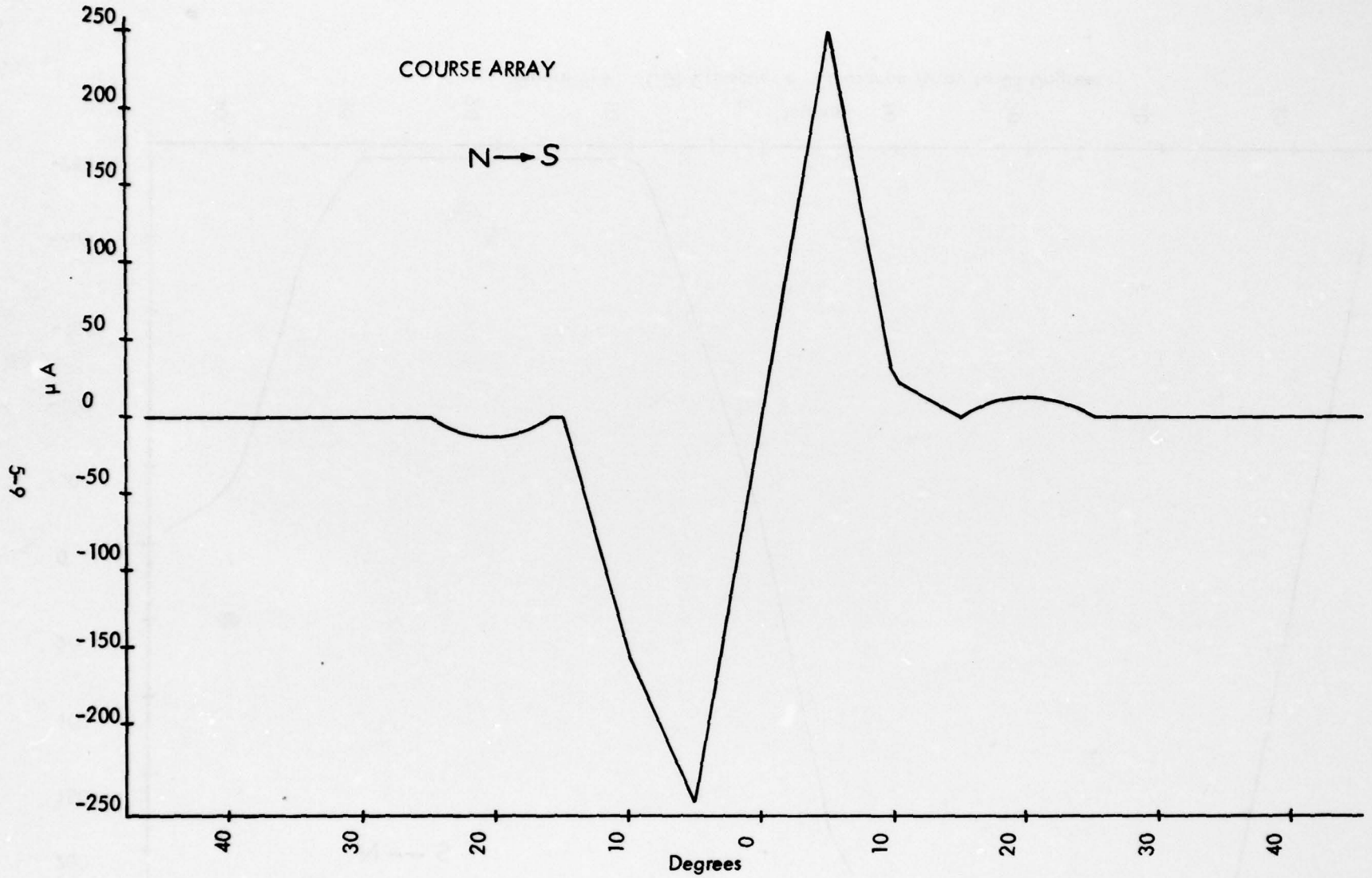

Figure 5-3. CDI Crossover of Course Array to 45 Degrees.

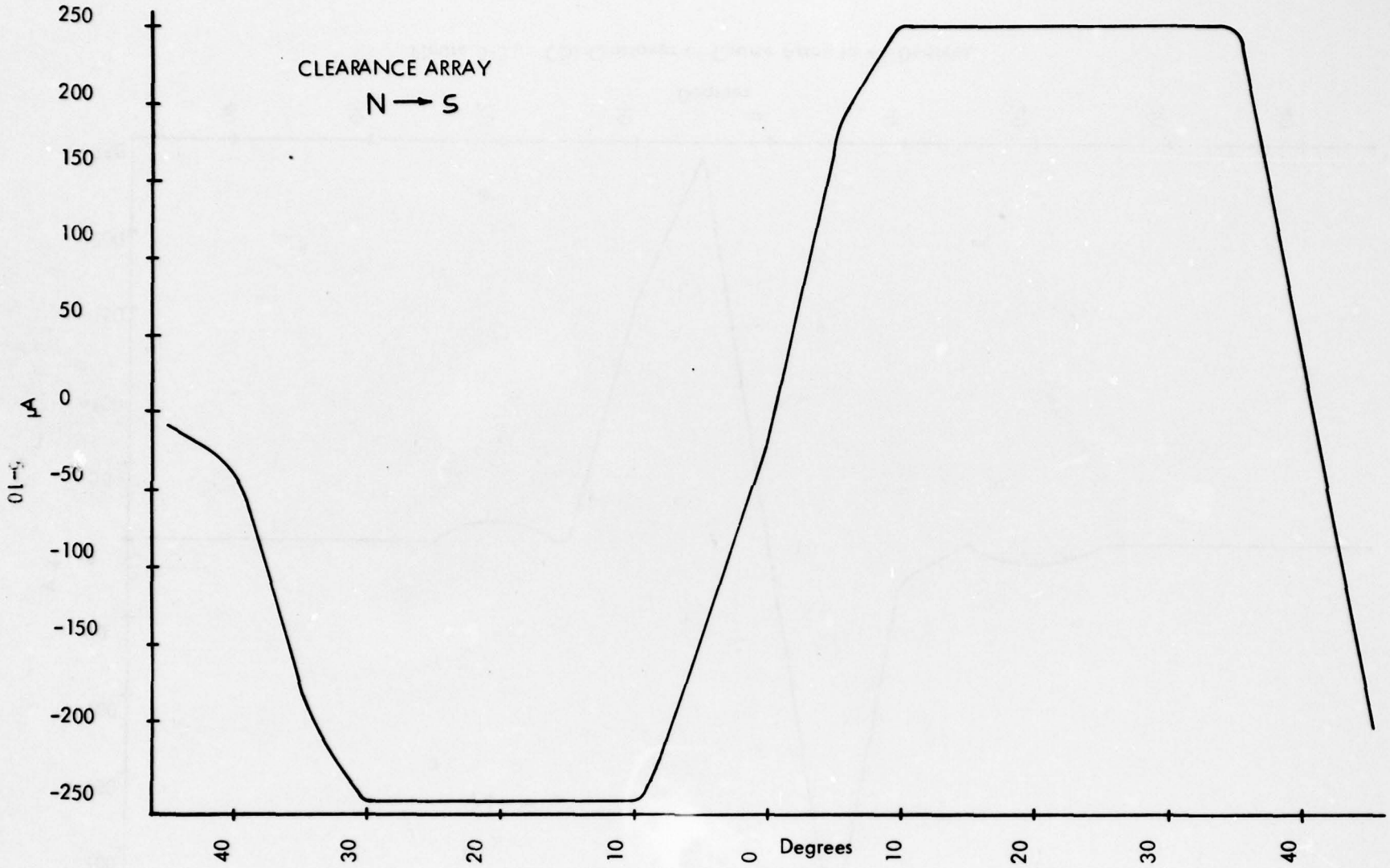

Figure 5-4. CDI Crossover of Clearance Array to 45 Degrees.

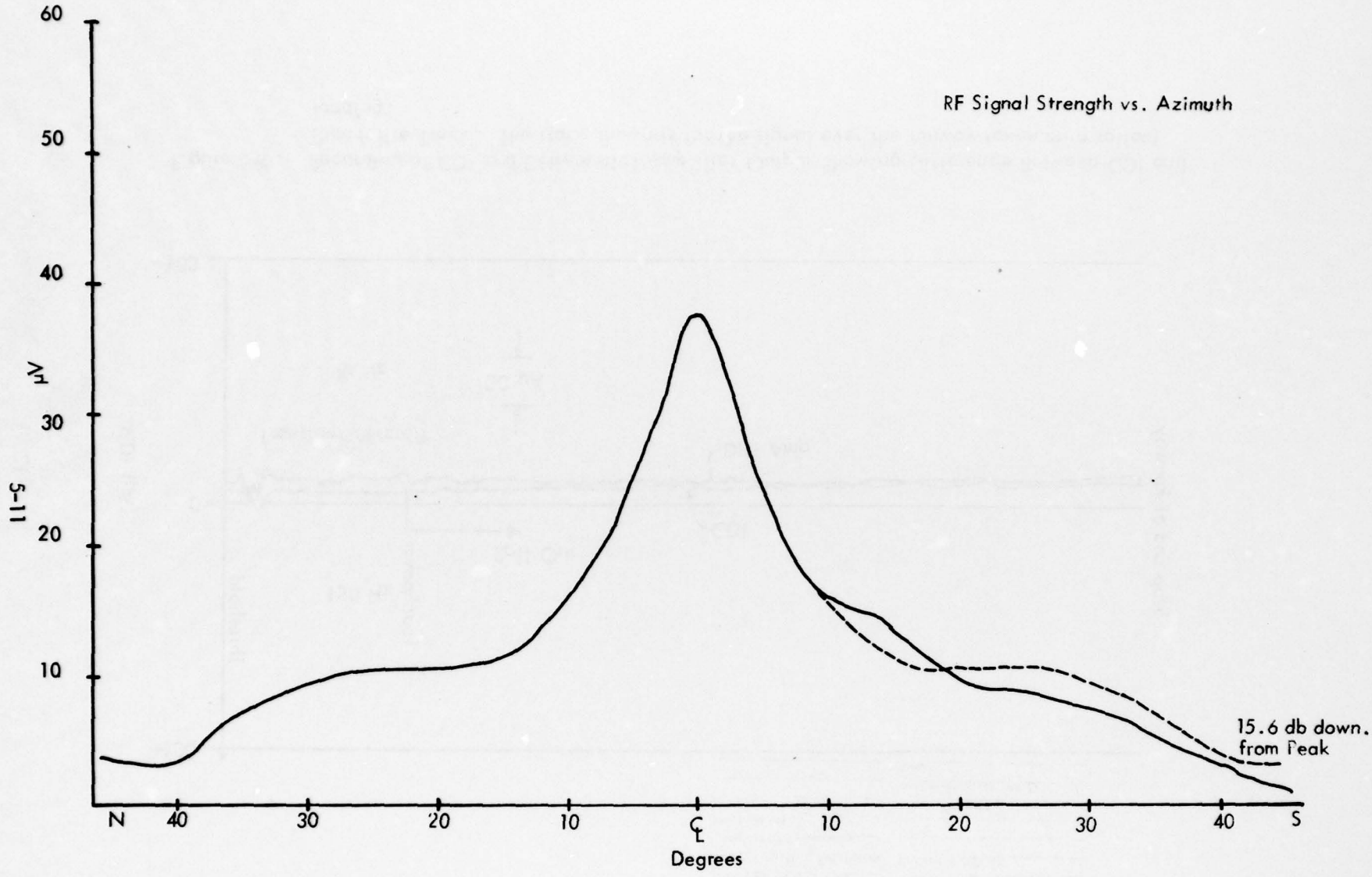

Figure 5-5. Data Taken During 6-Mile Orbit, 1500 Feet Elevation.

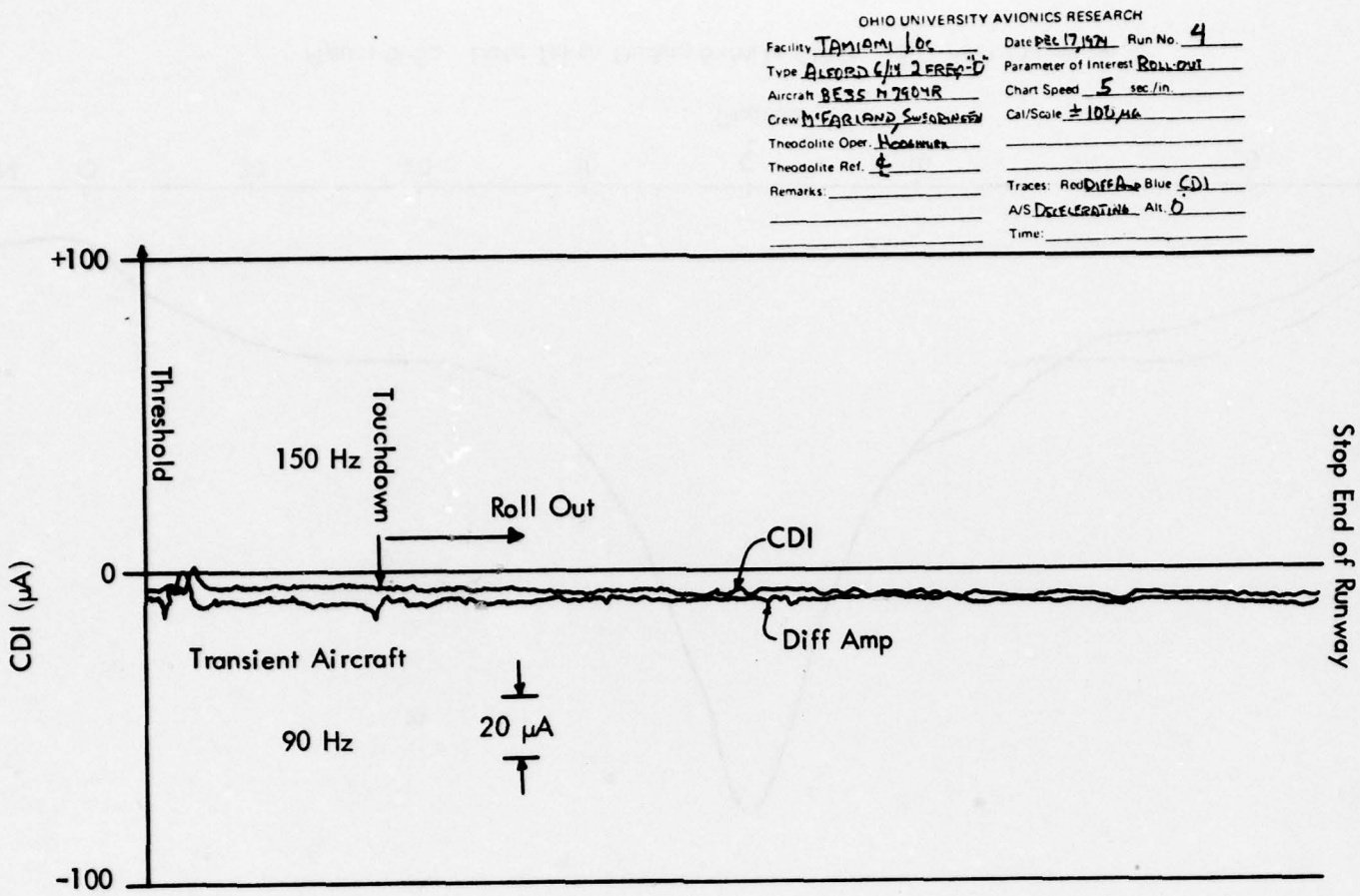

Figure 5-6. Recording of CDI and Differential Amplifier Output Showing Difference Between CDI and Theodolite Track. The trace shown is for the signal over the runway taken on a rollout landing.

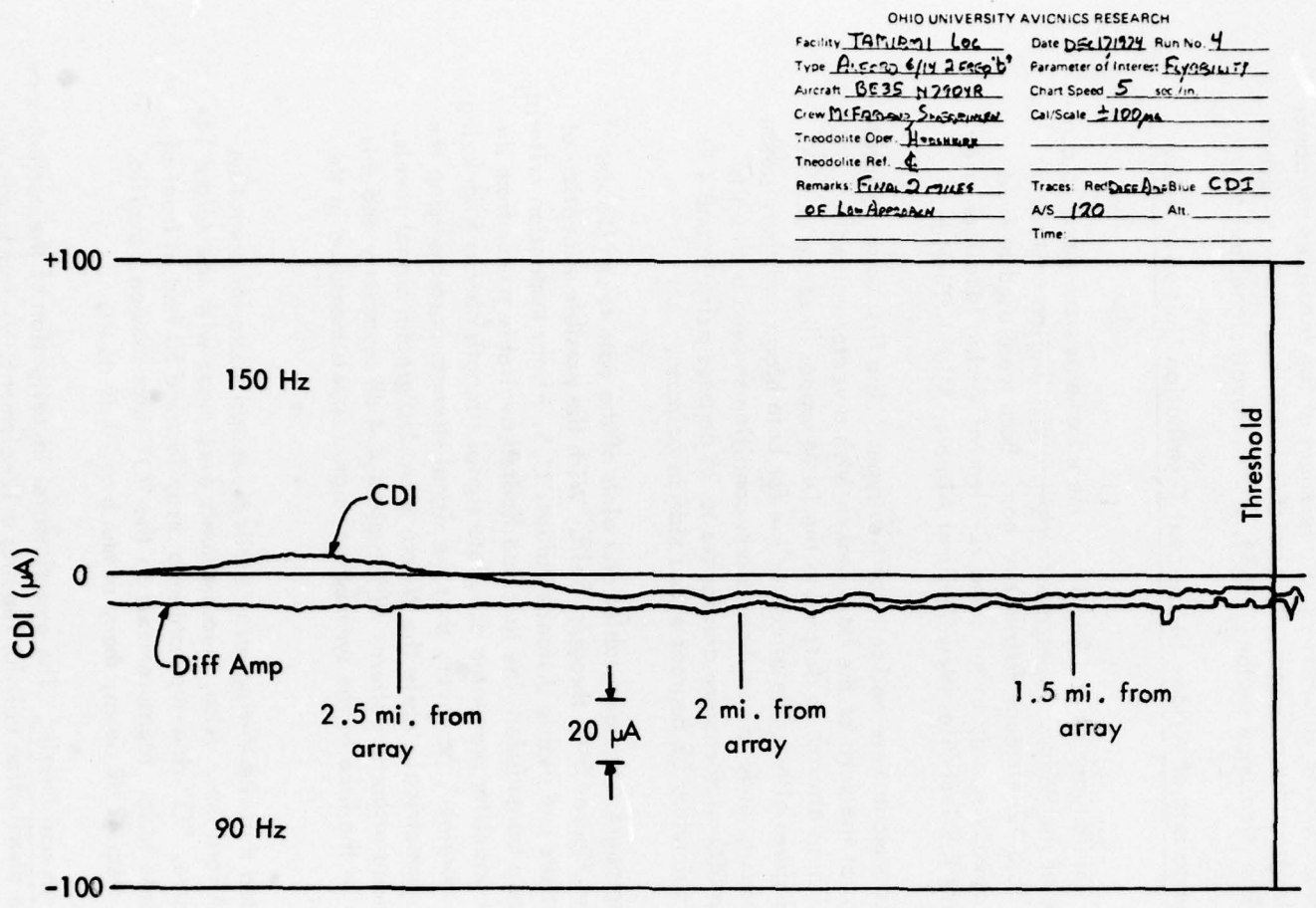

Figure 5-7. Recording of CDI and Differential Amplifier for Approach to Landing Shown in Previous Figure.

e. With 4.75 watts delivered to the course array (the approximate 3 dB-down alarm point for a nominal 10 watt array), a 5 microvolt signal is not available at the edge of 10 degree sector, 18 miles from the array at 1500 feet. The signal is adequate on centerline at this distance and altitude.

f. A 9 dB signal reduction or taper from centerline to 10 degrees reduces the signal below usable values when at the edges of the localizer clearance sector 1. At six miles from the antennas, in spite of a 15 dB taper from centerline to the edge of localizer clearance sector 2 (35°), a 5 microvolt signal exists.

C. Initial Comparison of Wilcox 14-Element Distribution Unit with Alford 12-Element Box.

1. Tests. On January 23 and 24, 1975, measurements were made to compare the performance of the Wilcox 14-element stripline distribution unit for a localizer with the Alford 12-element distribution box. Both were used to feed 111.9 MHz radio frequency energy to the same 12-element V-ring localizer array at the Ohio University ILS Test Site, New Tamiami Airport, Miami, Florida.

The measurements made were basically of two types. The first were complete sets of signal readings at the ports of the boxes taken with a vector voltmeter. The second were orbits with an aircraft to determine the DDM values in space at 1500 feet, 6 miles, ± 45 degrees either side of centerline for both broad and sharp alarm conditions. Measurements made in the sharp alarm condition showed both units produced greater than 300 microampere clearances to 35 degrees azimuth and 150 microamperes to approximately 39 degrees either side in azimuth.

In the following pages are shown tables and plots of the data taken (Tables 5-5 through 5-11 and Figures 5-8 through 5-18. With the possible exception of signal strength limitations and usable distance values, U.S. Flight Inspection criteria appear to be met. Long transmission line runs and limited available power from the solid state localizer transmitter prevented complete signal strength checks from being made. Evidence was obtained, however, that the signal strength patterns using the Alford unit are more symmetrical, while the Wilcox provided greater signal levels. The Wilcox unit provided airborne patterns with typical 4.4 dB asymmetry and this is difficult to explain in the face of the symmetrical signal levels measured in the transmission lines.

It should be noted that the V-ring array earlier was optimized for operation with the 12-element Alford Box. Also, measurements were made with the Alford 14-element, traveling-wave, "O" ring-type antenna array located 50 feet in front of the V-rings used in these tests. Measurements on the "O" rings showed parasitic excitation to be more than 42 dB down, many as much as 70 dB down.

2. Conclusions and Results. The experimental investigation of the performance of the Wilcox stripline distribution unit for feeding a 12-element, V-ring localizer

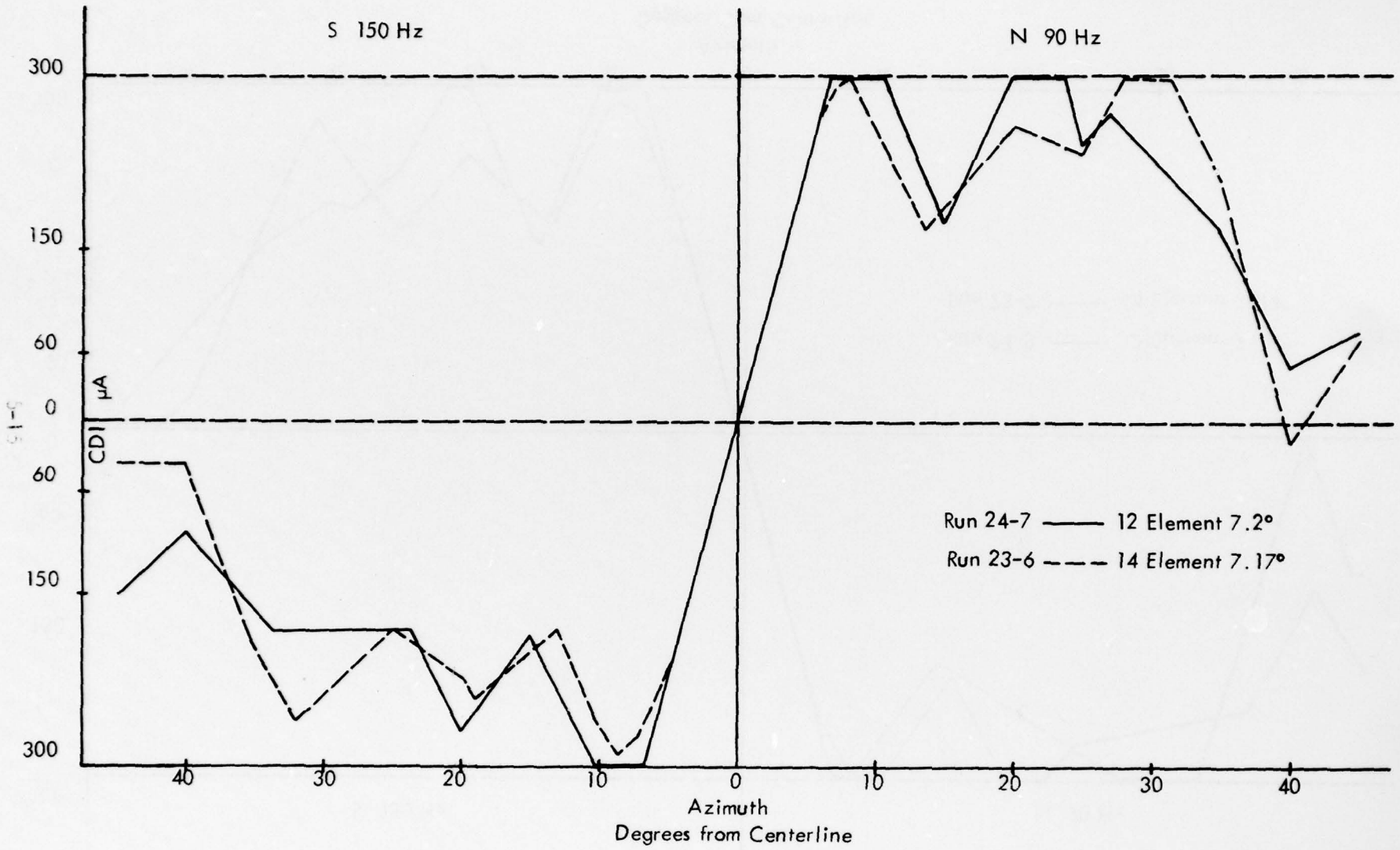

Figure 5-8. Broad Alarm - CDI - North to South Runs.

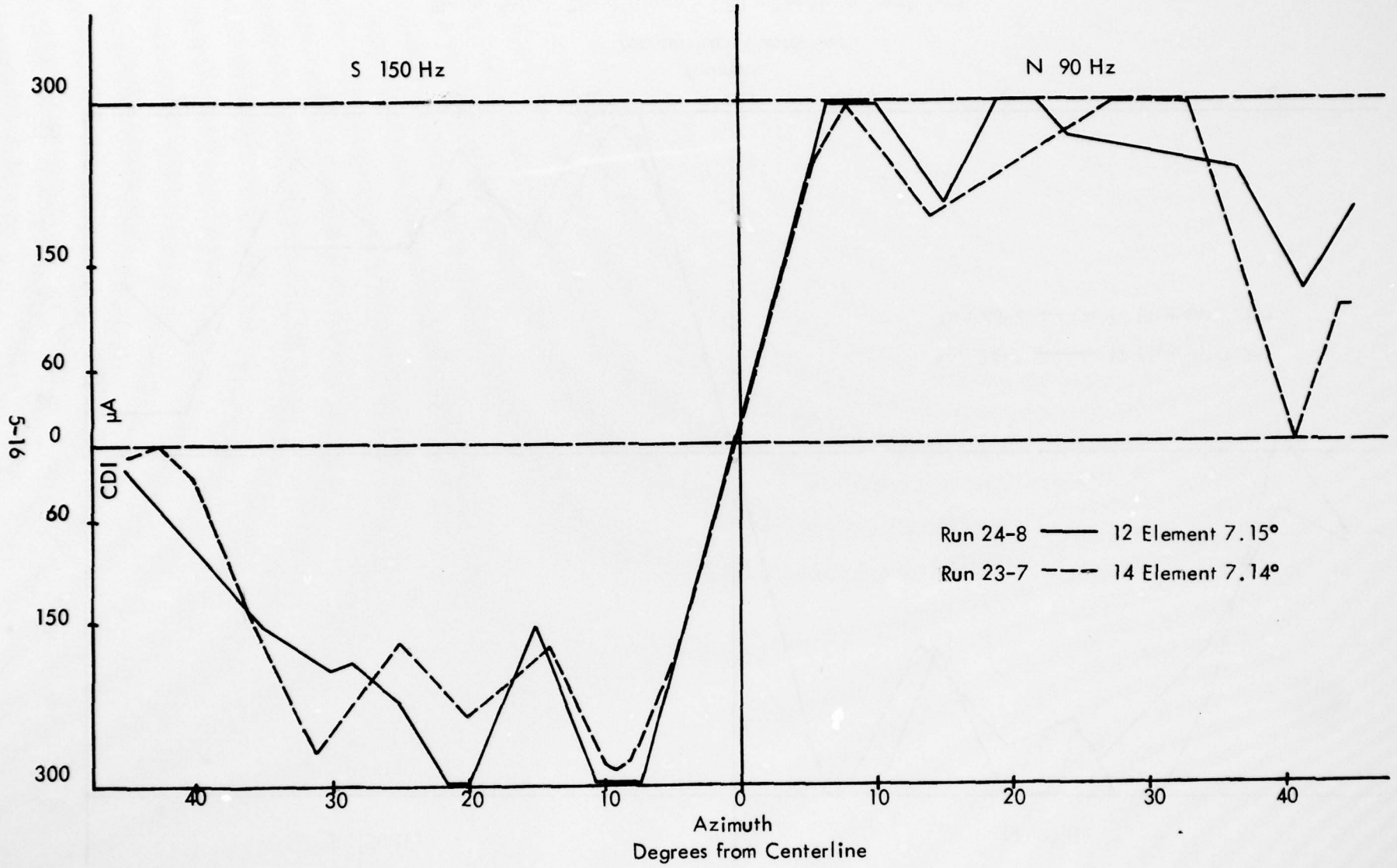

Figure 5-9. Broad Alarm - CDI - South to North Runs.

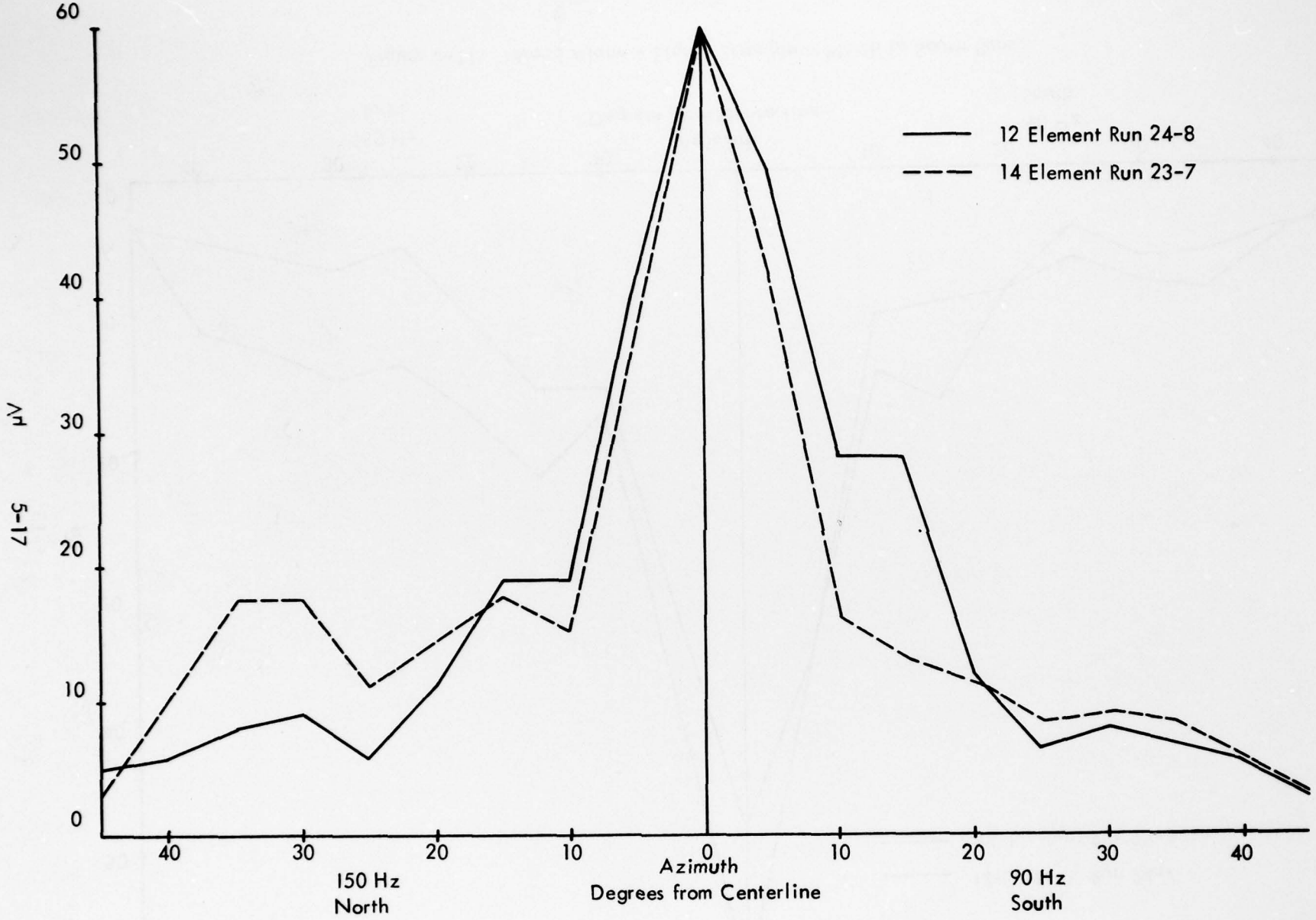

Figure 5-10. Broad Alarm - Signal Strength - South to North Runs.

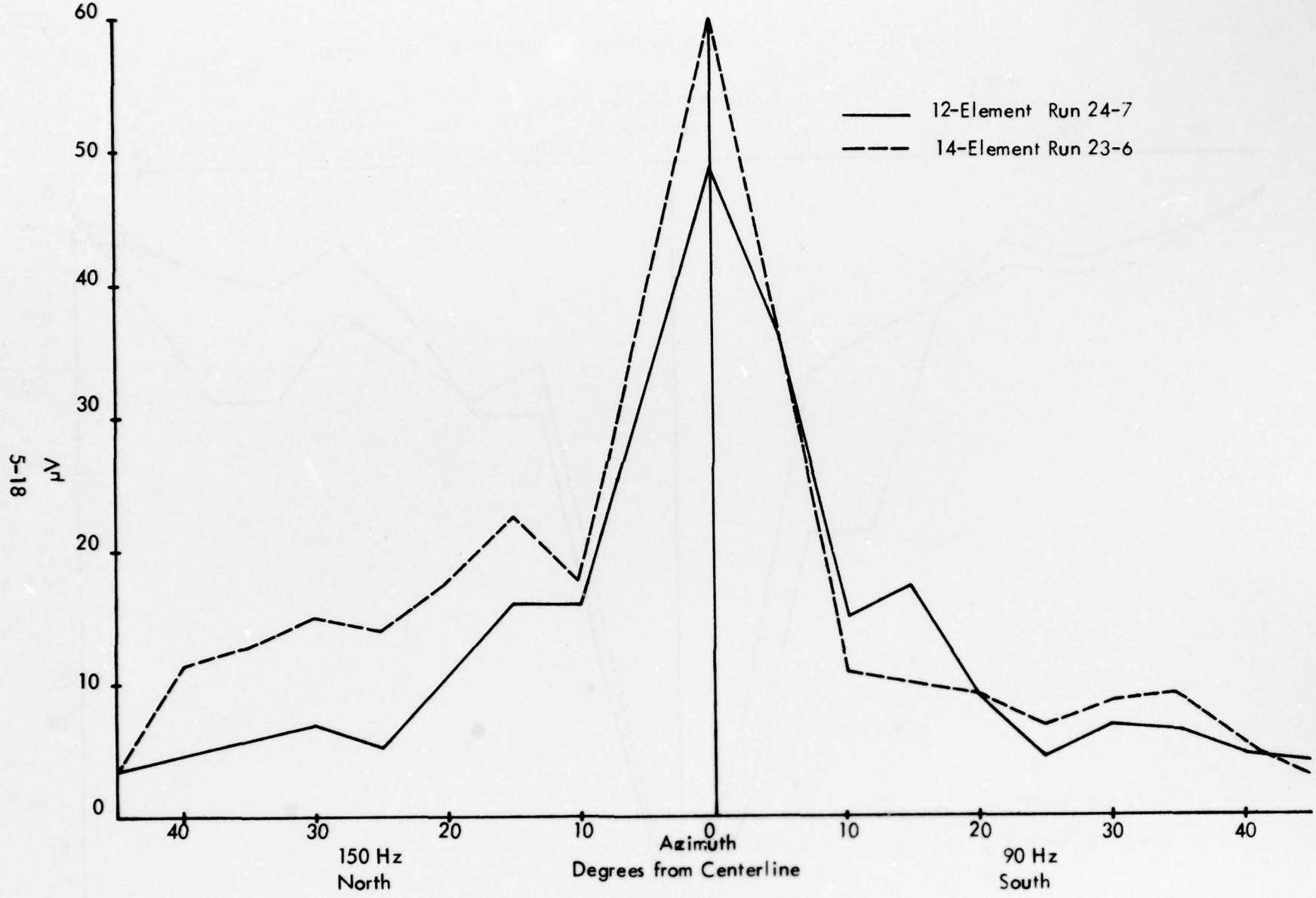

Figure 5-11. Broad Alarm - Signal Strength - North to South Runs.

ANTENNA FEED LINE	PHASE DEGREES
1	-7
2	-3.9
3	-3.6
4	-6.7
5	-5.3
6	-1.4
* 7	0
8	-6.5
9	-7.2
10	-3.5
11	-3.5
12	-6.5

*Reference Antenna

Table 5-5. Antenna Feed Line Measurements.

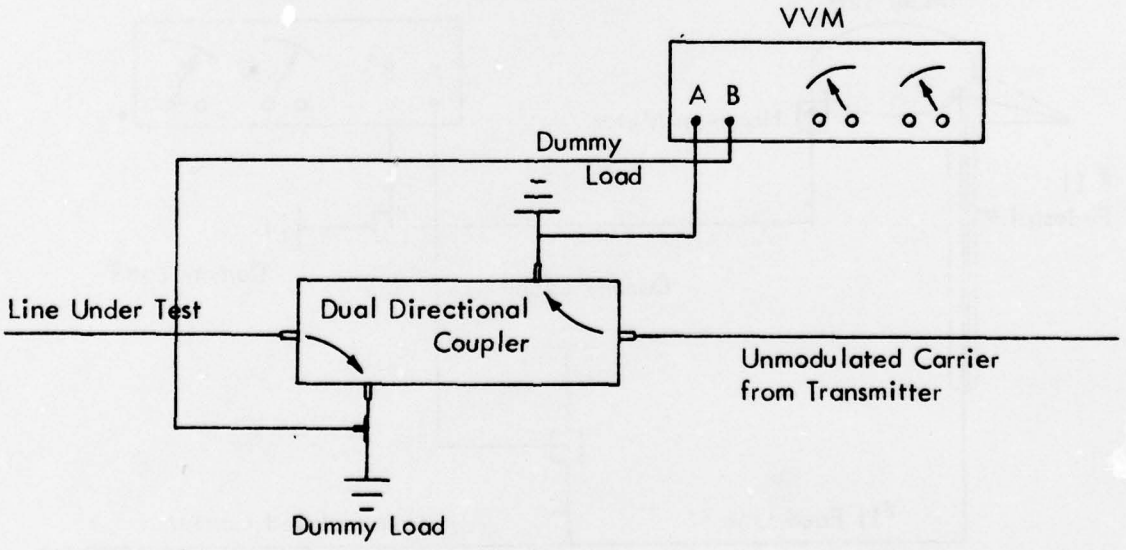

Figure 5-12. Antenna Feed Line Electrical Length Test Setup.

ANTENNA	RELATIVE AMPLITUDE dB	PHASE DEGREES
1	-2.4	-1.0
2	-2.6	-0.4
3	-2.6	-0.1
4	-2.5	0
5	-2.5	-0.5
6	-2.5	-0.2
7	-2.5	-0.7
8	-2.45	-0.7
9	-2.6	-0.7
10	-2.6	0
* 11	-2.6	0
12	-2.5	-1.0

*Reference Antenna

Table 5-6. Antenna Element Measurements.

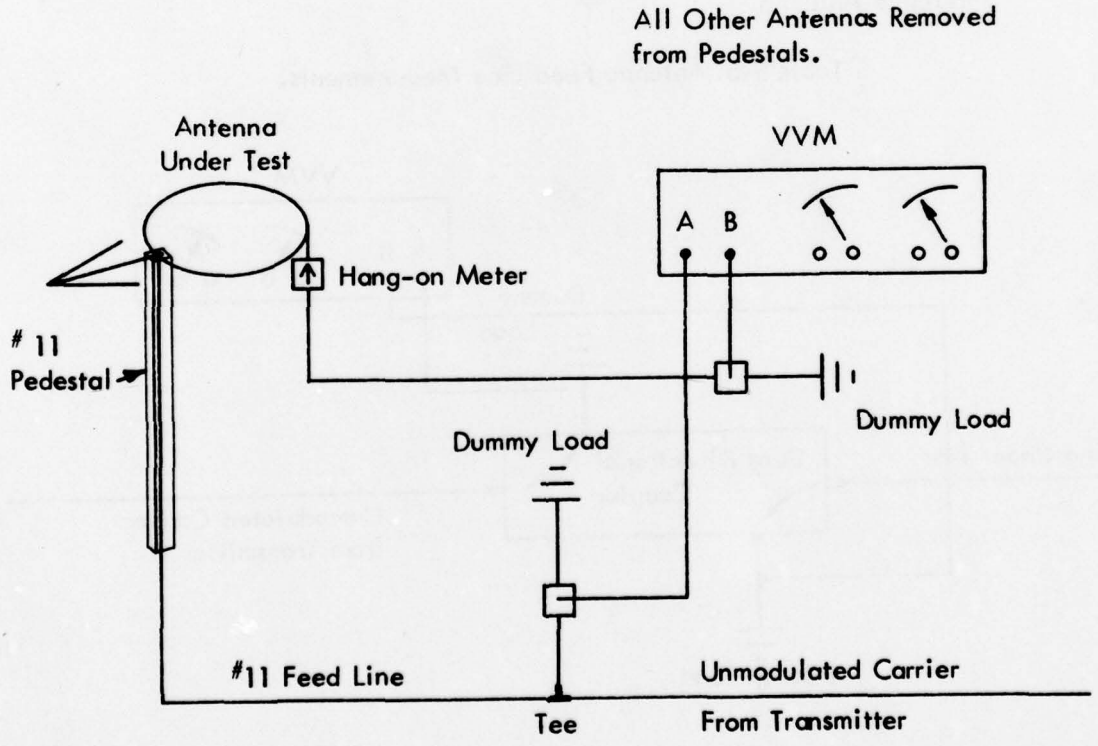

Figure 5-13. Antenna Element Test Setup.

PORT	CARRIER PORT FED		SIDEBAND PORT FED	
	RELATIVE AMPLITUDE dB	PHASE	RELATIVE AMPLITUDE dB	PHASE
*J1	-25.3	0	-21.7	0
J2	-19.2	+1.2	-17.8	-0.4
J3	-21.3	-1.5	-15.0	-2.5
J4	-16.2	-0.1	-13.9	-0.6
J5	-11.7	+1.4	-9.5	-1.1
J6	-6.7	+2.4	-8.8	+3.1
J7	-6.8	+2.1	-8.8	+2.8
J8	-11.7	+1.4	-9.6	-1.0
J9	-16.0	+0.3	-14.0	-0.4
J10	-21.3	-1.6	-15.3	-2.6
J11	-19.2	+0.2	-17.8	-1.4
J12	-25.2	+0.5	-21.6	+0.4

*Reference Antenna

+180°

Table 5-7. Alford 12-Element Distributions. All Ports Terminated in 50 Ω Dummy Loads.

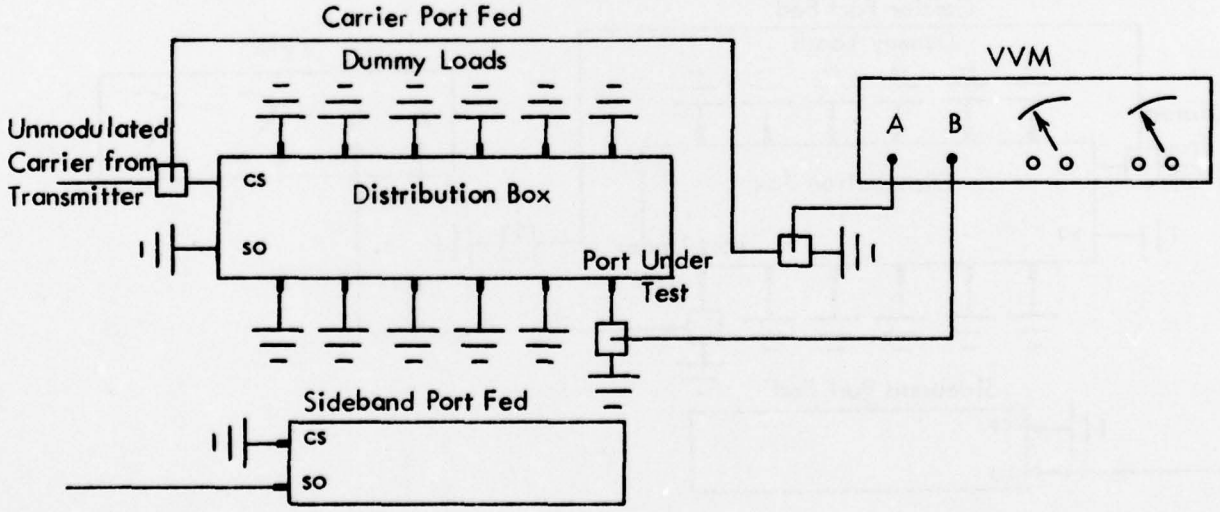

Figure 5-14. Alford 12-Element Test Setup.

PORT	CARRIER PORT FED		SIDEBAND PORT FED	
	RELATIVE AMPLITUDE dB	PHASE DEGREES	RELATIVE AMPLITUDE dB	PHASE DEGREES
J15	-31.2	+3.2	-17.4	+1.5
J14	-20.1	+4.0	-20.1	-2.6
J13	-20.2	+3.0	-14.1	+1.2
J12	-14.4	+1.0	-17.2	0
J11	-14.4	-0.3	-12.2	+0.6
J10	-6.8	+0.2	-8.5	+0.4
W1J1 *	-6.8	0	-8.5	0
W2J1	-14.8	-0.3	-12.2	0
W3J1	-14.8	+1.5	-17.1	+0.6
W4J1	-20.3	+0.4	-14.0	+0.6
W5J1	-20.0	+2.0	-20.0	-3.2
W6J1	-31.0	+1.8	-17.4	+1.3

+180°

*Reference Antenna

Table 5-8. Wilcox 14-Element Distributions.
All Ports Terminated in 50 Ω Dummy Loads.

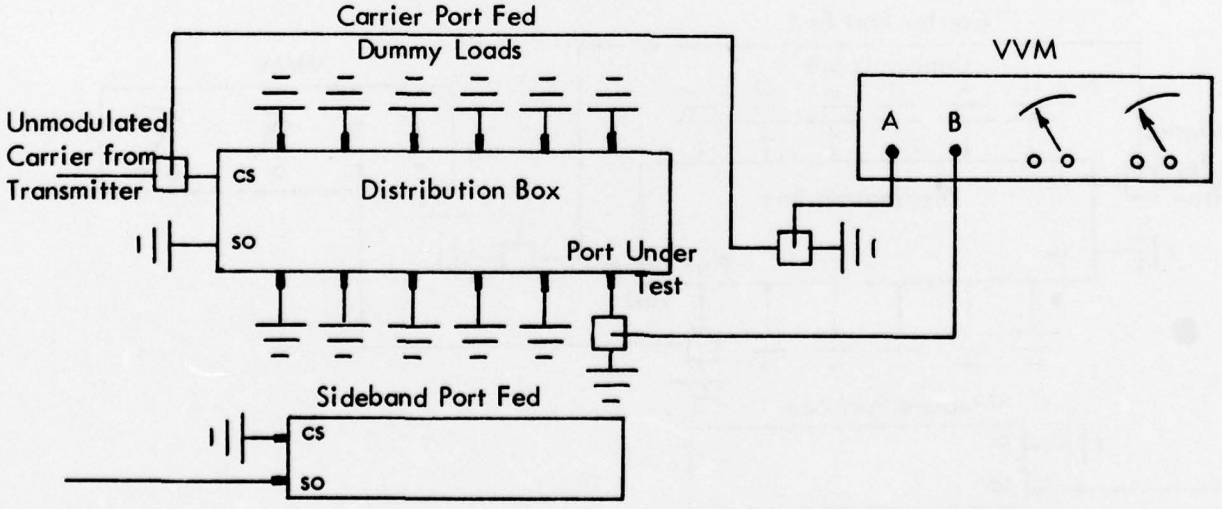

Figure 5-15. Wilcox 14-Element Test Setup.

12-ELEMENT BOX			14-ELEMENT BOX		
ANTENNA	RELATIVE AMPLITUDE	PHASE	ANTENNA	RELATIVE AMPLITUDE	PHASE
1	-32.6	-1.8	1	-28.0	+2.0
2	-29.2	-1.2	2	-31.0	+8.0
3	-26.8	-2.0	3	-25.2	+4.7
4	-25.4	0	4	-27.6	+9.0
5	-21.0	-2.0	5	-22.4	+5.0
6	-19.0	+1.3	6	-18.8	+3.0
* 7	-19.0	0	7	-18.6	0
8	-20.8	-1.5	8	-22.5	+3.6
9	-25.5	+1.0	9	-28.0	+7.3
10	-26.9	0	10	-25.2	+4.0
11	-29.1	0	11	-31.0	+4.0
12	-32.7	-2.0	12	-28.0	-1.7

±180°

*Reference Antenna

Table 5-9. Sideband Distributions as Measured on Antennas.

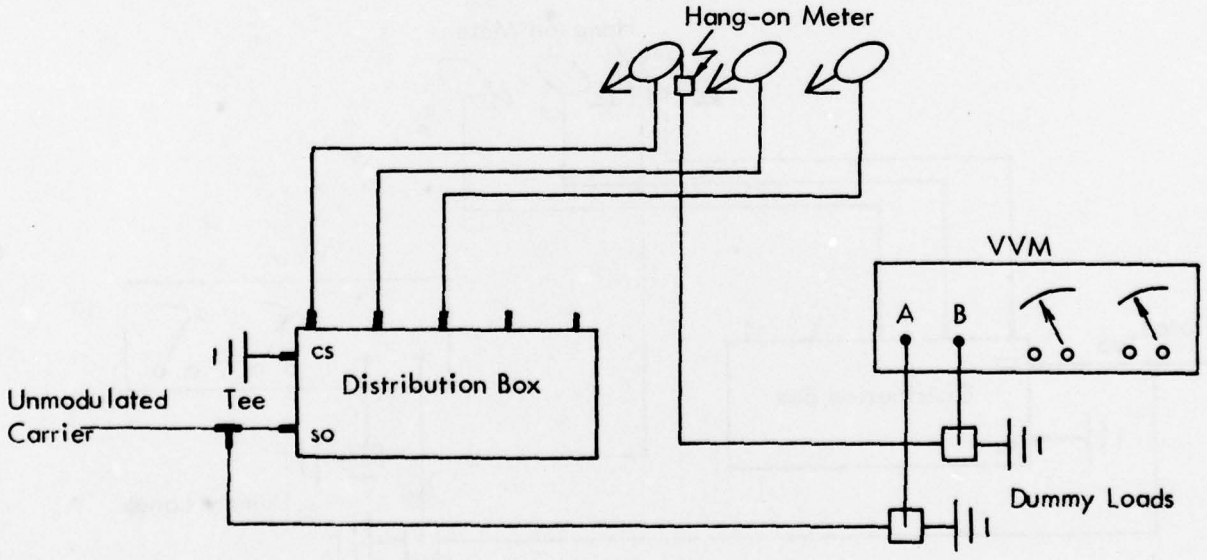

Figure 5-16. Sideband Test Setup.

12-ELEMENT BOX			14-ELEMENT BOX		
ANTENNA	RELATIVE AMPLITUDE	PHASE	ANTENNA	RELATIVE AMPLITUDE	PHASE
1	-36.8	-9.7	1	-43.4	+6.0
2	-30.6	-10.5	2	-31.6	+0.5
3	-32.7	0	3	-31.4	+6.0
4	-27.2	-10.0	4	-25.8	-9.4
5	-23.2	-4.8	5	-26.1	-0.5
6	-18.4	+3.2	6	-18.7	+5.0
* 7	-18.4	0	7	-18.6	0
8	-23.0	-5.7	8	-26.3	-0.5
9	-27.2	-10.0	9	-26.0	-10.3
10	-32.6	+1.4	10	-31.5	+3.5
11	-30.2	-6.5	11	-31.4	-4.2
12	-36.2	-8.5	12	-42.5	-2.0

*Reference Antenna

Table 5-10. Carrier Distributions as Measured on Antennas.

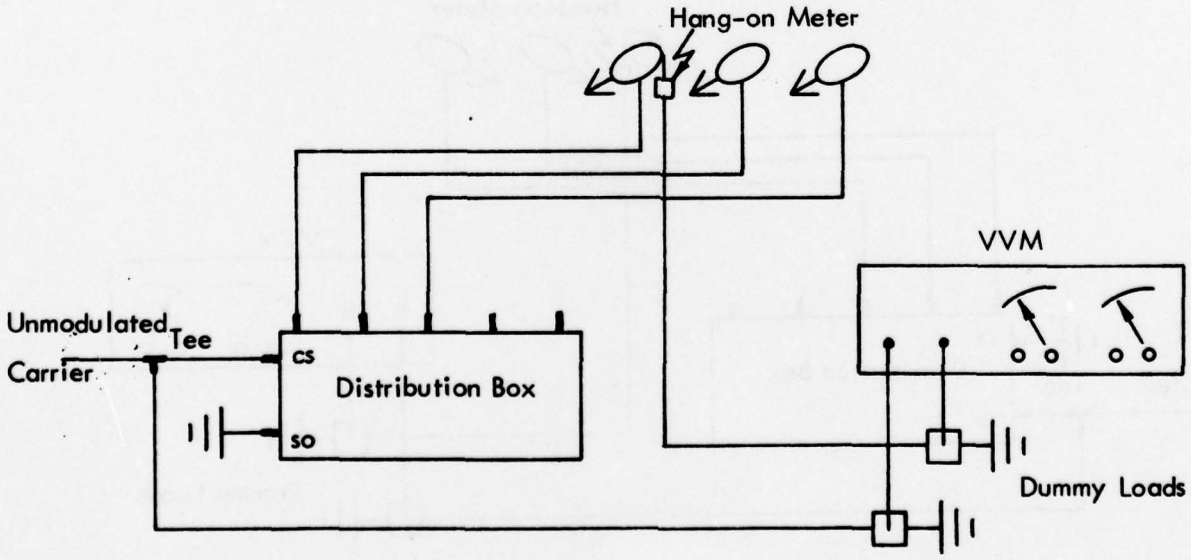

Figure 5-17. Carrier Test Setup.

12-ELEMENT BOX			14-ELEMENT BOX		
ANTENNA	RELATIVE AMPLITUDE dB	PHASE DEGREES	ANTENNA	RELATIVE AMPLITUDE dB	PHASE DEGREES
1	-34.8	-13.0	1	-34.5	+14.0
2	-29.5	-14.0	2	-30.3	+9.0
3	-30.2	-8.0	3	-29.8	+16.0
4	-26.0	-15.5	4	-25.0	-1.0
5	-22.0	-12.0	5	-24.0	+9.5
6	-18.0	-3.6	6	-17.5	+12.0
* 7	-17.5	0	7	-18.0	0
8	-21.4	-3.4	8	-24.9	0
9	-26.0	-6.0	9	-25.5	-8.0
10	-30.0	+3.6	10	-29.1	+3.2
11	-29.0	-4.8	11	-30.6	-3.0
12	-34.2	-5.6	12	-35.0	-2.8

*Reference Antenna

Table 5-11. System Normal - Antenna Amplitudes and Phases.

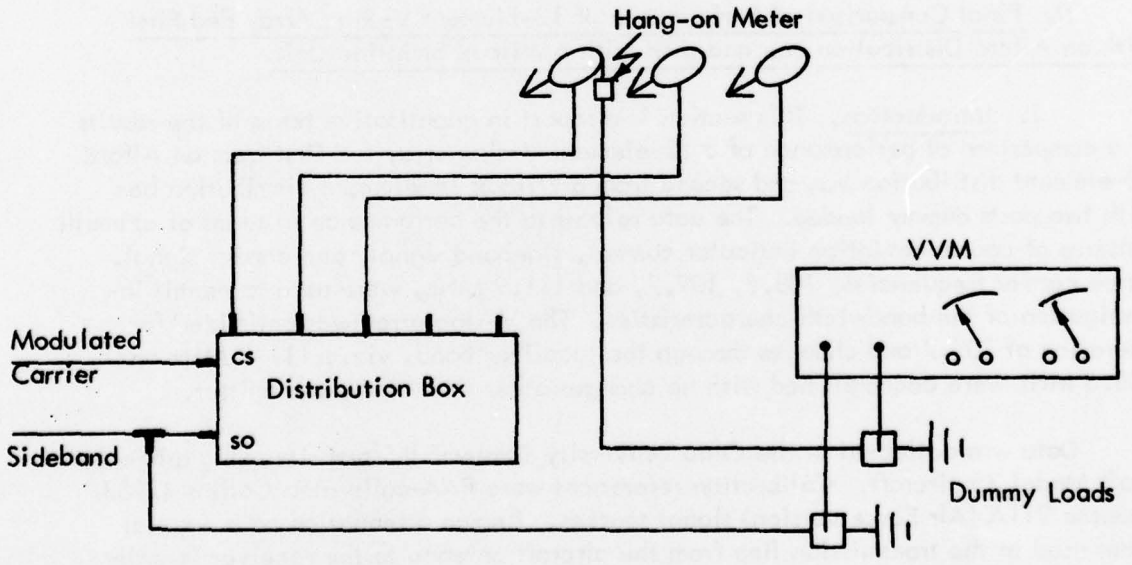

Figure 5-18. System Normal Test Setup.

has yielded several noteworthy results. For comparison purposes an Alford 12-element distribution box was used as a reference.

a. Both Wilcox and Alford distribution units provided more than 150 microamperes of clearance in the sector ±35 degrees about centerline, even for a 7.2 degree path width which is greater than the broad alarm condition.

b. Converting the 14-element Wilcox box to 12-element operation by means of dummy loads on two ports poses no special problems.

c. Course sectors were linear to 240 microamperes for the Wilcox and 300 microamperes for the Alford.

d. A given carrier sideband ratio provided the same course widths for both systems.

e. The Wilcox unit provided greater clearance in the 25 to 35 degree sectors, whereas the Alford unit provided greater clearance in the 20-0-20 degree sector. Both provided amounts of clearance in excess of those required by the U.S. Flight Inspection Manual.

f. The Wilcox unit provided typically 4 dB greater signal strength in the 20 to 35 degree sectors.

D. Final Comparison of Performance of 12-Element V- Ring Array Fed First with an Alford Distribution Box and then with a Wilcox Stripline Unit.

1. Introduction. This section is a report in quantitative terms of the results of a comparison of performance of a 12-element V-ring array fed first from an Alford 12-element distribution box and second from a Wilcox 14-element distribution box with two ports dummy loaded. The data relates to the performance in terms of azimuth patterns of course deviation indicator current, sideband signal, and carrier signal. Three carrier frequencies, 108.5, 109.7, and 111.9 MHz, were used to permit investigation of the bandwidth characteristics. The V-ring array was optimized for operation at 109.7 and changes through the localizer band, viz., 111.9 MHz and 108.5 MHz were accomplished with no changes other than at the transmitter.

Data was collected at the Ohio University Tamiami ILS test site using a Beechcraft Model 35 aircraft. Calibration references were FAA-calibrated Collins 479S3/ Boonton 211A (Air Force version) signal sources. Known attenuation pads were at times used in the transmission line from the aircraft antenna to the receiver in order to keep the signal level in a region of the AGC curve where reasonable accuracy could be obtained from the typically non-linear AGC response. The data for operation at 111.9 MHz was taken on one day while the data for 108.5 and 109.7 MHz was taken on another day.

Orbits were flown at 1500 feet altitude at a range of six miles from the site. The principal reference for altitude was a standard pressure altimeter backed up by a radar altimeter. The range of six miles was determined by use of area navigation equipment. A theodolite located on extended centerline of the runway approximately 20 feet to the rear of the transmitting antennas was used to provide the azimuth marks. These were recorded every 5 degrees in general but every one degree between ±5 degrees of centerline.

2. Discussion of Data. Both the Alford and Wilcox distribution boxes provided acceptable clearance to beyond 35 degrees in azimuth when the array was operating at the broad alarm limit of 7 degrees. (See Figures 5-19 through 5-29). These give assurance that clearance for all acceptable path widths will be met. Minimum clearance points for both distribution systems occur at 15 degrees azimuth which places it fortunately in the sector where currently only 150 microamperes of clearance is required. Both systems provided at least 10 microamperes of clearance margin over this minimum requirement.

Because potential multipath problems should be considered when a particular localizer array is selected, special knowledge of sideband radiation patterns is important. Figures 5-30 through 5-39 provide normalized sideband and carrier distribution radiation patterns for each of the distribution units. Organization of the plots is such as to provide direct comparison of the Wilcox and Alford units at each of the three frequencies and then direct comparison of each distribution unit over the frequency band.

Table 5-12 shows the taper in field strength distributions as one moves away from the centerline. Although there is clearly a frequency dependence, it is not an easily predictable characteristic of the distribution system. Unless specific values for the frequency to be used are known, a 15 dB taper value should be assumed for the edge of the 35 degree sector. Ten dB appears to be adequate to cover the edge of the 10 degree sector. These may impose some problems in meeting the U.S. Flight Inspection specifications where long transmission lines are run from solid state transmitters to the array.

In addition, special attention was given to signal strength versus distance comparisons for the 12-element array with these feed systems. A Wilcox solid state transmitter was used throughout the experiment. Table 5-13 gives receiver terminal voltage versus distance, on centerline, 1500 feet altitude, out to 19 miles from the array.

Azimuth patterns of signal strength also derived from AGC were recorded for the complete array. The most important of these are in Figures 5-40 through 5-42

Again, although there are obvious changes as the frequency is altered, there is no general trend established by these sample test frequencies (108.5, 109.7, 111.9 MHz) either with respect to the band or the distribution system used.

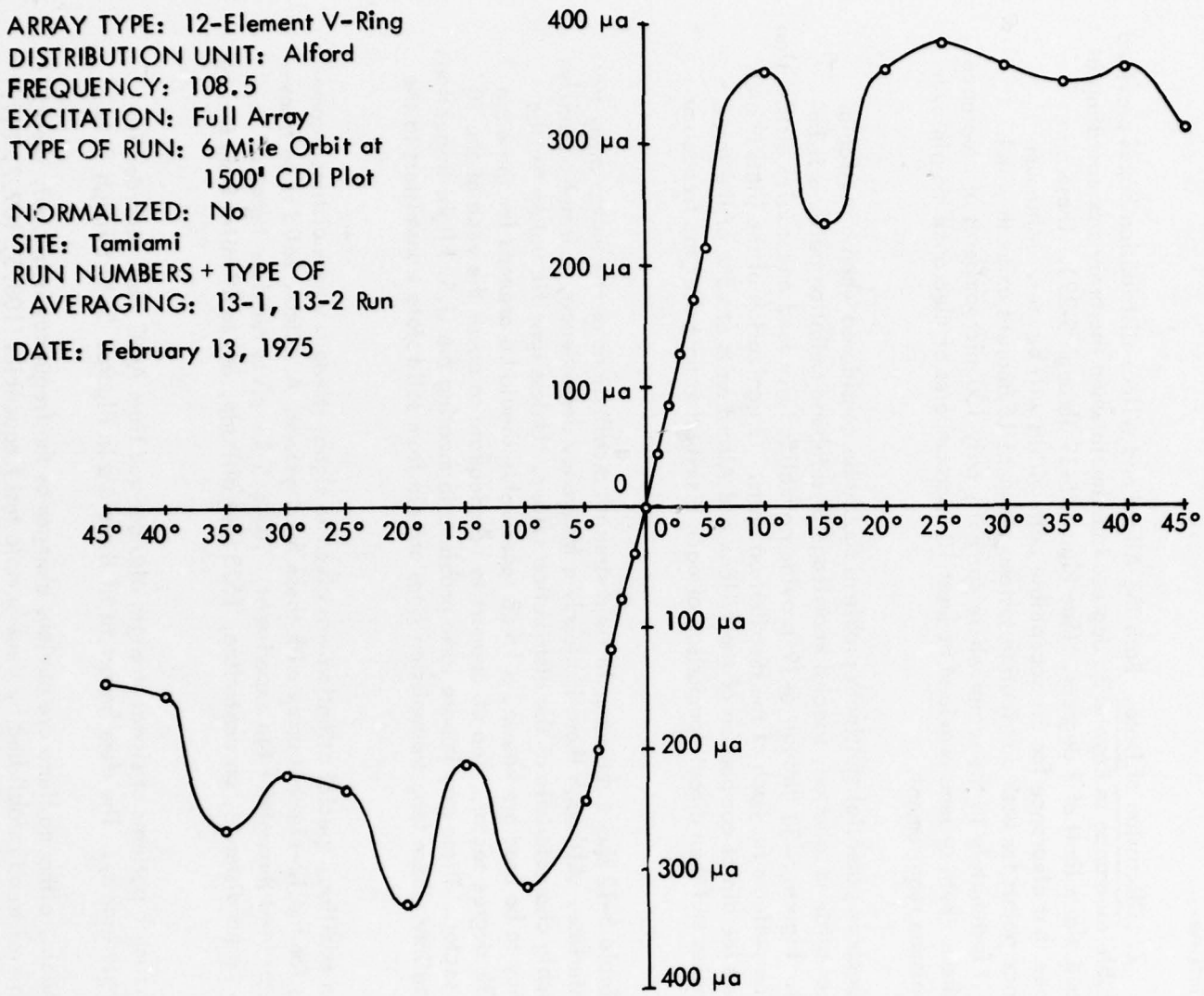

Figure 5-19. Plot of CDI versus Azimuth, Alford Box, 108.5 MHz.

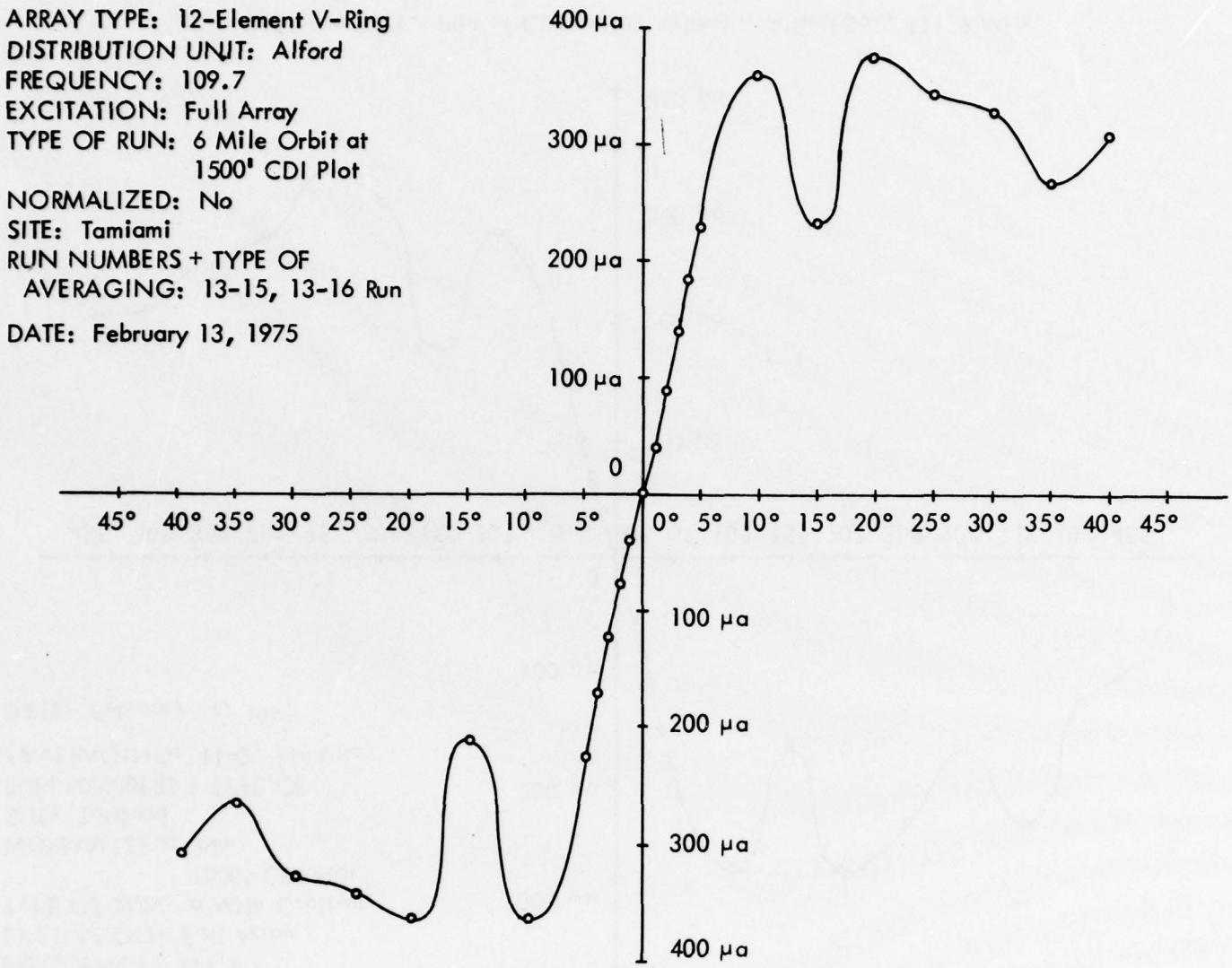

Figure 5-20. Plot of CDI versus Azimuth, Alford Box, 109.7 MHz.

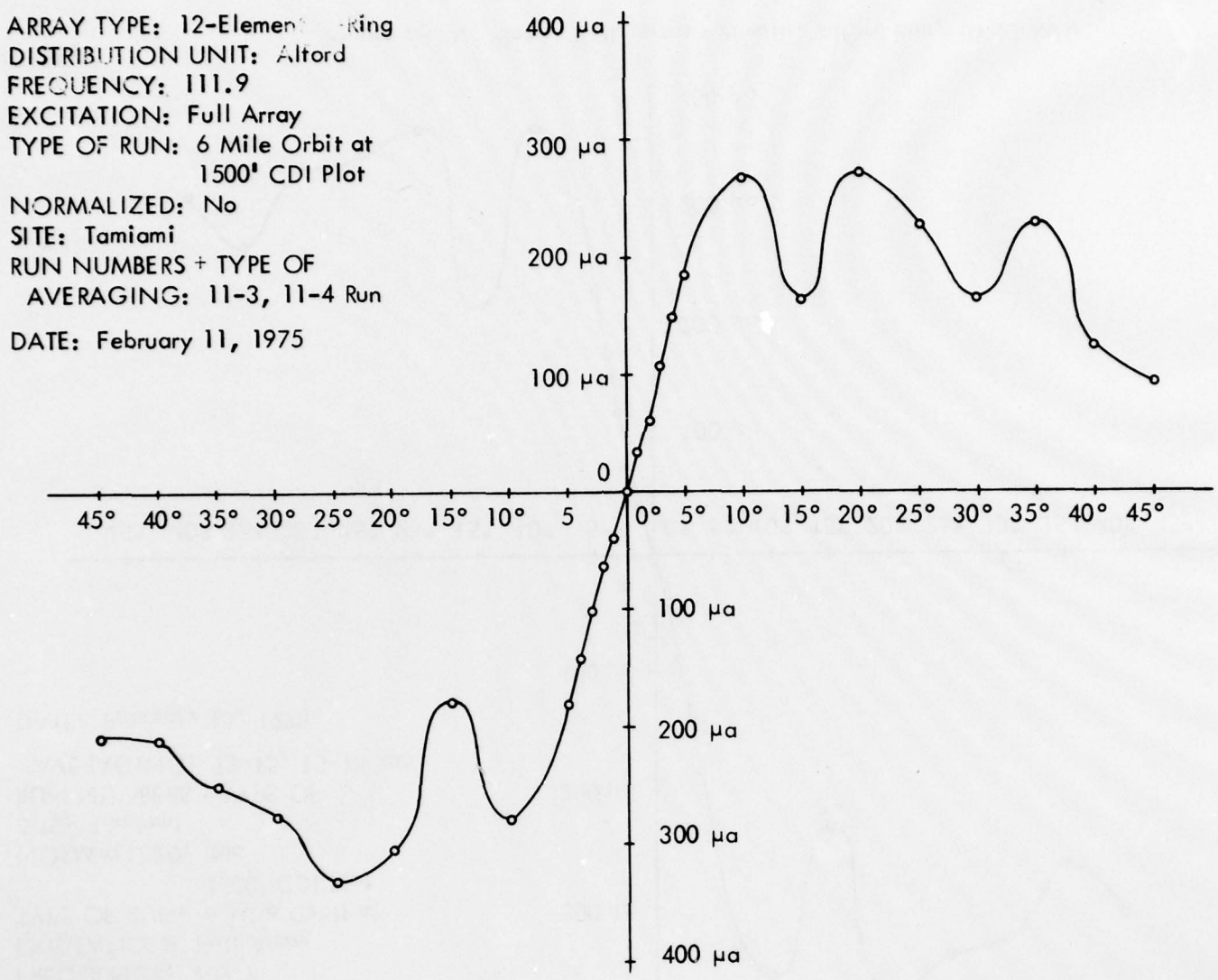

Figure 5-21. Plot of CDI versus Azimuth, Alford Box, 111.9 MHz.

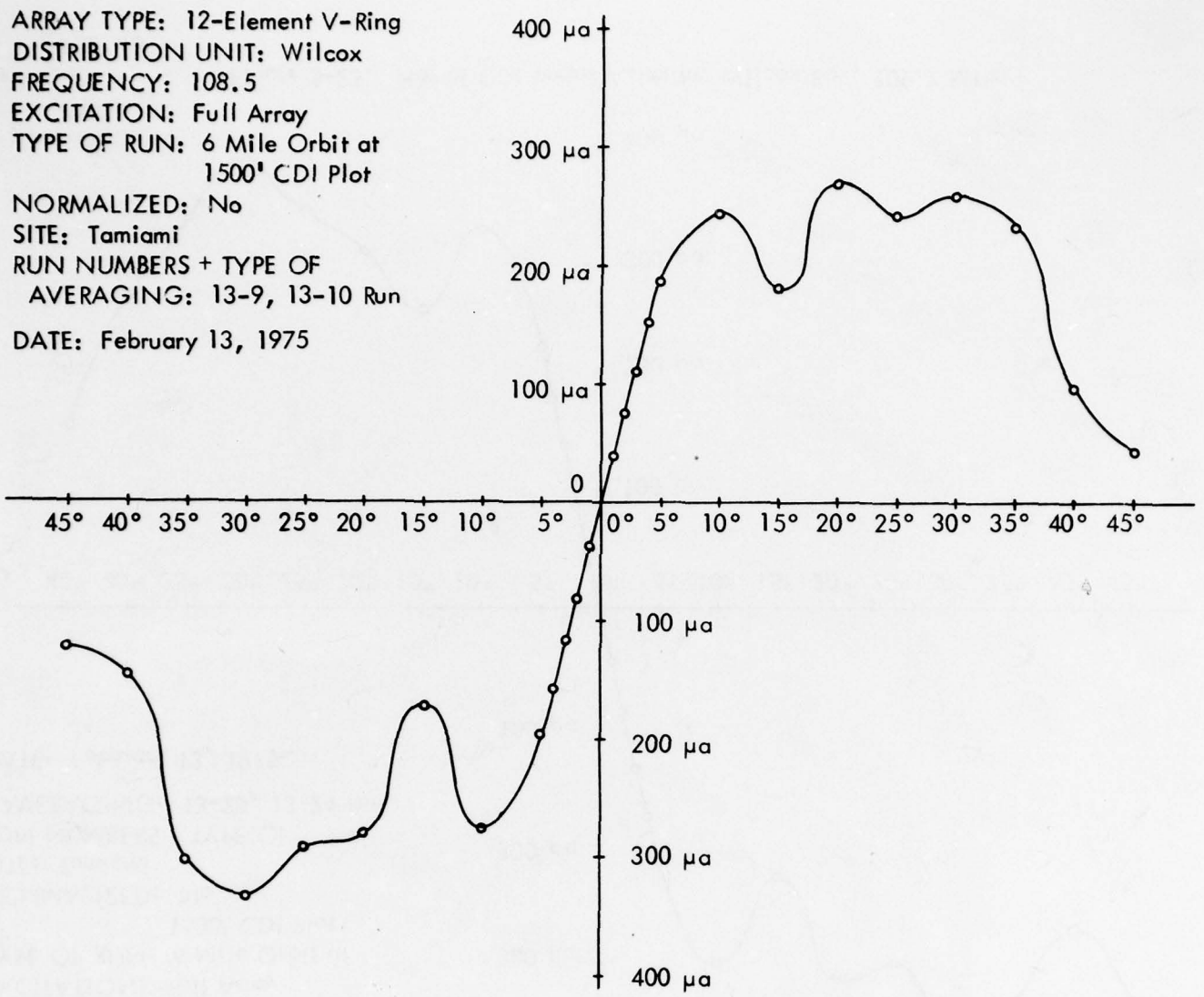

Figure 5-22. Plot of CDI versus Azimuth, Wilcox Box, 108.5 MHz.

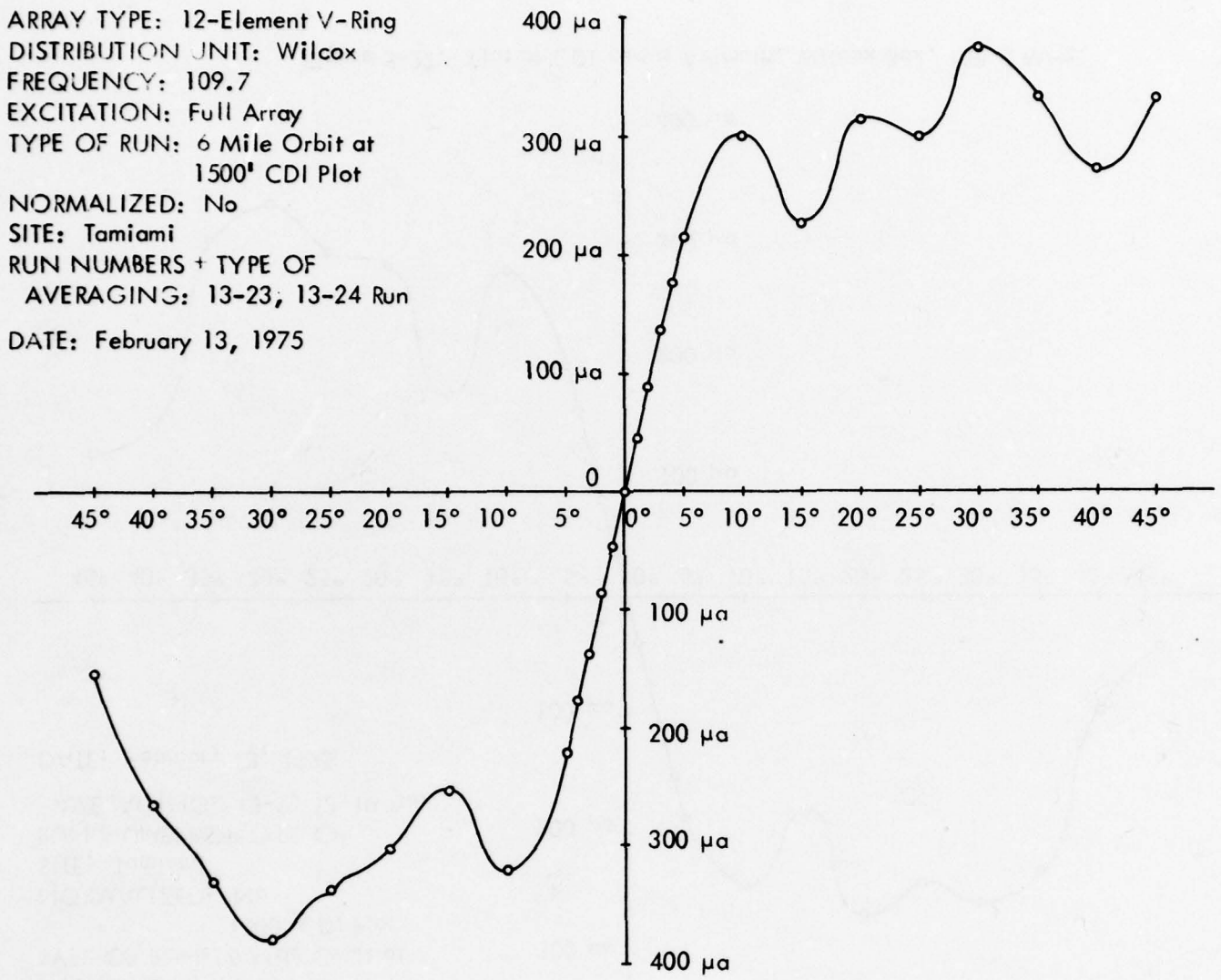

Figure 5-23. Plot of CDI versus Azimuth, Wilcox Box, 109.7 MHz.

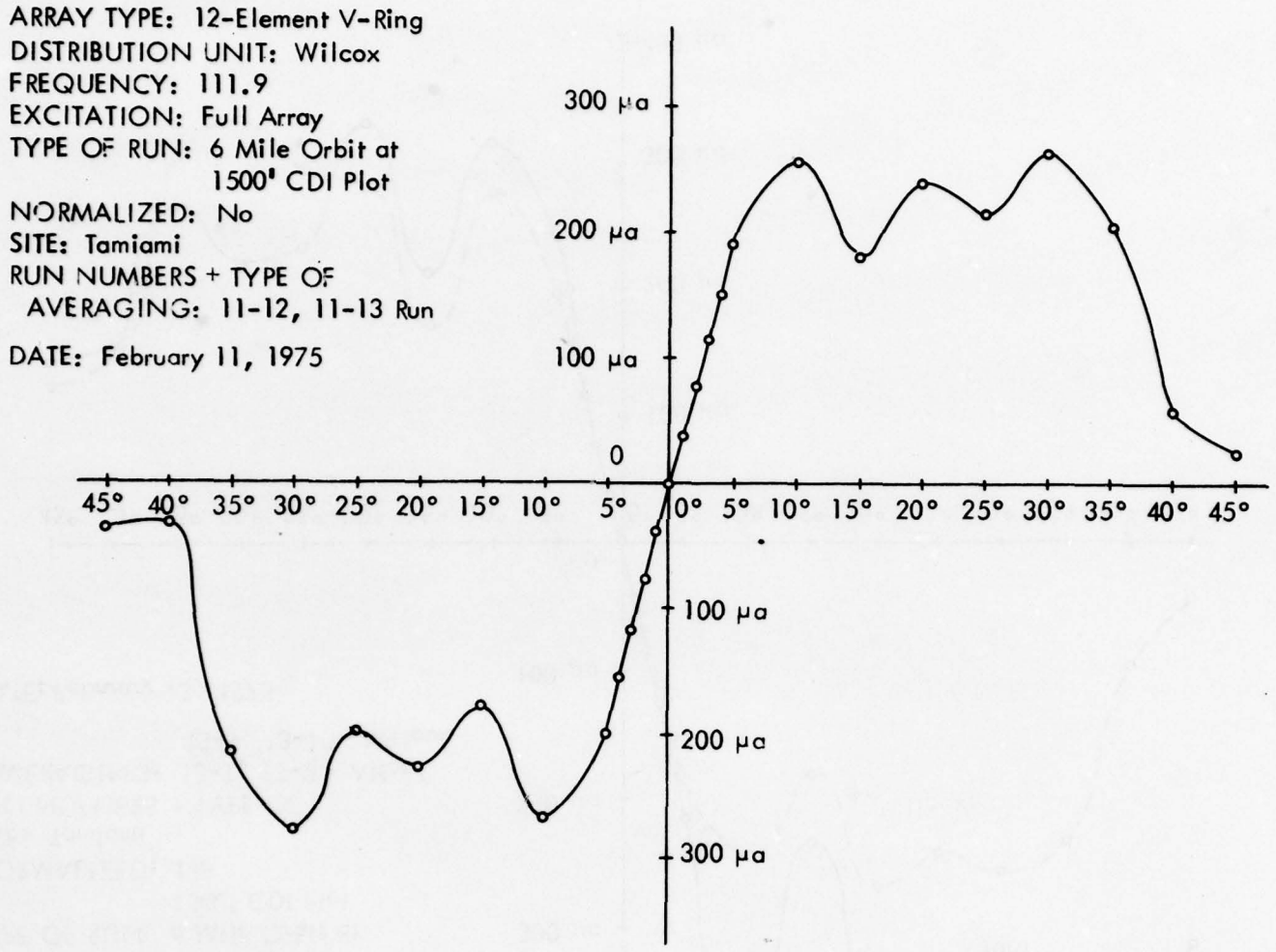

Figure 5-24. Plot of CDI versus Azimuth, Wilcox Box, 111.9 MHz.

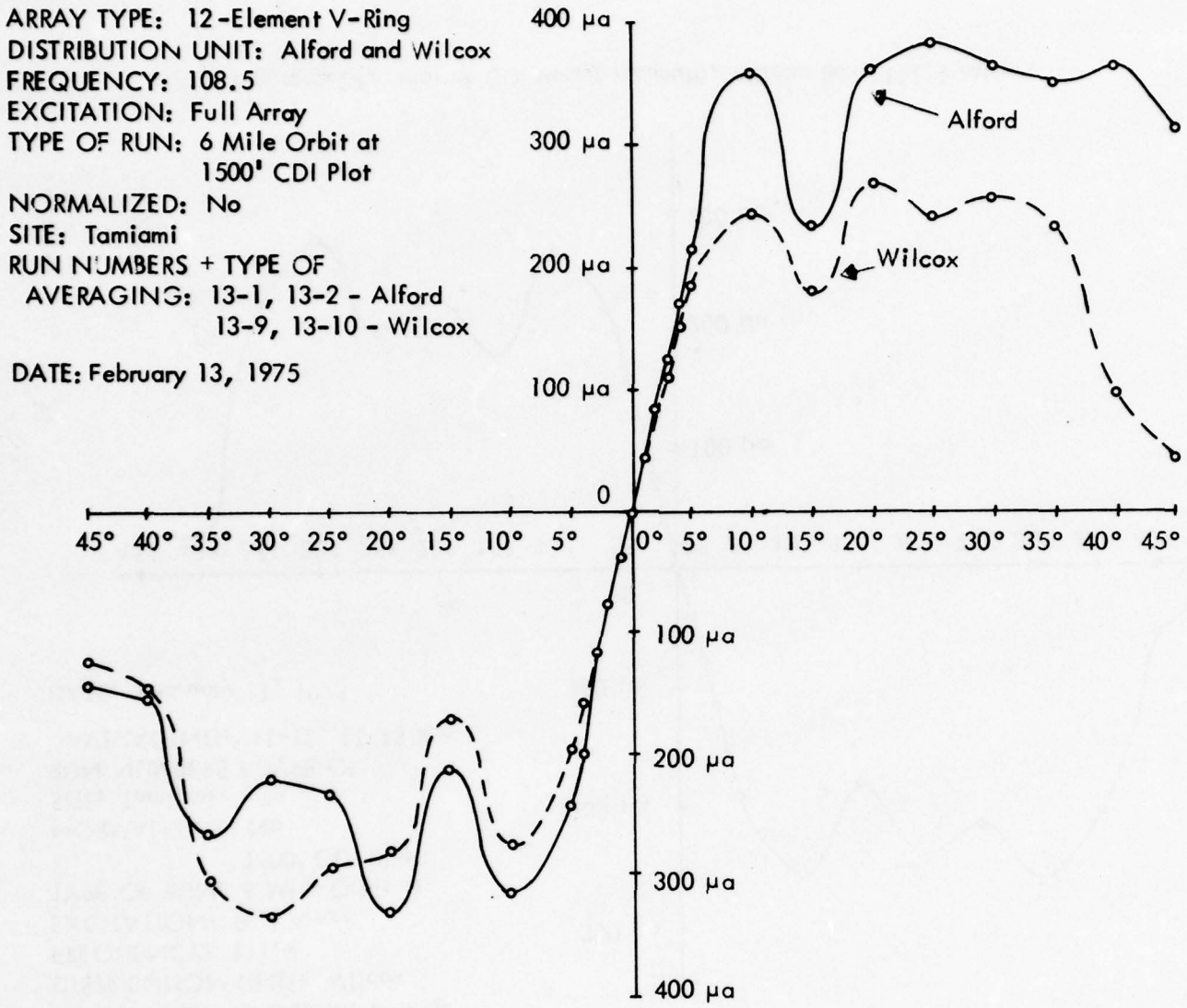

Figure of 5-25. Plot of CDI versus Azimuth, Alford and Wilcox Boxes, 108.5 MHz.

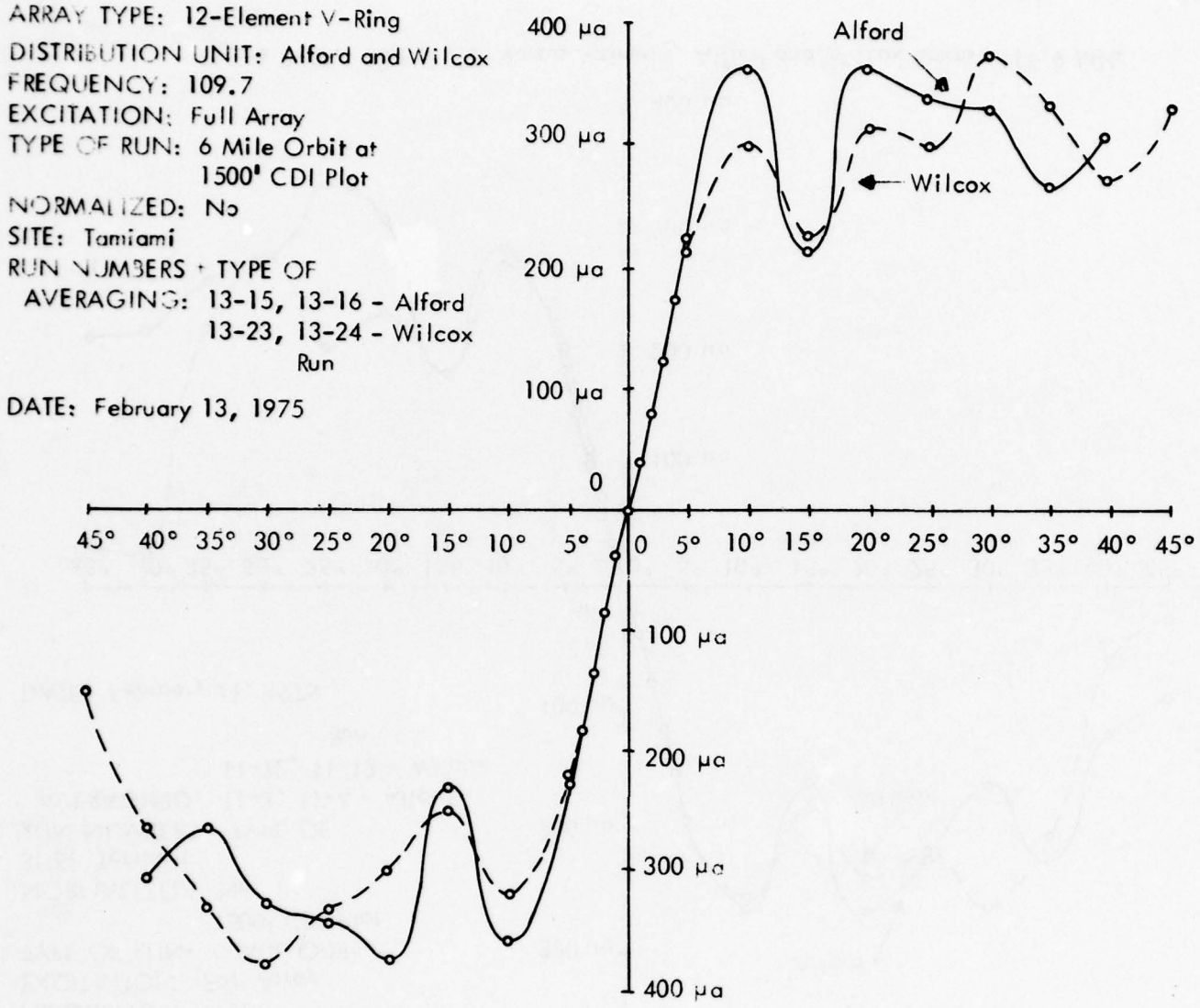

Figure 5-26. Plot of CDI versus Azimuth, Alford and Wilcox Boxes, 109.7 MHz.

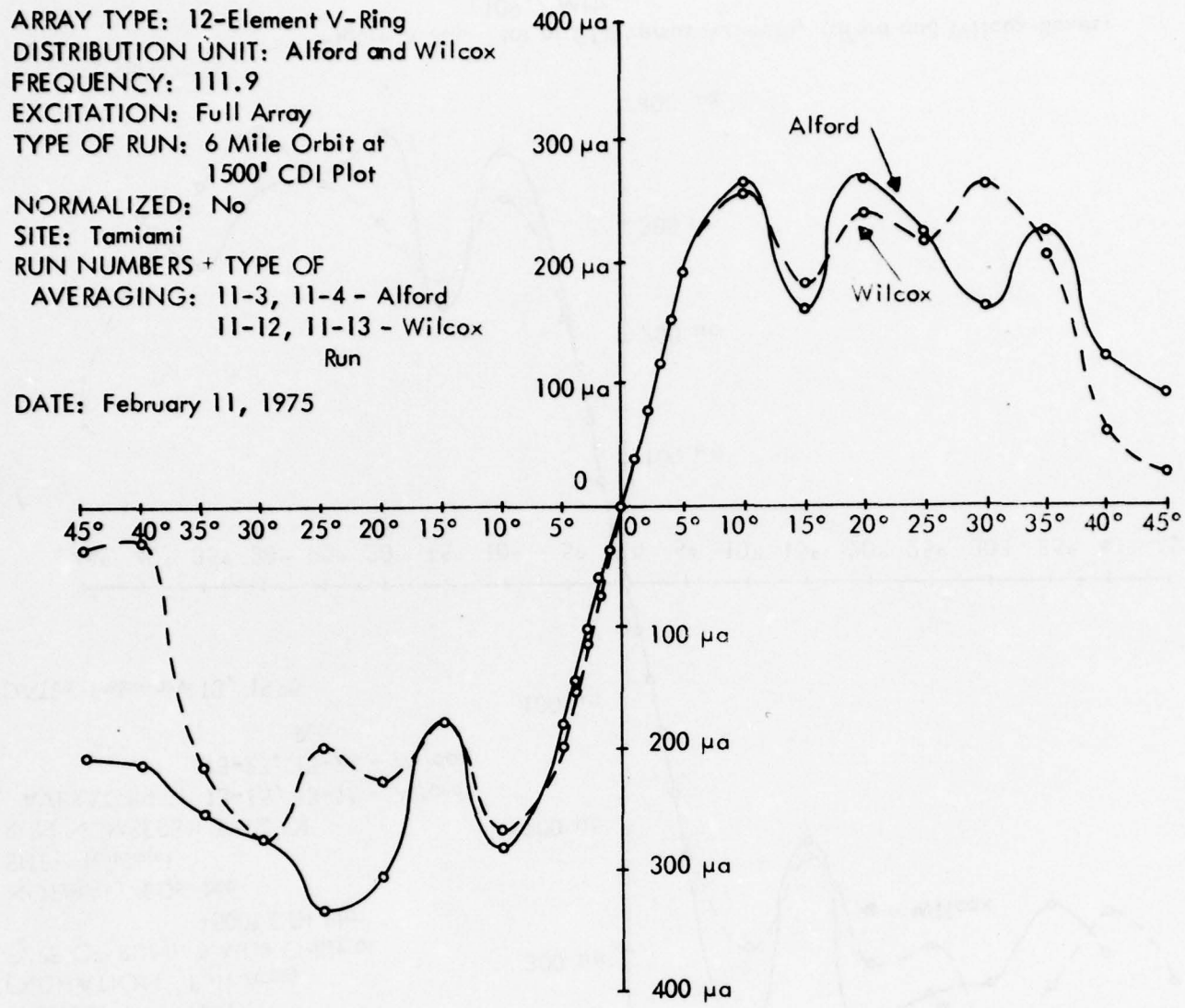

Figure 5-27. Plot of CDI versus Azimuth, Alford and Wilcox Boxes, 111.9 MHz.

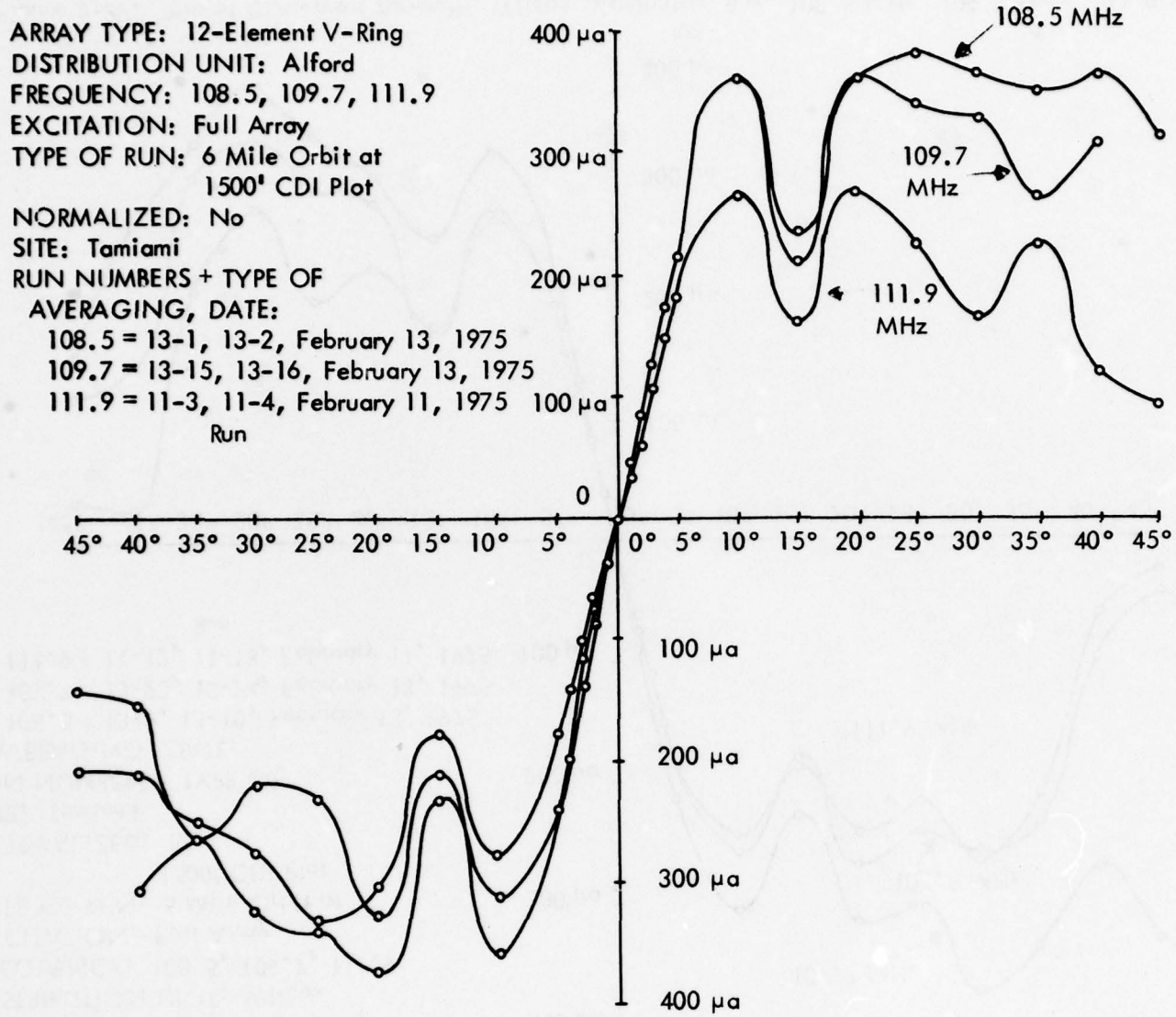

Figure 5-28. Plot of CDI versus Azimuth, Alford Distribution Box, 108.5 MHz, 109.7 MHz, 111.9 MHz.

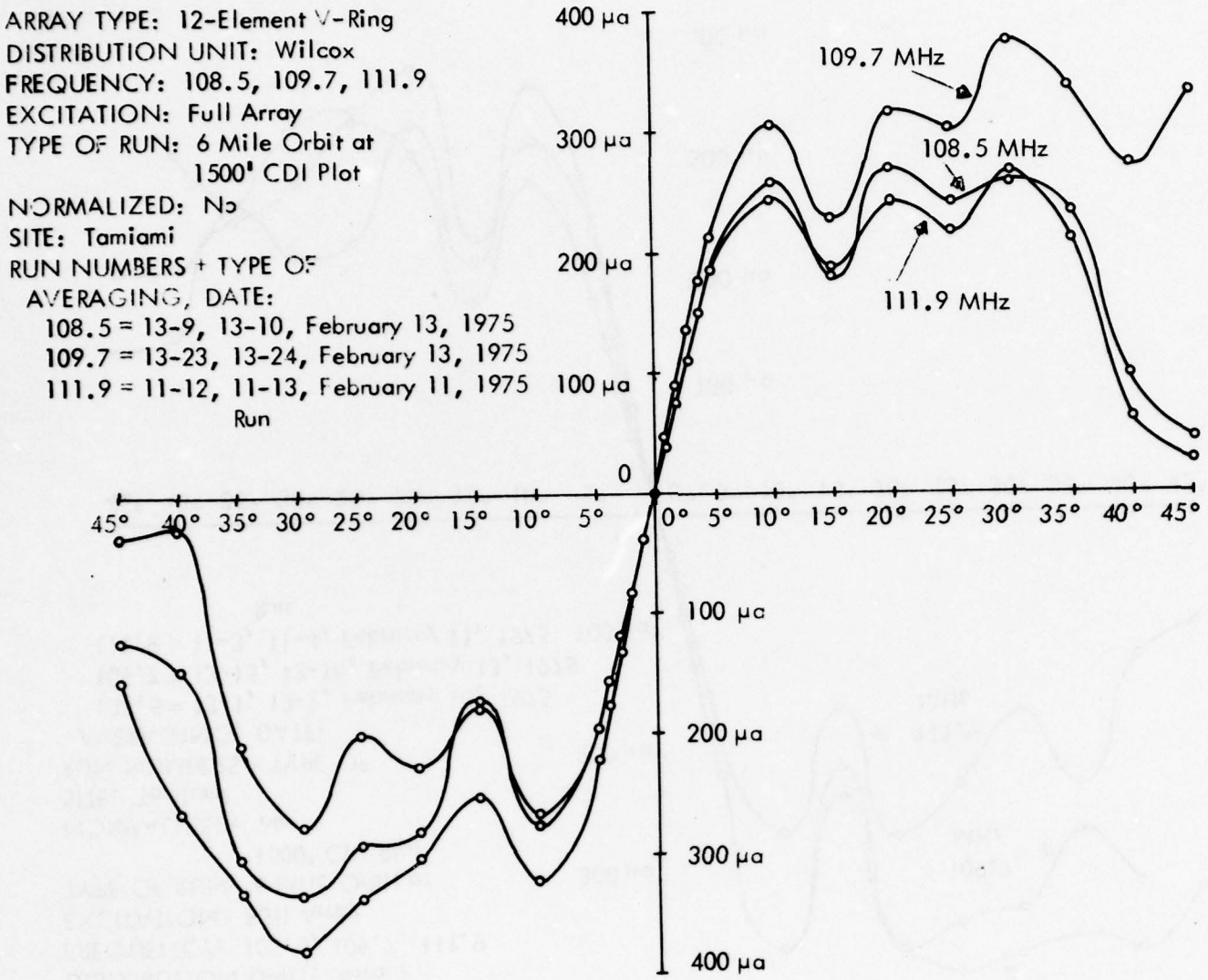

Figure 5-29. Plot of CDI versus Azimuth, Wilcox Distribution Box, 108.5 MHz, 109.7 MHz, 111.9 MHz.

Array Type: 12-Element V-Ring
Distribution Unit: Alford and Wilcox
Frequency: 108.5
Excitation: Sideband Only
Type of Run: 6 Mile Orbit at 1500'
Normalized: Unity Centerline Carrier
Site: Tamiami
Run Numbers + Type of Averaging:

13-5, 13-6 - Alford
13-13, 13-14 - Wilcox
Run + Azimuth

Date: February 13, 1975

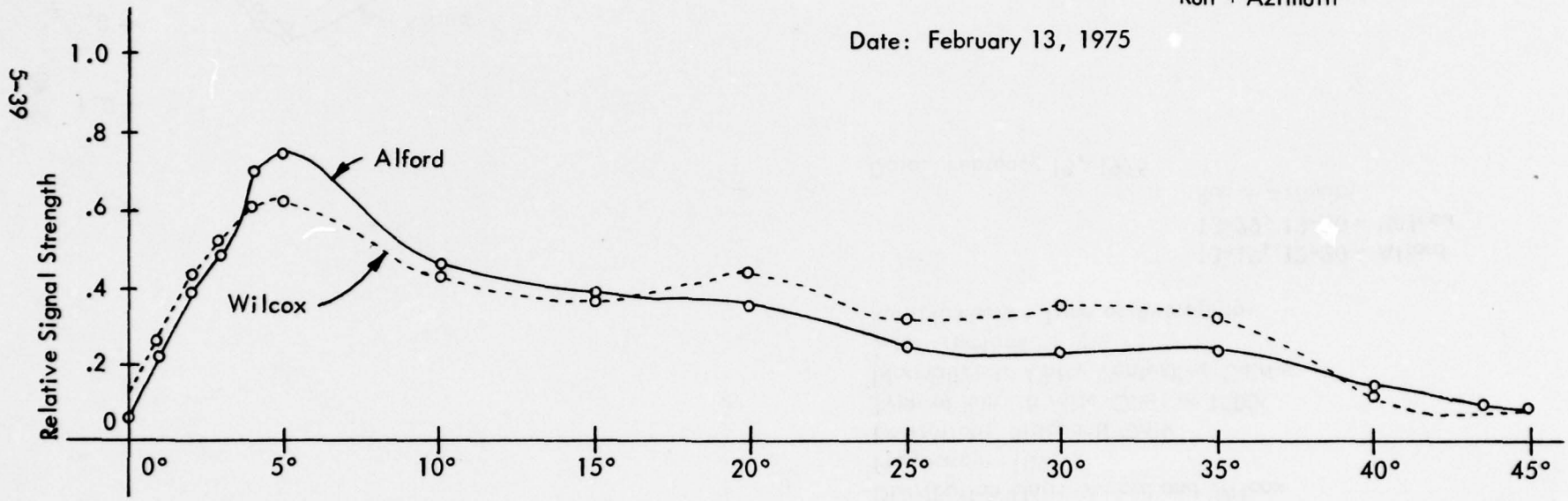

Figure 5-30. Plot of Sideband Signal versus Azimuth, Alford and Wilcox Boxes, 108.5 MHz.

Array Type: 12-Element V-Ring
Distribution Unit: Alford and Wilcox
Frequency: 109.7
Excitation: Sideband Only
Type of Run: 6 Mile Orbit at 1500'
Normalized: Unity Centerline Carrier
Site: Tamiami
Run Numbers + Type of Averaging:

13-19, 13-20 - Alford
13-29, 13-30 - Wilcox
Run + Azimuth

Date: February 13, 1975

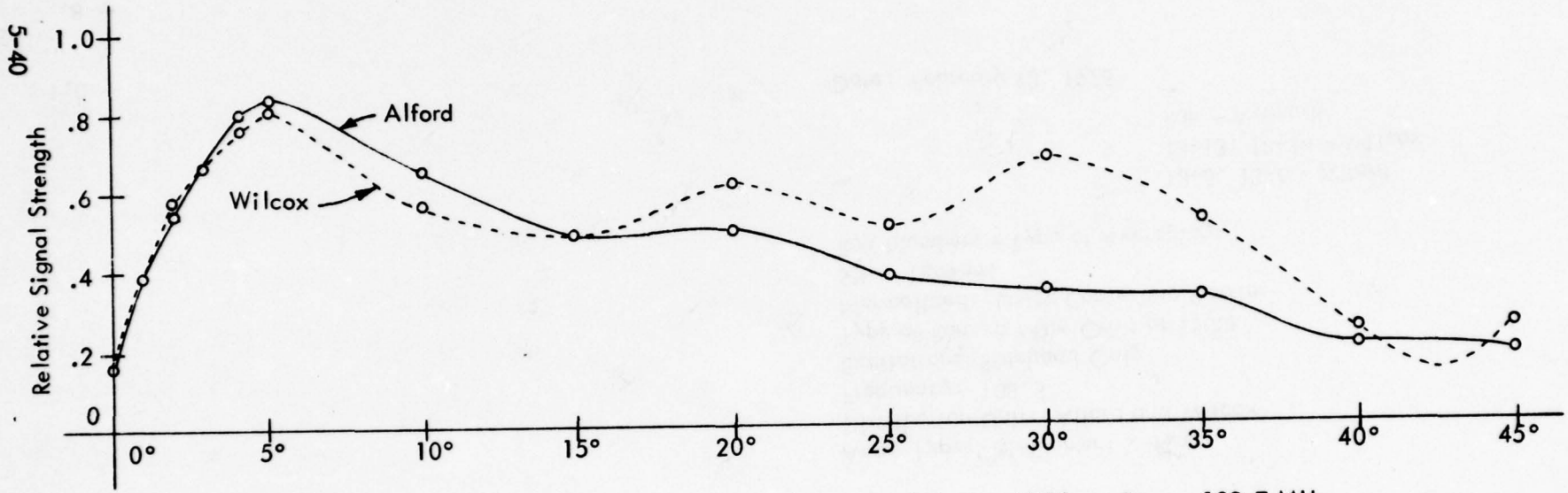

Figure 5-31. Plot of Sideband Signal versus Azimuth, Alford and Wilcox Boxes, 109.7 MHz.

Array Type: 12-Element V-Ring
Distribution Unit: Alford and Wilcox
Frequency: 111.9
Excitation: Sideband Only
Type of Run: 6 Mile Orbit at 1500'
Normalized: Unity Centerline Carrier
Site: Tamiami
Run Numbers + Type of Averaging:

11-7, 11-8 - Alford
11-16, 11-17 - Wilcox
Run + Azimuth

Date: February 11, 1975

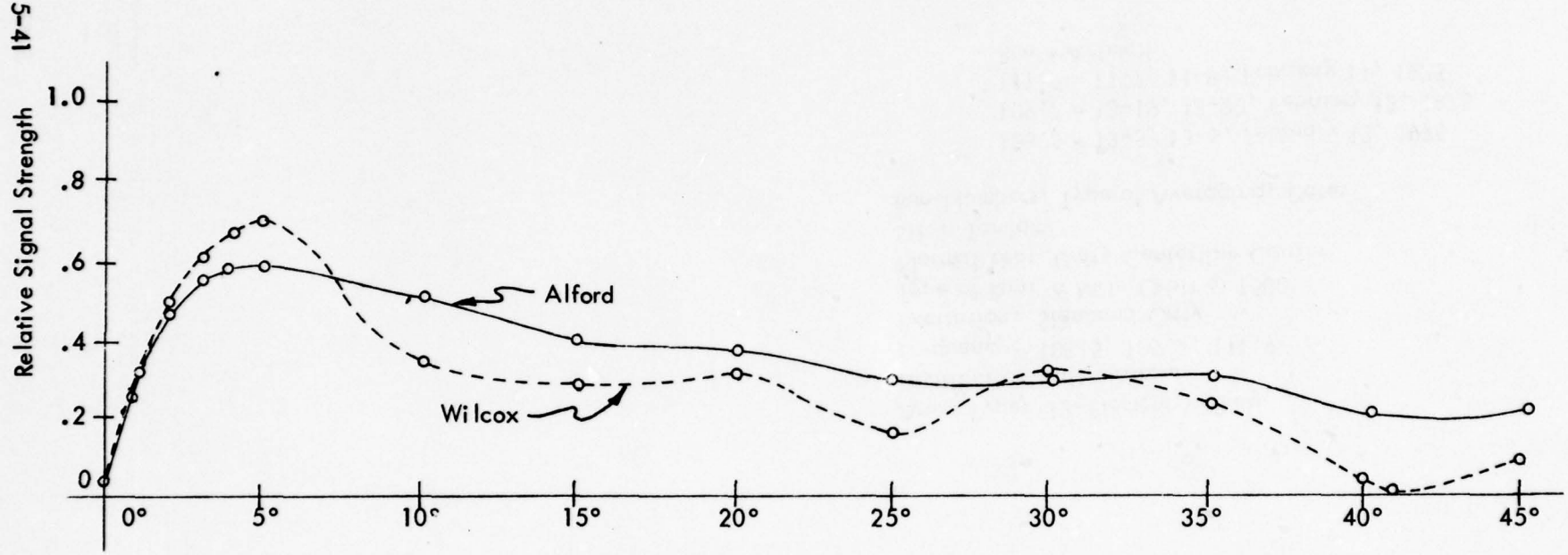

Figure 5-32. Plot of Sideband Signal versus Azimuth, Alford and Wilcox Boxes, 111.9 MHz.

Array Type: 12-Element V-Ring
Distribution Unit: Alford
Frequency: 108.5, 109.7, 111.9
Excitation: Sideband Only
Type of Run: 6 Mile Orbit at 1500'
Normalized: Unity Centerline Carrier
Site: Tamiami
Run Numbers, Type of Averaging, Date:

108.5 = 13-5, 13-6, February 13, 1975
109.7 = 13-19, 13-20, February 13, 1975
111.9 = 11-7, 11-8, February 11, 1975
Run + Azimuth

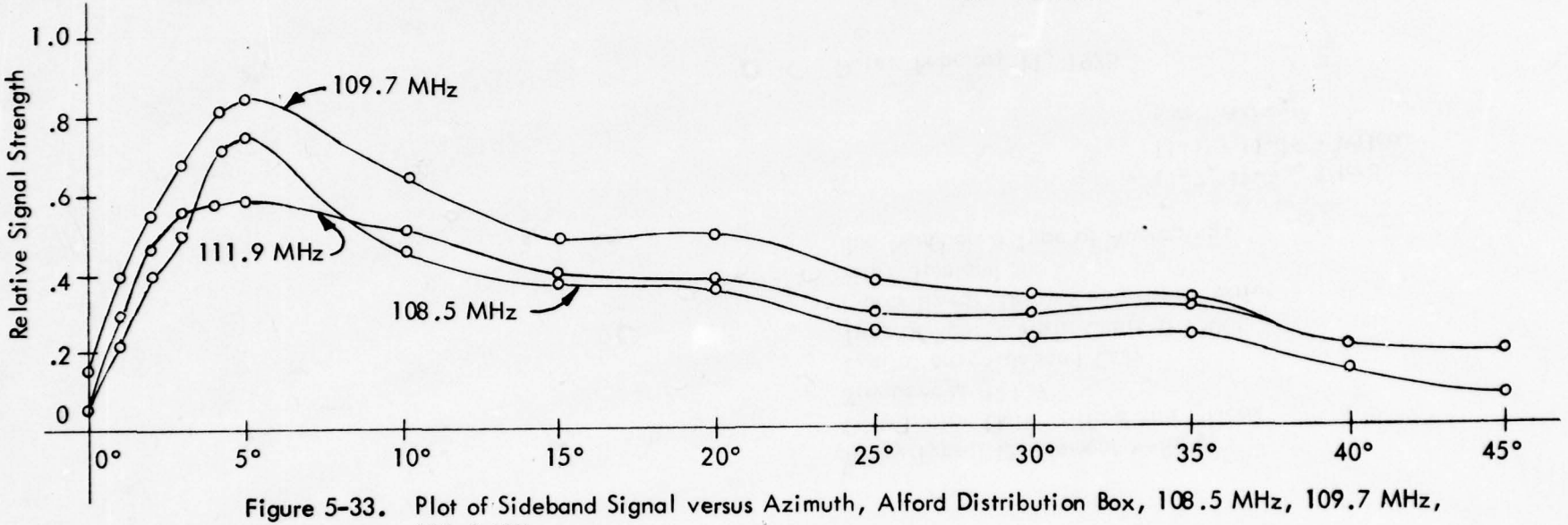

Figure 5-33. Plot of Sideband Signal versus Azimuth, Alford Distribution Box, 108.5 MHz, 109.7 MHz, 111.9 MHz.

Array Type: 12-Element V-Ring
Distribution Unit: Wilcox
Frequency: 108.5, 109.7, 111.9
Excitation: Sideband Only
Type of Run: 6 Mile Orbit at 1500'
Normalized: Unity Centerline Carrier
Site: Tamiami
Run Numbers, Type of Averaging, Date:

108.5 = 13-13, 13-14, February 13, 1975
109.7 = 13-29, 13-30, February 13, 1975
111.9 = 11-16, 11-17, February 11, 1975
Run + Azimuth

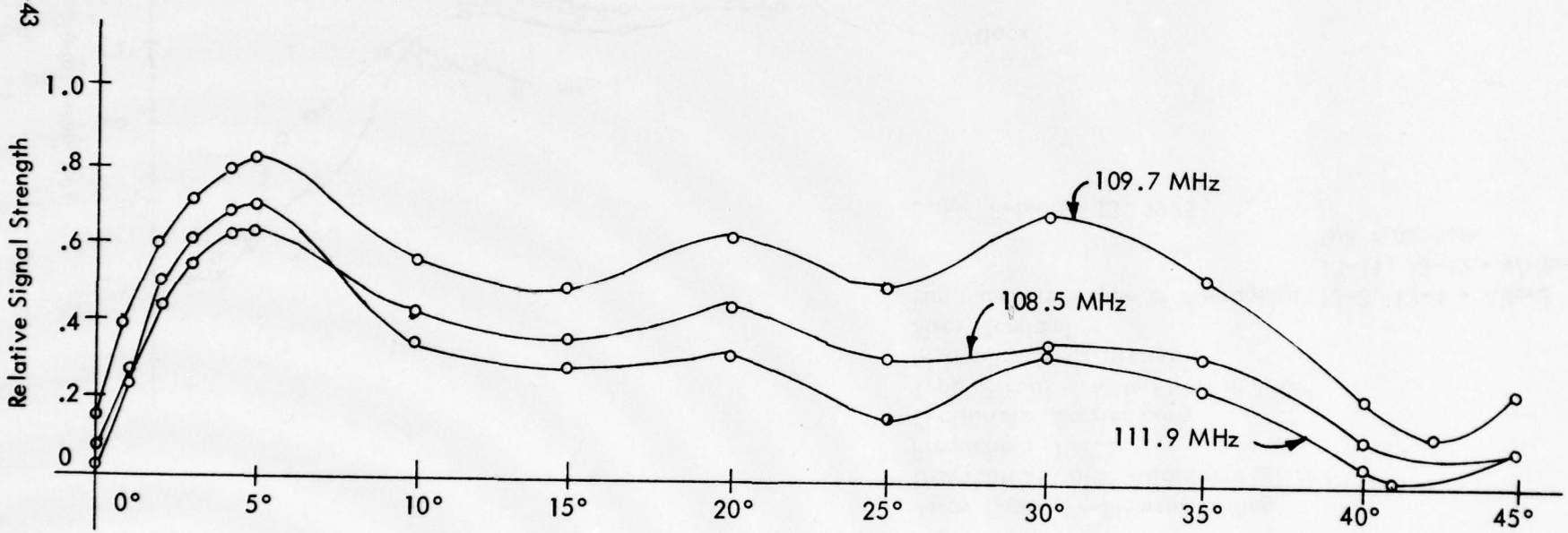

Figure 5-34. Plot of Sideband Signal versus Azimuth, Wilcox Distribution Box, 108.5 MHz, 109.7 MHz, 111.9 MHz.

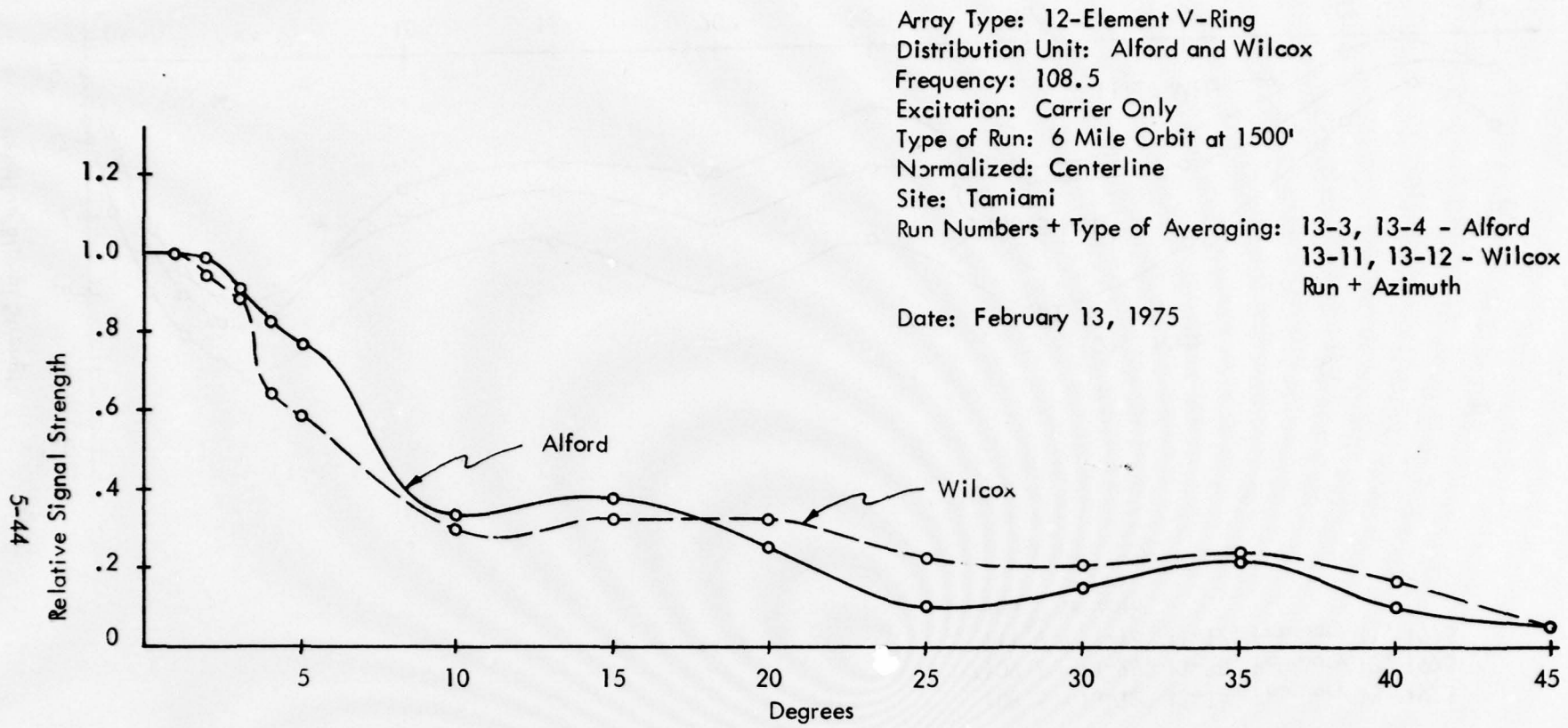

Figure 5-35. Plot of Carrier Strength versus Azimuth, Alford and Wilcox Boxes, 108.5 MHz.

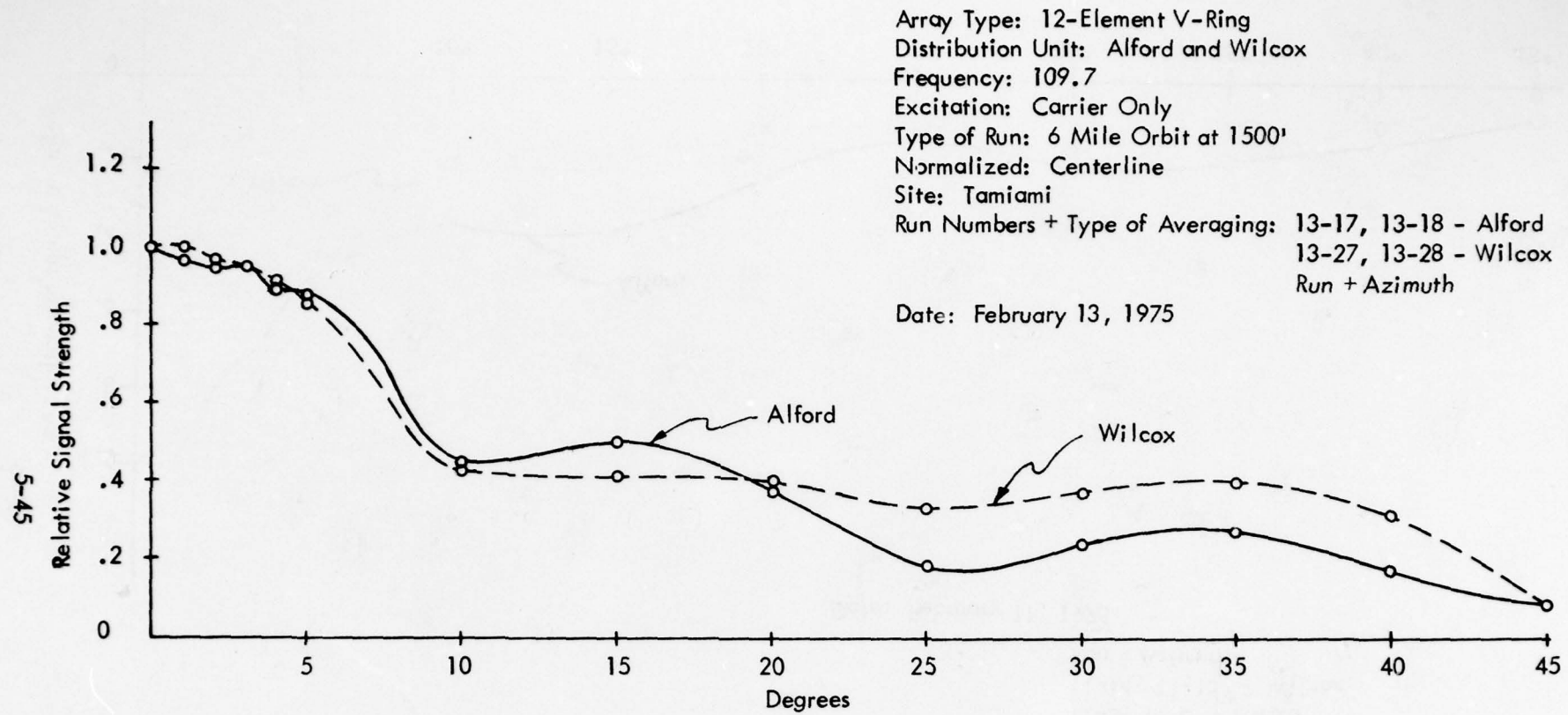

Figure 5-36. Plot of Carrier Strength versus Azimuth, Alford and Wilcox Boxes, 109.7 MHz.

Array Type: 12-Element V-Ring
Distribution Unit: Alford and Wilcox
Frequency: 111.9
Excitation: Carrier Only
Type of Run: 6 Mile Orbit at 1500'
Normalized: Centerline
Site: Tamiami
Run Numbers + Type of Averaging:

11-5, 11-6 - Alford
11-14, 11-15 - Wilcox
Run + Azimuth

Date: February 11, 1975

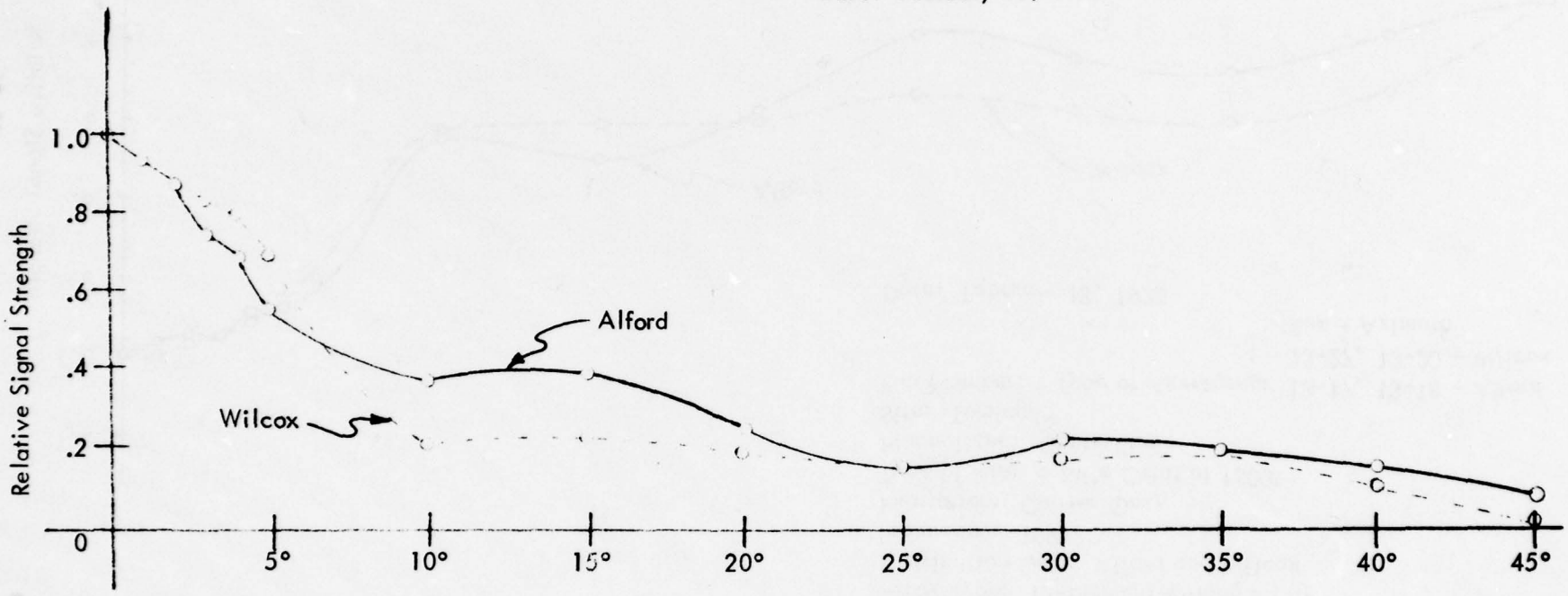

Figure 5-37. Plot of Carrier Strength versus Azimuth, Alford and Wilcox Boxes, 111.9 MHz.

Array Type: 12-Element V-Ring
Distribution Unit: Alford
Frequency: 108.5, 109.7, 111.9
Excitation: Carrier Only
Type of Run: 6 Mile Orbit at 1500'
Normalized: Centerline
Site: Tamiami
Run Numbers, Type of Averaging, Date:

108.5 = 13-3, 13-4, February 13, 1975
109.7 = 13-17, 13-18, February 13, 1975
111.9 = 11-5, 11-6, February 11, 1975
Run + Azimuth

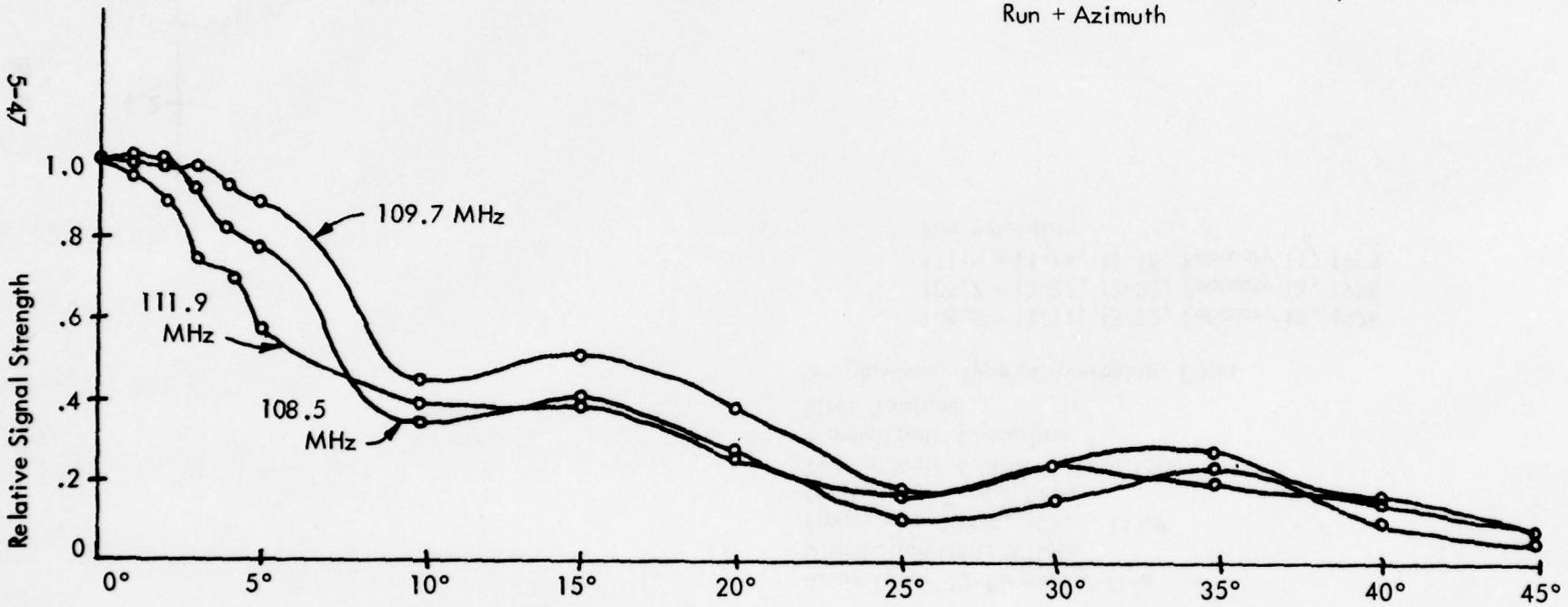

Figure 5-38. Plot of Carrier Strength versus Azimuth, Alford Distribution Box, 108.5 MHz, 109.7 MHz, 111.9 MHz.

Array Type: 12-Element V-Ring
Distribution Unit: Wilcox
Frequency: 108.5, 109.7, 111.9
Excitation: Carrier Only
Type of Run: 6 Mile Orbit at 1500'
Normalized: Centerline
Site: Tamiami
Run Numbers, Type of Averaging, Date:

108.5 = 13-11, 13-12, February 13, 1975
109.7 = 13-27, 13-28, February 13, 1975
111.9 = 11-14, 11-15, February 11, 1975
Run + Azimuth

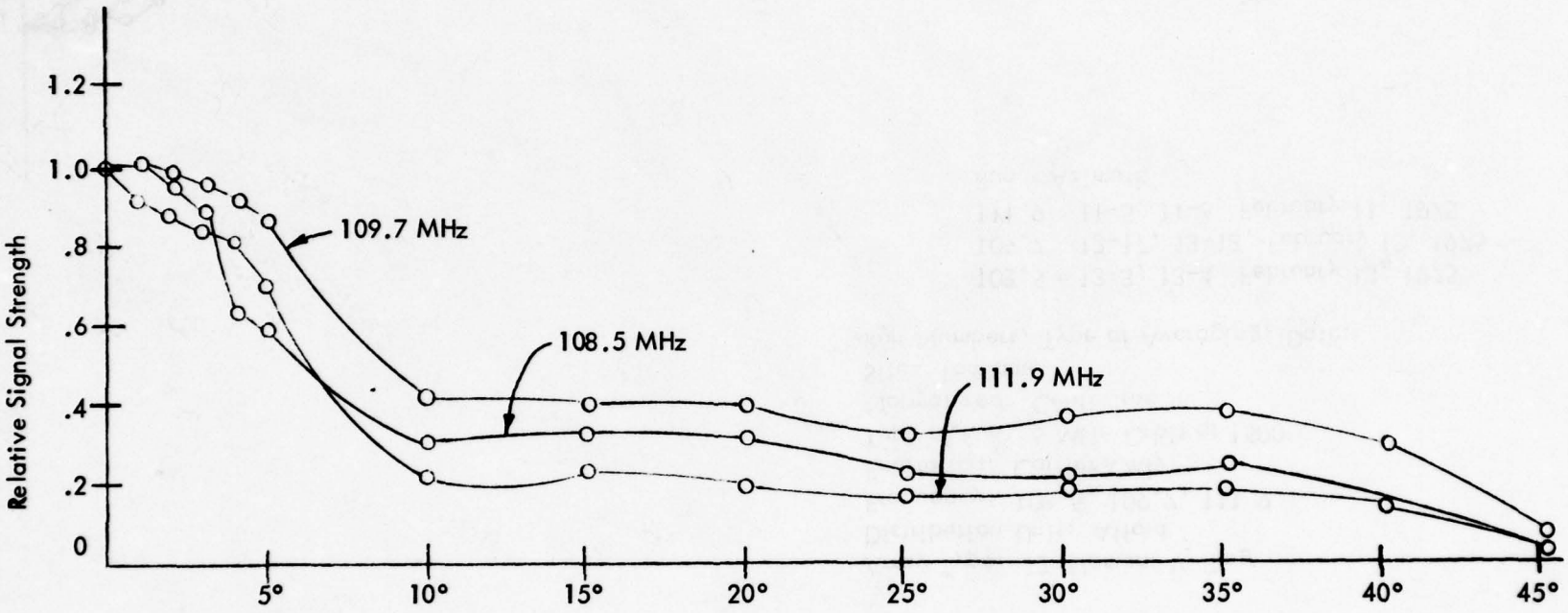

Figure 5-39. Plot of Carrier Strength versus Azimuth, Wilcox Distribution Box, 108.5 MHz, 109.7 MHz, 111.9 MHz.

To minimize the possibility of problems occurring in meeting the signal strength requirements for usable distance, it is recommended that the 3 dB power reduction for alarm limit be changed to 0.5 dB when solid state transmitting equipment is in use. The characteristics of the solid state circuit devices together with implementation of closed loop power level control make the 3 dB figure unrealistic and unnecessary.

Symmetry of signal is typically within one dB for both units, with variations observed as frequency was changed.

dB Taper to 10 Degrees			
	108.5 MHz	109.7 MHz	111.9 MHz
Alford	3.4	6.9	7.3
Wilcox	7.5	8.4	9.6
dB Taper to 35 Degrees			
	108.5 MHz	109.7 MHz	111.9 MHz
Alford	10.2	12.6	12.0
Wilcox	12.4	10.1	14.0

Table 5-12. dB Taper for Three Frequencies with Alford and Wilcox Distribution Systems. Data from 6-mile orbit at 1500 feet.

a. Comments on Data Reduction. Curves show the small circles that indicate points for which analog-to-digital data reduction were performed on the original flight recordings.

Two types of averaging were employed in presentation of the data in graphic form.

1. RUN averaging - Values for the same azimuth from south-to-north and north-to-south runs were averaged. This tends to reduce any error which might result from system lags.

2. AZIMUTH averaging - On sideband only and carrier only runs a second averaging was used. Values for azimuths equidistant north and south of the centerline extended were averaged. Since the array design is inherently symmetric about the centerline, this removes accidental asymmetries and presents a picture less dependent on environmental effects.

Distance Miles	Wilcox		Alford	
	μVolts	dB/1μVolt	μVolts	dB/1μVolt
19	1.21	1.66	0.96	-0.35
18	1.32	2.41	1.48	3.41
17	1.48	3.41	1.66	4.38
16	1.75	4.86	2.06	6.28
15	1.48	3.41	2.28	7.16
14	2.01	6.06	2.57	8.20
13	3.69	11.34	3.25	10.24
12	4.25	12.75	4.25	12.75
11	4.70	13.44	4.93	13.86
10	5.60	14.96	5.82	15.30
9	5.73	15.16	7.57	17.58
8	7.79	17.83	9.56	19.61
7	12.04	21.61	10.30	20.26
6	14.90	23.46	14.20	20.26
5	19.80	25.93	20.80	26.36
4	28.00	28.94	32.70	30.29
3	49.30	33.86	47.80	33.59
2	85.10	38.60	85.10	38.60

Table 5-13. Microvolts at Receiver Input as Function of Distance from Array Along Extended Centerline at 1500 Feet Altitude. Frequency 109.7 MHz, Wilcox and Alford distribution systems to 12-element V-ring array. These potentials at the receiver should be regarded as relative and are not referenced to the FAA DC-3 calibrated values.

Array Type: 12-Element V-Ring
Distribution Unit: Alford and Wilcox
Frequency: 108.5
Excitation: Full Array
Type of Run: 6 Mile Orbit at 1500' AGC Plot
Normalized: Centerline
Site: Tamiami
Run Numbers + Type of Averaging:

13-1, 13-2 - Alford
13-9, 13-10 - Wilcox
Run + Azimuth

Date: February 13, 1975

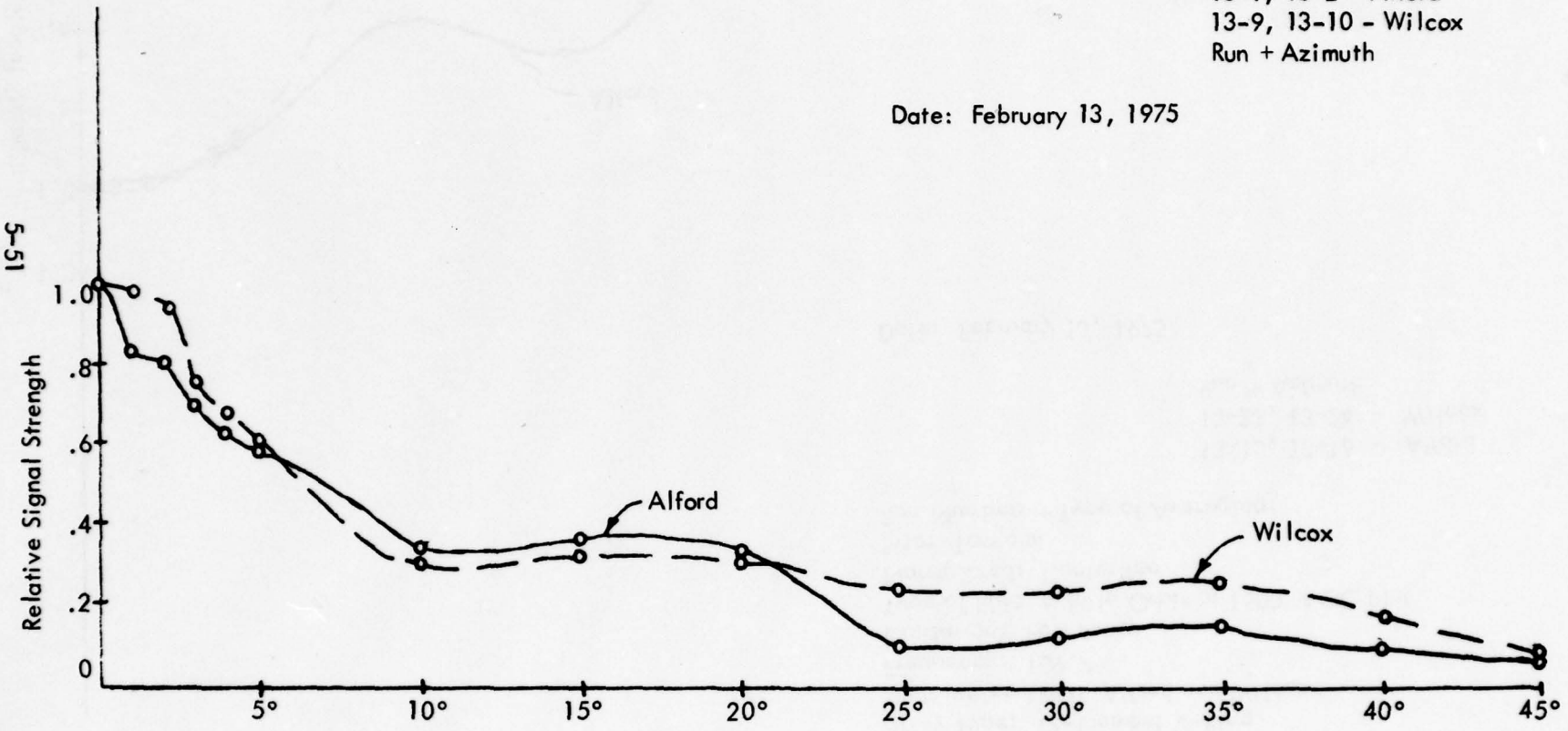

Figure 5-40. Plot of AGC Derived Signal Strength versus Azimuth, Alford and Wilcox Boxes, 108.5 MHz.

Array Type: 12-Element V-Ring
Distribution Unit: Alford and Wilcox
Frequency: 109.7
Excitation: Full Array
Type of Run: 6 Mile Orbit at 1500' AGC Plot
Normalized: Centerline
Site: Tamiami
Run Numbers + Type of Averaging:

13-15, 13-16 - Alford
13-23, 13-24 - Wilcox
Run + Azimuth

Date: February 13, 1975

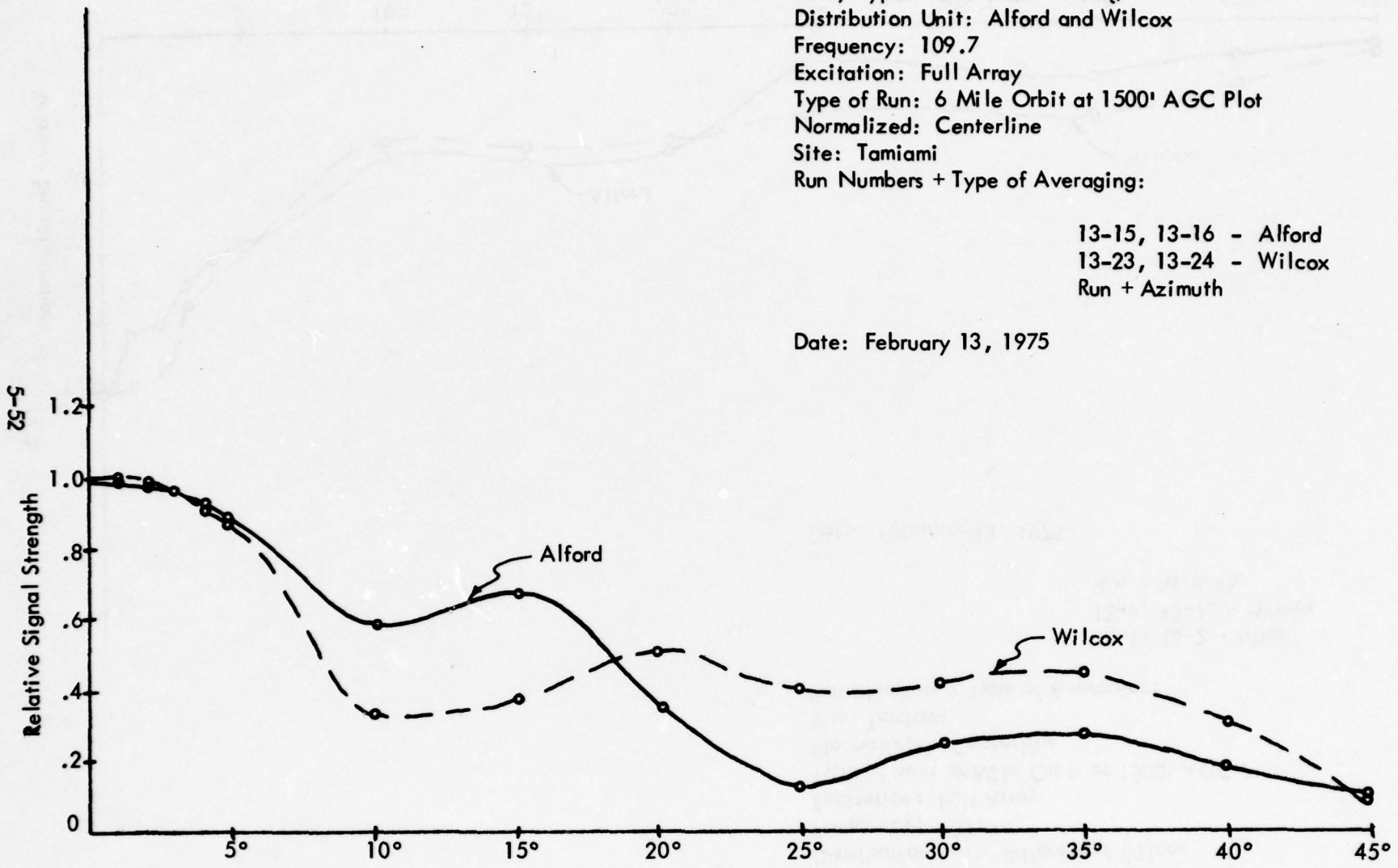

Figure 5-41. Plot of AGC Derived Signal Strength versus Azimuth, Alford and Wilcox Boxes, 109.7 MHz.

Array Type: 12-Element V-Ring
Distribution Unit: Alford and Wilcox
Frequency: 111.9
Excitation: Full Array
Type of Run: 6 Mile Orbit at 1500' AGC Plot
Normalized: Centerline
Site: Tamiami
Run Numbers + Type of Averaging:

11-3, 11-4 - Alford
11-12, 11-13 - Wilcox
Run + Azimuth

Date: February 11, 1975

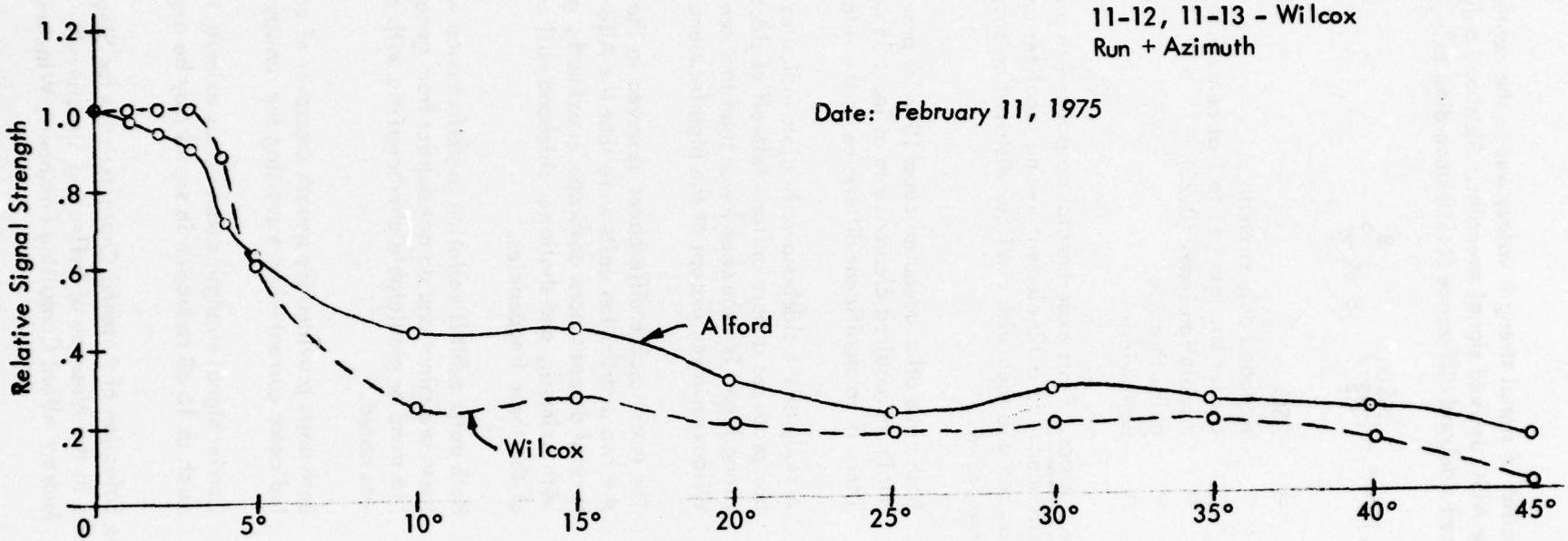

Figure 5-42. Plot of AGC Derived Signal Strength versus Azimuth, Alford and Wilcox Boxes, 111.9 MHz.

Normalization of signal strength values was to the centerline value for carrier only runs and for AGC derived signal strengths. Sideband only signals were adjusted to give normalized sideband difference (NSD) according to*:

$$0.155 = m\left(\frac{NSD}{CS}\right) \qquad \theta = \frac{\theta_o}{2}$$

Where NSD = 2SO
SO = sideband only strength
CS = carrier strength (set to 1 at centerline)
m = modulation index (0.20)
θ = azimuth angle
θ_o = path width

3. Conclusions. From experimental data taken to provide a direct comparison of the performance of a 12-element V-ring localizer array fed first with an Alford distribution box and then with a Wilcox distribution stripline unit, the following conclusions are drawn.

a. Both units offer adequate capability for providing more than minimum required clearance to at least 35 degrees in azimuth. There is no significant difference in the relative performance.

b. A study of the sideband-only plots indicates that the Alford box produces a more uniform fall-off of sideband signal strength and is somewhat lower than that produced by the Wilcox stripline except at the high frequency edge.

c. The most notable differences observed in the performance of the two distribution units were that the Alford box provided several degrees more coverage in azimuth, generally less taper with azimuth, and shallower sideband null on centerline at two of the three frequencies.

d. Both units exhibit variation in performance with frequency but these are minot and do not detract from general performance. No trend or predictable characteristic with change in frequency was noted.

e. Both units provided for smooth crossover of course deviation indicator current when traversing the runway centerline extended.

f. Carrier signal strength taken versus azimuth indicates that as much as 15 dB reduction in signal may be expected as one moves

* "A Guide for the Selection of Antenna Characteristics for Single Frequency and Two Frequency Localizers in the Presence of Reflecting Structures". Preliminary Edition, August 15, 1972. Andrew Alford Consulting Engineers, Winchester, Mass. 01890.

out to 35 degrees. This is in comparison to a drop of approximately 12 to 13 dB when moving from 10 to 18 miles on centerline at a constant altitude. Differences observed in the performance of the two distribution units with respect to signal strength are not considered significant.

E. Figure of Merit Analysis for Alford 14/6 Array.

1. Introduction. This section presents normalized curves of sideband and carrier signal distributions in azimuth for the Alford 14/6 localizer array. The normalization is accomplished to permit a direct comparison with curves for other arrays and relative figures of merit established.

Data was obtained from tests with a two-frequency, single array capture effect localizer system performed during December, 1974, at the Ohio University Tamiami test site in Miami, Florida.

The localizer was adjusted to have a main course path width of four degrees and a clearance path width of 8 degrees. When both frequencies were activated simultaneously, a minor adjustment was made to return the total path width to four degrees.

Six nautical mile orbits were flown at 1500 feet altitude using a Beechcraft Model 35 equipped with the Ohio University Minilab II. Azimuth reference was by theodolite with five degree marks telemetered manually by the operator (one degree marks within five degrees of the centerline). Altitude was maintained with reference to a standard barometric altimeter backed up by a radar altimeter. Radial distance was held by use of area navigation equipment.

2. Presentation of Data. Data was collected in the form of strip chart recordings of AGC voltage in the receiver when various ports of the distribution box were fed with carrier energy at 109.7 MHz. The receiver AGC was calibrated by applying various known signals to the antenna terminals with a Boonton 211A signal generator. Since for a given system the signal at the receiver input terminals will be proportional to the signal strength at the antenna (assuming symmetry, constant attitude with respect to polarization, and constant antenna to receiver line parameters), the AGC may be converted to relative signal strength in space.

The data was carefully analyzed and the results are presented in the following figures:

Figure 5-43 presents the azimuthal distribution of main carrier signal strength normalized to the value on centerline. Readings equidistant on either side of the centerline and readings taken on orbits in each direction have been averaged to remove the effects of instrument lag and of accidental asymmetries due to environmental effects.

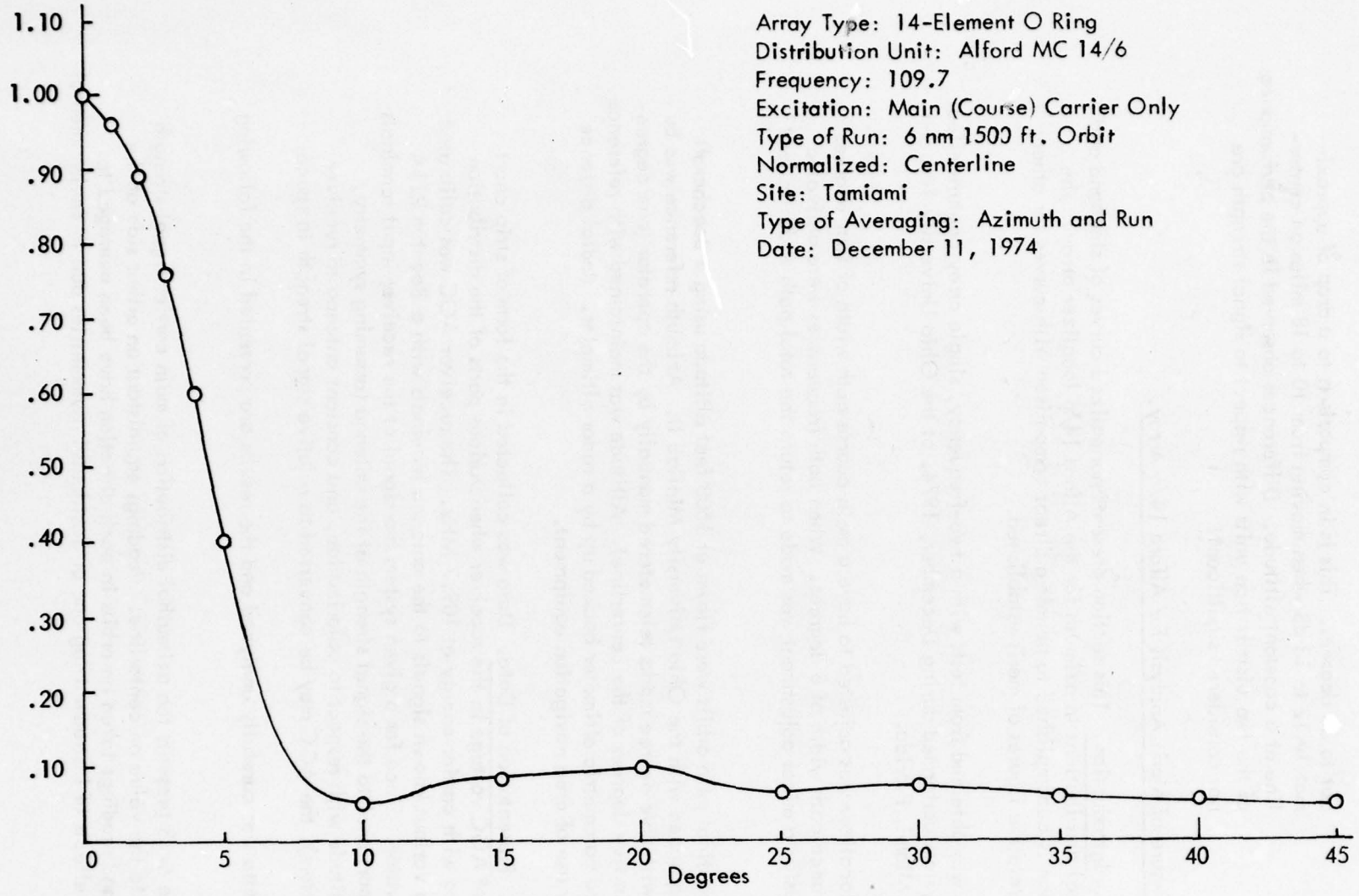

Figure 5-43. Normalized Main Carrier Pattern.

Figure 5-44 plots the signal strength of the clearance carrier normalized to its centerline value. As in Figure 5-43, both run and azimuth averaging are employed.

Figure 5-45 shows the main sideband only pattern plotted as normalized sideband difference (NSD). Course width is 4 degrees for the main (14) array.

Figure 5-46 shows the clearance sideband only NSD. Course width is 8 degrees for the clearance (6) array.

Figure 5-47 combines the main (course) and clearance sideband only NSD patterns for convenience in comparison. Since each NSD pattern has been normalized for comparison with the same unit (hypothetical) localizer, these patterns are not directly applicable to multipath analysis without further information concerning relative absolute signal strengths and a careful evaluation of the capture effect properties of specific receivers. They do, however, illustrate the broad clearance signal obtained with a very narrow azimuthal main signal spread.

3. Conclusions.

a. The main (course) sideband only signal strength pattern of the Alford MC 14/6 two-frequency, single array localizer shows a very high figure of merit with respect to multipath immunity from 10 degrees to 45 degrees off centerline (the extent of the test orbits).

b. The clearance sideband only pattern indicates that the required broad azimuth coverage has been achieved.

c. Minimal multipath is to be expected even under severe environmental conditions with properly functioning receivers.

F. Investigation of Alford MC 14/6 Two-Frequency Localizer Monitor Performance Under Attenuation and Phase Fault Conditions.

1. Introduction. This section covers tests made by Ohio University Avionics personnel at Tamiami Airport from May 14, 1975 to May 19, 1975, on the Alford MC 14/6 localizer array and its monitoring system.

Strip chart recordings were made by truck using the Ohio University Minilab II to record minimum clearances over a 70 degree orbit centered on the runway centerline and with a radius of 1000 feet. Results of these orbital ground runs are presented in Table 5-14 for those runs for which clearance dropped below 200 microamperes CDI.

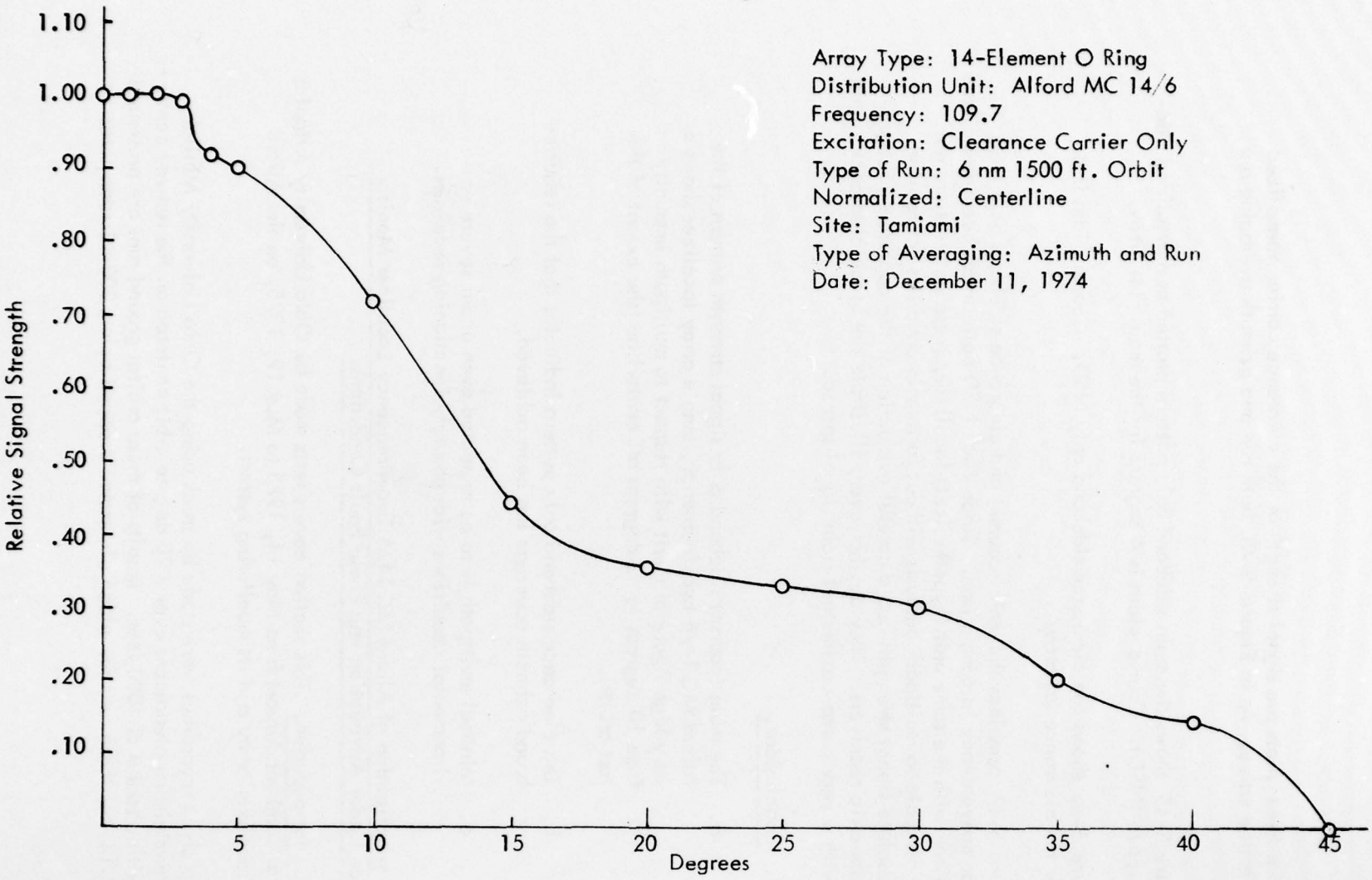

Figure 5-44. Normalized Clearance Carrier Pattern.

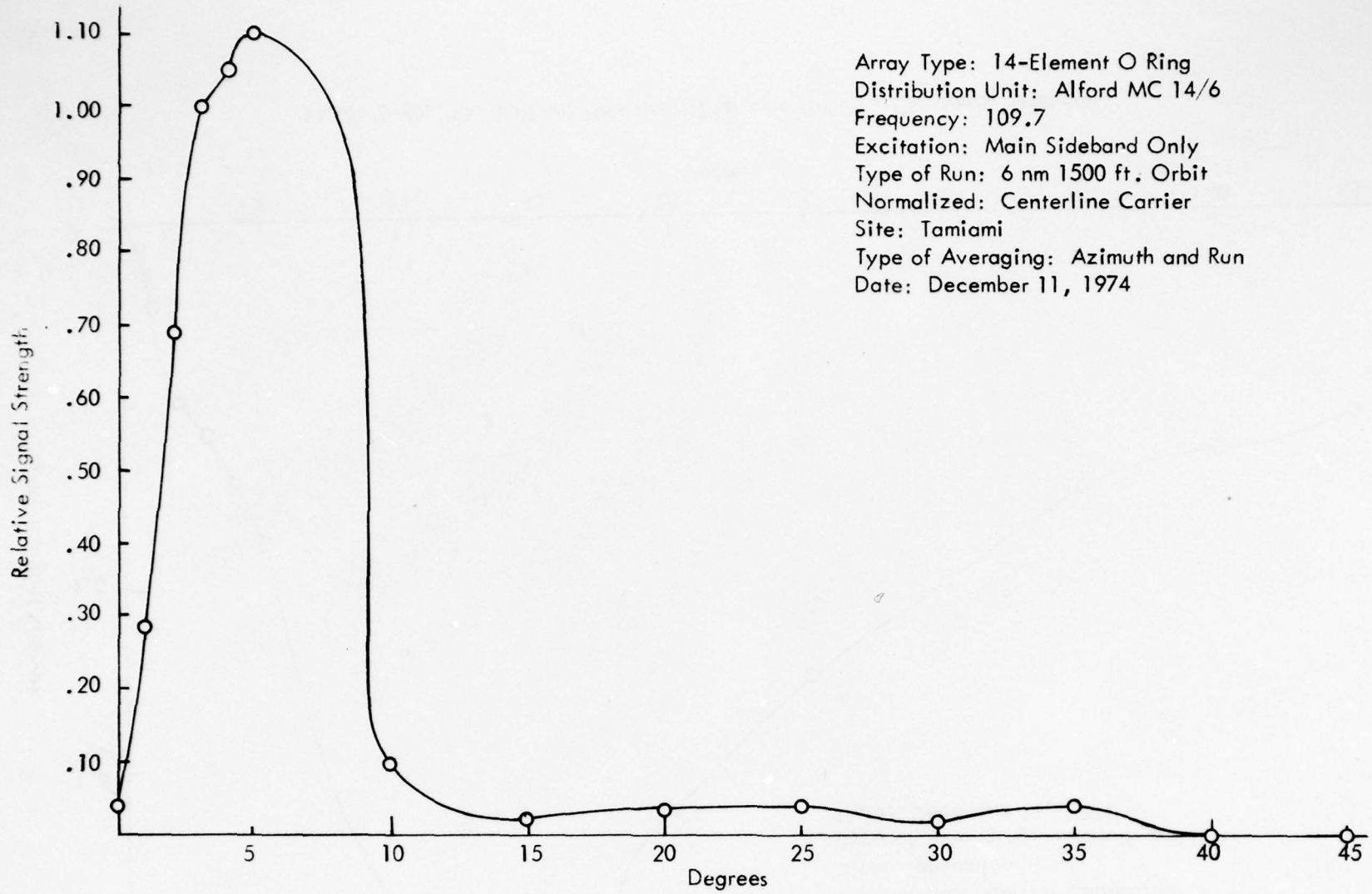

Figure 5-45. Normalized Sideband Difference (NSD) - Main Sideband.

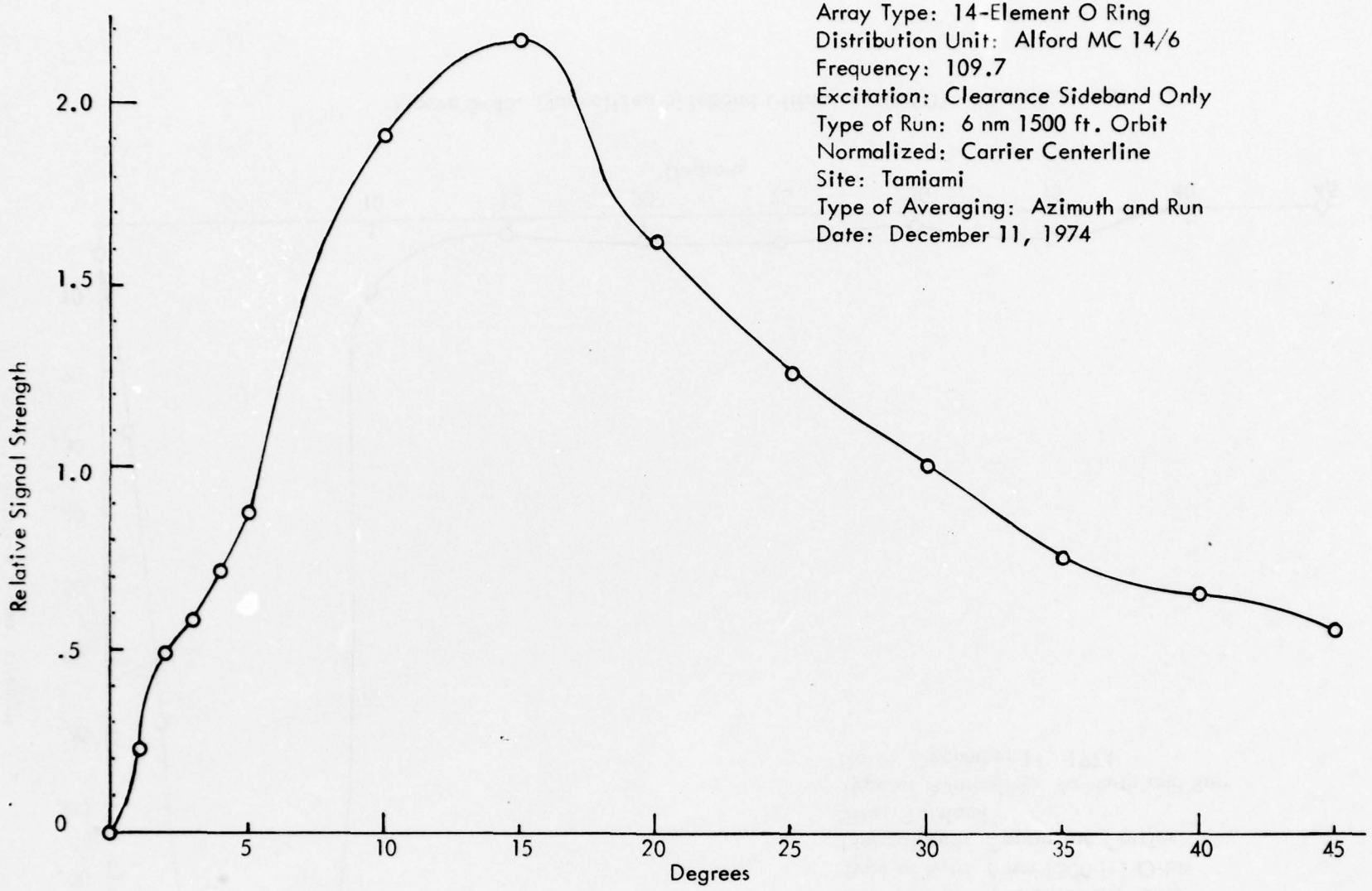

Figure 5-46. Normalized Sideband Difference (NSD) - Clearance Sideband.

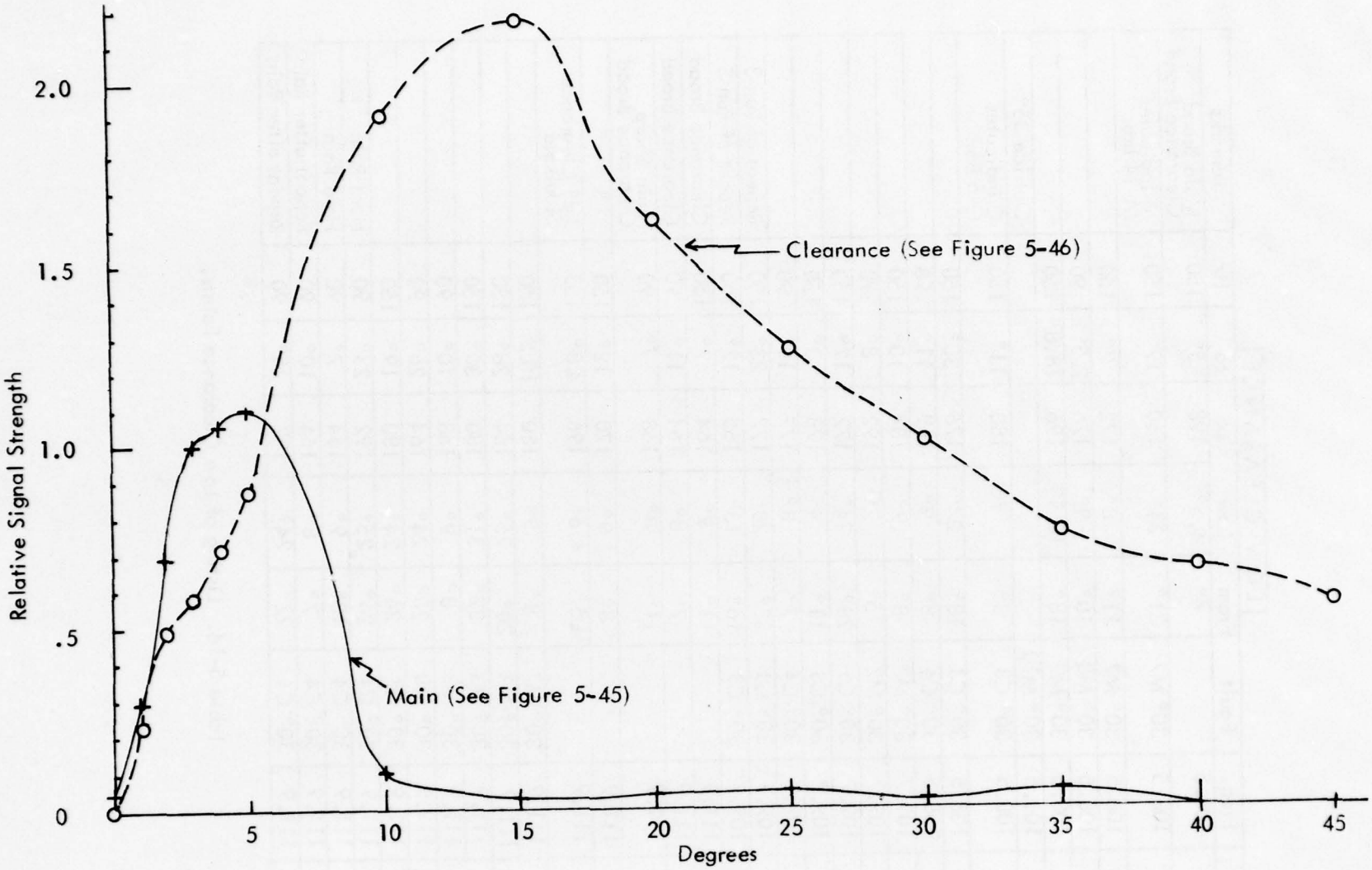

Figure 5-47. Main and Clearance NSD Patterns.

LOW CLEARANCE

Run	Freq.	Fault	From	Low	μa	to	Hz	Remarks
15-28	108.5		4°	4.5°	198	5°	150	Main Broad Clearance Brand
15-39	108.5	30° M7	31°	24°	160	19°	150	M indicates M-14 box
15-39	108.5	30° M7	11°	8°	172	7°	150	
15-40	108.5	30° M8	10°	8°	176	2.5°	90	
15-41	108.5	30° M9	18°	18.5°	196	18.8°	150	
15-42	108.5	30° M10						Outside 35°
15-50	108.5	30° C3	8°	9°	180	11°	150	C indicates C-6 Box
15-50	108.5	30° C3	18°	24°	176	30°	150	
15-51	108.5	30° C4	8°	9°	169	11°	90	
13-35	109.7	30° M7	8°	9°	184	10°	150	
13-35	109.7	30° M7	5°	7°	192	8°	90	
14-3	109.7	30° C3	28°	24°	172	17°	150	
14-3	109.7	30° C3	11°	4°	178	3°	150	
14-5	109.7	30° C4	7°	8°	177	10°	90	
14-11	109.7	30° C3	33°	28°	172	23°	150	Repeat of Run 3
14-11	109.7	30° C3	16°	13°	165	12°	150	Repeat of Run 3
16-6	111.9		11°	9°	164	7°	150	Clearance Broad
16-6	111.9		7°	8°	164	11°	90	Clearance Broad
16-9	111.9		11°	8°	168	7°	90	Main Sharp Clearance Broad
16-9	111.9		8°	9°	170	12°	150	" "
17-9	111.9		4.5°	4.6°	196	4.8°	150	3 dB Clearance Sideband
17-17	111.9	30° M7	8°	9°	180	10.5°	150	
17-17	111.9	30° M7	20°	25°	164	28°	150	
17-18	111.9	30° M8	32°	31°	180	30°	150	
17-18	111.9	30° M8	8°	9°	168	10°	90	
17-18	111.9	30° M8	20°	24°	164	26°	90	
17-28	111.9	30° C3	26°	24°	180	19°	150	
17-29	111.9	30° C4	26°	25°	192	23°	90	Hard Rain
17-29	111.9	30° C4	10°	9°	164	7°	90	Hard Rain
17-30	111.9	30° C4	7°	8°	164	10°	90	Repeat after Rain
17-30	111.9	30° C4	22°	24°	192	25°	90	Repeat after Rain

Table 5-14. Listing of Low Clearance Points.

In order to obviate the effects of observer and instrument lag, the truck was stopped and accurately positioned at the centerline and at the course edges. At these points readings were made with a digital meter and entered in the log.

2. Data and Analysis. In making the tests of monitor action, three types of faults were used. First, a 3 dB attenuation was inserted in each of the M14 lines, each of the C6 lines, and in the course and clearance sideband-only lines. All monitor readings and alarm indications (if any) are noted together with the measured field quantities.

This data is presented in Tables 5-15, 5-16, and 5-17 for the three frequencies used (108.5, 109.7, and 111.9 MHz). An asterisk (*) after a reading indicates an alarm. An A, U, or D preceding a reading indicates the relationship of the monitor alarm to the field conditions as shown in Figure 5-48.

		Path	
		In Tolerance	Out of Tolerance
Monitor	Happy	A	D
	Unhappy	U	A

Figure 5-48. Criteria for Assessing Acceptability of System Status.

An A response is acceptable while a U response is undesirable but conservative. The D, defective, response is not to be tolerated since it represents an unsafe condition.

Tables 5-18, 5-19, and 5-20 present the results of inserting a 30 degree phase lag at each of the above-mentioned points. The same symbols are used.

In order to check the monitor responses further, a series of variable phase retard faults was used. In these tests the phase was varied from a minimum until a monitor indicated an alarm condition.

Tables 5-21, 5-22, and 5-23 present this data. Here the asterisk (*) indicates an alarm, and the right hand column gives the phase lag which was just sufficient to initiate the alarm. Table 5-24 summarizes the monitor alarms catalogued in Tables 5-15 to 5-20.

3. Tests to Determine Operating Parameters of Equipment. All distribution units and antenna measurements were made at a frequency of 109.7 MHz. Transmitting equipment was retuned for each frequency. Null checks, alignment, width and fault checks were made at an accurately marked 1000-foot circle with the truck-mounted Minilab.

LINE	MAIN		SIM CLR		FIELD			REMARKS
	CRS	WDH	CRS	WDH	CL	090	150	
N	022	165	002	140				
1	022	161	003	147	2.1	151	147	M-14 Box
2	022	161	003	142	5.0	149	148	
3	022	161	003	140	2.0	149	145	
4	022	166	002	140	3.5	148	149	
5	022	170	002	145	0.5	154	149	
6	022	172	002	142	2.9	156	154	
7	023	180	U 020*	153	0.2	163	154	
8	020	172	U-013*	119	1.6	161	154	
9	021	170	009	150	0.3	160	150	
10	020	163	008	154	1.6	153	148	
11	020	161	004	148	-1.4	153	141	
12	022	160	004	140	0.9	150	142	
13	021	162	006	148	-1.9	152	141	
14	022	161	008	151	0.7	151	145	
N	023	165	008	151	-1.6	152	147	
c1	023	166	007	147	3.9	151	149	c indicates C-6 Box
c2	022	165	008	141	0.9	153	146	
c3	022	170	U 024*	U 177*	2.9	154	151	
c4	020	165	U-014*	130	0.2	158	147	
c5	020	161	011	151	2.2	152	147	
c6	020	162	007	142	0.8	154	145	
CRS SO	018	A 117*	006	160	2.1	109	107	
CLR SO	020	162	010	122	-0.2	153	144	
N	021	165	002	142	0.9	157	148	

N = normal (no fault) runs.
* = alarm.

Monitor data in DDM times 1000.
Field data CDI microamperes.
Negative course figures indicate 90 Hz.

Table 5-15. Monitor Response Data, 108.5 MHz. (Fault = 3 dB Attenuation in Line Indicated).

LINE	MAIN		SIM CLR		FIELD		150	REMARKS
	CRS	WDH	CRS	WDH	CL	090		
1	010	140	-005	151	-2.3	159	141	M-14 Box
2	008	138	-004	150	-3.2	155	140	
3	008	134	-005	142	-4.5	154	136	
4	008	136	-010	148	-4.8	154	136	
5	008	138	-010	150	-6.2	161	138	
6	008	142	-010	145	-6.3	164	141	
7	008	153	-008	148	-6.4	169	144	
8	008	150	-017	130	-4.6	167	146	
9	008	151	-013	157	-4.7	163	140	
10	008	149	-010	165	-4.5	161	137	
11	008	145	-014	150	-5.7	157	132	
12	008	141	-019	142	-6.4	157	130	
13	006	141	-016	150	-7.5	159	131	
14	008	144	-013	160	-8.3	160	131	
N	008	147	-013	152	-5.7	159	134	
c1	010	145	-014	148	-6.3	165	138	c indicates C-6 Box
c2	010	145	-014	140	-4.2	164	140	
c3	010	150	-014	165	-4.5	168	143	
c4	010	149	-022?	148	-4.8	164	142	
c5	010	142	-016	140	-5.1	162	138	
c6	010	146	-018	142	-5.2	162	141	
CRS	008	102?	-018	150	-2.7	116	100	
CLR	010	150	-008	113?	-4.4	158	142	
N	011	150	-011	158	-4.7	160	141	

N = normal (no fault) runs. Monitor data in DDM times 1000.
Field data CD' microamperes.

Note: Alarm indications were not set before the 109.7 MHz data were taken and thus are not listed here. However, given the approximate ± 15 and ± 30 DDM alarm limits for the CRS and WDH channels respectively, as determined from the data in Table 5-22, the boxed values show potential alarm conditions.

Table 5-16. Monitor Response Data, 109.7 MHz. (Fault = 3 dB Attenuation in Line Indicated).

LINE	MAIN		SIM CLR		FIELD			REMARKS
	CRS	WDH	CRS	WDH	CL	090	150	
N	019	159	-014	099	1.2	143	140	Rain
1	018	180	-012	102	0.5	143	142	M-14 box
2	018	180	-010	105	4.0	142	143	
3	017	177	-008	102	0.2	143	138	
4	016	178	-013	099	14.7	131	141	
5	018	180	-007	111	-0.3	150	144	
6	019	181	-005	110	1.4	155	150	
7	019	184	U-026*	088	1.3	158	153	
8	020	180	U 028*	U 142*	4.2	157	158	
9	020	180	U 000*	115	4.0	154	154	
10	018	181	-007	112	4.6	152	147	1830Z
	021	181	-010	105				1900 Z
11	020	180	-007	115	3.5	148	144	
12	020	175	-012	101	0.0	148	140	
13	018	177	-010	103	-0.5	149	142	
14	019	178	-010	109	-1.8	150	140	
N	019	180	-012	103	1.4	151	146	2000Z 1975 May 16
N	020	182	-010	102	6.8	149	156	1230Z 1975 May 17 80°F
c1	020	186	U 000*	110	6.7	150	157	c indicates C-6 box
c2	020	187	U 002*	104	5.3	150	154	
c3	020	189	U-038*	090	5.4	155	156	
c4	021	190	U 024*	U 148*	3.8	154	154	
c5	020	182	-018	098	4.2	152	152	
c6	020	183	-011	099	3.2	152	150	
CRS SO	016	A 133*	-008	103	4.7	102	103	
CLR SO	020	181	-009	120	2.7	151	147	
N	020	182	-007	110	3.7	151	147	1310Z 82°F

N = normal (no fault) runs.

Monitor data in DDM times 1000.
Field data CDI microamperes.

Table 5-17. Monitor Response Data, 111.9 MHz. (Fault = 3 dB Attenuation in Line Indicated).

LINE	MAIN		SIM CLR		FIELD			REMARKS
	CRS	WDH	CRS	WDH	CL	090	150	
N	018	161	-002	140	-2.2	158	147	
1	010	155	-006	138	-5.5	158	141	M-14 box
2	008	159	004	149	-10.6	160	137	
3	A 002*	146	009	150	-14.4	168	134	
4	A 000*	143	-010	125	-18.9	176	130	
5	A-001*	140	000	125	-17.1	180	130	
6	005	145	003	140	-12.6	174	137	
7	007	149	U-123*	U+19*	-6.4	167	144	
8	028	177	U 170*	U 280*	0.7	156	153	
9	029	178	-008	122	9.4	149	161	
10	A 034*	181	A-036*	A 095*	12.8	141	165	
11	A 032*	176	000	143	13.6	143	162	
12	030	170	A-018*	125	11.5	143	156	
13	024	165	U-014*	130	6.2	149	148	
14	022	162	-004	140	2.4	150	146	
N	016	160	-006	140	-1.7	158	146	
c1	018	160	U 013*	152	-2.2	158	145	c indicates C-6 box
c2	015	155	004	136	-2.6	158	145	
c3	010	150	U-027*	U 006*	2.5	159	146	
c4	024	173	U 146*	U 320*	-1.0	158	149	
c5	019	162	U-055*	139	-2.9	157	146	
c6	018	161	-010	130	-1.2	158	146	
CRS SO	013	148	-004	140	-1.9	126	115	
CLR SO	016	157	U-029*	U 076*	-2.1	159	145	
N	017	160	006*	140	-2.6	158	146	

N = normal (no fault) runs.
* = alarm.

Monitor data in DDM times 1000.
Field data CDI microamperes.
Negative course figures indicate 90 Hz.

Table 5-18. Monitor Response Data, 108.5 MHz, May 15, 1975. (Fault = 30° Retard in Line Indicated).

LINE	MAIN		SIM CLR		FIELD			REMARKS
	CRS	WDH	CRS	WDH	CL	090	150	
N	011	150	-011	158	- 4.7	160	141	
1	007	145	-006	152	- 8.4	158	133	M-14 box
2	003	150	-001	161	-12	159	131	
3	002	145	-006	162	-17.2	169	126	
4	005	135	-021	131	-19.3	177	125	
5	005	130	-010	127	-20.5	180	124	
6	002	133	-006	156	-15.4	179	130	
7	000	137	-165?	009?	- 9.2	171	137	
8	020	161	122 ?	300?	- 0.3	156	150	
9	023	169	-028	115	5.5	150	157	
10	027 ?	170	-018	125	10.9	143	162	
11	026 ?	163	-010	153	10.9	142	157	
12	024	156	-040?	120	8.4	145	150	
13	018	155	-030	134	1.9	148	143	
14	016	153	-012	155	- 0.6	152	140	
N	010	150	-020	148	- 4.7	158	141	
					- 3	142	141	After heavy rain
N	010	152	-008	130	- 1.7	156	148	May 14 1200 Z
c1	008	152	010 ?	140	- 6	159	136	c indicates C-6 box
c2	007	149	004	131	- 4.3	158	136	
c3	003	145	- 140?	008?	- 6.2	162	135	
c4	015	165	148 ?	300?	- 4.9	159	138	
c5	011	159	-063 ?	075?	- 4.3	157	137	
c6	010	158	-017	122	- 5.7	160	136	
CRS	005	D 140	-011	130	- 5.3	124	104	
CLR	008	151	-036	055	- 5.7	162	135	
N	010	155	-010	130	- 4.7	160	136	

N = normal (no fault) runs.
* = alarm.
? = (see note Table 5-16).

Monitor data in DDM times 1000.
Field data CDI microamperes.
Negative course figures indicate 90 Hz.

Table 5-19. Monitor Response Data, 109.7 MHz, May 14, 1975. (Fault - 30° Retard in Line Indicated).

LINE	MAIN		SIM CLR		FIELD			REMARKS
	CRS	WDH	CRS	WDH	CL	090	150	
N	020	182	-007	110	3.7	151	147	Normal
1	013	178	-008	105	-0.5	148	140	M-14 box
2	012	180	U-002*	117	-3.4	151	138	
3	A 004*	166	A 006*	120	-10.0	156	131	
4	A 002*	165	D-012	098	-12.4	165	129	
5	A 003*	165	D-008	099	-14.2	172	130	
6	D 009	170	A 009*	122	-8.2	171	138	
N	020	173	002	132				New Normal
7	018	177	U-120*	U 006*	-2.4	159	144	
8	025	200	U 135*	U 240*	7.3	148	155	
9	U 036*	203	-009	099	13.7	140	164	
10	A 042*	212	A-028*	083	18.6	134	166	
11	A 042*	203	A 003*	113	18.5	131	160	
12	A 039*	200	D-010	103	16.7	133	152	
13	U 034*	196	-004	112	9.8	138	145	
14	U 032*	192	U 008*	129	7.7	141	143	
N	026	190	U 004*	120	3.1	147	145	86°F
N	020	172	-002	130				
N	026	190	004*	120	3.1	147	145	Normal
c1	022	189	U 022*	133	3.0	149	144	c indicates C-6 box
c2	024	187	U 018*	121	2.3	149	143	
c3	020	180	U-145*	U-006*	0.6	152	142	
c4	021	190	U 149*	U 280*	-1	150	139	
c5	010	180	U-062*	U 108*	-1.2	149	140	
c6	010	179	-017	092	0.3	151	143	
CRS SO	008	U 143*	-018	100	-0.3	150	141	
CLR SO	010	D 175	U-026*	A 036*	0.4	097	092	
N	020	172	-001	132				Normal

N = normal (no fault) runs.
* = alarm.

Monitor data in DDM times 1000.
Field data CDI microamperes.
Negative course figures indicate 90 Hz.

Table 5-20. Monitor Response Data, 111.9 MHz.
(Fault = 30° Retard in Line Indicated).

LINE	MAIN CRS	MAIN WDH	SIM CLR CRS	SIM CLR WDH	PHASE RETARD	REMARKS
1					64°	No alarm
2	007	160	005*	148	37.5°	M-14 box
	001*				59°	
3	003*	143	006*	148	30°	
4	001*	142	-011	120	29°	
5	001*	142	-002	120	27°	
6	001*	140	005	140	39°	
7	017	160	-017*	125	4°	
	013	155		100*	10°	
8	017	160	009*	152	4°	
	018	164		169*	7°	
9	030*	178	-006	120	34°	
10	026	171	-020*	117	18°	
	030*	175		119	23°	
11	030*	162	-001	140	25°	
12	030*	171	-017*	122	30°	
13	030*	169	-017*	122	51°	
14	030*	165	002	143	64°	
c1	017	160	006*	145	16°	c indicates C-6 box
c2	016	159	006*	140	29°	
c3	017	160	-018*	123	5°	
	016	158		100*	11°	
c4	017	161	005*	145	3°	
	018	163		168*	7°	
c5	018	160	-018*	123	10°	
	018	152		100*	24°	
c6						No Alarms
CRS SO	010	130*	-005	138	45°	
CLR SO	016	158	-018*	100*	21°	
N	017	160	-007	138		

N = normal (no fault) runs.
* = alarm.

Monitor data in DDM times 1000.
Field data CDI microamperes.
Negative course figures indicate 90 Hz.

Table 5-21. Monitor Response to Phase Lags Just Sufficient to Initiate Alarm, 108.5 MHz.

LINE	MAIN CRS	MAIN WDH	SIM CLR CRS	SIM CLR WDH	PHASE RETARD	REMARKS
N	009	157	-011	130	0	1730 Z 1975 May 13
1	-002	140	-021	127	69°	M-14 box
2	-004	145	-002*	149	52°	
	-005*	147		148	55°	
3	000	140	003*	140	26°	
	-005*	137		142	31.5°	
4	-005*	137	-020	109	32°	
5	-005*	133	-008	110	31°	
6	002	138	-002*	135	34°	
	003*	132		132	45°	
7	009	151	-002*	118	5°	
	007	149		092*	11.5°	
	-004*	132			49°	
8	012	156	-002*	139	2.5°	
	013	160		153*	7°	
	023*				37.5°	
9	023*	171	-026	108	34°	
10	017	161	-026*	113	10°	
	023*	170		098	24°	
11	023*	168	-009	130	24.5°	
		180	-003*	138	54°	
12	023*	165	-026*	108	27°	
13	023*	160	-026*	110	52°	
14	022	158	+006	142	69°	
c1	009	151	-001*	138	21°	c indicate C-6 box
c2	007	148	-002*	125	36°	
c3	009	151	-025*	117	2°	
	008	150		091*	8°	
c4	010	153	-005*	139	2°	
	011	155		160*	6°	
c5	010	155	-027*	113	7°	
	011	155		091*	20°	
c6	013	158	-022	098	69°	
CRS SO	006	125*	016	130	41°	
CLR SO	009	152	025	090*	18°	

N = normal (no fault) runs.
* = alarm.

Monitor data in DDM times 1000.
Field data CDI microamperes.
Negative course figures indicate 90 Hz.

Table 5-22. Monitor Response to Phase Lags Just Sufficient to Initiate Alarm 109.7 MHz.

LINE	MAIN CRS	MAIN WDH	SIM. CLR CRS	SIM. CLR WDH	PHASE RETARD	REMARKS
N	026	177	000	132		
1	016	160	000	134	67°	No Alarm M-14 box
2	014	168	014*	143	46°	
3	016	165	014*	145	21°	
	009*	155		148	38°	
4	009*	159	004	129	28°	
5	009*	159	007	120	31°	
6	013	165	014*	143	29°	
	009*	149		142	51°	
7	020	172	-010*	125	3°	
	019	170		093*	10°	
8	020	162	013*	147	3°	
	021	177		163*	6°	
9	033*	192	013*	099	36°	
10	033*	190	000	112	30°	
11	033*	182	002	139	24°	
12	032*	179	012	118	27°	
13	032*	173	009	125	50°	
14	031	160	003	142	72°	No Alarms
N	020	172	-002	130		
c1	020	160	009*	137	14°	c indicates C-6 box
c2	020	160	009*	130	22°	
c3	020	160	-014*	120	2°	
	019	170		096*	8°	
c4	020	172	009*	141	2.5°	
	020	173		162*	6°	
c5	020	173	-009*	110	21°	
	020	175		098*	38°	
c6	020	175	-009*	118	16°	
	020	174		099*	36°	
CRS SO	016	144*	-001	131	26°	
CLR SO	020	175	000	98*	18°	

N = normal (no fault runs.
* = alarm.

Monitor in DDM times 1000.
Field data CDI microamperes.
Negative course figures indicate 90 Hz.

Table 5-23. Monitor Response to Phase Lags Just Sufficient to Initiate Alarm, 111.9 MHz.

	MAIN		SIM CLR	
	CRS	WDH	CRS	WDH
A	11	2	6	2
U	3	1	30	13
D	1	1	3	0

Table 5-24. Summary of Monitor Alarms Classified According to Figure 5-43. This summary includes the results for the fault tests at the frequencies of 108.5 and 111.9 MHz only.

Transmitter modulation was set at 20%, ± 0.2% for each frequency. Frequencies, VSWR, insulation resistance, modulator distortion, and total distortion at the audio harmonic frequencies were established within published tolerances.

Null checks were made for each pair of antennas being fed through the distribution unit. Unmodulated carrier from the course transmitter was fed to the SO input of the M-14 distribution box. CS port and the SO feed line were dummy loaded. All antenna feed lines and combiner box ports were dummy loaded except those associated with the antennas under test. The clearance transmitter was off.

NULL CHECKS M-14			
Antenna Pair	Null	In	Remarks
1 and 14	24 inches	150 Hz	
2 and 13	4 inches	90 Hz	
3 and 12	22 inches	150 Hz	
4 and 11	16 inches	150 Hz	Shallow Null
5 and 10	17 inches	150 Hz	
6 and 9	22 inches	150 Hz	
7 and 8	155 inches	90 Hz	
Composite Sideband	24 inches	150 Hz	

Table 5-25. Null Checks of Antenna Pairs.

No reason was found for the large shift of antenna pair 7 and 8, and the composite sideband null seems to indicate the reading to be in error.

Null checks were made on the center three antenna pairs, feeding unmodulated carrier from the course transmitter to the SO port of the C-6 distribution box with the CS port and feed lines dummy loaded. Lines to the combiner box and output ports were dummy loaded except those associated with the antenna pair under test. Input ports to the M-16 box were also dummy loaded.

NULL CHECKS C-6		
Antenna Pair	Null	In
5 and 10	3 inches	150 Hz
6 and 9	35 inches	90 Hz
7 and 8	28 inches	150 Hz
Composite	11 inches	90 Hz

Table 5-26. Null Checks of Center Antenna Pairs.

Power measurements were made at the output of the combiner unit using a Bird Thruline wattmeter with the system fed normally (both course and clearance). A Thruline body was inserted between the output port and antenna feed line being measured.

POWER TO ANTENNA FEEDLINE					
	Power (mw)			Power (mw)	
Port	250 mw Element	1w Element	Port	250 mw Element	1w Element
1	10*	6	14	13*	8
2	10*	6	13	14*	8.8
3	27*	18	12	40*	28
4	112*	80	11	138*	110
5	225*	192	10		200*
6		400*	9		440*
7		300*	8		310*

* Measured, others from conversion curve.

Table 5-27. Antenna Feedline Power.

Ports 8 through 14, which feed the predominantly 90 Hz portion of the antenna array, show consistently higher power than ports 1 through 7, which feed the 150 Hz side.

Power was also measured at the input ports to the monitor box. All measurements are with the 250 mw element.

Port	Power (mw)	Port	Power (mw)
1	2	14	3.5
2	2	13	3
3	5	12	7
4	20	11	26
5	38	10	45
6	100	9	105
7	60	8	58.5

Table 5-28. Power at Monitor Box Inputs.

Phasing checks were conducted using various antennas. These were made with a Thruline body with 250 mw element inserted in the antenna line being investigated. The PFCD was used for the readings.

COURSE TRANSMITTER PHASING		
Antenna	DDM	Comments
4	----	Insufficient level - 90 Hz predominant
5	20 - 150 Hz	
6	0	Reference
7	0	
8	13 - 150 Hz	
9	15 - 150 Hz	
10	2 - 90 Hz	
11	14 - 150 Hz	

Table 5-29. Course Transmitter Phasing.

CLEARANCE TRANSMITTER PHASING		
Only antennas 7 and 8 had sufficient level to calibrate the PFCD.		
Antenna 7	0 DDM	Reference
8	22 DDM	150 Hz

Table 5-30. Clearance Transmitter Phasing.

Antenna 7 was selected to phase both course and clearance transmitters as a quick phasing check for stability could be made with both transmitters operating.

A complete set of fault check readings was made with the PFCD at the 1000-foot circle. Readings were taken on centerline and at the 2° course width markers. These checks were made at a frequency of 111.9 MHz. The checks were not made at the time of the Minilab checks, and alignment and 4° course width were adjusted to accommodate the PFCD.

Figure 5-49, 30° Dephasing, is a plot of centerline readings of the Minilab for the three test frequencies and the PFCD at 111.9 MHz.

Figure 5-50 is the width reading of the monitor, Minilab and PFCD for 30° dephasing at 111.9 MHz.

The correlation between the PFCD and the Minilab appears to be very good.

Carrier equality showed a slight drift over a period of three days with no adjustments made to the equipment.

Date	Time	Course Carrier	Clearance Carrier	Remarks
May 18	8:00a.m.	7 DDM-150 Hz	10 DDM-150 Hz	Equipment set for 0 Allignment
May 18	4:00p.m.	8 DDM-150 Hz	12 DDM-150 Hz	Fault Tests During Day
May 19	8:00a.m.	6 DDM-150 Hz	13 DDM-150 Hz	Equip. on Overnight
May 19	6:00p.m.	6 DDM-150 Hz	12 DDM-150 Hz	Fault Tests During Day
May 20	7:30a.m.	7 DDM-150 Hz	11 DDM-150 Hz	Equip. on Overnight

Table 5-31. Carrier Equality Drift Measurements.

Antenna phasing changes were noted, the extremes being:

Date	Time	Course	Clearance	Remarks
May 18	5:30 p.m.	0	0	Equip. Rephased
May 19	7:30 a.m.	10 DDM-90Hz	6 DDM-150 Hz	Heavy Rain Overnight

Table 5-32. Antenna Phase Changes.

Power measured at the transmitter also showed some instability.

Date	Time	Course CS	Course SO	Clearance CS	Clearance SO
May 19	5:30 p.m.	12	140	12	450
May 20	7:45 a.m.	11+	137	12	440

Table 5-33. Transmitter Power Drift.

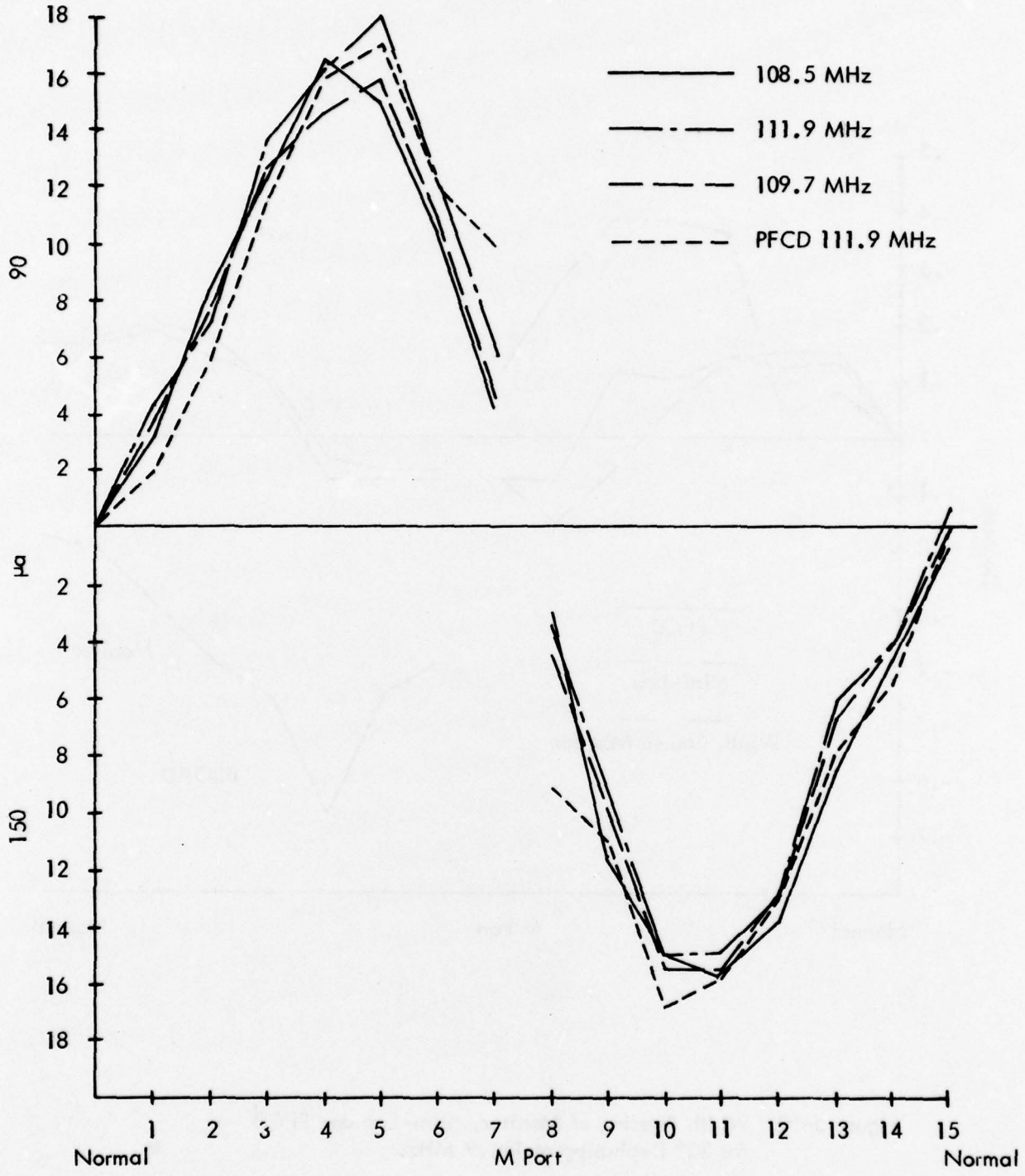

Figure 5-49. 30° Dephasing, Centerline Readings, Mini-Lab.

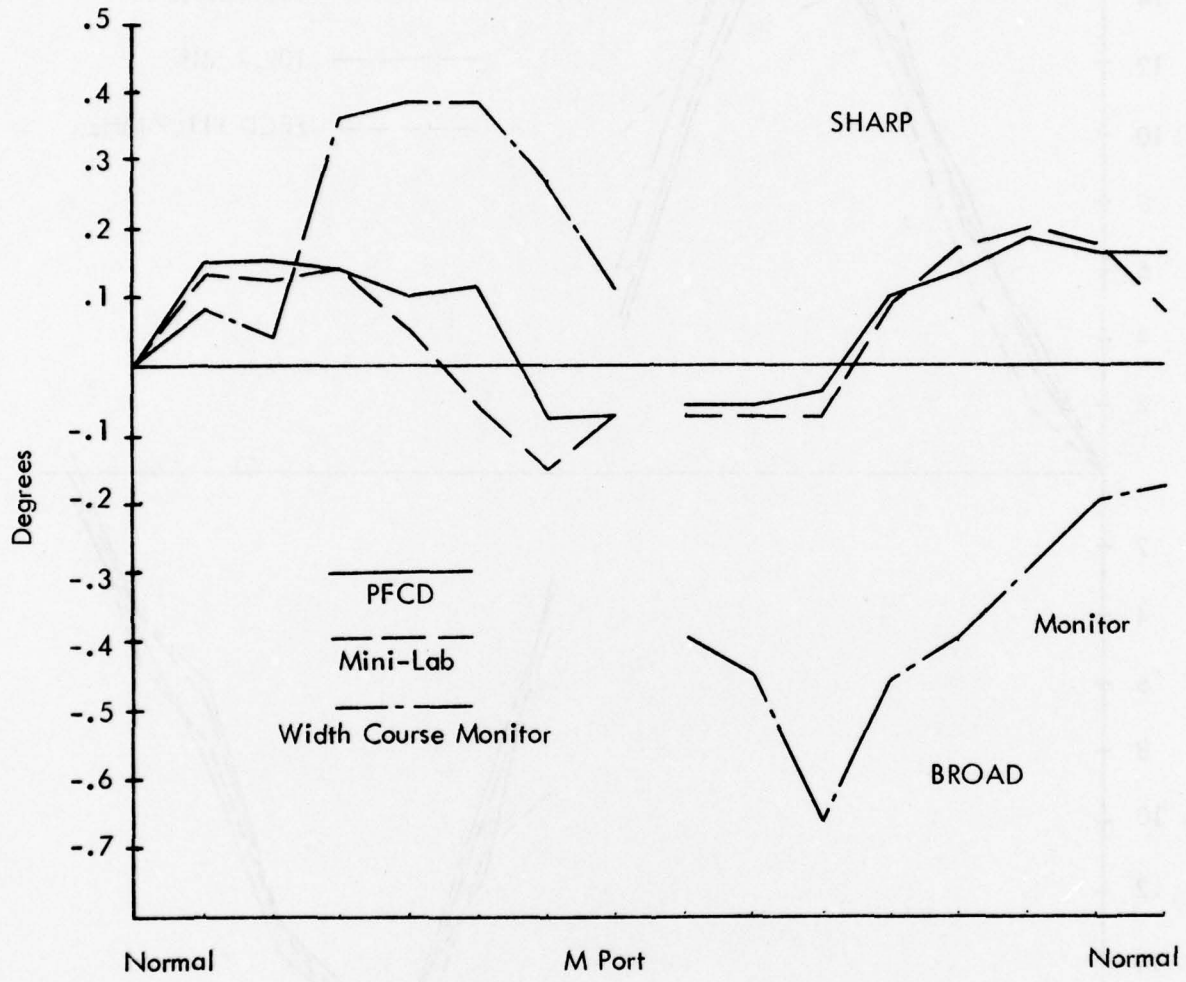

Figure 5-50. Width Reading of Monitor, Mini-Lab and PFCD for 30° Dephasing at 111.9 MHz.

G. Discussion of Total Monitor System Response. Figure 5-51 shows a block diagram of the MC-14/6 Alford Array System with monitors. This section treats a performance study of these monitors under induced fault conditions.

1. Pre-Combiner Clearance Monitor. During fault testing of the Alford MC-14/6 Localizer Array, monitor responses were recorded for the simulated clearance and pre-combiner clearance monitors for 3 dB signal attenuation and 30 degree phase retardation faults. The faults were introduced into the 14 course element feed lines, the 6 clearance element feed lines, and the course sideband only and clearance sideband only feed lines.

The simulated clearance monitor signal is obtained by combining the +16 degree and -16 degree analog monitor signals of the MC-14/6 array, and then separating out the CS signal for use as a 0 degree clearance monitor signal, and combining the CS and SO signals, with appropriate phasing and attenuation to get a synthetic 4 degrees off-course (.155 DDM) signal.

The pre-combiner clearance monitor signal is obtained by combining the appropriate clearance signals from the C-6 distribution network before the clearance signals are combined in the combiner box with the course signals, with the combined signal then subsequently being fed to the single course/clearance antenna array.

Tables 5-34, 5-35 and 5-36 list the simulated clearance and pre-combiner clearance monitor responses to the 3 dB fault test at the three test frequencies of 109.7, 108.5 and 111.9 MHz.

The columns labeled "measured" contain the monitor data as recorded, while the columns labeled "normalized" contain the deviations of the monitor from the normal, or initial values.

Tables 5-37, 5-38, and 5-39 are the respective data at the three test frequencies for the 30 degree fault test.

Examinations of Tables 5-34, 5-35, and 5-37 show that the pre-combiner clearance course and width monitors were insensitive to the faults inserted in the 14 course signal feed lines. This point was noted while taking the data and the recording of the responses was discontinued during further fault testing of the course signal line to expedite the fault testing.

When the 3 dB attenuator was inserted in the clearance signal feed lines, the pre-combiner clearance course and width monitor responses were erratic at the 109.7 MHz frequency, as were the width responses at the other two frequencies. However, at 108.5 and 111.9 MHz the pre-combiner clearance monitor course responses appear to follow a pattern with the monitor shift being smallest for attenuation of elements 1 and 6, larger for elements 2 and 5, and greatest for elements 3 and 4, which elements also receive the greatest sideband power.

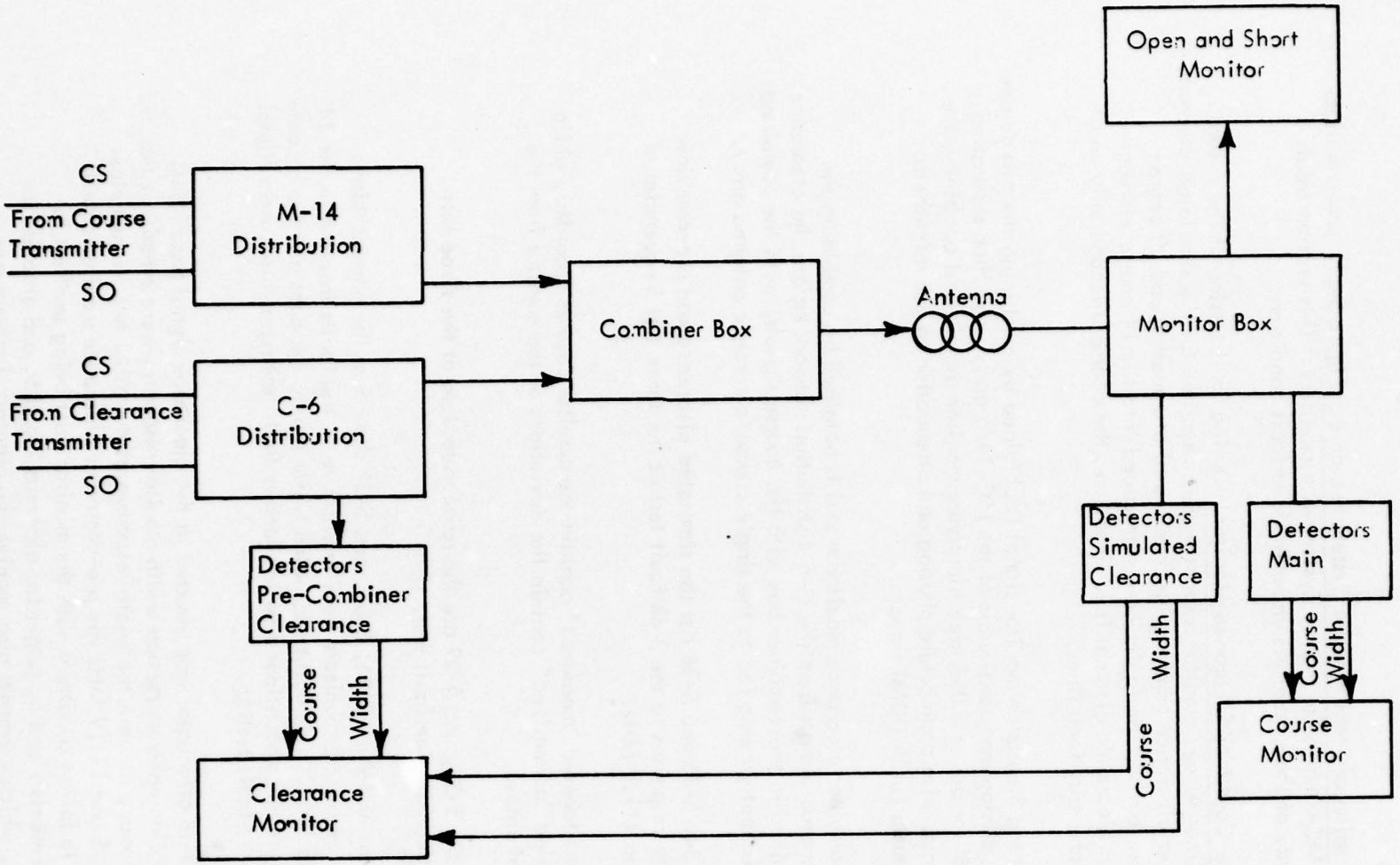

Figure 5-51. Block Diagram - MC-14/6 Alford Array System.

Faulted Line	MEASURED				NORMALIZED			
	Simulated Clearance		Pre Clearance		Course		Width	
	CRS	WID	CRS	WID	Simulated	Pre	Simulated	Pre
N	-004	161	008	163	000	000	000	000
1	-005	151	007	155	-001	-001	-010	-008
2	-004	150	006	155	-000	-002	-011	-008
3	-005	142	006	156	-001	-002	-019	-007
4	-010	149	006	157	-006	-002	-012	-006
5	-010	150	006	266	-006	-002	-011	-008
6	-010	145	006	160	-006	-002	-016	-003
7	-008	148	006	163	-004	-002	-013	000
8	-017	130	007	160	-013	-001	-031	-003
9	-013	157	007	168	-009	-001	-004	+005
10	-010	165	006	162	-006	-002	+004	-001
11	-014	150	006	160	-010	-002	-011	-003
12	-019	142	006	162	-015	-002	-019	-001
13	-016	150	007	164	-012	-001	-011	+001
14	-013	160	006	163	-009	-002	-001	000
N	-013	152	007	165	-009	-001	-009	+002
					000	000	000	000
C-1	-014	147	005	154	-001	-002	-004	-011
C-2	-014	140	006	151	-001	-001	-012	-014
C-3	-014	165	010	167	-001	+003	+017	+002
C-4	-022	148	003	165	-008	-004	-004	000
C-5	-016	140	006	150	-003	-001	-012	-015
C-6	-018	142	007	159	-005	-000	-010	-006
N	-011	158	007	162	+002	-000	+006	-003
CRS_{SO}	-018	150	007	162	-007	-000	-008	000
CLR_{SO}	-008	113	005	118	+003	-002	-045	-044

Table 5-34. Simulated Clearance and Pre-Combiner Clearance Monitor Responses to 3 dB Fault Test at 109.7 MHz.

Faulted Line	MEASURED				NORMALIZED			
	Simulated Clearance		Pre Clearance		Course		Width	
	CRS	WID	CRS	WID	Simulated	Pre	Simulated	Pre
N	002	140	006	160	000	000	000	000
1	003	147	006	160	+001	000	+007	000
2	003	142	006	161	+001	000	+002	+001
3	003	140	006	160	+001	000	000	000
4	002	140	006	160	000	000	000	000
5	002	145	006	160	000	000	+005	000
6	002	142	006	160	000	000	+002	000
7	020	153	007	160	+018	+001	+013	000
8	-013	119	006	160	-015	000	-021	000
9	009	150	006	160	+007	000	+010	000
10	008	154	006	160	+006	000	+014	000
11	004	148	006	161	+002	000	+008	+001
12	004	140	006	160	+002	000	000	000
13	006	148	006	160	+004	000	+008	000
14	008	151	006	160	+006	000	+011	000
N	008	151	006	160	+006	000	+011	000
					000	000	000	000
C-1	007	147	007	159	-001	+001	-004	-001
C-2	008	141	008	153	000	+002	-010	-007
C-3	024	177	019	186	+016	+013	+026	+026
C-4	-014	130	-008	152	-022	-014	-021	-008
C-5	011	151	003	147	+003	-003	000	-013
C-6	007	142	004	147	-001	-002	-009	-013
N	002	142	006	160	-006	000	-009	000
CRS_{SO}	006	150	006	161	+004	000	+008	+001
CLR_{SO}	010	122	005	118	+003	-001	-020	-042

Table 5-35. Simulated Clearance and Pre-Combiner Clearance Monitor Responses to 3 dB Fault at 108.5 MHz.

Faulted Line	MEASURED				NORMALIZED			
	Simulated Clearance		Pre Clearance		Course		Width	
	CRS	WID	CRS	WID	Simulated	Pre	Simulated	Pre
N	-012	101	009	160	000		000	000
1	-012	102			000		+001	
2	-010	105			+002		+004	
3	-008	102			+004		+001	
4	-013	099			-001		-002	
5	-007	111			+005		+010	
6	-005	110			+007		+009	
7	-026	88			-014		-013	
8	+028	142			+040		+041	
9	000	115			+012		+014	
10	-007	112			+005		+013	
11	-007	115			+005		+014	
12	-012	101			000		000	
13	-010	103			+002		+002	
14	-010	109			+002		+008	
N	-010	102	010	171	+002		+001	
					000	000	000	000
C-1	000	110	008	165	+010	-002	+008	-006
C-2	-002	104	006	160	+008	-004	+002	-011
C-3	-038	90	-006	165	-028	-016	-012	-006
C-4	+024	148	028	198	+034	+018	+046	+027
C-5	-018	098	018	165	-008	+008	-004	-006
C-6	-011	099	014	173	-001	+004	-003	+002
N	-007	110	010	172	+003	000	+008	+001
CRS_{SO}	-008	103	011	173	-001	+001	-007	+001
CLR_{SO}	-009	120	010	141	-002	000	+010	031

Table 5-36. Simulated Clearance and Pre-Combiner Clearance Monitor Reponses to 3 dB Fault Test at 111.9 MHz.

Faulted Line	MEASURED				NORMALIZED			
	Simulated Clearance		Pre Clearance		Course		Width	
	CRS	WID	CRS	WID	Simulated	Pre	Simulated	Pre
N	-011	158	007	162	000	000	000	000
1	-006	152	007	162	+005	000	-006	000
2	-001	161	007	161	+010	000	+003	-001
3	-006	162	007	161	+005	000	+004	-001
4	-021	131	007	161	-010	000	-027	-001
5	-010	127	007	161	+001	000	-031	-001
6	-006	156	007	161	+005	000	-002	-001
7	-165	009	006	161	-154	-001	-149	-001
8	+122	300			+133		+142	
9	-028	115			-017		-043	
10	-018	125			-007		-033	
11	-010	153			+001		-005	
12	-040	120			-029		-038	
13	-030	134			-019		-024	
14	-012	155			-001		-003	
N	-020	148	007	161	-009	-010	-010	-001
	-008	130	002	131	000	000	000	000
C-1	+010	140	+015	145	+018	+013	+010	-016
C-2	+004	131	-034	121	+012	-036	+001	-040
C-3	-140	008	-100	060	-132	-102	-122	-101
C-4	+148	300	+100	280	+156	+098	+170	+119
C-5	-063	075	+039	182	-055	+037	-055	+021
C-6	-017	122	+020	180	-009	+018	-008	+019
N	-010	130	+002	165	-002	000	000	+004
CRS_{SO}	-011	130	+002	163	-001	000	000	-002
CLR_{SO}	-036	055	+007	130	-026	+005	-075	-035

Table 5-37. Simulated Clearance and Pre-Combiner Clearance Monitor Response to 30° Phase Fault at 109.7 MHz.

Faulted Line	MEASURED				NORMALIZED			
	Simulated Clearance		Pre Clearance		Course		Width	
	CRS	WID	CRS	WID	Simulated	Pre	Simulated	Pre
N	-002	140	006	161	000	000	000	000
1	-006	138			-004		-002	
2	004	149			+006		+009	
3	009	150			+011		+010	
4	-010	125			-008		-015	
5	000	125			+002		-015	
6	003	140			+005		000	
7	-123	019			-121		-121	
8	+170	280			+168		+140	
9	-008	122			-006		-018	
10	-036	095			-034		-045	
11	000	143			+002		+003	
12	-018	125			-016		-015	
13	-014	130			-012		-010	
14	-004	140			-002		000	
N	-006	140	006	161	-004	000	000	000
					000	000	000	000
C-1	013	152	-010	147	+019	-016	+012	-014
C-2	004	136	-029	125	+010	-035	-004	-036
C-3	-027	006	-092	115	-021	-098	-134	-046
C-4	146	320	100	280	+152	+094	+180	+119
C-5	-055	139	041	180	-049	+035	-001	+019
C-6	-010	130	022	179	-004	+016	-010	+018
N	-006	140	006	161	000	000	000	000
CRS_{SO}	-004	140	006	161	+002	000	000	000
CLR_{SO}	-029	076	010	130	-023	+004	-064	-031

Table 5-38. Simulated Clearance and Pre-Combiner Clearance Monitor Response to 30° Phase Fault at 108.5 MHz.

Faulted Line	MEASURED				NORMALIZED			
	Simulated Clearance		Pre Clearance		Course		Width	
	CRS	WID	CRS	WID	Simulated	Pre	Simulated	Pre
N	-007	110	010	172	000	000	000	000
1	-008	105			-001		-005	
2	-002	117			+005		+007	
3	+006	120			+013		+010	
4	-012	098			-005		-012	
5	-008	099			-001		-011	
6	-009	122			-002		+012	
7	-120	006			-013		-004	
8	+135	240			+142		+130	
9	-009	099			-002		-011	
10	-028	083			-021		-027	
11	+003	113			+010		+003	
12	-010	103			-003		-007	
13	-004	112			+003		+002	
14	+008	129			+015		+019	
N	+004	120	010	170	+011		+010	-002
					000	000	000	000
C-1	022	133	006	157	+018	-004	+013	-013
C-2	018	121	-028	132	+014	-038	+001	-038
C-3	-145	-006	-090	123	-149	-100	-126	-047
C-4	149	280	105	292	+145	+095	+160	+122
C-5	-062	108	047	190	-066	+037	-012	+020
C-6	-017	092	027	190	-021	+017	-028	+020
N	-008	110	009	171	-012	-001	-010	+001
CRS_{SO}	-018	100	009	172	-010	000	-010	+001
CLR_{SO}	-026	036	012	135	-018	+003	-026	-036

Table 5-39. Simulated Clearance and Pre-Combiner Clearance Monitor Response to 30° Phase Fault at 111.9 MHz.

The pre-combiner clearance monitors were insensitive to the 3 dB attenuation of the course sideband feed power, and the pre-combiner clearance course monitor was insensitive to the 3 dB attenuation of the clearance sideband feed power. However, the pre-combiner clearance width monitor registered -.044, -.042, and -.031 DDM shifts for the 3 dB attenuation of the clearance sideband feed power at the three test frequencies.

When the 30 degrees phase fault was inserted in the clearance signal feed lines, the pre-combiner clearance monitor course and width channels exhibited a definite response pattern at the three test frequencies. The course and width channel DDM shifts were smallest for elements 1 and 6, increasing to a maximum DDM shift for elements 3 and 4, with negative shifts, or shifts into 90 Hz predominance, when the 30 degrees phase fault was inserted in the lines feeding elements 1, 2, and 3, and positive shifts, or 150 Hz predominance, for the fault in the lines feeding elements 4, 5, and 6. The pre-combiner clearance monitor channels were insensitive to the insertion of the 30 degrees phase fault in the course sideband power feed lines, and the pre-combiner clearance course monitor was only slightly sensitive (greatest shift + .005 DDM) to insertion of the 30 degrees phase fault in the clearance sideband power feed line. However, shifts of 0.035, -.031 and -.036 DDM were registered by the pre-combiner clearance width monitor with the 30 degrees phase fault in the clearance sideband power feed line.

A comparison of the pre-combiner clearance monitor responses with the simulated clearance monitor responses, indicates that the simulated clearance monitor is overly sensitive to a number of faults.

2. Monitor Response to Far-Field Out-of-Tolerance Conditions.

a. Low Clearance Conditions. Results of orbital ground runs are presented in Table 5-14 for those runs for which clearance dropped below 200 microamperes CDI. According to the U.S. Standard Flight Inspection Manual, the minimum clearance tolerances are as follows:

> From 0 degrees to 10 degrees either side of the runway centerline the clearance should linearly increase to 175 μamperes and then maintain 175 μamperes to 10 degrees.
>
> From 10 degrees to 35 degrees either side of the runway centerline the clearance must be greater than 150 μamperes.
>
> For the localizer course set to a broad alarm condition, the corresponding values are 160 μamperes to 10 degrees and 135 μamperes from 10 degrees to 35 degrees.

Applying the above criteria to the data in Table 5-14, one finds out-of-tolerance conditions for five cases (Runs 15-39, 15-51, 17-18, 17-29, 17-30). Three of the out-of-tolerance conditions (Runs 15-51, 17-29, 17-30) were registered as alarm conditions by the pre-combiner clearance monitors (see Tables 5-38 and 5-39 for the monitor response to the indicated faults).

The two other marginally low clearance conditions were obtained with a 30 degrees phase fault in the course feed lines #M7 at 108.5 MHz which gave a minimum clearance of 172 μamperes at 8 degrees and #M8 at 111.9 MHz with a minimum clearance of 168 μamperes at 9 degrees. The 30 degrees phase fault in line #M7 at 108.5 MHz resulted in a 10 μamperes shift of the main course monitor which is 67% of the alarm limit of 15 μamperes, while the fault in line #M8 at 111.9 MHz registered only a 5 μampere shift for a 33% alarm condition on the main course monitor.

b. Course Alignment or Course Width Out-of-Tolerance. Table 5-40 lists the out-of-tolerance conditions of the main localizer course alignment and main course width. Also listed in Table 5-40 are the monitor alarm conditions that were recorded for these specific fault conditions. As can be seen, there are three dangerous (D) conditions listed for which the monitors failed to alarm. The tolerance limits used in determining the far-field conditions were ±15 μamperes for the centerline alignment and ±30 μamperes for the course width. The corresponding alarm limits are ±0.015 DDM and ±0.030 DDM.

3. Conclusions.

a. Clearance for the Alford MC 14/6 tested proved to be adequate for all +35° to -35° 1000-foot ground orbits run.

b. The system exhibited some course and width drift during rain showers accompanied by temperature changes.

c. The installation exhibited some asymmetry. In one case this approached the 10% limit called for in Section 217.5(5)a of the Flight Inspection Manual.

d. Monitor action as implemented is unsatisfactory.

i. There is considerable drift with temperature and/or humidity.
ii. The simulated clearance section is over-sensitive and erratic.
iii. The pre-clearance section showed no sensitivity to most of the faults applied. It alarmed only once and falsely (U).

Frequency	System Fault	Field Conditions		Monitor Alarms	
		Out-of Tolerance	Shift from Nominal (μ Amperes)	Monitor	Shift from Nominal DDM
108.5	3 db crs. so. line	width	41	main width	.048
109.7	3 db crs. so. line	width	42	main width	.038
111.9	3 db crs. so. line	width	46	main width	.049
108.5	30° M4 line	cl. align.	16.9	main course	.018
108.5	30° M5 line	cl. align.	15.1	main course	.017
108.5	30° M10 line	cl. align.	15.0	main course	.017
108.5	30° M11 line	cl. align.	15.6	main course	.015
108.5	30° crs. so. line	width	32	NONE	.012
109.7	30° M5 line	cl. align.	15.8	NONE	.006
109.7	30° M10 line	cl. align.	15.6	main course	.016
109.7	30° M11 line	cl. align.	15.6	main course	.015
109.7	30° crs. so. line	width	34	NONE	.015
111.9	30° M4 line	cl. align.	15.8	main course	.018
111.9	30° M5 line	cl. align.	17.6	main course	.017
111.9	30° M10 line	cl. align.	15.2	main course	.022
111.9	30° M11 line	cl. align.	15.1	main course	.022
111.9	30° crs. so. line	width	51	main course	.041

Table 5-40. Monitor Alarms for Out-of-Tolerance Conditions of Course Centerline Alignment or Course Width.

e. A review of the data taken during fault testing of the Alford MC 14/6 localizer array and integral monitoring circuits revealed 5 fault conditions which produced an out-of-tolerance condition in the far-field that was not accompanied by an alarm indication of either the main course and width monitor or the pre-combiner clearance monitor. Two of the out-of-tolerance conditions were marginal low clearances inside the 10 degrees sector from the centerline, one out-of-tolerance condition was misalignment of the course centerline, and two out-of-tolerance conditions were excessive broadening of the course width.

H. 1976 Tests of Monitor Performance of the Alford MC 14/6 Two Frequency Localizer System under Attenuation and Phase Fault Conditions.

1. Introduction. This section covers tests made by Ohio University Avionics personnel, an engineer from the Andrew Alford Consulting Engineers Company, and personnel from the FAA, at the Ohio University Tamiami Test Site. The tests were performed from March 3, 1976 to March 19, 1976 and from April 30, 1976 to May 4, 1976 on the Alford MC 14/6 localizer array and its monitoring system, which is shown in block diagram form in Figure 5-52.

Following an analysis of data taken previously (in April and May of 1975) the analog, simulated-clearance monitors were eliminated because they were found to be overly sensitive and erratic. Also, adjustments were made by the Alford Company on the pre-combiner clearance monitor and the common aperture combiner networks to optimize the performance of these networks.

Fault testing of the array was then performed at the three test frequencies of 108.5 MHz, 109.7 MHz, and 111.9 MHz. Monitor responses and ground field data were recorded for 3 dB attenuation faults and for variable phase retard faults inserted in the individual antenna feed lines and in both the course transmitter and the clearance transmitter carrier and sideband feed lines. For the phase fault tests, the phase was varied until the first monitor alarm was obtained.

Strip chart recordings were made by truck using a King KX 175B localizer receiver and a specially designed audio processor to record minimum clearances over a 70 degree orbit centered on the runway centerline and with a radius of 1000 feet. Also for each fault, the truck was positioned at the centerline and the course edges (±2 degrees), and at these points the CDI readings were recorded using a digital meter.

For those faults which produced an out-of-tolerance condition at the 1000 foot distance, airborne data was then recorded, again using the King receiver and associated processor circuit in the Ohio University Beechcraft - 35 aircraft together with the Ohio University Minilab installation.

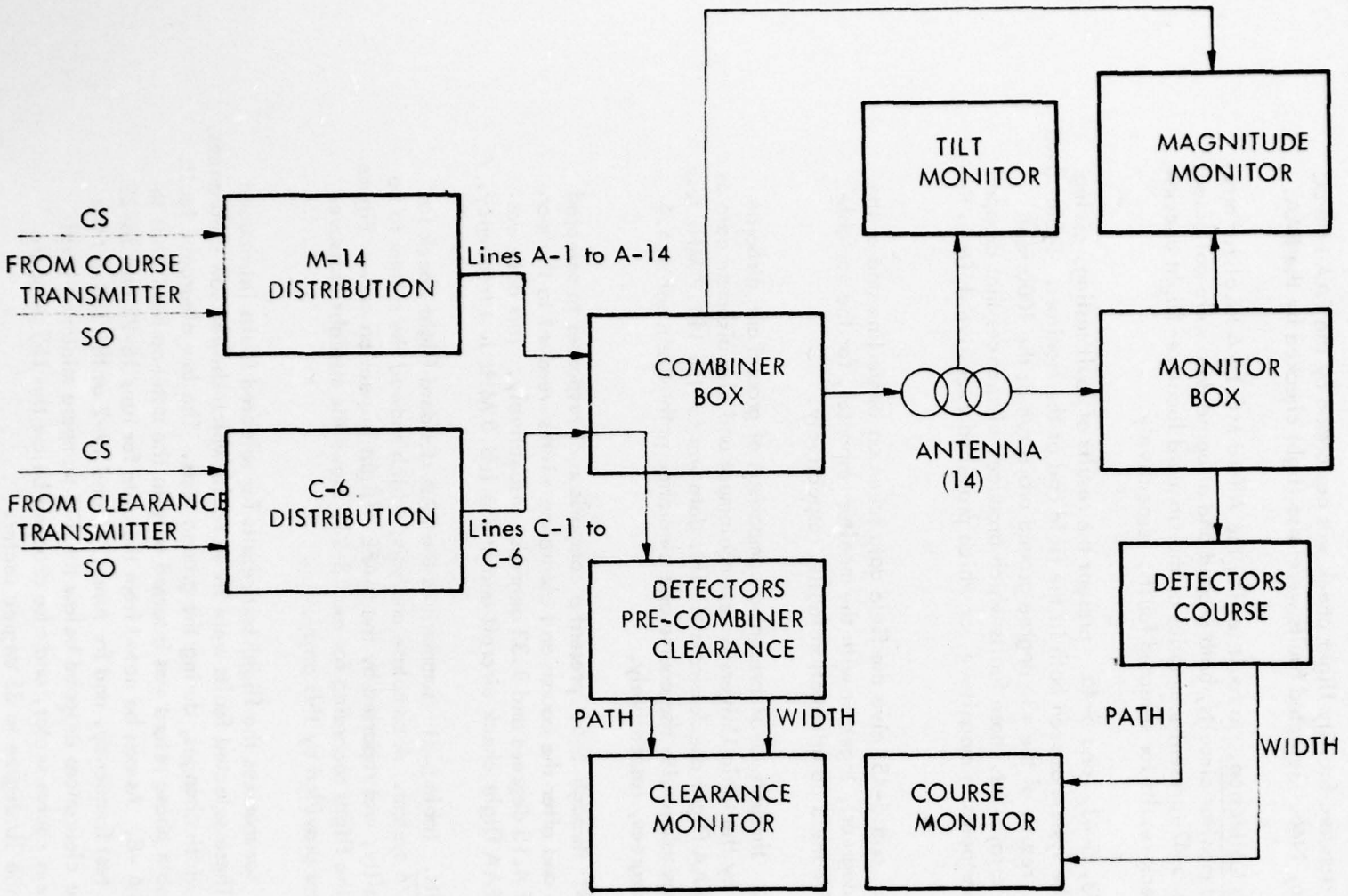

Figure 5-52. Block Diagram - MC-14/6 Alford Array System Revised 1976 Tests.

Neither the antennas nor the array was adjusted electrically or physically to accommodate changes in frequency over the band (108.5 - 111.9 MHz).

Finally, a standard facility flight check was performed by the FAA NAFEC team with a DC-6, N46. Selected faults were also flight checked by the FAA.

2. Data Collection. In fault testing the Alford MC 14/6 localizer array and its associated monitor circuits, both ground and airborne data were collected. Tables 5-41 and 5-42 present summaries of the standard localizer flight checks and the flight check results for selected faults, respectively.

Tables 5-43, 5-43, and 5-45 present the results of fault testing, giving the responses of the system as seen both in the field and at the monitors. Table 5-43 compiled from the results of the ±35 degree ground orbits run at the 1000 foot distance from the array, lists those faults which produced clearances that dropped below 200 microamperes in magnitude, or which produced excessive shifts in the course width.

Tables 5-44 and 5-45 give the field data taken on centerline and at the course edges (±2 degrees), together with the monitor responses, for the variable phase faults and for the 3 dB attenuation faults, respectively.

Figures 5-53 through 5-57 present a comparison of ground and airborne data as collected by the Ohio University test equipment and also airborne data as collected by the FAA flight check aircraft. This data was for the 111.9 MHz test frequency, and was taken with the course and clearance path widths set at 4.4 degrees and 9.5 degrees, respectively.

Figures 5-58 through 5-63 present a comparison of responses to selected faults both before and after the course and clearance widths were set to the more optimum values of 4.15 degrees and 8.33 degrees, respectively. This data was collected by the FAA flight check aircraft and at the 108.5 MHz test frequency.

3. Results. Table 5-41 summarizes the FAA standard flight check for the Alford MC 14/6 system. A complete analysis, which showed the system to be of Category II quality, was reported by the NAFEC flight inspection crew. Figure 5-53, which is the flight recording for run 18-21, shows the straight crossover and high clearances provided by this array.

Table 5-42 summarizes the flight test results for selected faults introduced into the system. These selected faults were those faults which showed low clearances, or excessive path width changes, during the ground tests. The low clearance faults arose when a variable phase retard was inserted only in the antenna feed lines to elements A-7 and A-8. As can be noted from the data for runs 18-28 and 18-29 at the 111.9 MHz test frequency, and for runs 19-1 and 19-2 at the 108.5 MHz test frequency, the clearances dropped below the 175 μampere minimum level inside the 10 degrees course sector, and also dropped below the 155 μampere minimum level in the 10 degree to 35 degree sector.

RUN	FREQ.	TYPE RUN	RESULT		REMARKS
18-1	111.9	Centerline Alignment	5 μa	90 Hz	Full Array
18-2	111.9	Mod. Bal.	2 μa	150 Hz	Full Array
18-3	111.9	Width ± 10°	4.29°		Course Only
18-4	111.9	Width ± 10°	4.20°		Course Only
18-5	111.9	Width ± 10°	9.57°		Clearance Only
18-6	111.9	Width ± 10°	9.48°		Clearance Only
18-7	111.9	Width ± 10°	4.47°		Full Array
18-8	111.9	Width ± 10°	4.39°		Full Array
18-9	111.9	Width ± 10°	5.6°		Full Array - Broad Alarm
18-11	111.9	Width ± 10°	3.75°		Full Array - Narrow Alarm
18-14	111.9	RTT	4 μa	90 Hz	Structure - Full Array
18-21	111.9	Orbit ± 35°	Minimum Clearances >| ± 250 μa		Full Array

Table 5-41. Summary of Localizer Standard Flight Check (FAA, DC-6 May 18, 1976).

RUN	FREQ.	FAULT		MINIMUM CLEARANCES			<155		min.	REMARKS
		LINE	Phase Retard				from	to	μa	
18/28	111.9	A-7	47°	+175 8.5°	+120 10.6°	+155 14.1°	21°s	34°s	+130	Low clearances apparently due to wide clearance only course width
							28°n	33°n	-95	
18/29	111.9	A-8	41°	-175 8°	-142 10°	-155 11.8°	22°n	28°n	-140	Low clearances apparently due to wide clearance only course width
							29°s	33°s	+120	
18/30	111.9	Cr.SB	31°	NONE						5.7° cw
19/1	108.5	A-7	45°	+175 8.8°	+120 11°	+155 14.5°	21°s	34°s	+125	Low clearances apparently due to wide clearance only course width
							29°n	33°n	-100	
19/2	108.5	A-8	51°	-175 7.8°	-88 10°	-155 35°	18°n	20°n	-150	Low clearances apparently due to wide clearance only course width
							28°s	35°s	+65	
19/3	108.5	A-8	51°							RTT Run average +7.5 μa
19/4	108.5	Cr.SB	36°	NONE						6.07° cw.
19/5	108.5	normal								Clearance only 8.89° cw.
19/6	108.5	normal								Clearance only 8.33° cw.

Table 5-42. Flight Check Results for Selected Faults (FAA, DC-6, May 18 and 19, 1976).

RUN	FREQ.	FAULT		MINIMUM CLEARANCES					REMARKS
		LINE	Phase Retard				<155 from	<155 to	min. μa	
19/7	108.5	normal								Full Array 4.15° cw.
19/8	108.5	A-7	41°	NONE					+165	at 11°s
									-170	at 32°n
19/9	108.5	A-8	40°	NONE					+200	at 32°s
									-180	at 10°n
19/10	108.5	A-8	40°	NONE						RTT Run average +3.8 μa
19/11	108.5	Cr.SB	44°	NONE						5.61° cw.
19/12	108.5	normal		NONE					+290	at 9°s
									-210	at 35°n
										course width - radio 1 - 4.14°
										- radio 2 - 4.27°

Table 5-42. (continued).

DATE	FREQ.	TEST CONDITION		LOW CLEARANCE				REMARKS
		Line	Fault	From	To	Min. CDI		
3-12-76	108.5	A-7	42°	7°	11°	178 μa	150 Hz	
3-12-76	108.5	A-7	42°	19°	31°	178 μa	150 Hz	
3-12-76	108.5	A-8	42°	20°	33°	155 μa	90 Hz	
3-12-76	108.5	A-8	42°	8°	15°	159 μa	90 Hz	
3-12-76	108.5	M-14 Sb Feed	43°	--	--	--	--	7.2° course width
3-12-76	108.5	M-14 Sb Feed	3 dB	--	--	--	--	9.3° course width
3-12-76	108.5	C-6 Sb Feed	3 dB	28°	29°	195 μa	150 Hz	
3-10-76	109.7	A-7	30°	8°	10°	193 μa	150 Hz	
3-10-76	109.7	A-7	30°	21.5°	28.5°	191 μa	150 Hz	
3-10-76	109.7	A-8	30°	8°	12°	186 μa	90 Hz	
3-10-76	109.7	A-8	30°	21°	30°	178 μa	90 Hz	
3-10-76	109.7	A-7	42°	7°	14°	155 μa	150 Hz	
3-10-76	109.7	A-7	42°	15.5°	33.5°	149 μa	150 Hz	
3-10-76	109.7	A-8	50°	8°	35°	114 μa	90 Hz	

Table 5-43. Ground Orbit Results for Those Faults Which Showed Less than 2000 Microamperes Clearance or Excessive Course Width Changes.

DATE	FREQ.	TEST CONDITION		LOW CLEARANCE				REMARKS
		Line	Fault	From	To	Min. CDI		
3-10-76	109.7	A-8	50°	27°	31°	148 μa	150 Hz	
3-10-76	109.7	A-7	57°	27°	35°	148 μa	90 Hz	
3-10-76	109.7	A-7	57°	6°	35°	95 μa	150 Hz	
3-10-76	109.7	A-8	55°	8°	35°	99 μa	90 Hz	
3-10-76	109.7	A-8	55°	26.5°	32.5°	133 μa	150 Hz	
3-10-76	109.7	M-14 Sb Feed	42°	--	--	--	--	7.5 course width
3-10-76	109.7	M-14 Sb Feed	3 dB	--	--	--	--	6.76 course width
3-10-76	109.7	C-6 Sb Feed	3 dB	25.5°	29°	178 μa	150 Hz	
3-9-76	111.9	A-7	30°	14.5°	15.5°	193 μa	150 Hz	
3-9-76	111.9	A-7	30°	26.5°	31°	189 μa	150 Hz	
3-9-76	111.9	A-8	30°	8°	12°	182 μa	90 Hz	
3-9-76	111.9	A-8	30°	21°	29°	170 μa	90 Hz	
3-9-76	111.9	M-14 Sb Feed	30°	--	--	--	--	6.0° course width
3-9-76	111.9	C-3	30°	23°	29°	187 μa	150 Hz	

Table 5-43. (continued).

DATE	FREQ.	TEST CONDITION		LOW CLEARANCE				REMARKS
		Line	Fault	From	To	Min. CDI		
3-9-76	111.9	C-4	30°	8°	10°	178 μa	90 Hz	
3-9-76	111.9	C-4	30°	21°	30°	172 μa	90 Hz	
3-9-76	111.9	M-14 SBO Feed	3 dB	--	--	--	--	6.17° course width
3-9-76	111.9	C-6 SBO Feed	3 dB	9°	12°	178 μa	90 Hz	
3-9-76	111.9	C-6 SBO Feed	3 dB	24°	31°	176 μa	90 Hz	
3-13-76	111.9	A-7	47°	27°	33°	135 μa	90 Hz	
3-13-76	111.9	A-7	47°	33°	35°	34 μa	90 Hz	
3-13-76	111.9	A-7	47°	7°	35°	121 μa	150 Hz	
3-13-76	111.9	A-8	40°	8.5°	15°	144 μa	90 Hz	
3-13-76	111.9	A-8	40°	16.5°	35°	140 μa	90 Hz	
3-13-76	111.9	A-8	40°	27°	30°	171 μa	150 Hz	
3-13-76	111.9	M-14 SBO Feed	41°	--	--	--	--	7.46 course width

Table 5-43. (continued).

AD-A074 425 OHIO UNIV ATHENS DEPT OF ELECTRICAL ENGINEERING F/G 17/7
IN-SERVICE IMPROVEMENTS AND MODERNIZATION OF ALL COMPONENTS OF --ETC(U)
JUL 78 DOT-FA75WA-3549
UNCLASSIFIED EER-35-1 FAA-RD-78-112-1 NL

5 OF 8
AD A074425

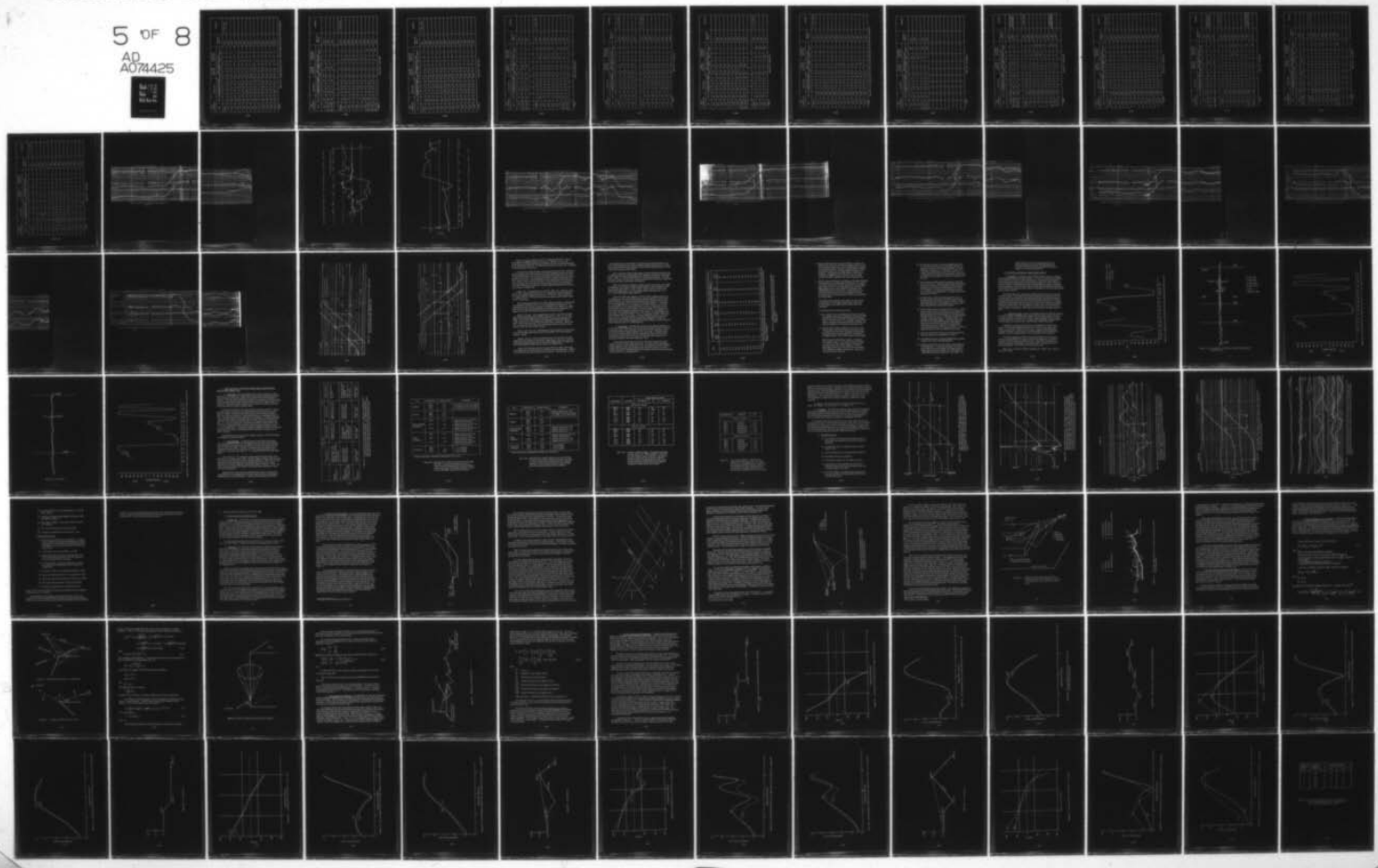

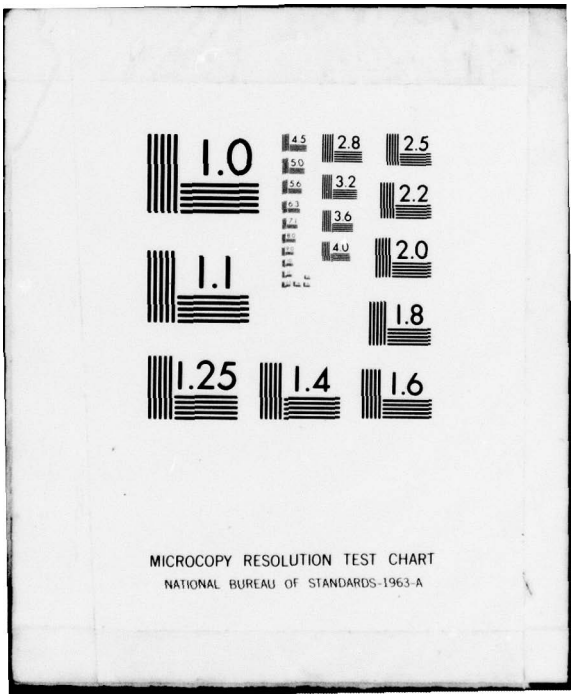
1.0
1.1
1.25
1.4
1.6
1.8
2.0
2.2
2.5
2.8
3.2
3.6
4.0
4.5
5.0
5.6
MICROCOPY RESOLUTION TEST CHART
NATIONAL BUREAU OF STANDARDS-1963-A

TEST CONDITION		FIELD DATA			COURSE MONITOR		CLEARANCE MONITOR		Magnitude Monitor	REMARKS
LINE	FAULT	μa change from normal			DDM change from normal					
		2°N	CL	2°S	path	width	path	width		
Normal	--	0	0	0	0	0	0	0	short	F = 108.5 MHz
A-1	72°	-6	-4	-9	-11*	-12	-2	0	open*	
A-2	55°	-4	-7	-11	-11*	-11	0	0	short	
A-3	30°	+1	-8	-7	-11*	-11	-2	0	short	
A-4	25°	+6	-10	-6	-11*	-10	-2	0	short	
A-5	24°	+9	-9	-9	-11*	-10	-2	0	short	
A-6	35°	+10	-8	-8	-11*	-11	-2	0	short	
A-7	41°	+12	-8	-8	-11*	-12	+1	0	short	
A-8	42°	-12	+11	+15	+11*	+18	-2	0	short	
A-9	27°	-12	+9	+10	+11*	+10	-2	0	short	
A-10	24°	-13	+10	+8	+11*	+10	-2	0	short	
A-11	24°	-16	+7	+6	+11*	+8	-2	0	short	
A-12	29°	-15	+8	-8	+11*	+7	-2	0	short	
A-13	59°	-20	+7	-3	+11*	+4	-2	0	short	

*Alarm

Table 5-44. Variable Phase Fault Data - Monitor Responses and Fixed Point Field Responses.

TEST CONDITION		FIELD DATA			COURSE MONITOR		CLEARANCE MONITOR		Magnitude Monitor	REMARKS
LINE	FAULT	μa change from normal			DDM change from normal					
		2°N	CL	2°S	path	width	path	width		
A-14	90°	-18	+3	-10	+11*	-1	-2	0	short	
CS "M-14"	48°	-14	+4	-4	0	-27*	-2	0	short	
SO "M-14"	43°	-55	+3	-46	-4	-27*	0	0	short	
Normal	--	0	0	0	0	0	0	0	short	F = 108.5 MHz
C-1	24°	-6	+2	0	0	-3	-11*	-9	short	
C-2	11°	-4	0	+1	0	-2	-11*	-7	short	
C-3	4°	-5	+1	0	+1	-1	-11*	+6	short	
C-4	4°	-7	+1	0	-1	-1	+11*	-5	short	
C-5	9°	-5	+2	-1	-1	-1	+11*	+2	short	
C-6	20°	-7	+1	0	-1	-1	+11*	-4	short	
CS "C-6"	53°	-8	+2	+1	-1	-1	-10	-37*	short	
CS "C-6"	47°	-8	+2	+2	-1	-1	-6	-27*	short	
SO "C-6"	41°	-6	+1	-1	-1	-1	+5	-29*	short	

*Alarm

Table 5-44. (continued).

TEST CONDITION		FIELD DATA			COURSE MONITOR		CLEARANCE MONITOR		Magnitude Monitor	REMARKS
LINE	FAULT	μa change from normal			DDM change from normal					
		2°N	CL	2°S	path	width	path	width		
Normal	--	0	0	0	0	0	0	0	short	F = 109.7 MHz
A-1	85°	+7	-4	-15	-12*	-15	0	-1	open*	
A-2	56°	+3	-8	-16	-12*	-11	0	-1	open*	
A-3	36°	-3	-14	-16	-13*	-13	0	-1	short	
A-4	29°	-9	-14	-15	-12*	-11	0	-1	short	
A-5	30°	-16	-17	-16	-12*	-12	0	0	short	
A-6	43°	-24	-19	-16	-13*	-14	0	0	short	
A-7	57°	-27	-19	-16	-12*	-15	0	-2	short	
A-8	55°	+5	+11	+18	+10	+26	-2	0	short	
A-9	39°	+11	+12	+10	+12*	+18	-1	-1	short	
A-10	29°	+11	+13	+7	+11*	+15	0	-1	short	
A-11	30°	+12	+11	+5	+12*	+13	0	-1	short	
A-12	33°	+11	+13	+2	+12*	+11	+1	0	short	
A-13	56°	+13	+3	-7	+12*	+7	+1	+1	short	

*Alarm

Table 5-44. (continued).

TEST CONDITION		FIELD DATA			COURSE MONITOR		CLEARANCE MONITOR		Magnitude Monitor	REMARKS
LINE	FAULT	μa change from normal			DDM change from normal					
		2°N	CL	2°S	path	width	path	width		
A-14	97°	+10	-1	-13	+11*	0	+1	0	open*	
CS "M-14"	41°	+10	-2	-11	+2	-28*	+1	0	short	
SO "M-14"	42°	+49	-1	-51	-5	-29*	0	-1	short	
Normal	--	0	0	0	0	0	0	0	short	F = 109.7 MHz
C-1	30°	0	-3	-3	-1	-2	-14*	-13	short	
C-2	14°	-3	-8	-6	-1	-2	-13*	-14	short	
C-3	6°	+3	-2	-7	-1	-2	-12*	-12	short	
C-4	7°	0	-7	-3	0	+2	+13*	+14	short	
C-5	12°	+2	-4	-2	-1	0	+11*	+7	short	
C-6	30°	+3	-7	-1	0	0	+13*	+10	short	
CS "C-6"	42°	+3	-2	-5	0	0	-8	-22	short	
SO "C-6"	37°	+5	0	-4	-1	-2	+4	-31*	short	

* Alarm

Table 5-44 (continued).

TEST CONDITION		FIELD DATA			COURSE MONITOR		CLEARANCE MONITOR		Magnitude Monitor	REMARKS
LINE	FAULT	μa change from normal			DDM change from normal					
		2°N	CL	2°S	path	width	path	width		
Normal	--	0	0	0	0	0	0	0	short	F = 109.7 MHz
A-7	30°	-9	-8	-7	-8	-12	0	0	short	
A-7	42°	-13	-11	-6	-11*	-14	0	-1	short	
A-8	30°	+10	+6	+12	+8	+14	-3	0	short	
A-8	50°	+14	+10	+18	+11*	+22	-2	0	short	
Normal	--	0	0	0	0	0	0	0	short	F = 111.9 MHz
A-1	58°	+3	-9	-11	-11*	-11	0	0	open*	
A-2	51°	0	-12	-15	-11*	-11	+1	0	open*	
A-3	28°	-4	-12	-15	-11*	-11	+1	0	short	
A-4	21°	-9	-10	-15	-11*	-11	+1	0	short	
A-5	23°	-12	-11	-16	-11*	-12	+1	0	short	
A-6	30°	-14	-13	-18	-11*	-13	+1	0	short	
A-7	39°	-15	-15	-16	-11*	-15	+1	0	open*	

* Alarm

Table 5-44. (continued).

TEST CONDITION		FIELD DATA			COURSE MONITOR		CLEARANCE MONITOR		Magnitude Monitor	REMARKS
LINE	FAULT	μa change from normal			DDM change from normal					
		2°N	CL	2°S	path	width	path	width		
A-8	46°	+9	+15	+6	+11*	+23	+1	0	--	
A-9	30°	+14	+11	+12	+11*	+15	-1	0	short	
A-10	24°	+16	+18	+10	+11*	+14	-1	-1	short	
A-11	22°	+14	+14	+5	+11*	+10	0	-1	short	
A-12	27°	+15	+17	+2	+11*	+10	0	-1	short	
A-13	53°	+18	+4	-7	+11*	+5	0	-1	short	
A-14	97°	+18	0	-18	+11*	+5	-1	0	open*	
CS "M-14"	32°	+13	0	-10	-5	-25*	+2	+2	short	
SO "M-14"	39°	+55	0	-52	+3	-25*	+2	+3	short	
Normal	--	0	0	0	0	0	0	0	short	F = 111.9 MHz
C-1	58°	+6	+1	-6	-2	-3	-27	-29*	short	
C-2	25°	+7	-1	-7	-2	-3	-27	-29*	short	
C-3	9°	+6	+1	-7	-2	-3	-29*	-29*	short	

* Alarm

Table 5-44. (continued).

TEST CONDITION		FIELD DATA			COURSE MONITOR		CLEARANCE MONITOR		Magnitude Monitor	REMARKS
LINE	FAULT	μa change from normal			DDM change from normal					
		2°N	CL	2°S	path	width	path	width		
Normal	--	0	0	0	0	0	0	0	short	F = 108.5 MHz
A-1	3 dB	+4	+2	0	+2	-2	-1	-1	open*	
A-2	3 dB	+9	+3	0	+3	-3	-1	-1	open*	
A-3	3 dB	+15	+6	-1	+3	-3	0	0	open*	
A-4	3 dB	+11	+5	+1	+3	0	-1	-1	open*	
A-5	3 dB	+11	+5	+5	+5	+7	-1	-1	open*	
A-6	3 dB	+7	+3	+8	+3	+8	-1	-1	open*	
A-7	3 dB	-1	+2	+11	+2	+12	-1	-1	open*	
A-8	3 dB	-7	-7	+4	-5	+1	-1	-1	open*	
A-9	3 dB	-6	-5	-2	-6	-3	-1	-1	open*	
A-10	3 dB	-5	-4	-8	-7	-8	-1	-1	open*	
A-11	3 dB	0	-4	-12	-6	-10	-1	-1	open*	
A-12	3 dB	+3	-8	-13	-5	-10	-1	-1	open*	
A-13	3 dB	+2	-9	-10	-4	-7	0	-1	open*	

* Alarm

Table 5-45. 3 dB Attenuation Fault Data - Monitor Responses and Fixed Point Field Responses.

TEST CONDITION		FIELD DATA			COURSE MONITOR		CLEARANCE MONITOR		Magnitude Monitor	REMARKS
LINE	FAULT	μa change from normal			DDM change from normal					
		2°N	CL	2°S	path	width	path	width		
C-4	8°	+10	+3	-4	+1	+2	+23	+25*	short	
C-5	25°	+9	+4	-5	+2	+2	+27*	+16	open*	
C-6	59°	+8	0	-1	+1	+2	+27*	+16	--	
CS "C-6"	43°	+9	+2	-3	0	-2	-10	-26*	short	
CS "C-6"	30°	+9	-2	-4	-1	-1	+4	-30*	short	

* Alarm

Table 5-44. (continued).

TEST CONDITION		FIELD DATA			COURSE MONITOR		CLEARANCE MONITOR		Magnitude Monitor	REMARKS
LINE	FAULT	μa change from normal			DDM change from normal					
		2°N	CL	2°S	path	width	path	width		
A-14	3 dB	+2	-5	-4	-3	-6	0	-1	open*	
CS "M-14"	3 dB	-20	-3	+21	+2	+37*	0	+5	open*	-2 dB RF Alarm Course Monitor
SO"M-14"	3 dB	+42	-2	-38	-4	-47*	-2	-1	short	
Normal	--	0	0	0	0	0	0	0	short	F = 108.5 MHz
C-1	3 dB	-1	-1	0	0	+1	+4	0	open*	
C-2	3 dB	+3	-1	+1	0	+1	+9	-1	open*	
C-3	3 dB	0	+2	+5	+2	+8	+33*	+45*	short	
C-4	3 dB	-3	-1	-2	-2	+1	-33*	-29*	short	
C-5	3 dB	+1	-1	-3	-1	0	-11	-20	short	
C-6	3 dB	+1	-2	-2	+1	+1	-3	-9	open*	
CS "C-6"	3 dB	-7	0	+6	-1	+7	+7	+39*	open*	-1 dB RF Alarm Clearance Monitor
SO "C-6"	3 dB	+3	+2	-1	-1	-1	-4	-46*	open*	

* Alarm

Table 5-45. (continued).

TEST CONDITION		FIELD DATA			COURSE MONITOR		CLEARANCE MONITOR		Magnitude Monitor	REMARKS
LINE	FAULT	μa change from normal			DDM change from normal					
		2°N	CL	2°S	path	width	path	width		
Normal	--	0	0	0	0	0	0	0	short	F = 109.7 MHz
A-1	3 dB	+4	0	+2	+1	-2	0	0	open*	
A-2	3 dB	+6	+1	0	+1	-2	0	0	open*	
A-3	3 dB	+9	+2	+1	+1	-4	0	0	open*	
A-4	3 dB	+5	0	+1	0	-2	-2	0	open*	
A-5	3 dB	+5	+1	+2	+3	+4	-1	0	open*	
A-6	3 dB	+4	0	+5	+1	+6	-1	0	open*	
A-7	3 dB	-4	-2	+9	+1	+11	-1	+1	open*	
A-8	3 dB	-9	-1	+4	-4	+3	0	0	open*	
A-9	3 dB	-6	-3	0	-5	-1	-1	0	open*	
A-10	3 dB	-5	-6	-3	-5	-5	-1	0	open*	
A-11	3 dB	-1	-5	-5	-5	-7	-1	0	open*	
A-12	3 dB	+1	-4	-6	-4	-7	-1	0	open*	
A-13	3 dB	+1	-4	-4	-3	-5	-1	0	open*	

* Alarm

Table 5-45. (continued).

TEST CONDITION		FIELD DATA			COURSE MONITOR		CLEARANCE MONITOR		Magnitude Monitor	REMARKS
LINE	FAULT	μa change from normal			DDM change from normal					
		2°N	CL	2°S	path	width	path	width		
A-14	3 dB	+2	-6	-6	-2	-4	0	0	open*	
CS "M-14"	3 dB	-33	-8	+29	+5	+48*	-1	+6	open*	-2 dB RF Alarm Course Monitor
SO "M-14"	3 dB	+41	+2	-33	-2	-43*	-1	-1	short	
Normal	--	0	0	0	0	0	0	0	short	F = 109.7 MHz
C-1	3 dB	+1	+1	-2	-1	+1	+2	-1	open*	
C-2	3 dB	+4	+3	-2	-2	0	+5	-3	short	
C-3	3 dB	+1	+4	+2	-2	+5	+23*	+33*	short	
C-4	3 dB	-2	-4	-5	-3	0	-25*	-20	short	
C-5	3 dB	0	-3	-8	-2	-2	-9	-16	short	
C-6	3 dB	-1	-4	-5	-3	-1	-2	-7	open*	
CS "C-6"	3 dB	-5	-2	+1	-5	+4	+5	+40*	open*	-1.5 dB RF Alarm Clearance Monitor
SO "C-6"	3 dB	+4	-1	-5	-4	-4	-5	-44*	short	

* Alarm

Table 5-45 (continued).

TEST CONDITION		FIELD DATA			COURSE MONITOR		CLEARANCE MONITOR		Magnitude Monitor	REMARKS
LINE	FAULT	μa change from normal			DDM change from normal					
		2°N	CL	2°S	path	width	path	width		
A-14	3 dB	+4	-6	-6	-1	-5	+1	+1	open*	
SO "M-14"	3 dB	+48	-2	-44*	-3	-42*	+1	+1	short	
Normal	--	0	0	0	0	0	0	0	short	F = 111.9 KHz
C-1	3 dB	-3	-2	-1	-1	-1	0	-3	open*	
C-2	3 dB	-2	-3	-1	-1	-1	+2	-6	short	
C-3	3 dB	-1	-5	+6	-1	+2	-6	+26	open*	
C-4	3 dB	-7	-6	+1	-1	+2	-6	0	open*	
C-5	3 dB	-3	-5	-2	-1	-3	-3	-11	short	
C-6	3 dB	-4	-5	+1	-1	-3	-1	-5	open*	
SO "C-6"	3 dB	+1	-4	+2	-1	-5	-3	-43 *	short	

* Alarm

Table 5-45. (continued).

TEST CONDITION		FIELD DATA			COURSE MONITOR		CLEARANCE MONITOR		Magnitude Monitor	REMARKS
LINE	FAULT	μa change from normal			DDM change from normal					
		2°N	CL	2°S	path	width	path	width		
Normal	--	0	0	0	0	0	0	0	short	F = 111.9 MHz
A-1	3 dB	+8	+1	-3	+1	-5	-1	0	short	
A-2	3 dB	+11	-1	-9	0	-5	-1	0	open*	
A-3	3 dB	+10	-1	-8	0	-6	-1	0	open*	
A-4	3 dB	+8	-5	-7	-1	-5	0	0	open*	
A-5	3 dB	+7	-1	-5	-1	-3	-1	0	open*	
A-6	3 dB	+2	-6	-7	-1	-2	0	0	open*	
A-7	3 dB	+9	+5	0	+5	+7	0	0	open*	
A-8	3 dB	-1	-3	0	-1	+4	+1	+1	open*	
A-9	3 dB	+1	-4	-4	-2	0	+1	+1	open*	
A-10	3 dB	+7	-4	-7	-2	-2	+1	+1	open*	
A-11	3 dB	+5	-7	-10	-1	-4	+1	+1	open*	
A-12	3 dB	+7	-6	-9	-2	-6	+1	+1	open*	
A-13	3 dB	+4	-7	-10	-2	-6	+1	+1	open*	

* Alarm

Table 5-45. (continued).

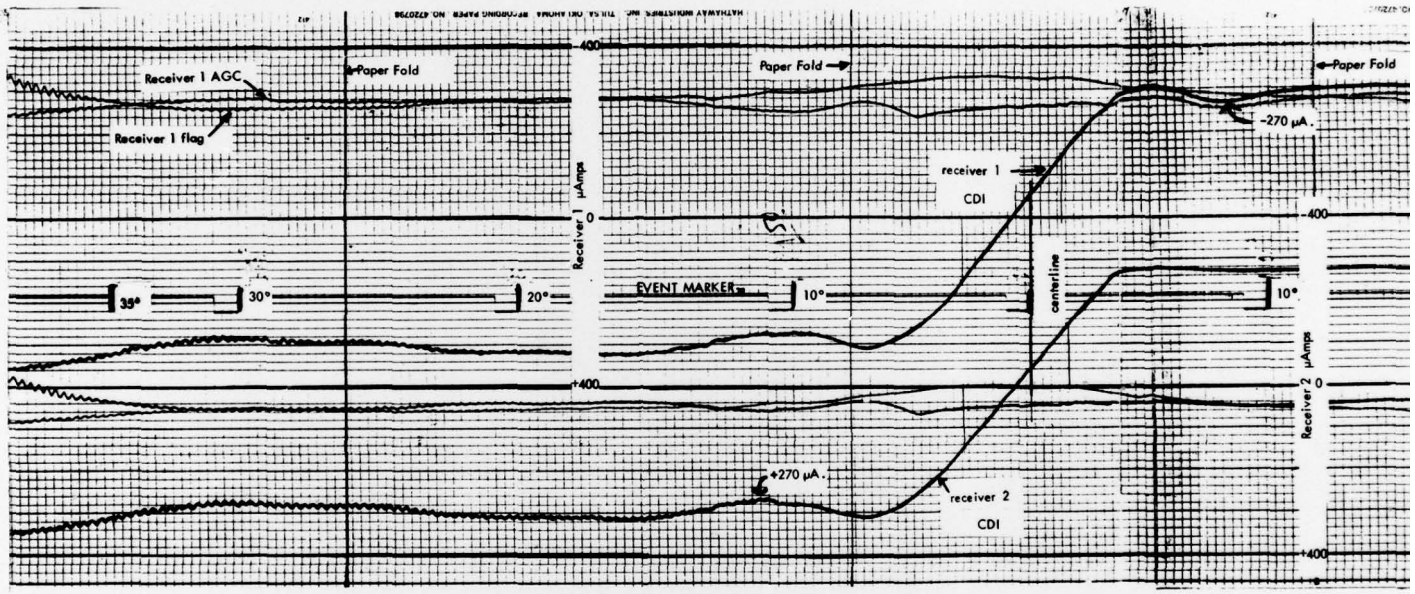

Figure 5-53. Run 18-21 (FAA-DC-6), Normal Configuration, ±35° Clearance Orbit--March 18, 1976.

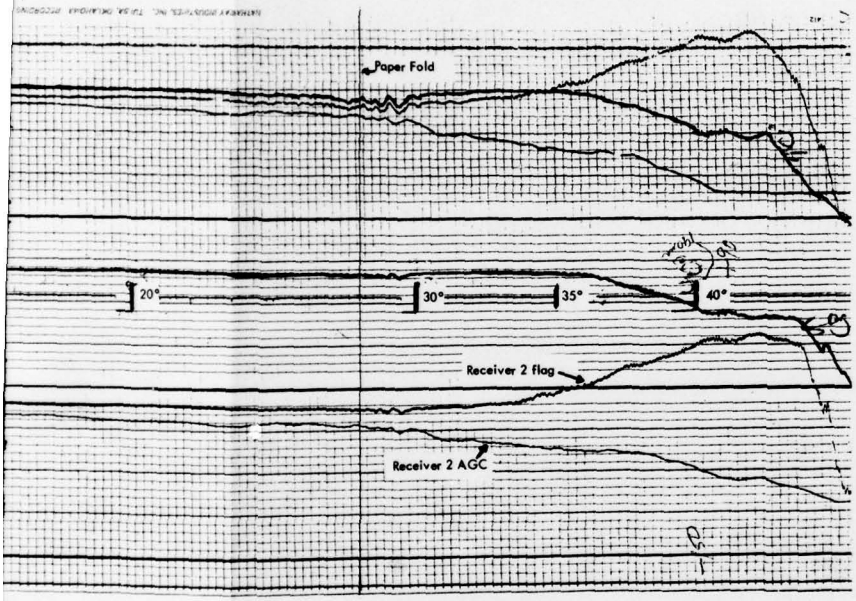
Paper Fold
20°
30°
35°
40°
Receiver 2 flag
Receiver 2 AGC

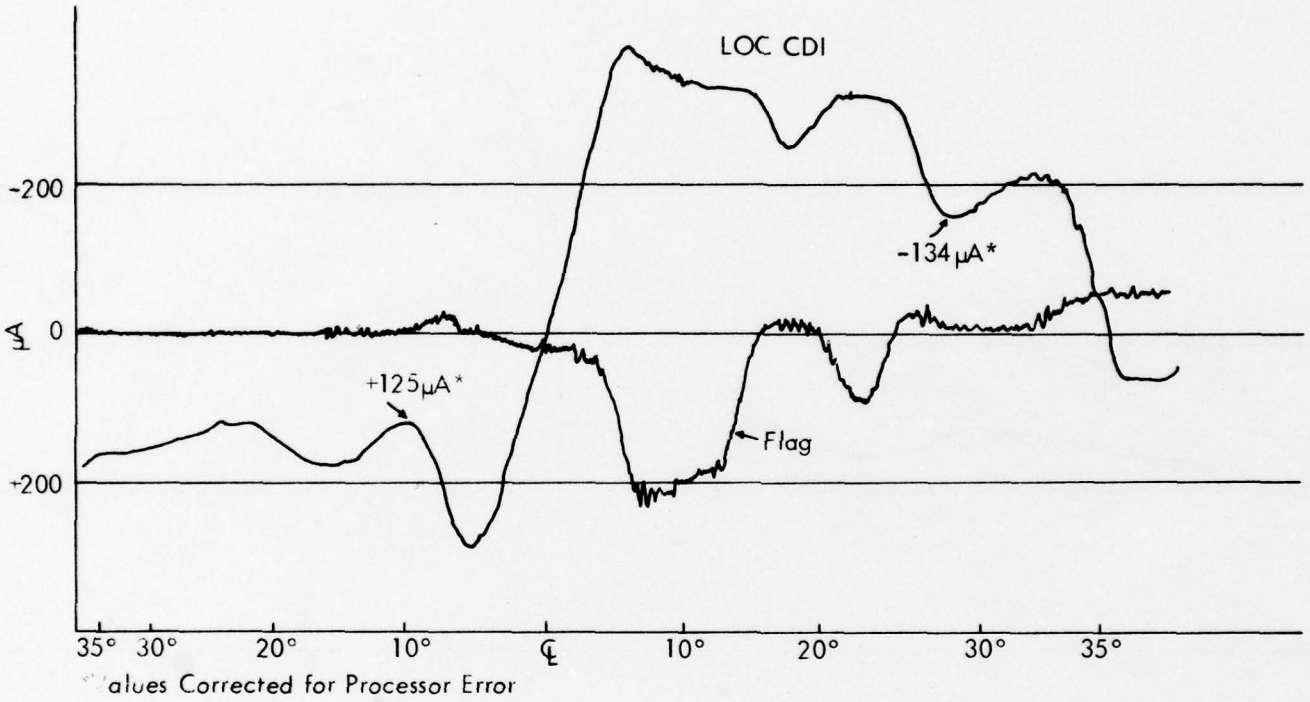

Figure 5-54. Ground Run, 47° Phase Retard in Line A-7, ±35° Clearance Orbit--March 13 1976.

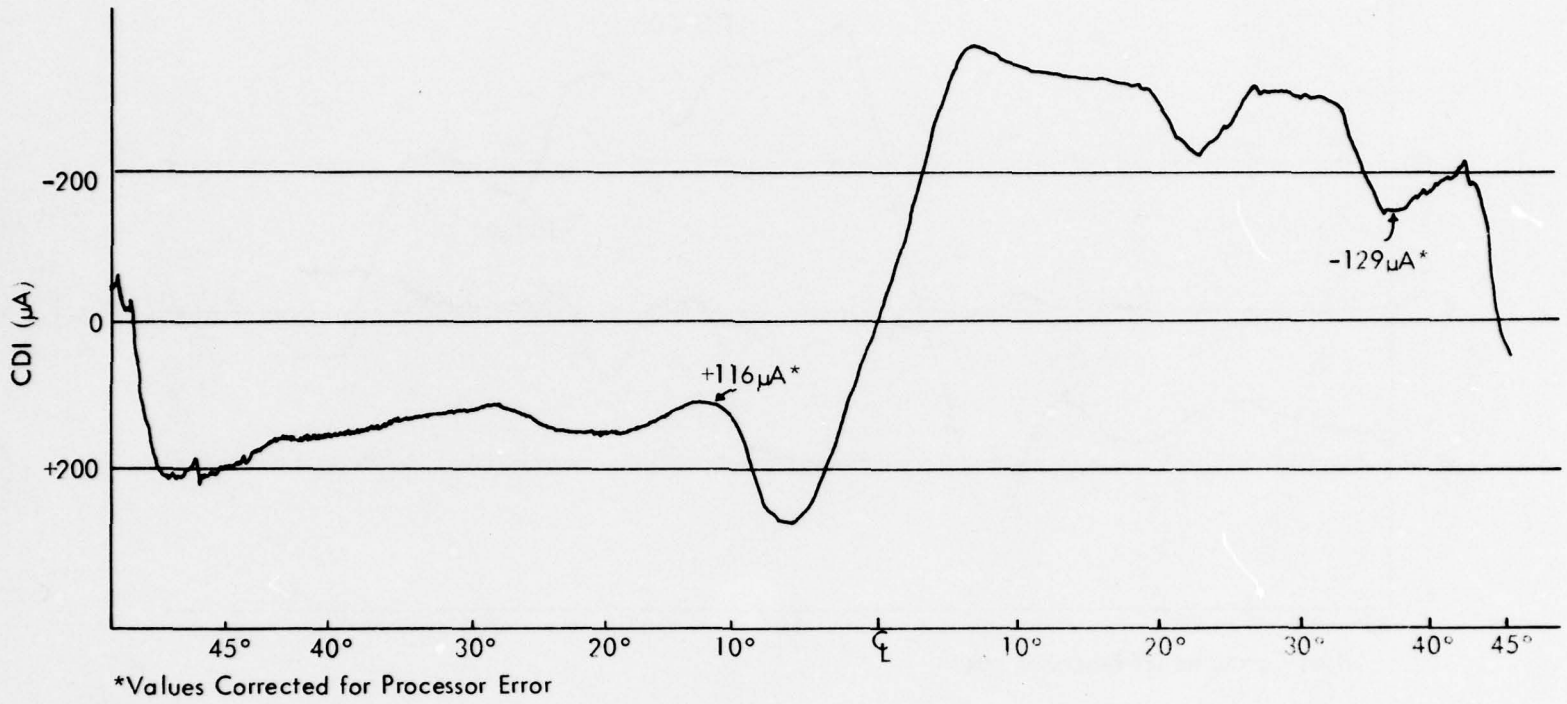

Figure 5-55. Orbit, 46° Phase Retard in Line A-7, ±35° Clearance Orbit--March 17, 1976.

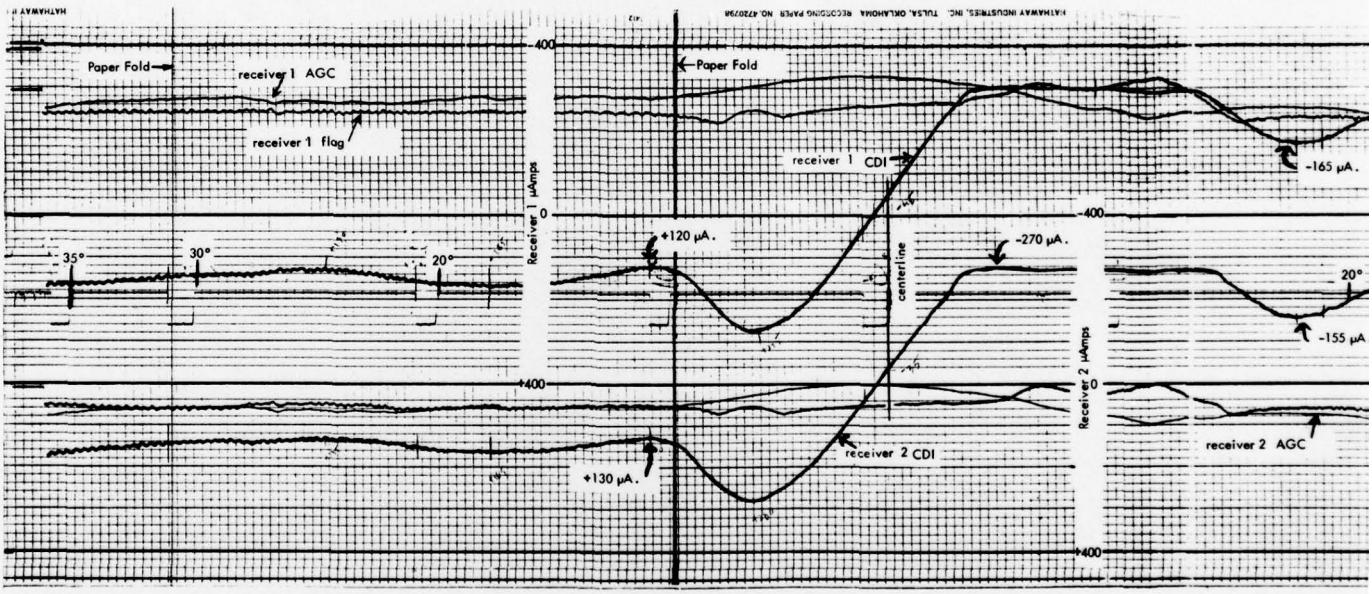

Figure 5-56. Run 18-28 (FAA-DC-6), 47° Phase Retard in Line A-7, ±35° Clearance Orbit--March 18, 1976.

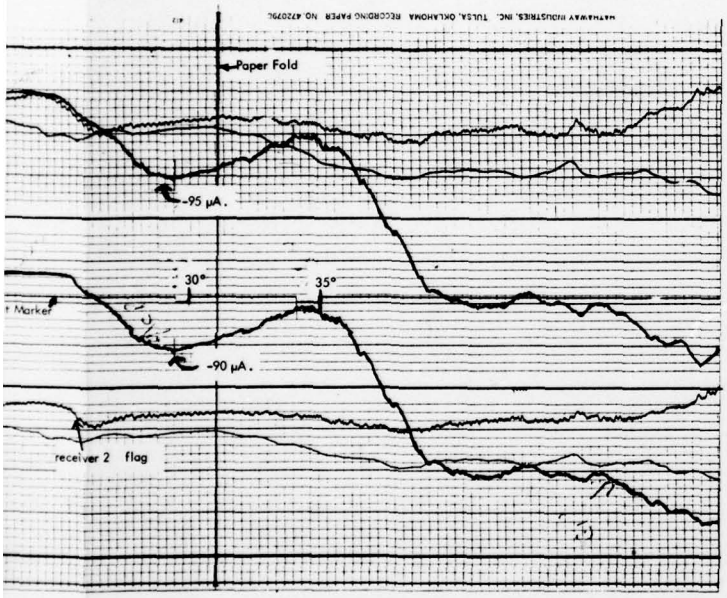
Paper Fold
-95 μA.
30°
35°
-90 μA.
receiver 2 flag

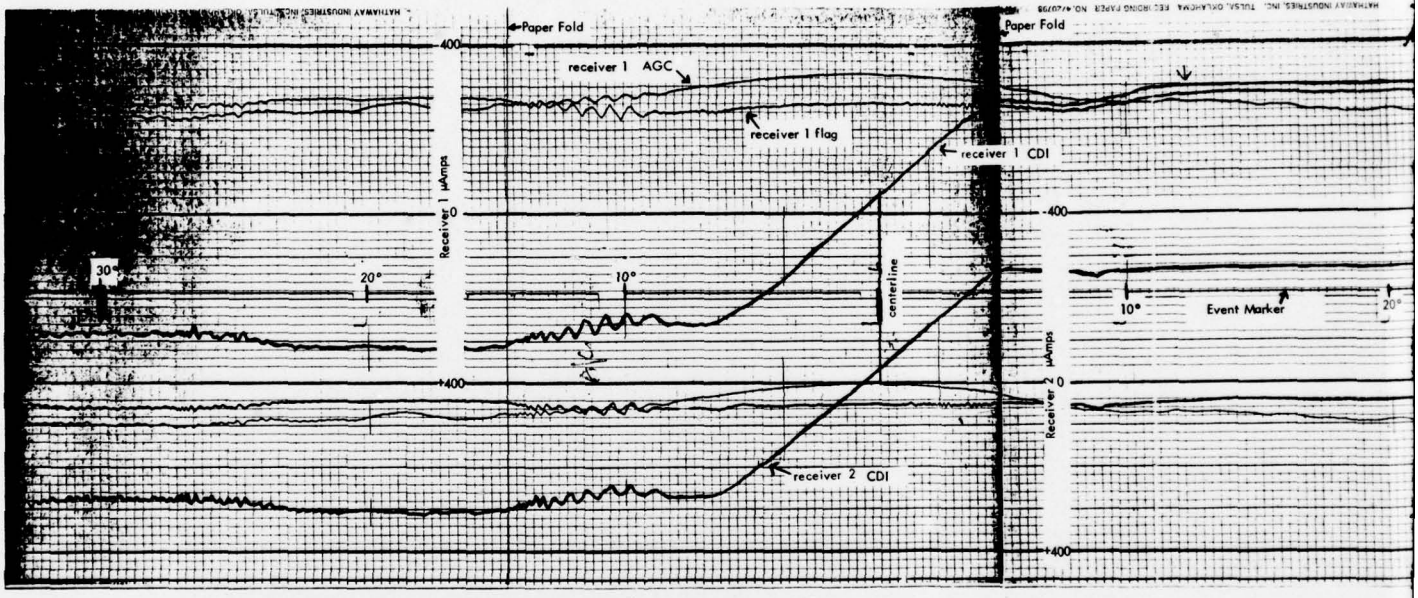

Figure 5-57. Run 18-30 (FAA-DC-6), 31° Phase Retard in M-14 SO Line, ±35° Clearance Orbit--March 18, 1976.

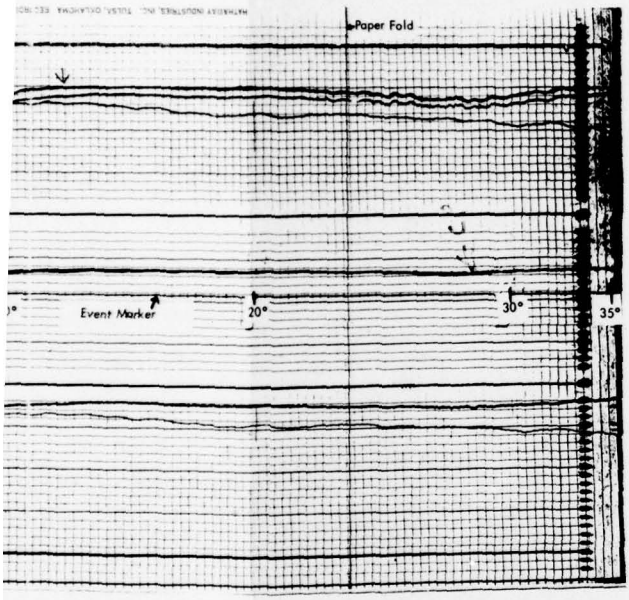
Paper Fold
Event Marker
20°
30°
35°

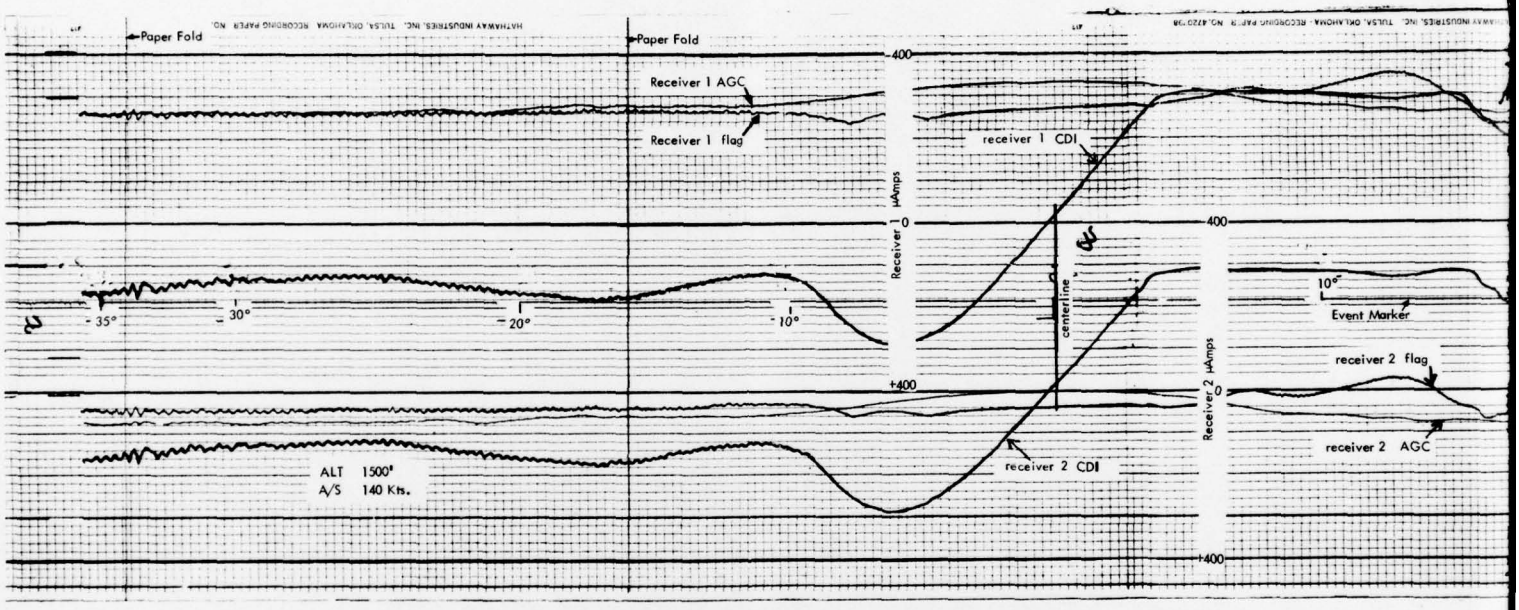

Figure 5-58. Run 19-2 (FAA-DC-6), 45° Phase Retard in Line A-7, Broad Course and Clearance Path Widths--March 19, 1976.

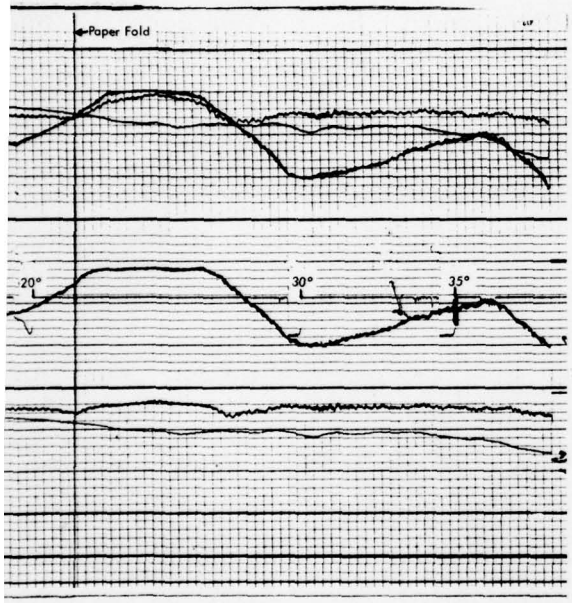
Paper Fold
20°
30°
35°

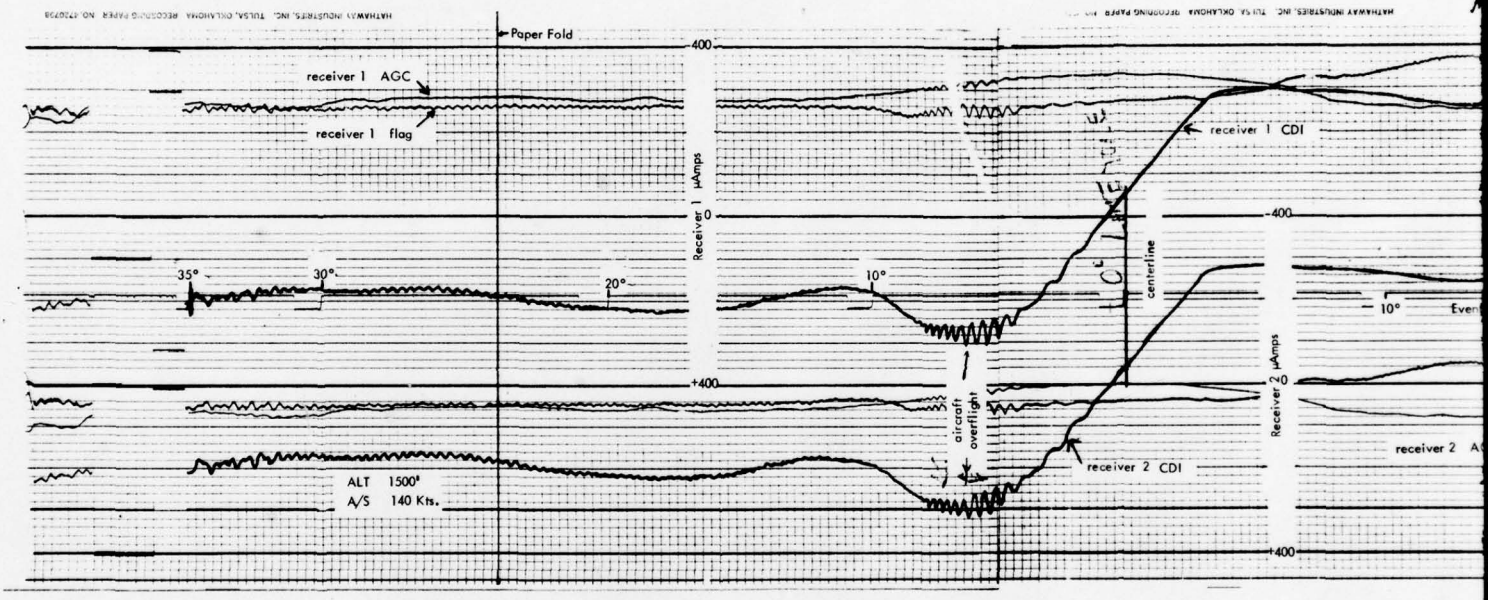

Figure 5-59. Run 19-8 (FAA-DC-6), 41° Phase Retard in Line A-7, Normal Course and Clearance Path Widths--March 19, 1976.

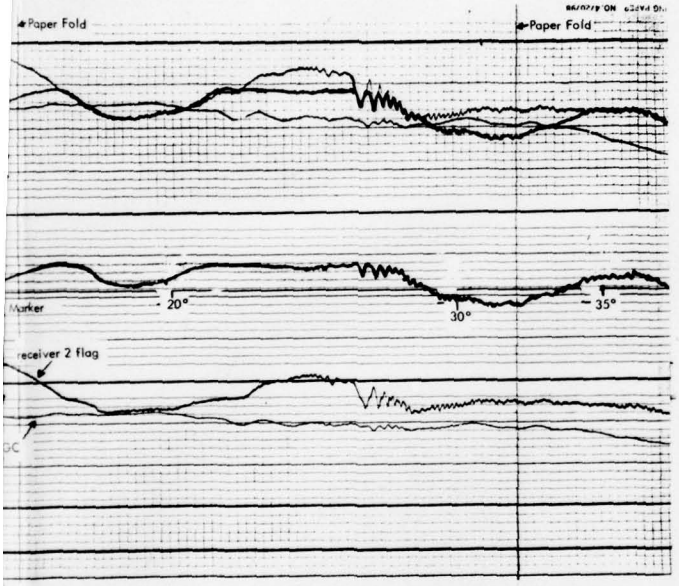

2

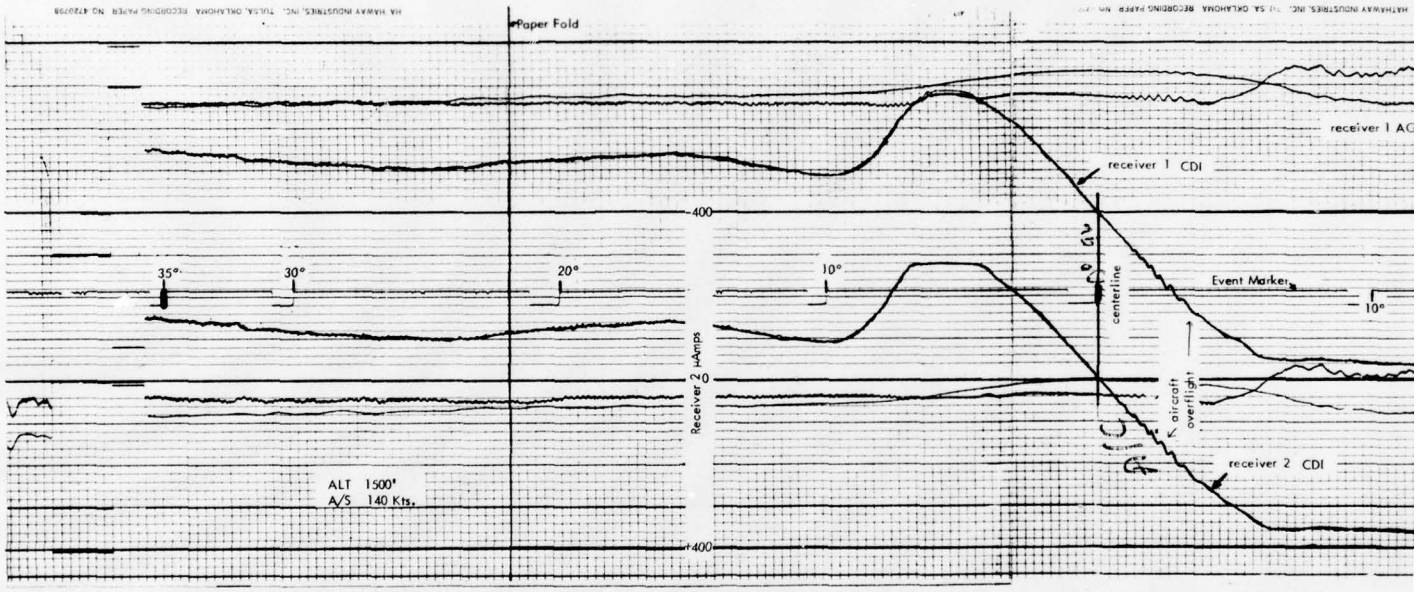

Figure 5-60. Run 19-2 (FAA-DC-6), 51° Phase Retard in Line A-8, Broad Course and Clearance Path Widths--March 19, 1976.

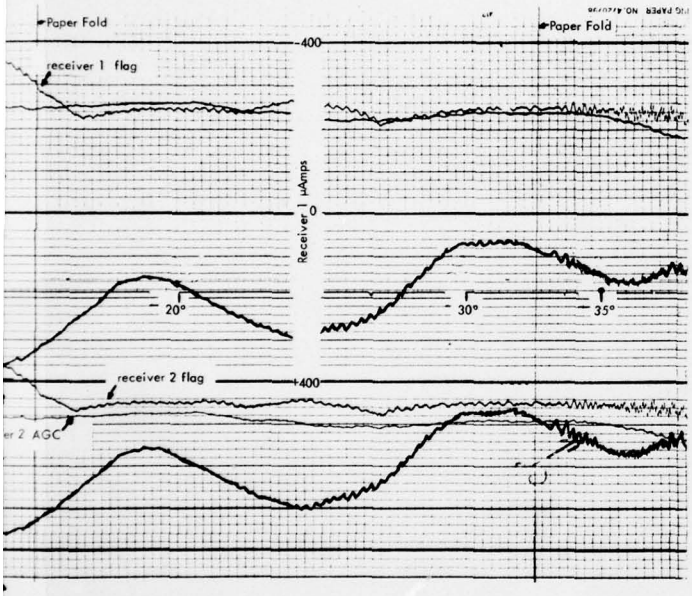
Paper Fold
receiver 1 flag
400
Receiver 1 μAmps
0
20°
30°
35°
Paper Fold
receiver 2 flag
400
er 2 AGC

2

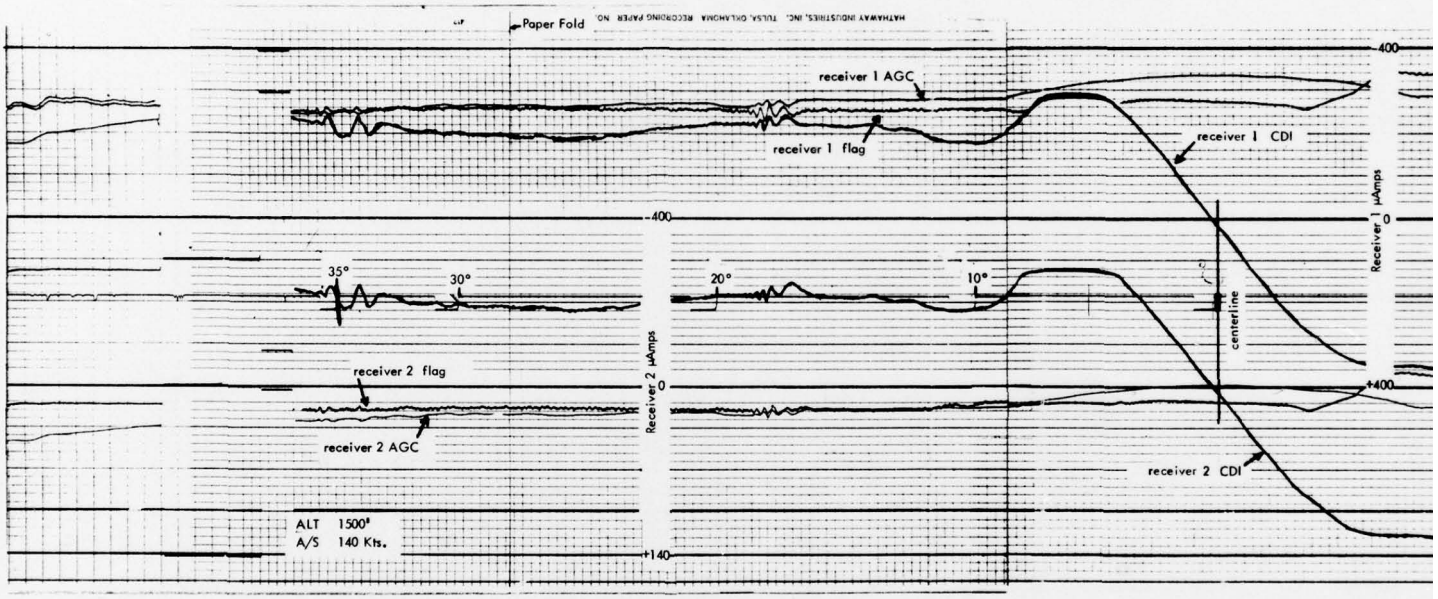

Figure 5-61. Run 19-9 (FAA-DC-6), 40° Phase Retard in Line A-8, Normal Course and Clearance Path Widths--March 19, 1976.

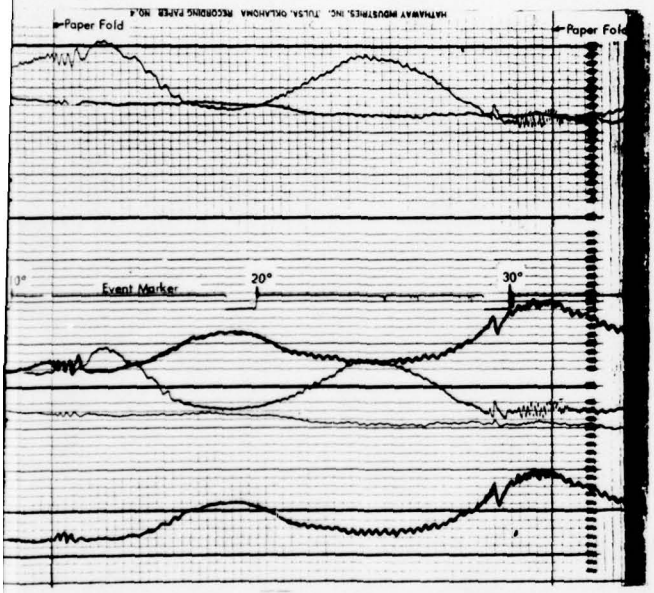
Paper Fold
Event Marker
20°
30°

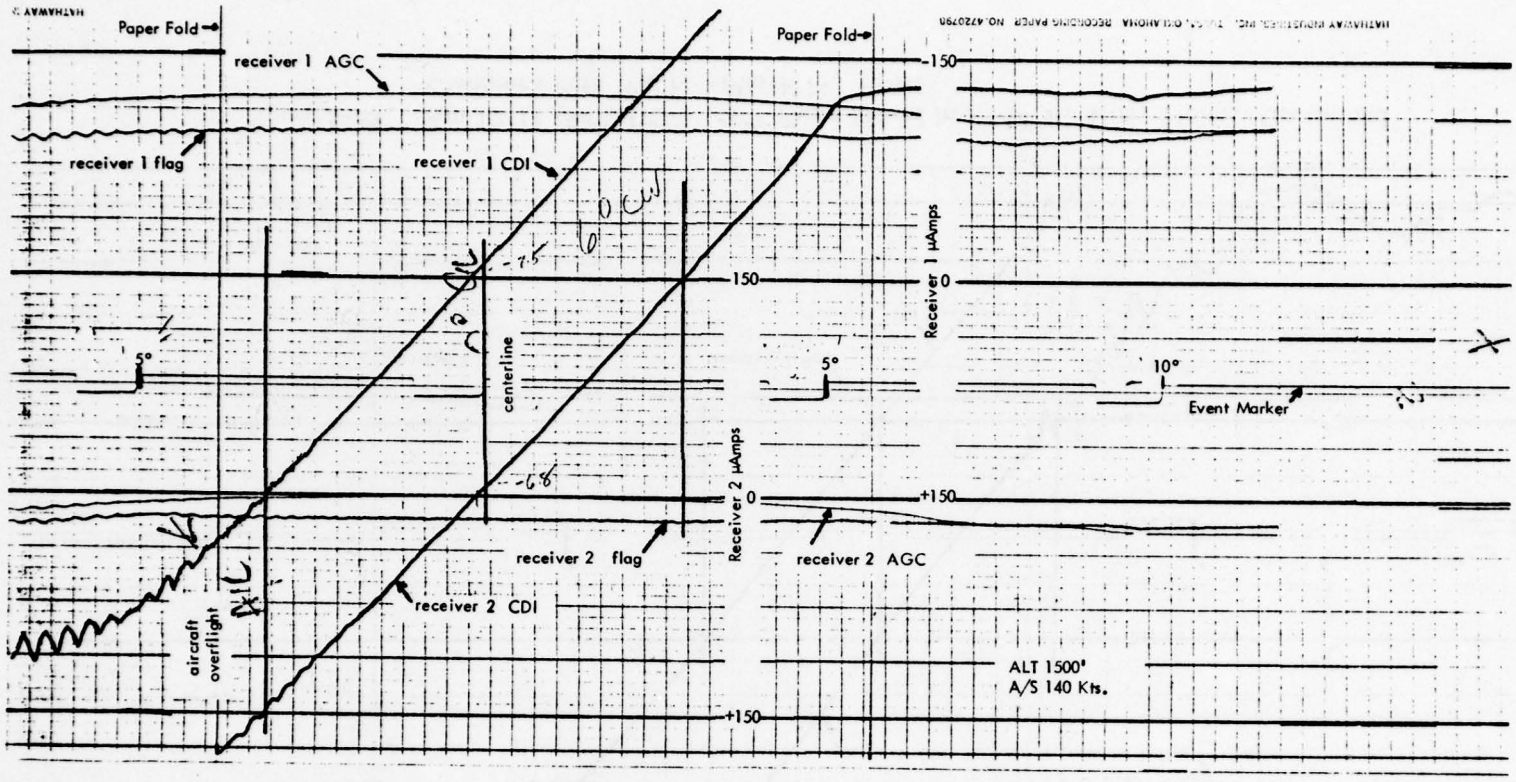

Figure 5-62. Run 19-4 (FAA-DC-6), 36° Phase Retard in M-14 SO Line, Broad Course and Clearance Path Widths--March 19, 1976.

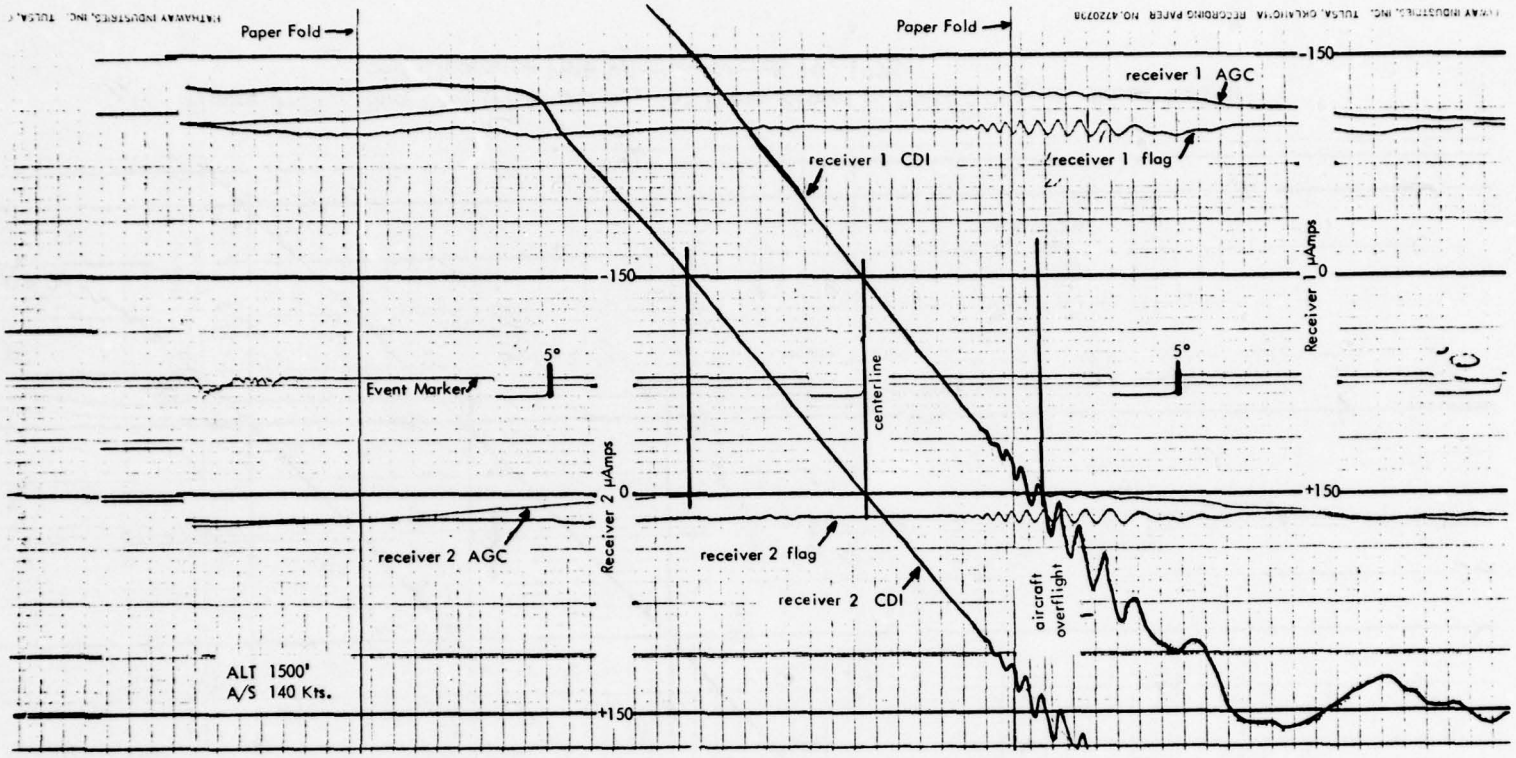

Figure 5-63. Run 19-11 (FAA-DC-6), 44° Phase Retard in M-14 SO Line, Normal Course and Clearance Path Widths--March 19, 1976.

Figure 5-54 is the clearance orbit for a 47 degree phase fault in line A-7, as recorded at the 1000 foot distance on the ground. Figures 5-55 and 5-56 are the flight recordings for the fault as recorded by the Ohio University Beechcraft and by the FAA DC-6 aircraft. The flight recording shown in Figure 5-56 corresponds to run 18-28 listed in Table 5-42.

As can be seen, good correlation exists among the 4 records (this includes the results from both of the receivers on the DC-6) even though the records were taken on three different days. The minimum clearances on the 150 Hz side of the runway centerline were 125 μa, 116 μa, 130 μa, and 120 μa, respectively, for the ground, BE-35, and the DC-6. The corresponding minimum clearances on the 90 Hz side were -134 μa, -129 μa, -90 μa, and -95 μa. The DC-6 results on the 90 Hz side of the centerline were lower than the Ohio University results, and this might be due to the flattening out of the DC-6 recorded responses at approximately -270 μa, as can be seen in Figure 5-56.

Figure 5-57, corresponding to run 18-30 in Table 5-42, illustrates the excessive width changes that occurred when a 31 degree phase retard was inserted in the course transmitter sideband only feed line. For this run, the path width was 5.7 degrees (150 μa to -150 μa) but the minimum clearance levels remained above 250 μa in magnitude.

After retuning the equipment to the 108.5 MHz test frequency, flight records were obtained with faults in the A-7, A-8, and sideband only feed lines. The clearance path width was then reset from 9.5 degrees to 8.33 degrees, the course path width (with the clearance transmitter on) was reset from 4.4 degrees to 4.15 degrees, and another set of flight records taken for the three faults.

Figures 5-58 and 5-59, corresponding to runs 19-1 and 19-8 with phase retard faults of 45 degrees and 41 degrees, respectively, in line A-7, show the effects of increasing sideband powers to sharpen the course and clearance path widths. For run 19-1, the clearance levels dropped to +120 μa and -100 μa on the 150 Hz side and on the 90 Hz side of the runway centerline, respectively. After correcting the path widths, the corresponding minimum clearance values, from run 19-8, were +160 μa and -170 μa.

Figures 5-60 and 5-61, corresponding to runs 19-2 and 19-9, show similar results for the phase retard faults in line A-8 (see Table 5-42 for the minimum clearance values).

Figures 5-62 and 5-63, corresponding to runs 19-4 and 19-11 for phase retard faults of 36 degrees and 44 degrees, respectively, in the course transmitter sideband only feed line, show that increasing the sideband power will lessen any path width broadening effects that are caused by the phasing fault.

Table 5-43 lists those results of the ground orbit runs, taken at the three test frequencies, for which the minimum clearance values dropped below ±200 μa or for which the path width broadened out excessively. From this data, only the

variable phase faults, when inserted in the feed lines to antenna numbers A-7 or A-8, or when inserted into the course transmitter sideband only feed line, are seen to give either below-tolerance clearance values in the ±35 degree sectors, or to show excessively broad course width values.

Table 5-44 lists both the monitor responses and the field data (centerline and ±2 degree points) for the variable phase faults necessary to initiate the first monitor alarm. Table 5-45 lists the same data for the 3 dB attenuation faults. Note that the data in Tables 5-44 and 5-45 has been normalized to indicate the changes from normal as seen either in the field or the monitors.

Table 5-46 lists the microampere changes as seen on centerline, at the 1000 foot distance, and the phase changes needed to obtain an alarm indication on the course monitor path channel. As can be seen, the best results occurred at the 108.5 MHz test frequency, where the greatest change in the field was +11 μa for a +0.011 DDM monitor alarm indication.

At the 111.9 MHz test frequency, 8 of the 14 field responses exceed 11 μa in magnitude when the corresponding monitor response registered an 0.011 DDM alarm indication. The maximum out-of-tolerance field condition occurred when line A-10 was faulted, and for this fault the field data exceed the 11 μa limit by 7 μa (corresponding to a total change in the field of +18 μa). At the 109.7 MHz test frequency, the monitor alarm limits were set at ±0.012 DDM, and the field responses exceed a 12 μa change in 7 of the 14 faults. The maximum out-of-tolerance field responses occurred when lines A-6 and A-7 were faulted. For these cases, the field data exceeded the -12 μa limit by -7 μa (corresponding to a total change in the field of -19 μa). Also, an examination of Table 5-46 shows that at the 109.7 MHz test frequency, the phase changes required to produce a monitor alarm were greater than the required phase changes at the other two frequencies, with the minimum phase fault required to produce an alarm indication being 21 degrees at the 111.9 MHz frequency.

4. Conclusions. The following conclusions concerning the performance of the Alford MC 14/6 localizer array are based on data taken by both the Avionics Engineering Center, Ohio University, and by the FAA flight inspection aircraft N-46 from the NAFEC Airport, Atlantic City, New Jersey. The data includes the results of 3 dB attenuation faults and variable phase retard faults inserted in the individual antenna feed lines as well as in both the course transmitter and clearance transmitter carrier and sideband feed lines.

The monitors detected most of the faults, within the monitor alarm limits. However, for some of the variable phase faults, the centerline field responses exceeded Category II limits with the path monitor just registering an alarm condition. As phase faults of greater than 22 degrees were required to produce the out-of-tolerance conditions, a slight tightening of the monitor limits should provide adequate monitor action for any reasonable fault.

LINE	Centerline Field Data (μampere change)			Line phase change needed to initiate course monitor path alarm (degrees) **		
	108.5 MHz	109.7 MHz	111.9 MHz	108.5 MHz	109.7 MHz	111.9 MHz
A-1	-4	-4	-9	72	85	58
A-2	-7	-8	-12	55	56	51
A-3	-8	-14	-12	30	36	28
A-4	-10	-14	-10	25	29	21
A-5	-9	-17	-11	24	30	23
A-6	-8	-19	-13	35	43	30
A-7	-8	-19	-15	41	57	39
A-8	+11	+11	+15	42	55	46
A-9	+9	+12	+11	27	39	30
A-10	+10	+13	+18	24	29	24
A-11	+7	+11	+14	24	30	22
A-12	+8	+13	+17	29	33	27
A-13	+7	+3	+4	59	56	53
A-14	+3	[illegible]	0	90	97	97

** Note: At the 109.7 MHz test frequency, the path alarm limits were ±0.012 DDM, while for the 108.5 MHz and 111.9 MHz test frequencies, these limits were reset to ± 0.011 DDM which are the limits for Category II operations.

Table 5-46. A Comparison of the Field Responses on Centerline and the Phase Faults Necessary to Produce a Monitor Alarm for the Three Test Frequencies.

a. Using a Portable ILS Receiver, Type FA-8766, at a distance of 1000 feet from the array, the clearance sideband power was set for an 8 degree width, and the course sideband power was set for a 4 degree course width. However, subsequent flight checking showed these widths to be 9.5 degrees and 4.4 degrees, respectively. This indicates that there might be a need to go to a 1500 foot or 2000 foot distance from the array for proper setting of the widths, especially that for the clearance array.

b. With the course and clearance transmitters in the above-mentioned broad settings, ground measurements to determine course alignment shifts, and to record minimum clearances over a 70 degree orbit centered on the runway centerline and at a distance of 1000 feet from the array were made for the 3 dB and for the variable phase faults in all the lines. Flight checks by both Ohio University and the FAA were then performed for those faults which showed out-of-tolerance conditions unaccompanied by monitor alarms.

The clearance and combined course widths were then reset to 8.33 degrees and 4.15 degrees respectively, as determined by flight check, and the effects of the critical faults were reexamined.

The following pertinent results were noted:

(1) For a number of the variable phase fault tests, the centerline alignment responses, as measured at a distance of 1000 feet from the array, shifted beyond Category II tolerance limits (± 11 μa) by at most 6 μa. However, the phase faults required to produce these out-of-tolerance conditions were between 22 degrees and 57 degrees in the faulted lines.

(2) With the phaser inserted in either line A-7 to A-8, and adjusted to give just a monitor alarm indication (usually for a phase retard of between 40 degrees and 50 degrees), inadequate clearances were noted in the +35 degrees to -35 degrees sector. This was with the broad width settings.

With the normal width settings, however, a 41 degree phase retard in line A-7 gave minimum clearance values of +165 μa and -170 μa, respectively, in the south and north sectors about the runway centerline. With 40 degree phase retard in line A-8, the minimum clearances were +200 μa and -180 μa, respectively. These results were determined by flight test.

(3) With the phaser inserted in the course sideband-only feed line, and adjusted to get an alarm indication (at about 42 degrees), the course width changed excessively, increasing to between 7.2 degrees and 7.5 degrees. However, decreasing the sideband power to get a width alarm gave only a change of from 4.74 degrees to 5.69 degrees. These values were measured on the ground at a distance of 1000 feet from the array.

(4) When measured by flight check, the change in path width was not as excessive. With the original broad width settings, the width was measured at 4.4 degrees and decreasing the sideband power to a broad alarm indication gave a width of 5.7 degrees. A 35 degree phase retard also registered an alarm condition and produced a 5.7 degrees course width. This was at 111.9 MHz.

(5) At 108.5 MHz, with the original broad width settings, a 36 degree phase retard gave a 6.07 degrees course width. After resetting the course and clearance widths, a 44 degree phase retard gave only a 5.61 degrees course width, with the normal (no fault) width being 4.2 degrees.

(6) With the phaser inserted in either line C-3 or C-4, a monitor alarm was noted with a phase setting of from 4 degrees to 6 degrees while the ground measurements indicated more than adequate clearances in the +35 degrees to -35 degrees sector. The alarm limits were set for a ±.011 DDM change in the clearance monitor path channel. As these limits are not specified in the United States Standard Flight Inspection Manual, the alarm limits were reset to ±.027 DDM, at which settings an alarm indication was obtained with a phase retard of 9 degrees to 10 degrees in lines C-3 and C-4. Adequate clearances were still noted for these cases.

(7) With the 3 dB attenuator inserted in the antenna feed lines, adequate clearances were obtained in all cases.

(8) Correlation between air and ground measurements was good except for the case of width determination.

(9) Stability of the Alford MC 14/6 localizer system appeared to be satisfactory. A continuous recording, over a 4-1/2 day period, of the course monitor, path channel DDM indicator showed maximum deviations of +.005 DDM and -.002 DDM setting (alarm settings are ±.011 DDM). The

weather during the 4-1/2 day recording period varied between brief intervals of very heavy thundershowers, intervals of continuous rainfall, and ended with approximately 1-1/2 days of bright sunshine.

I. Watts-Hollins Small Aperture Slotted-Cable Localizer.

1. Introduction. The slotted-cable localizer antenna conceived, designed, and fabricated by the Watts Prototype Company is intended to provide the ILS engineer with an option for a low-cost, easily installed array. The present unit consists of a slotted-cable approximately three inches in diameter backed by a slotted-cable pick-up for the monitor. This slotted-cable spaced approximately one quarter wavelength behind the radiating cable serves as a reflector. Both cables are oriented perpendicular to the centerline of runway nine left, at the Ohio University ILS Test Site, New Tamiami Airport, Miami, Florida.

The slotted-cable array was positioned 1600 feet from the stop end of nine left at Tamiami Airport. The slotted-cable radiating element and its parallel companion, a slotted-cable monitor antenna, are placed approximately 5 feet above the ground. These antennas are located at the Ohio University ILS Test Site along with an Alford 14-element traveling wave antenna array and a 12-element V-ring array. To simplify feeding the slotted-cable array, the cables to the Alford System were extended using 125 feet of RG-214 cable. The associated loss resulted in only 3.6 watts of carrier power available at the antenna. These tests were run January 23 through January 27, 1976.

2. Discussion of Data. Orbits were attempted initially at 1000 feet elevation at 6 nautical miles. Insufficient signal strength from the array to permit the receiver to operate satisfactorily prompted the decision to make subsequent orbits at 2 miles. Available data shown in Figure 5-64 indicates that no significant misrepresentation of DDM patterns was experienced by using the shorter radius for the orbits.

Inadequate and asymmetrical clearances were obtained in the back course region. Far-field orbit measurements were made with the monitor slotted-cable removed with virtually no effect on the localizer. Rotation of the transmitting antenna 180 degrees in azimuth gave a clear demonstration that the asymmetrical condition was a site-induced effect and was not associated with the antenna.

It should be noted that an Alford 14-element traveling wave O-ring type antenna is located 1000 feet to the rear of the slotted-cable and a 12-element V-ring array is 50 feet beyond the Alford antennas. Conceivably the Alford array could be perturbing a space pattern of the slotted-cable. The principal area of pattern deformation is in the 90 Hz sector of the back course.

Figure 5-65 is given to illustrate a flyability run. Figure 5-66 shows an orbit at 111.9 MHz.

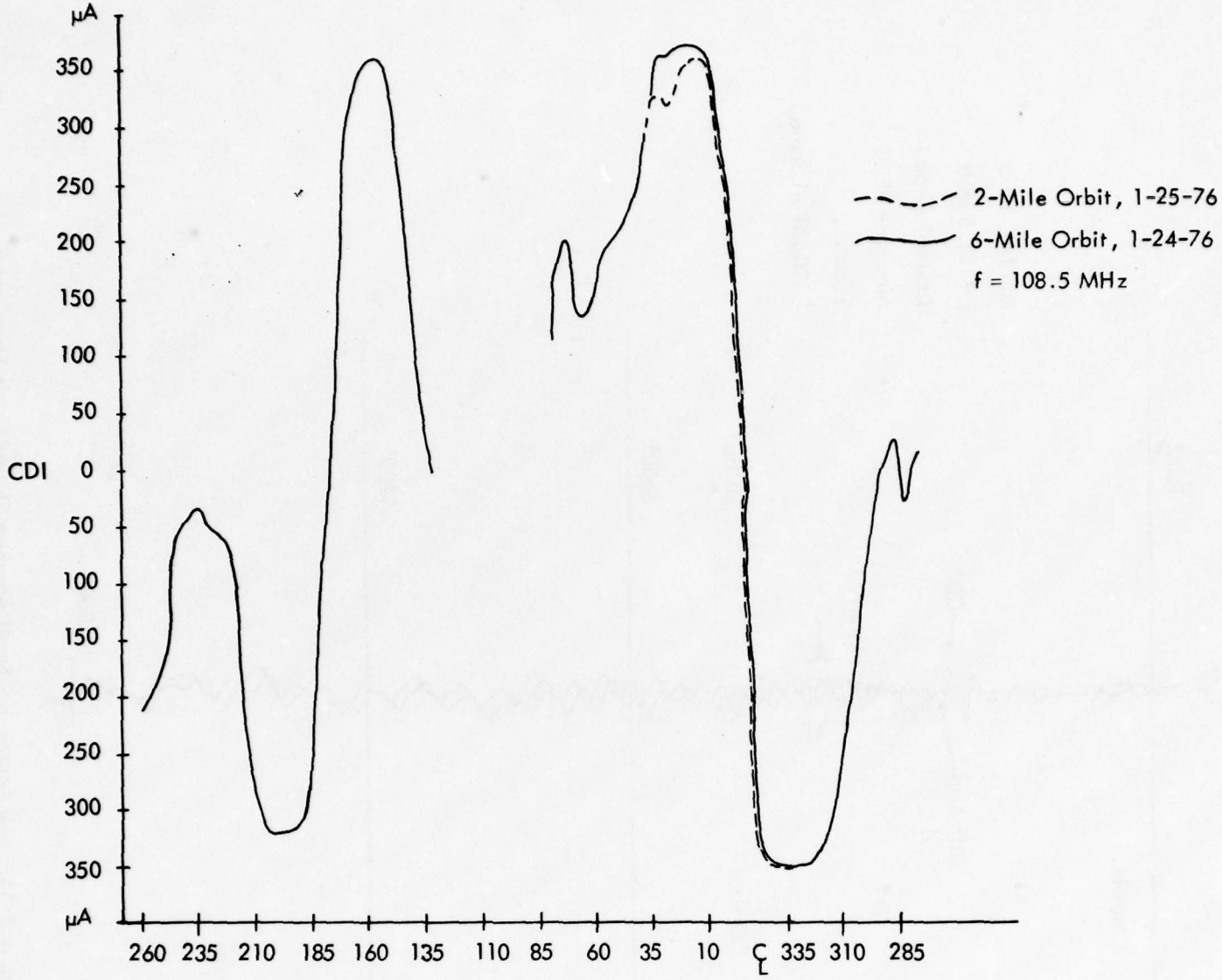

Figure 5-64. Comparison of 6 and 2-Mile Orbits of Small Aperture Slotted-Cable Localizer.

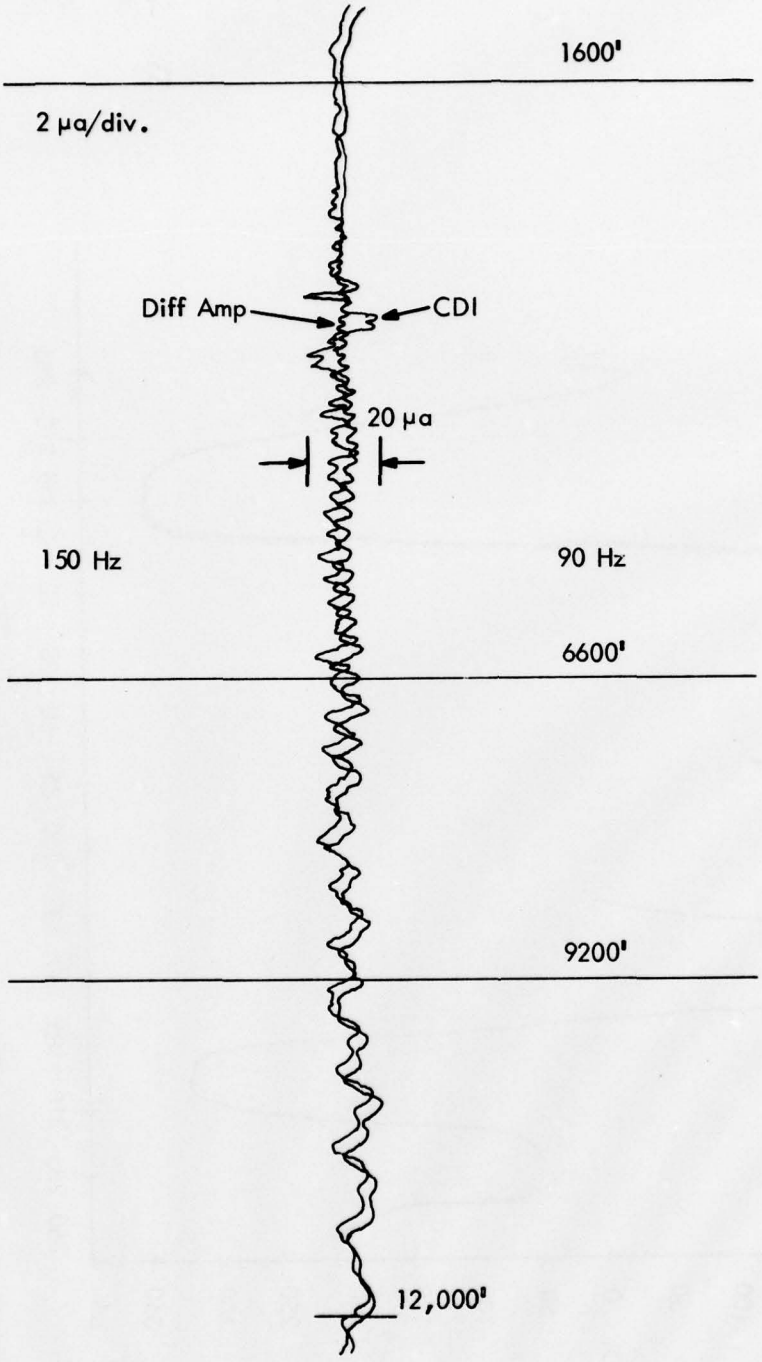

Figure 5-65. Low Approach - Small Aperture Slotted Cable Localizer - January 25, 1976.

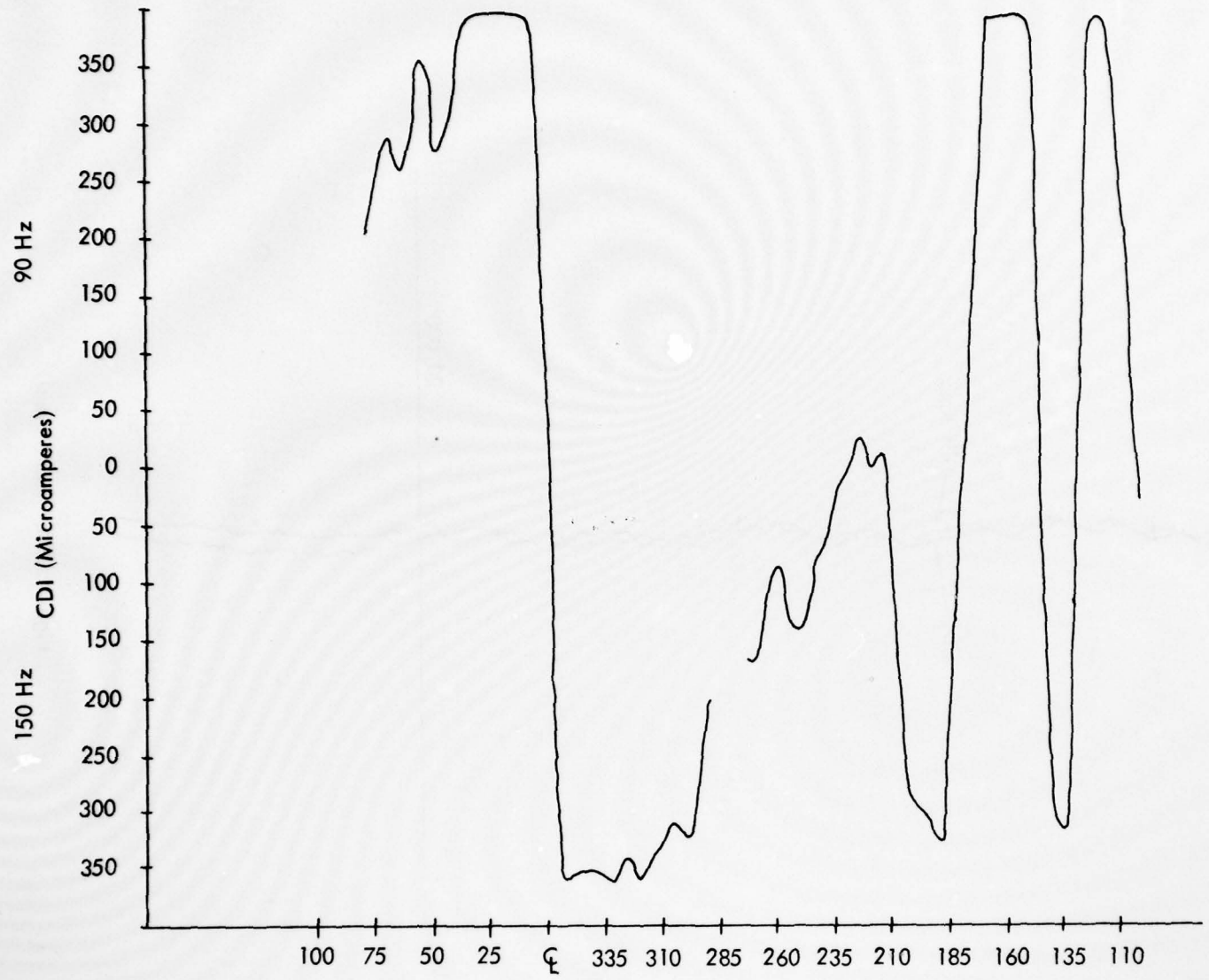

Figure 5-66. Plot of Localizer CDI vs. Azimuth for a 2 mile run at f = 111.9 on January 27, 1976 of Localizer Array.

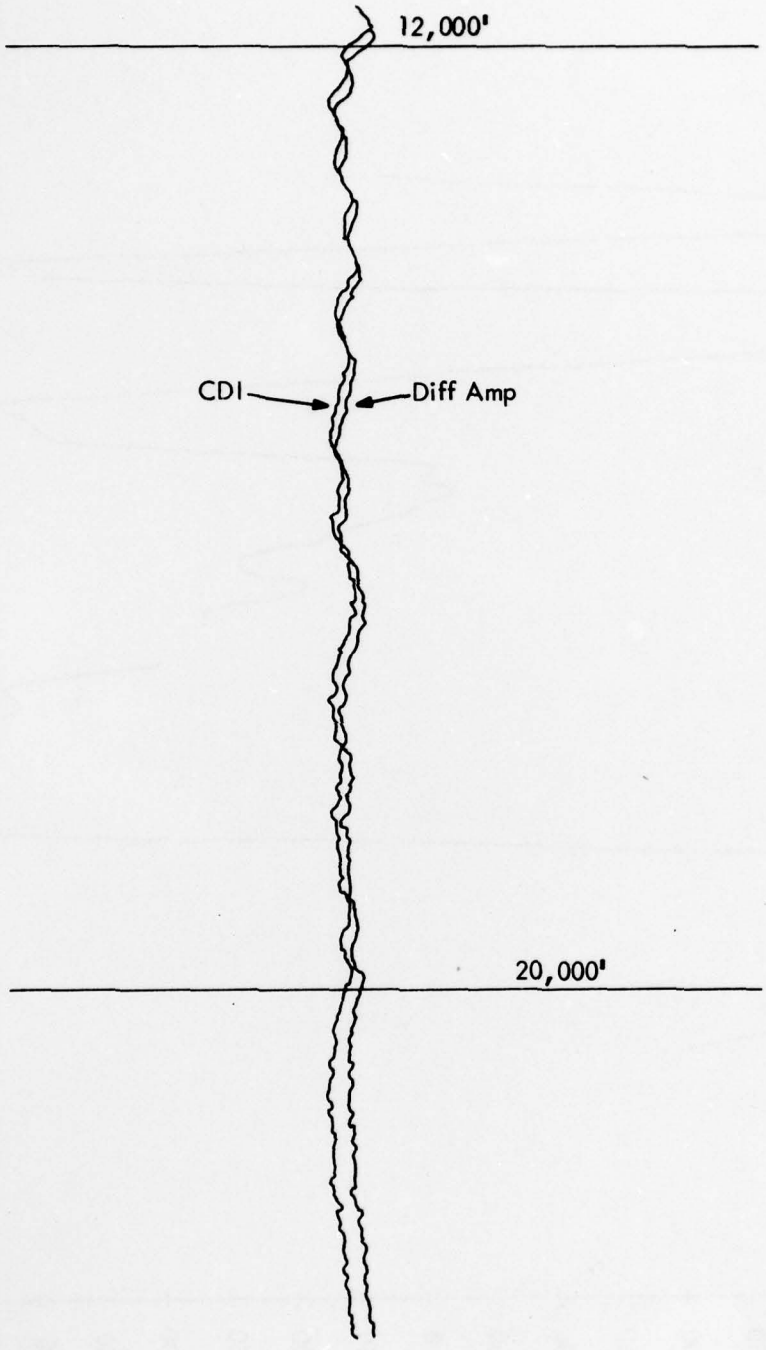

Figure 5-65. (continued).

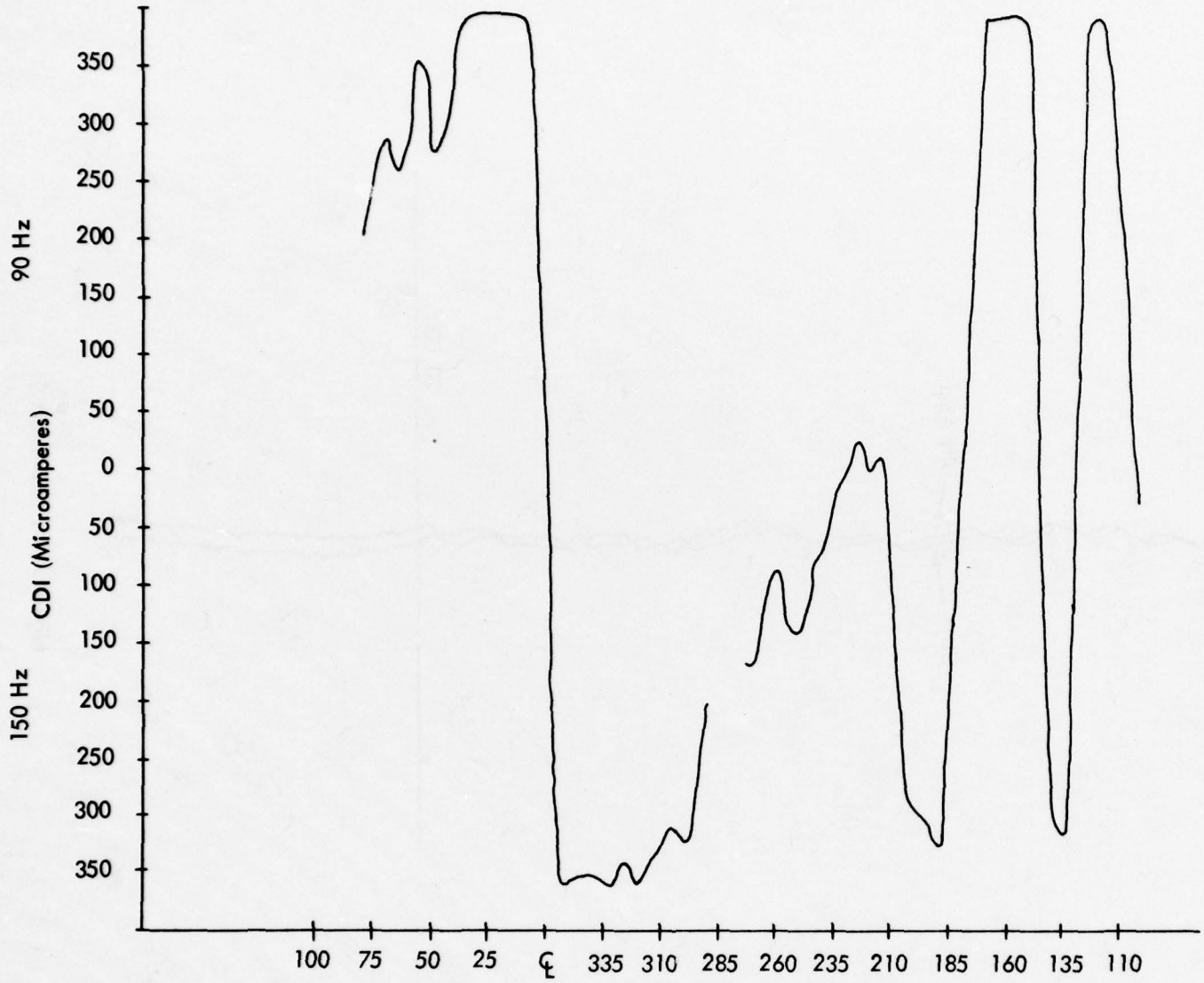

Figure 5-66. Plot of Localizer CDI vs. Azimuth for a 2 mile run at f = 111.9 on January 27, 1976 of Localizer Array.

J. Flight Test Results of the Small and Medium Aperture Hollins Slotted-Cable Localizer Antenna Array.

1. Introduction. The data presented in this section was taken in order to determine how well the Hollins slotted cable localizer antenna array (both small and medium aperture) performance compared with respect to FAA specifications for a localizer. The tests that provided this information were performed at the New Tamiami Airport (Florida) under favorable weather conditions and with no abnormalities in the ground plane (the effect of other antennas in the vicinity of the antenna under test will be mentioned as it applies to specific tests).

Preliminary flight checks were made by Ohio University to determine whether any major faults were present in the antenna before more extensive tests were performed by NAFEC. These tests were performed by the Ohio University aircraft Bonanza-35 using the Minilab as a data collection device on September 25 and 27, 1976. As these tests indicated no anomalies in the antenna, an in-depth evaluation was performed by NAFEC on September 28, 29 and 30, 1976 in the FAA DC-6 aircraft N46. The NAFEC tests were completed in accordance with a predetermined format for localizer certification on each of three frequencies (108.5, 109.7, and 111.9 MHz) with both the small and medium aperture antenna resulting in a total of six test configurations. As frequency changes necessitated retuning of the antennas, monitor and ground checks were performed after each frequency change to insure pattern integrity.

Representations from the FAA, Watts Prototype Company, and Ohio University were present for all phases of testing.

2. Data Collection. As the performance of the slotted-cable antenna array was evaluated by NAFEC on three frequencies and the Ohio University tests were performed on two frequencies, the graphical data presented here was derived from the NAFEC test flights. It should be noted, however, that at points where comparisons between the Ohio University and NAFEC data are possible, there is agreement on most points (see Table 5-47 for a summary of Ohio University's flight tests).

Tables 5-48 and 5-49 provide the general operating characteristics of the antenna arrays indicating course widths, clearance ranges, and front course structures for the three frequencies and for various operating conditions. Table 5-50 provides information on the usable distance of the antennas taken at 18 nmi for several altitudes (the altitude of interest for certification purposes is 1500 ft.). Table 5-51 depicts the system operation for different carrier/SBO phase relationships on each of the three frequencies.

Dephasing tests on the morning of September 30 revealed an unexplainable large difference in the degradation of the course width due to equal advances and retardations in the carrier/SBO phase. A check of the transmitters carrier/SBO

	f = 108.5 MHz		f = 111.9	
	Small Aperture	Medium Aperture	Small Aperture	Medium Aperture
SIGNAL DISTRIBUTION	3dB taper from 0-±10° 11dB taper from 0-±35° 11dB taper from 10-18nmi along centerline	15dB taper from 0-±10° 8 dB front to back ratio	10dB taper from 0-±35° 7dB front to back ratio	10-15dB taper from 0-±10°
DDM DISTRIBUTION AT BROAD ALARM (7.2° course width)	Excellent Clearance Good back course Symmetry acceptable	Good front course clearance (CDI > 220μa for ±35°) Unacceptable back course clearance	Excellent Clearance Good back course Symmetry acceptable	Deficient-flag below acceptable limits at ±10° at 18nmi (Due to low signal level)
R.F. COVERAGE	Marginal at ±10°, 18 nmi, 1500'	Marginal at ±10°, 18 nmi, 1500'	Marginal at ±10°, 18 nmi, 1500'	Marginal at ±10°, 18 nmi, 1500'

Table 5-47. Summary of Ohio University Flight Test Results. These tests were performed prior to and independent of the NAFEC test flights. The radiation characteristics observed by the Ohio University test team as listed in this summary are in general agreement with the NAFEC test results wherever comparisons can be made.

TEST	FREQUENCY	COURSE WIDTH	COMMENTS
(BROAD)	108.5 109.7 111.9	7.6° 7.5° 7.1°	min of 310 μa at 35° into 150 Hz min of 300 μa at 35° into 150 Hz min of 320 μa at 35° into 150 Hz
(SHARP)	108.5 109.7 111.9	3.6° 3.0° 3.0°	
BACK COURSE (NORMAL)	108.5 109.7 111.9	5.6° 5.8° 6.3°	adequate clearance to 38° into 90 Hz, 30° into 150 Hz adequate clearance to 45° into 90 Hz, 32° into 150 Hz adequate clearance to 40° into 90 Hz, 44° into 150 Hz
ORBIT (NORMAL)	108.5 109.7 111.9	6.1° 6.2° 7.0°	adequate clearance 65° into 90 Hz, 95° into 150 Hz adequate clearance 55° into 90 Hz, 80° into 150 Hz adequate clearance 48° into 90 Hz, 60° into 150 Hz
STRUCTURE	108.5 109.7 111.9	-- 3.0° 3.0°	± 11 μa scallops* ± 15 μa scallops ± 14 μa scallops

* These represent peak instantaneous deviations from "on course".

Table 5-48. Data Summary for Small Aperture Array for FAA Flight Test Data. As seen by this summary, there are no out-of-tolerance characteristics for the small aperture antenna array; there are adequate clearances in Sector II and an acceptable course structure in Sector I.

TEST	FREQUENCY	COURSE WIDTH	COMMENTS
(BROAD)	108.5	7.0°	adequate clearance to ± 58°
	109.7	--	min of 200 μa at 33° into 150 Hz
	111.9	7.2°	min of 200 μa at 33° into 150 Hz
(SHARP)	108.5	2.3°	
	109.7	2.5°	
	111.9	2.9°	
BACK COURSE (NORMAL)	108.5	6.1°	adequate clearance to ± 10°
	109.7	5.4°	adequate clearance to ± 11°
	111.9	6.3°	adequate clearance to ± 11°
ORBIT (NORMAL)	108.5	6.1°	adequate clearance to 57° into 150 Hz, 53° into 90 Hz
	109.7	5.8°	adequate clearance to ± 54°
	111.9	6.3°	adequate clearance to ± 53°
STRUCTURE (NORMAL)	108.5	6.0°	± 6 μa scallops *
	109.7	3.0°	± 10 μa scallops
	111.9	2.9°	± 10 μa scallops

* These represent peak instantaneous deviations from "on course".

Table 5-49. Data Summary for Medium Aperture Array for FAA Flight Test Data. This summary indicates in-tolerance conditions in all but the back course which does not show adequate clearance. The front course structure provides a smooth path with minimal perturbations due to scalloping.

FREQUENCY	ALTITUDE	Signal Strength (μVolts)		
		10°(150 Hz)	CL	10°(90 Hz)
MEDIUM ARRAY				
108.5	1000'	4.7	13	5.9
108.5	4500'	35	1000	24
109.7	1000'	3.1	8.5	2.9
109.7	4500'	26	57	21
111.9	1000'	4.1	10	3.3
111.9	1500'	4.5	17	5.4
111.9	4500'	24	60	14
SMALL ARRAY				
108.5	1000'	4.1	4.7	4.7
108.5	4500'	22	29	26
109.7	1000'	4.1	3.8	3.5
109.7	4500'	32	29	29
111.9	1000'	3.5	3.5	3.5
111.9	1500'	4.1	5.9	5.5
111.9	4500'	24	32	26

Table 5-50. Summary of Usable Distance. The pertinent parameters listed are those at the 1500 foot altitude, ± 10° points for which tolerance levels are defined. Although the majority of these points do not meet the required 5 microvolt level, the usable distance for these arrays has been classified as marginal due to the degree of uncertainty in measuring such small signals.

FREQUENCY	PHASING	CW
SMALL ARRAY		
108.5	Advanced	8.2°
108.5	Retarded	6.7°
109.7	Advanced 34°	11.5°
109.7	Retarded 34°	7.6°
111.9	Advanced 34°	7.0°
111.9	Retarded 34°	7.2°
MEDIUM ARRAY		
108.5	Advanced	7.7°
108.5	Retarded	7.2°
109.7	Advanced 34°	8.5°
109.7	Retarded 34°	7.5°
111.9	Advanced	8.2°
111.9	Retarded	7.6°

Table 5-51. Carrier/SBO Dephasing. These tests were performed as a basic system test. As a result of these tests, a phasing error in the transmitter was detected by the fact that phase advances and retardations of equal magnitude did not produce equal degradations in the course width.

generation circuitry showed that the transmitter's phase shifter had not been optimally aligned during frequency changes. The problem was corrected and flight tests resumed. Although all tests conducted before September 30 were performed with a non-optimally phased transmitter, the results obtained from those tests are valid; the effects of the adjustment error can only be seen in Table 5-51 which is concerned with carrier/SBO phasing. After the transmitter had been realigned, a symmetrical course width degradation was observed with phase advances and retardations of equal magnitude.

3. Results. Experimental results with relevant comments are shown in Tables 5-48 through 5-51 and Figures 5-67 through 5-71.

4. Conclusions. The following conclusions concerning the Hollins slotted-cable localizer antenna constructed by the Watts Prototype Company are based on data taken by both the Avionics Engineering Center, Ohio University, and by an FAA NAFEC Flight Measurement DC-6 aircraft. These tests were performed at the New Tamiami Airport between September 25 and September 30, 1976.

Two versions of the localizer slotted cable array were tested, the small and medium aperture array, on each of three frequencies: 108.5, 109.7 and 111.9 MHz. Although some variations were noticed on the above frequencies, the measurements showed that antenna performance can be expected to be reasonably consistent over the entire localizer band. The following results reflect typical antenna performance for all of the above frequencies (from both NAFEC and OU data).

a. Small Aperture Array.

(1) The minimum course observed was 3 degrees given the carrier/SBO ratio available from the Wilcox solid state transmitter.

(2) At broad alarm there was adequate clearance through sectors I and II.

(3) The RF and DDM patterns were reasonably symmetrical.

(4) Polarization effects were negligible.

(5) Front-to-back ratio at 6.0 nmi, 1500 ft. was 7 dB.

(6) Usable distance along centerline was 20 nmi with a transmitter power of 6.8 watts at the antenna input and an antenna height of 54 inches.

(7) At 18 nmi, 1500 ft., the signal strength along centerline was 1 dB above FAA requirements when the RF was reduced 1 dB to alarm.

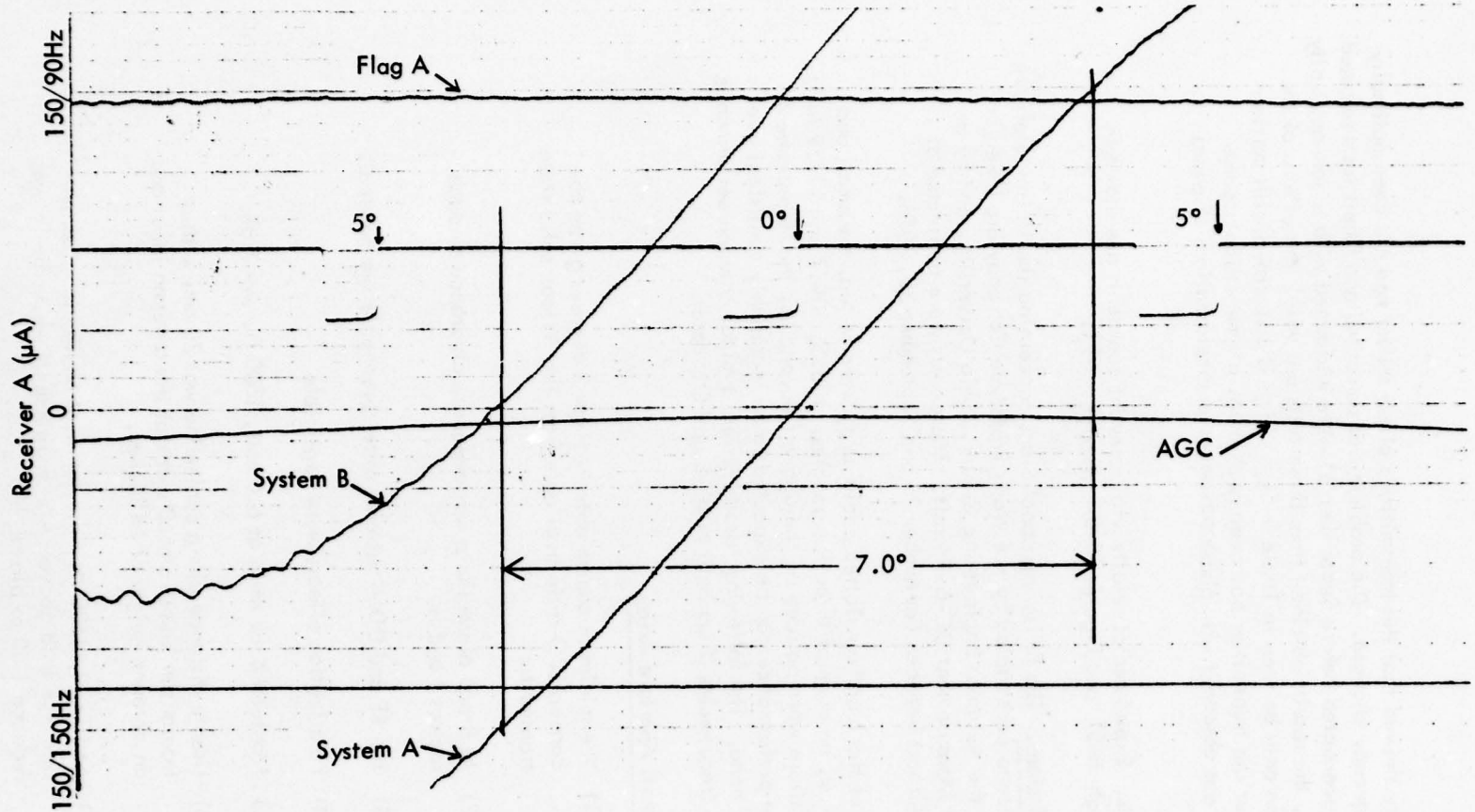

Figure 5-67. Course Width at Broad Alarm, 1500' Altitude at 6 Nautical Miles for the Medium Aperture Antenna Array at 108.5 MHz. This strip-chart recording presents the CDI reading when the flight check aircraft flew perpendicular to the localizer course. This recording shows reasonable linearity in Sector I.

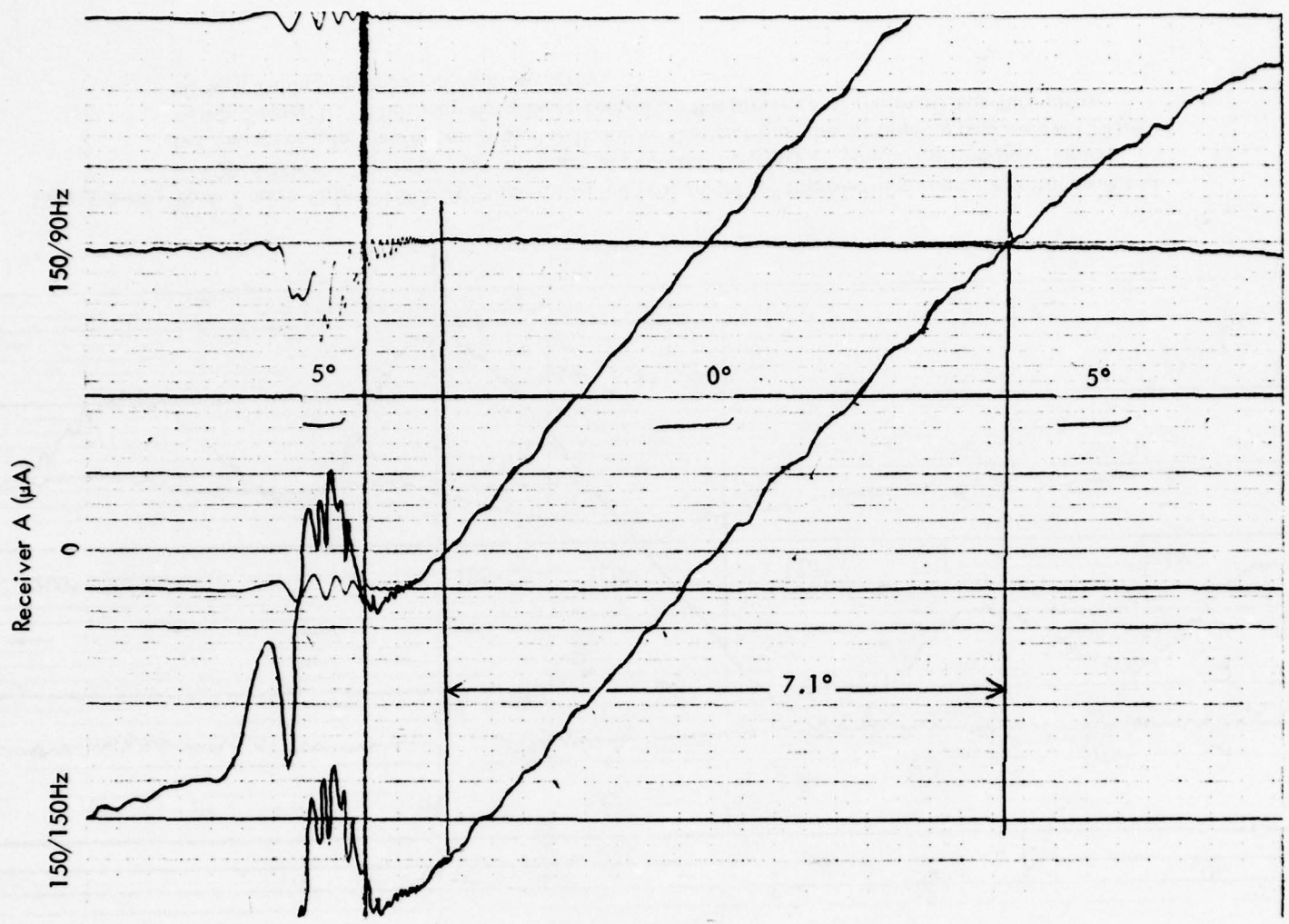

Figure 5-68. Course Width at Broad Alarm, 1500' Altitude at 6 Nautical Miles for the Small Aperture Antenna Array at 111.9 MHz. This strip-chart recording presents the CDI reading when the flight check aircraft flew perpendicular to the localizer course. This recording shows reasonable linearity in Sector I. The variations in the CDI trace around the 5°/150Hz point is due to another aircraft between the localizer array and the flight check aircraft.

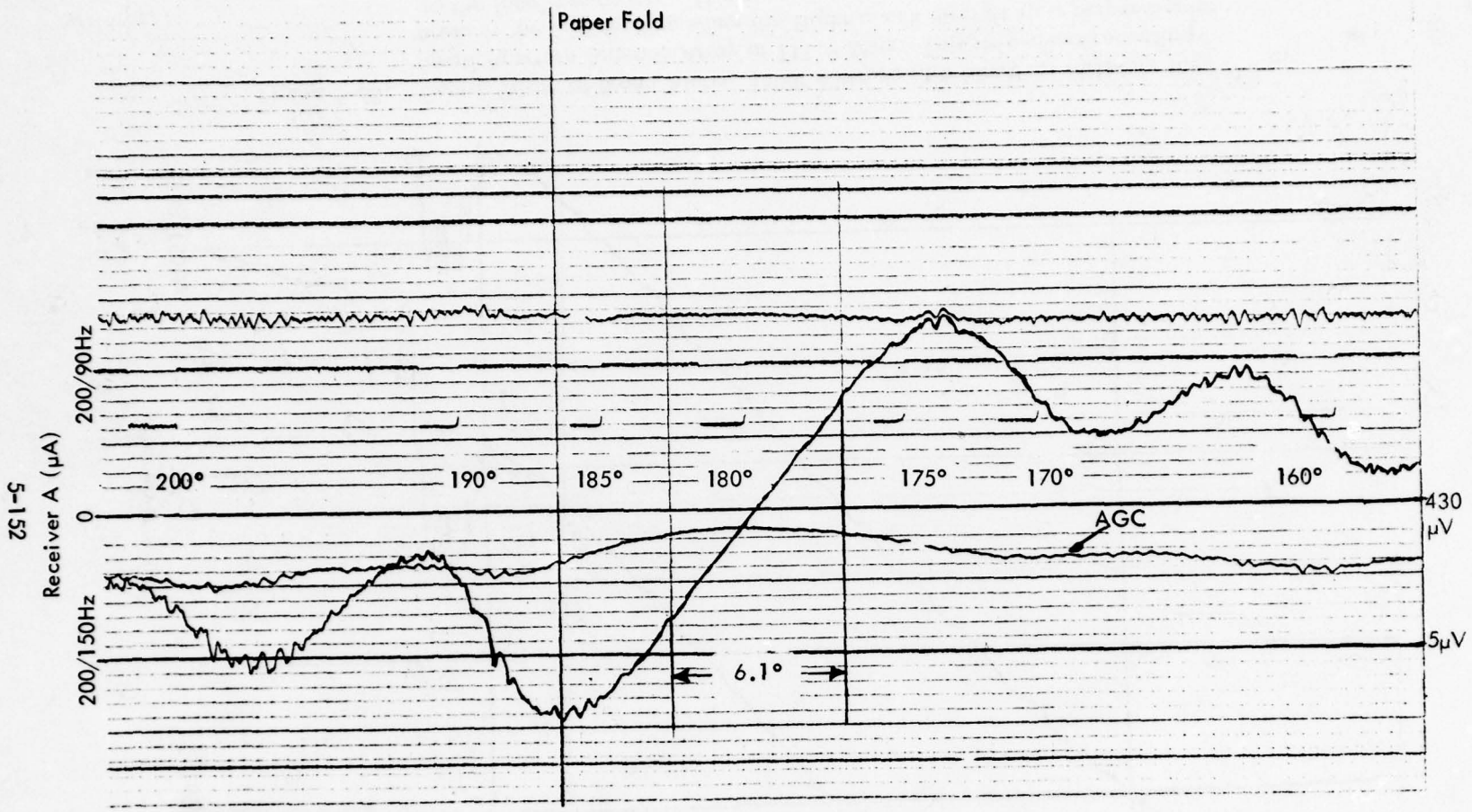

Figure 5-69. Back Course Orbit, 1000' Altitude at 6 Nautical Miles for the Medium Aperture Antenna Array at 108.5 MHz. This recording indicates acceptable linearity in Sector I of the back course, but unacceptable clearances in Sector II due to the fact that the clearances drop below 150 μA within Sector II. This may have been caused by the presence of the small aperture array 50 feet behind the medium aperture array.

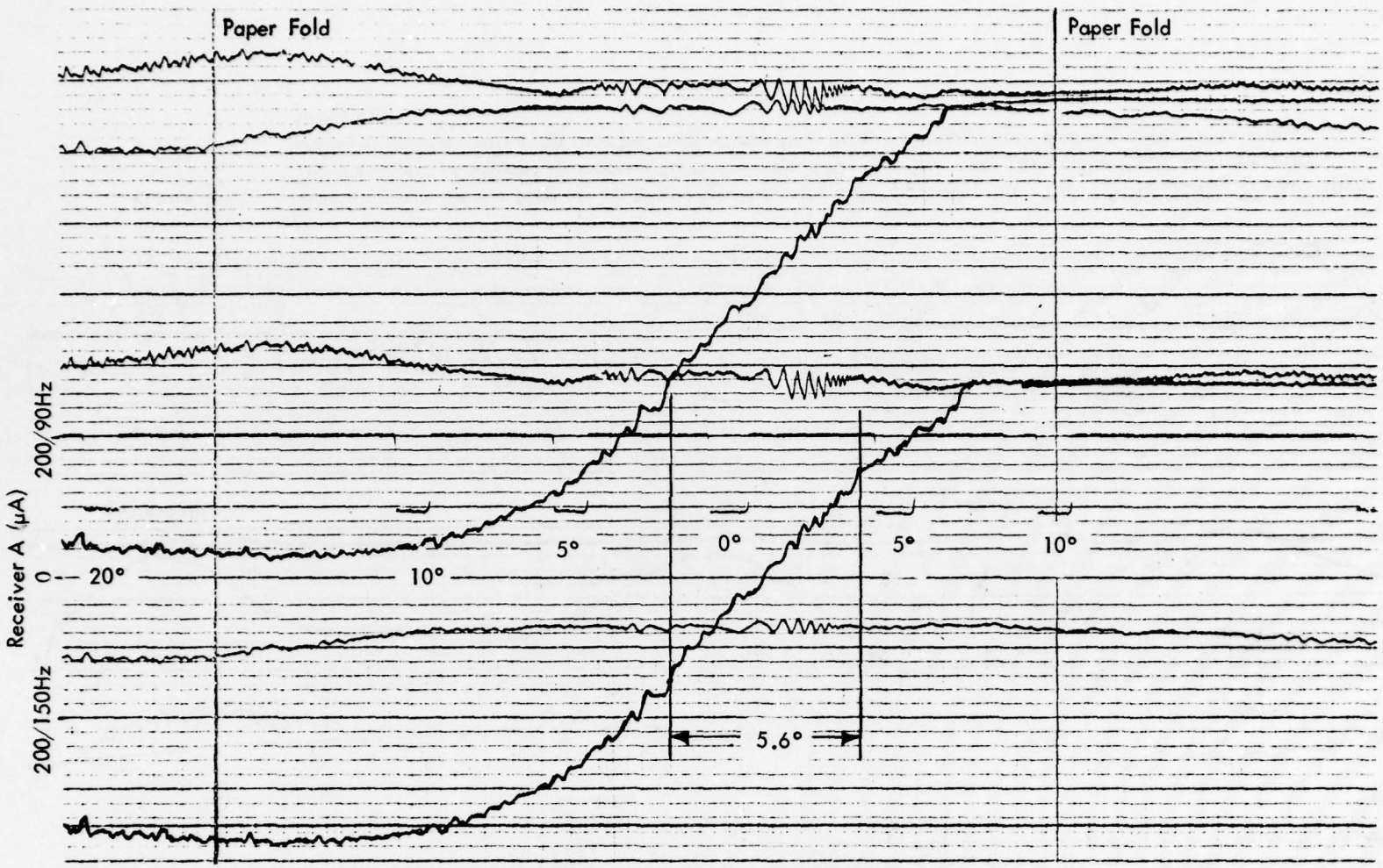

Figure 5-70. Back Course Orbit, 1000' Altitude at 6 Nautical Miles for the Small Aperture Antenna Array at 108.5 MHz. This recording indicates acceptable linearity in Sector I and above-tolerance clearances in Sector II.

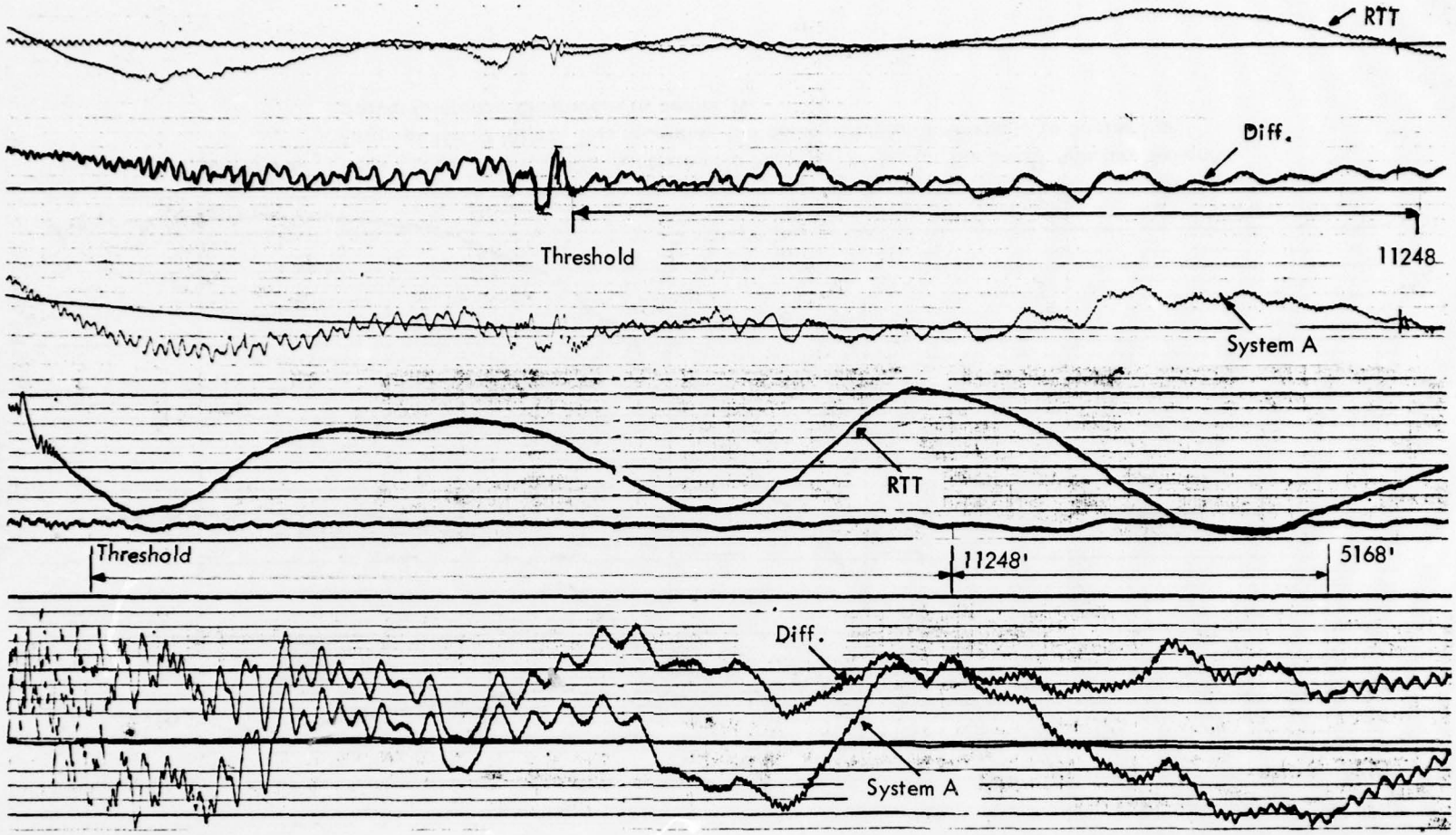

Figure 5-71. Structure Runs for the Medium (Top) and Small Aperture Antenna Arrays on 109.7 MHz (Scale: 37.5μA/inch). The parameter of interest is denoted "Diff." which is the true localizer path. The small aperture array produces greater scalloping than the medium aperture array, although both arrays provide in-tolerance structures.

(8) The array at 1500 ft., 6 nmi measured between 1 and 2 dB below a dipole.

(9) At 18 nmi, the signal strength dropped 3 dB between 1500 and 1000 ft. elevation.

(10) Signal taper at 1500 ft., 18 nmi was 3 dB from centerline to ± 10 degrees.

(11) The back course pattern was found to be flyable.

(12) Scalloping in approach zone 3 was less than ± 15 μa.

b. Medium Aperture Array.

(1) Minimum course was found easily adjustable to 2.4 degrees or less. Between minimum course and broad alarm, RF and DDM patterns were acceptable and reasonably symmetrical. Polarization for medium array was similar to the small array characteristics.

(2) Front-to-back ratio at 6 nmi, 1500 ft. was 8 dB.

(3) Usable distance along centerline was greater than 20 nmi with a transmitting power of 6.8 watts at the antenna input and an antenna height of 54 inches.

(4) At 18 nmi, 1500 ft., the signal strength along centerline was 8 dB above FAA requirements with 6.8 watts at the antenna input.

(5) The array at 1500 ft., 6 nmi measured 8 dB above a dipole.

(6) Signal level taper from 10 to 18 nmi was measured at 11 dB.

(7) Signal level taper from centerline to ± 10 degrees was 10 dB.

(8) The localizer back course was not found to be flyable.

(9) Scalloping in approach zone 3 was less than ± 10 μa.

Note: (4) and (7) above indicate that the medium array does not provide adequate coverate at 18 nmi, ± 10 degrees.

Although both antennas provided only marginal coverage at 18 nmi, the manufacturer felt that an additional 3 dB of signal power could be realized (which would result in adequate power) by physically raising the slotted cable antennas above

the ground. Also, the nonflyable back course pattern of the medium aperture antenna was not resolved but may have been affected by the location of the small array which was located 50 ft. behind the medium aperture antenna.

VI. TERRAIN-SENSITIVE MODELING OF ILS SYSTEMS

A. The Ohio University ILS Modeling Center.

1. Introduction. A Center for ILS Mathematical Modeling has been established at Ohio University. Its modeling capability includes the best of previously-developed models plus a new and improved glide slope model based on the Geometrical Theory of Diffraction and a new technique for modeling the receiver capture effect for two-frequency systems. These models have been validated against flight measurements with good agreement. An efficiently organized combination of computer main frame processing capability, disk storage, and input/output capability, including on-line graphic plotting capability, has been obtained and can be dedicated to mathematical modeling tasks. The modeling center staff has received experience in the use of the models, and already several results of practical interest to the FAA have been obtained.

It is recommended that this center be consulted by the FAA when computer modeling results can be helpful in making crucial decisions regarding problem ILS sites.

2. Background. For over twelve years research into means for predicting the performance of ILS systems in non-ideal environments using computer modeling has been underway. From the first efforts by Ohio University in 1965 to a multi-year effort by the Transportation Systems Center completed in 1976, the FAA has been supporting ILS mathematical modeling development. As a result of this effort several sophisticated and accurate models have been developed, but have remained scattered in various locations around the country. In order to provide for a central location where the various models could be systematically organized and be ready when needed, the FAA provided funds for the Avionics Engineering Center of Ohio University to establish an ILS Modeling Center.

After a survey of previous modeling work it became evident that while the modeling of environmental effects on ILS localizer performance had been relatively well accomplished, validated, and documented (primarily by the Transportation Systems Center work), glide slope terrain effect modeling had not been validated against measurements since the early work at Ohio University. Also, some of the assumptions made in the previous glide slope terrain models were somewhat questionable for certain types of terrain. Thus it was decided that while it was important to have operational localizer models available in the modeling center, the major effort in improving existing models and model validation should be made for the glide slope models.

For each type of model (glide slope and localizer) a survey and discussion of the available models is made including the availability of the various models at the modeling center. New glide slope models have been developed based on the Geometrical Theory of Diffraction and on work performed by the Transportation Systems Center. Finally, detailed descriptions are presented of the computer data input required by the new OUGS glide slope model, and the mathematical model developed by Ohio University to model the receiver capture effect for two frequency systems.

3. Available Glide Slope Models. During the past decade considerable time and effort have been spent in the attempt to model mathematically the effects of uneven terrain on the performance of the ILS glide slope. An important part of the work done by Ohio University in forming the ILS Mathematical Modeling Center was to review and evaluate the past glide slope models, choosing the best ones for inclusion in the modeling center computer system. As a result of this evaluation effort it was determined that for certain types of terrain, most noticeably upsloping terrain, none of the models was capable of giving accurate results. Furthermore, if the existing programs were modified so as to include the shadowing effects of upsloping terrain the computer running time would be exorbitant. For this reason a new glide slope model based on the Geometrical Theory of Diffraction (GTD) was developed by Ohio University. This new model will be discussed fully in the next section. First, however, a discussion of the previously existing glide slope models, some of which have been incorporated into the modeling center computer files, is in order.

The first attempt to predict mathematically the effects of uneven terrain on glide slope performance by Ohio University was made in 1965. [1]* This work was continued and expanded during the following years. [2,3] The basic approach used was that of physical optics. The ground itself was assumed to be a good conductor, and the currents induced at a given point on the surface of the ground by each glide slope antenna were calculated neglecting the effects of terrain in other areas. In other words, the currents on an upsloping section of ground would not be affected by radiation reflected from the ground in front of the upslope. Also, shadowing was not treated very precisely, in that electromagnetic energy diffracted over a ridge would not affect reflections from the bottom of the next valley. These two types of terrain reflection mechanisms are illustrated in Figure 6-1.

Once the approximate ground currents are found, the fields which they radiate must be determined. There are several basic radiation integrals which may be used for this process. The simplest of these is quite straightforward to evaluate but requires that the illuminating antenna and the receiving antenna both be in the electromagnetic far zone of the section of ground over which the currents are being integrated. This requirement forces one to divide the reflecting ground into small areas and then to integrate over each separate area. The size of these integration areas varies from model to model, but is on the order of several feet square. Even though the resulting integrations are very straightforward, dividing a 500 ft. by 4,000 ft. reflecting surface into 500,000 squares and adding the fields reradiated from each square is quite time consuming. Running times on the order of hours can be expected.

* See page 6-126 for references for Section VI.

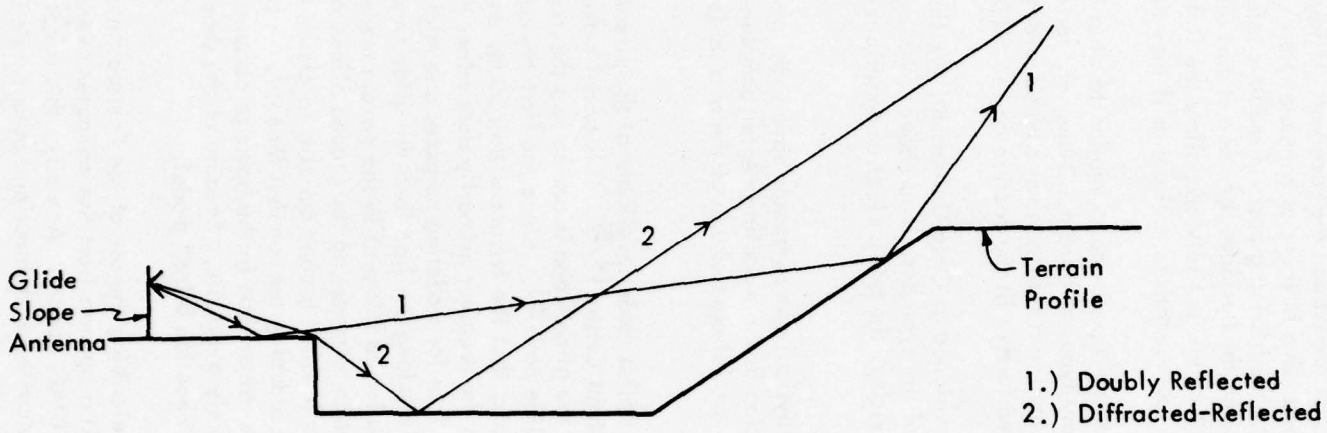

Figure 6-1. Examples of Terrain Reflection Mechanisms Normally Neglected in Physical Optics Terrain Models.

After the fields reradiated by the ground currents have been calculated, there still exists the problem of determining the effects of blockage caused by upslopes or hills between the ground currents being considered and the receiver. Using physical optics to calculate these effects is very expensive in terms of computer time since determining the fields incident on each point of the blocking upslope requires integrating over all of the ground between the antenna and the upslope. Because of this difficulty the physical optics models usually neglect this blockage entirely and allow the fields radiated by the ground currents to pass through any subsequent obstructions as if they did not exist.

While the above may seem to be a poor approximation to what happens physically, good results can be obtained for many types of terrain. However, terrain with severe dropoffs and/or upslopes may yield incorrect results when treated with the above physical optics models. This will be discussed further in the section on the GTD glide slope model.

In addition to the models developed at Ohio University, Westinghouse has also developed a physical optics model of the type described above. While differing in detail from those developed at Ohio University, the basic electromagnetic techniques and assumptions appear to be similar.

Since the above described physical optics models have such long running times, none of them was chosen for inclusion in the modeling center computer. If needed, this type of model can be obtained as a special case of one of the available models to be described later in this section.

The most advanced physical optics model available at the present time is that developed by the Transportation Systems Center [4,5]. This model makes use of the fact that while the first Fresnel zone for the glide slope is one to two thousand feet long it is less than 100 feet wide for a 3° glide path [6]. Since the first Fresnel zone ground reflections are dominant, this indicates that the terrain within 50 ft. on either side of the line from the glide slope mast to the receiver primarily determines the effects of the terrain on the glide path in space. Thus for modeling purposes one might approximate the terrain by using the terrain profile along the line from the glide slope to the aircraft. If one then makes a linear approximation to this profile, the terrain model of Figure 6-2 results. This two-dimensional approach to modeling the ground allows one to perform the X-direction radiation integral on the induced ground currents in closed form using asymptotic methods, thus drastically reducing the running time [7]. A typical site might be modeled in a few hundred seconds rather than in the hours of computer time required by the physical optics models previously available. Because of the shape of the terrain model, this is often referred to as a "Venetian blind" model.

If one refers to the manual describing the use of the Transportation Systems Center (TSC) glide slope model (reference 5) it appears from the computer listings that the model requires a very large amount of FORTRAN coding. Actually, this is not the case, since most of the TSC computer code is concerned with input and output. As the method for inputing the modeling data used by the TSC model was not suitable for the needs of the Ohio University modeling center, only the actual computational part of the TSC model was

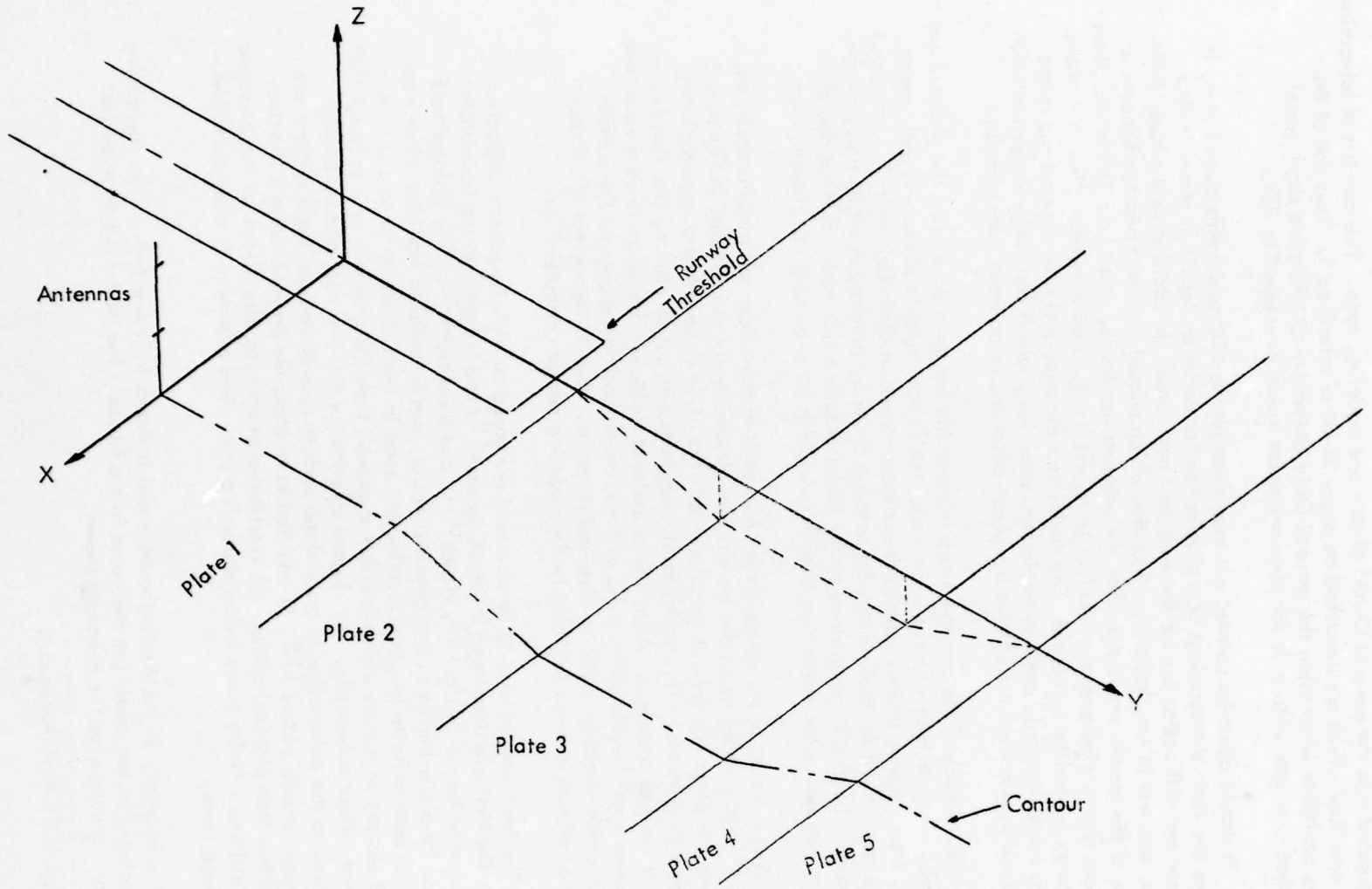

Figure 6-2. Terrain Approximated as Perfectly-Conducting Plates.

incorporated into the general OUGS glide slope modeling code. This consists of subroutines SCAT and SUM which are described on pages 32-38 of reference 5. Thus one of the options available when using the general Ohio University OUGS glide slope model described in a later section is the physical optics model developed by TSC.

It should again be pointed out that although the TSC model runs much faster, it still has the basic shortcomings of a physical optics model as described above in that blockage and diffraction are for the most part neglected. In addition to the basic limitations, an error in the shadowing algorithm which caused incorrect results whenever a portion of the terrain was higher than the antenna was found. Also, the TSC model gives erroneous results whenever the receiver (aircraft) is located anywhere other than above the runway centerline extended. The model uses the $\exp(-j\omega t)$ time dependence rather than the more commonly used (by engineers) $\exp(+j\omega t)$, which can easily cause confusion when modeling antenna currents with a phase advanced or retarded from nominal.

While much of the previous work in modeling has been done using the physical optics approach, other techniques have been used. While not capable of dealing with uneven terrain, image theory models such as the one developed at Ohio University* are useful in calculating the effects of perturbing antenna currents, heights, A ratio, etc., on the glide path. The OUGS glide slope model includes such a flat earth model as one of its modeling options. One advantage of such a model is its extremely fast running time.

An extension of the image theory approach to more than one plate is described by Raju [8]. His model treats the terrain two-dimensionally as indicated in Figure 6-2 Each separate plate can reflect specularly as if the glide slope antenna were radiating rays rather than waves. This model totally neglects diffraction effects, and thus is obviously of limited accuracy. Also, the calculated fields will be discontinuous each time a reflection point "walks off" a plate as the receiver position changes. For certain types of terrain it can be made to give useful results. Due to its neglect of important diffraction effects, it is not included in the modeling center computer files.

The next three models to be discussed are based on high-frequency diffraction theory. The first was developed by Westinghouse [9] and is based on the half-plane scattering solutions of Senior [10], Woods [11], and Bromwich [12]. The isolated half plane can be easily handled using physical optics, and is useful in modeling glide slope sites which have a finite length flat reflecting zone in front of the antenna and then drops off sharply to terrain which is either shadowed from the antennas or is so rough that it does not reflect coherently. An elegant solution for this was obtained by Redlich and applied to the calculation of glide slope performance of various image systems over finite length ground planes [13]. In addition to treating the problem using diffraction theory rather than physical optics, the Westinghouse solution also allows for the presence of an additional infinite plane below the half plane. This extension is made quite easily using image theory.

The geometry of the Westinghouse model is shown in Figure 6-3. The ray mechanisms included in the model are indicated in the figure. The model is said to be fast running and accurate for the geometry shown.

*See Section XI.A of this report.

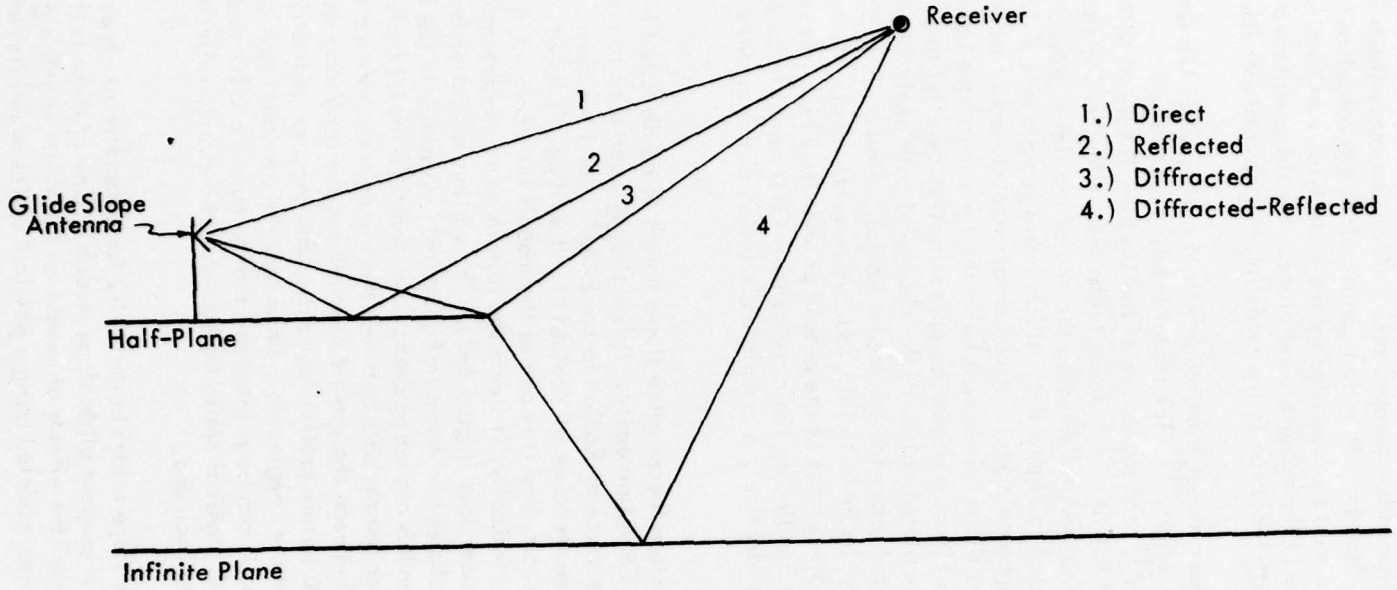

Figure 6-3. Geometry of Glide Slope Terrain Problem as Treated by Westinghouse Using Half-Plane Diffraction. The Four Types of Rays Included Are Indicated.

While this model is capable of producing worthwhile results for the particular geometry it is capable of handling, it has two basic shortcomings. One is that it can model only one type of terrain, the drop-off. It cannot be used to model upslopes, undulating terrain, downslope followed by upslope, etc., which obviously limits its usefulness severely. The other is that the diffraction contributions are calculated for a half plane, whereas actual terrain must be supported by the underlying earth which will affect the diffraction from the end of the upper ground plane. For these reasons a model of this type was not felt to be worth inclusion in the modeling center computer files.

The second diffraction theory model is an outgrowth of earlier Ohio University work prior to the beginning of the effort.[14] The model is based on Keller's Geometrical Theory of Diffraction[15] and makes use of the Uniform Theory of Diffraction as developed by Kouyoumjian and Pathak.[16] These techniques allow for the rigorous treatment of the diffraction from the wedge formed by the end of the finite ground plane and the supporting earth as indicated in Figure 6-4, which makes it more able to model the actual terrain than the Westinghouse model. It can simultaneously model transverse and longitudinal edges. However, the receiver must be in the far zone of the upper ground plane, i.e., the rays indicated in Figure 6-4 must be approximately parallel to each other. This model was used to provide calculated values of the change of path angle with tide level for null reference and sideband reference systems at Kodiak, Alaska which agreed closely with measurements made by the FAA.* This model is currently available in the Modeling Center computer files. Since most of the ground geometries which this model is capable of handling can also be handled by the more general GTD model to be described next, and since its basic theory is identical, a complete discussion of this model will not be given.

The last of the three diffraction theory glide slope models to be discussed is the GTD model recently developed at Ohio University. It has already been used to supply predictions of capture effect performance at Kodiak to the FAA[17], and has been validated with FAA flight measurements taken at Kodiak.** It will be discussed in detail in the next section of this report, and it is one of the models incorporated in the OUGS general glide slope model. Basically, it treats the terrain as a two-dimensional profile in the same way the TSC model does (Figure 6-2). The various reflection and diffraction mechanisms which it includes are shown in Figure 6-5. Contrary to the assumptions made in the physical optics models regarding shadowing, the GTD model includes shadowing and diffraction effects for terrain both between the transmitting antenna and the particular ground segment and between the ground segment and the receiving antenna. The model can accomodate up to 20 terrain profile segments. For complex geometries some ray contributions must be, and are, neglected. However, the dominant rays are all included. For comparison purposes, it can be pointed out that to obtain a GTD model approximately equivalent to the TSC physical optics model only the direct, reflected, and diffracted rays would need to be included.

Discussion of the GTD glide slope model in detail is, for completeness, preceded by discussion of several other special purpose glide slope models. One of these is the model developed at Ohio University to model the effects of terrain on the Watts end-fire glide slope array.[18] The terrain itself was modeled using a physical optics model similar

*See Section VI.B of this report.

**See Section VI.C of this report.

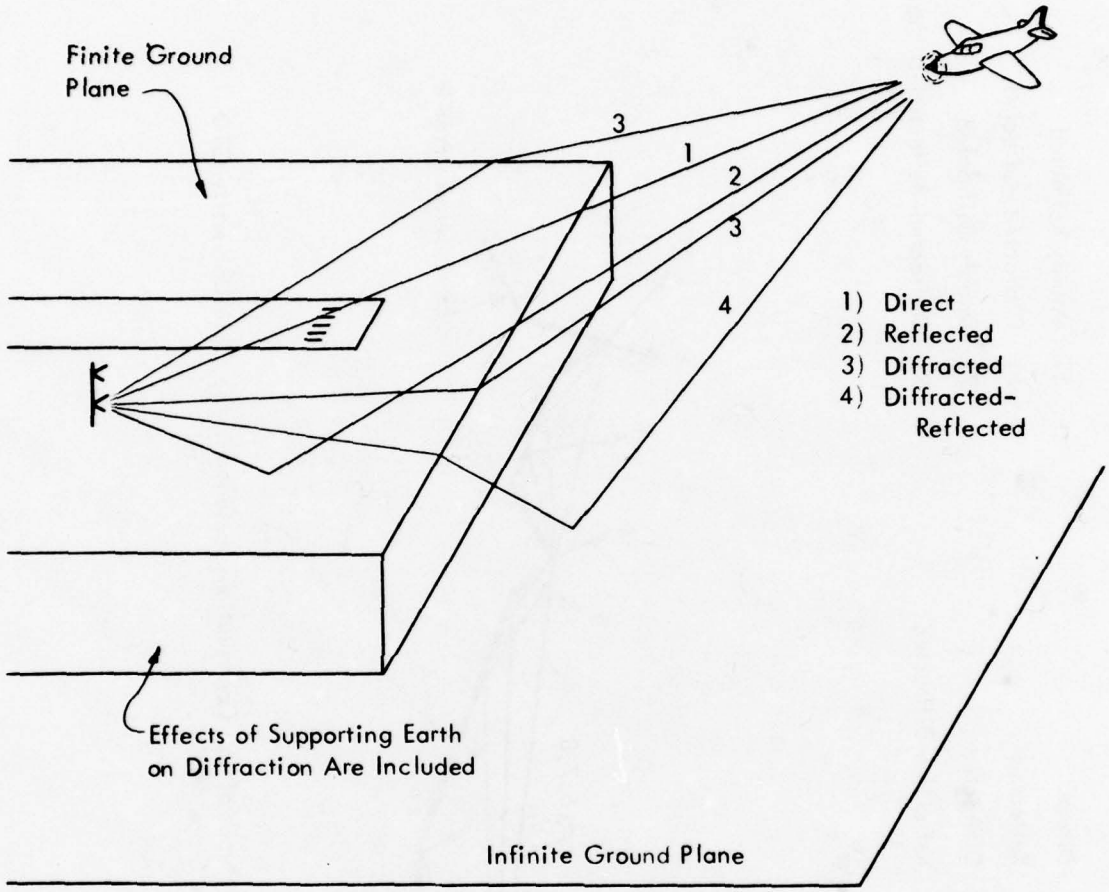

Figure 6-4. Geometry of Glide Slope Terrain Problem as Treated by OU Far Zone GTD Model. Aircraft is constrained to be in far zone of finite ground plane.

1) Direct
2) Reflected
3) Diffracted
4) Reflected-Diffracted
5) Doubly Reflected
6) Diffracted-Reflected
7) Doubly Diffracted
8) Diffracted-Reflected-Diffracted

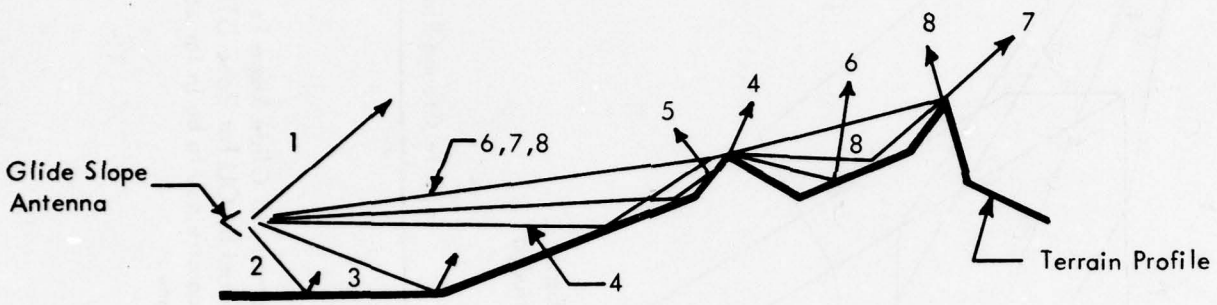

Figure 6-5. The 8 Types of Ray Contributions Included in the Ohio University GTD Glide Slope Model.

to that described in reference [3]. This model is available for use although not implemented on the Modeling Center computer. Normally, it is quite straightforward to modify an existing glide slope model to accomodate a different type of system if the antenna parameters are known. The difficult part of the modeling is involved with the terrain effects, and this part of the model will normally be unchanged regardless of the type of system to be modeled.

Another special-purpose glide slope model is one which extends the two dimensional terrain profile type of model to include the effects of reflections from hills or buildings. Ramakrishna and Sachidananda developed a model which treated the majority of the reflecting terrain as one flat plate, but used physical optics to calculate the reflections from a hill near the glide slope site [19]. The Transportation Systems Center developed a subroutine which used physical optics to add reflections from hills or buildings modeled by flat plates to the reflections obtained from the two-dimensional terrain model described above [5]. The advantage of this technique is that compute-bound 3-D physical optics calculations are used only for those parts of the terrain where necessary. The technique has not been validated against measured data as yet, however. The TSC subroutine described has been modified and some errors in it corrected and is currently available on the Modeling Center computer. It has not yet been validated or incorporated into the OUGS general glide slope model.

The last type of special-purpose glide slope model to be discussed is not concerned with modeling terrain or hangar effects but rather with the effects of reflections from aircraft parked near the glide slope antennas. Since these obstacles are large and are in the near zone of the glide slope antennas, somewhat different methods are required when calculating the fields radiated by the currents induced in the aircraft. Additionally, an aircraft is a complicated shape and reflections from it can be calculated only approximately. A physical optics model for aircraft reflection effects on the glide slope was developed at Ohio University by Rondini [8]. It approximated the reflections and/or blockage by the aircraft by using physical optics to calculate the fields reflected from a conducting plate having approximately the same outline as the aircraft. This program is available at the Modeling Center, but because of its specialized nature has not been incorporated into the Modeling Center's computer files.

4. The Ohio University GTD Glide Slope Model. In the previous section a brief description of the newly-developed GTD glide slope model was given as a part of the general discussion of available glide slope models. All of the other models discussed in that section have either been documented previously and reference made to that documentation or, as in the case of the Westinghouse physical optics model, documentation is not available to Ohio University. In this section documentation for the new GTD model is provided.

The GTD approach to finding the electromagnetic fields reflected from rough terrain can be broken into two parts: a geometrical process of finding which rays exist and where their reflection and/or diffraction point(s) lie, and a mathematical process

of evaluating the magnitude and phase of the corresponding electric field at the receiver location. The rays included in the present GTD model were shown in Figure 6-5. In this section we will provide a theoretical background for the method, discuss how the rays are determined geometrically, and compare the GTD model with the TSC physical optics model. Instructions for using the model, which is a part of the OUGS hybrid glide slope model, are contained in the Section VI.A.7.

a. Theoretical Background for GTD Model. In 1896 Sommerfeld published his classical work on the diffraction from a perfectly-conducting half-plane.[20] This work has been extended by Keller into a Geometrical Theory of Diffraction [15] which can be applied to wedge geometries other than the half plane (which it treats as a 0° wedge) as shown in Figure 6-6. The fields at the field point can be found by finding geometrically the direct, reflected and diffracted rays and combining the corresponding complex field contributions at the field point. The technique is applicable only as a high frequency approximation, so all problem dimensions must be large in comparison to the wavelength.

Using the GTD one can express the diffracted field as

$$\bar{E}^d(s) \simeq \bar{\bar{D}}(Q_E) \cdot \bar{E}^i(Q_E) A(s)\, e^{-jks} \tag{6.1}$$

where

$\bar{\bar{D}}(Q_E)$ is the dyadic edge diffraction coefficient.

$\bar{E}^i(Q_E)$ is the field incident on the edge at the diffraction point Q_E.

$A(s)$ is the geometrical optics spreading factor equal to $\sqrt{\frac{s'}{s(s+s')}}$ for sperical wave incidence.

s' is the distance from the source to the edge.

s is the distance from the diffraction point to the field point.

In the case of a perfectly conducting wedge (used for ILS modeling),

$$\bar{\bar{D}}(Q_E) = -\hat{\beta}'_o \hat{\beta} D_s - \hat{\phi}'\hat{\phi} D_h \tag{6.2}$$

where

$$\hat{\beta}'_o = \hat{s}' \times \hat{\phi}'$$

$$\hat{\beta} = \hat{s} \times \hat{\phi}$$

and where $\hat{s}$, $\hat{s}'$, $\hat{\phi}$, and $\hat{\phi}'$ are defined in Figure 6-7. It has been shown that [15]

$$D_{s,h}(\phi,\phi',\beta_o) = \frac{e^{[-j\,\pi/4]} \sin \pi/n}{n\sqrt{2\pi k}\sin\beta_o}\left[\frac{1}{\cos \pi/n - \cos\left(\frac{\phi-\phi'}{n}\right)} \mp \frac{1}{\cos \pi/n - \cos\left(\frac{\phi+\phi'}{n}\right)}\right] \tag{6.3}$$

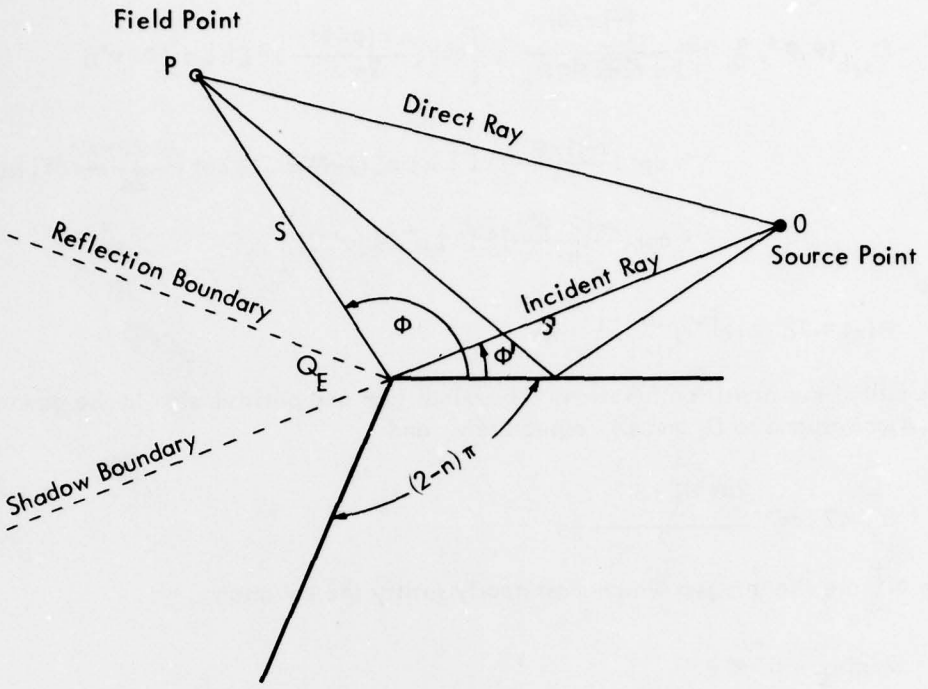

Figure 6-6. Wedge Diffraction Geometry and Coordinates.

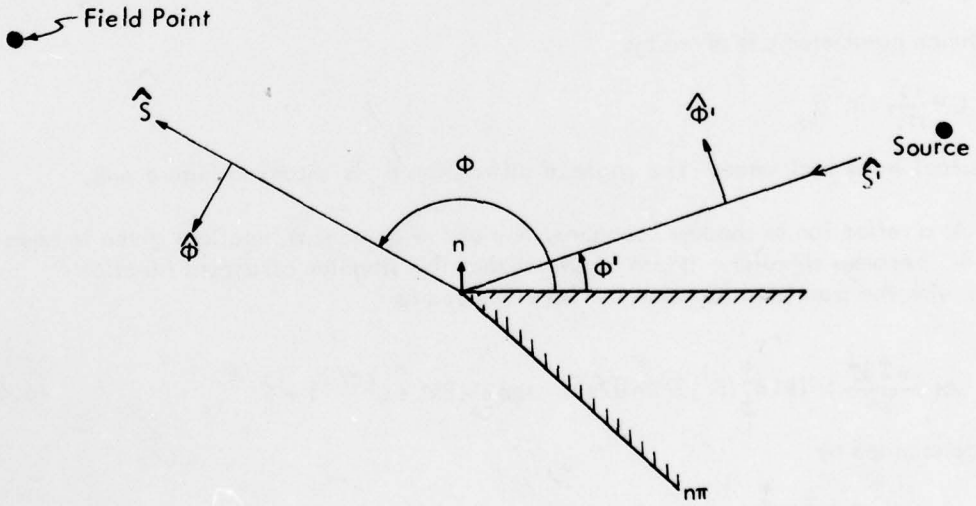

Figure 6-7. Illustration of Diffraction Unit Vectors.

for the case where the observation point is not close to a reflection or shadow boundary. If this is not the case, then equation 6.3 can be written more generally as

$$D_{s,h}(\phi,\phi',\beta_o) = \frac{-e^{[-i\pi/4]}}{2n\sqrt{2\pi k}\sin\beta_o} \times \left[\cot\left(\frac{\pi+(\phi-\phi')}{2n}\right) F[kLa^+(\phi-\phi')]\right.$$

$$+ \cot\left(\frac{\pi-(\phi-\phi')}{2n}\right) F[kLa^-(\phi-\phi')] \mp \{\cot\left(\frac{\pi+(\phi+\phi')}{2n}\right) F[kLa^+(\phi+\phi')]$$

$$\left. + \cot\left(\frac{\pi-(\phi+\phi')}{2n}\right) F[kLa^-(\phi+\phi')]\}\right] \cdots \qquad (6.4)$$

where

$$F(x) = 2i\sqrt{|x|}\, e^{ix} \int_{|x|}^{\infty} e^{-i\tau^2}\, d\tau \qquad (6.5)$$

and is called the transition function. The minus sign and positive sign in the equations 6.3 and 6.4 correspond to D_s and D_h respectively, and

$$a^{\pm}_{\mp} = 2\cos^2\left(\frac{2n\pi N^{\pm}_{\mp} - \beta^{\pm}}{2}\right)$$

where $N^{\pm}_{\mp}$ are the integers which most nearly satisfy the equation

$$2\pi n N^{+}_{-} - \beta^{+}_{-} = \pi$$

$$2\pi n N^{-}_{+} - \beta^{+}_{-} = -\pi$$

with

$$\beta^{\pm}_{\mp} = \phi \pm \phi'$$

The distance parameter L is given by

$$L = \frac{ss'}{s+s'}\sin^2\beta_o$$

for spherical wave incidence. The angle of diffraction β_o is shown in Figure 6-8.

At a reflection or shadow boundary, one of the cotangent functions given in equation 6.4 becomes singular. It can be shown that this singular cotangent function together with the transition function can be expressed as

$$\cot\left(\frac{\pi \pm \beta^{\pm}_{\mp}}{2n}\right) F[kLa^{\pm}_{\mp}(\beta^{\pm})] \simeq n\left[\sqrt{2\pi kL}\ \operatorname{sgn}\epsilon - 2kL\,\epsilon\, e^{i\pi/4}\right] e^{i\pi/4} \qquad (6.6)$$

with ϵ determined by

$$\epsilon = \pm\beta^{\pm}_{\mp} \mp 2\pi n N^{\pm}_{\mp} + \pi \qquad (6.7)$$

and $\epsilon \ll 1$.

This expression is bounded and continuous at shadow and reflection boundaries.

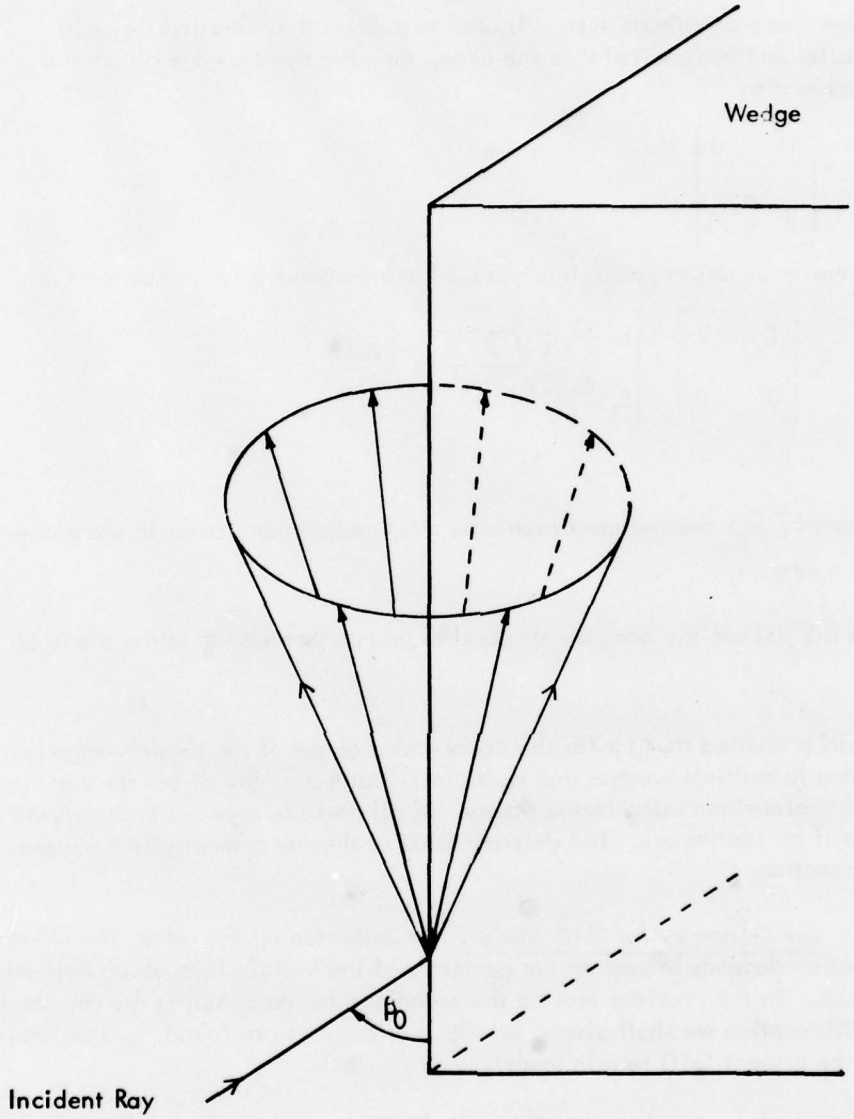

Figure 6-8. Diffraction Angle β_0 and Cone of Diffracted Rays.

These expressions may appear formidable, but they have been programmed in FORTRAN and can be evaluated in much less time than is required for performing a physical optics type of integration over the ground surface.

If an edge fixed coordinate system is used to express the radiation fields in components parallel and perpendicular to the edge, then the dyadic edge diffraction coefficient is reduced to

$$\bar{\bar{D}}(Q_E) = \begin{bmatrix} -D_s & 0 \\ 0 & -D_h \end{bmatrix} \tag{6.8}$$

Equation 6.1 can easily be decomposed into parallel and perpendicular components as

$$\begin{bmatrix} E_d^{''}(s) \\ E_d^{\perp}(s) \end{bmatrix} = \begin{bmatrix} -D_s & 0 \\ 0 & -D_h \end{bmatrix} \begin{bmatrix} E_i^{''}(Q_E) \\ E_i^{\perp}(Q_E) \end{bmatrix} \sqrt{\frac{s'}{s(s+s')}}\, e^{-jks} \tag{6.9}$$

where

$E_i^{''}(Q_E)$ and $E_i^{\perp}(Q_E)$ are the components parallel and perpendicular to the plane of incidence, respectively.

$E_d^{''}(s)$ and $E_d^{\perp}(s)$ are the components parallel and perpendicular to the plane of diffraction.

The results presented thus far for the canonical problem of the single wedge can be easily extended to multiple wedges and multiple diffraction. The direct ray contributions are easily determined using image theory. If all possible rays are included, the resulting field will be continuous. The determination of the ray geometry is discussed in the following section.

b. Ray Geometry for GTD Model. As indicated by the name, the Geometrical Theory of Diffraction depends in part on the geometry of the various rays which determine the reflected fields. In the previous section the technique for determining the ray amplitude was shown. In this section we shall discuss briefly how the rays are found, and which rays are included in the present GTD terrain model.

The numbering scheme used in describing the terrain model is shown in Figure 6-9. Note that the diffraction from the first and last terrain edges (2 and 2(M+1) for M segments) is not included, so that one does not need to compensate for truncating the terrain profile when determining the scattered fields. Referring back to Figure 6-5, one can see some of the possible rays which can exist in general--reflected, diffracted, reflected-diffracted, doubly diffracted, etc. In fact, for even a simple profile such as that formed by the first four segments in Figure 6-9, there can exist an infinite number of possible rays. Consider a ray which propagates from the upper antenna to edge 8, diffracts to edge 4,

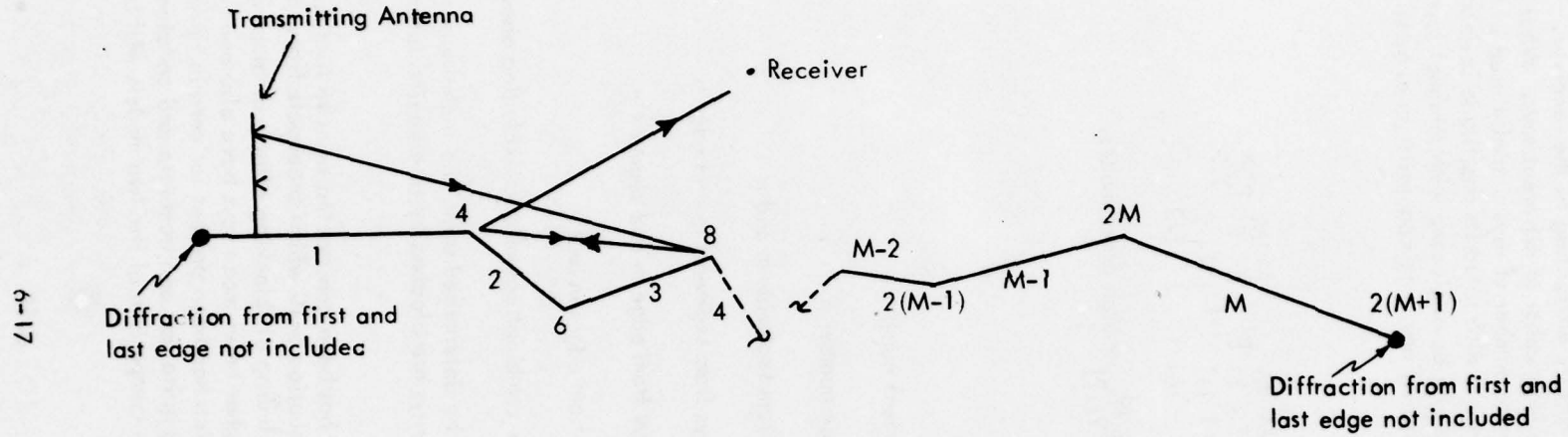

Figure 6-9. Numbering of Terrain Profile Plates and Curves.

diffracts back to edge $\hat{o}$, etc., until finally diffracting to the receiver. This one ray path can actually give rise to an infinite number of different rays. What allows the method to give meaningful results with the finite number of rays actually used in the model (Figure 6-5) is that each time the ray is diffracted its amplitude is decreased, so that after one or two diffractions the ray can usually be neglected with minimal loss in accuracy. If one considers all rays up to two interactions, one can write an expression for the total radiation field $\bar{E}^t$ as follows:

$$\bar{E}^t = \bar{E}^{di} + \sum_{i=1}^{M} \bar{E}_i^r + \sum_{i=2}^{M} \bar{E}_{2i}^d + \sum_{i=1}^{M} \sum_{\substack{j=1 \\ j\neq i}}^{M} \bar{E}_{i,j}^{rr} + \sum_{i=1}^{M} \sum_{\substack{j=2 \\ j\neq 2i}}^{M} \bar{E}_{i,2j}^{rd}$$

$$+ \sum_{\substack{i=2 \\ i\neq 2j}}^{M} \sum_{j=1}^{M} \bar{E}_{2i,j}^{dr} + \sum_{i=2}^{M} \sum_{\substack{j=2 \\ j\neq i}}^{M} \bar{E}_{2i,2j}^{dd} + \text{high order modes.} \qquad (6\text{-}10)$$

where

$\bar{E}^{di}$ = Direct ray

$\bar{E}_n^r$ = Reflected ray from segment number n

$\bar{E}_n^d$ = Diffracted ray from edge number n

$\bar{E}_{mn}^{rr}$ = Doubly reflected rays from segments m and n

$\bar{E}_{mn}^{rd}$ = Reflected diffracted rays from segments m and edge n

$\bar{E}_{mn}^{dr}$ = Diffracted reflected rays from edge m and segment n

$\bar{E}_{mn}^{dd}$ = Doubly diffracted rays from edges m and n

High order modes = all possible combinations of rays excluding above

The amplitude of each ray can be determined using the techniques presented in the previous section. If any of the rays are blocked by intervening terrain, they must be set equal to zero.

The present GTD terrain model has been constructed so as to find and evaluate all of the rays described in equation 6-10 which propagate from the glide slope antenna toward the receiver, including all blocking effects of intervening terrain. In addition, several of the higher order mode rays have also been added to eliminate pattern discontinuities which had been present for certain terrain profiles considered. The GTD model is quite fast and accurate and compares favorably with the TSC physical optics model. A comparison of the two models will be made in the next section.

c. Physical Optics and GTD Comparison. Contained in the following set of figures are comparisons of results obtained using the physical optics (TSC Subroutine) and GTD terrain reflection models for five different terrain profiles. The first two terrain profiles are for actual airfields where the models have been validated; Kodiak, Alaska and Carswell AFB, Texas.[21] The remaining three were chosen to illustrate differences between the two models. For each of the five comparisons the terrain profile is given, followed by calculated CDI for a 1000 ft level run above the runway centerline extended and calculated radiation patterns for the upper and lower antennas as they would be measured by the 1000 ft level run receiver. In all five cases a null reference system is modeled.

The results of the first two comparison cases are shown in Figures 6-10 through 6-17 For both of these terrain profiles the two different methods agree fairly well. The calculated CDI curves within the $\pm$75 microampere range agree well, and the antenna patterns agree closely in general shape. Both models agreed well with measured flight data [21]

The next three sets of comparisons are for terrain profiles which contain a downslope followed by varying amounts of upslope. The first profile, shown in Figure 6-18, has no upslope at all, but rather a flat horizontal section of ground following the downslope. Both models agree quite well for this terrain profile, as shown in Figures 6-19 to 6-21.

In Figure 6-22, the downslope is followed by a moderately severe 4% upslope which has its peak at an angle of +0.95 degrees from the base of the antenna mast. Note the serious discrepancies between the results of the two models presented in Figures 6-23 to 6-25 This discrepancy is due to the approximation made by the TSC model that signals reflected from the 1000 foot long ground plane can pass through the following upsloping terrain, and to the fact that the TSC physical optics model does not correctly handle the shadowing when the terrain is higher than the antenna. The GTD model includes all of the important rays for this geometry and includes all blockage effects and thus is the more accurate of the two models. The physical optics model is seen in Figures 6-24 and 6-25 to be capable of producing antenna patterns for this terrain which are generally correct in shape, but do not have the proper relative amplitudes and null positions.

A very severe upslope which is not likely to be encountered in practice but is included to illustrate the shortcomings of the physical optics model when dealing with severe upslopes is shown in profile in Figure 6-26. The terrain has a 7% grade and the highest point makes an angle of 1.72 degrees with the horizontal at the mast location. Comparing the CDI curves of Figures 6-19 and 6-27 it is evident that the TSC physical optics model predicts that this severe upslope will have a negligible effect on the path angle, width, and symmetry, while the GTD model shows the expected increase in the path angle. The calculated antenna patterns of Figures 6-28 and 6-29 show that for this terrain the physical optics model produces a poor approximation to the more accurate patterns as calculated by the GTD model.

Comparisons of the running time for various numbers of terrain profile segments are tabulated in Table 6-1. For small numbers of plates the GTD model is faster than the TSC physical optics model, but as the number of plates increases the GTD model

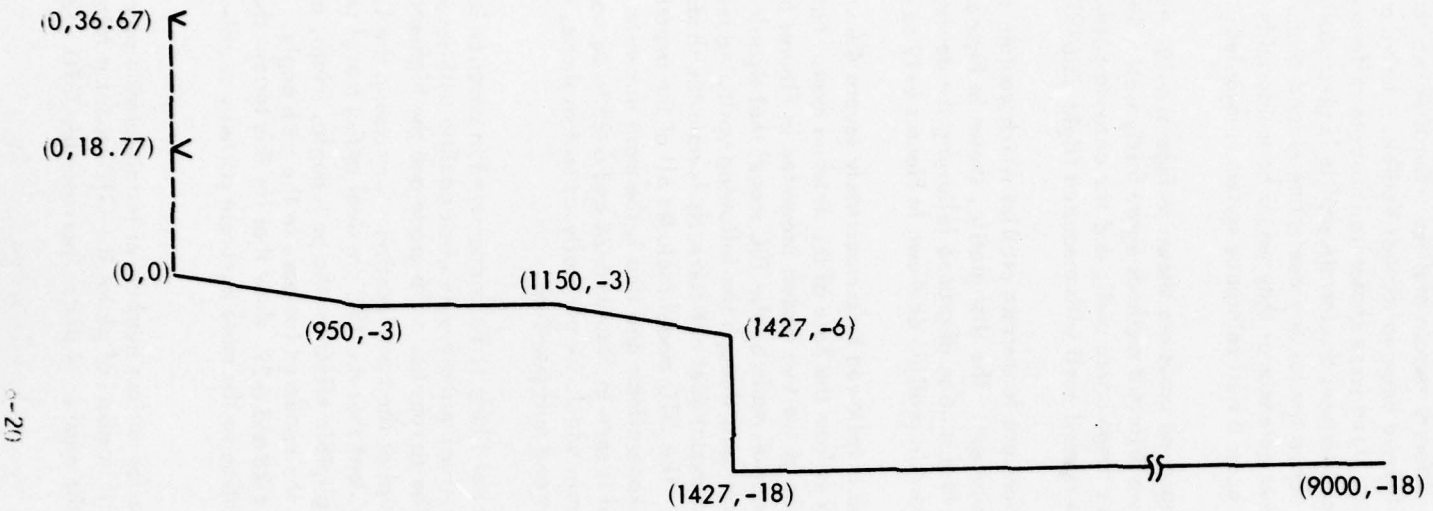

Figure 6-10. *Profile of Terrain* in the Reflecting Zone of the Kodiak, Alaska Glide Slope.

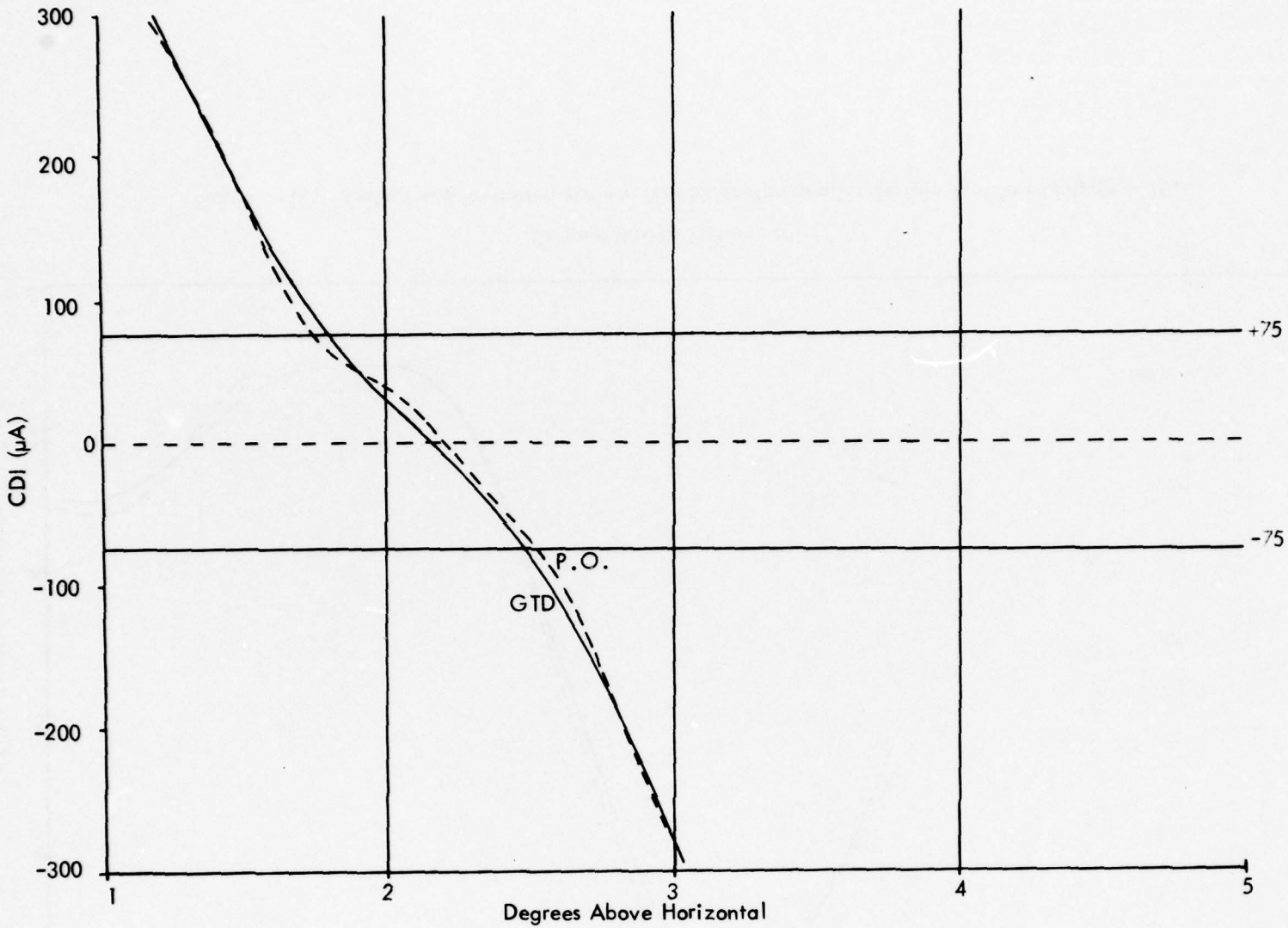

Figure 6-11. Calculated CDI for 1000 Foot Level Run for Terrain Profile of Figure 6-10.

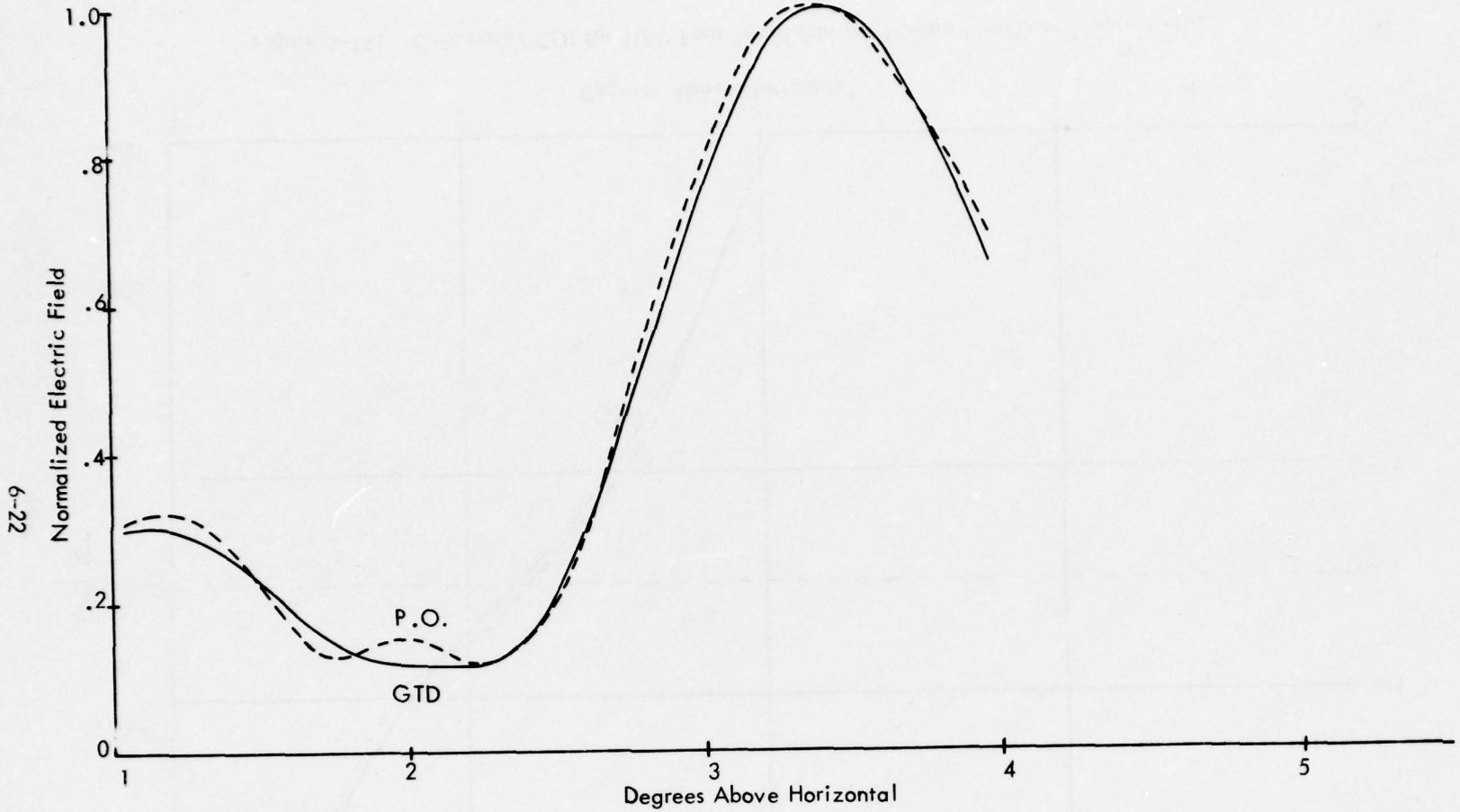

Figure 6-12. Calculated Radiation Pattern for Upper Antenna for Terrain Profile of Figure 6-10.

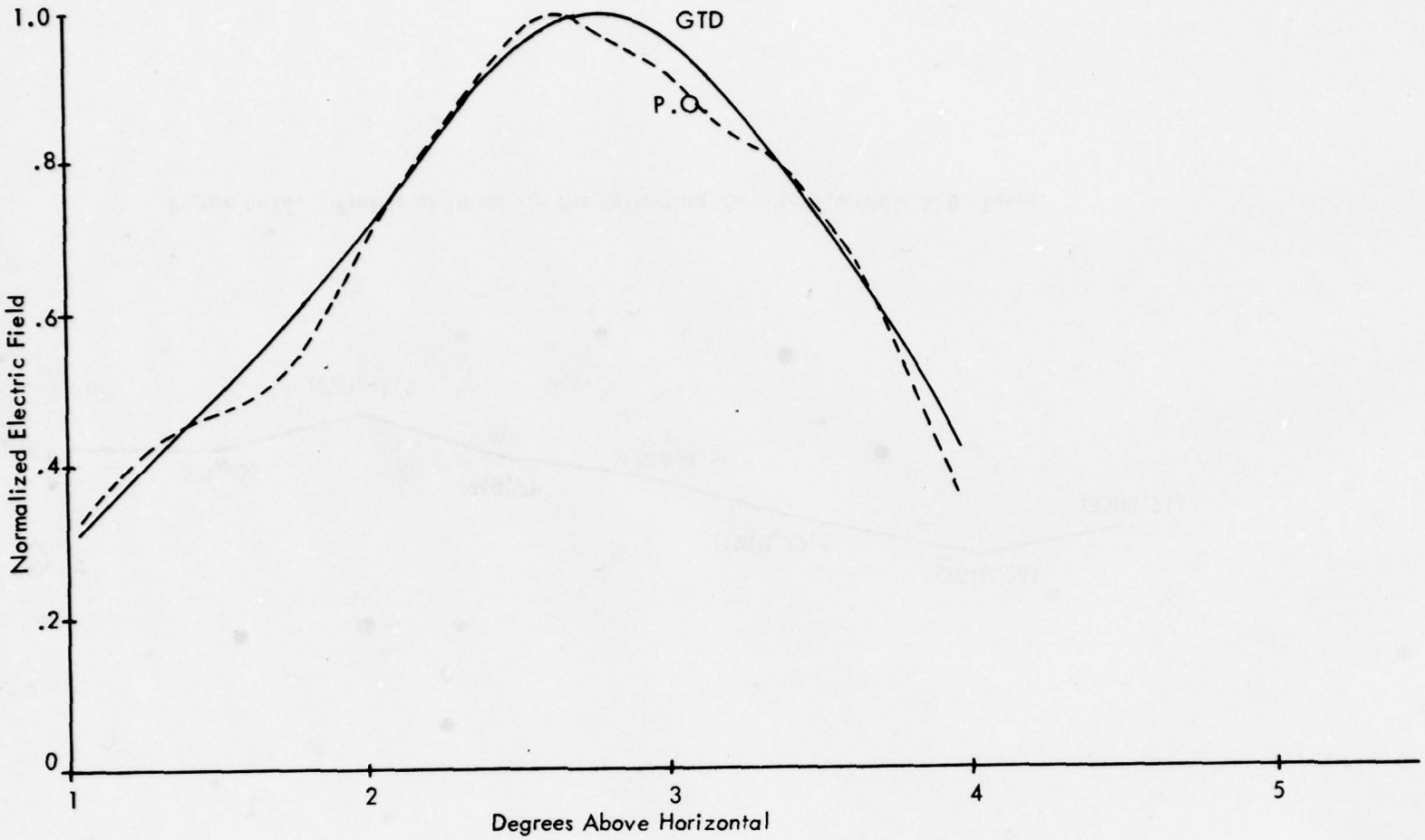

Figure 6-13. Calculated Radiation Pattern for the Lower Antenna for the Terrain Profile of Figure 6-10.

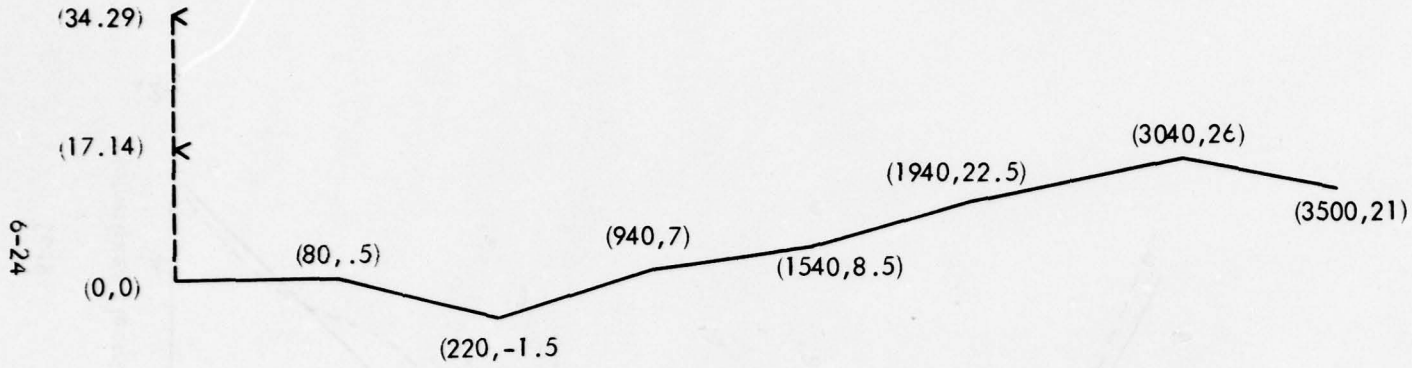

Figure 6-14. Profile of Terrain in the Reflecting Zone for Carswell AFB, Texas.

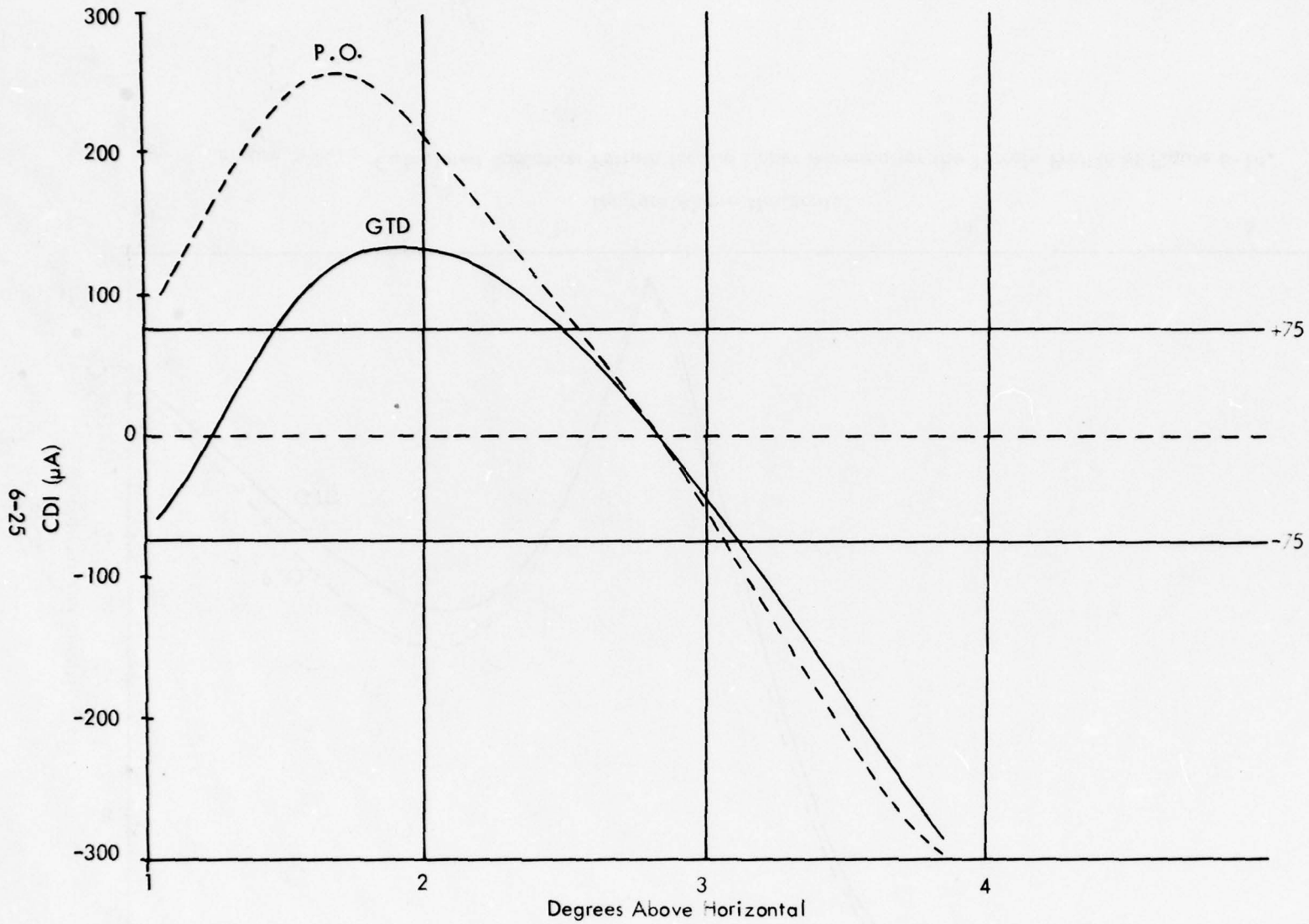

Figure 6-15. Calculated CDI for the Terrain Profile of Figure 6-14.

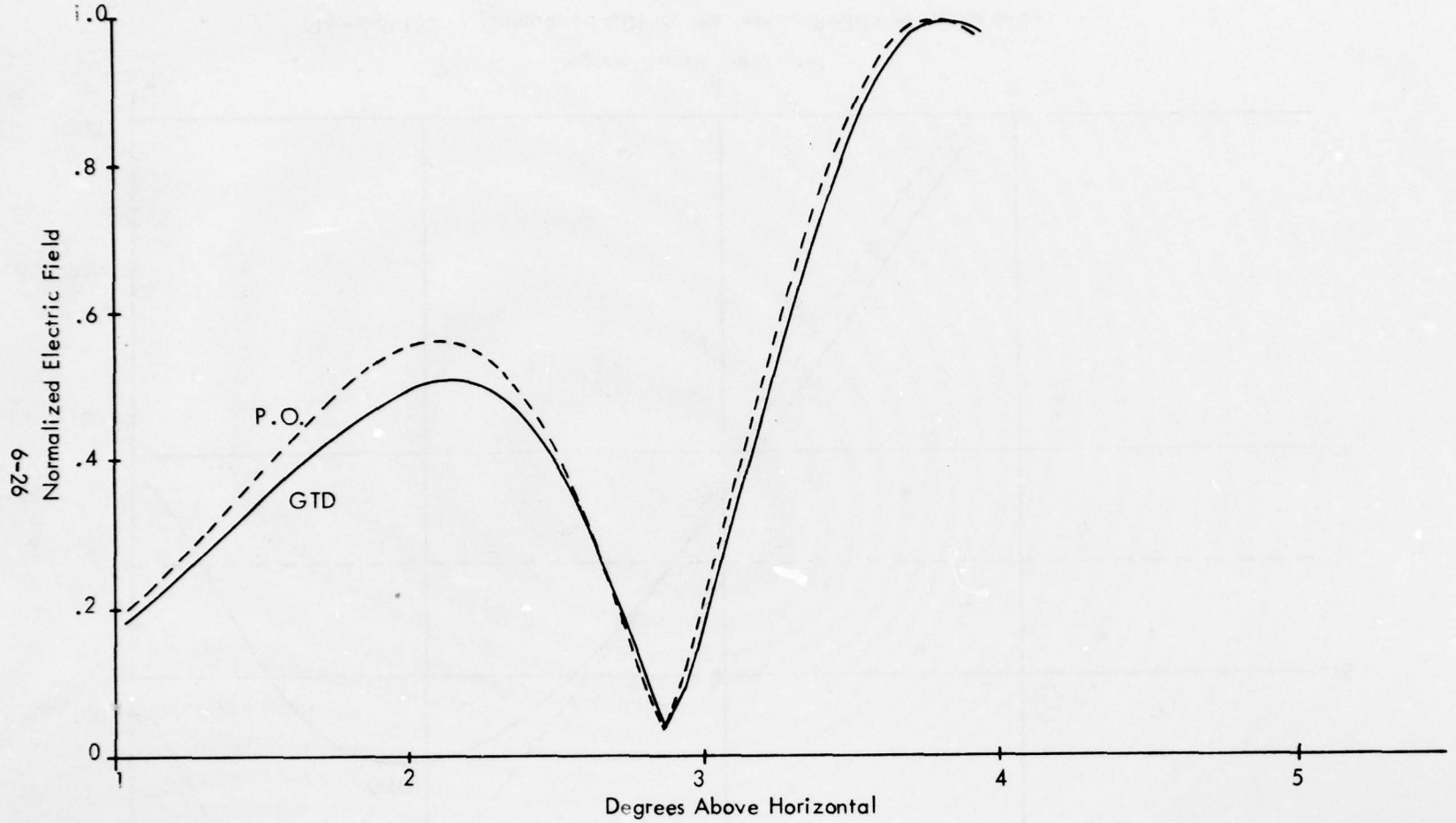

Figure 6-16. Calculated Radiation Pattern for the Upper Antenna for the Terrain Profile of Figure 6-14.

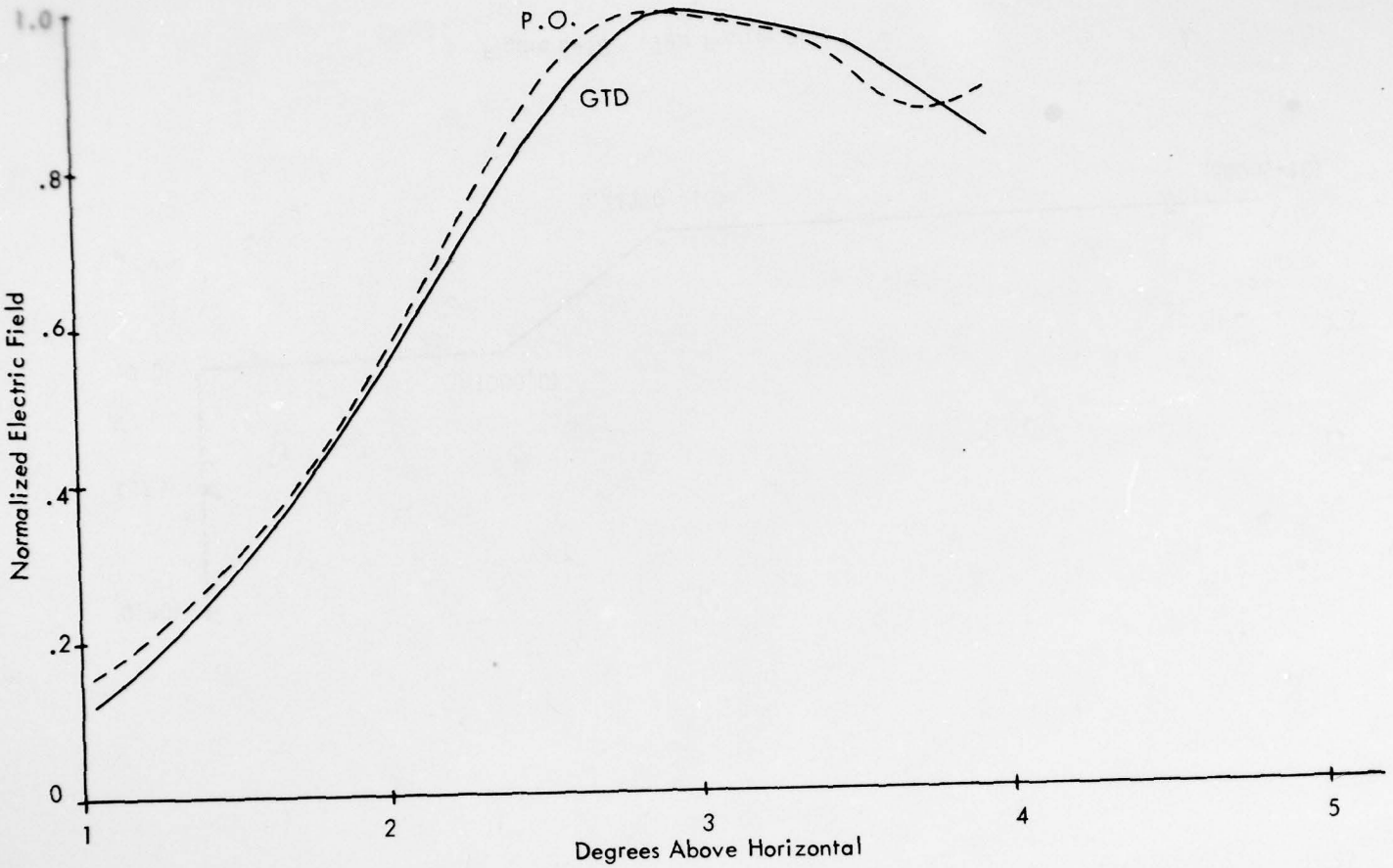

Figure 6-17. Calculated Radiation Pattern for the Lower Antenna for the Terrain Profile of Figure 6-14.

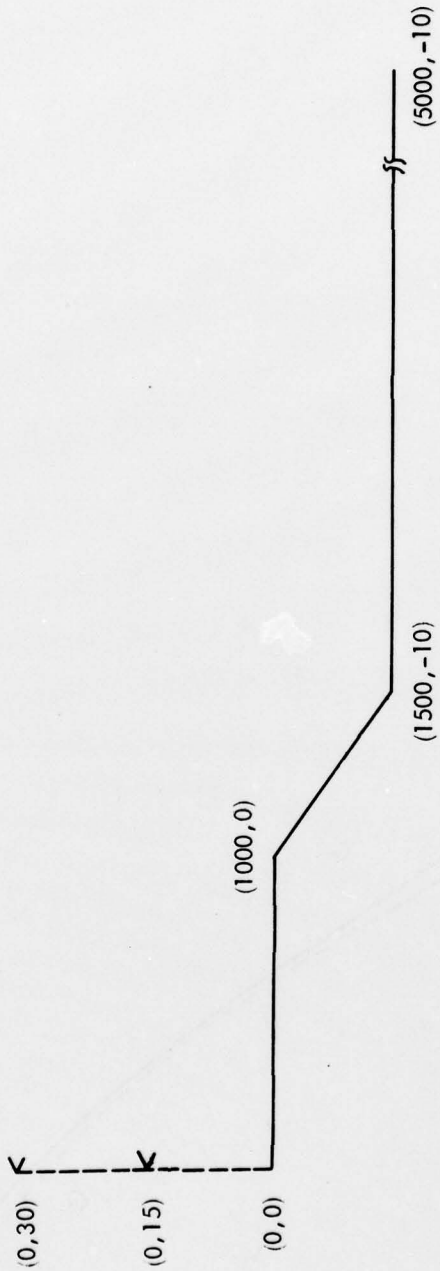

Figure 6-18. Test Profile No. 1.

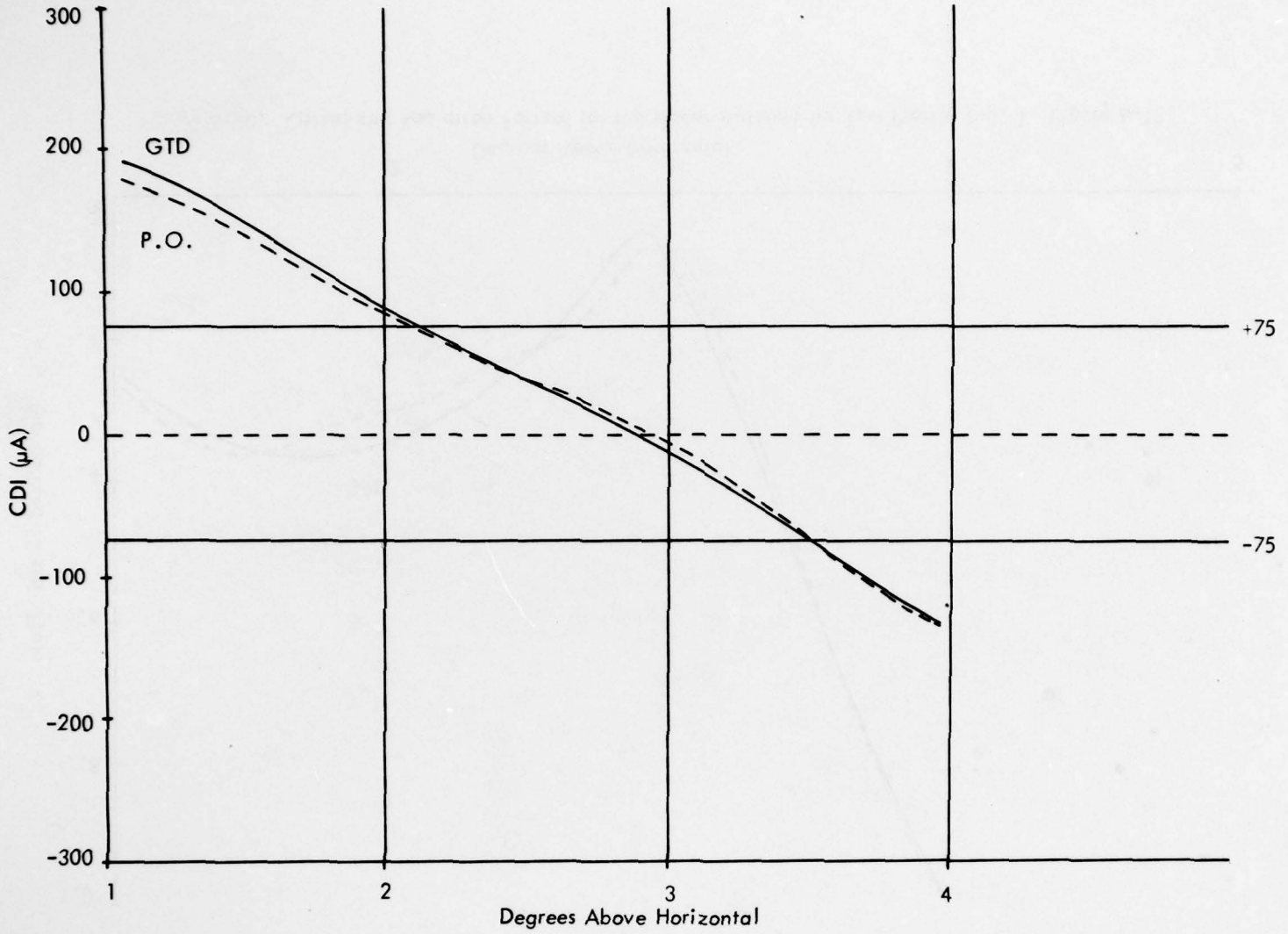

Figure 6-19. Calculated CDI for Test Profile No. 1, Figure 6-18.

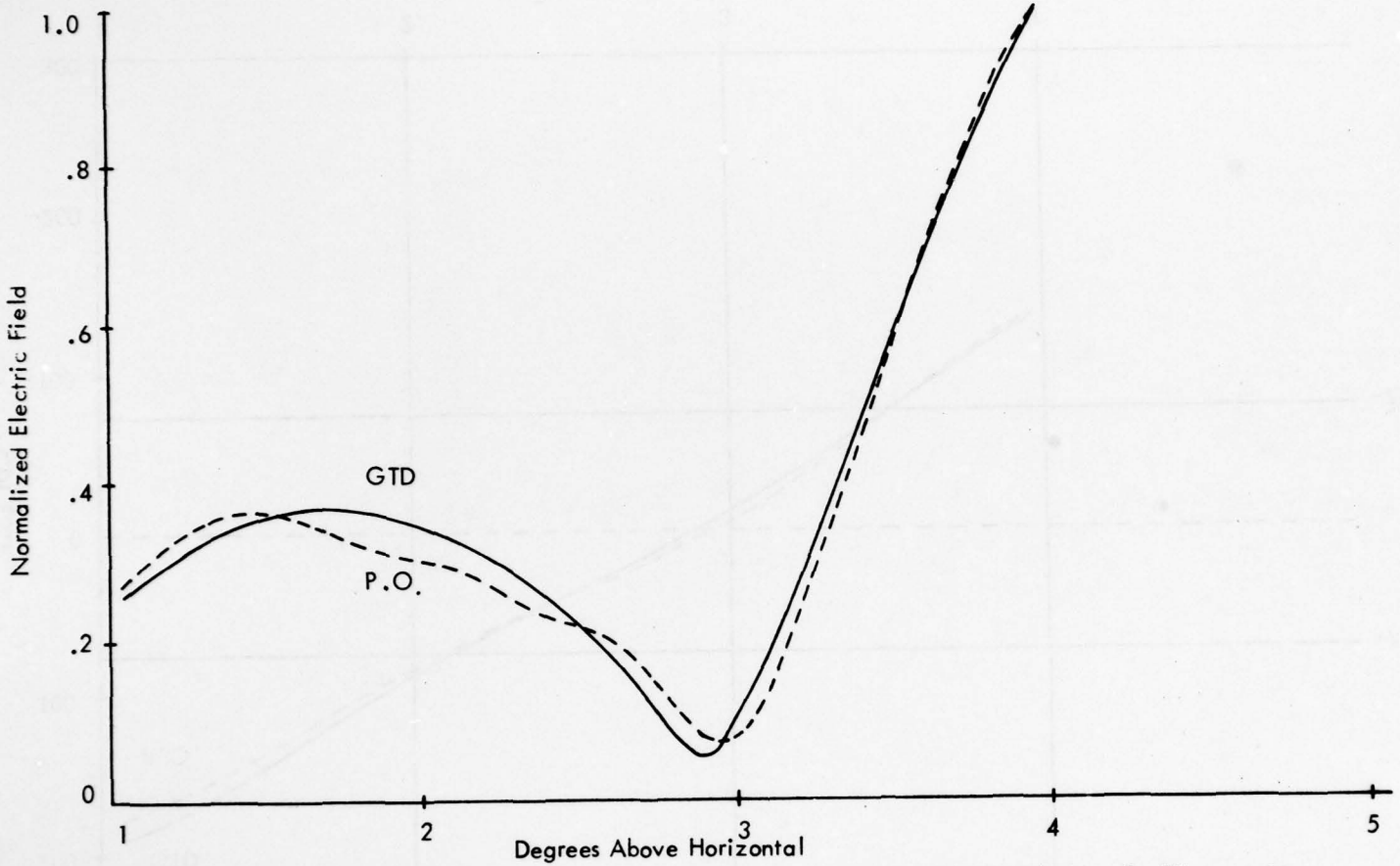

Figure 6-20. Calculated Radiation Pattern for the Upper Antenna for Test Profile No. 1, Figure 6-18.

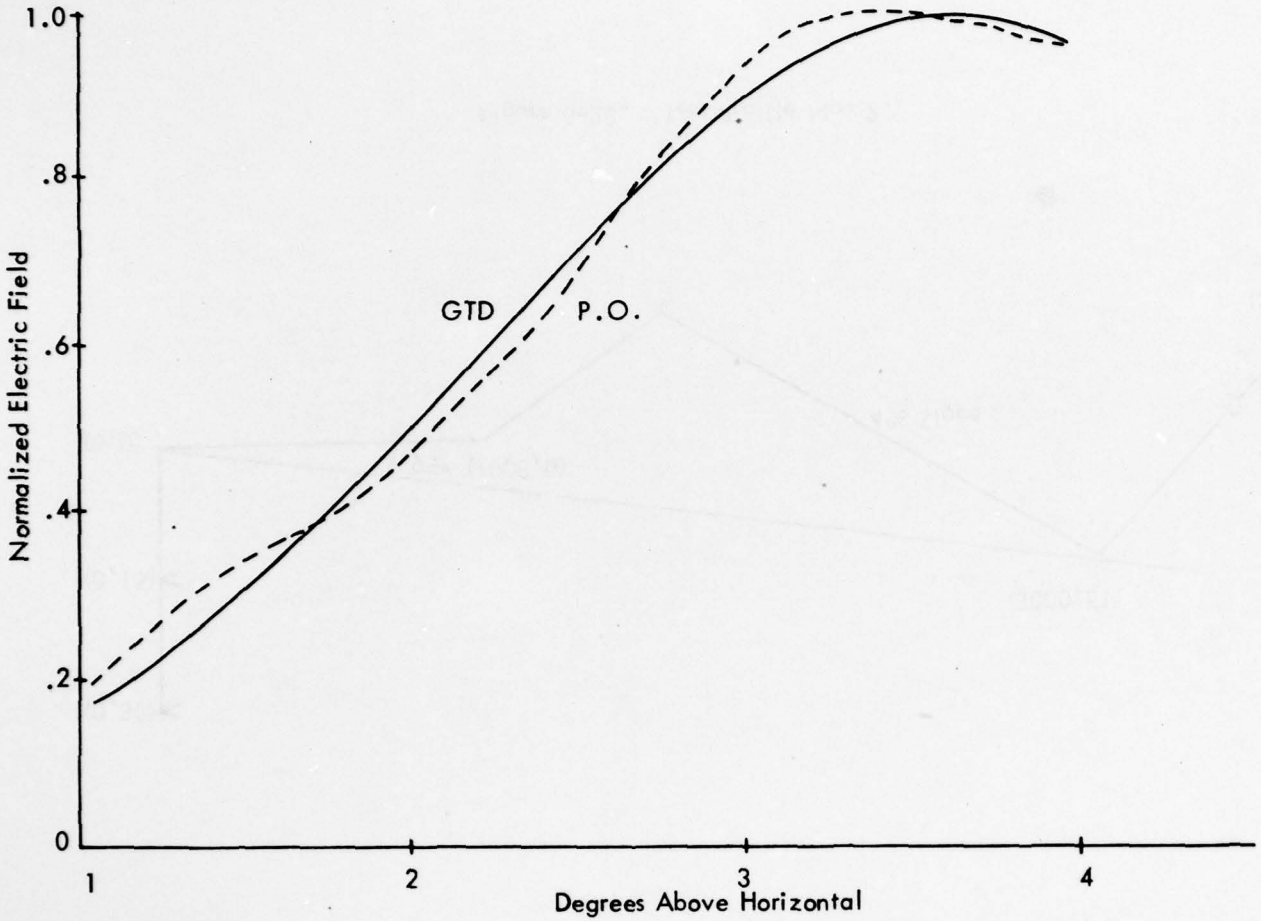

Figure 6-21. Calculated Radiation Pattern for the Lower Antenna for Test Profile No. 1, Figure 6-18.

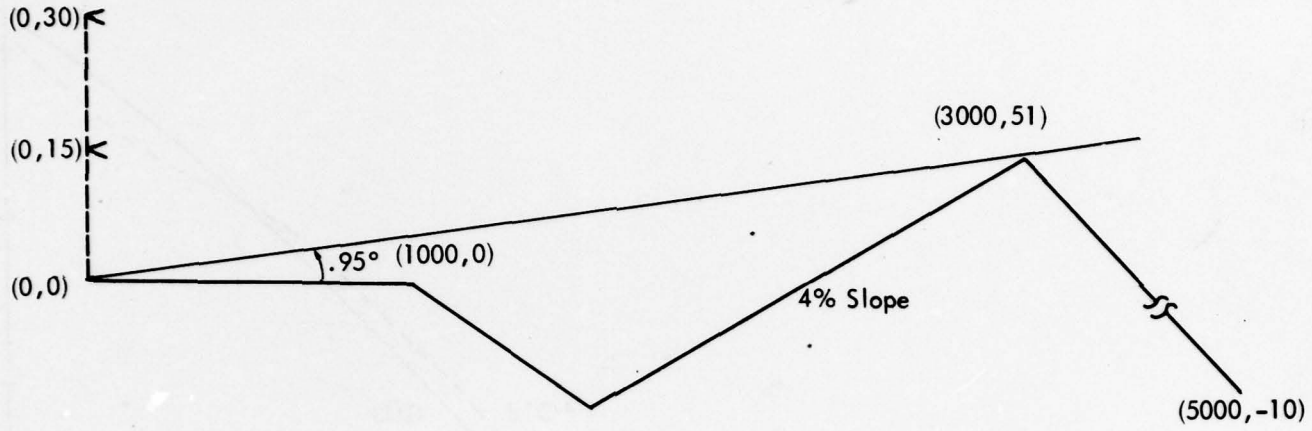

Figure 6-22. Test Profile No. 2.

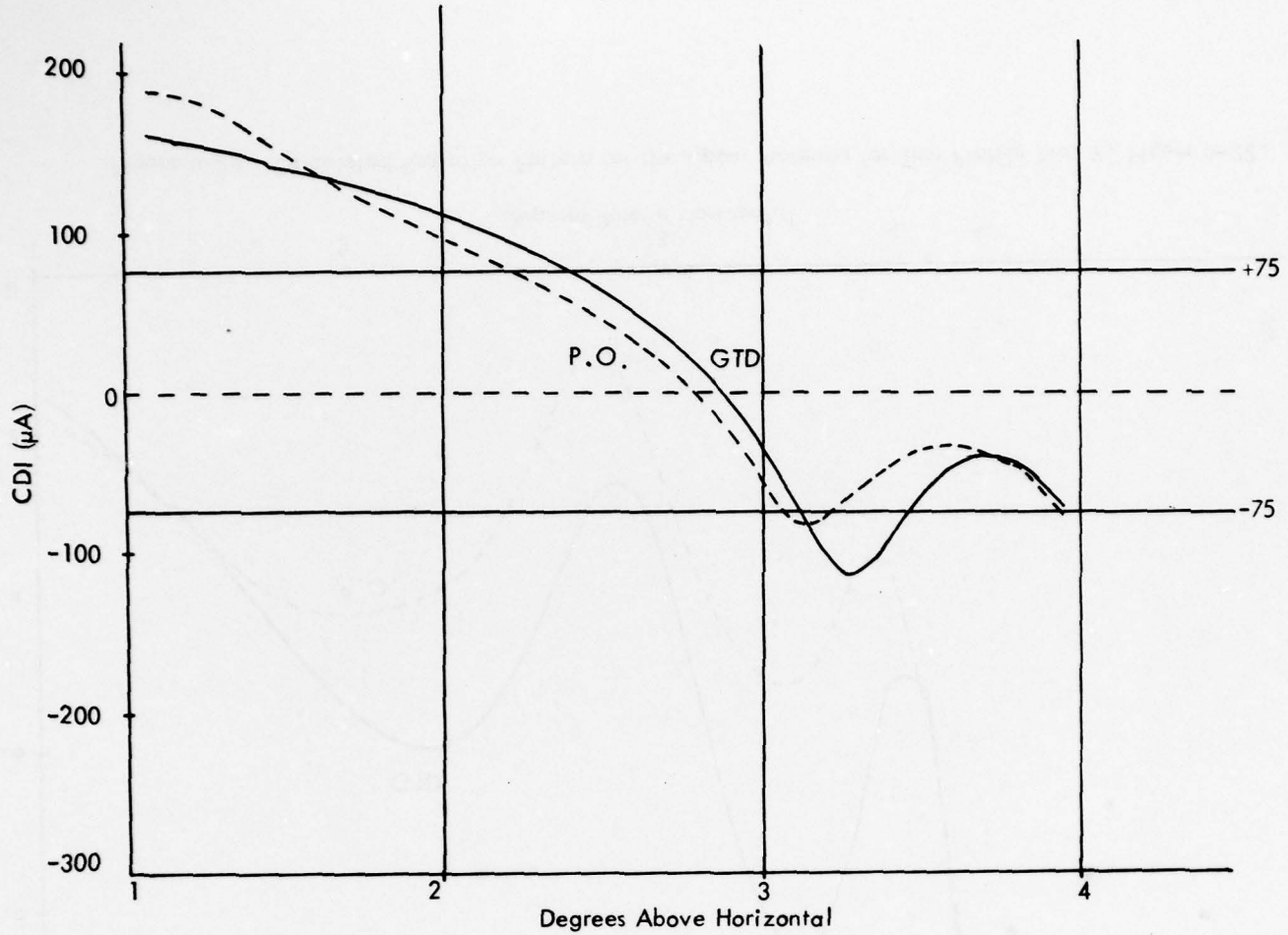

Figure 6-23. Calculated CDi for Test Profile No. 2, Figure 6-22.

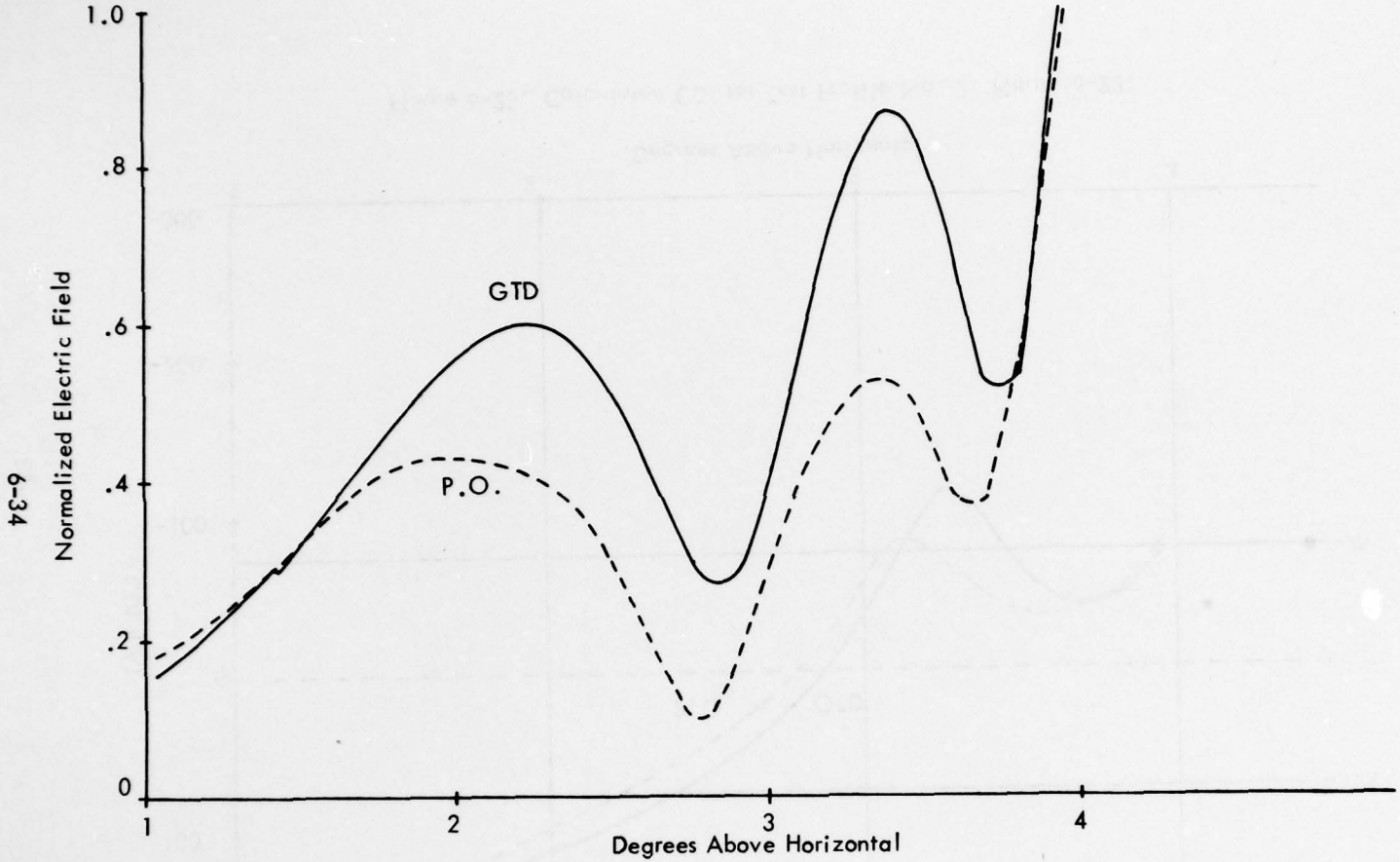

Figure 6-24. Calculated Radiation Pattern for the Upper Antenna for Test Profile No. 2, Figure 6-22.

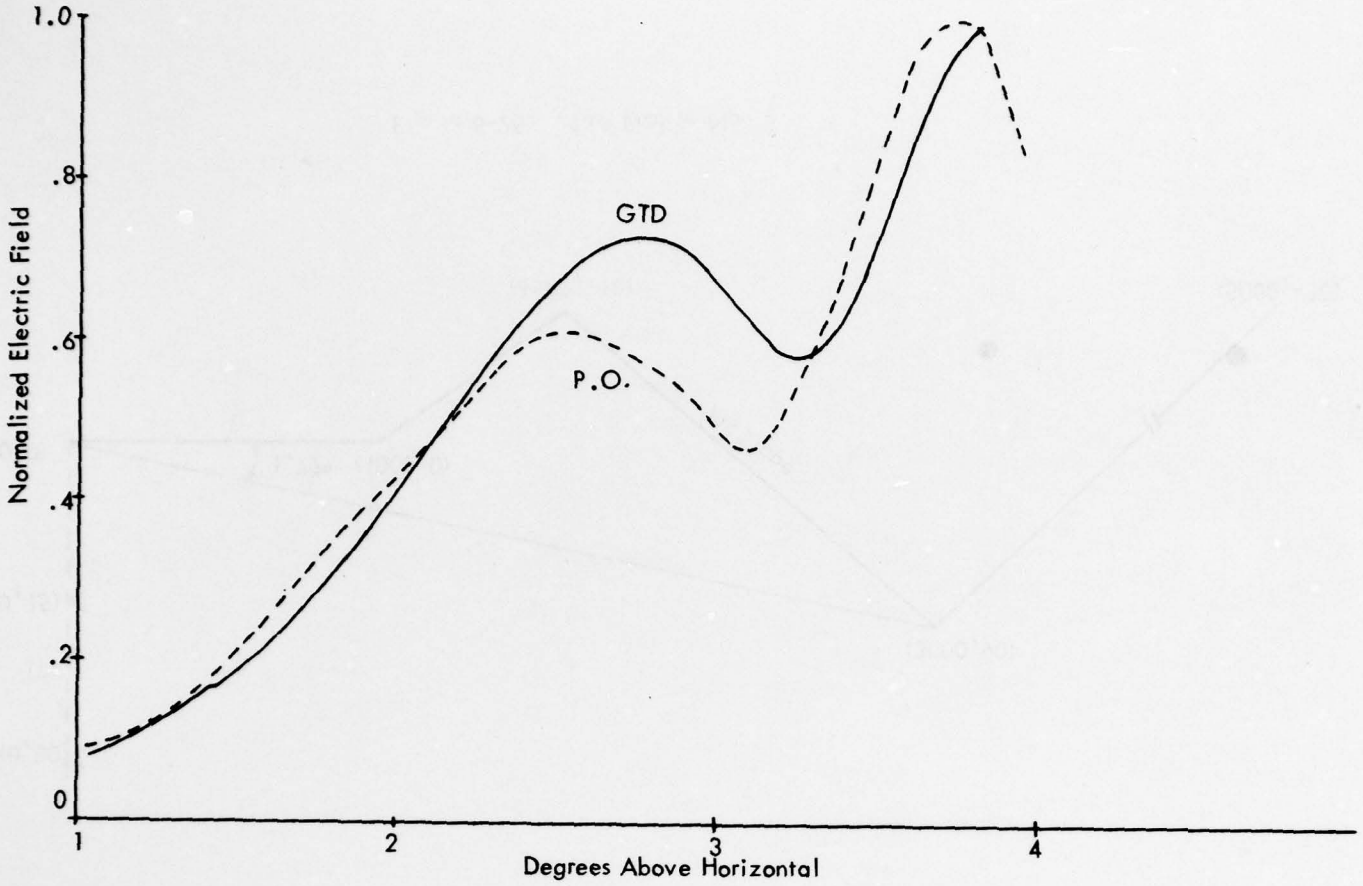

Figure 6-25. Calculated Radiation Pattern for the Lower Antenna for Test Profile No. 2, Figure 6-22.

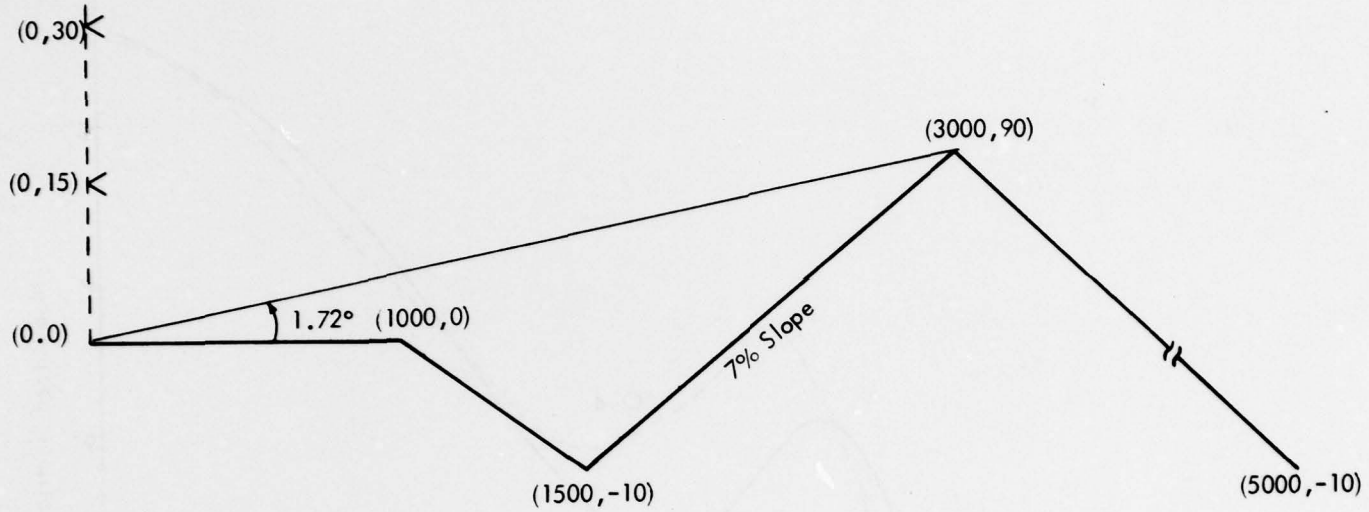

Figure 6-26. Test Profile No. 3.

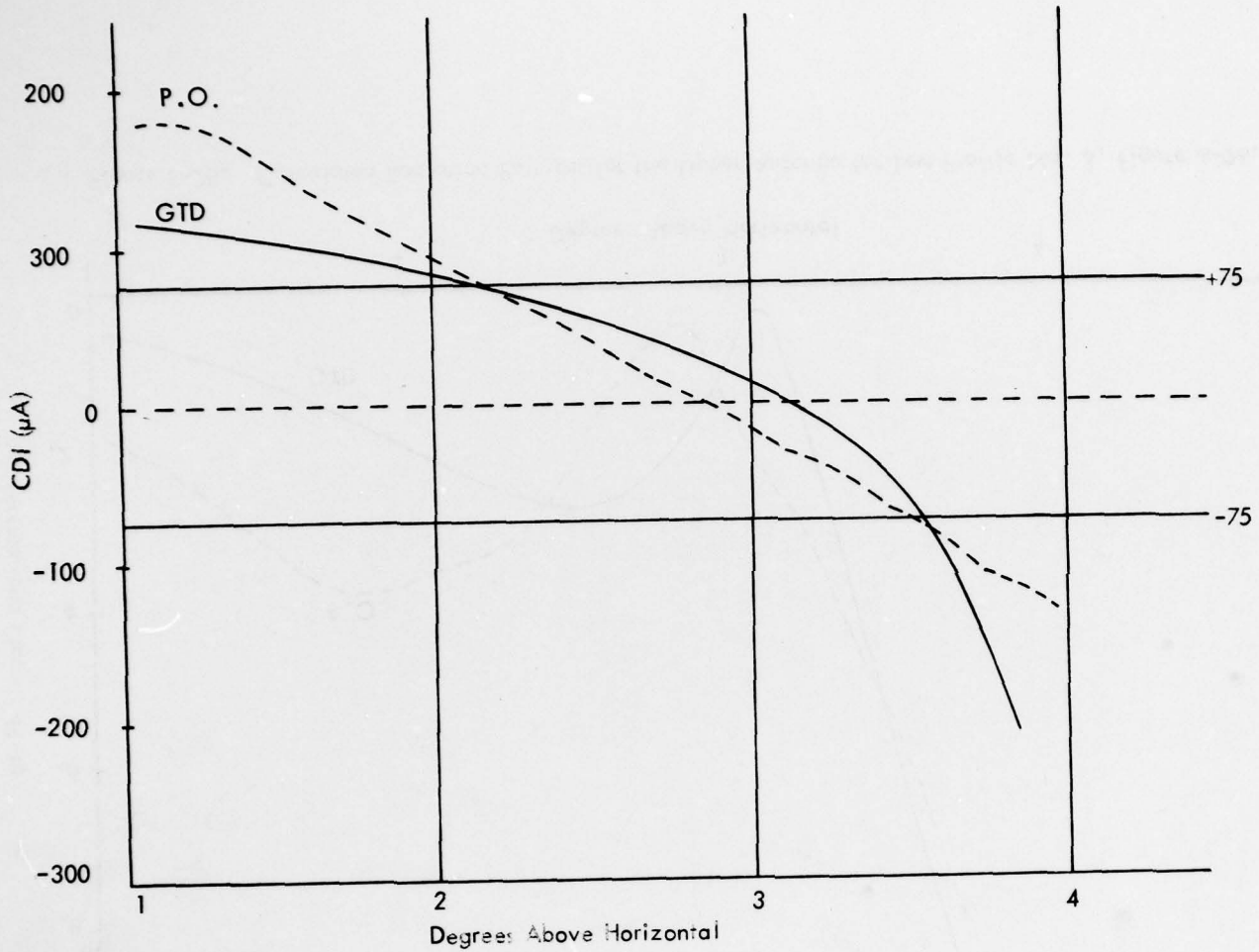

Figure 6-27. Calculated CDI for Test Profile No. 3, Figure 6-26.

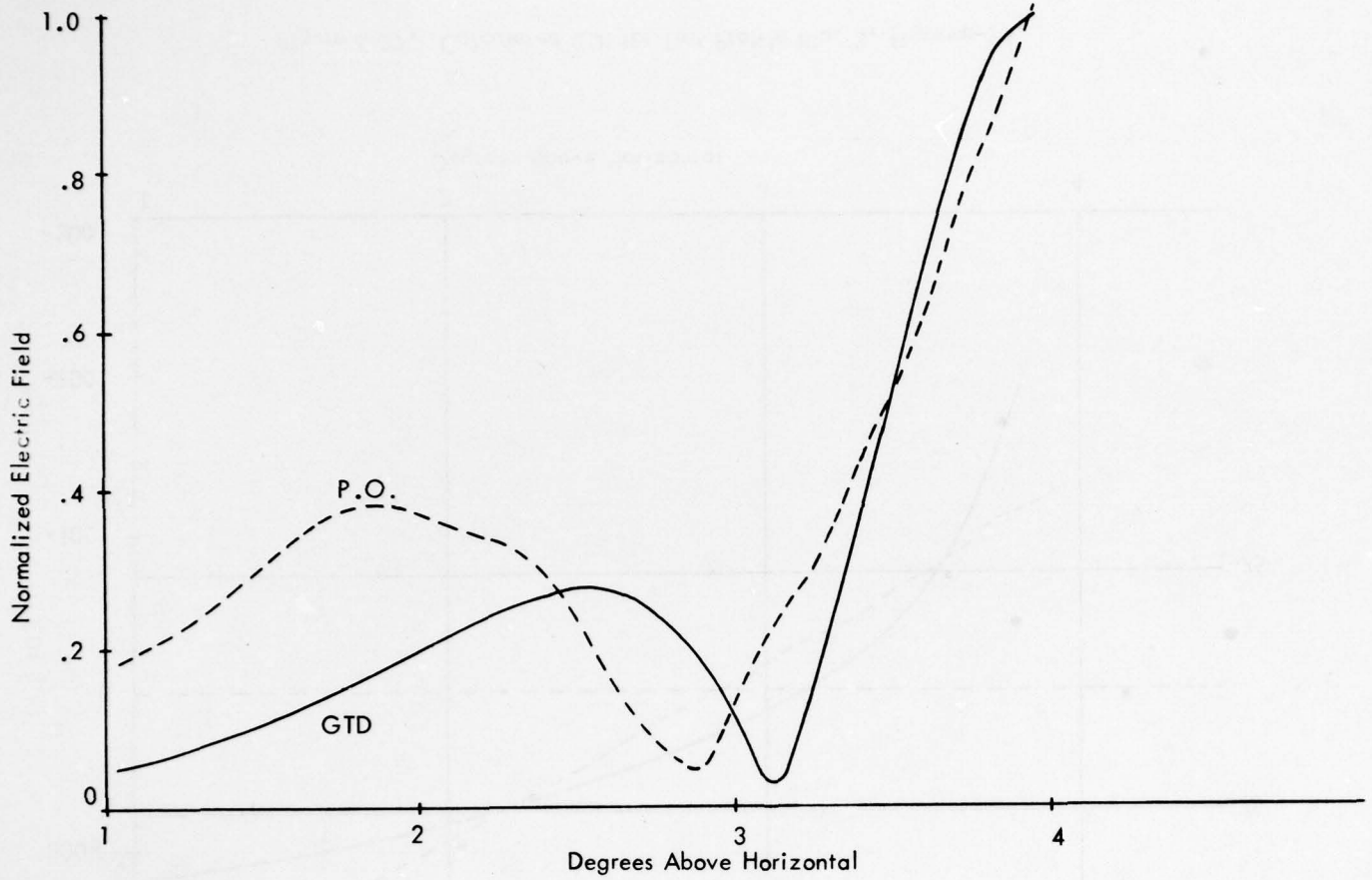

Figure 6-28. Calculated Radiation Patterns for the Upper Antenna for Test Profile No. 3, Figure 6-26.

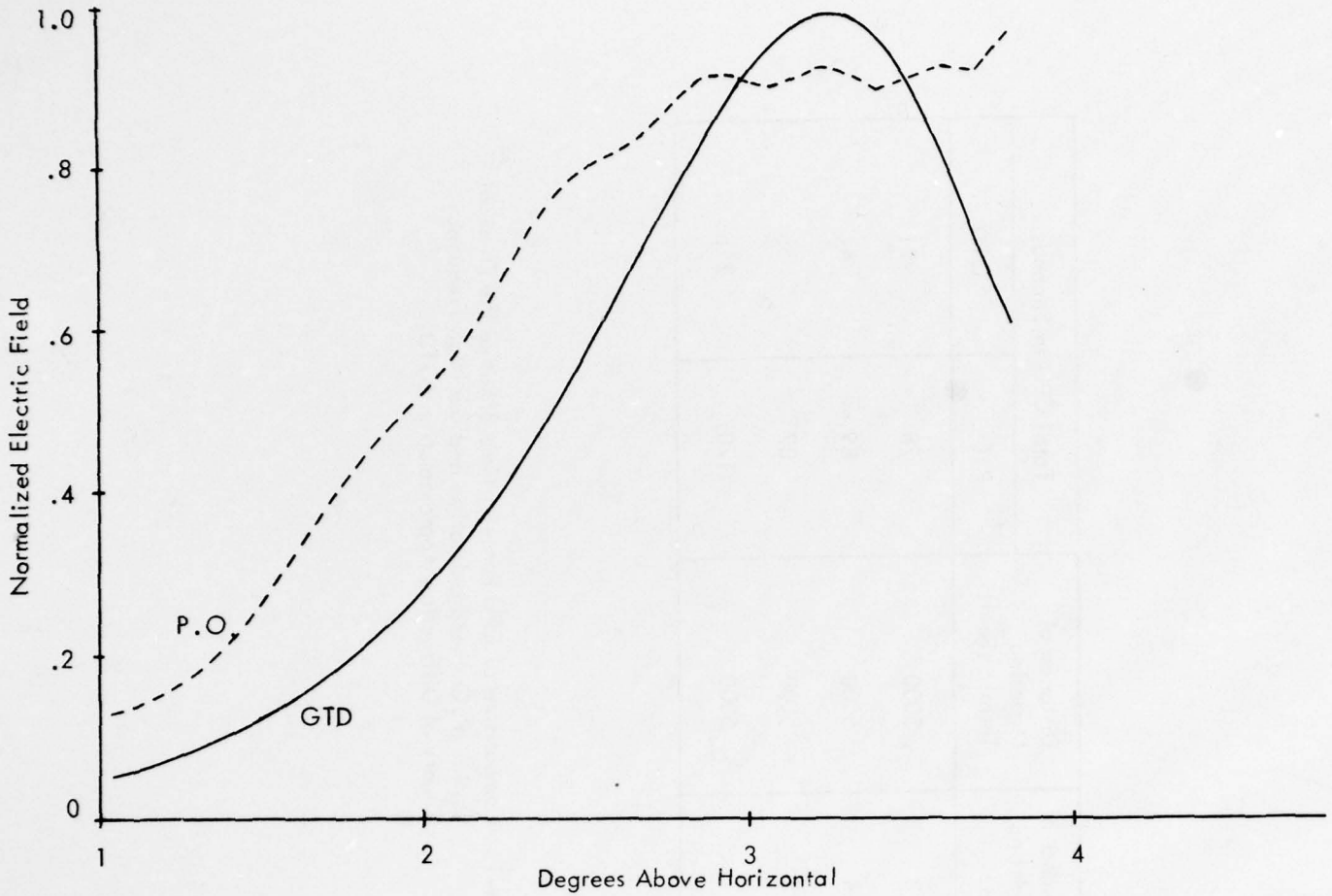

Figure 6-29. Calculated Radiation Patterns for the Lower Antenna for Test Profile No. 3, Figure 6-26.

Normalized Electric Field

.8 .6 .4 .2

6-26

Number of Modeling Plates	Distance of Modeling Terrain (Feet)	Total CPU in Seconds	
		P.O.	GTD
3	5000	78	21
4	5000	89	41
5	5000	87	56
7	5000	170	215

Table 6-1. Comparisons of CPU Running Time Between the Physical Optics (P.O.) Approximation and the High Frequency Theory of Diffraction Approximation (GTD).

AD-A074 425 OHIO UNIV ATHENS DEPT OF ELECTRICAL ENGINEERING F/G 17/7
IN-SERVICE IMPROVEMENTS AND MODERNIZATION OF ALL COMPONENTS OF --ETC(U)
JUL 78 DOT-FA75WA-3549
UNCLASSIFIED EER-35-1 FAA-RD-78-112-1 NL

6 OF 8
AD
A074425

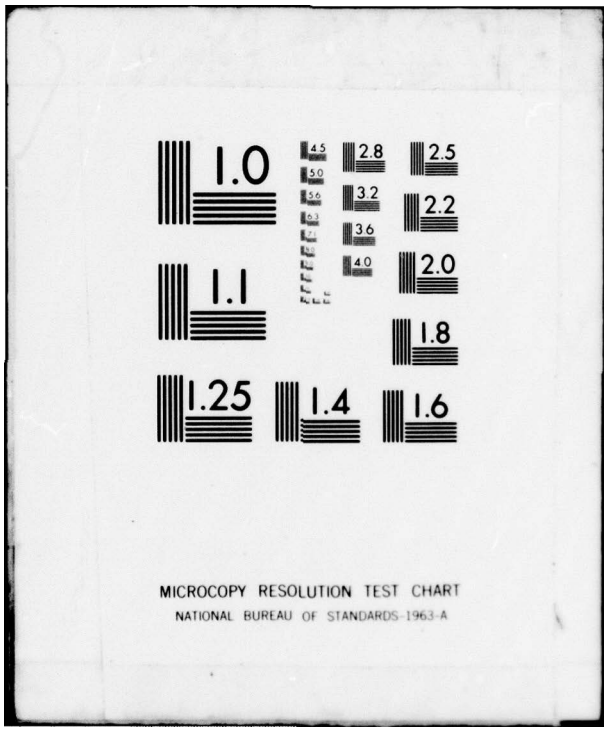
1.0
1.1
1.25
1.4
1.6
1.8
2.0
2.2
2.5
2.8
3.2
3.6
4.0
4.5
5.0
5.6
6.3
MICROCOPY RESOLUTION TEST CHART
NATIONAL BUREAU OF STANDARDS-1963-A

becomes slower as more possible combinations for producing contributing rays must be investigated. It should be again pointed out that the GTD model includes many more interaction effects than does the TSC model, so that the comparison is somewhat biased towards the physical optics model. A GTD model of comparable accuracy could be constructed using only the direct, reflected and diffracted rays, rather than the 8 types of rays presently included, and with the blocking effects of intervening terrain neglected. This GTD model would run much faster than the physical optics model and be capable of producing equivalent results. Rather than develop such a model, however, it was felt more productive to develop the model which is described here with its much more extensive capabilities.

5. OUGS--The Hybrid Glide Slope Program. The Ohio University Glide Slope model (OUGS) is a combination of three of the previously discussed glide slope models--the flat earth image theory model, the TSC physical optics model, and the Ohio University GTD model. The three models are combined in such a way that results obtained from each are easily compared, and so that the input data format is identical for each of the models. This allows efficient comparison of results obtained using different models for the same glide slope site.

As mentioned previously, the entire TSC model is not included in OUGS--only the two subroutines concerned with calculating the fields reflected from the terrain. The input to these subroutines and output from them is handled entirely by OUGS. Thus some of the problems which were encountered in using the TSC model, such as inconvenient phase convention and current input format, have been corrected. In addition, the capability of the OUGS calling program makes the TSC electromagnetic subroutines much more useful than if they were called by the full TSC model.

This incorporation of the TSC physical optics approach with OUGS is possible because the glide slope modeling problem can basically be divided into two parts. One part of the problem is: given the location and frequency of a glide slope antenna, the location of the aircraft receiver, and the topography between the two, calculate the electromagnetic fields at the position of the receiver. This is the electromagnetic theory part of the modeling problem and can be accomplished in three basic ways in OUGS--image theory, physical optics (TSC), or diffraction theory (GTD). In OUGS there are separate subroutines dedicated to these three types of calculations.

The second part of the problem is concerned with the input to these subroutines and the output from them. The subroutines must be furnished with properly formatted terrain information, antenna position information, frequency, and receiver location. This has to be repeated for each glide slope antenna. The electromagnetic fields output by the given subroutine must then be combined in the proper way to produce a calculated CDI or Differential Amplifier value. This depends upon the antenna currents for the SBO, CSB, and Clearance signals, and the position and (for differential amp output) telemetry settings of theodolite.

The advantages of the new Ohio University GTD electromagnetic model over previously available terrain models have already been discussed. However, it is useful for cross-checking and increasing the confidence level of the results to compare calculations obtained using different modeling techniques. The OUGS program makes this quite easy. In addition, the OUGS calling program makes the GTD and the physical optics models more accurate than before by including previously neglected phenomena in the OUGS model.

One of the parameters included for the first time is theodolite position, including eyepiece height above ground, and theodolite reference angle and width angle for pattern A measurements. While it has long been recognized that the position of the theodolite can have significant effect on the flight measurement results, especially in the case of pattern A measurements, previous glide slope models have neglected this parameter completely. In addition to computing elevation angles from the theodolite eyepiece location rather than from the base of the mast or the runway centerline as was previously done, the OUGS model calculates the theodolite telemetry signal (assuming perfect tracking) as well as the CDI at the location of the aircraft and subtracts the two to produce a calculated differential amplifier output which can be compared directly with the differential amplifier trace from a flight recording since it includes all of the pertinent parameters.

Another parameter included for the first time is clearance signal. A technique for modeling the receiver capture effect has been developed at Ohio University and incorporated into the OUGS model so that the effect of the clearance signal can be included in the CDI calculation if desired. This capability makes the model much more useful in modeling capture effect systems than previous models. The technique used for modeling the receiver capture effect is outlined under **Supplemental Data.**

In addition to including effects which previous models have neglected, the OUGS model, in conjunction with another computer program recently developed by Ohio University called POSTOUGS, can greatly reduce the computer running time required to model the effects of changes in the antenna currents, (relative phasing, sideband power, clearance power) or the theodolite position. As mentioned earlier, the electromagnetic modeling subroutines require only the terrain, antenna location, receiver location, and frequency to perform their calculations. Once these calculations are completed, the results can be used to calculate CDI's or differential amplifier values for any number of perturbations of antenna phasing, power levels, or theodolite positions. As the electromagnetic calculations are by far the most time consuming portion of the model, much time can be saved by not repeating them unnecessarily. Thus modeling the effects of antenna phasing, sideband power, or clearance power on the glide slope performance can be performed with very little computer time required even for very complex terrain.

The organization of OUGS and POSTOUGS is indicated in Figure 6-30. The three blocks labeled GTD, PO, and Image represent the three available terrain models--the GTD model discussed in the previous section, the SCAT and SUM subroutines from the

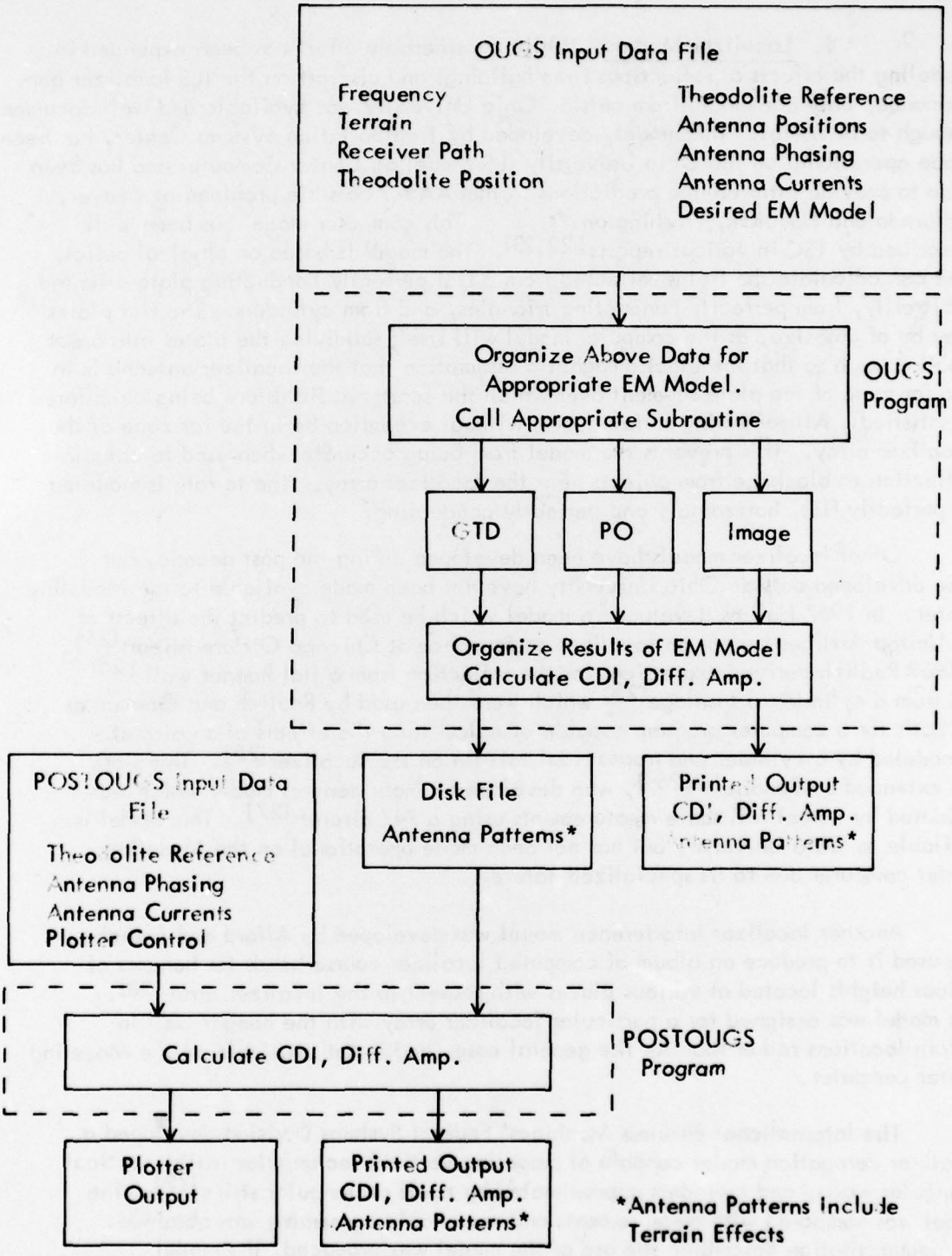

Figure 6-30. Organization of OUGS and POSTOUGS Programs.

TSC physical optics model[5], and an image theory model obtained by inputting flat ground of infinite extent to the GTD model (this is electromagnetically equivalent to an image theory model).

6. Localizer Models. While considerable effort has been expended in modeling the effects of reflections from buildings and aircraft on the ILS localizer performance, only one model from outside Ohio University was available and well documented enough to be useful. This model, developed by Transportation Systems Center, has been made operational on the Ohio University ILS Modeling Center Computer and has been used to provide interference predictions to theFAA for possible problems at Denver, Colorado and Hoquiam, Washington.* This computer model has been well described by TSC in various reports[22,23]. The model is based on physical optics, and can calculate the fields reflected from a flat perfectly conducting plate oriented arbitrarily, from perfectly conducting triangles, and from cylinders. The flat plates may be of any size, as the computer model will itself subdivide the plates into areas small enough so that the electromagnetic assumption that the localizer antenna is in the far zone of the plate segment over which the scattered fields are being calculated is satisfied. All reflecting surfaces must without exception be in the far zone of the localizer array. This prevents the model from being accurate when used to calculate reflection or blockage from objects near the localizer array. The terrain is modeled as perfectly flat, horizontal, and perfectly conducting.

Other localizer models have been developed during the past decade, but those developed outside Ohio University have not been made available to the Modeling Center. In 1967 Hollins developed a model which he used to predict the effects of the United Airlines hangar on localizer performance at Chicago O'Hare airport[24]. In 1969 Redlich derived expressions for the reflection from a flat hangar wall [25] and from a cylindrical fuselage[25] which were then used by Redlich and Gorman as the basis for a computer program capable of calculating the effects of an aircraft as modeled by a cylinder and trapezoidal tail fin on the localizer[25]. This work was extended by Rondini[8,26], who developed a more general model which was validated by actual full scale measurements using a 747 aircraft[27]. This model is available to Ohio University but has not been made operational on the Modeling Center computer due to its specialized nature.

Another localizer interference model was developed by Alford and French, who used it to produce an album of computed localizer course bends for hangars of various heights located at various places with respect to the localizer array[28]. This model was designed for a particular localizer array with the hangar wall in certain locations rather than for the general case, and is not available on the Modeling Center computer.

The International Business Machines' Federal Systems Division developed a localizer derogation model capable of modeling vertical rectangular walls, vertical triangular walls, and cylinders approximated by small rectangular strips[29]. The model was compared with measurements and reasonable agreement was obtained. No documentation describing the use of the model was produced, the model evidently having been developed for internal (to IBM) use only. This model is not operational on the Ohio University Modeling Center computer.

*See Sections VI.D and E of this report.

As previously mentioned, the ILS localizer computer model developed by TSC is fully operational on the Modeling Center computer. This model is based on physical optics, as are all of the localizer models which have been developed. The TSC model was chosen for implementation because it is very well documented, readily available, and has produced reasonably good agreement when compared with measurements [30].

7. Supplemental Data.

a. Input Data Format for the OUGS Hybrid Glide Slope Terrain Model. In previous sections of this report the basic organization and purpose of the OUGS hybrid glide slope terrain model were presented and discussed. In this section the format of the input data required by the OUGS program will be given.

A sample set of input data is shown in Figure 6-31a. Reference should be made to this figure when reading the following input description. The resulting output is shown in Figure 6-31b.

The input data for one particular modeling geometry is divided into one comment card and 5 sections of input. The comment card begins with an asterisk and is the first card for each geometry to be modeled. Following this card are the 5 sections of numerical data:

1. Terrain Data
2. Theodolite Data
3. Antenna Data
4. Pattern Control
5. Output Control

If more than one geometry is to be modeled on one computer run, a blank line is left after the last data for the previous geometry followed with the comment card for the next geometry. If some sections of data do not change for the next geometry, they need not be repeated. The last data line of each computer run must contain periods in the first three columns. Each section card contains the section number in column 15, with the first 10 columns available for comments. The data input in each section is organized as follows:

(1) Terrain Data

In this section the terrain information is encoded and the type of electromagnetic terrain model to be used is determined. The first line of this section (following the section 1 card) is formatted 10X, 3I5, and contains the variables NE, NRAY, and ICON. NE is the number of corners in the terrain profile, NRAY specifies the type of calculation to be made,

NRAY - 0 for flat earth
NRAY - 1 for GTD
NRAY - 2 Physical optics

```
*     CEGC. SET-UP
  SECTION      1
NO. OF PTS     8     1
COORDS.          0.0          0.0          0.0
COORDS.          0.0     1250.000          0.0
COORDS.          0.0     2000.000    -84.3
COORDS.          0.0     2320.000    -98.3
COORDS.          0.0     3680.000    -17.3
COORDS.          0.0     3870.000    -21.3
COORDS.          0.0     4040.000    -56.3
COORDS.          0.0    60000.000    -56.3
SECTION        2
THEOD                  -275.112  95.4       5.167      3.0        2.7
SECTION        3
ANT. DATA      3       332.0        .40        .321          .90
POSITION       1       -301.015  0.         14.250
CURR.      -0.5        -3.495    1.         -3.495     .484          -3.495
POSITION       2       -300.0      0.       28.50
CURR.      1.00        3.0       -0.5       0.0
POSITION       3       -298.309    0.       42.75
CURR.       -0.5       4.499     0.0        0.0        .484          4.499
SECTION        4
PATTERN        2    51     0      0.00       57300.0    1000.
PATTERN                             0.00      1270.      1000.
SECTION        5
OUTPUT         2     2     1
...
```

Figure 6-31a. Sample Input Data for OUGS Program.

THE INPUT DATA FOR THIS SIMULATION IS AS FOLLOWS:

FIELDS CALCULATED WITH CTD

CESAC SET-UP

THE PLATE DATA IS:
THE NUMBER OF EDGES IS 4

POSITION OF VERTICES:	X(COORD.)	Y(COORD.)	Z(COORD.)
	0.0	0.0	0.0
	0.0	12700.000	0.0
	0.0	23600.000	-14.300
	0.0	23200.000	-28.300
	0.0	36800.000	-17.300
	0.0	38700.000	-21.300
	0.0	46400.000	-56.300
	0.0	60000.000	-56.300

THE FACILITY DATA IS:
NA= 3 FREQ= 552.000 LAMBDA= 2.963 M= 0.400 N= 0.301 AC150= 0.900

THE THEODOLITE DATA IS:

X(COORD.)	Y(COORD.)	Z(COORD.)	PATH REF. ANGLE	WIDTH REF. ANGLE
-27[illegible].112	[illegible]5.433	5.167	3.100	0.700

THE ANTENNA DATA IS:

ANTENNA	X(COORD.)	Y(COORD.)	Z(COORD.)	ISS(MAG.)	ISS(PHS.)	ICS(MAG.)	ICS(PHS.)	ICC(MAG.)	ICC(PHS.)
1	-361.015	0.0	14.250	-0.50000	-3.495	1.00000	-3.495	0.48400	-3.495
2	-300.000	0.0	28.500	1.00000	0.0	-0.50000	0.0	0.0	0.0
3	-238.358	0.0	42.750	-0.50000	4.499	0.0	0.0	0.48400	4.499

THE PATTERN CUT FOR THIS SIM. IS:
THE PATTERN IS A STRAIGHT LINE CUT WITH THE INITIAL COORDINATES- X= 0.0 Y= 57300.000 Z= 1000.000

THE FINAL COORDINATES- X= 0.0 Y= 12700.000 Z= 1000.000

THE OUTPUT DATA IS AS FOLLOWS:

X	Y	[illegible]	ALPHA	DCDI	CDI	FTI	FTIPHA	ET2	ET2PHA	ET3	ET3PHA	ECSMAG	ESSMAG
0.0	57300.0[illegible]	1[illegible].000	0.936	231.2	721.6	0.3690-03	165.6	0.5820-03	162.1	0.5130-03	157.7	0.7770-04	0.4520-04
0.0	56400.[illegible]	1[illegible].000	1.012	232.0	714.0	0.3740-03	165.8	0.5950-03	162.4	0.5190-03	158.1	0.8090-04	0.4690-04
0.0	55[illegible].[illegible]	1[illegible].000	1.024	232.1	714.6	0.3780-03	166.0	0.6040-03	162.7	0.5230-03	158.4	0.8450-04	0.4880-04
0.0	54624.0[illegible]	1[illegible].000	1.045	290.5	709.3	0.3940-03	166.2	0.6190-03	163.0	0.5220-03	159.1	0.8870-04	0.5070-04
0.0	53732.[illegible]	1[illegible].000	1.063	288.3	703.5	0.4070-03	166.4	0.6240-03	163.3	0.5260-03	159.7	0.9320-04	0.5270-04
0.0	52841.[illegible]	1[illegible].000	1.081	245.6	696.9	0.4170-03	166.6	0.6340-03	163.7	0.5140-03	160.7	0.9790-04	0.5480-04
0.0	51949.[illegible]	1[illegible].000	1.099	242.4	689.7	0.4270-03	166.9	0.6440-03	164.1	0.5150-03	161.7	0.1030-03	0.5700-04
0.0	51057.[illegible]	1[illegible].000	1.118	278.5	681.7	0.4380-03	167.2	0.6530-03	164.6	0.5110-03	162.7	0.1080-03	0.5940-04
0.0	5 164.[illegible]	1[illegible].000	1.136	273.9	672.5	0.4490-03	167.5	0.6690-03	165.0	0.5060-03	163.7	0.1140-03	0.6180-04
0.0	49272.[illegible]	1[illegible].000	1.159	269.7	664.2	0.4600-03	167.8	0.6810-03	165.5	0.5010-03	165.2	0.1200-03	0.6460-04
0.0	48[illegible].000	1[illegible].000	1.183	263.2	653.1	0.4720-03	168.2	0.6910-03	166.1	0.4950-03	166.7	0.1270-03	0.6720-04
0.0	4744.[illegible]	1[illegible].000	1.203	256.0	641.2	0.4830-03	168.6	0.7020-03	166.7	0.4840-03	168.3	0.1340-03	0.6990-04
0.0	46[illegible].[illegible]	1[illegible].000	1.226	248.9	629.2	0.4930-03	169.0	0.7130-03	167.5	0.4800-03	171.2	0.1420-03	0.7260-04
0.0	45734.0[illegible]	1[illegible].000	1.250	239.3	614.4	0.5120-03	169.5	0.7240-03	168.2	0.4720-03	172.3	0.1510-03	0.7540-04
0.0	44812.0[illegible]	1[illegible].000	1.274	229.4	599.6	0.5260-03	170.1	0.7360-03	169.1	0.4640-03	174.6	0.1590-03	0.7800-04
0.0	43920.0[illegible]	1[illegible].000	1.300	219.6	583.8	0.5420-03	170.7	0.7480-03	170.0	0.4560-03	177.5	0.1690-03	0.8130-04
0.0	43028.0[illegible]	1[illegible].000	1.327	230.4	566.8	0.5560-03	171.3	0.7630-03	171.1	0.4490-03	-179.3	0.1800-03	0.8570-04
0.0	4214.[illegible]	1[illegible].000	1.356	136.9	549.5	0.5760-03	172.0	0.7740-03	172.2	0.4420-03	-175.8	0.1910-03	0.8930-04
0.0	41244.[illegible]	1[illegible].000	1.385	146.0	532.1	0.5950-03	172.7	0.7880-03	173.4	0.4360-03	-172.6	0.2030-03	0.9310-04
0.0	4134[illegible].000	1[illegible].000	1.416	174.7	514.2	0.6150-03	173.6	0.8040-03	174.7	0.4330-03	-169.8	0.2170-03	0.9700-04
0.0	3948.[illegible]	1[illegible].000	1.445	153.6	496.2	0.6380-03	174.5	0.8220-03	176.1	0.4320-03	-168.3	0.2310-03	0.1010-03
0.0	3853.[illegible]	1[illegible].000	1.481	152.9	476.4	0.6630-03	175.4	0.8420-03	177.7	0.4340-03	-168.7	0.2470-03	0.1050-03
0.0	3767.[illegible]	1[illegible].000	1.516	142.9	460.8	0.6900-03	176.4	0.8650-03	179.2	0.4390-03	-169.3	0.2650-03	0.1100-03
0.0	36784.0[illegible]	1[illegible].000	1.553	133.5	443.5	0.7220-03	177.5	0.8910-03	-179.2	0.4470-03	-169.5	0.2843-03	0.1150-03
0.0	35872.0[illegible]	1[illegible].000	1.592	124.6	426.5	0.7570-03	178.5	0.9210-03	-177.6	0.4570-03	-168.2	0.3060-03	0.1200-03
0.0	3500.[illegible]	1[illegible].000	1.633	116.6	409.6	0.7960-03	179.5	0.9550-03	-176.2	0.4660-03	-161.4	0.3300-03	0.1260-03
0.0	3419.0[illegible]	1[illegible].000	1.675	108.6	392.4	0.8410-03	-179.6	0.9940-03	-174.8	0.4730-03	-154.9	0.3570-03	0.1320-03
0.0	3321.[illegible]	2[illegible].000	1.720	100.4	374.6	0.8910-03	-178.8	0.1040-02	-173.7	0.4740-03	-145.1	0.3870-03	0.1390-03
0.0	3234.0[illegible]	1[illegible].000	1.766	91.7	355.7	0.9480-03	-178.1	0.1080-02	-172.9	0.4650-03	-132.3	0.4220-03	0.1470-03
0.0	3143.[illegible]	1[illegible].000	1.818	82.0	335.3	0.1010-02	-177.7	0.1130-02	-172.5	0.4440-03	-129.6	0.4620-03	0.1550-03
0.0	3054.[illegible]	1[illegible].000	1.872	71.1	313.9	0.1080-02	-177.5	0.1170-02	-172.5	0.4030-03	-126.2	0.5040-03	0.1650-03
0.0	2964.[illegible]	1[illegible].000	1.928	59.3	292.6	0.1150-02	-177.5	0.1210-02	-172.9	0.3410-03	-120.3	0.5620-03	0.1760-03
0.0	2875.[illegible]	1[illegible].000	1.988	45.4	269.3	0.1230-02	-177.9	0.1230-02	-173.7	0.2620-03	-107.0	0.6240-03	0.1870-03
0.0	27864.0[illegible]	1[illegible].000	2.052	32.3	235.5	0.1310-02	-178.4	0.1240-02	-174.9	0.2070-03	-74.8	0.6950-03	0.1980-03
0.0	2697.[illegible]	1[illegible].000	2.120	20.3	202.0	0.1380-02	-179.0	0.1220-02	-176.1	0.2730-03	-35.9	0.7770-03	0.2080-03
0.0	2608.0[illegible]	1[illegible].000	2.192	10.5	165.3	0.1450-02	-179.6	0.1170-02	-177.1	0.4557-03	-15.5	0.8700-03	0.2150-03
0.0	2518.[illegible]	1[illegible].000	2.270	5.1	159.5	0.1510-02	-179.9	0.1080-02	-177.2	0.6870-03	-10.3	0.9730-03	0.2180-03
0.0	2429.[illegible]	1[illegible].000	2.354	-2.0	156.5	0.1560-02	-179.8	0.9970-03	-175.6	0.9250-03	-10.0	0.1090-02	0.2150-03
0.0	2340.[illegible]	1[illegible].000	2.444	-5.3	113.9	0.1660-02	-178.7	0.9090-03	-171.9	0.1130-02	-11.1	0.1220-02	0.2040-03
0.0	2251.[illegible]	1[illegible].000	2.541	-6.6	101.7	0.1770-02	-177.7	0.8510-03	-167.6	0.1260-02	-10.9	0.1360-02	0.1880-03
0.0	2162.[illegible]	1[illegible].000	2.646	-5.6	70.3	0.1920-02	-177.4	0.8010-03	-166.9	0.1350-02	-6.5	0.1540-02	0.1680-03
0.0	2072.[illegible]	1[illegible].000	2.760	-2.3	49.1	0.2080-02	-178.6	0.8780-03	-173.3	0.1530-02	2.9	0.1750-02	0.1420-03
0.0	1983.[illegible]	1[illegible].000	2.885	0.4	25.1	0.2190-02	179.3	0.1390-02	169.0	0.1700-02	7.7	0.1990-02	0.9820-04
0.0	1894.[illegible]	1[illegible].000	3.021	-1.0	-6.3	0.2230-02	178.4	0.1250-02	58.5	0.2250-02	4.4	0.2250-02	0.5980-04
0.0	1803.[illegible]	1[illegible].000	3.171	-7.1	-43.7	0.2300-02	179.4	0.4420-03	-3.2	0.2200-02	-0.2	0.2520-02	0.1690-03
0.0	1716.[illegible]	1[illegible].000	3.336	-5.4	-77.4	0.2480-02	179.1	0.7330-03	5.2	0.1950-02	5.7	0.2840-02	0.3290-03
0.0	1626.0[illegible]	1[illegible].000	3.520	-5.5	-116.8	0.2450-02	176.6	0.1480-02	7.5	0.2910-02	5.1	0.3170-02	0.5450-03
0.0	1537.[illegible]	1[illegible].000	3.724	-10.4	-165.6	0.2480-02	-180.0	0.1950-02	-3.5	0.1090-02	-10.4	0.3460-02	0.8500-03
0.0	1448.0[illegible]	1[illegible].000	3.954	-3.1	-207.6	0.2440-02	176.9	0.2630-02	1.4	0.4160-03	1.2	0.3750-02	0.1170-02
0.0	1359.[illegible]	1[illegible].000	4.215	15.6	-244.7	0.2520-02	-179.8	0.2740-02	-2.4	0.1410-02	178.6	0.3910-02	0.1520-02
0.0	1270.0[illegible]	1[illegible].000	4.512	46.4	-277.2	0.2450-02	-177.0	0.3090-02	-5.6	0.2460-02	-177.3	0.3890-02	0.1620-02

THE PATH ANGLE IS 2.[illegible] THE WIDTH ANGLE IS 0.731 THE LOWER WIDTH IS 2.623 THE UPPER WIDTH IS 5.[illegible] SYMMETRY IS 0.471

Figure 6-31b. Sample Output Data from OUGS Program.

and ICON specifies whether or not extra information from the GTD subroutine will be printed out as follows:

ICON - 0 no extra messages
ICON - 1 full ray information
ICON - which rays exist

If ICON values of 1 or 2 are chosen, only a few receiver positions should be specified as a large amount of output for each receiver point will be produced. The remaining data lines in this section are formatted 10X, 3F10.3 and contain the x, y, z coordinates of one of the terrain profile corners, in order, going outward from the antenna mast toward the threshold. The coordinate system is shown in Figure 6-32 with z vertical and the terrain invariant in the x direction, so that the x coordinate of each edge is usually input as zero.

(2) Theodolite Data

Following the theodolite section card (2 in column 15) is one line of data containing the theodolite information. As is the case of actual RTT flight measurements, all angles are measured from the location of the theodolite eyepiece relative to horizontal. Also, for the Pattern A flyability calculations the difference between the theodolite CDI output and the CDI calculated at the receiver position is calculated and printed, and the reference path angle and width for the theodolite is input in this line of data. The format is 20X, 5F10.3; the first 3 numbers are the x, y, and z coordinates of the theodolite eyepiece, and the last two are the reference path angle and width.

(3) Antenna Data

Following the antenna data section card (3 in column 15) are the data describing the antennas. The first card describes the glide slope facility. The format of this card is 10X, I5, 5X, 4F10.3, and the card contains the number of antennas, the frequency in megahertz, the depth of modulation (as a decimal--not per cent), nominally 0.4, the A ratio, nominally 0.3 for a 3.0° path angle, and, for systems with a clearance signal, the depth of modulation for the clearance, nominally 0.9. The following data in this section consists of two lines for each antenna. The first line is formatted 10X, I5, 5X, 3F10.3, and contains the antenna number and the x, y, and z coordinates of the center of the antenna. The second line has a format 10X, 6F10.3, and contains the magnitude and phase of the complex sideband only sideband current (I_{ss}), carrier-sideband sideband current (I_{cs}), and clearance carrier current (I_{cc}), in order. The example in Figure 6-31 contains values derived from measurements; the nominal currents for the 3 common image type systems are as follows:

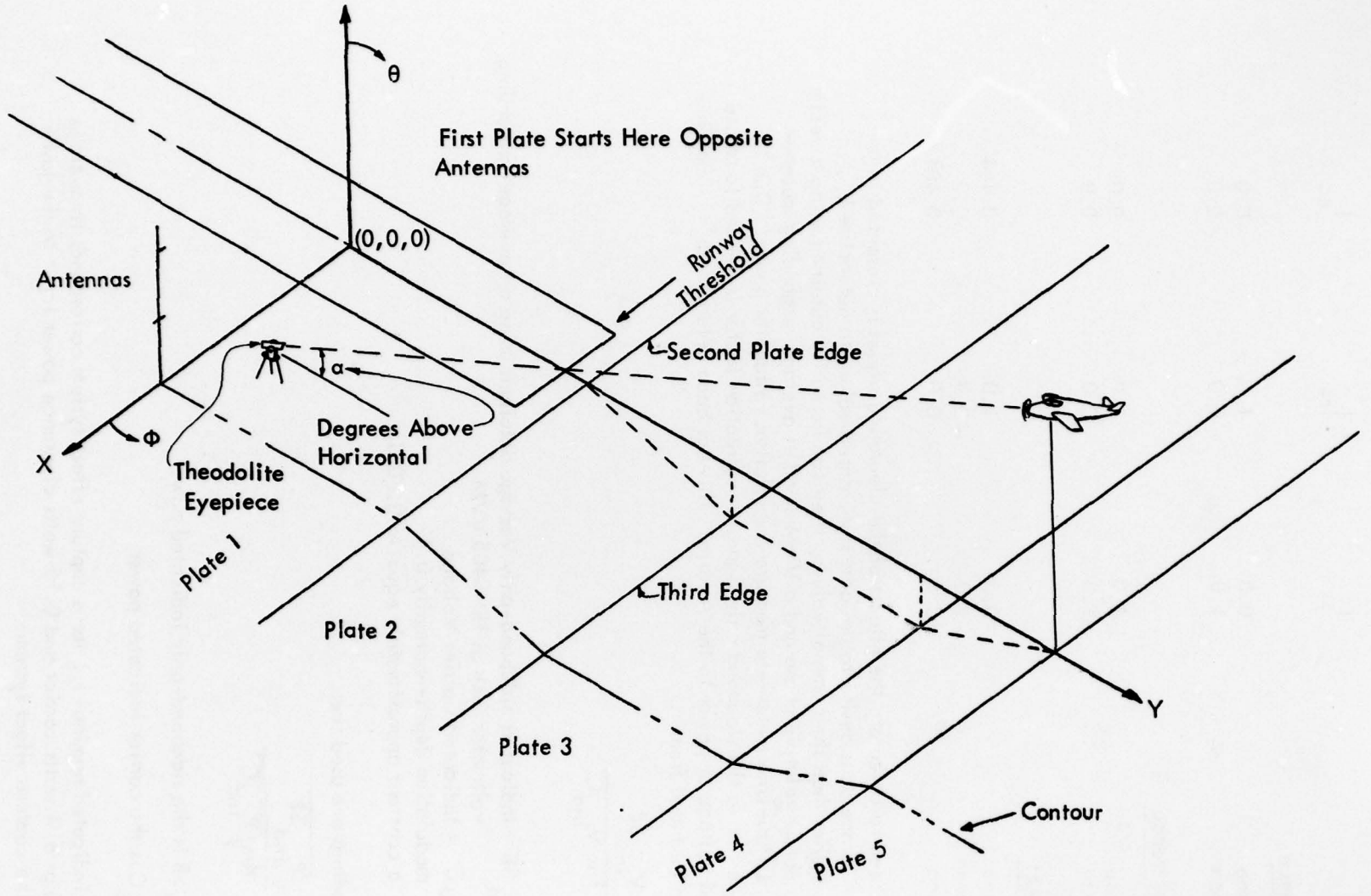

Figure 6-32. Coordinate System for Input to OUGS.

	I_{ss}	I_{cs}	I_{cc}
Null Reference			
lower antenna	0.0	1.0	0.0
upper antenna	1.0	0.0	0.0
Sideband Reference			
lower antenna	-1.0	1.0	0.0
upper antenna	1.0	0.0	0.0
Capture Effect			
lower antenna	-0.5	1.0	0.484
middle antenna	1.0	-0.5	0.0
upper antenna	-0.5	0.0	0.484

The method used to calculate the effects of the clearance signal is presented in a later section. If one does desire to use actual measured values to determine I_{ss}, I_{cs}, and I_{cc} rather than the nominal values, they can be easily obtained using a vector voltmeter to obtain relative phase and a VVM or other average responding meter--such as a Bird Thru-Line meter--to measure the relative voltage or power. Due to the lack of carrier in the sideband only signal a correction factor is needed to relate the measured voltage or power to the A ratio. This has been determined * and the A ratio can be found from

$$A = \frac{V_{ind}SB}{K m V_{ind}C}$$

where

$V_{ind}SB$ = Indicated Sideband-only Voltage obtained using an average-responding voltmeter such as HP-8405 VVM

$V_{ind}C$ = Indicated Carrier Voltage

m = modulation depth--normally 0.4

K = a constant approximately equal to 0.80235

If power readings are used then

$$A = \frac{\sqrt{P_{ind}SB}}{Km\sqrt{P_{ind}C}}$$

where

$P_{ind}SB$ is the sideband-only indicated power

$P_{ind}C$ is the carrier indicated power

The indicated nominal I_{cc} for a capture effect system corresponds to average power readings of 4 watts carrier and 0.15 watts clearance power input to the lower antenna of the capture effect system.

*See Section XI.D of this report.

(4) Pattern Data

Following the pattern section card (4 in column 5) are the input cards which control the path flown by the simulated aircraft--in other words, the receiver locations. The first line contains the information determining the type of pattern cut, the number of receiver positions where results are to be calculated, a print output option, and the coordinates of the initial receiver position. The format of this card is 10X, 3I5, 5X, 3F10.3. The second card determines the final position of the receiver and is formatted 30X, 3F10.3. The second and third numbers input on the first card do not depend on the type of cut chosen. The second number is the number of receiver positions, and the third is set equal to 0 if path angle, width, and symmetry calculations are to be made (usually only when a level run, straight line cut is chosen) and to 1 otherwise. The other input quantities depend on the type of pattern cut chosen as follows:

---Constant Radius Cut---Implemented by placing a 1 value for the first number on the first pattern card. For this cut the aircraft is simulated as flying a constant-radius vertical arc centered at the origin of the coordinate system and in the y-z plane (x=0). The first two floating point numbers on the first card contain the pattern radius and initial elevation angle measured from the origin (the elevation angle is equal to 90 - θ), and the second floating point number on the second pattern card contains the final elevation angle.

---Linear Cut---Implemented by placing a 2 in the first integer input, first card. For this cut the simulated aircraft flies in a straight line from the first position to the final one, where the x, y, and z coordinates of the first position are encoded in the floating point inputs of the first pattern card, and the x, y, and z coordinates of the final position are encoded in the second card.

---Hyperbolic Cut---The simulated aircraft will fly a hyperbolic path of constant angle alpha measured at the theodolite eyepiece with respect to horizontal when a 3 is encoded in the first position of the first card. The value of alpha is encoded in the third floating point position of the first card. The initial and final x and y coordinates are encoded in the first and second floating point positions of the two cards, with the first position coordinates on the first card.

(5) Output Control

Following the output section card (5 in column 15) is a card which controls the graphical output format. The format of this card is 10X, 3I5, 5X, 4F10.3, and the input variables and their functions are given in order as follows:

MAKTAP	0 output section bypassed
	1 Calcomp tape generated
	2 line printer plot directly following printed output
	3 both Calcomp and line printer plot

(A fifth option, a plot on the Hewlett Packard XY plotter, is available when using the POSTOUGS model discussed in the next section.)

IX	x-axis variable	1	y distance (feet)
		2	alpha angle with respect to theodolite (degrees)
IY	y-axis variable	1	CDI
		2	DCDI differential amp
		3	ET (1) magnitude of field from antenna 1
		4	ETPHA (1) phase of field from antenna 1
		5	ET(2) magnitude of field from antenna 2
		6	ETPHA (2) phase of field from antenna 2
		7	ET (3) magnitude of field from antenna 3
		8	ETPHA (3) phase of field from antenna 3
		9	ESSMAG composite magnitude of sideband only radiated fields
		10	ECSMAG composite magnitude of carrier and sideband radiated fields
		11	|CDI| absolute value of CDI

XMAX max. point on x-axis (Calcomp)
XMIN min. point on x-axis (Calcomp)
YMAX max. point on y-axis (Calcomp)
YMIN min. point on y-axis (Calcomp)

When the OUGS program is run the above described set of data is read by the program on logical unit 5. The program produces two output files. The one on unit 6 (the file is named OUGS PRINTOUT C) is shown in Figure 6-31b for the input data of Figure 6-31a. The plane data, facility data, etc., input in the data stream are organized and reproduced for identification purposes. For each receiver location the coordinates are printed and the elevation angle alpha measured from the theodolite eyepiece is calculated and printed. The next two columns contain the simulated differential amplifier CDI and the aircraft receiver CDI as calculated by the model. The next six columns contain the relative complex electric fields radiated by each antenna, magnitude and phase. The final two columns contain the magnitude of the relative carrier-sideband and sideband only signals at the receiver location. In these calculations the glide slope antennas are assumed to have a dipole pattern and the receiving antenna is assumed to be omni-directional and horizontally polarized. The last line of the output contains calculated values for path angle, width, etc., but are applicable only for level run calculations. A line printer plot of the CDI was also printed but is not reporduced here in order to save space.

The second output file produced by OUGS is on unit 10 (the file is named OUGS FILE10 C) and contains the input data and the relative complex electric fields at each receiver location for each antenna. This output can be used by the POSTOUGS program to calculate values of CDI, DCDI, etc. for glide slope systems which have the same antenna heights and terrain, and for the same set of receiver positions, but with different antenna phasing, A ratio, clearance signal, theodolite position, or with different variables plotted on the line printer plot. The advantage of this is that the electromagnetic field calculations do not need to be repeated each time one desires to change the A ratio, investigate the phasing of the antennas, etc. Since the electromagnetic calculations are the most lengthy part of the calculation time by far, this greatly increases the

efficiency of parameter investigations which do not require a change in antenna heights. In addition, the POSTOUGS program can be used to generate plots on the Modeling Center Hewlett Packard X-Y plotter. Use of the POSTOUGS program is described in the following section.

b. POSTOUGS Program. As mentioned previously in this report, the POSTOUGS program can be used in conjunction with OUGS to reduce greatly the computer running time when performing parameter studies that do not require changes in antenna heights or receiver position. Also, the POSTOUGS program can control the Hewlett-Packard X-Y plotter.

The POSTOUGS program reads input data on both units 5 and 10. The unit 10 input is the data file written previously on unit 10 by OUGS (the OUGS FILE10 C file). This file contains all of the data describing the glide slope facility which will be unchanged in the POSTOUGS calculations. The data read by POSTOUGS on unit 5 is that which can change from the OUGS calculations. An example of a POSTOUGS unit 5 input file is shown in Figure 6-33. This input file can be compared with the OUGS input file of Figure 6-31a. Comparing the two files it is evident that the terrain data and pattern data, which cannot be changed, are not included in the POSTOUGS unit 5 input file. The theodolite data, antenna currents, and output control are included. The POSTOUGS file of Figure 6-33 combined with the OUGS unit 10 output produced for the OUGS data file of Figure 6-31a will cause the POSTOUGS program to calculate glide slope information for the site described by the data of Figure 6-31a but with the A ratio changed from 0.42 to 0.38. Also, the POSTOUGS program will produce a file of data which can be plotted on the Hewlett Packard X-Y plotter rather than the line printer plot produced by OUGS. The POSTOUGS program will generate the desired data in a few seconds, while running the OUGS program again with the new A ratio would require approximately one minute of computer calculation (cpu) time.

The POSTOUGS program produces a printed putput on unit 6 which is identical with that of Figure 6-31b (the file is named POSTOUGS PRINTOUT C). It also has a unit 11 output which is read by a Hewlett Packard X-Y plotter program developed at Ohio University (the file name is POSTOUGS PLOT11 C). To use the HP plotter following execution of POSTOUGS one enters on the computer terminal:

.avplot postougs plot11 c 1

where avplot is the name of the plotting routine, postougs plot11 c is the data file to be plotted, and the number 1 plot is to be plotted. Note that if OUGS ran with several different sets of data, then POSTOUGS will also run for all of the same cases, as this information is on the unit 10 file read by POSTOUGS. Thus POSTOUGS may produce data on unit 11 for several plots.

```
THEOD                  -275.112   95.4      5.167     3.0       0.7
ANT. DATA      3       332.(       .4?       .321        .9?
CURR.      -0.5        -3.495     1.        -3.495     .484      -3.495
CURR.      1.9?        0.(        -0.5      0.9
CURR.       -0.5       4.499      0.9       0.0       .484      4.499
OUTPUT         4    2     1       4.5       0.50       3??.     -3??.
```

Figure 6-33. Sample Input Data for POSTOUGS Program.

c. Mathematical Modeling of Receiver Capture Effect. Two-frequency ILS systems are used both in localizer and glide slope installations when there is a need to keep reflections from terrain obstacles, hangars, buildings or other reflecting surfaces from disturbing the radiation patterns which guide the aircraft. In general a two frequency ILS utilizes two distinct radiation patterns resulting in two distinct DDM (difference in depth of modulation) patterns on two carrier frequencies separated by 8 KHz. The course pattern is structured so that most of its energy is concentrated in a narrow beam along the flight path of the landing aircraft. It provides guidance for the aircraft and directs a minimum of radiation to the reflecting obstacles previously mentioned. The clearance pattern is such that minimum radiation is directed along the aircraft flight angle and maximum radiation to other angles. The clearance pattern also is modulated at high DDM levels in the directions of maximum radiation (causing a strong fly left or fly right signal with the localizer and a strong fly up signal with the glide slope). The receiving antenna voltage is made up of the two signals 8 KHz apart whose relative amplitudes depend on where the receiving antenna is located in the two patterns. When one received voltage is at least ten times the magnitude of the other, the recovered DDM is very nearly the same as the DDM of the larger signal alone. The receiver is then said to be "captured" by the larger signal. Recovered DDM is a function of the signal voltage ratios, the DDM of each signal alone, the SDM (sum of the depths of modulation) of each signal alone, and the relative phase of the 90 and 150 Hz audio signals of each carrier. An approximate analytic expression can be derived which is useful in calculating the DDM for a two frequency system when the signal ratio is less than ten.

The solution for such an expression is contained in a paper by the Andrew Alford Consulting Engineers. [31] Using this work a computer subroutine was written which has been included in the OUGS program for calculating ILS antenna patterns, thus providing a calculation for DDM which includes an approximation for the capture process. Details of the expression used are given later in this section. The expression is not exactly the same as the one in the Alford paper, and the resulting expression has sufficient generality to be reduced to either the two frequency localizer or glide slope system. An example of the results obtained using the subroutine as written for the two-frequency capture effect glide slope is given in the following paragraphs.

Figure 6-34 is a graphical illustration of the change in DDM which occurs as the clearance carrier $+E_{cc}$ is increased with respect to the course carrier E_c. Plots are made for various DDM values for the course signal alone resulting in a family of curves. Notice that for carrier level ratios of 10:1 or greater the DDM approaches the value which would result from the large carrier alone. Figure 6-35 is the same kind of plot, but it points out the capability to determine how a phase change of carrier audio with respect to course audio (in this case a 180° difference) affects the DDM.

The equations used in these plots are derived using a number of assumptions. One class of assumptions requires that the receiver have certain "ideal" properties among

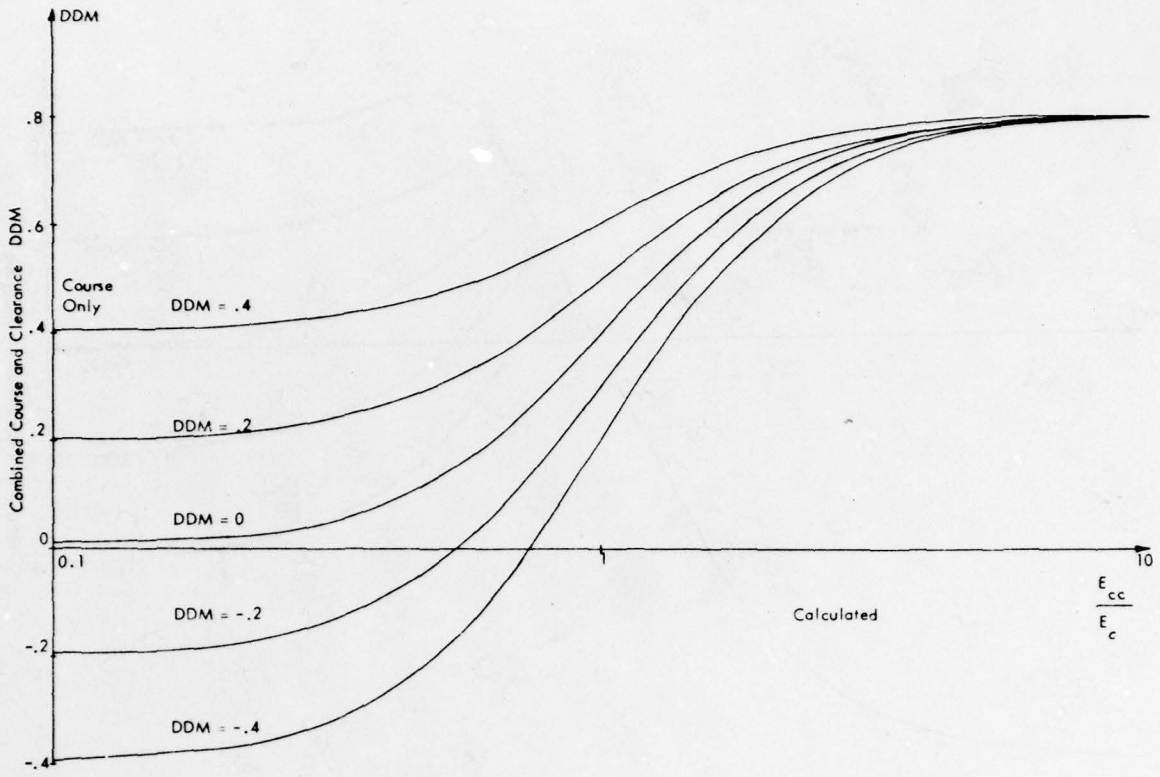

Figure 6-34. Calculated Values of DDM Versus the Ratio of the Clearance Carrier Signal (E_{cc}) to the Course Carrier Signal (E_c) for Various Values of Course Signal Only DDM. The course signal audio modulation is in phase with that of the clearance signal.

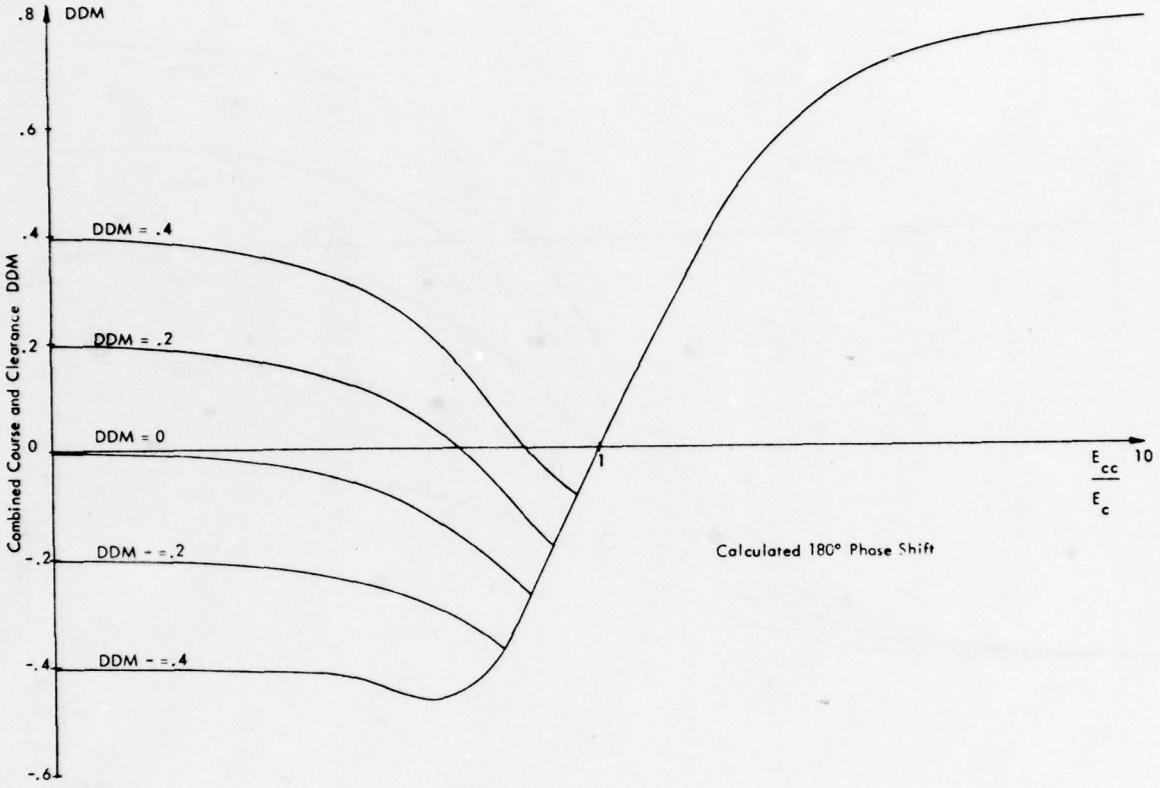

Figure 6-35. Calculated Values of DDM Versus the Ratio of the Clearance Carrier Signal (E_{cc}) to the Course Carrier Signal (E_c) for Various Values of Course Signal Only DDM. The course signal audio modulation is 180° out of phase with that of the clearance signal.

which are: an ideal linear detector which does not distort the signal, an ideal AGC (automatic gain control) which keeps a constant dc level at the output of the detector, ideal 90 and 150 Hz filters which completely separate the 90 and 150 Hz audio components, ideal detectors and summing and differencing circuits which provide dc voltages proportional to the sum and difference of the 90 and 150 Hz components for the CDI (course deviation indicator) and the FLAG. Another class of assumptions is simplifying assumptions used to make the mathematics more tractable. Laboratory experiments were set up so that the DDM families of curves calculated in Figures 6-34 and 6-35 could be duplicated experimentally. These curves taken with a Narco UGR2-A glide slope receiver, are shown in Figures 6-36 and 6-37. It is felt that there is sufficient agreement between the calculated and experimental results to warrant the use of the computer subroutine in the two frequency ILS modeling work.

The test setup is shown in Figure 6-38. The detected audio is taken from the receiver and is processed in a separate audio processor which more nearly approximates the ideal processor than does the receiver's own processor. A diagram of the audio processor is shown in Figure 6-39. The non-ideal behavior of this processor is apparent in its inability to reach 0.8 DDM when a large predominance (10:1) of clearance signal is present. This occurs because the 90 Hz filter passes some 150 Hz which subtracts from the 150 Hz filter output, thus causing an error. Figure 6-40 shows the details of the 90/150 Hz audio generation.

The mathematics representing the two frequency ILS signals is developed in a very clear manner in the paper by the Alford organization. An equation is derived (no. 42 in the paper) which gives the DDM indicated by the receiver as a function of the DDM's of the course and clearance signals alone and the ratio of the carrier levels of the clearance and course signals. This equation is given below for reference.

$$DDM = \frac{d + .2546\, q^2 [2\bar{d} - d]}{1 + .2546\, q^2 [1 + \frac{1}{4}(d-\bar{d})^2]} \qquad (6.11)$$

where

d = DDM of larger carrier
$\bar{d}$ = DDM of smaller carrier
$q = \frac{\text{smaller carrier amplitude}}{\text{larger carrier amplitude}}$

This equation can be used to produce a family of curves like those in Figure 6-41. The DDM is calculated up to $E_{cc}/E_c < 1$ with $q = E_{cc}/E_c$

d = DDM of course signal
$\bar{d}$ = DDM of clearance signal

For $E_{cc}/E_c > 1$ with $q = E_c/E_{cc}$

d = DDM of clearance signal
$\bar{d}$ = DDM of course signal

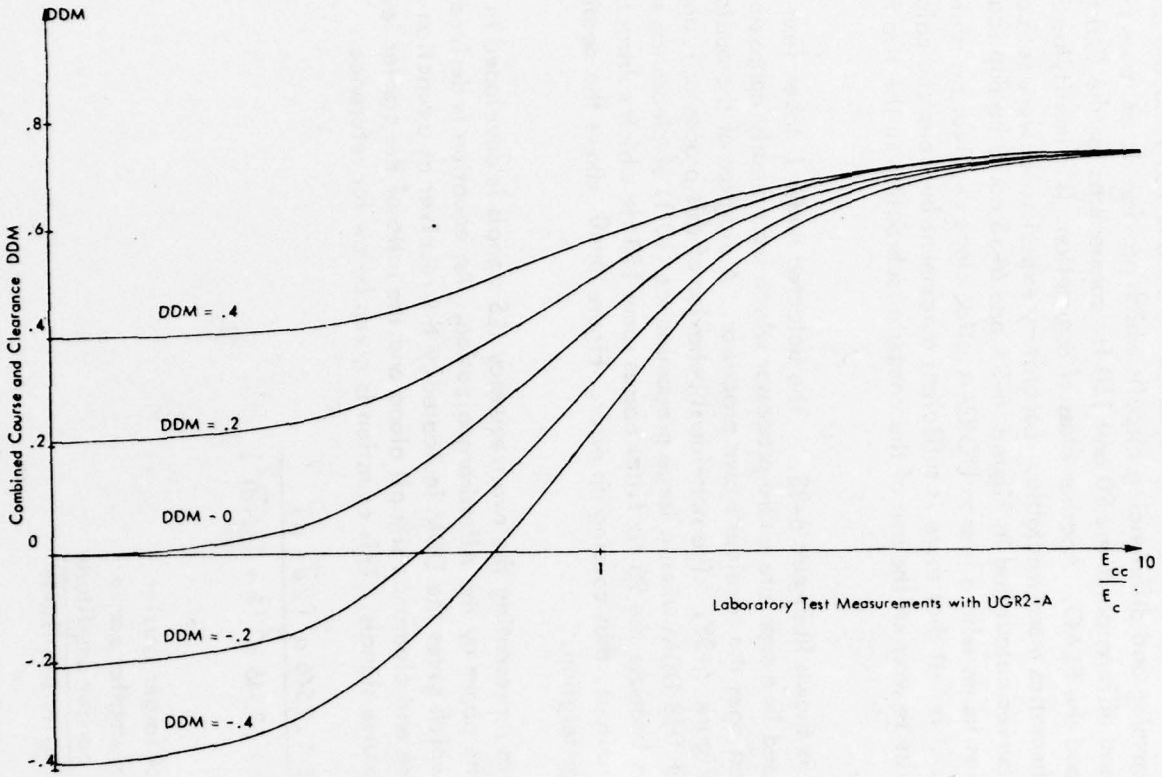

Figure 6-36. Measured Values of DDM Versus the Ratio of the Clearance Carrier Signal (E_{cc}) to the Course Carrier Signal (E_c) for Various Values of Course Signal Only DDM. The course signal audio modulation is in phase with that of the clearance signal.

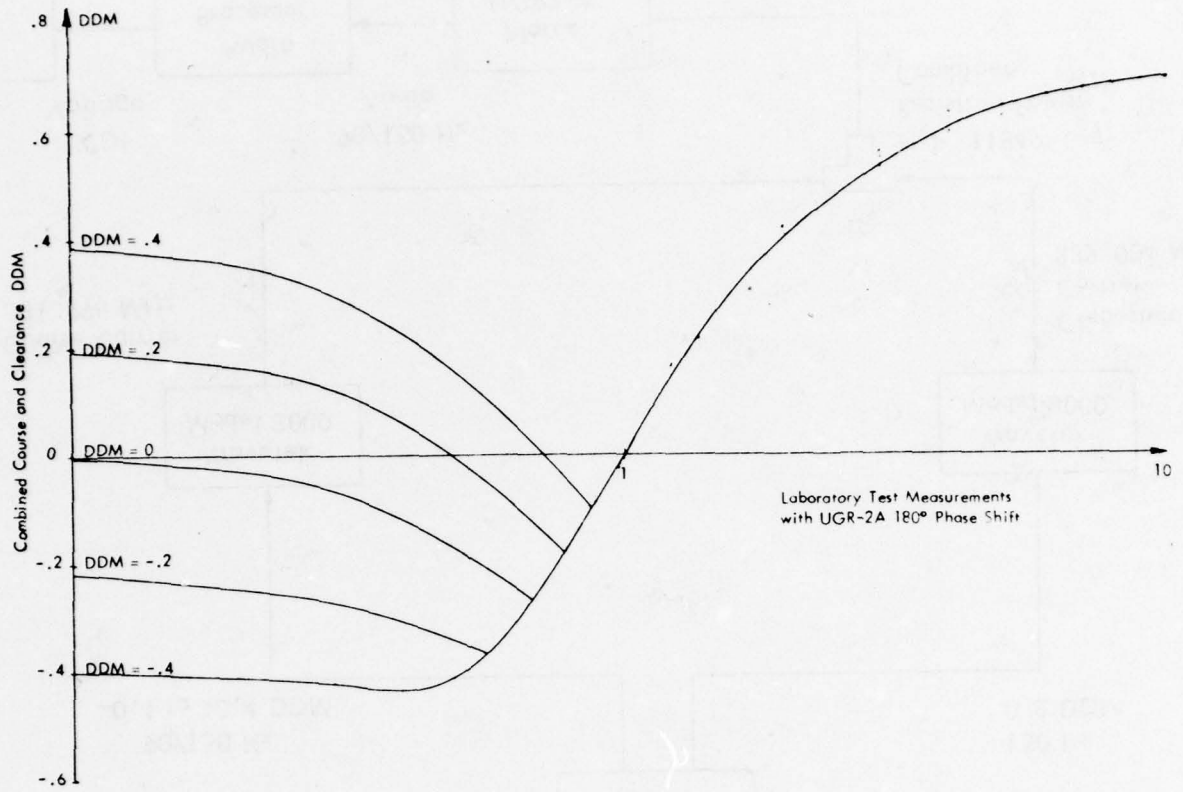

Figure 6-37. Measured Values of DDM Versus the Ratio of the Clearance Carrier Signal (E_{cc}) to the Course Carrier Signal (E_c) for Various Values of Course Signal Only DDM. The course signal audio modulation is 180° out of phase with that of the clearance signal.

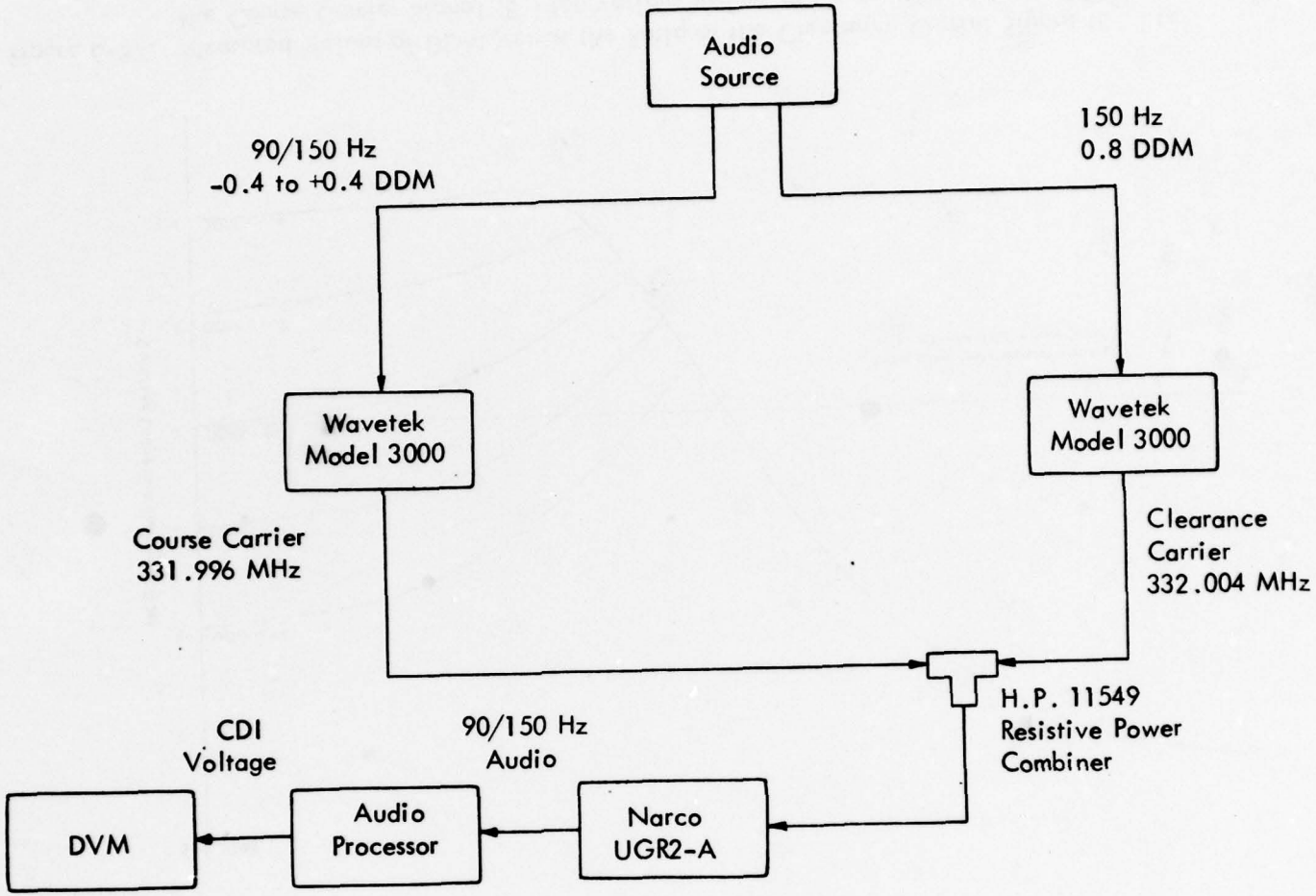

Figure 6-38. Block Diagram of the Experimental Setup Used to Obtain the Measured Curves of Figures 6-36 and 6-37. The Audio Processor is shown in Figure 6-39 and the Audio Source in Figure 6-40.

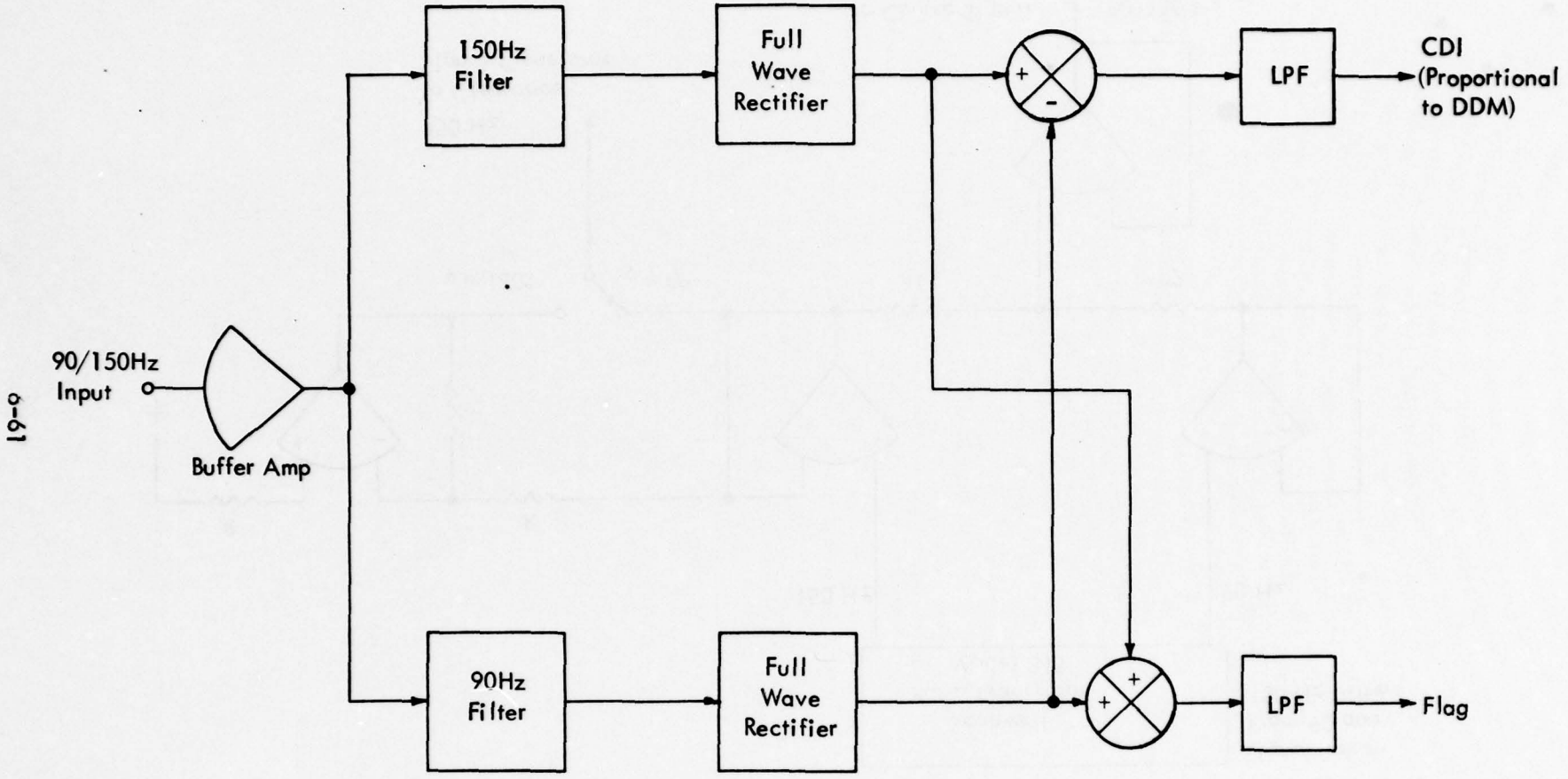

Figure 6-39. Block Diagram of the Audio Processor Used to Obtain the Values of DDM Shown in Figures 6-36 and 6-37 and Indicated in the Block Diagram of Figure 6-38.

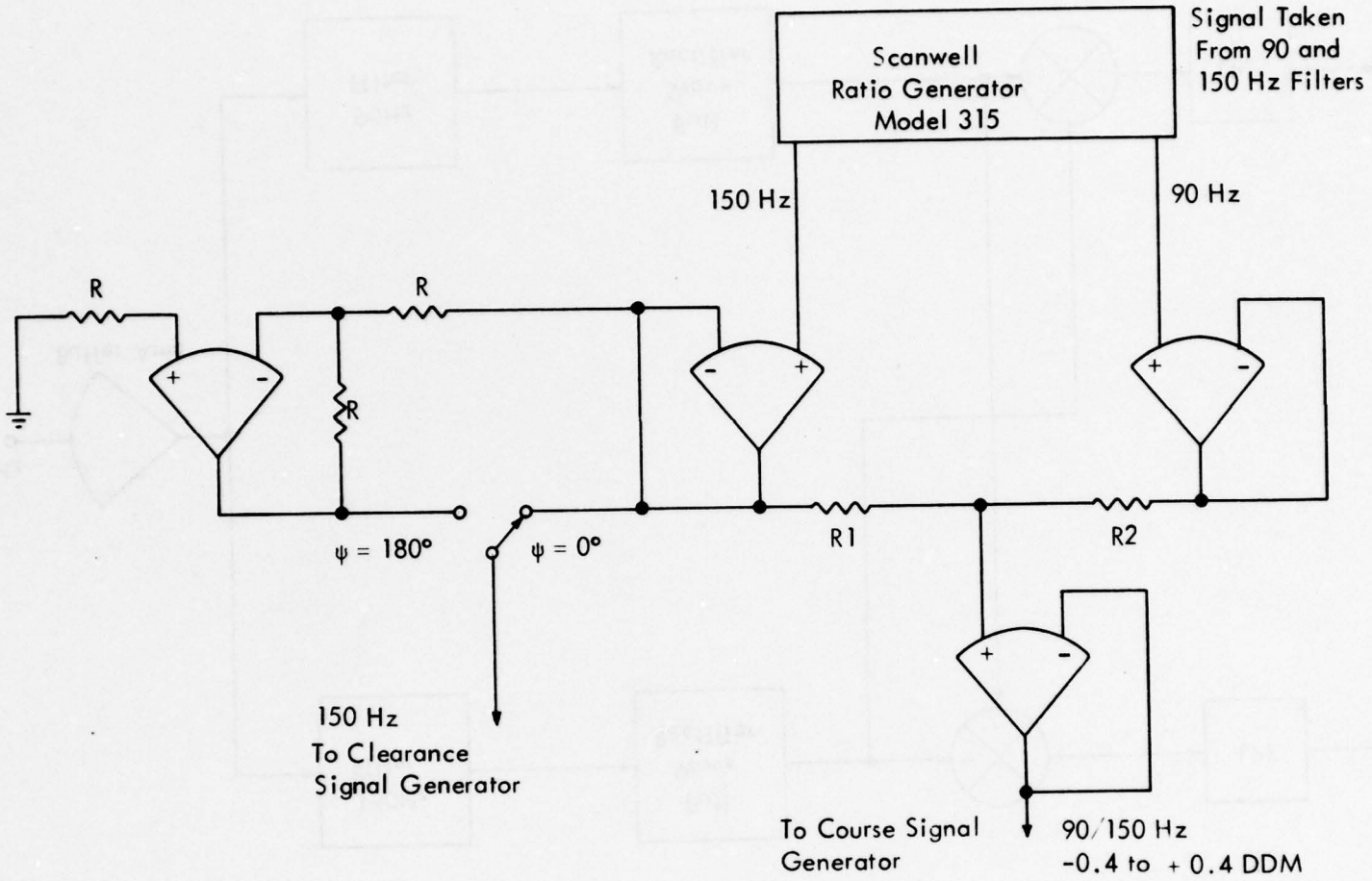

Figure 6-40. Circuit Schematic of the Audio Source Used to Obtain the Values of DDM Shown in Figures 6-36 and 6-37 and Indicated in the Block Diagram of Figure 6-38.

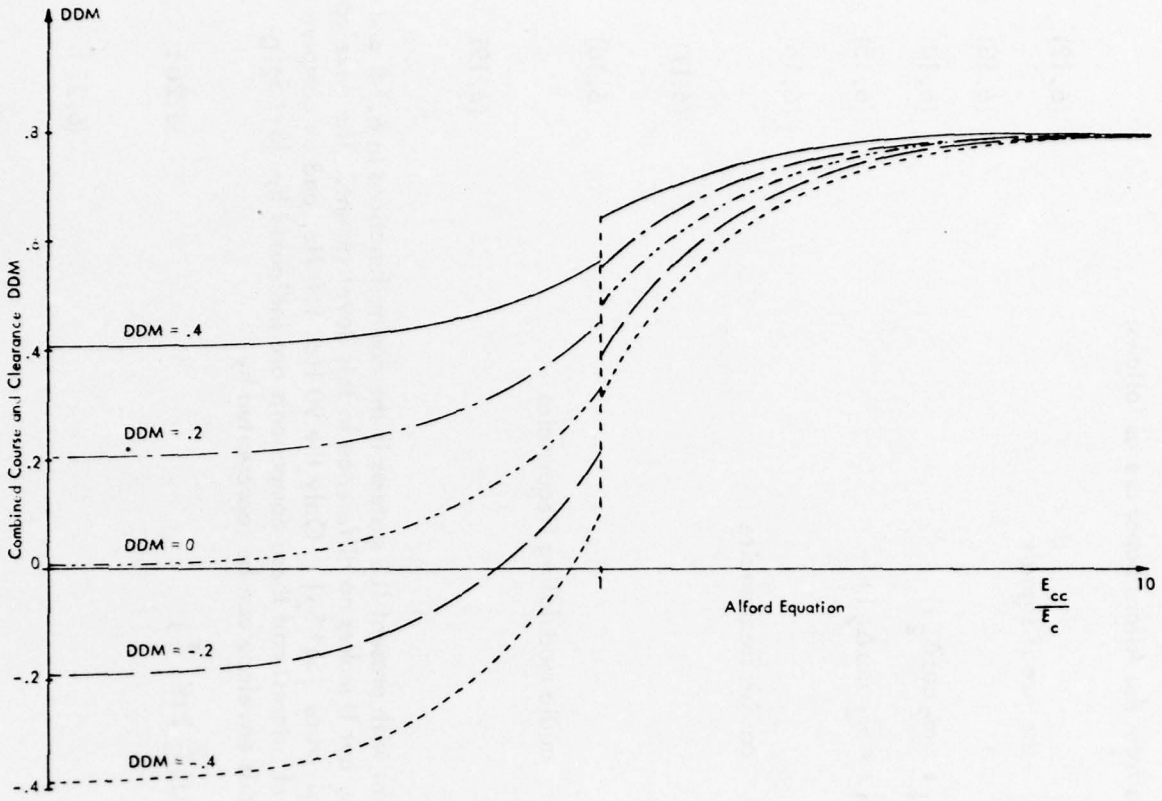

Figure 6-41. Calculated Values of DDM Versus the Ratio of the Clearance Carrier Signal (E_{cc}) to the Course Carrier Signal (E_c) for Various Values of Course Signal DDM Calculated Using the Alford Equation. The course signal audio modulation is in phase with that of the carrier signal.

These curves are shown in Figure 6-4 and it can be seen that there is a discontinuity at $E_{cc}=E_c$. The discontinuity is caused by an approximation used in the development of the equation. A slightly different development with a different approximation is used here to produce an equation which does not have this discontinuity and which in addition is a function of the audio phase.

Defining equations from the Alford paper are as follows:

$$S_1 = A \cos \omega_1 t \qquad (6.12)$$

$$S_2 = B \cos \omega_2 t \qquad (6.13)$$

the two rf signals

$$A = a(1 + m_1 \cos \Delta_1 t + m_2 \cos \Delta_2 t) \qquad (6.14)$$

$$B = b(1 + \bar{m}_1 \cos \Delta_1 t + \bar{m}_2 \cos \Delta_2 t) \qquad (6.15)$$

$$f_1 = \frac{\omega_1}{2\pi} \qquad (6.16)$$

carrier frequencies

$$f_2 = \frac{\omega_2}{2\pi} \qquad (6.17)$$

$$f_{90} = \frac{\Delta_1}{2\pi} \qquad (6.18)$$

audio modulating frequencies

$$f_{150} = \frac{\Delta_2}{2\pi} \qquad (6.19)$$

It would be more consistent with present ILS systems if the cosine functions in (6.14) and (6-15)were sine functions, but it makes no difference in this development. The envelope after linear detection is given as $|S_1+S_2|$. Only the 90 Hz, 150 Hz, and dc components of this envelope are of interest and these components are indicated by $|S_1+S_2|_0$. The Alford papers show this envelope can be represented by

$$|S_1+S_2|_0 = A(1+U)\frac{2}{\pi} E(K, \frac{\pi}{2}) \qquad (6.20)$$

where

$$U = \frac{B}{A} \qquad (6.21)$$

$$K^2 = \frac{4U}{(1+U)^2} \qquad (6.22)$$

and $E(K, \frac{\pi}{2})$ is the complete elliptic integral of the second kind of modulus K.

In the Alford paper an approximation

$$1 + .2546\,U^2 \simeq (1+U)\frac{2}{\pi}\,E\left(K, \frac{\pi}{2}\right) \tag{6.23}$$

is substituted into (6-20) and further simplification results in (6-11). Another approach is to recognize that

$$E\left(K, \frac{\pi}{2}\right) = \frac{\pi}{2}\left[1 - \left(\frac{1}{2}\right)^2 K^2 - \left(\frac{1\cdot 3}{2\cdot 4}\right)^2 \frac{K^4}{3} - \left(\frac{1\cdot 3\cdot 5}{2\cdot 4\cdot 6}\right)^2 \frac{K^6}{5} - \ldots\right] \text{ if } K^2 < 1 \tag{6.24}$$

and substitute into (6.20).

From (6.21) and (6.22) we have

$$K^2 = \frac{4AB}{(A+B)^2} \tag{6.25}$$

Now letting $A = a(1+f)$ and $B = b(1+g)$ and substituting into (6.25) we obtain, after minor simplification,

$$K^2 = \frac{4ab}{(a+b)^2}\,\frac{1+f+g+fg}{1+2\left(\frac{af}{a+b}+\frac{bg}{a+b}\right)+\left(\frac{af}{a+b}+\frac{bg}{a+b}\right)^2} \tag{6.26}$$

Keeping the first three terms of the binomial series approximation (for $\frac{1}{1+x}$) to the denominator of (6-26), we have

$$K^2 \simeq \frac{4ab}{(a+b)^2}\,(1+f+g+fg)\left[1 - 2\left(\frac{af}{a+b}+\frac{bg}{a+b}\right)+\left(\frac{af}{a+b}+\frac{bg}{a+b}\right)^2\right]$$

Multiplying and keeping first order modulation terms results in

$$K^2 \simeq \frac{4ab}{(a+b)^2}\left(1 + \frac{b-a}{a+b}\,f + \frac{a-b}{a+b}\,g\right) \tag{6.27}$$

Let

$$q = \frac{b}{a} \tag{6.28}$$

and substitute into (6.27) to obtain

$$K^2 = \frac{4q}{(1+q)^2}\left[1 + \frac{1-q}{1+q}\,(g-f)\right] \tag{6.29}$$

Equation (6.29) is now substituted into (6.24) where terms up to K^8 only are retained. When K^2 is expanded in the power series, only the constant and first order modulation

terms are kept. Defining

$$C_1 = \left(\frac{1}{2}\right)^2 \quad C_2 = \left(\frac{1\cdot 3}{2\cdot 4}\right)^2 \quad C_3 = \left(\frac{1\cdot 3\cdot 5}{2\cdot 4\cdot 6}\right)^2 \quad C_4 = \left(\frac{1\cdot 3\cdot 5\cdot 7}{2\cdot 4\cdot 6\cdot 8}\right)^2$$

we obtain

$$E(K, \tfrac{\pi}{2}) = \frac{\pi}{2}\left\{1 - C_1\frac{q}{(1+q)^2} - C_2\left[\frac{q}{(1+q)^2}\right]^2 - C_3\left[\frac{q}{(1+q)^2}\right]^3 - C_4\left[\frac{q}{(1+q)^2}\right]^4 - (g-f)\left(\frac{1-q}{1+q}\right)\left[C_1\frac{q}{(1+q)^2} + 2C_2\left[\frac{q}{(1+q)^2}\right]^2 + 3C_3\left[\frac{q}{(1+q)^2}\right]^3 + 4C_4\left[\frac{q}{(1+q)^2}\right]^4\right]\right\} \tag{6.30}$$

which can be simplified using the self-evident D notation as

$$E(K, \tfrac{\pi}{2}) = \frac{\pi}{2}\{1 - D_1 - D_2 - D_3 - D_4 - (g-f)\left(\frac{1-q}{1+q}\right)[D_1 + 2D_2 + 3D_3 + 4D_4]\}$$

or further simplified to

$$E(K, \tfrac{\pi}{2}) = \frac{\pi}{2}\left[D_D - (g-f)\left(\frac{1-q}{1+q}\right)(D_N)\right] \tag{6.31}$$

Equation (6.20) can be written

$$\left|S_1 + S_2\right|_0 = (A+B)\frac{2}{\pi}E(K, \tfrac{\pi}{2})$$

or

$$\left|S_1 + S_2\right|_0 = [a(1+f) + b(1+g)]\frac{2}{\pi}E(K, \tfrac{\pi}{2})$$

Using the above approximation to $E(K, \frac{\pi}{2})$ this becomes

$$\left|S_1 + S_2\right|_0 = [a(1+f) + b(1+g)]\left[D_D - (g-f)\left(\frac{1-q}{1+q}\right)D_N\right]$$

$$= (a+b)D_D + (af+bg)D_D + ag\left(\frac{1-q}{1+q}\right)D_n + afg\left(\frac{1-q}{1+q}\right)D_n$$

$$+ bg\left(\frac{1-q}{1+q}\right)D_N + bg^2\left(\frac{1-q}{1+q}\right)D_N - af\left(\frac{1-q}{1+q}\right)D_N$$

$$- af^2\left(\frac{1-q}{1+q}\right)D_N - bf\left(\frac{1-q}{1+q}\right)D_N - bfg\left(\frac{1-q}{1+q}\right)D_N$$

which can be simplified, after dropping higher order modulation terms, to

$$\left|S_1 + S_2\right|_0 = (a+b)D_D \{1 + [\frac{1}{1+q} - (\frac{1-q}{1+q})\frac{D_N}{D_D}](m_1 \cos\Delta_1 t + m_2 \cos\Delta_2 t)$$

$$+ [\frac{q}{1+q} + (\frac{1-q}{1+q})\frac{D_N}{D_D}](\bar{m}_1 \cos\Delta_1 t + \bar{m}_2 \cos\Delta_2 t)\} \qquad (6.32)$$

One now sees how the depth of modulation in terms of the detected envelope is dependent upon the depth of modulation of the original carriers (i.e.: $m_1, m_2, \bar{m}_1, \bar{m}_2$) and the relative amplitudes of the two original carriers as represented by q. The two 90 Hz components can be summed and the two 150 Hz components can be summed to find the depth of modulation of 90 Hz, and the depth of modulation of 150 Hz. The difference is, of course, ddm.

$$M_{90} = [\frac{1}{1+q} - (\frac{1-q}{1+q})\frac{D_N}{D_D}]m_1 + [\frac{q}{1+q} + (\frac{1-q}{1+q})\frac{D_N}{D_D}]\bar{m}_1$$

$$M_{150} = [\frac{1}{1+q} - (\frac{1-q}{1+q})\frac{D_N}{D_D}]m_2 + [\frac{q}{1+q} + (\frac{1-q}{1+q})\frac{D_N}{D_D}]\bar{m}_2$$

$$ddm = M_{150} - M_{90} = [\frac{1}{1+q} - (\frac{1-q}{1+q})\frac{D_N}{D_D}]d + [\frac{q}{1+q} + (\frac{1-q}{1+q})\frac{D_N}{D_D}]\bar{d} \qquad (6.33)$$

where

$$d = m_2 - m_1 \qquad (6.34)$$

and

$$\bar{d} = \bar{m}_2 - \bar{m}_1 \qquad (6.35)$$

Equation (6.33) relates the ddm resulting from the two carriers to the ddm of each carrier alone (d and $\bar{d}$) and the ratio of the two carrier levels, q. This equation can be applied to either localizer or glide slope two frequency systems. With the localizer, for instance, d can be the ddm calculated at a given observation point for the course signal, $\bar{d}$ would then be the ddm calculated for the same observation point for the clearance signal and q would be the ratio of the magnitudes of the electric fields at the observation point (or the ratio of the voltages produced on an antenna at the observation point by the two signals). A similar situation exists with the capture effect glide slope except that the ddm of the clearance signal does not vary as a function of angle. The clearance carrier is modulated only with 150 Hz so the $\bar{d}$ in this case is a constant equal to the depth of modulation of the 150 Hz on the clearance carrier.

It is possible to re-write (6.33) for the capture effect glide slope to calculate the effect of varying the phase of the 150 Hz signal on the clearance carrier with respect to the 150 Hz on the course carrier. It might be desirable to make calculations to simulate transmitter faults which would result in such a phase shift. To accomplish this the two 150 Hz components in the detected envelope must be added as phasor quantities rather than scalars.

$$ddm = \left\{ \left[\left[\frac{1}{1+q} - \left(\frac{1-q}{1+q} \right) \frac{D_N}{D_D} \right] m_2 + \left[\frac{q}{1+q} + \left(\frac{1-q}{1+q} \right) \frac{D_N}{D_D} \right] \bar{m}_2 \cos \psi \right]^2 \right.$$
$$\left. + \left[\left[\frac{q}{1+q} + \left(\frac{1-q}{1+q} \right) \frac{D_N}{D_D} \right] \bar{m}_2 \sin \psi \right]^2 \right\}^{\frac{1}{2}} - \left[\frac{1}{1+q} - \left(\frac{1-q}{1+q} \right) \frac{D_N}{D_D} \right] m_1 \qquad (6.36)$$

Notice that $\bar{m}_1$ does not appear in (6.36). This is because there is no 90 Hz modulation on the clearance carrier for the capture effect glide slope. It may be more convenient to write (6.35) in terms of the ddm of the course signal. This may be accomplished by recalling that:

$$d = m_1 - m_2 \qquad (6.34) \quad \text{and} \quad 2m = m_1 + m_2 \qquad (6.37)$$

where m is the nominal depth of modulation of each audio frequency on the carrier (normally m = 0.4). From (6.34) and (6.37) we have

$$m_1 = \frac{2m + d}{2} \qquad (6.38)$$

and

$$m_2 = \frac{2m - d}{2} \qquad (6.39)$$

Substituting (6.38) and (6.39) into (6.36) and defining $\bar{m}_2 = M_{c150}$, the depth of modulation of the 150 Hz on the clearance carrier, we obtain for the capture effect glide slopes:

$$ddm = \left\{ \left[\left[\frac{1}{1+q} - \left(\frac{1-q}{1+q} \right) \frac{D_N}{D_D} \right] \left(\frac{2m+d}{2} \right) + \left[\frac{q}{1+q} + \left(\frac{1-q}{1+q} \right) \frac{D_N}{D_D} \right] M_{c150} \cos \psi \right]^2 \right.$$
$$\left. + \left[\left[\frac{q}{1+q} + \left(\frac{1-q}{1+q} \right) \frac{D_N}{D_D} \right] M_{c150} \sin \psi \right]^2 \right\}^{\frac{1}{2}} - \left[\frac{1}{1+q} - \left(\frac{1-q}{1+q} \right) \frac{D_N}{D_D} \right] \left(\frac{2m-d}{2} \right) \qquad (6.40)$$

Equation (6.40) is the one used in the OUGS glide slope model, and in the plots of Figures 6-34 and 6-35. It does not have the discontinuities of the Alford expression, but averages the discontinuity as can be seen by comparing Figures 6-34 and 6-41.

An expression for SDM (sum of the depths of modulation) which is proportional to the Flag current, can easily be developed with the equations derived thus far.

8. ILS Modeling Center Facilities. The establishment of the ILS Modeling Center at Ohio University has been concerned not only with the development, programming, and validation of the computer software models themselves, but has also involved obtaining the computer support equipment necessary for the efficient use of the models and organizing this equipment so that a minimum amount of man-hours is expended in modeling ILS sites on the computer. At the present time a very complete and efficient combination of computer main frame and peripheral input/output devices has been established and is available to the Avionics Engineering Center for ILS modeling purposes.

The main computer available to the Modeling Center is the Ohio University IBM 370/158 computer. This computer mainframe is used very efficiently in a time shart mode by virtue of being controlled by the IBM VM/370 operating system. The ILS Modeling Center has access to this mainframe via 7 direct lines, so that simultaneous modeling work may be performed by different staff engineers without interference. In addition to these direct lines, several telephone dial-up access lines exist, so that Modeling Center staff have access to the computer when at home or even when out of town if necessary.

The ILS computer models, input data, and important output data are stored on 14 cylinders of an IBM 3350 disk drive. These files are protected from unauthorized access by frequently-changed passwords. In addition, the contents are periodically copied to magnetic tape so that a recent permanent copy of the computer models and data is always available. The computer mainframe and disk drives are located in the Ohio University computer center and are maintained by the Computer Center staff.

Located in the same building as the Modeling Center (Clippinger Laboratories), but not in the actual Modeling Center itself, is a Harris Remote Job Entry Station. This device is connected to the IBM 370/158 and is capable of reading card input at 300 cards/minute and printing output at a rate of 300 lines/minute.

The most frequently used Modeling Center computer terminal is the Digital Equipment Corporation Decwriter II and Hewlett-Packard 7203A graphic plotter shown in Figure 6-42. The terminal produces printed output at a rate of 30 characters per second, and is directly connected to the IBM 370/158 main computer. The plotter is connected to the Decwriter terminal. While the Calcomp plotter had been available previously, the necessity of producing a tape, obtaining the tape from the Computer Center and mounting it on the Calcomp plotter made plotting quite inefficient. The HP plotter connected directly to the Decwriter terminal is a much more efficient system and the Calcomp plotter is rarely used at this time.

In addition to the Decwriter terminal there are two other printing teletype terminals which are available. These print at a rate of 10 characters per second. In addition, four CRT display terminals (ITT Asciscopes) are available. These may either be connected to the main computer using one of the direct line connections or may be connected via a dial-up line and the telephone handset plugged into a built-in acoustic

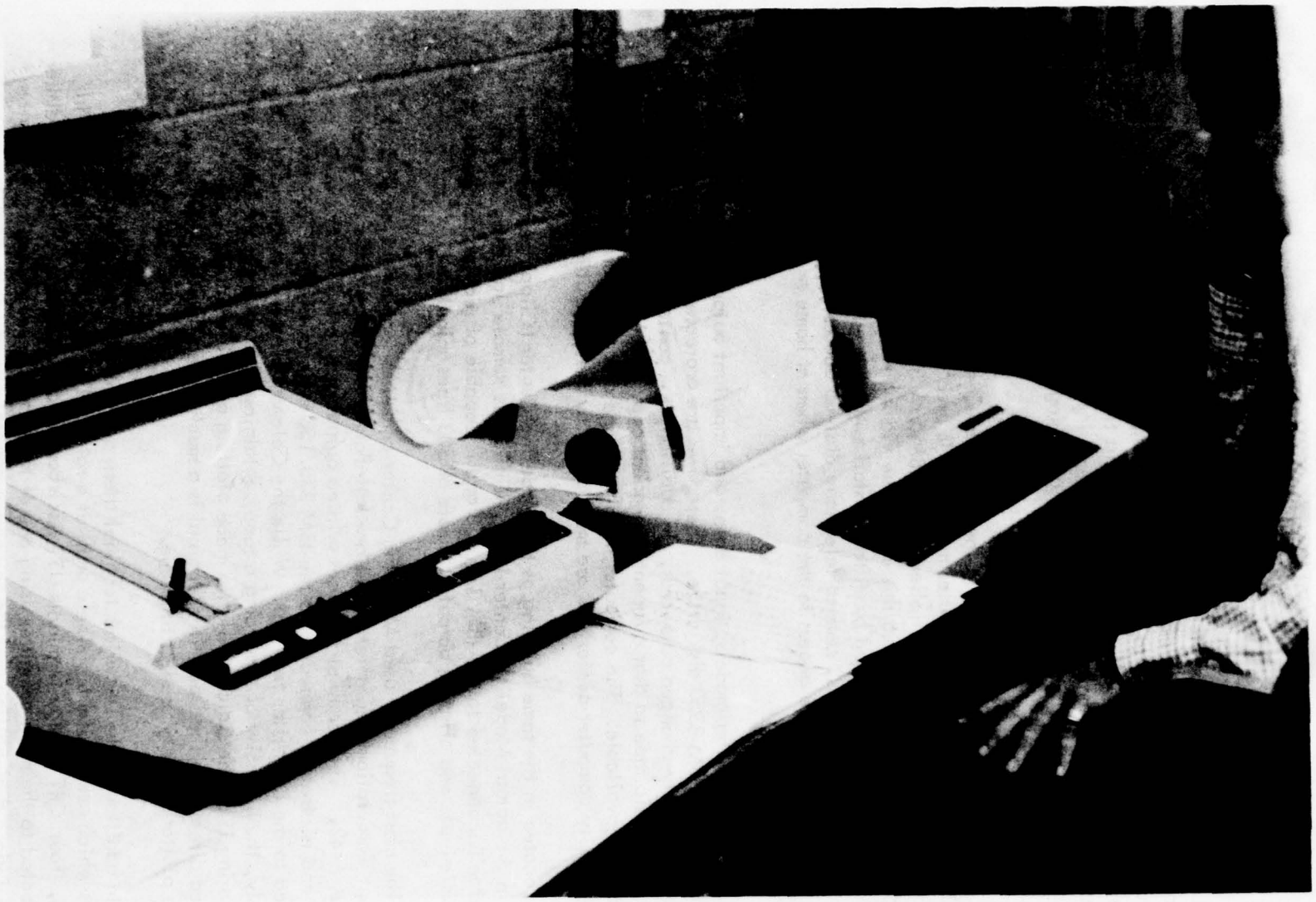

Figure 6-42. Digital Decwriter II 30 Character/Second Terminal and Hewlett-Packard 7203A Graphic Plotter Being Used by a Research Engineer in the ILS Modeling Center.

coupler in the top of the Asciscope. These terminals are portable and may be used at home or other remote locations when necessary. They are capable of 30 characters per second output. One 120 character-per-second terminal is available.

The above facilities are either located in the Modeling Center or are readily available, and insure that the computer modeling can be performed as efficiently as possible within the present state-of-the-art.

9. Summary. An ILS Modeling Center has been established at Ohio University. At this center the most advanced computer models for predicting the effects of non-uniform terrain and reflections from hangars and other objects on the performance of ILS glide slope and localizer have been collected and implemented on the Ohio University IBM 370/158 computer.

The effects of terrain on glide slope performance can be predicted using several different models. The model developed by Transportation Systems Center has been made operational on the Modeling Center computer. In addition, the basic electromagnetic subroutines of this model have been combined with a new model, based on the Geometrical Theory of Diffraction, which has been developed at Ohio University under this effort. Combined in a program called OUGS, this combination of glide slope terrain effect modeling is the most powerful and efficient available. This model has been validated with FAA flight measurements taken at Kodiak, Alaska and has also been used to predict the performance of a capture effect system there.

The effects of buildings and other scatterers on ILS localizer performance can be predicted using the TSC localizer model. This model has been validated by TSC and is currently operational on the Modeling Center computer. Predictions of localizer performance at Denver, Stapleton and Hoquiam, Washington, have been made by Ohio University using this model.

In addition to the above models other special purpose models are available in the Modeling Center in card form but have not yet been made operational on its computer. One example of this type of model is one capable of calculating the effects of large aircraft parked near a glide slope or localizer antenna on the system performance.

An efficient and complete set of computer peripherals, such as I/O terminals, disk storage devices and a graphical plotter, has been assembled and organized so that the computer models may be used efficiently and the results displayed quickly and accurately.

B. Theoretical Models Applied to the Kodiak, Alaska Glide Slope.

1. Airfield Geometry. The glide slope facility at Kodiak, Alaska presents a difficult siting problem. A significant portion of the reflecting surface illuminated by the glide slope antenna is ocean, and thus the path angle is affected by the tide level. This effect is increased over that which would normally be encountered since:

(a) Tidal variations in Alaska are large.

(b) The choice of low path angles--approximately 2°--means higher antennas and thus greater illumination of the ocean.

Thus far both null reference and sideband reference systems have been site-tested at Kodiak. The null reference system had objectionably large tidal variations of path angle, and the sideband reference system presents monitoring difficulties in the Alaskan environment.

The purpose of this study is to predict the performance of a proposed capture effect system by using mathematical modeling. However, in order to build confidence in the model, calculated results for the two systems already tried are also given and compared with measured data.

The Kodiak airfield was modeled as shown in Figure 6-43. The model extends "infinitely" far in the +y and -y directions and in the -x direction; i.e., no ground variations in these directions are included. The 400 foot antenna offset is included in the Physical Optics flyability calculations. Otherwise the ground model is essentially 2-dimensional and has not been varied, except for the tidally affected distance d, throughout the work reported here. The ocean surface is assumed to be flat, which is a good approximation for the grazing incidence angles encountered, and the ground and ocean are assumed perfectly conducting.

The frequency for all calculations is 330.8 MHz, with the corresponding wavelength being 2.97 feet. The A ratio for all calculations is 0.289.

2. Calculated Results for Null Reference and Sideband Reference Systems Compared with Flight Measurements. In order to build confidence in the modeling techniques, calculations of path angle, path width, and path symmetry for high, mean, and low tide levels were performed for the null reference and sideband reference systems for which measurements were available. The calculations are valid at large distances from the facility; i.e., ~30,000 feet or more from touchdown. In order to compare the two methods, most of the calculations were done twice, once with a program furnished to Ohio by Transportation Systems Center (TSC), and again using a program developed by Ohio University personnel. Since the TSC program and the OU program are entirely different and are based on different electromagnetic techniques and assumptions, agreement between the two would be a strong indication that accurate results were being obtained by both programs.

The results obtained are compared in Tables 6-2 and 6-3. While the agreement is not exact, it is quite good and, in most cases, is within measurement accuracy tolerances. In Table 6-3 the symmetry factor S is given by:

$$S = \frac{\alpha_u - \alpha_p}{\alpha_u - \alpha_l}$$

where α_p is the path angle, α_u is the upper 75 μA width angle, and α_l is the lower 75 μA width angle, so that $\alpha_u - \alpha_l$ is the path width. This symmetry factor S gives a direct measure

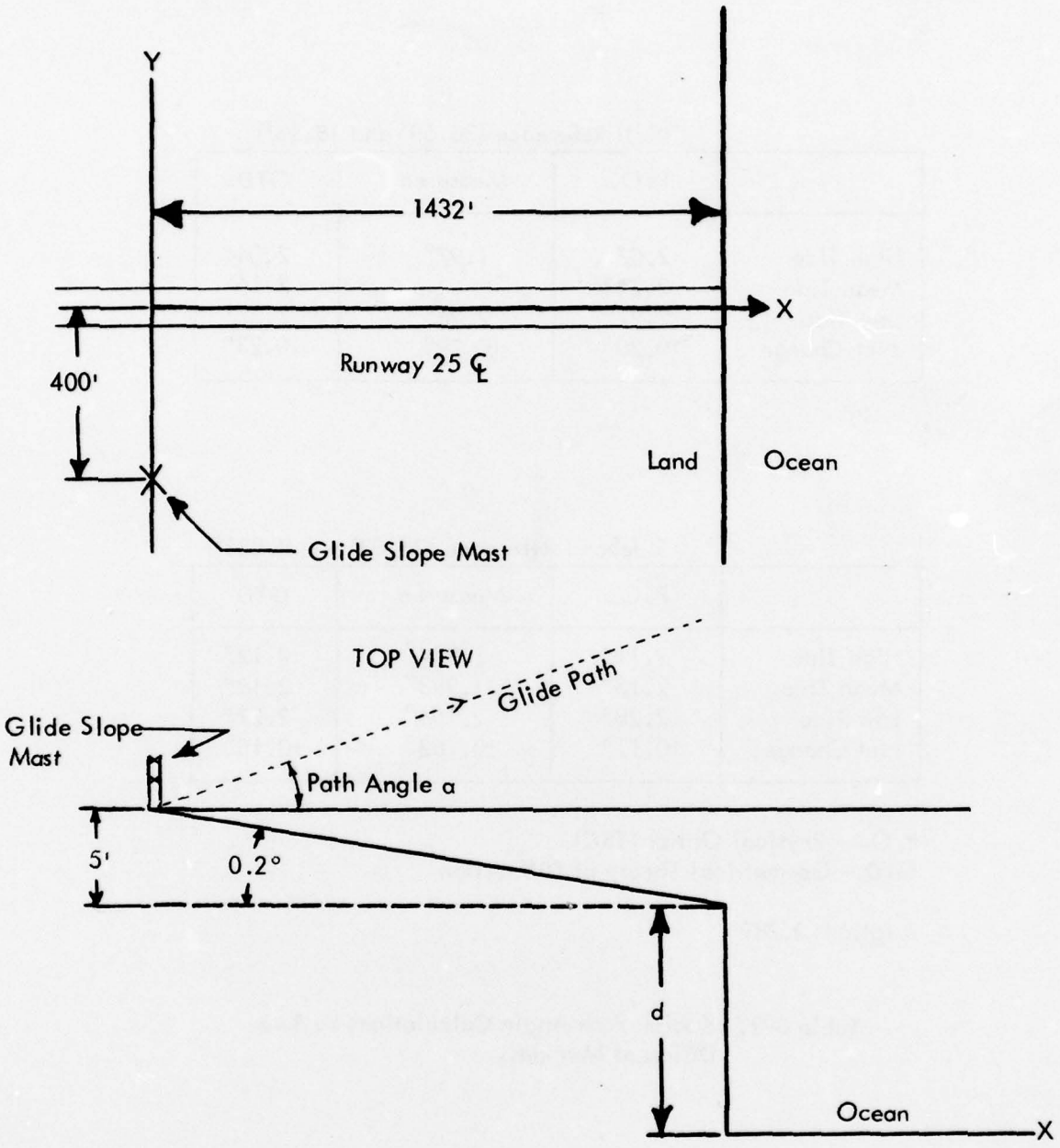

	d
High Tide	8.9'
Mean Tide	15'
Low Tide	21.6'

Figure 6-43. Model of Kodiak Airfield.

Null Reference (36.68' and 18.34')

	P.O.	Measured	GTD
High Tide	2.07°	1.97°	2.04°
Mean Tide	2.24°		2.14°
Low Tide	2.27°	2.26°	2.27°
Net Change	+0.20°	+0.29°	+0.23°

Sideband Reference (28.03' and 8.833')

	P.O.	Measured	GTD
High Tide	2.11°	1.944°	2.12°
Mean Tide	2.18°	1.993°	2.18°
Low Tide	2.28°	2.106°	2.27°
Net Change	+0.17°	+0.162°	+0.15°

P.O. - Physical Optics (TSC)
GTD - Geometrical Theory of Diffraction

A ratio = 0.289

Table 6-2. Kodiak Path Angle Calculations by Two Different Methods.

Null Reference (36.68' and 18.34')

	P.O.		Measured		GTD	
	α_w	S	α_w	S	α_w	S
High Tide	0.50°	.563			0.70°	.58
Mean Tide	0.88°	.352			0.90°	.47
Low Tide	0.57°	.351			0.85°	.32

Sideband Reference (27.03' and 8.833')

	P.O.		Measured	GTD	
	α_w	S	α_w	α_w	S
High Tide	0.68°	.559	.68°	.66°	.541
Mean Tide	0.81°	.457	.86°	.78°	.481
Low Tide	0.76°	.276	.94°	.73°	.390

A ratio = 0.289

Table 6-3. Kodiak Path Width and Symmetry Calculations

$\pm$ 75 μA path width and symmetry factor S.

α_w = path width

$$S = \frac{\alpha_u - \alpha_p}{\alpha_w}$$

α_u = upper 75 μA path angle

α_p = path angle

of the symmetry as required in 217.5, paragraph 14, of the U.S. Flight Inspection Manual. Category I glide slopes are required to have no worse than a 40%, 60% unbalance of width above and below path. Thus the S factor should be between 0.4 and 0.6. Measured path width was not made available to Ohio for the null reference system, and measured path symmetry data was not made available for either system.

The data marked P.O. is based on the physical optics approach [3,4] (used by TSC), while the GTD data was calculated with a code developed by Ohio University using the Geometrical Theory of Diffraction. [32]

Further information on the path structure for the sideband reference system is contained in Figure 6-44, which shows % DDM vs. path angle for the three tide levels.

At this point it may be useful to give a short explanation of the reflection processes which determine the system antenna performance at the Kodiak site. Referring to Figure 6-43, we see that there are basically two reflecting surfaces--the airfield itself and the ocean. One might at first expect that the far zone antenna patterns (and thus the path angle) would be determined by the ocean reflections, since the ocean area is so much larger than the airfield area and the specular reflection point (for the upper antenna at least) is on the ocean surface for angles up to about 2°. If this were the case, however, then lowering the ocean level would effectively increase the antenna heights and lower the path angle. In fact, for the two systems tried so far, just the opposite effect was measured and calculated; i.e., as the tide lowered the path angle went up. Thus the ocean surface is not the dominant reflecting surface for any part of the flight path, but merely perturbs the stronger signal reflected from the airfield.

This perturbation effect of the ocean is illustrated in Figure 6-45. Here two calculated far zone patterns for an antenna located at the Kodiak glide slope mast position (Figure 6-43) at a height of 23.10 feet are shown. The pattern marked "mean tide" is for the ground geometry of Figure 6-43 with d = 15.0 feet. The pattern marked "infinite ground coincident with airfield" is the pattern which would exist if the 0.2° slope airfield plane extended to ± ∞ in all directions. The difference between the two patterns must then be due to the diffraction effects of the terminating end of the airfield (which are included in the calculations) and to the ocean surface reflection. These perturbing effects are shown clearly by the curve marked "MEAN TIDE - INFINITE GROUND PLANE", which is simply the difference between the two patterns. It is evident that the ocean reflection and diffraction effects tend to add an oscillation to the primary pattern produced by the airfield ground plane as they phase in and out with it. Thus the amount and direction of the path angle change does not simply depend on whether or not the ocean has risen or fallen, but rather depends in a complex way on the relative phasing between the dominant reflection from the airfield and the perturbing reflection from the ocean. Thus the path angle might go up, down, or remain the same depending upon the relative phasing of the two reflected signals.

That this is the case is shown in the data of Table 6-3, which contains calculated data for a capture effect system in the Kodiak environment. Note that for this system the path angle goes down with the lowering of the tide. In the next section

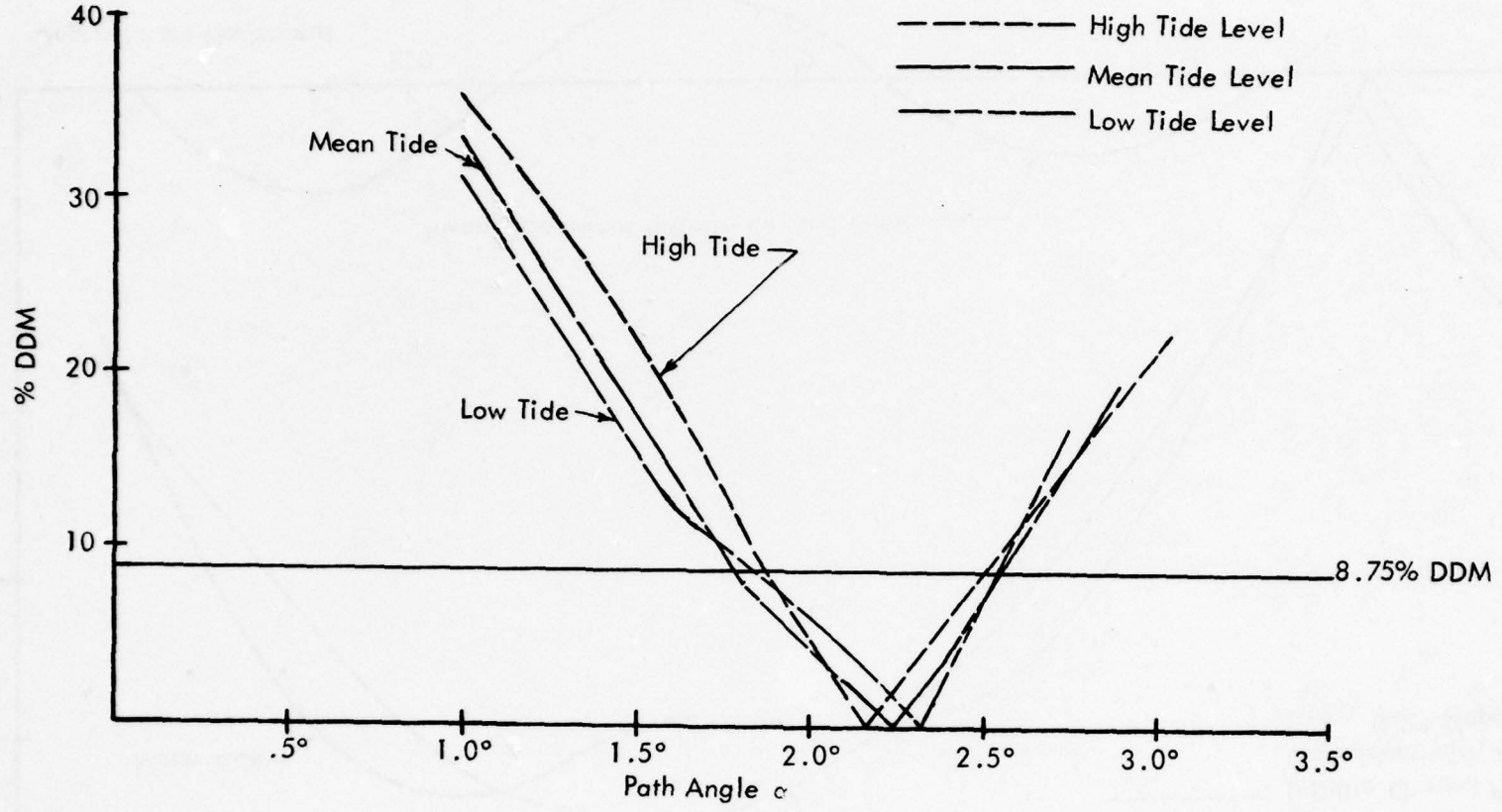

Figure 6-44. DDM vs Path Angle for the Kodiak Sideband Reference Glide Slope Calculated Using the GTD Code.

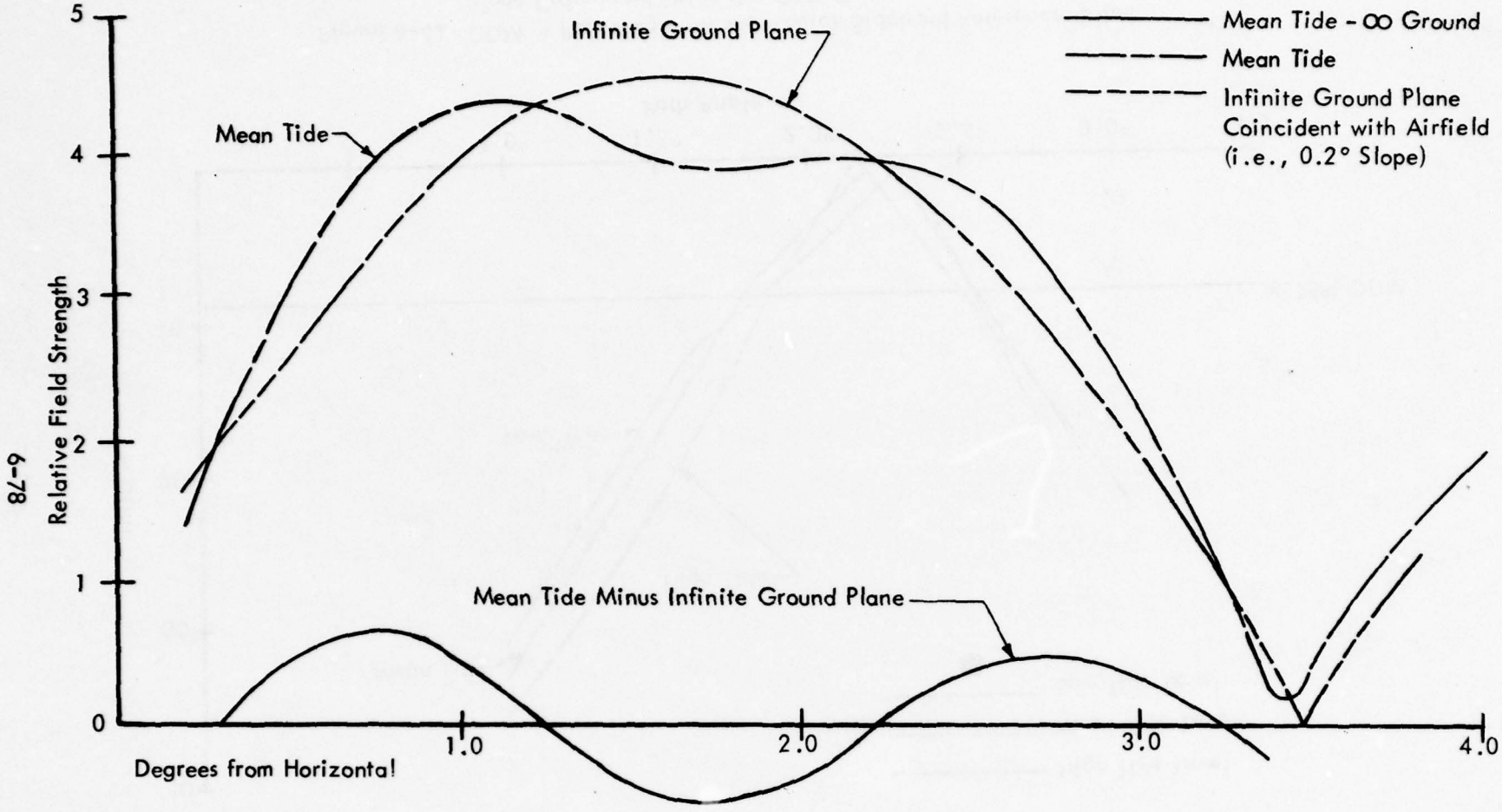

Figure 6-45. Calculated Antenna Patterns for the Kodiak Geometry and an Ideal Flat Ground Plane Subtracted to Show Perturbing Effect of Ocean Reflections. Antenna Height is 23.10', $\lambda = 2.97'$.

Capture Effect (57.0', 38.0', 19.0')

	P.O.	Measured	GTD
High Tide	1.93°		1.98°
Mean Tide	1.86°		1.91°
Low Tide	1.85°		1.84°
Net Change	-0.08°		-0.14°

A ratio = 0.289

Table 6-4. Calculated Path Angles for Untried Capture Effect System.

calculated path angles for capture effect systems with lower antennas increase as the tide goes out, and for a null reference system the highest calculated path angle occurs at mean tide. Thus the tidal effects on path angle depend not only on the tide level but also on the antenna heights.

3. Predicted Results for Possible Future Glide Slope Installation at Kodiak. In Figure 6-46 and the upper section of Tables 6-6 and 6-7, data on a capture effect system with a calculated mean tide path angle of 2.23° is presented. The data in Figure 6-46 and Table 6-6 is calculated using physical optics, while geometrical diffraction theory was used for the data in Table 6-7. The agreement between the two methods is not exact, but the general trends agree very well. The path angle variation from high to low tide is 0.104° as calculated using physical optics. The diffraction theory results indicate a path angle decrease of 0.021° going from high to mean tide, and a 0.063° increase going from mean to low tide. This phenomenon has been explained in the previous section. The disagreement between the two methods is small, and is due to slight differences between the two in determining the relative magnitude and phase between the signal reflected from the airfield and that from the ocean. Calculations using both methods agree that the tidal effects on the capture effect system path angle will be relatively small.

Both methods also agree that the ±75 μA path width angles are not symmetrically located around the 0 μA path angle for the low tide condition, but this was also true for the two systems which have thus far been tried (see Table 6-3).

The flyability run shows a general rise in path angle for all three tide heights up to about 12,000 feet from touchdown. At this point the low tide path begins to lower, but this path is already too high. The roughness within 6000 feet is not of high amplitude, and a large part of it would be damped out by the CDI indicator inertia.

Tables 6-5 and 6-6 also show data for capture effect and null reference systems with antenna heights adjusted to produce a higher path angle. In both cases the shift of path angle with tide is quite low. For the null reference system in particular the calculated path angle shift is less than the shift which occurred when the antennas

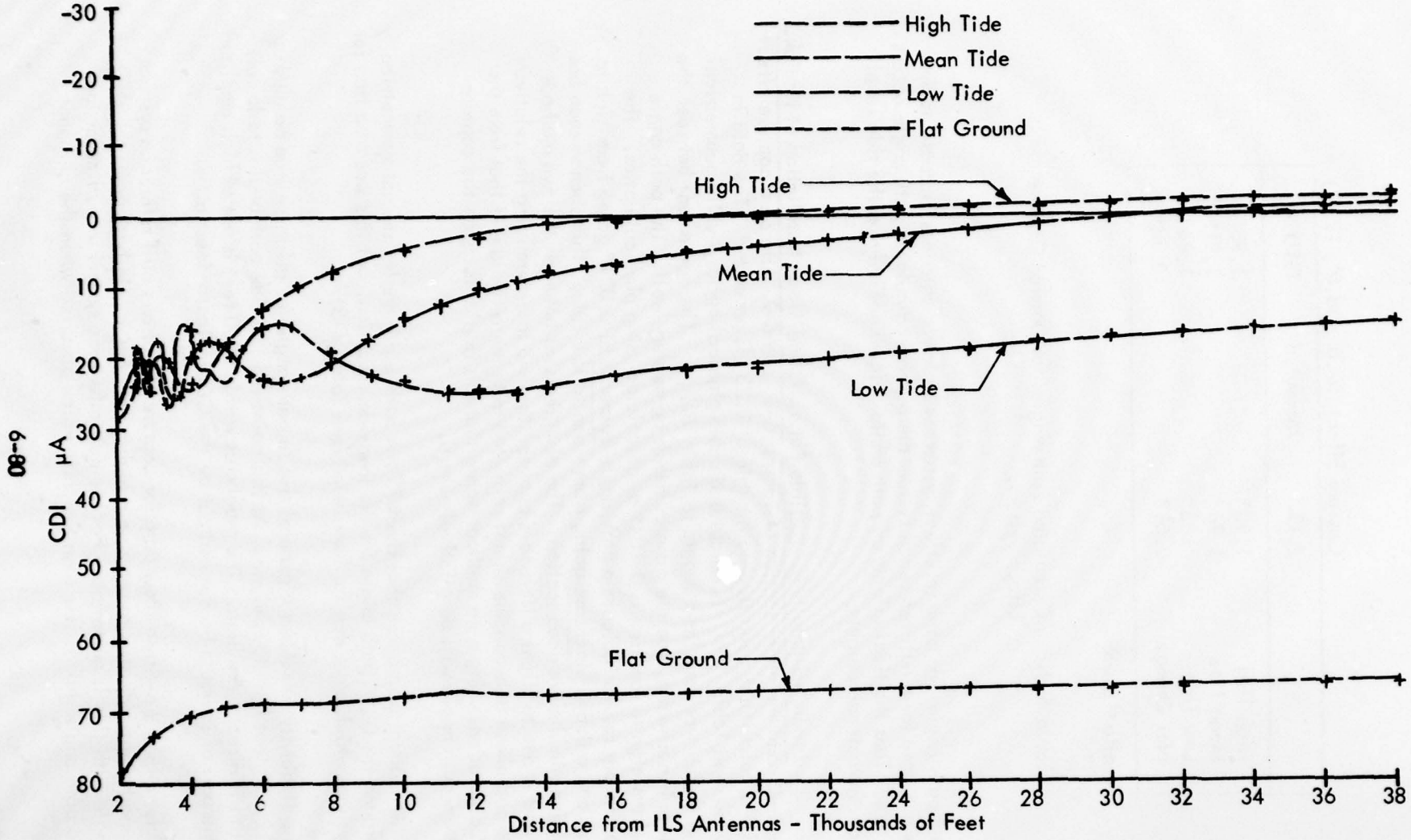

Figure 6-46. Calculated Flyability Runs for a Capture Effect System with Antenna Heights of 51', 34', and 17' and an A ratio of 0.289. The Simulated Flight Path Is at a 2.23° Angle Measured from Horizontal, with Touchdown at the X-Y Origin of Figure 6-43.

were adjusted to a 2.2° path angle (see Table 6-2). This would be explained in part by noting that the lower antenna heights for the 2.4° path angle would tend to illuminate the ocean less than would be the case for the higher antenna heights needed for a 2.2° path angle.

4. Summary and Conclusions. A null reference system with a 2.26° path angle (mean tide) was found to be unacceptable when installed at Kodiak, Alaska due to a 0.29° increase in the path angle as the tide changed from high to low. This increase in path angle with lowering tide level is contrary to what would be predicted using image theory. However, the increase in path angle was confirmed by two different calculations made at Ohio University. One, based on physical optics, calculated a path angle increase of 0.20°; the other, based on the geometrical theory of diffraction, resulted in a calculated path angle increase of 0.23°.

A sideband reference system was also tried, and also had a measured increase in path angle as the tide level changed from high to low. The measured path angle increase was 0.162°, and the calculated path angle increases were 0.17° and 0.15° as calculated using physical optics and geometrical diffraction respectively. Predicted results for a capture effect system at Kodiak with a 2.23° path angle (mean tide) calculated using physical optics indicate a path angle increase of 0.104° from high to low tide, while a geometrical theory of diffraction calculation predicts a 0.063° net change, indicating a significant improvement to be gained from using a capture effect system. Other calculated results indicate that significant reduction in the tidal variations could also be made by increasing the mean tide path angle to 2.4°.

Finally, it should be pointed out that the variation of path angle with tide level for the image systems discussed here depends in a rather complex way on the antenna height and phasing as well as on the tide level. Calculated results indicate that for certain antenna heights the path angle will go down as the tide level lowers.

C. Validation of Mathematical Models Using the Kodiak, Alaska Glide Slope.

1. Introduction. The establishment of a commissionable glide slope facility at the Kodiak, Alaska airfield has been in progress since 1973, but has not yet been accomplished. The reason is that a significant portion of the reflecting surface in front of the glide-slope antennas is ocean, and at the latitude of Kodiak the tidal variations are on the order of 12 feet from low to high tide. This variation in the level of the ocean would be expected to cause the glide-path angle to vary with the tide level since common, image type glide-slope systems make use of signals reflected from the ground to form the glide-path structure.

The expected variation was observed in two different tests. In October, 1973, a null reference system was installed and flight checked but was found to have unacceptably large variations in path angle due to the tidal effects. A sideband reference system was tested in December of 1973. This system showed less path angle variation than the null reference, but was still unacceptable due to difficulties in monitoring its performance in the presence of snow.

While the path angle variations were not unexpected, both the amount of the change and the direction of the change seemed to violate the conventional wisdom. The site did have a flat, 1400 foot-long section of ground between the antennas and the ocean, which normally would be considered adequate to produce an acceptable glide path, especially since the mean sea level was 15 feet below the level of the runway. More puzzling than the size of the variations, however, was the fact that as the ocean level dropped, the path angle increased. This is contrary to what would be predicted using image theory, and at the time made an engineering evaluation of the site very difficult.

During June of 1976 consideration was given to this problem, and a decision was made to use mathematical modeling to analyze the Kodiak site.

Detailed information on the Kodiak glide slope tests was received [33], including a large number of actual flight recordings which were of high quality and which were accurately logged so that the time of the flight was known. Tide tables were also included so that the tide level during each flight could be determined. Finally, better topographic information, including the relationship between the antenna heights and the surrounding terrain, was made available. With the receipt of this package of well-documented data, it was decided to determine how closely the mathematical model predictions could be correlated with actual flight measurements. Also, revised predictions of capture effect performance were made and communicated to the FAA. [17]

Although mathematical modeling of terrain effects on glide-slope performance has been under investigation since 1965[1], very few attempts to correlate computed results with flight measurements at an actual glide slope facility have been reported. Documented correlation attempts were performed by Ohio University and reported in 1966 [2] and 1968. [3] The correlation reported in the 1966 report was reasonably good, that in the 1968 report rather poor. In all cases flyability type flight measurements were used so that a quantitative measure of the correlation could not readily be obtained. Background information such as antenna heights, phasing, offsets, A ratios, etc.) was not included in either report.

Since 1968 a considerable amount of research in glide slope terrain modeling has been performed, and some good technical results have been obtained, but no documented attempts to correlate these new modeling capabilities with measured data from glide slope facilities have been published. Since the modeling programs available today are more sophisticated than those available in the 60's, another validation attempt seemed to be quite worthwhile. The results are reported in this section.

Two different computer modeling codes were used to obtain the results presented. One is based on physical optics and was developed by the Transportation Systems Center [4] and made available to Ohio University. Its basic electromagnetic assumptions and approximations are approximately the same as were used in the two validation attempts previously mentioned. The program is, however, computationally much more efficient in terms of required computer time. The other code is based on the Geometrical Theory of Diffraction [32] and was developed recently at Ohio University. Both codes are limited to terrain which has no lateral variation.

2. Results. Comparisons were made both for level flight (Pattern B) measurements and RTT (radio telemetering theodolite) flyability (Pattern A) measurements. [34] The level run flight measurements are considered in tabulated form in Table 6-5. This contains the basic quantitative information contained in a level flight recording: path angle, width angle, and path symmetry. The symmetry factor is defined here to agree with previous calculations on the Kodiak site. The only input parameter to the computer model that was changed in calculating the results for the various tide levels was the tide level itself, thus making the correlation relatively independent of any bias. Further discussion of the input data to the models can be found in (3) and (4) of this section.

	FAA Measured			Calculated OU GTD			Calculated Physical Optics		
	α_p	α_w	S	α_p	α_w	S	α_p	α_w	S
High Tide	1.99	0.54	0.59	2.050	0.562	0.572	2.023	0.612	0.621
NR Mean Tide	2.02	0.68	0.60	2.094	0.715	0.508	2.105	0.731	0.522
Low Tide	2.29	0.68	0.28	2.255	0.627	0.353	2.274	0.568	0.327
High Tide	1.98	0.68	0.57	2.043	.722	.558	2.050	0.720	0.561
SBR Mean Tide	1.99	0.85	0.53	2.053	.871	.531	2.063	0.838	0.552
Low Tide	2.13	0.93	0.38	2.201	.994	.314	2.225	0.870	0.302

α_p = path angle, i.e., angle at which 0 μA CDI occurs
α_w = total width, i.e., angle between ±75 μA CDI points
α_u = angle at which -75 μA occurs
α_l = angle at which +75 μA occurs
$\alpha_w = \alpha_u - \alpha_l$
S = symmetry factor = $\dfrac{\alpha_u - \alpha_p}{\alpha_w}$

Table 6-5. Comparison of Measured and Calculated Results for Kodiak NR and SBR Tests.

Referring to Table 6-5, the calculated and measured path angles are seen to increase as the tide level lowers. This is contrary to what would be predicted using simple image theory, as was pointed out previously, and rather strongly points out the need for sophisticated mathematical modeling (i.e., physical optics or GTD rather than image theory models) to predict correctly the path characteristics at sites with irregular terrain.

The agreement between the calculated and measured path angles is quite good, with the GTD results being within 0.08° and the physical optics within 0.10° of measured values at worst case. The worst discrepancy occurs for the physical optics calculation of

Capture Effect (51', 34', 17')

	α_p	α_L	α_u	α_w	S
High Tide	2.219°	1.910°	2.596°	.686°	.550
Mean Tide	2.224°	1.834°	2.649°	.815°	.521
Low Tide	2.323°	1.748°	2.643°	.895°	.358

Capture Effect (47', 31.33', 15.67')

	α_p	α_L	α_u	α_w	S
High Tide	2.473°	2.101°	2.869°	.768°	.516
Mean Tide	2.528°	2.049°	2.878°	.829	.422
Low Tide	2.551°	2.104°	2.856°	.752	.406

Null Reference (34.42', 17.21')

	α_p	α_L	α_u	α_w	S
High Tide	2.305°	1.889°	2.700°	.811°	.487
Mean Tide	2.415°	1.939°	2.678°	.739°	.356
Low Tide	2.386°	2.068°	2.589°	.521°	.390

Table 6-6. Path Data for Several Untried Systems Calculated Using Physical Optics.
α_p - path angle α_L, α_u - lower and upper 75 μ A angles

$$S = \frac{\alpha_u - \alpha_p}{\alpha_w} \qquad \alpha_w = \alpha_u - \alpha_L$$

Capture Effect (51', 34', 17')

	α_p	α_L	α_U	α_w	S
High Tide	2.251°	1.964°	2.587°	.623°	.540
Mean Tide	2.230°	1.904°	2.639°	.735°	.557
Low Tide	2.293°	1.851°	2.673°	.823°	.462

Capture Effect (47', 31.33', 15.67')

	α_p	α_L	α_U	α_w	S
High Tide	2.483°	2.145°	2.863°	.718°	.530
Mean Tide	2.508°	2.105°	2.901°	.796°	.493
Low Tide	2.560°	2.113°	2.894°	.780°	.428

Null Reference (34.42', 17.21')

	α_p	α_L	α_U	α_w	S
High Tide	2.248°	1.883°	2.671°	.788°	.536
Mean Tide	2.379°	1.864°	2.721°	.857°	.398
Low Tide	2.419°	2.039°	2.672°	.633°	.400

Table 6-7. Path Data for Several Untried Systems Calculated Using the Geometrical Theory of Diffraction.

the low tide path width for the null reference system. This is apparently due to a basic assumption made in the derivation of the physical optics model regarding the ocean illumination, which will be discussed in relation to the CDI versus angle plots presented later in this section. It should be pointed out that the measurements themselves are subject to error, so that the discrepancies in the table may be due to measurement errors rather than modeling inaccuracy.

Although Table 6-5 provides all of the parameters normally tabulated from a Pattern B flight check, a more comprehensive and illuminating view of the calculation accuracy can be obtained from the plots of course deviation indication (CDI) versus angle presented in Figures 6-47 through 6-52. The measured curves are taken from FAA flight recordings. It is evident that the calculated curves agree quite well with the measurements for the most part. Figures 6-47, 6-48 and 6-49 are for the null reference system for high, mean, and low tides respectively, while Figures 6-50, 6-51 and 6-52 are for the sideband reference system. Referring first to the null reference graphs, note that the agreement between the GTD and physical optics calculations is quite good except for the low tide case, where the two differ in shape for low angles. Since the GTD curve agrees very well with the measured curve, it would seem the physical optics calculation is in error. This is probably due to the different way the two models deal with shadowing effects. At low tide a significant portion of the ocean surface is shadowed from the glide-slope antennas by the edge of the land. The physical optics model makes the assumption that the portion of the ocean shadowed by the land is not illuminated at all, while the GTD model is more realistic in assuming that while the visible portion of the ocean is illuminated directly, the entire ocean surface is also illuminated by radiation diffracted by the end of the ground at the ocean edge. Further investigation reveals that specular reflection from the ocean surface is cut off by the land edge at about 1.65°, which is approximately the angle where the physical optics calculation shows the greatest departure from the GTD results and the measured data. Note that despite the abrupt drop from land to ocean surface in the low tide case, it is evident from Figure 6-49 that the GTD model reproduces the bends in the measured curve quite accurately. This is the reason that the GTD gives better results when calculating the low tide path width.

Figures 6-50, 6-51, and 6-52 show similar comparisons for the sideband reference system. The major source of disagreement between the calculated and measured curves is that the calculated path angles are consistently higher than measured. This could be due to slight errors in determining the antenna heights. The shapes of the curves agree quite well. Note from Figure 6-52 that for the low tide case, where the terrain discontinuity is most severe, the GTD model again shows better agreement with the measured curve, especially for the low angles where the specular reflection from the ocean is being shadowed by the land's edge. For angles just below 2°, both the measured and GTD curves are concave down while the physical optics curve is concave up. The disagreement is not as great as for the null reference system, perhaps due to the fact that the lower antennas for the sideband system illuminate the ocean less.

Figures 6-53 to 58 are calculated and measured plots of CDI versus distance for Pattern A flyability runs down the runway centerline. The measured curves are taken from the differential amplifier trace of FAA recordings made using the RTT. In order to more

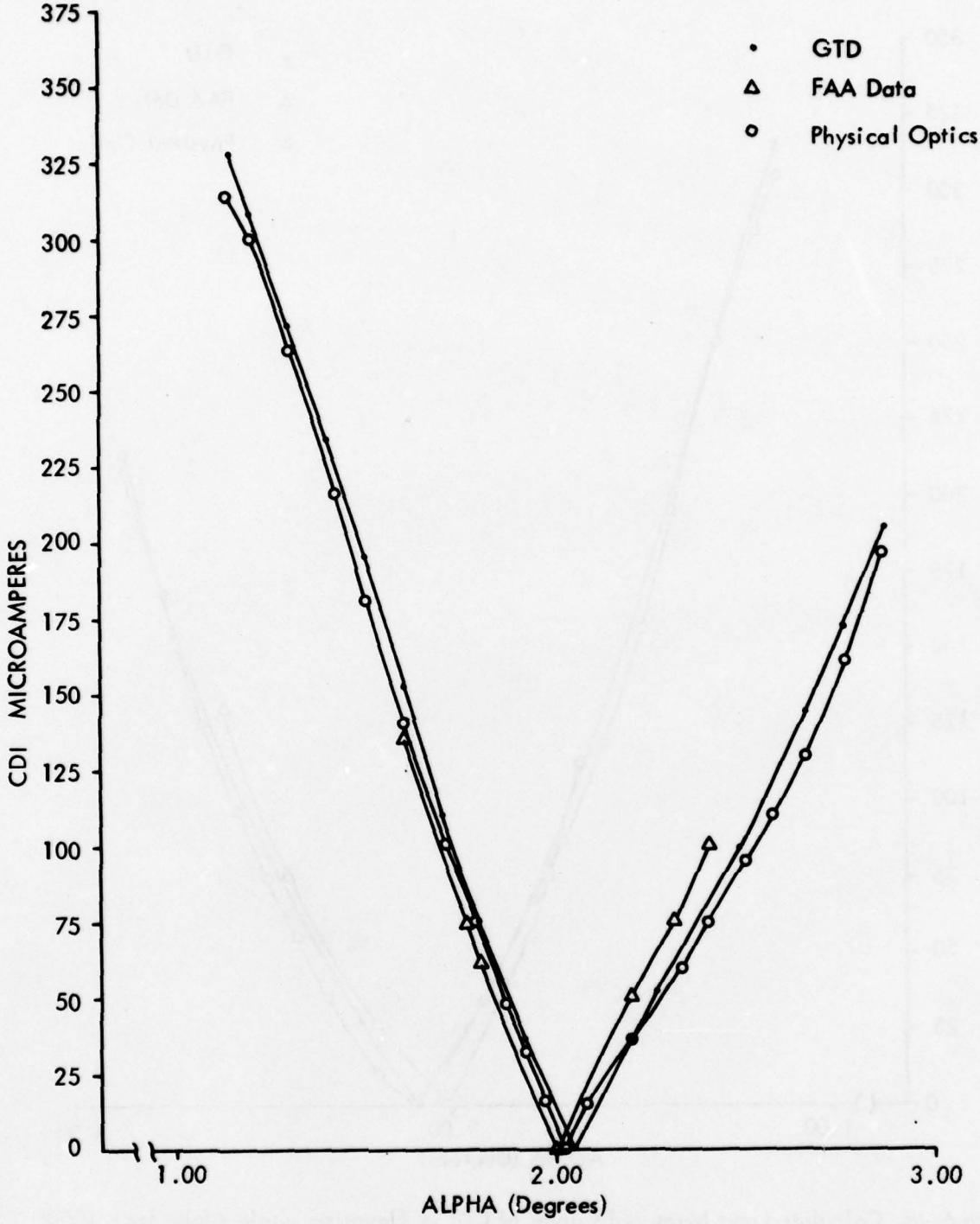

Figure 6-47. Calculated and Measured Curves of CDI vs. Elevation Angle Alpha for a 1000' High Level Run (Pattern B) Flight Measurement Along the Runway Centerline for the Null Reference System at High Tide.

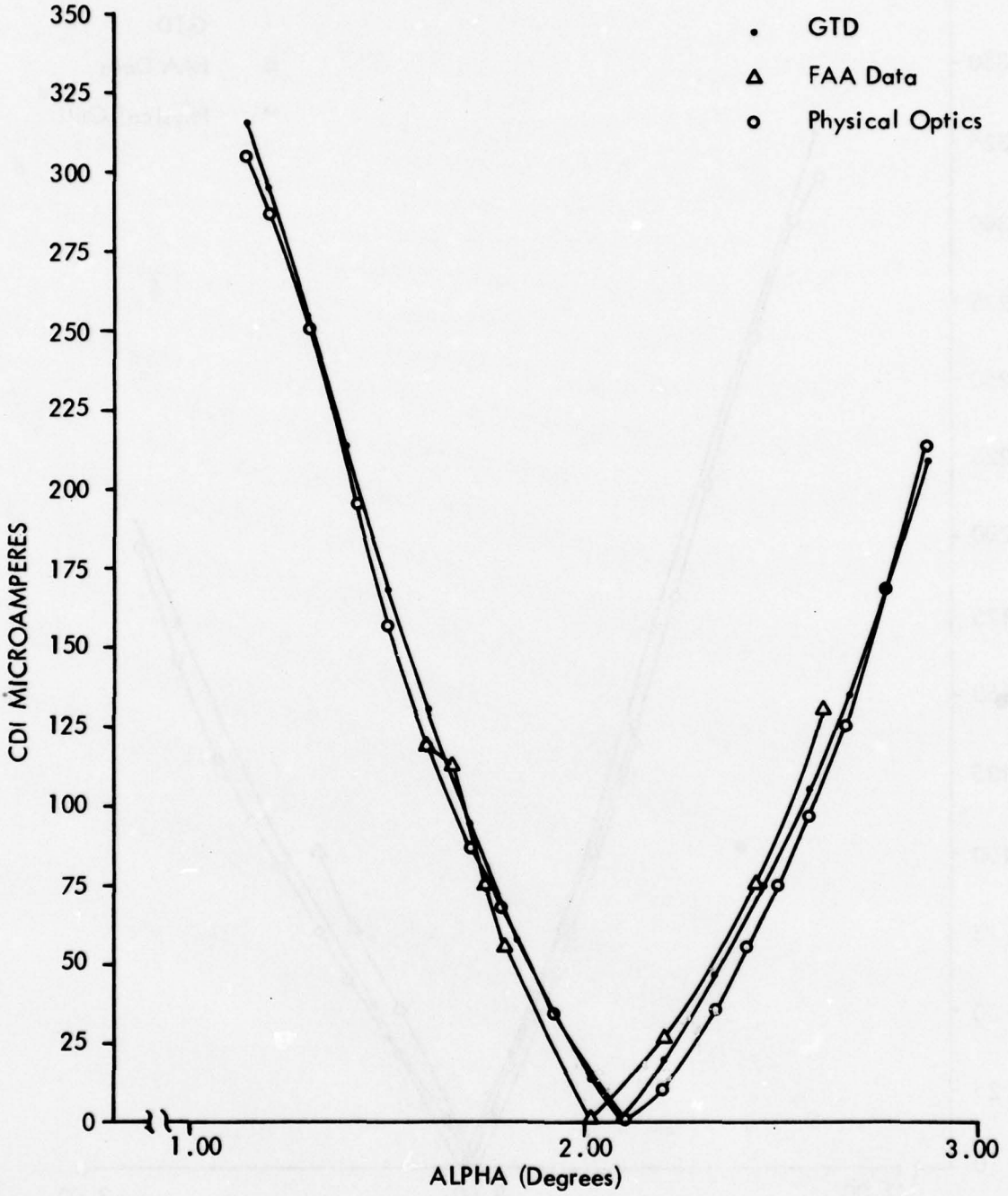

Figure 6-48. Calculated and Measured Curves of CDI vs. Elevation Angle Alpha for a 1000' High Level Run (Pattern B) Flight Measurement Along the Runway Centerline for the Null Reference System at Mean Tide.

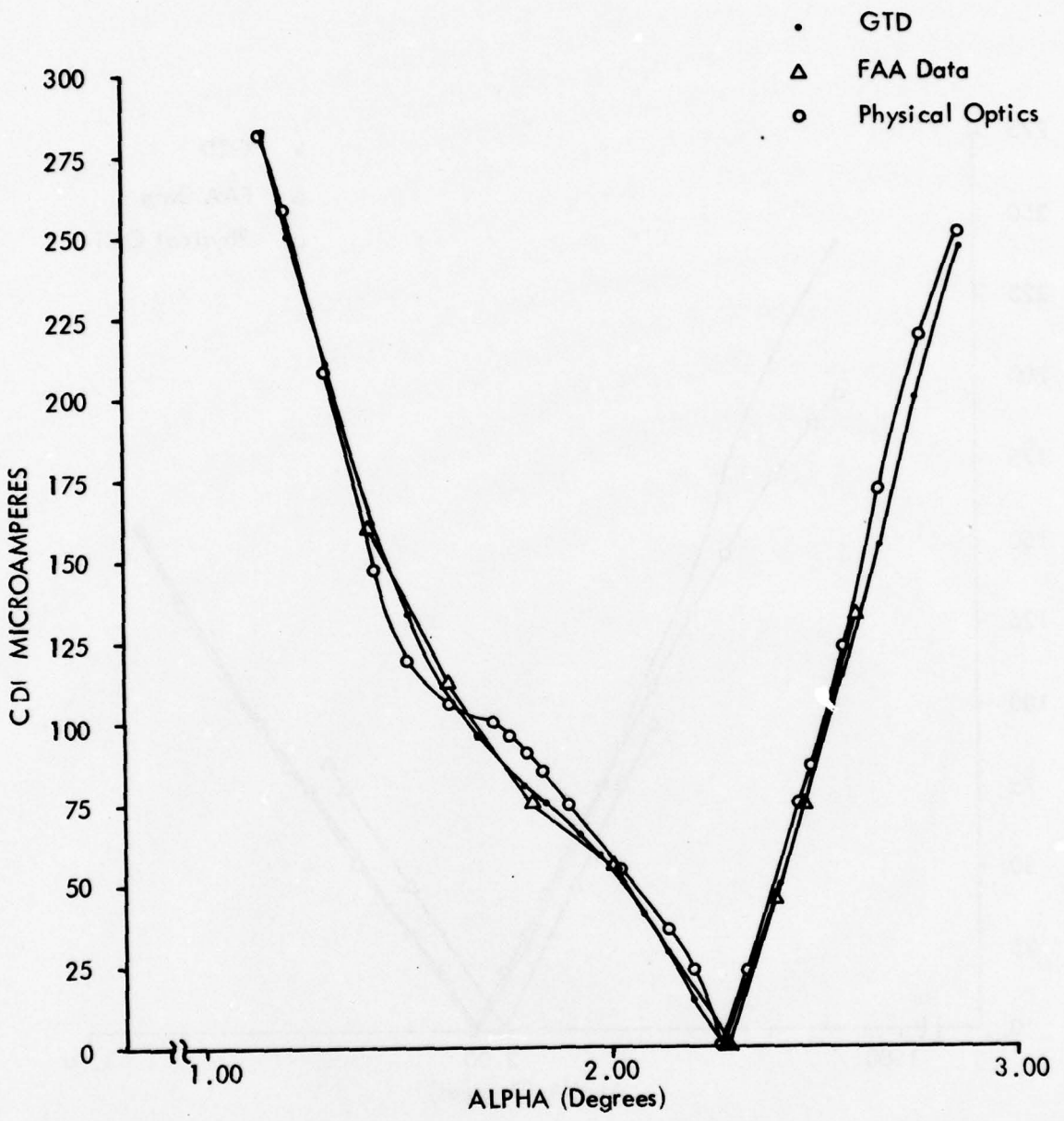

Figure 6-49. Calculated and Measured Curves of CDI vs. Elevation Angle Alpha for a 1000' High Level Run (Pattern B) Flight Measurement Along the Runway Centerline for the Null Reference System at Low Tide.

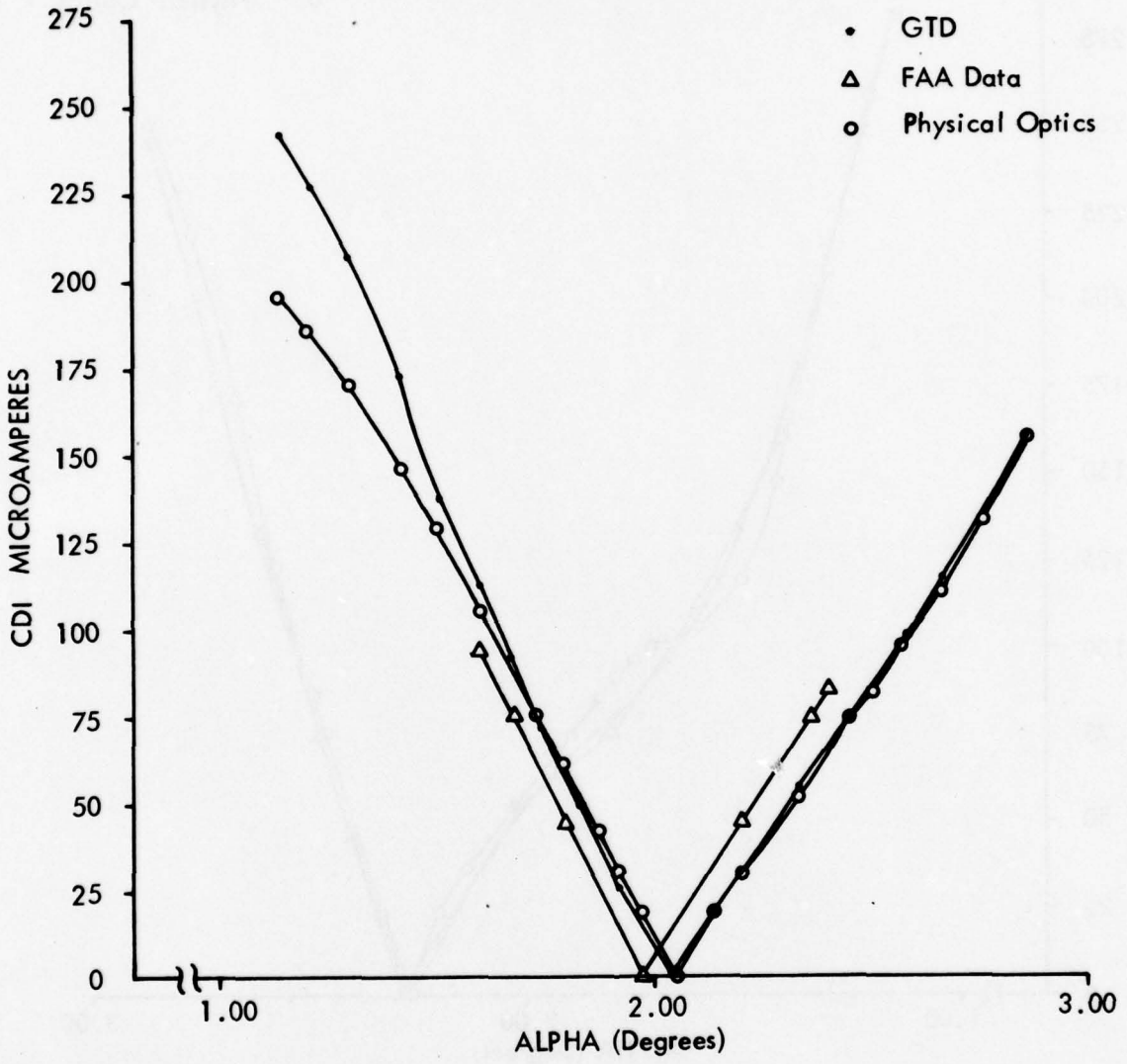

Figure 6-50. Calculated and Measured Curves of CDI vs. Elevation Angle Alpha for a 1000' High Level Run (Pattern B) Flight Measurement Along the Runway Centerline for the Sideband Reference System at High Tide.

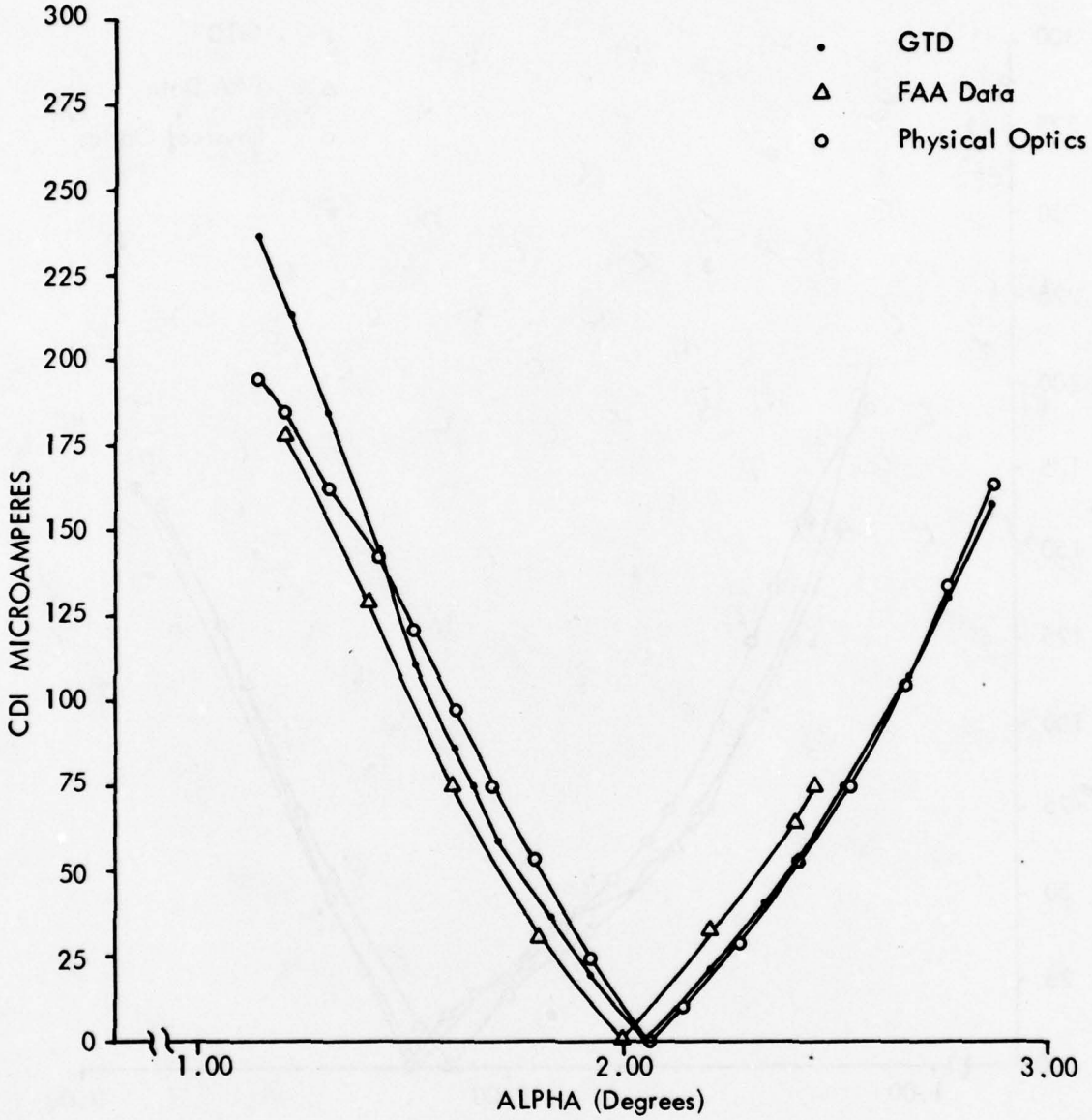

Figure 6-51. Calculated and Measured Curves of CDI vs. Elevation Angle Alpha for a 1000' High Level Run (Pattern B) Flight Measurement Along the Runway Centerline for the Sideband Reference System at Mean Tide.

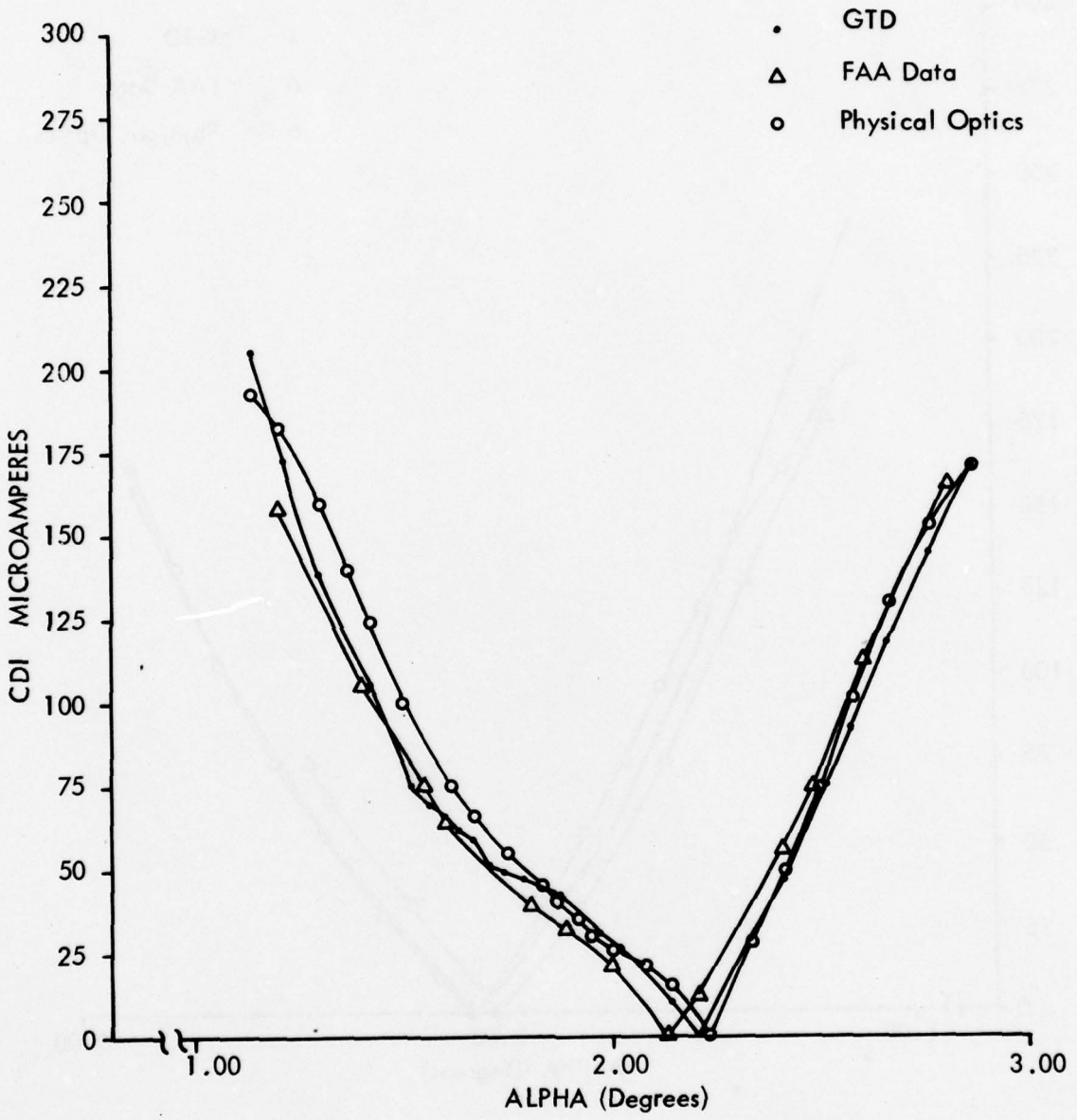

Figure 6-52. Calculated and Measured Curves of CDI vs. Elevation Angle Alpha for a 1000' High Level Run (Pattern B) Flight Measurement Along the Runway Centerline for the Sideband Reference System at Low Tide.

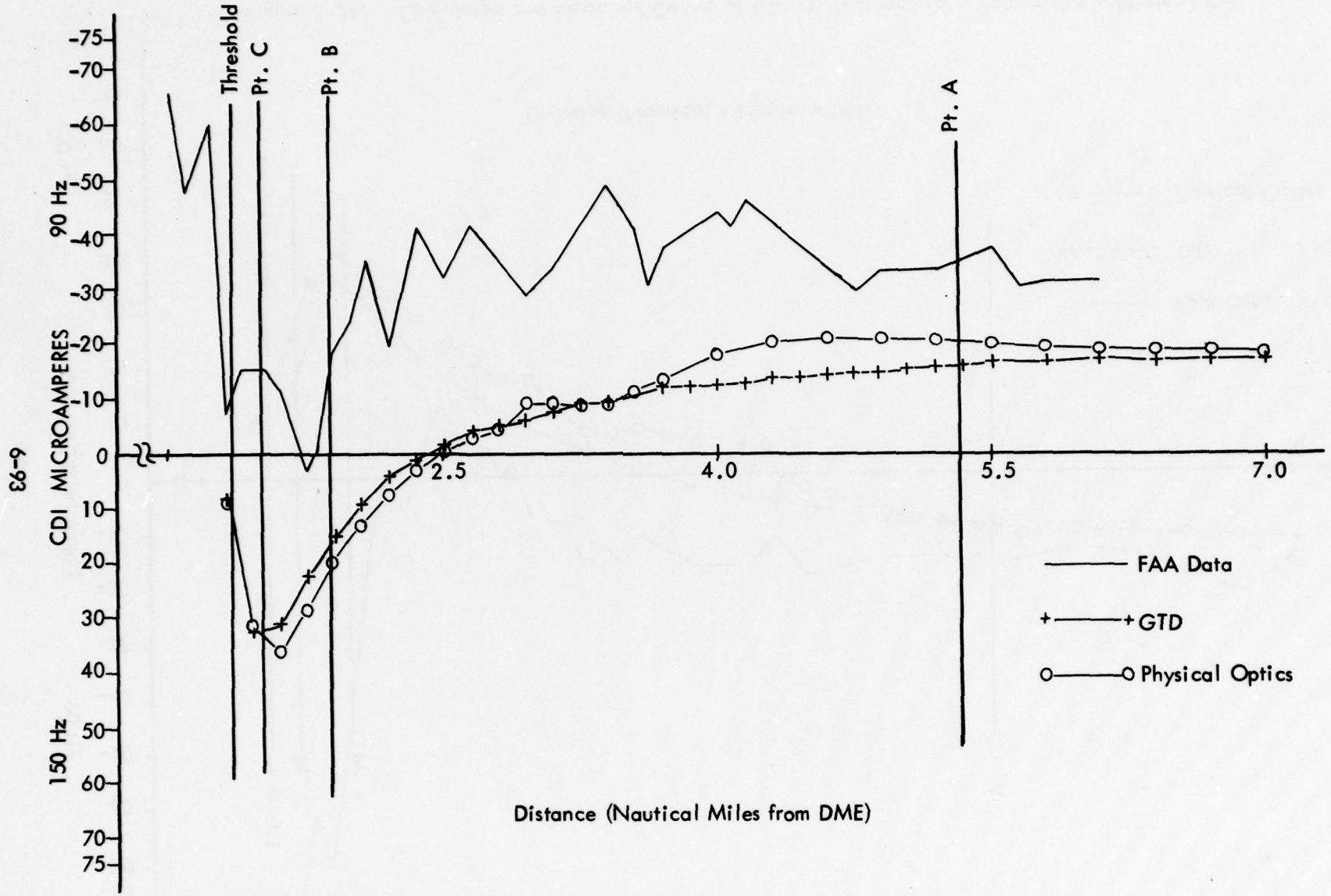

Figure 6-53. Calculated and Measured Curves of CDI vs. Distance for a Pattern A Flight Along the Runway Centerline for the Null Reference System at High Tide.

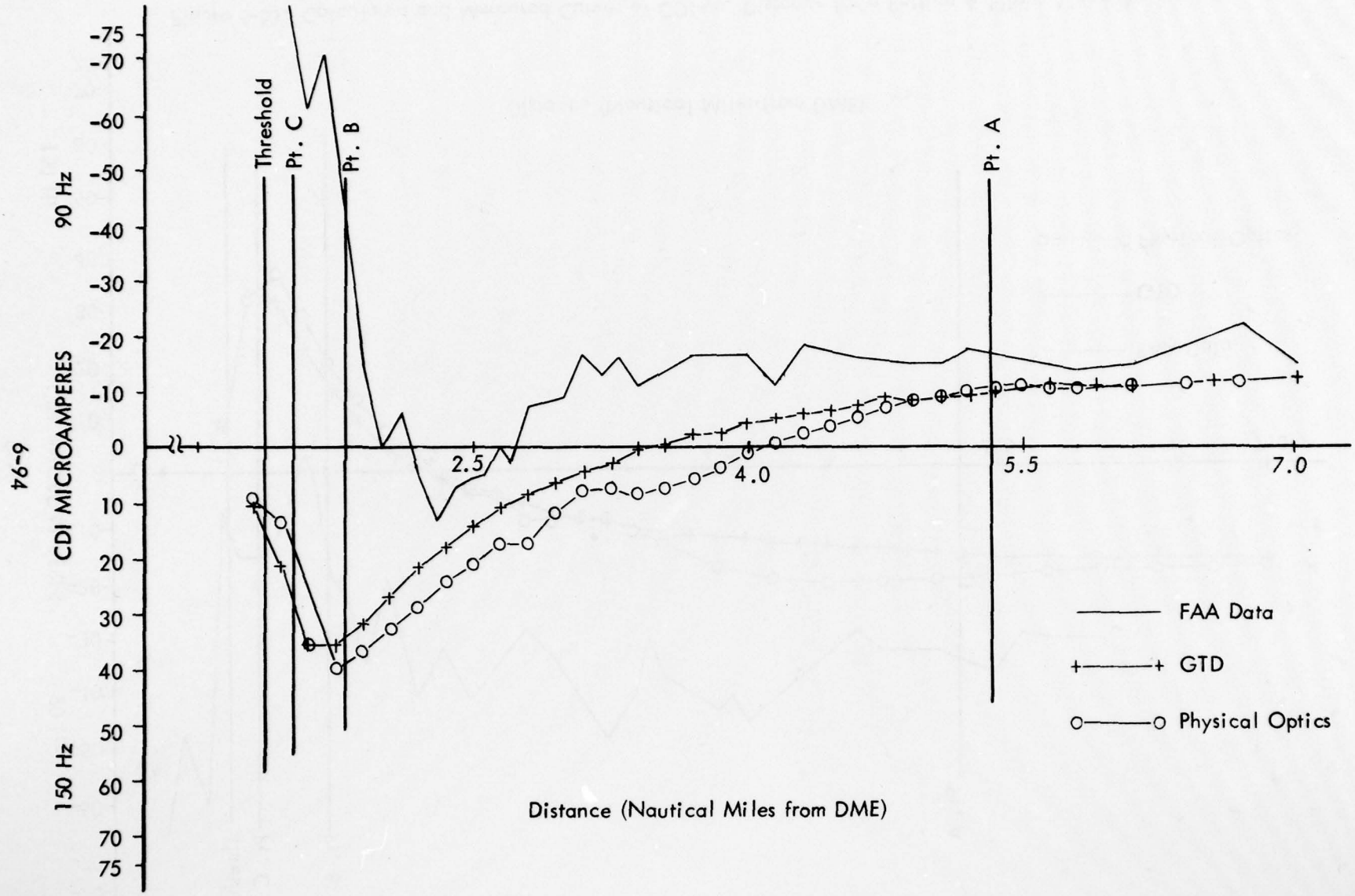

Figure 6-54. Calculated and Measured Curves of CDI vs. Distance for a Pattern A Flight along the Runway Centerline for the Null Reference System at Mean Tide.

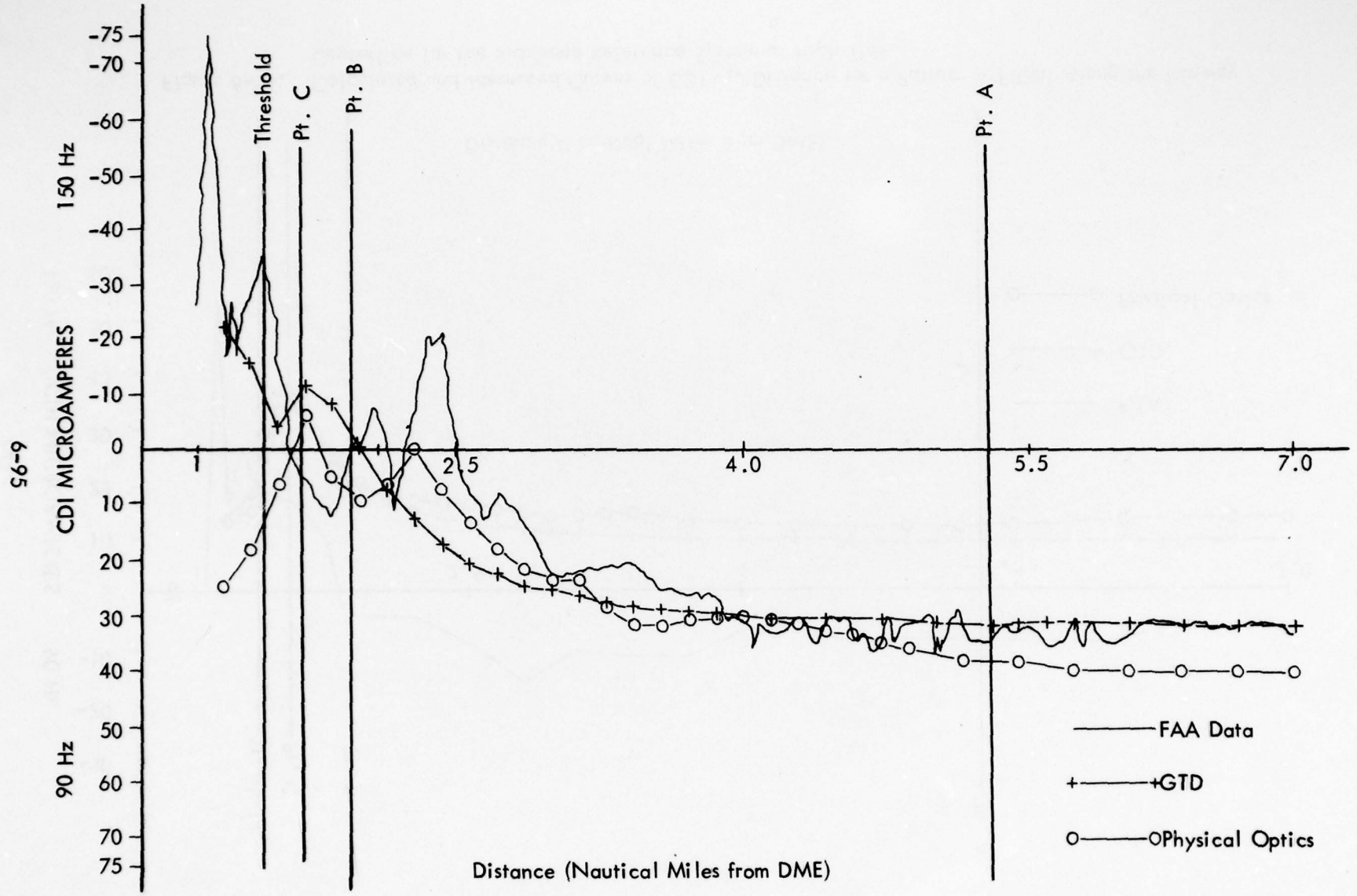

Figure 6-55. Calculated and Measured Curves of CDI vs. Distance for a Pattern A Flight along the Runway Centerline for Null Reference System at Low Tide.

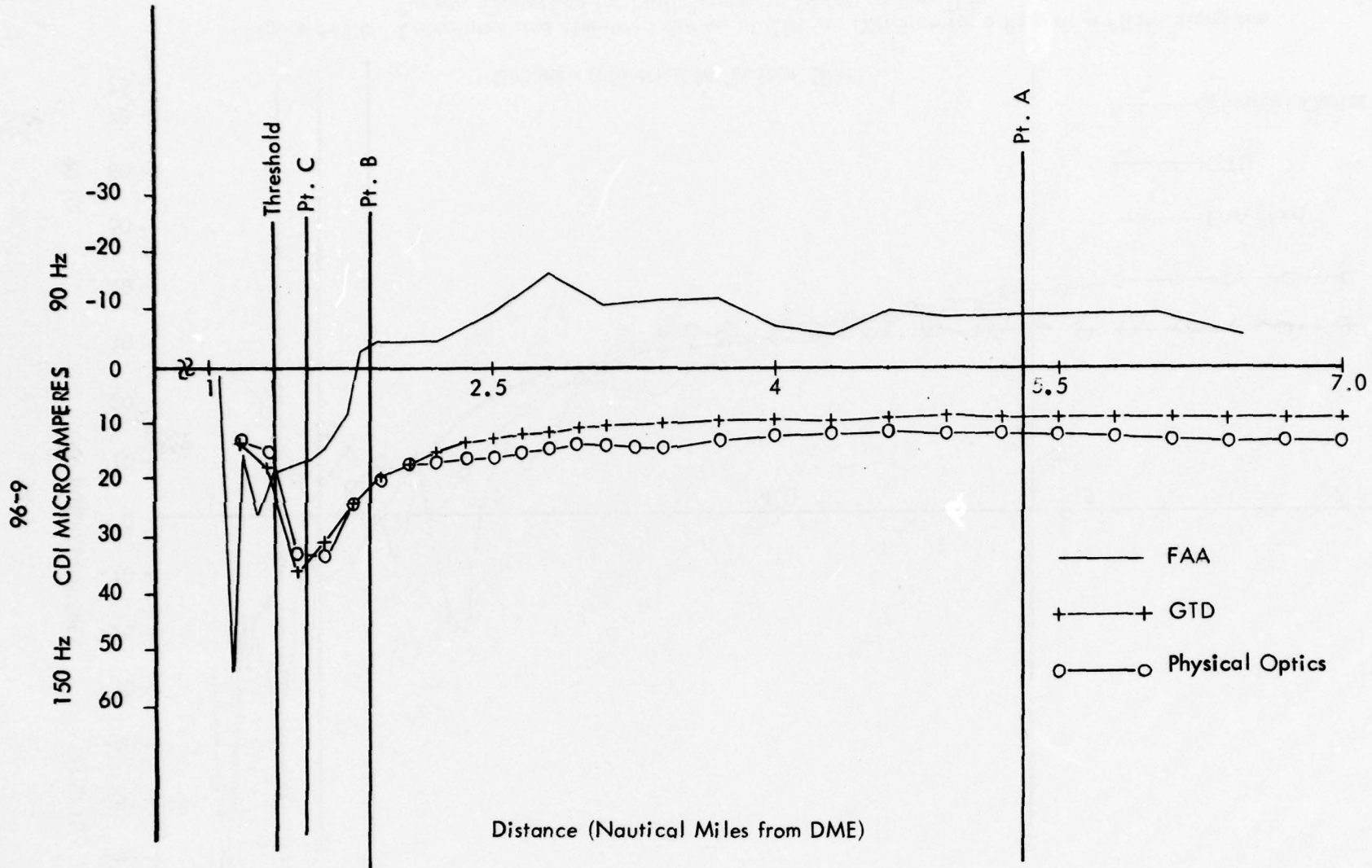

Figure 6-56. Calculated and Measured Curves of CDI vs. Distance for a Pattern A Flight Along the Runway Centerline for the Sideband Reference System at High Tide.

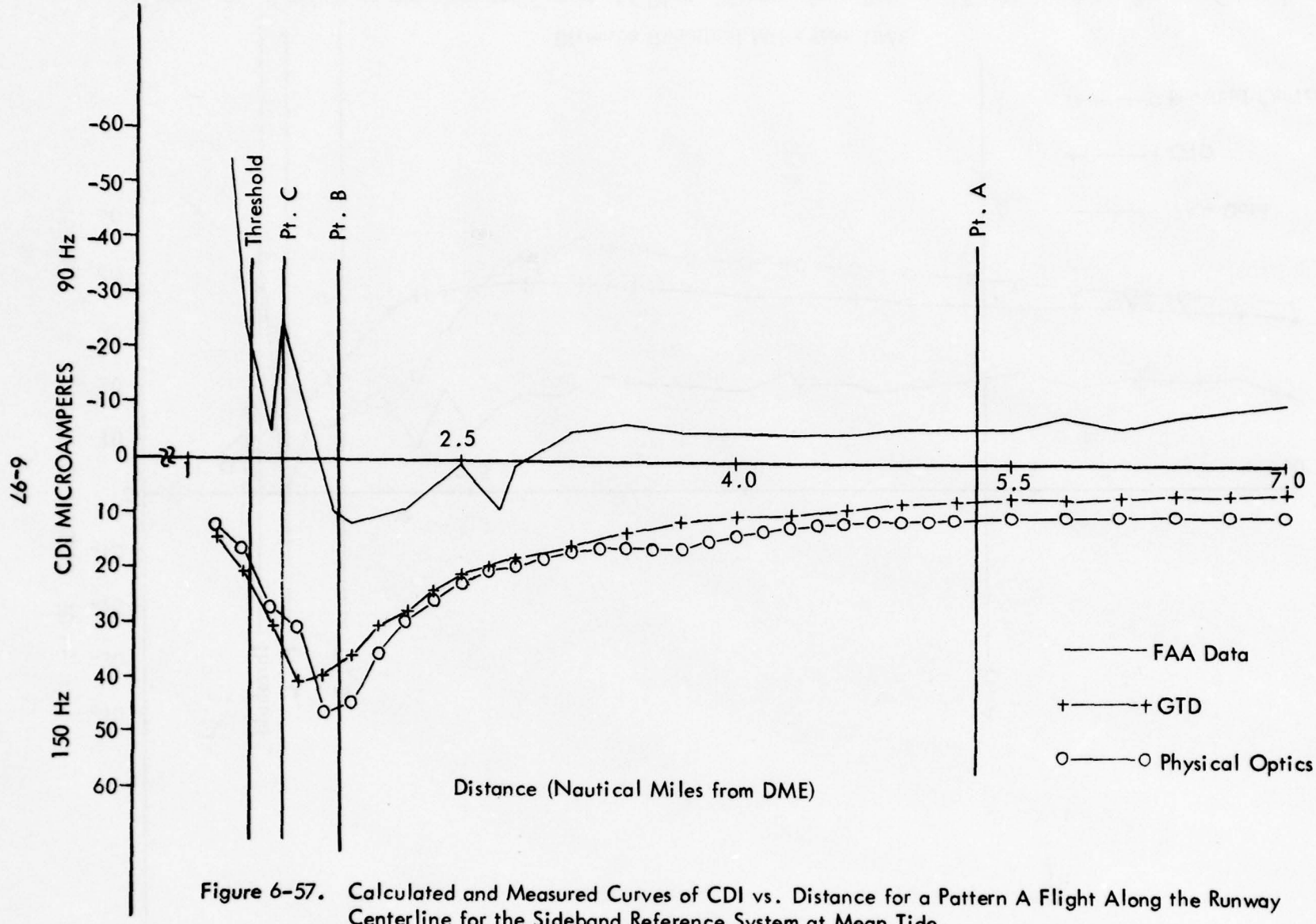

Figure 6-57. Calculated and Measured Curves of CDI vs. Distance for a Pattern A Flight Along the Runway Centerline for the Sideband Reference System at Mean Tide.

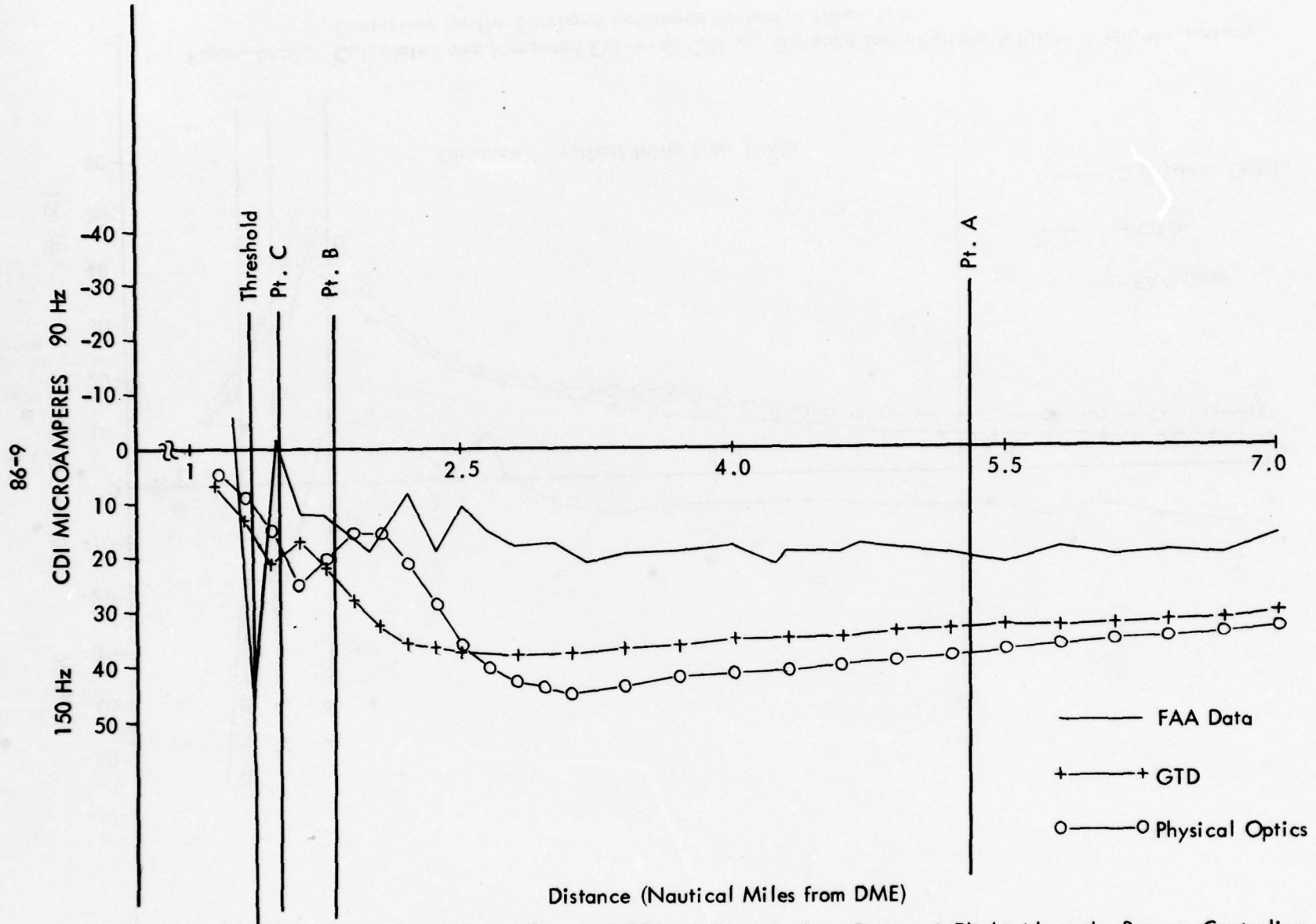

Figure 6-58. Calculated and Measured Curves of CDI vs. Distance for a Pattern A Flight Along the Runway Centerline for the Sideband Reference System at Low Tide.

accurately model this situation the computer models simulated an aircraft flying a hyperbolic path which maintained a constant angle from the theodolite position. The angle which was flown by the simulated aircraft was not the theodolite reference angle, but rather the path angle determined by the level run measurements. In this way the simulated aircraft would be flying approximately the same course flown by a pilot keeping his CDI meter centered. At each simulated aircraft position the CDI was calculated. The angle from the theodolite position was also calculated, and converted to equivalent RTT microamperes by including in the modeling input the theodolite reference angle and reference path width. These two CDI's were then subtracted to obtain the calculated differential amplifier traces which were plotted in Figures 6-53 through 6-58.

The agreement between the calculated and measured data, while reasonably good, is not as good as was obtained for the Pattern B measurements. This is probably due in part to both the greater complexity and subsequent possible inaccuracy of the measurement technique (due to tracking error or non-linearities) and to the possible modeling inaccuracy involved in calculating CDI's with the receiver relatively close to the glideslope antennas.

Referring first to the null reference curves, in all cases the calculated curves reproduce the general trends of the measurements quite well, showing the rise in the path encountered during low tide conditions. The GTD curves are smoother than the physical optics curves. However, the roughness of the physical optics curves does not correlate well with the flight measurements, but appears rather to be due to the assumptions regarding ocean illumination discussed earlier. The fine structure in the recordings is due to noise and to reflections from terrain discontinuities or other reflecting objects too small to be included in the terrain profile input to the models. Note that the Pattern A measurements do not have the same path angle as the Pattern B measurements. If the average differential amplifier value for the region between 5 and 7 miles from the localizer is converted to degrees, approximately 1.99, 2.05, and 2.25° for high, mean, and low tide path angles results. Except for the high tide case, these path angles differ from those measured and tabulated in Table 6-5 and agree more closely with those obtained from the models.

The calculated and measured Pattern A curves for the sideband reference system are contained in Figures 6-56 through 6-58. Again, the general trends in the path as the approach is made are calculated correctly by both models. The high tide calculations show the path rising, the mean tide shows the path rising then falling again, and the low tide case calculations agree with the slight drop in the path indicated by the measurements.

Also, as was the case for the null reference measurements, the path angles indicated by the Pattern A measurements for the sideband reference system do not agree precisely with those obtained from the Pattern B runs. Converting the differential amplifier readings for the 5 to 6 mile range into path angles, yields 1.95, 1.97, and 2.12° for the high, mean, and low tide cases respectively, which differ from the figures in Table 6-5. These differences are not due to changing tide levels, as can be seen from information contained in part (4) of this section, Figure 6-64, but rather to

differences in the measurements. This measurement inconsistency explains why the calculated path angles of Table 6-5 agree more closely with the measured path angles than do the calculated and measured flyability curves.

3. Data Requirements for Accurate Modeling. In general the parameters required to describe and model an ILS system are well known, but the relative importance of the various parameters and the accuracy to which they must be determined is worth some discussion. The following data must be known to varying degrees of accuracy.

(a) Magnitude and phase of the exciting current on each antenna and the radiation pattern of the antennas, magnitude and phase.

(b) Position of each radiator with respect to the center of the runway at threshold.

(c) Terrain with respect to runway threshold (including manmade obstructions, reflecting objects, etc.).

(d) Position of the aircraft receiver with respect to threshold.

(e) Position of the theodolite with respect to threshold.

The threshold of the runway is an arbitrary reference, but the point is that all positions must be known in relation to each other. Accuracy and precision requirements for this data can now be examined.

For the null reference system it is only necessary to find the amplitude ratio between the SBO and CSB currents (since they go to different antennas), and the phase between the two. The amplitude ratio is commonly known as the A ratio in FAA literature and is known to affect only the width angle and (in some cases) the symmetry but not the path angle. Presently power meters with ±5% of full scale accuracy are used in monitoring CSB and SBO power to the antennas. This means that often readings are made on the low end of the scale where there is probably less than ±5% accuracy. More accurate measurements would provide better data for modeling although this is not a particularly critical point. The importance of the relative phase between the SBO and CSB signals is seen by looking at an expression for difference in depth of modulation (DDM) of the 90 and 150 Hz audio signals received by the aircraft. For a receiver with a linear envelope detector, a good approximation for DDM is given by the following equation:

$$DDM = \left| \frac{E_{ss}}{E_{cs}} \right| \cos \Phi \qquad \Phi = \text{phase of } E_{ss} - \text{phase of } E_{cs}$$

where E_{ss} is the sideband only signal and E_{cs} is the carrier sideband signal. This equation is consistent with the expression for space modulation found in the FAA training material. [35] When irregular terrain is encountered, ideal nulls in E_{ss} do not exist, and the phase between E_{ss} and E_{cs} does not change 180° instantaneously in the E_{ss} null. In this case, then, the path angle (i.e., the angle at which zero microamperes CDI is encountered) is determined

by the phase angle Φ becoming 90°. Clearly, if the excitation current of an antenna is shifted in phase, this can shift the path angle as well as changing the width angle. Since the phase characteristics are so dependent on terrain, it is difficult to say in general how much a given change in phase will affect the path angle. For the Kodiak terrain, a phase change of 5° was found to cause a path angle change of 0.03°, in one case. To model correctly a glide slope it is very important to establish this phase angle as accurately as possible. There appears to be no really good way to measure relative SBO and CSB phase on the ground with a null reference system. Fortunately quadrature phasing from the air provides essentially the same information. The phase of E_{ss} and E_{cs} in the far-field can be checked with the computer model and the phase of the currents corrected until the proper far-field phase relationship exists.

The comments made for the NR generally hold for the SBR and CEGS systems. The path and width angles are usually more sensitive to the antenna current magnitudes and phases than for the NR because there are more complex arrays with SBO and CSB currents in the same antennas. A set of calculations for path and width change for a given perturbation in an antenna current should be used in establishing the required accuracy and precision in antenna current measurements.

The position of the antennas must be established in three dimensions and referenced properly to the terrain surrounding the antenna mast. It is well known that the antenna heights affect the path angle, path symmetry and ultimate flyability of the path. The heights are commonly measured with respect to the concrete base of the antenna mast since this is a good solid reference point. It is very important, however, that a good survey reference this elevation with the rest of the terrain on an accurate contour map. The antenna heights used in the computer model will not be those measured with respect to the base of the mast, but must be referred to the intersection of the mast and the extension of the first piece of ground profile extended through the mast. Figure 6-59 shows how these heights were related in the case of the Kodiak ground profile.

FAA manuals provide extensive discussion of the need for offset in the antenna locations in the direction perpendicular to the runway centerline to provide compensation for near-field misphasing as the aircraft approaches threshold, so it is sufficient to say that it is important to have accurate information as to the offset if the path structure is to be modeled accurately near threshold. It is important to check for antenna offset, i.e., vertical alignment, in the direction parallel to the runway centerline as well. Since at glide slope frequencies the phase varies in free space at about 10 degrees per inch, a half inch offset could cause a significant path angle difference due to phase error in the same way as could an error in the phase of the excitation current. Another advantage of far-field airborne phasing is that it implicitly compensates for vertical misalignment by forcing the SBO and CSB to have the proper phase in the far field.

The terrain can be represented for modeling purposes by a contour map, with pictures if necessary. The models used for Kodiak do not allow for lateral variations in ground elevation, i.e., in the direction perpendicular to the runway centerline. The entire ground reflecting area is assumed to have the same profile as the actual ground profile along a line from the transmitting antenna to the aircraft. This line does not change much until the

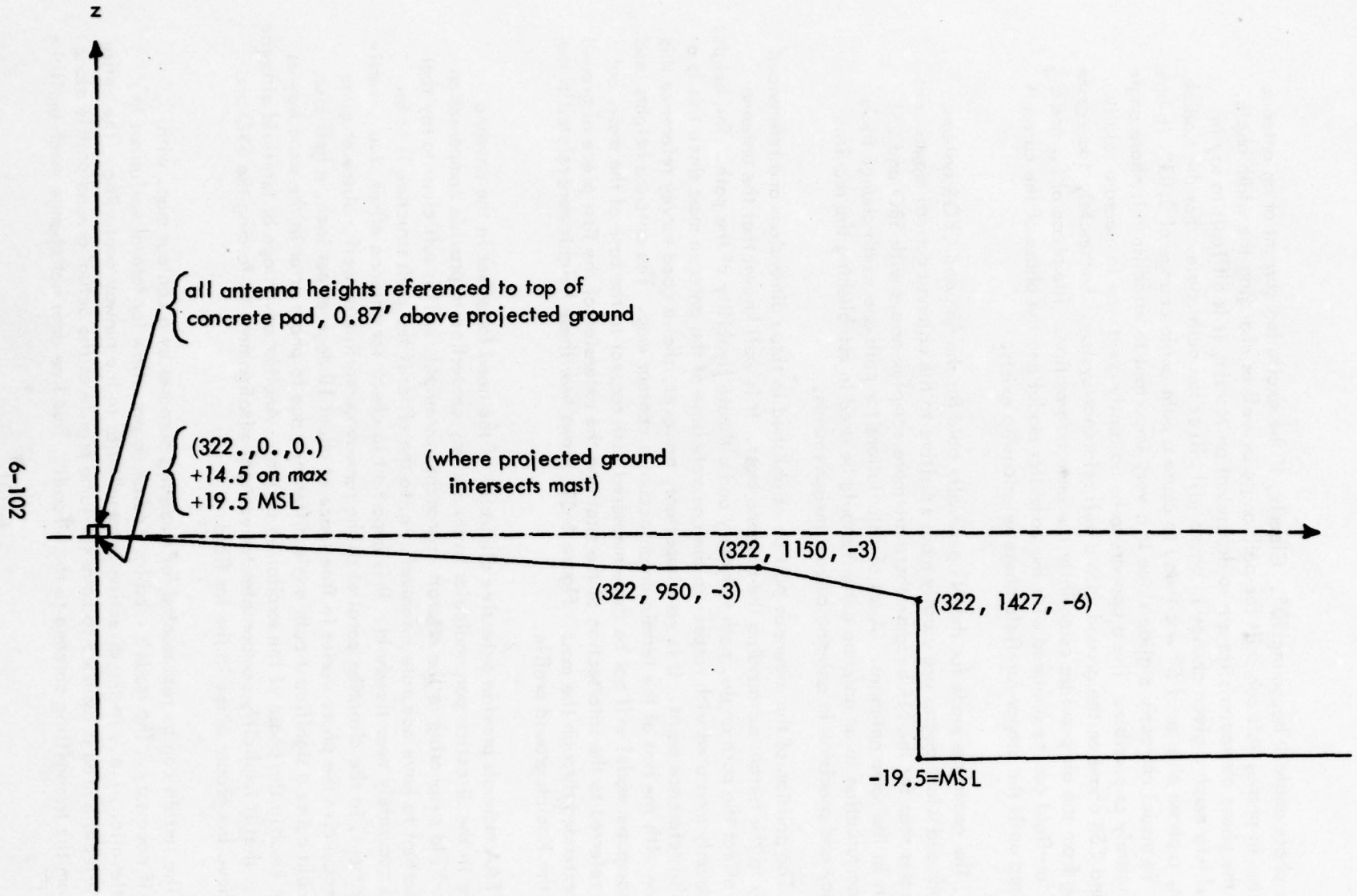

Figure 6-59. Ground Profile for Kodiak Modeling Calculations.

aircraft is fairly close to the threshold. The width of the first Fresnel zone is less than 150 feet, so in many cases it is a good assumption that the lateral variation in ground, if any, does not affect the calculations appreciably. Good engineering judgment is required in deciding whether lateral variations may be neglected. In a case where significant energy will be reflected from ground (i.e., hills) or objects not on the line from the transmitting antenna to the aircraft, a more complex model must be used in the calculations.

The position of the aircraft is generally considered a variable in calculations of this type, and the position is normally generated by the computer program which simulates some predetermined aircraft path. In order for the calculations to best match the flight measurements or vice versa, the positions used in the model and for the flight measurement must coincide as closely as possible. In the model the position of the aircraft is calculated exactly with respect to the coordinate system, while during flight measurements the aircraft elevation angle is measured by theodolite. This fact makes it important to know the position of the theodolite during flight measurements for best agreement with calculated results. Accuracy in establishing the position of the theodolite and the aircraft becomes increasingly important as the aircraft approaches the threshold.

4. Documentation of Data Used in Model Validation. The data used in the modeling of Kodiak was taken from a well-documented package of flight recordings and other data sent by the FAA Alaska Region. [33] The following paragraphs explain the manner in which the data received was processed for use in the models.

a. Excitation Currents in Antennas. To specify the antenna excitation currents, the A ratio, calculated from the CSB and SBO power measurements, and the phase as determined by far-field phasing are sufficient. The power measurements received from the FAA were quoted from memory and were used as a starting point in determining the A ratio. Using equation (6.41), see Section VI, D, of this report:

$$A = \frac{\sqrt{P_{ss}^{i} / P_{c}^{i}}}{.8m} \qquad (6.41)$$

where P_{ss}^{i} and P_{c}^{i} are indicated SBO and carrier power, respectively, and m is the modulation depth; usually m = 0.4. The A ratio is found to be 0.36 for the NR, and 0.306 for the SBR. Using these values gave poor agreement for the width values, and the final values used were 0.39 for the NR and 0.265 for the SBR. Considering that the measurements were made with a 100 milliwatt element, the reading could be in error as much as ± 5 milliwatts which provides some justification for adjusting the A ratio in the calculations. In the NR case the phases of the antenna currents were corrected until there was approximately zero calculated phase difference in E_{ss} and E_{cs} in the far field well below path. For the SBR, the SBO and CSB phase difference was set to exactly 180 degrees in the lower antenna. The phase of the SBO current in the upper antenna was corrected until there was approximately zero degrees calculated phase difference in E_{ss} and E_{cs} in the far field well below path.

b. Positions of the Radiators. For the null reference measurements, several flights were made at mean tide periods and a graph made of glide-slope angle versus upper antenna height. Using this emperical relationship, the best estimate for the proper upper antenna height for a 2.05° path angle was made. This point is the star on the graph in Figure 6-59 and indicates a height of 35.8 feet. The lower antenna was set at half that, or 17.9 feet, with both measured from the concrete base of the antenna mast. For modeling purposes these heights were then referred to the intersection of the mast and the extended average ground plane by adding 0.87 feet to both heights (see Figure 6-60).

c. Terrain Data. The terrain in this case consists of both ground and ocean. The ground data was taken from an elevation map, part of which is shown in Figure 6-61. The point at the threshold arbitrarily referenced at +10' is actually +15' MSL. A ground profile plot is made in Figure 6-60 for points along a line from the transmitting antennas in the direction parallel to the runway centerline. To a good approximation the ground reflecting terrain can be considered to be made up of five straight line segments as shown in Figure 6-60. The distance from the ground segment to the ocean surface was found from the tide plots provided by the FAA shown in Figures 6-63 and 6-64. The times from the NR flight log (Figure 6-62) were used to determine the tide height from Figure 6-63. The level runs calculated were runs 2, 8, and 13 for NR; 4, 8, and 13 for the SBR. RTT runs 3, 9, and 14 were calculated for the NR system, and runs 18, 25, and 31 for the SBR system.

d. Aircraft Position. Calculations were made for level runs using a 1000 foot altitude, coming in from a distance of 50,000 feet out to 20,000 feet out from the glide-slope mast. The RTT flight comparisons were made with constant angle calculations, covering approximately the same range as the flight recordings showed, i.e., from about 7 to 1 nautical miles from the localizer. The theodolite position, reference angle, and reference width were input to the model and the calculated differential amplifier output (assuming perfect tracking) was produced by the model.

5. Summary. Correlation between calculations of glide-slope performance and actual FAA flight measurements was shown to be good for both the GTD and physical optics models when applied to both null reference and sideband reference systems tested on Runway 25 at Kodiak, Alaska. The GTD model calculated the path angle to within 0.08° for both the null reference and sideband reference systems for three different tide levels. The corresponding figures for the physical optics model are 0.08° and 0.10°. Very good correlation was also obtained for path width and symmetry. Both models were also used to simulate flyability (Pattern A) measurements. The correlation was generally good, but not as good as for the Pattern B level run cases. It should be pointed out that for some cases the path angles determined from Pattern A flyability measurements did not agree with those obtained from Pattern B level run measurements.

To the authors' knowledge such correlations have been documented only twice before. As these previous correlations were for flyability runs only, this is the first time that quantitative comparisons (i.e., actual angular differences measured in degrees) between mathematical model results and FAA measurements have been reported.

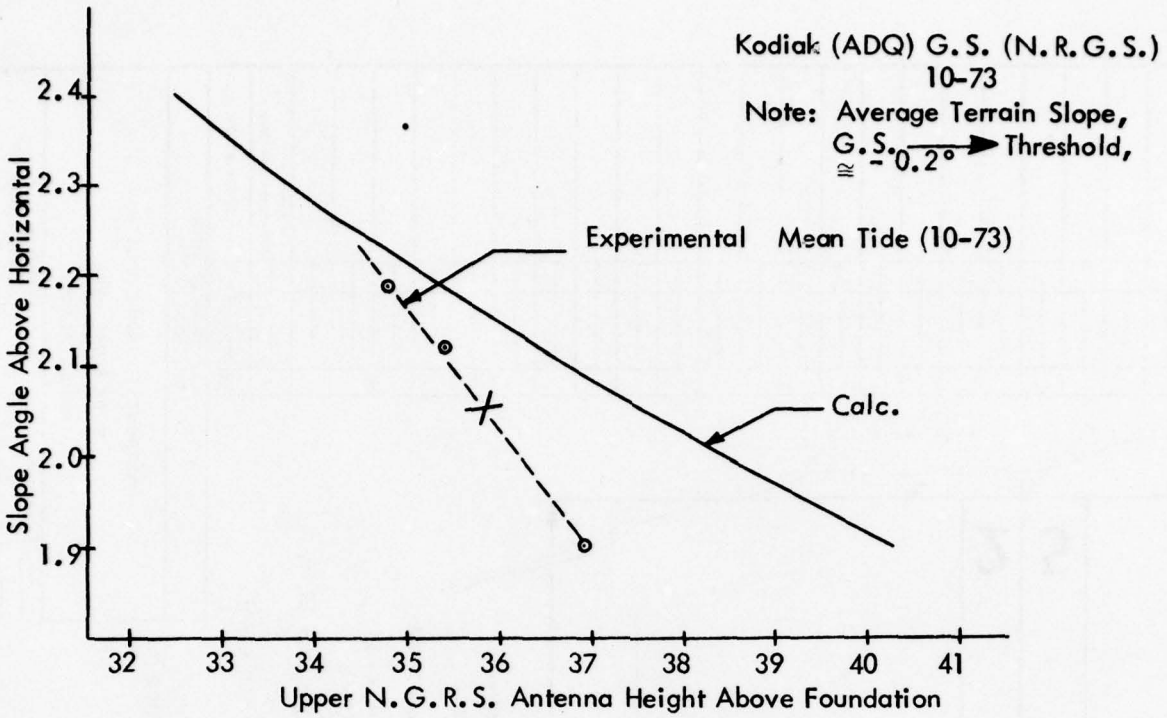

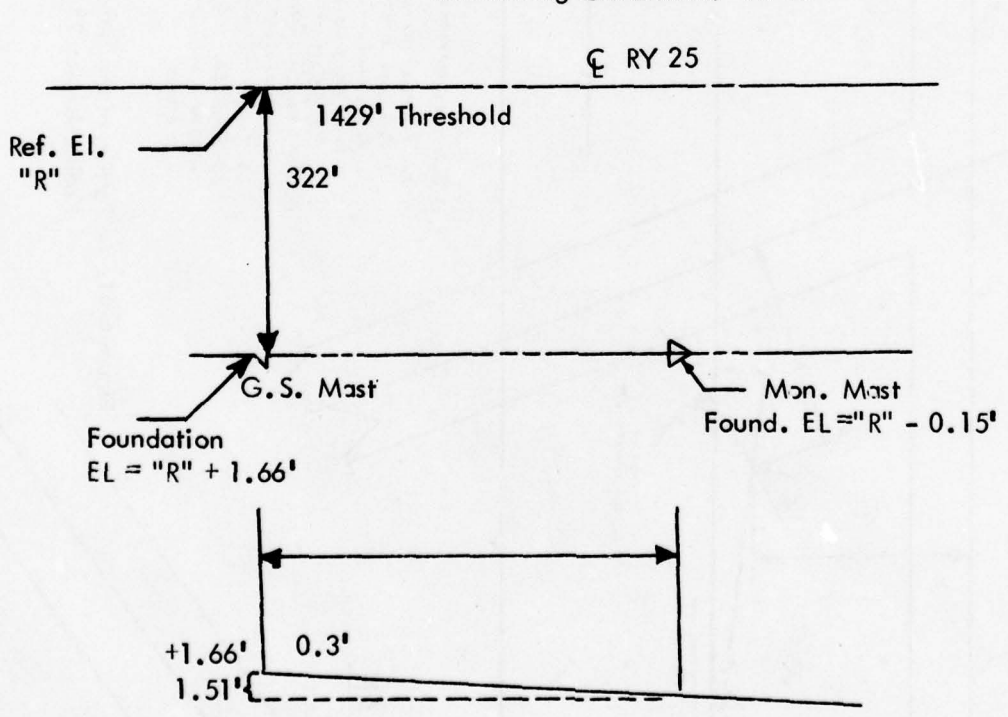

Figure 6-60. Graph for Experimental Determination of Upper Antenna Height for NR.[33]

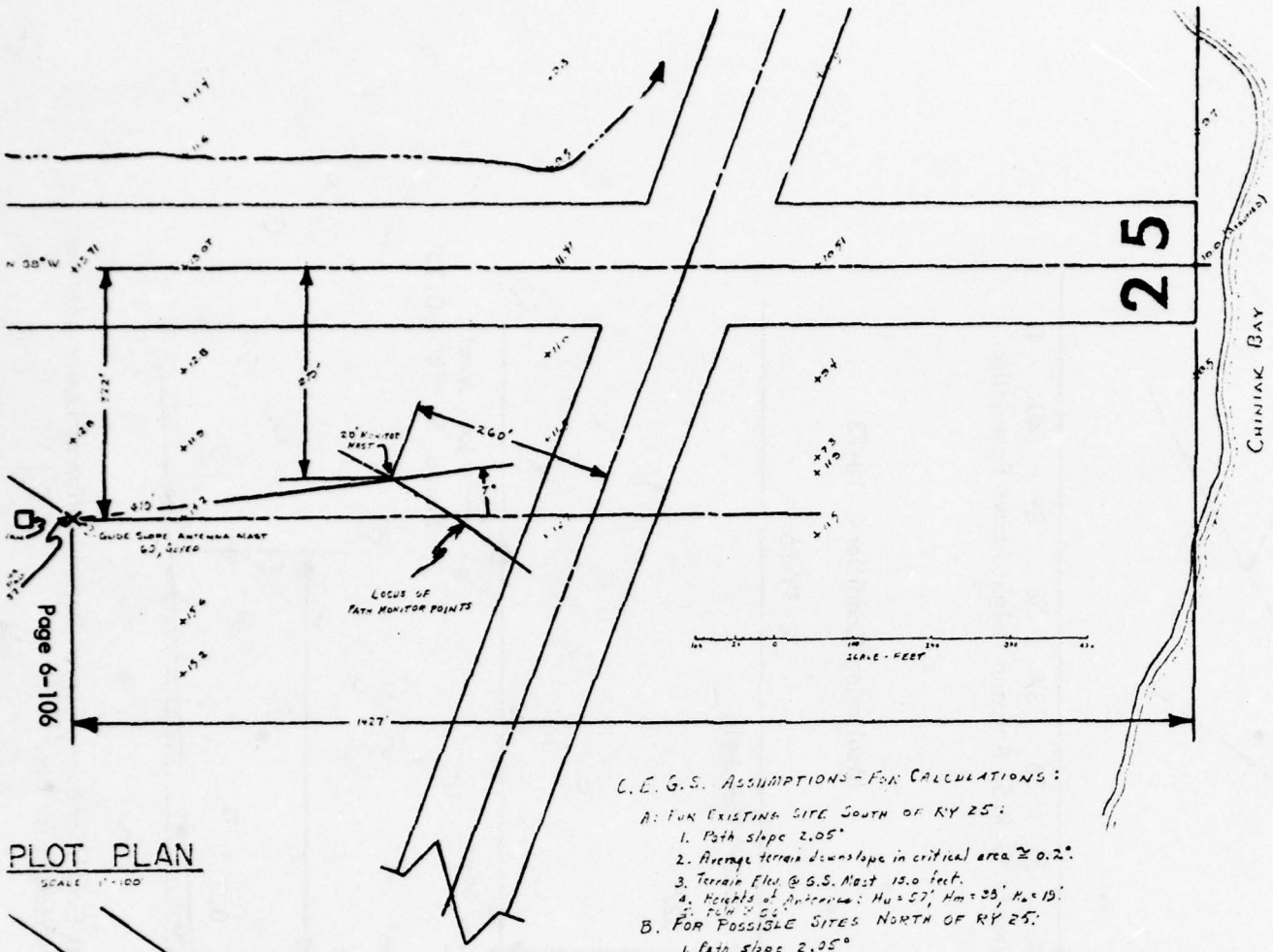

PLOT PLAN

SCALE 1" = 100

C. E. G. S. ASSUMPTIONS - FOR CALCULATIONS:

A. FOR EXISTING SITE SOUTH OF RY 25:
1. Path slope 2.05°
2. Average terrain downslope in critical area ≅ 0.2°.
3. Terrain Elev @ G.S. Mast 13.0 feet.
4. Heights of Antennas: $H_u = 57'$, $H_m = 38'$, $H_L = 19'$.
5. TCH ≅ 56'

B. FOR POSSIBLE SITES NORTH OF RY 25:
1. Path slope 2.05°
2. Average longitudinal Terrain Slope in Critical Area is 0.
3. Terrain Elev. @ G.S. Mast is 10.0 feet
4. Heights of Antennas: $H_u = 62.1'$, $H_m = 41.4'$, $H_L = 20.7'$
5. TCH ≅ 50'

NO	DATE	BY	DESCRIPTION
1	9-24-73	LMS	U.S. 70813 ESTABLISH DRAWING

DEPARTMENT OF TRANSPORTATION
FEDERAL AVIATION ADMINISTRATION

INSTRUMENT LANDING SYSTEM
GLIDE SLOPE AREA
KODIAK, ALASKA

PREPARED BY | SUBMITTED BY | APPROVED BY

Figure 6-61. Portion of the Terrain Contour Map for Kodiak Runway 25 Glide Slope.

PARTIAL FLIGHT CHECK LOG, KODIAK (ADQ) NULL-REFERENCE GLIDE SLOPE

N-76 (DC-3) 13 Oct. 1973

RCDG. NO.	TIME AL. DAYLIGHT	TIDE STAGE	RUN TYPE AND RMKS After Final Antenna Move.
1	1430	HI	LVL, WIDTH AND ANGLE (NARROW)
2	1440	HI	LVL, WIDTH AND ANGLE, "NORMAL" AS LEFT
3	1500	HI	RTT ON LOC ℄, ON PATH
4	1520	HI	RTT, ON LOC, 75 μA ABOVE PATH (SYMM.)
5	1525	HI	LVL, WIDTH AND ANGLE, ON 150 Hz SIDE LOC
6	1530	HI	RTT, SYMMETRY CK 75 μA BLO. PATH
7	1615	HI	LVL, WIDTH AND ANGLE, ON 90 Hz SIDE LOC
8	1645	MID	LVL, WIDTH AND ANGLE "NORMAL" ANGLE 2.02, WIDTH 0.68
9	1655	MID	RTT APCH ON PATH, ON LOC ℄
10	1708	MID	RTT APCH ON PATH, ON LOC ℄
11	1715	MID	RTT SYMM. CK, LOC ℄, 75 μA ABV. PATH
12	1724	MID	RTT SYMM. CK, LOC ℄, 75 μA BLO. PATH
13	2000	LO	LVL, WIDTH AND ANGLE, "NORMAL" ANGLE 2.29, WIDTH 0.68
14	2015	LO	RTT APCH ON PATH, ON LOC ℄
15	2025	LO	RTT APCH ON PATH, ON LOC ℄
16	2030	LO	RTT 75 μA ABV. PATH, ON LOC ℄
17	2045	LO	RTT 75 μA BLO. PATH, ON LOC ℄ (SYMM. CK)

CHECK SEQUENCE SELECTED BY BOB DAME, OF WASHINGTON, D.C., FLT. STDS. OFFICE

This sheet by G.A.H., AAL-431,
11 Nov. '76

Figure 6-62. Flight Log for Null Reference Tests [33].

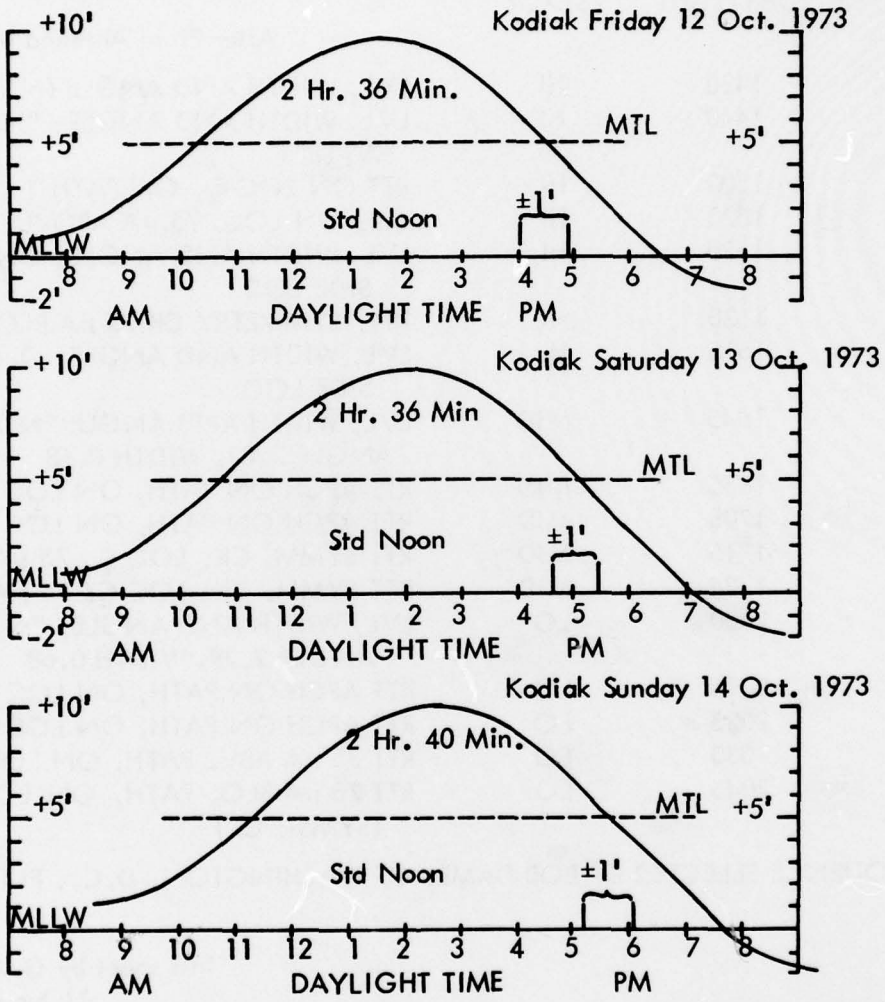

Note: Working periods for a desired tide level; allowable variation of ±1 Foot.

(a) Mean Tide Level (MTL)= book time ± 30 min.

(b) Max. or Min.:= book time ± 1 hour.

Figure 6-63. Tide Plots for NR Tests. [33]

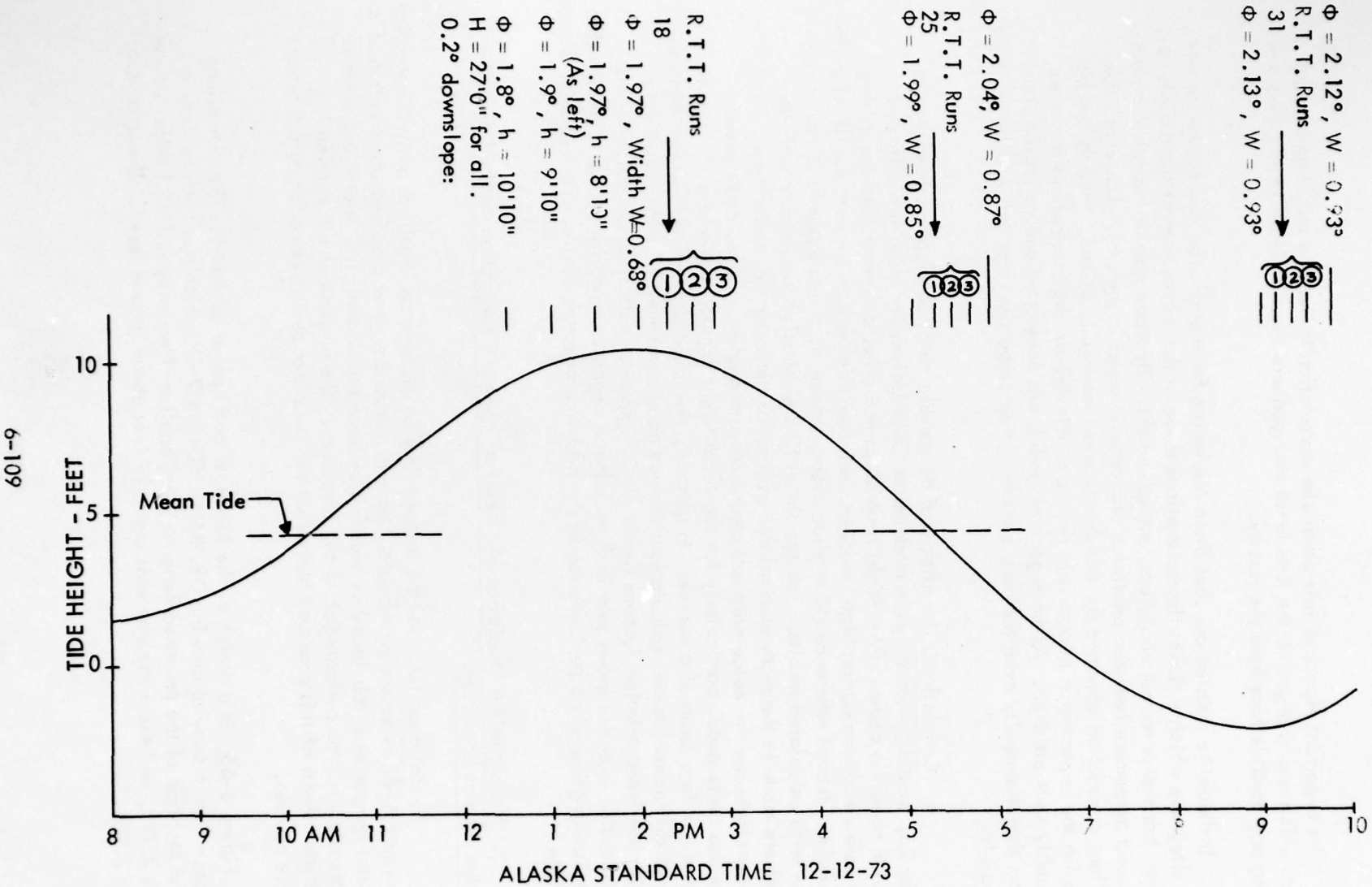

Figure 6-64. Tide Plots for SBR Tests. [33]

An important aspect of this particular correlation is that the only input to the models which was changed as the tide level changed was the tide level itself, thus removing any possible bias from the results.

It should be pointed out that these results are for a particular and somewhat unusual site, one which satisfies the assumptions made in the derivations of the models very well (no transverse terrain variations, smooth earth). Thus one cannot expect to obtain such good agreement between predicted and actual values in general. However, the excellent correlation obtained for this site proves that mathematical modeling can be used with the expectation of accurate results on sites where the assumptions made are reasonably well satisfied. As more general models are developed and validated, one expects that eventually even the most complex glide slope sites can and will be modeled accurately.

6. Conclusions. The effects of the terrain on glide-slope performance at Runway 25, Kodiak, Alaska, were modeled at Ohio University using two different computer modeling codes. FAA flight recordings and other pertinent data describing glide-path conditions during high, medium, and low tide periods for both a null reference (NR) and a sideband reference (SBR) glide-slope systems were available for direct comparison with calculated results. The terrain at Kodiak satisfies reasonably well the assumptions made in the mathematical derivations for the computer codes used. The agreement between the calculated and measured path angles, widths, and symmetry figures was quite good, particularly for the level flight comparisons where the agreement was within a tenth of a degree. In general, the Ohio University GTD (geometrical theory of diffraction) model calculations showed good agreement with measured data and with the Transportation Systems Center P.O. (physical optics) model calculations. This validation exercise shows that both models are capable of providing usable information for predicting glide-slope performance in the presence of rough terrain with two dimensional variations.

D. Mathematical Prediction of Effects of Hangar Construction on the Denver Stapleton Airport Localizer.

1. Introduction. At the present time an eight-loop localizer array is operational on Runway 26L-8R at Stapleton Airport, Denver, Colorado. The proposed construction of a new metal hangar near this localizer was felt to have the potential of interfering electromagnetically with the performance of the localizer. The purpose of this section is to predict the effects of this proposed hangar on the localizer performance for both the front and back courses.

Figure 6-65 is a sketch of the localizer and hangar geometry. The dimensions were taken from a copy of drawing DR.RM-D 400-40477-IX which had been revised to show the location of the proposed hangar. The localizer frequency is 110.3 MHz, course width is 3.79°, and the array elements are 6.17 feet above ground level. The approach angle is 2.75°.

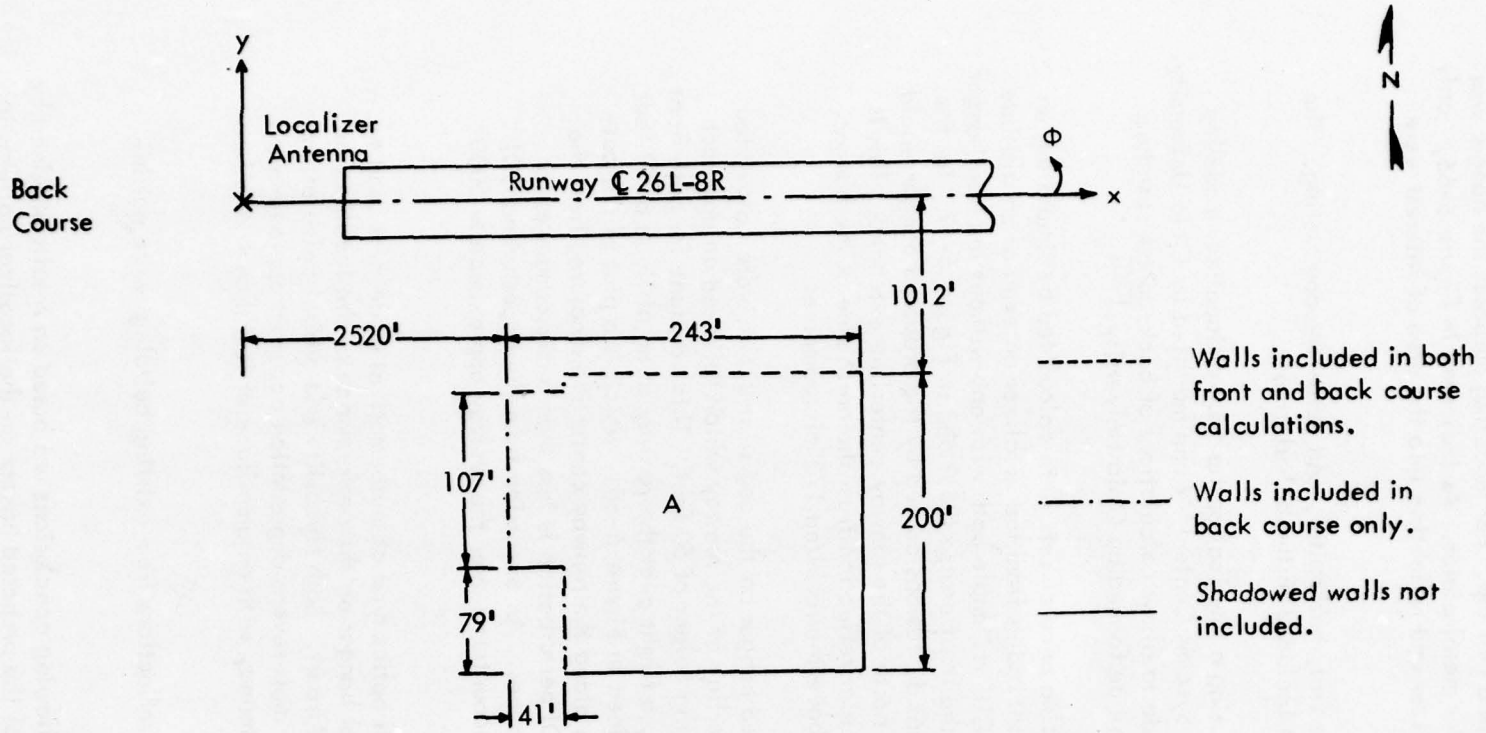

Figure 6-65. Building A Geometry and Relation to Localizer Antenna - Denver Stapleton Runway 26L-8R. Building A is 32 feet high.

The hangar is to be metal with a flat top. For modeling purposes the hangar was assumed to be made of flat rectangular metal plates. As indicated in Figure 6-66, only those plates illuminated by the localizer and reflecting into the area of interest were included in the calculations.

The ground was assumed to be flat, horizontal, and perfectly-conducting. The effects of existing buildings were not included in the calculations.

The calculations were made using a physical optics type of localizer modeling program developed at Transportation Systems Center [22] and modified by Ohio University. In particular, modifications were made to allow calculations of back-course structure. This program is based on previous work performed by Ohio University. [36]

2. Results. Off-course clearance effects were calculated by simulating an orbital flight at a constant 15,000-foot radius from the localizer antenna at an altitude of 1000 feet. The resulting plots of CDI vs. angle both with and without the new hangar present are shown in Figure 6-66 for the front course (26L) and in Figure 6-67 for the back course (8R). The only significant deviations caused by the proposed hangar would be in the front course from 10 to 18° north of the runway centerline extended. This is the approximate direction of the specular reflection from the north side of the hangar. Even in this region the CDI is well above the required 175 microamperes.

Possible effects of the proposed hangar on the course structure were calculated by simulating a flight along the centerline of the runway which followed an approach angle of 2.75° with a threshold crossing height of 50 feet. This was done for both front course and back course. In addition, a flight over the runway at an altitude of 50 feet was simulated. The results are combined in Figure 6-68, which is a plot of the calculated CDI envelope versus distance along the runway centerline measured from the localizer antenna. The predicted CDI perturbation is less than 5 microamperes for both the front and back course approaches. An excursion from the unperturbed CDI of up to 20 microamperes could be encountered over the runway approximately 5000 feet in front of the localizer antenna.

3. Summary. A physical optics type of mathematical model was used to predict the effects of a proposed metal hangar on the performance of the localizer on Runway 26L-8R at Denver Stapleton Airport. Both flyability and orbital calculations were made. These indicated that the most severe degradation occurred approximately 5000 feet in front of the localizer antenna, with an amplitude of less than ± 20 microamperes from nominal.

Terrain effects and effects of reflections from existing buildings were not included in the model.

4. Conclusions. The following conclusions are based on results obtained by mathematically modeling the effects of the proposed hangar on the localizer patterns in space for Runway 26L-8R at Denver Stapleton Airport.

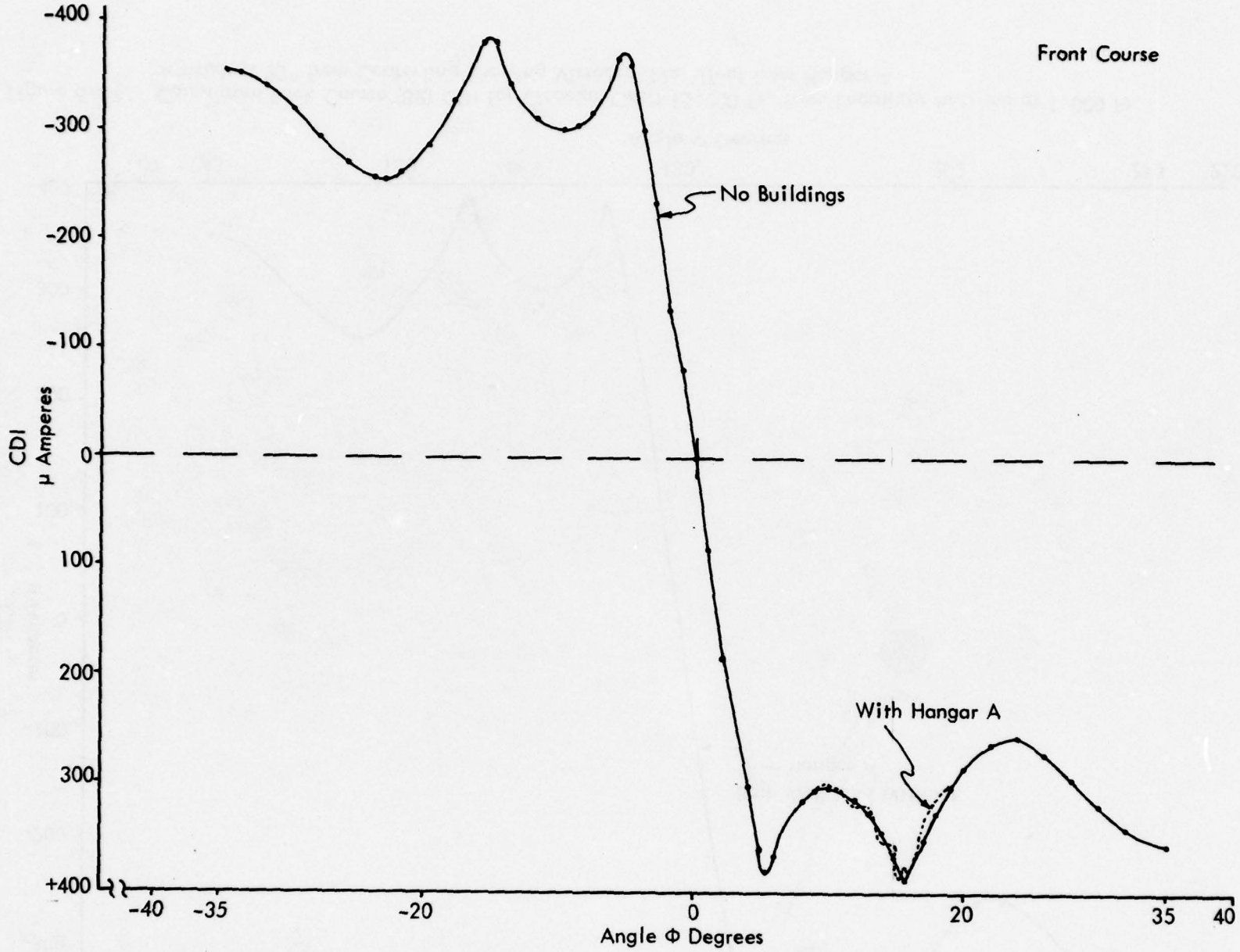

Figure 6-66. Calculated Front Course (26L) for Circular Orbit 15,000 Ft. from Localizer Antenna at 1,000 Ft. Altitude ±35° from Centerline Showing Slight Perturbing Effect of Hangar A.

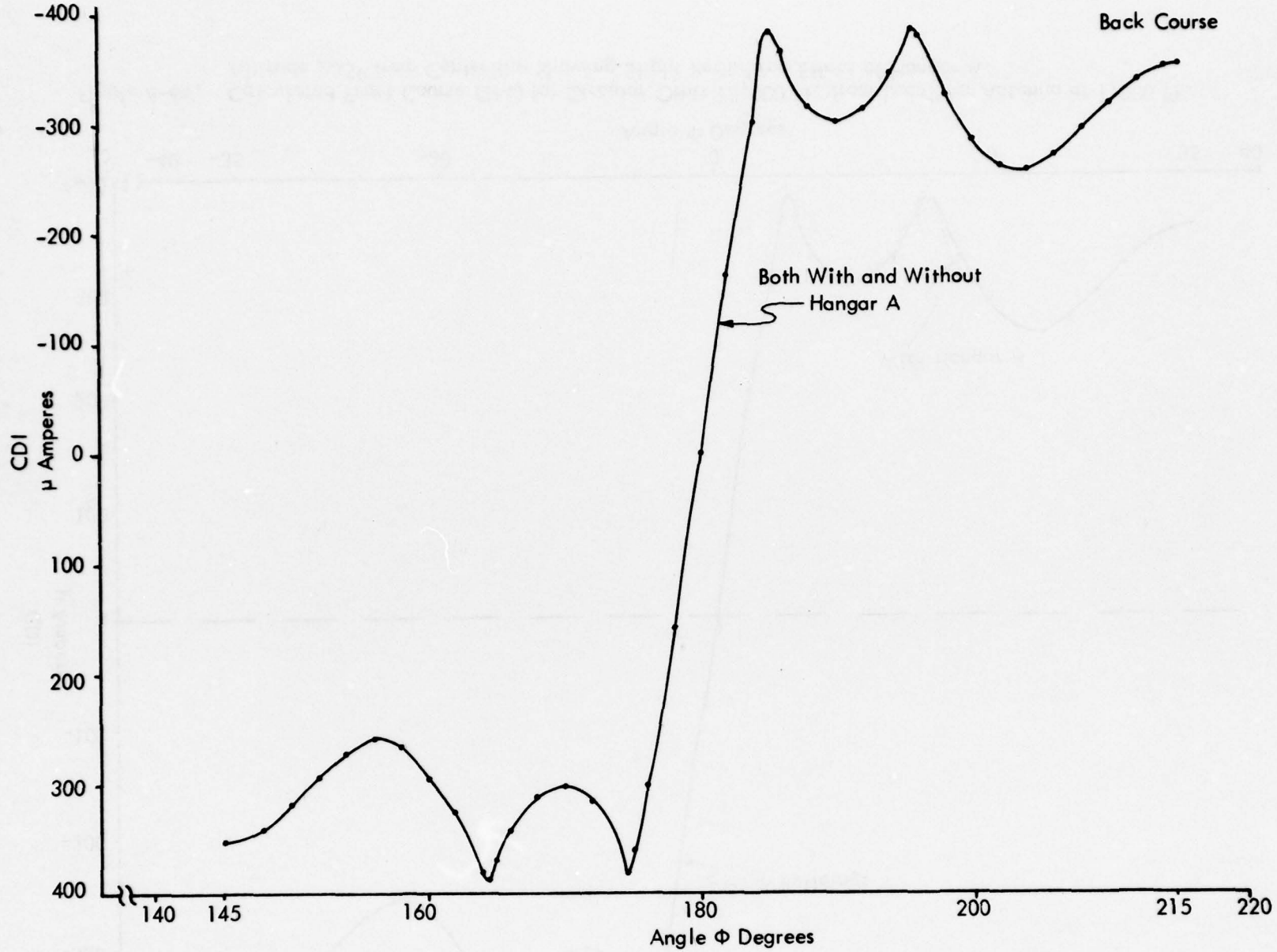

Figure 6-67. Calculated Back Course (8R) CDI for Circular Orbit 15,000 Ft. from Localizer Antenna at 1,000 Ft. Altitude ± 35° from Centerline Showing Virtually No Effect from Hangar A.

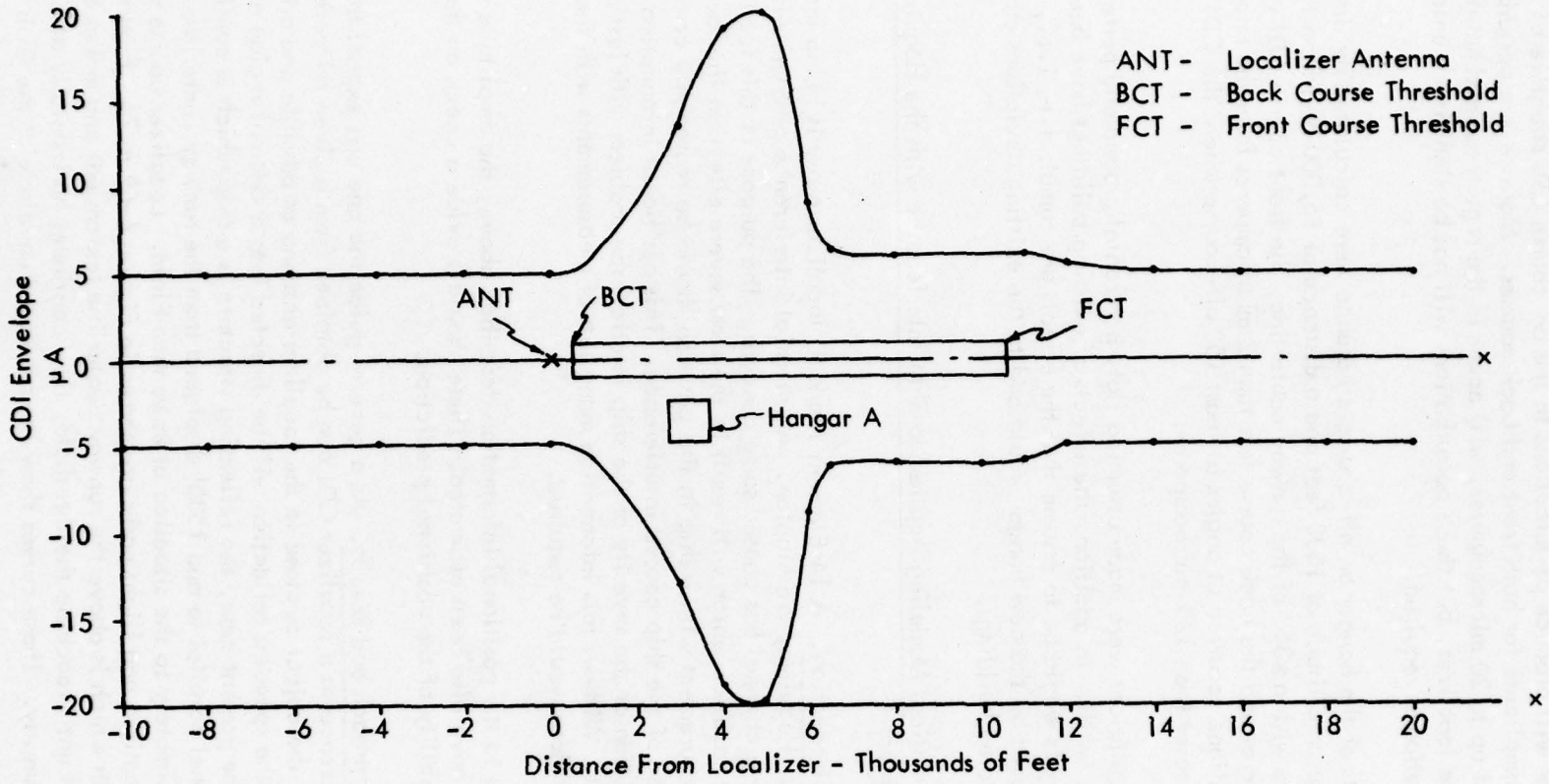

Figure 6-68. Stapleton Field Localizer CDI Envelope for a 2.75° Flight Angle (from Horizontal) Above Runway Centerline Due to Derogation Caused by Proposed Hangar A. Between thresholds the simulated aircraft maintains a 50' altitude.

The hangar will produce perturbations in the on course CDI structure of less than ±5 microamperes amplitude for both front and back courses. More severe perturbations, with amplitudes of up to 20 microamperes, will occur in the region approximately 5000 feet in front of the localizer, but these perturbations will not be significant unless Category III operation is required.

The effects of the hangar on off-course clearance were calculated by simulating an orbital flight at an altitude of 1000 feet and a distance of 15,000 feet from the localizer. For angular sectors within ±35° of the runway centerline, the front course CDI varied less than 15 microamperes and the back course less than 2 microamperes from the unperturbed CDI. These variations occurred at angles at least 15° off-course where the CDI was (and remained) greater than 175 microamperes.

These calculations were made assuming flat, horizontal ground and perfectly-conducting hangar walls. In addition, the effects of existing buildings have been neglected. A worst-case analysis would be to assume that the effects are cumulative, i.e., that the CDI deviation caused by the new hangar would add to the existing deviations due to previously constructed buildings.

E. Mathematical Modeling Applied to Ship Interference with the Hoquiam, Washington Localizer.

1. Introduction. A 14-Element Mark ID localizer array is being installed at Bowerman Field, Hoquiam, Washington. A potential interference problem with ships in a nearby shipping channel has caused some concern. The purpose of this section is to predict the ship location which will result in the most severe effect on the localizer CDI. A flight measurement with a ship in this position should be reasonably certain to be the worst case of the ship caused interference. This positional information will permit a determination of the severity of the ship interference problem with just one flight measurement. Without this information many sets of measurements with the ship in various positions would be required.

In addition to the positional information described above, the amplitude of the CDI perturbations have also been estimated. These should provide a check on the accuracy and reliability of the positional prediction.

2. Approach and Results. As a general guideline one can expect that the most severe interference to a localizer CDI can be obtained from a given reflecting object by locating the object as close to the localizer antenna as possible and orienting the object so that the specular reflection will be directed into a critical region of the flight path. For the present case, the reflecting structure is a ship which is confined to a shipping channel parallel to and 1500' displaced from the runway centerline. This corresponds approximately to the situation at Bowerman Field. Localizer course perturbations for various ship locations and flight paths are shown in Figures 6-69 to 74. Figures 6-69 to 71 are for a flight path which is above the runway centerline (extended) and makes a 3° angle with the horizontal until reaching the threshold, then continues horizontally at a 50' elevation above the runway. These curves show the predicted envelope of the CDI; the

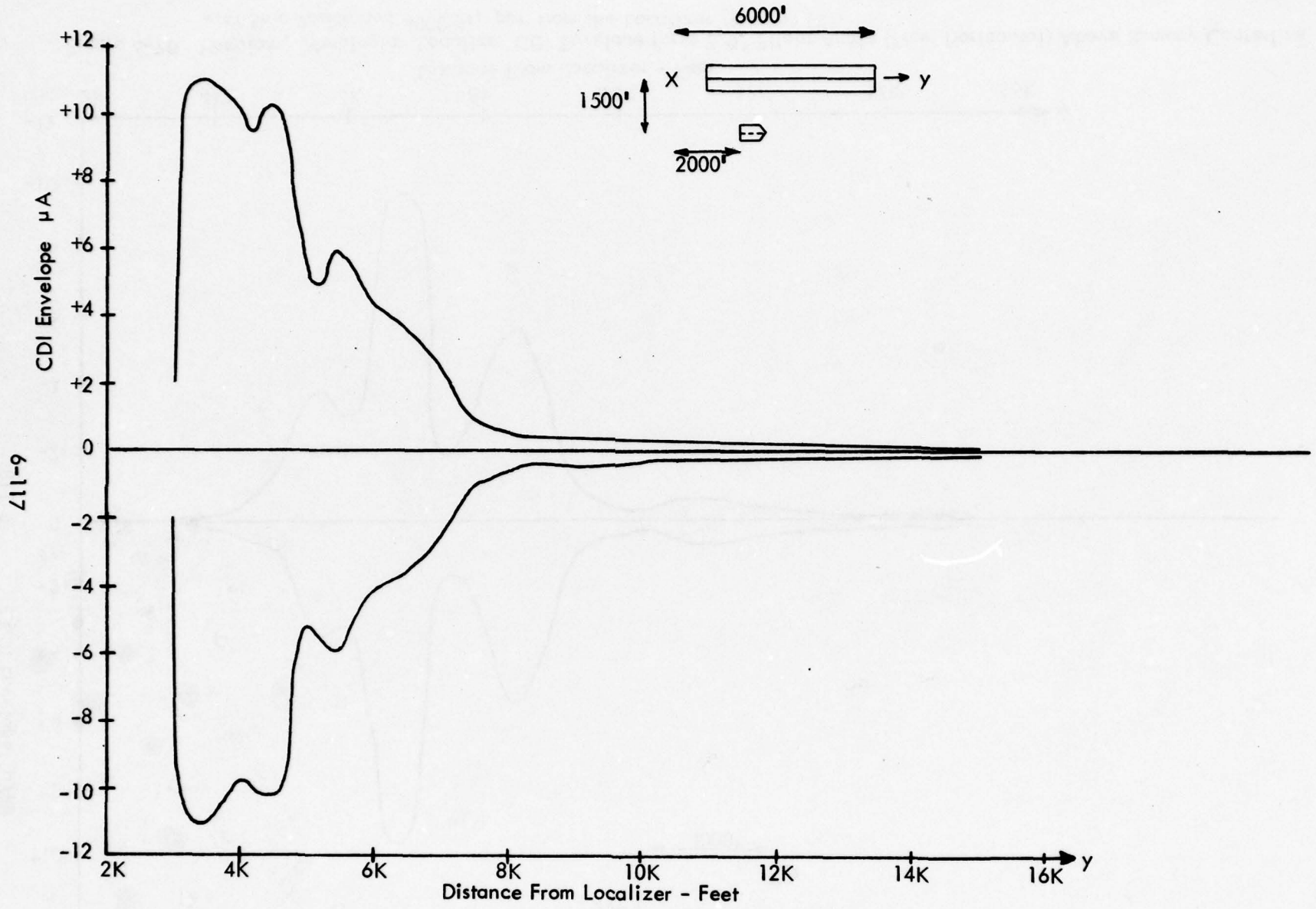

6-117

Figure 6-69. Hoquiam, Washington Localizer CDI Envelope for a 3.0° Flight Angle (From Horizontal) Above Runway Centerline with Ship Positioned 2000 Ft. out from the Localizer Antenna (X).

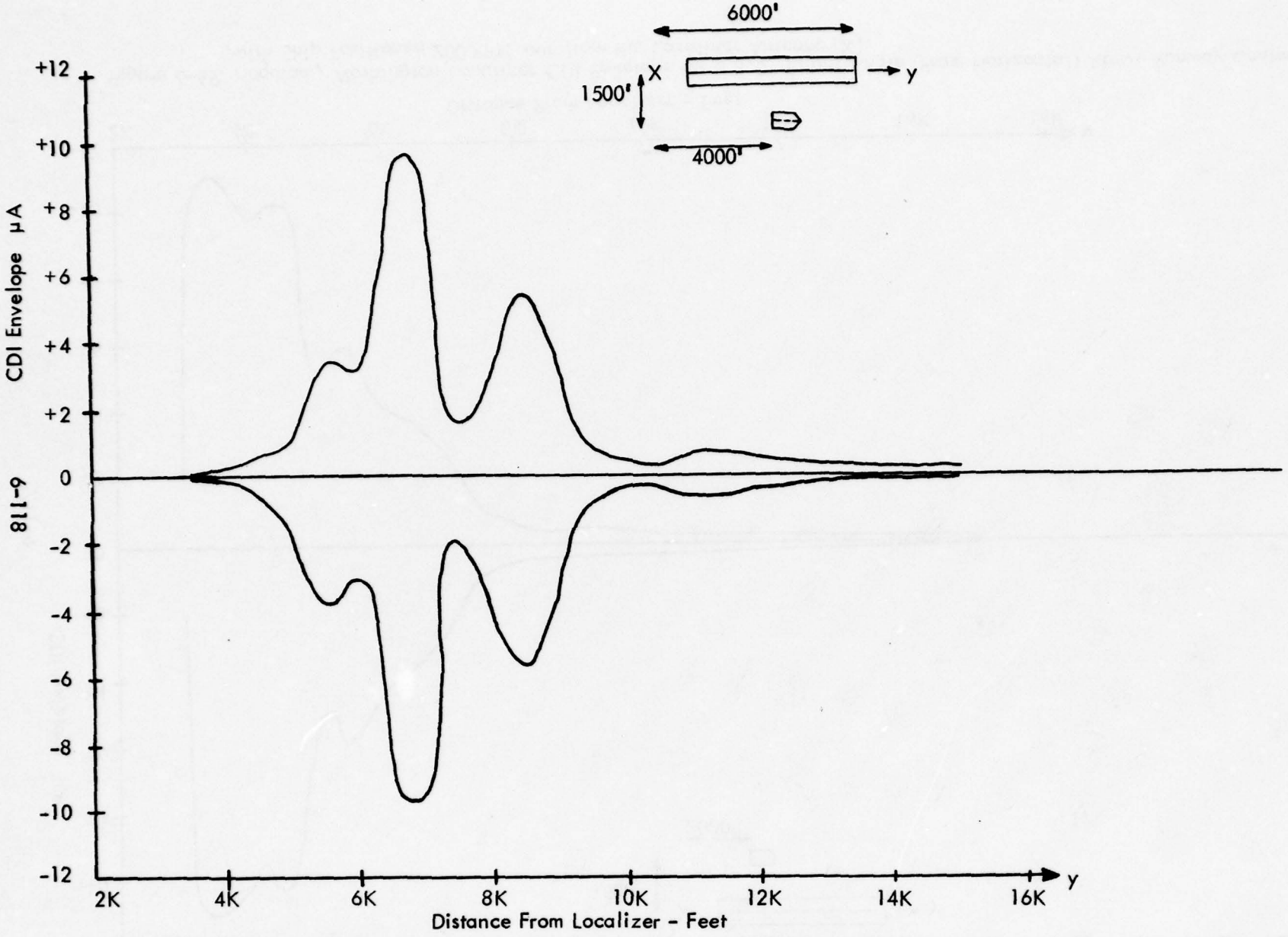

Figure 6-70. Hoquiam, Washington Localizer CDI Envelope for a 3.0° Flight Angle (From Horizontal) Above Runway Centerline with Ship Positioned 4000 Ft. out from the Localizer Antenna (X).

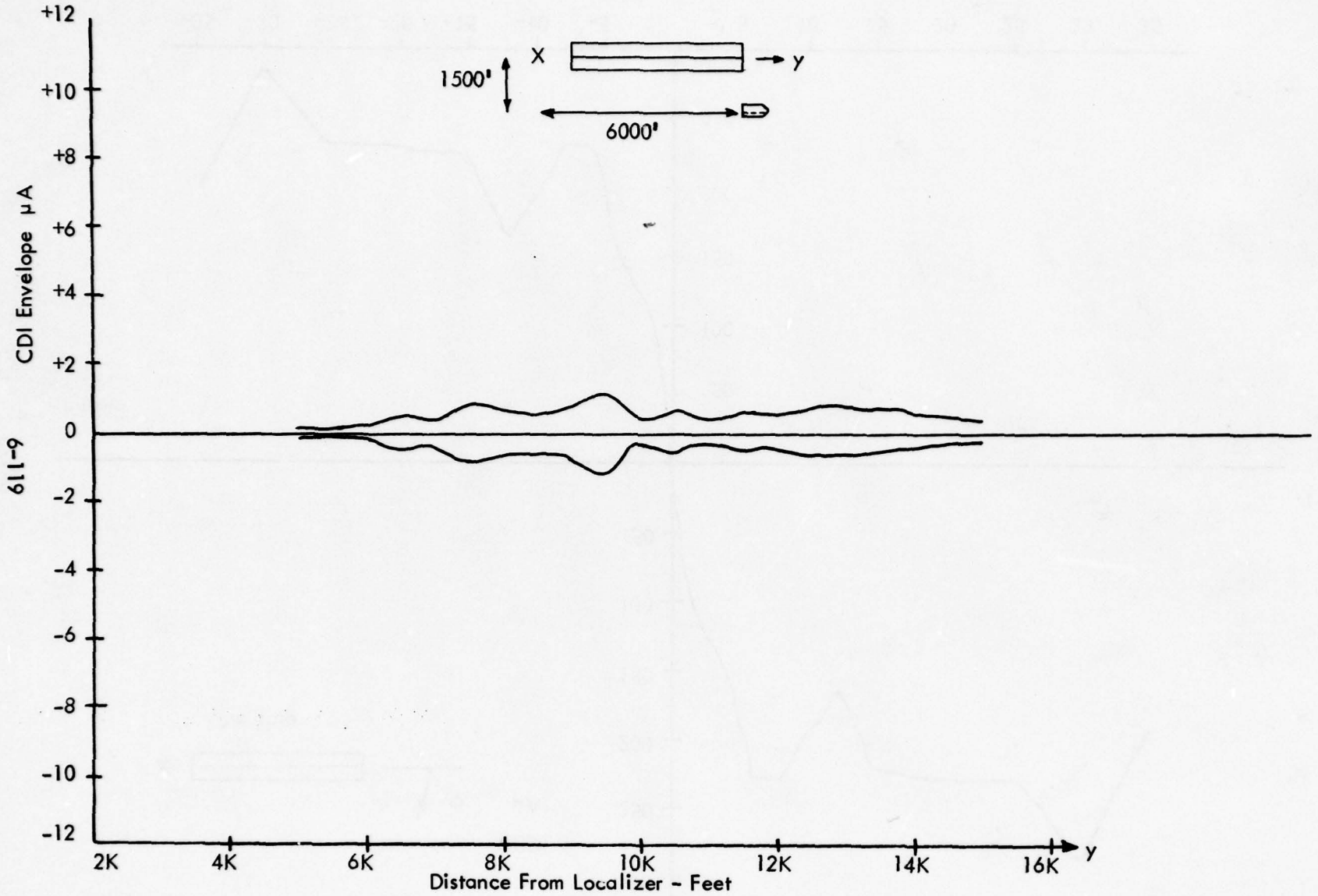

Figure 6-71. Hoquiam, Washington Localizer CDI Envelope for a 3.0° Flight Angle (From Horizontal) Above Runway Centerline with Ship Positioned 6000 Ft. out from the Localizer Antenna (X).

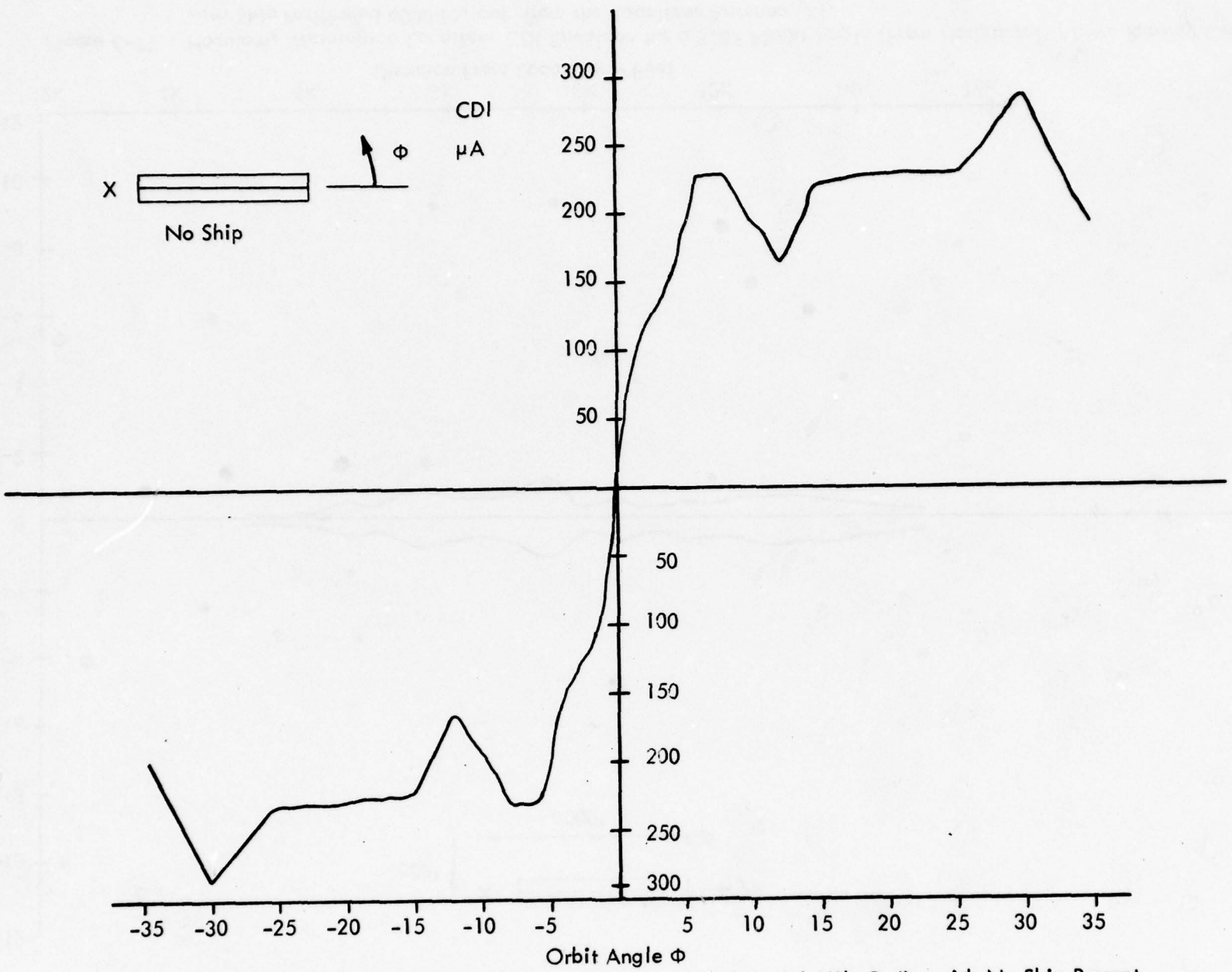

Figure 6-72. Predicted CDI for Orbital Flight at 1000 Ft. Altitude and 6 Mile Radius with No Ship Present.

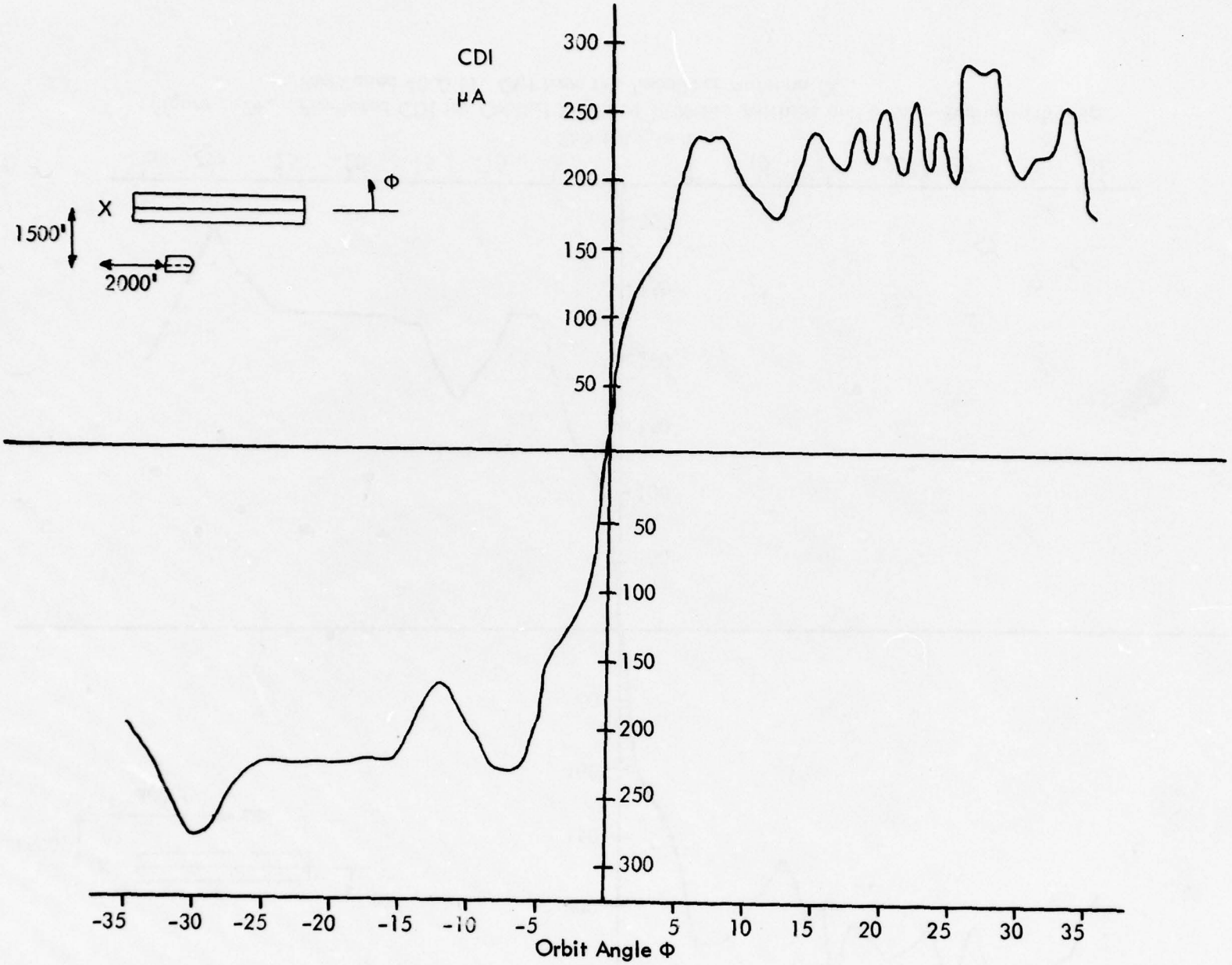

Figure 6-73. Predicted CDI for Orbital Flight at 1000 ft. Altitude and 6 Mile Radius with Ship Positioned 2000 ft. out from the Localizer Antenna (X).

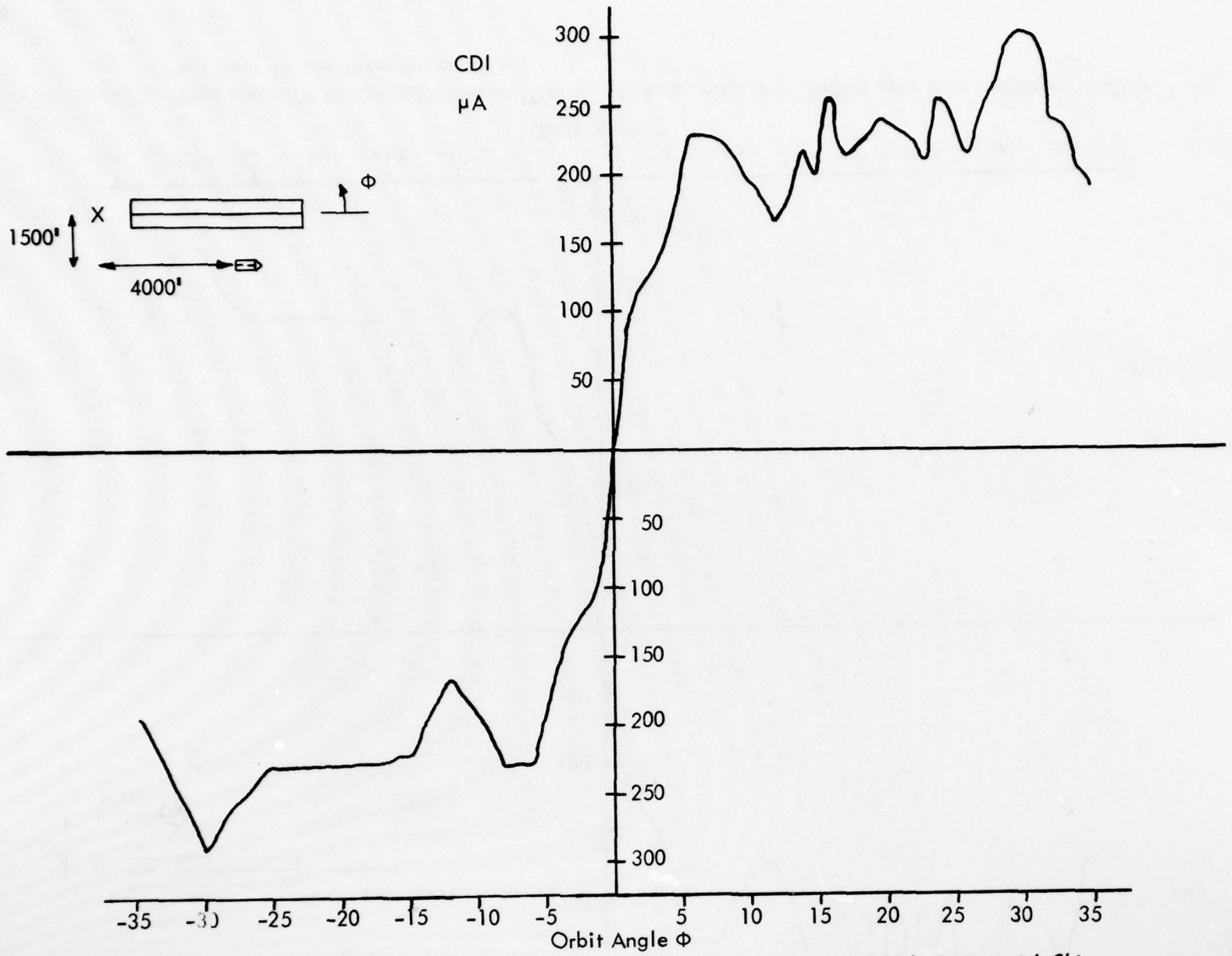

Figure 6-74. Predicted CDI for Orbital Flight at 1000 Ft. Altitude and 6 Mile Radius with Ship Positioned 4000 Ft. Out from the Localizer Antenna (X).

the actual CDI values should be within this envelope. The largest CDI deviations are with the ship positioned 2000 ft. out from the localizer, but these deviations occur inside the threshold. Thus it would appear from Figure 6-70 that for the most severe effect the ship should be positioned approximately 4000 ft. out from the localizer, and that the maximum CDI roughness will occur just outside threshold and be less than ± 11 μA from nominal.

Figures 6-71 to 74 are calculated CDI's for ±35° orbital runs at a height of 1000 ft. and a range of 6 (nautical) miles. From this data it is evident that the effect of the ship is to add a ripple to the unperturbed CDI on the side opposite the ship; i.e., in the direction of the specular reflection. This ripple is small enough that the CDI should remain within ±15 μA of the nominal, unperturbed CDI.

These results were obtained using a physical optics type of localizer modeling program developed at Transportation Systems Center[22] and modified by Ohio University. This program is based on previous work performed by Ohio University.[36] The CSB and SBO radiation patterns for the 14-Element Mark ID array shown in Figure 6-75 were used by the modeling program to determine the illumination of the ship. The relative amplitude of the two patterns was adjusted to provide an approximate course width of 6°.

The scale of the patterns in Figure 6-75 is such that highly accurate determination of the pattern structure for small angles is quite difficult, and thus a small deviation from the nominal course width could not be avoided. This deviation should not severely affect the results obtained.

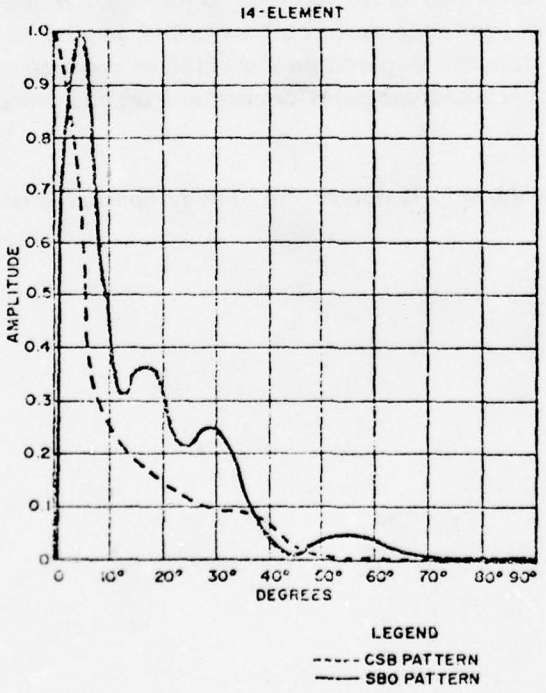

Figure 6-75. Antenna Radiation Patterns for 14-Element Mark ID LPD Array.

The modeling program requires that the interfering object(s) be modeled using combinations of flat plates. Figure 6-76 illustrates the model of the ship which uses vertical flat plates. Two plates are used for the body of the ship itself, one for the side and one for the bow. The dashed plates were not included because these portions of the ship are shadowed. Three narrow vertical plates were used to model the ship superstructure, the outline approximating a ship with a bridge and two loading cranes. The total height of the ship is 100 ft., with the superstructure accounting for 60 ft. of the total.

3. Summary. A physical optics type of mathematical model was used to predict the effects of a nearby ship on the Hoquiam, Washington localizer. While the predictions must be considered approximate due to the difficulty of accurately modeling the reflections from a ship, the results show that the effects of the ship will not cause a severe degradation of the localizer CDI structure in space.

Both flyability and orbital calculations were made. These indicate that the most severe effects will occur when the ship is located approximately 4000 ft. out from the localizer antenna.

4. Conclusions. The following are conclusions based on a brief analytical study of the effects on the localizer patterns in space of ships operating in a channel near the runway.

For a channel parallel to the runway and 1500 feet to the side, a 500-foot long ship with total height of 100 feet will produce perturbations in the on-course structure of ±11 micromaperes. Reflections from the ship can be expected to produce scallops in the clearance pattern amounting to ±15 microamperes deviation from the unperturbed pattern.

The worst-case location for the ship is abeam the runway approximately 4000 feet out from the localizer array.

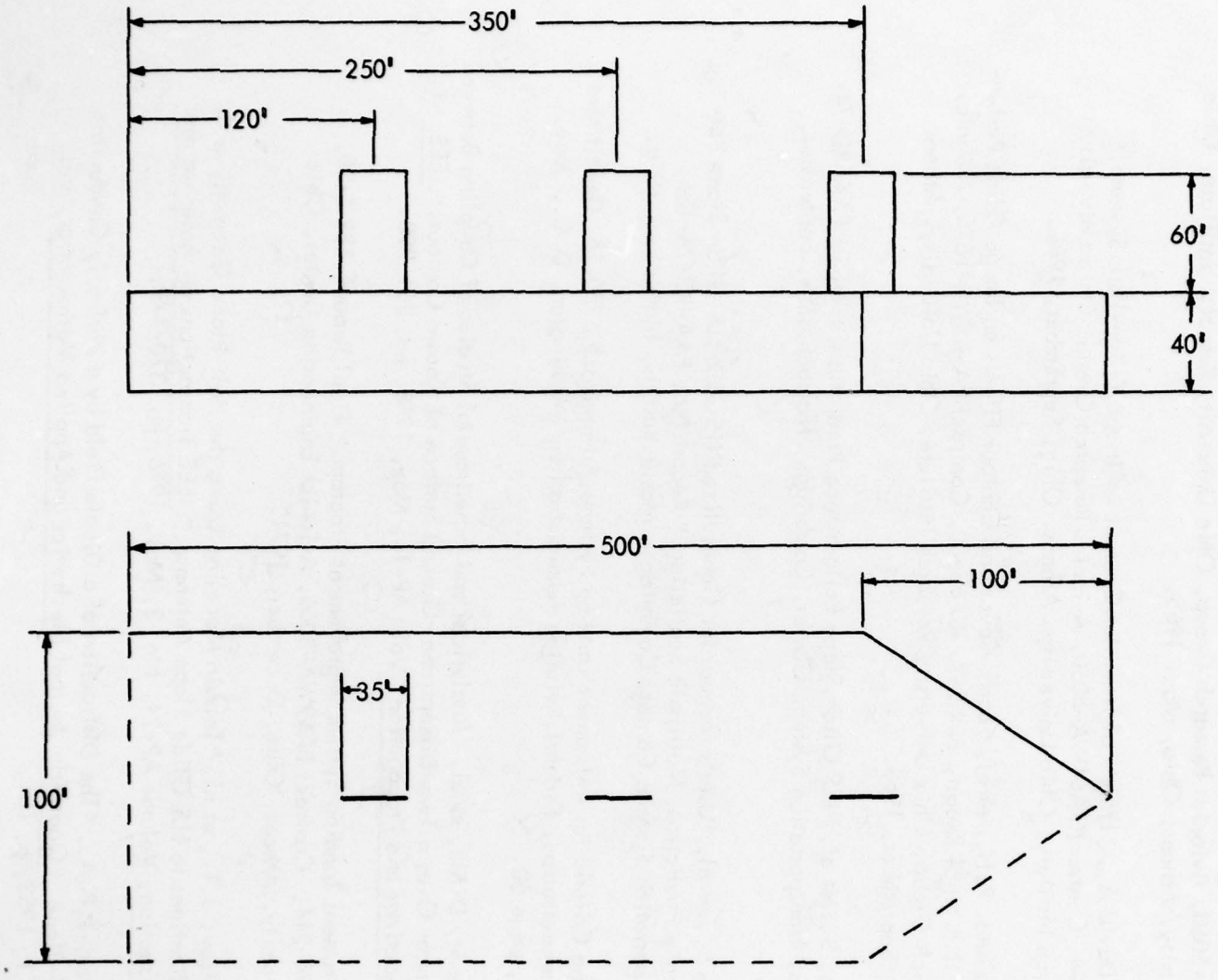

Figure 6-76. Ship Modeled Using Five Vertical Flat Plates.

F. References for Section VI.

[1] McFarland, R.H., David Hill, and Donald Luttermoser, "Earth Cover and Contour Effects on Image Glide Paths," Final Report, EER 5-1, RD 65-30, Contract FA-64WA-5060, Avionics Research Group, Ohio University Research Institute, Ohio University, Athens, Ohio, May, 1965.

[2] Hill, David A., "Effects of Irregular Contour on Image Glide-Path Systems," EER 5-4, Contract FA64WA-5060, Avionics Research Group, Ohio University Research Institute, Ohio University, Athens, Ohio, September, 1966.

[3] McFarland, R.H., et al, "Earth Cover and Contour Effects on Image Glide Paths--Phase II," Final Report, EER 5-7, RD 68-60, Contract FA-67WA-1676, Avionics Research Group, Ohio University Research Institute, Ohio University, Athens, Ohio, September, 1968.

[4] Morin, S., et al, "ILS Glide Slope Performance Prediction," Report FAA-RD-74-157.B, Transportation Systems Center, Cambridge, Massachusetts, September, 1974.

[5] Morin S., et al, "User's Manual for Generalized ILSGLD-ILS Glide Slope Performance Prediction: Multipath Scattering," Report No. FAA-RD-76-186, Transportation Systems Center, Cambridge, Massachusetts, November, 1976.

[6] "Siting Criteria for Instrument Landing Systems," Handbook 6750.16, Department of Transportation, Federal Aviation Administration, Washington, D.C., June, 1971, page 50.

[7] Cunnold, D.M., et al, "Analytical and Experimental Studies of Coupling Between Antennas Over a Two-Dimensional Ground Surface of Known Contour," IEEE Transactions and Propagation, Vol. AP-16, May, 1968, pp. 291-298.

[8] "Instrument Landing System Improvement Program," Final Report, EER 5-20, RD-74-214, Contract FA69WA-2066, Avionics Engineering Center, Ohio University, Athens, Ohio, December, 1974.

[9] Godfrey, J.T., et al, "Terrain Modeling Using the Half-Plane Geometry with Applications to ILS Glide Slope Antennas," IEEE Transactions on Antennas and Propagation, Volume AP-24, No. 3, May, 1976, pp. 370-378.

[10] Senior, T.B.A., "The Diffraction of a Dipole Field by a Perfectly Conducting Half-Plane, "Quarterly Journal Mechanics and Applied Mathematics, Vol. VI, Part 1, 1953, p. 101.

[11] Woods, B.D., "The Diffraction of a Dipole Field by a Half-Plane," Quarterly Journal Mechanics and Applied Mathematics, Volume X, Part 1, 1957, p. 90.

[12] Bromwich, T.J.I.A., Proceedings of the London Mathematical Society, Vol. 14, 1915, p. 450.

[13] Redlich, R.W., "Computed Performance of Glide Slope Arrays on Sites with Limited Ground Plane," IEEE Transactions on Aerospace and Electronic Systems, Vol. AES-7, No. 5, September, 1971.

[14] Luebbers, R.J., R.G. Kouyoumjian, and L. Ton-That, "GTD-AMP Computer Program Description," Report 4066-2, The Ohio State University, Department of Electrical Engineering, Columbus, Ohio, prepared under Contract F 30603-75-C-0051 with Rome Air Development Center.

[15] Keller, J.B., "Geometrical Theory of Diffraction," Journal Optical Society of America, Vol. 52, 1962, pp. 116-130.

[16] Kouyoumjian, R.G., and P.H. Pathak, "A Uniform Geometrical Theory of Diffraction for an Edge in a Perfectly Conducting Surface," IEEE Proceedings, Vol. 62, No. 11, November, 1974, pp. 1448-1461

[17] Luebbers, R.J., private communication to Mr. Rial Sloan, AAF-421, Department of Transportation, Federal Aviation Administration, FOB 10A, 800 Independence Avenue, Washington, D.C., May 1977.

[18] Tran, H.B., "Investigation of the Effects of Irregular Contour on the Watts Two-Antenna Slotted-Cable, End-Fire Glide-Slope System," Master of Science Thesis, Avionics Engineering Center, Department of Electrical Engineering, Ohio University, Athens, Ohio 45701, March 1975.

[19] Ramakrishna, S., and M. Sachidananda, "Calculating the Effect of Uneven Terrain on Glide Path Signals," IEEE Transactions on Aerospace and Electronic Systems, Vol. AES-10, No. 3, May, 1974, pp. 380-384.

[20] Somerfeld, A., "Mathematische Theorie der Diffraktion," Math. Ann. Vol. 47, 1896.

[21] Luebbers, R.J., L.H. Mitchell, Vichate Ungvichian, and R.H. McFarland, "Mathematical Modeling of Terrain Effects on ILS," Final Task Report (Carswell), Avionics Engineering Center, Department of Electrical Engineering, Ohio University, Athens, Ohio, July,1977.

[22] Chin, G., et al, "Instrument Landing System Scattering," Report No. FAA-RD-72-137, Transportation Systems Center, Cambridge, Massachusetts, December, 1972.

[23] Chin, G., et al, "User's Manual for ILSS (Revised ISLOC): Simulation for Derogation Effects on the Instrument Landing System," Report No. FAA-RD-76-217, Transportation Systems Center, Cambridge, Massachusetts, December, 1976.

[24] Hollins, Clinton G., "Effects of United Air Lines' Proposed Type B-747 Hangar on Localizer Courses at O'Hare International Airport," prepared for United Air Lines under UAL Contract Number 21147 by Scanwell Laboratories, Springfield, Virginia, December 1967.

[25] "Instrument Landing System Improvement Program," Interim Report, EER 5-11, RD 71-30, Contract FA69WA-2066, Avionics Engineering Center, Department of Electrical Engineering, Ohio University, Athens, Ohio, October, 1971.

[26] Rondini, Robert, "A Study of Diffraction of Electromagnetic Waves Around Large Stationary Aircraft and Its Effects on Instrument Landing System Guidance Signals," (Dissertation), Avionics Engineering Center, Department of Electrical Engineering, Ohio University, Athens, Ohio, June, 1976.

[27] Rondini, Robert, and R.H. McFarland, "Experimental Validation of Boeing 747 ILS Signal Scattering Calculations for Critical Area Determination," Final Report, FAA Report Number RD-74-57, Report EER 18-1, Avionics Engineering Center, Department of Electrical Engineering, Ohio University, Athens, Ohio, January, 1974.

[28] Alford, Andrew, and Edward French, "Album of Computed Localizer Course Bends Caused by Flat Reflecting Walls," Contract DOT-FA70WA-2253, Andrew Alford Consulting Engineers, Winchester, Massachusetts, July, 1970.

[29] "Multipath and Diffraction Effects of Structures on Localizer Systems," Report No. FAA-RD-70-20, Federal Systems Division, International Business Machines Corporation, Gaithersburg, Maryland; prepared for Federal Aviation Administration, Systems Research and Development Service, Washington, D.C., August, 1970.

[30] Chin, G., et al, "ILS Localizer Performance Study Part 1 Dallas/Fort Worth Regional Airport and Model Validation--Syracuse Hancock Airport," Report FAA-RD-72-96, Transportation Systems Center, Cambridge, Massachusetts 02142, July, 1972.

[31] Alford, Andrew, Gordon Robertson, and Barry Flahive, "Theory of the Capture Effect in Linear Reflectors Applied to Two Frequency ILS Localizer Systems," Andrew Alford Consulting Engineers, 120 Cross Street, Winchester, Massachusetts 01890, October, 1975

[32] Kouyoumjian, R.G., "The Geometrical Theory of Diffraction and Its Application," Topics in Applied Physics, Volume 3, Springer-Verlag, Berlin, Germany, 1975.

[33] Sandors, Gus J., Chief, Approach/Landing Aids Branch, AAF-20, FAA- Private communication of material collected and organized by George A. Hannon of FAA Alaskan Region, December 3, 1976.

[34] "Flight Check Manual" by Ohio University, Avionics Engineering Center, Athens, Ohio.

[35] FAA Manual FV-106-1, Amplitude Modulation, Aeronautical Center, Oklahoma City, Oklahoma, February, 1971.

[36] Redlich, R.W. and J.T. Gorman, "Disturbances of ILS Localizer Signals by Reflections from Large Hangars," IEEE Transactions on Aerospace and Electronic Systmes, November, 1969.

VII. SINGLE FREQUENCY DISCRIMINATION AGAINST REFLECTIONS (MULTIPATH)

A. General. The use of a single frequency and single transmitter but with different modulation techniques is an attractive concept to avoid the current requirement of a separate clearance transmitter and associated components used in the contemporary two-frequency systems. Reference is made to SRDS Report FAA-RD-74-214, pages 83-88, where switched beam techniques are discussed. During the course of the work effort covered by this report, the priority on the investigation of this technique was never high enough to allow a more complete investigation. A substantial effort is required to insure that maximum advantage is obtained without a requirement for alteration of airborne equipment.

VIII. SYSTEM PERFORMANCE STANDARDS

A. Proposed Criteria for Classification of Glide Slope Records with Respect to Quality.

1. General. Experience has shown that on occasion the ILS engineer is furnished flight records which are to be used for evaluation of facility performance, a basis for effecting changes in station parameters or for system modification. Unfortunately, the quality of the records is found to vary and in some cases it may be such that the records are of no use for making engineering judgments. The real danger is that an engineer might unknowingly accept poor data and make fallacious judgments that result in increased costs, wasted time and even embarrassment. The purpose of this section is to provide some criteria for qualifying flight data and thus provide indicators as to the degree of credibility appropriate for the records. In general, the complete set of records should be given the designation.

2. Definition of Classes of Records. Four classes of records are defined principally to correlate with uses for which certain records may be appropriate. The highest classification AA is needed to qualify Category II and III facilities and to validate mathematical modeling predictions. Class A is satisfactory for qualifying Category I facilities and for general analyses. Class B records must be used with reservation when making engineering judgments and certifying any facility. Class U is unsatisfactory and should not be used except in desperate circumstances. One certainly will recognize that certain features may cause a low classification to be applied; whereas if only certain pieces of information are needed and these are not the parameters that are deficient in the recording, then the record may be classified to a provisional higher rating. The provision is that the record be limited to the specialized use which is not affected by the items in the record of poor quality.

The criteria are listed in Table 8-1 on the following page. Some values are more arbitrary than others, but since quantification is necessary specific values are identified.

3. Rationale. Some subjective comments may be useful in helping the user obtain a better intuitive feel for the significance of the various tolerances.

Modulation balance or tone adjustment is an excellent method of establishing compatibility between airborne and ground based equipment. It is an easy adjustment and a non-critical measurement which usually shows little effect of terrain. Irregularities in the recordings of equality produced by radiating carrier signals (CSB) only indicate possible leakage of sideband signals from the transmitting system. If present, this leakage should, of course, be eliminated.

Theodolite placement is critical in establishing the references necessary for a quality recording. The theodolite location has been changed by order several times during the past decade. Even permanent emplacements have been found in error due to a contractor misreading a plan. Assumptions as to the location are risky. Present

PARAMETER	CLASS AA	A	B	U
MODULATION	0 ± 2 μa	0 ± 3 μa	0 ± 5 μa	> 5 μa
THEODOLITE PLACEMENT	Documented	Specified	Assumed	Unknown
THEODOLITE	Angular elevation marks - uniform 2.0 to 4.0° elevation	Irregularity compensation one mark to another	Irregularity <30% no compensation	Gross Irregularities
REFERENCES	Set within 0.1° of avg. path 3% of width	0.20° of avg. path <5% of width	0.30° of avg. path <10% of width	>0.3of path >10%
THEODOLITE TRACK	Rate <10 μa/sec continuous om --→ threshold lag< 10μa	<20 μa	<30 μa	> 30 μa
		<20 μa	<30 μa	> 30 μa
FLIGHT TRACK	Within ± 30 μa of CDI zero reference	± 40 μa of CDI zero reference	± 60 μa of CDI zero reference	> 60 μa
DIFFERENTIAL AMPLIFIER	Verified <± 2 μa accuracy through range ± 30 μa of CDI and theodolite	<± 3 μa	<± 5 μa	> 5 μa
REPEATABILITY	< 5 μa except for 20 μa/200 max 10 μa	<10 μa	<20 μa	> 20 μa
NOISE	All traces <2 μa p-p	<3 μa p-p	<5 μa p-p	> 5 μa p-p
LEGIBILITY	Trace width <1 μa unambiguous om-threshold	<2 μa	<2 μa Ambiguity present	Ambiguities present
LABELS	Applied all traces and scales	Most labeled	Assumed values	Some parameters unknown
EXTRANEOUS MARKS	None	Few	Several	Frequent

Table 8-1. Proposed Criteria for Glide Slope Recordings.

location optimizes for direct readout of path location from a differential amplifier trace and for creature comfort while operating the instrument; however, if a location is incorrect but known, it is possible to correct the data using calculations and thus salvage the effort.

The theodolite angle and width values should very nearly duplicate those of the electronic facility in order to make the direct readout an accurate reproduction of the path in space in terms of elevation degrees.

The quality of tracking is strongly dependent on the proficiency of the theodolite operator. The resultant trace must reflect an aircraft track which above all else is evident of a physically realizable aircraft flight track. This is a necessary but not sufficient condition for a quality record. Further, the pilot should track a reasonably smooth zero CDI indication to within 30 microamperes to insure that the assumptions of linearity made in the differential amplifier subtraction is not introducing significant error. Since the objective is to depict the position of the zero DDM line in space, the best base would be for the aircraft to fly the zero line precisely and have the theodolite merely tell where the aircraft is.

The differential amplifier is an electronic device which can be set to perform subtractions very accurately. Fortunately this amplifier is usually good enough that tight tolerance is not difficult to achieve.

The item of repeatibility is the principal, overt means of recognizing a quality record. If one can take two or more records and have them essentially overlay, then one may have great confidence that the records do indeed present a correct picture of the path in space, in the presence of a stable physical world.

Unfortunately noise contaminates quantities to be measured in this world. The objective is to introduce as little additional noise as possible when making an observation. Noise from the receiver itself, the recorder, and differential amplifier can and should be reduced to the point where it is not evident on the records.

Recorder operator techniques can go a long way towards eliminating problems of legibility. It is usually a matter of professionalism and attention to detail. Interlacing traces with similar intensities of the trace indications add confusion but with astuteness the recorder operator can eliminate this problem. Labels should be placed on the records promptly and in sufficient detail so that there is no question as to the circumstances present for the observation. Usually there is some prime item to be identified for the record and this is usually done. More of a problem, however, are the subtleties which are frequently not documented and with the passage of time and the fading of human memory the record becomes useless or worse yet, misleading. Marks not germane to the record should not be on the strip chart to reduce the probability of error in analysis or obliteration of a key item.

If the flight data collection team dedicates itself to the production of high quality records, and studies what the technical requirements are, the probability is very high that high quality records will be produced by observing common sense.

B. STI Report.

Article 1B6 under Statement of Work in Contract FA74WA-3549:

"Study and analyze the complete overall air-ground ILS system performance and develop new overall system performance standards. Many of the present airborne and ground standards were developed in the past without regard for each other, and consequently, there is a great need for up-to-date overall system performance standards. It is believed that some parameters are too restrictive while others may be relaxed without hurting system performance."

A two part report, ILS Glide Slope Standards, subtitled "Part I: A Review of Flight Inspection Standards Affecting Landing Performance and Comparison with Limits Evolved from System Analysis" by Lee Hofmann, Warren Clement, Dunstan Graham, and Gary Teper of Systems Technologies, Inc., Byron Wiscons and David Hammel of Collins Radio Company, and Richard H. McFarland of Ohio University, and "Part II: Validation of Proposed Flight Inspection Filter Systems and Responses of Simulated Aircraft on Coupled Approaches" by Lee Hofmann, John Shanahan and Dunstan Graham, has been used as a basis for consideration of this problem.

Several Avionics Engineering Center engineers and consultants have become familiar with the STI work (under DOT Contract FA74WA-3340) - one, Dr. Richard H. McFarland, Center Director, is listed as an author of Part I - since this study is so closely related to work being done at Ohio University.

It is the consensus of senior staff here that since the STI project involved only computer simulation of ILS systems and computer validation of simulation results, there should be real-world tests before new standards affecting aviation safety are adopted.

Much real data needs to be gathered and suitably analyzed before definitive conclusions can be drawn. Quite a bit of this data is already on file for ILS systems which have been checked out under the present and previous contracts. More will be obtained as time goes on.

Priorities for tasks under Contract FA74WA-3549 have not been such as to permit a sufficiently large scale effort to produce specific recommendations for system-wide standards; however, as a byproduct of ongoing studies, a sound basis has been laid for future efforts in this direction.

IX. RANGE MEASUREMENT FROM LOCALIZER SIGNALS

A. System Description. The concept of a position-determining system operating on a modified ILS localizer signal was described in block-diagram form by Forrest Yetter, ARD 721. His system is illustrated in Figure 9-1. As originally presented, the system allows distance measurement using marker beacon and localizer signals. See Chapter IV, Section G, for documentation of a precision marker-beacon receiver which provides plus or minus six feet dispersion in marker location during approach. The work reported here concentrates on that portion of Yetter's total system which determines rate of change or distance with time (proportional to groundspeed).

For concept feasibility studies, the system is configured with a stable clock at the localizer site which generates a reference signal for an RF sampler. Carrier energy is coupled from the localizer transmitter to the sample input port of the sampler (mixer), and an audio signal is produced which is modulated on the localizer output for transmission to the aircraft. Note that through the use of the RF sampler, the audio tone varies in phase in step with any variations present in the localizer carrier signal.

In the aircraft, a localizer receiver obtains localizer carrier, 90-150 Hz sidebands, and the audio tone. RF energy is coupled out to an airborne RF sampler, which is driven by a clock to produce an audio tone, just as in the ground system described above. In addition, the receiver audio output is filtered to recover the detected audio tone transmitted from the ground.

The ground-derived tone is used as the reference input to a phase detector in the aircraft; the air-derived tone contains phase variations with respect to the ground-derived tone. These variations occur due to aircraft movement with respect to the localizer, and, as will be described later, occur at approximately a 24 Hz rate for a 120 Kt. approach speed. Note that it is assumed any Doppler effects on the ground-derived audio tone are negligible compared to effects on the localizer's 110 MHz frequency. In addition, any frequency shifts on the (unstabilized) localizer carrier frequency are cancelled in the phase detector since these variations will appear on both ground and air-derived audio tones. The resulting phase-detector output in the aircraft will be due to aircraft radial velocity with respect to the localizer array.

Yetter then specifies a digital counter to determine the Doppler count based on movement through 110 MHz phase changes. The remainder of the block diagram relates to the marker-beacon location function and is not addressed in this section.

B. System Assembly for Concept Demonstration.

1. Predicted System Parameters. The groundspeed sensor operates on detection of phase change from a stationary ground transmitter (the ILS localizer) due to aircraft motion. The rate of phase change in cycles per second is the Doppler rate observed in the aircraft. In order to allow system calibration, Table 9-1 was produced to illustrate expected system parameters. Column headings are described as follows:

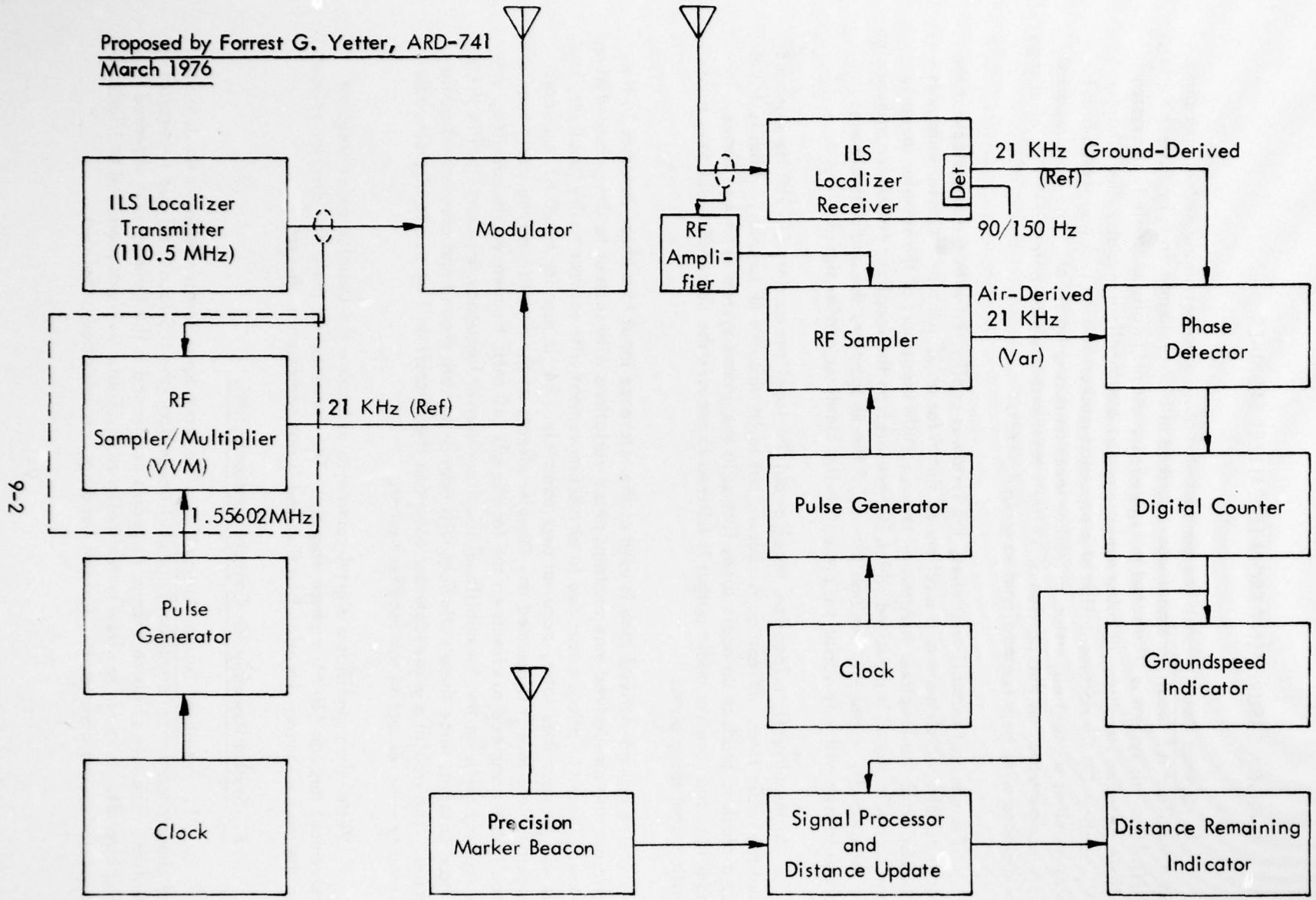

Figure 9-1. ILS Distance Measuring System.

AD-A074 425 OHIO UNIV ATHENS DEPT OF ELECTRICAL ENGINEERING F/G 17/7
IN-SERVICE IMPROVEMENTS AND MODERNIZATION OF ALL COMPONENTS OF --ETC(U)
JUL 78 DOT-FA75WA-3549
UNCLASSIFIED EER-35-1 FAA-RD-78-112-1 NL

7 OF 8
AD A074425

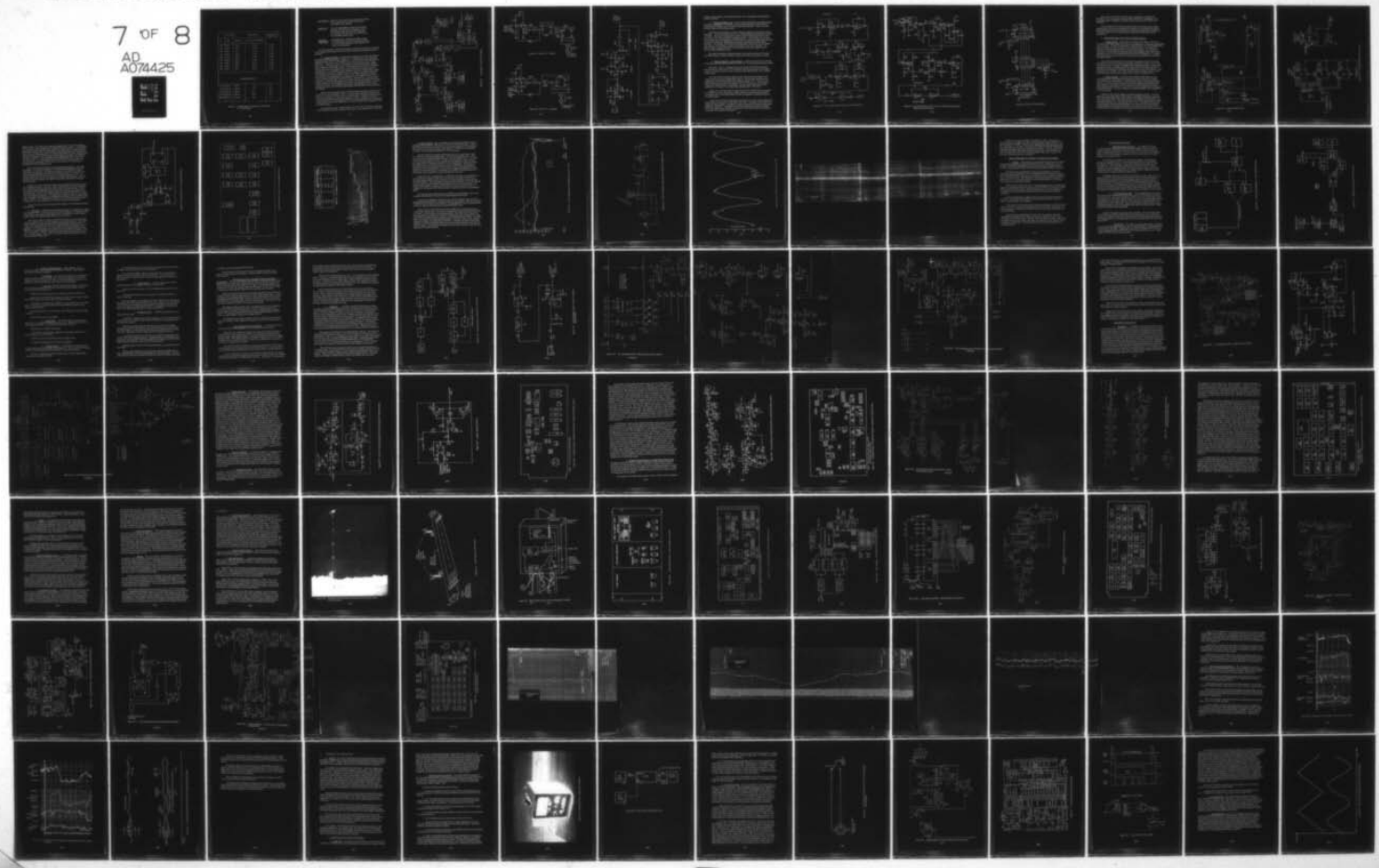

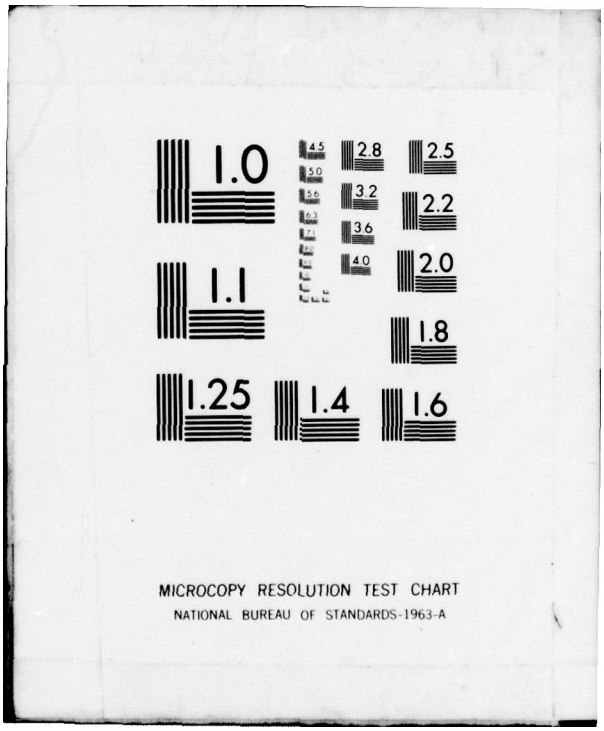
1.0
1.1
1.25
1.4
1.6
1.8
2.0
2.2
2.5
2.8
3.2
3.6
4.0
4.5
5.0
5.6
6.3
7.1
MICROCOPY RESOLUTION TEST CHART
NATIONAL BUREAU OF STANDARDS-1963-A

A/C Velocity			Phase Count	Equivalent Clock Offset - Hz
kt	mph	feet/sec	λ/sec at 110.497 MHz	
60	69.0	101.2	11.36	0.160
70	80.5	118.1	13.26	0.187
80	92.0	134.9	15.15	0.213
90	103.5	151.8	17.04	0.240
100	115.0	168.7	18.94	0.267
110	126.5	185.5	20.83	0.293
120	138.0	202.4	22.72	0.320
130	149.5	219.3	24.62	0.347
140	161.0	236.1	26.51	0.373
CALIBRATION DATA				
37.5	43.12	63.24	7.1	0.1
75.0	86.24	126.49	14.2	0.2
112.49	129.36	189.73	21.3	0.3
149.98	172.48	252.97	28.4	0.4
187.48	215.60	316.22	35.5	0.5

Table 9-1. Predicted System Parameters at 110.497 MHz (λ = 8.9075 Feet).

A/C Velocity: Given in knots, miles per hour, and feet per second. This is range-rate, the aircraft radial velocity with respect to the localizer.

Phase Count: Given in wavelengths per second at the localizer frequency (110.497 MHz for this study). This is the measure of aircraft motion effect (Doppler) due to motion with respect to the localizer array. It is the primary system output.

Equivalent Clock Offset: A calibration aid. This frequency offset is equal in the demonstration system to the phase divided by 71, which is the multiplication factor applied to the clocks in the RF samplers.

As will be discussed in the following sections, the basic system output is processed in three separate phase detection circuits to derive alternative groundspeed outputs for evaluation.

2. Ground Installation. A detailed block diagram of the ground and airborne groundspeed installations appears in Figure 9-2. On the ground, a Sulzer frequency standard operating at 5 MHz with a stability of 1×10^{-10} drives the GR 1164 frequency synthesizer. A frequency of 3.112 MHz is output and used to drive pulser #1 (see Figure 9-3). The output pulses at 1.556 MHz are used to synchronize the HP8405A vector voltmeter (VVM) sampler circuit. For this application, the VVM is modified by removing the locked-loop sampling circuit normally used, and synchronizing to the external signal. In the modified vector voltmeter, the input 1.556 MHz signal is used to sample the RF input signal, taken from the driver stage of the localizer transmitter. The IF output of the vector voltmeter is then 21 KHz. This audio signal is limited, divided by four, bandpass filtered, and modulated onto the localizer transmitter output by insertion into the IDENT TONE TEST input. See Figure 9-5 for circuit documentation. To facilitate this experiment, the ident tone was removed from the localizer output, although in later development, this removal would not be necessary. As shown in the block diagram, this modulation takes place in the transmitter AGC circuitry. Modulation levels are set to produce approximately 25% modulation with the audio tone, at 5,250 Hz.

Note that the frequencies chosen to demonstrate the groundspeed concept are constrained by the vector voltmeter circuitry. Far more freedom of choice for audio tone frequency is available in further work, in which the vector voltmeter would not be used, but would be replaced by a custom-designed mixer circuit. In addition, the Sulzer frequency standard and GR frequency synthesizer would be replaced by an oven-controller crystal oscillator with similar stability but with custom frequency output designed for this groundspeed system.

This ground installation was fabricated for use with the TV-34 localizer transmitter at Ohio University's test site at Albany, Ohio airport. Tests discussed later in this report

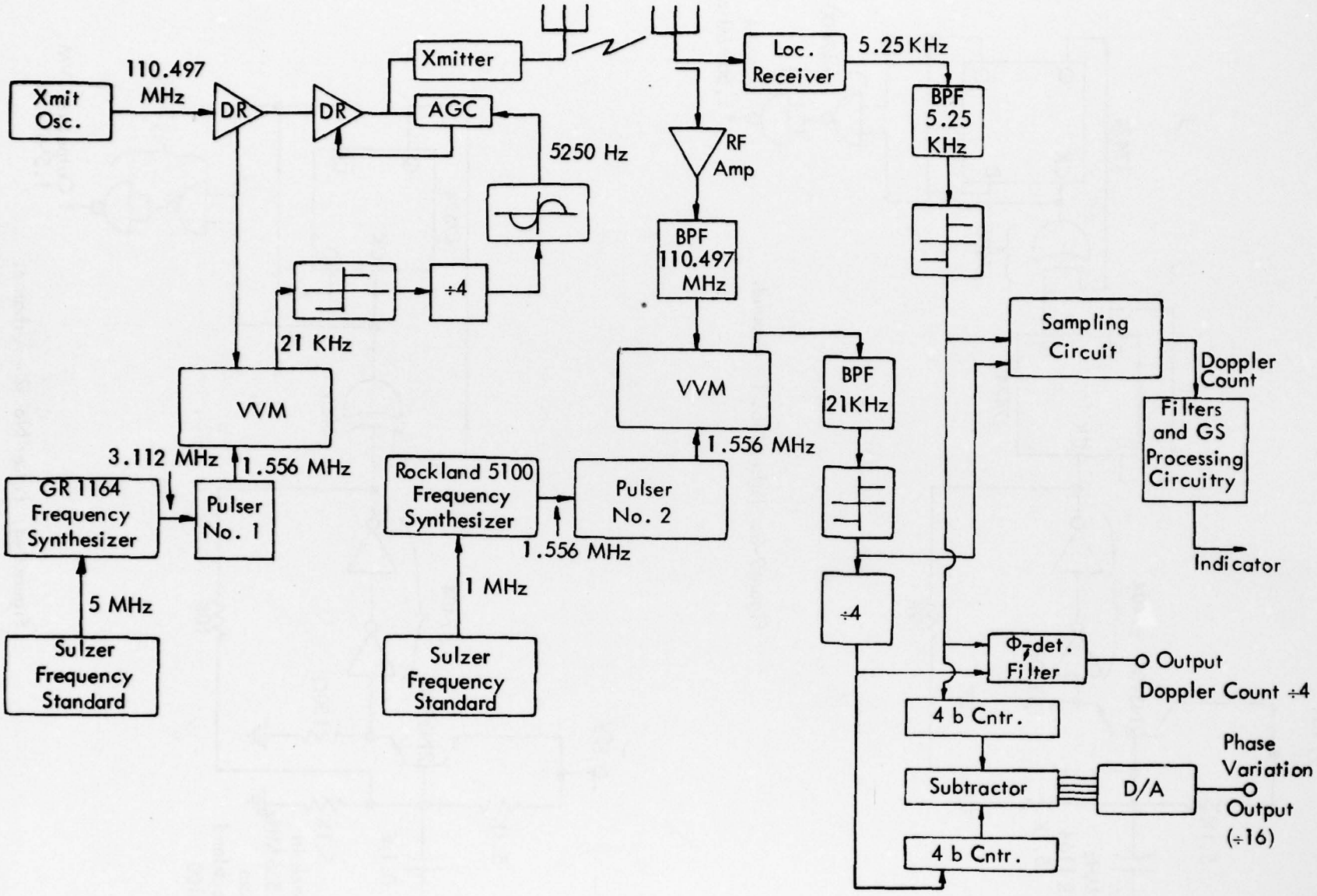

Figure 9-2. Groundspeed System Block Diagram.

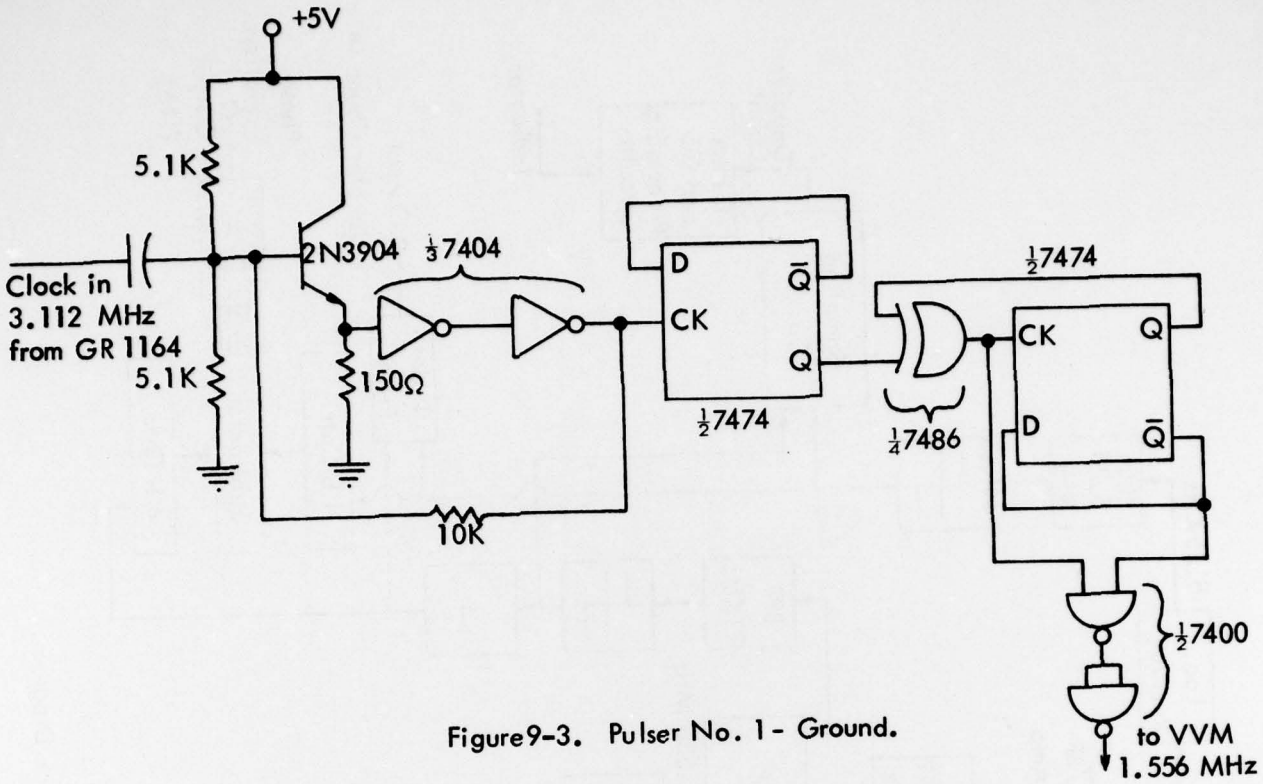

Figure 9-3. Pulser No. 1 - Ground.

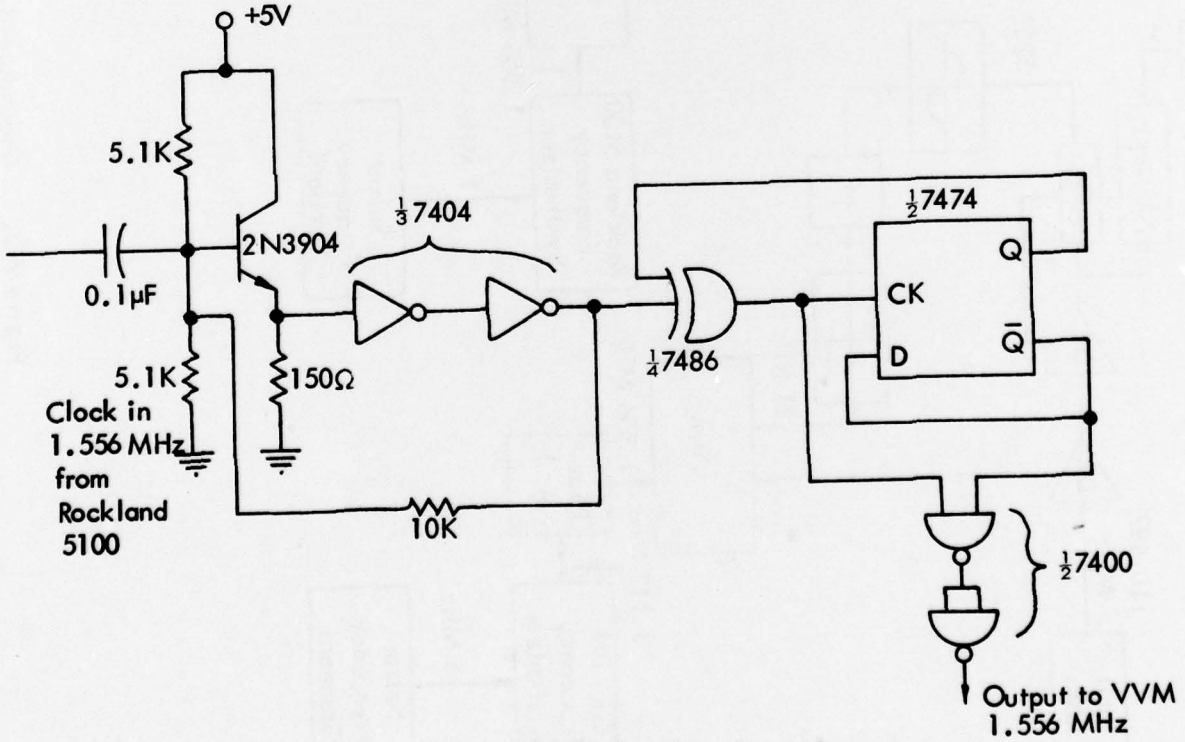

Figure 9-4. Pulser No. 2 - Airborne.

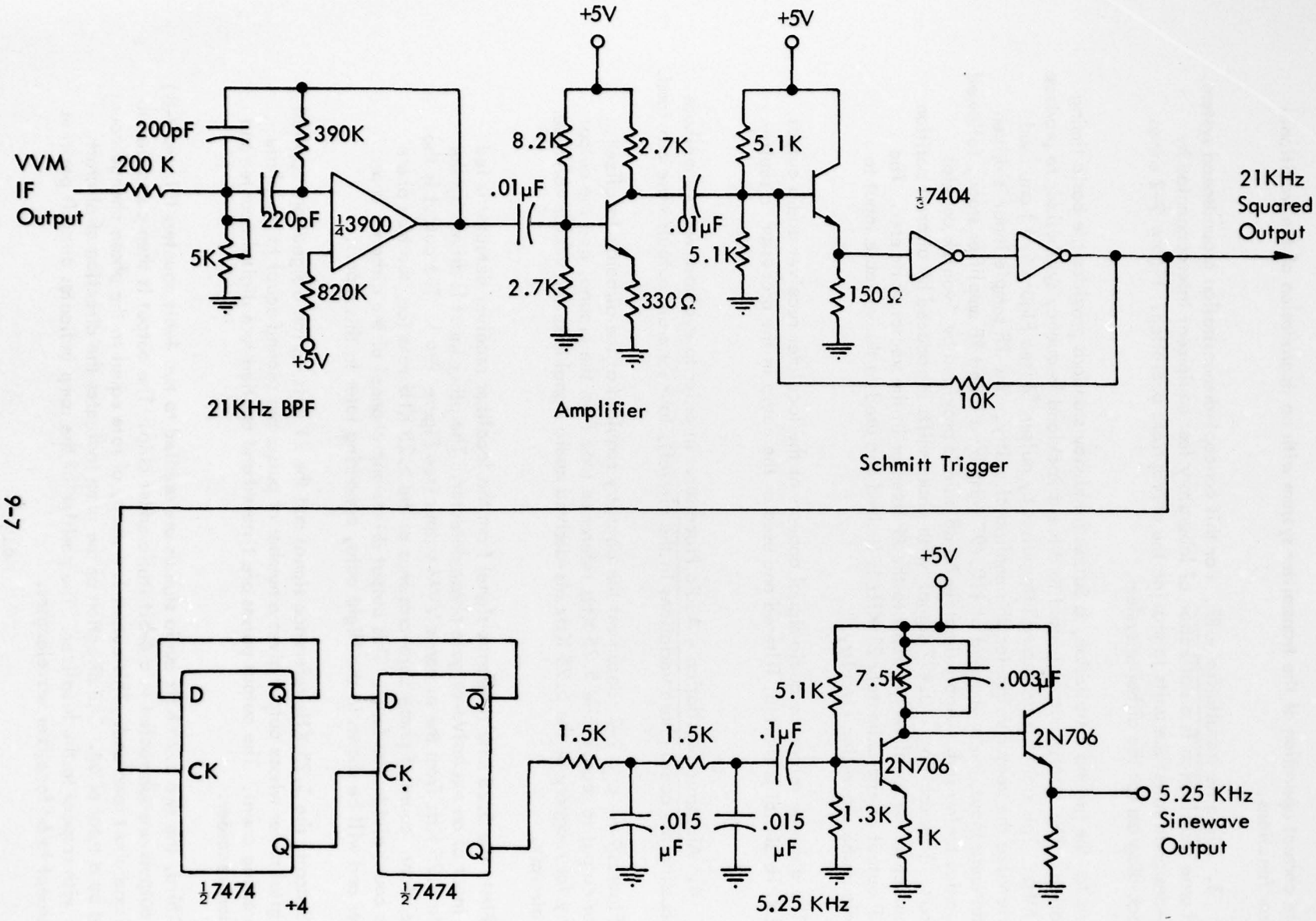

Figure 9-5. Transmitter Modulation Generating Circuitry.

indicate correct operation of the transmitter system with no degradation of the traditional localizer functions.

3. Airborne Installation - RF. For this concept-demonstration groundspeed system, the airborne installation is a collection of laboratory test equipment interconnected by custom-designed interface units to provide the appropriate operation. Figure 9-2 shows the block diagram for the airborne system.

As for the ground installation, a Sulzer frequency standard provides the basic timing information. The 1 MHz output is used to drive a Rockland frequency synthesizer to produce 1.556 MHz. This signal is processed into pulses by pulser #2 (see Figure 9-4) and used to synchronize the vector voltmeter RF sampling circuitry. The RF sample input is driven by an antenna input, narrowbanded at 110.497 MHz by a tuned RF amplifier stage, followed by a coaxial tuning stub. Approximately 60 dB gain is provided by Avantek coaxial amplifiers. The resulting 110.497 signal (with phase shifts introduced by aircraft position with respect to the localizer) is input to the RF sampler in the vector voltmeter. The audio IF output at approximately 21 KHz is limited and used as the variable input to the audio phase processing circuitry.

The airborne reference audio signal appears at the localizer receiver audio output. This 5250 Hz signal is limited, filtered and used as the audio in the processor circuitry.

4. Airborne Installation - Audio Processor. In order to evaluate various methods for processing the audio phase variations in the aircraft, four separate outputs were provided.

Figures 9-6 and 9-7 document the circuitry required at the airborne localizer receiver output to recover the 5.25 KHz reference tone from the ground, and the output circuitry for recovery of the 5.25 KHz air-derived audio signal from the vector voltmeter in the aircraft.

First, the 5.25 KHz reference signal from the localizer receiver detector is fed to one input of an exclusive-or gate phase detector. The other input is driven by the variable 5.25 KHz from the airborne VVM output (see Figure 9-6). The output is the nondirectional count of phase zero-crossings at the 5.25 KHz rate (or, the true phase change count divided by four). This output drives one channel of the airborne chart recorder and will be shown in the flight data, appearing later in this report.

Second, the 5.25 KHz reference signal and the 21 KHz variable signal are applied to a digital mixer whose output gives a number of pulses per second equal to the phase zero-crossing count. The output pulses are filtered and applied to a digital counter and to a chart recorder.

Third, the two 5.25 KHz audio signals are applied to two 4-bit counters (Figure 9-8) whose outputs are subtracted in a 4-bit static adder chip. The output is then converted to analog and chart recorded. This output is a ramp, of rate equal to the phase change count divided by a total of 64. The direction of the ramp indicates the direction of aircraft motion with respect to the localizer. The position of the ramp indicates aircraft position with respect to 64 localizer wavelengths.

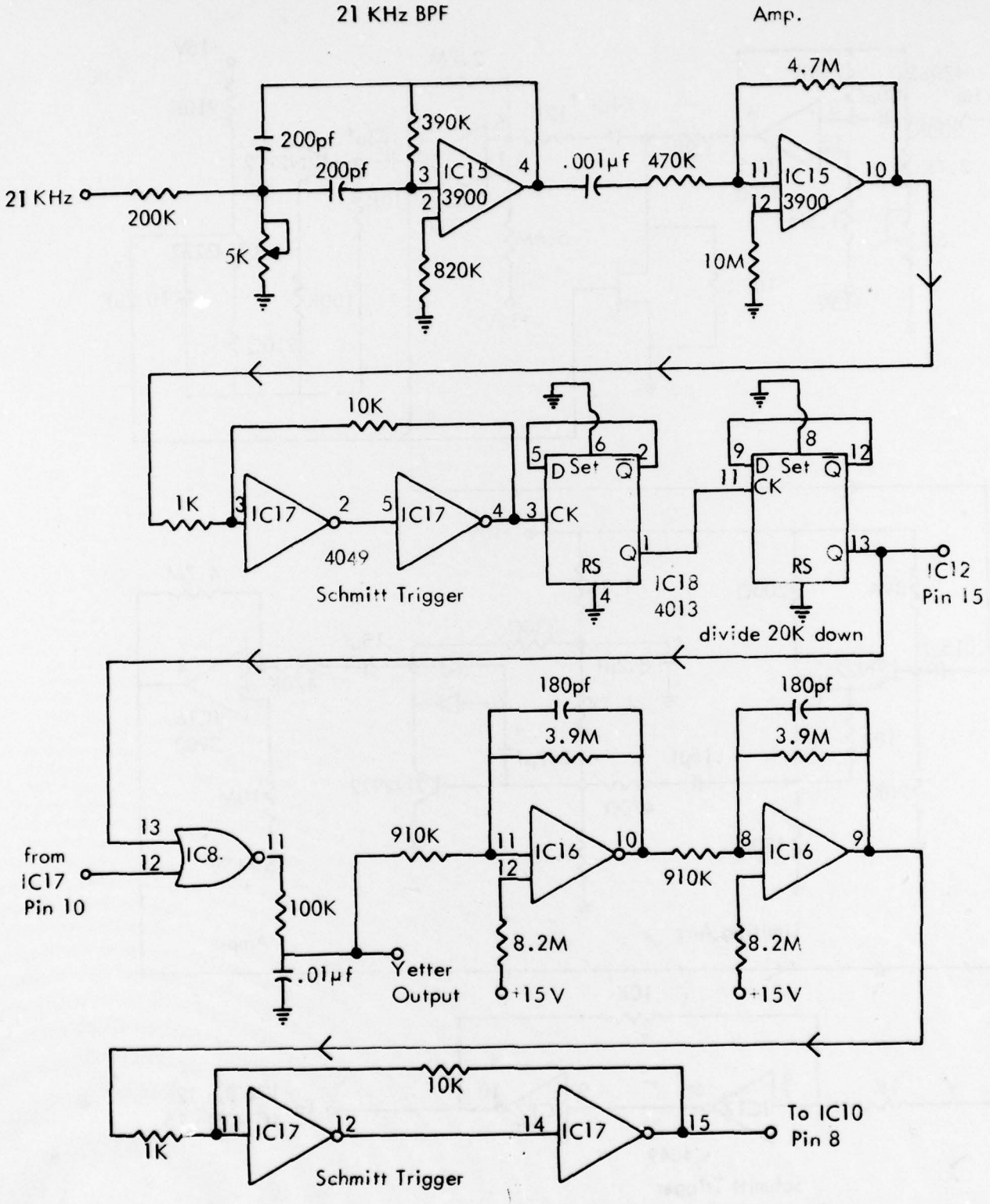

Figure 9-6. 21 KHz Input Conditioning and 5 KHz Phase Detector.

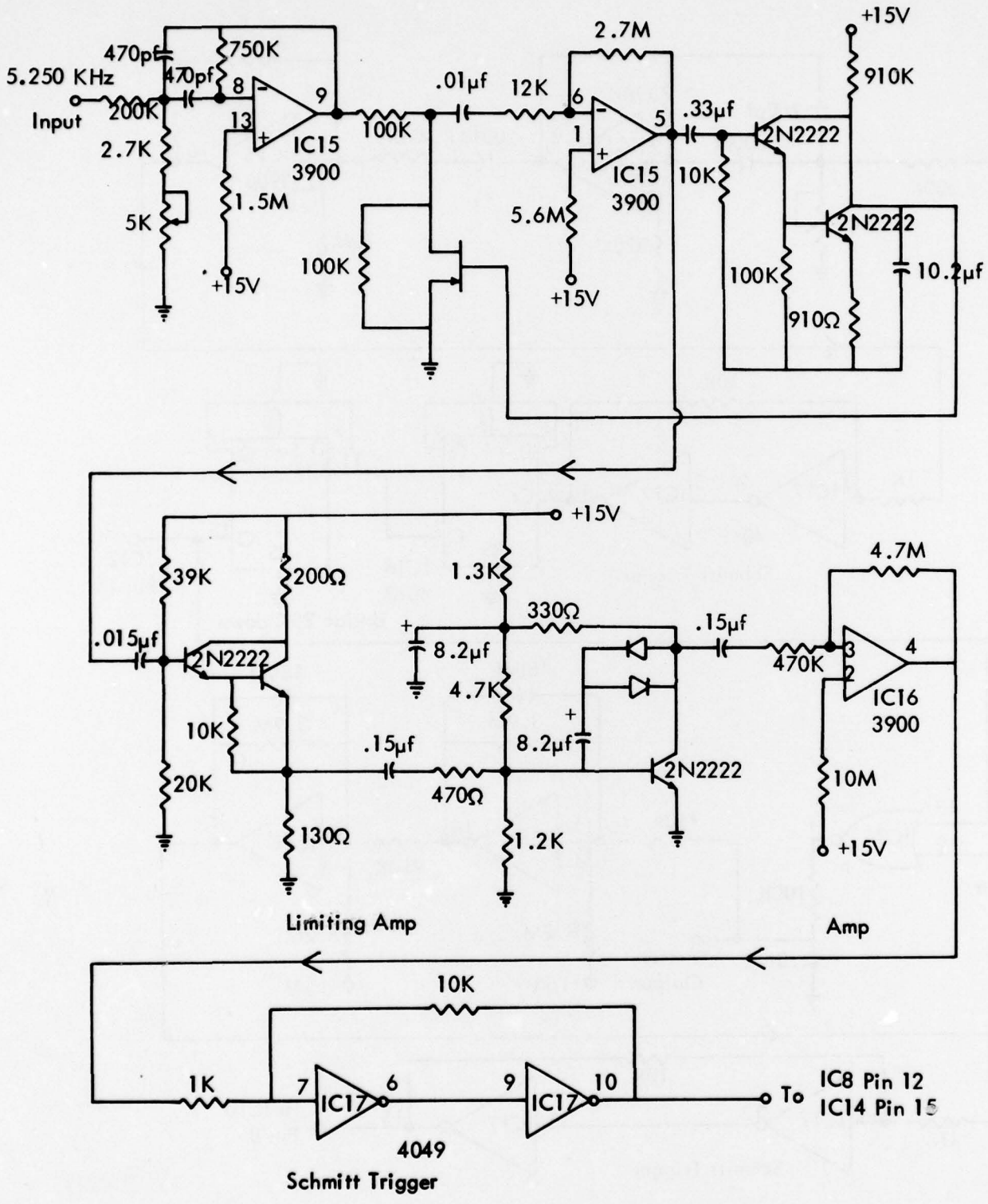

Figure 9-7. Input Conditioning Circuitry for the 5.250 KHz Reference Tone Modulated on the Localizer.

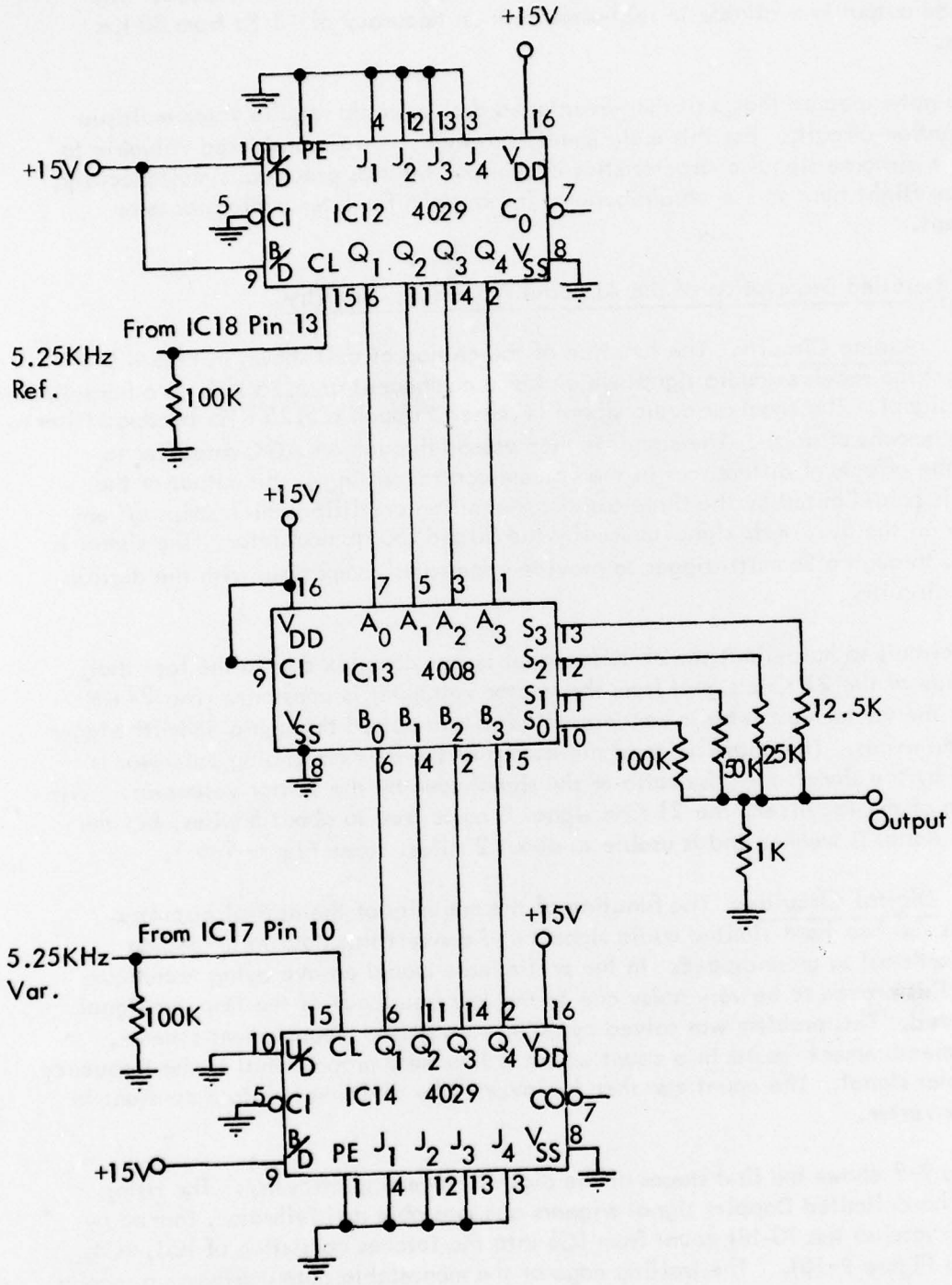

Figure 9-8. Directional Phase Detector.

Fourth, the output of the exclusive-or gate is processed in a digital circuit followed by a D to A to provide an analog output proportional to groundspeed. The groundspeed output is available in real-time with an accuracy of ±1 Kt from 30 Kts to 150 Kts.

It is not expected that a further-developed design would require these multiple phase detection circuits. For this experiment, however, it was considered valuable to measure the airborne signal characteristics in as many ways as practical simultaneously, to minimize flight time and to obtain general information for later audio processor development.

C. Detailed Description of the Airborne Processing Circuitry.

1. Analog Circuits. The function of the analog circuit shown in Figure 9-7 is to convert the receiver audio signal which has a component at 5.25 KHz to a hard-limited 5.25 KHz signal. The receiver audio signal is passed through a 5.25 KHz bandpass filter to reduce the amount of noise. The signal is then passed through an AGC amplifier to eliminate the effects of differences in the volume control setting. The output of the AGC amp is hard-limited by the three-transistor-limiting amplifier which strips off any modulation on the 5.25 KHz signal caused by the 90 and 150 Hz modulator. The signal is then passed through a Schmitt trigger to provide edge rates compatible with the digital processing circuitry.

The circuit to hard-limit the 21 KHz signal is less complex due to the fact that the amplitude of the 21 KHz signal from the vector voltmeter is constant. The 21 KHz signal from the vector voltmeter is bandpass-filtered and passed through a Schmitt trigger to square the edges. The phase noise at the output of the 21 KHz analog processor is determined by the signal-to-noise ratio of the signal seen by the vector voltmeter. Within the beam of the localizer, the 21 KHz signal is noise free to about 5 miles, but the backcourse signal is weaker and is usable to about 2 miles. (See Figure 9-6).

2. Digital Circuitry. The function of the majority of the digital circuitry is to process the two hard-limited audio signals and convert this data to an analog output proportional to groundspeed. In the preliminary model an averaging technique was used. This proved to be very noisy due to the low frequency of the Doppler signal to be measured. This problem was solved by going to a period measurement scheme. The period measurement results in a count which is inversely proportional to the frequency of the Doppler signal. The count can then be inverted by dividing it into a constant in a D to A converter.

Figure 9-9 shows the first stages of the digital processing circuitry. The rising edge of the hard-limited Doppler signal triggers a monostable multivibrator, formed by IC10, which latches the 10-bit count from IC6 into the latches consisting of IC3, IC4, and IC5 (see Figure 9-10). The trailing edge of the monostable output triggers a second monostable formed by IC11 which resets the count in IC6. The counter then proceeds to count the pulses from the oscillator formed from two gates of IC8 until the edge of another Doppler cycle triggers the monostable. The result is that the 10-bit count in the three latches is proportional to the time between the rising edges of the two preceding

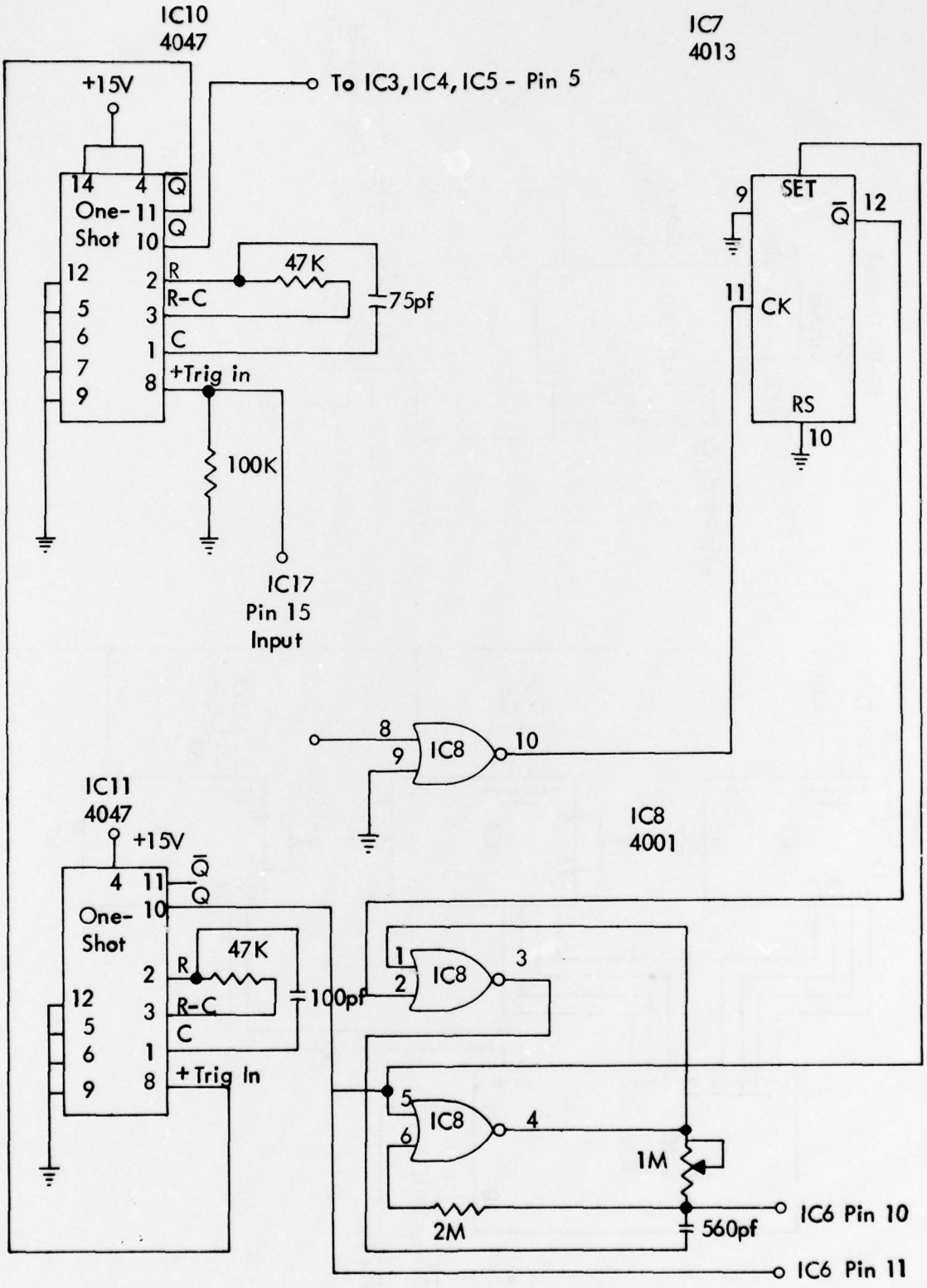

Figure 9-9. Processor Control Circuit.

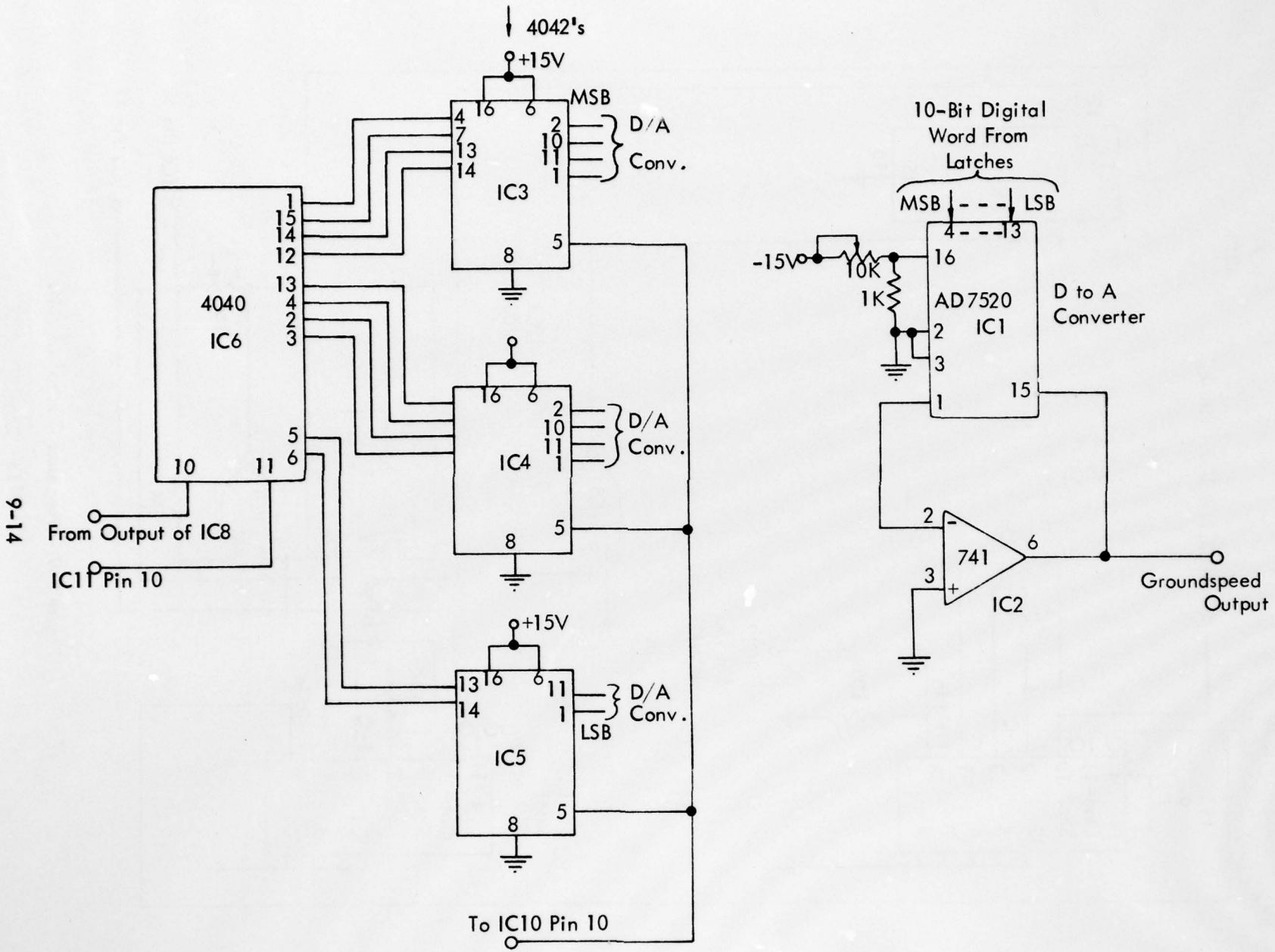

Figure 9-10. Groundspeed Computational Circuitry.

Doppler cycles. The 10-bit count is used as the digital input of a CMOS multiplying D to A converter, IC1, configured in the feedback loop of an op-amp. In the feedback loop, instead of multiplying the analog input by the digital word, the analog signal is divided by the digital word. Since the digital word is proportional to the period of the Doppler signal and the analog input is a constant determined by a resistor voltage divider, the output is proportional to the frequency of the Doppler input signal. The remaining circuitry in Figure 9-9 is used to disable the groundspeed output if the count overruns counter IC6, i.e., if the Doppler frequency is so low the counter reaches a full count before the next Doppler cycle arrives. In this case the circuit assumes zero groundspeed and sets the output to zero.

Figure 9-8 shows the schematic of the directional phase detector. The 4-bit up-counter in IC12 counts the reference 5.25 KHz frequency obtained from the audio modulated on the localizer. The 4-bit down-counter in IC14 counts the variable 5.25 KHz signal obtained by dividing the 20 KHz VVM output by 4. The count in IC14 is then subtracted from the count in IC12 in a 4-bit adder contained in IC13. The resulting 4-bit number is D to A converted by the resistor array to produce a ramp, the direction of which is determined by whether the aircraft is approaching or receding from the localizer.

Figure 9-11 is the schematic of a digital mixer and lowpass filter used to process the full Doppler frequency. The mixer works by sampling the 21 KHz VVM output by the 5.25 KHz signal, obtained from the localizer audio in a D type flip-flop. Since the two signals are harmonically related, the output of the flip-flop won't change under static conditions. If the 21 KHz is offset slightly from the 5.25 KHz signal, the output will be the difference frequency. The digital filter is needed because, due to the phase noise, the edges of both signals can be shifted slightly, leading to noisy transitions of the output waveform. The retriggerable multivibrator will not allow the second flip-flop to change state if two or more edges occur within the on-time of the monostable.

Figure 9-12 shows the physical layout of the processor and is included for documentation purposes.

D. Calibration. Calibration of the groundspeed output is accomplished by introducing a frequency offset into the system while the plane is stationary. The frequency offset is equivalent to a corresponding groundspeed which would produce the same frequency offset by means of the Doppler shift if the plane were in motion.

The frequency offset is created by adjusting the frequency of the Rockland 5100 frequency synthesizer away from the frequency which causes a zero beat. The change in the synthesizer frequency alters the VVM sampling frequency which results in a change in the frequency of the VVM IF of 71 times the change in the frequency of the synthesizer. The multiplication occurs because the VVM IF output frequency is the difference in frequency between the incoming 110.5 MHz and the 71st harmonic of the sampling frequency. Table 9-2 relates the frequency offset of the synthesizer to the equivalent groundspeed. Figure 9-13 is a recording of groundspeed output for several different frequency offset values.

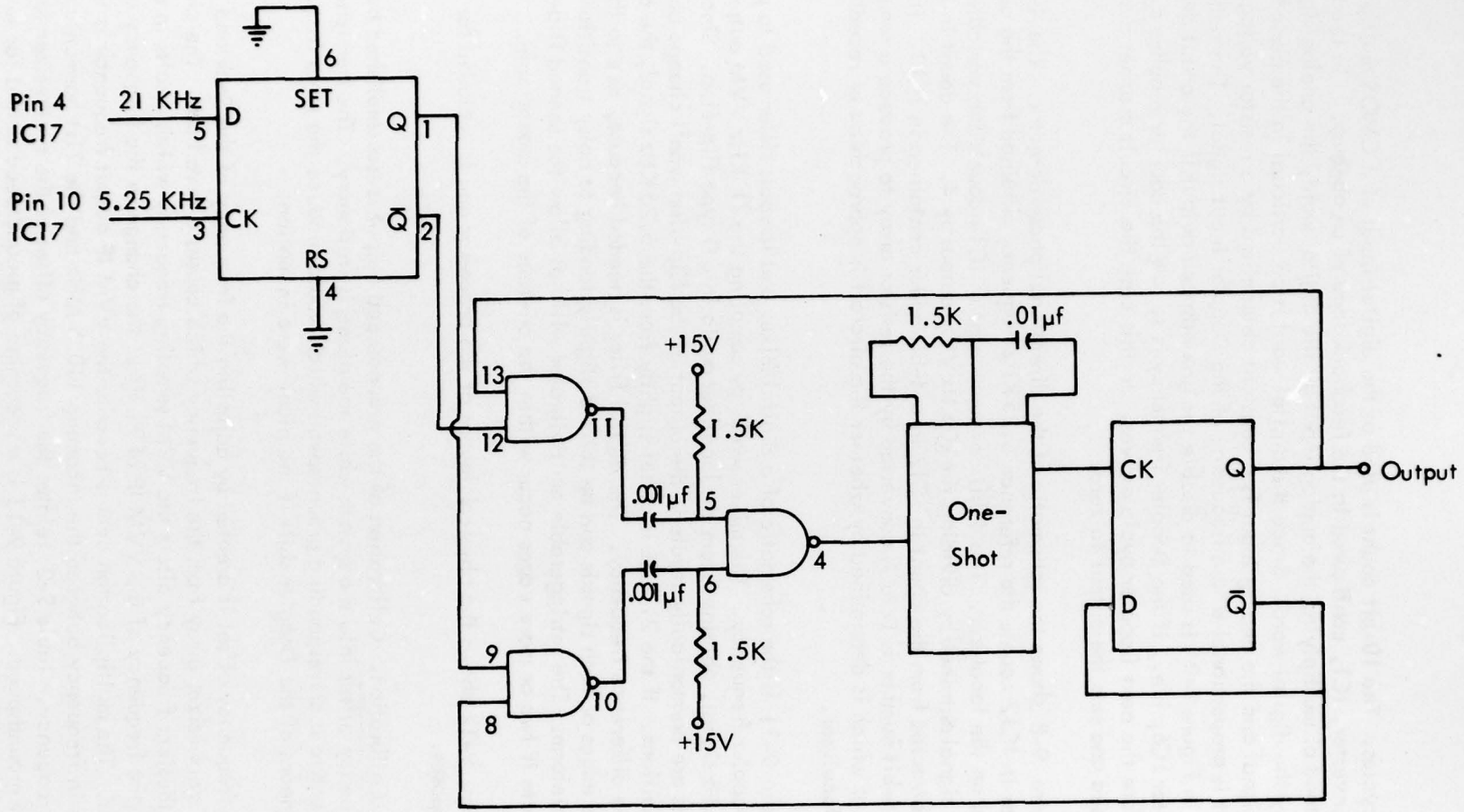

Figure 9-11. Mixer and Filter for Full Doppler Processing.

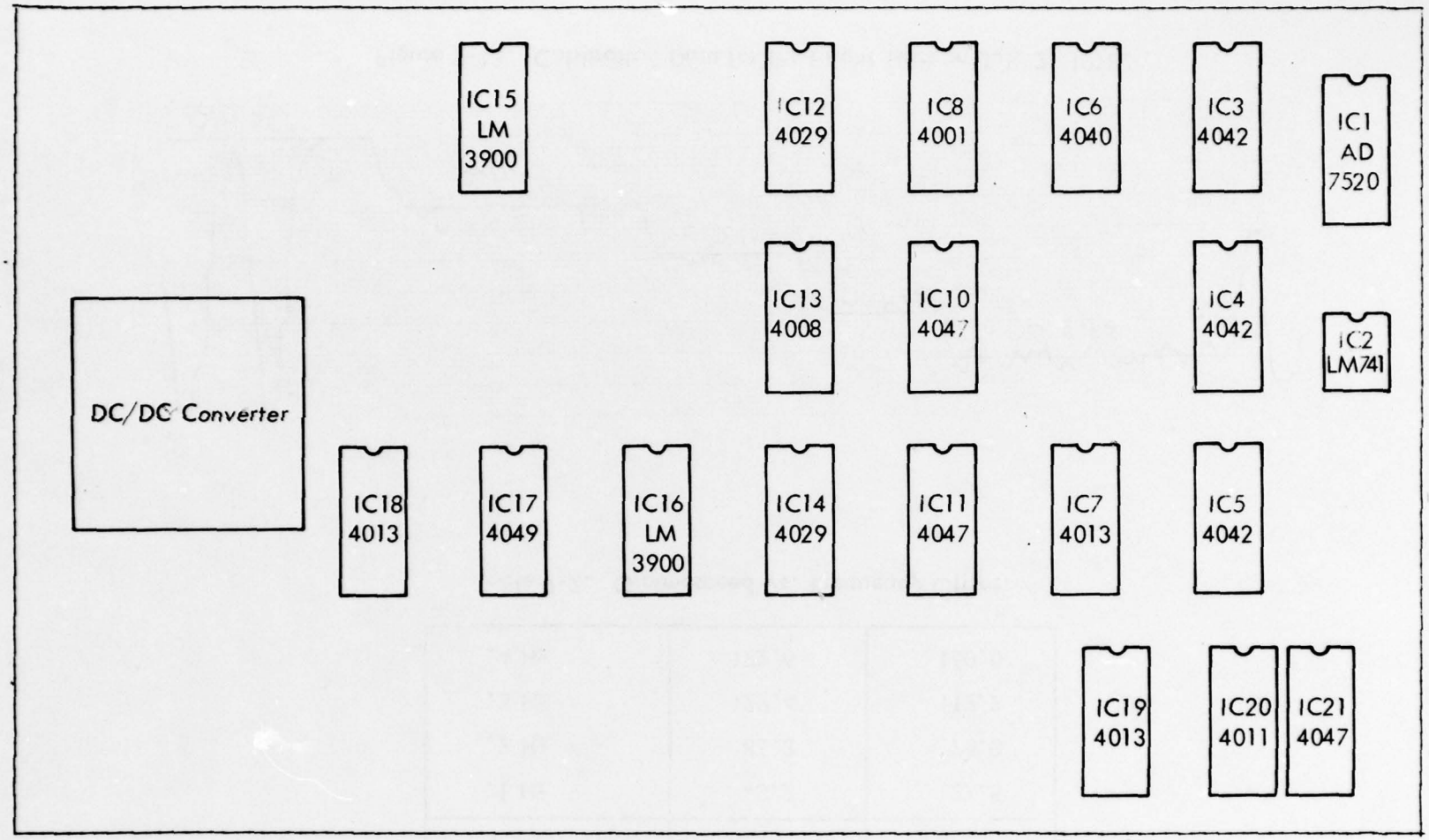

Figure9-12. Physical Layout of the Groundspeed Processor.

Synthesizer Frequency Offset	Equivalent Groundspeed	
	MPH	KNOTS
.1 Hz	43.2	37.5
.2 Hz	86.3	75.0
.3 Hz	129.4	112.2
.4 Hz	172.6	150.0

Table 9-2. Groundspeed Vs. Frequency Offset.

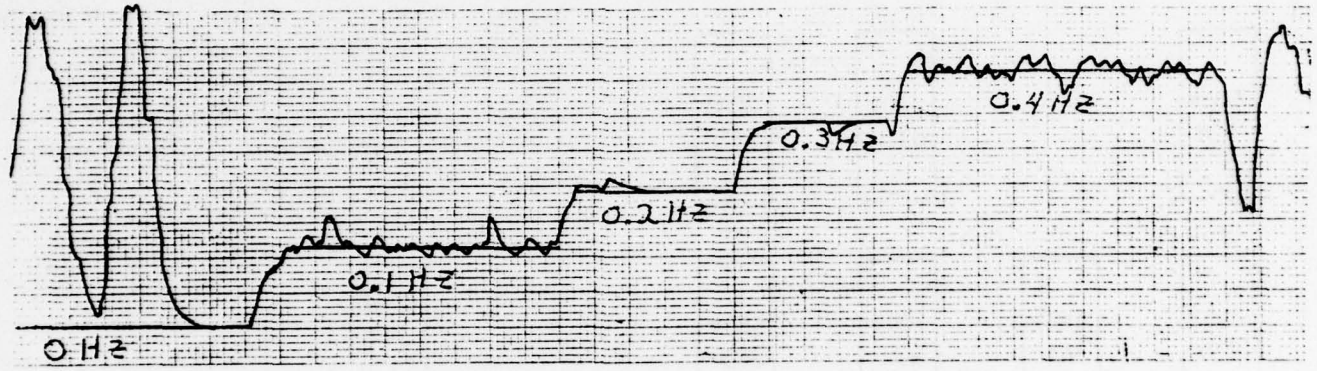

Figure 9-13. Calibration Data for the Flight Tests on July 2, 1978.

E. Flight Evaluation. After successfully ground testing the groundspeed system, preparation was made for the flight test in Avionics' DC-3 Flying Laboratory. After the first flight test indicated low RF sensitivity in the airborne equipment, the engineering effort was focused on attaining greater usable distance. The RF section was modified to provide a narrow bandpass characteristic with increased gain.

The second flight test consisted of calibration and four low approaches. Figure 9-14 shows the data from these approaches. The first two approaches, plots A and B were made with an indicated airspeed of 90 Kts. The third approach, plot C, was made with an indicated airspeed of 120 Kts. During the fourth approach, shown in plot D, the aircraft crossed the beacon at a speed of 90 Kts, accelerated to a speed of 140 Kts, then decelerated to a speed of 90 Kts and continued the approach. During these four approaches the accuracy was estimated to be within $\pm$ 3 Kts and the repeatability, as can be seen from the charts, is good. The dip in the indicated groundspeed plots occurs directly over the localizer array. At that point the aircraft is moving perpendicular to the localizer signal causing the received groundspeed to go to zero.

Following the four low approaches, two 360° turns were made in the approach area. A map of the area is shown in Figure 9-15 and the data is presented in Figure 9-16. The highest speed indication occurs at points 1 and 4 when the plane is moving directly toward the localizer. The lowest speed indication occurs at points 1 and 3 on the extended runway centerline when the plane is flying perpendicular to the localizer signals. The velocity of the airplane, referenced to the ground, is a vector quantity and only the component in the direction of the localizer antenna is being measured in this groundspeed system.

The flight data shows that the system is insensitive to aircraft heading and to pitch. Anywhere inside the beacon the system provides groundspeed information.

At very low groundspeeds, the data rate from the lane crossings is too low for the analog groundspeed processor to compute accurately the groundspeed. Above this threshold, at about 30 Kts, the output is quite reliable. The groundspeed can still be determined even at very low speeds by looking directly at the phase detector output.

Figure 9-17 is the last portion of the chart recording of a low approach from the beacon to the localizer array. This was the third approach made and the indicated airspeed was 120 Kts. The top trace is the analog groundspeed. The middle trace is the output of a phase detector consisting of an exclusive-or gate followed by a low pass filter. Each cycle of this waveform represents a change in aircraft position of about 36 feet. The bottom trace is the output of the directional phase detector. Each of the cycles of this waveform represents a change in aircraft position of 576 feet. In addition, the output of this phase detector can be used to determine whether the aircraft is moving toward or away from the localizer antenna. This directional characteristic can be seen at the point where the plane passes over the localizer antenna.

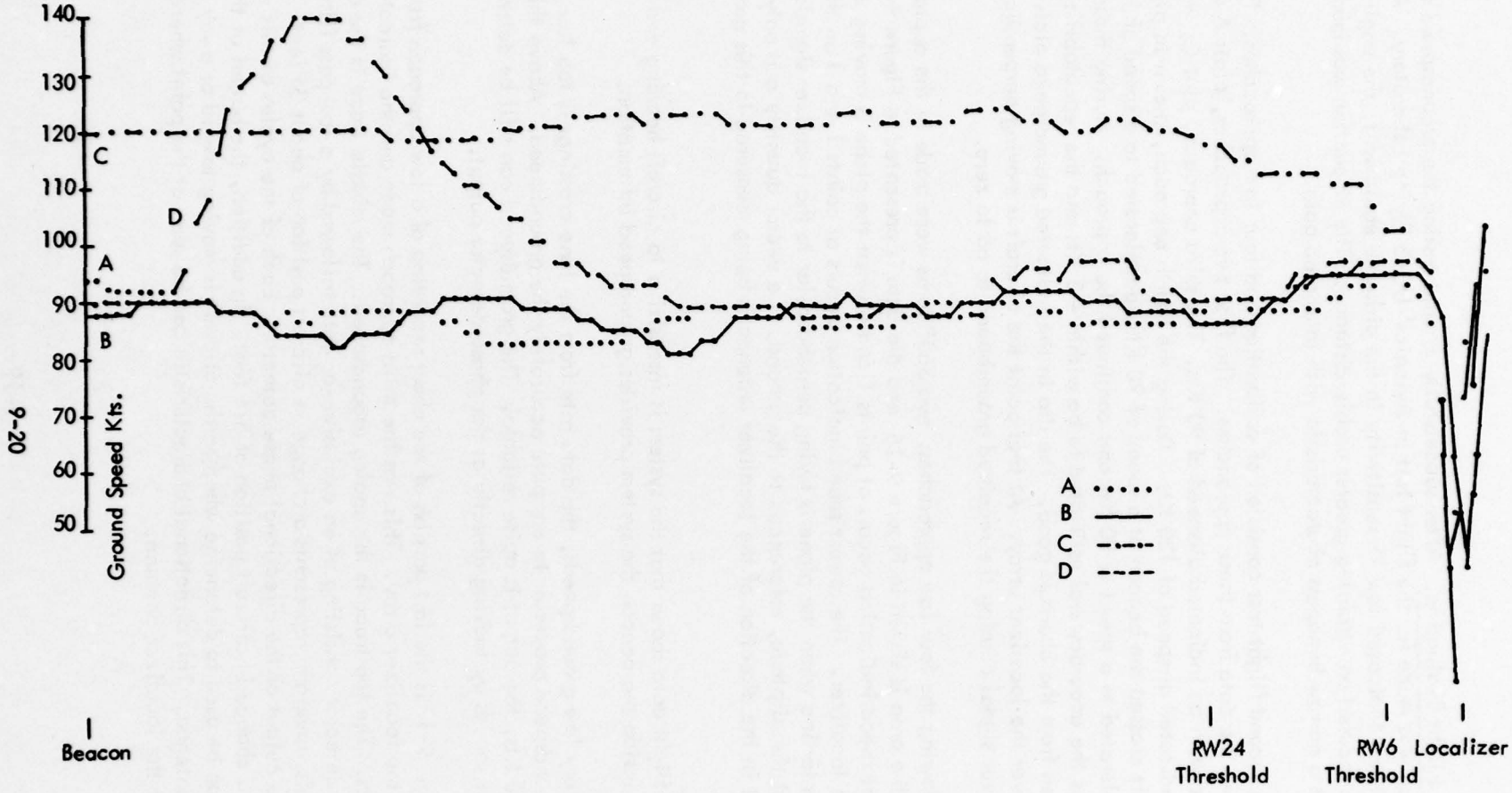

Figure 9-14. Four Low Approaches from the Flight Test on July 26, 1976.

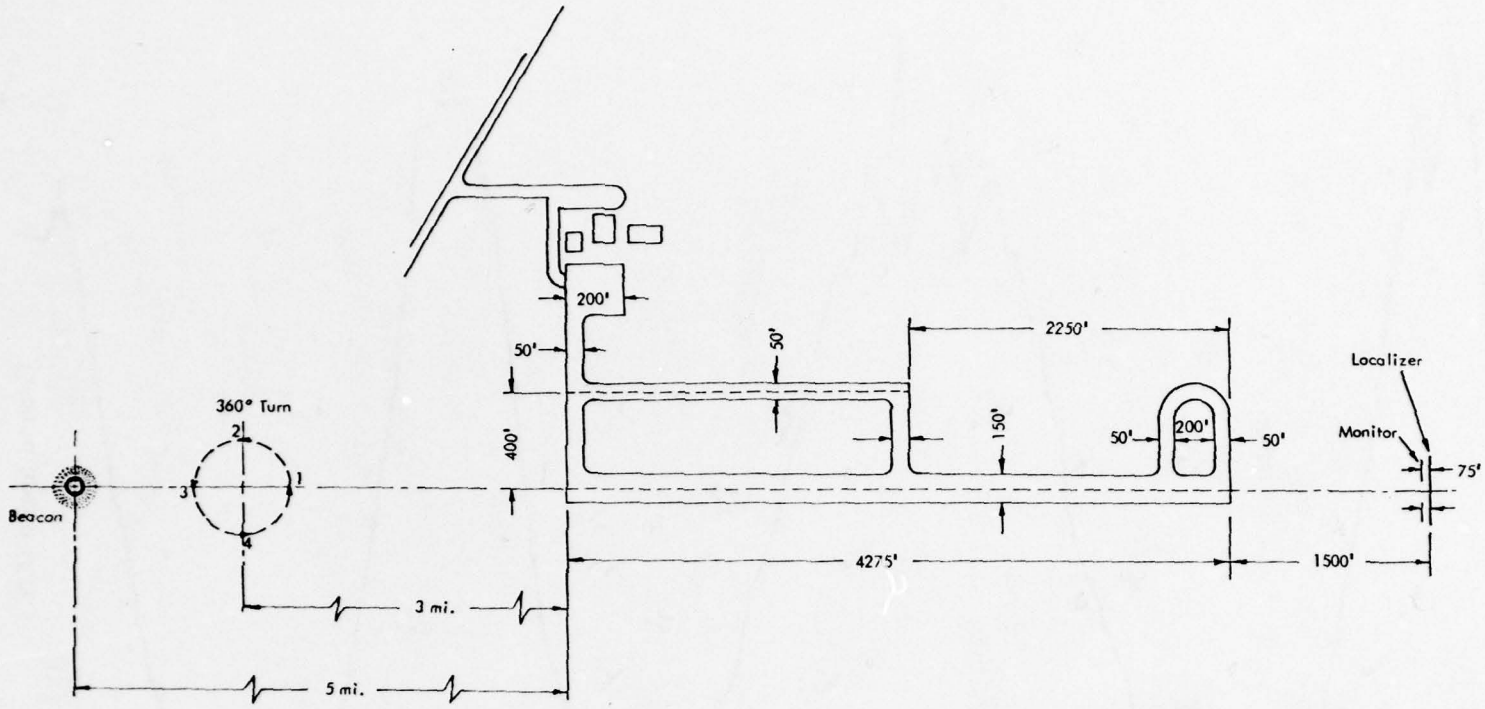

Figure 9-15. 360° Turns Made at Ohio University Test Site at Albany, Ohio.

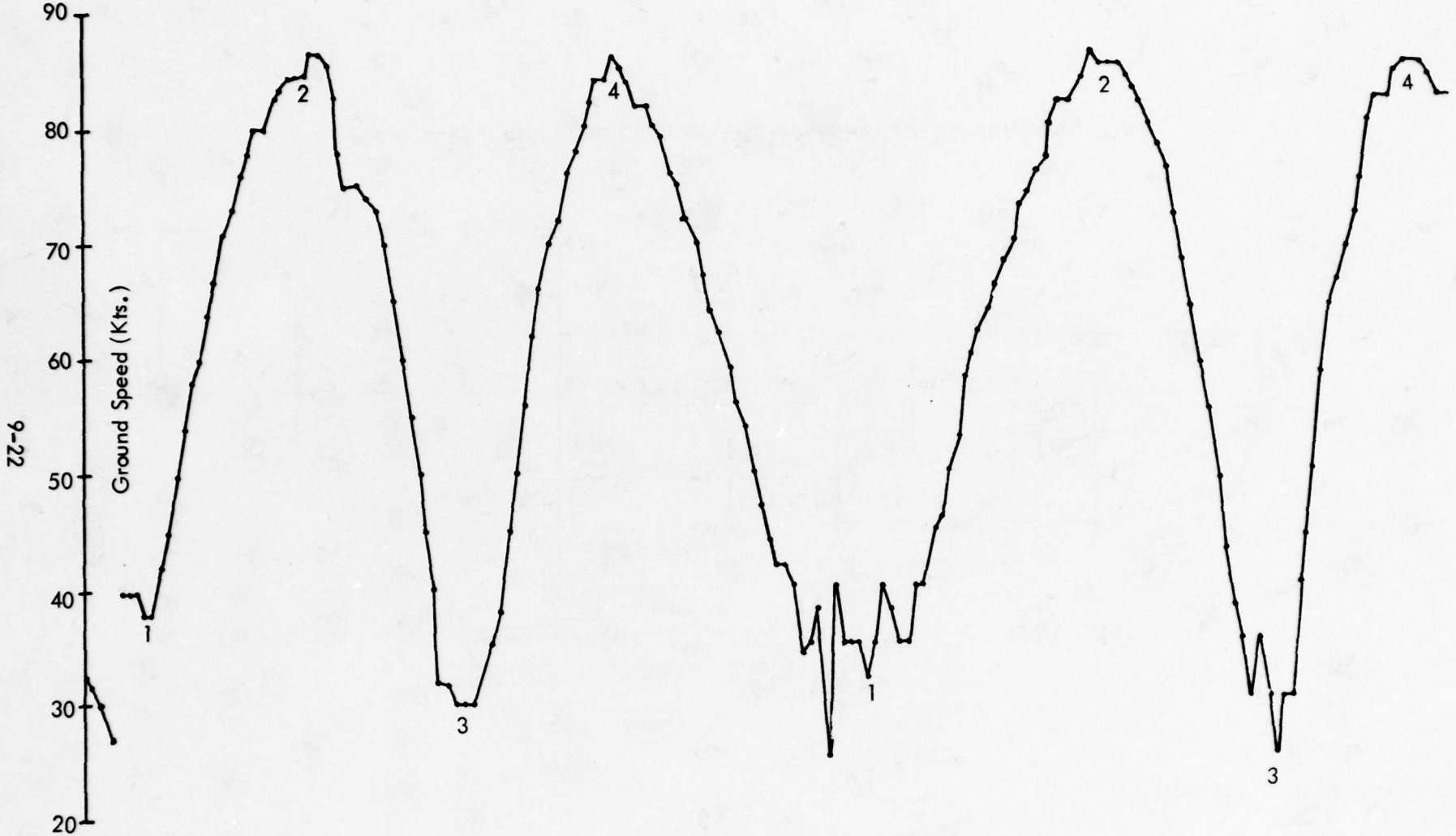

Figure 9-16. Two 360° Turns from the Flight Test on July 26, 1976.

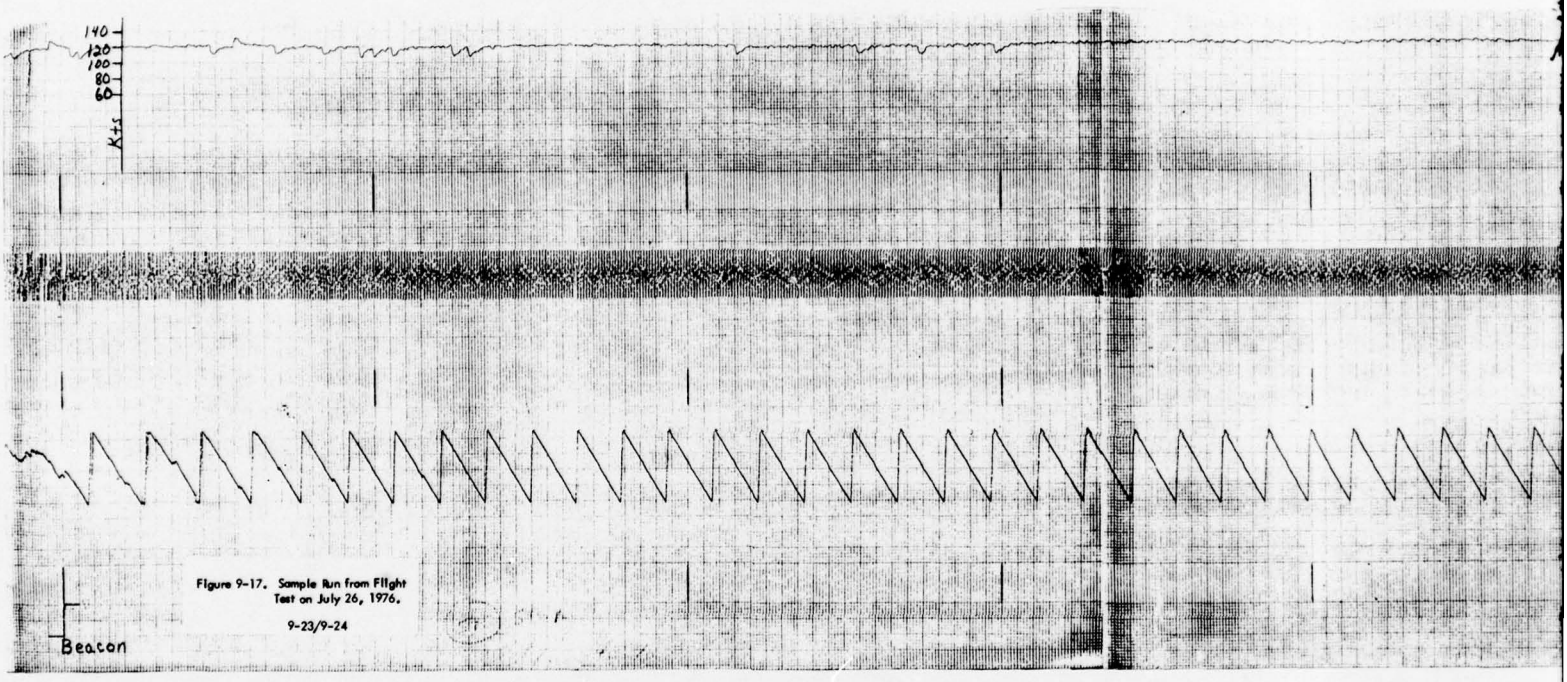

Figure 9-17. Sample Run from Flight Test on July 26, 1976.

9-23/9-24

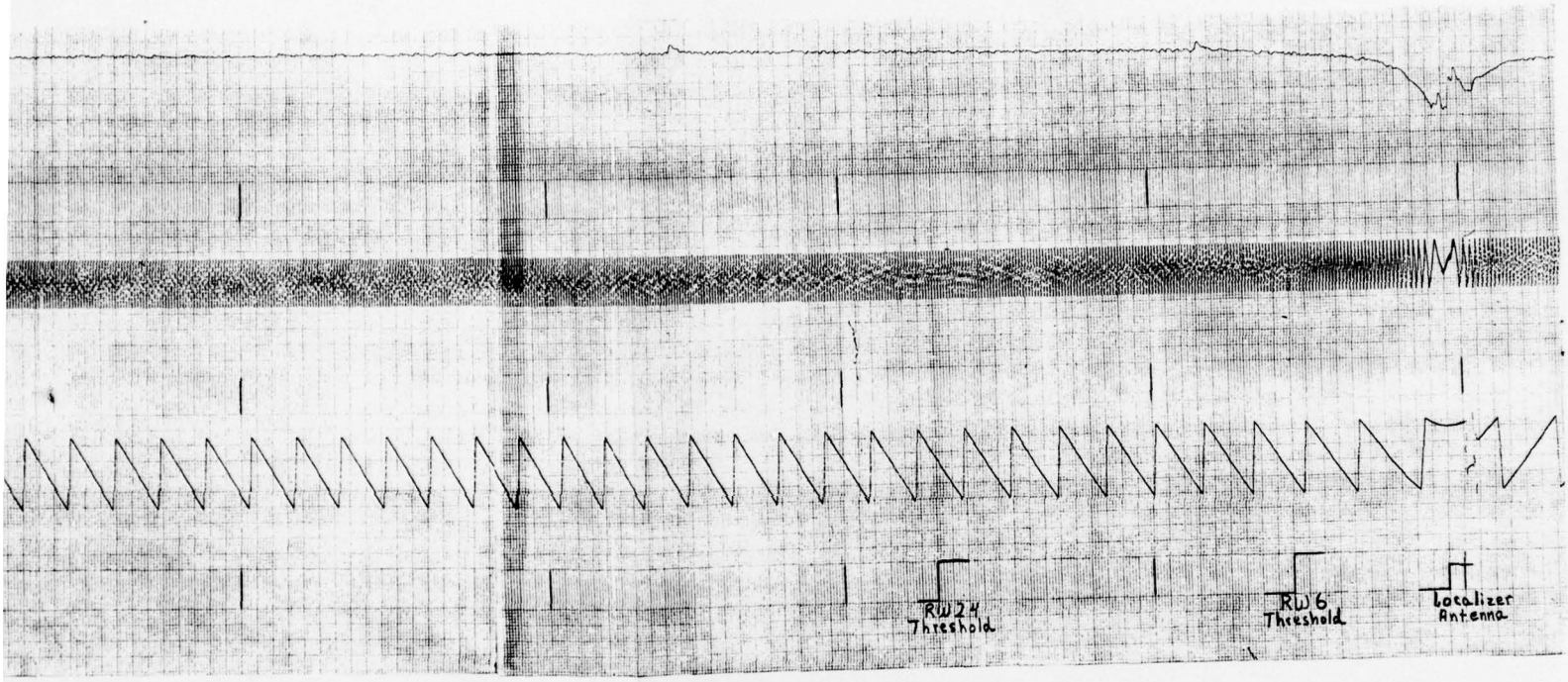
RW 24
Threshold
RW 6
Threshold
Localizer
Antenna

A flight test was made at NAFEC on September 23, 1976. The purpose of this flight test was to compare the output from the groundspeed system with that of the photo-theodolites at NAFEC. The system had undergone some modifications since the data reported here was recorded. The results of this flight were contaminated by noise on the theodolite data, and are not available for this report. However, a preliminary inspection of the data revealed that the improvements made in the groundspeed processor had reduced the noise on the analog groundspeed output and, in general, the data was well-behaved and much as expected.

F. Approach Range-Rate and Windspeed: Evaluation and Development.

1. General. Ohio University was tasked by the FAA to evaluate audio-tone approach range-rate equipment fabricated by ITP, Inc. of Washington, D.C. for the FAA. Additionally the equipment was to be interfaced to an airborne localizer receiver with appropriate filtering, and flight-tested using Ohio University's localizer.

The audio range-rate equipment was delivered by the FAA to the Avionics Engineering Center on December 7, 1977. A Bendix RNA-26-CF navigation receiver was selected by Ohio University for use in this work since it is a sensitive and relatively quiet, solid-state receiver. The RNA-26-CF was bench-checked and found to have a sensitivity of 2 μV. A navigation audio tap was provided just before the VOR filter in the receiver to retrieve received data.

Ohio University Avionics personnel, using FAA-suggested and locally-generated designs, constructed and evaluated a variety of 10 KHz filters for interfacing the range-rate system to the receiver output. These filter designs met with varying degrees of success due to the critically small phase shifts being used to transfer the range-rate information.

The filter design finally accepted utilizes the Seiko SL-62R mechanical filter at 10 KHz, with suitable shock mounting to minimize vibration effects. This filter module is described below in more detail.

Ohio University, after initial system evaluation and reports to the FAA Technical Officer, was asked to modify the range-rate system to improve output data quality and noise performance. The laboratory and flight-evaluation work which fulfilled this task are discussed below.

FAA studies have indicated that the presence in the cockpit of range-rate (approximate groundspeed) and touchdown zone wind can significantly aid a pilot in overcoming the wind-shear threat. Therefore, Ohio University was asked to demonstrate simultaneous operation of an audio-tone range-rate system and a wind telemetry system to provide this cockpit data. This section reports on the resulting development and evaluation program.

2. Approach Range-Rate System.

a. Range-Rate System Description. The Doppler Range-Rate (or, approximately, groundspeed) System derives groundspeed information from the frequency difference between an on-board precision clock and a stable 10 KHz subcarrier transmitted on the localizer. In order to measure the extremely small frequency differences, the 10 KHz signal is multiplied in frequency and compared at a higher frequency to the airborne clock.

Two methods were evaluated for recovering the Doppler; the multiplying detector and the sampler detector. The multiplying detector uses a phase-locked loop (PLL) to multiply the frequency of the 10 KHz signal by a factor between 100 and 1000 times. The result is then compared with the on-board clock in a phase comparator to obtain the Doppler signal. The sampler detector samples the incoming 10 KHz signal with a 10 MHz signal from the on-board clock in a high speed sample-and-hold module to obtain directly the Doppler signal.

The Doppler frequency is processed to read directly in knots, range-rate. Two Doppler processors were evaluated, the synchronous and non-synchronous processors. The synchronous processor tries to hold the Doppler signal at a constant phase by switching the on-board clock above and below the incoming frequency derived from the localizer signal. The average value of the resultant switching waveform is proportional to the groundspeed. The asynchronous processor measures the Doppler frequency directly with a precision frequency-to-voltage converter developed at Ohio University. The output can be displayed on a digital or analog meter or recorded on a chart recorder.

b. Initial System Evaluation. The groundspeed system was assembled on the bench and evaluated initially with no receiver or RF generator involvement (see Figure 9-18). The ground installation (with the "air" clock installed due to clock tuning problems for this test) is connected directly to either the multiplier (phase-locked loop) detector or to the sampler detector. The airborne clock reference signal is also provided to the detector being used. Doppler signal output from the detector is fed to the Doppler processor which, in synchronous mode, controls the airborne clock. Output is read on the fast-slow and DVM modules.

Results of this preliminary testing were encouraging. The clean 10 KHz signal from the ground installation produced quiet and accurate outputs on the multiplying detector in synchronous mode, and on both detectors in non-synchronous (free-run) mode. The sampling detector was somewhat noisier in synchronous mode (±3-6 Kt), as had been shown at ITP.

c. RF-Link Tests. The system was reconfigured as shown in Figure 9-19, with the RF signal generator and receiver interposed between the ground installation and the airborne equipment. The generator was crystal-controlled at 114.9 MHz, and could be modulated from 0 to 100% by the 10 KHz ground tone from the clock. Additionally, 90-150 Hz tones could be provided.

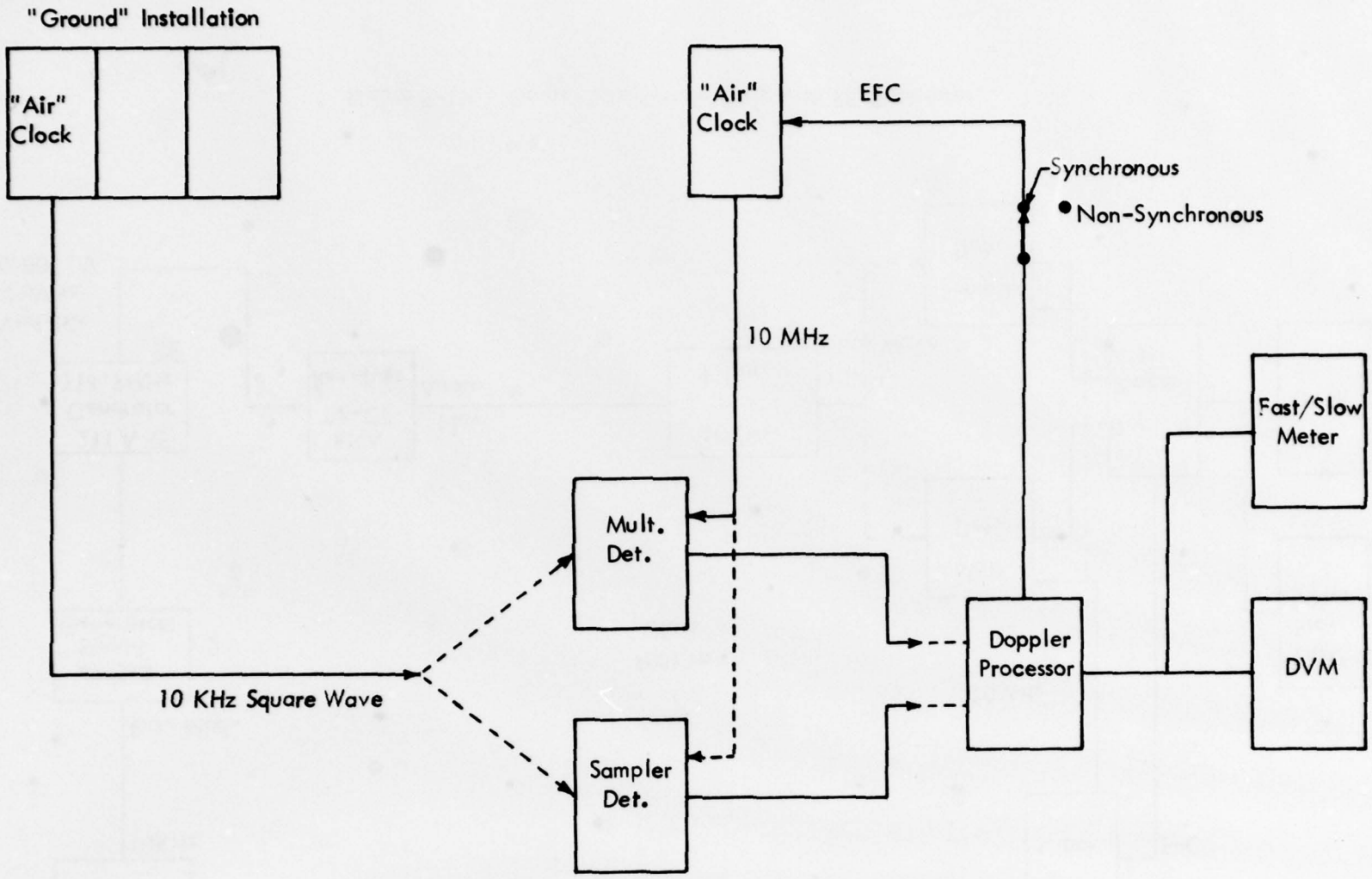

Figure 9-18. Initial Test Configuration - Audio Range-Rate System.

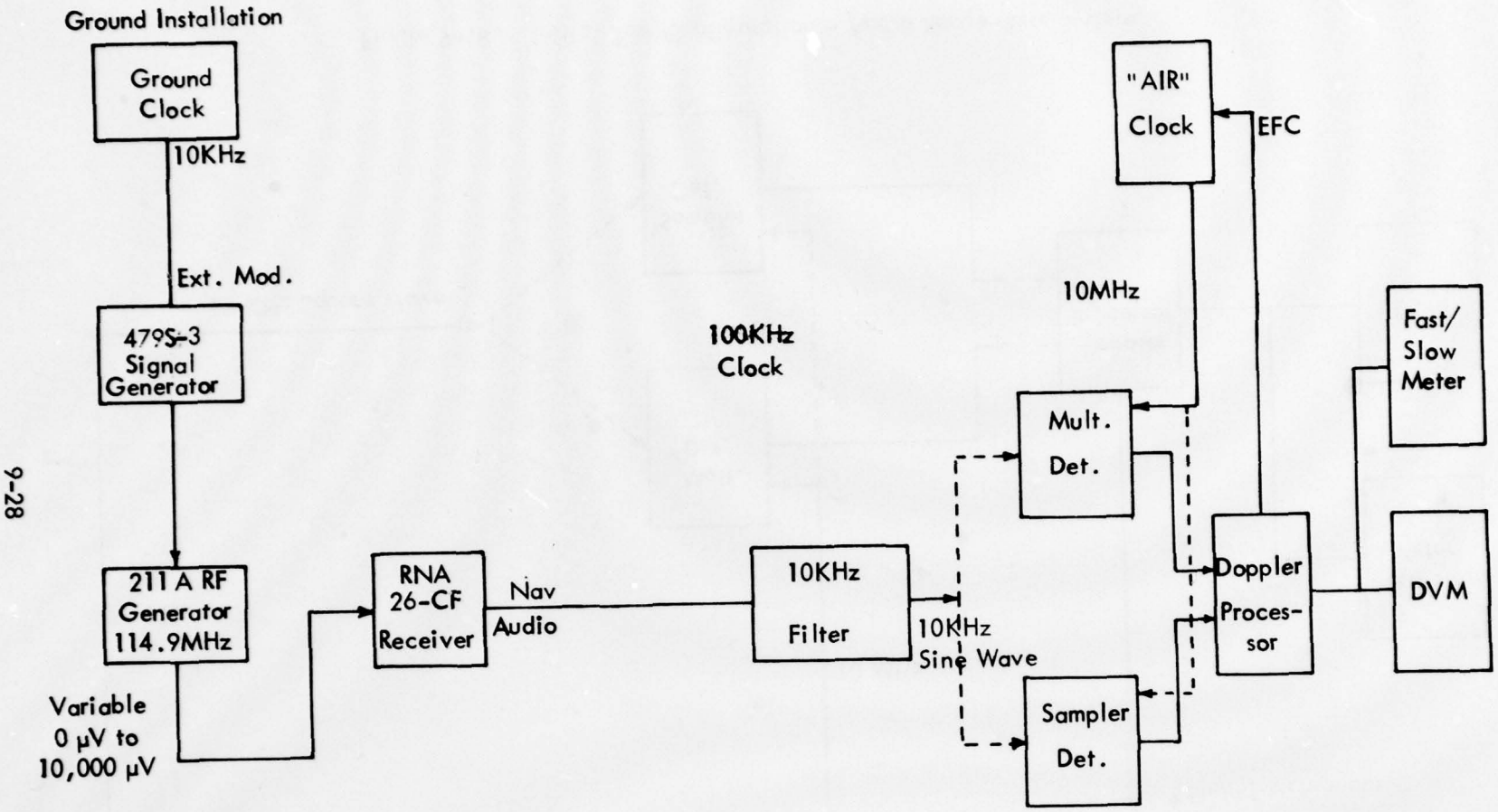

Figure 9-19. Range-Rate System Tests with RF Generator.

d. Individual Module Checkout. During checkout, several items were modified from the original ITP construction to provide a clean electrical environment for detector evaluation.

1) Mainframes. The 6-position mainframe causes interference with the countdown processes in both clocks. This causes output jitter. The clock problem was traced to the presence of cables on the rear panel BNC connectors. The problem was solved by buffering all outputs which go to the backplane.

2) Air Clock. By-pass capacitors were installed on the Oscillator Power Supply to ground (pin 3 to pin 2) and from Oven Power Supply to ground (pin 14 to pin 15) on the clock unit.

Shielded wire shield ground clips were soldered to eliminate 10 MHz noise.

Digital noise, and some 10 MHz, appears on the tops of logic countdown pulses. The noise was found not to interfere with the countdown process.

Line drivers, with 50 ohm output impedance, were provided on the two 10 MHz outputs. Without these, cable attachment to front-panel BNC connectors caused serious waveform distortion.

The SN7414 amplifier chip was replaced with a 74S04 chip to improve 10 MHz waveforms.

Loose PC board screws were tightened.

3) Ground Clock. The 10 KHz output was out-of-service upon arrival. Two inoperative SN7490 chips were found. When replaced, the clock module operated normally. No cause for the chip failure was found.

Shield clips were soldered to avoid noise.

In this module, the power supply appeared to be generally free of noise, so by-pass capacitors were not installed.

10 MHz line drivers were installed for the front panel outputs.

A loose bracket holding the clock module was tightened.

4) Doppler Processor. The frequency-to-voltage converter in the non-synchronous processor drifts with temperature. (This fact was earlier reported by ITP). The R/C oscillator should be replaced by a clock-derived signal.

A 0.1 μF capacitor was added to the DVM output to reduce high-frequency noise riding on the output DC level.

R7 comparator offset control was identified and adjusted for correct operation on Doppler input levels expected from the two detectors.

It was found that Doppler inputs must remain positive to avoid undesirable operation of the non-synchronous mode input comparator. This comparator uses positive and ground voltage references, and thus cannot compare to a negative voltage properly.

5) Sampler Detector. The input comparator for 10 KHz required adjustment for input signal level from the 10 KHz filter.

The output offset was adjusted to insure that Doppler output would not swing below zero.

A 50-ohm terminating resistor was provided at the 10 MHz input BNC connector for matching.

The circuit appears to work properly (with some noise present in the output of the sampler) when driven directly by the ground clock. However, even the interposition of the filter causes significant noise increases in the output, and use with the receiver link produces unusable Doppler signals. Such operation is consistent with jitter in the sampling pulse position, or in the input waveforms.

6) Multiplier Detector. A 50-ohm terminating resistor was added at 10 MHz input.

A line driver is needed on the 10 MHz output port. This was not added at this time, since the unit could be evaluated using low-capacitance scope probes without disturbing the waveform.

The 562 phase-locked loop can accept sine waves to very low amplitudes. Accordingly, since the filter produces a very clean 10 KHz sine wave at 0.5 v p-p, the input comparator was by-passed and the filter output applied directly to the 562 loop input. Reasoning is that any comparator jitter is eliminated in this way.

It was observed that the PLL is affected very adversely by the presence of the 10 MHz clock input for Doppler generator. Apparently there is feed-through on this board which causes problems. For the remainder of the evaluation, the PLL itself was isolated from any signal input other than the 10 KHz loop input.

Countdown logic in the PLL enclosure operates below v_{cc} specification due to filter choke.

The PLL crystal attempts to set the loop center frequency at 10-20 KHz too high. Experimentation with crystal loading failed to correct the problem. With the crystal removed, the loop locks tightly on direct clock input, but with too much noise

at 10 MHz when locked through the 10 KHz filters.

This unit should have buffers and line drivers installed on 10 MHz circuitry whenever external connection is possible. Waveform distortion and level decrease result otherwise.

e. Preliminary Conclusions from Module Checkout and System Re-Evaluation. The two clock modules were radiating or conducting 10 MHz to other parts of the system through power supply paths and evidenced waveform distortion due unterminated cables being driven directly by TTL gates. The waveform distortion was causing erratic operation of voltage comparators downstream, and the 10 MHz leakage was apparently causing improper operation of the multiplier detector module.

When the stray RF was reduced, and waveforms improved, it was found that the multiplier detector would no longer operate to produce stable Doppler output. Further investigation of this module discovered that the crystal reference for the PLL was operating approximately 10-20 KHz high, and that it could not be "pulled" by the loop to lock stably onto the incoming signal. With the crystal removed, and with direct clock input into the multiplier module, correct operation is obtained.

The sampler module evidences noise at the sampler output even in the presence of a "perfect" direct-connected clock input at 10 KHz. When connected to the receiver output, the noise at the sampler output masks the Doppler signal completely. In fact, even with direct-connected 10 KHz clock signal passed through the 10 KHz filters, no usable Doppler is output by the sampler detector.

The Doppler processor module operates correctly, assuming correct adjustment of the non-synchronous mode comparator for Doppler input level (which changes due to noise).

f. System Modification and Development. A conversation with the Technical Officer (TO) on December 17, 1977 resulted in the following plan:

Ohio University would revise the phase-lock loop in the multiplier detector to operate without a crystal reference at 1 MHz, and would evaluate system operation with this change. The requisite changes were made and flight test and bench test data showed that the 1 MHz Multiplier Detector was indeed an improvement over the 10 MHz Multiplier Detector originally received. In addition, the sampler detector operating at 10 MHz was judged to be unworkable.

The Technical Officer visited Ohio University on December 27, 1977 to receive firsthand the data and conclusions arrived at by Ohio University. In the ensuing discussions the following plan was agreed upon by the Technical Officer and Ohio University.

Since the 1 MHz data was a distinct improvement over the data from the original detector, but the data rate was judged to be too low by the Technical Officer, an attempt would be made to produce a 5 MHz Multiplier Detector. Furthermore, the data produced

by the sampler detector indicated that further work in this area was not warranted and all components from the Sampler Detector were returned to the Technical Officer. In addition Ohio University was to work on optimizing the filtering of the groundspeed output to improve the presentation.

Ohio University performed the above work in close cooperation with the Technical Officer, resulting in a 5 MHz Multiplier Detector with a reasonable data rate and with much of the data stability of the 1 MHz system. Output filtering was added to improve the output. In addition, the synchronous Doppler Processor was redesigned to incorporate improvements conceived during the course of the work. The resulting system achieved the goals originally proposed by the Technical Officer.

Ohio University received a third clock module from the Technical Officer. The new clock was modified to produce a larger frequency excursion with the allowable control voltage. The new clock significantly increased the speed of the synchronous processor, reducing the filter requirements at the output and lead to the design of the 9 MHz loop (Figure 9-20), which was to make use of the 1 MHz multiplier detector and the synchronous processor to achieve higher data rates while using the more accurate detector. Although fully designed on paper, the time remaining on this contract did not allow fabrication and testing of this idea.

g. Schematics. A conclusion reached by Ohio University during the course of the work on the range-rate system is that the factor limiting the accuracy of the groundspeed output is the amount of noise on the 10 KHz tone received from the ground. In trying to improve the signal to noise ratio of this signal, many different filters and filter configurations were tested. A general conclusion reached early on was that the mechanical filter produced the cleanest output of all the filters tested but had the disadvantage of vibration pick-up or microphonics. Considerable effort was spent comparing the different mechanical filters and circuits along with the different methods of decoupling the filters from the mechanical operating environment. The optimum configuration proved to be a Seiko Filter Model SL-62R operating in the circuit of Figure 9-21 with foam padding packed around the entire circuit. Although bench tests continued on alternate filters the Seiko filter circuit was used exclusively in flight tests.

Figure 9-22 is the schematic of the 1 MHz Multiplier Detector. The circuit uses a Signetics NE562 phase-lock loop chip with an RC oscillator to multiply the 10 KHz input signal to 1 MHz which is compared in a phase comparator to a 1 MHz signal derived from the system clock, to produce the Doppler output signal. The Doppler output signal was very clean and produced low-noise groundspeed output, but the update time was on the order of 3 to 5 seconds depending on the groundspeed. Much of the subsequent work on the range-rate system was directed toward improving the data rate.

The most obvious way to increase the data rate is to increase the frequency of the Doppler signal. Since the 10 KHz subcarrier frequency had been specified, the only way to increase the Doppler frequency was to increase the multiplication factor in the detector. Figure 9-23 is the schematic of the 5 MHz multiplier detector. The phase detector and voltage-controlled oscillator (VCO) were different from those used

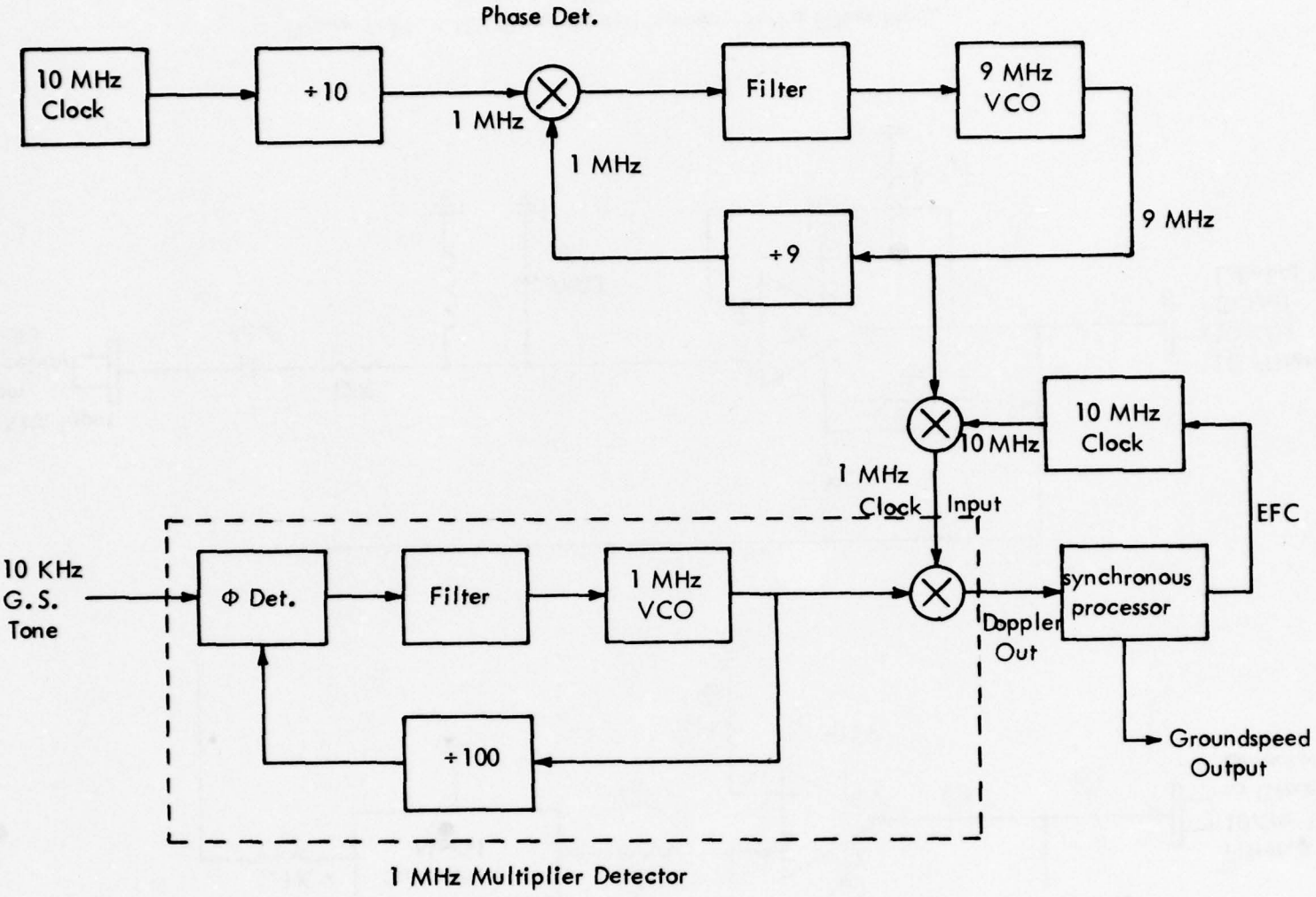

Figure 9-20. Revised Synchronous Processing of 1 MHz Data.

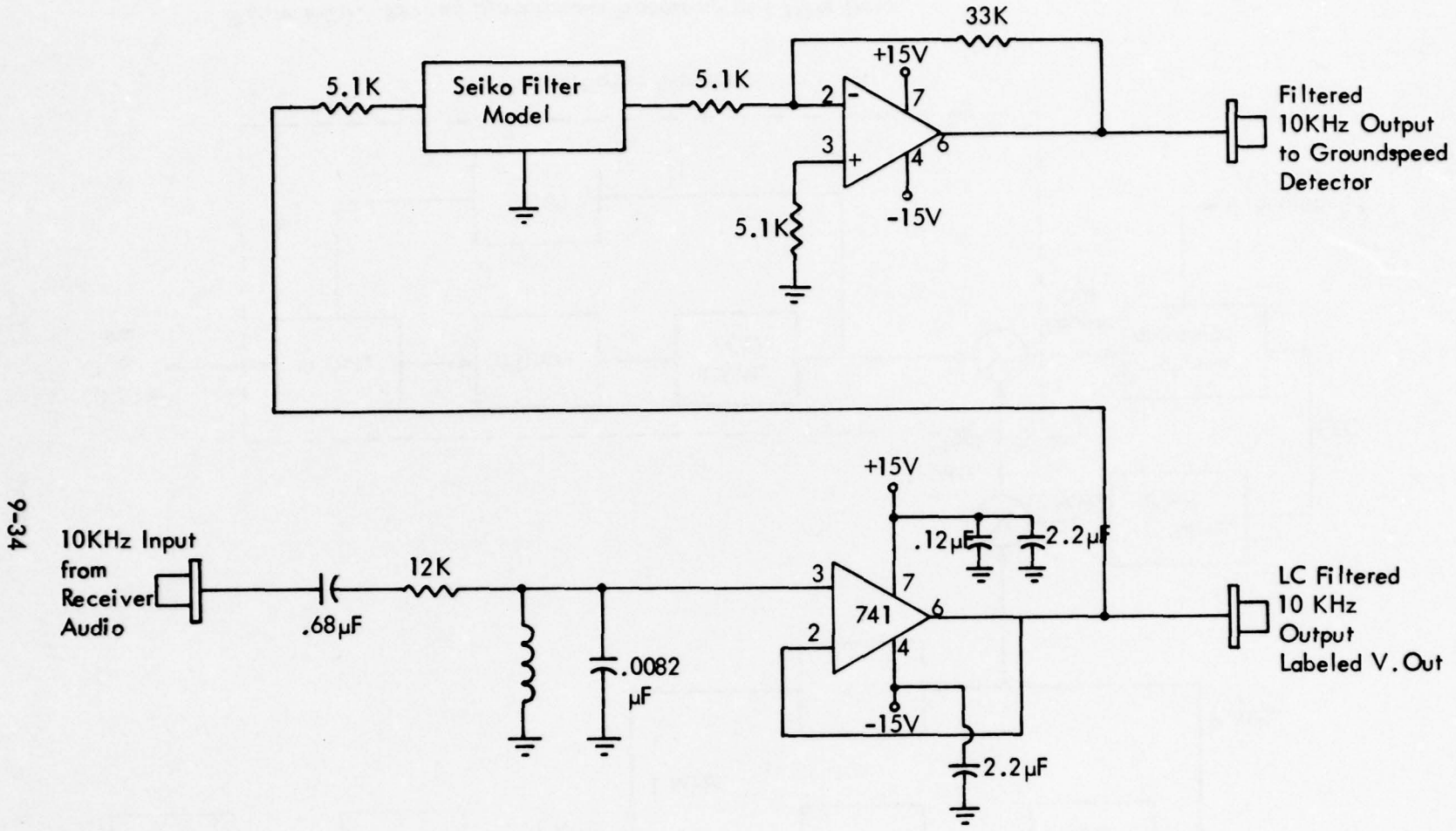

Figure 9-21. ILS Groundspeed System, Seiko Filter Module, Model SL-62R.

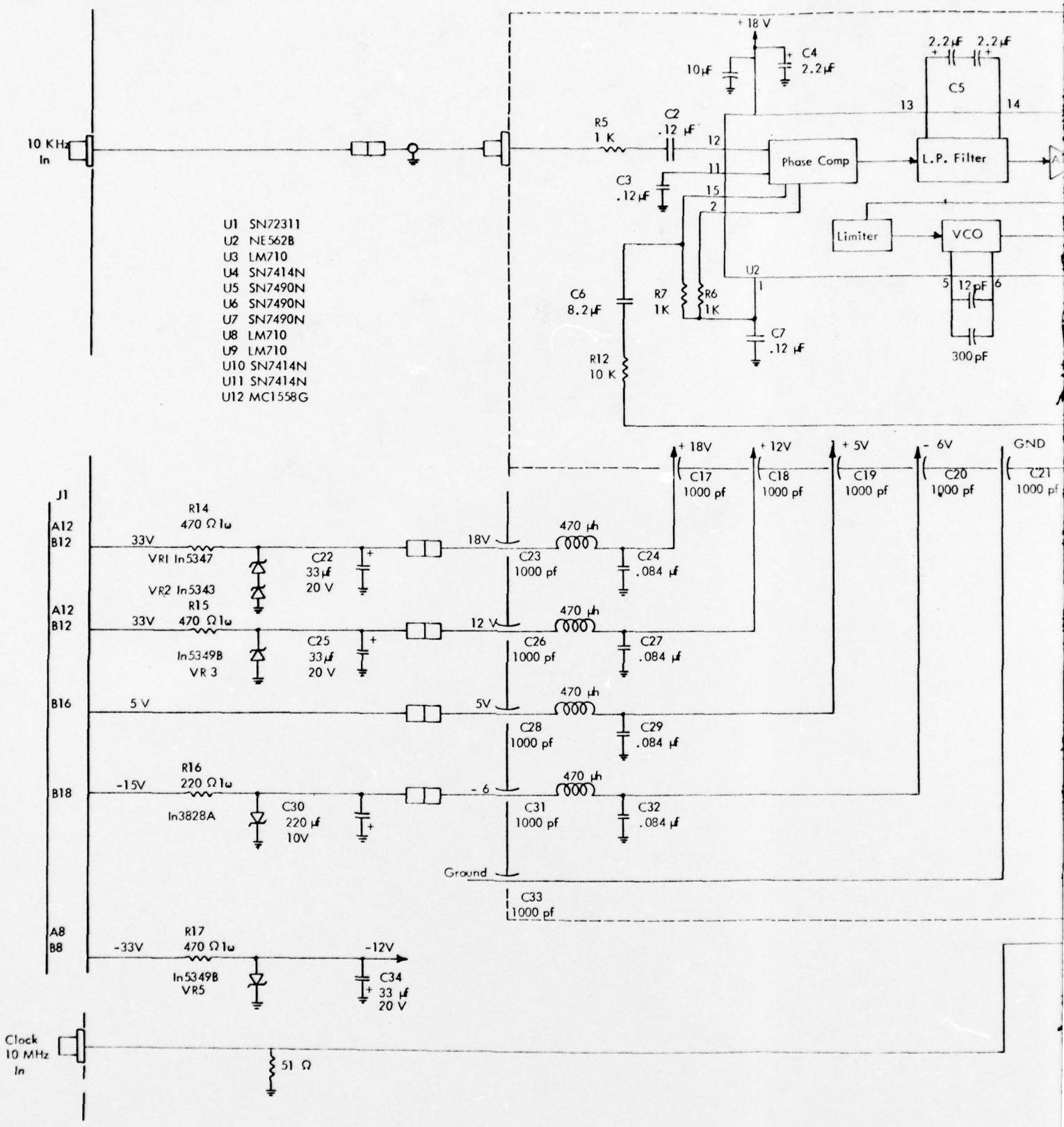

Figure 9-22. ILS Groundspeed System 1 MHz Multiplier Detector Module.

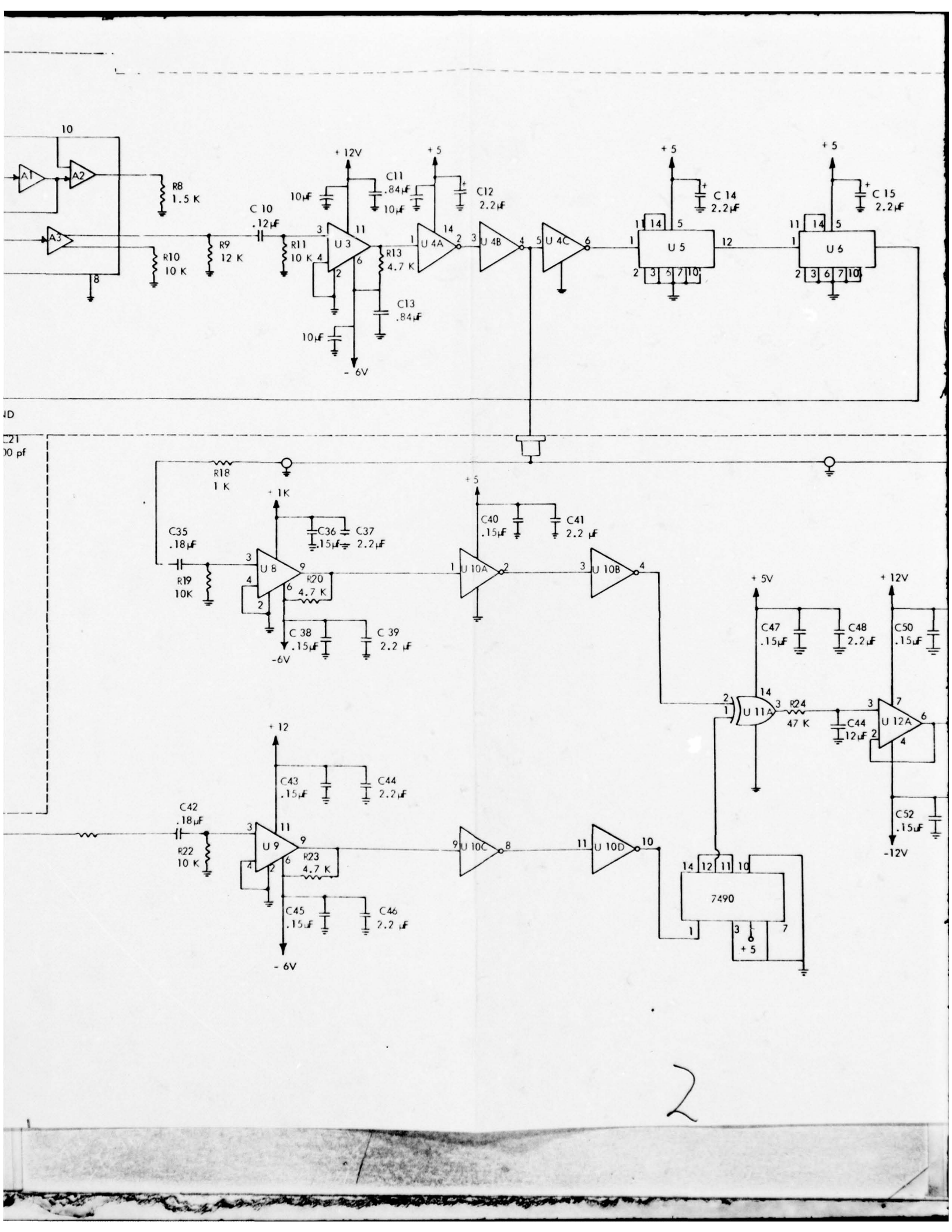
10
A1
A2
A3
8
R8
1.5 K
R10
10 K
R9
12 K
C 10
.12μF
+ 12V
10μF
C11
.84μF
10μF
+ 5
C12
2.2μF
R11
10 K
U 3
R13
4.7 K
C13
.84μF
10μF
- 6V
U 4A
U 4B
U 4C
+ 5
C 14
2.2μF
U 5
+ 5
C 15
2.2μF
U 6
ND
C21
00 pf
R18
1 K
+ 1K
C35
.18μF
R19
10K
C36
.15μF
C37
2.2μF
U 8
R20
4.7 K
C 38
.15μF
C 39
2.2 μF
-6V
+ 5
C40
.15μF
C41
2.2 μF
U 10A
U 10B
+ 5V
C47
.15μF
C48
2.2μF
+ 12V
C50
.15μF
U 11A
R24
47 K
C44
12μF
U 12A
C52
.15μF
-12V
+ 12
C43
.15μF
C44
2.2μF
C42
.18μF
R22
10 K
U 9
R23
4.7 K
C45
.15μF
C46
2.2 μF
- 6V
U 10C
U 10D
7490
+ 5

2

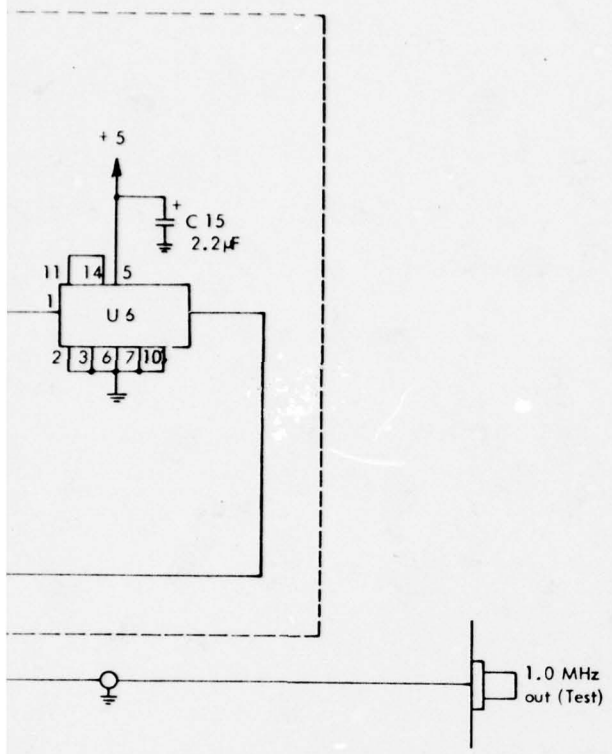
+ 5
C 15
2.2μF
11
14
5
1
U 6
2
3
6
7
10

1.0 MHz
out (Test)

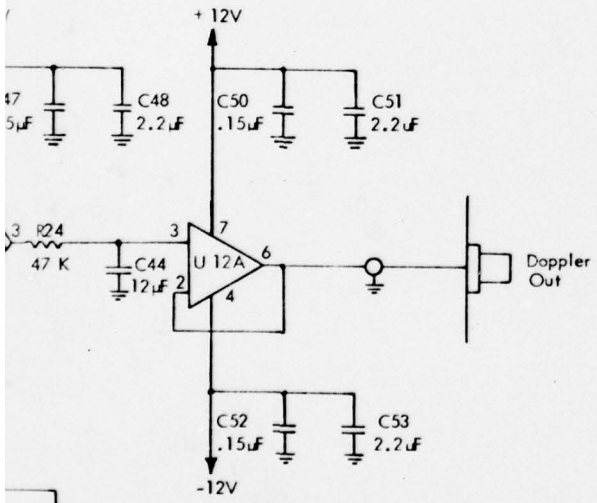
+ 12V
C48
2.2μF
C50
.15μF
C51
2.2μF
R24
47 K
C44
12μF
U 12A
Doppler
Out
C52
.15μF
C53
2.2μF
-12V

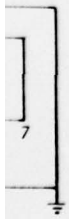

3

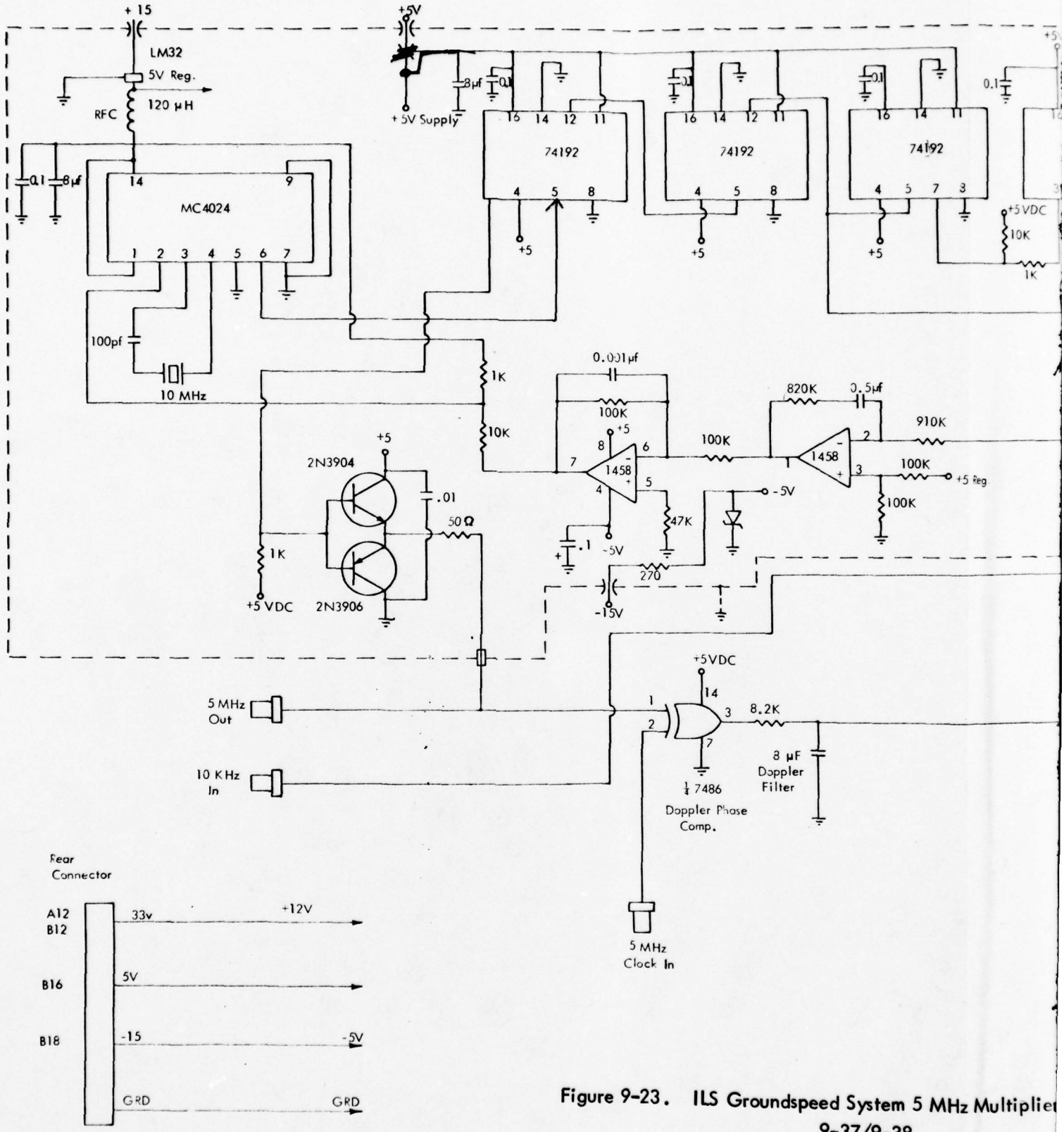

Figure 9-23. ILS Groundspeed System 5 MHz Multiplier

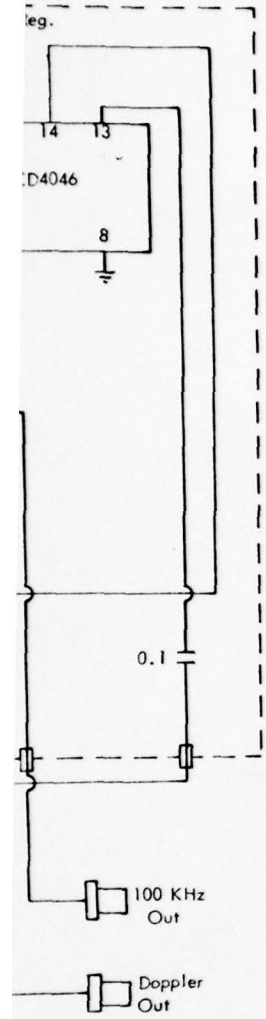

Detector Module.

in the 1 MHz loop because it was considered desirable to use a crystal for the VCO timing element. The output signal from the loop is compared with a 5 MHz clock signal to produce the Doppler output.

Figure 9-24 is the schematic of the Doppler processor module. The schematic contains the circuitry for both the synchronous and non-synchronous processors. The non-synchronous processor performs the frequency-to-voltage conversion by measuring the period of the Doppler signal, which is inversely proportional to the groundspeed output desired, and dividing this quantity into a constant by means of a multiplying digital-to-analog (D/A) converter in the feedback loop of an op-amp. Calibration pots were provided on the board for use with either the 5 MHz or the 1 MHz detectors. Selection is made by moving two jumper wires.

The synchronous processor operates by switching the reference clock between its upper and lower limits in order to keep the Doppler signal at a predetermined phase angle. The average value of the switching voltage is proportional to groundspeed and can be calibrated directly. The synchronous processor measures positive or negative groundspeed (relative to the localizer) while the non-synchronous measures the absolute value of the groundspeed only over the range of 40 to 190 Kts. Also shown on this schematic is the non-synchronous processor calibrator which can be used to calibrate this processor over its full range of operation.

Figure 9-25 is a schematic of the fast-slow module. Although this module was built by ITP, its schematic is included here because a schematic was not provided at the time of delivery to Ohio University.

Figure 9-26 is the schematic for the clock module. This module was modified by the addition of line drivers to buffer the outputs from load variations. Additional power supply filtering was also added to reduce the interaction between modules. One of the 10 MHz outputs was modified on each module by the addition of a flip-flop to produce a 5 MHz output to operate with the 5 MHz detector.

3. Analog Wind Telemetry System.

a. Introduction. In response to the need for a simplified, low-cost wind telemetry system for the wind shear project currently underway, the analog wind telemetry system was designed and evaluated. This telemetry system transmits analog wind information to the aircraft by amplitude modulating the localizer carrier with an audio sine-wave signal whose frequency is proportional to the wind velocity. This frequency is then recovered from the audio output of a standard localizer receiver for processing of the wind data. During the evaluation of this telemetry system, two different types of airborne wind data processors were tested to provide a comparison of alternative methods. The simplest data processor tested consisted of an integrated-circuit frequency-to-voltage converter plus appropriate signal conditioning circuitry to drive a microammeter, thus providing an analog readout of the transmitted wind. A second data processor consisted of a dedicated frequency counter, calibrated to display the wind directly in knots. This system is designed entirely with digital techniques and provides a seven-segment readout of the wind information.

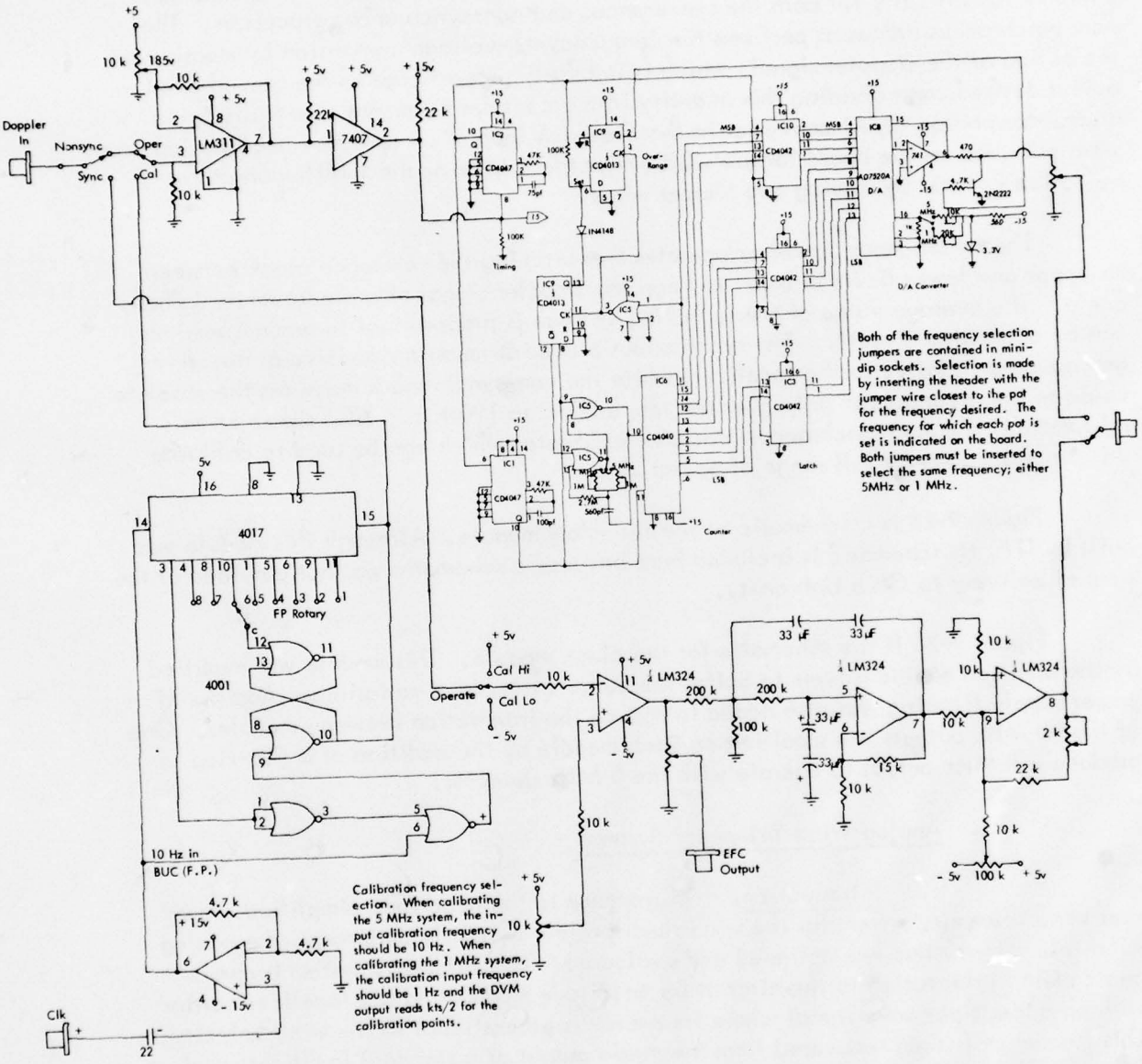

Figure 9-24. ILS Groundspeed System - Doppler Processor Module.

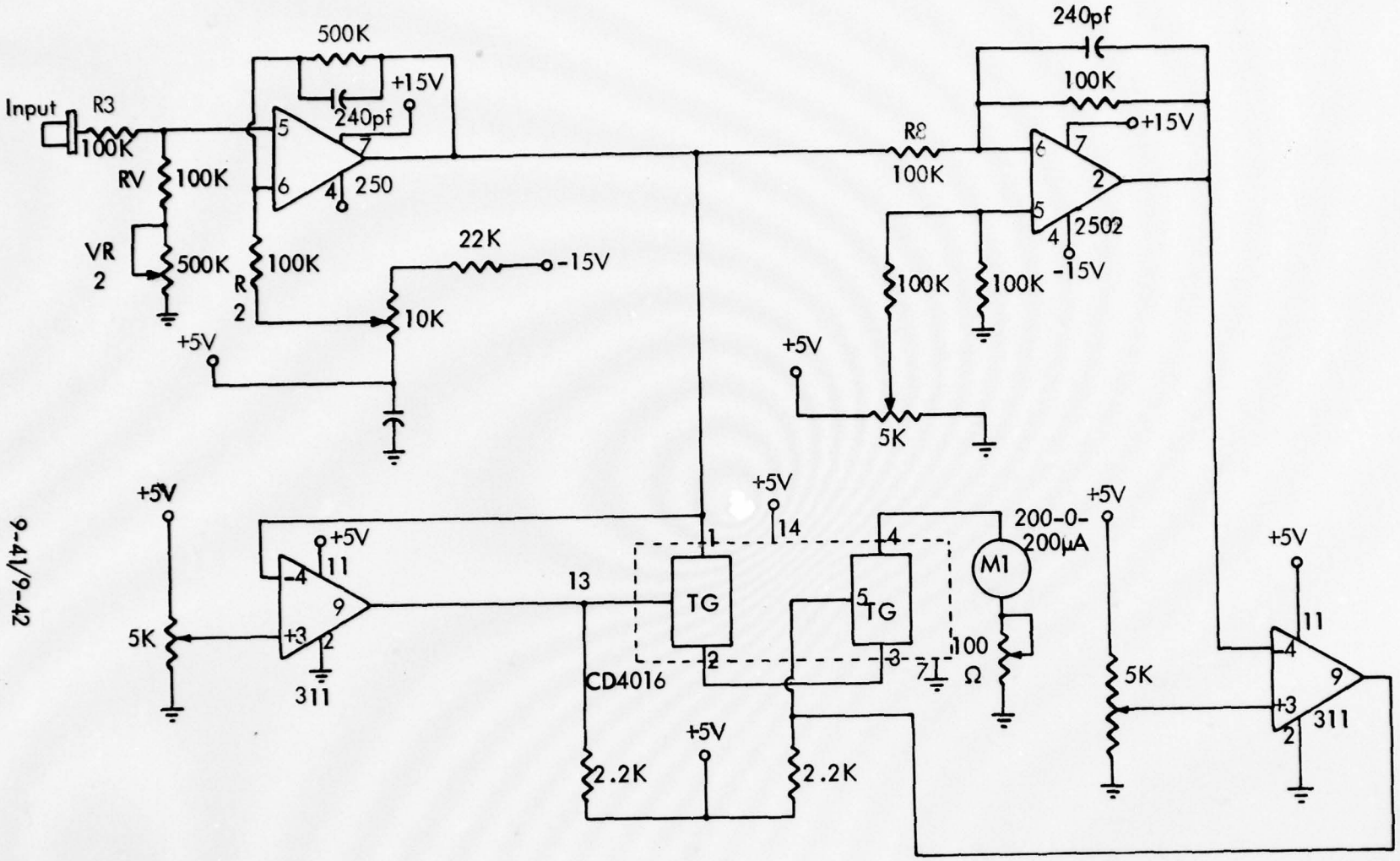

9-41/9-42

Figure 9-25. ILS Groundspeed System, Fast-Slow Module.

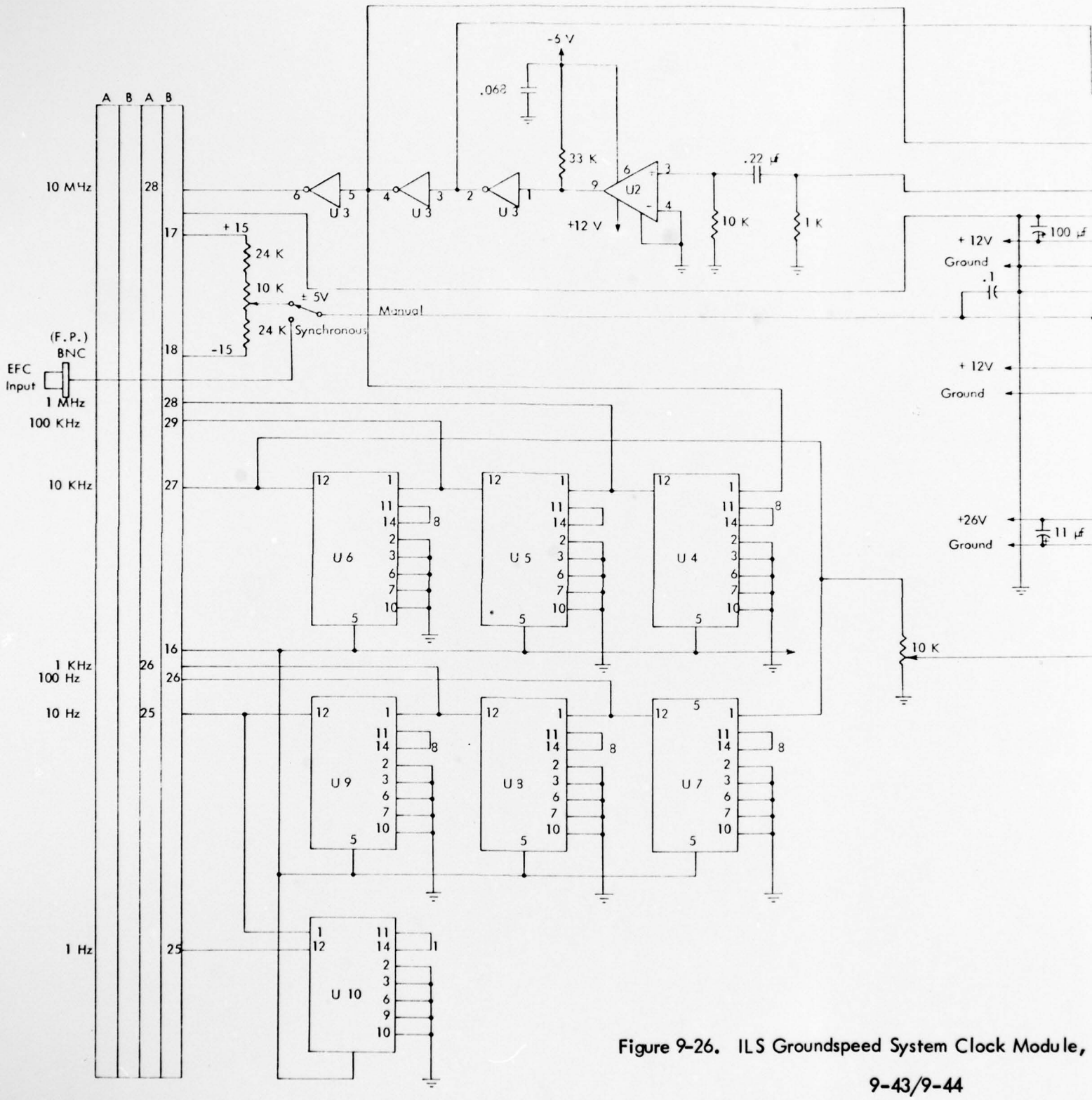

Figure 9-26. ILS Groundspeed System Clock Module,

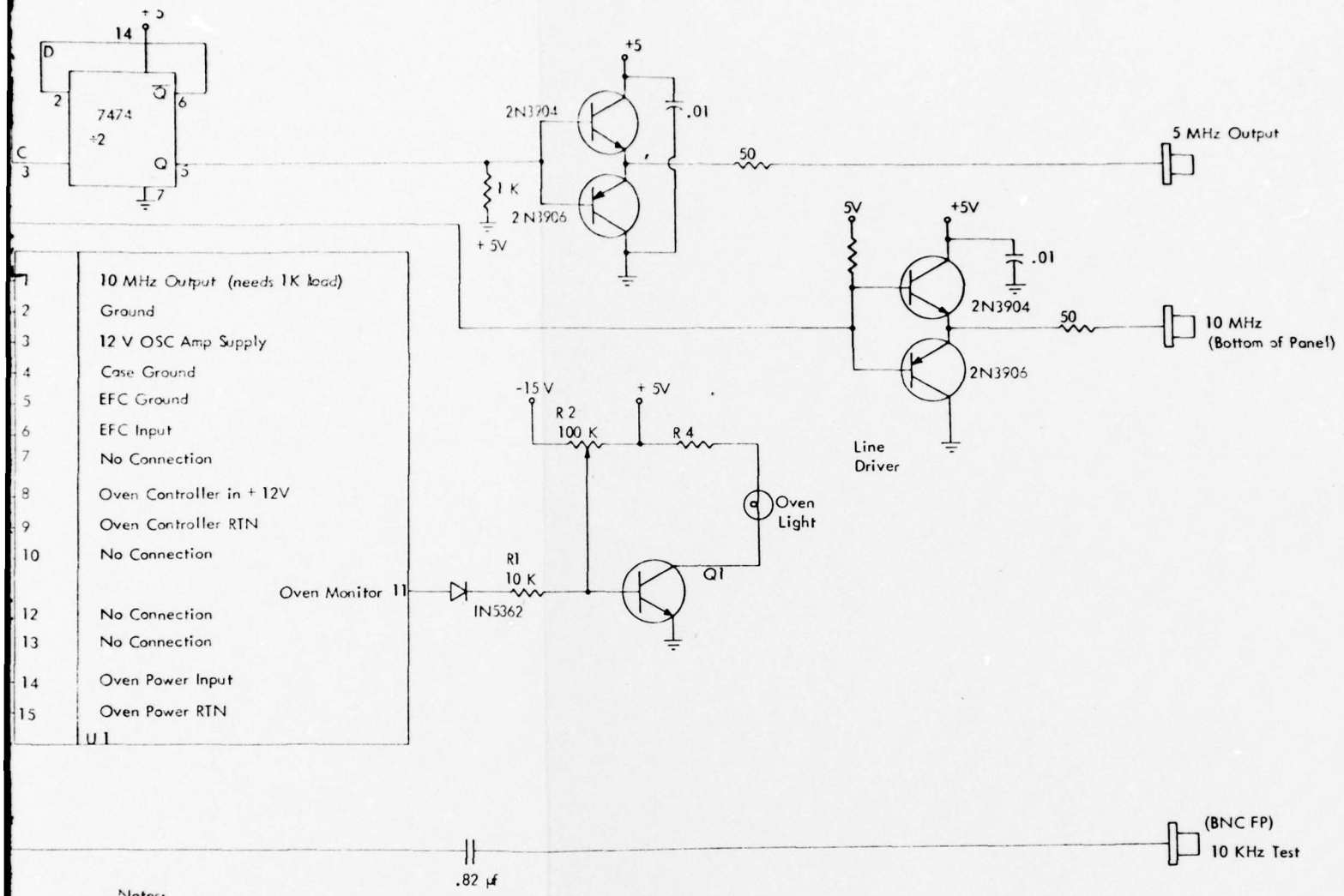

Notes:

U 1	10544A
U 2	µA 710
U 3	SN7414
U 4	SN7490A
U 5	SN7490A
U 6	SN7490A
U 7	SN7490A
U 8	SN7490A
U 9	SN7490A
U 10	SN7490A
Q 1	2N2222

Modified.

b. Ground Installation. The modulation of the localizer carrier with the correct wind data requires two circuits, the anemometer transmitter shown in Figure 9-27 and the localizer modulator shown in Figure 9-28. The anemometer transmitter is located at the anemometer and provides a signal whose frequency is dependent upon the wind velocity as measured by the anemometer. Functionally, the anemometer transmitter operates as follows: The voltage output of the anemometer is applied to the input of the differential amplifier constructed from one-half of IC1. This signal is then scaled by the inverting amplifier formed by the other half of IC1 so that the output of the inverting amplifier equals 5 volts for anemometer wind measurements of 50 knots. The inverting amplifier formed by IC2 is then used to offset the 5 volt signal by 5 volts so that the wind information is now scaled from 0 to +10 volts. The Teledyne 9400 v/f converter designated IC3 is configured so that this 0-10 volt signal swing will cause a variation in the frequency output at pin 6 of 5495 Hz to 6495 Hz respectively. This provides 10 Hz/knot sensitivity with 5995 Hz equal to 0 knots. Nominally, R21 will be used to adjust the lower frequency limit and R20, the upper frequency limit; but in practice it may be found that a series of adjustments of both potentiometers at both frequency limits will be necessary for correct calibration of the anemometer transmitter output. The output of pin 6 of IC3 is a digital signal and is applied to transistor Q1 which provides current drive capability. This frequency-formatted wind data is then coupled through transformer T1 to provide a floating output that is connected to the localizer modulator via a twisted pair. The localizer modulator circuit is located at the localizer transmitter and performs two functions, the first function being the addition of the 10 KHz groundspeed signal to the wind signal. This is accomplished by IC1 which is configured to provide for differential amplification of the wind signal from the anemometer transmitter and then addition of the 10 KHz groundspeed signal through use of an inverting amplifier. The amplitude of the added wind signal is adjustable by means of R5 which is extemally accessible. The second function of the localizer modulator is to provide the required drive capabilities for impression of the two tones upon the AGC of the localizer transmitter. This is accomplished by means of the line driver composed of transistors Q1 and Q2. Figure 9-29 is a component layout diagram for the anemometer transmitter board.

c. Airborne Installation. For airborne evaluation, two separate data processors were constructed on separate boards and mounted within a single Tektronix TM500 module. The method of data recovery for the two processors differs in that one processor uses analog techniques and provides an analog meter output, while the other processor uses digital techniques and provides a seven-segment display output. The circuitry required for signal conditioning and flag generation is common to both processors and was incorporated into the analog processor board with outputs shared by the digital processor board.

1) Analog Data Processor. The analog data processor was constructed on a printed circuit board; and since it contains the circuitry common to both processors, it is by itself a complete wind data processor. The wind output data is in the form of a DC current proportional to the wind velocity and is used to drive a center-zero galvanometer. Due to space limitations, this meter is mounted separately from the Tektronix TM500 module.

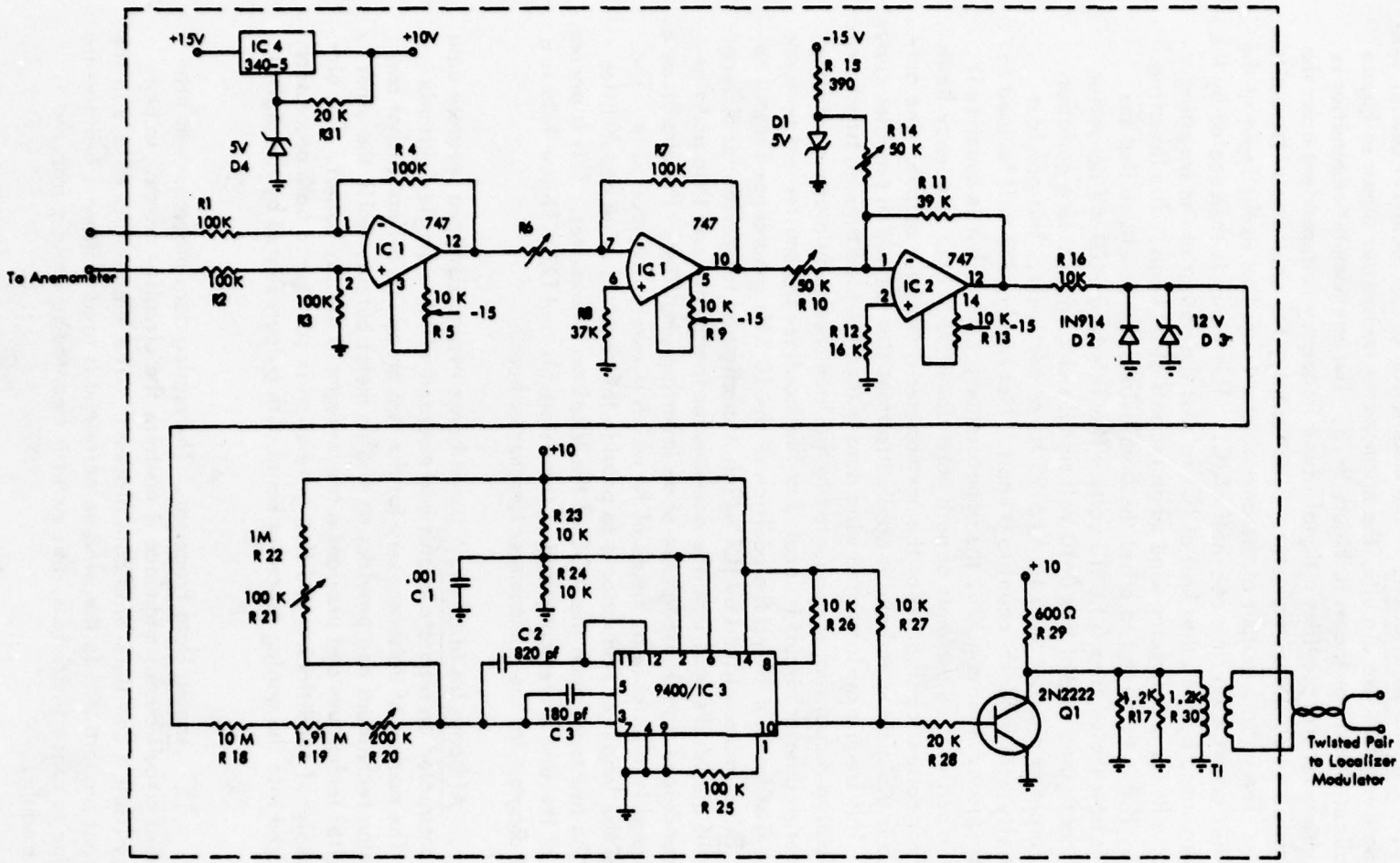

Figure 9-27. Circuit Schematic Anemometer Transmitter Analog Wind Telemetry System.

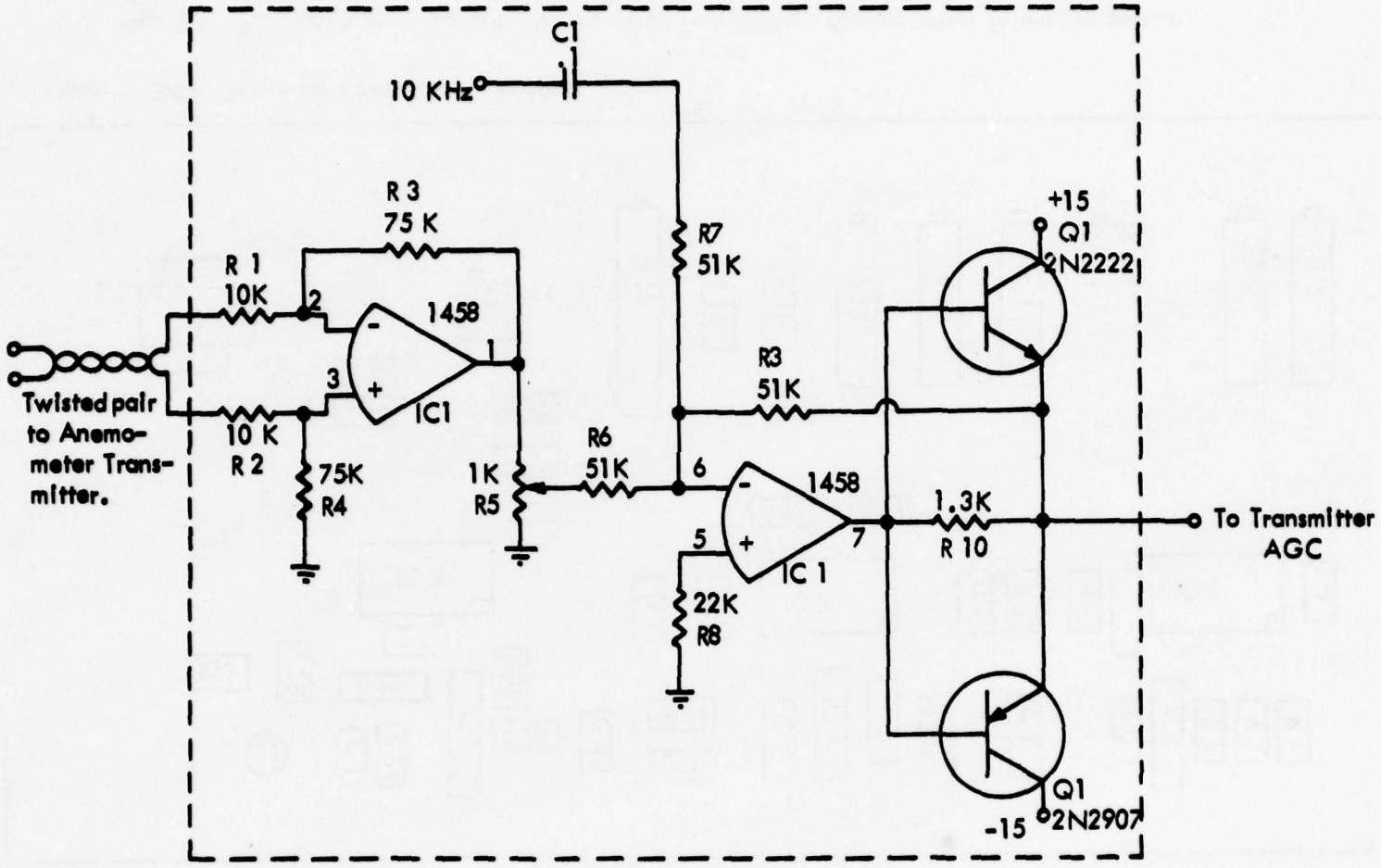

Figure 9-28. Localizer Modulator Circuit.

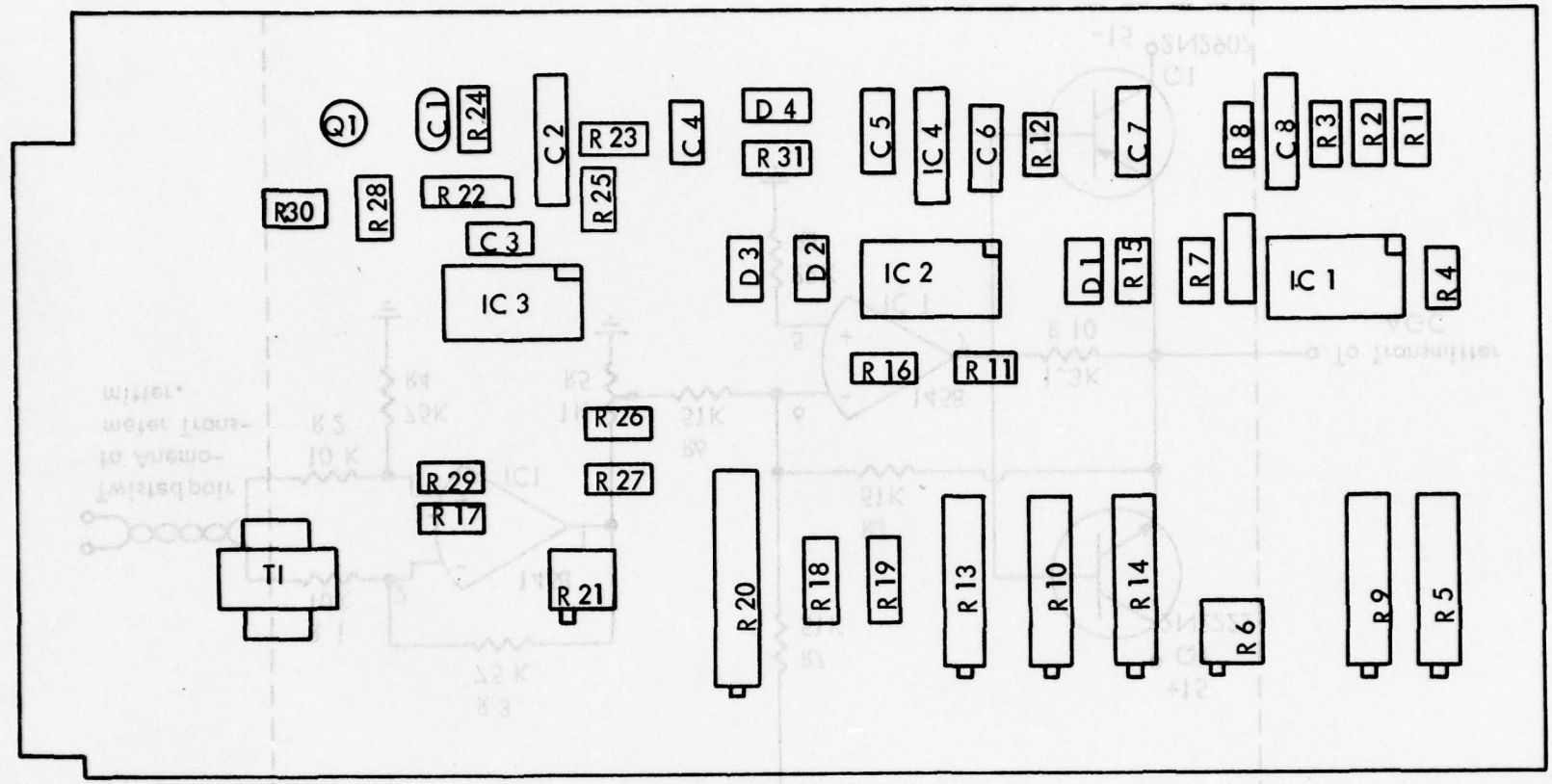

Note: C4 - C8 are for power supply by-pass.

Figure 9-29. Component Layout, Anemometer Transmitter, Analog Wind Telemetry System.

The schematic for the analog wind data processor is shown in Figure 9-30 and the board component layout diagram in Figure 9-31. In operation, the audio output of a standard localizer receiver is applied to the input of the processor and is filtered by the concatenated second order Butterworth low-pass and high-pass filters composed of IC1. The filtered signal is then half-wave rectified by the circuit of IC2 with a gain adjustment provided by R10. The rectified signal must have an amplitude of at least four volts. The rectified signal is then hard-limited by the inverter pair of IC3 which contains positive feedback so that the output of pin 4 of IC3 is a CMOS level digital signal. Further signal processing is accomplished by the frequency detection circuit fromed by IC4, IC5, and IC6. The output at pin 6 of IC6 is a digital waveform that will clock at the frequency of the input to pins 4 and 12 of IC4 only if the frequency of this input is in the approximate range of 4 KHz to 9 KHz. This "filtered" signal is then applied to the one-shot of IC10 whose output will be high if the input is not clocking, indicating a FLAG condition on the wind telemetry system. A low signal will be present if the input is clocking which indicates the wind telemetry tone is present. The FLAG signal is used to light an incadescent lamp on the front of the Tektronix module providing an indication of the wind telemetry system status. The circuitry described thus far is that which is common to both systems; the required outputs are supplied to the digital processor board by means of a patch connection.

The remaining circuitry on the analog data processor board is that which is unique to the analog processor. The clocking digital signal designated WIND DIG carries the wind information in its frequency and is shifted to a bi-polar signal by the divider network of R15 and R16 to provide a suitable input for the Teledyne 9400 frequency-to-voltage converter of IC7. Since the 9400 f/v converter operates on zero crossings, diodes D3 and D4 are provided for protection from excessive input voltages. Actual output voltage of the 9400 is not critical as long as the voltage varies in the range less than 0 to 5 volts over the frequency range of interest. IC8 provides a pair of analog switches that select at the output pins 9 and 10 the output of the 9400 in the event of no flag indication of a meter zeroing voltage provided by R30 if there is a FLAG indication. The two stages of IC9 provide the meter drive circuitry. The first stage is required for level shifting so that the output at pin 10 of IC9 is a bi-polar signal that is zero volts for an audio input to the processor of 5995 Hz. This bi-polar signal is then buffered through the second stage of IC9 to provide a current source to drive a microammeter connected in a floating load configuration. Meter zeroing is accomplished by the adjustment of R28 and the meter full-scale calibration by R39. In addition, the output of pin 10 of IC9 is applied to an inverting amplifier on the digital processor board to provide a front panel analog output for monitoring purposes.

2) Digital Processor/Indicator for Analog Wind Telemetry Data.
The digital processor/indicator is a dedicated frequency counter scaled to display the transmitted wind velocity directly in knots. The basic time base for the processor is derived from the airborne 10 KHz clock required for the accompanying range-rate system. The wind tone frequency measurement is made over a one second time interval. In order to facilitate testing of the processor a BCD-to-analog converter was included to provide an analog output of wind velocity.

The schematic of the digital data processor is shown in Figure 9-32 and component

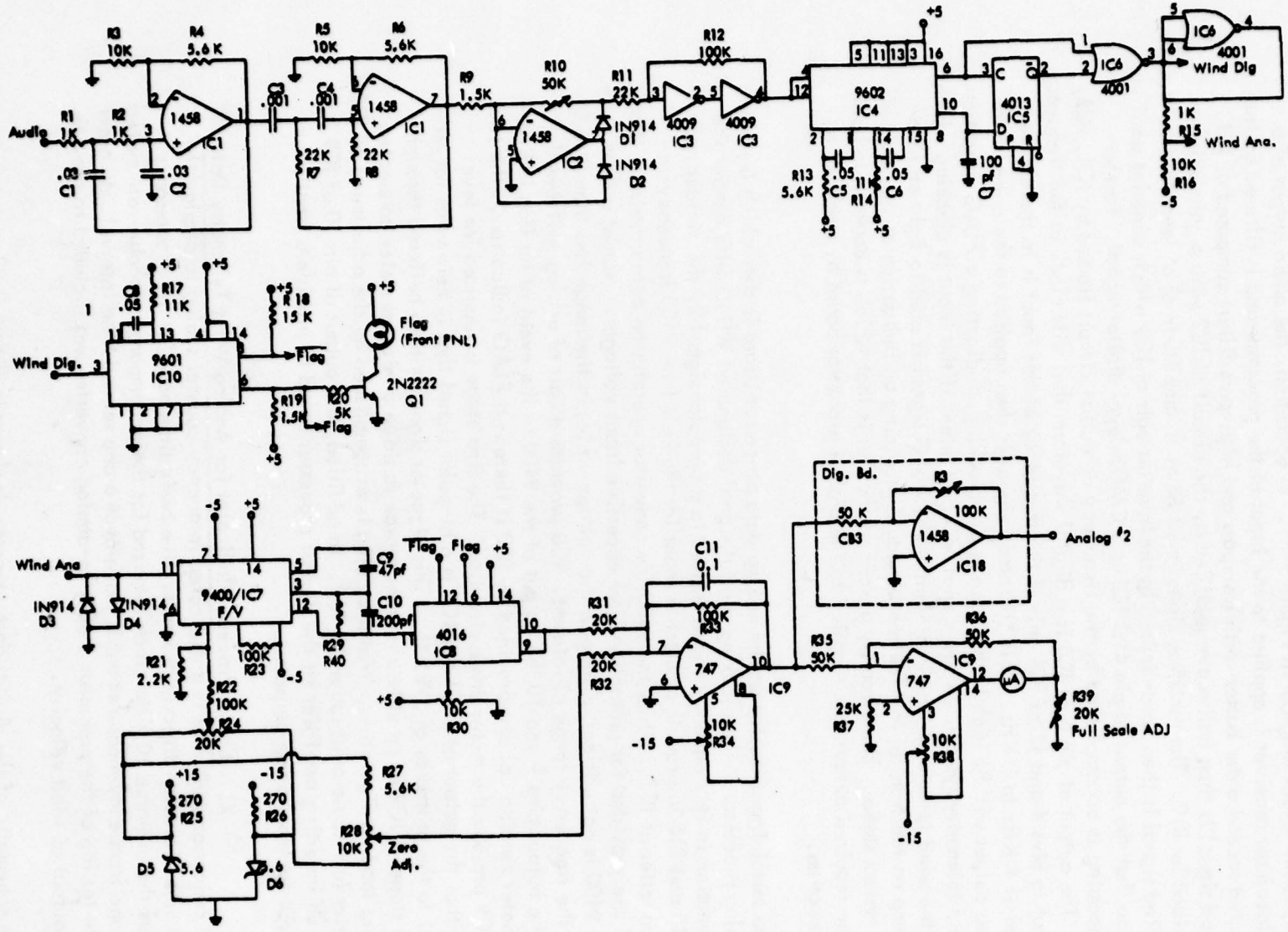

Figure 9-30. Circuit Schematic Analog Data Processor, Analog Wind Telemetry System.

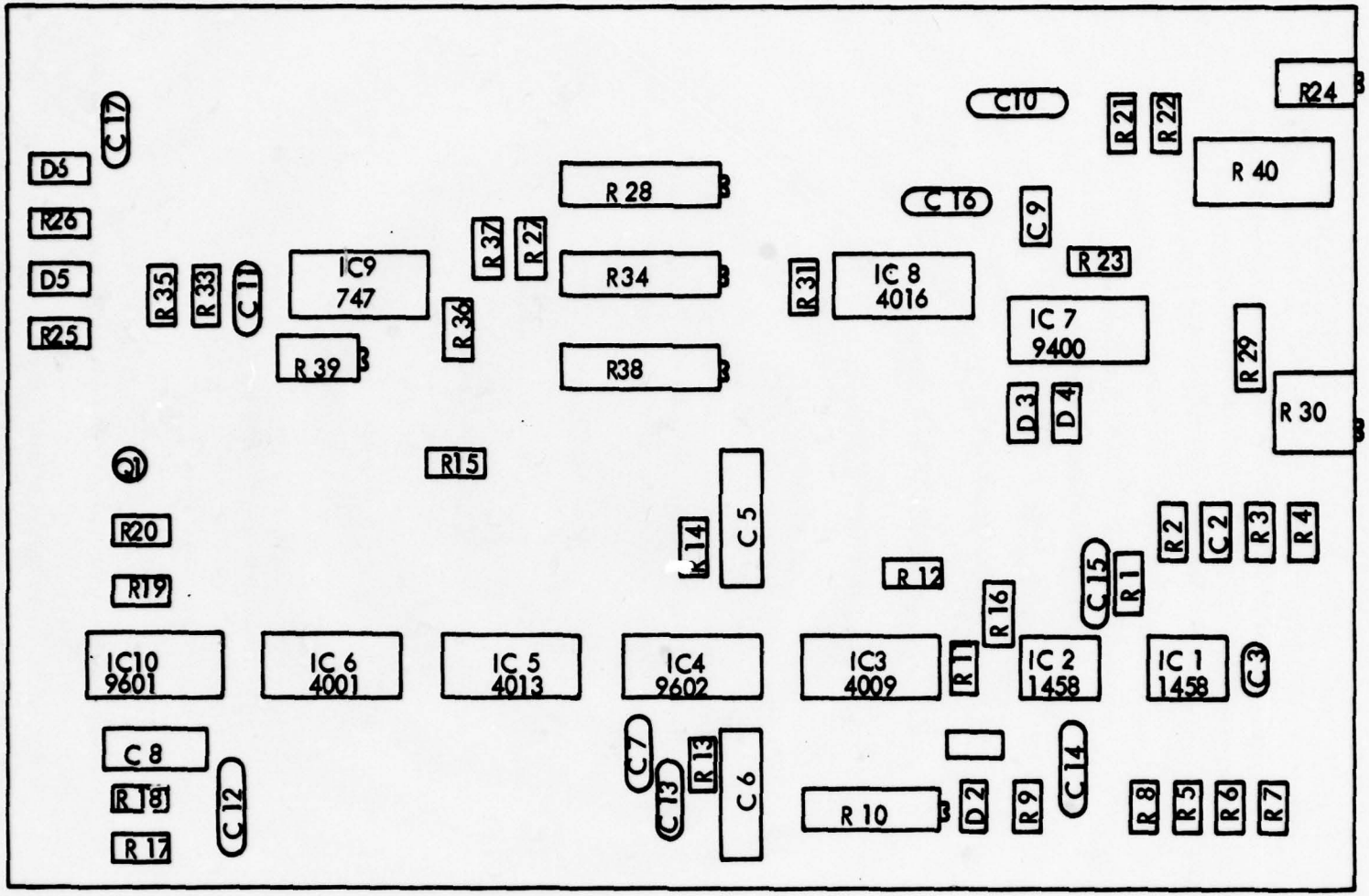

Note: C12, C13, C14, C15, C16, and C17 are for power supply by-pass.

Figure 9-31. Components Layout, Analog Data Processor, Analog Wind Telemetry System.

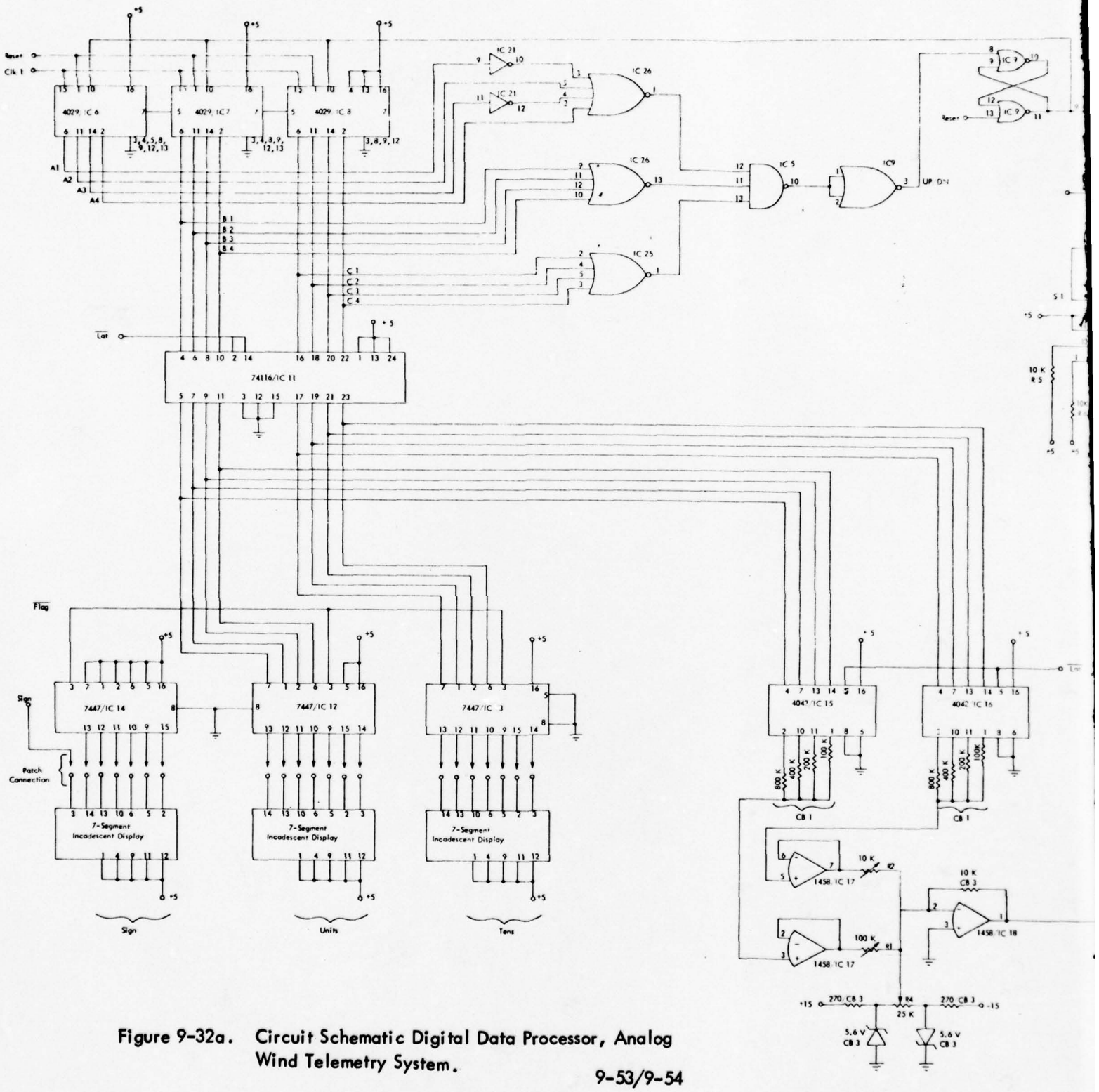

Figure 9-32a. Circuit Schematic Digital Data Processor, Analog Wind Telemetry System.

9-53/9-54

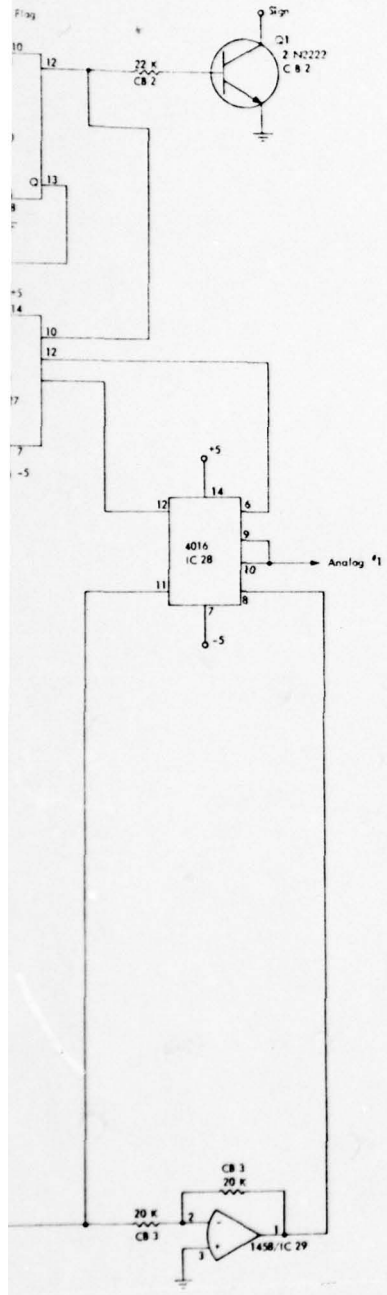
Sign
Q1
2 N2222
C B 2
22 K
CB 2
Q
13
+5
14
10
12
17
7
-5
+5
14
12
6
9
4016
IC 28
10
Analog #1
11
8
7
-5
CB 3
20 K
20 K
CB 3
2
1
3
1458/IC 29

2

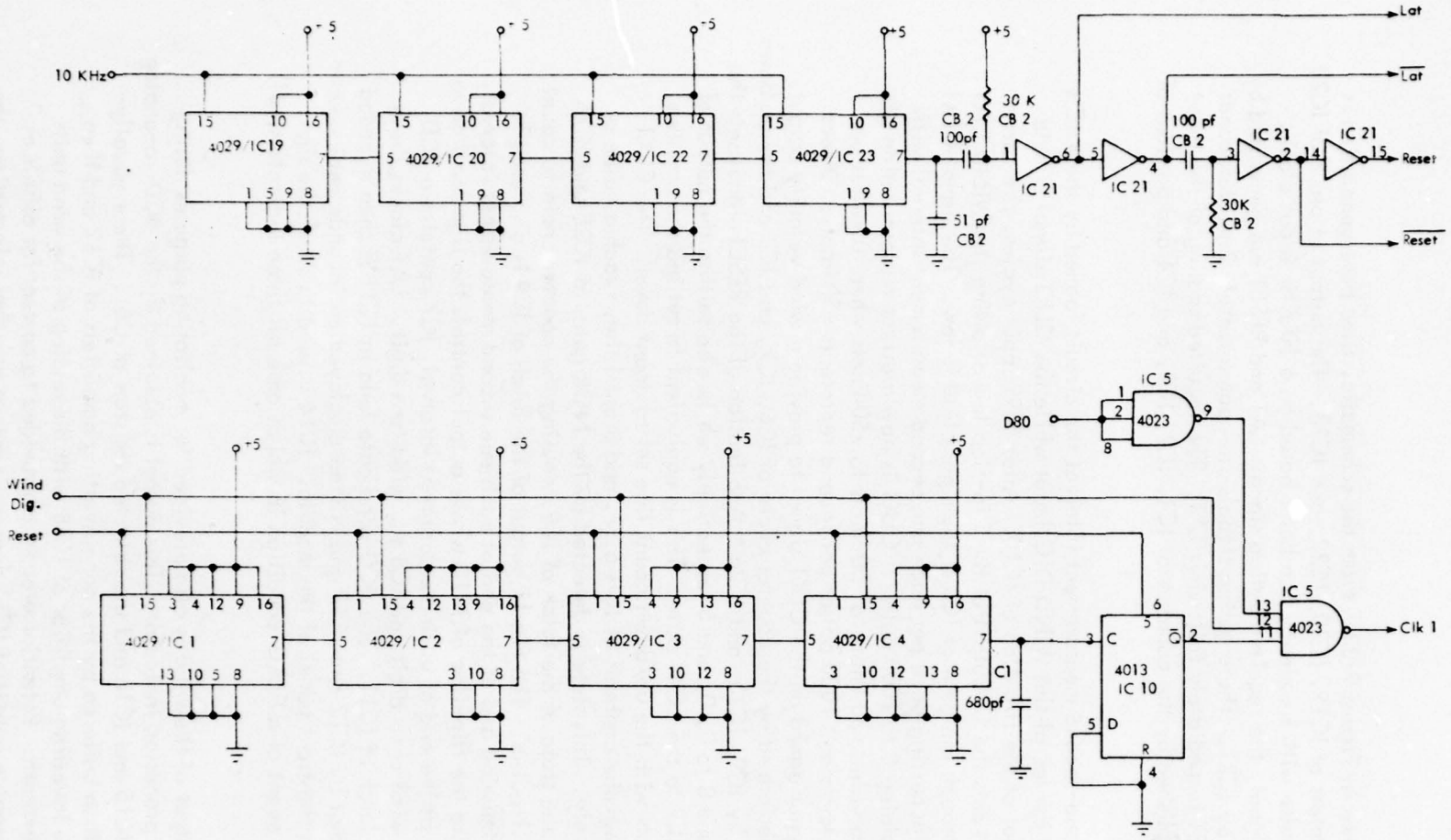

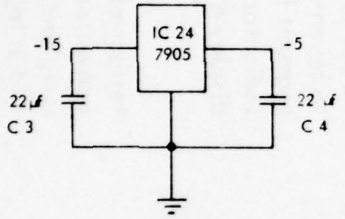

Figure 9-32b. Circuit Schematic Digital Data Processor, Analog Wind Telemetry System.

layout diagram is shown in Figure 9-33. From the schematic, time base generation is performed by the counters of IC19, IC20, IC22, and IC23. The output at pin 7 of IC23 is a negative going pulse with frequency one hertz based on a 10 KHz input clock. From this one hertz signal, the required gating signals LAT and RESET are generated by the one shots formed by IC21. These gating signals are approximately 2 microseconds in duration with RESET immediately following LAT. The required scaling of the input wind signal is accomplished by the counters of IC1, IC2, IC3, and IC4 and portions of IC5 and IC10.

During each one-second measurement interval the circuit formed by these IC's remove the first 5499 cycles of the WIND DIG input while the CLK1 signal is held HIGH by the $\overline{Q}$ output of the flip-flop of IC10. After 5499 input cycles, the carry output of pin 7 of IC4 sets the $\overline{Q}$ output of the flip-flop low allowing the WIND DIG signal to be passed through the gate of IC5 if the signal D80 is low. The signal CLK1 then is a pulse group occurring once per each one second measurement interval with the pulse group containing 0 to 1000 pulses. CLK1 is now a direct representation of the wind velocity of a value -50 knots to +50 knots to +50 knots where 0 pulses per second indicates -50 knots and 1000 pulses per second represents +50 knots. Direct counting can then be performed on the CLK1 signal to provide a wind velocity output. This direct count is performed by the counter chain of IC6, IC7, and IC8 and the up/down count control formed by IC9, IC25, and IC26. Application of the RESET signal sets the counters of IC6, 7, and 8 to 0, 0, and 5 respectively while also setting the output of the latch formed by IC9 to the LOW state. This is equivalent to setting the counters to a value of -50 knots with the up/down count line set to dount down. The CLK1 signal then counts down the contents of IC's 6, 7, and 8 until they reach a value of 5, 0, and 0 respectively. This state is detected by the NOR gates of IC25 and IC26 and is used to toggle the state of the latch of IC9, causing the counter chain to count up for additional CLK1 pulses. The pin 11 output of the latch of IC9 is also used to indicate the sign of the wind and at the end of each one second measurement interval, the sign is clocked into the flip-flop of IC10 whose output controls the sign lamp drive transistor Q1. Also, at the end of each measurement interval, IC7 contains a BCD representation of the wind units digit and IC8 the wind tens digit. LAT clocks these values into the 8-bit latch of IC11. The BCD wind data held in IC11 is then decoded to seven-segment format by IC12 and IC13 and is then displayed on incandescent seven-segment indicators on the front panel of the module. IC14 is used to drive the sign indicator only in the event of a FLAG condition in which case all three indicators will display 8's.

An analog output of the wind is also provided for monitoring purposes during testing of the digital processor/indicator. This output is obtained by the BCD-to-analog converter formed by IC15 and IC16 and the selected resistors of CB1. These equally-weighted values are then buffered by the non-inverting amplifiers of IC17 and then added together by the inverting amplifier of IC18 with the analog of the wind units digit weighted by one-tenth. Potentiometer R4 is provided to correct for offsets as required. Since the analog output of IC18 does not contain any sign information, the output is applied to a unity gain inverting amplifier of IC29 and then the output of

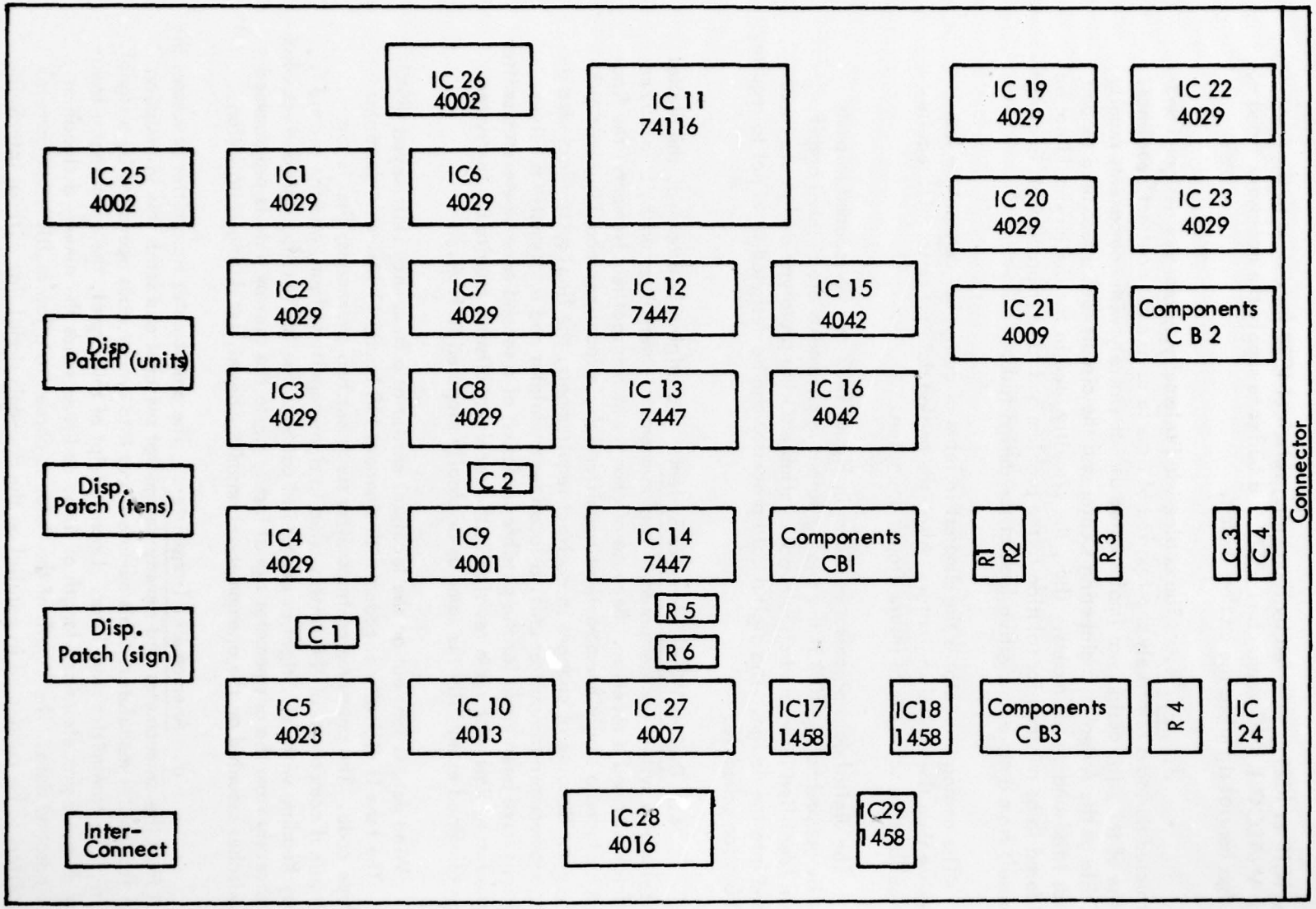

Note: All unmarked capacitors are for power supply by-pass.

Figure 9-33. Components Layout, Digital Data Processor, Analog Wind Telemetry System.

either IC18 or IC29 is selected by the analog switch of IC28 for output to the front panel ANALOG 1 BNC connector. IC27 is a buffer to supply the necessary + and -5 volt sign control signal to the analog switch.

d. Results. The analog wind telemetry system was designed and constructed during a relatively short period of time so as to meet contract deadlines. Because of this, the design was implemented almost entirely with components readily available at the Avionics Engineering Center and the circuit techniques used tended towards tried-and-tested means. Thus, the circuitry used in the design should not be considered to be minimal for solution to the problem and some improvements in design may result from a more innovative look at the design task.

The analog indicator is the simplest in terms of design but may not be less expensive than the digital indicator. Also, the analog data processor will require some calibration schedule to insure proper operation.

The digital data processor as shown in Figure 9-32 can be reduced in parts count by approximately 40% if the analog output requirements are deleted and if certain identified integrated circuits not available during prototype design are incorporated into the design. The digital data processor can be designed so as not to require a calibration schedule.

4. Digital Wind Telemetry System. As originally proposed, the digital wind telemetry system was composed of two anemometer-transmitter units, a localizer modulator unit and a receiver. Because of changes in contract requirements, the final system included a single anemometer-transmitter unit, a localizer modulator unit and a receiver. Because of changes in contract requirements, the final system included a single anemometer-transmitter unit, a localizer modulator and a telemetry receiver. Provisions have been made for the possible inclusion of a second anemometer-transmitter at some future time with some revision in the receiver software required. The system design remained essentially the same as originally proposed to FAA.

Wind data is sent out on the localizer carrier as a frequency shift keyed (FSK) tone. The tone is digitally encoded with standard 110 baud, 11 bits-per-character teletype code. The anemometer-transmitter sends out two characters; first is the longitudinal component of the runway wind in sign-magnitude form, and the second is runway heading with left, right or center indication. The transmitting unit derives wind data directly from the anemometer signal input, while the runway data is programmed via switches mounted on the anemometer-transmitter board, set during installation.

a. Anemometer Transmitter. The anemometer transmitter processes the signal from the anemometer and runway designator switches and sends this information to the transmitter modulator. This module is put into synchronous operation by a signal sent from the transmitter modulator. Upon receipt of this signal, the anemometer transmitter delays a predetermined length of time, and then sends the runway designation and windspeed data. The length of the delay is chosen to allow multiple anemometer transmitters to be connected in parallel on the one-pair signal line without interfering

with the data from each other. Each anemometer transmitter is electronically switched off the signal line except when actually sending data. Physically, the anemometer transmitter is mounted at the base of the anemometer tower. The signal from the anemometer is amplified and low-pass filtered before being converted in an analog-to-digital converter. The anemometer signal is then multiplexed along with the runway designator data into a universal asynchronous receiver transmitter (UART). This chip serializes the data and adds parity bits. The serial data stream is sent to the tone encoder circuitry and from there is switched onto the signal line. The anemometer transmitter provides all the siganl conditioning and the analog-to-digital conversion, and consequently determines the basic accuracy and resolution of the system.

b. Transmitter Modulator. The transmitter modulator receives the tones sent by the anemometer transmitters and re-encodes the serial bit stream for modulating on the localizer transmitter. This module sends a synchronization tone down the signal line each second. The timing for this pulse is crystal controlled; however, it is suppressed for 1 cycle to assure synchronization during the next cycle if tones are present on the signal line. Upon reception of the serial data tones, the transmitter modulator recovers the digital signal by means of tone decoders and then re-encodes the serial data on tones compatible with the localizer transmitter and the 10 KHz range-rate system tone. This signal is then summed with the groundspeed tone and the composite signal is modulated onto the localizer transmitter. The localizer modulator module provides for control of the levels of the wind telemetry tones and 10 KHz tone and controls the modulation percentage allowed to each.

c. Receiver. The wind telemetry receiver performs the functions of decoding the tones received from the detected output of the localizer receiver and recovering the digital serial bit stream. A serial-to-parallel conversion is then performed to recover the original parallel data word. The data is processed for eventual output on the front panel LED displays plus analog output via digital-to-analog converters (D/A). The receiver provides parity checking to reduce erroneous data caused by data channel noise and filtering of the windspeed data. The runway data is presented just as received; however, in order to change the displayed data, the new runway data must be received identically twice in two consecutive time frames.

At power-up, the receiver enters a calibration mode in which the display cycles through all displayable characters and then the display and analog outputs are set to plus and minus full scale followed by a zero. The LED displays will display $\pm$ 79 Kts. and the analog outputs will go from plus to minus full scale to zero. The analog outputs are offset (the output is always positive). The receiver module provides precise timing and decoding of the incoming signal.

The recorder calibration routine in the receiver starts at -79 Kts on the displays and the corresponding most negative output on the analog output lines. The chart recorder should be adjusted to read -79 Kts with the zero control. The calibration routine will then output +79 at which time the recorder should be set to read +79 Kts with the gain or span adjustment. The calibration routine will then output a zero which should be checked on the recorder for center scale. The routine will repeat the calibration output a second time so that any errors caused by the interaction between the zero and gain controls can

be eliminated.

d. Transmitted Data Format. The windspeed data is sent to the airborne receiver as a sequence of digital bits encoded into the transmitted carrier as frequency shift keying (FSK). During most of the cycle between updates, the tone sent to the aircraft is a 1923 Hz tone. This indicates a mark or a digital '1'. The presence of this tone for longer than 1/10 of a second indicates that the transmitter is not in the process of data transmission. When the transmitter sends a byte of data, it first sends a start bit which consists of a 2650 Hz tone for 1 bit-time (9 msec). Both the transmitter and the receiver must know what the bit-time will be in advance. In this system that time is fixed at 1/110 second. When the receiver receives the start bit, it expects that during the next 10 bit-times that data will be transmitted. The first eight data bits following the start bit are the eight data bits of either the windspeed or the runway identification with the least significant bit (LSB) first and the Most Significant Bit (MSB) last. The two bits following the data bits are the parity bit followed by a stop bit. The parity bit provides the system with error detection in that the sense of the parity bit is such that the number of 1's sent in the data word plus the parity bit will be even. If the parity bit has the wrong sense, the data will not be used. The stop bit is always '1' and indicates to the receiver that the data byte transmission is complete.

e. System Schematic Diagrams. The schematic diagrams for the digital wind telemetry system as constructed for evaluation are shown on the following pages as Figures 9-34 through 9-45.

5. Data and Discussion. During the groundspeed-wind telemetry effort, various flight evaluations were performed to test circuitry improvements and system modules. The data reported here represents a sample of the data recorded to demonstrate system operation.

Figure 9-46 is a chart recording of groundspeed and airspeed made on March 13, 1978. This was a flight test of the synchronous processor with the 5 MHz detector using the Seiko filter. The groundspeed and airspeed traces noticeably follow the same trends; however, since the windspeed is not known, the true groundspeed is not known either. As indicated on the chart, there was a tailwind during this pass.

Figure 9-47 is a chart recording made on February 15, 1978. This pass was made with the Seiko filter, the 5 MHz detector and the non-synchronous processor. During the pass an airspeed change from 90 Kts to 150 Kts was made. As can be seen from the chart, the groundspeed followed the airspeed with some delay caused by the sampled nature of the groundspeed and the output filtering.

Figure 9-48 shows a chart recording of the anemometer output superimposed onto a chart recording of the output of the digital wind telemetry system. The wind telemetry output closely follows the output. The differences in the traces are caused by 1) the sampled nature of the wind telemetry system which has a sampling time of 1 second, 2) a 4 Kt jump in the wind telemetry system caused by improper operation of tone decoders, the fix for this problem has been investigated but has not been implemented yet.

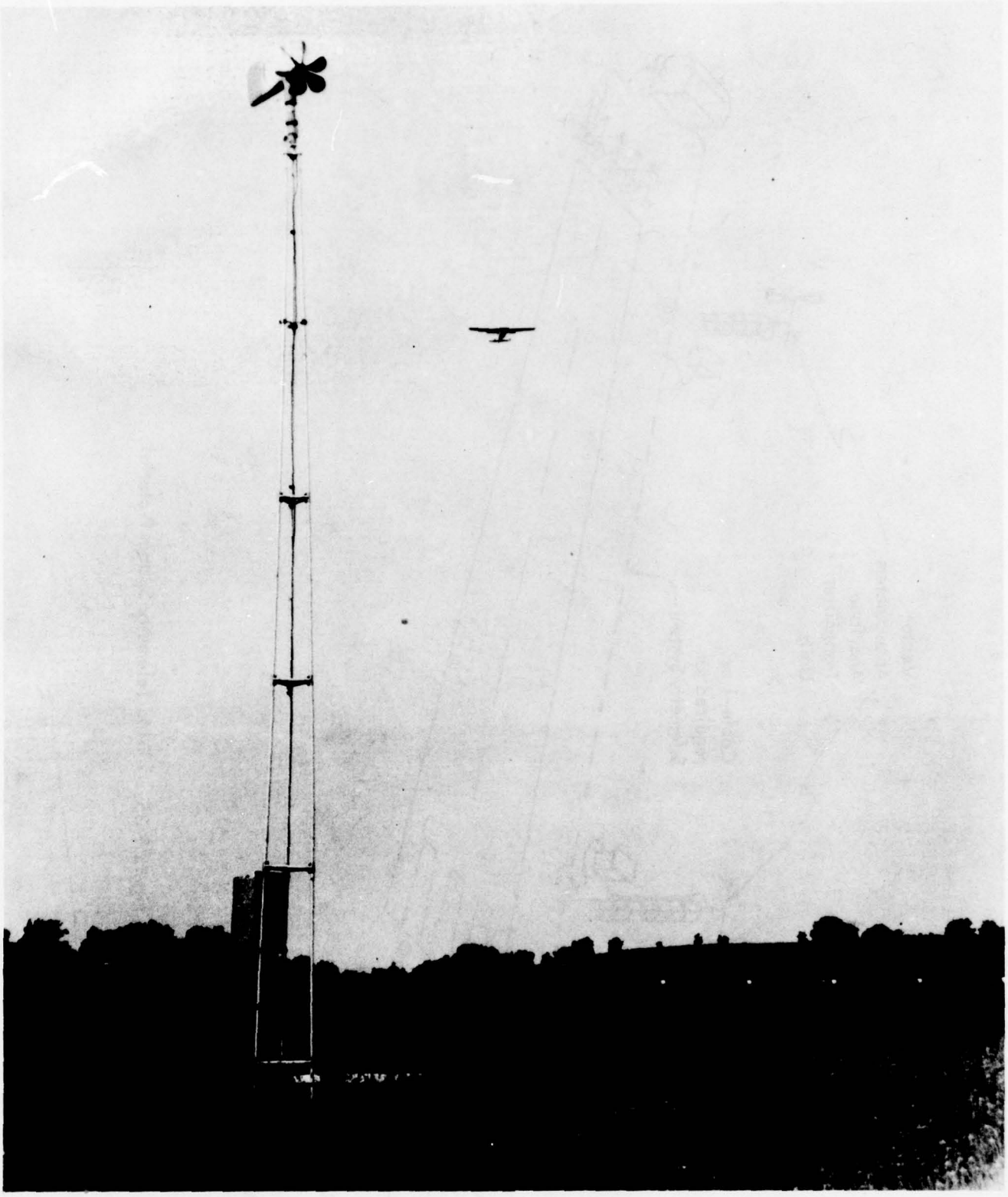

Figure 9-34. Photograph of Wind Telemetry Anemometer and Transmitter at Ohio University Airport.

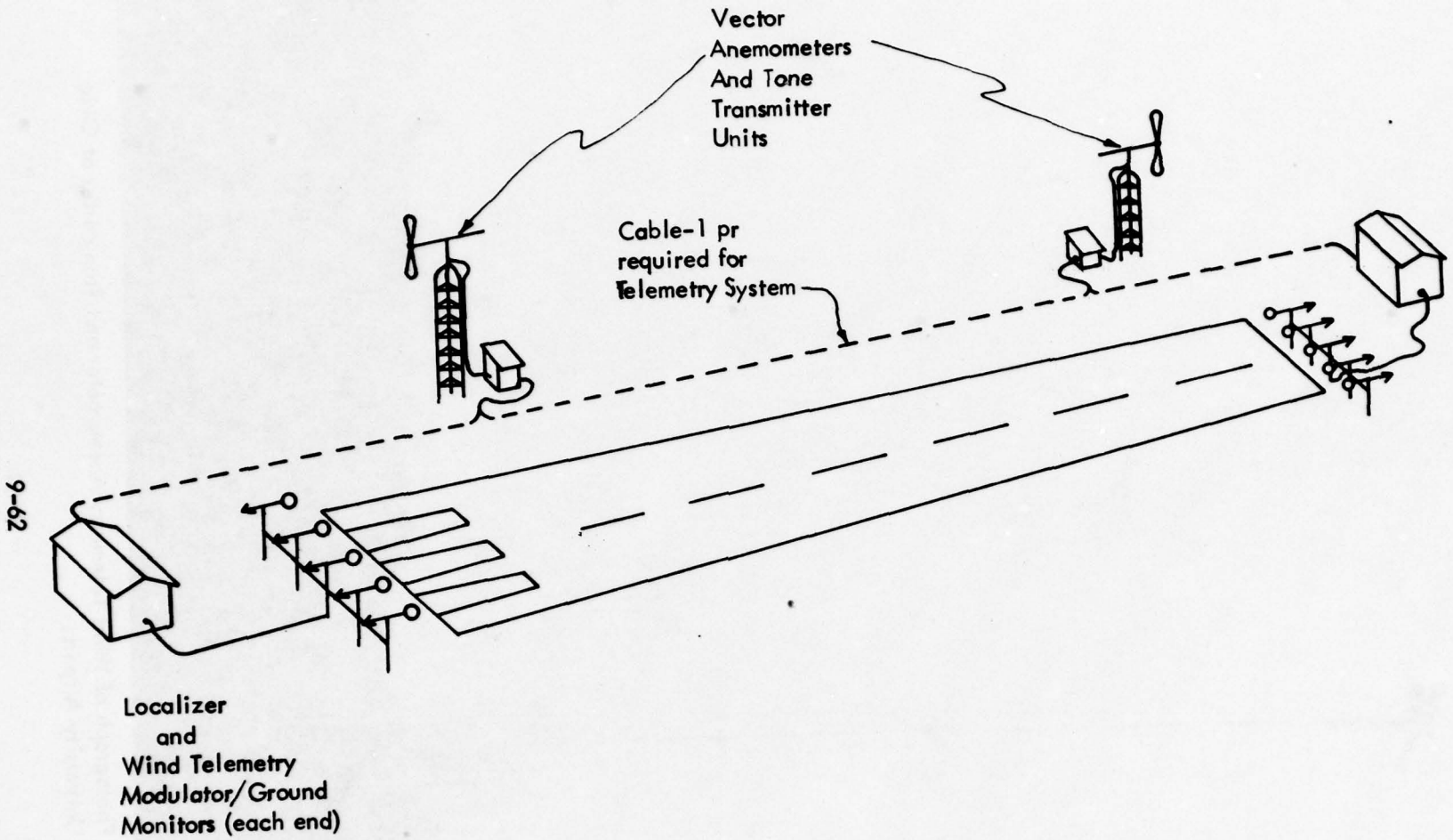

Figure 9-35. Wind Telemetry System Pictorial.

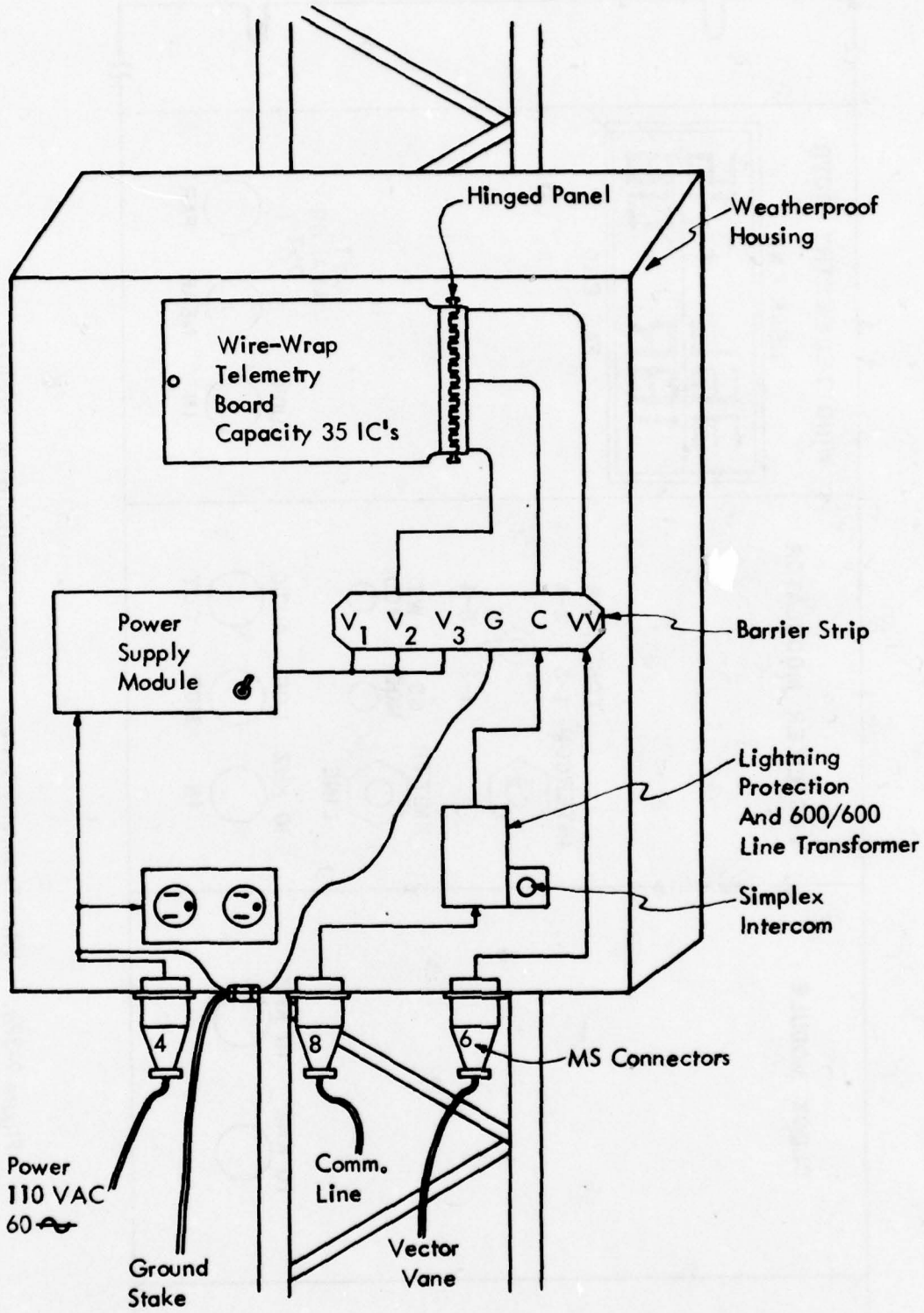

Figure 9-36. Wind Telemetry System Ground Anemometer Transmitter Unit.

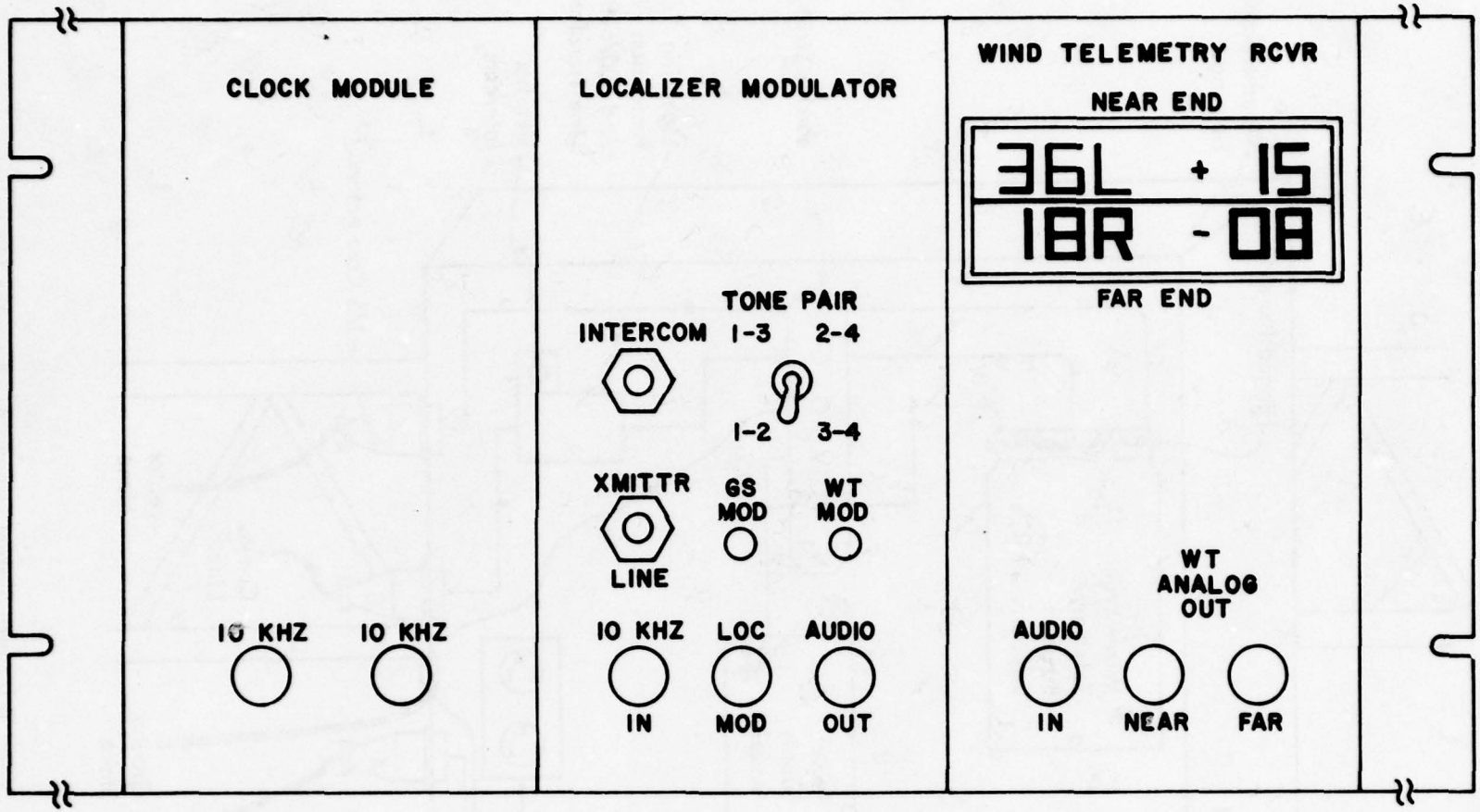

Figure 9-37a. Wind Telemetry System: Ground Installation at Localizer.

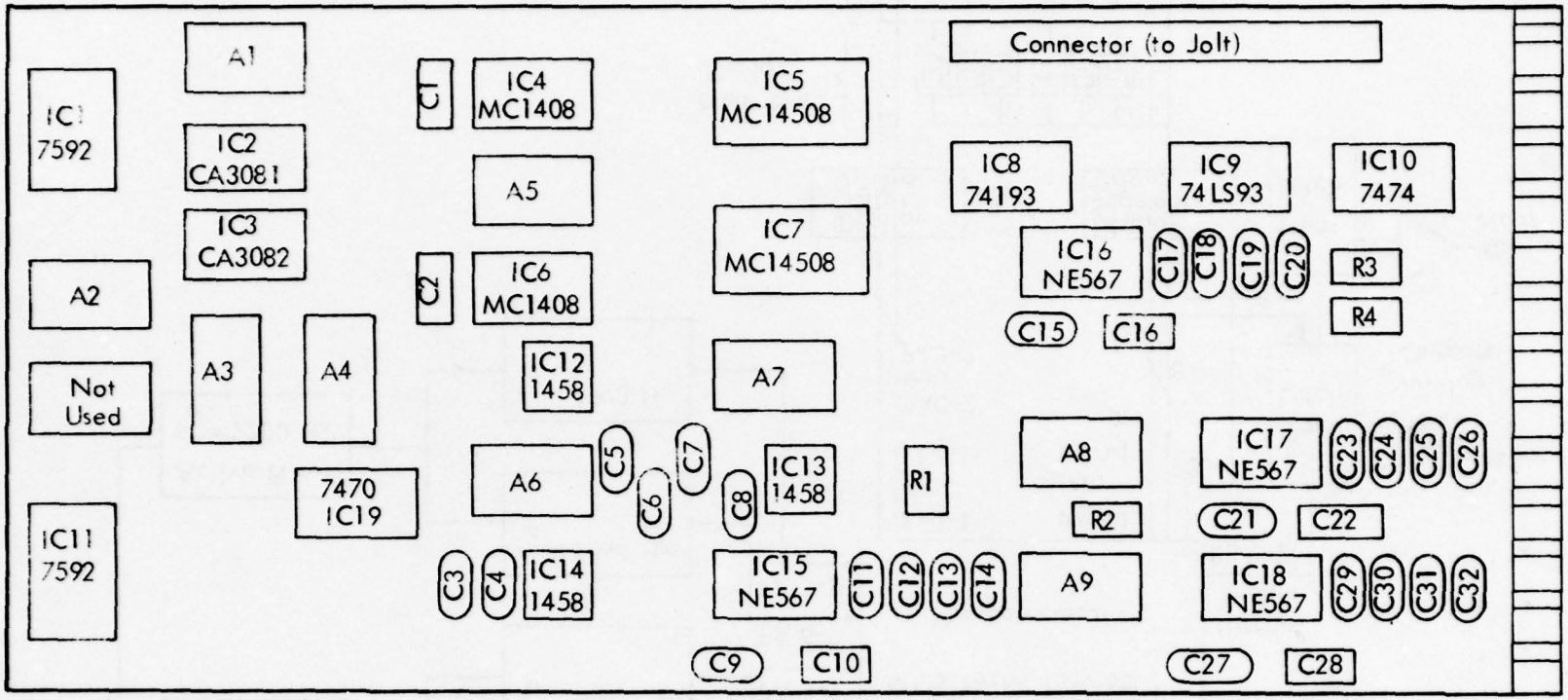

Note: Capacitors not shown are used for power supply by-pass.

Figure 9-37b. Digital Wind Telemetry Receiver Component Layout.

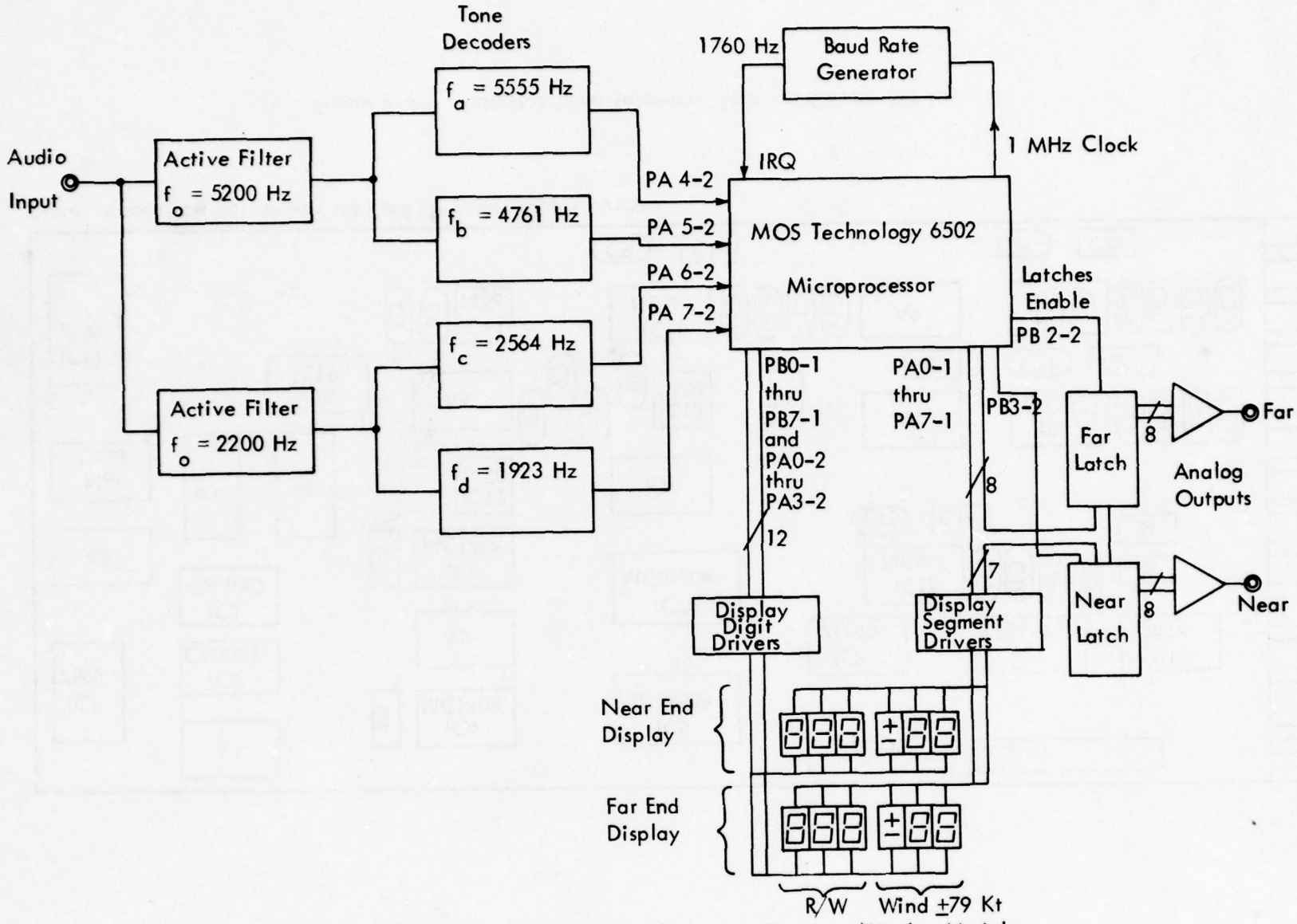

Figure 9-37c. Block Diagram: Wind Telemetry Receiver/Display Module.

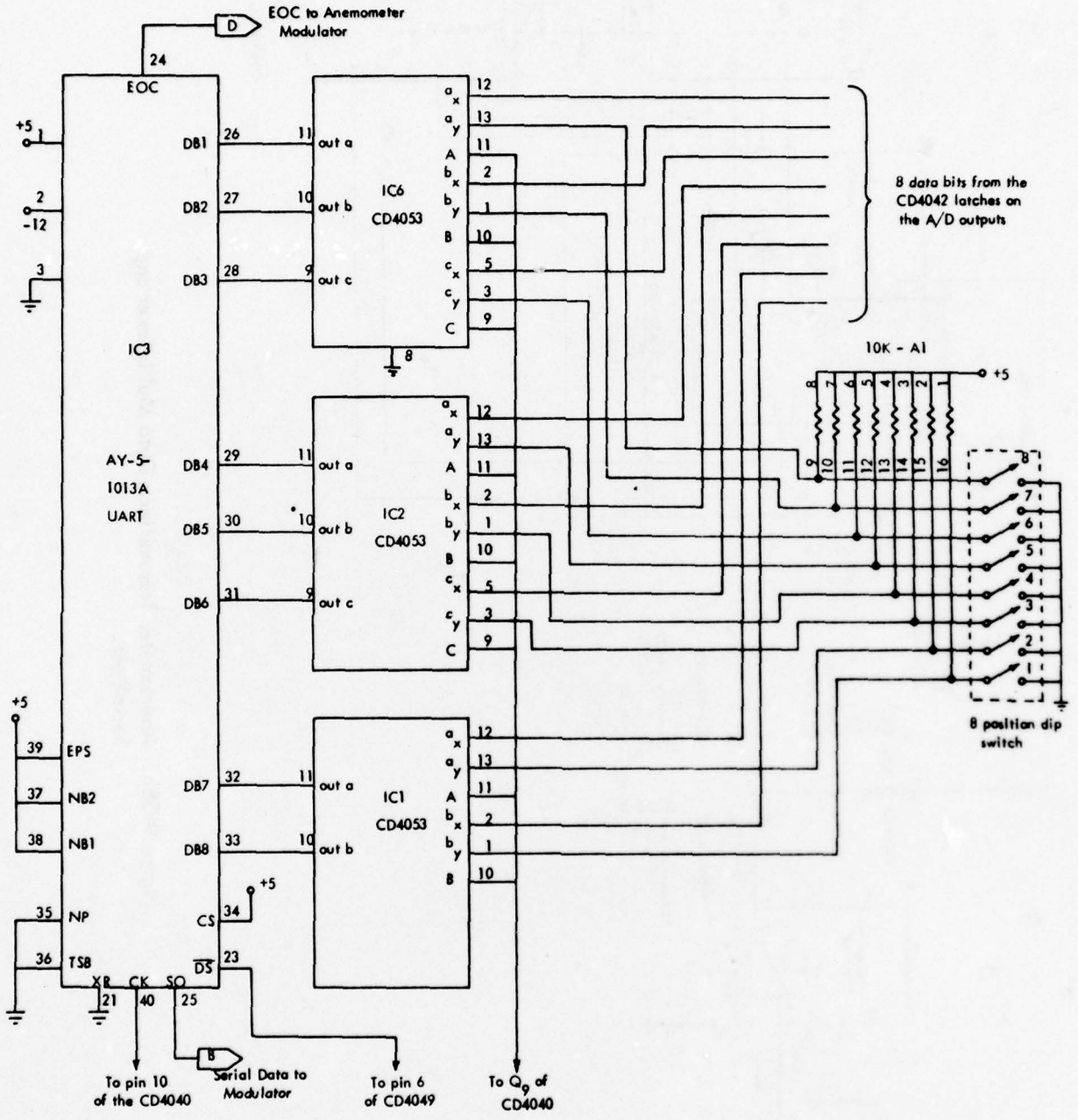

Figure 9-38a. Anemometer Transmitter: Data Multiplexer and Serializer.

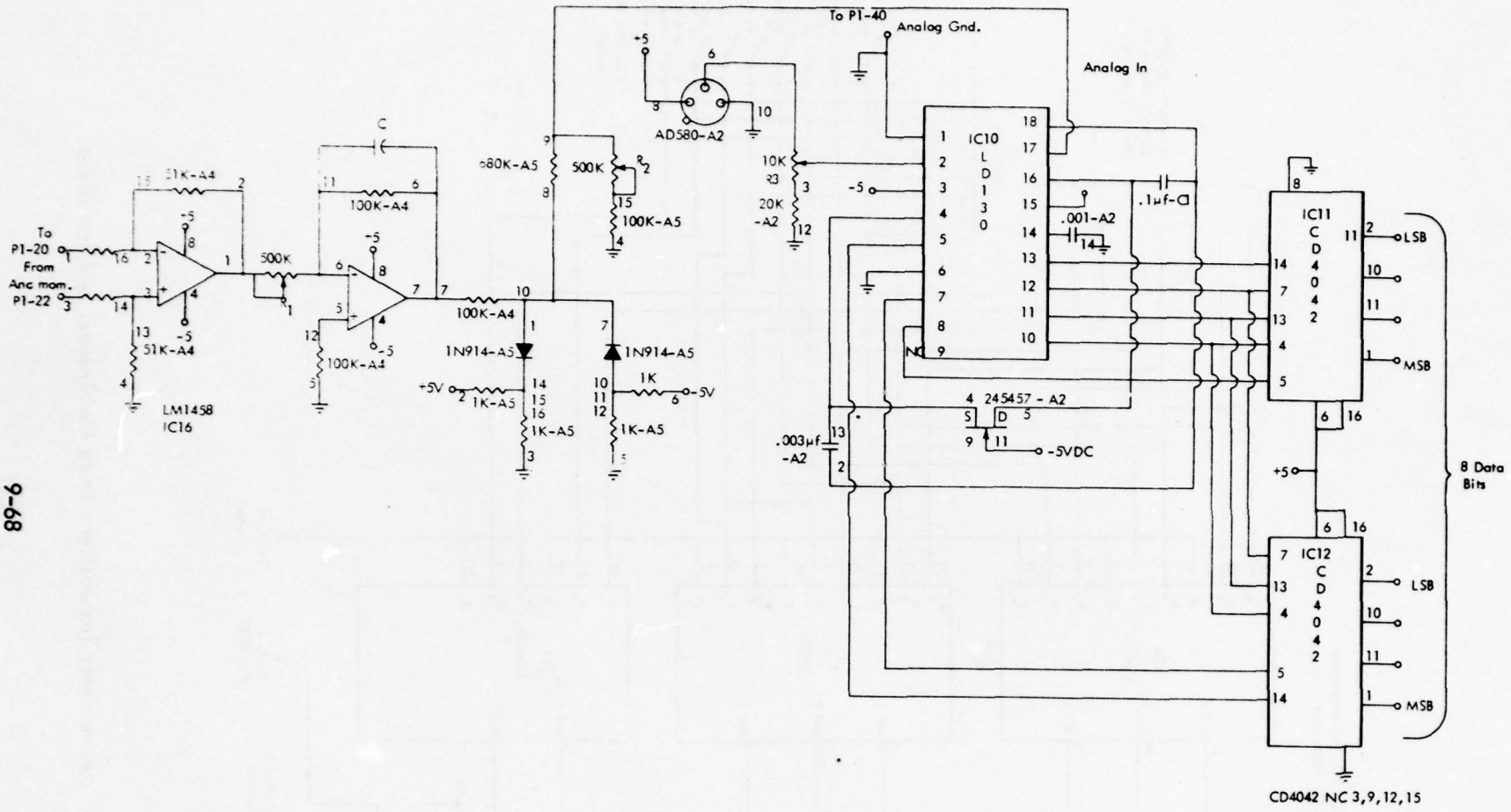

89-6

Figure 9-38b. Anemometer Transmitter: Data Multiplexer and Serializer.

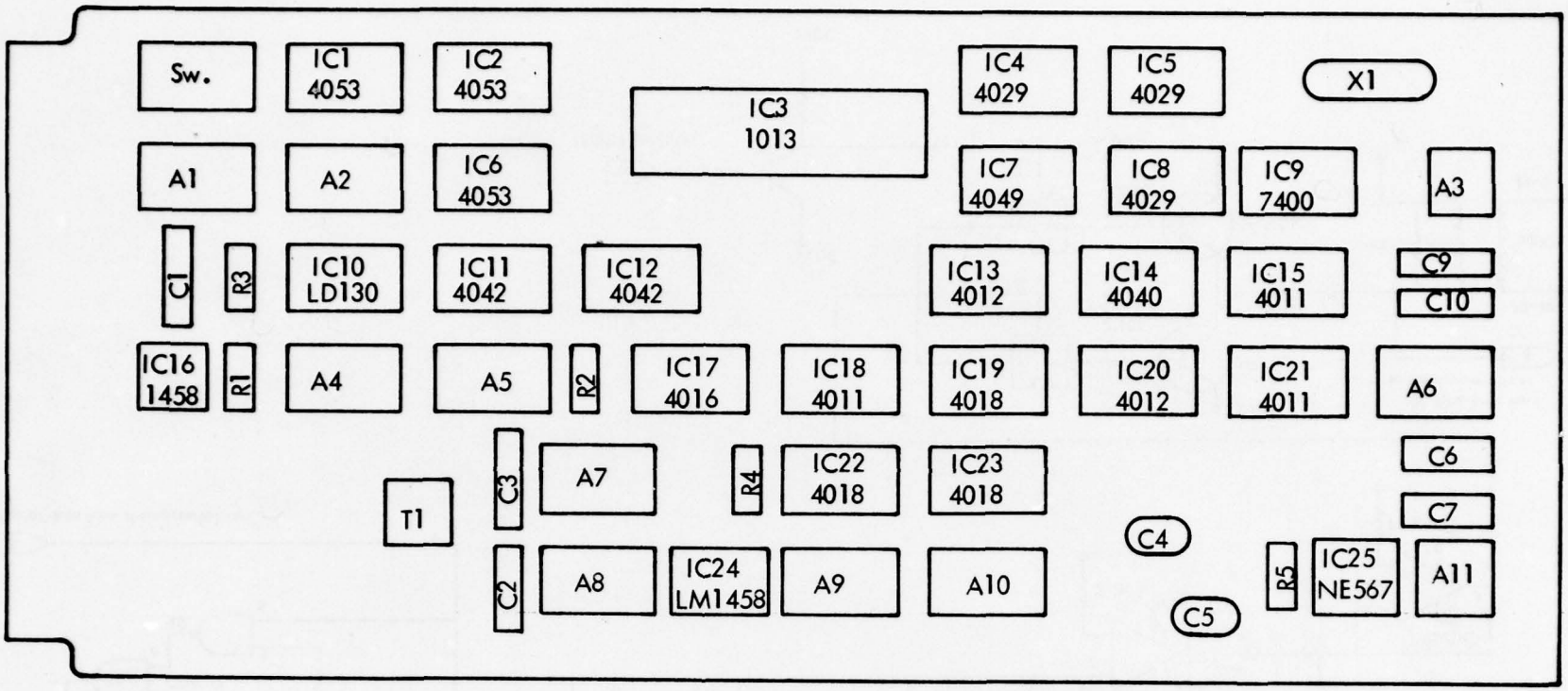

69-6

+5 P1 - 71 and 72
GND P1 - 1 and 2
-5 P1 - 12
-12 P1 - 62

All caps not shown are for power supply by-pass.

Figure 9-39. Components Layout, Anemometer Transmitter Digital Wind Telemetry System.

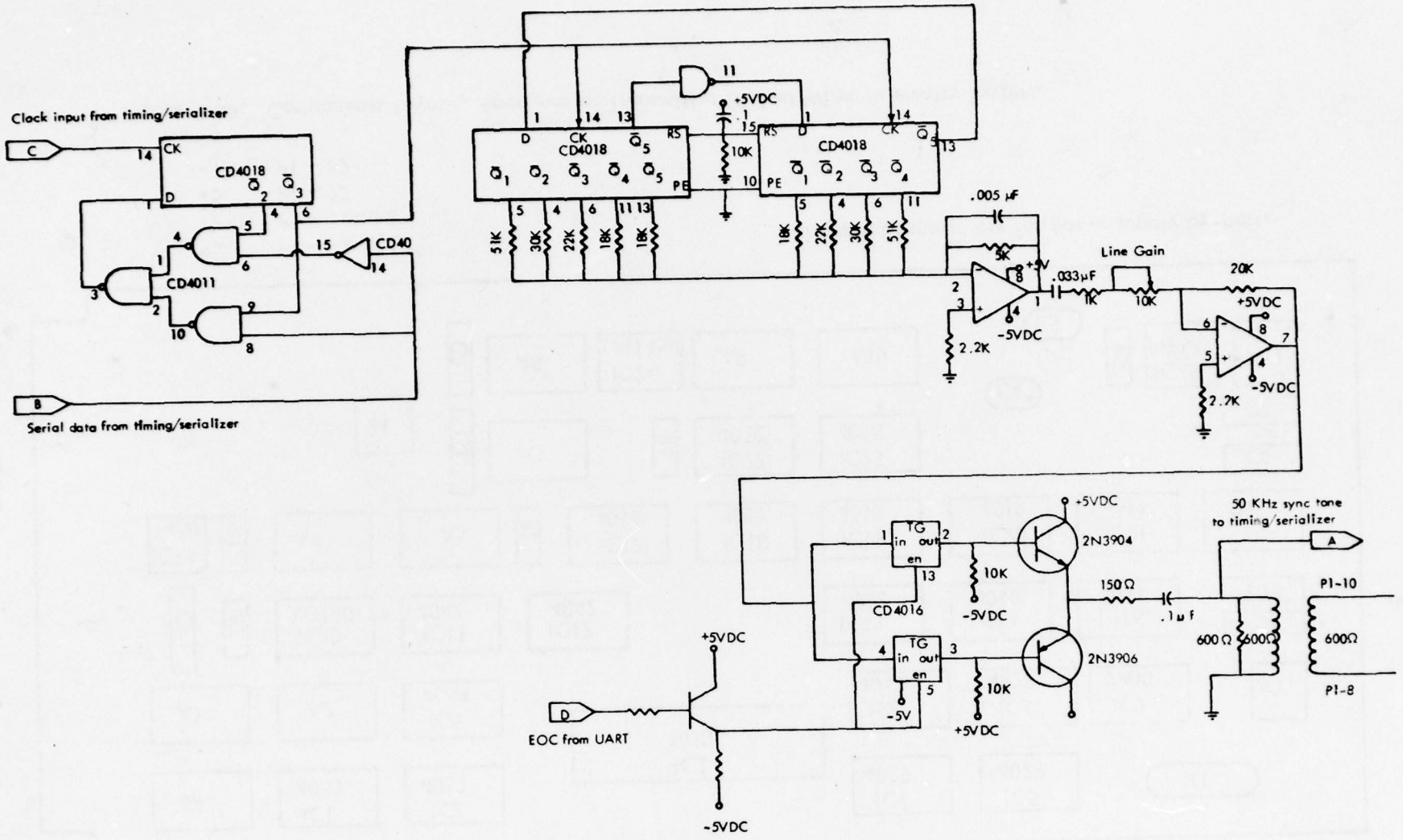

Figure 9-40. Anemometer Transmitter: Tone Generation and Switching.

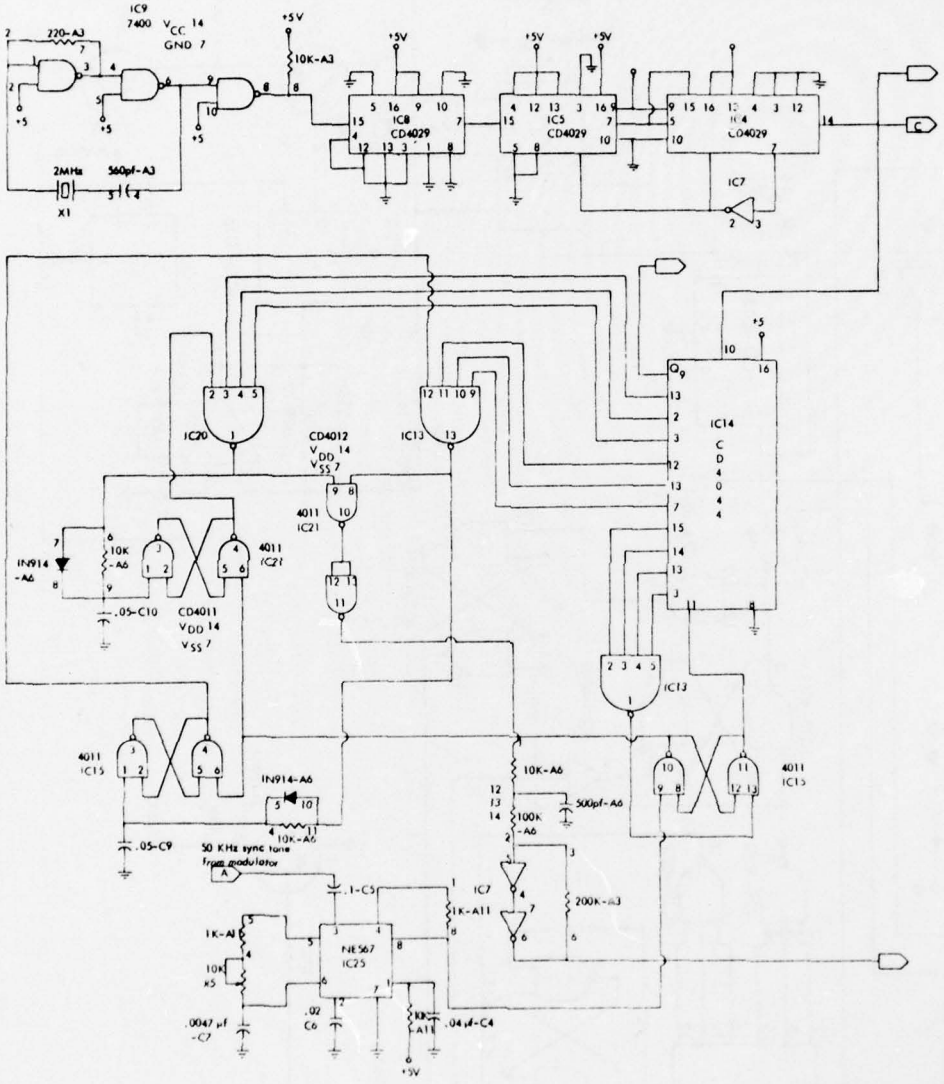

Figure 9-41. Anemometer Transmitter: Clock Generation and Controller.

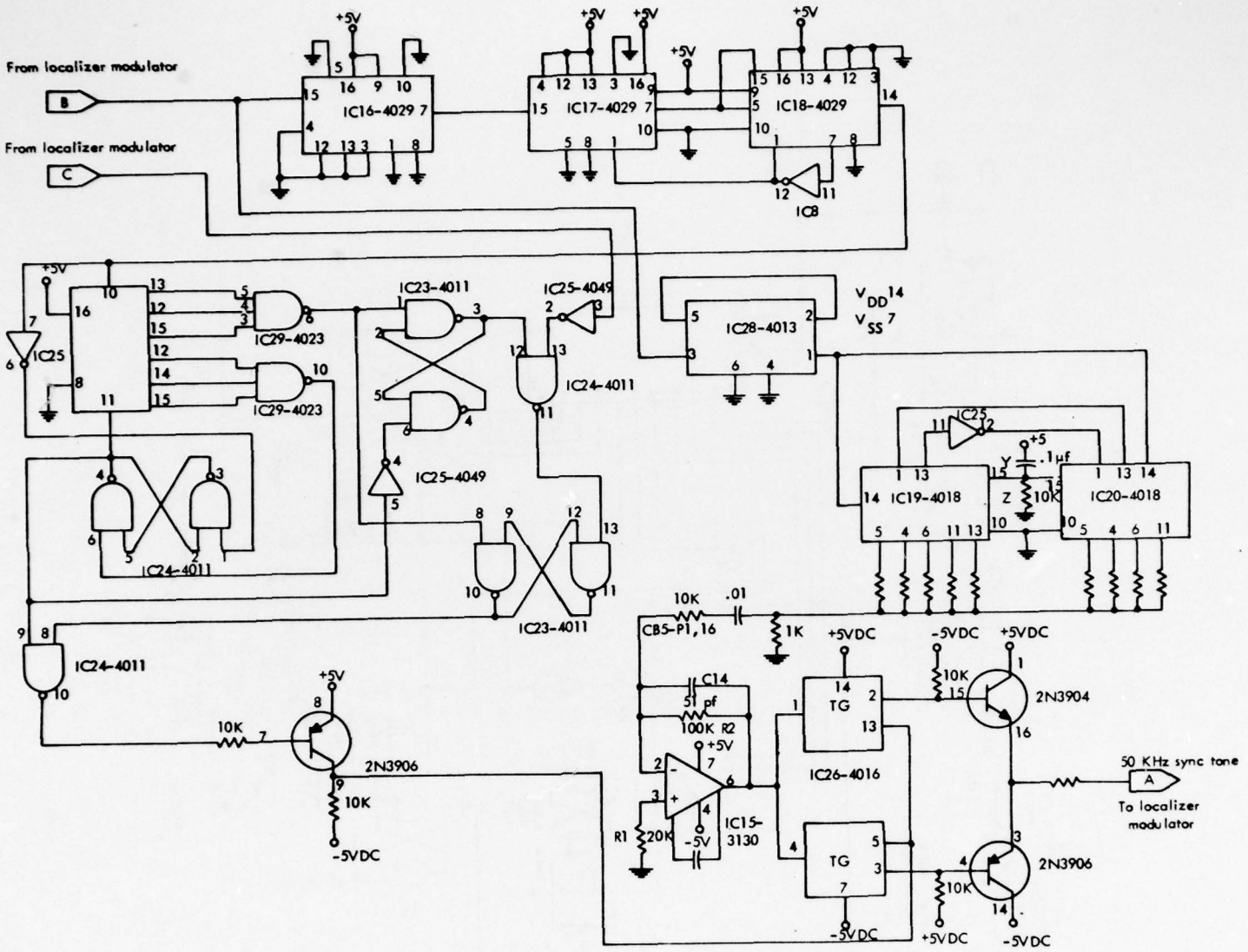

Figure 9-42. Localizer Transmitter: Timing and Synchronizing Tone Generation.

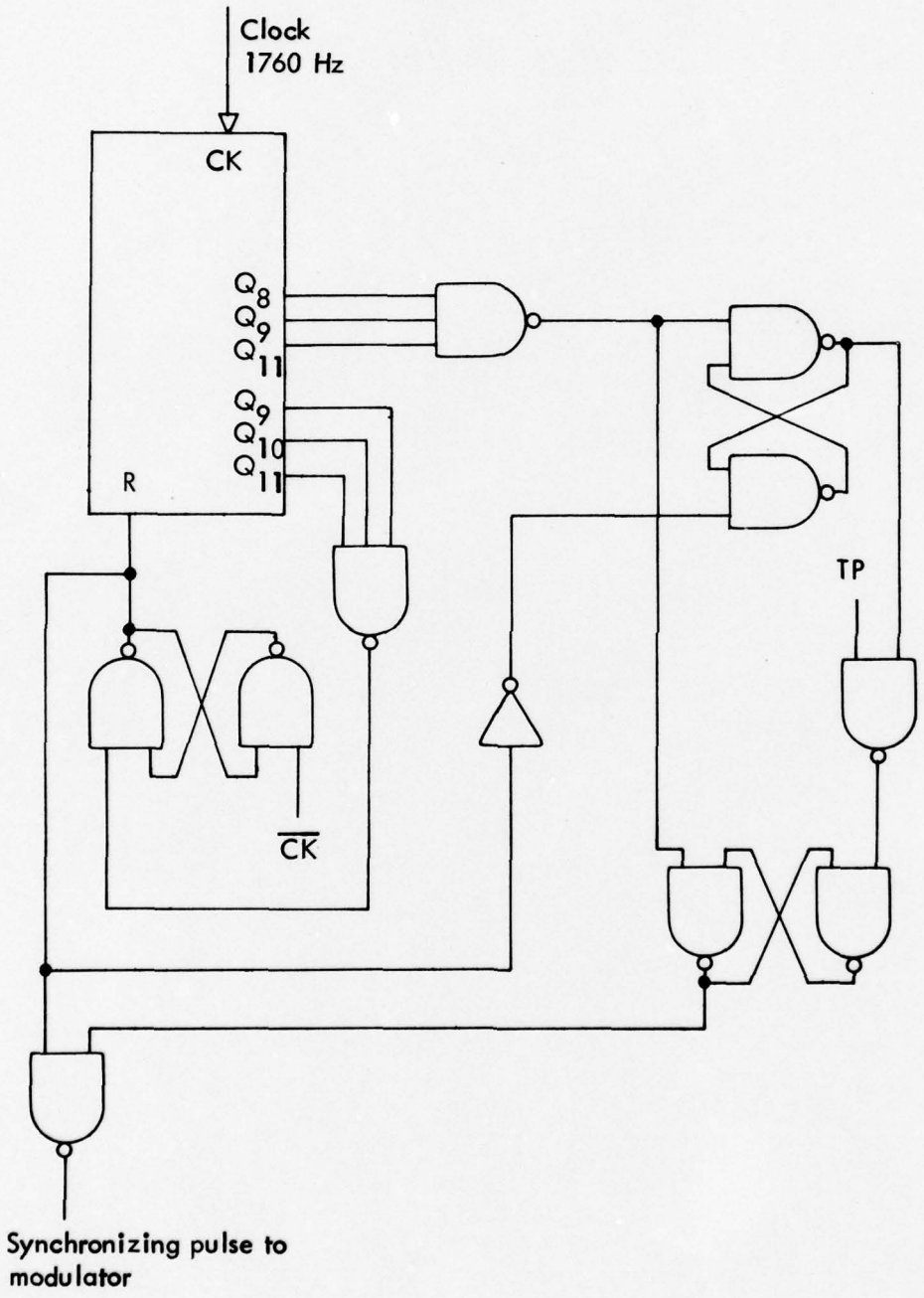

Figure 9-43. Localizer Modulator Synchronization Pulse Generation.

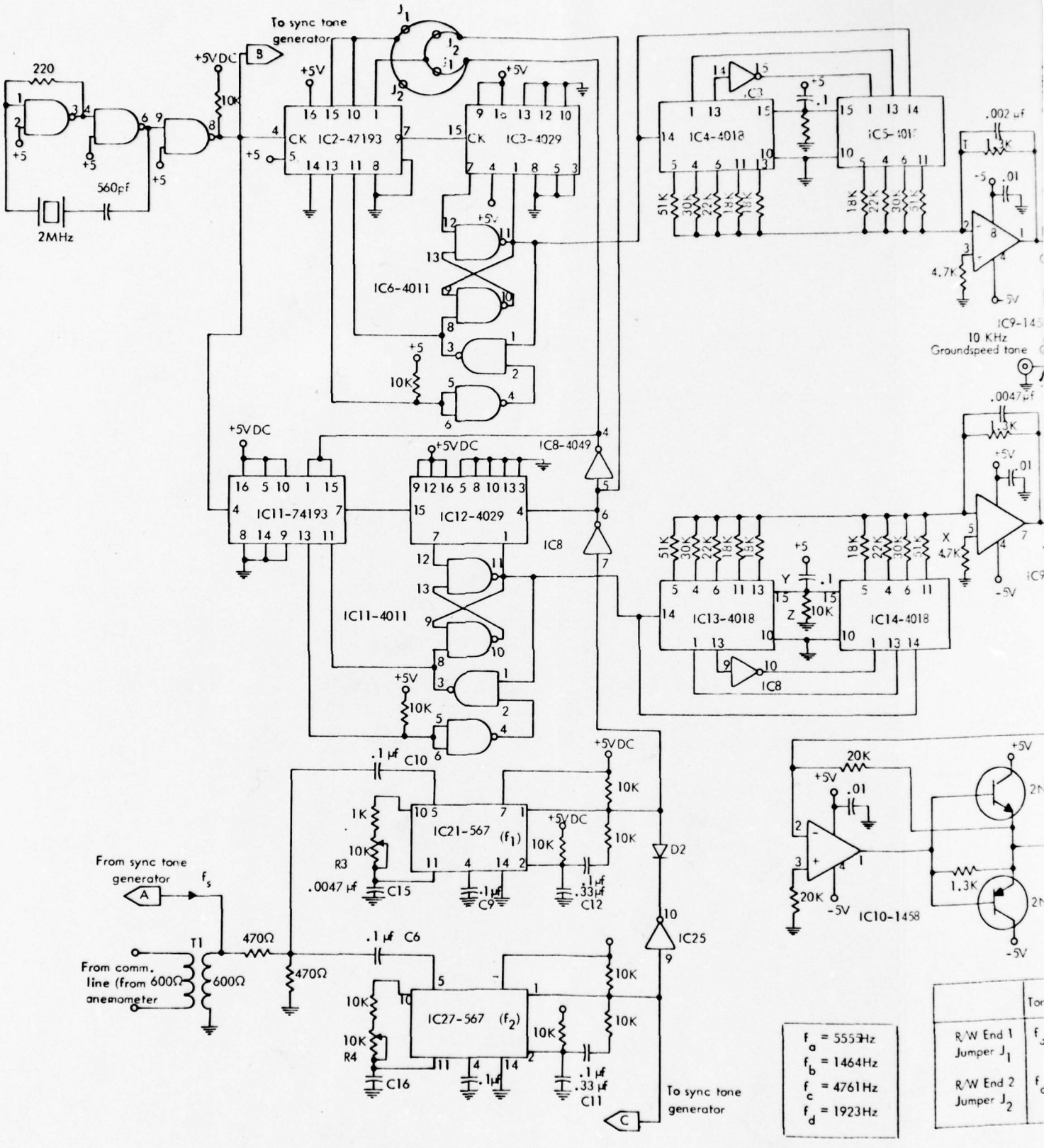

Figure 9-44. Localizer Modulator: Tone Detection, Tone Generation and Modulation.

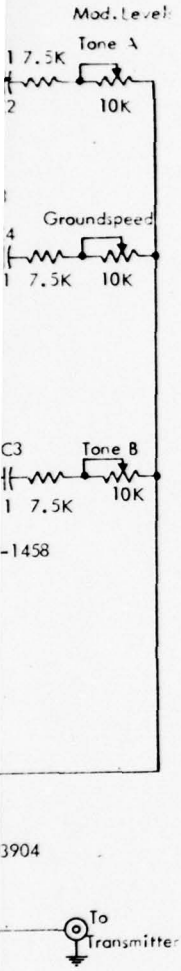

e A	Tone B
f_c	f_b/f_d
f_a	f_b/f_d

IC1 - 7400
IC2,11 - 74193
IC3,12,16,17,18 - 4029
IC4,5,13,14,19,20 - 4018
IC6,7,23,24 - 4011

IC8,25 - 4049
IC9,10 - 1458
IC21,27 - 567
IC22 - 4040
IC26 - 4016

IC28 - 4013
IC29 - 4023
IC15 - CA3130

C1 ⟶ C10 - .1μf

C11,12 - .33μf
C13 - .0047μf
C14 - 51pf
C15,C16 - .0047μf
C17 - 8μf

R_1 - 20K
R_2 - 100K
R_3, R_4 - 10K to turn pot.
R_5 - 220Ω
D_1 - IN2032 4.9V Zener
T_1 - 600Ω/600Ω XFMR
D_2 - IN914

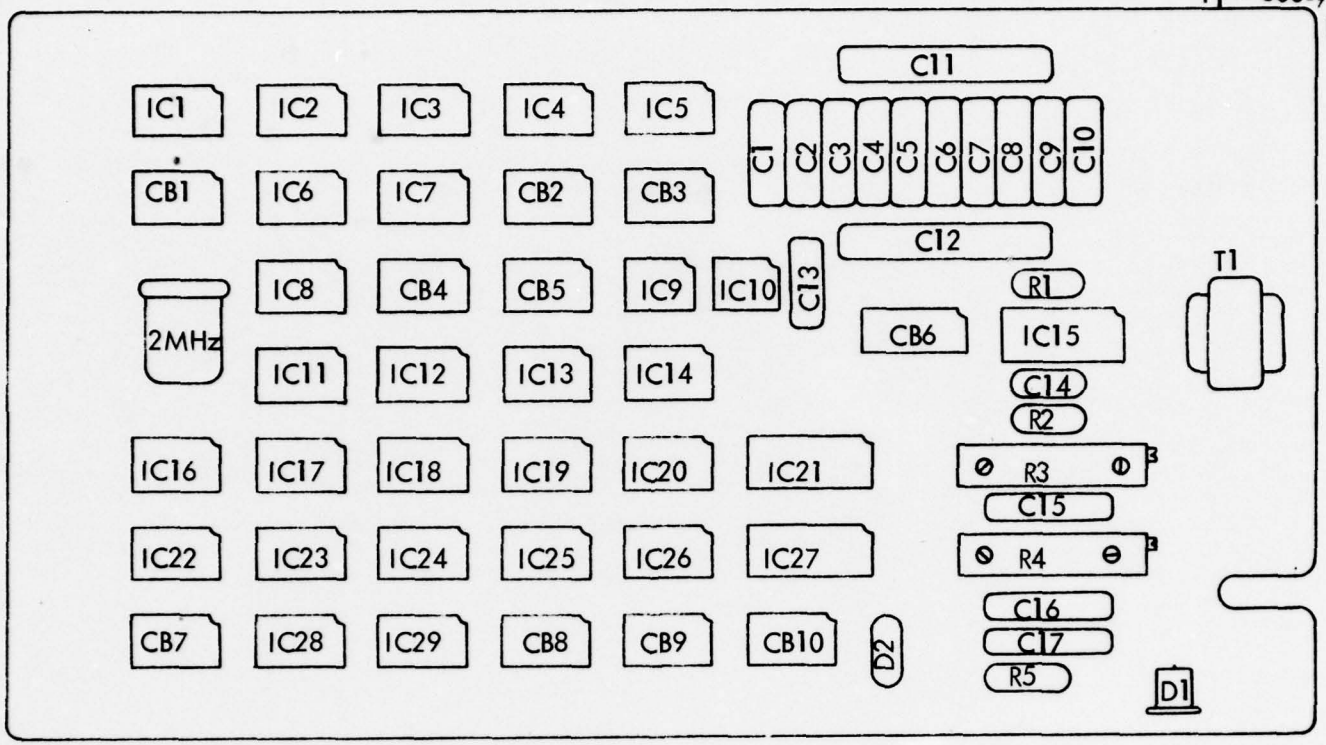

(CB - Component Block)

9-77/9-78

Figure 9-45. Localizer Modulator and Sync Tone Generator (Viewed from Component Side of Board).

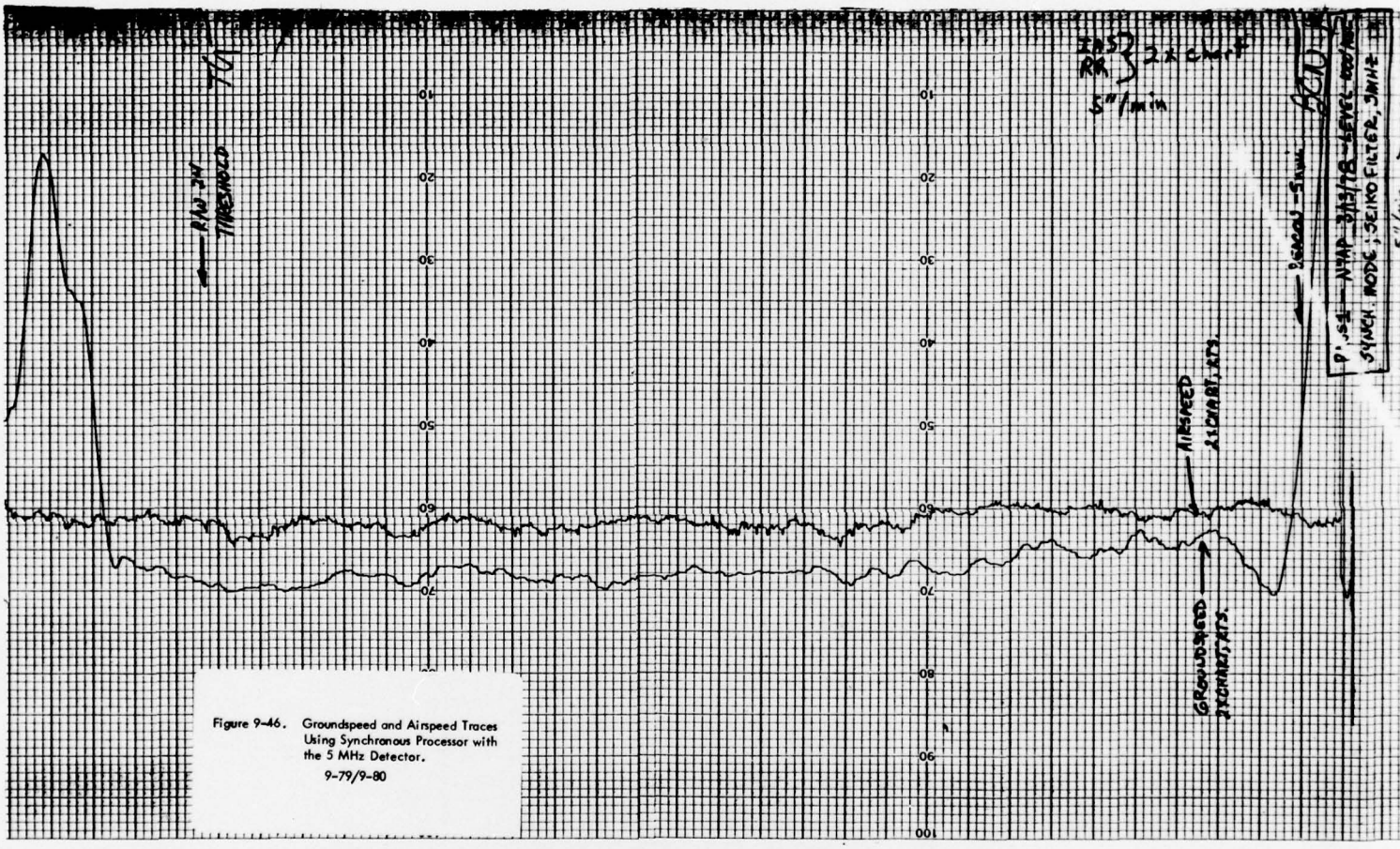

Figure 9-46. Groundspeed and Airspeed Traces Using Synchronous Processor with the 5 MHz Detector.

9-79/9-80

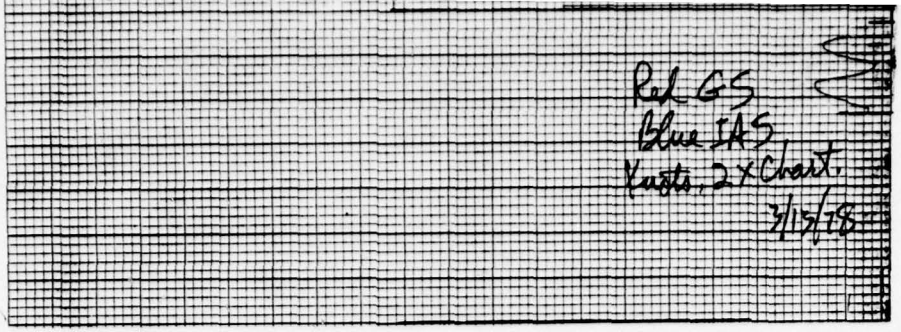

2

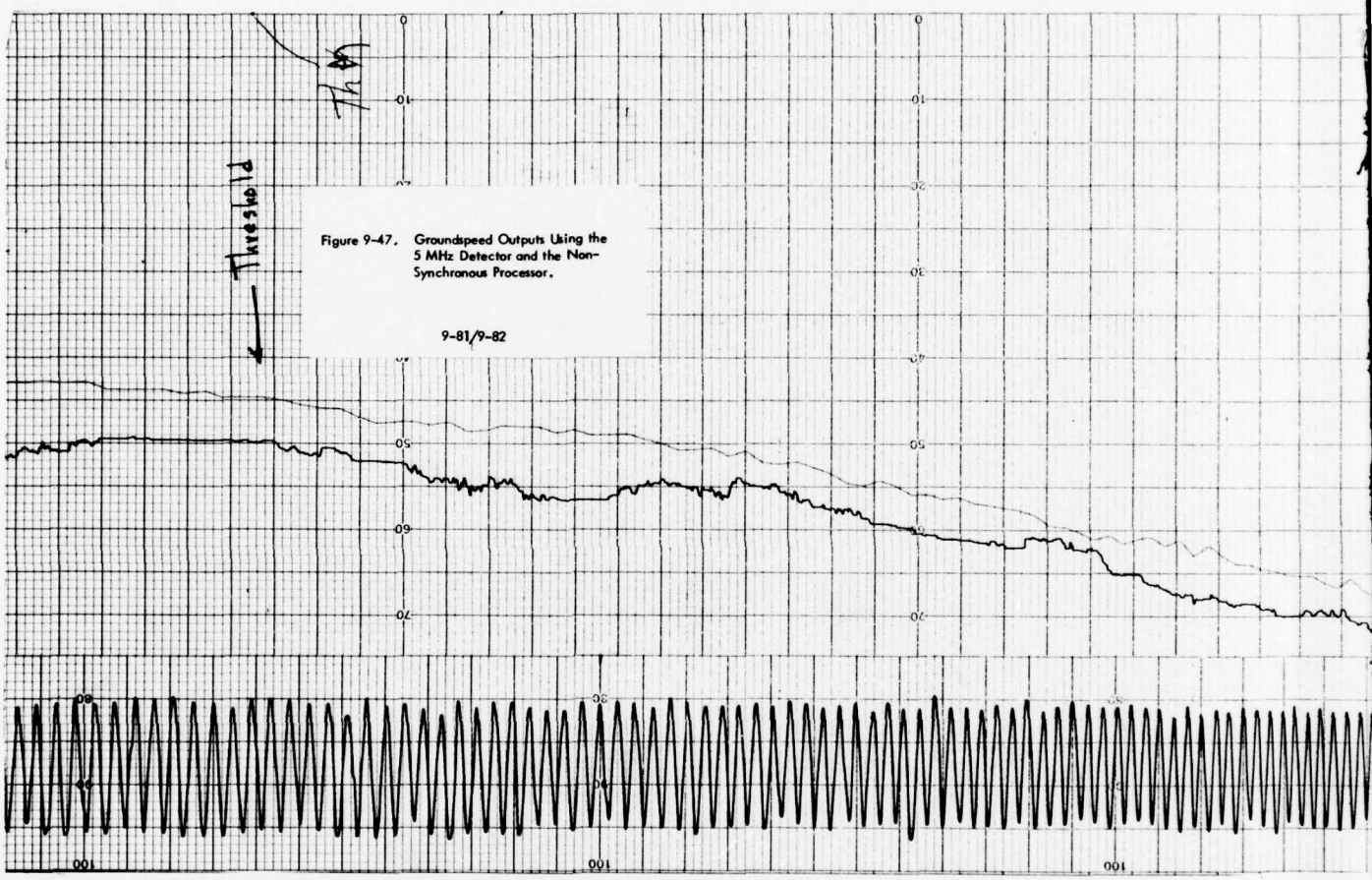

Figure 9-47. Groundspeed Outputs Using the 5 MHz Detector and the Non-Synchronous Processor.

9-81/9-82


Baseline - 5 mm

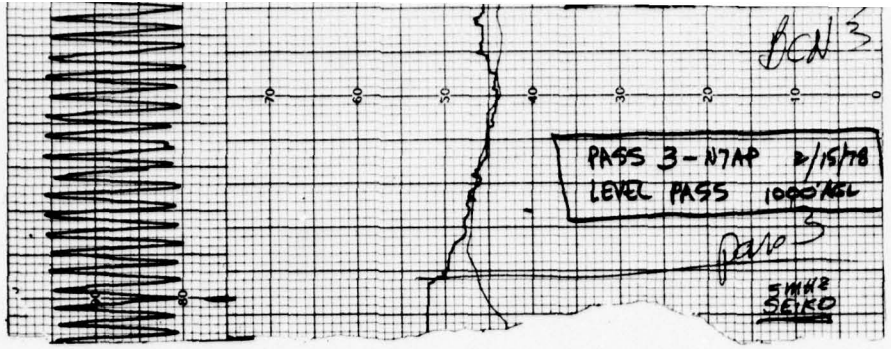
DCN 3
PASS 3 - N7AP 9/15/78
LEVEL PASS 1000'AGL
pass 3
SMKE
SEKO

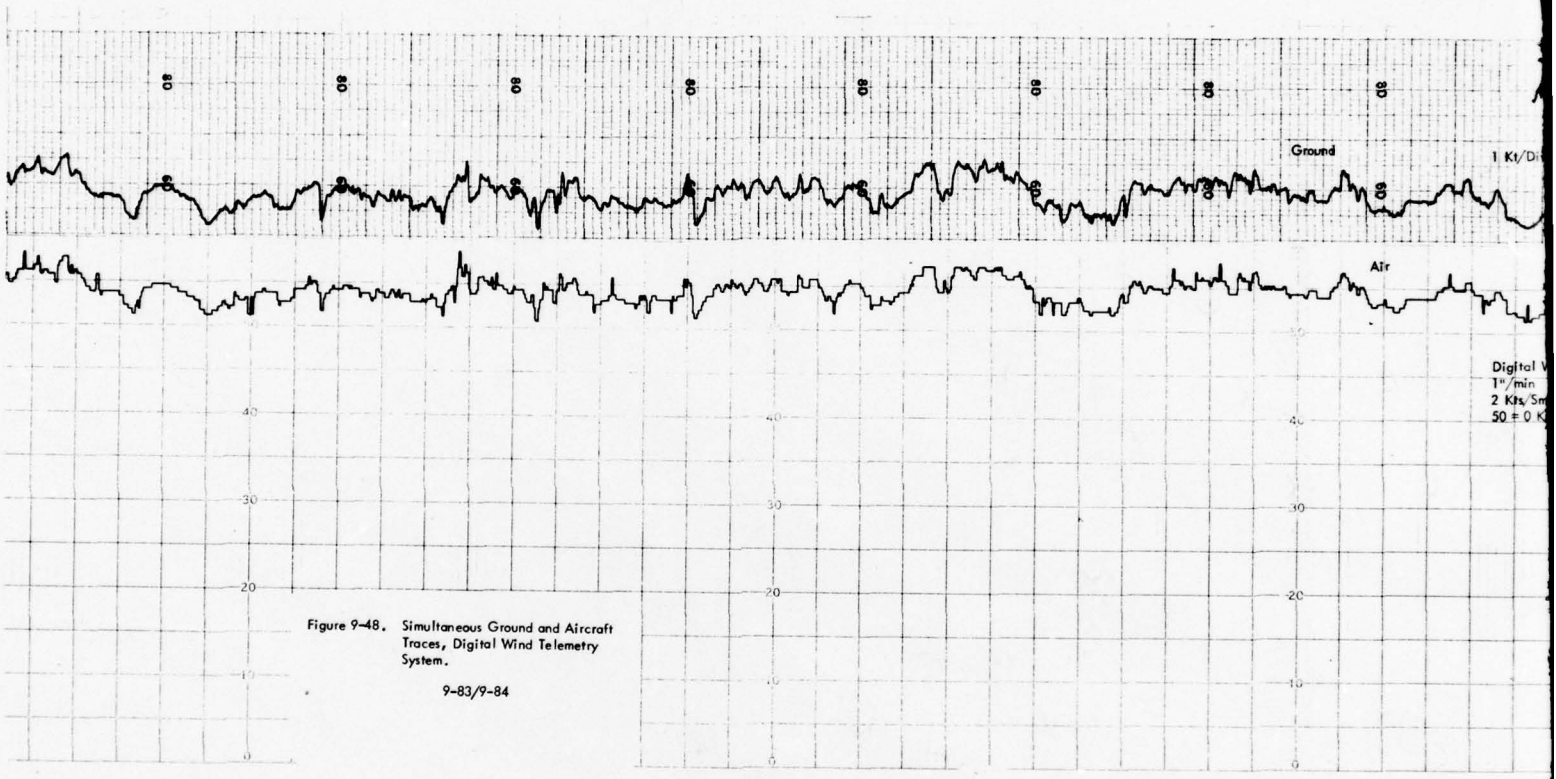

Figure 9-48. Simultaneous Ground and Aircraft Traces, Digital Wind Telemetry System.

9-83/9-84

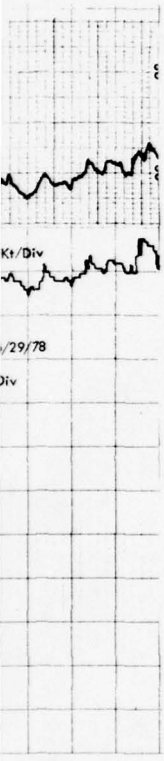

2

Figure 9-49 is a composite chart recording of simultaneous wind telemetry system and groundspeed system flight tests. As indicated on the chart the top trace is indicated airspeed (IAS), the second trace is groundspeed data, the third trace is wind telemetry output data and the bottom trace is the anemometer output recorded on the ground. The wind telemetry output closely follows the anemometer data and the groundspeed generally follows the airspeed data.

Figure 9-50 is a composite chart recording of simultaneous wind telemetry and groundspeed system flight tests during a pass when a large change in airspeed was made. The groundspeed output closely follows the shape of the airspeed chart while the wind telemetry output is not affected by these changes.

Figure 9-51 is a chart recording of the analog wind telemetry system output along with the anemometer output. Both of the analog systems closely follow the ground recording; however, the digital output is inverted. Both versions of the analog wind telemetry system provide an extremely accurate representation of the ground winds in the airplane.

G. Conclusions and Recommendations. The development and evaluation program has shown two feasible methods for obtaining a groundspeed analog on approach using the existing localizer carrier for information transfer. Additionally, touchdown zone wind information can simultaneously be made available to the aircraft.

Data obtained on the approach groundspeed systems showed resolutions to 1 Kt are possible. Absolute accuracy is estimated at ±1 Kt. Wind telemetry accuracy is ±1 Kt for both the analog and digital systems.

Usable distance depends upon localizer transmitter parameters. During flight evaluations at Ohio University, usable distances in excess of twenty miles were measured.

In the course of the work, an altemative groundspeed processor design was produced, but time did not allow prototyping and evaluation. It is felt that this promising avenue should be pursued; the 9 MHz multiplier detector should allow low-noise groundspeed data with high data rate.

New, low-cost atomic clock modules should be incorporated into the prototype system, at least, to facilitate evaluation.

Two wind telemetry systems were developed to show the range of capabilities and complexity of such systems. Both systems operated as expected, with the exception of an occasional data sync error in the digital system. A design fix for this error was produced, but contract schedules did not allow its implementation. Both systems evidence accuracy of ±1 Kt when transmitting the longitudinal wind component to the aircraft.

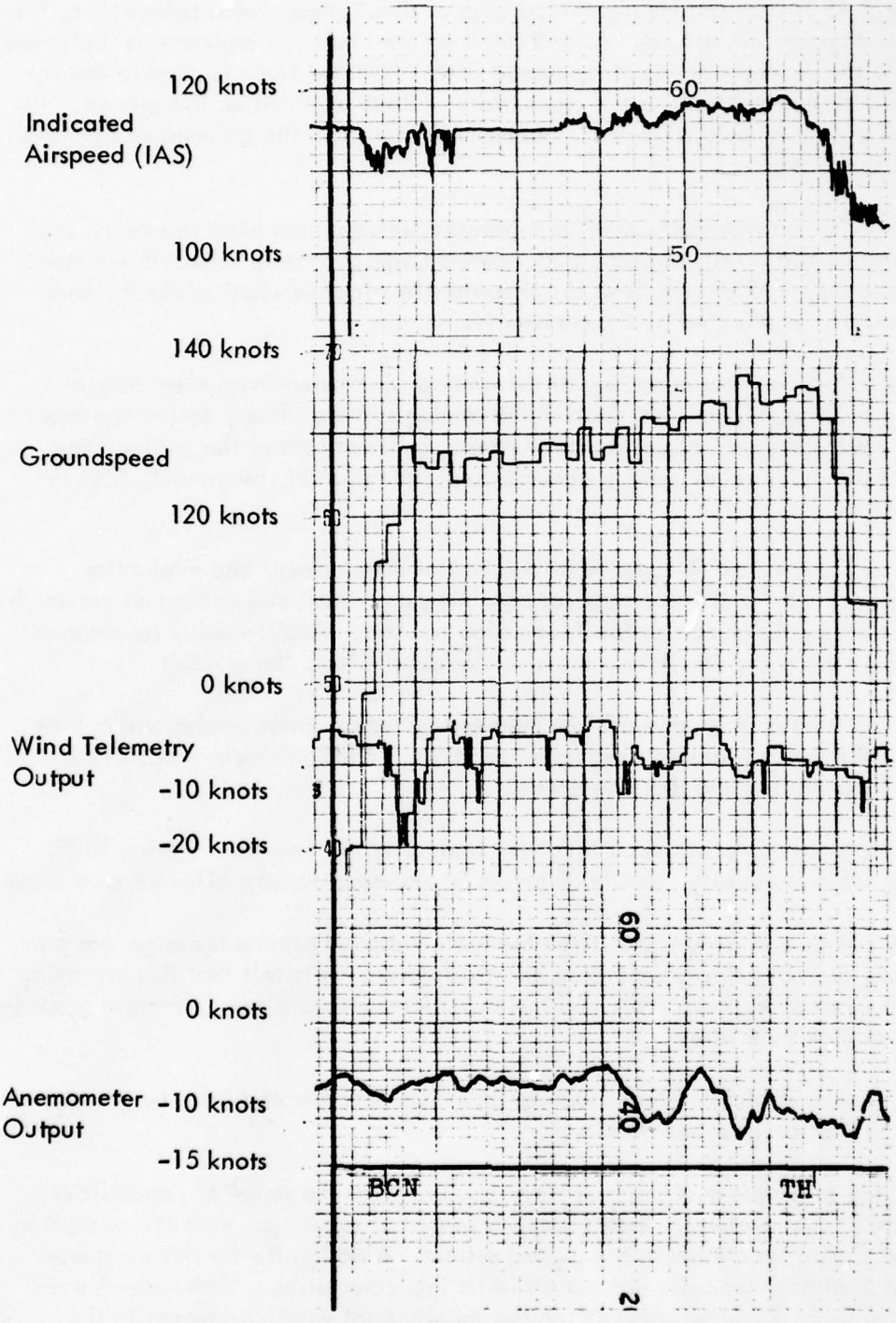

Figure 9-49. Simultaneous Wind Telemetry and Groundspeed Outputs.

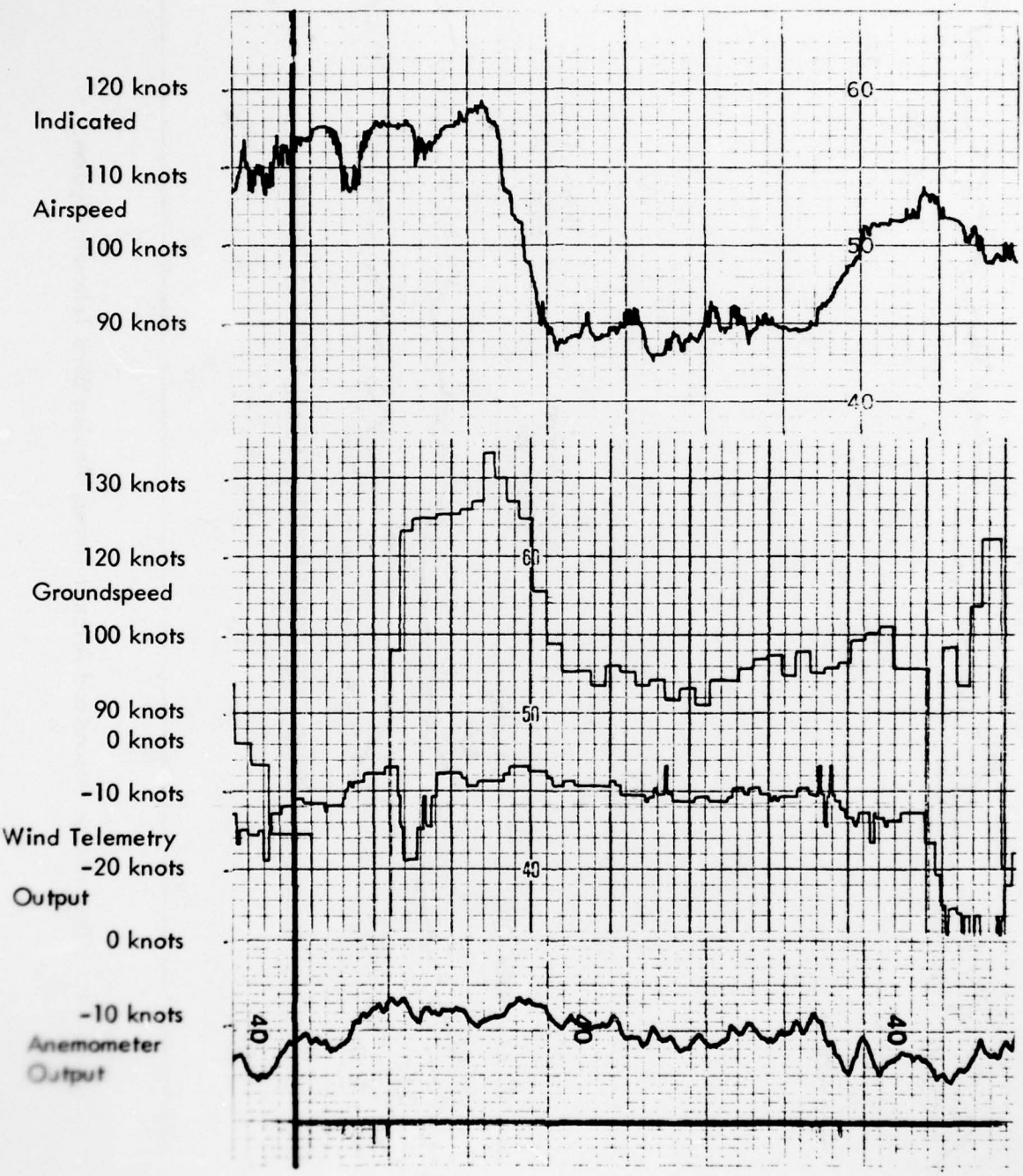

Figure 9-50. Simultaneous Wind Telemetry and Groundspeed Tests with a Change in Airspeed.

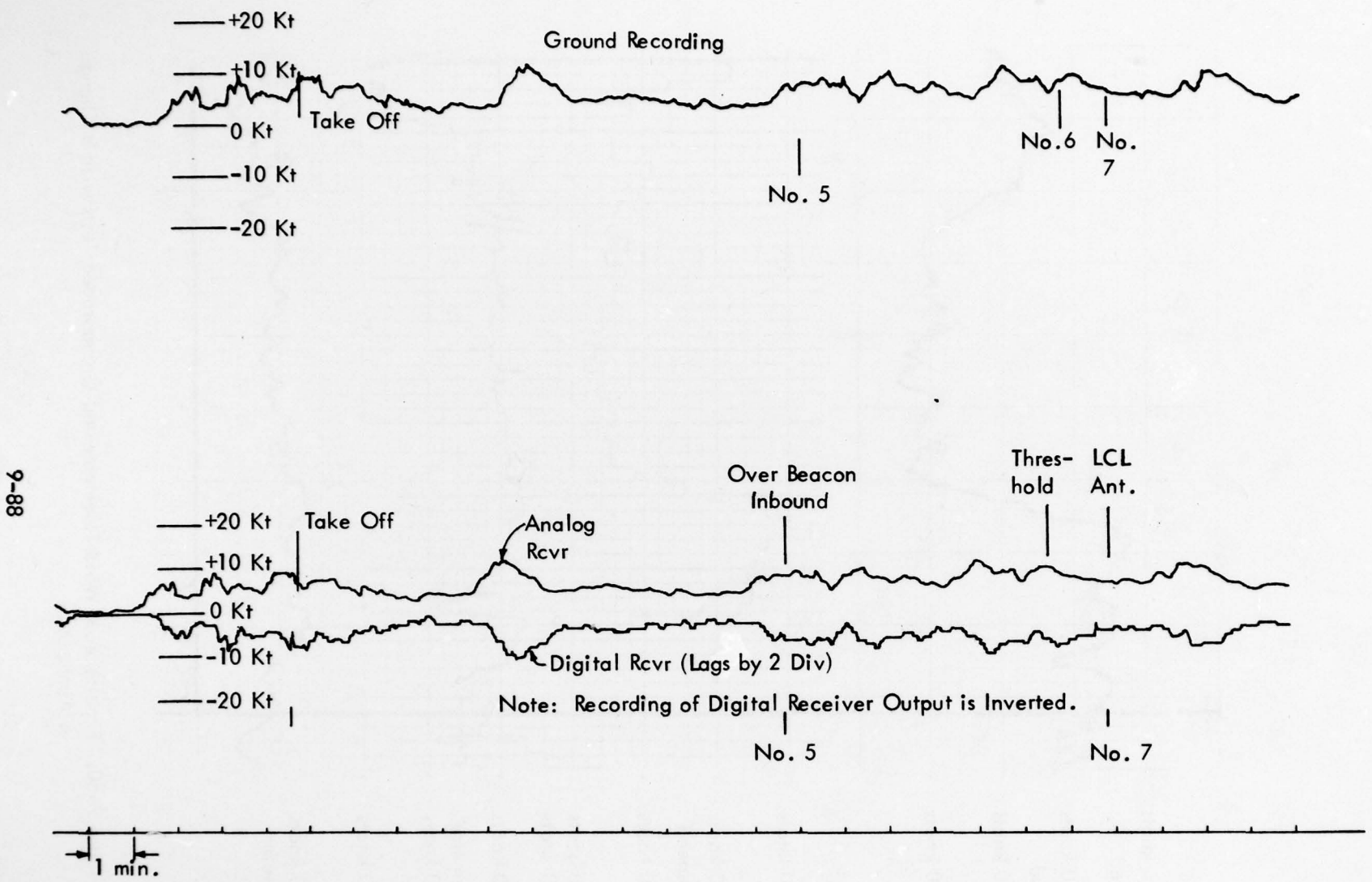

9-88

Figure 9-51. Simultaneous Ground and Aircraft Traces, Analog Wind Telemetry System.

The digital wind telemetry system, as prototyped, contains elements included for evaluation only, and contains a second set of tone encoders and decoders. These should be eliminated and a streamlined prototype produced for formal demonstration of the concept.

Although the digital wind telemetry system was demonstrated to operate as expected, the tone decoder circuitry is considered marginal. Time did not permit the replacement of this circuitry with an altemate design, similar to a data communication modem, which will clear up the occasional incorrect data sync event. This uncomplicated circuit change should be accomplished.

The groundspeed and wind telemetry systems should be packaged in standard avionics boxes for formal concept demonstration.

The demonstrations of approach groundspeed and touchdown zone wind telemetry indicate the feasibility of this alternate use for the ILS localizer. With relatively little additional effort, these systems can be demonstrated to provide the necessary flight data inputs for pilot aid in combatting the wind-shear problem.

X. PROCESSING OF ILS FLIGHT DATA

A. General. The Avionics Engineering Center has developed digital processing methods for ILS flight data, to support the light-aircraft digital data collection system in the Minilab Mark III. Digital format provides for flexible storage and utilization of ILS flight data in later comparisons with computer models of predicted ILS performance.

Two methods are contemplated in the final system. In the first, flight recordings are produced on analog charts and labeled as to run number, trace identification and chart scales. Upon return to the Avionics Engineering Center from a field site, each chart is rerun through the recorder with a dry pen, and an operator manually follows the recorded trace by means of a potentiometer voltage divider which drives the recorder pen. This voltage is digitized and recorded on digital magnetic tape. Using the Avionics Engineering Center remote-access computer facilities, the data is placed in formatted disk files and reviewed for reasonableness (placement of event marks, presence of communications radio interference, etc.). Each data point is then scaled to microamps and corrected by computer for Minilab receiver calibration curves, to take out any nonlinearities in the glide slope receivers at the higher CDI values.

Using theodolite event marks recorded on the chart during the flight and subsequently digitized along with the data, the theodolite angle is matched with Minilab summer amplifier output data for Pattern B runs. Pattern A data is processed using matched event marks between runs to correct for ground speed changes from one run to the next.

The disk resident data files are then converted to digital plotter format, and the Avionics Engineering Center remote-connected plotter produces graphs on preprinted axis forms. The results are presented as graphs of CDI versus theodolite angle for Pattern B approaches and as CDI versus distance in the case of Pattern A approaches.

For the second method, the manual graph digitizing step will be removed. The cassette from the Minilab data system will be fed directly to the central computer from a remote terminal, either in the field by telephone or from direct-connected terminals at the Avionics Engineering Center. Data formatting and scaling routines, and plot production, proceed as described above.

In this manner, the Avionics Engineering Center continues to develop a data processing capability for ILS evaluation data. The system will in the future accept digital data directly from the Minilab digital data collection module. Meanwhile, the one manual step of analog chart digitizing remains as an interface between flight data and report-quality graphs produced by computer.

1. Analog Strip-Chart to Digital Data Translator.

a. Introduction. The ability to digitize previously recorded analog strip-chart data in an efficient manner so that the data can be analyzed by a digital computer

can be a great aid in the data reduction task of flight test results. To this end, the Analog Strip-Chart to Digital Data Translator, Figure 10-1, was designed and constructed. To use the data translator, an analog strip chart that contains the previously recorded data is run through an analog recorder with an operator manually tracking the recorded data with a dry pen. The position of the manually-operated pen is sensed by the data translator and is encoded into a BCD format for recording on a digital magnetic tape recorder. Sample rates of the data translator are adjustable so that the operator can work the manual track at a comfortable speed that allows good resolution of the data conversion. The end result is a magnetic tape with all of the flight data encoded in a digital format that allows automatic data analysis on a digital computer.

b. Setup and Operating Procedure. The required additional equipment for use with the data translator is an analog strip-chart recorder of the type that the data was originally recorded on, a Kennedy Model 1600/360 Incremental Magnetic Tape Recorder, and a regulated reference supply (0-10 volts). The proper interconnection of the devices is shown in Figure 10-2.

To operate the data translator proceed as follows:

1. Connect the equipment as shown in Figure 10-2 but do not apply power to any of the equipment. Remove the connection between the recorder input and the data translator.

2. Load the analog strip-chart to be encoded onto the paperfeed reel of the analog recorder. Ensure that the pens of the recorder are dry or in the raised position so that the original data is not destroyed. Set zero reference on the recorder.

3. Ensure that the RECORD switch of the data translator is in the OFF position and turn the translator POWER switch to ON.

4. Load the Kennedy Incremental Magnetic Tape Recorder as per the instructions in its operating manual.

5. Set the reference supply to approximately 5 volts and turn it on.

6. Rotate the REF VOLT potentiometer of the data translator fully counter-clockwise and adjust the reference supply so that the DPM reads 0.999. Care should be taken so that the DPM does not overflow.

7. Connect strip-chart recorder input to RECORDER output of the data translator and adjust the gain of the recorder as required.

8. Select a comfortable speed on the strip-chart recorder that is commensurate with the dynamic characteristics of the data being translated. Based on this selected value, the sampling rate of the translator is chosen. This sampling rate should be no less than one sample per second of real time data. These values must later be supplied to the computer software for meaningful data reduction. Alternatively, samples may be

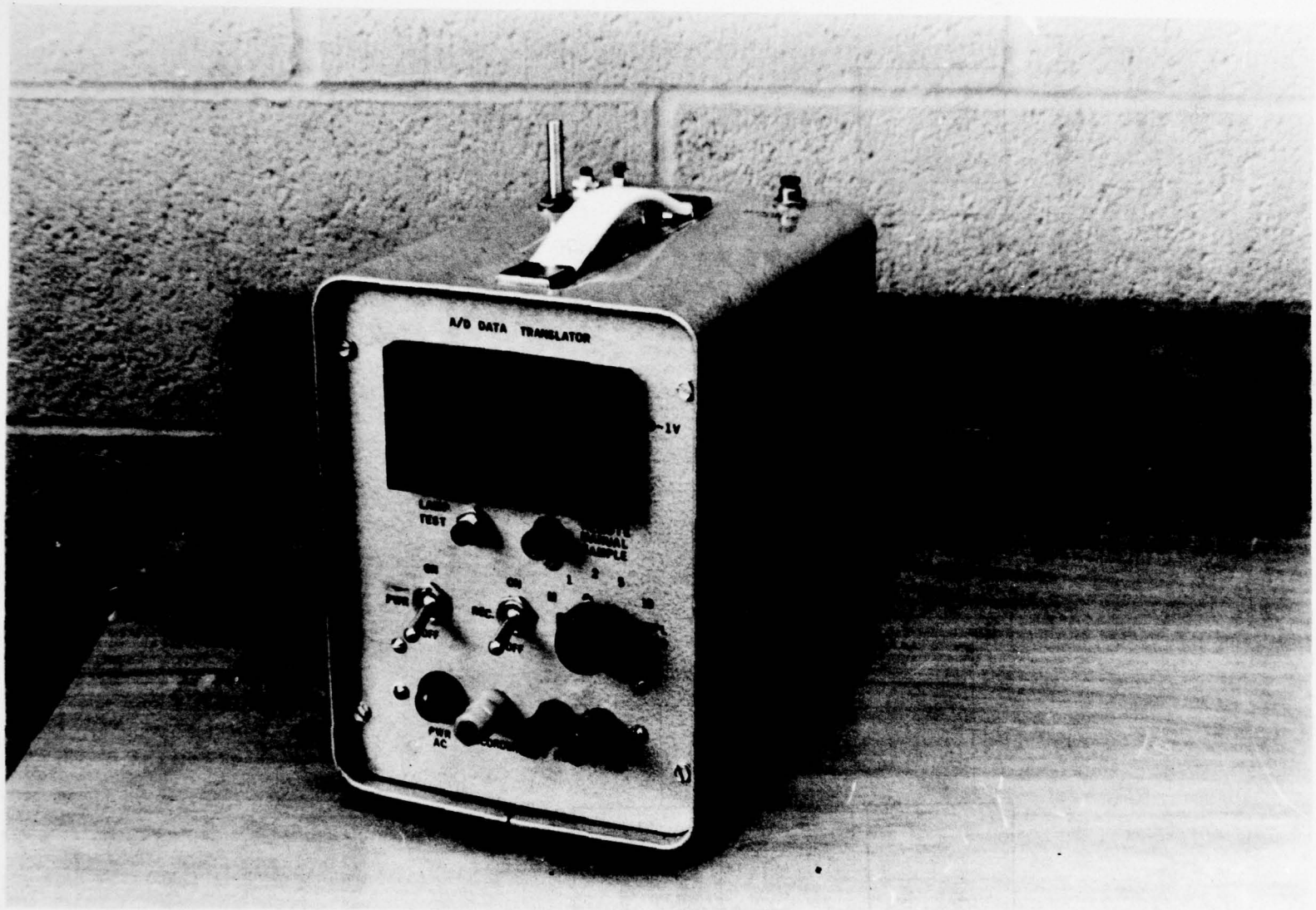

Figure 10-1. Analog Strip-Chart to Digital Data Translator.

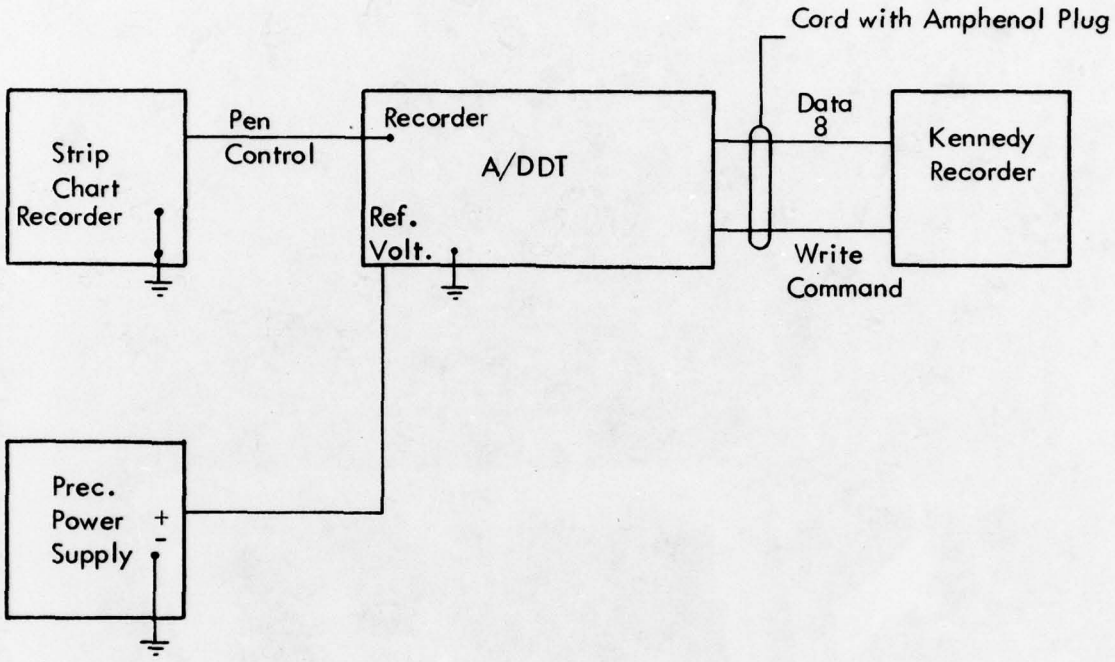

Figure 10-2. Data Translator Operational Setup.

taken manually, either locally with the button on top of the Data Translator, or remotely using a switch and plug combination as shown in Figure 10-3. In this case, an accurate record of each sample point is imperative.

9. To start recording, move the RECORD switch to ON and use the REF VOLT potentiometer to follow the strip-chart data with the dry pen. Three different event marks can be recorded along with the data. Pushing EVENT 1 will record a binary one on the data tape and pushing EVENT 2 will record a binary two on the tape. If both event buttons are pushed simultaneously, a binary three will be recorded. Each time an event mark is recorded, the A/DDT will emit a soft "beep". A listing of all events, in order, must be supplied to the software during data reduction.

10. To end the recording, turn the RECORD switch to OFF and insert a file gap on the magnetic tape using the Kennedy's front panel control. The recorded data is now ready for computer reduction.

c. Circuit Description. The circuit schematic for the data translator is shown in Figures 10-4 and 10-5. The main function of the unit is an analog-to-digital conversion which is performed by a Datel DM-3000 digital panel meter. Besides providing a useful display for the data translator, the DM-3000 also provides the encoded information in the form of a TTL compatible BCD output. For simplicity, only one BCD digit of the DPM output is recorded in one byte of the Kennedy recorder. The order that the digits are written is: 1's, 10's, 100's, followed by the event mark, if any. Since the A/D function of the unit is provided by the DPM, the remaining circuit is used to gate the required data to the input of the Kennedy recorder and then provide a write command to the recorder based on the sample rate selected.

In Figure 10-4, IC1-1 is a timer that is used to set the sampling rate of the translator in conjunction with the RC time constant selected by the SAMPLE FREQ switch (S3). Rates of 1,2,5, and 10 samples per second are selectable in addition to manual sampling. Section A of the SAMPLE FREQ switch selects either the timer output or the Manual Sample circuit output and sends it to IC1-5, a 74121 one-shot. Each time the one-shot senses a falling edge at its input, it outputs a positive pulse of about 102 msec. These pulses serve as start pulses for the DPM sampling circuitry.

Once the A/D conversion is completed, the E.O.C. output of the DPM goes low (see Figure 10-5. This signal controls the write pulses to the Kennedy recorder and multiplexes the output of the DPM to the input of the recorder at the appropriate time. When the E.O.C. signal goes low, the trigger input to the monostable flip-flop of IC1-4 goes high, causing the output of IC1-4 to go high for approximately 63 msec. This in turn enables the astable multivibrator IC1-6. During the 63 msec that IC1-6 is enabled, four output pulses occur. These four pulses are sent to the Kennedy recorder as write commands to cause four bytes to be written on the magnetic tape. The pulses are also used to control the digit multiplexing required to the input of the Kennedy recorder. The number of write pulses generated is counted by a two stage binary counter, IC2-3. The value of the counter output is used to control the digit multiplexers, IC2-1 and IC2-4. A timing diagram is shown in Figure 10-6.

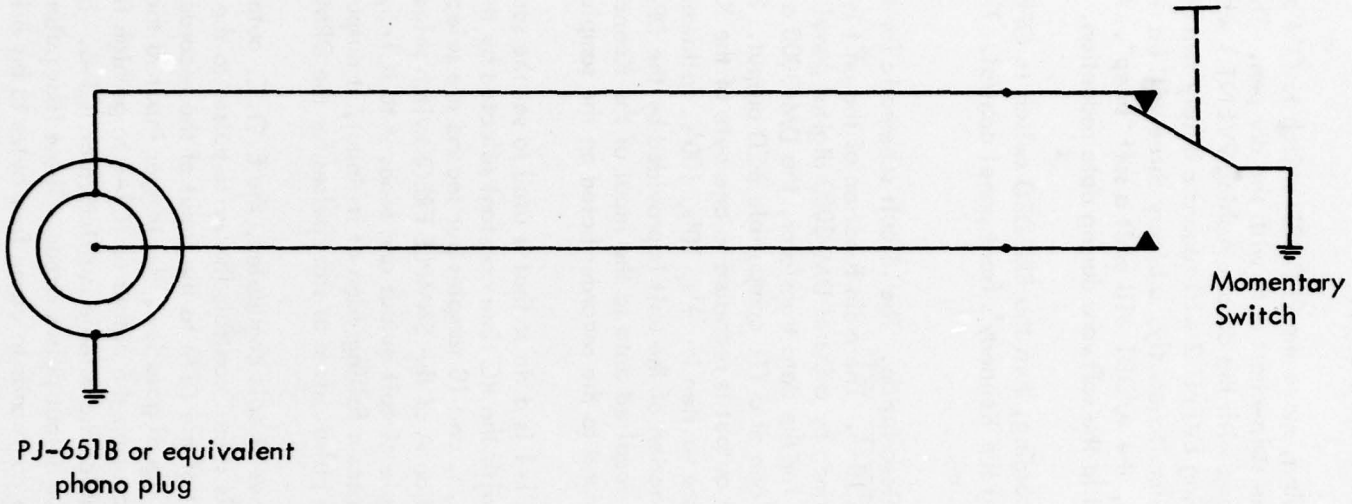

Figure 10-3. Remote Manual Sample Control Switch for Analog/Digital Data Translator.

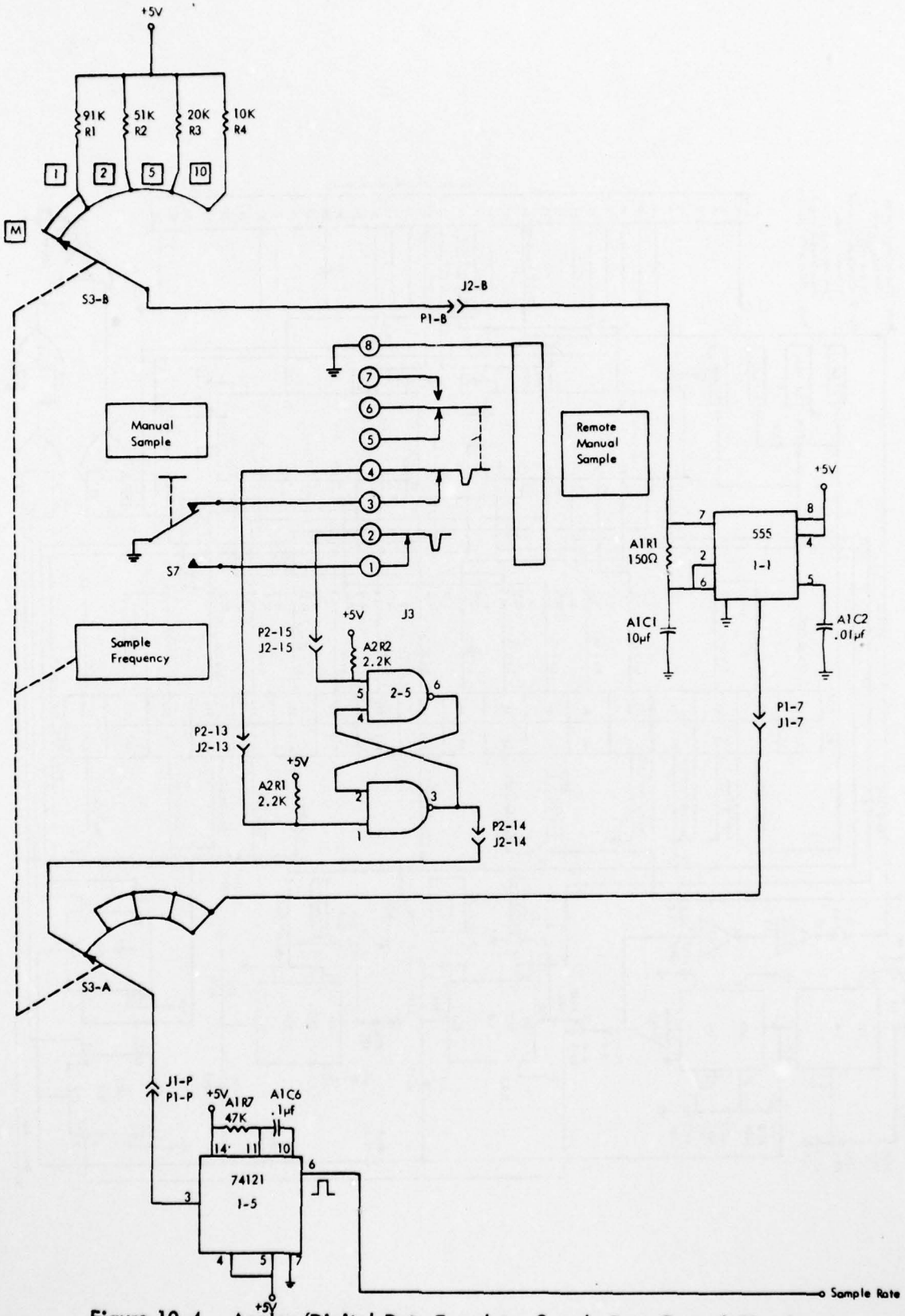

Figure 10-4. Analog/Digital Data Translator Sample Rate Control Circuit.

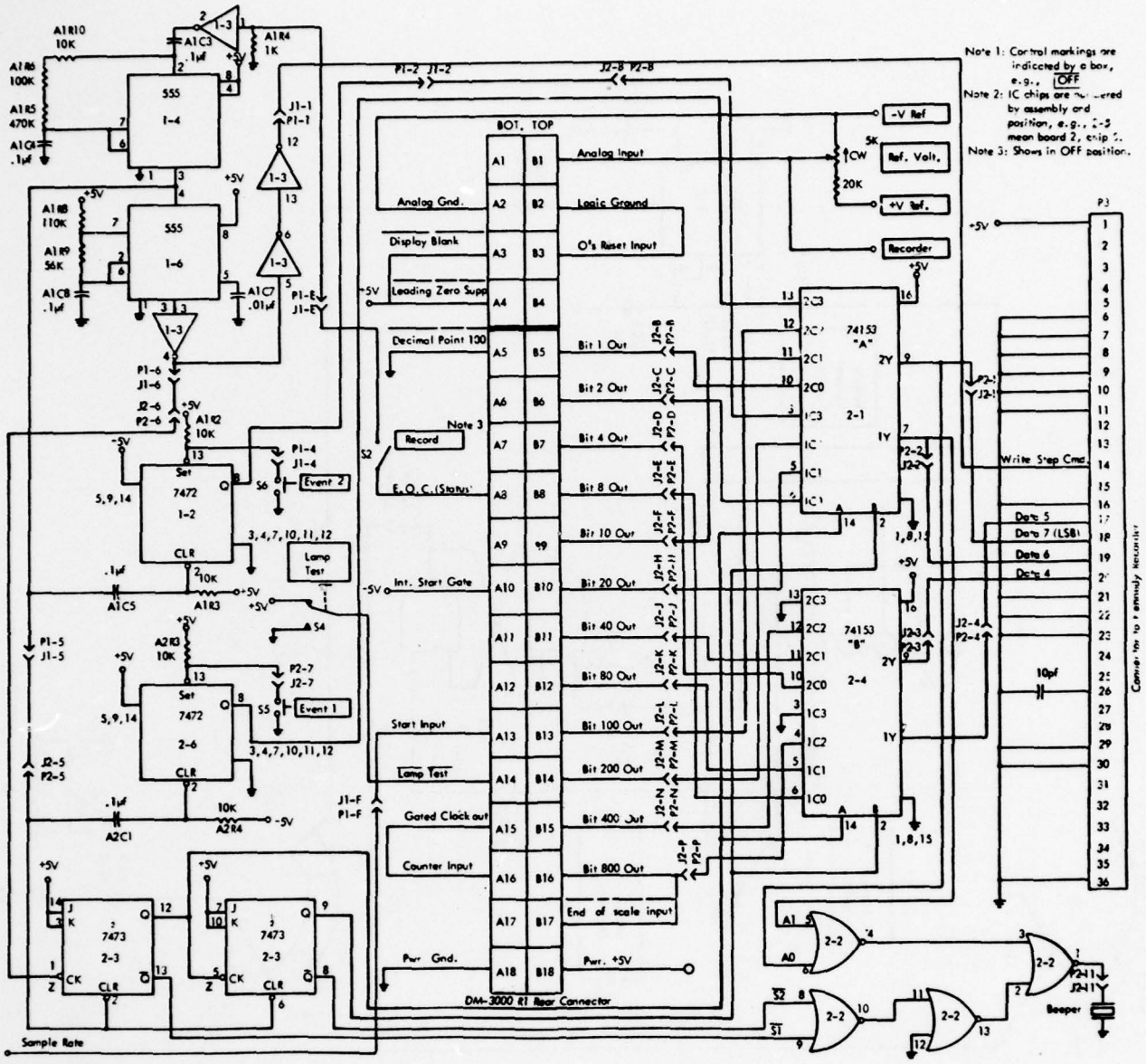

Figure 10-5. Analog/Digital Data Translator Schematic.

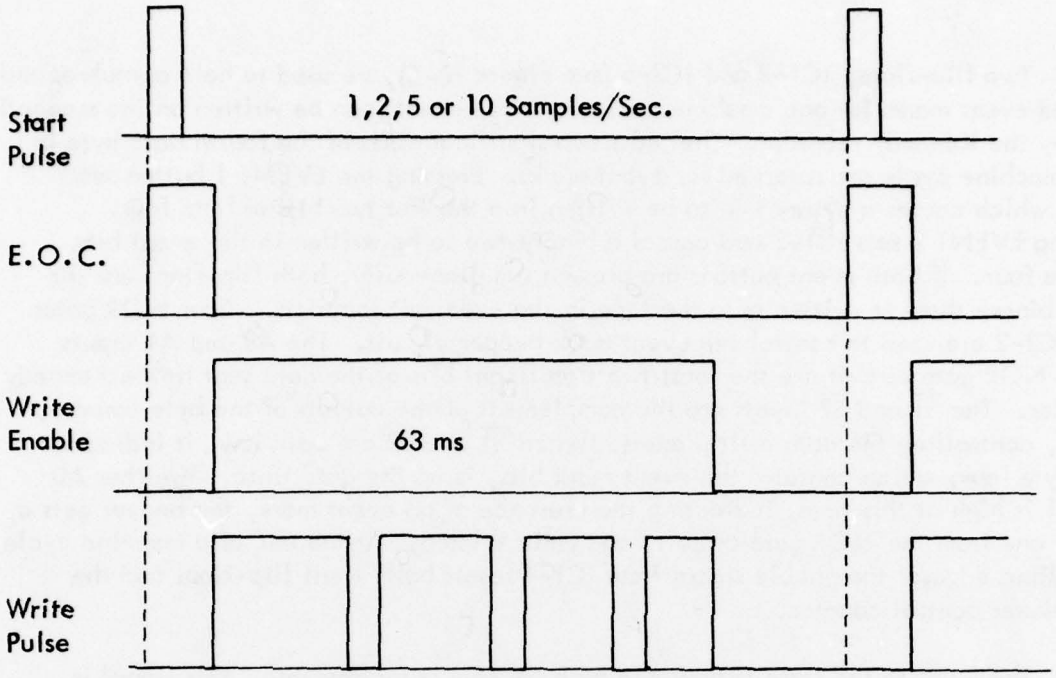

Figure 10-6. Timing Diagram.

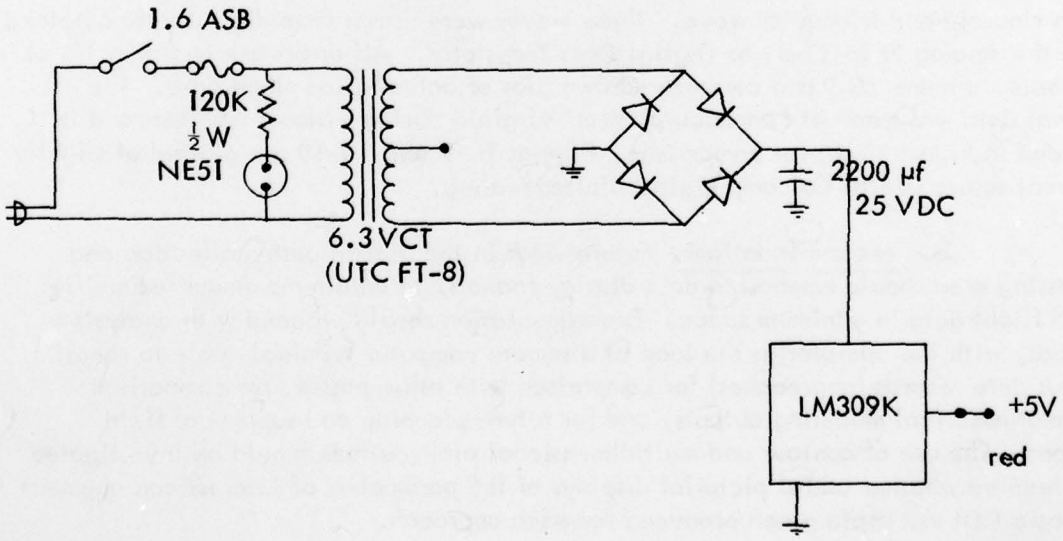

Figure 10-7. Data Translator Power Supply.

Two flip-flops, IC1-2 and IC2-6 (see Figure 10-5), are used to hold asynchronously entered event marks for one machine cycle until the events can be written on the magnetic tape by the Kennedy recorder. The least two significant bits of the fourth data byte in each machine cycle are reserved for event marks. Pressing the EVENT 1 button sets IC2-6 which causes a binary one to be written into the last two bits of byte four. Pressing EVENT 2 sets IC1-2 and causes a binary two to be written in the event bits of byte four. If both event buttons are pressed simultaneously, both flip-flops are set and a binary three is written onto the tape in the event bit location. Four NOR gates from IC2-2 are used to control the event mark beeper circuit. The A0 and A1 inputs to the NOR gate circuit are the least two significant bits of the data sent to the Kennedy recorder. The $\overline{S1}$ and $\overline{S2}$ inputs are the complement of the outputs of the byte counter, IC2-3, controlling the data multiplexers. When $\overline{S1}$ and $\overline{S2}$ are both low, it indicates that byte four, which contains the event mark bits, is on the data lines. If either A0 and A1 is high at this time, indicating the presence of an event mark, the beeper gets a binary one from the NOR gate circuit, and emits a beep. At the end of a machine cycle, the falling edge of the enable signal from IC1-4 resets both event flip-flops and the multiplexer control counter.

The input to the DPM is provided by a 5K ohm potentiometer. This signal is also the input to the analog strip-chart recorder.

A standard 309 voltage regulator is used to provide the power supply for the unit. A schematic of the complete power supply is shown in Figure 10-7.

d. Sample Data Sets. Three sample data conversions are supplied in Figures 10-8 and 9 to indicate system performance. Figure 10-8 shows a computer-drawn sinusoid and triangular wave. These waves were drawn from digital data obtained using the Analog Strip-Chart to Digital Data Translator. All errors are less than 1% of full scale. Figure 10-9 is a computer-drawn plot of actual glide slope data. The original data was made at Parkersburg, West Virginia during Video ARTT tests and is included in Figure 10-10 for comparison. Figures 10-9 and 10-10 are plotted at slightly different scales due to Calcomp digital plotter scaling.

e. Recommendations. Future work in the digital data-collection and processing area should emphasize data display formats, to obtain maximum readability of ILS flight data in minimum space. Experimentation should proceed with analysis methods, with the operator in the loop at a remote computer terminal, able to recall various data records (approaches) for comparison with other passes, for comparison with mathematical modeling outputs, and for future planning and support of field missions. The use of contour and multidimensional plot routines should be investigated to determine whether useful pictorial displays of ILS parameters of interest can augment the basic CDI vs. angle graph produced for each approach.

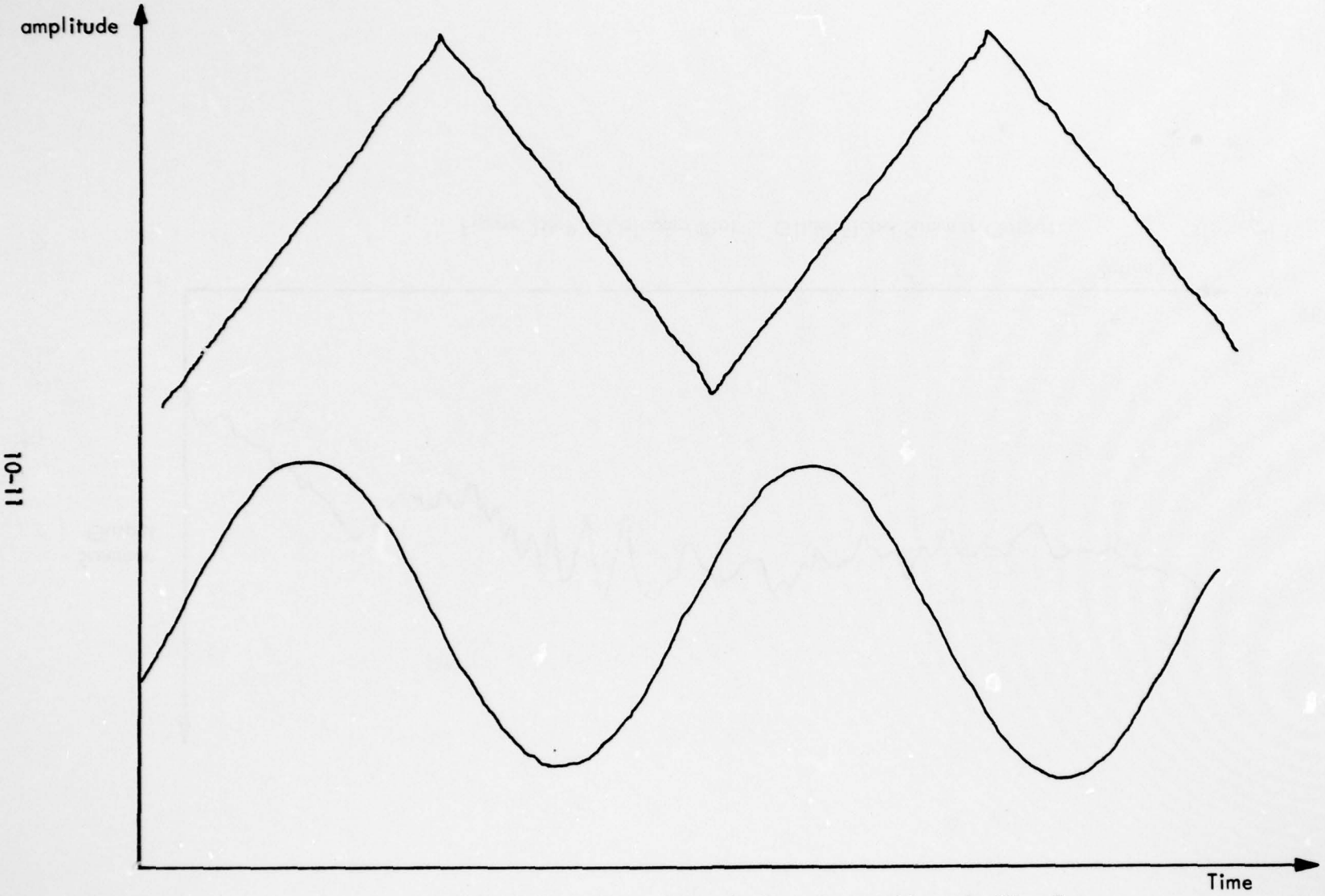

Figure 10-8. Calcomp Plot of Sample Sinusoid and Triangular Waveforms.

AD-A074 425 OHIO UNIV ATHENS DEPT OF ELECTRICAL ENGINEERING F/G 17/7
IN-SERVICE IMPROVEMENTS AND MODERNIZATION OF ALL COMPONENTS OF --ETC(U)
JUL 78 DOT-FA75WA-3549
UNCLASSIFIED EER-35-1 FAA-RD-78-112-1 NL

8 OF 8
AD A074425

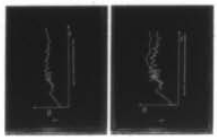

END
DATE FILMED
11-79
DDC

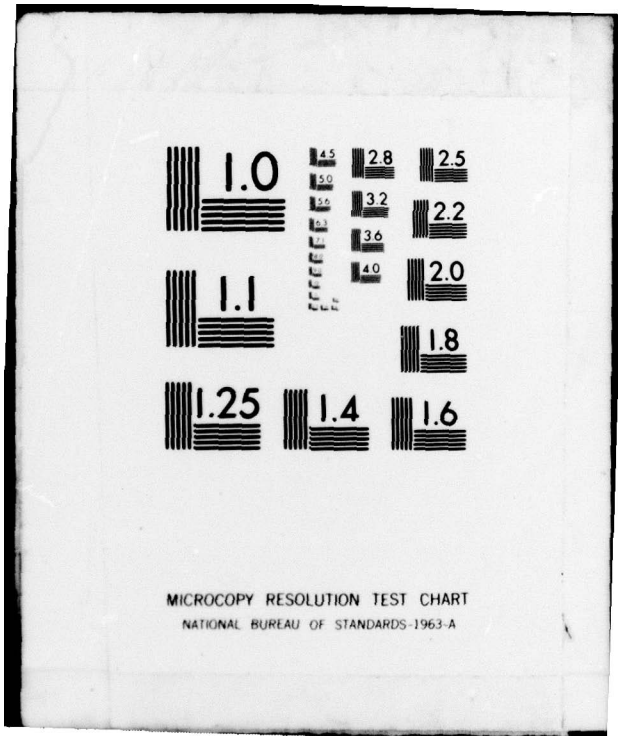
1.0
1.1
1.25
1.4
1.6
1.8
2.0
2.2
2.5
2.8
3.2
3.6
4.0
4.5
5.0
5.6
MICROCOPY RESOLUTION TEST CHART
NATIONAL BUREAU OF STANDARDS-1963-A

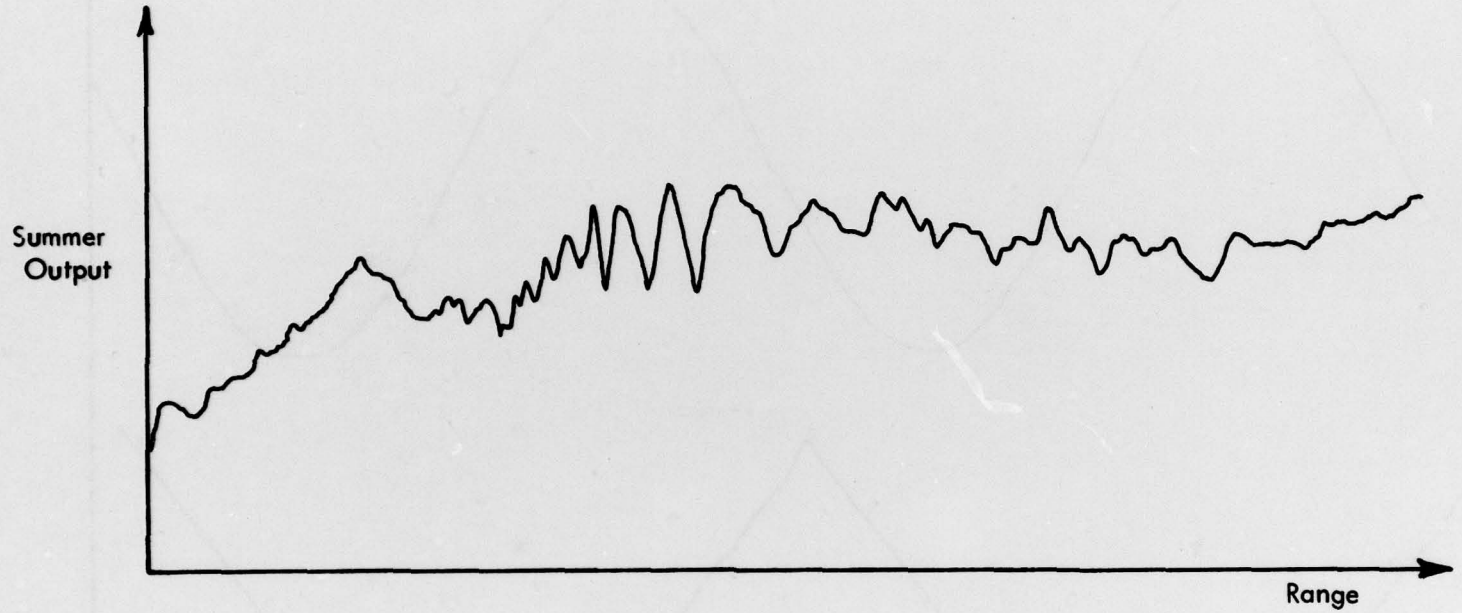

Figure 10-9. Calcomp Plot of Glide Slope Summer Output.

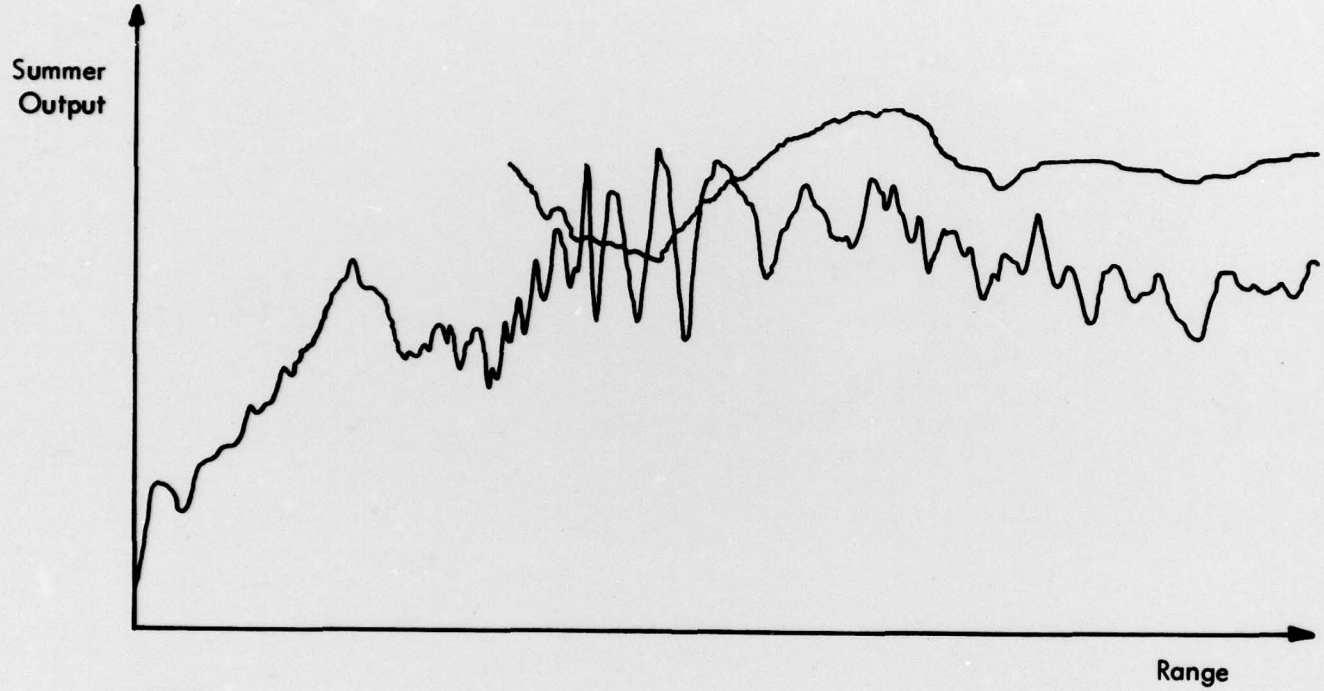

Figure 10-10. Actual Glide Slope Data Used for Data Conversion Comparison.